

THE JOURNAL of the Acoustical Society of America

Vol. 102, No. 4

October 1997

MEETING PROGRAM SUMMARY**SAN DIEGO MEETING****1–5 DECEMBER 1997**

(see pp. 1953–1954)

ACOUSTICAL NEWS—USA

1913

USA Meetings Calendar

1918

ACOUSTICAL NEWS—INTERNATIONAL

1921

International Meetings Calendar

1921

REVIEWS OF ACOUSTICAL PATENTS

1923

SELECTED RESEARCH ARTICLE [10]

The dynamic coupling between piezoceramic actuators and a beam

M. J. Brennan, S. J. Elliott, R. J. Pinnington

1931

The influence of different timbre attributes on the perceptual segregation of complex-tone sequences

Punita G. Singh, Albert S. Bregman

1943

GENERAL LINEAR ACOUSTICS [20]

The forward projection of harmonic pressure fields using the generalized internal source density method

Peter R. Stepanishen

1955

A method for acoustic scattering by slender bodies. I. Theory and verification

Zhen Ye, Emile Hoskinson, Richard K. Dewey, Li Ding, David M. Farmer

1964

A method for acoustic scattering by slender bodies. II. Comparison with laboratory measurements

Li Ding, Zhen Ye

1977

Acoustical characterization of absorbing porous materials through transmission measurements in a free field

Celse K. Amédin, Yvan Champoux, Alain Berry

1982

Dynamic compressibility of air in porous structures at audible frequencies

Denis Lafarge, Pavel Lemarinier, Jean F. Allard, Viggo Tarnow

1995

The usage of standard finite element codes for computation of dispersion relations in materials with periodic microstructure

M. Åberg, P. Gudmundson

2007

Acoustical properties of irregular and fractal cavities

B. Sapoval, O. Haeberlé, S. Russ

2014

Helmholtz equation—least-squares method for reconstructing the acoustic pressure field

Zhaoxi Wang, Sean F. Wu

2020

Measurements of newly defined intensimetric quantities and their physical interpretation

Domenico Stanzial, Nicola Prodi

2033

AEROACOUSTICS, ATMOSPHERIC SOUND [28]

Analytical solutions for outdoor sound propagation in the presence of wind

Kai Ming Li, Qiang Wang

2040

(Continued)

CONTENTS—Continued from preceding page

The sound field of an arbitrarily oriented quadrupole near ground surfaces	Kai Ming Li, Shahram Taherzadeh	2050
UNDERWATER SOUND [30]		
Further evidence that the sound-speed algorithm of Del Grosso is more accurate than that of Chen and Millero	Christopher S. Meinen, D. Randolph Watts	2058
A comparison of quasi-continuous wave and broadband travel time techniques in the prediction of long-range reverberation	Kevin B. Smith, Erick B. Cushman	2063
The perfectly matched layer for acoustic waves in absorptive media	Qing-Huo Liu, Jianping Tao	2072
Modulations of detectable pulse response time spread in shallow water resulting from a combination of sound-speed variability and bottom loss	Charles L. Monjo, Hien Nguyen, Harry A. Deferrari	2083
Far-field acoustic holography onto cylindrical surfaces using pressure measured on semicircles	Andrew N. Norris	2098
ULTRASONICS, QUANTUM ACOUSTICS, AND PHYSICAL EFFECTS OF SOUND [35]		
Stoneley wave excitation by a bounded beam at the down-step of a thin layer on a substrate	R. Briers, O. Leroy, G. Shkerdin	2108
Spectral statistics in damped systems: Diffuse field decay curvature for materials characterization	John Burkhardt	2113
A liquid wedge as generating technique for Lamb and Rayleigh waves	R. Briers, O. Leroy, G. Shkerdin	2117
Finite difference predictions of P - SV wave propagation inside submerged solids. I. Liquid–solid interface conditions	Girish Dahake, S. M. Gracewski	2125
Finite difference predictions of P - SV wave propagation inside submerged solids. II. Effect of geometry	Girish Dahake, S. M. Gracewski	2138
Solid–liquid interface reconstructions from ultrasonic time-of-flight projection data	Douglas T. Queheillalt, Haydn N. G. Wadley	2146
STRUCTURAL ACOUSTICS AND VIBRATION [40]		
A modeling technique for active control design studies with application to spacecraft microvibrations	G. S. Aglietti, S. B. Gabriel, R. S. Langley, E. Rogers	2158
Vibration of truss structures	Joseph E. Bondaryk	2167
Transmission of sound across a trusslike periodic panel; 2-D analysis	Michael El-Raheb, Paul Wagner	2176
NOISE: ITS EFFECTS AND CONTROL [50]		
Implementation of an active headset by using the H_∞ robust control theory	Mingsian Bai, Dunjay Lee	2184
Individual differences in susceptibility to the “irrelevant speech effect”	Wolfgang Ellermeier, Karin Zimmer	2191
ARCHITECTURAL ACOUSTICS [55]		
Use of pseudo-random sequences and a single microphone to measure surface impedance at oblique incidence	Jing-Fang Li, Murray Hodgson	2200
PHYSIOLOGICAL ACOUSTICS [64]		
A time domain binaural model based on spatial feature extraction for the head-related transfer function	Zhenyang Wu, Francis H. Y. Chan, F. K. Lam, Joseph C. K. Chan	2211
Influence of contralateral noise on distortion product latency in humans: Is the medial olivocochlear efferent system involved?	Anne Lise Giraud, Jocelyne Wable, André Chays, Lionel Collet, Sylviane Chéry-Croze	2219
Effects of electrode configuration on psychophysical strength-duration functions for single biphasic electrical stimuli in cats	David W. Smith, Charles C. Finley	2228
Model calculations of the effects of wide-band inhibitors in the dorsal cochlear nucleus	Michael C. Reed, Jacob J. Blum	2238

CONTENTS—Continued from preceding page

Two-tone rate suppression boundaries of cochlear ganglion neurons in chickens following acoustic trauma	Lin Chen, Patricia G. Trautwein, Nicholas Powers, Richard J. Salvi	2245
PSYCHOLOGICAL ACOUSTICS [66]		
Multidimensional scaling of complex sounds by school-aged children and adults	Prudence Allen, Cheryl-Ann Bond	2255
Discrimination of changes in the spectral shape of noise bands	Niek J. Versfeld	2264
Coherence masking protection in brief noise complexes: Effects of temporal patterns	Peter C. Gordon	2276
The role of spread excitation and suppression in simultaneous masking	Brian C. J. Moore, Deborah A. Vickers	2284
A probe-signal study of auditory discrimination of complex tones	Nicholas I. Hill, Peter J. Bailey, Philip Hodgson	2291
Identification of multidimensional stimuli containing speech cues and the effects of training	Laurel A. Christensen, Larry E. Humes	2297
Auditory profile analysis: Is there perceptual constancy for spectral shape for stimuli roved in frequency?	Hedwig Gockel, Hans Colonius	2311
Perceptual segregation of a harmonic from a vowel by interaural time difference and frequency proximity	C. J. Darwin, R. W. Hukin	2316
The effect of head rotations on vertical plane sound localization	Stephen Perrett, William Noble	2325
Dichotic beats of mistuned consonances	M. Patrick Feeney	2333
Auditory localization, detection of spatial separateness, and speech hearing in noise by hearing impaired listeners	William Noble, Denis Byrne, Kim Ter-Horst	2343
SPEECH PRODUCTION [70]		
The development of speech adaptation to an artificial palate	Shari R. Baum, David H. McFarland	2353
Acoustic correlates of English and French nasalized vowels	Marilyn Y. Chen	2360
Correlation dimension of electroglottographic data from healthy and pathologic subjects	Alison Behrman, R. J. Baken	2371
Locus equations in the light of articulatory modeling	Samir Chennoukh, René Carré, Björn Lindblom	2380
SPEECH PERCEPTION [71]		
Timing of pitch movements and accentuation of syllables in Dutch	Dik J. Hermes	2390
Speech intelligibility as a function of the number of channels of stimulation for signal processors using sine-wave and noise-band outputs	Michael F. Dorman, Philipos C. Loizou, Dawne Rainey	2403
Development and evaluation of a German sentence test for objective and subjective speech intelligibility assessment	Birger Kollmeier, Matthias Wesselkamp	2412
MUSIC AND MUSICAL INSTRUMENTS [75]		
Specifying spectra for musical scales	William A. Sethares	2422
Optimal undercuts for the tuning of percussive beams	J. Petrolito, K. A. Legge	2432
LETTERS TO THE EDITOR		
Green's tensor function for Lamb's problem: The general anisotropic case [20]	Martin Spies	2438
Leaky-Rayleigh wave detection at air-solid interfaces by optical heterodyne interferometry [20]	Michel de Billy, Laszlo Adler, Gerard Quentin	2442
Comment on "Modal analysis of a structure in a compressible fluid using a finite element/boundary element approach" [J. Acoust. Soc. Am. 99, 1949–1957 (1996)] [20]	Ardhendu G. Pathak, Purnima Jaliha	2445

CONTENTS—Continued from preceding page

Response to “Comment on ‘Modal analysis of a structure in a compressible fluid using a finite element/boundary element approach’ ” [J. Acoust. Soc. Am. 102, 2445–2447 (1997)] [20]	M. D. McCollum, Clementina M. Siders	2448
ERRATA		
Erratum: “Reflection and refraction of longitudinal wave at an interface between two micropolar elastic solids in welded contact” [J. Acoust. Soc. Am. 97, 822–830 (1995)]	S. K. Tomar, M. L. Gogna	2452
TECHNICAL NOTES AND RESEARCH BRIEFS		
Numerical estimation of the influence of ground impedance on sound propagation	L. Rahovich, M. Slonim, Ts. Zlotnick	2453
The influence of the oxygen mask on long-time spectra of continuous speech	Milan Vojnović, Miomir Mijić	2456
CUMULATIVE AUTHOR INDEX		2459

NOTES CONCERNING ARTICLE ABSTRACTS

1. The number following the abstract copyright notice is a Publisher Item Identifier (PII) code that provides a unique and concise identification of each individual published document. This PII number should be included in all document delivery requests for copies of the article.
2. PACS numbers are for subject classification and indexing. See June and December issues for detailed listing of acoustical classes and subclasses.
3. The initials in brackets following the PACS numbers are the initials of the JASA Associate Editor who accepted the paper for publication.

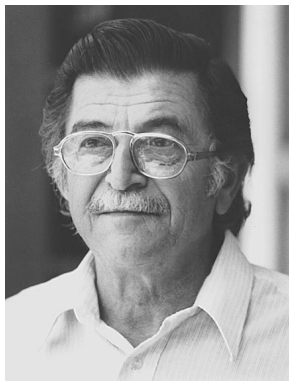
Document Delivery: Copies of articles can be ordered for \$15 per copy from the AIP/Member Society document delivery service “Articles in Physics,” 75 Varick Street, New York, NY 10013; Fax: 212-301-4060; Telephone: 800-480-PHYS (800-480-7497) (in U.S. and Canada), or 212-301-4000; E-mail: articles@aip.org; URL: <http://www.aip.org/articles.html>

Elaine Moran

Acoustical Society of America, 500 Sunnyside Boulevard, Woodbury, New York 11797

Editor's Note: Deadline dates for news items and notices are 2 months prior to publication.

Isadore Rudnick • 1917–1997



We are saddened to announce the death of Isadore Rudnick, who died Friday, 22 August, in Los Angeles, California. Izzy joined ASA in 1940 and in the fifty-seven years as a member, he served the Acoustical Society in a variety of appointed and elected offices. Izzy was awarded the Biennial Award in 1948, the first Silver Medal in Physical Acoustics in 1975, and the Gold Medal in 1982. This brief notice is published here to let all of his friends and colleagues know of his passing. A full obituary will appear in a future issue of JASA.

LAWRENCE A. CRUM
President
Acoustical Society of America

Annual Report of the Editor-in-Chief for the Calendar Year Ending 31 December 1996

This is the annual report to the Executive Council of the Society concerning the activities of the Editor-in-Chief and his colleagues on the Editorial Board of the *Journal* of the Society, as well as other matters related to the *Journal* during the 1996 year.

1. Financial and Pages Published

The total number of *Journal* text pages (articles, letters, front text material, and indices) published in 1996 (Volumes 99 and 100) was 7567, an increase of 3%. This figure includes the indexes of both volumes but does not include the technical programs of meetings in Indianapolis and Honolulu for which the total number of text pages (abstracts plus author indexes) was 462, nor does it include the 1996 Supplement containing the References to Contemporary Papers on Acoustics, with 535 text pages. The latter appeared as Part 2 of the August 1996 issue. Including all of the above, the total number of text pages published in 1996 was 8564. The corresponding figure for 1995 was 8224, giving an increase of 4%. Comparing indexed pages (pages excluding indexes and References), the number published in 1996 was 7793 and in 1995 was 7415, a 4% increase. The record size of the joint program for Honolulu accounts for nearly half of the percentages of increase. Table I lists in two columns the number of numbered pages published in the last 10 years. Column I gives the total text pages as defined above. Column II gives indexed pages as defined above.

Page charge acceptance was 48%, below the expected 50% of the total text pages published, exclusive of meeting programs and references. The current page charge is \$80.00 per printed page. Acceptance of page charges is not mandatory. The existence of a mandatory page fee (now \$160.00 per page) for published pages over 12 may have reduced the acceptance of voluntary charges. Some authors have published articles in parts to avoid mandatory fees.

The Executive Council's budget for 1996 limited total pages for the *Journal* (exclusive of meeting programs and References) to 7700 pages. By month-to-month monitoring of the publication schedule the Editorial Department at AIP and the Editor-in-Chief adhered to this budget, with cooperation from the Associate Editors.

2. Personnel and Editorial Mechanics

During the year 1996 the following changes in editorial personnel took place, some already reported in the semi-annual report to the Executive Council in December 1996.

Associate Editor Juergen Schroeter for Speech Processing and Communication Systems (43.72) asked to be replaced at the end of his three-year term. In consultation with the Technical Committee on Speech Communication, the Editor-in-Chief has appointed James L. Hieronymus of AT&T Bell Labs. to be the new Associate Editor.

Associate Editor Michael Porter for Underwater Sound (PACS 43.30) asked to be replaced after four years of service. In consultation with the Chairs of the Underwater Acoustics and Acoustical Oceanography Technical Committees, the Editor-in-Chief has appointed Stanley A. Chin-Bing of NRL Stennis Space Center to be the new Associate Editor.

Associate Editor James H. Miller for Underwater Sound (PACS 43.30) asked to be replaced after four years of service. In consultation with the Chairs of the Underwater Acoustics and Acoustical Oceanography Technical Committees, the Editor-in-Chief appointed David L. Bradley of Pennsylvania State University to be the new Associate Editor.

The number of submissions and acceptances in Physiological Acoustics (PACS 43.64) has increased, requiring the appointment of an additional

TABLE I. Number of pages published in the last ten years.

Year	Text total I	Indexed II
1987	5021	4346
1988	5753	5079
1989	5934	5421
1990	6710	6088
1991	7162	6333
1992	7818	6982
1993	7899	7013
1994	8278	7403
1995	8224	7415
1996	8564	7793
Ten-year average	7136	6387

TABLE II. Distribution of articles among categories in JASA, 1996.

Category	Number of articles	Total pages	Pages per article
10. Tutorial	12	138	11.5
20. General Linear Acoustics	102	876	8.6
25. Nonlinear Acoustics, Macrosonics	51	384	7.5
28. Aeroacoustics, Atmospheric Sound	20	164	8.2
30. Underwater Sound	85	867	10.2
35. Ultrasonics, Quantum Acoustics, Physical Effects of Sound	43	365	8.5
38. Transduction	15	115	7.7
40. Structural Acoustics and Vibration	69	578	8.4
50. Noise: Its Effects and Control	10	109	10.9
55. Architectural Acoustics	12	105	8.8
58. Acoustical Measurements	10	75	7.5
60. Acoustic Signal Processing	19	167	8.8
64. Physiological Acoustics	69	769	11.1
66. Psychological Acoustics	96	892	9.3
70,71,72. Speech Communication	90	913	10.1
75. Music and Musical Instruments	18	165	9.2
80. Bioacoustics	32	283	8.8
1996 Total Articles and Letters	753	6965	9.2
1995 Total Articles and Letters (for comparison)	741	6728	9.1

Associate Editor. The Editor-in-Chief appointed Brenda L. Lonsbury-Martin of the University of Miami Ear Institute.

Being an Associate Editor of our *Journal* requires, in addition to ability and experience in a branch of acoustics, a considerable dedication to the Society and to the field of Acoustics. The Editor-in-Chief expresses his gratitude to both the retiring and the continuing Associate Editors, and to those institutions which support their editorial efforts, on behalf of our contributions, our members, and the Society.

The editorial mechanics of the *Journal* at AIP continues with the able participation of Editorial Supervisor Lin Miller and Rosalind Nissim as Chief Production Editor, with help from Andrea Witt, Connie Nedohon, and Jennifer Mackey. The Editor-in-Chief is especially grateful to this entire group for their capable, diligent, and cheerful assistance.

3. Subject Coverage and Emphasis in the *Journal*

Table II presents data on the number of articles published in the various categories of our subject classification system (PACS) during the year 1996 together with the number of associated pages, and the average number of pages per article in each category. Note that some categories average almost 50% more pages per article than other categories.

From 1995 to 1996 the number of articles and letters published increased about 1.6%, and the number of pages increased 3%. The average

length increased to 9.2 pages in 1996 compared to 9.1 in 1995. This slight increase is the result of more tutorial papers. There was a marked increase in the number of pages published in nonlinear acoustics, ultrasonics, physiological acoustics, and speech communication. There was decreased publication in transduction, noise, architectural acoustics, measurements and signal processing.

In Volumes 99 and 100 published in 1996 there were 548 pages devoted to acoustical news, technical notes, reviews, and indices. Distribution is shown in Table III, which also contains the corresponding figures for 1991 through 1995. The distribution changes little from year to year.

4. Meeting Programs in 1996

The program of the 131st meeting of the Society in Indianapolis, Indiana contained 160 pages of abstracts and author index with a total of 678 abstracts. The program appeared as Part 2 of the May issue. All authors of papers in meeting programs are currently indexed in the *Journal*, but the abstracts are not peer reviewed. The program of the 132nd meeting of the Society (3rd joint meeting with ASJ) in Honolulu contained 302 pages of abstracts and author index with a total of 1333 abstracts, a new record. The program appeared as Part 2 of the October issue.

5. Acceptance and Rejection of Manuscripts Submitted to the *Journal* for Publication in 1996

The relevant figures are presented in Table IV in the same form as that used previously. A few more manuscripts were accepted and a few less were rejected in 1996 than in 1995. There are 4% fewer papers under review currently than a year ago, but enough backlog to be entirely adequate for continuity of publication. The overall rejection rate was approximately 24%. The largest percentages of rejection in 1996 were architectural, underwater, speech, aeroacoustics, physiological, musical, and ultrasonics.

The Society owes a continuing debt of gratitude to the Associate Editors who process manuscripts, and to the dedicated reviewers who examine them. A list of 1479 reviewers during the year 1996 will be published in the August issue with an expression of appreciation for their services.

6. Outside-U.S.A. Papers Published in the *Journal*

Publication activity in the *Journal* from outside the U.S.A. led in 1996 to the equivalent of 321 articles and letters in the *Journal* compared with 308 in 1995. Forty-two percent of *Journal* authorship was outside U.S.A. The distribution among 37 countries was as follows: United Kingdom 53, Canada 40, France 26, Japan 21, Netherlands 19, Australia 17, Germany 16, Sweden 15, Belgium 14, China 11, Italy 11, India 10, Denmark 9, Taiwan 7, Spain 5, Hong Kong 4, Korea 4, Russia 4, Belarus 3, Brazil 3, Norway 3, Poland 3, Singapore 3, Austria 2, Greece 2, New Zealand 2, Portugal 2, with Byelorussia, Czech, Estonia, Israel, Saudi Arabia, South Africa, Switzerland, and Ukraine represented.

7. Review and Tutorial Papers

In 1996 each issue had a review and/or tutorial paper, with emphasis on tutorial. The October issue contained an Editorial on the subject of "Tutorials."

TABLE III. Page distribution of complementary material for 1991–1996.

	1991	1992	1993	1994	1995	1996
Technical Notes, Research Briefs, and FORUM	17	11	21	20	25	28
Acoustical News—U.S.A.	95	89	107	89	108	114
Acoustical News—International	11	12	16	12	16	14
Standards News	32	35	29	20	27	31
Book Reviews	28	17	12	19	12	16
Patent Reviews	135	116	121	110	103	102
Cumulative Author Indexes	16	18	20	20	20	18
Volume Indexes	193	207	213	238	220	213
Errata	15	10	6	9	6	12
TOTALS	542	515	535	537	537	548

TABLE IV. Acceptance and rejection of manuscripts submitted to JASA in 1996.

Category	Manuscripts received in 1996	Manuscripts accepted in 1996	Manuscripts rejected in 1996	Manuscripts sent back for revision 1996	Manuscripts under review at end of 1996
10 Martin (Tutorial Review)	10	7	1	3	2
20 Greenspon	77	65	12	55	81
Norris	56	26	15	30	21
25 Breazeale	47	46	2	34	44
28 Sutherland	25	8	4	12	8
30 Miller	90	45	18	31	77
Porter	29	30	20	29	4
Chin-Bing	22	0	0	3	19
35 Bass	71	44	18	50	33
38 Ehrlich	15	17	1	19	6
40 Remington	30	5	0	4	23
Burroughs	68	53	7	40	22
50 Daigle	30	20	4	11	6
55 Quirt	18	11	9	8	4
58 Ehrlich	18	13	1	15	9
60 Krolik	28	11	2	15	20
64 Frisina	80	38	16	29	17
66 Hall	58	21	6	20	11
Feth	0	10	7	10	—
Jesteadt	53	26	2	19	6
Dye	37	22	7	14	17
70 Lofqvist	39	25	12	17	3
71 Strange	63	8	14	15	25
Fox	0	36	6	34	—
72 Schroeter	14	5	4	3	2
Hieronymus	13	0	2	4	7
75 Strong	41	21	9	23	16
80 Dunn	42	48	1	15	4
TNRB Ostergaard	3	4	0	1	0
1996 TOTALS	1077	665	200	527	487
1995 Totals (for comparison)	1102	647	216	487	507

8. Technical Notes and Research Briefs

In 1996 this *Journal* section contained 5 brief reports of recent research results in various fields, and also contained 28 abstracts of graduate dissertations in acoustics.

9. Book Reviews

In 1996 the *Journal* published 12 book reviews. Fewer book reviewers are producing than before. The Society is deeply appreciative to those book reviewers who have handled their assignments capably and have submitted their reviews in a reasonable time.

10. Patent Reviews

A dedicated corps of 14 patent reviewers published reviews for an average of 47 reviews per month in 1996. These reviews benefit our readers, particularly those who are concerned with new acoustical applications, devices and instruments.

11. References to Contemporary Papers in Acoustics

The 1996 issue of this document, compiled by computer by Richard Stern, appeared in the summer as Part 2 of the August 1996 issue. It contained 535 text papers, fewer than last year because the maximum number of PACS number references per paper has been reduced. This bibliographical coverage of acoustical information from around the world is a valuable part of the material on acoustics distributed to all members of the Society, and to all non-member subscribers to the *Journal*.

12. Standards News and Standards

This section of the *Journal* continues to provide the essential news of the work of the various standards committees on acoustics, as well as availability of standards in acoustics published by the Society and others. The role of the Society in the publication of standards is very important.

13. News Sections

These sections provide up-to-date information about the work of the Society Office, the activities of the various Society committees and the regional chapters, changes in membership lists, personal notes about members and obituaries, and a calendar of meetings of relevant societies for both the U.S.A. and around the world. The *Journal* is now collecting international information for the ICA.

14. Acoustics 1996

Two newsworthy recent acoustical advances were selected by the President and the Editor-in-Chief for news coverage. Brief versions were solicited, prepared, submitted, and were published both in *Physics News in 1996*, and in the January 1997 issue of our *Journal*.

15. Times of Appearance of the *Journal*

Release by AIP to the printer has been on schedule consistently. The Editor-in-Chief appreciates the diligent efforts of our publication staff to maintain the schedule during a heavy publication year.

16. Supplementary Publication Media

The *Journal* became available to members bimonthly on CD-ROM in 1996. Back issues through 1961 are also on CD-ROM. Preparations began for future on-line availability of the *Journal*.

17. Echoes

The Society newsletter edited by Alice Suter provided 4 issues in 1996 containing news about the Society, its members and meetings, and press publicity about sound. Each issue had a feature article on an acoustical subject. Subjects in 1996 were "Active Noise Control," "Designing the Sonic Environment," "Facets of Medical Ultrasound," and "Paradoxical Music."

The Editor-in-Chief expresses his deep appreciation for the generous and capable support he has received from all connected with the editing and production of the *Journal*.

DANIEL W. MARTIN
Editor-in-Chief
May 1997

Robert V. Shannon becomes New Associate Editor of the *Journal*



Robert V. Shannon



Walter Jesteadt

In July 1997 Dr. Robert V. Shannon of the House Ear Institute in Los Angeles, California, became a new Associate Editor of the *Journal* for papers in Psychological Acoustics (PACS 43.66). He succeeded Walter Jesteadt of the Boys Town National Research Hospital in Omaha, Nebraska, who completed a three-year term of faithful and effective service. The Editor-in-Chief is happy to express his deep appreciation to Dr. Jesteadt and to his institution for support services.

Robert Shannon received his B.A. degree in mathematics and psychology from the University of Iowa in 1971. He received a Ph.D. in psychology in 1975 from the University of California in San Diego, after serving as a research assistant in the Harvard Laboratory of Psychophysics.

From 1975 to 1978 he was a Postdoctoral Research Fellow, first at the Institute for Perception (Netherlands), then at the University of California at Irvine. From 1978 to 1985 he was in the Department of Otolaryngology at the University of California, San Francisco, becoming an Assistant Professor in 1982. From 1985 to 1989 Shannon was engaged in research at Boys Town National Institute and was an Associate Professor at Creighton University School of Medicine in the Department of Otolaryngology. Since 1989 he has been at the House Ear Institute where he is currently Head, Auditory Implants and Perception Department.

Shannon's principal research interest has been in electrical stimulation of the human auditory system and the development of implantable auditory prostheses. He has authored or co-authored over 48 research publications, many of them in our *Journal*.

The Editor-in-Chief and his colleagues welcome Dr. Robert V. Shannon to membership on the Editorial Board.

DANIEL W. MARTIN
Editor-in-Chief

ASA gives awards at the 48th International Science and Engineering Fair

The Acoustical Society of America presented special awards at the 48th International Science and Engineering Fair (ISEF) to four students whose projects were most outstanding in the field of acoustics.

The first place award of \$500 went to Ehren Biglari, 16, of Covenant Christian Academy, Huntsville, Alabama for his project entitled, "Computationally efficient speech coding algorithm." In his project, Ehren designed and implemented a real-time speech coding algorithm based on nonlinear methods of speech data compression and play-back. The 48th ISEF was held 10–16 May at the Commonwealth Convention Center in Louisville, Kentucky. The fair included 1089 student-finalists in ninth through twelfth grade who represented 47 states, the District of Columbia, Puerto Rico, and 22 other countries. The students competed for ISEF grand awards, as well as numerous special awards, including ASA awards.

The ASA presented three honorable mention awards to: Paul Henderson, 16, Henderson Home School, Charlotte, North Carolina, for his project, "Equalizer tuning for feedback reduction: Phase III—Digital Fourier analysis;" Gregory Charvat, 17, Gross Pointe South High School, Gross Pointe, Michigan, for his project, "Identifying and reducing radio frequency interference by spectrum analysis;" Melissa Meyer, 17, Tullahoma High School, Tullahoma, Tennessee, for her project, "Music analysis with MIDI and fractal dimensions: Two-year study."



FIG. 1. Ann Clock Eddins (l), Chair of the ASA Judging Panel, with winners of ASA awards at the 48th International Science and Engineering Fair. From l-r: Ehren Biglari, Melissa Meyer, Gregory Charvat, and Paul Henderson.

All four award winners (see Fig. 1) received a one-year student membership in ASA. The winners were among 40 projects determined by the ASA judging team to be within the Society's area of interest. The ASA judges were Ann Clock Eddins, Chairperson, and David A. Eddins, both of Indiana University.

ASA awards presented at Dallas Science Fair

Each spring approximately 50000 students from 400 schools in an eight county area of North Texas compete in science fairs. From these competitions 786 projects qualified and were entered in the 40th Annual Dallas Morning News/Toyota Regional Science and Engineering Fair; forty-five of these projects dealt with acoustics.

Six judges from the Acoustical Society selected two Senior Division and two Junior Division projects for First Place awards; a third Junior Division project was selected for ingenuity. In each case students were strikingly experimental, interpreted their results, and showed clear understanding of salient acoustical principles.

In the Senior Division Megan Eschbach, Clark High School, investigated resonant properties of different woods; she had people evaluate tonal variations in bowed and plucked strings strung across wooden top plates on a cigar box. David Moore, Townview Magnet School, evaluated musical interval ratios in classical and rock music using scores of Beethoven and Jimi Hendrix (see Fig. 1).

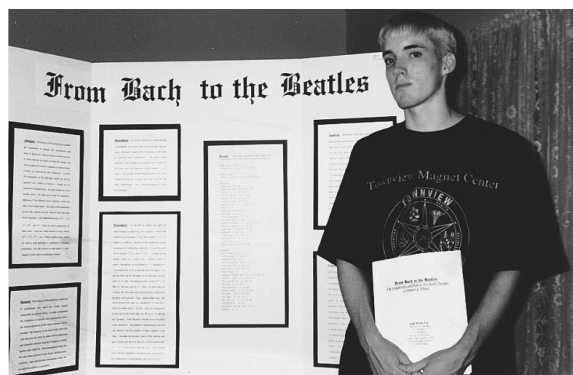


FIG. 1. David Moore, winner of the ASA's First Place Senior Division Award at the Dallas Science and Engineering Fair.

In the Junior Division Steven Lamb, Austin Academy, used tuning forks of known pitch and a PVC pipe partially filled with water (a quarter wave length resonator) to calculate the speed of sound. Hallie Randel, Highland Park Junior High School, investigated how pitch of musical notes depended on thickness and length of vibrating strings. The judges also recognized Matt Paschal, Benjamin Franklin Middle School, for investigating effects of soothing or discordant music on accuracy and speed with which rats learn to run a complex maze.

Laurie Bornstein, Ted Carnes, Ray Daniloff, Bob Lange, Deborah Rekart, and Jack Wrightson represented the Society this year.

MICHAEL DALY

Correction

The caption for Fig. 9 in the report on the 130th meeting of the Acoustical Society of America [J. Acoust. Soc. Am. **99**, 1801 (1996)] is incorrect. The photo is reprinted below with the correct caption.

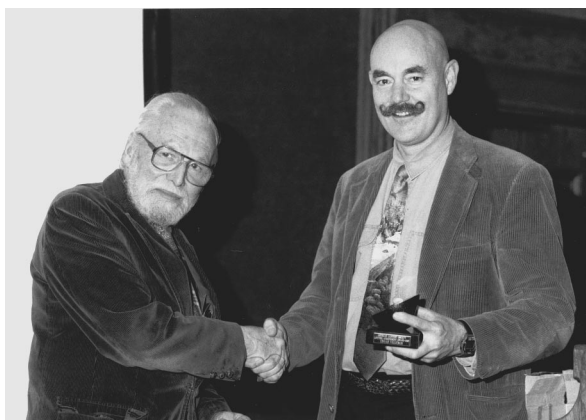


FIG. 9. Mead C. Killion (r) presents the American Auditory Society's Lifetime Achievement Award to Edgar Villchur in recognition of his several contributions to high-fidelity sound reproduction and to signal processing for the hearing impaired. The award was presented to Mr. Villchur on 29 November 1995 at the 130th meeting of the Acoustical Society of America.

Regional Chapter News

Greater Boston: On Thursday evening, 1 May 1997, the Greater Boston Chapter held a spring meeting at the newly renovated Jordan Hall, the first major renovation since the New England Conservatory opened this landmark building in 1903. Clete Davis, senior consultant with R. Lawrence Kirkegaard and Associates, Inc., the project acoustical consultants, began the evening with a slide lecture overviewing the acoustical aspects of the project and especially the noise and vibration controls for the Hall's new super quieted HVAC system. Concerts may now be scheduled in the summer months fulfilling a longstanding dream and need of the Conservatory. Following Clete's lecture, the group toured Jordan Hall and continued up

close inspection of all the Hall's details that achieved a very quiet, yet fully air-conditioned environment (below RC10). A scheduled concert had to be cancelled due the guest performer's illness, but a senior conservatory student performed an original composition in an impromptu recital to the delight and enthusiastic appreciation of all.

The New England Conservatory of Music was founded in 1867; Jordan Hall was a gift of Eben D. Jordan, II, heir to the Jordan Marsh merchant trade business and an accomplished amateur musician. The architecture firm of Wheelright & Haven, whose work includes Boston landmarks such as Horticultural Hall and Cambridge's Harvard Lampoon building, was chosen to design the Hall. On its opening night in 1903, the Hall was proclaimed a unique acoustic marvel.

After nearly a century of constant use (an estimated 16000 performances), Jordan Hall was aged and inefficient, dark and dreary. It lacked air conditioning and accessibility for the disabled as well as comfortable seats and adequate services. The goal of the Jordan Hall restoration was to return the building to its original finish and ambiance while integrating much-needed climate control, accessibility for the disabled, and improved amenities. Of paramount importance was the preservation of the Hall's renowned acoustics. Ann Beha Associates led a five-year design effort that culminated in a condensed five-month construction period. Jordan Hall was awarded a 1996 Massachusetts Historical Commission Preservation Award, a Victorian Society in America's Preservation Commendation, and a Preservation Award from the Boston Preservation Alliance

Annual Reports of Technical Committees

Physical Acoustics

This report summarizes the activities of the Physical Acoustics Technical Committee (PATC) over the past year.

The technical program at the Honolulu meeting consisted of six special sessions and five session of contributed papers. These eleven sessions contained a total of 36 invited and 97 contributed papers. The special sessions were: "Laser Acoustics" chaired by Tsuguo Sawwada, James Wagner, and Kazushi Yamanaka; "Implosion Acoustics I: Sonochemistry, Cavitation, and Bubbles," "Implosion Acoustics II: Sonoluminescence Theory," and "Implosion Acoustics III: Sonoluminescence Experiments" all chaired by Robert Apfel, Hiroyasu Nomura, and Nai-chyuan Yan, "Thermoacoustics I" and "Thermoacoustics II" co-sponsored with Engineering Acoustics and The American Physical Society, chaired by Steve Garrett and Yoshimasa Narahara. Sessions of contributed papers (and chairs) were: "Nonlinear Acoustics I: Propagation in Solids" (James Tencate and Akira Nakamura), "Nonlinear Acoustics II" (Robin Cleveland and Hideto Mitome), "Outdoor Sound Propagation" (James Chambers), "General Topics in Propagation" (Sameer Madanshetty and Mitsuhiro Ueda), and "General Topics in Physical Acoustics" (Thomas Matula and Kenshiro Takagi).

The Fall meeting of the PATC was held in the Waialua room of the Sheraton Waikiki hotel. Approximately 70 people attended. First time attendees were invited to stand and tell the other attendees something about themselves.

Some highlights of the PATC meeting include the following items. Thanks were expressed to Anthony Atchley and Carr Everbach, the PATC representatives at the Technical Program Organizing Committee meeting. Tom Matula reported progress on the PATC web page. The page is now up.

Issues brought forward from the Technical Council include the report titled "ASA Member Analysis." There was some discussion about membership trends and the members were in agreement with the report. Plans for special sessions at the State College and Seattle meetings were discussed.

Two technical initiatives were approved by the Technical Council, \$300 for web page support and \$300 for a PATC student reception at the Penn State meeting.

The Physical Acoustics Summer School was held 21–28 June with a total of 50 participants. Approximately one half the participants were advanced graduate students in physical acoustics. The Physical Acoustics Summer School is sponsored by the Office of Naval Research in cooperation with the Acoustical Society of America and the National Center for Physical Acoustics.

Logan Hargrove and James Sabatier organized an Acoustic Demonstration session at the AAAS meeting in Seattle. Speakers were Anthony Atchley, Bruce Denardo, Robert Keolian, Andres Larraza, and James Sabatier. Approximately 75 people attended the session. Larry Crum and Lo-

gan Hargrove also organized a session on Sonoluminescence and Sonochemistry at the same meeting. The speakers were Larry Crum, William Moss, Andrew Szeri, Kenneth Suslick, and Michael Hoffman.

JAMES M. SABATIER
Chair

USA Meetings Calendar

Listed below is a summary of meetings related to acoustics to be held in the U.S. in the near future. The month/year notation refers to the issue in which a complete meeting announcement appeared.

- 1997**
- 1–5 Dec. 134th meeting of the Acoustical Society of America, San Diego, CA [ASA, 500 Sunnyside Blvd., Woodbury, NY 11797, Tel.: 516-576-2360; FAX: 516-576-2377; E-mail: asa@aip.org; WWW: <http://asa.aip.org>].
- 1998**
- 9–13 Feb. 1998 Ocean Sciences Meeting, San Diego, CA [American Geophysical Union, 2000 Florida Ave., N.W., Washington, DC 20009, Tel.: 202-462-6900; FAX: 202-328-0566; WWW: <http://www.agu.org>].
- 5–8 April NOISE-CON 98, Ypsilanti, MI [Noise Control Foundation, P.O. Box 2469, Arlington Branch, Poughkeepsie, NY 12603; Tel.: 914-462-4006; FAX: 914-463-0201; E-mail: noisecon98@aol.com; WWW: users.aol.com/noisecon98/nc98_cfp.html].

- 20–26 June 135th meeting of the Acoustical Society of America/16th International Congress on Acoustics, Seattle, WA [ASA, 500 Sunnyside Blvd., Woodbury, NY 11797, Tel.: 516-576-2360; FAX: 516-576-2377; E-mail: asa@aip.org; WWW: <http://asa.aip.org>].
- 7–12 July Vienna and the Clarinet, Ohio State Univ., Columbus, OH [Keith Koons, Music Dept., Univ. of Central Florida, P.O. Box 161354, Orlando, FL 32816-1354, Tel.: 407-823-5116; E-mail: kkons@pegasus.cc.ucf.edu].
- 13–17 Sept. American Academy of Otolaryngology—Head and Neck Surgery, San Francisco, CA [American Academy of Otolaryngology—Head and Neck Surgery, One Prince St., Alexandria, VA 22314; Tel.: 703-836-4444; FAX: 703-683-5100].
- 12–16 Oct. 136th meeting of the Acoustical Society of America, Norfolk, VA [ASA, 500 Sunnyside Blvd., Woodbury, NY 11797, Tel.: 516-576-2360; FAX: 516-576-2377; E-mail: asa@aip.org; WWW: <http://asa.aip.org>].

- 1999**
- 27–30 June ASME Mechanics and Materials Conference, Blacksburg, VA [Mrs. Norma Guynn, Dept. of Engineering Science and Mechanics, Virginia Tech, Blacksburg, VA 24061-0219; FAX: 540-231-4574; E-mail: nguynn@vt.edu; WWW: <http://www.esm.vt.edu/mmconf/>]. Deadline for receipt of abstracts: 15 January 1999.

ACOUSTICAL NEWS—INTERNATIONAL

Walter G. Mayer

Physics Department, Georgetown University, Washington, DC 20057

Meeting of the International Commission on Acoustics

The International Commission on Acoustics met at Penn State on 21 and 22 June 1997 to discuss upcoming ICA (International Congress on Acoustics) meetings and the new governance which will begin in 1998. The next ICA meeting will be in Seattle in June of 1998, and Larry Crum (President of ASA) and Charles Schmid (Executive Director of ASA) reviewed the preparations for that meeting. Rome will be the site for the meeting in 2001. Sonoko Kuwano and Hideki Tachibana presented a proposal for Kyoto for the year 2004, and the Commission said they will consider it along with any other sites which are proposed. Sonoko Kuwano is shown in Fig. 1 with members of the Commission who attended the Penn State meeting.



FIG. 1. Back row (left to right): Gilles Daigle, Peter Bury, Sonoko Kuwano, Tor Kihlman (Chair), Gerhard Sessler, Gunnar Rasmussen (Vice-Chair), Suk Wang Yoon, Asbjorn Krogstad, Renhe Zhang. Front row: Gérard Quentin, Hideki Tachibana, Stephen Crandall, Lawrence Crum. —Photo by Charles Schmid.

The Commission also discussed the new method by which the ICA will be governed which will be more representative of acoustics from around the world. At the Seattle meeting the assembly will meet for the first time. It consists of delegates from over 40 acoustical societies. Nominees for the positions on the Commission will be presented to the Assembly for a vote on Thursday, 25 June 1998, at the ICA Seattle meeting, and the newly elected Commission will then meet on the following Saturday.

CHARLES SCHMID

Executive Director

Lisbon to host Acustica 98—September 1998

The Portuguese Acoustical Society (SPA), the Spanish Acoustical Society (SEA), and the Iberoamerican Acoustical Federation (FIA) will hold a joint congress in Lisbon, Portugal, 14–16 September 1998. The official languages will be Portuguese, Spanish, and English. The main topics are expected to be architectural acoustics, acoustic materials, bioacoustics, effects of noise on man, electroacoustics, noise mapping, signal processing, and urban noise. The program will include invited lectures, contributed papers, workshops, and a technical exhibition. The congress will also be host to the First Symposium of the Iberoamerican Acoustical Federation; the symposium will be on industrial and environmental noise.

Further information is available from ACUSTICA 98, CAPS-Instituto Superior Técnico, Ave. Rovisco Pais, 1096 Lisboa Codex, Portugal; Fax: +351 1 3523014; e-mail: capsist@alfa.ist.utl.pt

Papers published in JASJ(E)

A listing of Invited Papers and Regular Papers appearing in the latest issue of the English language version of the *Journal of the Acoustical Society of Japan*, JASJ(E), was published for the first time in the January 1995 issue of the Journal. This listing is continued below.

The September issue of JASJ(E), vol. 18, No. 5 (1997) is a Special Issue on Ultrasonics and contains the following papers:

- Peter A. Lewin and Qian Zhang “Nonresonant transducers for ultrasound imaging”
T. Kobayashi, H. Tsai, and S. Ueha “Vibrating-plate viscometer using a triangular bimorph transducer”
K. Sawada, Y. Miyahana, and K. Ishii “Precise target strength pattern measurement in an indoor tank”
Y. Koike, M. Kihara, J. Satonobu, K. Nakamura, and S. Ueha “A peripherally bolted torsional Langevin vibrator with large diameter”
Hai-Ying Huang, T. Kamakura, and Y. Kumamoto “Acoustic streaming and temperature elevation in focussed Gaussian beams”
K. Nagai, M. Ohmaru, K. Mizutani, and T. Yokoyama “Spacing of transducer elements in transmitter and receiver arrays to collect data for ultrasonic tomography”
K. Mizutani, N. Wakatsuki, H. Yoshida, and K. Nagai “An amplitude phase modulation (APM) using a shear horizontal (SH) plate-mode wave device”
Taibao Li “An implementation study of dynamic compensation of hand motion component in pulsed Doppler ultrasound”
R. Murayama “Nondestructive evaluation of formability in cold rolled steel sheets using electromagnetic acoustic transducer for shear horizontal plate waves”

International Meetings Calendar

Below are announcements of meetings to be held abroad. Entries preceded by an * are new or updated listings with contact addresses given in parentheses. Month/year listings following other entries refer to issues of the *Journal* which contain full calendar listings or meeting announcements.

October 1997

- 7–10 1997 IEEE Ultrasonics Symposium, Toronto. 2/96
8–10 Acoustics Week in Canada 1997, Windsor. 12/96
23–26 Reproduced Sound 13, Windermere. 2/97
30–31 Swiss Acoustical Society Meeting, Bern. 6/97

November 1997

- 9–13 *Asia Pacific Vibration Conference 97, Kyongju, Korea. (Intercom Services, 4 Fl. Jisung Bldg., 645-20 Yoksam 1-dong, Kangnam-gu, Seoul 135-081, Korea; Fax: +82 2 3452 7292; e-mail: intercom@sobak.kornet.nm.kr)
19–21 WESTPRAC'97, Hong Kong. 10/96
27–30 IOA Autumn Conference: Environmental Noise, Windermere. 2/97, 6/97

December 1997

- 16–17 *Underwater Acoustics Conference, Loughborough, UK. (Institute of Acoustics, 5 Holywell Hill, St. Albans, Herts AL1 1EU, UK; Fax: +44 1727 850 533; e-mail: acoustics@clus1.ulcc.ac.uk)
15–18 5th International Congress on Sound and Vibration, Adelaide. 10/96

February 1998

- 2–6 Ultrasonic Technological Processes-98, Moscow. 6/97

March 1998

4–5

***4th Annual Conference of the Society of Acoustics of Singapore**, Singapore. (W. Gan, c/o Acoustical Services Pte Ltd., 209-212 Innovation Centre, NTU, Nanyang Avenue, Singapore 6397989, Republic of Singapore; Fax: +65 7913665, e-mail: wsgan@singnet.com.sg)

23–27

DAGA 98 (German Acoustical Society Meeting), Zürich. 8/96

31–2

***Acoustics 98**, Cranfield University, UK. (Institute of Acoustics, 5 Holywell Hill, St. Albans, Herts AL1 1EU, UK; Fax: +44 1727 850 533; e-mail: acoustics@clus1.ulcc.ac.uk)

May 1998

10–14

***6th Meeting of the European Society of Sonochemistry**, Rostock-Warnemünde, Germany. (D. Peters, FB Chemie, University of Rostock, Buchbinderstr. 9, 18051 Rostock, Germany; Fax: +49 381 498 1763; e-mail: ess6@chemibm1.chemie1.uni-rostock.de)

18–22

7th Spring School on Acoustooptics and Applications, Gdańsk. 8/97

25–27

Noise and Planning 98, Naples. 2/97

June 1998

8–10

EAA/EEAA Symposium “Transport Noise and Vibration,” Tallinn. 10/96

9–12

8th International Conference on Hand-Arm Vibration, Umea. 6/97

20–28

Joint Meeting of the 16th International Congress on Acoustics and 135th Meeting of the Acoustical Society of America, Seattle. 6/97

September 1998

7–9

***Nordic Acoustical Meeting 98**, Stockholm, Sweden. (Swedish Acoustical Society c/o Ingemansson AB, Box 47321, 10074 Stockholm, Sweden; Fax: +46 818 2678; e-mail: nam98@ingemansson.se)

14–16

***Biot Conference on Poromechanics**, Louvain-la-Neuve, Belgium. (J.-F. Thimus, Unité de Génie civil, Université catholique de Louvain, Place du Levant 1, 1348 Louvain-la-Neuve, Belgium; Fax: +32 10

472179; e-mail: biotconf@gc.ucl.ac.be; Web: www.gc.ucl.ac.be/ge/geotech/geomater.html#biotconf)

***ACUSTICA 98**, Lisbon. 10/97

***35th International Conference on Ultrasonics and Acoustic Emission**, Chateau of Třešt, Czech Republic. (H. Kotschová, Geophysical Institute AS Boční II/401, 14131 Prague 4, Czech Republic; Fax: +42 2 761 549; e-mail: hko@ig.cas.cz; Web: www.ig.cas.cz)

November 1998

16–18

20

Inter-Noise 98, Christchurch. 4/96

***Recreational Noise**, Queenstown, New Zealand. (P. Dickenson, NZ Ministry Health, PO Box 5013, Wellington, New Zealand; Fax: +64 4 496 2340; e-mail: philip.dickerson@mohwn.synet.net.nz)

23–27

30–4

ICBEN 98: Biological Effects of Noise, Sydney. 12/96
5th International Conference on Spoken Language Processing, Sydney. 6/97

March 1999

15–19

Joint Meeting of DAGA, EAA Forum Acusticum, and 137th Meeting of the Acoustical Society of America, Berlin. 6/97

June 1999

28–30

***1st International Congress of the East European Acoustical Association**, St. Petersburg, Russia. (EEAA, Moskovskoe Shosse 44, St. Petersburg 196158, Russia; Fax: +7 812 127 9323; e-mail: krylspb@sovam.com)

July 1999

4–9

***10th British Academic Conference in Otolaryngology**, London, UK. (BOA-HNS, The Royal College of Surgeons, 35-43 Lincoln's Inn Field, London WC2A 3PN, UK; Fax: +44 171 404 4200)

September 1999

1–4

***15th International Symposium on Nonlinear Acoustics (ISNA-15)**, Göttingen, Germany. (W. Lauterborn, Drittes Physikalisches Institut, Universität Göttingen, Bürgerstr. 42-44, 37073 Göttingen, Germany; Fax: +49 551 39 7720; e-mail: lb@physik3.gwdg.de)

REVIEWS OF ACOUSTICAL PATENTS

Daniel W. Martin

7349 Clough Pike, Cincinnati, Ohio 45244

The purpose of these acoustical patent reviews is to provide enough information for a Journal reader to decide whether to seek more information from the patent itself. Any opinions expressed here are those of reviewers as individuals and are not legal opinions. Printed copies of United States Patents may be ordered at \$3.00 each from the Commissioner of Patents and Trademarks, Washington, DC 20231.

Reviewers for this issue:

SAMUEL F. LYBARGER, 101 Oakwood Road, McMurray, Pennsylvania 15317

D. LLOYD RICE, 11222 Flatiron Drive, Lafayette, Colorado 80026

CARL J. ROSENBERG, Acentech Incorporated, 33 Moulton Street, Cambridge, Massachusetts 02138

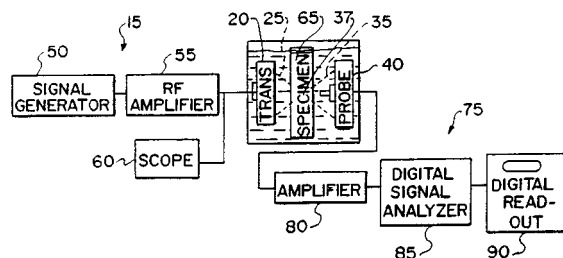
ROBERT C. WAAG, University of Rochester Medical Center, 601 Elmwood Avenue, Rochester, New York 14642

5,623,095

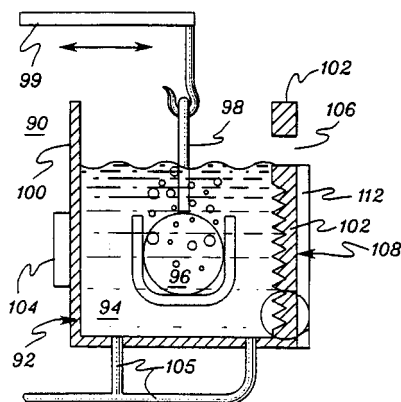
43.35.Vz METHOD FOR CHEMICALLY ANALYZING A SOLUTION BY ACOUSTIC MEANS

Laurence S. Beller, assignor to the United States of America
22 April 1997 (Class 73/61.49); filed 24 November 1995

In this apparatus for determining the solution concentration and type for a specimen **64**, the specimen is immersed between ultrasonic focusing transducer **20** and sensor **40**. Variable sound intensities over a range between 0 and cavitation are used. "Each solution goes through 'saturation'



peaks and valleys one or more times in this intensity range;... the location, in terms of intensity, of these peaks and valleys is unique to the solvent/solute combination."—DWM



through the wall to allow bubbles of gas from manifold **112** to form between the serrations, thereby adding absorption to the scattering process.—DWM

5,627,319

43.38.Md MOTION ACOUSTIC HOLOGRAPH

Ronald J. Greene, Sun City, CA

6 May 1997 (Class 73/605); filed 12 February 1996

This patent describes a "new acoustic motion holography process" involving two steps at different times. "In the first step or freezing, the generation of the 3-D interference pattern is delayed and only the one-dimensional information about the wave, its frequency, amplitude and phase is frozen in-time and recorded. The second step or unfreezing, done at a later time then requires the simultaneous generation, decoding and illumination of the 'live' 3-D interference pattern by causing two identical sets of highly coherent one-dimensional waves to interfere while being simultaneously illuminated." For example, "when an acoustic string instrument is plucked the emerging waves would be frozen one-dimensionally in-time in an analogue record, tape or CD. In the second step, at a later time upon the generation of the 'live' 3-D interface pattern with its simultaneous illumination, the same emerging waves are unfrozen and the released waves would then continue to proceed out from the acoustic string instrument as if it were still actually present, while long removed."—DWM

5,579,792

43.35.Zc APPARATUS FOR UNIFORM CLEANING OF WAFERS USING MEGASONIC ENERGY

David Stanasolovich *et al.*, assignors to International Business Machines Corporation
3 December 1996 (Class 134/184); originally filed 19 April 1993

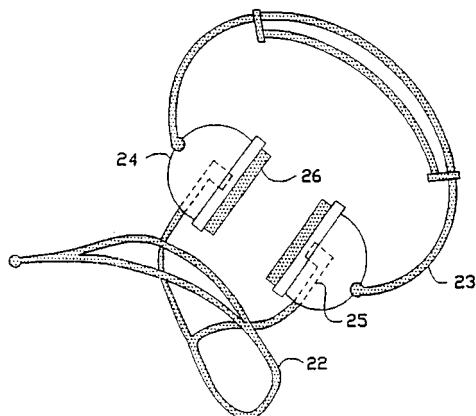
In this ultrasonic bath **92** for cleaning articles with sonic power, a semiconductor wafer **96**, for example, is suspended within cleaning fluid **94** in the path of radiation from transducer **104**. The opposite sidewall **102** is designed to be anti-reflective by its serrated shape, and by tiny holes drilled

5,627,902

**43.38.Si MAGNETIC RESONANCE IMAGING
COMPATIBLE AUDIO HEADSET**

Mokhtar Ziarati, assignor to Resonance Technology, Incorporated
6 May 1997 (Class 381/187); originally filed 11 February 1991

Magnetic resonance imaging for medical analysis uses magnetic fields which can affect or damage electromagnetic audio devices in the vicinity of the patient. Associated noise can annoy the patient both in noise level and in sound spectrum. The headset of this patent supplies musical masking sound to the patient through tubes **22** from a transducer either outside the magnetic



field or of a type (e.g., piezoelectric) not responsive to the magnetic field. The earphones **24** have circumaural cups **26** to attenuate the acoustical noise for the patient. Electrical filters in the audio system attenuate electrical noise resulting from the high magnetic fields.—DWM

5,598,479

**43.50.Gf DEVICE FOR REDUCING TIRE/ROAD
SURFACE NOISE**

Thomas Dodt *et al.*, assignors to Continental Aktiengesellschaft
28 January 1997 (Class 381/71); filed in Germany 29 January 1994

In order to reduce the noise generated by an automobile tire running on road surface at variable speed, this patent provides resonator absorbers mounted, for example, on the inner surface of the partially surrounding wheel well, and adjusts the resonance frequency in accordance with wheel rotation rate so that the resonators are tuned to the tire noise frequency.—DWM

5,623,130

**43.55.Dt SYSTEM FOR ENHANCING ROOM
ACOUSTICS**

Arthur M. Noxon, Eugene, OR
22 April 1997 (Class 181/30); filed 20 November 1995

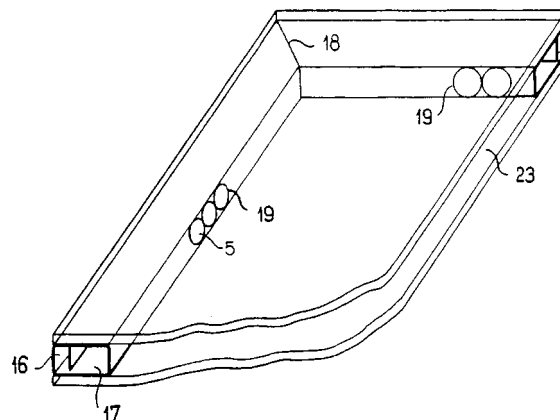
The system referred to in the patent is a series of absorptive baffles (such as medium density glass fiber), arrayed in a room perpendicular to the walls or ceiling, preferably at the corner where the wall and ceiling meet, and preferably sealed tight against the room boundary. The baffles might be spaced about two feet apart. The baffles as described in the patent have an edge surface, which makes it easier to install the baffle in a bracket or channel.—CJR

5,598,669

43.55.Ti ACOUSTIC INSULATING BOX

Mohamed A. Hamdi *et al.*, assignors to Saint Gobain Vitrage International "Les Miroirs"
4 February 1997 (Class 52/144); filed in France 16 July 1992

The "box" in the title of this patent refers to the air- or gas-filled enclosure between two parallel panes of glass and the frame separating them for heat (and sound) insulating glazing. Orifices **5** and **19** in the frame connect to a peripheral waveguide to improve the acoustical insulation performance of the window, by detuning "acoustic and mechanical waves which arise respectively in the air or gas space and on the walls when the



double-walled box system is subjected to an incident acoustic field." A computing method using acoustic and mechanical finite elements allows the internal acoustic modes of the air space and the eigenmodes of the glass panels to be determined, in order to effect reduction of the noise and vibration transmission.—DWM

5,626,629

**43.64.Me PROGRAMMING OF A SPEECH
PROCESSOR FOR AN IMPLANTABLE COCHLEAR
STIMULATOR**

Michael A. Faltys *et al.*, assignors to Advanced Bionics Corporation
6 May 1997 (Class 607/57); filed 31 May 1995

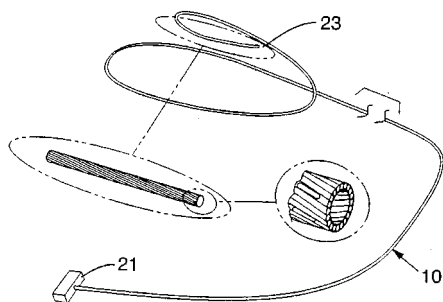
A method and apparatus are shown for fitting an auditory stimulation system. In one version a programmer is coupled to an implanted electrode to determine an estimated threshold stimulation current for an electrode channel. A number of figures assist in describing the device and method.—SFL

5,630,839

**43.64.Me MULTI-ELECTRODE COCHLEAR
IMPLANT AND METHOD OF MANUFACTURING
THE SAME**

Scott S. Corbet III *et al.*, assignors to PI Medical Corporation and the University of Washington
20 May 1997 (Class 607/137); filed 18 August 1995

A multi-electrode cochlear implant is shown that has 20 or more insulated wires wound around a flexible insulated tube. The wires are coated with an insulating material to hold them in place. An ultraviolet laser beam



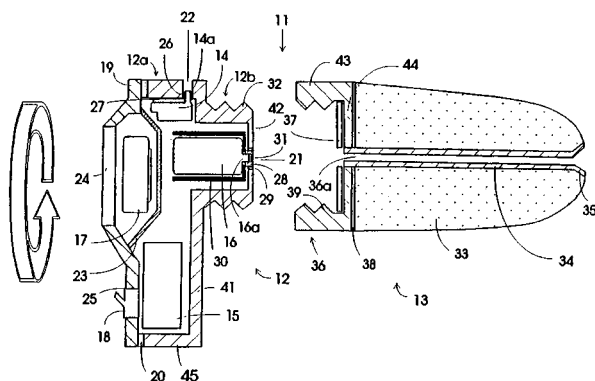
is focused on selected small areas to remove the insulation from each wire so that contacts will be made at appropriate locations along the basilar membrane.—SFL

5,631,965

43.66.Vt HEARING PROTECTOR

Joseph S. Chang and Yit C. Tong, Victoria, Australia
20 May 1997 (Class 381/72); filed in Australia 19 June 1992

The patent shows an ear protector that has a microphone, amplifier, and receiver feeding a signal into an eartip fitting snugly into the ear canal.



The output of the amplifier is adjusted to limit the signal output to a comfortable level.—SFL

5,590,241

43.72.Dv SPEECH PROCESSING SYSTEM AND METHOD FOR ENHANCING A SPEECH SIGNAL IN A NOISY ENVIRONMENT

Sangil Park *et al.*, assignors to Motorola, Incorporated
31 December 1996 (Class 395/2.36); filed 30 April 1993

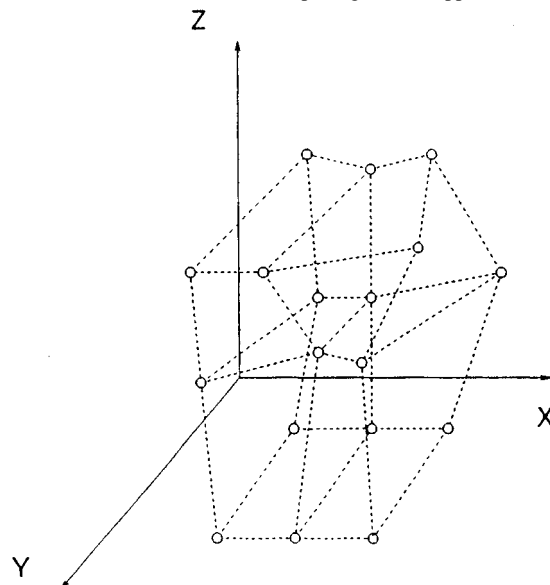
This noise reduction system is arranged much like a typical two-microphone system, in which one microphone picks up a voice signal plus a noise component, while a second microphone is placed to pick up only the noise. The difference is that, in this case, the voice microphone is an accelerometer sensor attached to the speaker's throat where it will be relatively insensitive to the noise component. A normal air microphone receives both speech and noise. An adaptive filter modifies the accelerometer signal by making the output more like those power components which are correlated between the two pickups and less like those power components which are uncorrelated between the pickups.—DLR

5,594,833

43.72.Gy RAPID SOUND DATA COMPRESSION IN CODE BOOK CREATION

Takeo Miyazawa, Tokyo, Japan
14 January 1997 (Class 395/2.3); filed in Japan 29 May 1992

This audio waveform compression system uses a type of neural network known as a Kohonen self-organizing map as a method of vector quantization of waveform samples. In a Kohonen network, multiple layers of neurons are interconnected. Input signals are applied to all layers



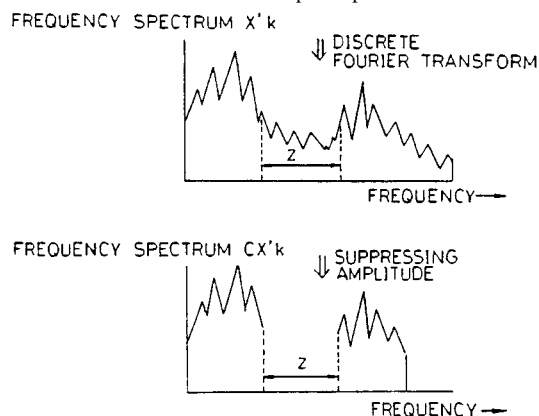
and any node can generate an output. In this case, the network computes a similarity measure referred to as a Voronoi division, in effect, clustering the waveform blocks. Representative "centroid" waveforms are chosen to represent each cluster in a codebook.—DLR

5,596,675

43.72.Gy METHOD AND APPARATUS FOR SPEECH ENCODING, SPEECH DECODING, AND SPEECH POST PROCESSING

Jun Ishii and Shinya Takahashi, assignors to Mitsubishi Denki Kabushiki Kaisha
21 January 1997 (Class 395/2.2); filed in Japan 21 May 1993

This patent describes a set of speech analysis techniques said to improve the quality of an encoded speech signal. One of the techniques addresses the transitions between voiced and unvoiced speech. During the transitions, a scheme of sliding the analysis window to different phases within a frame interval is based on the speech power within the window. A



second technique suppresses low-amplitude harmonics located between the formant regions. This is said to reduce noise levels. A third technique is similar in that low-amplitude regions of a Fourier spectrum are suppressed.—DLR

5,596,676

43.72.Gy MODE-SPECIFIC METHOD AND APPARATUS FOR ENCODING SIGNALS CONTAINING SPEECH

Kumar Swaminathan *et al.*, assignors to Hughes Electronics
21 January 1997 (Class 395/2.17); filed 1 June 1992

This speech vocoder uses a collection of code-excited linear prediction (CELP) coding techniques. Frames of input speech are divided into two overlapping subframes and analyzed to determine the short-term (spectrum) and long-term (pitch) predictor values. The spectral frames are processed to broaden the bandwidths, converted to line spectral frequency (LSF) coefficients, and vector quantized with a set of LSF codebooks. This results in a classification of the input frame as voiced, unvoiced, transient, or background noise. Depending on this result, various optimizations are chosen for the CELP encoding process.—DLR

5,596,677

43.72.Gy METHODS AND APPARATUS FOR CODING A SPEECH SIGNAL USING VARIABLE ORDER FILTERING

Kari Jarvinen and Olli Ali-Yrkko, assignors to Nokia Mobile Phones Limited
21 January 1997 (Class 395/2.29); filed in Finland 26 November 1992

This speech coder selects the optimum linear prediction analysis order based on the signal characteristics, so as to reduce the transmission bitrate without significantly reducing the speech quality. An initial analysis is done with a fixed LPC order, such as 14th order. The speech is then resynthesized using orders ranging from 4 to 14. A loop including both short- and long-term parameters and the perceptual weighting filter is used to determine the lowest usable LPC order.—DLR

5,592,585

43.72.Ja METHOD FOR ELECTRONICALLY GENERATING A SPOKEN MESSAGE

Bert Van Coile *et al.*, assignors to Lernout & Hauspie Speech Products N.C.
7 January 1997 (Class 395/2.15); filed 26 January 1995

This patent consists of a broad and coarse description of a text-to-speech synthesis system while giving little detail on the underlying approach being used. Acknowledgment is made of the requirement of being able to generate phonetic content of the message independently of the prosodic content. Most of the discussion deals with the application of previously published methods for handling the mechanics of pitch, duration, and amplitude changes and the phonetic transcription. The patent appears to be a collection of old ideas wrapped in new terminology.—DLR

5,592,545

43.72.Kb VOICE ENHANCEMENT SYSTEM AND METHOD

Helena S. Ho *et al.*, assignors to DSC Communications Corporation
7 January 1997 (Class 379/347); filed 2 December 1993

This voice enhancement system for telephone applications is intended to detect and correct several distortions typically introduced by the telephone network. Such distortions include multiple passes of low-frequency

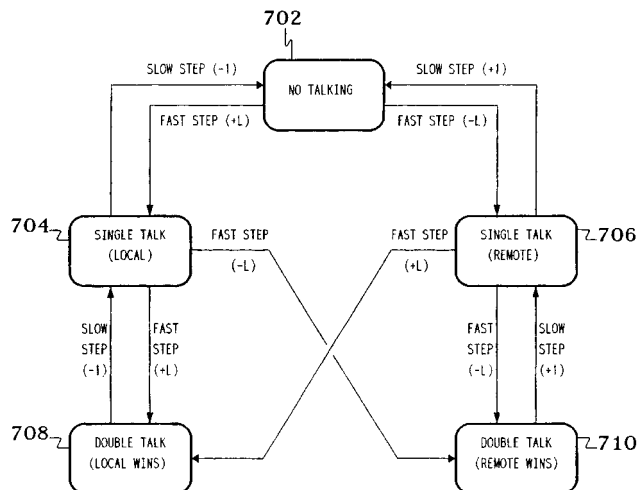
attenuation, inappropriate amplification of loud signals, and transmittal of background sounds during speech silences. A gain control system is sensitive to power levels in low-frequency and voice-band regions. Lookup tables of gain coefficients allow the system to mix the input signal with various equalized versions of the input.—DLR

5,592,547

43.72.Kb PROCESSING AUDIO SIGNALS USING A DISCRETE STATE MACHINE

Carol Wu and Seo P. Ng, assignors to Intel Corporation
7 January 1997 (Class 379/390); filed 24 November 1993

This patent addresses the problem of feedback in speakerphone systems as it arises in the context of a microphone and loudspeaker attached to a personal computer. The strategy disclosed for controlling the feedback



signal consists of detection of microphone and line-signal power levels and differing rates of switchover between local and remote signals being fed to the local loudspeaker and being transmitted.—DLR

5,592,586

43.72.Kb VOICE COMPRESSION SYSTEM AND METHOD

Sidhartha Maitra *et al.*, assignors to Multi-Tech Systems, Incorporated
7 January 1997 (Class 395/2.29); filed 8 January 1993

This complex patent discloses a speech coding system, but includes hardware digital logic, software architecture, and system configuration aspects of providing efficient real-time voice and data communications. The speech coder uses linear prediction with vector quantization of the long-term (pitch) predictions. Speech sampled at 8 KHz is compressed to 9200 bits per second and then integrated into the computer system's fax and modem data communications system.—DLR

5,596,678

43.72.Kb LOST FRAME CONCEALMENT

Karl T. Wigren and Rolf A. Bergstroem, assignors to Telefonaktienbolaget LM Ericsson
21 January 1997 (Class 395/237); filed in Sweden 11 June 1993

This is an elaboration of several patents recently issued to the same authors on the topic of strategies for generating "fill-in" speech frames in a communications receiver when frames of the transmitted signal are lost. The disclosure of the patent is particularly tricky in that it is not stated directly in the patent text. Instead, several alternative solutions are described, along with advantages and disadvantages of each. The actual implementation is

then revealed in the form of several pages of Pascal source code, which the reader must unravel in order to understand.—DLR

5,596,680

43.72.Kb METHOD AND APPARATUS FOR DETECTING SPEECH ACTIVITY USING CEPSTRUM VECTORS

Yen-Lu Chow and Erik P. Staats, assignors to Apple Computer, Incorporated
21 January 1997 (Class 395/257); filed 31 December 1992

This speech presence detector uses a combination of power levels and zero crossing features to detect the beginning of an acoustic event. It then performs linear prediction cepstral analysis on subsequent frames of the input signal to determine when the event ends and whether it should be classified as speech or one of a variety of background sounds such as beeps, clicks, or office environment sounds.—DLR

5,590,242

43.72.Ne SIGNAL BIAS REMOVAL FOR ROBUST TELEPHONE SPEECH RECOGNITION

Biing-Hwang Juang and Mazin G. Rahim, assignors to Lucent Technologies, Incorporated
31 December 1996 (Class 395/2.54); filed 24 March 1994

This speech recognition enhancement system involves a method of processing cepstral vectors of the speech signal so as to remove or reduce any of a number of nonspeechlike "bias" conditions. The system is said to be effective in reducing not only additive noise, but convolutive channel distortions as well as Lombard and other articulation-modifying effects. Training speech data containing the targeted bias effects is processed to determine cepstral coefficients. The relative probabilities of speechlike versus nonspeechlike events are used iteratively to identify and construct centroids of the bias components. These can then be used to subtract the bias, leaving a cleaner speech signal.—DLR

5,594,834

43.72.Ne METHOD AND SYSTEM FOR RECOGNIZING A BOUNDARY BETWEEN SOUNDS IN CONTINUOUS SPEECH

Shay-Ping T. Wang, assignor to Motorola, Incorporated
14 January 1997 (Class 395/2.62); filed 30 September 1994

This patent describes the application of a technique described as a polynomial classifier to the problem of word boundary detection in a continuous speech recognizer. The task is presented as if spoken words were separated by certain distinct sounds referred to as delimitive sounds. Speech frames are processed to compute linear prediction cepstral vectors. A polynomial is then formed as the sum of various powers of the cepstral coefficients. It is supposed that similarities among the polynomial values can be used to classify the delimitive sounds.—DLR

5,596,679

43.72.Ne METHOD AND SYSTEM FOR IDENTIFYING SPOKEN SOUNDS IN CONTINUOUS SPEECH BY COMPARING CLASSIFIER OUTPUTS

Shay-Ping T. Wang, assignor to Motorola, Incorporated
21 January 1997 (Class 395/2.45); filed 26 October 1994

This is another patent issued to the same author as the above reviewed United States Patent 5,594,834, describing the application of a polynomial cepstral classifier to speech recognition tasks. As in the related patent, speech frames are processed to compute linear prediction cepstral vectors. A polynomial is formed as the sum of various powers of the cepstral coefficients. In this case, multiple versions of the polynomial are computed and a

voting procedure is applied to determine which polynomial expansion is the most successful in classifying the speech events.—DLR

5,631,434

43.75.Tv FILTERING APPARATUS FOR AN ELECTRONIC MUSICAL INSTRUMENT

Toda Hiroyuki, assignor to Yamaha Corporation
20 May 1997 (Class 84/661); filed in Japan 11 October 1989

Many musical instruments have fewer significant tonal harmonics at high fundamental frequencies than at low. To reproduce this condition in electronically simulated tone, without the need to store different tone spectra for each key on the keyboard, this electronic musical instrument uses a digital low-pass filter with its cutoff frequency controlled by the keycode signal which also controls the frequency of the computer-generated input signal to the filter. For tone spectra which change with duration of the tone, it is also possible to vary the cutoff frequency with time after keying.—DWM

5,585,583

43.75.St INTERACTIVE MUSICAL INSTRUMENT INSTRUCTION SYSTEM

Randall L. Owen, assignor at Maestromedia, Incorporated
17 December 1996 (Class 84/470 R); filed 14 October 1993

"A musical instrument instruction system utilizes a CD-ROM electronic storage medium to store audio and video musical instrument instructional materials. Instructional materials are accessed utilizing a computer which provides an interactive system in which animation, voice, music, video and imagery are integrated in essentially real time and under complete control of the music student. The system permits the student to access the instructional materials in a variety of ways, and control the parameters governing the presentation of the instructional materials, including control of the tempo of the music and whether or not displays of the manner of playing the musical instrument will be shown with a displayed notation or tablature relating to the selected musical piece. A mixer is provided for combining musical output of the practice instrument with musical output generated by the computer corresponding to the selected musical piece."—DWM

5,606,971

43.80.Qf METHOD AND DEVICE FOR SHEAR WAVE ELASTICITY IMAGING

Armen P. Sarvazyan, assignor to Artann Corporation
4 March 1997 (Class 128/660.02); filed 13 November 1995

A focused ultrasound transducer remotely induces a shear wave in tissue by sending modulated ultrasonic pulses. A shear wave at the frequency of the modulating signal is detected. The shear modulus and dynamic shear viscosity are determined from measured values of shear wave velocity and attenuation. The intended use is detection of abnormalities characterized by changes in the mechanical properties of tissue.—RCW

5,617,863

43.80.Qf ULTRASONIC DIAGNOSTIC IMAGE SCANNING TECHNIQUES

David N. Roundhill et al., assignors to Advanced Technology Laboratories, Incorporated
8 April 1997 (Class 128/661.01); filed 12 June 1995

In these techniques, ultrasonic beams are initially transmitted along directions at the lateral sides of the image field. Subsequent beams are alternately transmitted on either side of the initial beams and at lateral locations that converge toward the center of the field until the full image field has been scanned. In an alternate technique, beams are initially transmitted on one side and then on the other side of the center of the image field, and

subsequent beams diverge laterally from the locations of the initially transmitted beams.—RCW

5,609,606

43.80.Sh ULTRASONIC ANGIOPLASTY BALLOON CATHETER

Matthew O'Boyle, assignor to Joe W. & Dorothy Dorsett Brown Foundation
11 March 1997 (Class 606/194); filed 7 June 1995

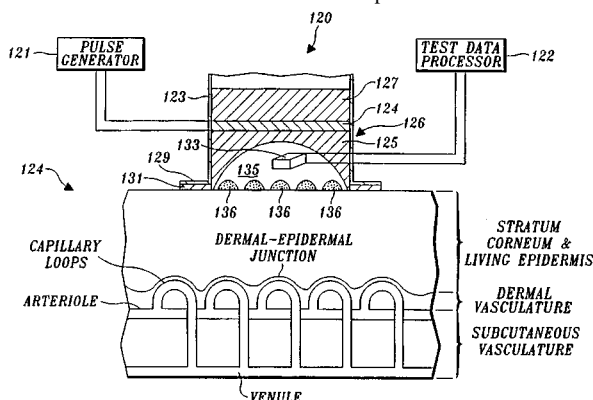
The balloon in this catheter has piezoelectric properties and may be inflated with a conductive contrast fluid that is injected proximally. The balloon is excited by a signal applied across the metallized surface of the balloon and the contrast fluid. Excitation of the deflated piezoelectric balloon at the site of a stenosis causes vibrations at the catheter tip to ablate the stenosis. Maintaining the vibrations while the balloon is inflated in the stenosis breaks up the stenosis, rather than pressing the stenosis against the blood vessel wall as in other angioplasty balloon catheters.—RCW

5,617,851

43.80.Sh ULTRASONIC TRANSDERMAL SYSTEM FOR WITHDRAWING FLUID FROM AN ORGANISM AND DETERMINING THE CONCENTRATION OF A SUBSTANCE IN THE FLUID

Lev M. Lipkovker, assignor to Endodermic Medical Technologies Company
8 April 1997 (Class 128/632); filed 14 March 1995

In this patent, which is a division of a prior application that resulted in U.S. Patent 5,421,816, Ultrasonic Transdermal Drug System, the system contains a substance concentration sensor 120 that includes an extraction transducer 126 with a container 123, and a substance sensing transducer 133. The extraction transducer also includes a piezoelectric ultrasonic trans-



ducer 124, a focusing lens 125, and a backing layer 127. Ultrasonic transducer pulses traumatize the skin, causing dermal-epidermal junction membranes and capillary endothelial joints to open, and to allow fluid to be drawn from the cavity for analysis.—RCW

5,618,275

43.80.Sh ULTRASONIC METHOD AND APPARATUS FOR COSMETIC AND DERMATOLOGICAL APPLICATIONS

Robert R. Bock, assignor to Sonex International Corporation
8 April 1997 (Class 604/290); filed 27 October 1995

High-intensity ultrasonic waves are applied to disrupt the skin and allow a therapeutic agent on the skin to penetrate the body. Ultrasonic waves that do not disrupt the skin may be applied afterward. The depth of penetration of the agent may be controlled by varying the burst length of the electric signals applied to the transducer.—RCW

5,606,972

43.80.Vj ULTRASONIC DOPPLER MEASUREMENT OF BLOOD FLOW VELOCITIES BY ARRAY TRANSDUCERS

Helen F. Routh, assignor to Advanced Technology Laboratories, Incorporated
4 March 1997 (Class 128/661.09); filed 10 August 1995

Peak and mean flow velocities are found from Doppler signals. The peak velocities are compensated by a function that depends on the array aperture dimension and relation of the aperture to the location of the Doppler sample volume. Mean velocities are combined with a function depending on the array to produce accurate mean values of velocity. The entire spectrum may be compensated by deconvolution of the received signal spectrum with an array distortion function, or by the use of Doppler reference signals for each array element as a function of element position in the array aperture.—RCW

5,606,973

43.80.Vj LIQUID CORE MICRODROPLETS FOR ULTRASOUND IMAGING

Karel J. Lambert and Edward G. Jablonski, assignors to Molecular Biosystems, Incorporated
4 March 1997 (Class 128/662.02); filed 7 June 1995

These microdroplets contain a biocompatible liquid encapsulated by a shell of amphiphilic biocompatible material. The microdroplets are prepared by milling a mixture of a solution of the shell material and vaporized liquid and then cooling the milled mixture to below the boiling point of the liquid.—RCW

5,606,974

43.80.Vj CATHETER HAVING ULTRASONIC DEVICE

Thomas M. Castellano *et al.*, assignors to Heart Rhythm Technologies, Incorporated
4 March 1997 (Class 128/662.06); filed 2 May 1995

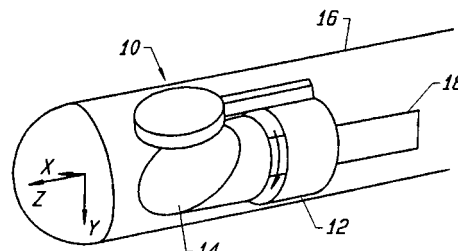
This catheter includes a piezoelectric transducer and temperature sensors mounted on the distal end.—RCW

5,606,975

43.80.Vj FORWARD VIEWING ULTRASONIC IMAGING CATHETER

David H. Liang and Bob S. Hu, assignors to Leland Stanford Junior University
4 March 1997 (Class 128/662.06); filed 19 September 1994

This catheter employs an ultrasound mirror 10 supported by a bearing 12. An ultrasound transducer 14 directs ultrasonic waves in the forward



direction along the axis of the catheter. The mirror is rotated relative to the transducer by a drive cable 18.—RCW

5,609,154

43.80.Vj DUPLEXER INCLUDING A VARIABLE CAPACITANCE DIODE FOR AN ULTRASOUND IMAGING SYSTEM

Ralph Oppelt and Markus Vester, assignors to Siemens Aktiengesellschaft
11 March 1997 (Class 128/661.01); filed in Germany 19 May 1994

The variable capacitance diode in this duplexer is connected between a transducer element and a receiver. The direction of the diode is opposite that of pulses emitted by a unipolar transmitter. For bipolar transmit pulses, two variable capacitance diodes that operate in opposite directions are connected in series.—RCW

5,609,155

43.80.Vj ENERGY WEIGHTED PARAMETER SPATIAL/TEMPORAL FILTER

Ismayil M. Guracar, assignor to Acuson Corporation
11 March 1997 (Class 128/661.09); filed 26 April 1995

In a fluid flow the mean velocity, variance, and energy of Doppler ultrasound signals from the flow are first estimated from autocorrelation values of the signal to obtain a set of parameters for a particular sampling time or location. An averaging process is then performed on two sets of the parameters that correspond to a number of sampling times, or on two sets of parameters that correspond to a number of different locations. The filtered parameters are then compared to thresholds to reject noise and clutter.—RCW

5,613,940

43.80.Vj SYNTHESIZING ARRAY FOR THREE-DIMENSIONAL SOUND FIELD SPECIFICATION

Anthony J. Romano, Washington, DC
23 March 1997 (Class 601/2); filed 22 January 1993

A sound field specified at N locations in an acoustic or elastodynamic medium is synthesized using an array of N reciprocal transducers driven by N linearly independent inputs. To produce the field, the impulse response or dyadic Green's function matrix is determined. Then a system of N equations is solved to obtain for the appropriate inputs.—RCW

5,617,862

43.80.Vj METHOD AND APPARATUS FOR BEAMFORMER SYSTEM WITH VARIABLE APERTURE

Christopher R. Cole *et al.*, assignors to Acuson Corporation
8 April 1997 (Class 128/661.01); filed 2 May 1995

In this method and apparatus, an ultrasonic imaging system includes connections to one or more transducer arrays of at least M elements each, a transmit beamformer with N processors, and a receive beamformer with N processors. Separate transmit and receive multiplexers permit switching between transmit firings to any contiguous N -element transmit or receive apertures completely within a transducer array or straddled across two arrays. The transmit and receive apertures for a given firing may be independently placed and need not coincide. Beamforming to create synthetic apertures of $P \times N \leq M$ elements is accomplished with a multiplexing arrangement by coherently summing the receive beamformer predetected output from P acquisition firings.—RCW

5,617,864

43.80.Vj METHOD AND APPARATUS FOR POSITIONING AND ULTRASONIC TRANSDUCER AND A DISPLAY SCREEN

James R. Stouffer *et al.*, assignors to Animal Ultrasound Services, Incorporated
8 April 1997 (Class 128/662.03); filed 4 August 1995

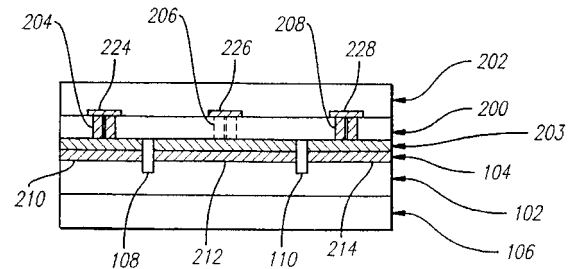
This method and apparatus allow the user to see simultaneously the device that positions the ultrasonic transducer and also the image that is being produced.—RCW

5,617,865

43.80.Vj MULTI-DIMENSIONAL ULTRASONIC ARRAY INTERCONNECT

Grazyna Palczewska and Ron Ho, assignors to Siemens Medical Systems
8 April 1997 (Class 128/662.03); filed 31 March 1995

In this interconnection arrangement, an ultrasonic transducer array with a piezoelectric ceramic layer 102 is separated in a longitudinal direction into n transducer groups. Each of these groups is separated in a transverse direction into m elements. A double-sided flex circuit 200 has a non-conductive base layer through which conductive vias 204, 206, 208 extend and are in electrical contact with a respective element. A conductive layer 203 on the bottom side of the flex is divided into a number of electrodes, each of which is in electrical contact with a respective one of the elements.



For each group, electrically conducting traces located on top of the flex circuit connect conductors in the flex circuit with external driving circuitry. Transducer groups with different numbers of elements are provided; some with element pairs excited by via common trace are for 1.5-D operation while others with separate traces for each element are for 2-D operation.—RCW

5,617,866

43.80.Vj MODULAR TRANSDUCER SYSTEM

Vaughn R. Marian, Jr., assignor to Acuson Corporation
8 April 1997 (Class 128/662.3); filed 5 January 1995

This system contains a small, handheld adapter that is permanently attached to an ultrasonic system console. The adapter permits rapid connection and disconnection of individual, sterilizable ultrasonic transducers. The individual transducers are easily stored at the site of the ultrasonic examination, and are submersible in a wide variety of liquids that include cleaning solutions and disinfectants.—RCW

5,619,998

43.80.Vj ENHANCED METHOD FOR REDUCING ULTRASOUND SPECKLE NOISE USING WAVELET TRANSFORM

Aiman A. Abdel-Malek, assignor to General Electric Company
15 April 1997 (Class 128/660.07); filed 11 March 1996

Signal-dependent noise in a coherent ultrasonic imaging system is reduced by nonlinear adaptive thresholding of received echo wavelet trans-

form coefficients. Steps in the method include: dividing the imaging system signal into a number of equal length subintervals; applying to each subinterval a discrete wavelet transformation that yields wavelet coefficients for a number of wavelet scales having different levels of resolution; deleting all of the coefficients that represent the finest wavelet scale; identifying for each

of the remaining scales the subinterval signal related to noise and to true signal through the use of adaptive nonlinear thresholding; selecting those coefficients that are identified with the true signal; setting to zero those coefficients identified as being related to noise; and inverse wavelet transforming the modified transform coefficients.—RCW

The dynamic coupling between piezoceramic actuators and a beam^{a)}

M. J. Brennan, S. J. Elliott, and R. J. Pinnington

ISVR, University of Southampton, Southampton, Hampshire SO17 1BJ, United Kingdom

(Received 24 March 1995; accepted for publication 23 October 1995)

This paper describes the coupling between piezoceramic actuators and flexural and longitudinal vibration of a beam. A comprehensive model, which incorporates the mass and stiffness of the actuator elements, is used to couple the actuators to a beam using the wave approach. Experimental results are presented, and it is shown that at high frequencies it is necessary to consider the dynamic loading of the actuator to accurately model the characteristics of the flexural vibration actuator. For the longitudinal actuator, however, it is shown that it is acceptable to neglect the dynamic loading of the actuator. The way in which the actuator affects the passive behavior of the beam is also considered by investigating the scattering of waves by the actuator. Wave scattering by a single-element piezoceramic actuator is also investigated and is shown to be negligibly small for the practical structures generally in current use. © 1997 Acoustical Society of America. [S0001-4966(97)04909-6]

PACS numbers: 43.10.Ln, 43.40.Vn, 43.40.Cw [PJR]

INTRODUCTION

Active control of beam vibration has been the subject of much research in recent years as the beam is a fundamental element of many structures. Vibrational energy propagates through such a structure in the form of flexural, longitudinal, and torsional waves, but much of the previous work has concentrated on the control of flexural waves, for example, Refs. 1–5. Recently, with the widespread use of piezoceramic elements,⁶ which are capable of acting both as flexural and longitudinal actuators, there has been research into the simultaneous control of flexural and longitudinal waves using this type of actuator.^{7,8} It is the coupling between a piezoceramic actuator and these wave types that is the subject of this paper.

Since the first model by Crawley and de Luis,⁶ which describes the static coupling of a piezoceramic actuator to a beam, several other models have been proposed that take into account the *static* loading of the actuator on the beam, for example, Refs. 9–11. Recently Charette *et al.*¹² have extended this analysis to investigate the *dynamic* loading effects of the actuator. These researchers developed a model of a single-element piezoceramic actuator fitted to a finite beam with arbitrary boundary conditions. Using Hamilton's principle together with the Rayleigh–Ritz method they modeled the dynamic behavior of the actuator coupled to the finite beam. This necessarily involved a *global* model of the structure which was complicated as it had to accommodate the modal behavior of the beam and the boundary conditions. Rivory *et al.*¹³ have also studied the coupling between a piezoceramic actuator and a finite beam. In their model of a two-element flexural vibration actuator fitted to a beam, they split the beam into active and passive sections, considering them separately, and then joining them together using appropriate

boundary conditions at the ends of the actuator. However, as they considered relatively small piezoceramic elements, they neglected the dynamic loading effects of the actuator. Their model was validated experimentally and was shown to describe adequately the behavior of the beam at its resonant frequencies, but at nonresonant frequencies the agreement between their predicted and experimental results was not as good. They concluded that this may have been because the impedance of the actuator was not included in their model.

A similar approach to that taken by Rivory *et al.*¹³ has been adopted in the work reported in this paper. The actuator and beam are split into active and passive sections which are modeled separately and then joined using suitable boundary conditions at the ends of the actuator. However, to keep the model simple, an infinite rather than a finite beam is used. The model expands on the one described by Gibbs and Fuller,¹⁴ where the beam response is modeled using flexural and longitudinal waves, and the actuator is modeled as a wave generator. The effects of the mass and stiffness of the actuator are investigated using the model, and experimental results are presented. The wave approach enables a *local* model of the structure to be developed which is much more simple than a global model as it does not have to incorporate the boundary conditions, or be able to describe the complicated modal behavior. One of the difficulties of this approach, however, is that to validate the model experimentally an “infinite” beam is required. As practical structures are finite in nature, then an “infinite” beam has to be approximated by fitting flexural and longitudinal anechoic terminations at the ends of the beam. Ways of accomplishing this are described and experimental results are presented.

Although the model of the actuator presented in this paper describes only the behavior of the structure in the vicinity of the actuator, it can be incorporated into complex structures by modeling uniform sections of beam as waveguides which can be represented by simple transformation matrices. Discontinuities in the structure can be modeled

^{a)}“Selected research articles” are ones chosen occasionally by the Editor-in-Chief that are judged (a) to have a subject of wide acoustical interest, and (b) to be written for understanding by broad acoustical readership.

using scattering matrices as described by von Flotow.¹⁵ Alternatively, the active section, including the impedance of the actuator, can be coupled to finite sections of beam in the way described by Rivory *et al.*¹³ In this paper the methods of Pines and von Flotow,² and Gibbs and Fuller¹⁴ are combined to describe the coupling between a piezoceramic actuator and a beam, and it is shown that a model of this complexity is required to describe accurately the coupling between a piezoceramic actuator configured to induce flexural motion.

The basic method applied in Sec. I of this paper uses the static models of a perfectly bonded actuator, which are well understood, to relate the voltages applied to the piezoceramic elements and the moments and forces generated by the actuator. These moments and forces are then treated as wave generators in the dynamic model of the structure as described by Brennan *et al.*¹⁶ The main part of the paper focuses on an actuator consisting of two elements, which are fitted to opposite sides of a beam. This is because this type of actuator can generate any combination of flexural and longitudinal waves provided that the piezoceramic elements are driven independently, as discussed by Gibbs and Fuller.¹⁴ As the model includes the mass and stiffness of the actuator, an examination of the passive effects of the actuator is also possible. In order to compare piezoceramics with other actuators, we can ignore these passive effects and this enables a simple analytical model to be developed. This simplified model, which is discussed in Sec. II, gives physical insight into the parameters which govern the relative magnitudes of the two wave types generated for a given applied voltage. In Sec. III, experimental observations are used to validate these theoretical models.

With a two-element actuator the generated flexural and longitudinal motion of the beam are uncoupled due to the symmetry of the device. However, if a single-element actuator, such as that described by Charette *et al.*¹² and Gibbs and Fuller,¹⁴ is fitted to a beam, the generated flexural and longitudinal motions are coupled. Both flexural and longitudinal waves are generated in response to a voltage applied to the actuator, and the passive effects of the actuator involve scattering between flexural and longitudinal waves and vice

versa. This is investigated theoretically in Sec. IV. There is also an Appendix which describes the design of the experimental rig and presents experimental results which characterize the behavior of the anechoic terminations.

I. TWO-ELEMENT ACTUATOR THEORY

The two-element actuator considered in this paper is shown in Fig. 1, where it is fitted to an infinite uniform beam. If the piezoceramic elements are driven in-phase, they generate a pair of in-plane forces F , which induce purely longitudinal motion, and if they are driven in anti-phase, they generate a pair of moments M , which induce purely flexural motion. The actuator can be considered as a wave generator as discussed by Brennan *et al.*,¹⁶ and this is depicted in Fig. 1, where A_1 and A_2 are flexural near-field waves, A_3 and A_4 are flexural propagating waves, and A_l and A_r are left- and right-going longitudinal waves. Assuming a linear system and applying the principle of superposition, both flexural and longitudinal waves can be generated simultaneously by applying appropriately phased voltages to the piezoceramic elements in a similar way to that discussed by Gibbs and Fuller.¹³ If the mass and stiffness of the piezoceramic elements are to be included in the theoretical model, then for the purpose of analysis the section of beam to which the piezoceramic elements are fixed has to be separated from the rest of the beam as shown in Fig. 2. It can be seen that the beam now has an active section which is connected to two passive sections. This model is similar to that discussed by Pines and von Flotow² and Miller,¹⁷ but as the piezoceramic elements are driven independently it includes both flexural and longitudinal motions. The principle behind the model is that as waves propagate independently on the uniform active and passive sections of the beam, these sections can be modeled using spatial transformation matrices. At each end of the actuator the waves are transformed to state vectors, and the passive beam sections are then coupled to the active section through these state vectors. The relationship between a state vector and the waves present on the beam at one of these junctions is given by the equation

$$\begin{bmatrix} u \\ w \\ \theta \\ M \\ Q \\ F \end{bmatrix} = \begin{bmatrix} u \\ w \\ w' \\ E_b I_b w'' \\ E_b I_b w''' \\ E_b S_b u' \end{bmatrix} = \begin{bmatrix} 0 & 0 & 1 & 0 & 0 & 1 \\ 1 & 1 & 0 & 1 & 1 & 0 \\ k_f & jk_f & 0 & -k_f & -jk_f & 0 \\ E_b I_b k_f^2 & -E_b I_b k_f^2 & 0 & E_b I_b k_f^2 & -E_b I_b k_f^2 & 0 \\ E_b I_b k_f^3 & -jE_b I_b k_f^3 & 0 & -E_b I_b k_f^3 & jE_b I_b k_f^3 & 0 \\ 0 & 0 & jk_l E_b S_b & 0 & 0 & -jk_l E_b S_b \end{bmatrix} \begin{bmatrix} A_1 \\ A_3 \\ A_l \\ A_2 \\ A_4 \\ A_r \end{bmatrix} \quad (1a)$$

where the wave components are defined in Fig. 1 and the sign convention is shown in Fig. 3. Here ' denotes the spatial derivative with respect to x , k_f is the flexural wave number, and k_l is the longitudinal wave number of the beam itself, j is $\sqrt{-1}$, E is Young's modulus, S is the cross-sectional

area, I is the second moment of area, and the subscript b denotes the beam. Equation (1a) can be written as

$$\mathbf{h} = \mathbf{H} \mathbf{a} \quad (1b)$$

where \mathbf{h} is the state vector, \mathbf{H} is the transformation matrix,

and \mathbf{a} is the vector of wave amplitudes. Force balance and continuity of displacement at the junctions can be applied to give the relationships between the state vectors at the junctions and the applied moments and forces. These are in turn related to the moments and in-plane forces generated at the ends of the actuator, which gives

$$\mathbf{h}_{Lp} = \mathbf{h}_{La} + \begin{bmatrix} 0 \\ 0 \\ 0 \\ M \\ 0 \\ F \end{bmatrix} \quad (2)$$

and

$$\mathbf{h}_{Rp} = \mathbf{h}_{Ra} + \begin{bmatrix} 0 \\ 0 \\ 0 \\ M \\ 0 \\ F \end{bmatrix}, \quad (3)$$

where the subscripts a and p denote the active and passive sections of the beam, and L and R are the left- and right-hand junctions as depicted in Fig. 2. These equations show that the state vectors on the passive sides of the junctions are equal to the state vectors on the active sides of the junction plus the moments and forces generated at the ends of the actuator. The moments and forces are related to the out-of-phase and in-phase components of the voltages V_0 and V_i , that are applied to the piezoceramic elements. These are given by

$$M = \alpha V_0, \quad (4a)$$

$$F = \beta V_i, \quad (4b)$$

where the coefficients α and β are the gains of the actuators. It should be noted that in the formulation used in this paper these moments and forces are those induced by the piezoceramic elements in the *active* section of the beam. Previous work, for example, Refs. 9 and 10, related the moments and forces induced in the *passive* beam by the piezoceramic elements. The coefficient α , derived in Ref. 9, is used in this work but it has been modified to account for the passive properties of the piezoceramic elements. For an actuator which has the same width as the beam it is given by

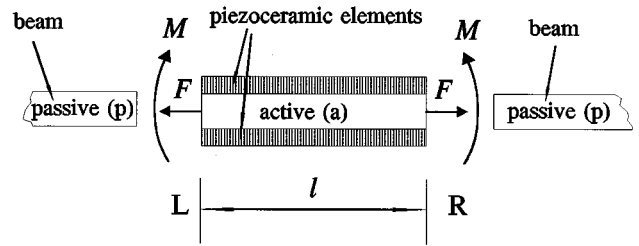


FIG. 2. Diagram showing the active and passive sections of the beam.

$$\alpha = \frac{M}{V_0} = \left(\frac{2E_b I_a}{t_b} \right) \left(\frac{6(1+T)}{6 + E_b/E_p T + 12T + 8T^2} \right) \frac{d_{31}}{t_p}, \quad (5)$$

where I_a is the effective second moment of area of the active section of the beam comprising the beam and the piezoceramic elements (the effective second moment of area accounts for the different Young's moduli of the beam and the piezoceramic elements), t_p is the thickness of the piezoceramic elements, $T = t_p/t_b$ is the thickness ratio of the piezoceramic elements to the beam, and d_{31} is the piezoelectric constant. It is interesting to note that for the actuator to induce a maximum bending strain in the beam for a given electric field $E = V_0 d_{31}/t_b$, there is an optimal thickness ratio as discussed in Refs. 9 and 11. The coefficient β is taken from Ref. 9, but as with the coefficient α it has been modified to account for the passive properties of the piezoceramic elements. For an actuator which has the same width as the beam this is given by

$$\beta = \frac{f}{V_i} = \left(\frac{2E_b S_a}{6 + E_b/E_p T} \right) \frac{d_{31}}{t_p}, \quad (6)$$

where S_a is the effective cross-sectional area of the active section (the effective area accounts for the different Young's moduli of the piezoceramic elements and the beam). The out-of-phase and in-phase voltages are related to the voltages V_1 and V_2 , applied separately to the actuator elements by

$$\begin{bmatrix} V_0 \\ V_i \end{bmatrix} = \begin{bmatrix} 1 & -\cos \phi \\ 1 & \cos \phi \end{bmatrix} \begin{bmatrix} V_1 \\ V_2 \end{bmatrix}, \quad (7)$$

where ϕ is the phase angle between the applied voltages V_1 and V_2 . Thus, given the applied voltages, the generated moments and forces can be determined using Eqs. (4)–(7). As mentioned previously, these moments and forces act as wave generators and are incorporated into the dynamic model by way of the state vectors at the ends of the actuator. Thus,

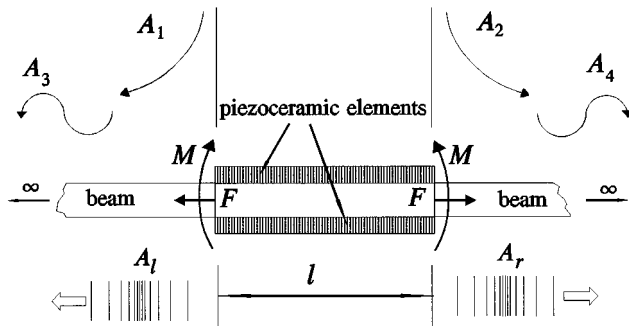


FIG. 1. A two-element piezoceramic actuator.

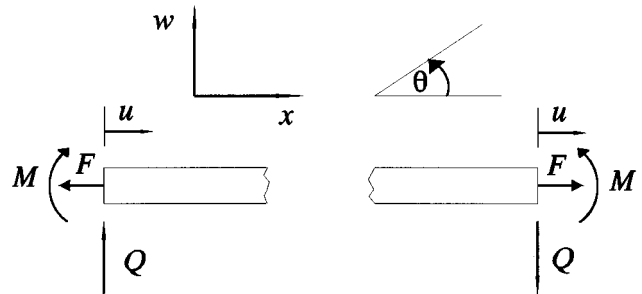


FIG. 3. Sign convention used with the state vectors.

Eqs. (2) and (3) can be transformed into wave-mode coordinates using Eq. (1b) to give

$$\mathbf{H}_p \mathbf{a}_{Lp} = \mathbf{H}_a \mathbf{a}_{La} + \begin{bmatrix} 0 \\ 0 \\ 0 \\ M \\ 0 \\ F \end{bmatrix} \quad (8)$$

and

$$\mathbf{H}_p \mathbf{a}_{Rp} = \mathbf{H}_a \mathbf{a}_{Ra} + \begin{bmatrix} 0 \\ 0 \\ 0 \\ M \\ 0 \\ F \end{bmatrix}, \quad (9)$$

where \mathbf{H}_a includes the mass and stiffness of the beam and the actuator elements and \mathbf{H}_p includes the mass and stiffness of the beam only. The relationship between the wave vectors \mathbf{a}_{Ra} and \mathbf{a}_{La} is given by

$$\mathbf{a}_{Ra} = \mathbf{T}_a \mathbf{a}_{La}, \quad (10)$$

where \mathbf{T}_a is the spatial transformation matrix for the active section of beam and is given by

$$\mathbf{T}_a = \begin{bmatrix} e^{k_{fa}l} & 0 & 0 & 0 & 0 & 0 \\ 0 & e^{jk_{fa}l} & 0 & 0 & 0 & 0 \\ 0 & 0 & e^{jk_{la}l} & 0 & 0 & 0 \\ 0 & 0 & 0 & e^{-k_{fa}l} & 0 & 0 \\ 0 & 0 & 0 & 0 & e^{-jk_{fa}l} & 0 \\ 0 & 0 & 0 & 0 & 0 & e^{-jk_{la}l} \end{bmatrix}, \quad (11)$$

where k_{fa} and k_{la} are the flexural and longitudinal wave numbers of the active section of beam which includes the beam and the piezoceramic elements. Substituting Eqs. (8) and (9) into Eq. (10) gives, after rearranging,

$$\mathbf{H}_p \mathbf{a}_{Rp} = \mathbf{H}_a \mathbf{T}_a \mathbf{H}_a^{-1} \mathbf{H}_p \mathbf{a}_{Lp} + \mathbf{Q}, \quad (12)$$

where

$$\mathbf{Q} = \mathbf{H}_a \mathbf{T}_a \mathbf{H}_a^{-1} \begin{bmatrix} 0 \\ 0 \\ 0 \\ -M \\ 0 \\ -F \end{bmatrix} + \begin{bmatrix} 0 \\ 0 \\ 0 \\ M \\ 0 \\ F \end{bmatrix}. \quad (13)$$

Equation (12) can be rearranged into a partitioned matrix equation to give the waves at junctions L and R in terms of the moments and forces applied:

$$[\mathbf{H}_p] - \mathbf{H}_a \mathbf{T}_a \mathbf{H}_a^{-1} \mathbf{H}_p \begin{bmatrix} \mathbf{a}_{Rp} \\ \mathbf{a}_{Lp} \end{bmatrix} = \mathbf{Q}. \quad (14)$$

This equation can be further rearranged to group the waves into incoming and outgoing waves. This actuator can therefore be represented by the simple block diagram shown in

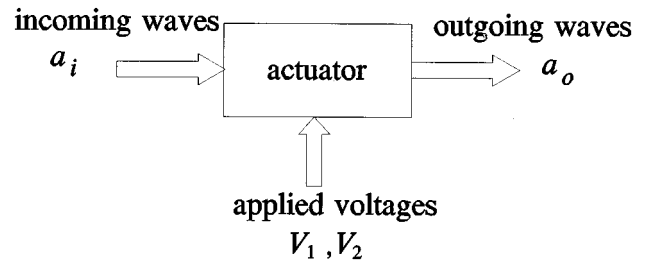


FIG. 4. Conceptual diagram of a piezoceramic actuator as a wave generator.

Fig. 4, and the expression relating the waves to the applied moments and forces is given by

$$\mu \mathbf{a}_i + \gamma \mathbf{a}_o = \mathbf{Q}, \quad (15)$$

where the wave vectors are given by

$$\mathbf{a}_i = \begin{bmatrix} A_{R1} \\ A_{R3} \\ A_{R1} \\ A_{L2} \\ A_{L4} \\ A_{Lr} \end{bmatrix} \quad (16a)$$

and

$$\mathbf{a}_o = \begin{bmatrix} A_{L1} \\ A_{L3} \\ A_{L1} \\ A_{R2} \\ A_{R4} \\ A_{Rr} \end{bmatrix}, \quad (16b)$$

and the matrices are given by

$$\mu = [(\mathbf{H}_p)_1 | (\mathbf{H}_p)_2 | (\mathbf{H}_p)_3 | (-\mathbf{H}_a \mathbf{T}_a \mathbf{H}_a^{-1} \mathbf{H}_p)_4 | \\ \times (-\mathbf{H}_a \mathbf{T}_a \mathbf{H}_a^{-1} \mathbf{H}_p)_5 | (-\mathbf{H}_a \mathbf{T}_a \mathbf{H}_a^{-1} \mathbf{H}_p)_6] \quad (17)$$

and

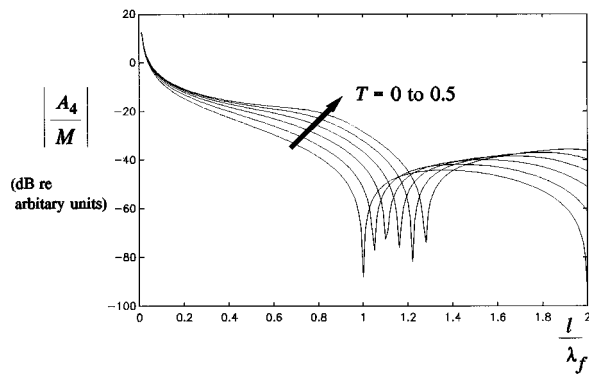
$$\gamma = [(-\mathbf{H}_a \mathbf{T}_a \mathbf{H}_a^{-1} \mathbf{H}_p)_1 | (-\mathbf{H}_a \mathbf{T}_a \mathbf{H}_a^{-1} \mathbf{H}_p)_2 | \\ \times (-\mathbf{H}_a \mathbf{T}_a \mathbf{H}_a^{-1} \mathbf{H}_p)_3 | (\mathbf{H}_p)_4 | (\mathbf{H}_p)_5 | (\mathbf{H}_p)_6], \quad (18)$$

where the subscripts 1–6 denote the columns of the respective matrices given in the curved brackets. Equation (15) gives a complete description of the active and passive effects of the actuator. The waves generated by the actuator in terms of the applied moments and forces can be determined by setting the incoming wave vector \mathbf{a}_i to zero and rearranging to give

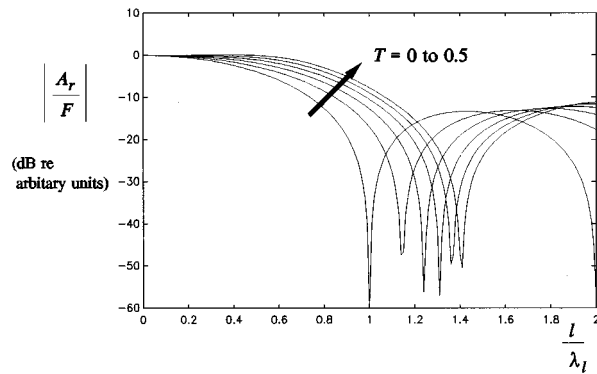
$$\mathbf{a}_o = \gamma^{-1} \mathbf{Q}. \quad (19)$$

The amplitudes of the generated propagating flexural and longitudinal waves are plotted as functions of the length of the piezoceramic actuator (on the beam) divided by the respective wavelengths in Fig. 5(a) and (b) for thickness ratio T , ranging from 0 to 0.5.

To examine the passive behavior of the piezoceramic elements, the applied moment has been increased with the thickness of the elements to maintain a constant *static* bending strain in the beam beneath the actuator, independent of



(a)

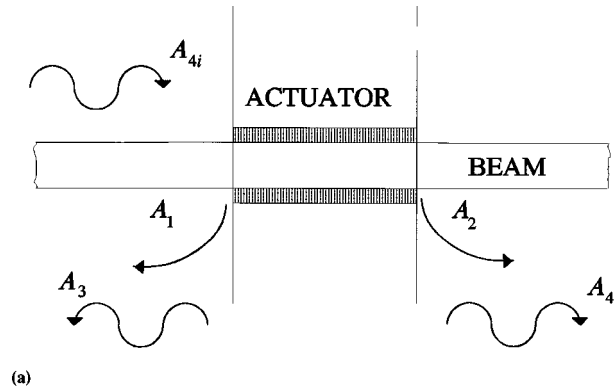


(b)

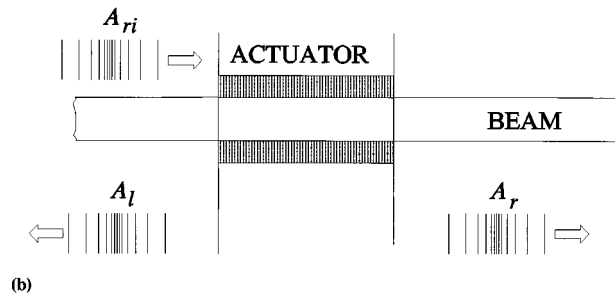
FIG. 5. Amplitudes of the lateral and longitudinal waves generated when the two-element piezoceramic actuator is driven (a) out-of-phase and (b) in-phase.

the thickness of the actuator elements. These figures show that the mass and stiffness of the piezoceramic elements have an effect on the amplitudes of the generated propagating waves. When the thickness of the piezoceramic elements are zero, which is equivalent to assuming that the elements have negligible mass and stiffness, then the amplitudes of the propagating waves reduce to zero when the length of the actuator equals an integer number of wavelengths of the generated propagating waves. For longitudinal motion this occurs at very high frequencies; for example, if a 100-mm-long actuator is fitted to a steel or aluminium beam, this occurs around 50 kHz, and is thus not a problem in most practical situations. For flexural motion, with the same actuator fitted to a 6-mm aluminium beam, this occurs at about 7 kHz and could thus be a problem, which is demonstrated later in the paper. It can be seen that at higher frequencies, and as the thickness of the piezoceramic elements is increased, the amplitudes of the propagating waves also increase. A possible reason for this is that the applied moment has to excite both the passive sections of beam and the thicker active section. At low frequencies the active section is seen as a stiffness by the applied moment rather than a beam section due to its relatively short length. As the impedance of a stiffness is proportional to $1/\text{frequency}$ and the impedance of a beam is proportional to $1/\text{frequency}^{1/2}$, the proportion of the applied moment available to drive the beam rather than the actuator increases with frequency.

The passive effects of the actuator can be determined by



(a)



(b)

FIG. 6. Scattering of waves by the two-element piezoceramic actuator: (a) scattering of flexural waves and (b) scattering of longitudinal waves.

setting the applied moments and forces to zero, and the outgoing waves can then be determined in terms of the incoming waves, i.e.,

$$\mathbf{a}_0 = -\boldsymbol{\gamma}^{-1} \boldsymbol{\mu} \mathbf{a}_i. \quad (20)$$

As the actuator is symmetric there is no scattering between longitudinal and flexural waves. An incident flexural wave will scatter into reflected and transmitted near-field and propagating waves as illustrated in Fig. 6(a), and an incident longitudinal wave will scatter into transmitted and reflected longitudinal waves as illustrated in Fig. 6(b). The way in which these two incident waves scatter into other wave types can be seen in Fig. 7, which has been calculated using the formulation above, Eq. (20), for various thickness ratios T . A check was made on the calculations; the amplitudes of the positive- and negative-going outgoing propagating waves were squared and summed and divided by the square of the incident propagating wave to check that this was unity. This is a necessary condition for any conservative junction as the power flow into the junction must equal the power flow out of the junction. Examination of Fig. 7(a)–(d) shows that a thicker actuator has a greater passive effect than a thinner actuator, as expected. It can also be seen that the amplitudes of the scattered waves are dependent on both the thickness ratio and frequency. The amplitude of the transmitted A_4 wave is at most attenuated by about 20% for a thickness ratio of 0.5, which means that the incident propagating wave would generally pass through most practical actuators without a large degree of attenuation. However, a near-field A_2 wave is generated and this amplitude increases to about 50% of the amplitude of the incident propagating wave for the same thickness ratio. The reflected negative-going flexural waves have surprisingly large amplitudes. The A_1 wave has

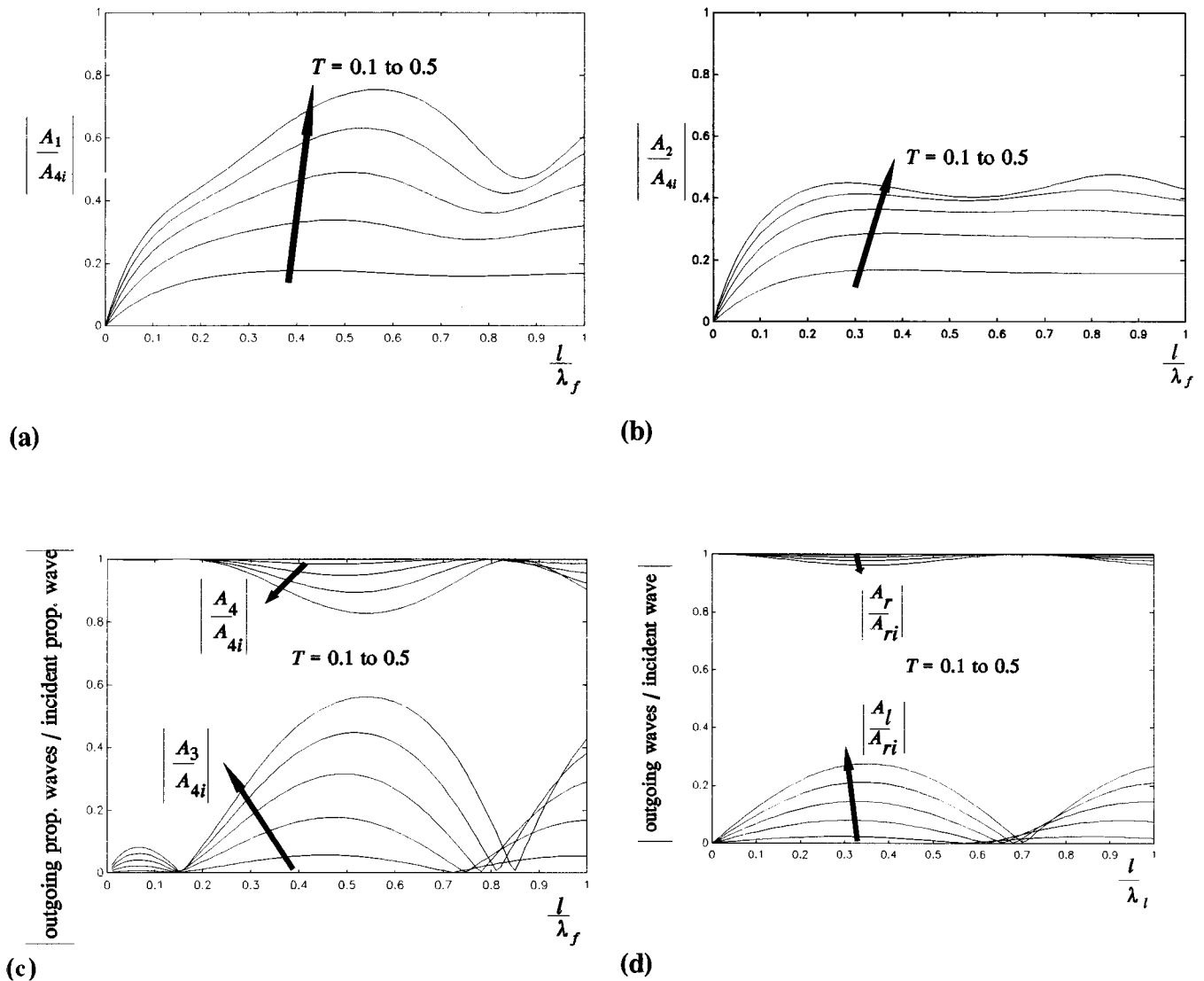


FIG. 7. Reflected and transmitted propagating and near-field flexural waves due to an incident propagating flexural wave and the passive effects of the two-element piezoceramic actuator, (a), (b), and (c), and the reflected and transmitted longitudinal waves due to an incident longitudinal wave (d) for various thickness ratios T , of the actuator to the beam: (a) reflected A_1 wave, (b) transmitted A_2 wave, (c) reflected and transmitted flexural A_3 and A_4 waves propagating waves, and (d) reflected and transmitted A_l and A_r longitudinal waves.

an amplitude approaching about 80% of the incident propagating wave for a thickness ratio of 0.5 and the A_3 wave has an amplitude of almost 60% of the incident wave for the same thickness ratio, but this varies considerably with frequency. This frequency-dependent behavior is similar to that of a spatially periodic structure as discussed by Cremer *et al.*,¹⁸ where there are frequencies at which the incident wave is transmitted readily and there are frequencies when the wave is reflected.

II. COMPARISON OF TWO-ELEMENT PIEZOCERAMIC ACTUATORS WITH OTHER ACTUATORS

The model of the actuator described above is comprehensive and allows analysis of the active and passive effects of the actuator. However, it is complicated and thus it is difficult to gain physical insight into other aspects of the actuator's behavior. Therefore a simplified model is used that ignores the passive effects of the piezoceramic elements and

this is shown in Fig. 8. The relationship between the generated flexural waves on either side of the actuator and the applied moments is given by¹⁶

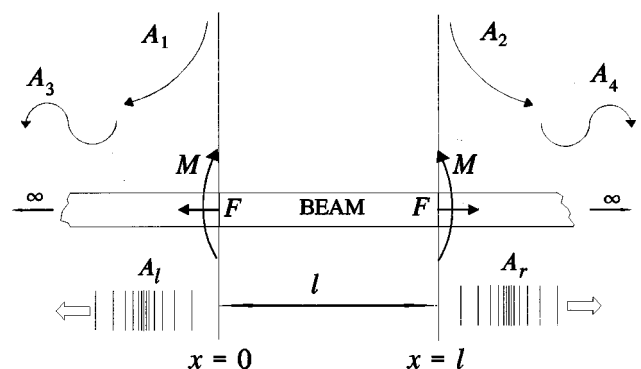


FIG. 8. Simplified model of a piezoceramic actuator fitted to a beam.

$$\begin{bmatrix} A_1 \\ A_2 \\ A_3 \\ A_4 \end{bmatrix} = \frac{1}{4E_b I_b k_f^2} \begin{bmatrix} 1 & e^{-k_f l} \\ -1 & -e^{k_f l} \\ -1 & -e^{-j k_f l} \\ 1 & e^{j k_f l} \end{bmatrix} \begin{bmatrix} -M \\ M \end{bmatrix}, \quad (21)$$

and the relationship between the generated longitudinal waves and the applied forces is given by¹⁶

$$\begin{bmatrix} A_l \\ A_r \end{bmatrix} = \frac{-j}{2k_l E_b S_b} \begin{bmatrix} 1 & e^{-j k_l l} \\ 1 & e^{j k_l l} \end{bmatrix} \begin{bmatrix} -F \\ F \end{bmatrix}. \quad (22)$$

The moments and forces are related to the out-of-phase and in-phase applied voltages, respectively, in a similar way to the complete model. However, the coefficients α and β are now smaller as the effects of the piezoceramic elements are ignored. It should be noted that the amplitudes of the generated waves predicted by these simple models are the same as those for the comprehensive model with the thickness of the elements is set to zero [see Fig. 5(a) and (b)].

The simple model allows comparison with other actuators that could be used as secondary sources in an active control system, such as force and moment actuators. To compare these cases, the power supplied to an infinite beam by the various actuators is calculated. If a lateral point force is applied to an infinite beam, then the flexural power that it supplies, P_f , is given by¹⁹

$$P_f = \frac{\omega |F|^2}{8E_b I_b k_f^3}. \quad (23)$$

The power supplied by a line moment is given by¹⁹

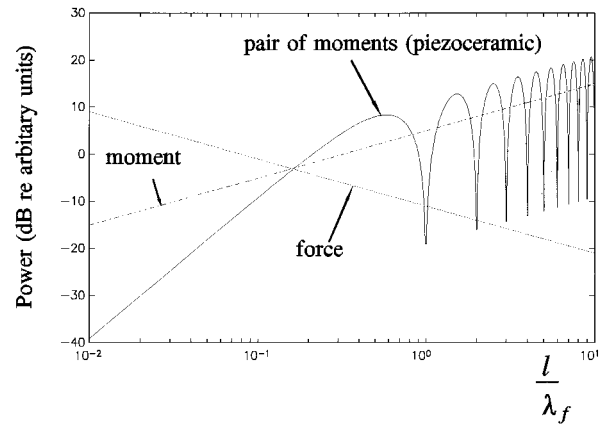
$$P_f = \frac{\omega |M|^2}{8E_b I_b k_f}. \quad (24)$$

The power supplied by a pair of moments a distance l apart, as shown in Fig. 8, is given by¹⁶

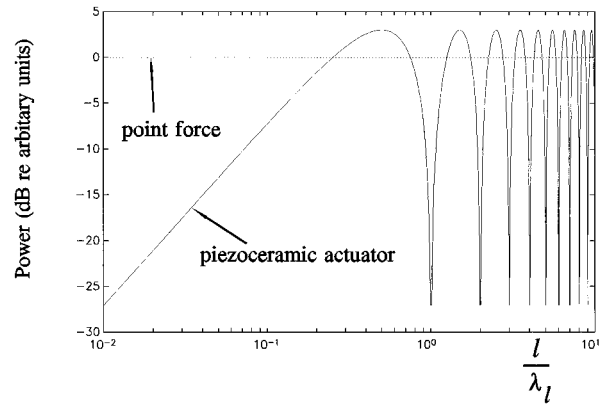
$$P_f = \frac{\omega |M|^2}{4E_b I_b k_f} (1 - \cos k_f l). \quad (25)$$

The power supplied by these actuators is plotted in Fig. 9(a) as a function of the length of the piezoceramic actuator divided by a flexural wavelength. For the generation of this graph the moments have a magnitude set equal to the product of the force and the length between the pair of moments l , and the power supplied by each actuator is normalized to this force. It can be seen that at low frequencies the force actuator supplies more power than the other two actuators. However, the other actuators supply more power as frequency increases, with the result that above a certain frequency the moment and piezoceramic actuators supply more power than the force actuator. At frequencies when the length of the piezoceramic actuator equals an integer number of flexural wavelengths, however, the power supplied by this actuator reduces to zero. It is clear that this actuator should ideally be operated in frequency regions close to where the length of the actuator is equal to an odd-integer number of half-flexural wavelengths.

The power supplied by an in-plane point force on an infinite beam is given by¹⁹



(a)



(b)

FIG. 9. Comparison of the power supplied to a beam by various actuators. (a) power supplied by actuators inducing lateral motion and (b) power supplied by actuators inducing longitudinal motion.

$$P_l = \frac{\omega |F|^2}{2k_l E_b S_b}, \quad (26)$$

and the power supplied by a pair of in-plane, in-phase forces such as that shown in Fig. 8 is given by¹⁶

$$P_l = \frac{\omega |F|^2}{2k_l E_b S_b} (1 - \cos k_l l). \quad (27)$$

These are plotted in Fig. 9(b) normalized to Eq. (26). It can be seen that the point force supplies much more power than the piezoceramic actuator at low frequencies, but at higher frequencies the maximum power supplied by the piezoceramic actuator is 3 dB greater than this. The trends for the flexural and longitudinal power supplied by a piezoceramic actuator are similar. At low frequencies, the power supplied is very small but increases with frequency until the length of the actuator equals half a longitudinal wavelength. The power then reduces to zero when the length of the actuator equals a whole wavelength. This pattern repeats with increasing frequency, but, unlike the flexural power, the maximum level of power supplied by the in-plane forces does not carry on increasing due to the nondispersive nature of longitudinal waves. The power equations (25) and (27) are similar to those derived by Gibbs and Fuller,¹⁴ but are written in

terms of the forcing function rather than the voltage supplied.

As these actuators have been proposed as suitable devices to simultaneously control flexural and longitudinal waves in a beam, see, for example Refs. 7 and 8, it is worth comparing the flexural and longitudinal power supplied to an infinite beam for a given supply voltage. A convenient way of doing this is to calculate the power transmitted in longitudinal and flexural waves as no power is transmitted in a flexural near-field wave provided it does not interact with other near-field waves. The power transmitted in a longitudinal wave A_r is given by¹⁹

$$P_l = \frac{1}{2} E_b S_b k_l \omega |A_r|^2, \quad (28)$$

and the power carried in a propagating flexural wave is given by

$$P_f = E_b I_b k_f^3 \omega |A_4|^2. \quad (29)$$

The ratio of these powers can thus be calculated by dividing Eq. (28) by (29). If we assume that the beam has a rectangular cross section, then

$$\frac{S_b}{I_b} = \frac{12}{t_b^2} \quad (30a)$$

and

$$k_l = \frac{t_b}{\sqrt{12}} k_f^2, \quad (30b)$$

and by combining Eqs. (28) and (29) with Eqs. (30a) and (30b), the ratio of the longitudinal to flexural power is given by

$$\frac{P_l}{P_f} = \frac{\sqrt{3}}{t_b k_f} \frac{|A_r|^2}{|A_4|^2}. \quad (31)$$

Consider now a pair of piezoceramic elements first being driven in-phase to generate an in-plane force F and producing a longitudinal wave A_r , and then the same elements being driven out-of-phase to generate a pair of moments M producing a flexural wave A_4 . By taking low-frequency approximations of the amplitudes of these waves given by Eqs. (21) and (22), i.e., assuming that $k_f l$ and $k_l l$ are much less than one, then, provided that the piezoceramic actuator is thin compared to the beam so that for the same in-phase and out-of-phase voltages $M \approx F t_b / 2$, the ratio of the amplitudes of the generated waves is given by

$$\left| \frac{A_r}{A_4} \right| \approx \frac{t_b}{3l} k_f. \quad (32)$$

If Eqs. (31) and (32) are combined, and noting that $k_f = 2\pi/\lambda_f$, where λ_f is a flexural wavelength, the ratios of the powers at low frequencies become

$$\frac{P_l}{P_f} = \frac{2\pi}{\sqrt{27}} \frac{t_b}{l} \frac{l}{\lambda_f}. \quad (33)$$

The ratio of the longitudinal to flexural power given by Eq. (31) together with the low-frequency approximation given by Eq. (33) are plotted in Fig. 10 as a function of the length of

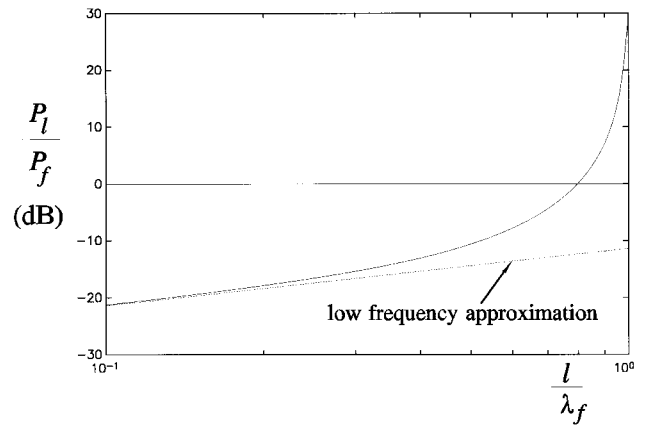


FIG. 10. Ratio of the longitudinal power to the flexural power supplied to a beam by a piezoceramic actuator where the thickness of the beam to the length of the actuator is 0.06.

the actuator divided by a flexural wavelength. It is clear from this figure that for a given magnitude of supply voltage the actuator generates more flexural power at low frequencies, but, above about four-fifths of a flexural wavelength, more longitudinal power is supplied to the beam. Examination of Eq. (33) shows that the important parameter that influences the ratio of the powers supplied at low frequencies is the thickness of the beam compared to the length of the actuator. For the graph in Fig. 10 this ratio is 0.06.

III. EXPERIMENTAL VALIDATION

An experiment was set up to validate the theory developed above. In order to do this simply a beam had to be configured so that it had both flexural and longitudinal anechoic terminations at each end. This was achieved by using exponentially shaped foam rubber for the flexural terminations and steel plates for the longitudinal terminations. The effectiveness of this arrangement is discussed in the Appendix. A schematic of the experimental rig is shown in Fig. 11 and the properties of the beam, plates, and actuator elements are given in Table I. The actuator was first driven with voltage V_0 over the frequency range 100 Hz to 1 kHz such that the actuator elements were forced in antiphase so that only flexural waves were generated. The amplitude of acceleration a_4 of the A_4 propagating wave was measured using

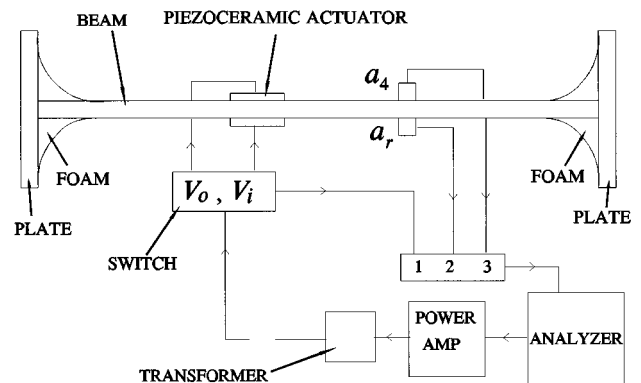


FIG. 11. Experimental setup to measure the flexural and longitudinal waves generated by the piezoceramic actuator.

TABLE I. Material properties of the beam, end plates, and PZT elements.

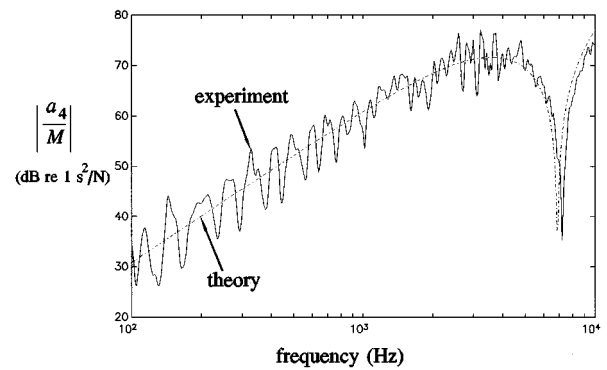
Beam	
Material	aluminium alloy
Density	2720 kg m ⁻³
Young's modulus	68.9 GN m ⁻²
Length	5 m
Width	30 mm
Thickness	6 mm
Plates	
Material	Mild steel
Density	7850 kg m ⁻³
Young's modulus	210 GN m ⁻²
Thick plate	3.29 mm (1/8")
Thin plate	1.65 mm (1/16")
Dimension	0.8 m×0.8 m
Piezoceramic (PZT) elements	
Young's modulus	59.5 GN m ⁻²
Density	7300 kg m ⁻³
Width	20 mm
Length	100 mm
Thickness	1.5 mm
Piezoelectric constant, d_{31}	212×10 ⁻¹² V m ⁻¹

an accelerometer and the frequency response function (FRF) a_4/V_0 was calculated using a Hewlett–Packard frequency response analyzer type 3566A. The FRF was multiplied by the gain of the transformer (which was 5) and the gain of the actuator calculated using Eq. (5) to give acceleration per unit moment applied. This is plotted in Fig. 12(a) together with the predicted response calculated using Eq. (19).

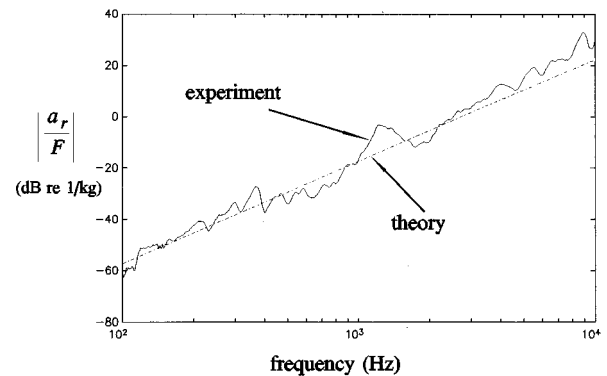
The actuator was then driven with voltage V_i over the same frequency range such that the piezoceramic elements were forced in-phase and only longitudinal waves were generated. The amplitude of acceleration a_r of the A_r wave was measured and the frequency response function a_r/V_i calculated by the analyzer. This was multiplied by the gain of the transformer, and the gain of the actuator calculated using Eq. (6), and the result is plotted in Fig. 12(b) together with the predicted response calculated using Eq. (19) or (22).

These figures show that the models of the static and the dynamic coupling of the actuator to the beam developed in this paper are reasonable representations of the actuator. The uneven nature of the measured responses is due to the imperfect anechoic terminations. It proved necessary to use a comprehensive model of the actuator that includes the passive effects of the piezoceramic elements to predict accurately the flexural behavior of the actuator, especially at high frequencies. To examine the difference between the comprehensive and simplified models, the predicted responses of the beam using these models are plotted in Fig. 13. It can be seen that at high frequencies, the difference between the predicted responses is significant. The simplified model, however, was found to be adequate to describe the longitudinal behavior over the frequency range tested, since in the experimental rig the thickness ratio of the piezoceramic elements to the beam was 0.25, and at 1 kHz the length of the actuator is only 0.02 of a longitudinal wavelength.

The measured ratio of the longitudinal to the flexural wave amplitudes for a given supply voltage can be calculated by dividing the measured FRFs, and the predicted ratio of



(a)



(b)

FIG. 12. Acceleration amplitudes of the flexural and longitudinal waves generated by the two-element piezoceramic actuator. (a) Acceleration amplitude of propagating flexural per unit moment applied. (b) Acceleration amplitude of the generated longitudinal wave per unit force applied.

wave amplitudes can be calculated using Eq. (19). These are plotted in Fig. 14. The gains relating the out-of-phase voltage to the applied moment and the in-phase voltage to the applied force were not used in the theoretical prediction; it was simply assumed that the moment applied when the piezoceramic elements were driven in antiphase was equal in magnitude to the product of the applied in-plane force when the piezoceramic elements were driven in-phase times half the thickness of the beam. The predicted and the measured results agree reasonably well (noting that the uneven nature of

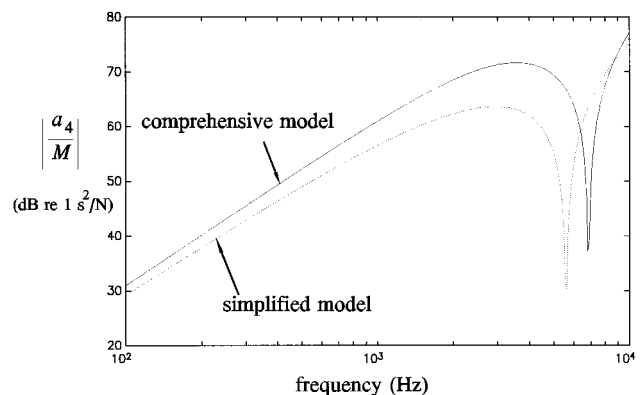


FIG. 13. The response of a beam to excitation by a two-element piezoceramic actuator showing the effects of neglecting the mass and stiffness of the piezoceramic elements (simplified model).

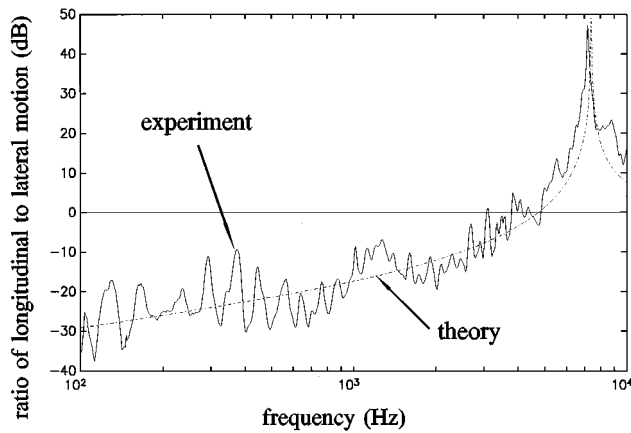


FIG. 14. Ratio of the longitudinal to flexural waves generated by the two element piezoceramic actuator.

the measured results is due to the imperfect anechoic terminations). With the actuator configuration used in the experiments it is clear that the amplitude of the generated longitudinal wave is much less than the flexural wave except at frequencies close to where the length of the actuator is half a flexural wavelength. As discussed above, the controlling factor that governs the ratio of these waves at low frequencies is the thickness of the beam compared to the length of the actuator.

IV. SINGLE-ELEMENT ACTUATOR

There are some situations where the use of a single-element actuator has been proposed. Although these are mainly on plates, Charette *et al.*¹² has suggested its use on a beam, as it leaves a free surface on the other side of the beam that can be used to fit a collocated sensor. One of the problems with this arrangement, however, is that it is not possible for the actuator to generate flexural and longitudinal waves independently. Any voltage applied to the actuator generates both flexural and longitudinal waves. Also, the passive waveguide behavior is coupled through the asymmetry of the configuration, so that flexural waves scatter into longitudinal waves and vice versa. The purpose of this section is to describe a model of the actuator so that these effects can be studied. A model similar to that discussed in Sec. I can be developed to describe this type of actuator. As the active section is now asymmetric due to the single element, the longitudinal internal force at the junction between the active and passive sections does not act on the neutral axis of the active section. Thus an additional moment of magnitude Fd

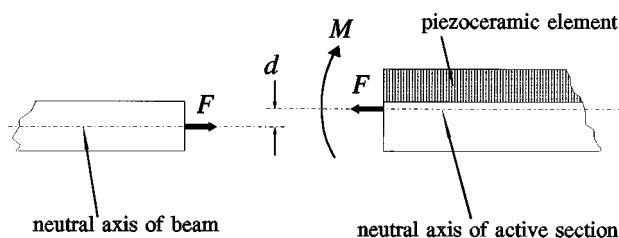


FIG. 15. Junction between the active section of beam containing a single-element piezoceramic actuator and the passive beam.

(where $d = E_p/E_b * t_p/2$ is the distance between the neutral axes of the active and passive sections of the structure) is applied to the active section as shown in Fig. 15. It is this moment that couples the passive flexural and longitudinal motion. The state vector on the active side of the junction thus has to be modified to account for this:

$$\begin{bmatrix} u \\ w \\ \theta \\ M \\ Q \\ F \end{bmatrix}_{\hat{a}} = \begin{bmatrix} u \\ w \\ \theta \\ M \\ Q \\ F \end{bmatrix}_a + \begin{bmatrix} 0 & 0 & -d & 0 & 0 & 0 \\ 0 & 0 & 0 & 0 & 0 & 0 \\ 0 & 0 & 0 & 0 & 0 & 0 \\ 0 & 0 & 0 & 0 & 0 & d \\ 0 & 0 & 0 & 0 & 0 & 0 \\ 0 & 0 & 0 & 0 & 0 & 0 \end{bmatrix} \begin{bmatrix} u \\ w \\ \theta \\ M \\ Q \\ F \end{bmatrix}_a, \quad (34a)$$

which can be written as

$$\mathbf{h}_{\hat{a}} = \mathbf{h}_a + \mathbf{T}\mathbf{h}_a. \quad (34b)$$

This can be rearranged to give

$$\mathbf{h}_a = (\mathbf{I} - \mathbf{T})\mathbf{h}_{\hat{a}}. \quad (35)$$

The single-element actuator can thus be modeled using similar analysis to the two-element actuator, but with \mathbf{a}_{La} replaced with $\mathbf{a}_{L\hat{a}}$, and \mathbf{a}_{Ra} replaced with $\mathbf{a}_{R\hat{a}}$. Also the second moment of area of the active section is calculated about the shifted neutral axis shown in Fig. 15. It should also be noted that the forces and moments generated by the actuator are half that for a two-element actuator for the same magnitude of supply voltage. The passive effects of the actuator are investigated by analyzing the way in which waves are scattered, as with the two-element actuator. However, in order to make a comparison between the scatter of flexural and longitudinal waves, the *power* transmitted in these waves is calculated. The scattering of the power transmitted in the waves from (a) an incident flexural propagating wave [A_{4i} in Fig. 6(a)], and (b) an incident longitudinal wave [A_{ri} in Fig. 6(b)], can be seen in Fig. 16(a) and (b), where P represents the power transmitted in the wave. For this example, the thickness ratio of the piezoceramic element to the beam is 0.5. It can be seen that there is very little wave conversion, and attenuation of the incident flexural and longitudinal waves is negligible as they pass through the actuator. In most practical situations discussed in the literature, the thickness of the actuator is less than half the thickness of the structure under control, therefore it can be concluded that in most situations the scattering of waves by a single-element actuator will be negligibly small.

The simplified model discussed in Sec. II can, of course, be used as an approximate representation of a single-element actuator. However, as noted above, it is not possible to generate flexural and longitudinal motion independently. For a relatively thin actuator the moment generated is approximately equal to the product of the generated force and half the thickness of the beam. In this case the ratio of the generated longitudinal to flexural waves is given by Eq. (32).

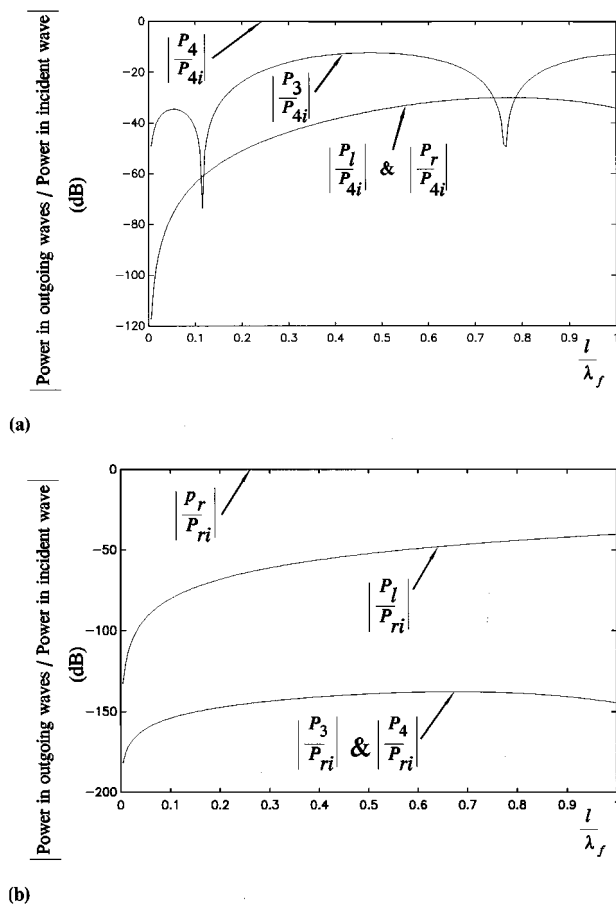


FIG. 16. The power in the scattered waves from incident propagating waves on a single-element piezoceramic actuator fitted to a beam with a thickness ratio of 0.5. (a) Power transmitted in the scattered waves from an incident flexural wave. Power transmitted in the scattered waves from an incident longitudinal wave.

V. CONCLUDING REMARKS

In this paper a wave model has been proposed as a way of investigating the dynamic coupling between either a one- or two-element piezoceramic actuator and a beam. The advantage of such a model is its simplicity, as only the behavior in the vicinity of the actuator has to be modeled. This has enabled a study of the both the active and passive characteristics of the actuators. The analysis has shown that the mass and stiffness of the actuators has very little effect on the longitudinal behavior over most practical frequencies of interest, and very simple models of the actuators which ignore the elements' mass and stiffness are adequate. The mass and stiffness of the actuators have a greater influence on the flexural behavior. Although at low frequencies, and for low thickness ratios, the effect is very small, at higher frequencies it has a much greater effect. It was found that a model which includes the passive effects of the actuator was required to accurately model the behavior of a two-element actuator fitted to an aluminium beam where the thickness ratio was 0.25. To validate the theoretical model an experimental rig had to be built where the beam had flexural and longitudinal anechoic terminations fitted to each end. The flexural termination consisted of exponentially shaped pieces of foam rubber and the longitudinal termination consisted of

flat plates that had a lateral characteristic impedance equal to the longitudinal characteristic impedance of the beam. The experiments showed that the wave model of the beam adequately represented the behavior observed in the experiments. It can be concluded that the optimum length of an actuator for flexural and longitudinal wave generation is half a respective wavelength. If the actuator is to be used to generate *both* wave types, then this is clearly not possible and a compromise would have to be reached. With this type of actuator the ratio of the generated waves for a given supply voltage is dependent upon frequency and the length of the actuator compared to the thickness of the beam.

APPENDIX

This Appendix describes the design of the flexural and longitudinal anechoic terminations fitted to the ends of the beam, and presents experimental results showing their effectiveness.

The flexural terminations consisted of exponentially shaped pieces of foam rubber about 0.6 m in length fitted to either side of each end of the beam as shown in Fig. 11. The intention was to progressively dampen the flexural waves as they approached the ends of the beam so that waves were not reflected with the result that the beam behaved as though it was infinite in length. These terminations had a negligible effect on the longitudinal behavior of the beam, and thus separate longitudinal terminations were required. The idea was that a structure with the same characteristic impedance of the beam should be fitted to each end so that the energy in the longitudinal waves would be transmitted into the structures. There would thus be no reflections, and the beam would behave as if it were infinite in length. The impedance match required can be achieved by connecting the beam to an infinite plate so that the longitudinal waves in the beam convert to flexural waves in the plate. As an infinite plate cannot be realized in practice, a heavily damped plate was used where the dimensions of the plate were chosen such that at the lowest frequency of interest the width of the plate was equal to one flexural wavelength. The thickness of the plate was chosen so that the characteristic impedance of the receiving plate, which is¹⁹

$$Z_{pl} = 8 \sqrt{\frac{E_{pl} \rho_{pl} h^4}{12(1 - \nu^2)}}, \quad (A1)$$

was equal to that for the beam under test:

$$Z_b = \rho_b c_l S_b, \quad (A2)$$

where the subscripts $_b$ and $_{pl}$ stands for the beam and plate, respectively, ρ is density, E is Young's modulus, c_l is the longitudinal wave speed in the beam, S is cross-sectional area, h is the thickness of the plate, and ν is Poisson's ratio. For the 6 mm×30 mm aluminium beam used here, a 5-mm steel plate was predicted as providing an anechoic termination.

The damping in the plate was achieved by bolting together two plates, one of half the thickness of the other, so that there was a thin layer of air between them. The damping in this system was considered to have contributions from two

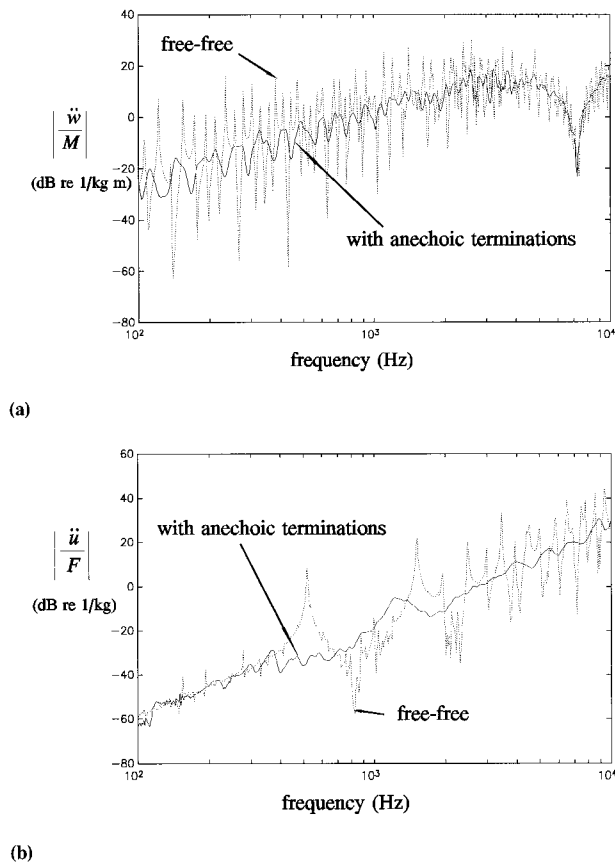


FIG. A1. Graphs showing the effectiveness of the anechoic terminations. (a) Amplitude of lateral beam acceleration per unit moment applied and (b) amplitude of longitudinal acceleration per unit force applied, with and without the anechoic terminations fitted.

different mechanisms; friction damping and squeeze film damping as discussed by Chow and Pinnington.²⁰ This method of damping was chosen rather than conventional constrained layer damping because of its simplicity. The dimensions of the plates used in the experiments are given in Table I.

To test the effectiveness of the anechoic terminations the beam was excited with and without the terminations fitted over the frequency range 100 Hz to 1 kHz. The beam was first suspended in the free-free configuration using thin cord and was excited by driving the two-element actuator such that flexural motion only was generated. The lateral acceleration, \ddot{w} , of the beam was then measured and the frequency response function between the acceleration and excitation moment computed. This is plotted in Fig. A1(a). The experiment was repeated, but with the actuator driven to excite purely longitudinal waves, and the longitudinal acceleration \ddot{u} of the beam measured. The frequency response function between the acceleration and excitation force was also computed and this is plotted in Fig. A1(b). The anechoic termi-

nations were then fitted to the beam and the measurements retaken; these results can also be seen in Fig. A1(a) and (b). It is clear from these graphs that although the terminations are not perfect, they do significantly change the characteristic of the beam so that the motion of the beam at any frequency is primarily due to traveling rather than standing waves, and thus the beam appears to be almost anechoically terminated for both flexural and longitudinal waves.

- ¹B. R. Mace, "Active Control of Flexural Vibrations," *J. Sound Vib.* **114**(2), 253–270 (1987).
- ²D. J. Pines and A. H. von Flotow, "Active Control of Bending Wave Propagation at Acoustic Frequencies," *J. Sound Vib.* **142**(3), 391–412 (1990).
- ³R. J. McKinnell, "Active Vibration Isolation by Cancelling Bending Waves," *Proc. R. Soc. London, Ser. A* **421**, 357–393 (1989).
- ⁴J. Scheuren, "Active Control of Bending Waves in Beams," *Proc. Inter-Noise* **85**, 591–595 (1985).
- ⁵S. J. Elliott and L. Billet, "Adaptive Control of Flexural Waves Propagating in a Beam," *J. Sound Vib.* **163**(2), 295–310 (1993).
- ⁶E. F. Crawley and J. de Luis, "Use of Piezoelectric Actuators as Elements of Intelligent Structures," *AIAA J.* **25**(10), 1373–1385 (1987).
- ⁷C. R. Fuller, G. P. Gibbs, and R. J. Silcox, "Simultaneous Active Control of Flexural and Extensional Power Flow in Beams," in *Proceedings of the International Congress on Recent Developments in Air and Structure Borne Sound and Vibration*, held in Auburn University (1990), pp. 657–662.
- ⁸R. L. Clark, J. Pan, and C. H. Hansen, "An experimental study of the active control of multiple wave types in an elastic beam," *J. Acoust. Soc. Am.* **92**, 871–876 (1992).
- ⁹E. F. Crawley and E. H. Anderson, "Detailed Models of Piezoceramic Actuation of Beams," in *Proceedings of the 30th Structures, Structural Dynamics and Materials Conference*, Mobile, AL (1989), pp. 2000–2010.
- ¹⁰B. T. Wang and C. A. Rogers, "Modelling of Finite-Length Spatially Distributed Induced Strain Actuators for Laminate Beams and Plates," *J. Intell. Mater. Syst. Struct.* **2**, 38–57 (1991).
- ¹¹S. J. Kim and J. D. Jones, "Optimal Design of Piezoactuators for Active Noise and Vibration Control," *AIAA J.* **29**(12), 2047–2053 (1991).
- ¹²F. Charette, C. Guigou, A. Berry, and G. Plantier, "Asymmetric actuation and sensing of a beam using piezoelectric materials," *J. Acoust. Soc. Am.* **96**, 2273–2283 (1994).
- ¹³J. F. Rivory, C. H. Hansen, and J. Pan, "Further Studies of the Dynamic response of a Simply Supported Beam Excited by a Pair of Out-of-Phase Piezoelectric Actuators," *J. Intell. Mater. Syst. Struct.* **5**, 654–664 (1994).
- ¹⁴G. P. Gibbs and C. R. Fuller, "Excitation of thin beams using asymmetric piezoelectric actuators," *J. Acoust. Soc. Am.* **92**, 3221–3227 (1992).
- ¹⁵A. H. von Flotow, "Disturbance Propagation in Structural Networks," *J. Sound Vib.* **106**, 433–450 (1986).
- ¹⁶M. J. Brennan, M. J. Day, S. J. Elliott, and R. J. Pinnington, "Piezoceramic Flexural and Longitudinal Wave Generators for Active Vibration Control," in *Proceedings of the Third International Congress on Air- and Structure Borne Sound and Vibration*, Montreal, Canada, 13–15 June 1994 (1994), Vol. 3, pp. 1469–1476.
- ¹⁷D. W. Miller, "Modelling and Active Modification of Wave Scattering in Structural Networks," Ph.D. thesis, Massachusetts Institute of Technology, 1988.
- ¹⁸L. Cremer, M. Heckl, and E. E. Ungar, *Structure-borne Sound* (Springer-Verlag, Heidelberg, 1988), 2nd ed.
- ¹⁹H. G. D. Goyder and R. G. White, "Vibrational Power Flow from Machines into Built Up Structures, Part I: Introduction and Approximate Analysis of Beam and Plate-like Foundations," *J. Sov. Laser Res.* **68**, 59–75 (1980).
- ²⁰L. C. Chow and R. J. Pinnington, "A Practical Industrial Method of Increasing Structural Damping in Machinery: Squeeze Film Damping with Air," *J. Sound Vib.* **118**(1), 123–139 (1987).

The influence of different timbre attributes on the perceptual segregation of complex-tone sequences^{a),b)}

Punita G. Singh^{c)} and Albert S. Bregman

Department of Psychology, McGill University, Montréal, Québec H3A 1B1, Canada

(Received 29 September 1995; revised 15 May 1997; accepted 21 May 1997)

Spectral factors such as differences in harmonic content are powerful cues in the perceptual organization of tone sequences. Temporal features such as rise time, however, have been shown to be poor cues [W. M. Hartmann and D. Johnson, *Mus. Perc.* **9**, 155–184 (1991)]. The relative influence of these timbral features on perceptual segregation was investigated. Complex tones were sequenced in a repeating ABA- “gallop” format, under four conditions in which tones A and B had the same or different timbres as defined by differences in numbers of harmonics and temporal-envelope features. A sequence started with A and B tones at the same F_0 . The F_0 difference between A and B then increased over the course of a trial, until a listener terminated the trial indicating perceptual segregation into sub-sequences comprising A and B tones, respectively. The F_0 difference required to reach this crossover point of segregation provided a measure of the efficacy of stimulus features of A and B as cues for perceptual organization. Sequences combining differences in harmonic structure and temporal envelope required the smallest F_0 change for segregation. Sequences of tones with the same harmonic structure and temporal envelope required larger changes in F_0 , while the other conditions fell in the middle of this range. The F_0 -tracking method used in this study facilitates measurement of the relative contribution of different stimulus features to stream segregation. It also holds potential as a tool using the point of segregation as a measure of the magnitude of timbre differences brought about by different physical features of sounds. © 1997 Acoustical Society of America. [S0001-4966(97)03309-2]

PACS numbers: 43.10.Ln, 43.75.Cd, 43.66.Jh, 43.66.Lj, 43.66.Mk [WJS]

INTRODUCTION

The perceptual organization of sound sequences is dependent on several factors (Bregman, 1990; Deutsch, 1982; Handel, 1989; Jones, 1976; McAdams and Bregman, 1979). Some factors that influence how sounds will be perceptually organized in a sequential context are the range of F_0 of the sounds, differences in spectral content and spatial location, and temporal proximity to other sounds. A sequence comprising pure tones that differ in frequency, for example, will at the appropriate tempo and frequency difference be perceived as splitting into sub-sequences within each of which the range of frequency differences is reduced.

A number of studies have investigated this perceptual segregation phenomenon using pure tones. Miller and Heise (1950) called the point of perceptual splitting the “trill threshold” while Dowling (1968) referred to the phenomenon as “rhythmic fission.” Bregman and Campbell (1971) called the perceptual splitting of a sequence into sub-sequences “stream segregation.” Van Noorden (1975) made a distinction between “fission,” the state when a sequence seems to be perceptually split into overlapping sub-

sequences, and “temporal coherence,” the state in which the elements of a sequence remain perceptually integrated in a single sequence.

Different paradigms have been used to study stream segregation. For sequences of pure tones, frequency changes are generally correlated with changes in pitch. Experimental tasks have thus often been designed to utilize perception of pitch relations. For example, in some experiments, listeners were asked to identify melodies, the notes of which were interleaved so that the input sequence was a composite of the component melodies (Dowling, 1968; Hartmann and Johnson, 1991). Correct identification of the melodies would imply that listeners had perceptually segregated the input sequence into streams corresponding to the individual melodies.

Temporal-order perception is also affected when an input sequence is perceptually segregated (Hirsh, 1974). The streams typically appear to overlap in time, making it difficult to judge the actual order of elements in the sequence (Dannenbring and Bregman, 1976). This striking aspect of the streaming phenomenon has also been used in experimental tasks to determine the occurrence of perceptual segregation (Bregman and Campbell, 1971).

In addition to changes in perceived pitch and temporal-order relations, the rhythmic percept associated with a sequence can also be a powerful cue indicating perceptual segregation or coherence. A paradigm employed by van Noorden (1975) and in the present experiment, illustrates this phenomenon quite effectively. Three-element sequences

^{a)}“Selected research articles” are ones chosen occasionally by the Editor-in-Chief, that are judged (a) to have a subject of wide acoustical interest, and (b) to be written for understanding by broad acoustical readership.

^{b)}Some of this research was presented at a meeting of the Acoustical Society of America in Ottawa [Singh and Bregman, *J. Acoust. Soc. Am.* **93**, 2363 (A) (1993)].

^{c)}Present address: 20-A Aurangzeb Road, New Delhi-110011, India.

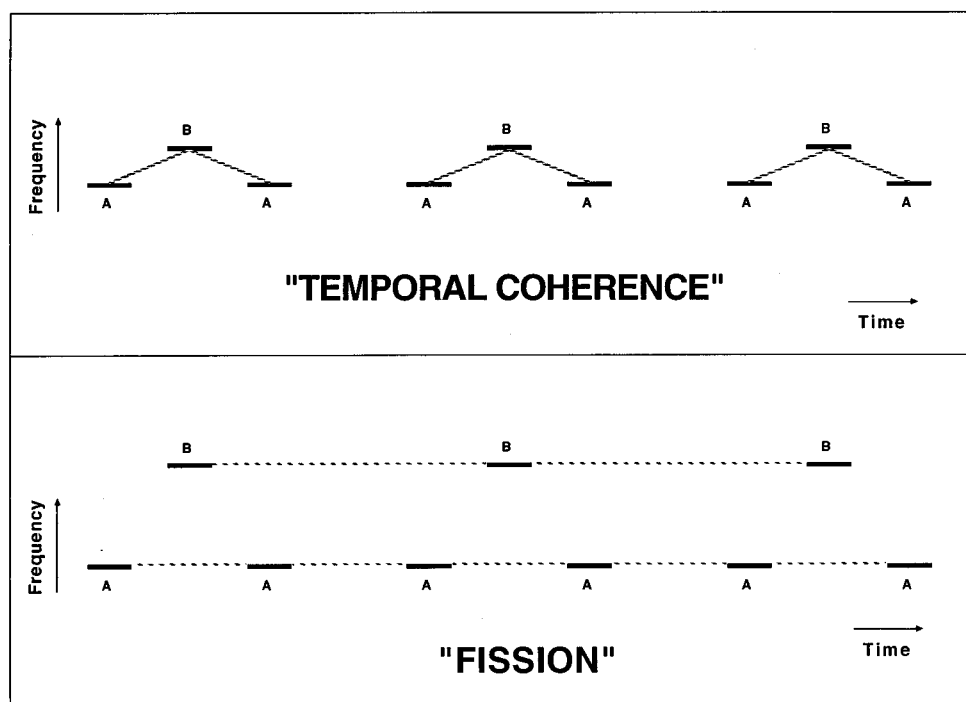


FIG. 1. The "ABA-" galloping sequence used by van Noorden (1975). The top panel represents retention of the galloping rhythm, in the "temporal coherence" state. The bottom panel illustrates the "fission" state, when the ABA- sequence perceptually segregates into overlapping sequences of A and B tones, with one sequence perceived to have double the tempo of the other.

composed of two tones A and B are created to form triplet patterns ABA as shown in Fig. 1. The ABA triplets are repeated with a gap equal to the duration of B inserted between repetitions. In the "temporal coherence" state, a sequence comprising such triplets appears to have a galloping rhythm. In the "fission" state, however, the sequence breaks up into perceptual streams comprising the A and B tones, respectively. Because of the temporal placement of the tones in the sequence, the sub-sequences will be isochronous, with the A tones perceived to repeat at a tempo twice that of the B tones. This dramatic change in rhythm is a useful cue indicating perceptual segregation.¹

While the study of stream segregation for pure-tone sequences is relatively straightforward, for sequences of complex tones, the situation is more complex. Complex tones may differ from each other along several dimensions simultaneously. Thus tones with the same F_0 may have very different spectra or onset-attack features. Would the type of segregation effects observed for sequences of pure tones hold for sequences comprising complex tones as well? If the sounds making up a sequence were produced by different instruments, would the formation of streams be dependent on the similarity of instrumental timbres or on the proximity of pitch as is typically the case for pure tones?

A number of studies have shown that stream segregation based on timbre differences is not only possible, but often more potent than segregation based on pitch differences (Iverson, 1993, 1995; Singh, 1987; Wessel, 1979). However, the manner in which stimulus features are manipulated to create timbre differences seems to be a crucial factor determining segregation. Spectral differences are particularly

powerful initiators of stream segregation. A sequence comprising sounds differing in spectral loci of components will typically break up into streams, within which the range of spectral differences is reduced, even if the sounds share the same F_0 (van Noorden, 1975; Singh, 1987). Timbre changes resulting from temporal differences, such as in attack and decay characteristics, however, have not proven to be very effective initiators of segregation (Hartmann and Johnson, 1991; Wessel, 1979).

Hartmann and Johnson (1991) investigated the influence of a variety of stimulus characteristics on stream segregation. Differences in amplitude-envelope shape were found to make no significant contribution to stream segregation. The relative dominance of spectral factors over temporal-envelope features was attributed to gross differences in peripheral channeling caused by spectral changes, and the absence or reduction of such differences given changes in envelope features alone.

"Peripheral channels" in their report imply physiological channels that are involved in the initial stages of auditory processing based on frequency (tonotopicity) or on ear of presentation (laterality). According to their viewpoint, tones exciting different peripheral channels will be more likely to segregate from each other than those exciting the same channels. In the absence of differences in peripheral channeling, however, Hartmann and Johnson declare that little or no stream segregation will be observed, "even in those cases where individual tones should clearly evoke images of different sources" (p. 155).

At odds with the prediction of Hartmann and Johnson (1991), Iverson (1993, 1995) found an effect of envelope

difference on stream segregation. Using edited samples of real instrument tones, Iverson found that, in addition to the usual spectral effects, sequences of tones with dissimilar temporal-amplitude envelopes received higher segregation ratings than sequences of tones with similar envelopes. Furthermore, tones with shorter attacks received higher ratings than tones with gradual attacks.

The conflict between the findings of Iverson and those of Hartmann and Johnson may be a result of the different stimuli used in the two studies. In most natural instrument sounds, the spectral and temporal dimensions may covary (Risset and Wessel, 1982). The separate contribution of these dimensions to stream segregation may therefore be difficult to ascertain. As admitted by Iverson (1993, p. 88), some “unquantified acoustic attribute” may have been correlated with the attack-time measures used in his study. Isolating the dynamic attributes that influenced streaming in his study clearly requires additional experiments using synthetic tones.

With synthetic sounds created in the laboratory, one can attempt to tease apart spectral and temporal dimensions and control them as independent variables in a streaming experiment. This was the intention of the present study. In particular, we wanted to determine the relative efficacy of differences in amplitude-envelope features, and harmonic content on stream segregation. A second goal was to devise a paradigm that would provide a common scale against which to measure or “titrate” the potency of different physical features as initiators of stream segregation. To obtain such a common measure, we used a variant of the van Noorden galloping ABA- sequence described earlier.

I. METHOD

A. Stimuli

Stimulus sequences were constructed following an ABA- format similar to that illustrated in Fig. 1. However, they were unlike those used by van Noorden (1975) in that the A and B sounds were complex, rather than pure tones, and could thus differ from each other along different timbral dimensions in addition to pitch (as defined by F_0). Tones A and B were selected to have the same or different timbre as defined by similarity or difference in spectral and temporal features described below. Thus monotimbral AAA- sequences as well as bitimbral ABA- sequences were included in the stimulus inventory.

Both A and B were 100 ms in duration. A 10-ms silence was inserted between the 100-ms long tones, so that the physical onset-to-onset interval between tones A-B-A was 110 ms. A gap of 120 ms was inserted between repetitions of the ABA triplets. This type of temporal structuring leads to a characteristic galloping rhythm, that is lost when the sequence perceptually segregates into isochronous streams of A and B tones, respectively.

Sequences of sounds with different spectral and temporal-amplitude envelope features² were constructed following a two-factor design to generate four presentation conditions as summarized in Fig. 2.

The A and B tones could have either:

		Harmonics (n)	
		SAME	DIFFERENT
Envelope (e)	SAME	Condition 1 (Se Sn)	Condition 3 (Se Dn)
	DIFFERENT	Condition 2 (De Sn)	Condition 4 (De Dn)

FIG. 2. Sequences were constructed following the four conditions illustrated above. The A and B tones in the ABA- sequence could have either (1) the same envelope and number of harmonics (SeSn), (2) different envelope and same number of harmonics (DeSn), (3) same envelope but different number of harmonics (SeDn), or (4) different envelope and different number of harmonics (DeDn). Each condition had eight sub-conditions as described in the text and in Table A1.

- (1) the same temporal envelope and same number of harmonics (SeSn)³;
- (2) different envelopes but same number of harmonics (DeSn);
- (3) same envelope, but different number of harmonics (SeDn); or
- (4) different envelopes and different number of harmonics (DeDn).

The spectral and temporal differences in design between individual sounds used in the stimulus sequences are illustrated in Fig. 3. The spectral factor had two levels, with tones constructed to have either the first two harmonics of the requisite F_0 , or the first four harmonics, added in phase at equal amplitudes. The two levels of the temporal factor corresponded to differences in the extent of rise and fall times. In one case, the tones had a 5-ms linear rise time with a 95-ms linear decay time. In the other case, the temporal-amplitude envelope was reversed so that the tones had a 95-ms rise time and a 5-ms decay time.

For each of the four sound designs illustrated in Fig. 3, a set of 25 tones ranging in F_0 from 262 to 524 Hz were

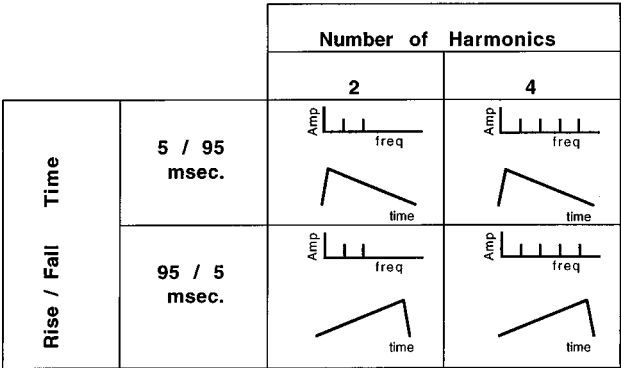


FIG. 3. Individual A and B sounds were constructed following a 2×2 design. The tones had either the first two or four harmonics of the required F_0 , and envelopes with either a sharp rise time and gradual fall time or a gradual rise time and sharp decay time as illustrated above.

synthesized. The 25 tones spanning this octave interval differed in F_0 from each other in quarter-tone steps, where a quarter-tone step is equivalent to a change in F_0 by half a semitone, i.e., by an amount equal to $2^{1/24}$ (or 3%) of the reference F_0 . All sounds were equalized in rms energy to compensate for the difference in the number of components. The entire set of tones was accessible via the control program described below for selection during the adaptive procedure used.

B. Apparatus

All sounds were synthesized digitally using the MITSYN software package for signal processing and analysis (Henke, 1990). Sound synthesis, stimulus presentation and data collection were controlled by a 486/50 microcomputer fitted with a Data Translation DT 2823 audio card set at a sampling frequency of 20 kHz and 16-bit resolution. The stimuli were filtered via TTE low-pass filters set at a cutoff frequency of 8 kHz with a 96 dB/oct roll off. Output presentation levels were controlled via a Tascam amplifier/mixer and verified with a GenRad 1565 sound level meter. The listener was seated in an IAC double-walled, sound-absorptive booth and received the stimuli binaurally via Sennheiser HD414 headphones at an overall sound-pressure level of about 70 dB.

C. Procedure

The stimuli were presented in an interactive procedure constructed using the MAPLE software package (Achim *et al.*, 1992). On each trial, a listener was presented with a repeating ABA sequence in which the F_0 difference between A and B was initially 0 Hz. As the trial proceeded, the F_0 difference between A and B increased in quarter-tone steps, following an ascending track (*re*: 262 Hz) or descending track (*re*: 524 Hz), until the sequence appeared to perceptually segregate. At this “crossover point,” the trial was terminated by the listener pressing a key on the computer terminal and the amount of F_0 change in quarter-tone steps was recorded.

Since attention has been shown to have an influence on perceptual segregation boundaries (van Noorden, 1975) listeners were specifically instructed to try to hold on to the galloping pattern despite the changes in F_0 . They were to terminate the trial only when the galloping rhythm was lost and they perceived the sequence to have segregated into streams.

The procedural control program monitored the selection of timbral features and fundamental frequencies of the A and B tones during a trial. For every four repetitions of the ABA-pattern, the F_0 of the middle tone B changed so that the F_0 interval between A and B accordingly changed by a quarter-tone. The direction of change of F_0 within a trial (up or down) and the order of particular sounds serving as A and B in the sequence were counterbalanced so that each of the four main conditions had eight subconditions. Features of individual sounds used in the 32 subconditions thus resulting, are

summarized in Table AI in the Appendix. The 32 stimuli were presented randomly in a block, with six replications obtained per subject.

D. Subjects

Ten listeners between the ages of 21 and 36 years were used as subjects. They all had normal hearing and had participated in auditory experiments before. All subjects were given a block of practice trials encompassing all stimuli used to familiarize them with the task prior to actual data collection. Individual results are described in Sec. II B.

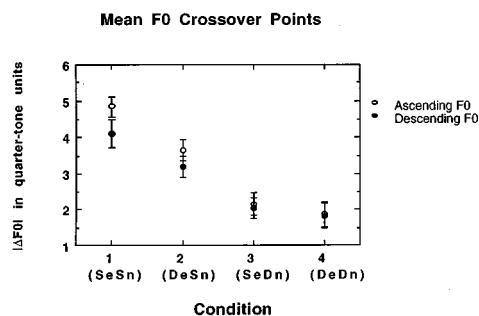
II. RESULTS

Mean F_0 values obtained at segregation crossover points for all subjects across replications for the 32 stimuli were highest for condition 1, getting progressively lower for conditions 2, 3, and 4. A two-way analysis of variance (ANOVA), with condition and direction of F_0 change considered as the two factors, revealed a highly significant effect for condition [$F(3,27) = 59.29$, $p < 0.000$],⁴ a significant effect of F_0 direction [$F(1,9) = 6.79$, $p < 0.027$], and a significant interaction between condition and F_0 direction [$F(3,27) = 7.21$, $p < 0.001$]. One-way analyses designed to probe the interaction between condition and F_0 direction revealed that the F_0 -direction factor was coming into play only in conditions 1 and 2 [$F(1,9) = 11.62$, $p < 0.007$ and $F(1,9) = 6.65$, $p < 0.029$, respectively]. For conditions 3 and 4, the F_0 -direction factor was not significant [$F(1,9) = 0.6$, $p = 0.467$ and $F(1,9) = 0.77$, $p = 0.754$, respectively].

To evaluate the effect of order of timbres of A and B in a sequence, the means corresponding to subconditions for conditions 2, 3, and 4 were analyzed via a three-way ANOVA with condition, F_0 direction, and A-B timbre order considered as the three factors. Subconditions for condition 1 (SeSn) were not included in this analysis since the sequences for this condition were monotimbral, i.e., of an AAA-format, where timbre order was not an issue. As expected, the effect of condition was highly significant [$F(2,18) = 33.40$, $p < 0.000$]. The main effect of F_0 direction, however, was not significant [$F(1,9) = 3.12$, $p = 0.109$] but the condition $\times F_0$ direction interaction remained [$F(2,18) = 4.31$, $p < 0.029$]. No effect of order of timbres A and B was found [$F(1,9) = 2.31$, $p = 0.161$].

Condition 1 (SeSn) was also analyzed to determine if there was any effect of absolute features of the sounds such as steepness of the amplitude envelope or the number of harmonics on the crossover points for monotimbral AAA-sequences. This was done via a three-way ANOVA with two levels for each of the three factors under consideration, i.e.: direction of F_0 change within a trial (up or down), steepness of rise time (5 or 95 ms) and number of harmonics (two or four).

The F_0 -direction factor proved to be highly significant [$F(1,9) = 11.66$, $p < 0.008$]. There was no effect of number of harmonics [$F(1,9) = 1.61$, $p = 0.235$] and of steepness of envelope [$F(1,9) = 4.00$, $p = 0.074$]. The interaction of en-



Condition	Comparisons	Ascending F(1,9)	Trials p	Descending F(1,9)	Trials p
1 vs. 2		37.51	< 0.000	37.73	< 0.000
1 vs. 3		171.19	< 0.000	62.22	< 0.000
1 vs. 4		89.64	< 0.000	39.93	< 0.000
3 vs. 4		4.09	= 0.072	2.22	= 0.168

FIG. 4. Mean $\Delta F0$ -crossover points (in quarter-tone steps) obtained for ten listeners for the four main conditions shown along the abscissa. Empty symbols correspond to crossover points for ascending $F0$ trials. Filled symbols represent descending $F0$ trials. Error bars correspond to the standard error of the data. Results of planned comparisons for different condition pairs are given at the bottom.

velope and $F0$ direction, however, was significant [$F(1,9) = 7.33, p < 0.023$]. The interaction was explored further via one-way analyses that revealed that $F0$ direction only made

a difference for envelopes with the sharper rise times [$F(1,9) = 19.99, p < 0.002$].

The main results of these analyses are summarized below:

- (1) The effect of condition (1, 2, 3, or 4) was highly significant.
- (2) Direction of $F0$ change made a significant difference to crossover points in conditions 1 and 2 but not 3 and 4.
- (3) The order of timbres for A or B tones did not contribute to any significant differences in crossover points.
- (4) Monotimbral AAA- sequences of sounds with envelopes with steep rise times (5 ms) had significantly higher $\Delta F0$ crossover points than sequences of sounds with more gradual rise times (95 ms) for ascending $F0$ trials.
- (5) The absolute number of harmonics (two or four) in AAA- sequences did not make a difference to crossover points.

$\Delta F0$ -crossover points averaged across listeners for the four main conditions of the experiment are shown in Fig. 4 for both ascending and descending $F0$ trials. Crossover points for individual listeners are listed in Tables I and II and discussed later. The ordinate in Fig. 4 gives the mean $F0$ difference between tones required for stream segregation in quarter-tone steps (where a quarter-tone is about 3% of the

TABLE I. Mean crossover points for the four main conditions for ascending $F0$ trials for individual listeners. Numbers in parentheses below the means are the respective standard errors. The last four columns of the table summarize the results of planned comparisons for conditions 1 vs 2, 1 vs 3, 1 vs 4, and 3 vs 4 for each listener. Overall means across subjects are also given at the bottom of the table for comparison.

Subject	Condition 1 (SeSn)	Condition 2 (DeSn)	Condition 3 (SeDn)	Condition 4 (DeDn)	1 vs 2 <i>p</i>	1 vs 3 <i>p</i>	1 vs 4 <i>p</i>	3 vs 4 <i>p</i>
S1	4.08 (0.23)	3.08 (0.27)	1.62 (0.08)	1.33 (0.14)	<0.057	<0.000	<0.001	=0.057
S2	4.67 (0.31)	3.58 (0.26)	2.62 (0.15)	2.62 (0.21)	<0.001	<0.003	<0.002	=1.000
S3	5.04 (0.14)	3.46 (0.22)	2.17 (0.14)	1.37 (0.08)	<0.002	<0.000	<0.000	<0.004
S4	6.33 (0.31)	4.17 (0.22)	3.54 (0.42)	2.46 (0.18)	<0.001	<0.002	<0.000	=0.057
S5	3.21 (0.27)	2.12 (0.21)	1.00 (0.20)	1.00 (0.13)	<0.005	<0.000	<0.001	=1.000
S6	4.42 (0.34)	3.21 (0.26)	0.92 (0.25)	0.75 (0.09)	<0.004	<0.001	<0.000	=0.469
S7	5.58 (0.14)	3.58 (0.17)	2.25 (0.09)	1.62 (0.18)	<0.000	<0.000	<0.000	<0.007
S8	4.96 (0.30)	4.50 (0.20)	1.29 (0.18)	0.79 (0.21)	=0.099	<0.001	<0.000	=0.166
S9	5.71 (0.74)	5.54 (0.81)	3.71 (0.94)	4.08 (0.68)	=0.855	<0.024	=0.174	=0.762
S10	4.42 (0.26)	3.25 (0.44)	2.46 (0.27)	2.62 (0.29)	<0.043	<0.002	<0.011	=0.589
Mean	4.84 (0.28)	3.65 (0.29)	2.16 (0.31)	1.87 (0.34)	<0.000	<0.000	<0.000	=0.072

TABLE II. Same as Table I, but for descending $F0$ trials.

Subject	Condition 1 (SeSn)	Condition 2 (DeSn)	Condition 3 (SeDn)	Condition 4 (DeDn)	1 vs 2 p	1 vs 3 p	1 vs 4 p	3 vs 4 p
S1	3.71 (0.18)	3.12 (0.14)	2.25 (0.13)	1.92 (0.17)	<0.013	<0.001	<0.002	=0.248
S2	3.21 (0.10)	2.87 (0.08)	2.37 (0.15)	1.96 (0.15)	=0.081	<0.005	<0.001	<0.030
S3	3.62 (0.29)	2.79 (0.23)	1.17 (0.10)	0.96 (0.15)	<0.030	<0.001	<0.001	=0.091
S4	7.00 (0.22)	4.92 (0.25)	3.54 (0.18)	2.67 (0.08)	<0.002	<0.000	<0.000	<0.008
S5	3.00 (0.17)	1.79 (0.22)	1.12 (0.19)	0.87 (0.17)	<0.000	<0.000	<0.000	=0.142
S6	3.29 (0.16)	2.67 (0.27)	1.25 (0.26)	0.79 (0.21)	<0.010	<0.001	<0.000	=0.193
S7	4.29 (0.08)	3.33 (0.10)	1.96 (0.15)	1.58 (0.12)	<0.003	<0.000	<0.000	=0.059
S8	4.50 (0.24)	3.58 (0.31)	1.29 (0.27)	0.87 (0.14)	<0.009	<0.000	<0.000	<0.041
S9	5.21 (0.41)	4.21 (0.44)	3.54 (0.51)	4.04 (1.09)	<0.042	<0.024	=0.285	=0.629
S10	3.29 (0.15)	2.58 (0.21)	2.00 (0.30)	2.67 (0.26)	<0.038	<0.016	=0.108	=0.161
Mean	4.11 (0.39)	3.19 (0.28)	2.05 (0.29)	1.83 (0.33)	<0.000	<0.000	<0.000	<0.168

reference $F0$). The abscissa shows the corresponding conditions as defined in Fig. 2.

A. General observations

Figure 4 shows a declining trend for crossover points across conditions 1–4 for both ascending and descending $F0$ trials. Crossover points for ascending trials were higher than those for descending trials for conditions 1 and 2, but not for conditions 3 and 4. The reason for this difference is not clear at present.

For both ascending and descending trials, the highest average $\Delta F0$ values were obtained for condition 1 (SeSn), in which A and B tones were designed to have the same timbre (i.e., the same temporal envelope and number of harmonics). Condition 1 (SeSn) serves as a reference condition with no changes in harmonic numbers or temporal envelopes across tones of the sequence. Planned comparisons between condition 1 and the other three conditions showed significant differences as summarized at the bottom of Fig. 4. Crossover points for condition 2 (DeSn), were significantly lower than those for condition 1 [ascending, $F(1,9)=37.51$, $p<0.000$; descending $F(1,9)=37.73$, $p<0.000$]. In this condition, A and B differed in envelope, but had the same number of harmonics. Crossover points were even lower for condition 3 (SeDn), in which A and B had the same envelopes, but differed in harmonic structure, and lowest for condition 4 (DeDn) in which A and B differed in both envelope and harmonic content.

The $\Delta F0$ values obtained for condition 3 were significantly lower than those for condition 2 [ascending $F(1,9)=36.86$, $p<0.000$; descending $F(1,9)=39.05$, $p<0.000$]. A difference in harmonic structure alone was thus more powerful in facilitating segregation of A and B than an envelope difference alone. Supplementing an envelope difference by a difference in harmonic numbers led to even further lowering of crossover points as is evident from a comparison of conditions 2 vs 4 [ascending, $F(1,9)=41.84$, $p<0.000$; descending $F(1,9)=22.89$, $p<0.001$]. Supplementing a harmonic difference with an envelope difference, however, did not lead to significant lowering of crossover points for condition 4 as contrasted with condition 3 [ascending, $F(1,9)=4.09$, $p=0.072$; descending $F(1,9)=2.22$, $p=0.168$].

Improved segregation for harmonic differences (condition 1 vs 3 and 1 vs 4) is not surprising, given the growing body of evidence implicating spectral differences as enhancers of stream segregation. The significant difference between condition 1 and 2, however, is contrary to the prediction of Hartmann and Johnson (1991) who found no effect of envelope differences on stream segregation. This may be constructed as supporting the case of Iverson (1993, 1995) for segregation based on onset differences, but it should be noted that the difference between conditions 3 and 4, which also differed from each other only in the envelope parameter, was not statistically significant.

B. Individual differences

Crossover points for individual listeners for the four main conditions of the experiment are presented in Tables I and II for ascending and descending $F0$ trials, respectively. These $\Delta F0$ values were obtained by averaging across the six replications for each listener. Standard errors are given in parentheses below the means. The mean results for all ten listeners are also given for comparison in the last row of the tables. The last four columns of each table summarize the results of planned comparisons of different conditions in terms of the level of statistical significance.

As can be seen from the tables, *absolute* $\Delta F0$ values were quite different for different listeners. Listener S4 for example, could hold an ascending-trial sequence together under condition 1 for 7 quarter-tone units on the average ($\approx 21\%$). Listener S5 on the other hand, achieved segregation at 3 quarter-tone units ($\approx 9\%$). However, *relative* differences between conditions showed the same declining trend as the mean data. Conditions 2, 3, and 4 were significantly different from the standard condition 1 (SeSn) for most listeners. However, the difference between condition 3 and 4 which was not statistically significant for the listener-averaged crossover values was statistically significant for some listeners.

Subjects in our experiment were not preselected on the basis of musical experience. However, different degrees of familiarity with music may have contributed to some of the individual differences observed. Pitt (1994) has observed that nonmusicians are more sensitive to changes in timbre than to changes in pitch in sound categorization tasks. Musicians on the other hand, tend to follow pitch relations more closely. Cho *et al.* (1994) also note that familiarity with particular instrument timbres may affect the relative weighting assigned by listeners to physical features of sounds.

In the present experiment, such factors may have contributed to differences in absolute values of crossover points. In reference to Tables I and II, listener S1 sings in a choir, listener S4 is an accomplished pianist, listener S5 plays the saxophone, and listener S8 (the first author) is a percussionist. Despite musical exposure being a common factor, the absolute values of crossover points for these listeners are different. However, as noted above, relative values show the same trend across these and other listeners.

To systematically evaluate the effect of musical training on stream segregation, experiments would have to be done in which subjects were selected not only on the basis of general musical experience *per se*, but also based on different types of musical experience.

III. GENERAL DISCUSSION

The results of the present experiment corroborate the importance of spectral differences in facilitating stream segregation. Conditions 3 (SeDn) and 4 (DeDn), under which the sounds in a sequence differed from each other in terms of number of harmonics, led to significantly lower $\Delta F0$ values for segregation than the reference condition 1 (SeSn), in which there was no difference between sounds in terms of harmonic structure. However, our listeners also attained sig-

nificantly lower crossover points for condition 2 (DeSn), under which changes were made only in the envelope feature of sounds. In this condition, the sounds comprising the sequence occupied the same peripheral channels at unison, differing only in the time course of evolution of amplitude. Their long-term power spectra were identical.

Though the mean crossover points for conditions 1 (SeSn) and 2 (DeSn) were significantly different, those for conditions 3 (SeDn) and 4 (DeDn) were not. The reason for the difference between these complementary conditions is not clear. It could be that for conditions 3 and 4 the $\Delta F0$ values were approaching "floor" limits. The harmonic structure difference alone was large enough to cause streaming without much change in pitch. The influence of the added envelope difference may thus not have been observable at this low end of the scale.

One could also speculate that in condition 2 (DeSn), the lack of a concurrent difference along the harmonic dimension allowed the envelope differences to be better detected. These perceived envelope differences were apparently adequate to enhance stream segregation so that segregation was achieved at lower $F0$ differences than the null standard. For condition 3 (SeDn), the spectral differences alone were a highly effective cue for segregation. The additional difference provided by a change in envelope in condition 4 (DeDn) apparently did not serve to enhance perceptual segregation of A and B any further.

A study by Grey (1978) investigating timbre discrimination in musical patterns suggests that sequences camouflage the temporal detail of individual sounds while amplifying spectral differences between sounds. Isolated contexts, on the other hand, appear to facilitate the comparison of temporal features of a pair of tones, such as differences in their rates of attack and decay (p. 471). The salient spectral difference between sounds used in condition 4 (DeDn) may have had such an obscuring effect on the concurrent envelope difference for our stimuli.

In the present study, onset-to-onset times between sounds were not adjusted for individual listeners to compensate for *perceptual* attack times of sounds with different envelopes. The perceptual correlate associated with envelope changes, while producing a timbre change, may also have provided a slight rhythmic cue (perceived as a difference in "accent" within the sequence). Any advantage obtained via this rhythmic cue, however, is observed only for condition 2 (DeSn) versus condition 1 (SeSn), not condition 4 (DeDn) versus 3 (SeDn), which should have similarly benefitted from this cue.

Iverson (1993, 1995) investigated the influence of such inadvertent rhythmic cues in a comparative study using sequences with elements spaced by physically equal onset-to-onset intervals as well as sequences in which the spacing of elements was adjusted in an attempt to provide equal perceptual onset-to-onset intervals. No difference between these two types of sequences was found in terms of stream-segregation measures. It thus seems unlikely that accent structure affected crossover points in our study. Furthermore, such an effect would have shown up as an A-B timbre order

effect in the statistical analyses described earlier, but was not observed.

Iverson (1993, 1995) found a correlation between dissimilarity measures of sounds and measures of stream segregation. He suggested that auditory stream segregation is based on the same dynamic and spectral acoustic attributes that influence similarity judgments. The same factors that allow listeners to discriminate sounds, should help in segregating them in a sequential context.

It is reasonable to assume that some differences must exist between sounds in a sequence, for subgroups such as streams to emerge. But how different must these differences be, in order to be successful initiators of stream segregation? Added to the problem of obtaining adequate measures of magnitude of difference, is that of having a common way of measuring the effects of differences along various stimulus dimensions.

With the $F0$ -tracking method used in the present experiment, we were attempting to provide such a measure that would allow comparisons of different stimulus features in terms of their contribution to the $\Delta F0$ segregation value. The method was successful for this purpose, in that it enabled a ranking of conditions in terms of crossover points in common, underlying $F0$ -change units.

In the present experiment, stimulus features were varied following the design table in Fig. 3. Tones corresponding to the four recipes illustrated clearly differed from each other in perceived timbre. Although timbre discrimination *per se* was not the goal of our study, discrimination experiments conducted by other investigators indicate that the type and magnitude of stimulus features manipulated by us should evoke discriminable changes in timbre (Samson *et al.*, 1993). The relative contribution of different physical features in evoking a perceived change in timbre, however, may be different. For example, Cho *et al.* (1993, 1994) found spectral factors to be more crucial to the normalization of instrument timbre than temporal factors such as attack times. In addition to differences in relative weighting of physical substrates of timbre, the perceived magnitude of timbre difference between sounds may also differentially affect stream segregation.

If the degree of perceived dissimilarity of timbres is indeed a predictor of stream segregation (Iverson, 1993, 1995), then the difference in crossover point in $F0$ units would also provide a measure of the discriminability of timbres contrasted in the sequence. Sequences of sounds with very different timbres would be likely to segregate at lower $\Delta F0$ values, while those with more subtle variations in timbre would segregate at higher $\Delta F0$ values. The relative values of crossover points would be an indicator of the degree of perceived difference between timbres despite different physical substrates contributing to the timbre difference. The method used here could thus potentially be used to obtain quantitative measures of timbre difference.

One limitation of the $F0$ -tracking method, however, relates to ranking of conditions such as 3 and 4 of the present experiment. For these conditions, the $\Delta F0$ crossover points appeared to be approaching limiting values at the lower end of the $\Delta F0$ scale. Indeed, it is possible to achieve stream segregation at unison ($\Delta F0 = 0$ Hz) for some types of timbre

contrasts between sounds (Iverson, 1993, 1995; Singh, 1987). This suggests development of an analogous tracking procedure based on tempo manipulation rather than frequency manipulation for sequences contrasting highly distinct timbres. Rate of presentation of sounds in a sequence is also one of the key factors bringing about segregation (van Noorden, 1975). Multitimbral sequences of complex tones at different fixed $\Delta F0$ values could be used as stimuli, and an adaptive procedure used with rate of presentation (ΔT) changing over the course of a trial. Listeners would terminate trials at ΔT values where segregation appeared to occur. Lower ΔT values (i.e., faster tempi) would presumably be required for sequences more resistant to segregation, while sequences comprising highly contrastive sounds more amenable to segregation would break apart at larger ΔT values (i.e., slower tempi). A wider range of timbre contrasts could thus be studied using this complementary procedure.

IV. CONCLUSIONS

The present study attempted to measure the relative efficacy of different stimulus dimensions for initiation of perceptual segregation of sequences. Sounds composing the sequences had the same or a different number of harmonics and temporal-amplitude envelopes. Maximal segregation was obtained for sequences that combined differences along both these dimensions, as characterized by low $\Delta F0$ values at the point of segregation. Differences in harmonic numbers were the next best at causing segregation. Monotimbral conditions in which the sounds in a sequence shared the same number of harmonics and envelope characteristics were the least susceptible to segregation (i.e., they had the highest $F0$ crossover points).

A surprising finding is that crossover points for sequences of sounds with envelope differences alone, though higher than the harmonic-number conditions, still proved to be significantly lower than the standard condition. Given the results of Hartmann and Johnson (1991), Iverson (1993, 1995), and the present study, the role of temporal cues in stream segregation clearly needs to be studied further. A wider range of envelope differences and temporal-envelope modulation differences could be included in future investigations.

The method used in the present study enabled measurement of the influence of different timbre attributes on perceptual segregation using $\Delta F0$ crossover points as a common denominator. The stimuli used were kept deliberately simple in the present experiment, but in future research, we hope to apply this adaptive procedure using complex stimuli with a wider range of spectral and temporal differences. With some streamlining in terms of specification of frequency stepsizes used, temporal points of change of $F0$, tempo of the sequence, etc., the method used in the present study holds promise for obtaining quantitative measures of stream segregation, as well as providing a way to measure differences in complex perceptual attributes such as timbre in common units.

TABLE AI. Summary of the features of the sounds used in construction of sequences ABA- for conditions 1, 2, 3, 4, and their subconditions.

Condition	Tone A		Tone B		F0 change direction
	Number of harmonics	Rise–fall time in ms	Number of harmonics	Rise–fall time in ms	
SeSn					
1.1	2	5/95	2	5/95	ascending
1.2	4	5/95	4	5/95	ascending
1.3	2	95/5	2	95/5	ascending
1.4	4	95/5	4	95/5	ascending
1.5	2	5/95	2	5/95	descending
1.6	4	5/95	4	5/95	descending
1.7	2	95/5	2	95/5	descending
1.8	4	95/5	4	95/5	descending
DeSn					
2.1	2	5/95	2	95/5	ascending
2.2	2	95/5	2	5/95	ascending
2.3	4	5/95	4	95/5	ascending
2.4	4	95/5	4	5/95	ascending
2.5	2	5/95	2	95/5	descending
2.6	2	95/5	2	5/95	descending
2.7	4	5/95	4	95/5	descending
2.8	4	95/5	4	5/95	descending
SeDn					
3.1	2	5/95	4	5/95	ascending
3.2	4	5/95	2	5/95	ascending
3.3	2	95/5	4	95/5	ascending
3.4	4	95/5	2	95/5	ascending
3.5	2	5/95	4	5/95	descending
3.6	4	5/95	2	5/95	descending
3.7	2	95/5	4	95/5	descending
3.8	4	95/5	2	95/5	descending
DeDn					
4.1	2	5/95	4	95/5	ascending
4.2	4	95/5	2	5/95	ascending
4.3	2	95/5	4	5/95	ascending
4.4	4	5/95	2	95/5	ascending
4.5	2	5/95	4	95/5	descending
4.6	4	95/5	2	5/95	descending
4.7	2	95/5	4	5/95	descending
4.8	4	5/95	2	95/5	descending

ACKNOWLEDGMENTS

Financial support for this project was provided by the Natural Sciences and Engineering Research Council of Canada. The authors are grateful to Pierre Ahad and Todd Mondor for technical and statistical assistance and to the editor and reviewers for their patience and suggestions.

APPENDIX

A summary of features of sounds used in construction of sequences ABA- for conditions 1, 2, 3, 4, and their subconditions is given in Table AI.

¹An audio example of the type of sequences used by van Noorden (1975) can be heard on the compact disc of Auditory Demonstrations distributed by the Acoustical Society of America.

²The terms “spectral” and “temporal” are used here in an operational sense to define the stimulus variables “harmonic structure” and “amplitude envelope,” respectively. In reality, it is not possible to separate the spectral from the temporal completely. A “temporal” feature such as sharp

attack time has a spectral consequence (in evoking high-frequency distortion in an output audio device) just as a “spectral” feature such as number of harmonics has a temporal consequence (in that the waveform becomes more complex).

³Note that for condition 1 (SeSn), the sequences are in effect monotonimbral, i.e., of an AAA- type while for the other conditions, the sequences were bitimbral, i.e., of an ABA- type. In this study A and B are used as timbre labels and do not have any bearing on the F0 relation between the tones. Thus AAA- sequences do not imply tones of the same F0, but rather of the same timbre, as defined by similarity of harmonic structure, envelope, or both of these features.

⁴The statistical program used was set to round off values to the third decimal place. The use of the expression “ $p < 0.000$ ” here and elsewhere, actually implies that the probability of obtaining the result purely by chance would be lower than 5 in 10 000 (i.e., $p < 0.0005$).

Achim, A., Bregman, A. S., and Ahad, P. (1992). MAPLE software documentation, Speech and Hearing Laboratory, Department of Psychology, McGill University, Montréal, Québec, Canada.

Bregman, A. S. (1990). *Auditory Scene Analysis: The Perceptual Organization of Sound* (MIT, Cambridge, MA).

- Bregman, A. S., and Campbell, J. (1971). "Primary auditory stream segregation, and the perception of order in rapid sequences of tones," J. Exp. Psychol. **89**, 244–249.
- Cho, J. L., Hall, M. D., and Pastore, R. E. (1993). "Stimulus properties critical to normalization of instrument timbre," J. Acoust. Soc. Am. **93**, 2402.
- Cho, J. L., Hall, M. D., and Pastore, R. E. (1994). "Normalization of musical instrument timbre," Center for Cognitive and Psycholinguistic Studies, SUNY, Binghamton, New York (unpublished).
- Dannenbring, G. L., and Bregman, A. S. (1976). "Stream segregation and the illusion of overlap," J. Exp. Psychol.: Hum. Perc. Perf. **2**, 544–555.
- Deutsch, D. (1982). "Grouping mechanisms in music," in *The Psychology of Music* (Academic, New York), Chap. 4.
- Dowling, W. J. (1968). "Rhythmic fission and perceptual organization," J. Acoust. Soc. Am. **44**, 369.
- Grey, J. M. (1978). "Timbre discrimination in musical patterns," J. Acoust. Soc. Am. **64**, 467–472.
- Handel, S. (1989). *Listening: An Introduction to the Perception of Auditory Events* (MIT, Cambridge, MA).
- Hartmann, W. M., and Johnson, D. (1991). "Stream segregation and peripheral channeling," Mus. Perc. **9**, 155–184.
- Henke, W. H. (1990). "MITSYN: A coherent family of command-level utilities for time signal processing," available from WLH, 133 Bright St., Belmont, MA 02178.
- Hirsh, I. J. (1974). "Temporal order and auditory perception," in *Sensations and Measurement*, edited by H. R. Moskowitz, B. Scharf, and J. C. Stevens (Riedel, Dordrecht, The Netherlands), pp. 251–258.
- Iverson, P. (1993). "Auditory stream segregation by musical timbre," Ph.D. dissertation, Cornell University, Ithaca, New York.
- Iverson, P. (1995). "Auditory stream segregation by musical timbre: Effects of static and dynamic acoustic attributes," J. Exp. Psychol.: Hum. Perc. Perf. **21**, 751–763.
- Jones, M. R. (1976). "Time, our lost dimension: Toward a new theory of perception, attention and memory," Psychol. Rev. **82**, 323–355.
- McAdams, S., and Bregman, A. S. (1979). "Hearing musical streams," Comput. Music J. **3**, 26–43.
- Miller, G. A., and Heise, G. A. (1950). "The trill threshold," J. Acoust. Soc. Am. **22**, 637–638.
- van Noorden, L. P. A. S. (1975). "Temporal coherence in the perception of tone sequences," Ph.D. dissertation, IPO, The Netherlands.
- Pitt, M. A. (1994). "Perception of pitch and timbre by musically trained and untrained listeners," J. Exp. Psychol.: Hum. Perc. Perf. **20**, 976–986.
- Risset, J. C., and Wessel, D. L. (1982). "Exploration of timbre by analysis and synthesis," in *The Psychology of Music*, edited by D. Deutsch (Academic, New York), Chap. 2.
- Samson, S., Zatorre, R., and Ramsay, J. (1993). "Multidimensional scaling of synthetic musical timbre: Perception of spectral and temporal characteristics," J. Acoust. Soc. Am. **93**, 2402.
- Singh, P. G. (1987). "Perceptual organization of complex-tone sequences: A tradeoff between pitch and timbre?," J. Acoust. Soc. Am. **82**, 886–899.
- Singh, P. G., and Bregman, A. S. (1993). "Spectro-temporal factors in the perceptual segregation of tonal sequences," J. Acoust. Soc. Am. **93**, 2363A.
- Wessel, D. L. (1979). "Timbre space as a musical control structure," Comput. Music J. **3**, 45–52.

The forward projection of harmonic pressure fields using the generalized internal source density method

Peter R. Stepanishen

Department of Ocean Engineering, University of Rhode Island, Narragansett, Rhode Island 02882

(Received 18 May 1996; accepted for publication 23 May 1997)

A previously developed generalized internal source density (GISD) method is extended to address the forward projection of harmonic pressure fields from normal velocity fields on a closed surface of revolution in a fluid. The GISD approach is based on decomposing the normal velocity field on the closed surface into a summation of circumferential orders where the pressure field for each order is associated with an internal linear source distribution of ring sources on the axis of revolution of the surface. The linear source distributions are formulated as integral equations of the first kind which are then solved using singular value decomposition methods. Far-field pressures are simply related to the Fourier transforms of the linear source distributions. Numerical results are presented to illustrate the forward projection of harmonic fields using the GISD method for both Dirichlet and Neumann problems. The numerical results for spherical and finite cylindrical vibrators illustrate the usefulness of the GISD method over a wide range of frequencies for both acoustic radiation and scattering problems. © 1997 Acoustical Society of America. [S0001-4966(97)04910-2]

PACS numbers: 43.20.Fn [ANN]

INTRODUCTION

Acoustic harmonic radiation from complex sources continues to be a subject of considerable interest for noise control in both air and underwater acoustics. A fundamental problem in the area is the forward and backward projection of a harmonic acoustic field from one region in space to another region. Forward projection is defined here as the projection of a normal velocity or pressure field on a closed surface S_m surrounding an acoustic source as illustrated in Fig. 1 to a more distant surface, whereas backward projection is defined here as the projection of the normal velocity or pressure field on S_m to a surface which is closer to the source. For the latter case the surface of interest may in fact be the surface of the acoustic source.

For an acoustic source in a free-space environment it is obvious that the solution of the forward projection problem can be obtained from the solution of either a classical Dirichlet or Neumann boundary value problem.^{1,2} From this point of view the solution of these classical problems is central to the basic projection problem of interest. Although there are a multitude of differing mathematical approaches which may be used to address these classical boundary value problems,^{1,2} the use of integral equation methods have become a method of present choice as a result of the increasing availability of computational tools.

Much of the recent work on the forward projection problem originated with the desire to predict the acoustic far field characteristics of acoustic sources. Horton and Innis,³ Chertock,⁴ Copley,⁵ and Schenck⁶ presented integral equation methods of predicting the far-field radiation patterns given normal velocity and/or pressure measurements on a closed surface containing the vibrating body. Typically, the method requires the solution of a surface integral equation to determine the surface pressure from normal velocity or vice versa. The surface pressure and normal velocity are then used in the Helmholtz integral equation to project the near-

field pressure information to the far-field pressure via relatively simple quadrature methods.

In 1930 von Karman proposed the use of an internal monopole source method to address axisymmetric flow about axisymmetric bodies.⁷ More recently, Stepanishen⁸⁻¹¹ and co-workers developed the internal monopole source density approach to evaluate acoustic radiation and scattering from three-dimensional bodies of revolution and two-dimensional cylinders with a plane of symmetry. During this same period Koopman and co-workers^{12,13} used a related superposition method to address the forward projection or radiation problem from a radiator of arbitrary shape. Tomalina^{14,15} also addressed the acoustic radiation from elastic structures during this same period using equivalent sources within the structure. In contrast to the works of Stepanishen and Koopman which are rooted in matching normal surface velocities over the body, Tomalina's work is based on minimizing a force distribution to determine the strengths of the internal sources.

A new mean-squared error approach was recently reported by Stepanishen¹⁶ to address the general forward and backward projection problem from complex three-dimensional bodies. The resulting generalized internal source density (GISD) method is an alternative to the use of acoustic holographic or other techniques of projecting acoustic fields and is based on representing the field over a closed surface of revolution in the fluid via internal linear distributions of ring sources on the axis of revolution of the body. The pressure fields of interest are thus viewed as resulting from finite length spatially variable line sources on the axis of revolution where the axial source strength distribution is determined from the prescribed surface field via a simple set of algebraic equations which is solved using singular value decomposition (SVD) methods. Forward and backward projection of the surface fields are simply obtained from the line source distributions. The velocity and pressure fields are ex-

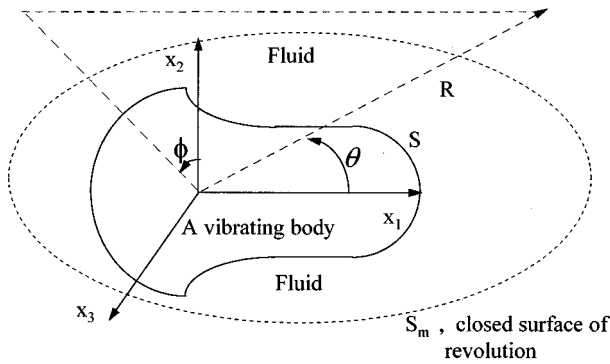


FIG. 1. An acoustic source or vibrating body in a fluid.

pressed as line integrals of the internal source distributions and far-field pressures are simply related to the Fourier transforms of the source distributions.

Although it was noted in the earlier work that the GISD method could be used to address either the Dirichlet or Neumann boundary value problems, the earlier development focused on the Dirichlet problem due to its importance for the backward projection problem. As a result of the importance of the Neumann problem in the forward projection or acoustic radiation and scattering areas, the analogous development of the GISD method for the Neumann problem is presented here. Numerical results are then presented to illustrate the accuracy of the GISD method in addressing some forward projection problems from spherical and end-capped cylindrical geometries. The results illustrate the accuracy of the field calculations using the GISD method to address acoustic radiation and scattering problems over a wide frequency range.

I. GENERAL THEORY

Consider a vibrating body with a surface S which is in contact with an external fluid as shown in Fig. 1. The forward and backward projection of a harmonic acoustic field from one region in space to another region has been previously addressed in detail¹⁶ for the problem where the harmonic pressure field on a closed surface of revolution S_m surrounding the body is presumed known from measurement. Since the Dirichlet boundary value problem was the focus of the previous development, the associated Neumann boundary value problem is addressed here. This latter problem is important in acoustic radiation and scattering studies.

It is apparent that $p(\vec{x})$, the harmonic pressure field external to S , must satisfy the reduced wave equation in the external fluid volume V , i.e.,

$$\nabla^2 p(\vec{x}) + k^2 p(\vec{x}) = 0, \quad \vec{x} \in V, \quad (1)$$

where k is the acoustic wave number. A standard separation of variables in the spherical coordinates (R, θ, ϕ) shown in Fig. 1 then leads to the following representation of $p(\vec{x})$

$$p(\vec{x}) = \sum_{n=-\infty}^{\infty} p_n(R, \theta) e^{jn\phi}, \quad \vec{x} \in V. \quad (2)$$

In addition, $p(\vec{x})$ must also satisfy the Sommerfeld radiation condition

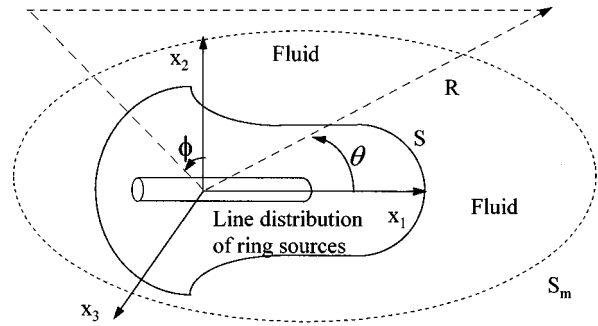


FIG. 2. A line distribution of ring sources in a body.

$$\lim_{R \rightarrow \infty} R \left[\frac{\partial p}{\partial R} + jkp \right] = 0. \quad (3)$$

For the case of specified Neumann boundary conditions on S_m it is obvious that the normal velocity $v(\vec{x})$ for $\vec{x} \in S_m$ can be decomposed into circumferential Fourier components as follows

$$v(\vec{x}(s)) = \sum_{n=-\infty}^{\infty} v_n(R(s), \theta(s)) e^{jn\phi}, \quad \vec{x}(s) \in S_m, \quad (4)$$

where s is a path parameter on S_m at $\phi=0$ and

$$v_n(R(s), \theta(s)) = \frac{\varepsilon_n}{2\pi} \int_{-\pi}^{\pi} v(\vec{x}(s)) e^{-jn\phi} d\phi, \quad (5)$$

where ε_n is the Neumann symbol, i.e., $\varepsilon_0 = 1$ and $\varepsilon_n = 2$ for $n \geq 1$.

In order to solve the Neumann boundary value problem represented by Eqs. (1)–(4), an internal linear distribution of ring sources along the axis of symmetry of S_m is introduced as shown in Fig. 2 for each circumferential order of interest. The circumferential variation of each distribution of ring sources is matched to a circumferential mode of interest for the surface pressure in Eq. (2) and the axial variation of each ring source distribution is formulated as the solution of a minimum mean-square error problem to satisfy the Neumann boundary condition in Eq. (4). Since the general procedure to solve the Neumann boundary value problem is identical to that presented earlier for the Dirichlet boundary value problem, only a brief development is presented here.

The pressure field resulting from the line source distribution of ring sources of radius a in free space with a specified circumferential variation $e^{jn\phi}$ as shown in Fig. 2 may be expressed as

$$P_n(\vec{x}) = \int_{-L}^L K_n(\vec{x}, z_0) q_n(z_0) dz_0, \quad (6)$$

where the kernel $K_n(\vec{x}, z_0)$ is the pressure at \vec{x} due to the ring source at z_0 , n is the circumferential order of interest and $q_n(z)$ is the strength of the ring source at z where $q_n(z) = 0$ for $|z| > L$. It is readily apparent from the nature of the source distribution that the kernel $K_n(\vec{x}, z_0)$ and $P_n(\vec{x})$ are both proportional to $e^{jn\phi}$ and can be expressed as

$$P_n(\vec{x}) = P_n(\vec{x})|_{\phi=0} e^{jn\phi} \quad (7)$$

and

$$K_n(\vec{x}, z_0) = K_n(\vec{x}, z_0)|_{\phi=0} e^{jn\phi}. \quad (8)$$

Furthermore, it follows from earlier work¹⁶ that the kernel $K_n(\vec{x}, z_0)$ may be expressed as follows for $ka \ll 1$ and all n :

$$K_n(\vec{x}, z_0) \approx \sin^{|n|} \theta(z_0) e^{jn\phi} h_n(kR(z_0)), \quad ka \ll 1, \quad (9)$$

where $\theta(z_0)$ and $R(z_0)$ are the spherical coordinates of a local coordinate system centered at z_0 on the axis of the internal source distribution and $h_n()$ are outgoing spherical Hankel functions of order n . It is noted that a previously introduced¹⁶ constant $K_{|n|}$ is now associated with the $q_n(z)$.

It is obvious that $P_n(\vec{x})$ satisfies the radiation condition and the reduced wave equation external to the source region for all n . The associated normal velocity on the surface S_m is readily obtained via the use of the linearized momentum equation, i.e.,

$$V_n(\vec{x}(s)) = \int_{-L}^L G_n(\vec{x}(s), z_0) q_n(z_0) dz_0, \quad (10)$$

where

$$G_n(\vec{x}(s), z_0) = \frac{j}{k\rho_0 c_0} \hat{n}_s \cdot \vec{\nabla}_s K_n(\vec{x}(s), z_0) \quad (11)$$

and $\rho_0 c_0$ is the characteristic impedance of the medium. A functional J_n is now introduced to measure the error between the specified modal velocity $v_n(R(s), \theta(s))$ and that due to the internal line source distribution of ring sources $V_n(\vec{x}(s))$ for $\vec{x} \in S_m$, i.e.,

$$J_n = \int_{S_m} |v_n(R(s), \theta(s)) e^{jn\phi} - V_n(\vec{x}(s))|^2 dS \quad (12)$$

which, in light of Eq. (7), can be reduced to

$$J_n = 2\pi \int |v_n(R(s), \theta(s)) - V_n(\vec{x}(s))|_{\phi=0}^2 r(s) ds, \quad (13)$$

where $r(s)$ is the radius of curvature in the circumferential direction.

From Eqs. (6) and (13) it is thus apparent that $q_n(z)$ must satisfy the following integral equation of the first kind

$$v_n(R(s), \theta(s)) = \int_{-L}^L G_n(\vec{x}(s), z_0)|_{\phi=0} q_n(z_0) dz_0. \quad (14)$$

Since the unknown distribution $q_n(z)$ may now be approximated using any of several methods^{16,17} which then lead to the following generic representation for $q_n(z)$

$$q_n(z) = \sum_{i=1}^N w_i^{(n)}(z) q_i^{(n)} \quad (15)$$

it then follows from Eqs. (14) and (15) that $v_n(R(s), \theta(s))$ can be represented as

$$v_n(R(s), \theta(s)) = \sum_{i=1}^N G_i^{(n)}(s) q_i^{(n)}, \quad (16)$$

where the $G_i^{(n)}(s)$ are defined as

$$G_i^{(n)}(s) = \int_{-L}^L G_n(\vec{x}(s), z_0)|_{\phi=0} w_i^{(n)}(z_0) dz_0. \quad (17)$$

As a result of the often ill posed nature of the inversion for integral equations of the first kind, the singular value decomposition (SVD) method is more generally preferred¹⁷ to determine the N unknown source densities $q_i^{(n)}$. To cast the problem into a form suitable for the SVD method consider now the following set of algebraic equations which results from the use of Eq. (16) and an $M > N$ point collocation on the surface S_m :

$$\sum_{i=1}^N G_i^{(n)}(s_m) q_i^{(n)} = v_n(R(s_m), \theta(s_m)), \quad m = 1, 2, \dots, M. \quad (18)$$

After expressing Eq. (18) in matrix form as

$$[G] \vec{q}^{(n)} = \vec{v}_n, \quad (19)$$

where $[G]$ is an $M \times N$ matrix with $M > N$, SVD methods can then be used to represent $\vec{q}^{(n)}$ as

$$\vec{q}^{(n)} = [G]^{-1} \vec{v}_n, \quad (20)$$

where $[G]^{-1}$ denotes the pseudoinverse of $[G]$. For the over determined system of interest here, SVD produces a solution that is the best approximation in the least-squares sense,¹⁷ i.e., the solution vector is determined so as to minimize $J^{(n)}$ where

$$J^{(n)} = |[G] \vec{q}^{(n)} - \vec{v}_n|^2. \quad (21)$$

The pressure field external to S_m in Fig. 1 can now be represented as a summation of fields associated with line source distributions of ring sources within S , i.e.,

$$p(\vec{x}) = \sum_{n=-\infty}^{\infty} e^{jn\phi} \int_{-L}^L K_n(\vec{x}, z_0)|_{\phi=0} q_n(z_0) dz_0, \quad \vec{x} \in V. \quad (22)$$

Furthermore, in the far field it is easily shown that

$$p(\vec{x}) \sim \frac{e^{-jkR}}{kR} \sum_{n=-\infty}^{\infty} j^{|n|+1} e^{jn\phi} \sin^{|n|} \theta \hat{Q}_n(k \cos \theta), \quad \vec{x} \in V, \quad (23)$$

where $\hat{Q}_n(k_z)$ is the Fourier transform of $q_n(z)$, i.e.,

$$\hat{Q}_n(k_z) = \int_{-L}^L e^{jk_z z_0} q_n(z_0) dz_0. \quad (24)$$

More generally, in light of the approximation for $q_n(z)$ in Eq. (15), $p(\vec{x})$ can be expressed as

$$p(\vec{x}) = \sum_{n=-\infty}^{\infty} \sum_{i=1}^N T_{ni}(R, \theta) q_i^{(n)} e^{jn\phi}, \quad \vec{x} \in V, \quad (25)$$

where

$$T_{ni}(R, \theta) = \int_{-L}^L K_n(\vec{x}, z_0)|_{\phi=0} w_i^{(n)}(z_0) dz_0. \quad (26)$$

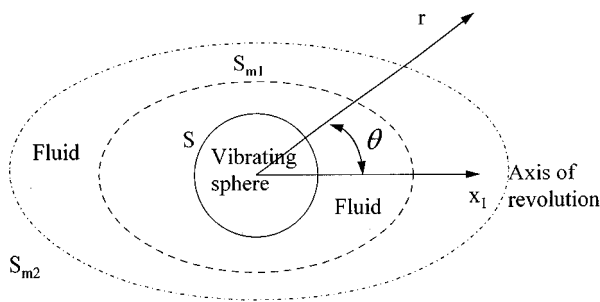


FIG. 3. A spherical source and the projection surfaces.

It is noted that the entire pressure and velocity fields external to S can thus be simply obtained from the linear source density distributions if they are contained within S .

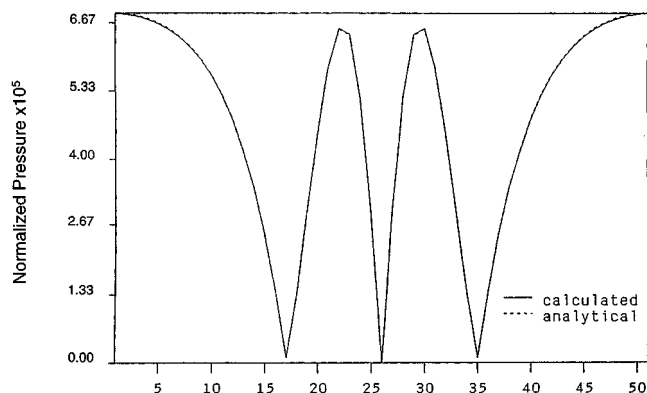
II. NUMERICAL RESULTS

Numerical results are now presented to illustrate some typical applications of the GISD method in forward projecting harmonic pressure fields. For the sake of brevity only axisymmetric field problems are addressed. Both Dirichlet and Neumann boundary problems are addressed using the GISD method where the Dirichlet problems are addressed using the GISD method presented in an earlier paper¹⁶ and the Neumann problems are addressed using the GISD method presented here in Sec. I. Field problems associated with spherical sources are first addressed since closed-form solutions are available for comparison purposes. Finite cylindrical sources are then addressed as a result of their importance in the radiation and noise control areas.

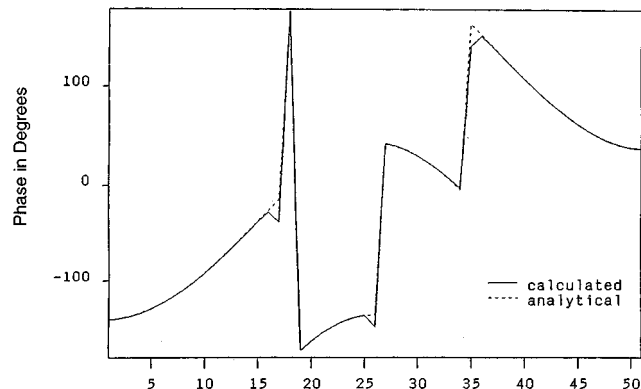
Consider first the forward projection of the pressure field resulting from a harmonically vibrating sphere of radius a as shown in Fig. 3 with the prescribed axisymmetric normal velocity distribution $V_n P_n(\cos \theta)$ which is an n th-order Legendre polynomial. The external pressure field in the surrounding fluid is simply obtained via separation of variables. Since the pressure and velocity fields are available in closed form, the analytical solutions can be used to verify the accuracy of the forward projection of acoustic fields using the GISD method.

The geometry of initial interest is shown in Fig. 3 where the surface over which the pressure is assumed to be known is denoted by S_{m1} , and the surface to which the pressure will be projected is denoted by S_{m2} . Although S_{m1} and S_{m2} are required to be surfaces of revolution, the present study utilized only ellipsoidal surfaces where the major and minor semiaxes are a_1 and b_1 for S_{m1} and a_2 and b_2 for S_{m2} . For each of the following cases the pressure was first evaluated over S_{m1} from the analytical result, the resulting Dirichlet problem was then solved via the use of the GISD method, and then the pressure on S_{m2} was simply evaluated via the line integral of the internal source density and compared to the corresponding analytical result.

The forward projection problem for a sphere of radius b which is harmonically vibrating in the third mode, i.e., $n = 3$, is first considered. The magnitude of the normalized pressure and the phase, which were obtained both analytically and via the GISD method with $a_1 = 2b$, $b_1 = b$, and



(a)



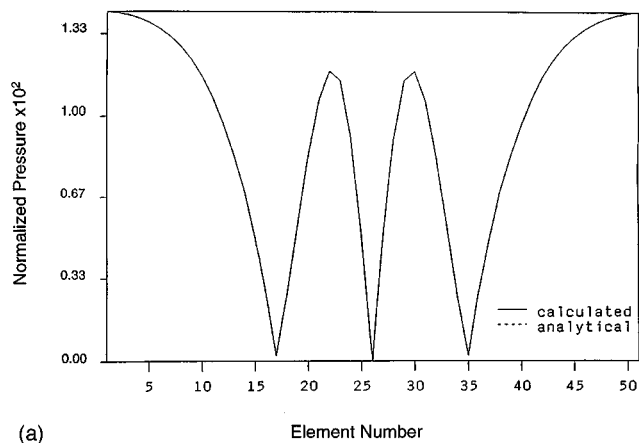
(b)

FIG. 4. Pressure on ellipsoidal surface due to normal velocity $V(b, \theta) = V_3 P_3(\cos \theta)$ on a spherical surface for $kb = 0.5$. (a) Magnitude, (b) phase.

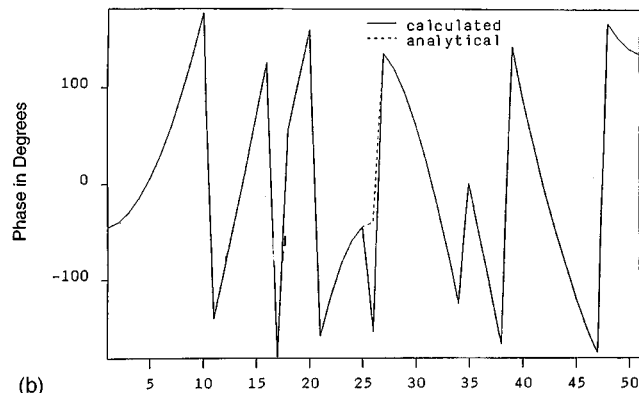
$a_2 = 16b$ with $b_2 = 8b$, are shown in Fig. 4 for $kb = 0.5$ and in Fig. 5 for $kb = 2$ as a function of element position on S_{m2} . The normalization factor for the pressure is $\rho_0 c_0 V_3$. It is noted that 51 equispaced angles were used on S_{m2} and 15 nonuniformly positioned internal sources were used along the axis of symmetry between $\pm 0.75b$ where the positions were determined from Gaussian-Legendre integration. Although some minor differences in phase are noted at the pressure nulls, the agreement is generally excellent. Such results are typical for the low- and midfrequency range.

Consider again the forward projection problem from the sphere where $n = 3$ and now $kb = 20$ which is considered here to be a high-frequency case. The effect of using 15, 25, and 35 nonuniformly positioned internal sources on the magnitude of the normalized pressure is shown in Fig. 6 where 101 equispaced angles were used on S_{m2} . In general, as kb increases the number of internal sources must also increase to maintain the same accuracy. Furthermore, as n increases both the number of internal sources and element positions on S_{m2} must increase to obtain acceptable accuracy.

As a second class of problems of interest, consider the Dirichlet problem of determining the normal velocity on a closed surface of revolution in a fluid from the pressure field on the surface. After determining the normal velocity on the closed surface, the normal component of the local intensity vector can then be simply determined and the power flow



(a)



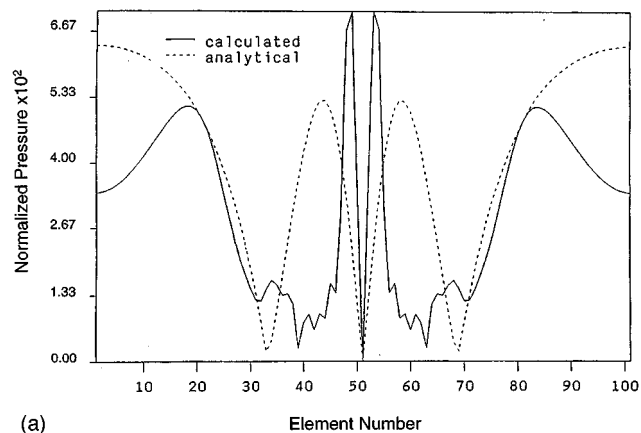
(b)

FIG. 5. Pressure on ellipsoidal surface due to normal velocity $V(b, \theta) = V_3 P_3(\cos \theta)$ on a spherical surface for $kb=2$. (a) Magnitude, (b) phase.

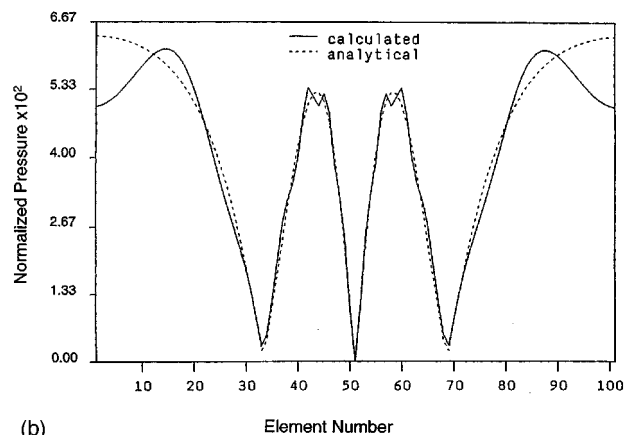
from the enclosed source can then be determined via an integration. Since the pressure and velocity fields are known in closed form for the specific case of a spherical source, the spherical source again provides an ideal test problem.

Consider again the geometry shown in Fig. 3 where the surface over which the pressure is assumed to be known is denoted by S_{m1} which is an ellipsoidal surface. In contrast to the preceding examples, the normal velocity on S_{m1} is to be determined. In the following example the pressure was first evaluated over S_{m1} from the analytical result and the resulting Dirichlet problem was then solved via the use of the GISD method. The normal velocity of interest on S_{m1} was then simply evaluated via a line integral of the internal source density and compared to the corresponding analytical result.

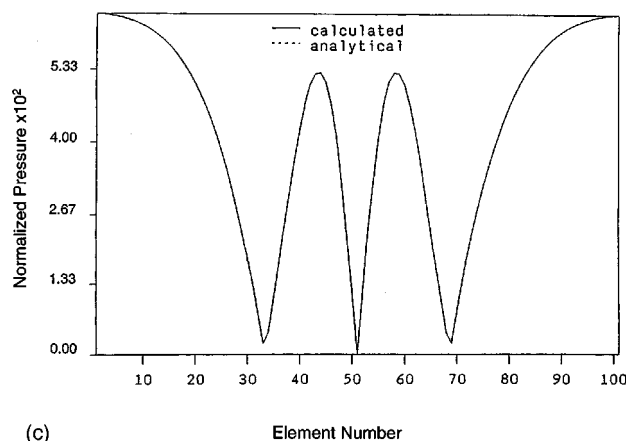
The simple case of a harmonically translating sphere, i.e., $n=1$, is now considered. The magnitude of the normalized normal velocity, which was obtained both analytically and via the GISD method, is shown as a function of element position on S_{m1} in Fig. 7 for the case of $kb=2.0$ with $a_1=4b$, $b_1=b$. The normalization factor for the normal velocity is V_1 . Once again 51 equispaced angles were used on S_{m1} and 15 nonuniformly positioned internal sources were used along the axis of symmetry between $\pm 0.75b$ where the positions were determined from Gaussian-Legendre integration. The results in Fig. 7 indicate the nature of the errors involved in using the GISD method. In general, the GISD solution oscillates about the exact solution due to the mean-



(a)



(b)



(c)

FIG. 6. The effect of varying the number of internal sources on the pressure magnitude on an ellipsoidal surface due to normal velocity $V(b, \theta) = V_3 P_3(\cos \theta)$ on a spherical surface for $kb=20$. (a) 15 sources, (b) 25 sources, (c) 35 sources.

square error formulation. Additional surface points and internal sources are required to further reduce the error as noted earlier.

Since the scattered field resulting from an acoustic plane wave impinging onto a rigid sphere is readily formulated as the solution of a classical Neumann problem, the scattered field is also readily obtained via the GISD method presented in Sec. II. Numerical results for the far-field scattering function as a function of θ are thus presented in Fig. 8(a)–(c) for $kb=0.1$, 1.0, and 10, respectively. For these cases 15 uniformly positioned internal sources were used along the axis

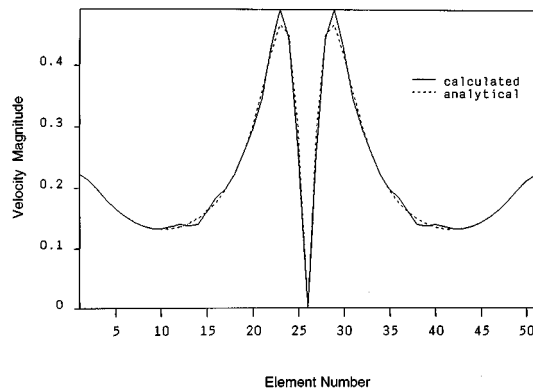


FIG. 7. Velocity magnitude on an ellipsoidal surface due to normal velocity $V(b, \theta) = V_1 P_1(\cos \theta)$ on a spherical surface for $kb = 2$.

of symmetry between $\pm 0.75b$. Analytical results for the far-field scattering function are readily obtained using eigenfunction expansion methods and are also presented in the figures. The change in the nature of the scattering from back-scattering to forward scattering as kb increases is clearly evident. It is also clearly apparent that the analytical and GISD results are in excellent agreement for the low- and midfrequency cases. In contrast to the earlier problems which involved a single mode or spherical harmonic, the scattered field involves a multimodal description in which the number of terms required for convergence increases with kb .

The Neumann problem for finite cylindrical source geometries is now briefly addressed. If the cylindrical source is mounted in an infinite cylindrical rigid baffle as illustrated in Fig. 9(a), the resulting axisymmetric Neumann problem can of course be solved via the use of integral transform methods whereas surface integral equation methods, e.g., CHIEF, can be used to address the more general cylindrical problem illustrated in Fig. 9(b). The more general cylindrical problem is, however, also readily addressed via the GISD method as illustrated below.

Consider now the case of a nonuniform velocity over a finite cylindrical surface of length L and radius b with hemispherical end caps as illustrated in Fig. 9(b). Several test problems involving a finite cylindrical surface with hemispherical end caps where $L = 2b$ have been addressed using the GISD method and the results have been compared to those obtained via the CHIEF method. For each problem the surface was subdivided into 101 elements with 41 elements on the cylindrical portion and 30 elements on each end cap and 25 internal sources were distributed along the axis. The normal velocity of the end caps was zero for all cases and the velocity of the cylinder was sinusoidal in space, i.e., $V_m \sin(m\pi x/L)$.

The real and imaginary parts of the normalized surface pressure on the finite cylinder where $L = 2b$ and $m = 1$ are presented as a function of element number in Fig. 10(a) and (b) for $kL = 0.1$ and 1.0 , respectively. Field pressure data on a spherical surface where $r = 5L$ are presented in Fig. 11(a) and (b) and for the same low- and midfrequency cases. As indicated by the data, the agreement between the GISD and CHIEF results is excellent both at the surface and in the

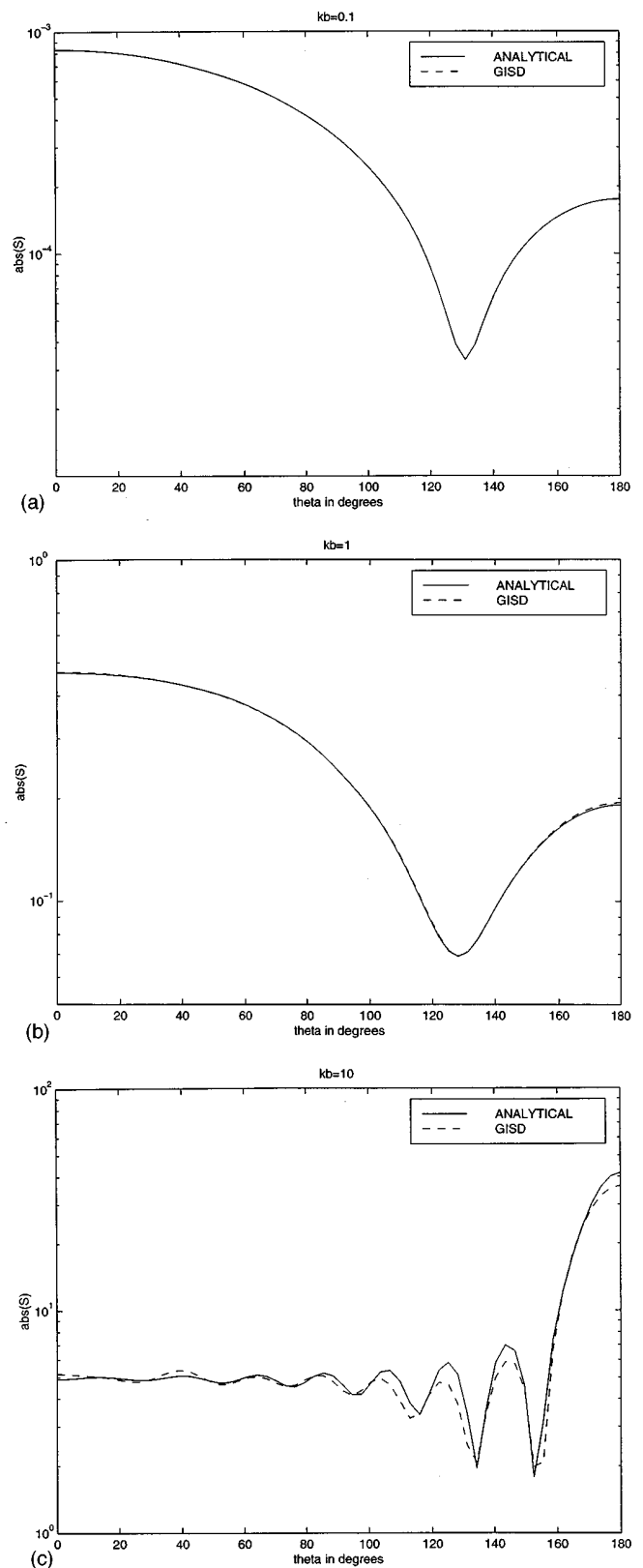


FIG. 8. Far-field scattering function versus θ for plane-wave scattering from a rigid sphere. (a) $kb = 0.1$, (b) $kb = 1.0$, (c) $kb = 10.0$.

field. The decay of the evanescent portion of the surface wave field is readily apparent for the low- and midfrequency case and, as expected, the effect decreases as kL increases.

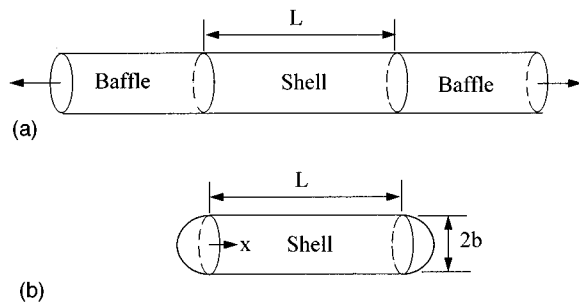


FIG. 9. Two models of cylindrical shells. (a) Baffled cylindrical shell, (b) cylindrical shell with hemispherical end caps.

Similar sets of data are presented in Figs. 12 and 13 for $m=5$, and once again the agreement is excellent.

III. SUMMARY AND CONCLUSIONS

The forward projection of acoustic fields is important in several areas including transducer and array calibration, noise prediction from structures, and source identification problems on structures. Since a new GISD method was recently presented¹⁶ in detail to address the forward and backward projection of harmonic fields for the Dirichlet problem, the basic method is applied here to address the Neumann problem, i.e., the projection of harmonic pressure fields from

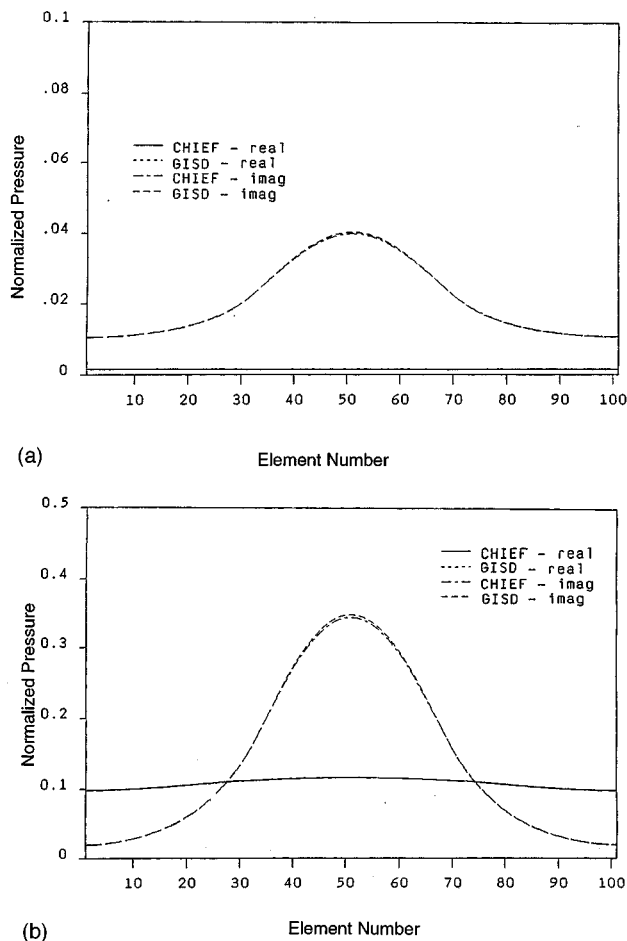


FIG. 10. Surface pressure on a finite cylinder with $L=2b$ and the normal velocity $V_1 \sin(\pi x/L)$. (a) $kL=0.1$, (b) $kL=1.0$.

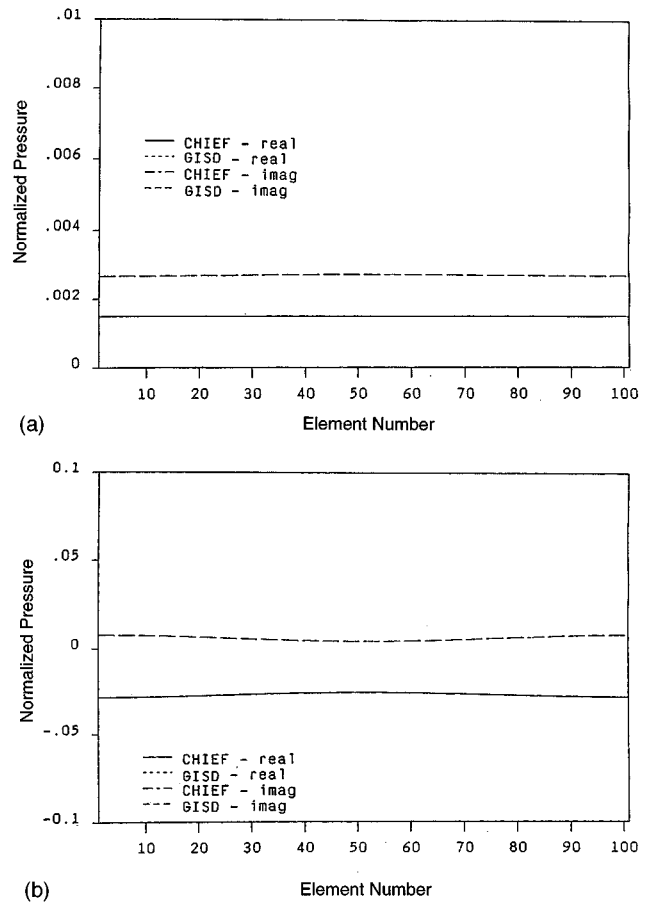
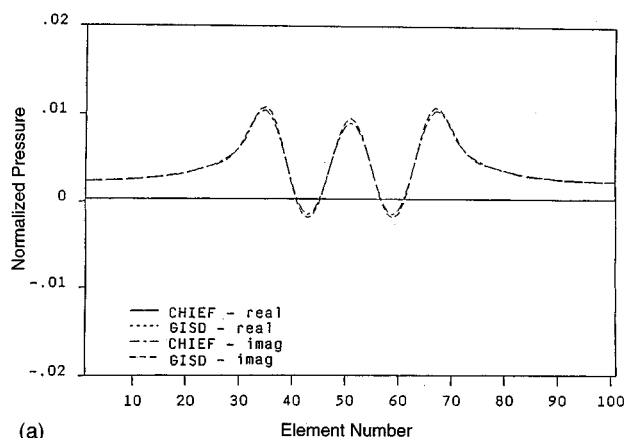


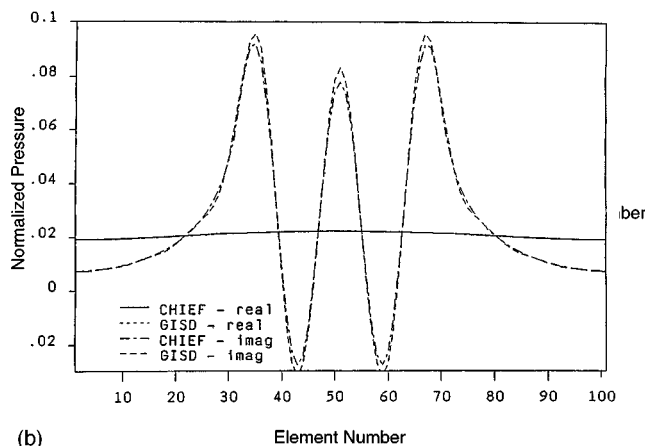
FIG. 11. Pressure at $r=5L$ from a finite cylinder with $L=2b$ and the normal velocity $V_1 \sin(\pi x/L)$. (a) $kL=0.1$, (b) $kL=1.0$.

a normal velocity field on a surface of revolution encompassing a complex three-dimensional source. The GISD method is based on decomposing the normal velocity field on the closed surface into a summation of circumferential orders where the pressure field for each order is associated with an internal linear source distribution of ring sources on the axis of revolution of the surface. The linear source distributions are formulated as integral equations of the first kind which are then solved using singular value decomposition methods. Far-field pressures are simply related to the Fourier transforms of the linear source distributions.

Numerical results are presented to illustrate the forward projection method denoted here as the GISD method from both spherical and finite cylindrical geometries. Since numerical results were not presented in the earlier paper for the Dirichlet problem, numerical results are presented here for the Dirichlet forward projection problems. An analytical solution for the spherical problem is used to illustrate the accuracy of the new GISD method for the forward projection of the pressure field for a Dirichlet problem. The numerical results indicate the excellent accuracy of the method over a wide range of normalized frequencies. Since the surface of interest can be readily selected for the Dirichlet problem, the GISD method is well suited to the forward projection of measured pressure fields on a closed surface which can be chosen to match the eccentricity of the source.



(a)

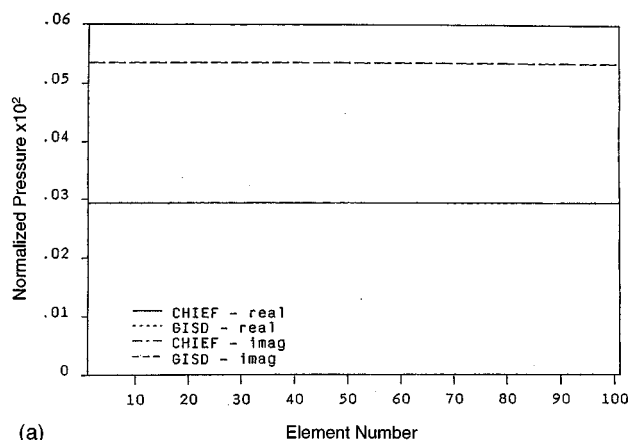


(b)

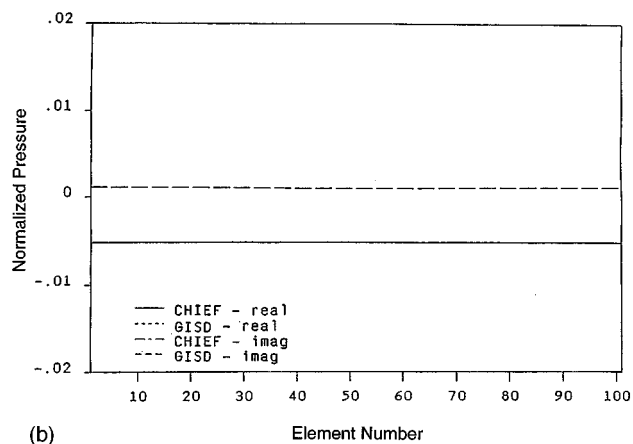
FIG. 12. Surface pressure on a finite cylinder with $L=2b$ and the normal velocity $V_5 \sin(5\pi x/L)$. (a) $kL=0.1$, (b) $kL=1.0$.

Numerical results for the forward projection of fields associated with the Neumann problem are also presented. Acoustic plane-wave scattering from a rigid body of revolution is readily addressed using the GISD method. Since a closed-form solution for the scattering from a rigid sphere is available, the scattered field was evaluated using the GISD method as a function of normalized frequency and angle. The results were shown to be in excellent agreement with the analytical results. Numerical results for a finite cylindrical shell with nonuniform normal velocities and hemispherical end caps are also presented. These results, which also encompass a wide range of frequencies, further illustrate the usefulness of the GISD approach for finite cylindrical geometries of practical interest.

In concluding it is noted that the GISD method provides an alternative to the use of more conventional boundary element methods of projecting fields from either Dirichlet or Neumann boundary data on a closed surface of revolution. In contrast to the use of the surface Helmholtz integral equation which exhibits uniqueness problems associated with an interior problem when addressing the exterior projection problem as noted by Schenck,⁷ there are no interior resonance problems associated with the GISD method. Also, unlike the boundary element methods which require the numerical evaluation of surface integrals with weakly singular kernels as in CHIEF⁷ or more strongly singular kernels as in the Burton and Miller formulation,¹⁸ the GISD method is more



(a)



(b)

FIG. 13. Pressure at $r=5L$ from a finite cylinder with $L=2b$ and the normal velocity $V_5 \sin(5\pi x/L)$. (a) $kL=0.1$, (b) $kL=1.0$.

simply implemented since the kernel is nonsingular. Finally, the simplicity of the GISD method for the far-field forward projection problem is noted where the far field is simply evaluated from the one-dimensional Fourier transforms of the linear source distributions of ring sources.

Although the present paper has focused on the use of the GISD method for the forward projection problem, the method is also readily applicable to the important backward projection problem.¹⁶ In particular, it is noted that the method provides an alternative to existing acoustic holographic methods of backward projecting pressure fields on a measurement surface enclosing a complex source in order to evaluate the pressure, normal velocity, and power flow at the surface of the source. Although the measurement surface must be smooth and rotationally symmetric about an axis of interest, the shape may be more conformal to the source of interest than spherical or cylindrical holographic methods. In contrast to the forward projection problem addressed in the present paper the evanescent portion of the source field can be expected to be of major importance in the backward projection problem.¹⁹⁻²¹ Work on the backward projection is in progress and will be reported at a later date.

Additional work is required to determine the limitations of the GISD method. In this regard several points are worthy of note. As noted earlier, the linear source density distributions for both the Dirichlet and Neumann problems have been formulated as the solutions of inhomogeneous integral

equations of the first kind which are often ill conditioned. It is apparent that the use of various approximations and quadrature methods naturally leads to underdetermined sets of algebraic equations and the use of SVD methods to solve the resultant equations is a necessity. It is equally apparent that smooth surfaces and distributions of interest are less likely to result in numerical problems. Although the pressure fields of interest are uniquely specified by the Dirichlet or Neumann boundary data, the source distributions are dependent upon the nature of the approximations. Work is presently in progress to address the limitations of the GISD method and the problem of obtaining the source distribution which provides the best estimate of the desired field.

ACKNOWLEDGMENT

The author wishes to thank Janet Hillenbrand for her assistance in obtaining the numerical results.

- ¹P. M. Morse and H. Feshbach, *Methods of Theoretical Physics* (McGraw-Hill, New York, 1953).
- ²I. Stakgold, *Boundary Value Problems of Mathematical Physics* (MacMillan, New York, 1967).
- ³C. W. Horton and G. S. Innis, Jr., "The computation of the far field radiation patterns from measurements made near the source," *J. Acoust. Soc. Am.* **76**, 1823–1828 (1984).
- ⁴G. Chertok, "Sound radiation from vibrating surfaces," *J. Acoust. Soc. Am.* **36**, 1305–1313 (1964).
- ⁵L. G. Copley, "Integral equation method for radiation from vibrating bodies," *J. Acoust. Soc. Am.* **41**, 807–816 (1967).
- ⁶H. A. Schenck, "Improved integral formulation for acoustic radiation problems," *J. Acoust. Soc. Am.* **44**, 41–58 (1968).
- ⁷T. von Karman, "Calculation of pressure distribution on airships hulls," NACA TM 574 (1930).
- ⁸P. R. Stepanishen and H. W. Chen, "Surface pressure and harmonic loading on shells of revolution using an internal source density method," *J. Acoust. Soc. Am.* **92**, 2248–2259 (1992).

- ⁹P. R. Stepanishen and H. W. Chen, "Acoustic harmonic radiation and scattering from shells of revolution using finite element and internal source density methods," *J. Acoust. Soc. Am.* **92**, 2248–2259 (1992).
- ¹⁰P. R. Stepanishen and S. Ramakrishna, "Acoustic radiation from cylinders with a plane of symmetry using internal multi-pole line-source distributions," *J. Acoust. Soc. Am.* **93**, 658–672 (1993).
- ¹¹S. Ramakrishna and P. R. Stepanishen, "Acoustic scattering from cylinders with a plane of symmetry using internal multi-pole line-source distributions," *J. Acoust. Soc. Am.* **93**, 673–682 (1993).
- ¹²G. H. Koopman, L. Song, and J. B. Fahline, "A method for computing acoustic fields based on the superposition principle," *J. Acoust. Soc. Am.* **86**, 2433–2438 (1989).
- ¹³J. B. Fahline and G. H. Koopman, "A numerical solution for the general radiation problem based on the combined methods of superposition and singular-value decomposition," *J. Acoust. Soc. Am.* **90**, 2808–2819 (1991).
- ¹⁴T. M. Tomilina, "Fast algorithm for sound field analysis based on fictitious sources method," *Int. Congress Acoust.* **19**, 433 (1989).
- ¹⁵Y. I. Bobrovnikskii and T. M. Tomilina, "Application of ESM to a calculation of a finite elastic structure radiation," *Sov. Phys. Acoust.* **36**, 334–338 (1990).
- ¹⁶P. R. Stepanishen, "A generalized internal source density method for the forward and backward projection of harmonic pressure fields from complex bodies," *J. Acoust. Soc. Am.* **101**, 3270–3277 (1997).
- ¹⁷W. H. Press, B. P. Flannery, S. A. Teukolsky, and W. T. Vetterling, *Numerical Recipes* (Cambridge U.P., Cambridge, England, 1986).
- ¹⁸A. J. Burton and G. F. Miller, "The application of integral equation methods to the numerical solution of some exterior boundary value problems," *Proc. R. Soc. London, Ser. A* **323**, 201–210 (1971).
- ¹⁹E. G. Williams, H. G. Dardy, and K. B. Washburn, "Generalized nearfield acoustical holography for cylindrical geometry: Theory and experiment," *J. Acoust. Soc. Am.* **81**, 389–407 (1987).
- ²⁰G. V. Borgiotti, "The power radiated by a vibrating body in an acoustic fluid and its determination from boundary measurements," *J. Acoust. Soc. Am.* **88**, 1884–1893 (1990).
- ²¹D. M. Photiadis, "The relationship of singular value decomposition to wave-vector filtering in sound radiation problems," *J. Acoust. Soc. Am.* **88**, 1152–1159 (1990).

A method for acoustic scattering by slender bodies.

I. Theory and verification

Zhen Ye^{a)}

Ocean Acoustics, Institute of Ocean Sciences, Sidney, British Columbia, Canada

Emile Hoskinson

Department of Physics, University of British Columbia, British Columbia, Canada

Richard K. Dewey

School of Earth and Ocean Sciences, University of Victoria, British Columbia, Canada

Li Ding^{b)}

National Research Institute of Fisheries Engineering, Hasaki, Ibaraki, Japan

David M. Farmer

Ocean Acoustics, Institute of Ocean Sciences, Sidney, British Columbia, Canada

(Received 26 November 1996; revised 6 May 1997; accepted 14 May 1997)

This paper presents a new approach for calculating sound scattering by slender scatterers. The method is based on the assumption that the sound scattering function can be approximated by superimposing the scattered waves from a series of small adjacent cylindrical elements, with each of these elements scattering sound as though it were part of an infinite straight cylinder of the same radius. Using the Kirchhoff integral theorem, the bistatic scattering function is derived rigorously within the accuracy of the assumption. To validate the approach, the solution is applied to sound scattering by fluid prolate spheroids, for which the exact solution is known. Numerical comparison with the exact solution reveals that the new approach is very versatile; it can predict scattering patterns remarkably comparable to that obtained by the exact solution for a wide range of incident angles. For incidence within approximately $\pm 20^\circ$ of the broadside direction, the scattering patterns predicted by the new method coincide uniformly with the exact results. Agreement in the absolute scattering amplitude slowly deteriorates as the incidence is tilted away from the broadside aspect. However, the method consistently produces scattering patterns highly correlated to the results from the exact solution; this is potentially useful for target identification based on pattern recognition techniques. The results also show that the new method works better on the whole as the elongation of the target increases. Furthermore, calculation of cross-correlation coefficients indicates that the present method works slightly better for rigid bodies than for weak fluid bodies. The low-frequency scattering by gas-filled spheroids is also considered. It is shown that near resonance the scattering is almost isotropic, in agreement with the prediction of previous simple analytic solution. © 1997 Acoustical Society of America. [S0001-4966(97)02109-7]

PACS numbers: 43.20.Fn, 43.20.Tb, 43.30.Gv [JEG]

INTRODUCTION

Acoustic scattering by slender bodies of revolution has been the subject of intensive study over the past few decades, and continues to be an active area of research. A reason for this is that a slender body can be used to model many important underwater targets such as marine animals, suspended sands, and sediment inhomogeneities.

Except for a few geometries, for which the technique of separation of variables can be used, such as sphere, infinite cylinder, and spheroid, no analytic solution can be derived to describe the scattering by an arbitrary slender scatterer. Approximate methods are thus often used. These include, to name a few, the volume integral method (Montroll and Hart,

1951), the *T*-matrix method (Waterman, 1969), the Kirchhoff approximate method (e.g., Gaunaurd, 1985), the geometrical theory of diffraction (Keller and Ahluwalia, 1971), the matched asymptotic expansions method (Tran Van Nhieu and Ywonne, 1994), the Sommerfeld–Watson transformation method (Rumerman, 1992), the boundary integral method (Schenck, 1968), and the cylinder method proposed by Junger (1982).

Recently, using the Kirchhoff integral theorem (e.g., Waterman, 1969) and the exact solution for infinite cylinders (Flax *et al.*, 1980), Ye (1997a) proposed a method for calculating the scattering of sound by a straight cylinder of finite length. The underlying assumption in this method states that a differential element of a finite cylinder scatters sound as though it were a part of an infinite cylinder of the same radius. Under this assumption, the method is considered to be rigorous as far as the scattering by the cylinder body is concerned. However, many scatterers of practical interest are

^{a)}Now at: Department of Physics, National Central University, Taiwan, ROC.

^{b)}Affiliated with Institute of Ocean Sciences, Sidney, British Columbia, Canada.

of slender shape, whose cross section can be approximated as circular with the radius varying along the longitudinal axis; this general scattering geometry is now referred to as the deformed cylinder in the literature. Therefore, a question immediately follows: can the new cylinder method be extended to describe the sound scattering by deformed cylinders?

The purpose of this paper is to present a new method for sound scattering by deformed cylinders based on the findings of Ye (1997a). Invoking the aforementioned assumption and following the line in Ye (1997a), the exact solution for an infinite straight cylinder will be used in the Kirchhoff integral theorem to obtain an analytic integral formula for the sound scattering by a deformed cylinder. As a test, the formula will be applied to prolate spheroids, and the results will be compared with the exact solution obtained by the variable separation method. Such a direct comparison will not only give us an accurate evaluation of the present approximate method, but also guide us in improving the method in the future. Although the method can be used for deformed cylinders of any material composition, here we will focus on fluid-filled deformed cylinders, i.e., no shear waves in the scatterers. Fluid-filled scatterers are particularly important, as they can be used to model the sound scattering by important targets such as fish and zooplankton.

There are significant practical reasons for pursuing a more accessible solution for the scattering from slender bodies, including those shapes for which an exact solution exists. One such example is the scattering from prolate spheroids. The exact solution [see, for example, Yeh (1967)] involves the summation of radial and azimuthal spheroidal wave functions, with coupled boundary conditions. Although analytically tractable, the numerical calculation of the exact prolate spheroid solution, in particular the radial spheroidal wave function, is extremely difficult and involves retaining accuracy beyond 128 bit resolution. The method described here is relatively "simple" and fast in comparison, and for higher frequencies, allows the calculation of an approximate scattering function for regions where the exact solution has difficulty converging.

I. THE MODEL

The cylinder model in Ye (1997a), which has been restricted to straight cylinders, can be extended to a slender body of revolution as follows. Consider an arbitrary slender scatterer located at the origin, with a cross section approximated as circular [Fig. 1(a)]. The points on the longitudinal axis, which need not be a straight line, are denoted by z ; the radius of the cross section is a function of z and written as $a(z)$. A unit plane wave is incident on the scatterer, and can be expressed as $p_i = e^{i\mathbf{k}_i \cdot \mathbf{r}}$ with the time factor $-i\omega t$ being suppressed. Here \mathbf{k}_i is the incident wave vector, with norm $k = \omega/c$, ω being the angular frequency and c the sound speed in the propagating medium. According to the Kirchhoff integral theorem, the scattered wave at far field can be written as

$$p_s(\mathbf{r}) \approx f(\mathbf{k}_i, \mathbf{k}_s) \frac{e^{ikr}}{r}, \quad (1)$$

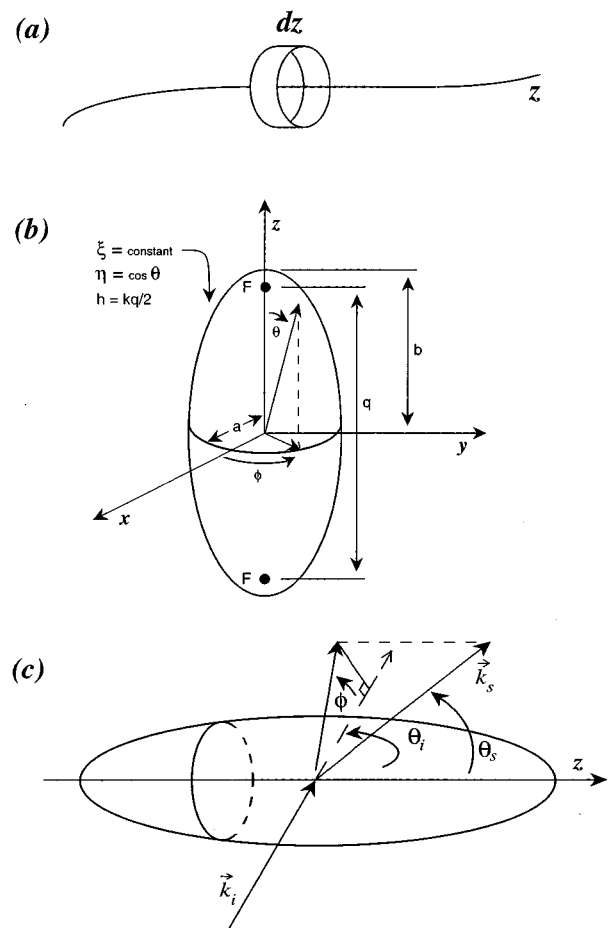


FIG. 1. Geometrical layout of the problem: (a) a deformed cylinder; (b) a prolate spheroid; (c) scattering coordinates for a prolate spheroid.

with the scattering function $f(\mathbf{k}_i, \mathbf{k}_s)$ being given by

$$f(\mathbf{k}_i, \mathbf{k}_s) = -\frac{1}{4\pi} \int_S ds' e^{-i\mathbf{k}_s \cdot \mathbf{r}} [\nabla' p_s(\mathbf{r}) + ik_s p_s(\mathbf{r})], \quad (2)$$

where \mathbf{k}_s is the scattered wave vector, \mathbf{n} is the outward normal on the surface of the scatterer, and the integration is performed on the surface.

From Eq. (2) it is clear that once the values of the scattered wave and its derivative on the surface are known, the scattering function can be evaluated from the surface integration. Unfortunately, no exact solution for the scattered wave can be deduced except for a few separable geometries. Approximate solutions are usually resorted to. One approximation is the well-known Kirchhoff approximation, in which the scattered wave is considered as an integral of the scattering from surface elements each of which has the reflection coefficient equal to that of an infinite plane surface. However, it has been found that such an approximation is restricted to high frequencies and rigid/soft scatterers. An alternative way of evaluating the scattered wave at the interface is to employ the assumption of Junger (1982) that a differential length of the body scatters sound as though it were part of an infinite cylinder of the same radius, for which an exact solution exists.

Consider a differential element dz of an elongated scatterer located at $\mathbf{r}(z)$. We approximate it as a straight cylinder element with radius $a(z)$, whose axis is represented by the unit vector $d\hat{z}$. Substituting the exact solution for the infinite cylinder (Flax *et al.*, 1980) into Eq. (2), the integral can be readily carried out following Ye (1997a). The resulting scattering function from this cylindrical element can be written as:

$$df(\mathbf{k}_i, \mathbf{k}_s) = \frac{-i dz}{\pi} \sum_{n=0}^{\infty} B_n(z) F_n(z) (-i)^n \times \cos(n\phi(z)) e^{i\mathbf{k}_i \cdot \mathbf{r}(z) - i\mathbf{k}_s \cdot \mathbf{r}(z)}. \quad (3)$$

The azimuthal angle $\phi(z)$ between the incident and scattering directions is defined in the plane perpendicular to the axis of the cylindrical element, and can be expressed as

$$\phi(z) = \cos^{-1} \left(\frac{[\hat{k}_i - (\hat{k}_i \cdot d\hat{z})d\hat{z}] \cdot [\hat{k}_s - (\hat{k}_s \cdot d\hat{z})d\hat{z}]}{|\hat{k}_i - (\hat{k}_i \cdot d\hat{z})d\hat{z}| |\hat{k}_s - (\hat{k}_s \cdot d\hat{z})d\hat{z}|} \right), \quad (4)$$

where \hat{k}_i and \hat{k}_s refer to the unit incident and scattering wave vectors. In Eq. (3),

$$B_n(z) = \frac{-i^n \epsilon_n [J_n(ka(z) \sin \theta_i) - \beta_n J_n'(ka(z) \sin \theta_i)]}{H_n^{(1)}(ka(z) \sin \theta_i) - \beta_n H_n^{(1)'}(ka(z) \sin \theta_i)}, \quad (5)$$

and

$$F_n(z) = \frac{\pi}{2i} (ka(z)) \times [H_n^{(1)'}(ka(z) \sin \theta_i) J_n(ka(z) \sin \theta_s) \sin \theta_i - H_n^{(1)}(ka(z) \sin \theta_i) J_n'(ka(z) \sin \theta_s) \sin \theta_s], \quad (6)$$

where

$$\theta_i = \cos^{-1}(\hat{k}_i \cdot d\hat{z}), \quad \theta_s = \cos^{-1}(\hat{k}_s \cdot d\hat{z}),$$

and

$$\beta_n = \frac{k\rho_1}{k_1\rho} \frac{J_n(k_1 a(z) \sin \theta_i)}{J_n'(k_1 a(z) \sin \theta_i)} = g h_c \frac{J_n(k_1 a(z) \sin \theta_i)}{J_n'(k_1 a(z) \sin \theta_i)},$$

in which ρ_1, ρ are the mass densities inside and outside the cylinder respectively, $a(z)$ is the radius of the cylindrical element, $g = \rho_1/\rho$, and $h_c = k/k_1$. In the above J_n is the n th order Bessel function of the first kind, $H_n^{(1)}$ is the Hankel function of the first kind, and ϵ_n is the Neumann factor given by

$$\epsilon_n = \begin{cases} 1, & n=0; \\ 2, & n=1,2,3,\dots \end{cases}$$

Furthermore, $J_n'(x)$ and $H_n^{(1)'}(x)$ denote $dJ_n(x)/dx$ and $dH_n^{(1)}(x)/dx$, respectively. Note that in the case of a rigid scatterer, where g and h_c go to infinity, $B_n(z) \rightarrow J_n'(ka(z) \sin \theta_i)/H_n^{(1)'}(ka(z) \sin \theta_i)$.

For the elongated scatterer, the total scattering function is the sum of the scattering functions of each such differential cylindrical element, and is written as

$$f(\mathbf{k}_i, \mathbf{k}_s) = \int df(\mathbf{k}_i, \mathbf{k}_s) = \int dz \frac{-i}{\pi} \sum_{n=0}^{\infty} B_n(z) F_n(z) (-i)^n \times \cos(n\phi(z)) e^{i\mathbf{k}_i \cdot \mathbf{r}(z) - i\mathbf{k}_s \cdot \mathbf{r}(z)}. \quad (7)$$

The integration is performed along the longitudinal axis of the scatterer, which need not be a straight line. As usual, the differential scattering cross section is defined as

$$\sigma(\mathbf{k}_i, \mathbf{k}_s) = |f(\mathbf{k}_i, \mathbf{k}_s)|^2. \quad (8)$$

The target strength is defined as usual

$$TS = 10 \log_{10} \sigma. \quad (9)$$

A few notes are appropriate here. (1) When $\mathbf{k}_s = \pm \mathbf{k}_i$, direct forward and back scatter, by the Wronskian identity

$$[J_n(x)H_n^{(1)'}(x) - J_n'(x)H_n^{(1)}(x)] = \frac{2i}{\pi x},$$

Eq. (7) becomes equivalent to a formula heuristically derived by Stanton (1989); a more detailed discussion of Stanton's work and how it could relate to the present method can be found in Ye and Furusawa (1995) and Ye (1997a). (2) The extension from a straight cylinder to a slender body ignores possible "tapering" effects due to the variation of radius along the longitudinal axis. At this moment, how to incorporate such effects properly remains an open issue. Intuitively, such effects are not important when the longitudinal length is much larger than the transverse dimension, and when incident angles are near broadside. (3) The assumption of Junger (1982), in fact, only takes into account the multiple reflection in the transverse direction inside the scatterer, while the possible multiple reflection between the ends of the scatterer along the longitudinal axis is ignored; therefore, intuitively this assumption is more appropriate for long scatterers and the accuracy of the approximation is expected to increase as the elongation increases. As the longitudinal dimension shrinks, the end reflection effects could become important. When the incidence is tilted toward the longitudinal axis, the longitudinal internal modes due to reflection from the ends are more to be likely excited, decreasing the accuracy of the new method. In addition, as the incident angle approaches the longitudinal axis, the exposed surface normal to the axis decreases and the scatterer becomes more transparent. Therefore the scattering amplitude is expected to drop generally. These points will be illustrated by numerical examples in later parts of the paper.

II. NUMERICAL COMPARISON AND DISCUSSION

A. The exact solution for a prolate spheroid

To evaluate the accuracy of the new method, we apply it to prolate spheroids of various aspect ratios because the exact solution for the prolate spheroids is known (e.g., Yeh, 1967; Furusawa, 1988). For this purpose, we first outline the exact solution.

A prolate spheroid is plotted in Fig. 1(b). The scattering geometry is shown in Fig. 1(c). Suppose that the foci of the spheroid are at $x=y=0$, $z=\pm 1/2q$. The distances from the point (x,y,z) to these foci are

$$r_1 = \sqrt{(z+1/2q)^2 + x^2 + y^2},$$

$$r_2 = \sqrt{(z-1/2q)^2 + x^2 + y^2}.$$

The prolate spheroidal coordinates ξ , η , and ϕ are defined as follows:

$$\xi = (r_1 + r_2)/q, \quad \eta = (r_1 - r_2)/q, \quad \phi = \tan^{-1}(y/x),$$

and therefore

$$z = \frac{1}{2}q\xi\eta, \quad x = \frac{1}{2}q\sqrt{(\xi^2-1)(1-\eta^2)} \cos \phi,$$

$$y = \frac{1}{2}q\sqrt{(\xi^2-1)(1-\eta^2)} \sin \phi.$$

Here ξ goes from 1 to ∞ , η from -1 to 1 , and ϕ from 0 to 2π . The major axis is thus $b = \frac{1}{2}\xi q$, and the minor axis $a = \frac{1}{2}q\sqrt{\xi^2-1}$. Throughout the paper we define the ratio aspect as $e = a/b$ and the aspect ratio as $1/e$.

The unit incident wave can be expressed in terms of spheroidal variables (p. 1502 in Morse and Feshbach, 1946),

$$p_i = e^{i\mathbf{k}_i \cdot \mathbf{r}} = e^{ik(z \cos \theta_i + x \sin \theta_i)}$$

$$= 2 \sum_{m=0}^{\infty} \sum_{n=m}^{\infty} \frac{\epsilon_m}{N_{mn}} i^n S_{mn}(h, \cos \theta_i)$$

$$\times S_{mn}(h, \eta) j e_{mn}(h, \xi) \cos m\phi, \quad (10)$$

where the incident direction is denoted in spherical variables as $\hat{\mathbf{k}}_i = \mathbf{k}/k = (\sin \theta_i, 0, \cos \theta_i)$. Moreover, we define $h = kq/2$. S_{mn} are the angular spheroidal functions, N_{mn} are their norm, and $j e_{mn}$ are the corresponding radial functions of the first kind. Similarly, the scattered wave can be represented in terms of the functions S_{mn} , and the linear combinations of radial functions of the first and second kinds $h_{mn} = j e_{mn} + i n e_{mn}$:

$$p_{\text{scat}}(\mathbf{r}) = 2 \sum_{m=0}^{\infty} \sum_{n=m}^{\infty} \frac{\epsilon_m}{N_{mn}} i^n A_{mn} S_{mn}(h, \cos \theta_i)$$

$$\times S_{mn}(h, \eta) h_{mn}(h, \xi) \cos m\phi. \quad (11)$$

The unknown coefficients A_{mn} are determined by the boundary conditions that require that both the pressure field and the normal component of displacement be continuous across the scattering surface (Furusawa, 1988).

The scattering function is obtained in the far field limit, i.e., $r \rightarrow \infty$, where $\xi \rightarrow \infty$, $\eta \rightarrow \cos \theta$, and

$$h_{mn} \rightarrow i^{-n-1} \frac{e^{ikr}}{kr}.$$

Thus we obtain

$$f(\mathbf{k}_i, \mathbf{k}_s) = \frac{2}{ik} \sum_{m=0}^{\infty} \sum_{n=m}^{\infty} \frac{\epsilon_m}{N_{mn}} A_{mn} S_{mn}(h, \cos \theta_i)$$

$$\times S_{mn}(h, \cos \theta_s) \cos m\phi, \quad (12)$$

where ϕ is the azimuthal angle between the incident and scattering wave vectors. We stress that the vectors \mathbf{k}_i and

TABLE I. The parameters used in the computation.

Material	Mass density (kg/m ³)	Sound speed (m/s)
Water (medium)	1000	1500
Weak fluid ^a	1040	1560
Rigid fluid ^b	∞	∞
Gas fluid ^c	1.29	340

^aWeak fluid scatterers may be used to model zooplankton or fish bodies.

^bRigid fluid scatter may be used to model suspended sands, shellfish, and submarines.

^cGas-filled scatterers can be used to model fish swimbladders and gas-filled bubbles.

\mathbf{k}_s are represented in the spherical coordinates at the far field as

$$\mathbf{k}_i = k(\sin \theta_i, 0, \cos \theta_i),$$

$$\mathbf{k}_s = k(\sin \theta_s \cos \phi, \sin \theta_s \sin \phi, \cos \theta_s),$$

where θ_i , θ_s are the angles from \mathbf{k}_i and \mathbf{k}_s to the positive z axis, respectively, and ranging from 0 to π .

Due to the complexity of spheroidal functions, the computation of the scattering function in Eq. (12) is by no means an easy task. In the past, only limited numerical results for special situations were given. Recently, the FORTRAN codes for the spheroidal functions from U.S. Naval Research Laboratory (NRL) (King *et al.*, 1970; Patz and Van Buren, 1981) were modified for use on an HP 9000 computer, and called from within the numerical analysis software package MATLAB. MATLAB routines were then used to construct the scattering function according to Eq. (12). The NRL programs, especially in the case of the radial functions, are limited in the range of h for which they can produce accurate results. As h increases, more and more terms of the series solutions need to be included to obtain convergence. Due to the oscillatory nature of these terms and the finite precision of the computer, accuracy is eventually lost. In our case, whereas the angular function values appear to be accurate for any h , the radial function values are only accurate for h below about 40. Calculation of the scattering function itself, however, becomes too expensive computationally above h of about 12.

In the case of a spheroid, the integral in Eq. (7) is performed along the longitudinal axis with z varying from $-b$ to b . The radius along the axis is calculated from the equation of a spheroid as $a(z) = e\sqrt{b^2 - z^2}$. By making the substitution $z = bt$, $dz = bdt$, it is possible to combine the two parameters k and b into the single parameter kb . The combination $\mathbf{k}_i \cdot \mathbf{r}(z)$ becomes $kb \cos \theta_i t$, $\mathbf{k}_s \cdot \mathbf{r}(z)$ becomes $kb \cos \theta_s t$, and $ka(z)$ becomes $kbe\sqrt{1-t^2}$. Integration is now performed with respect to t , with limits -1 and 1 . If the reduced scattering amplitude $f/2b$ is calculated, Eq. (7) becomes a function of kb instead of k , and b . The associated reduced target strength is defined as $20 \log_{10}|f/2b|$.

B. Comparison and discussion

To compare the deformed cylinder model and the exact solution, we consider fluid-filled prolate spheroids. The physical parameters used are listed in Table I.

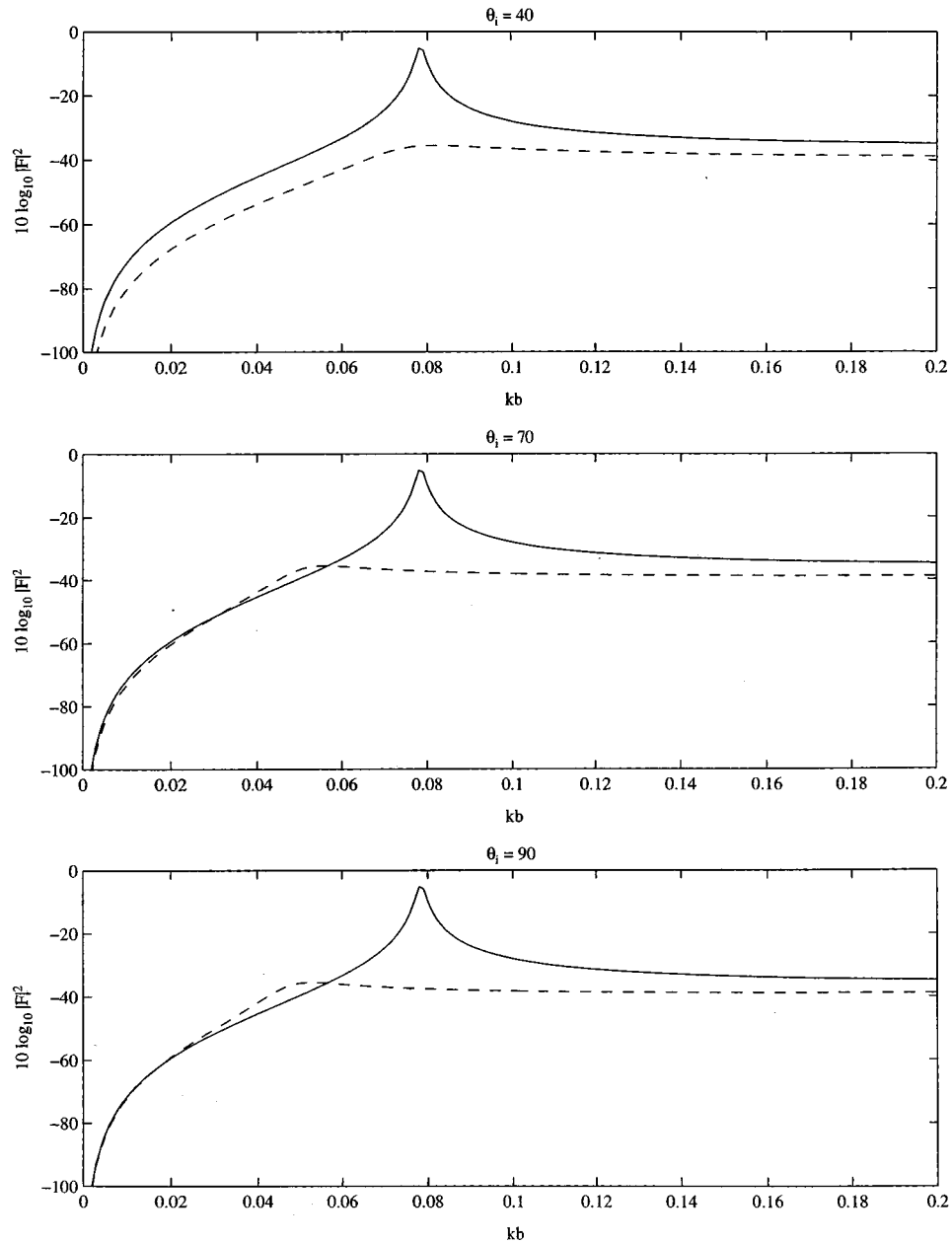


FIG. 2. Backscattering target strength of a prolate spheroid gas bubble as a function of kb for three incident angles. The dashed and solid lines refer respectively to the results from the new approach in Eq. (7) and the analytic solution in Eq. (13).

1. Gas spheroids

Sound scattering by a gas-filled spheroid poses a difficult problem (Furusawa, 1988). Previous attention has been restricted to low-frequency cases, where the pulsating mode dominates the scattering and the scattering strength is greatly enhanced at resonance, a useful feature for detecting fish with swimbladders. Using a hybrid method, Ye (1997b) derived a simple solution for the resonant scattering of a gas-filled prolate spheroid. The simple scattering function is

$$f = \frac{R_0}{\omega_0^2/\omega^2 - 1 - ikR_0}, \quad (13)$$

with ω_0 is the resonance frequency given by

$$\omega_0/\omega_e = e^{-1/3}(1-e^2)^{1/4} \left[\ln \frac{1+\epsilon}{e} \right]^{-1/2}, \quad \epsilon = \sqrt{1-e^2}$$

and

$$R_0 = b \left[\frac{\ln \frac{1+\epsilon}{e}}{\epsilon} \right]^{-1}.$$

Here ω_e is the resonant frequency of an equivalent sphere which has the same volume as the prolate spheroid. It is interesting to note that the resonant scattering by the gas-filled prolate spheroid is approximately *isotropic*. Note that since the calculation of the sound scattered by a gas spheroid

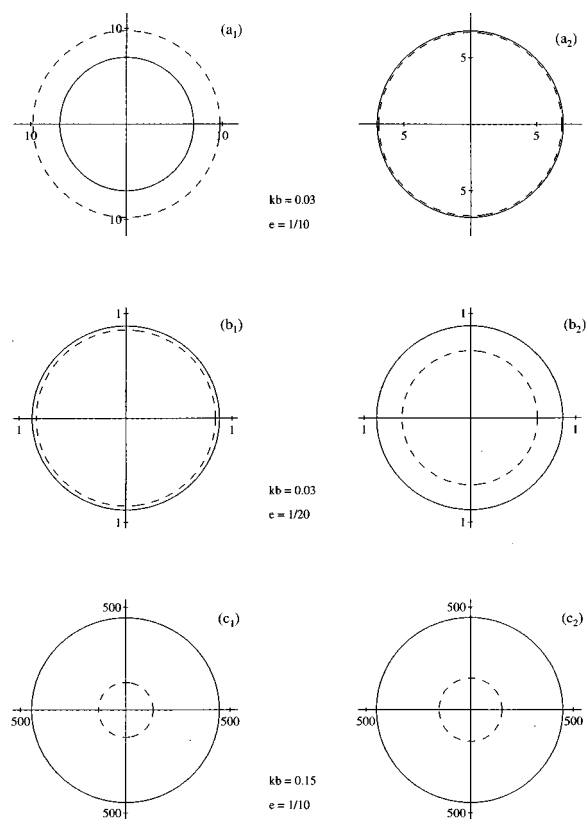


FIG. 3. Scattering pattern of the prolate spheroid gas bubble for different aspect ratios and at various incident angles. The plots have been scaled by a factor of 10^6 .

using the exact modal series solution is rather complicated because of resonance, in this paper we will not use the exact solution. A discussion of the problem will be presented in a forthcoming paper.

We consider a gas prolate spheroid whose equivalent sphere has the radius of 1 cm. Figure 2 shows the back-scattering target strength as a function of kb for a bubble with aspect ratio 10 at three incident angles, 40° , 70° , and 90° . The last one corresponds to the broadside incidence. In this figure, the dashed and solid lines refer to the results from the present approach and the analytic approach, respectively. Here we see that (1) the resonance occurs at kb about 0.08; (2) the new method does not reproduce the sharp resonance feature; however, (3) for frequencies away from the resonance peak, the results from the two methods seem agreeable, with best agreement in the broadside incidence case and at very low frequencies. The reason why the approximate method does not reproduce the resonant peak may be that it cannot take into account longitudinal pulsation mode properly. In fact, the approximate method only considers transverse pulsation (Ye, 1997b).

Figure 3 plots the scattering cross section for the scattered wave as a function of scattering angle for different aspect ratios and at various incident angles. The dashed and solid lines refer to the results from the present approach and the analytic approach. The curves in (a_1) and (a_2) are the results for the aspect ratio 10 at broadside and 70° incidence, respectively. The curves in (b_1) and (b_2) show the results

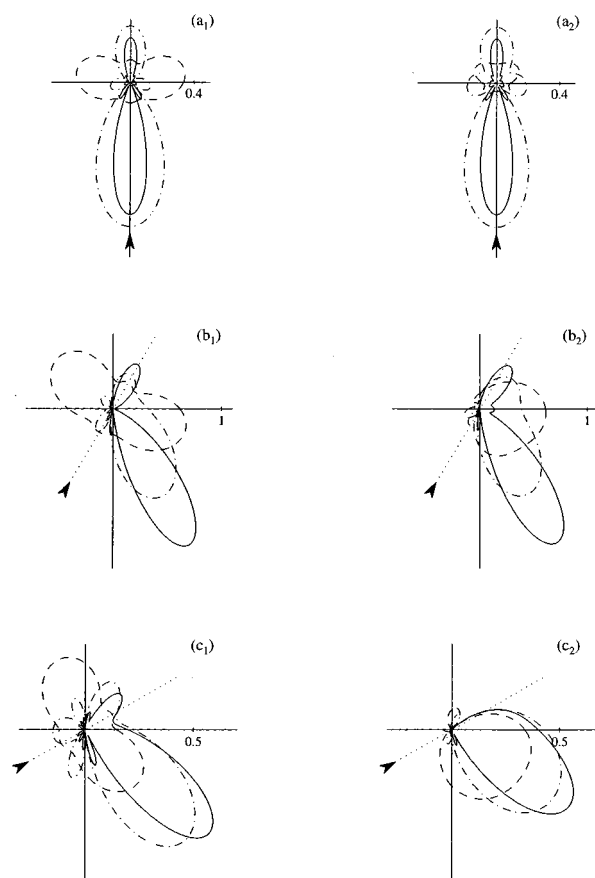


FIG. 4. The normalized scattering patterns for the prolate spheroids considered in Yeh (1967). In accordance with Yeh, the normalized scattering amplitude $|fk/2|$ is plotted. The solid line in (a_1) and (a_2) has been multiplied by $1/2$, and the dashed line in (b_1) and (b_2) has been multiplied by 2.

for an aspect ratio 20 at these two incident angles. In plots (a_1) , (a_2) , (b_1) , and (b_2) , kb is set at 0.03, which is close to resonance. It is interesting to note that the present approach does indicate isotropic scattering at around resonance for aspect ratios of 10 and 20. Further numerical computation shows that the isotropy in the scattering patterns exists even for larger aspect ratios. At certain angles of incidence, the approximate result matches the simple analytic solution. Comparing (a_1) to (a_2) , and (b_1) to (b_2) , we see that the scattering pattern depends on the incident angles only weakly. These features remain for higher frequencies. For example, the plots in (c_1) and (c_2) present the result for $kb=0.15$ at the incident angles 90° (c_1) and 40° (c_2) for the aspect ratio 10. Here it is clear that the scattering pattern is almost omnidirectional, and similar to that predicted from the simple analytic solution.

2. Weak fluid spheroids

a. Comparison with published results. First we reconsider the cases considered by Yeh (1967), who first calculated the sound scattering by a liquid prolate spheroid using the exact modal series solution. Comparing with Yeh's results not only assists us in evaluating the present approxi-

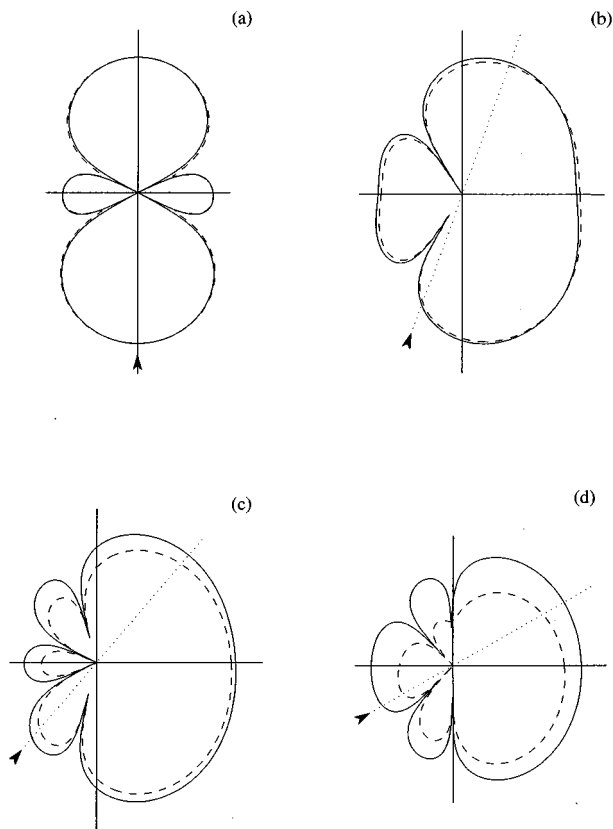


FIG. 5. The reduced target strength scattering pattern for the weak fluid prolate spheroid of aspect ratio 10 at $kb=5$. The arrow indicates the direction of the incident plane wave.

mate method, but also provides a verification of our implementation of the exact solution. The parameters used in the computation are $g=0.5$, $h_c=1$. The volume of the prolate spheroid is normalized as $(4\pi/3)h^3\xi(\xi^2-1)$ and set to be $40\pi/3$.

Figure 4 plots the scattering pattern for various eccentricities at different incident angles 90° , 60° , 30° in (a), (b), and (c), respectively. The incident direction is denoted by the arrows in the figure. The dashed lines, dotted-dashed lines, and solid lines are for $\xi=100$, 1.05, 1.006, respectively; the corresponding aspect ratios are calculated as 1.0005 (nearly sphere), 2.8645, 9.1701. In accordance with Yeh, the normalized function $|fk/2|$ is plotted versus scattering angles. The plots (a_1) , (b_1) , and (c_1) present our implementation of the exact solution, and (a_2) , (b_2) , and (c_2) the present approach. By examining both Yeh's and our results, we believe our exact implementation is working properly. We note, however, that the arrows in Yeh are pointing in the wrong directions. These plots show that (1) for high aspect ratios, the approximate results agree with the exact solution remarkably well for the broadside incidence; the agreement is also reasonable for 70° incidence, i.e., 20° from the normal incidence, but the agreement in amplitude deteriorates as the incident direction is tilted further away from the broadside direction, as expected; (2) even when the incident direction is set at 60° away from the broadside direction, the main scattering lobe is still comparable to that obtained from the exact solution for the case with aspect ratio 10; (3) the

present approach does not work well as the spheroid approaches a sphere, since in this case the ignored longitudinal modes may contribute significantly.

Next we further explore the validity of the present method by considering other examples. In the computation, for simplicity we restrict our attention to the case that the scattering vector is in the same plane as the incident wave vector, and $kb=5$ is used unless otherwise noted. The physical parameters for the scatterer are listed in Table I.

b. $e=1/10$ case. Figure 5 presents the results for the scattering pattern in dB, i.e., the reduced target strength define earlier, for different incident angles. All plots in this figure have been separately scaled by a normalization such that the minimum value in each plot is zero. The arrow indicates the direction of the incident plane wave, which is at 90° , 70° , 50° , 30° , respectively. The approximate results from Eq. (7) represented by the dashed lines are compared against the exact results shown by the solid line. In general, the approximate results compare favorably with the exact results. The agreement is strikingly good when the incidence is near the broadside direction [Fig. 5(a) and (b)]. The agreement in the scattering amplitude deteriorates when the incidence is further away from the broadside direction, but much of the structure is retained in the scattering function. Even when the incidence is aimed at 40° from the broadside as in Fig. 5(c), the results are encouraging. We also note that in all cases the present approach can predict the general shape of the scattering pattern quite well. In particular, the node structure in the scattering pattern is reproduced accurately. A further computation of the scattering pattern as a function of azimuthal angles at given incident and scattering angles also supports the above features.

Now we consider the characteristics of forward scattering and backscattering, correspondingly $\hat{k}_s=\hat{k}_i$ and $\hat{k}_s=-\hat{k}_i$, as these are two important special cases. In Fig. 6, we plot the reduced forward and backward scattering target strength $20\log_{10}(|f/2b|)$ as a function of the tilt angle (θ_i) at $kb=5$. The solid line and dashed line refer to the results from the exact solution and Eq. (7), respectively. It is interesting to see here that the forward scattering target strength from the exact solution is almost constant for all incident angles. Again remarkable agreement is seen when the incidence is near the broadside direction. In both forward and backward scatter cases, the approximate results compare well with the exact solution, although the forward scatter seems to have a slightly better fit. If we set 3 dB as the tolerance of error, the present approach is accurate for incidence more than 35° from the broadside direction for the weak scatter. In the backscatter case, the present approach reproduces the node structure well.

In Fig. 7, we plot the reduced forward and backward scattering target strength as a function of kb for three different incident angles. The solid line refers to the results from the exact solution, whereas the other lines are from Eq. (7). The solid line in this figure actually contains four superimposed lines: three from the exact solution for all three incident angles and one from the approximation for broadside incidence. The fact that the results from the exact solution

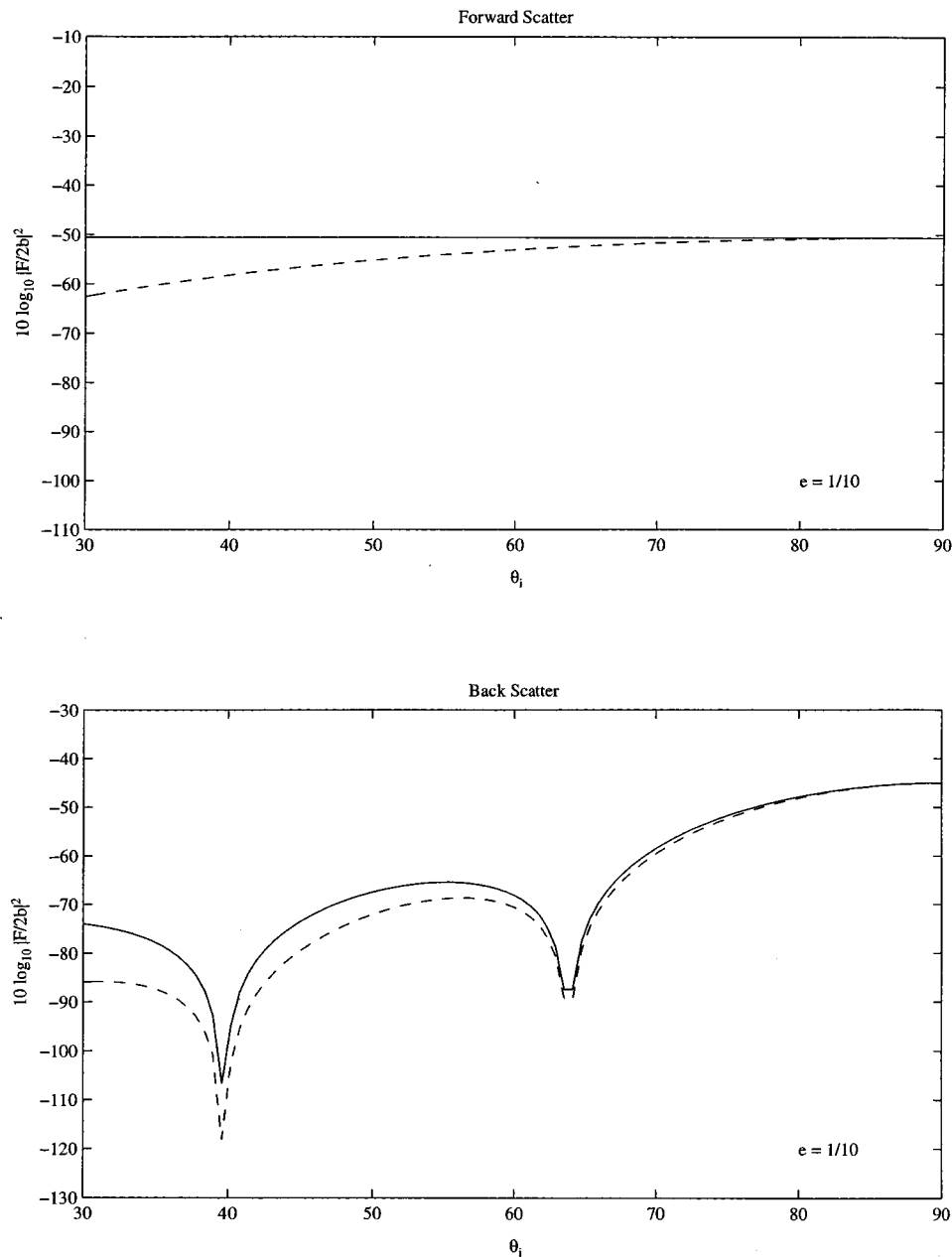


FIG. 6. The reduced forward and backward scattering target strength as a function of tilt angles at $kb=5$ for the weak fluid case. The aspect ratio $1/e$ is 10.

coincide with each other for the three incident angles reiterates the invariance of the forward scatter in the exact solution, as seen in Fig. 6. Again, the results from the present method agree very well in shape with those of the exact solution. For $\theta=70^\circ$ and 90° , the approximate results also agree in magnitude with the exact solutions within our tolerance of error. In particular, the approximate results coincide with the exact results when $\theta=90^\circ$, i.e., at broadside direction. For $\theta=30^\circ$, the approximate result differs from the exact result by as much as 10 dB. However, it is important to note that it appears as if this discrepancy will not deteriorate as the acoustic frequency increases, a region of poor convergence for the exact solution. Furthermore, the difference between the approximate and exact results varies regularly with increasing frequency. This suggests that the proposed method can be used at high frequencies, where the present

implementation of the exact solution may have difficulties.

c. Effect of eccentricity. Figure 5 shows that agreement between the approximate and exact results degrades as the incidence is tilted away from the broadside direction. Now we examine how the elongation can affect the agreement. Take the worst case in Fig. 5(d) as an example. Figure 8 shows the scattering pattern in dB for various ratio aspects e at incident angle 30° . As in Fig. 5, all plots in Fig. 8 have been separately scaled by a normalization such that the minimum value in each plot is zero. The arrow indicates the direction of the incident plane wave. It is clear that as the elongation increases, the agreement improves. However, the results suggest that the agreement cannot be improved further when the aspect ratio exceeds a certain value ($1/e \approx 20$).

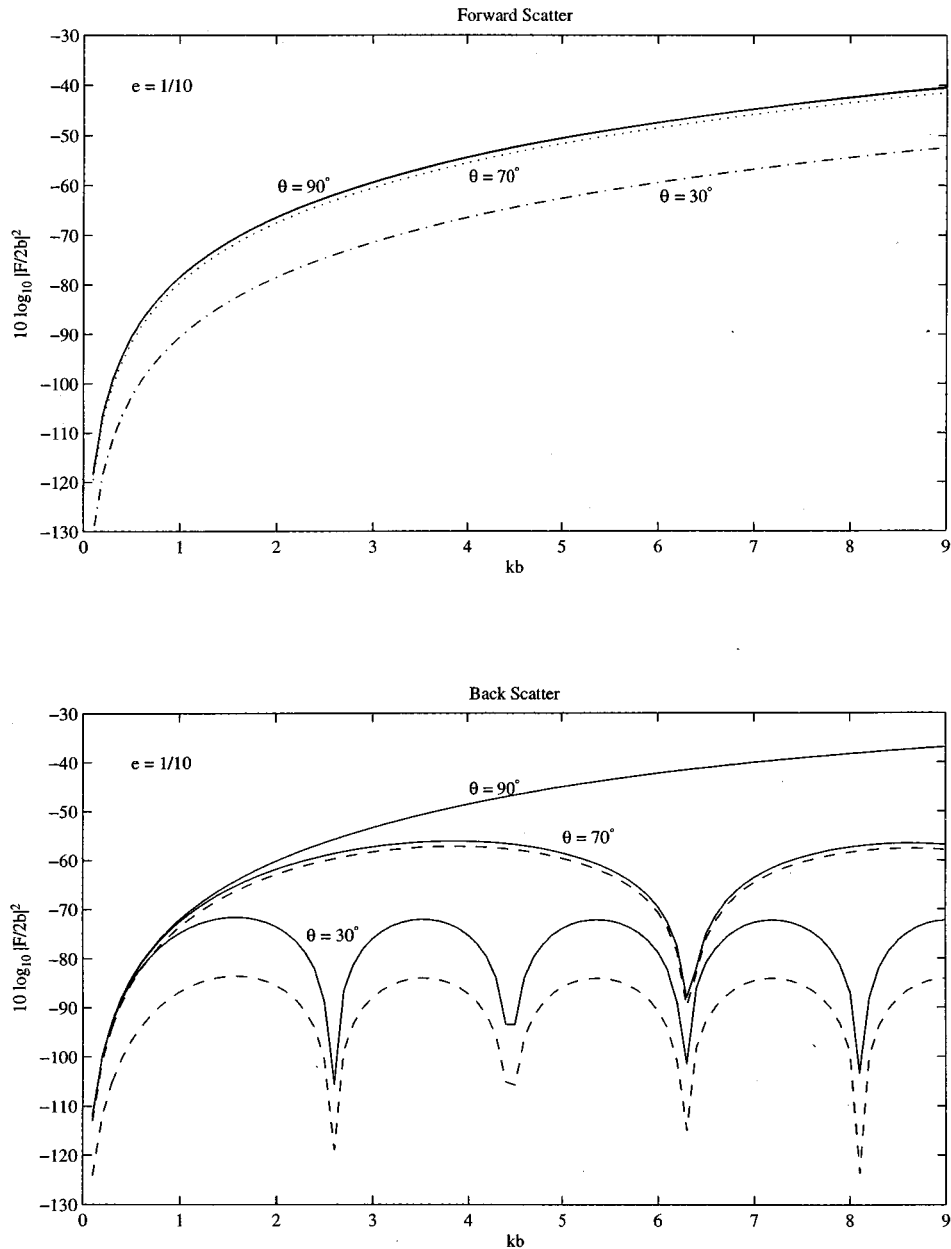


FIG. 7. The reduced forward and backward scattering target strength as a function of kb for three different incident angles for the weak fluid case. The aspect ratio is 10.

3. Rigid spheroids

We first consider an asymptotic formula for the rigid spheroid case. Using the Kirchhoff approximation, one can deduce an asymptotic solution for the back scattering cross section of a rigid scatterer at high frequencies (Gaunaud, 1985),

$$\sigma_{bs} = \frac{R_1 R_2}{4}, \quad (14)$$

where R_1 , R_2 are the principle radii of curvature at incidence, which can be computed for known surfaces. For the prolate spheroid case, we obtain

$$\sigma_{bs}(\theta) = \frac{1}{4} b^2 e^4 (\cos^2 \theta + e^2 \sin^2 \theta)^{-2}, \quad (15)$$

where θ is the incident angle [Fig. 1(b)], b is the major axis, e is the ratio aspect, and $a = eb$ is the minor axis. For the broadside incidence, $\theta = 90^\circ$, the reduced asymptotic back-scattering target strength $10 \log_{10}(\sigma_{bs}/(2b)^2)$ is calculated as -12.04 dB.

a. $e = 1/10$ case. On the whole, the scattering features for the rigid prolate spheroids draw many similarities to that for the weak fluid prolate spheroids discussed above. In Fig. 9 we present the scattering pattern in dB for different incident angles. The arrow in these plots indicates the direction of the incident plane wave, which is at 90° , 70° , 50° , 30° , respectively. In this figure the approximate results from Eq. (7) represented by the dashed lines are compared against the exact results shown by the solid line.

We see that (1) similar to the weak fluid case, the

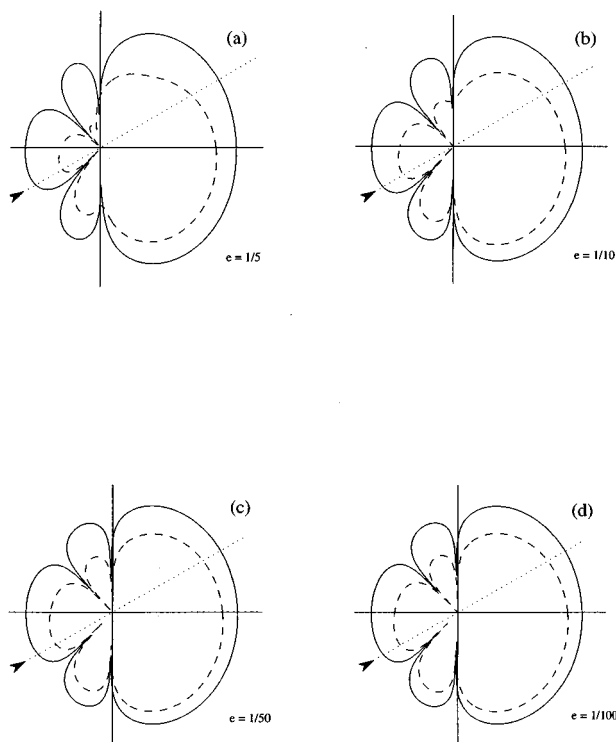


FIG. 8. The reduced target strength scattering pattern for the weak fluid prolate spheroid with various ratio aspects. The incident angle is 30° , and $kb = 5$.

present approach continues to predict a scattering pattern comparable to the exact solution; (2) compared to the fluid case, the agreement is better for most of the scattering angles, and in fact, Fig. 9 shows that the approximate results are within our tolerance of error for a wider range of incident and scattering angles; poor agreement is only seen for certain scattering angles; (3) the best agreement is where the incidence is near the broadside direction, and agreement deteriorates as the incident direction moves away from the broadside aspect; (4) interestingly, even when the incident direction is tilted further away from the broadside such as to 60° in Fig. 9(d), the approximate result still compares reasonably well to the exact result in the forward direction [Fig. 9(c) and (d)] (note that here the forward direction means any scattering direction which satisfies $\phi_s = 0$); (5) differing from the weak fluid case, the approximate method predicts more node structures than the exact solution [e.g., Fig. 9(d)]; (6) comparison of Figs. 5 and 9 indicates that the present approach works slightly better for rigid bodies than for weak fluid bodies with respect to the absolute scattering amplitude, whereas it works better for weak fluid bodies than for rigid bodies with regard to the node structure.

Figure 10 shows the reduced forward and backward scattering target strength as a function of the tilt angle at $kb = 5$. The solid line refers to the exact solution, whereas the other lines are from Eq. (7), as before. The agreement between the approximate and exact results are excellent, especially in the forward scatter case. If the tolerance of error is set at 3 dB as before, the present method can be regarded

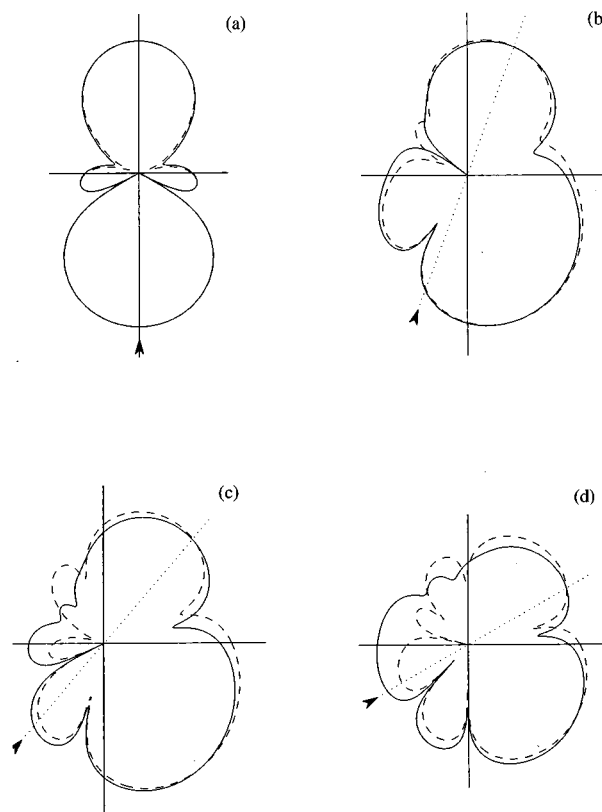


FIG. 9. The reduced target strength scattering pattern for the rigid prolate spheroid of aspect ratio 10 at $kb = 5$. The arrow indicates the direction of the incident plane wave.

as accurate for incidence deviated from the broadside direction by as much as 50° .

Figure 11 plots the reduced forward and backward scattering target strength as a function of kb for three different incident angles. The solid line and dashed line refer to the results from the exact solution and Eq. (7), respectively. We see that: (1) in the forward scatter case, the approximate results basically coincide with the exact results for the three different tilt angles; (2) in the backscatter case, the approximate result coincides with the exact result when incidence is broadside [also these results approach that from the asymptotic result from Eq. (15)]; (3) the agreement is also excellent for the case $\theta = 70^\circ$; (4) as the incidence moves away from the broadside direction by as much as 60° , the numerical difference between the approximate and exact results increases, but they agree remarkably well in shape and node structure; (5) similar to the weak fluid case, the discrepancy between the two results will not deteriorate as the acoustic frequency increases, and the difference between the approximate and exact results varies regularly with increasing frequency. Furthermore, calculation shows that exact results vary about the asymptotic values for $kb > 2$. For example, besides the broadside incidence, the exact result varies near the asymptotic values of -34.04 dB and -49.57 dB from Eq. (15) at $\theta = 70^\circ$ and 30° , respectively.

b. Effects of eccentricity. Again we inspect the effect of eccentricity. Figure 12 presents the scattering pattern in dB for various ratio aspects e at incident angle 30° . As in the

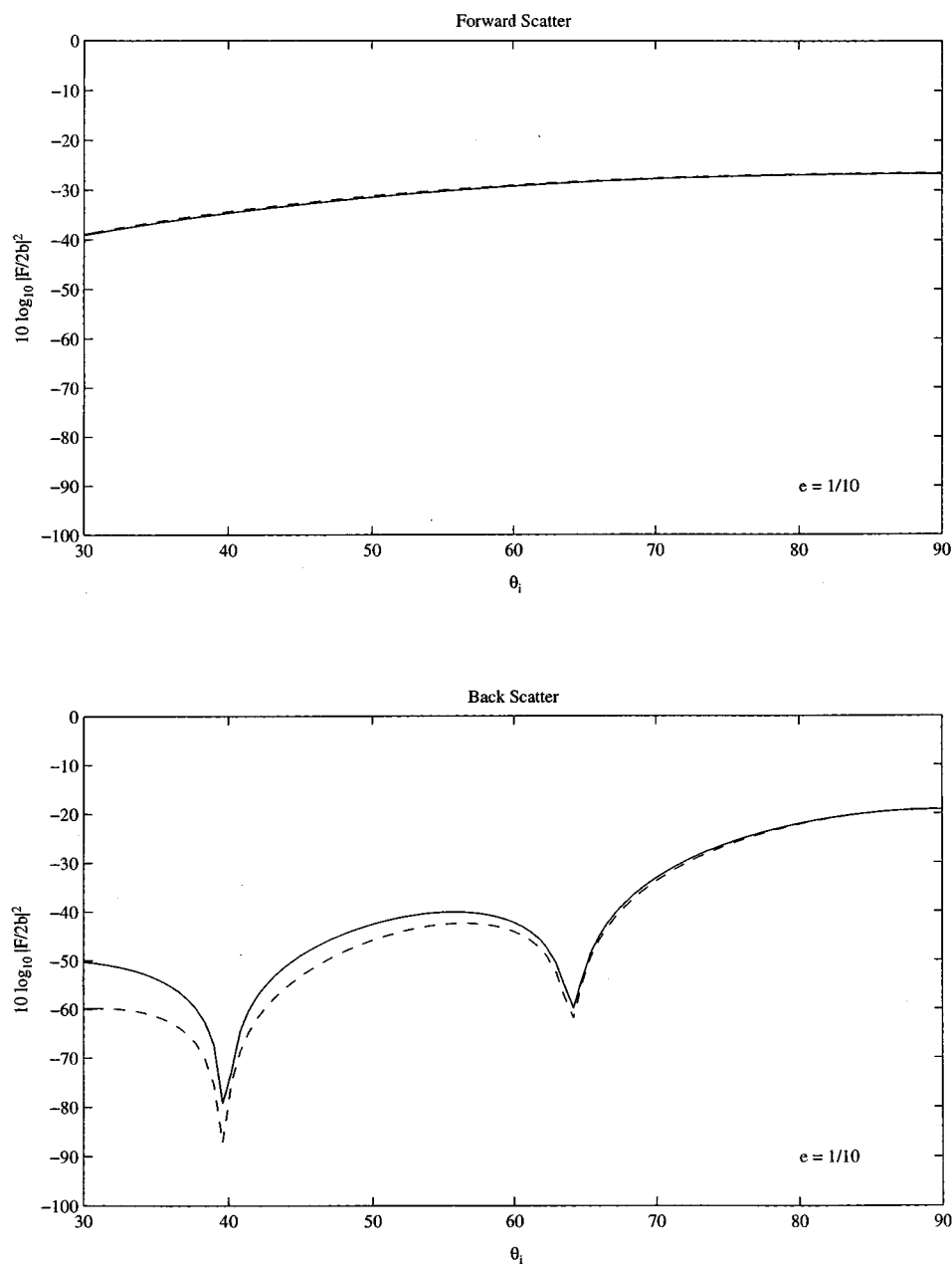


FIG. 10. The reduced forward and backward scattering target strength as a function of tilt angles at $kb=5$ for the rigid case. The aspect ratio is 10.

above, all plots in Fig. 12 have been separately scaled by a normalization such that the minimum value in each plot is zero. The arrow indicates the direction of the incident plane wave. Clearly, as the elongation increases, the agreement improves. However, comparison of (c) and (d) implies that the agreement cannot be improved further when the aspect ratio exceeds a certain value.

C. Normalized cross correlation between the approximate and exact results

Although agreement between the approximate and exact solutions may deteriorate as the incidence is tilted away from the broadside direction, the approximate method can produce scattering patterns consistent with the exact solution. This would be useful for applications in which the overall scatter-

ing patterns instead of the absolute magnitudes are important and relevant. For example, discerning target characteristics such as the animal species, it is the overall scattering pattern that plays a more important role in data analysis and modeling. An heuristic but convenient way of evaluating the general validity of the approximate method in predicting scattering pattern may to compute the normalized cross correlation coefficient between the approximate and exact results. The normalized cross-correlation coefficient between two sets of data, $X = (x_1, x_2, \dots, x_n)$ and $Y = (y_1, y_2, \dots, y_n)$, is defined as

$$\langle X, Y \rangle \equiv \frac{\sum_{i=1}^n x_i y_i}{\sqrt{\sum_{i=1}^n x_i^2} \sqrt{\sum_{i=1}^n y_i^2}}. \quad (16)$$

Clearly $\langle X, Y \rangle$ varies from -1 to 1 by the Schwarz inequality. The larger $\langle X, Y \rangle$, the better the two sets of data fit. The

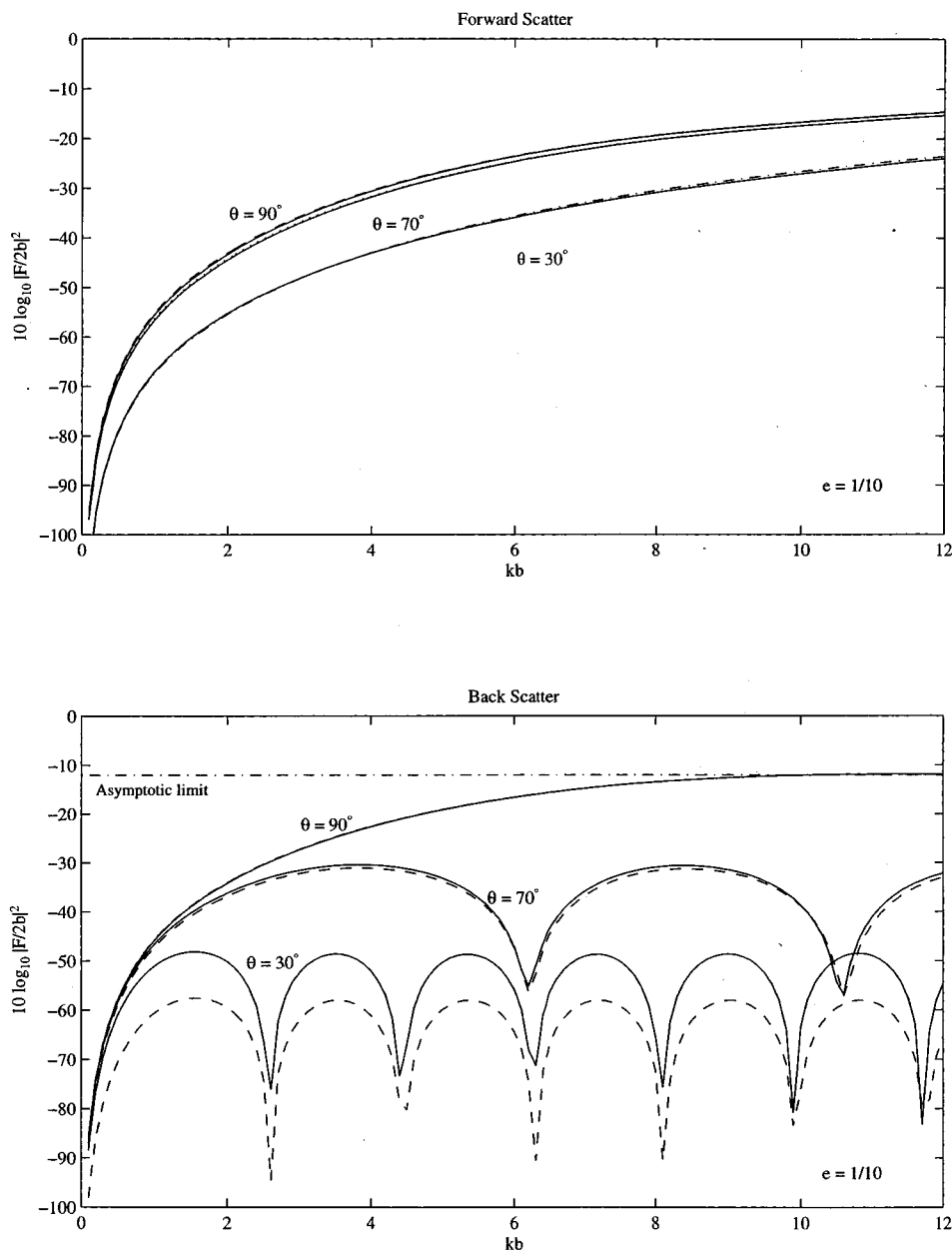


FIG. 11. The reduced forward and backward scattering target strength as a function of kb for three different incident angles for the rigid case. The aspect ratio is 10.

best overall fit should occur when the coefficient equals one. In the present paper, the scattering cross section is used in the cross-correlation calculation.

In Table II, we present the calculated normalized cross-correlation coefficients for the weak and rigid spheroids considered in Figs. 5 and 9. From Table II, the following features are evident. (1) The results from the present approach are highly correlated to that from the exact solution for all the cases considered, implying that the present approach can be used for a wide range of situations. At the normal incidence, the approximate results coincide uniformly with the exact results. (2) The coefficient decreases slightly as the incidence is tilted away from the broadside direction. (3) It shows that the present approach works slightly better for the rigid spheroids. This seems reasonable because no internal waves can be excited in rigid scatterers, thereby supporting

our earlier assumption of neglecting the longitudinal internal waves generated at the ends of scatterers.

The effect of eccentricity on the cross-correlation coefficient is presented in Table III. When the incident direction is not on the broadside aspect, the coefficient increases as the elongation of the target increases, which is in accordance with what has been expected from the theory. And the cross-correlation coefficients are greater in the rigid case than in the weak fluid case.

III. SUMMARY

In this paper, we presented a new and computationally easy method for calculating the sound scattering function of slender bodies. The validity of the new method is examined thoroughly by applying it to prolate spheroids for which the

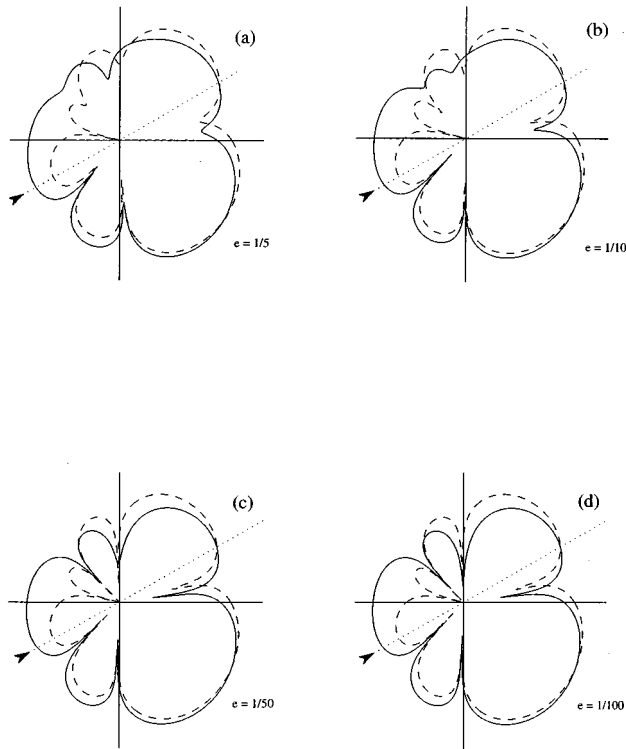


FIG. 12. The reduced target strength scattering pattern for the rigid prolate spheroid with various ratio aspects. The incident angle is 30° , and $kb=5$.

exact solution is known. The comparison with the exact solution indicates that the new method is powerful in predicting accurate bistatic scattering patterns for a wide range of situations. The results predicted by the method are shown to be highly correlated with the exact results. However, we also notice some discrepancies between the model and the exact results. Undoubtedly, these discrepancies can be attributed to the approximations involved in the method. As observed in the study, the present model is comparatively more accurate for high aspect ratios, and near broadside incidence. To improve the accuracy of the present model, the aforementioned possible “tapering” effects due to the variation of radius and effects of the internal waves excited due to the ends may have to be taken into account, which is beyond the scope of the present study. In the present paper, however, we do not intend unrealistically to solve all the problems.

Although fluid scatterers have been predominantly con-

TABLE II. The calculated normalized cross-correlation coefficients. Aspect ratio=10.

Incident angle ($^\circ$)	Weak fluid	Rigid fluid
90	1.000	1.000
70	0.996	0.998
50	0.984	0.988
30	0.944	0.956

TABLE III. The calculated normalized cross-correlation coefficients for various aspect ratios from Figs. 8 and 12, with $\theta_i=30^\circ$.

Aspect ratio	Weak fluid	Rigid fluid
5	0.929	0.941
10	0.944	0.956
50	0.947	0.963
100	0.947	0.964

sidered in this paper, it is clear from the derivation that the new method can be easily implemented to study scattering by scatterers of any other material composition such as elastic materials. In a following paper, we shall apply this approach to calculate scattering by fish and compare with experimental measurements.

ACKNOWLEDGMENTS

We thank Dr. M. Furusawa and Dr. A. L. Van Buren for useful communications on the numerical computation of the spheroidal functions. The work received support from the Department of Fisheries and Oceans, Canada, and the National Central University, Taiwan.

Flax, L., Varadan, V. K., and Varadan, V. V. (1980). “Scattering of an obliquely incident acoustic wave by an infinite cylinder,” *J. Acoust. Soc. Am.* **68**, 1832–1835.

Furusawa, M. (1988). “Prolate spheroidal models for predicting general trends of fish target strength,” *J. Acoust. Soc. Jpn. (E)* **9**, 13–14.

Gaunard, G. C. (1985). “Sonar cross sections of bodies partially insonified by finite sound beams,” *IEEE J. Ocean Eng.* **OE-10**, 213–230.

Junger, M. C. (1982). “Scattering by slender bodies of revolution,” *J. Acoust. Soc. Am.* **72**, 1954–1956.

Keller, J. B., and Ahluwalia, D. S. (1971). “Diffraction by a curved wire,” *SIAM (Soc. Ind. Appl. Math.) J. Appl. Math.* **20**, 390–405.

King, B. J., Baier, R. V., and Hanish, S. (1970). “A FORTRAN computer program for calculating the prolate spheroidal radial functions of the first kind and second kind and their first derivatives,” *NRL Rep. No.* 7012.

Montroll, E. W., and Hart, R. W. (1951). “Scattering of plane waves by soft obstacles. II. Scattering by cylinders, spheroids, and disks,” *J. Appl. Phys.* **22**, 1278–1289.

Morse, P. M., and Feshbach, H. (1946). *Method of Theoretical Physics* (McGraw-Hill, New York).

Patz, B. J., and Van Buren, A. L. (1981). “A FORTRAN computer program for calculating the prolate spheroidal angular functions of the first kind,” *NRL Rep. No.* 4414.

Rumerman, M. L. (1992). “Application of the Sommerfeld–Watson transformation to scattering of acoustic waves obliquely incident upon cylindrical shells,” *J. Acoust. Soc. Am.* **91**, 2502–2509.

Schenck, H. A. (1968). “Improved integral formation for acoustic radiation problems,” *J. Acoust. Soc. Am.* **44**, 41–58.

Stanton, T. K. (1989). “Sound scattering by cylinders of finite length. III. Deformed cylinders,” *J. Acoust. Soc. Am.* **86**, 691–705.

Tran Van Nhieu, M., and Ywonne, F. (1994). “Sound scattering by slender bodies of arbitrary shape,” *J. Acoust. Soc. Am.* **95**, 1726–1733.

Waterman, P. C. (1969). “New formulation of acoustic scattering,” *J. Acoust. Soc. Am.* **45**, 1417–1429.

Ye, Z., and Furusawa, M. (1995). “Modeling of target strength of swim-bladder fish at high frequencies,” *J. Acoust. Soc. Jpn. (E)* **16**, 371–379.

Ye, Z. (1997a). “A novel approach to acoustic scattering by cylinders of finite length,” *J. Acoust. Soc. Am.* **102**, 877–884.

Ye, Z. (1997b). “Low-frequency acoustic scattering by gas-filled prolate spheroids in liquids,” *J. Acoust. Soc. Am.* **101**, 1945–1952.

Yeh, C. (1967). “Scattering of acoustic waves by a penetrable prolate spheroid. I. Liquid prolate spheroid,” *J. Acoust. Soc. Am.* **42**, 518–521.

A method for acoustic scattering by slender bodies.

II. Comparison with laboratory measurements

Li Ding^{a)}

National Research Institute of Fisheries Engineering, Hasaki, Ibaraki, 314-04 Japan

Zhen Ye^{b)}

Institute of Ocean Sciences, Sidney, British Columbia V8L 4B2, Canada

(Received 26 November 1996; revised 6 May 1997; accepted 14 May 1997)

This paper describes a comparison between a sound scattering model for slender bodies proposed in Ye *et al.* [J. Acoust. Soc. Am. **102**, 1964–1976 (1997)], and laboratory measurements of forward and bistatic scattering by individual fish [Ding, J. Acoust. Soc. Am. **101**, 3398–3404 (1997)]. A prolate spheroid target made of styrofoam is also measured to help verify the model, and it is found that the model results agree reasonably well with the measurements of the styrofoam target. Scattering of fish is assumed to be primarily due to fish flesh and swimbladder, which are modeled as liquid filled and gas filled, respectively. An asymmetric prolate spheroid is used to approximate the geometry of both fish body and swimbladder. It is shown in the modeling that fish body (flesh) is more important in determining the forward scattering at the frequency of interest (38 kHz), while in the case of bistatic scattering, swimbladder is still dominant. The model appears able to produce results in good agreement with the measurements of bistatic scattering, for incident angles within $\pm 40^\circ$. For forward scattering, the model results of fish body follow well the general trends of the data for one side of incident angles, but for the other side, do not show as large variability as the data, suggesting more complex structures involved. When the scattering by swimbladder is added coherently to that of fish body, the total scattering is stronger than the data. Therefore it remains an open question how to combine contributions from fish body and swimbladder when their scattering strengths are not significantly different. © 1997 Acoustical Society of America. [S0001-4966(97)02209-1]

PACS numbers: 43.20.Fn, 43.20.Tb, 43.30.Gv [JEG]

INTRODUCTION

Sound scattering by slender bodies has been a subject of general interest in underwater acoustics over the past years, since it can be used to model scattering by a number of underwater targets such as fish and zooplankton. While there exist several theoretical models for this problem, including the Kirchhoff approximation model (Gaunaurd, 1985) and the cylinder model (Junger, 1982), many of these models are either limited to certain frequency regions and ideal geometries, or too complicated to be of much practical use. For practical applications, a model preferably should be both versatile and easy to compute, yet with sufficient accuracy. Recently, Ye *et al.* (1997) proposed a model for calculating scattering by deformed cylinders or slender bodies, extended from an earlier version which is limited to uniform cylinders (Ye, 1997). This model has been applied to prolate spheroids and compared with exact solutions. The comparison indicates that the model produces results that agree well with the exact solutions for relatively large aspect ratios and incident angles not too far away from the broadside direction. The performance deteriorates as the aspect ratio decreases and the incident angle gets closer to the end-fire directions, which is within expectation as the model does not take into account reflections from the ends of the object.

This sequential paper compares the model of Ye *et al.* (1997) with laboratory measurements of sound scattering by a styrofoam prolate spheroid and an individual fish. Measuring a simple target such as a prolate spheroid helps verify the model. Modeling of scattering by fish is a typical application of the model, as many species of fish have a slender body and swimbladder with the aspect ratio ranging from 5 to 7 for body and from 5 to 9 for bladder (Furusawa, 1988). Unlike earlier model studies which focus mainly on backscattering of fish, we shall examine the model in a more general perspective than backscatter, by comparing it with laboratory measurements of forward and bistatic scattering by fish (Ding, 1997), as there is potential application of forward scatter in detection of fish with acoustic scintillation techniques (Curran *et al.*, 1994). We believe that such a comparison will guide us not only in improving theoretical models but also in conducting future experiments towards using the concept of forward and bistatic scatter in fish detection.

I. EXPERIMENTAL RESULTS

It is well-known that acoustic backscatter of fish can be used to detect and quantify fish at sea (MacLennan and Simmonds, 1992). However, sound scattering in other directions can also be exploited for such a purpose. Although less known in fisheries acoustics, forward scatter has recently been used in discerning migrating salmon in the Fraser river of B.C., Canada, with an acoustic scintillation flowmeter deployed across the river (Curran *et al.*, 1994). Recently, Ding

^{a)}Affiliated with Institute of Ocean Sciences, Sidney, British Columbia V8L 4B2, Canada.

^{b)}Now at: Department of Physics, National Central University, Taiwan.

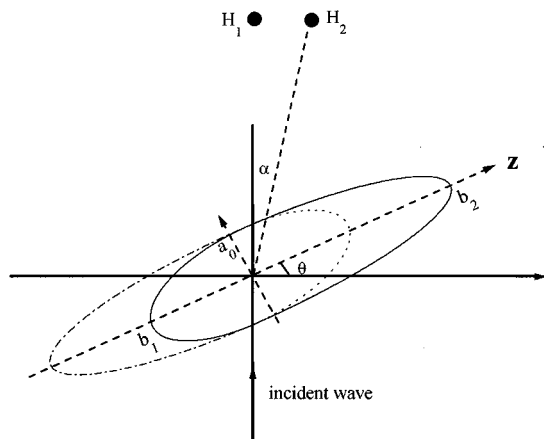


FIG. 1. An asymmetric prolate spheroid used to approximate fish body and swimbladder. It is composed of two symmetric spheroids, each of which has a minor axis of $2a_0$ and a major axis $2b_1$ or $2b_2$. The spheroid is tilted relative to the incident waves, with θ being the tilt angle. Also shown are hydrophone positions relative to the target.

(1997) conducted a novel experiment on sound scattering by fish. In addition to measurement of backscatter, he focused on measuring forward and bistatic scattering by individual fish.

The experiment was carried out in a fresh water tank, 15 m long, 10 m wide, and 10 m deep. A 38-kHz split-beam transducer was mounted on the floor of the tank, looking upward to the water surface. A hydrophone was suspended 7.69 m away from the transducer. A target was suspended horizontally between the hydrophone and transducer, and was aligned together with the hydrophone on the beam axis of the transducer with the help of the split-beam outputs of the transducer. This hydrophone received forward scattered signals (i.e., scattered signals in the same direction as the incident signals) from the target. The target was tilted relative to the beam axis with a computer-controlled rotating system such that the incident angle of sound was changed. A second hydrophone was placed at the same depth as the first one, but positioned at the first null of the acoustic beam. This was used to measure bistatic scattered signals. The hydrophone positions relative to the target are shown in Fig. 1, and details of the experiment are referred to Ding (1997).

Here we present measurements of two acoustic targets. One is a prolate spheroid made of styrofoam, and the other is a Japanese mackerel (*Scomber Japonicus*) of fork length 33.4 cm and weight 424 g. Styrofoam prolate spheroids have been used in precise backscattering measurements and it was found that the measurements were in good agreement with the model in Furusawa (1988) (Sawada *et al.*, 1996). Figure 2 shows the measured forward and bistatic scattering amplitude (dark and open circle) of the styrofoam prolate spheroid, in terms of target strength, versus the tilt angle or incident angle. Relative to the target, the receiving hydrophone is at an angle (i.e., α in Fig. 1) of 20.2° off the beam axis of the transducer. The forward scatter is fairly flat, varying between -25 dB and -28 dB. The bistatic scatter decreases from -33 dB around incident angle -45° to a minimum of -38 dB around -5° , and then increases toward positive angles. For the bistatic scatter, positive angles correspond to

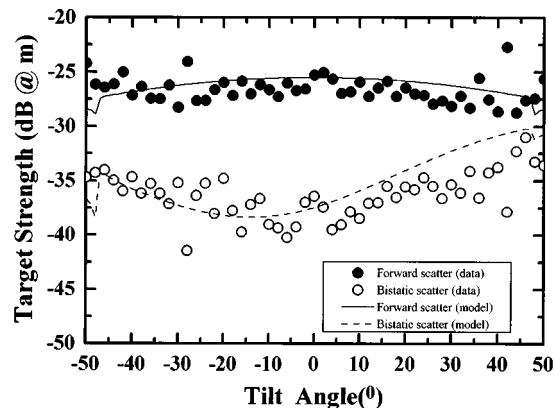


FIG. 2. Forward and bistatic scattering strength of the styrofoam target. The scatter plots are the measurement results and the curves show the model results.

the axis normal to the target moving farther away from the hydrophone (H_2). There are exceptional data points at -28° and 42° in both the forward and bistatic scatter, possibly due to some interference. Except for these points, the data show well-defined general trends. The curves are model results to be discussed below.

The measured forward scattering amplitude of the fish is shown in Fig. 3(a), where a positive angle corresponds to the fish head moving toward the transducer. The open circle and dark circle represent results when the fish was in the dorsal and side aspect, respectively. It is seen that the majority of the data vary between -27 and -17 dB, with a few points in the dorsal aspect falling below -27 dB at tilt angles between -10° and -20° . Figure 3(b) shows the bistatic scattering of

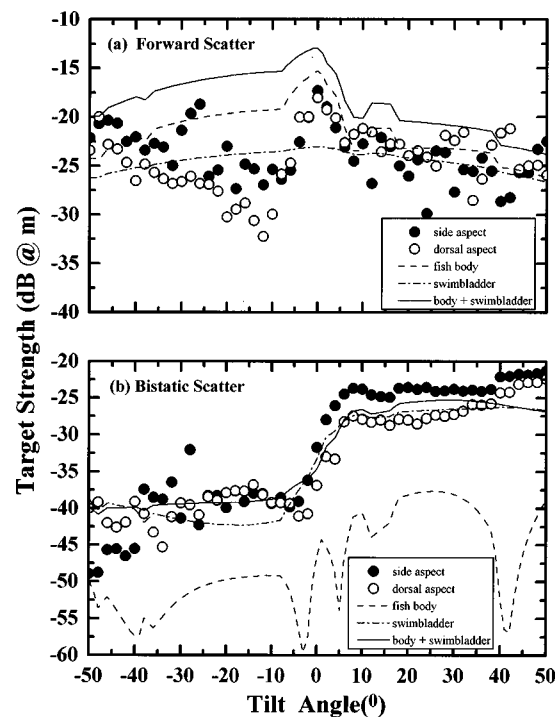


FIG. 3. Forward and bistatic scattering strength of fish. Scatter plots are the measurements from Ding (1997), and line plots are the modeling. (a) Forward scattering; (b) bistatic scattering.

TABLE I. Geometry and acoustic properties for a styrofoam target and different parts of a Japanese Mackerel, used in the modeling. ρ : density; c : sound speed (longitudinal); c_s : shear wave speed; $2b_1$ and $2b_2$: major axes of the prolate spheroids used to form an asymmetric one; $2a_0$: minor axis; The ρ , c data of fish flesh are from Shibata (1970).

	ρ (kg m ⁻³)	c (m s ⁻¹)	c_s (m s ⁻¹)	$2a_0$ (cm)	b_1 (cm)	b_2 (cm)
water	1000	1450				
fish flesh	1065	1580		5.46	13.36	20.04
swimbladder	1.24	345		2.59	3.38	5.64
styrofoam	20	653.7	441.7	1.5	5.0	5.0

the fish, with the same legends. Relative to the fish, the receiving hydrophone is at an angle of 21° off the beam axis of the transducer. When the tilt angle is positive, the measured scattering amplitude increases rapidly and then stabilizes at some level. When the angle is negative, the scattering drops first and then stabilizes. We shall compare model results with the data shown in Figs. 2 and 3 in the following section.

II. COMPARISON AND DISCUSSION

In this study, we assume that scattering by fish is due to fish flesh and swimbladder, and ignore scattering from the other parts of the fish. Fish flesh is modeled as liquid filled and swimbladder as gas filled, respectively. Both are assumed to support no shear waves. In our initial effort to examine the effectiveness of the theoretical approach, we shall use prolate spheroids for simplicity to approximate the shapes of both swimbladder and fish body. However, the real shape of a fish is rarely symmetric like a prolate spheroid. In most cases, the shape of a fish is thicker near the head, and tapers off towards the tail. To reflect the asymmetry, we use a more realistic but still simple geometry, composed of two prolate spheroids, each of which has the same minor axis but a different major axis, as shown in Fig. 1. The radius of a cross section along the z axis (major axis) can be written as

$$a(z) = \begin{cases} a_0 \sqrt{1 - (z/b_2)^2} & 0 \leq z \leq b_2 \\ a_0 \sqrt{1 - (z/b_1)^2} & -b_1 \leq z \leq 0, \end{cases} \quad (1)$$

where $2a_0$ is the minor axis, and $2b_1$ and $2b_2$ the major axes. The parameters can be easily measured from the fish body and x-ray images of the swimbladder. For the fish used in the experiment, the parameters are given in Table I, which also includes acoustic properties of fish flesh (from Shibata, 1970) and swimbladder. Using Eq. (1) for the varying radius, the scattering function can be computed from Eqs. (4)–(7) in Ye *et al.* (1997).

For the styrofoam target, the compressional wave speed (C) and shear wave speed (C_s) can be computed from its Young's modulus (E), Poisson ratio (σ) and density (ρ), using the following equations:

$$C = \sqrt{\frac{E(1-\sigma)}{\rho(1+\sigma)(1-2\sigma)}}, \quad (2)$$

$$C_s = \sqrt{\frac{E}{2\rho(1+\sigma)}} \quad (3)$$

(Clay and Medwin, 1977). The results are also given in Table I. Although the shear wave speed is not negligible

compared to the compressional one, our model does not consider shear waves and we shall keep this in mind when making comparison.

A. Forward scattering

Let us first examine the model result for the styrofoam target in Fig. 2. It is seen that the model result (solid curve) is in very good agreement with the data (dark circle) for incident angles up to $\pm 40^\circ$. After that, the data appear to increase slightly while the model tends to continue to drop. We expect the model to become less accurate as the incident angle increases. The agreement between the model and measurements also implies that shear waves are not important in the forward scattering of the styrofoam target.

The model results for the forward scattering by fish are shown as the curves in Fig. 3(a), where the dashed line is for fish body (flesh), the dash-dot line for swimbladder, and the solid line for the total scattering, which is obtained by adding coherently the complex scattering functions of fish body and swimbladder, as in Clay and Horne (1994). As indicated in Ding (1997), when the fish was tilted, it deviated slightly from the beam axis, and the deviation was measured with the split beam for calibration. The deviation modifies both the incident and scattering angle, and thus the results in Fig. 3(a) are not exactly forward scattering (i.e., incident angle equal to scattering angle), but slightly bistatic scattering. The deviation angles have been incorporated to calculate the curves in Fig. 3(a) (when measuring the artificial target, the deviation angle was trivial and thus not recorded).

The maximum forward scattering target strength (TS) in Fig. 3(a) is -17.31 dB and -18.00 dB, for the side aspect and dorsal aspect, respectively. The calculated forward scattering TS due to fish body is -15.31 dB, about 7 dB larger than that due to swimbladder, implying that the fish body is a more important factor in the forward scattering. This is in contrast to the case of backscattering by fish, in which swimbladder usually dominates (Foote, 1985). The total forward scattering TS, resulting from coherent summation, is found to be -12.96 dB, that is, 4–5 dB higher than the measurement.

Figure 3(a) shows that the dashed line (due to the fish body) appears to follow quite well the general trends of the measurements for positive angles, although the data are somewhat scattered. In the negative angle region, the data drop significantly as the tilt angle deviates from zero, and then increase with the angle. Such a feature is not seen in the dashed line, although it drops initially at the negative angles.

This suggests that more complex structures may exist on this side of the fish body, but are not modeled.

The dash-dot line (due to swimbladder) is seen to be nearly flat across the entire range of angles, and it appears that the contribution made by the swimbladder would be to lift the total scattering strength entirely above the data. Nevertheless, we also see that the model results of fish body (flesh) agree reasonably well with the data, at least for the positive angles. This indicates that the simple coherent summation may be inadequate and some mechanism of interaction between fish body and swimbladder should be considered. It is also observed that neither fish flesh nor swimbladder clearly predominates in forward scattering for the frequency (38 kHz) and the fish we used; other parts of the fish (e.g., bones and organs) may also play a role in this case. The above analysis also points to the necessity of acquiring accurate information of the acoustic properties (i.e., sound speed and density) of fish flesh, in addition to that of swimbladder, for proper modeling of forward scattering.

B. Bistatic scattering

The model results of bistatic scattering of the fish, however, give us a completely different picture, as shown in Fig. 3(b), with the same legends as in Fig. 3(a). The aforementioned position deviation has also been incorporated here. It is seen that the dash-dot line (due to swimbladder) is much higher than that due to fish body, and is very close to the measurements for angles within $\pm 40^\circ$. The total scattering does not depart significantly from the dash-dot line, indicating that the swimbladder is the dominant factor in this case, in contrast to the case of forward scattering. The data appear to increase for angles larger than 40° and decrease for angles less than -40° , which is not seen in the model results. This may be due in part to the fact that the model produces less accurate results as the incident angle increases, as discussed in Ye *et al.* (1997).

Referring to the styrofoam target, it is seen that the model result of bistatic scatter (dashed line in Fig. 2) follows quite well the trends of the data, for incident angles from -45° to the minimum point. After that, the model result appears to be higher (within 3 dB in general) than the data. It looks somewhat peculiar that the model result for the styrofoam target does not agree with the data as well as in the case of the fish, given that the artificial target has a much simpler structure. One possible reason is that there may still have existed slight position deviation as mentioned above, which was thought to be small enough to be ignored. In addition, shear waves are ignored in our model, and may also contribute to the discrepancy. The swimbladder is modeled as filled with air, supporting no shear waves.

It is important to note that in Fig. 2 where the target had little off-axis position deviation, both the measurement and the model results depend weakly on the incident angle (compared with the backscattering measurements in Sawada *et al.*, 1996), particularly in the case of forward scattering. Our analysis indicates that when there is no position deviation, the model results of the forward and bistatic scatter of the fish are also very smooth with respect to the incident angle (not shown here), similar to the curves in Fig. 2. This

suggests that much of the variability near normal incidence in the fish data are not inherent but due to the position deviation, and strengthens an earlier conclusion (Ding, 1997) that the variability of forward scatter is much less than that of backscatter of the same target. The less variability of forward scatter could be understood more intuitively from the viewpoint of phase interference of scattered signals from different parts of a target, as discussed in Ding (1997): Consider an ideal case where a target is approximated by a line array of scatterers. The path (from source to scatterer to receiver) difference between the scatterers is zero in the case of forward scattering, whereas in the case of backscattering the path difference is proportional to $\sin \theta / \lambda$, with θ being incident angle and λ being wavelength, and thus the resulting phase difference can cause strong interference, leading to strong variation in backscatter with respect to the incident angle.

III. CONCLUSION

In this paper we have made an effort to compare the theoretical model developed in Ye *et al.* (1997) with the forward and bistatic scattering measurements by Ding (1997). Our analysis indicates that the fish body (flesh) is more important than the swimbladder in determining forward scattering of the fish at the frequency of interest (38 kHz). For bistatic scattering, however, the swimbladder is still the dominant factor. This suggests that in future experiments, the acoustic properties of fish flesh should also be measured accurately.

In the case of forward scattering, we find the model produces results very close to the data of the styrofoam prolate spheroid for incident angle up to $\pm 40^\circ$. For the fish, the model results due to the body agree well with the data for positive angles, but fails to follow the data for negative angles, suggesting that more complex structures may be involved. The results also indicate that the coherent summation of the calculated scattering by the fish body and the swimbladder overestimates the forward scattering strength. It is thus speculated that fish body (flesh) and swimbladder may have to be treated as a coupling acoustic system, instead of being considered separately.

The model also agrees reasonably well with the bistatic scatter data of the styrofoam target, despite the fact that the model does not include shear waves. In the case of bistatic scattering of fish where the swimbladder dominates, the model results appear to agree even better with the measurements for incident angles within $\pm 40^\circ$.

It must be emphasized that the theoretical model is easy to implement and compute and the chosen geometry is simple with only a few parameters. While it is more realistic to develop a model based on an ellipsoid for application in fisheries acoustics, such a task appears very difficult at this stage (to our knowledge, numerical computation of ellipsoidal wavefunctions is difficult and has not been documented in the literature). Our work here is a reasonable step towards the more complicated problem, and as a first-order approximation, has produced encouraging results. As demonstrated above, it is believed that the model should have general ap-

plications for slender targets such as fish, when incident angle of sound is not too close to end-on directions.

ACKNOWLEDGMENTS

Constructive comments from Dr. M. Furusawa, of Tokyo University of Fisheries, Japan, are greatly appreciated. The work received supports from the Science and Technology Agency of Japan, in the form of an STA fellowship to LD, and from Department of Fisheries and Oceans, Canada and the National Central University, Taiwan (ZY). Technical support in the experiment (LD) from the Fisheries Acoustics group at the National Research Institute of Fisheries Engineering of Japan is also gratefully acknowledged.

Clay, C. S., and Horne, J. K. (1994). "Acoustic models of fish: The Atlantic cod (*Gadus morhua*)," J. Acoust. Soc. Am. **96**, 1661–1668.
Clay, C. S., and Medwin, H. (1977). *Acoustical Oceanography* (Wiley, New York).
Curran, T., Lemon, D., and Ye, Z. (1994). "The acoustic scintillation flow-

meter: Applications for a new environmental tool," J. Can. Hydrographic Asso., No. 49, 24–29.

Ding, L. (1997). "Direct laboratory measurement of forward scattering by individual fish," J. Acoust. Soc. Am. **101**, 3398–3404.
Foote, K. G. (1985). "Rather high frequency sound scattering by swimbladder fish," J. Acoust. Soc. Am. **78**, 688–700.
Furusawa, M. (1988). "Prolate spheroidal models for predicting general trends of fish target strength," J. Acoust. Soc. Jpn. (E) **9**, 13–24.
Gaunaurd, G. C. (1985). "Sonar cross sections of bodies partially insonified by finite sound beams," IEEE J. Ocean Eng. **OE-10**, 213–230.
Junger, M. C. (1982). "Scattering by slender bodies of revolution," J. Acoust. Soc. Am. **72**, 1954–1956.
MacLenna, D. N., and Simmonds, E. J. (1992). *Fisheries Acoustics* (Chapman & Hall, London).
Sawada, K., Miyano, Y., and Ishii, K. (1996). "Precise target strength pattern measurement in an indoor tank," J. Acoust. Soc. Jpn. (submitted).
Shibata, K. (1970). "Study on details of ultrasonic reflection from individual fish," Bull. Fac. Fish. Nagasaki Univ. **29**, 1–82.
Ye, Z. (1997). "An approach to sound scattering by cylinders of finite length," J. Acoust. Soc. Am. (in press).
Ye, Z., Hoskinson, E., Dewey, R. K., Ding, L., and Farmer, D. M. (1997). "A method for acoustic scattering by slender bodies. I. Theory and verification," J. Acoust. Soc. Am. **102**, 1964–1976.

Acoustical characterization of absorbing porous materials through transmission measurements in a free field

Celse K. Amédin, Yvan Champoux, and Alain Berry

Département de Génie mécanique, Université de Sherbrooke, Sherbrooke, Québec J1K 2R1, Canada

(Received 30 July 1996; accepted for publication 2 July 1997)

Various results are presented to experimentally validate the theoretical modeling of the acoustic radiation of a circular piston through a thin layer of porous absorbing material, as worked out by Amédin *et al.* [J. Acoust. Soc. Am. **98**, 1757–1766 (1995)]. This theoretical modeling is subsequently exploited for the development of an acoustical characterization method for porous absorbing materials. The method is based on acoustical pressure measurements taken at two different positions in an open baffled tube radiating into the material to be characterized and at a given point above the material, and on an iterative process of numerical resolution. The reliability of the method is evaluated by means of numerical simulations and by comparisons using the two-layer method in an impedance tube [J. Acoust. Soc. Am. **74**, 1577–1582 (1983)]. The preliminary tests show that the new method can be used to experimentally characterize the specific acoustic impedance and the propagation constant of porous absorbing materials *in situ*. © 1997 Acoustical Society of America. [S0001-4966(97)04510-4]

PACS numbers: 43.20.Gp, 43.20.Ye, 43.55.Ev, 43.58.Bh [JEG]

INTRODUCTION

Various techniques are proposed in literature for the acoustical characterization of porous absorbing materials. Most of these techniques are limited by the conditions of their application. This is typical of methods based on impedance tube measurements,^{1,2} which necessitate prior taking up of several samples of the material tested. This is also the case with the free-field measurement method,^{3–6} mostly because of the difficulty in establishing basic hypotheses (very wide samples, plane wave hypotheses, critical spacing between acoustic field measuring microphones, etc.). Because of these limitations, the aforementioned methods are essentially suitable for laboratory acoustical characterizations.

In practice, having at one's disposal an acoustical characterization method *in situ* would be more practical and more useful. Such a method would have several advantages, the most noteworthy being to provide manufacturers of porous absorbing materials with continuous and real time monitoring of the acoustical and physical parameters of their products. Recent practical work carried out by Champoux and Ross⁷ has in effect demonstrated that it is possible to calculate the thermal resistance of a fibrous insulating material from acoustical measurements. More precisely, experimental measurements of acoustic pressure radiated through a material from an open, baffled waveguide have first been used in conjunction with a simplified model to estimate the acoustical propagation constant of the material. Other experimental results have subsequently shown the existence of good correlation between the estimated propagation constant and the thermal resistance, which is the main parameter for the physical characterization of thermal insulating material.

The technique developed by Champoux and Ross is very promising. However, the simplified model used to describe the acoustical phenomena limits the application of this method to materials of very large thickness. Moreover, the

model does not provide a complete acoustical characterization of absorbing porous materials, because it does not evaluate the specific acoustic impedance of the material. It became apparent that a better understanding of the acoustic phenomena in question, and maybe of other physical parameters, will probably lead to the generalization of the Champoux and Ross technique on low thickness materials. For the purpose of taking better account of these acoustic phenomena, a previous paper dealt with the theoretical modeling of a baffled piston radiating through a thin layer of porous absorbing material. Results of numerical simulations showed that the theoretical framework thus established is rigorous and usable for purposes of acoustical characterization.

The object of the present study is to exploit this theoretical framework to develop an acoustical characterization method for porous absorbing materials, based on transmission measurements in a free field. Section I sums up and supplements the theoretical framework previously established. Section II deals with an experimental validation of the theoretical framework by comparing theoretical results and experimental measurements taken with three samples of materials. Section III displays developments leading to the new method of acoustical characterization, as well as numerical and experimental validations for this method.

I. THEORETICAL BACKGROUND RESULTS

A previous paper⁸ dealt with sound radiation of a baffled, circular piston through a thin layer of absorbing porous material (Fig. 1) which can be processed as an equivalent, homogeneous, and isotropic fluid. It showed that sound pressure p_1 in the material and acoustic pressure p_2 in the acoustic medium above the material can respectively be modeled by the expressions

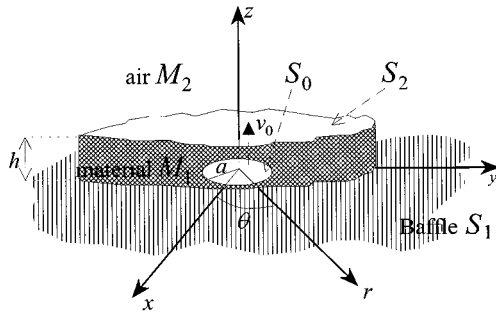


FIG. 1. Problem geometry.

$$p_1(M) = ja\omega\nu_0 \frac{\rho_1}{\Omega} \times \int_0^\infty \frac{1 + [1 + \exp(2\eta_1 z_M)] Q_1(\mu)}{\eta_1} \times J_0(\mu r_M) J_1(\mu a) \exp(-\eta_1 z_M) d\mu, \quad (1)$$

and

$$p_2(N) = ja\omega\nu_0 \frac{\rho_2}{\Omega} \int_0^\infty \frac{Q_2(\mu)}{\eta_2} \times J_0(\mu r_N) J_1(\mu a) \exp(-\eta_2 z_N) d\mu. \quad (2)$$

In Eqs. (1) and (2), j is the square root of -1 , a is the piston radius, ω is the angular frequency of the wave, ν_0 is the uniform velocity of the piston, ρ_1 and Ω , respectively, indicate the density and porosity⁹ of the material, ρ_2 is the density of the acoustic medium, and J_0 and J_1 are the Bessel functions of the first kind of order 0 and 1, respectively. Points M (in the material) and N (above the material) have cylindrical coordinates (r_M, θ_M, z_M) and (r_N, θ_N, z_N) in a coordinate system whose origin is at the center of the piston. The terms η_1 , η_2 , Q_1 , and Q_2 are complex variables defined as functions of Ω , ρ_1 , and ρ_2 , of the integration variable μ , of the wave numbers k_1 and k_2 in the material and in the acoustic medium, respectively, and of the finite thickness h of the layer of material:⁸

$$\eta_1 = \sqrt{\mu^2 - k_1^2}, \quad \eta_2 = \sqrt{\mu^2 - k_2^2},$$

$$Q_1(\mu) = \frac{-(\rho_1 \eta_2 - \Omega \rho_2 \eta_1) \exp(-(\eta_1 + \eta_2)h)}{(\rho_1 \eta_2 - \Omega \rho_2 \eta_1) \exp(-(\eta_1 + \eta_2)h) + (\rho_1 \eta_2 + \Omega \rho_2 \eta_1) \exp((\eta_1 - \eta_2)h)},$$

and

$$Q_2(\mu) = \frac{2\Omega \rho_1 \eta_2}{(\rho_1 \eta_2 - \Omega \rho_2 \eta_1) \exp(-(\eta_1 + \eta_2)h) + (\rho_1 \eta_2 + \Omega \rho_2 \eta_1) \exp((\eta_1 - \eta_2)h)}.$$

The density ρ_1 of the absorbing porous material is a complex value; it is defined by the relation^{9,10}

$$\frac{\rho_1}{\Omega} = \frac{k_1 Z_c}{\omega}, \quad (3)$$

where Z_c is the characteristic acoustic impedance of the material. In other respects, the wave number k_1 can be defined as a function of the propagation constant in the material:

$$\gamma = jk_1. \quad (4)$$

The two latter relations indicate that besides the thickness h of the material, γ and Z_c are the only parameters of the material involved in Eqs. (1) and (2). These parameters constitute the intrinsic elements of acoustical characterization of a given medium.⁹

In practice, Eq. (1) is of little interest because of the great difficulty in experimentally measuring the acoustic field in the material. The acoustic pressure \bar{p}_0 averaged over the piston surface will become more useful later on in this paper (Sec. III). This pressure \bar{p}_0 is defined by the relation

$$\bar{p}_0 = \frac{1}{\pi a^2} \int_{S_0} p_1(P) dS_P, \quad (5)$$

where S_0 indicates the piston surface. By exploiting Eq. (1) to express $p_1(P)$ and in noting that z_P is zero, Eq. (5) becomes

$$\bar{p}_0 = \frac{ja\omega\nu_0}{\pi a^2} \frac{\rho_1}{\Omega} \int_0^\infty \frac{1 + 2Q_1(\mu)}{\eta_1} J_1(\mu a) \times \left(\int_0^{2\pi} \int_0^a J_0(\mu r_P) r_P dr_P d\theta \right) d\mu,$$

or

$$\bar{p}_0 = \frac{2j\omega\nu_0}{a} \frac{\rho_1}{\Omega} \int_0^\infty \frac{1 + 2Q_1(\mu)}{\eta_1} J_1(\mu a) \times \left(\int_0^a J_0(\mu r_P) r_P dr_P \right) d\mu. \quad (6)$$

The Bessel functions J_0 and J_1 satisfy the relation¹¹

$$\int_0^a J_0(\mu r_P) r_P dr_P = \frac{a}{\mu} J_1(\mu a).$$

Application of this relation in Eq. (6) then supplies the final expression of \bar{p}_0 :

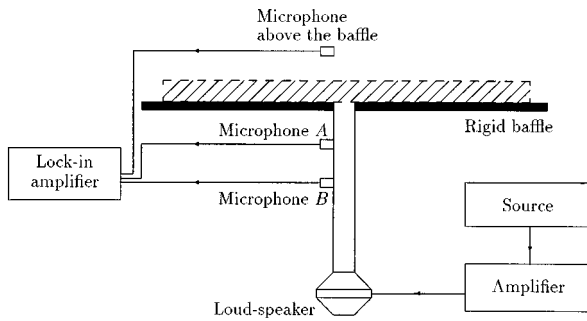


FIG. 2. Instrumentation chain schematic.

$$\bar{p}_0 = 2j\omega\nu_0 \frac{\rho_1}{\Omega} \int_0^\infty \frac{1+2Q_1(\mu)}{\mu\eta_1} (J_1(\mu a))^2 d\mu. \quad (7)$$

Equation (7) can be used in calculating the radiation impedance Z_r of a baffled piston radiating through an absorbing porous layer of finite thickness:

$$Z_r = \frac{\pi a^2 \bar{p}_0}{\nu_0} = 2j\pi a^2 \omega \frac{\rho_1}{\Omega} \int_0^\infty \frac{1+2Q_1(\mu)}{\mu\eta_1} (J_1(\mu a))^2 d\mu. \quad (8)$$

Apart from the term $2Q_1(u)$ which is a correction related to the finite thickness of the material, Eq. (8) is equivalent to the expression of the radiation impedance of a baffled piston radiating into a semi-infinite medium.¹²

II. EXPERIMENTAL VALIDATION OF THE THEORY

A. Experimental procedure

1. Experimental setup

Figure 2 illustrates the experimental setup and the instrumentation which were used for experimental manipulations in a semi-anechoic room. The rigid baffle is a $4\text{ m} \times 2\text{ m} \times 0.019\text{ m}$ plywood panel. A circular hole is cut at the center of the baffle so that a brass tube 1 m in length with an inside radius of 0.0225 m can be terminated at the same level as the top surface of the baffle. It is agreed that sound radiation at the end of the tube is equivalent to the uniform radiation of a circular baffled piston,¹³ as long as the wavelength remains at least six times greater than the tube radius. The other end of the tube is terminated with a loudspeaker creating acoustic excitation in the tube. The loudspeaker is driven by a function generator that provides a steady sinusoidal signal. An amplifier, placed between the generator and the expansion chamber, provides control for a higher than 100-dB acoustic pressure inside the tube and 75 dB above the baffle. Two openings are made in the tube wall in order to introduce microphones. An estimation of the acoustic velocity can be obtained from the microphone readings. Another microphone is used to measure the pressure field at any point above a material sample resting on the baffle. The three microphones have a diameter of $\frac{1}{4}$ in.; they are connected through preamplifiers to a lock-in amplifier providing amplitude and phase to the signals picked up.

2. Description of the samples

The theoretical formulation of Sec. I assumes that the material resting on the baffled tube is an homogeneous and isotropic equivalent fluid medium. Taking into account the fact that an homogeneous material is not readily found, three samples of material have been retained for the experimental manipulations.

The first two are SIF[®] reticulated foams 2.85 cm and 5.35 cm thick, manufactured by the Foamex company. They are respectively called SIF 1 and SIF 2 in the rest of this paper. Their porosity are larger than 97% and their density equal to 1.75 lb/pi^3 . They are used industrially to build anechoic chambers or for noise insulation. The two samples are homogeneous and isotropic. Their acoustical characteristics are about the same, but their thickness is essentially different, and so are their absorbing properties.

The third sample is a fiberglass wool OC 705 manufactured by Fiberglass Canada. It is a rigid material with a density of 6 lb/pi^3 and with a thickness of 5.3 cm. It is generally used for thermal insulation. This material is rather heterogeneous. It does not respect the basic hypothesis of theoretical formulation, but has nevertheless been retained for the experimental validation tests, for the information its use can provide on the importance of homogeneity in the theoretical formulation.

3. Measurement of the acoustic velocity and the acoustic pressure at the open end of the tube

According to the theoretical formulation in Sec. I, it is essential to know the velocity ν_0 at the tube output, in order to compare theoretical results with experimental results. This velocity depends not only on frequency but also on the signal generator's output level and the acoustic load created by the sample of material resting on the baffled tube. A well-documented² experimental technique has been used to quantify this velocity ν_0 , as well as the acoustic pressure \bar{p}_0 at the tube output. From the measurement of acoustic pressures p_A and p_B at two distinct points A and B of the tube (in which only plane waves are propagated), it is easily shown that

$$\nu_0 = \frac{p_B \cos(kz_A) - p_A \cos(kz_B)}{j\rho_0 c_0 \sin(kd)} \quad (9)$$

and

$$\bar{p}_0 = \frac{p_A \sin(kz_B) - p_B \sin(kz_A)}{\sin(kd)}, \quad (10)$$

where z_A and z_B designate the respective distances of measurement points A and B from the baffle, d is the distance between these two points ($d = |z_B - z_A|$), c_0 , ρ_0 , and k , respectively, designate the speed of sound, density of the air, and wave number in the tube.

Equation (9) provides an experimental estimate of ν_0 , with the fundamental hypothesis whereby this value represents the overall velocity at the tube output. Instead of incorporating this experimental estimate of ν_0 in the theoretical formulation of Sec. I, a unitary speed has instead been considered for theoretical calculations. The experimental mea-

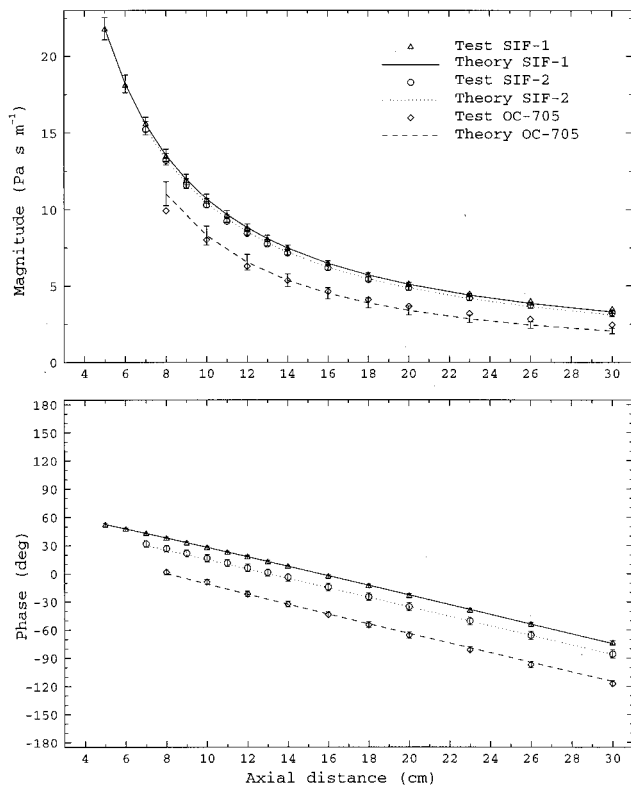


FIG. 3. Comparison between theory and experience for the normalized transfer function H measured above the sample on the main axis of the tube. Samples SIF 1, SIF 2, and OC 705. Frequency=500 Hz.

measurements of the acoustic field created by the tube radiation through the material have therefore been normalized by the experimental estimate of ν_0 before being compared with theoretical predictions. It is therefore the transfer function H between the acoustic pressure radiated by the tube above the material and the velocity at the tube termination

$$H = \frac{p_2(N)}{\nu_0},$$

that has served as element of comparison between theory and experiment. The results of this comparison are outlined in Sec. II B.

Equation (10) assumes that the acoustic pressure is uniform at the output point of the tube. This is questionable because it is easy to demonstrate from Eq. (1) and in the simpler case where the tube radiates in a semi-infinite medium with a uniform velocity,^{13,14} that the acoustic pressure is not perfectly uniform at the tube output. Equation (1) will however be very useful in Sec. III, because it will be assumed that it provides an indirect measurement of the average acoustic pressure at the tube output.

B. Experimental results and comparison with the predictions

The propagation constant γ and the specific acoustical impedance Z_c of the three material samples must be known in order to validate the theoretical model of Sec. I. These acoustical characteristics have been determined using the two thickness technique in an impedance tube,¹ and they

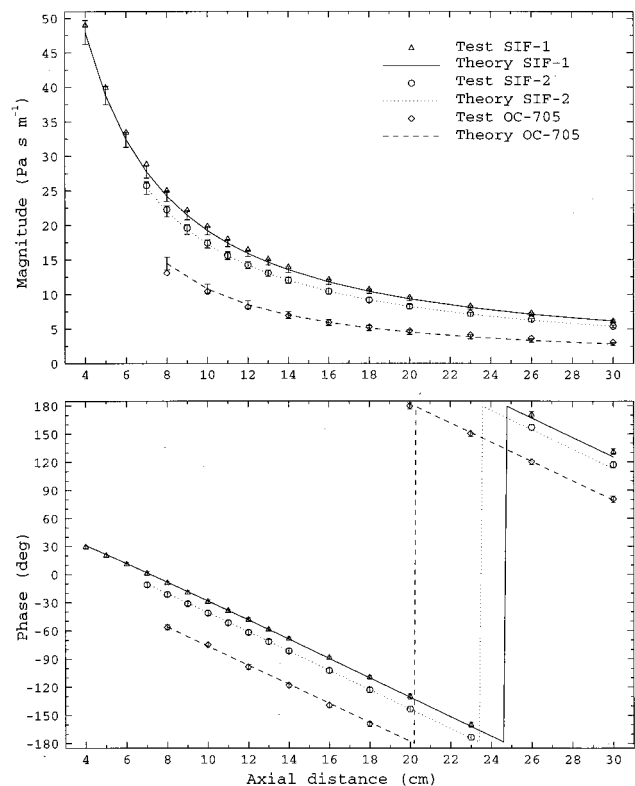


FIG. 4. Comparison between theory and experience for the normalized transfer function H measured above the sample on the main axis of the tube. Samples SIF 1, SIF 2, and OC 705. Frequency=1000 Hz.

were then incorporated in the theoretical model to obtain the predictions which have then been compared to the experimental values H . The comparisons have been made by first considering measurement points located at various distances from the baffled tube axis, and then measurement points located at a vertical distance of 10 cm from the baffle. The results of these comparisons are outlined below.

1. On-axis measurements

The comparisons between theoretical and experimental on-axis responses are represented by Figs. 3, 4, 5, and 6 which correspond respectively to 500 Hz, 1000 Hz, 1500 Hz, and 2000 Hz frequencies. In these four figures, the term “axial distance” indicates the measurement point position in relation to the tube termination. Globally, the theoretical results and the experimental measurements are highly concordant. The uncertainty bars have been associated with theoretical predictions because they reflect uncertainties in the various measured input values of the model (sound velocity, microphone positioning, thickness of material, and uncertainties in lock-in amplifier ratings). Amplitude discrepancies are especially noticeable at measurement points closest to the top surface of the sample. There probably is, at the very output of the material, a “near-field” zone in which the sensor microphone causes turbulence not taken into account in the theoretical modeling. Phase divergences are caused in great part by uncertainties related to measuring microphone positions and to sound velocity in the acoustic medium. The phase is very sensitive to the microphone position when the

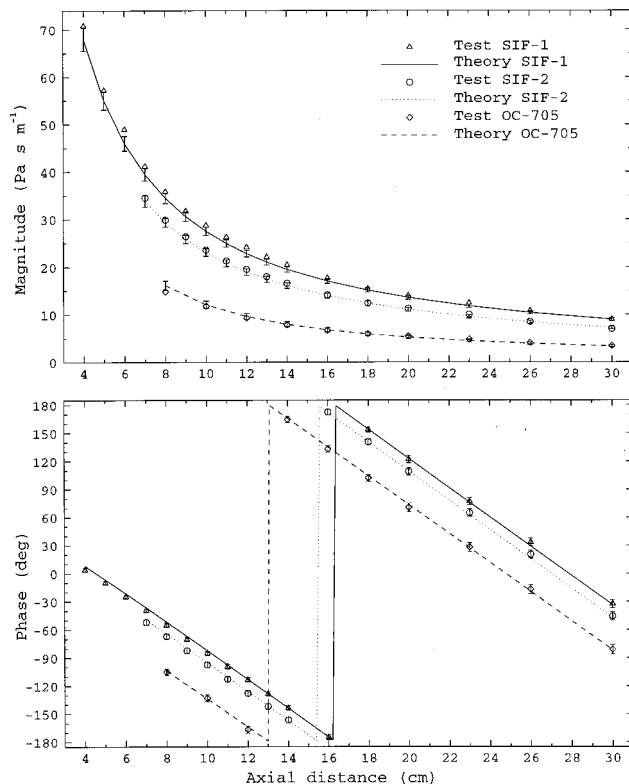


FIG. 5. Comparison between theory and experience for the normalized transfer function H measured above the sample on the main axis of the tube. Samples SIF 1, SIF 2, and OC 705. Frequency=1500 Hz.

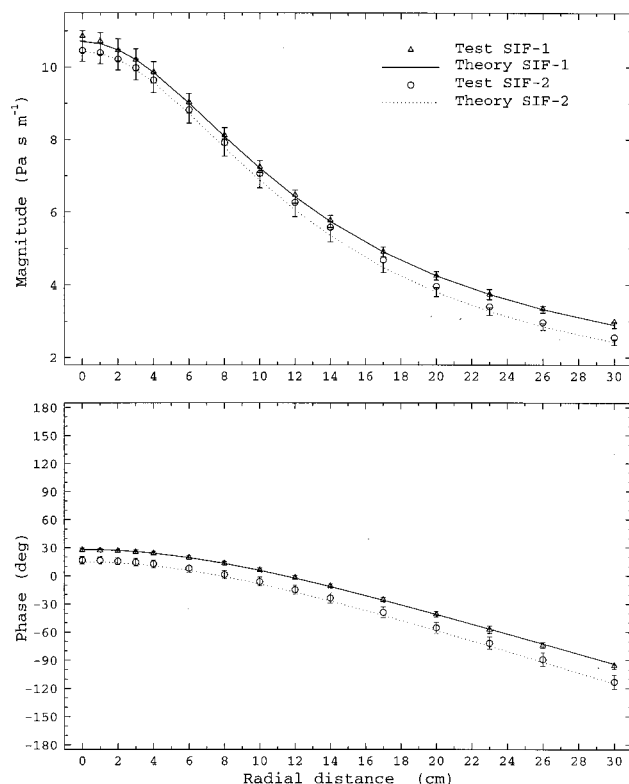


FIG. 7. Comparison between theory and experience for the normalized transfer function H measured radially at 10 cm above the sample. Samples SIF 1 and SIF 2. Frequency=500 Hz.

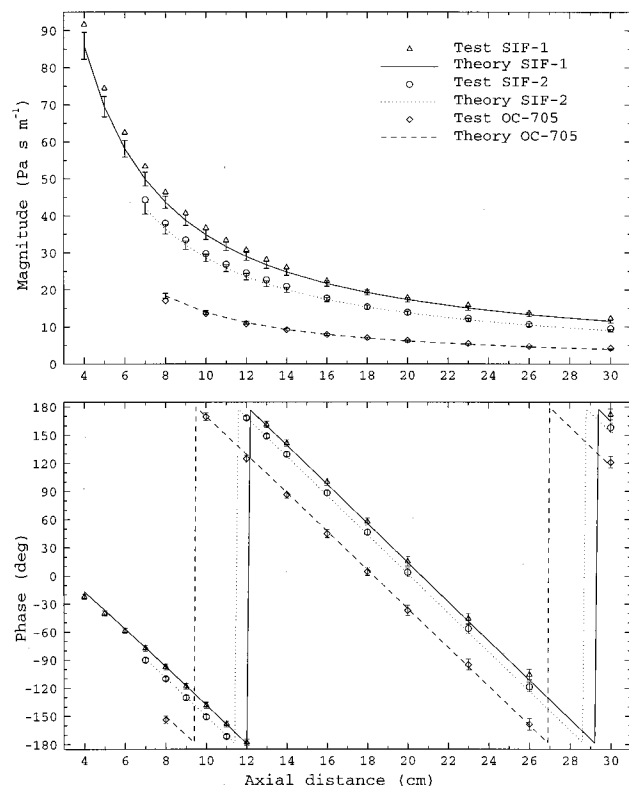


FIG. 6. Comparison between theory and experience for the normalized transfer function H measured above the sample on the main axis of the tube. Samples SIF 1, SIF 2, and OC 705. Frequency=2000 Hz.

microphone is located near the material. The pressure amplitude is not very sensitive to microphone location.

With SIF 1 and SIF 2 wool, the theoretical results compare very well with experimental measurements, especially at 500 Hz or at 1000 Hz. At frequencies of 1500 Hz and 2000 Hz, the discrepancies between theory and experiment can reach 7% in amplitude and 4 degrees in phase. The discrepancies are weaker with SIF 2 wool. That could be due to the fact that SIF 2 wool is more absorbent than SIF 1 wool (because of its larger thickness).

Because of heterogeneity, results obtained with OC 705 wool vary slightly in relation with the side of the material facing the open tube. Results shown in Figs. 3, 4, 5, and 6 about this sample are in fact averages of results obtained for the material tested on both sides. With this sample, axial response comparisons also give acceptable results: discrepancies between theory and experience are very weak phase-wise (less than 2 degrees), but they can reach 11% in amplitude.

Comparisons thus show that the axial response of a baffled tube radiating through either one of three samples is reasonably well predictable through the proposed theoretical modeling in Sec. I. Although this type of modeling presumes a homogeneous material, satisfactory results were nevertheless obtained in the case of OC 705 wool.

2. Off-axis measurements

Figures 7, 8, 9, and 10, respectively illustrate comparisons at 500, 1000, 1500, and 2000 Hz, between the theoret-

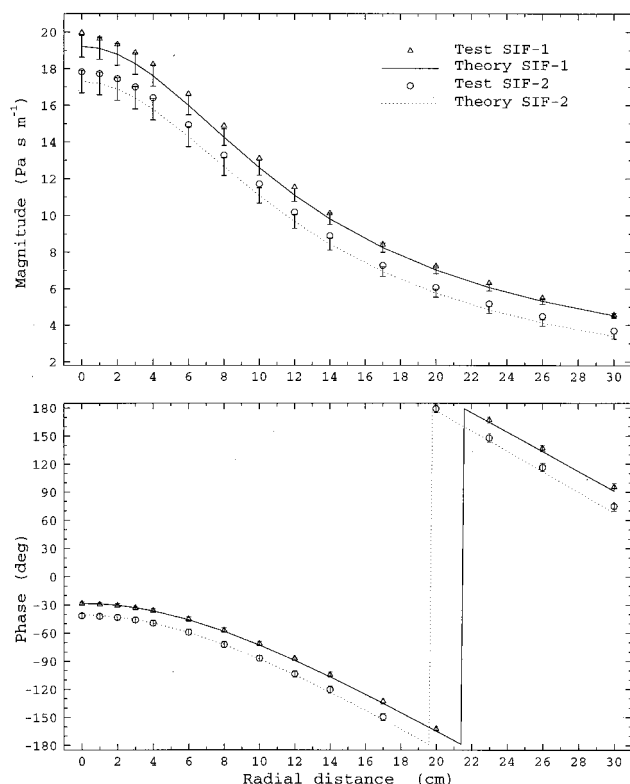


FIG. 8. Comparison between theory and experience for the normalized transfer function H measured radially at 10 cm above the sample. Samples SIF 1 and SIF 2. Frequency=1000 Hz.

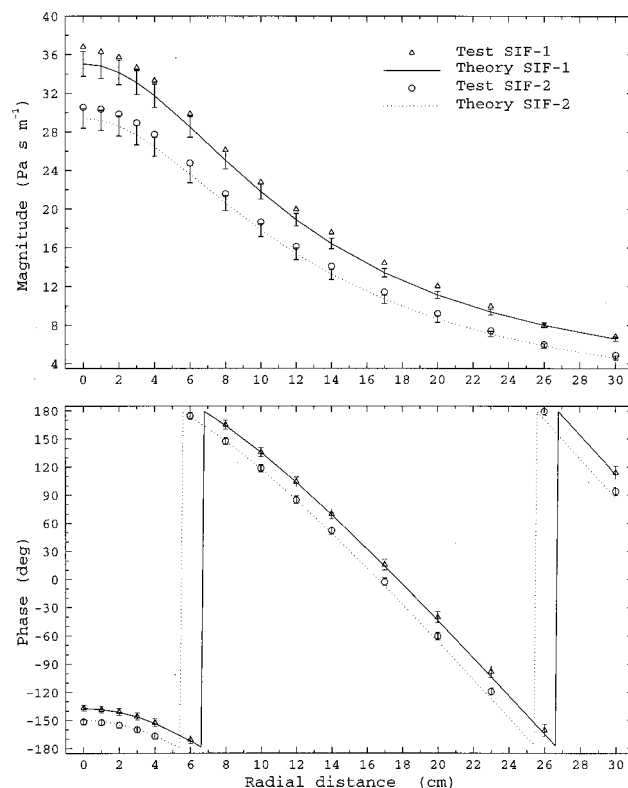


FIG. 10. Comparison between theory and experience for the normalized transfer function H measured radially at 10 cm above the sample. Samples SIF 1 and SIF 2. Frequency=2000 Hz.

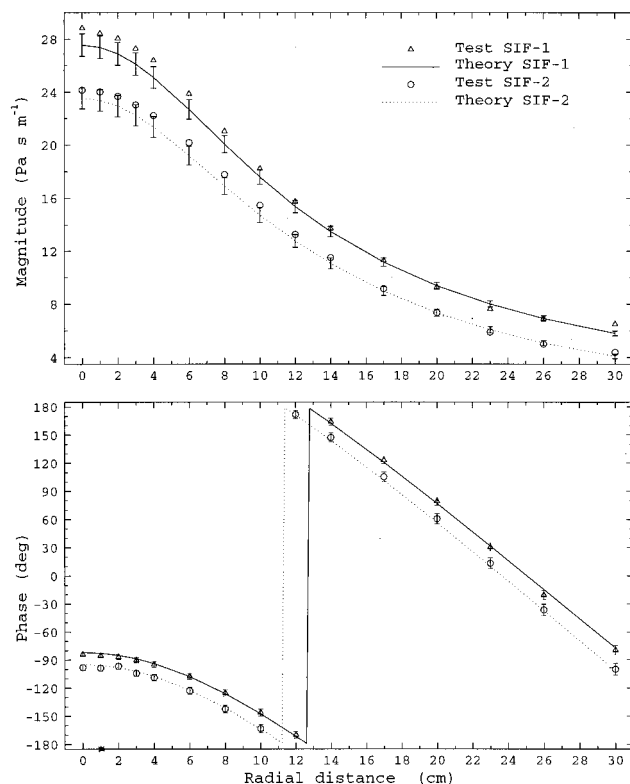


FIG. 9. Comparison between theory and experience for the normalized transfer function H measured radially at 10 cm above the sample. Samples SIF 1 and SIF 2. Frequency=1500 Hz.

ical predictions and the experimental measurements, in the case of measurement points located at a vertical distance of 10 cm from the baffle. The distance between one measurement point and the tube axis is termed “radial distance” in these four figures. Fiberglass OC 705 is no longer used for these comparisons because its heterogeneous character was found more critical in the radial direction. Conclusions already reached concerning samples SIF 1 and SIF 2 in the axial response analysis, are still worthwhile for radial radiation: Theory can predict experimental measurements very well, especially at 500 and 1000 Hz, while weak divergences occur at 1500 and 2000 Hz. Discrepancies between theory and experience are smaller than 6 degrees in phase and 5% in amplitude.

In conclusion, it must be noted that comparisons have revealed very close agreement between theory and experience with the tube radiating through thin samples of absorbing porous materials. The various figures showed that the theoretical formulation satisfactorily reflects experimental observations. Discrepancies are relatively small between theoretical values and measurements, in amplitude as well as in phase.

III. ACOUSTICAL CHARACTERIZATION OF POROUS MATERIAL VIA TRANSMISSION MEASUREMENT IN FREE FIELD

This section deals with the development of an acoustical characterization method for absorbing porous materials via free-field transmission measurements. The problem consists

to estimate the propagation constant γ and the acoustical impedance characteristic Z_c of these materials. The acoustic radiation of a baffled open tube through a finite layer of porous material and the theoretical model that has been experimentally validated in the previous section are been exploited to resolve the problem. The procedure developed to determine the intrinsic acoustical characteristics will first be described, and results of the numerical simulations and comparisons with the two-thickness method in an impedance tube¹ will be introduced to test the validity of the new method.

A. Description of the method

A porous absorbing material whose acoustical characteristics γ and Z_c are unknown is resting on an open baffled tube of a radius a . It is assumed that the tube termination in contact with the material act as a piston vibrating uniformly at a velocity v_0 . The main idea is to use two measurements of the acoustic pressure radiated by the tube to determine the unknown γ and Z_c . A first approach was developed by considering two measurements of the sound pressure above the material. Experimental validation trials for this first approach have not yielded satisfactory results due to lack of sensitivity of these measurements to the acoustical characteristics of the material. The spatial variations of the acoustic field above the material were too weak. The selected approach was developed by measuring the average sound pressure \bar{p}_0 at the tube output (under the material) as well as the sound pressure at one location above the material. The sensitivity of this second approach to the acoustical characteristics of the sheet of material is then much higher. Obtaining the average pressure value \bar{p}_0 can however constitute a big problem, because of the great difficulty in making direct pressure readings at the tube output. In the framework of this operation, \bar{p}_0 is measured with the same experimental technique with which the velocity v_0 was measured at the tube output (cf. Sec. II A). In other words, it is assumed that Eq. (10) provides an indirect measurement of \bar{p}_0 from the acoustic pressure taken at two points of the tube.

For the remainder of this paper, this developed procedure will be called the transmission method, meaning that its base is the sound pressure transmitted through the material. For easier reading of the text, acoustic pressure at point N above the material will from now appear as $p(N)$ instead of $p_2(N)$. Measurements of \bar{p}_0 and $p(N)$ will be used to invert Eqs. (2) and (7), and extract characteristics γ and Z_c of the material as per the procedure outlined below.

It was already underlined in Sec. I that Eqs. (2) and (7) depend essentially on γ and Z_c ; they can thus be written

$$p(N) = v_0 H_N(\gamma, Z_c) \quad (11)$$

and

$$\bar{p}_0 = v_0 H_0(\gamma, Z_c), \quad (12)$$

where $H_N(\gamma, Z_c)$ and $H_0(\gamma, Z_c)$ are given under the forms

$$H_N(\gamma, Z_c) = ja\omega \frac{\rho_2}{\Omega} \int_0^\infty \frac{Q_2(\mu)}{\eta_2} \times J_0(\mu r_N) J_1(\mu a) \exp(-\eta_2 z_N) d\mu \quad (13)$$

and

$$H_0(\gamma, Z_c) = 2j\omega \frac{\rho_1}{\Omega} \int_0^\infty \frac{1 + 2Q_1(\mu)}{\mu \eta_1} (J_1(\mu a))^2 d\mu. \quad (14)$$

It is impossible to analytically extract the unknown γ and Z_c from a system formed by Eqs. (11) and (12). An iterative procedure based on the fixed-point method was then worked out to determine the two unknowns. The procedure requires initial values of γ and Z_c , which are chosen from the following simplifications of the physical problem.

Assuming that the material has infinite thickness, the sound pressure radiated by the tube at point N of this semi-infinite material is formulated^{13,14}

$$p(N) = \frac{j\omega v_0}{2\pi} \frac{\rho_1}{\Omega} \int_{S_0} \frac{\exp(-jk_1 R_{NP})}{R_{NP}} dS_P, \quad (15)$$

where R_{NP} refers to the distance between the point N and a point P on surface S_0 of the tube termination. Equations (3) and (4) allow transformation of Eq. (15) to yield

$$p(N) = \frac{\gamma Z_c v_0}{2\pi} \int_{S_0} \frac{\exp(-\gamma R_{NP})}{R_{NP}} dS_P. \quad (16)$$

An approximation of the integral in Eq. (16) then gives the relation

$$p(N) \approx \frac{\gamma Z_c v_0 a^2}{2} \frac{\exp(-\gamma R_N)}{R_N}, \quad (17)$$

in which R_N designates the distance between point N and the center of surface S_0 . The approximation used in Eq. (17) implies that radius S_0 is small compared to the acoustic wavelength and that the measurement point is far enough from surface S_0 . A similar approximation was obtained for the average pressure \bar{p}_0 at the tube output, assuming that \bar{p}_0 corresponds to the acoustic pressure at a point of S_0 found at a distance r_0 from the center of S_0 :

$$\bar{p}_0 \approx \frac{\gamma Z_c v_0 a^2}{2} \frac{\exp(-\gamma r_0)}{r_0}. \quad (18)$$

The second condition on which this approximation is based is not met in the case of Eq. (18), which corresponds to a measurement point located on S_0 . The validity of this equation is however not very important in the present context as the objective sought is simply limited to obtaining the initial values for the numerical resolution procedure. On the other hand, it is essential to determine an appropriate value of r_0 to introduce in Eq. (18). That has been done by using another approximation of \bar{p}_0 . From the radiation impedance of a baffled piston in a semi-infinite medium,^{12,15} it can in effect be shown that for a radius a much smaller than the acoustic wavelength, an approximation of \bar{p}_0 is in the form

$$\bar{p}_0 \approx v_0 Z_c \left(\frac{8\gamma a}{3\pi} - \frac{\gamma a^2}{2} \right). \quad (19)$$

However, under the same restrictions, an approximation of Eq. (18) is

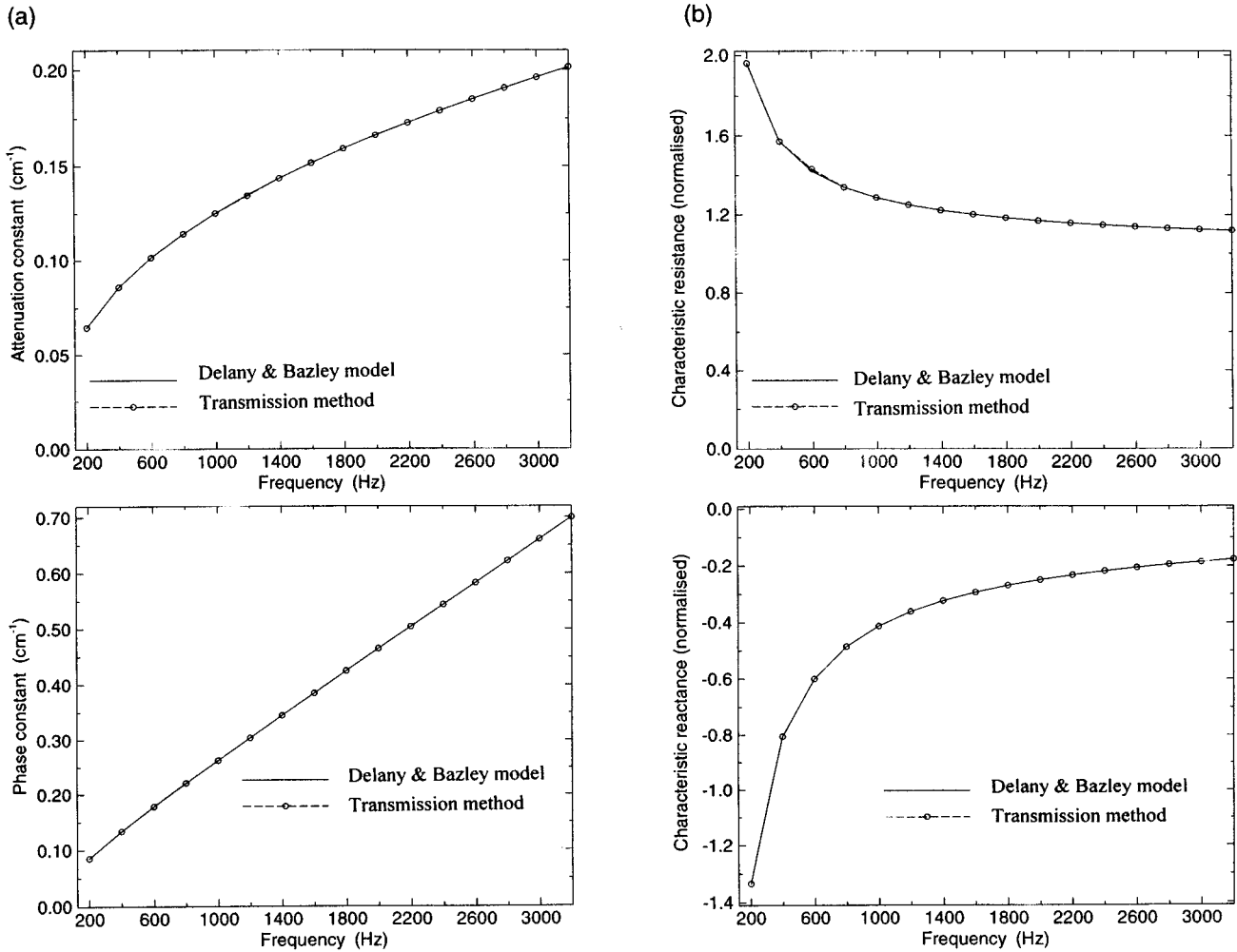


FIG. 11. Comparison between the Delany and Bazley model (direct approach) and the transmission method (inverse approach). Air flow resistance $\sigma = 10$ cgs rayls/cm. (a) Propagation constant. (b) Normalized characteristic impedance.

$$\bar{p}_0 \approx \frac{\gamma Z_c \nu_0 a^2}{2} \left(\frac{1}{r_0} \gamma \right). \quad (20)$$

Equations (19) and (20) then lead to

$$r_0 \approx \frac{3\pi}{16} a.$$

This value of r_0 is thus chosen in Eq. (18).

By dividing Eq. (17) by Eq. (18), an initial value γ_0 of the propagation constant is obtained:

$$\gamma_0 = h_\gamma[p(N), \bar{p}_0], \quad (21)$$

where h_γ is defined by

$$h_\gamma[X, Y] = \frac{\ln(r_0 Y) - \ln(R_N X)}{R_N - r_0}. \quad (22)$$

This initial value is then used in Eq. (17) to obtain an initial value Z_{c0} of the characteristic acoustical impedance,

$$Z_{c0} = h_Z[p(N), \gamma_0], \quad (23)$$

where the h_Z is defined by

$$h_Z[X, Y] = \frac{2R_N X}{Y \nu_0 \exp(-Y R_N)}. \quad (24)$$

These initial values are utilized in an iterative procedure beginning at iteration i ($i \geq 0$) with a calculation of the terms $p(N)_i$ and \bar{p}_{0i} , which are defined from Eqs. (13) and (14):

$$p(N)_i = \nu_0 H_N(\gamma_i, Z_{ci}) \quad (25)$$

and

$$\bar{p}_{0i} = \nu_0 H_0(\gamma_i, Z_{ci}). \quad (26)$$

Convergence tests are then carried out by evaluating the relative discrepancies $|\bar{p}_0 - \bar{p}_{0i}|/|\bar{p}_0|$ and $|p(N) - p(N)_i|/|p(N)|$. It was assumed that the procedure converges when the discrepancies are both less than 10^{-6} . If the convergence criteria are not respected, the procedure is continued at iteration $(i+1)$ from the following corrections:

$$\gamma_{i+1} = \gamma_i - h_\gamma[p(N)_i, \bar{p}_{0i}] + \gamma_0 \quad (27)$$

and

$$Z_{ci+1} = Z_{ci} - h_Z[p(N)_i, h_\gamma[p(N)_i, \bar{p}_{0i}]] + Z_{c0}. \quad (28)$$

The next subsection presents the numerical and experimental validations of the iterative resolution procedure.

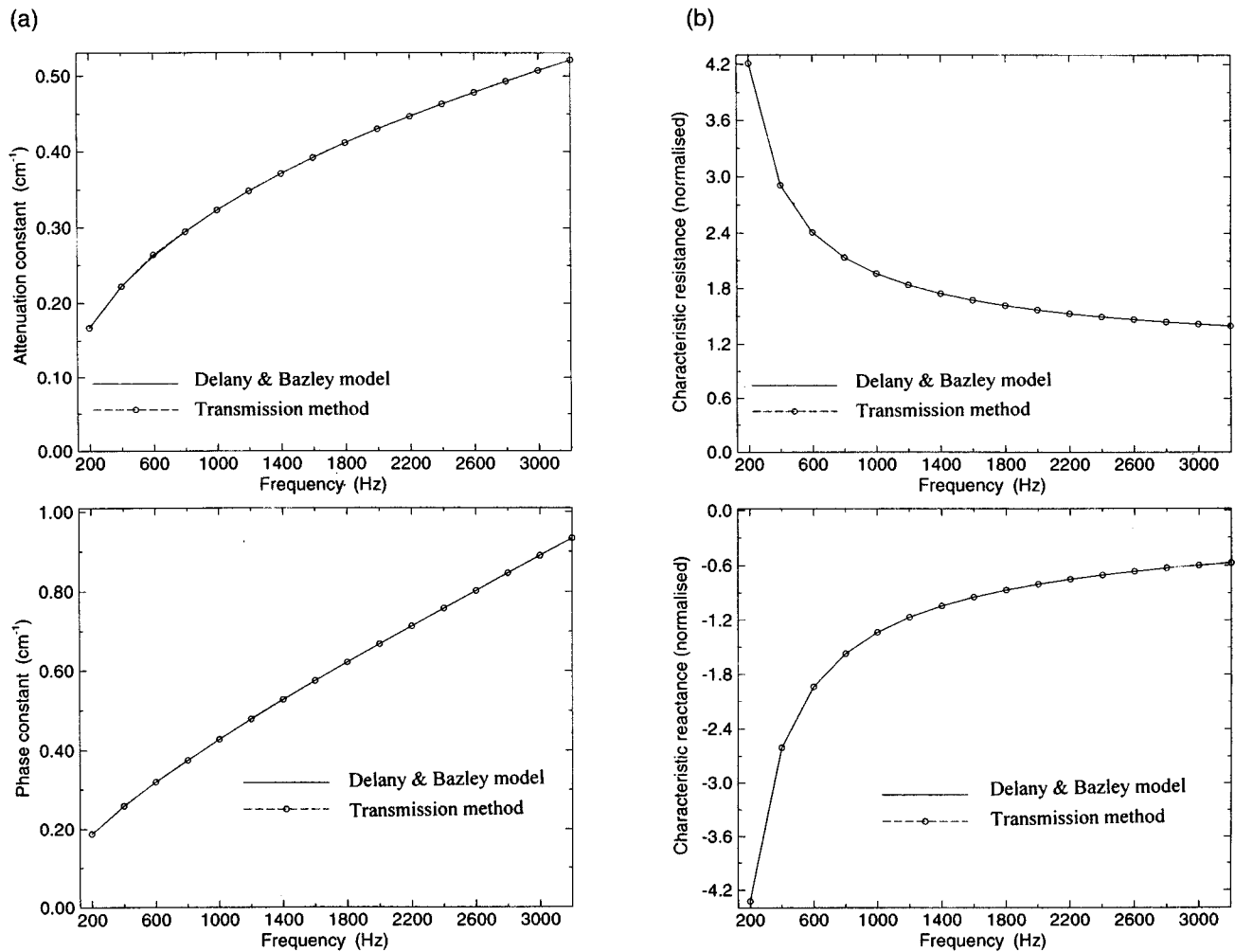


FIG. 12. Comparison between the Delany and Bazley model (direct approach) and the transmission method (inverse approach). Air flow resistance $\sigma = 50$ cgs rays/cm. (a) Propagation constant. (b) Normalized characteristic impedance.

B. Validations of the transmission method

1. Numerical simulations

Numerical simulations have been carried out considering a baffled circular piston with a 2.25-cm radius over which a 5-cm-thick porous absorbing material is resting. The acoustical characteristics γ and Z_c are simulated with the Delany and Bazley¹⁶ empirical model, allowing the characterization of a material as a function of wave frequency f and air flow resistance σ in the material:

$$\gamma = \frac{2\pi f}{c_0} \left(10.3 \left(\frac{f}{\sigma} \right)^{-0.59} + j \left(1 + 10.8 \left(\frac{f}{\sigma} \right)^{-0.70} \right) \right),$$

$$Z_c = \rho_0 c_0 \left(1 + 9.08 \left(\frac{f}{\sigma} \right)^{-0.75} - j 11.9 \left(\frac{f}{\sigma} \right)^{-0.73} \right).$$

In these two relations, ρ_0 and c_0 refer, respectively, to the density and speed of sound in air. Assuming that the piston vibrates with a uniform velocity equals to one, Eqs. (2) and (7) are then used to calculate $p(N)$ and \bar{p}_0 , respectively, the point N being taken on the piston axis at 10 cm from the piston surface. The calculated values are then introduced in the iterative procedure as if they were measured experimentally, and then estimations of γ and Z_c from the transmission

method are compared to the initial characteristics supplied by the Delany and Bazley model.

Figures 11 and 12 represent comparisons between the Delany and Bazley model (direct approach) and the transmission method (inverse approach), for materials whose air flow resistance is equal to 10 cgs rays/cm and 50 cgs rays/cm, respectively. The transmission method correctly predicts the characteristics given by the Delany and Bazley model, since the discrepancies between the two techniques are all less than 1%. The curves illustrating the results almost coincide.

More generally, the numerical simulations have revealed that the transmission method is potentially usable on a wide scale of porous materials, because comparisons with the Delany and Bazley model still show excellent air flow resistance larger than 50 cgs rays/cm. It must be emphasized that a solution is reached after only a few numbers of iterations (less than 20 iterations in most cases). The transmission method convergence is however slower at low frequencies. This is probably due to a longer wavelength compare to the distance between the measurement point N and the tube output. This lowers the sensitivity of the resolution procedure. For a frequency below 600 Hz, the transmission method will

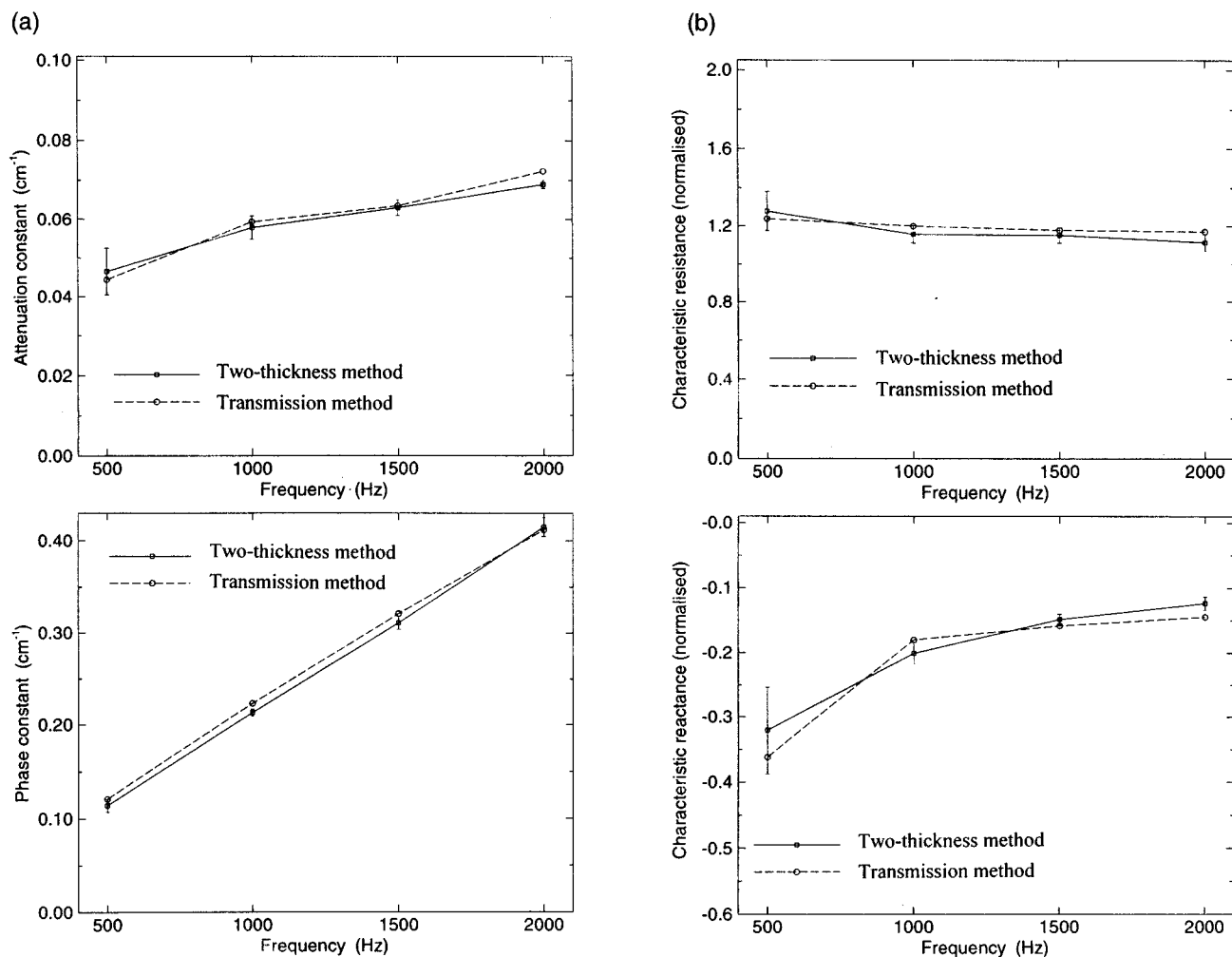


FIG. 13. Comparison between the two-thickness method and the transmission method for sample SIF 1. (a) Propagation constant. (b) Normalized characteristic impedance.

converge only if point N is more than 15 cm above the baffle. It thus appears that at low frequencies, the measurement point above the material has to be far enough from the baffle to ensure convergence of the iterative resolution procedure.

2. Experimental validation

Experimental validation of the transmission method is achieved by means of comparisons with the results obtained with the two-thickness method in an impedance tube.¹ The three samples SIF 1, SIF 2, and OC 705 described in Sec. II A were used for the experimental manipulations. Various experimental results in Sec. II B have thus been used for the purpose of introducing the measured values in the iterative procedure of the transmission method. For each material and for each frequency (500, 1000, 1500, and 2000 Hz), five cases were considered for the positioning of the pressure point above the material. This point was taken on the tube axis, at 8, 10, 16, 20, and 23 cm above the baffle. The average results obtained with various positions are then compared to the acoustical characteristics γ and Z_c determined by the two-thickness method in an impedance tube. It must be emphasized that at 500 Hz, only the results obtained with

positions at 16, 20, or 23 cm above the baffle were taken into account. In effect, as in the case of numerical simulations, the method has diverged at 500 Hz when the pressure point was located at less than 15 cm above the baffle.

Figures 13 and 14 illustrate the comparison between the transmission method and the two-thickness method, for samples SIF 1 and SIF 2, respectively. The results of both methods compare fairly well. Only the characteristic reactance shows discrepancy higher than 10%. Classical methods of acoustical characterization¹ show equivalent discrepancies. It can then be concluded that the transmission method works satisfactorily with samples SIF 1 and SIF 2.

Figure 15 shows, on the other hand, that the two methods give substantially different results with the sample OC 705, especially in the case of the characteristic reactance where discrepancies are fairly important. Since it has already been shown that the pressure field above the material is theoretically adequately predicted (cf. Sec. II B), the divergence between the two methods is probably due to a faulty theoretical prediction of the sound pressure \bar{p}_0 at the tube output. The theoretical modeling proposed in Sec. I assumes in effect that the porous medium is homogeneous. The experimental results of Sec. II B show that the theoretical model is

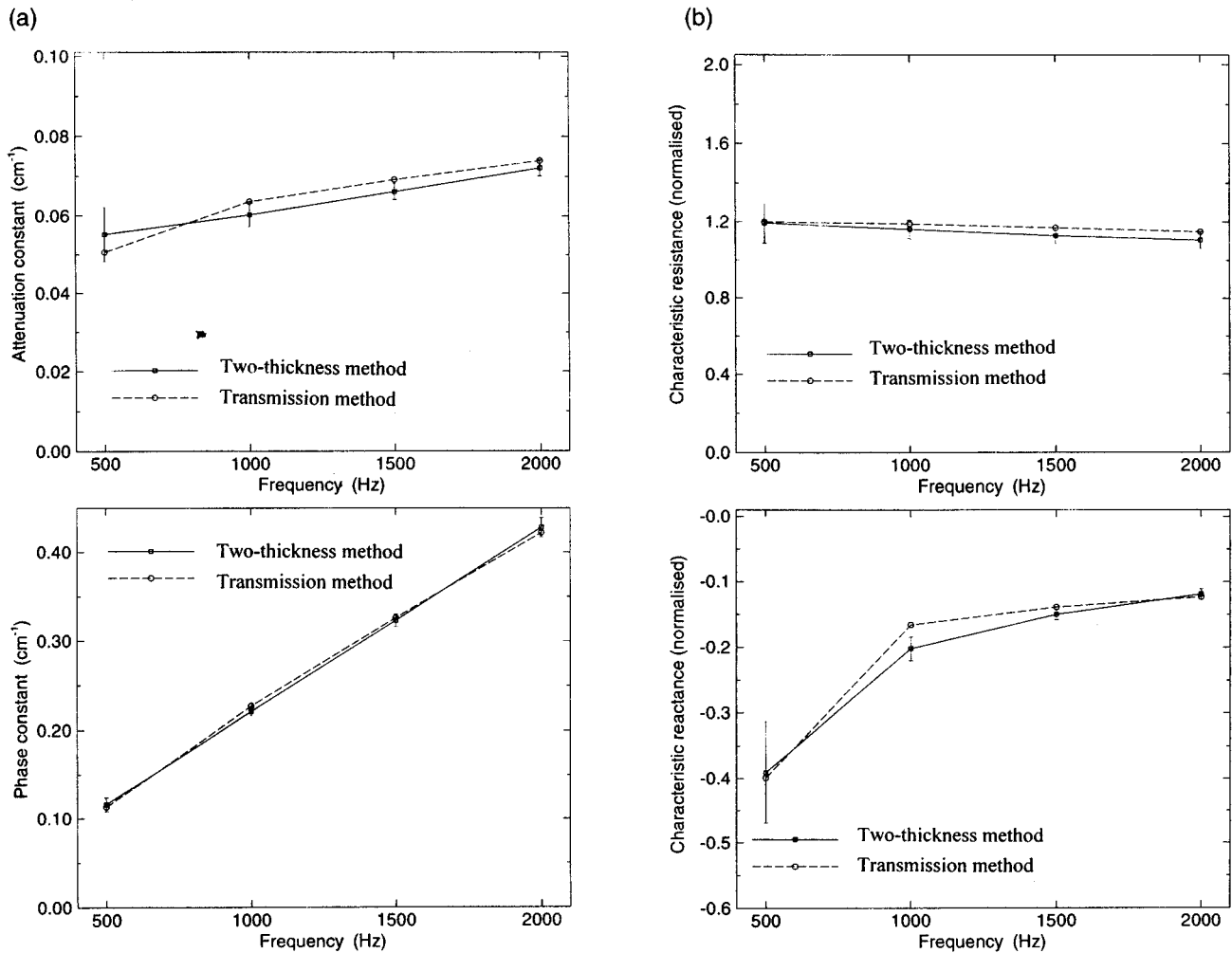


FIG. 14. Comparison between the two-thickness method and the transmission method for sample SIF 2. (a) Propagation constant. (b) Normalized characteristic impedance.

not very sensitive to heterogeneity, in the prediction of the acoustic field above the material. This may not still be the case at the tube output, when the incident wave meets the surface of a heterogeneous material.

IV. CONCLUDING REMARKS

The first part of this paper dealt with the experimental validation of the theoretical framework established in a previous paper⁸ to model the acoustic radiation of an open baffled tube through a thin absorbing porous material. Experimental manipulations made with three samples of material have in effect shown excellent agreement between theory and experience. This theoretical framework was exploited in the second part of the paper to develop a characterization technique of acoustic absorbing porous material, called the transmission method. It is based on an iterative procedure of numerical resolution and on measurements of the acoustic pressure on both faces of a sample of material through which a baffled open tube radiates. A measurement point is taken in the semi-infinite medium above the material. Two other pressure measurement must be carried out on two locations of the baffled tube to be able to experimentally estimate the radiating velocity of the baffled tube and the acoustic pres-

sure at the tube output. The numerical simulations and the experimental validation tests demonstrated that the transmission method works satisfactorily. Only in the case of a heterogeneous material that it was found that the method did not give acceptable results. This is probably due to some limitation in the theoretical framework which is normally designed to work on a homogeneous and isotropic medium.

The experimental technique used in this study to estimate the acoustic pressure \bar{p}_0 at a baffled tube output is based on the assumption that the acoustic pressure is uniform at the tube output. In reality, it is not exactly the case. It is likely that a more direct pressure measurement at the tube output would increase the efficiency of the transmission method.

Unlike the acoustical characterization methods in a Kundt tube (two-thickness method and two-cavity method¹), the transmission method is making use of wave transmission phenomena instead of reflection, and it is nondestructive because it does not necessitate specimen removal. In addition, the transmission method takes into account the low thickness of the material to be characterized, and the experimental setup to be utilized is easy to assemble. This method is thus potentially applicable to *in situ* situations, for example for

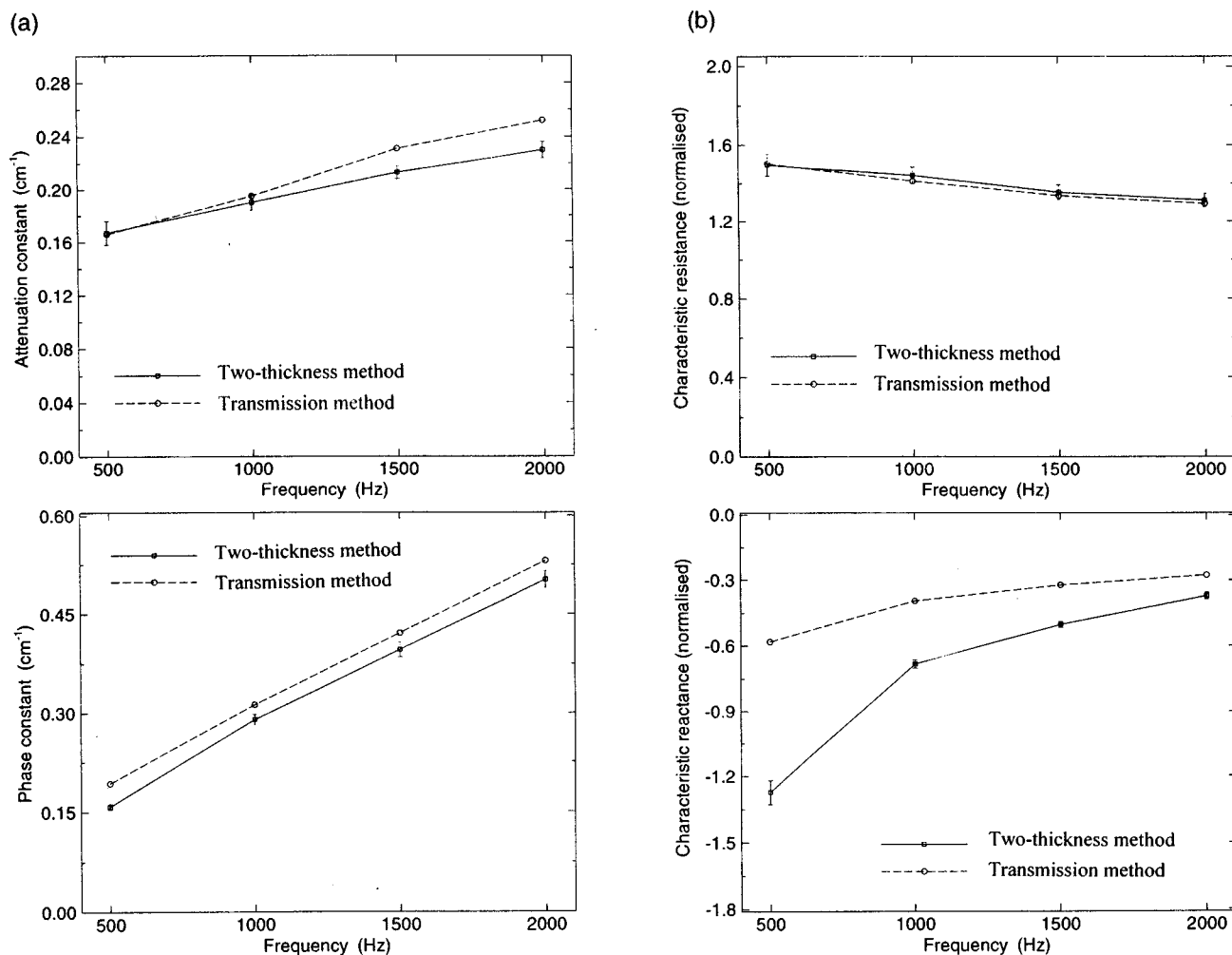


FIG. 15. Comparison between the two-thickness method and the transmission method for sample OC 705. (a) Propagation constant. (b) Normalized characteristic impedance.

continuous real time monitoring of materials on a production line. It must also be noted that the transmission method requires three acoustic measurements, whereas the Kundt tube methods necessitate four measurements (two measurements for each thickness or each cavity). The experimental manipulations involved in the transmission method are probably faster than in the Kundt tube methods. However, the numerical processing required by the transmission method may be significant depending on the frequency and the power of the computer available. It is thus difficult to clearly establish the speed of this method as compared with in tube Kundt methods.

In all cases, the transmission method introduces an interesting new avenue for acoustical characterization of absorbing porous materials. A phase of experimentation with a great variety of materials will eventually have to be carried out in order to test the method on a wider scale. A parametric study based on frequency, thickness of material, and radius of the baffled tube should also be considered to better establish the limitations of the new method. Modifications will also have to be conceived to make the theoretical framework applicable to the processing of heterogeneous and anisotropic materials. Subsequently, this method could be used to

establish a quality control method based on acoustic measurements for the physical parameters of porous absorbing materials.

ACKNOWLEDGMENT

This work was supported by the Natural Sciences and Engineering Research Council of Canada (NSERC).

- ¹C. D. Smith and T. L. Parrott, "Comparison of three methods for measuring acoustic properties of bulk materials," *J. Acoust. Soc. Am.* **74**, 1577–1582 (1983).
- ²ASTM C 384-90, "Standard Test Method for Impedance and Absorption of Acoustical Materials by the Impedance Tube Method," revised in 1990.
- ³J.-F. Allard and B. Sieben, "Measurement of acoustic impedance in a free field with two microphones and a spectrum analyser," *J. Acoust. Soc. Am.* **77**, 1617–1618 (1985).
- ⁴J.-F. Allard and Y. Champoux, "In situ two-microphone technique for the measurement of the acoustic surface impedance of materials," *Noise Control Eng. J.* **32**, 15–23 (1989).
- ⁵A. J. Cramon and C. G. Don, "Reflection of impulses as a method of determining acoustic impedance," *J. Acoust. Soc. Am.* **75**, 382–389 (1984).
- ⁶T. Legouis and J. Nicolas, "Phase gradient method of measuring the acoustic impedance of materials," *J. Acoust. Soc. Am.* **81**, 44–50 (1987).
- ⁷Y. Champoux and M.-J. Ross, "Measurement of thermal resistivity of

- insulating material using an acoustical technique," *Noise Control Eng. J.* **40**, 151–158 (1993).
- ⁸C. K. Amédin, A. Berry, Y. Champoux, and J.-F. Allard, "Sound field of a baffled piston source covered by a porous medium layer," *J. Acoust. Soc. Am.* **98**, 1757–1766 (1995).
- ⁹C. Zwikker and C. W. Kosten, *Sound Absorbing Materials* (Elsevier, Amsterdam, 1949), Chap. 1.
- ¹⁰Y. Champoux and M. R. Stinson, "On acoustical models for sound propagation in rigid frame porous materials and the influence of shape factors," *J. Acoust. Soc. Am.* **92**, 1120–1131 (1992).
- ¹¹P. M. Morse and H. Feshbach, *Methods of Theoretical Physics* (McGraw-Hill, New York, 1953), Part II, p. 1322.
- ¹²P. M. Morse and K. U. Ingard, *Theoretical Acoustics* (McGraw-Hill, New York, 1968), Chap. 7.
- ¹³L. E. Kinsler, A. R. Frey, A. B. Coppens, and J. V. Sanders, *Fundamentals of Acoustics* (Wiley, New York, 1982), 3rd ed., Chap. 8.
- ¹⁴F. Fahy, *Sound and Structural Vibration* (Academic, Orlando, 1987), Chap. 3.
- ¹⁵C. Lesueur, *Rayonnement Acoustique des Structures* (Eyrolles, Paris, 1988), Chap. 3.
- ¹⁶M. E. Delany and E. N. Bazley, "Acoustical properties of fibrous absorbent materials," *Appl. Acoust.* **3**, 105–116 (1970).

Dynamic compressibility of air in porous structures at audible frequencies

Denis Lafarge, Pavel Lemarinier, and Jean F. Allard

Laboratoire d'Acoustique associé au CNRS, URA 1101, Faculté des Sciences du Mans, Avenue Olivier Messiaen, BP 535, 72017 Le Mans Cedex, France

Viggo Tarnow

Department of Applied Engineering Design and Production, DTU, Akademivej Bygning 358, DK 2800 Lyngby, Denmark

(Received 24 February 1996; revised 9 June 1997; accepted 16 June 1997)

Measurements of dynamic compressibility of air-filled porous sound-absorbing materials are compared with predictions involving two parameters, the static thermal permeability k'_0 and the thermal characteristic dimension Λ' . Emphasis on the notion of dynamic and static thermal permeability—the latter being a geometrical parameter equal to the inverse trapping constant of the solid frame—is apparently new. The static thermal permeability plays, in the description of the thermal exchanges between frame and saturating fluid, a role similar to the viscous permeability in the description of the viscous forces. Using both parameters, a simple model is constructed for the dynamic thermal permeability $k'(\omega)$, which is completely analogous to the Johnson *et al.* [J. Fluid Mech. **176**, 379 (1987)] model of dynamic viscous permeability $k(\omega)$. The resultant modeling of dynamic compressibility provides predictions which are closer to the experimental results than the previously used simpler model where the compressibility is the same as in identical circular cross-sectional shaped pores, or distributions of slits, related to a given Λ' . © 1997 Acoustical Society of America. [S0001-4966(97)00310-X]

PACS numbers: 43.20.Gp, 43.20.Jr, 43.55.Ev [JEG]

INTRODUCTION

In air-filled sound-absorbing media, the frequency dependence of the compressibility, which varies from the isothermal to the adiabatic value when frequency increases, plays an important role when a precise prediction of sound absorption versus frequency is needed. Beranek¹ has suggested (1942) that at low frequencies the cycle of condensation and rarefaction of the enclosed air is isothermal due to the thermal exchanges between air and frame. The frequency dependence of compressibility was calculated by Zwicker and Kosten² for pores in the form of circular cross-sectional shaped cylinders and slits. Other shapes of pores were studied later.³ It may be noticed that for cylindrical pores the compressibility depends on the shape of the cross section. For a given hydraulic radius \bar{r} (\bar{r} is two times the ratio of the area to the perimeter of the cross section), this dependence can be neglected in a first approximation. In porous media with other geometries of the frame, the frequency dependence of compressibility was the same (Zwicker and Kosten,² Attenborough,⁴ Allard *et al.*⁵) as in circular cross-sectional shaped pores. The radius is related to the flow resistivity with an adjustable factor which takes into account the specificity of the geometry for the different porous frames. The adequation of such models is limited by the fact that cylindrical pores generally do not exist in porous media. A qualitative description of the effect of pore constrictions was given by Zwicker and Kosten.² A precise description of compressibility in a pore made up of an alternating sequence of circular cross-sectional shaped cylinders was performed by Champoux and Stinson.⁶ An aim to relate the frequency

dependence of compressibility to nonacoustical measurements was performed later by Attenborough.⁷ In this paper the porous material was modeled as a log-normal size distribution of tortuous slits widths. Pore size distribution can be determined nonacoustically for some materials. A parameter which characterizes the high-frequency behavior of compressibility, i.e., the thermal characteristic dimension, was identified by Champoux and Allard.⁸ This parameter Λ' is twice the ratio between the pore volume V_p and surface S_p and is sometimes referred to as the Kozeny radius: $\Lambda' = 2V_p/S_p$. It generalizes the notion of hydraulic radius for the case of arbitrary geometries of the frame and reduces to it for the case of cylindrical pores. This definition was inspired by the definition of the characteristic viscous dimension (Johnson *et al.*^{9,10}) Λ , which characterizes the viscous interaction between air and frame at high frequencies. At sufficiently high frequencies the thermal exchanges between air and frame mainly occur in a small layer close to the frame, where temperature depends on the local distance to the frame (as if the frame-air interface was plane). A normalized dynamic compressibility $\beta(\omega)$ will be used in the present work, defined by

$$\frac{\beta(\omega)}{K_a} \langle p \rangle = \frac{1}{\rho_0} \langle \rho \rangle, \quad (1)$$

where K_a is the adiabatic bulk modulus of air, ρ_0 the air density at rest, and $\langle p \rangle$ and $\langle \rho \rangle$ the macroscopic acoustic pressure and density, respectively. (In the present paper, the symbol $\langle \rangle$ denotes an intrinsic air-phase average.) When frequency increases, $\beta(\omega)$ tends to

TABLE I. Viscous and thermal parameters for both porous media.

	Flow resistivity $\sigma \text{ Nm}^{-4} \text{ s}$	Viscous permeability $k_0 \text{ m}^2$	Characteristic thermal dimension $\Lambda' \text{ m}$	M'	Thermal permeability $k'_0 \text{ m}^2$
Foam	6000	0.3×10^{-8}	6.1×10^{-4}	0.3	1.3×10^{-8}
Glass wool	2300	0.8×10^{-8}	2.1×10^{-3}	0.03	1.7×10^{-8}

$$\beta(\omega) = 1 - (\gamma - 1)(1 + i) \frac{\delta'}{\Lambda'} \quad (2)$$

In this equation, $\delta' = (2\nu'/\omega)^{1/2}$ is the thermal skin depth (with $\nu' = \nu/\text{Pr}$, ν being the kinematic viscosity and Pr the Prandtl number), and γ is the specific heat ratio. The imaginary part in $\beta(\omega)$ produces absorption, whereas the real part is related to the speed of sound. The characteristic dimensions Λ' and Λ can be evaluated from the attenuation or the wave speed of ultrasonic pulses successively measured with different gases saturating the porous frame.¹¹ The parameter Λ' can also be obtained with the BET method¹² of measuring specific surfaces (pore surface S_p for a unit mass of frame). The frame, at liquid nitrogen temperature, adsorbs a multimolecular layer of the surrounding gas (krypton can be chosen to increase the sensitivity for the case of glass wools and reticulated foams, because S_p is much smaller than for the case of powders and materials generally measured). A measurement of the adsorbed volume of krypton provides an evaluation of S_p , and the specific volume V_p is deduced from the two densities of the frame and the solid, or from direct measurement of the porosity and frame density. Previous measurements of Λ' obtained from both methods (BET and ultrasonic measurements) are in a good agreement.¹¹

Acoustic measurements are performed on layers set on a rigid impervious baking. The frame of the porous media is always supposed to be motionless. The flow resistivity of the studied media is small (see Table I). For these materials, at low frequencies, where the transition between the isothermal and adiabatic compressibility occurs, it may be shown in the context of the Biot model¹³ that the frame tends to become motionless due to the weakness of the viscous forces. A simple model for the frequency dependence of compressibility consists in replacing the porous structure by an equivalent one with circular cross-sectional shaped pores having a radius equal to Λ' . The asymptotic behavior of the predicted compressibility at high frequencies is correct. When frequency decreases, the frequency dependence of compressibility is difficult to predict, due to the increasing range of the thermal interaction between frame and air. The same problem arises for the viscous interaction at low frequencies. One approach consists in using a low-frequency parameter, the viscous static permeability related to the flow resistivity σ by

$$k_0 = \eta/\sigma, \quad (3)$$

where η is the viscosity of air. The flow resistivity and the permeability are easily measurable, and when frequency tends to zero provide the essential information concerning the viscous interaction. With the parameters Λ , k_0 , and formation factor α_∞/ϕ , Johnson *et al.*¹⁰ have suggested a gen-

eral expression for the dynamic viscous permeability $k(\omega)$ defined by

$$\phi \langle \mathbf{v} \rangle = - \frac{k(\omega)}{\eta} \nabla \langle p \rangle, \quad (4)$$

where ϕ is the porosity (1-volumen concentration of frame material), and $\langle \mathbf{v} \rangle$ is the macroscopic velocity field. Isotropy of the porous solid is assumed for simplicity. For anisotropic structures, $k(\omega)$ is a symmetric tensor of rank two. Numerical simulations and experiments have shown that the modeling by Johnson *et al.* is very robust.

In the present work, a thermal analogue of the dynamic viscous permeability is defined by setting at any frequency

$$\phi \langle \tau \rangle = \frac{k'(\omega)}{\kappa} \frac{\partial}{\partial t} \langle p \rangle, \quad (5)$$

where $\langle \tau \rangle$ is the macroscopic excess temperature in air, and κ is the coefficient of thermal conduction. The quantity $k'(\omega)$ has the same dimensions as $k(\omega)$ (length squared). When the frame has a sufficient thermal capacity for the compressibility $\beta(\omega)$ to reach the isothermal value γ at low frequencies, the excess temperature τ can be considered to vanish at the pore walls (this replaces the no-slip condition $\mathbf{v} = \mathbf{0}$ for viscous flow) and a static “thermal permeability” k'_0 exists. This parameter provides the missing low-frequency thermal information and is shown to be equal to the inverse trapping constant of the porous frame (the trapping constant is defined for instance in Ref. 14 and in Appendix B). We suggest that the function $k'(\omega)$ can be modeled in a manner similar to the permeability function $k(\omega)$ with the parameters Λ' , k'_0 , and porosity ϕ . A general connection between $k'(\omega)$ and $\beta(\omega)$ is also established, leading to a simple expression for the compressibility function $\beta(\omega)$. Developments and justifications are reported in the different Appendices A, B, and C.

Precise and fast evaluations of compressibility are now available with a new method developed by Tarnow,¹⁵ based on measurement of the frequency and the quality factor of the quarter-wavelength resonance in a closed tube where a layer of porous material is set. Predictions with the new model are compared to measurements performed with the method developed by Tarnow.

It is to be noted that the homogenization of the visco-thermal linearized acoustic equations in a gas-filled porous structure has been previously considered by Sanchez-Palencia and Levy.¹⁶ These authors stated the microscopic boundary value problem which enables calculating the macroscopic coefficient $\langle \tau \rangle / \langle p \rangle$ [$-i\omega k'(\omega)/\phi\kappa$ in our notations] from the microstructures. However, no attempt was

made to extract from this definition a simple modeling of the frequency dependence of compressibility. A previous attempt to generalize Johnson *et al.* model of dynamic permeability $k(\omega)$ to the compressibility function $\beta(\omega)$ was made by Champoux and Allard.⁸ However, the thermal permeability function was not considered and the role played by the inverse trapping constant k'_0 was not apparent. The concept of thermal permeability and the resulting modeling of $\beta(\omega)$ were suggested by one of the authors in a thesis dissertation.¹⁷

I. DYNAMIC PERMEABILITY FUNCTIONS

A. Dynamic viscous permeability

In a porous medium, a static flow which corresponds to an averaged fluid velocity $\langle \mathbf{v} \rangle$ is related to the gradient of the averaged pressure $\nabla \langle p \rangle$ by the Darcy law:

$$\phi \langle \mathbf{v} \rangle = -\frac{k_0}{\eta} \nabla \langle p \rangle. \quad (6)$$

In the frequency domain, and for disturbances characterized by a long wavelength ($\lambda \gg l$, where l is typical of the pore or grain size) this static law can be replaced by

$$\phi \langle \mathbf{v} \rangle = -\frac{k(\omega)}{\eta} \nabla \langle p \rangle, \quad (7)$$

where $k(\omega)$ is the dynamic permeability. It has been shown by Johnson *et al.*¹⁰ (see also Avellaneda and Torquato,¹⁴ Appendix D) that $k(\omega)$ could be replaced at high frequencies by the following asymptotic expression, analogous to (2):

$$k(\omega) = \frac{\nu \phi}{-i\omega \alpha_\infty} \left[1 - (1+i) \frac{\delta}{\Lambda} \right], \quad (8)$$

where α_∞ is the tortuosity, Λ is the viscous characteristic dimension, and $\delta = (2\nu/\omega)^{1/2}$ is the viscous skin depth. Assuming that the three parameters, $F = \alpha_\infty/\phi$ (formation factor), k_0 , and Λ , provide a sufficient information on the geometry, an approximation for $k(\omega)$ between the high- and the low-frequency range has been worked out by Johnson *et al.*¹⁰ The permeability $k(\omega)$ is the frequency response of an invariant, causal, linear system, and the poles, the zeros, and the branch points of $k(\omega)$ are located on the imaginary negative axis in the complex ω plane. Analytical functions having these properties are expected to provide fairly good approximations for $k(\omega)$ in the intermediate real frequency range, if they tend to the limits given by Eqs. (6) and (8) for small and large ω . The following expression, which satisfies all the required properties, was suggested as the simplest possible ansatz:

$$k(\omega) = k_0 / [(1 - (M/2)i\tilde{\omega})^{1/2} - i\tilde{\omega}], \quad (9)$$

where M is the following dimensionless shape factor:

$$M = \frac{8\alpha_\infty k_0}{\phi \Lambda^2}, \quad (10)$$

and the dimensionless frequency $\tilde{\omega}$ is defined as

$$\tilde{\omega} = \frac{\omega}{\nu} \frac{k_0 \alpha_\infty}{\phi}. \quad (11)$$

B. Dynamic thermal permeability

In a porous material having a rigid frame filled by air, a macroscopic description of the thermal exchanges between frame and air is needed to predict the compressibility of the equivalent fluid. This description will be obtained with the help of the concept of dynamical thermal permeability.

Two linearized equations which link pressure, density, and temperature variations of air considered as an ideal gas, the equation of thermal conduction and the equation of state, may be written (see for example Ref. 3)

$$\kappa \nabla^2 \tau = \frac{T_0}{P_0} \left(\rho_0 C_v \frac{\partial p}{\partial t} - P_0 C_p \frac{\partial \rho}{\partial t} \right), \quad (12)$$

$$\frac{\partial p}{\partial t} = \frac{P_0}{\rho_0 T_0} \left(\rho_0 \frac{\partial \tau}{\partial t} + T_0 \frac{\partial \rho}{\partial t} \right). \quad (13)$$

In these equations, T_0 and P_0 are the static temperature and pressure, and C_v and C_p are the specific heats (per unit mass) at constant volume and pressure, respectively. The acoustic density ρ is related to the velocity \mathbf{v} by

$$\frac{\partial \rho}{\partial t} = -\rho_0 \nabla \cdot \mathbf{v}. \quad (14)$$

Eliminating $\partial \rho / \partial t$ between Eqs. (12) and (13), and making use of the relation

$$\frac{\rho_0 T_0}{P_0} (C_p - C_v) = 1, \quad (15)$$

which is valid for ideal gas, gives, in the volume V of air,

$$\rho_0 C_p \frac{\partial \tau}{\partial t} = \kappa \nabla^2 \tau + \frac{\partial p}{\partial t} \quad (\mathbf{r} \in V). \quad (16)$$

The thermal capacity and conductivity of the frame, for usual porous media, is generally very large compared to air. In a first approximation the frame can be considered as a thermostat, and the acoustical temperature τ at the contact surface ∂V with the frame can be set equal to zero:

$$\tau = 0 \quad (\mathbf{r} \in \partial V). \quad (17)$$

Equation (16) and the boundary condition (17) describe the thermal diffusion in the fluid. They constitute the thermal counterpart of the linearized equations $\rho_0 (\partial \mathbf{v} / \partial t) = \eta \nabla^2 \mathbf{v} - \nabla p$ ($\mathbf{r} \in V$) and $\mathbf{v} = \mathbf{0}$ ($\mathbf{r} \in \partial V$) for inertial/viscous effects. [The term $(\eta + \zeta/3) \nabla (\nabla \cdot \mathbf{v})$, where ζ is the second viscosity, is not written in the above Navier–Stokes equation because incompressibility of air may be assumed at the pore scale, see Appendix A, Eq. (A5c).] This suggests the definition of a “thermal permeability” $k'(\omega)$ by means of Eq. (5), in analogy with Eq. (4). The use of the denomination “thermal permeability” is not completely appropriate, because a permeability (viscous or magnetic) is related to vectors, and the thermal permeability links two scalar quantities. Nevertheless, the designation is used to emphasize the formal similarity with the viscous permeability. In Appendix A, the first-principles definition of the frequency-dependent viscous and thermal permeabilities and the recipe for their calculation are derived through the generalization of the homogenization

procedure employed by Zhou and Sheng¹⁸ in the purely viscous case.

When $\omega \rightarrow 0$ and the frame is considered as a thermostat, the excess temperature in air $\langle \tau \rangle$ is proportional to the pressure derivative $\partial \langle p \rangle / \partial t$ and a thermal Darcy's law is obtained

$$\phi \langle \tau \rangle = \frac{k'_0}{\kappa} \frac{\partial}{\partial t} \langle p \rangle. \quad (18)$$

The real constant $k'_0 = \lim_{\omega \rightarrow 0} k'(\omega)$ plays the role of a static thermal permeability. Under some conditions examined in Appendices A and B, it is related to the trapping constant¹⁴ Γ of the frame by

$$k'_0 = 1/\Gamma. \quad (19)$$

(The definition of Γ is recalled in Appendix B.)

The trapping constant can be predicted from numerical simulations for simple geometries (Schwartz *et al.*¹⁹). Experimentally, nuclear magnetic resonance (NMR), which is used to characterize the geometry of porous frames (Straley *et al.*²⁰), could provide experimental evaluations of Γ . The excitation corresponds to the induced parallelism of nuclear spins in water. Two physical phenomena, a large de-excitation in the saturating fluid, and a noninstantaneous relaxation on contact with the frame, have prevented until now an evaluation of Γ by NMR for plastic foams and glass wools.

When ω is large, the harmonic compressions/dilatations become adiabatic and $\rho_0 C_p \langle \tau \rangle / \langle p \rangle \rightarrow 1$. More precisely, taking into account the presence of a thin thermal boundary layer at the pore walls yields⁸

$$\langle \tau \rangle = \frac{\langle p \rangle}{\rho_0 C_p} \left[1 - (1+i) \frac{\delta'}{\Lambda'} \right], \quad (20)$$

where it has been assumed that the pressure is a local constant—a condition justified in Appendix A—and that the temperature profile in the boundary layer is the same in the limit of high frequencies as that near a flat surface. This excludes more complicated and “fractal” pore surfaces. The asymptotic expression for $k'(\omega)$ that can be deduced from (5) and (20) is

$$k'(\omega) = \frac{\nu' \phi}{-i\omega} \left[1 - (1+i) \frac{\delta'}{\Lambda'} \right]. \quad (21)$$

The exact frequency dependence of $k'(\omega)$ in the whole range of frequencies needs an exact description of the geometry of the frame. However, as shown in Appendix C, the function $k'(\omega)$ verifies the same general analytical properties as $k(\omega)$. An approximate expression depending on a small number of parameters can be obtained by following the method developed by Johnson *et al.* described in Sec. I A. The following three parameters expression may be suggested for $k'(\omega)$:¹⁷

$$k'(\omega) = k'_0 / [(1 - (M'/2) i \bar{\omega}')^{1/2} - i \bar{\omega}'], \quad (22)$$

which involves the following (dimensionless) shape factor M' :

$$M' = 8k'_0 / \phi \Lambda'^2, \quad (23)$$

and the reduced frequency

$$\bar{\omega}' = \frac{\omega}{\nu'} \frac{k'_0}{\phi}. \quad (24)$$

This modeling depends on three independent geometrical parameters, for instance k'_0 , M' , and $F' = 1/\phi$. These parameters play the same role as parameters k_0 , M , and F in the previous description of the viscous permeability.

II. DYNAMIC COMPRESSIBILITY

To describe sound propagation at the macroscopic level in rigid air-saturated material, the knowledge of two response factors will be required. One is the dynamic tortuosity

$$\rho_0 \alpha(\omega) \frac{\partial \langle \mathbf{v} \rangle}{\partial t} = -\nabla \langle p \rangle, \quad (25)$$

obviously related to the dynamic viscous permeability [$\alpha(\omega) = -\nu \phi / i \omega k(\omega)$]. A second convenient response factor is the normalized dynamic compressibility $\beta(\omega)$, defined by Eq. (1), which can be rewritten:

$$\frac{\beta(\omega)}{K_a} \frac{\partial \langle p \rangle}{\partial t} = -\nabla \cdot \langle \mathbf{v} \rangle. \quad (26)$$

[This is obtained by using Eq. (14) and the identity $\langle \nabla \cdot \mathbf{v} \rangle = \nabla \cdot \langle \mathbf{v} \rangle$, which is valid for materials having an uniform porosity; see for example Pride *et al.*²¹ and Marle.²²] With this definition $\beta(\omega) \rightarrow 1$ when $\omega \rightarrow \infty$. Looking for plane wave solutions varying as $\exp[i(qx - \omega t)]$, Eqs. (25) and (26) yield the propagation constant and characteristic impedance of the medium

$$q = \omega \left(\alpha(\omega) \beta(\omega) \frac{\rho_0}{K_a} \right)^{1/2}, \quad (27)$$

$$Z = \left(\frac{\alpha(\omega)}{\beta(\omega)} \rho_0 K_a \right)^{1/2}. \quad (28)$$

Thus α and β provide all pertinent information on the propagation in the medium.

The scaled compressibility $\beta(\omega)$ is directly related to the thermal permeability $k'(\omega)$ by means of the relation

$$\beta(\omega) = \gamma + (\gamma - 1) \frac{i \omega k'(\omega)}{\nu' \phi}. \quad (29)$$

A proof is given in Appendix A. Using Eq. (22), the following simple model for frequency dependence of dynamic scaled compressibility has thus been obtained:

$$\beta(\omega) = \gamma - (\gamma - 1) \left[1 + \frac{1}{-i \bar{\omega}'} \left(1 - \frac{M'}{2} i \bar{\omega}' \right) \right]^{1/2} - 1, \quad (30)$$

where the shape factor M' and reduced frequency $\bar{\omega}'$ are expressed by Eqs. (23) and (24) in terms of the parameters k'_0 , Λ' , and ϕ .

It may be noticed that a similar expression for $\beta(\omega)$ was proposed by Champoux and Allard [Eq. (19) of Ref. 8]. It is, however, written in such a way that a mixing occurs between the inertial/viscous and thermal parameters, and it coincides

with the present one only if the adjustable parameter σ' is set equal to $\eta\alpha_\infty/k'_0$. The present derivation gives a physical meaning to σ' in Ref. 8 and shows that Eq. (19), which was extrapolated from an expression valid for cylindrical pores, is a reasonable general hypothesis for the frequency dependence of compressibility.

III. VISCOUS AND THERMAL PERMEABILITY IN CYLINDRICAL PORES AND IN SYSTEMS OF SLITS WITH A LOG-NORMAL DISTRIBUTION FOR THE SEMI-THICKNESS

A. Cylindrical pores

In a cylindrical pore having a cross section with dimensions much smaller than the wavelength, velocity \mathbf{v} is perpendicular to the cross section, and the pressure is uniform over a cross section. Thus the viscous and thermal problem happen to have exactly the same mathematical form. This identity was noted before^{3,23} and it leads to the following obvious relations, valid for cylindrical pores:

$$k'(\omega) = k(\text{Pr } \omega), \quad (31)$$

$$k_0 = k'_0, \quad (32)$$

$$M = M', \quad (33)$$

$$\Lambda = \Lambda', \quad (34)$$

$$\alpha_\infty = 1. \quad (35)$$

A test for the model consists in predicting the compressibility with Eq. (30), and comparing with exact calculations, for circular, triangular, or rectangular cross-sectional shaped cylindrical pores. The characteristic dimensions are equal to two times the ratio of the area to the perimeter of the cross section. The viscous permeability can be calculated for the different shapes.²⁴ Results of the exact calculations, and calculations performed with Eq. (30), are close to each other. It may be noticed that for cylindrical pores the thermal static permeability can be evaluated by measuring the flow resistivity σ

$$\sigma = \eta/k_0, \quad (36)$$

$$k'_0 = k_0 = \eta/\sigma. \quad (37)$$

B. Systems of slits with a log-normal distribution for the semi-thickness

The study, restricted to the viscous interaction, of a system of parallel slits with a log-normal distribution for the semi-thickness b , was initially performed by Yamamoto and Turgut.²⁵ This study was adapted by Attenborough⁷ in order to predict the dynamic tortuosity and compressibility in porous media. A brief description of the model, with further developments to predict the dependence of the characteristic dimension Λ' and the transition frequency for the compressibility on the parameters of the model, are given in what follows. These developments also present a nontrivial illustration of the model described in the previous sections. A

distribution $e(b)$ is used, defined from the variable w , $-\infty < w < \infty$, related to b by $b = \exp[-w \ln 2]$, and the distribution f for w , given by

$$f(w) = \frac{1}{v\sqrt{2\pi}} \exp[-(w - w_a)^2/2v^2]. \quad (38)$$

The precise meaning of $e(b)$ can be deduced from Eq. (10) of Ref. 25, which gives the viscous permeability k_0 when $\alpha_\infty = 1$

$$k_0 = \frac{\phi}{3} \int_0^\infty b^2 e(b) db. \quad (39)$$

Let $s(b)db$ be the total area of slits of semi-thickness between b and $b + db$ per unit area of porous material. A direct consequence of the definition of $s(b)$ is

$$\int_0^\infty s(b) db = \phi. \quad (40)$$

The permeability can be written

$$k_0 = \frac{1}{3} \int_0^\infty b^2 s(b) db, \quad (41)$$

and $s(b)$ is related to $e(b)$ by

$$s(b) = \phi e(b). \quad (42)$$

For a unit volume of porous material, the volume of air is equal to ϕ , and the area related to the surface of the pores in contact with air inside the volume, is twice the number N of the pores, which is given by

$$N = \int_0^\infty \frac{s(b)}{2b} db. \quad (43)$$

The characteristic dimensions are given by

$$\Lambda = \Lambda' = \left[\int_0^\infty \frac{e(b)}{b} db \right]^{-1}. \quad (44)$$

They can also be obtained from Eqs. (20) and (37) of Ref. 7, which can be used to evaluate Λ in Eq. (8) of the present paper. Equations (35) and (41) of Ref. 7 can also be used, but the right-hand sides of both equations must be multiplied by α_∞ . The different methods give the same result

$$\Lambda = \Lambda' = 2b_a \exp[-(v \ln 2)^2/2]. \quad (45)$$

When the system of parallel slits is canted at an angle ϑ , the two characteristic lengths are given by the above expressions, and k_0 and k'_0 are given by

$$k'_0 = \alpha_\infty k_0 = \phi(b_a^2/3) \exp[2(v \ln 2)^2], \quad (46)$$

where b_a is related to w_a by $b_a = \exp[-w_a \ln 2]$. The characteristic dimensions and the thermal permeability depend on b_a and v , and not on tortuosity $\alpha_\infty = 1/\cos^2 \vartheta$. When $v = 0$, these expressions give the same results as for a simple slit of semi-thickness b_a . The dynamic normalized compressibility $\beta(\omega)$ can be evaluated from the dynamic tortuosity. A simpler and equivalent evaluation can be obtained more directly by using

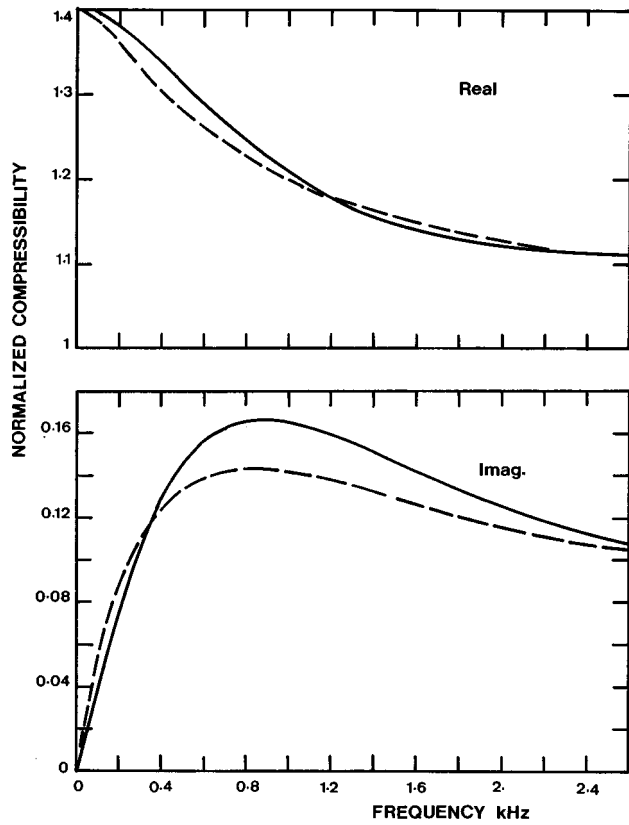


FIG. 1. Predicted normalized compressibility $\beta(\omega)$ for a slit and a system of slits, related to $\Lambda' = 0.2$ mm; slit —; system of slits (with $\nu = 0.5$) ----.

$$\beta(\omega) = \int_0^\infty \beta_b(\omega) e(b) db, \quad (47)$$

where $\beta_b(\omega)$ is the compressibility in a slit having a semi-width b , given by

$$\beta_b(\omega) = 1 + (\gamma - 1) \tanh \left[b \left(\frac{-i\omega}{\nu'} \right)^{1/2} \right] \bigg/ b \left(\frac{-i\omega}{\nu'} \right)^{1/2}. \quad (48)$$

The asymptotic expression of $\beta(\omega)$ when $\omega \rightarrow \infty$, compared to Eq. (2), provides the same expression for Λ' as Eq. (45). When $\omega \rightarrow 0$, Eq. (29) can be rewritten

$$\beta(\omega) = \gamma + (\gamma - 1) \frac{i\omega k'_0}{\nu' \phi}, \quad (49)$$

and the asymptotic expression of $\beta(\omega)$ given by Eqs. (47) and (48) provides the same expression for $k'_0(0)$ as Eq. (46). The compressibility is represented in Fig. 1 for $\Lambda' = 0.2$ mm, and $\nu = 0$ and 0.5. In the first case the compressibility is the same as in a slit of semi-thickness $b = 0.1$ mm. In the second case, b_a and k'_0 are given by Eqs. (45) and (46). The high-frequency representation of $\beta(\omega)$ [Eq. (2)] is already a good approximation at 2500 Hz, for both cases. At very low frequencies, the imaginary part of $\beta(\omega)$ depends linearly on ω , as indicated by Eq. (49). At last, when ν increases from 0 to 0.5, the maximum for the imaginary part, at the transition frequency, is shifted toward the low frequencies. This shift is not obvious in Fig. 1, due to the broadness

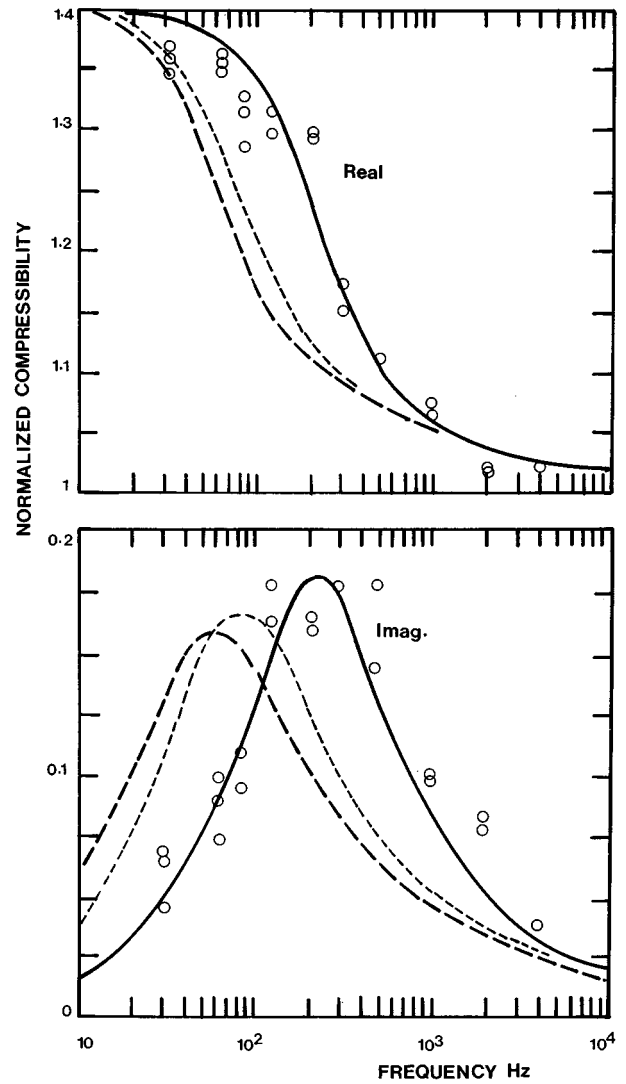


FIG. 2. Measured and predicted normalized compressibility $\beta(\omega)$ for the foam. Measurement $\circ\circ\circ$; prediction $M' = 0.3$ —; prediction $M' = 1$ (circular cross-sectional shaped tube) ----; prediction with Attenborough's model -----.

of the peaks compared to the small value of the shift, which is close to 50 Hz.

IV. TWO EXAMPLES

The compressibility of air in a reticulated plastic foam and a glass wool with thin fibres of diameter close to $6 \mu\text{m}$ has been evaluated with a new method which is simpler than the classical one where the acoustic impedance is measured for a layer successively backed by an impervious rigid plate, and set in front of a quarter-wavelength cavity. This new method is described in Ref. 15. The measured compressibilities are represented in Fig. 2 for the foam and Fig. 3 for the glass wool. The uncertainty of the measurements is about 0.04 for the imaginary and the real part of the compressibility at 100 Hz. The measured values are more spread about than predicted by this uncertainty, probably due to the fact that the different samples of both materials studied cannot be characterized by identical acoustic parameters. The previous measurements by Champoux and Stinson^{6,26} present a

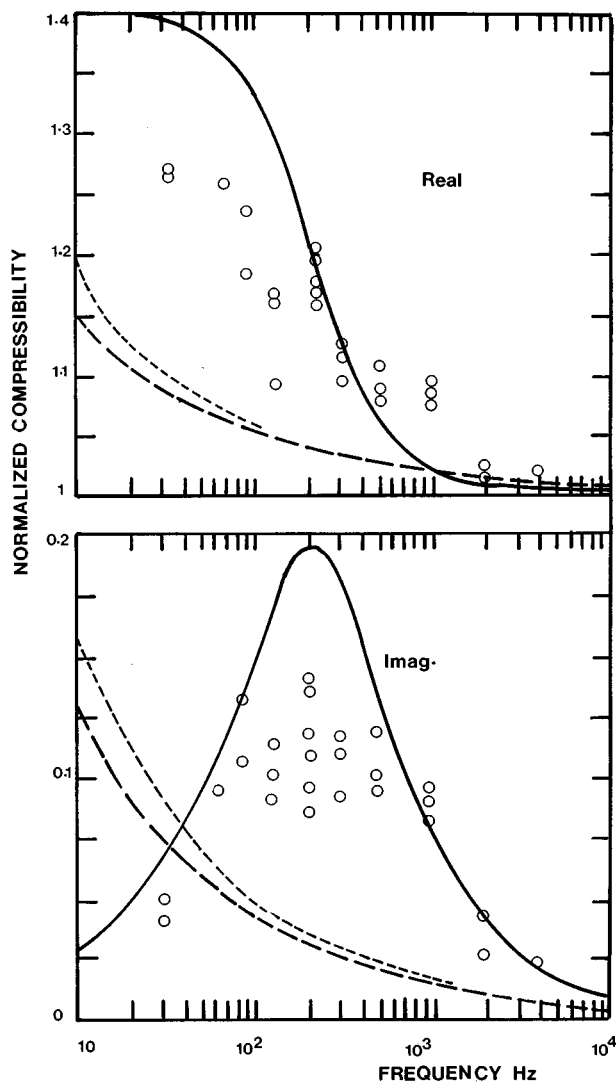


FIG. 3. Measured and predicted compressibility $\beta(\omega)$ for glass wool. Measurement $\circ\circ\circ$; prediction $M'=0.03$ —; prediction $M'=1$ (circular cross-sectional shaped tube) — — —; prediction with Attenborough's model - - - - -.

slightly smaller order of magnitude of the error. Their evaluations were obtained with a Kundt tube. Measurement method developed by one of the authors can be performed quickly, and frequencies lower than 50 Hz can be reached easily. The characteristic dimensions Λ' have been measured with the BET method described in the Introduction.

The measured dimensions Λ' are indicated in Table I. For both materials, the compressibility is compared with the one in a circular cross-sectional shaped pore of radius R equal to Λ' , which is obtained by setting $M'=1$ in Eq. (30). The agreement between prediction and measurement is poor for the foam and very bad for the glass wool for the cylindrical model. An unambiguous result is that the cylindrical model with $R=\Lambda'$ does not predict the location of the transition frequency where the imaginary part of the compressibility is maximum. The distance between the predicted and measured location is very large for glass wool, and noticeable for plastic foam. For both materials, the model based on the system of slits does not provide predictions in better

agreement with measurements if Λ' is fixed at the measured value. For both materials, predictions obtained from the model developed by Attenborough⁷ have been compared with the measured compressibility. The measured tortuosity for both materials is smaller than 1.05 and the difference between the evaluations obtained from Eqs. (35) and (41) of Ref. 7, and Eq. (47) of the present work, are negligible. Equation (45) has been used to relate v and b_a with the measured value of Λ' , and the high-frequency behavior of compressibility is the same as for the cylindrical model. For the first material, the best fit between prediction and measurement is obtained for $v=0$. The predicted compressibility is represented for $v=0$, $b_a=\Lambda'/2$. An increase of v , b_a , and v , being related by Eq. (45), does not noticeably modify the location of the maximum of the imaginary part, but simultaneously, the maximum decreases and becomes noticeably smaller than the measured value. For the second material, the predicted compressibility is also represented for $v=0$, $b_a=\Lambda'/2$. The dependence of compressibility on v , b_a , and v , being related by Eq. (45), is very weak, and the agreement between prediction and measurement is not improved when v increases. The weak dependence of the compressibility on v for frequencies higher than the transition frequency, and the behavior of the imaginary part around the transition frequency, can also be observed in Fig. 1.

As indicated in Sec. I, it has not been possible to evaluate k'_0 nonacoustically from the measurement of the trapping constant by methods involving NMR. Without a comparison between acoustic and precise nonacoustical measurement of k'_0 , it is only possible to verify that the order of magnitude of the acoustical evaluations of k'_0 , under the hypothesis that Eq. (30) is valid, are not unphysical. Using the measured values for Λ' , the coefficient M' has been adjusted to obtain the correct transition frequency where the imaginary part of β is maximum. The values of the thermal permeability k'_0 indicated in Table I have been evaluated by using Eq. (23) and the information of measured Λ' and fitted M' . The Darcy permeabilities k_0 were obtained by independent measurements of the flow resistivity σ . The measured porosities are indicated in Table I. The method of measuring porosity is close to the one described in the book by Zwikker and Kosten.²

With the adjusted value of M' , the agreement between prediction and experience is very good for foam. It is not as good for glass wool because the fibers do not have a sufficient thermal capacity for the compressibility to reach the isothermal value at low frequencies, and the imaginary part of β does not reach the predicted value for the maximum. In an aim of simplicity, the model has not been modified to take this effect into account. (The effect of the small thermal capacity of the frame has been studied by Tarnow.²⁷ See Appendix B for a simple criterion which ensures that this effect is small.) The important fact for the glass wool is that the transition frequency predicted by the one parameter model (with this parameter being equal to the characteristic length Λ') is very far from the actual frequency. This is related to the very small value of M' , which must be equal to one if the circular cross-sectional shaped model is valid. The volume of fiber per unit volume of glass wool is very small,

about 1/1000. A previous study²⁸ on periodic lattices of spheres indicates that the modeling of the viscous permeability by Eq. (9) is robust, but M becomes very small at low concentrations. The same trend is observed experimentally for M' . In fact, exact calculations of the various parameters are not difficult to perform for regular arrays of cylinders in a dilute limit and the mentioned behavior $M, M' \rightarrow 0$ with $\phi \rightarrow 1$ can be checked explicitly.²⁹ For identical circular pores and slits, $M' = 1$ and 0.66, respectively. For the log-normal distribution, M' increases with ν and is always larger than 0.66. These representations cannot be used when $M' \ll 1$ to predict compressibility.

By inspection of the Johnson *et al.* function (9) it may be observed that in a limit $M \rightarrow 0$, a simple, one relaxation time, “Debye” scaling³⁰ occurs, $k/k_0 \rightarrow 1/(1 - i\tilde{\omega})$, as long as the frequency fulfills $M\tilde{\omega} \ll 1$ —which is the case for most of the relaxational pattern. Disregarding effects related to the finite thermal capacity of the solid, the same trend will occur for the thermal quantities, and we may expect that for small M' a “Debye” scaling will apply to k' (as long as $M'\tilde{\omega}' \ll 1$). In terms of the compressibility β this means that we should, in this limit, obtain $\beta \approx \gamma - (\gamma - 1)[-i\tilde{\omega}'/(1 - i\tilde{\omega}')]$. It can be easily verified that this simple form of β could have been used in Fig. 3 in place of the given two parameters prediction ($M' = 0.03$, $\Lambda' = 2.1 \times 10^{-3}$ m).

The above simple form for β can be used to recover in a more direct manner the given value $k'_0 = 1.7 \times 10^{-8}$ m² of the thermal permeability for glass wool. The characteristic frequency f_c where $\text{Im}(\beta)$ is maximum corresponds in this case to $\tilde{\omega}' = 1$, i.e., the thermal permeability can be estimated by means of the relation $k'_0 = \nu' \phi / (2\pi f_c)$. With $f_c \approx 200$ Hz, as indicated by the measurements in Fig. 3, we obtain $k'_0 = 1.68 \times 10^{-8}$ m² in agreement with the previous result. For glass wool the simplified Debye expression for β related to very small concentrations can be used to evaluate k'_0 .

For foam, the acoustically measured thermal permeability is larger than the viscous permeability by a factor close to 4. This factor is equal to 2 for glass wool. Like glass wool, reticulated foam can be considered a fibrous material. It may be noticed that a fibrous material having parallel fibers, in a flow parallel to the fibers, can be considered as one pore limited by the surface of the fibers. In that case, the thermal and the viscous permeability are equal. If the flow is perpendicular to the fibers, the thermal permeability is the same as in the previous case, but the viscous permeability is approximately decreased by a factor of 2.²³ In fact, an exact calculation for regular arrays of cylinders in a dilute limit predicts this factor of 2.²⁹ The fibers in the porous foam are not parallel and their sections are more like triangles than circles. We do not know whether taking into account these details on the structure yields the desired factor of 4 for foam.

V. CONCLUSION

The present study presents a simple extension to thermal effects of an approach worked out by Johnson *et al.* for viscous effects. This modeling uses two parameters for predicting the dynamic compressibility of air in reticulated foams and glass wools. The thermal characteristic dimension and

the thermal permeability have been used, which characterize the thermal exchanges between air and frame in the high- and low-frequency range, respectively. Due to the complexity of the frame of these materials, it has not been possible to compare the acoustically evaluated static permeability with predicted values. Comparison with measurements of related quantities like the trapping constant would be an interesting complement to the present study.

ACKNOWLEDGMENT

The authors thank A. Gedeon (Laboratoire de Chimie des Surfaces, University of Paris VI) for the measurements of the specific surfaces.

APPENDIX A: MICROSTRUCTURAL APPROACH

Under the excitation of an external harmonic source with frequency ω , the air motion inside the porous material is completely characterized, at the microscopic level, by values of the velocity $\mathbf{v}(\mathbf{r}, \omega)$, excess pressure $p(\mathbf{r}, \omega)$, and excess temperature $\tau(\mathbf{r}, \omega)$. In the framework of linearized acoustics, air being considered as an ideal gas, these variables obey the following coupled equations in the porous domain V :

$$-i\omega\rho_0\mathbf{v} = -\nabla p + \eta\nabla^2\mathbf{v} + (\eta/3 + \zeta)\nabla(\nabla \cdot \mathbf{v}), \quad (\text{A1a})$$

$$-i\omega \frac{1}{P_0} (p - (P_0/T_0)\tau) = -\nabla \cdot \mathbf{v}, \quad (\text{A1b})$$

$$-i\omega\rho_0 C_p \tau = -i\omega p + \kappa \nabla^2 \tau. \quad (\text{A1c})$$

The boundary conditions at the contact surface with the frame are

$$\mathbf{v} = \mathbf{0}, \quad (\mathbf{r} \in \partial V) \quad (\text{A1d})$$

and

$$\tau = 0, \quad (\mathbf{r} \in \partial V). \quad (\text{A1e})$$

The general solution of Eqs. (A1a)–(A1d) for any nontrivial frame geometry would be difficult, if not impossible. For instance, significant coupling effects between viscous and thermal effects can occur if the porous material contains cavities which are weakly coupled with the main pores. Nevertheless, for the materials studied, i.e., air-filled glass wools and reticulated foams, the frame is made of fibers which occupy a small part of the volume, and the interplay between viscous and thermal effects can be neglected in a first approximation. One may identify a dimensionless small parameter ϵ in the problem that would enable significant simplifications for the viscous permeability and thermal permeability calculation. Like in the work by Zhou and Sheng¹⁸ this small parameter is defined as the ratio between two length scales, $\epsilon = l/L$, in which the small scale l is given by the typical pore size, and the large scale L is given by the product of the air sound speed $c = \sqrt{K_a/\rho_0}$ and an intrinsic viscous relaxation time $\vartheta_v = l^2/\nu$. The characteristic frequency $2\pi/\vartheta_v$ is a rough estimate of a viscous rollover frequency where, when ω increases, a transition occurs between a viscous dominated regime and an inertia dominated regime. The Prandtl number Pr is of order 1 (~ 0.71 for air) and the thermal rollover frequency where a transition occurs between

isothermal and adiabatic regimes, is expected to be on the same order as the viscous rollover frequency. For air saturating usual acoustic materials with $l \approx 10^{-4}$ m, ϵ is on the order of 10^{-4} .

By expressing time in units of ϑ_v and lengths in units of l , Eqs. (A1a)–(A1d) may be written in dimensionless form

$$-i\omega \mathbf{v} = -\frac{1}{\epsilon} \nabla p + \nabla^2 \mathbf{v} + \left(\frac{1}{3} + \frac{\zeta}{\eta}\right) \nabla(\nabla \cdot \mathbf{v}), \quad (\text{A2a})$$

$$-i\omega \left(p - \frac{\gamma-1}{\gamma} \text{Pr } \tau\right) = \frac{-1}{\gamma\epsilon} \nabla \cdot \mathbf{v}, \quad (\text{A2b})$$

$$-i\omega \text{Pr } \tau = -i\omega p + \nabla^2 \tau, \quad (\text{A2c})$$

$$\mathbf{v} = \mathbf{0} \quad (\mathbf{r} \in \partial V), \quad (\text{A2d})$$

$$\tau = 0 \quad (\mathbf{r} \in \partial V). \quad (\text{A2e})$$

Here, p is in units of $L \eta^2 / \rho_0 l^3$ following the assumption that the macroscopic pressure gradient should be on the same order as $\eta v / l^2$ in accordance with Darcy's law (6). Similarly, τ is in units of $L \eta^3 / \rho_0^2 \kappa l^3$ following the assumption that the pressure derivative $\partial p / \partial t$ should be on the same order as $\kappa \tau / l^2$ in accordance with the thermal analogue of Darcy's law (18). As in the Zhou and Sheng treatment,¹⁸ these assumptions are justified by our consistent derivation of the two ‘‘Darcy's laws’’ from Eqs. (A2a) to (A2e). The following thermodynamic identities were used in writing Eqs. (A2b) and (A2c):

$$\frac{P_0}{T_0 \rho_0 C_p} = \frac{\gamma-1}{\gamma}, \quad (\text{A3a})$$

$$\kappa = \frac{\eta C_p}{\text{Pr}}. \quad (\text{A3b})$$

A brief discussion of the validity of boundary condition (A2e) is given in Appendix B.

The existence of a small parameter ϵ associated with rapid fluctuations in the structure of the air-filled porous domain can now be taken into account using the well-known method of homogenization. We assume that the different fields depend on two scales: a slow scale $\mathbf{x} = \mathbf{r} / L$ and a fast scale $\mathbf{y} = \mathbf{x} / \epsilon = \mathbf{r} / l$. We shall derive the global (macroscopic) equations governing sound propagation using a two-scale expansion

$$\mathbf{v}(\mathbf{x}, \mathbf{y}) = \mathbf{v}_0(\mathbf{x}, \mathbf{y}) + \epsilon \mathbf{v}_1(\mathbf{x}, \mathbf{y}) + \dots, \quad (\text{A4a})$$

$$p(\mathbf{x}, \mathbf{y}) = p_0(\mathbf{x}, \mathbf{y}) + \epsilon p_1(\mathbf{x}, \mathbf{y}) + \dots, \quad (\text{A4b})$$

$$\tau(\mathbf{x}, \mathbf{y}) = \tau_0(\mathbf{x}, \mathbf{y}) + \epsilon \tau_1(\mathbf{x}, \mathbf{y}) + \dots, \quad (\text{A4c})$$

$$\nabla = \epsilon \nabla_x + \nabla_y. \quad (\text{A4d})$$

Substituting (A4a)–(A4d) into (A2a)–(A2e) and collecting powers of ϵ yields the leading order equations

$$\nabla_y p_0 = 0, \quad (\text{A5a})$$

$$-i\omega \mathbf{v}_0 = -\nabla_x p_0 - \nabla_y p_1 + \nabla_y^2 \mathbf{v}_0, \quad (\text{A5b})$$

$$\nabla_y \cdot \mathbf{v}_0 = 0, \quad (\text{A5c})$$

$$i\omega \left(p_0 - \frac{\gamma-1}{\gamma} \text{Pr } \tau_0\right) = \frac{1}{\gamma} (\nabla_x \cdot \mathbf{v}_0 + \nabla_y \cdot \mathbf{v}_1), \quad (\text{A5d})$$

$$-i\omega \text{Pr } \tau_0 = -i\omega p_0 + \nabla_y^2 \tau_0. \quad (\text{A5e})$$

These equations are supplemented by absorbing conditions on the air–solid interface

$$\mathbf{v}_0 = 0, \quad \mathbf{v}_1 = 0, \dots \quad (\mathbf{r} \in \partial V), \quad (\text{A5f})$$

$$\tau_0 = 0, \dots \quad (\mathbf{r} \in \partial V). \quad (\text{A5g})$$

Equation (A5a) shows that p_0 , independent of coordinate \mathbf{y} , may be regarded as the externally applied pressure. Equations (A5e), (A5a), and (A5g) then indicate that, to the lowest order, the temperature field originates from a spatially uniform, harmonic, heating in the air domain, with perfect absorbing conditions on the solid boundaries. Equation (A5c) indicates that to the lowest order, the velocity field may be regarded as incompressible on the \mathbf{y} scale.

The fields p_1 , \mathbf{v}_0 , and τ_0 are solutions to two independent set of linear equations, Eqs. (5c), (A5d), and (A5f) on one hand, and Eqs. (A5d) and (A5g) on the other hand. Hence, they may be formally expressed as linear operators acting on the source terms $-\nabla_x p_0$ and $-i\omega p_0$, i.e.,

$$p_1 = \mathbf{P}(\mathbf{x}, \mathbf{y}) \cdot (-\nabla_x p_0), \quad (\text{A6a})$$

$$\mathbf{v}_0 = \vec{\mathbf{V}}(\mathbf{x}, \mathbf{y}) \cdot (-\nabla_x p_0), \quad (\text{A6b})$$

$$\tau_0 = \Theta(\mathbf{x}, \mathbf{y})(-i\omega p_0). \quad (\text{A6c})$$

The linear operators Θ , \mathbf{P} , and $\vec{\mathbf{V}}$ are, respectively, scalar, vector, and second rank tensor operators. By substituting Eqs. (A6a)–(A6c) into the two independent set noted above, we get the generic equations satisfied by the operators \mathbf{P} , $\vec{\mathbf{V}}$, and Θ

$$\nabla_y \mathbf{P} - i\omega \vec{\mathbf{V}} - \nabla_y^2 \vec{\mathbf{V}} = \vec{\mathbf{I}}, \quad (\text{A7a})$$

$$\nabla_y \cdot \vec{\mathbf{V}} = \mathbf{0}, \quad (\text{A7b})$$

$$\vec{\mathbf{V}} = \vec{\mathbf{0}} \quad (\mathbf{r} \in \partial V) \quad (\text{A7c})$$

and

$$-i\omega \text{Pr } \Theta - \nabla_y^2 \Theta = I, \quad (\text{A8a})$$

$$\Theta = 0 \quad (\mathbf{r} \in \partial V). \quad (\text{A8b})$$

In these equations $\vec{\mathbf{I}}$ and I are the unit second rank tensor and unit scalar operators [$(\vec{\mathbf{I}})_{ij} = I \delta_{ij}$ where δ_{ij} is the Kronecker symbol]. Given the solutions $\vec{\mathbf{V}}$ and Θ , the dynamic viscous and thermal permeabilities $k(\omega)$ and $k'(\omega)$ may be directly calculated by averaging \mathbf{v}_0 and τ_0 over the \mathbf{y} variable

$$\langle \mathbf{v}_0 \rangle_y = \langle \vec{\mathbf{V}}(\mathbf{x}, \mathbf{y}) \rangle_y \cdot (-\nabla_x p_0), \quad (\text{A9})$$

$$\langle \tau_0 \rangle_y = \langle \Theta(\mathbf{x}, \mathbf{y}) \rangle_y (-i\omega p_0). \quad (\text{A10})$$

Comparing Eqs. (A9) and (A10) with the two dynamic Darcy's laws (4) and (5), we get

$$\vec{k}(\omega) = \phi \langle \vec{\mathbf{V}}(\mathbf{x}, \mathbf{y}) \rangle_y \quad (\text{A11})$$

as the definition of the permeability tensor, and

$$k'(\omega) = \phi \langle \Theta \rangle_y \quad (\text{A12})$$

as the definition of the (scalar) thermal permeability. The dimensionless permeabilities given by (A11) and (A12) must be multiplied by l^2 to recover the dimensionalized quantities in Eqs. (4) and (5).

The remaining microscopic equation (A5d) may serve to establish the general connexion (29) between thermal permeability and compressibility. Averaging (A5d) gives

$$i \left(p_0 - \frac{\gamma-1}{\gamma} \text{Pr} \langle \tau_0 \rangle_y \right) = \frac{1}{\gamma} (\nabla_x \cdot \langle \mathbf{v}_0 \rangle_y + \langle \nabla_y \cdot \mathbf{v}_1 \rangle_y). \quad (\text{A13})$$

The second term on the right-hand side of (A13) is now shown to be zero. Let V_R be a large sphere of radius R centered at the origin. Then

$$\langle \nabla_y \cdot \mathbf{v}_1 \rangle_y = \frac{1}{V_R} \int_{V_R} \nabla_y \cdot \mathbf{v}_1(\mathbf{x}, \mathbf{y}) d\mathbf{y} = \frac{1}{V_R} \int_{\partial V_R} \mathbf{v}_1 \cdot \mathbf{n} d\mathbf{y}.$$

The surface ∂V_R consists of two parts: $(S_R)_i$ is the part of the pore surface within V_R , and $(S_R)_e$ is the part of the surface of the large sphere within the pore domain. Using the boundary condition $\mathbf{v}_1 = \mathbf{0}$ on $(S_R)_i$ we have

$$\langle \nabla_y \cdot \mathbf{v}_1 \rangle_y = \frac{1}{V_R} \int_{(S_R)_e} \mathbf{v}_1 \cdot \mathbf{n} d\mathbf{y},$$

and letting $R \rightarrow \infty$ we finally arrive at

$$\langle \nabla_y \cdot \mathbf{v}_1 \rangle_y = 0. \quad (\text{A14})$$

By using Eq. (A14) and Eqs. (A10) and (A12), the averaged equation (A13) can then be rewritten

$$-\nabla_x \cdot \langle \mathbf{v}_0 \rangle_y - i\omega p_0 = \gamma + (\gamma-1) \text{Pr} \frac{k'(\omega)}{\phi} i\omega. \quad (\text{A15})$$

This ratio represents the dimensionless, frequency-dependent compressibility function $\beta(\omega)$. [Reintroducing dimensionalized variables on the left-hand side of Eq. (A15) a factor $L\tilde{\omega}\tilde{p}/\tilde{\nu}$ appears where tilded quantities are reference quantities. Using the identifications $\tilde{p} = L\eta^2/\rho_0 l^3$, $L = \sqrt{K_a/\rho_0(l^2/\nu)}$, and $\tilde{\nu} = \tilde{\omega}l$, it may be checked that this factor coincide with the adiabatic bulk modulus K_a .] Reintroducing dimensionalized variables on the right-hand side of Eq. (A15), the product $k'(\omega)\omega$ must be written $[k'(\omega)/l^2] \times (\omega l^2/\nu)$ and the final result is

$$\beta(\omega) = \gamma + (\gamma-1) \frac{i\omega}{\nu'} \frac{k'(\omega)}{\phi}, \quad (\text{A16})$$

with $\nu' = \nu/\text{Pr}$.

APPENDIX B: RELATION WITH DIFFUSION-CONTROLLED REACTIONS

1. Trapping constant

The trapping constant can be defined as follows. Inside the fluid that saturates the frame, an excitable solute is created with a spatially constant density s . The solute diffuses with a diffusion constant D , and is instantly relaxed on contact with the frame. The equations governing the diffusion-controlled process are

$$\frac{\partial u}{\partial t} - D \nabla^2 u = s \quad (\mathbf{r} \in V) \quad (\text{B1})$$

$$u = 0 \quad (\mathbf{r} \in \partial V), \quad (\text{B2})$$

where u is the concentration of solute per unit volume of saturating fluid. At equilibrium, $\partial u/\partial t = 0$, and the trapping constant is given by

$$\Gamma = s / (\langle u \rangle \phi D). \quad (\text{B3})$$

The trapping constant is related to the *mean survival time* θ of solute particles by

$$\theta = 1/\Gamma \phi D. \quad (\text{B4})$$

Application of Eq. (B3) gives

$$\theta = \langle u \rangle / s. \quad (\text{B5})$$

2. Frequency-dependent mean survival time and relation with thermal permeability

A similar survival problem can be defined in harmonic regime when the excitable solute is created with a spatially constant density $s e^{-i\omega t}$. The frequency-dependent mean survival time is defined by (Torquato and Avellaneda³¹)

$$\theta(\omega) = \langle u(\omega) \rangle / s, \quad (\text{B6})$$

where $u(\omega)$ solves the diffusion-controlled problem

$$-i\omega u - D \nabla^2 u = s \quad (\mathbf{r} \in V), \quad (\text{B7})$$

$$u = 0 \quad (\mathbf{r} \in \partial V), \quad (\text{B8})$$

where s is a spatial constant. Note that $\theta(0)$ is just the standard static survival time (B4).

A comparison between Eqs. (B7) and (B8) and the thermal diffusion equations Eqs. (16) and (17) shows identical problems (with substitutions $s = -i\omega p/\rho_0 C_p$, $u = \tau$, $D = \nu' = \kappa/\rho_0 C_p$) provided the pressure p can be considered as a spatial constant at the pore scale. It was noted in Appendix A that this constancy follows from the simple two-scale analysis [see Eq. (A5a)] and that it is a reasonable hypothesis for the materials studied. Hence, the following identity is obtained:

$$k'(\omega) = \nu' \phi \theta(\omega), \quad (\text{B9})$$

where $\theta(\omega)$ corresponds to $D = \nu'$. Setting $\omega = 0$ in Eq. (B9) and using (B4) yields relation (19) between static thermal permeability k'_0 and trapping constant Γ .

3. Condition on the heat capacity of the porous solid

So far we have assumed the validity of the boundary conditions $\tau = 0$ on the air–solid interface. A static thermal permeability exists and an isothermal low-frequency limit for the compressibility $\lim_{\omega \rightarrow 0} \beta(\omega) = \gamma$ is obtained by using Eq. (A16). This assumption is justified only in a limit where the ratio

$$r = \frac{(\rho_0 C_p)_{\text{air}} \phi}{(\rho_0 C_p)_{\text{solid}} (1 - \phi)} \quad (\text{B10})$$

of the heat capacity coefficients is small: $r \ll 1$. For usual porous foams this ratio is on the order of 1/20. However,

greater values can be found in the case of light glass wools. The effect of finite heat capacity of the solid on the low-frequency limit of $\beta(\omega)$ can be predicted by means of simple calorimetric considerations. In a quasi-static limit for compressions and dilatations, the excess temperature has sufficient time to equalize in the air and solid part. Thus in the limit $\omega=0$ we may write

$$[(\rho_0 C_p)_{\text{air}} \phi + (\rho_0 C_p)_{\text{solid}} (1 - \phi)] \frac{\partial \langle \tau \rangle}{\partial t} = \phi \frac{\partial \langle p \rangle}{\partial t}. \quad (\text{B11})$$

A comparison between Eqs. (5) and (B11) shows that in this quasi-static limit $k'(\omega)$ behaves like $\nu' \phi r / -i\omega(1+r)$. The general relation (A16) between $k'(\omega)$ and $\beta(\omega)$ still applies to this case because the boundary conditions $\tau=0$ were not explicitly used. Making use of this connection finally yields

$$\lim_{\omega \rightarrow 0} \beta(\omega) = \frac{\gamma + r}{1 + r}. \quad (\text{B12})$$

Equation (B12) shows that the effect of finite heat capacity of the solid can be ignored when $r \ll 1$ (this is the mentioned criterion in Sec. IV). The boundary conditions $\tau = 0$ then lead to reasonable results and a static thermal permeability may be assumed to exist.

APPENDIX C: SINGULARITIES OF THERMAL RESPONSE FUNCTIONS

As shown by Johnson *et al.*¹⁰ (Appendix A), the two response functions $k(\omega)$ and $\alpha(\omega) \equiv \nu \phi / -i\omega k(\omega)$ are analytic functions of ω everywhere in the complex plane except for values of ω on the negative imaginary axis. Thus any pole, branch point, or zero of these functions lies on the imaginary axis. We wish to point out that the same general properties apply to the thermal functions $k'(\omega)$ and $\alpha'(\omega) \equiv \nu' \phi / -i\omega k'(\omega)$.

The definitions of $k'(\omega)$ and $\alpha'(\omega)$ are

$$\phi \langle \tau \rangle = \frac{k'(\omega)}{\kappa} \frac{\partial}{\partial t} \langle p \rangle, \quad (\text{C1})$$

$$\rho_0 C_p \alpha'(\omega) \frac{\partial}{\partial t} \langle \tau \rangle = \frac{\partial}{\partial t} \langle p \rangle, \quad (\text{C2})$$

where τ and p verify the local equations

$$\rho_0 C_p \frac{\partial \tau}{\partial t} = \kappa \nabla^2 \tau + \frac{\partial p}{\partial t}, \quad (\mathbf{r} \in V), \quad (\text{C3})$$

$$\nabla p = \mathbf{0} \quad (\mathbf{r} \in V), \quad (\text{C4})$$

$$\tau = 0 \quad (\mathbf{r} \in \partial V). \quad (\text{C5})$$

[Equation (C4) is written because of Eq. (A5a).]

In order to study the singularities of the functions $k'(\omega)$ and $\alpha'(\omega)$, we imagine a volume of the porous sample enclosed by a thin membrane, which is allowed to be moving through the solid without disturbing it, while being impervious to the fluid. It is assumed that the membrane behaves as an adiabatic wall (Woods³²). The singularities of response factors are related to unforced oscillations of the system, and we shall prove that the latter are purely damped. Due to Eq.

(C1), a pole of $k'(\omega)$ means that there exists a nontrivial solution to the above microscopic equations, having the property that $p=0$. This occurs if the membrane is a pressure-release surface. The pressure term in (C3) is not present, and we are left with the Fourier equation of heat diffusion

$$\rho_0 C_p \frac{\partial \tau}{\partial t} = \kappa \nabla^2 \tau. \quad (\text{C6})$$

The oscillations $\exp(-i\omega t)$ of the system hence defined, are unforced oscillations: since $p=0$, no mechanical power arises from a displacement of the membrane, and the following boundary condition guarantees that no thermal power is entering the system

$$\oint_{\partial V_f} \bar{\tau} \partial_i \tau n_i dS = 0. \quad (\text{C7})$$

Here, ∂V_f is the closed boundary of the fluid volume V , made of the pore walls ∂V and contact surfaces with the confining membrane; n_i are the components of the unit normal to ∂V_f , and $\bar{\tau}$ is the field complex conjugate of τ . This condition (C7) is automatically satisfied because the integrand is identically zero on the pore walls and membrane, due to, respectively, boundary conditions (C5) and membrane adiabaticity. From heat equation (C6) we have

$$-i\omega \rho_0 C_p \int_V \bar{\tau} \tau dV = \kappa \int_V \bar{\tau} \nabla^2 \tau dV. \quad (\text{C8})$$

Finally, because of the following identity

$$\bar{\tau} \nabla^2 \tau = \partial_i (\bar{\tau} \partial_i \tau) - \partial_i \bar{\tau} \partial_i \tau, \quad (\text{C9})$$

and boundary conditions (C7), Eq. (C8) becomes

$$\omega = -i\nu' \frac{\int_V |\nabla \tau|^2 dV}{\int_V |\tau|^2 dV}. \quad (\text{C10})$$

Therefore, any pole of $k'(\omega)$ lies on the negative imaginary axis.

A pole of $\alpha'(\omega)$ means that there exists a nontrivial solution to the microscopic equations (C3)–(C5), having the property that $\langle \tau \rangle = 0$, where $\langle \tau \rangle$ is the mean excess temperature in the fluid. Here the membrane is sealed off so that a nonvanishing pressure may arise. As before, no mechanical power is entering the system since the membrane is motionless, and the boundary condition (C7) is fulfilled. From Eq. (C3) we have

$$-i\omega \rho_0 C_p \int_V \bar{\tau} \tau dV = \kappa \int_V \bar{\tau} \nabla^2 \tau dV - i\omega \int_V \bar{\tau} p dV.$$

The second integral in the right-hand side is identically zero since p is a constant and $\langle \tau \rangle = 0$. Hence, the same result (C10) is obtained, proving that any pole of $\alpha'(\omega)$ lies on the negative imaginary axis. To complete the proof and obtain that any zero or branch point of $k'(\omega)$ or $\alpha'(\omega)$ must occur on the negative imaginary axis, one proceeds exactly as indicated by Johnson *et al.*,¹⁰ Appendix A.

¹L. L. Beranek, "Acoustic impedance of porous materials," J. Acoust. Soc. Am. **13**, 248–260 (1942).

- ²C. Zwikker and C. W. Kosten, *Sound Absorbing Materials* (Elsevier, New York, 1949).
- ³M. R. Stinson, "The propagation of plane sound waves in narrow and wide circular tubes, and generalization to uniform tubes of arbitrary cross-sectional shapes," *J. Acoust. Soc. Am.* **89**, 550–558 (1991).
- ⁴K. Attenborough, "On the acoustic slow wave in air-filled granular media," *J. Acoust. Soc. Am.* **81**, 93–102 (1987).
- ⁵J. F. Allard, C. Depollier, and A. Aknine, "Acoustical properties of partially reticulated foams with high and medium flow resistance," *J. Acoust. Soc. Am.* **79**, 1734–1740 (1986).
- ⁶Y. Champoux and M. R. Stinson, "Experimental investigation of models of sound wave propagation in air saturated porous media," *J. Acoust. Soc. Am.* **88**, 121 (1990).
- ⁷K. Attenborough, "Models for the acoustical properties of air saturated granular media," *Acust. Acta Acust.* **1**, 213–226 (1993).
- ⁸Y. Champoux and J. F. Allard, "Dynamic tortuosity and bulk modulus in air-saturated porous media," *J. Appl. Phys.* **70**, 1975–1979 (1991).
- ⁹D. L. Johnson, J. Koplik, and L. M. Schwartz, "New pore size parameter characterizing transport in porous media," *Phys. Rev. Lett.* **57**, 2564–2567 (1986).
- ¹⁰D. L. Johnson, J. Koplik, and R. Dashen, "Theory of dynamic permeability and tortuosity in fluid saturated porous media," *J. Fluid Mech.* **176**, 379–402 (1987).
- ¹¹P. Leclaire, L. Kelders, W. Lauriks, M. Melon, and B. Castagnède, "Determination of the viscous and the thermal characteristic lengths of plastic foams by ultrasonic measurements in helium and air," *J. Appl. Phys.* **80**, 2009–2012 (1996).
- ¹²S. Brunauer, P. H. Emmett, and E. Teller, "Absorption of gases in multimolecular layers," *J. Am. Chem. Soc.* **60**, 309–319 (1938).
- ¹³A. Bardot, B. Brouard, and J. F. Allard, "Frame decoupling at low frequency in thin porous layers saturated by air," *J. Appl. Phys.* **79**, 8223–8229 (1996).
- ¹⁴M. Avellaneda and S. Torquato, "Rigorous link between fluid permeability, electrical conductivity and relaxation times for transport in porous media," *Phys. Fluids A* **3**, 2529–2540 (1991).
- ¹⁵V. Tarnow, "Measurement of sound propagation in glass wool," *J. Acoust. Soc. Am.* **97**, 2272–2281 (1995).
- ¹⁶T. Levy and E. Sanchez-Palencia, "Equations and interface conditions for acoustic phenomena in porous media," *J. Math. Anal. Appl.* **61**, 813–834 (1977).
- ¹⁷D. Lafarge, "Propagation du son dans les matériaux poreux à structure rigide saturés par un fluide viscothermique: Définition de paramètres géométriques, analogie électromagnétique, temps de relaxation," Ph.D. thesis, Université du Maine, Le Mans, France (1993).
- ¹⁸M.-Y. Zhou and P. Sheng, "First-principles calculations of dynamic permeability in porous media," *Phys. Rev. B* **39**, 12 027–12 039 (1989).
- ¹⁹L. M. Schwartz, N. Martys, D. P. Bentz, E. J. Garboczi, and S. Torquato, "Cross-properties relations and permeability estimation in model porous media," *Phys. Rev. E* **48**, 4584–4591 (1993).
- ²⁰C. Straley, A. Matteson, S. Feng, and L. M. Schwartz, "Magnetic resonance, digital analysis, and permeability of porous media," *Appl. Phys. Lett.* **51**, 1146–1148 (1987).
- ²¹S. Pride, A. Gangi, and F. D. Morgan, "Deriving the equations of motion for porous isotropic media," *J. Acoust. Soc. Am.* **92**, 3278–3290 (1992).
- ²²C. Marle, "Écoulements monophasiques en milieux poreux," *Rev. Inst. Français du Pétrole* **22**, 1471–1509 (1967).
- ²³J. F. Allard, *Propagation of Sound in Porous Media: Modeling Sound Absorbing Materials* (Chapman & Hall, London, 1993).
- ²⁴A. Craggs and J. G. Hildebrandt, "Effective densities and resistivities for acoustic propagation in narrow tubes," *J. Sound Vib.* **92**, 321–331 (1984).
- ²⁵T. Yamamoto and A. Turgut, "Acoustic wave propagation through porous media with arbitrary pore size distributions," *J. Acoust. Soc. Am.* **83**, 1744–1751 (1988).
- ²⁶Y. Champoux, "Etude expérimentale du comportement acoustique des matériaux poreux à structure rigide," Ph.D. thesis, Carleton University, Canada (1991).
- ²⁷V. Tarnow, "Compressibility of air in fibrous materials," *J. Acoust. Soc. Am.* **99**, 3010–3016 (1996).
- ²⁸A. M. Chapman and J. J. L. Higdon, "Oscillatory Stokes flow in periodic porous media," *Phys. Fluids A* **4**, 2099–2116 (1992).
- ²⁹Y. Auregan, private communication.
- ³⁰D. W. Davidson and R. H. Cole, "Dielectric relaxation in glycerol, propylene glycol, and *n*-propanol," *J. Chem. Phys.* **19**, 1484–1490 (1951).
- ³¹S. Torquato and M. Avellaneda, "Diffusion and reaction in heterogeneous media: Pore size distribution, relaxation times, and mean survival time," *J. Chem. Phys.* **95**, 6477–6489 (1991).
- ³²L. C. Woods, *The Thermodynamics of Fluid Systems* (Oxford U.P., New York, 1986).

The usage of standard finite element codes for computation of dispersion relations in materials with periodic microstructure

M. Åberg and P. Gudmundson

Department of Solid Mechanics, Royal Institute of Technology, 100 44 Stockholm, Sweden

(Received 9 June 1996; accepted for publication 2 July 1997)

A method with which standard finite element programs can be used to compute dispersion relations in periodic composites is proposed. The method is applied to two composite microstructures: a two-phase laminate and a fiber composite. The dispersion relations computed for the laminate are compared with a known analytical solution and the agreement is very good. The dispersion relations computed for the fibrous composite are compared with an existing approximate model and experimental results from the literature. The agreement between the approximate model, the experiments, and the computations is very good in the wave guide case and satisfactory for the wave reflect case. © 1997 Acoustical Society of America. [S0001-4966(97)04310-5]

PACS numbers: 43.20.Jr, 43.20.Gp, 43.20.Mv, 43.35.Cg [JEG]

INTRODUCTION

Structural materials are inhomogeneous on small scales. In metals and ceramics the grain size usually defines the microstructural scale, and in composites it is the ply thickness, fiber dimension, or inclusion size that defines this scale. Generally, the inhomogeneous character of the material is ignored in engineering applications; the continuum hypothesis is assumed. The accuracy of this assumption is good if the stress and strain fields vary slowly compared to the microstructural length. In certain situations, however, this is not the case. Close to crack tips, for example, the stress and strain field vary strongly over microstructural lengths. Also, if the wavelength becomes sufficiently small, waves in inhomogeneous materials experience dispersion (i.e., phase and group velocities depend on the wavelength), as has been measured by Tauchert and Guzelsu,¹ Robinson and Leppelmeier,² Sutherland and Lingle,³ and Kinra *et al.*⁴ among others. In practice it is often impossible to analyze such problems using the conventional techniques of stress and strain calculations, therefore a number of simplified models, which take the microstructure into account, have been proposed.

One widely used technique is to smear out the effect of the microstructure and to calculate homogenized, or effective, properties as functions of the properties of the constituents. The so-called self-consistent scheme⁵ has been developed and applied by Sabina *et al.* for the study of dispersion in materials with aligned and randomly oriented spheroids as inclusions.^{6,7} Yang and Mal use a similar technique (the generalized self-consistent model) to study the dispersion in random fiber composites.⁸ Random fiber composites have also been studied by Beltzer and Brauner by the use of the Kramers–Kronig relations.^{9,10}

Another approach is to assume that the material is periodic and to apply an asymptotic multivariable expansion. One set of variables deals with the global stress and strain variations in the body, while the other set of variables take care of the rapid variations within a unit cell of the periodic material. The process is outlined in a number of texts; see, for example, Sanchez-Palencia and Zaoui,¹¹ Parton and

Kudryavtsev,¹² Murakami *et al.*,¹³ or Murakami and Hegemier.¹⁴ To the authors' knowledge there are, however, relatively few examples of this procedure being carried out to the point where quantitative comparisons with the results of other theories or experiments can be made.

Murakami *et al.* consider a laminate and derive approximate constitutive equations containing the microstructure. In order to assess the accuracy of the model, Murakami *et al.* calculate the dispersion relations resulting from their model and compare it with the exact results obtained by Sve.¹⁵ Murakami and Hegemier use the same technique to model composites with hexagonally arranged fibers. Apart from the approximation involved with the expansion, another approximation is introduced based on a study by Murakami *et al.*¹⁶ The hexagonally shaped unit cell boundary is approximated by a circle. From the resulting constitutive equations, the dispersion relation is calculated and compared with the experiments done by Tauchert and Guzelsu, and Sutherland and Lingle. Hence, it is unknown if the discrepancy between the calculated and the measured dispersion is due to the approximation made by the expansion and the simplified boundary or effects not accounted for, such as fiber-matrix slip or attenuation.

For the purpose of comparison there is, thus, a need for exact dispersion relations. In the one-dimensional case, i.e., a laminate, Sve and Delph *et al.* have obtained and discussed analytical solutions of dispersion relations.^{17,18} For more complicated geometries one has to resort to numerical methods such as the finite element method.

The so-called stiffness method, which can be perceived as a finite element method, was used by Dong and Nelson to study wave motion in laminated plates.¹⁹ Datta and co-workers used a refined version of the stiffness method to study wave motion in laminated plates and laminates.^{20,21} Minagawa *et al.* use a mixed variational formulation and a new energy quotient to compute the dispersion relations for laminates, fiber composites with square fibers, and chequerboard composites, among others.^{22–24} Naciri *et al.* use the finite element method to compute the dispersion and damping relations for a viscoelastic fibrous composite with square

fibers.²⁵ The abovementioned finite element formulations result in eigenvalue problems with in general Hermitian stiffness and mass matrices. Nelson and Navi split the equations into real and imaginary parts and obtain a formulation which is used for computations of dispersion in a fiber composite with square fibers.²⁶ Orris and Petyt formulate a real eigenvalue problem using the fact that a complex eigenvalue problem with Hermitian matrices can be restated as a eigenvalue problem with real matrices at the expense of doubled matrix dimensions.²⁷ They then use this to compute dispersion in a periodically supported beam and a skin rib structure.

The methods mentioned above are, of course, generally applicable. It is, however, time consuming to apply them to a specific problem. Therefore it would be desirable to be able to use standard procedures included in most of the wide spread standard finite element codes for real valued field equations. Langlet *et al.* use a finite element code which handles complex fields called ATILA to compute dispersion,²⁸ however, most standard codes do not have this capability. A nice thing with standard codes is that they automatically compute the stiffness and mass matrices and that constraints can easily be implemented; also the whole arsenal of pre- and post-processing that usually comes with these packages makes modeling and analysis of the results faster and more straightforward. This paper presents a procedure with which standard finite element programs for real valued fields can be used to compute dispersion relations. This method is then applied to two examples: a laminate and a fiber composite.

I. STATEMENT OF PROBLEM

A. Governing equations

Consider propagation of a harmonic wave in a periodic material. By periodic it is here meant that the material can be divided into finite-sized identical, so-called periodic cells. Thus one single cell completely describes the material. The governing equations are

$$\sigma_{ij,j} = \rho \frac{\partial^2 u_i}{\partial t^2}, \quad (1)$$

$$\sigma_{ij} = C_{ijkl} \epsilon_{kl}, \quad (2)$$

and

$$\epsilon_{kl} = \frac{1}{2}(u_{k,l} + u_{l,k}). \quad (3)$$

Here, σ_{ij} is the stress tensor, ϵ_{kl} the strain tensor, u_i the displacement vector, C_{ijkl} the stiffness tensor, and ρ the density. In all tensor equations the usual summation convention is assumed and differentiation with respect to a Cartesian coordinate is denoted by a comma. Note that the stiffness and the density may both depend on position periodically.

Now look for solutions of the form

$$u_m(x_n, t) = U_m(x_n) e^{-i\omega t}, \quad (4)$$

where $U_m(x_n)$ is, in general, a complex valued function. As a consequence, the stresses and the strains will be given by

$$\sigma_{ij}(x_n, t) = \Sigma_{ij}(x_n) e^{-i\omega t} \quad (5)$$

and

$$\epsilon_{ij}(x_n, t) = E_{ij}(x_n) e^{-i\omega t}. \quad (6)$$

The equations of motion may now be written as

$$\Sigma_{ij,j} + \rho \omega^2 U_i = 0, \quad (7)$$

$$\Sigma_{ij} = C_{ijkl} E_{kl}, \quad (8)$$

and

$$E_{kl} = \frac{1}{2}(U_{k,l} + U_{l,k}). \quad (9)$$

The periodic material is divided into periodic cells. Due to the periodicity the displacement vectors at equivalent points in different periodic cells are related through²⁹

$$U_m(x_n) = U_m(x_n + l_n) e^{-ikn_j l_j}, \quad (10)$$

where k denotes the wave number, n_j the direction cosines of wave propagation, x_n a position vector, and l_n the vector connecting equivalent points in the periodic cells. From Eqs. (8) and (9) it follows that the stresses in the points under consideration satisfy an equivalent periodicity relation, thus

$$\Sigma_{ij}(x_n) = \Sigma_{ij}(x_n + l_n) e^{-ikn_j l_j}. \quad (11)$$

A single periodic cell is now considered. For each point on the boundary of the cell there exists an equivalent periodic point for which relations (10) and (11) are valid. For corner points of the cell, in particular, there exists more than one equivalent periodic point. Excluding for a moment the singular case of corner points, the pair of equivalent points on the boundary of the periodic cell have outward normal vectors in opposite directions. Hence the traction vectors, S_m , are defined by

$$S_m(x_n) = \Sigma_{mj}(x_n) n_j \quad (12)$$

and satisfy the following periodicity equation:

$$S_m(x_n) \mp S_m(x_n + l_n) e^{-ikn_j l_j}. \quad (13)$$

Thus the boundary conditions on the outer surfaces of the periodic cell are given by Eqs. (10) and (13). Because very few of the standard finite element programs in solid mechanics handle complex valued displacements, the displacement and other fields are split into real and imaginary parts. That is,

$$U_m(x_n) = U_m^{\text{Re}}(x_n) + i U_m^{\text{Im}}(x_n), \quad (14)$$

$$S_m(x_n) = S_m^{\text{Re}}(x_n) + i S_m^{\text{Im}}(x_n). \quad (15)$$

In doing this, Eq. (7) splits into the equations,

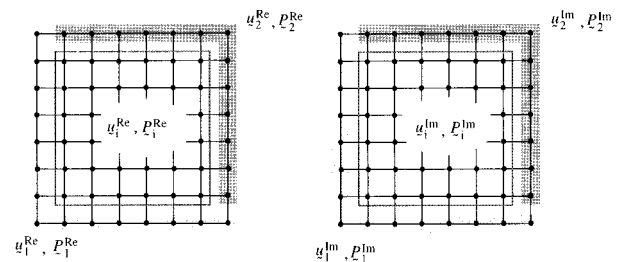


FIG. 1. Principle of the division and labeling of nodal displacements and nodal forces.

$$\Sigma_{ij,j}^{\text{Re}} + p\omega^2 U_i^{\text{Re}} = 0, \quad (16)$$

$$\Sigma_{ij,j}^{\text{Im}} + p\omega^2 U_i^{\text{Im}} = 0,$$

for the real and imaginary parts, respectively. Boundary conditions (10) and (13) transform into

$$U_m^{\text{Re}}(x_n) = U_m^{\text{Re}}(x_n + l_n) \cos(kn_j l_j) + U_m^{\text{Im}}(x_n + l_n) \sin(kn_j l_j), \quad (17)$$

$$U_m^{\text{Im}}(x_n) = U_m^{\text{Im}}(x_n + l_n) \cos(kn_j l_j) - U_m^{\text{Re}}(x_n + l_n) \sin(kn_j l_j)$$

and

$$S_m^{\text{Re}}(x_n + l_n) = -S_m^{\text{Re}}(x_n) \cos(kn_j l_j) + S_m^{\text{Im}}(x_n) \sin(kn_j l_j), \quad (18)$$

$$S_m^{\text{Im}}(x_n + l_n) = -S_m^{\text{Im}}(x_n) \cos(kn_j l_j) - S_m^{\text{Re}}(x_n) \sin(kn_j l_j).$$

B. Finite element formulation

Since the real and imaginary parts are uncoupled in Eq. (16), it is possible to solve the eigenvalue problem defined by Eqs. (16), (17), and (18) using two identical, unit cell shaped, finite element meshes—one for the real part and one for the imaginary part. If the boundaries of the two meshes are coupled by the displacement boundary conditions in Eq. (17), the boundary conditions for the tractions are fulfilled automatically due to the way that most standard finite element codes implement condition (17).

In order to highlight this, consider the two identical two-dimensional meshes in Fig. 1 representing a quadratic unit cell. The finite element formulation of Eq. (16) is

$$\left(\begin{bmatrix} [K] & 0 \\ 0 & [K] \end{bmatrix} - \omega^2 \begin{bmatrix} [M] & 0 \\ 0 & [M] \end{bmatrix} \right) \begin{bmatrix} \mathbf{u}_i^{\text{Re}} \\ \mathbf{u}_1^{\text{Re}} \\ \mathbf{u}_2^{\text{Re}} \\ \mathbf{u}_i^{\text{Im}} \\ \mathbf{u}_1^{\text{Im}} \\ \mathbf{u}_2^{\text{Im}} \end{bmatrix} = \begin{bmatrix} \mathbf{p}_i^{\text{Re}} \\ \mathbf{p}_1^{\text{Re}} \\ \mathbf{p}_2^{\text{Re}} \\ \mathbf{p}_i^{\text{Im}} \\ \mathbf{p}_1^{\text{Im}} \\ \mathbf{p}_2^{\text{Im}} \end{bmatrix}. \quad (19)$$

Here the vector \mathbf{u}^{Re} , the real part of the displacement, is partitioned into \mathbf{u}_i^{Re} , \mathbf{u}_1^{Re} , and \mathbf{u}_2^{Re} denoting the internal nodes, the nodes of set 1, and the nodes of set 2, respectively. The real parts of the corresponding nodal forces are labeled \mathbf{p}_i^{Re} , \mathbf{p}_1^{Re} , and \mathbf{p}_2^{Re} . The imaginary counterparts have the superscript “Im” instead of “Re.” The submatrices $[K]$ and $[M]$ are the stiffness and mass matrices, of a single mesh, respectively. Boundary conditions (17) have the following appearance:

$$\begin{bmatrix} \mathbf{u}_i^{\text{Re}} \\ \mathbf{u}_1^{\text{Re}} \\ \mathbf{u}_2^{\text{Re}} \\ \mathbf{u}_i^{\text{Im}} \\ \mathbf{u}_1^{\text{Im}} \\ \mathbf{u}_2^{\text{Im}} \end{bmatrix} = [Q] \begin{bmatrix} \mathbf{u}_i^{\text{Re}} \\ \mathbf{u}_2^{\text{Re}} \\ \mathbf{u}_i^{\text{Im}} \\ \mathbf{u}_2^{\text{Im}} \end{bmatrix}. \quad (20)$$

The constraint matrix $[Q]$ can be schematically written as

$$[Q] = \begin{bmatrix} [I] & 0 & 0 & 0 \\ 0 & [C] & 0 & [S] \\ 0 & [I] & 0 & 0 \\ 0 & 0 & [I] & 0 \\ 0 & -[S] & 0 & [C] \\ 0 & 0 & 0 & [I] \end{bmatrix}, \quad (21)$$

where $[C]$ and $[S]$ are diagonal block matrices containing the sine and cosine factors of Eq. (17). Substitution of Eq. (20) into (19) and premultiplication by $[Q]^T$ yields the following system of equations:

$$[Q]^T \left(\begin{bmatrix} [K] & 0 \\ 0 & [K] \end{bmatrix} - \omega^2 \begin{bmatrix} [M] & 0 \\ 0 & [M] \end{bmatrix} \right) [Q] \begin{bmatrix} \mathbf{u}_i^{\text{Re}} \\ \mathbf{u}_2^{\text{Re}} \\ \mathbf{u}_i^{\text{Im}} \\ \mathbf{u}_2^{\text{Im}} \end{bmatrix} = \begin{bmatrix} \mathbf{p}_i^{\text{Re}} \\ [C]\mathbf{p}_1^{\text{Re}} + \mathbf{p}_2^{\text{Re}} - [S]\mathbf{p}_1^{\text{Im}} \\ \mathbf{p}_i^{\text{Im}} \\ [C]\mathbf{p}_1^{\text{Im}} + \mathbf{p}_2^{\text{Im}} + [S]\mathbf{p}_1^{\text{Re}} \end{bmatrix}. \quad (22)$$

When a standard finite element code computes the eigenfrequencies and eigenmodes, the vector on the right-hand side of Eq. (22) is set to zero. In Eq. (22) this corresponds to an absence of body forces on the internal node set and the fulfillment of the traction boundary conditions in Eq. (18). In other words, the boundary conditions of Eq. (18) are automatically fulfilled if Eq. (17) is fulfilled.

Thus by having two identical finite element meshes and implementing the constraints of Eq. (17), the eigenfrequencies ω , which can be shown to be double eigenvalues, can be computed for any given wave number, k , and wave direction, n_j . This procedure makes it possible to compute the dispersion relation for the periodic material.

C. Phase and group velocity

When the dispersion relation is known two velocities may be calculated—the phase and group velocities. The phase velocity, c_p , is the speed with which a point of constant phase moves through the medium. If the eigenfrequency is known for a given wave number the components of the phase velocity is calculated according to

$$c_{pi} = \frac{\omega}{k} n_i. \quad (23)$$

The group velocity is the speed at which energy travels through the medium. The components of the group velocity vector, c_{gi} , are found from

$$c_{gi} = \frac{\partial \omega}{\partial k_i}. \quad (24)$$

Here, $k_i = kn_i$ are the components of the wave vector. Note that the direction of the group velocity is not necessarily the same as the direction of wave propagation. Following Kline an expression for the group velocity in terms of boundary displacements and boundary forces may be derived.³⁰ Begin by defining

$$\Psi_j = \frac{1}{T} \int_0^T \dot{u}_i(x_m, t) \sigma_{ij}(x_m, t) dt. \quad (25)$$

Here, a dot denotes derivation with respect to time and T is the period of the plane wave. Evaluated, this becomes

$$\Psi_j = \frac{\omega}{2} (U_i^{\text{Re}} \Sigma_{ij}^{\text{Im}} - U_i^{\text{Im}} \Sigma_{ij}^{\text{Re}}), \quad (26)$$

where U_i^{Re} and U_i^{Im} are defined as in Eqs. (4) and (14), and Σ_{ij}^{Re} and Σ_{ij}^{Im} are defined by Eq. (5) and the relation

$$\Sigma_{ij}(x_i) = \Sigma_{ij}^{\text{Re}}(x_i) + i \Sigma_{ij}^{\text{Im}}(x_i). \quad (27)$$

The time average of the total energy density, E , in a point can be written as

$$E = \frac{1}{T} \int_0^T \rho \dot{u}_i(x_m, t) \dot{u}_i(x_m, t) dt. \quad (28)$$

With the notation of Eqs. (4) and (14) this becomes

$$E = \frac{\omega^2}{2} \rho [U_i^{\text{Re}} U_i^{\text{Re}} + U_i^{\text{Im}} U_i^{\text{Im}}]. \quad (29)$$

Now the average power P per unit area with normal vector n_j may be written in terms of Ψ_j as

$$P = \frac{1}{\Gamma} \int_{\Gamma} \Psi_j n_j d\Gamma, \quad (30)$$

where Γ is a representative surface element. The average energy in a representative volume may be expressed as

$$E = \frac{1}{V} \int_V E dV, \quad (31)$$

where V is the representative volume.

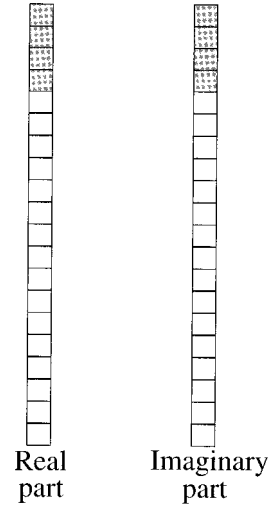


FIG. 2. The simple meshes used for the laminate. The shadowed elements denote material 1 and the unshadowed material 2.

For a periodic material the representative volume, V , and surface, Γ , may be defined from a single periodic cell. The component of the group velocity in the normal direction of Γ , n_i , then takes the value

$$c_{gi} n_i = \frac{V \int_{\Gamma} (U_i^{\text{Re}} S_i^{\text{Im}} - U_i^{\text{Im}} S_i^{\text{Re}}) d\Gamma}{\omega \Gamma \int_V \rho [U_i^{\text{Re}} U_i^{\text{Re}} + U_i^{\text{Im}} U_i^{\text{Im}}] dV}. \quad (32)$$

The right-hand side of Eq. (32) gives the ratio between average energy flux through the unit cell in the direction of the normal of the surface Γ and average total energy in the unit cell. Equation (32) is suitable for finite element computations. The integrals are then exchanged by sums, and U_i and S_i are taken as the nodal displacements and nodal forces, respectively.

II. EXAMPLES

A. Laminate

In order to certify the above presented method, dispersion relations for an elastic two phase laminate were computed using the standard finite element program ABAQUS³¹ and compared with the exact solution due to Sve. In the case of laminates the meshes were very simple. Two rows of 20 square eight-node biquadratic plain strain elements—one row for the real and imaginary parts, respectively—were used (see Fig. 2). In order to avoid false eigenfrequencies, the model should be as thin as possible in the direction of translation symmetry. In this case only one row of elements should be used. The value of the wave number, k , and the direction of wave propagation, n_i , was given and ABAQUS was used to compute the eigenfrequencies. The values of the material and geometric parameters used are found in Table I.

TABLE I. Material and geometric properties of the laminate. The density is denoted ρ , the relative thickness of a ply is denoted D , and λ and μ are Lamé's constants.

ρ_2 / ρ_1	μ_2 / μ_1	λ_1 / μ_1	λ_2 / μ_1	$D_1 / (D_1 + D_2)$	$D_2 / (D_1 + D_2)$
3	50	2.33	75	0.2	0.8

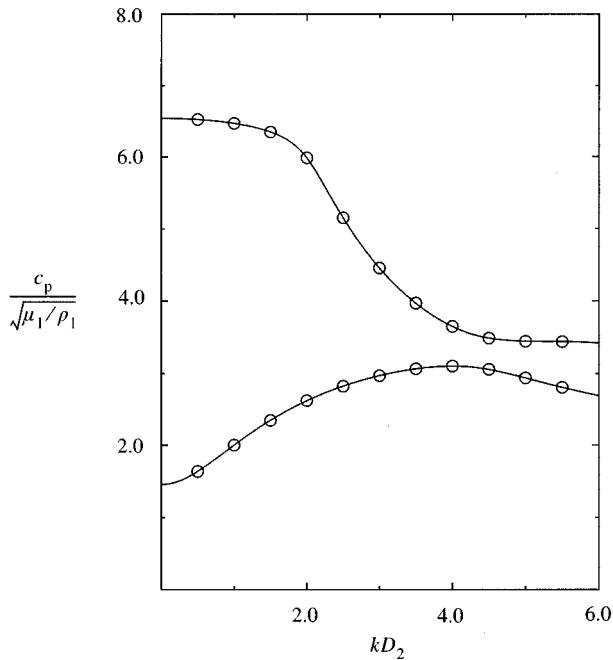


FIG. 3. Dimensionless phase velocity as functions of dimensionless wave number for the laminate. The wave vector and the normal of the plies make a 75-deg angle. The solid line is due to Sve (Ref. 15) and the circles (○) are the computed values.

Subscripts 1 and 2 refer to material 1 and 2, respectively. The density is denoted ρ , the relative thickness of a ply is denoted D , and λ and μ are Lamé's constants. As an example the results for wave propagation where the wave vector and the normal of the plies make a 75 degree angle is presented in Fig. 3. A dimensionless phase velocity is plotted as a function of a dimensionless wave number. The solid line is the relation found by Sve and the circles are points computed by use of ABAQUS. The difference between calculated and computed values was less than 0.1%. The comparison was made for several other wave vector angles and in all cases the agreement was equally good.

B. Hexagonal fiber composite

In order to assess the accuracy of Murakami and Hegemier's model, finite element computations were made on a hexagonally arranged fiber composite. The parameter values used correspond to the epoxy boron composite used by Murakami and Hegemier and are given in Table II. The unit cell was modeled using 416 eight-node brick elements in each mesh. The mesh used is shown in Fig. 4 (remember that two meshes have to be used although only one mesh is shown). Note that only one layer of elements is used in the direction

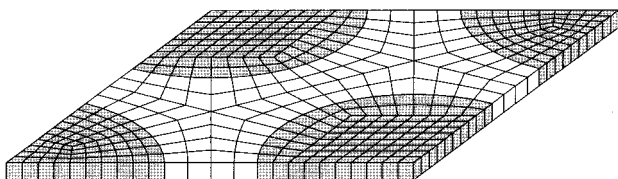


FIG. 4. The finite element mesh used for the fibrous composite.

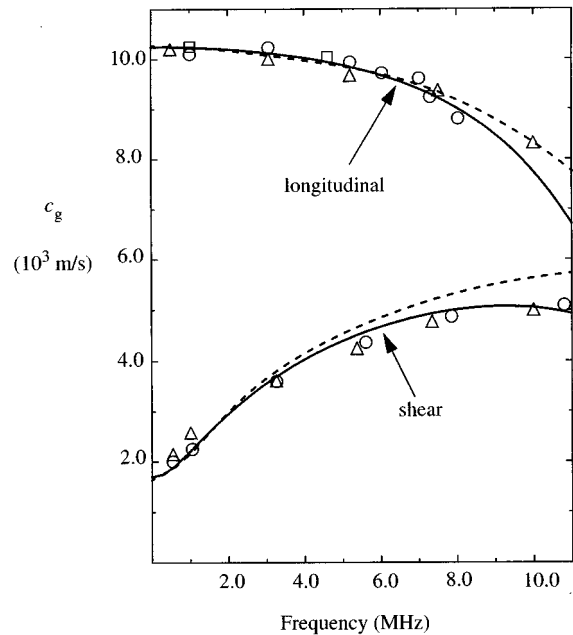


FIG. 5. Group velocity of wave guide modes as functions of frequency for the fibrous composite. Solid curve, computed values. Dashed curve, Murakami and Hegemier (Ref. 14). Symbols, Tauchert and Guzelsu (Ref. 1).

of translation symmetry. In order to check the convergence of the computed eigenfrequencies a few computations were also done for a mesh with roughly four times as many elements. The difference in group velocity between the coarser mesh that was used and the finer mesh was roughly one percent. Figure 5 shows a comparison between the computed dispersion relation (the solid curve), experiments done by Tauchert and Guzelsu (the symbols are the ones used in their work), and the dispersion relations due to Murakami and Hegemier (the dashed curve) for the so-called waveguide

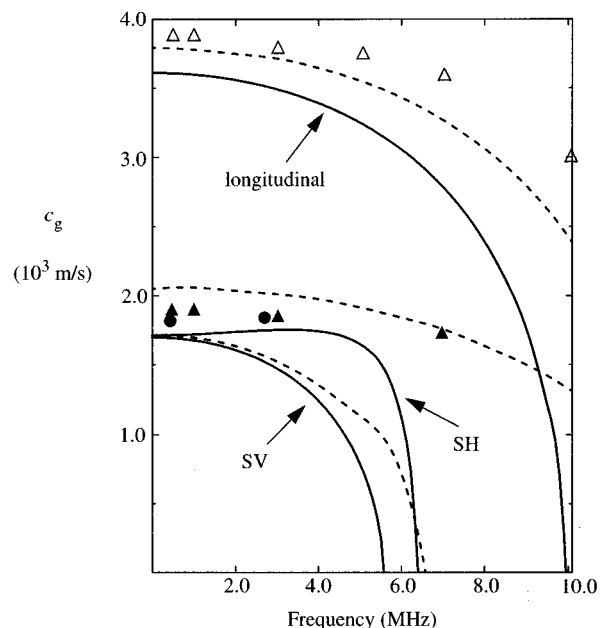


FIG. 6. Group velocity of wave reflect modes as functions of frequency for the fibrous composite. Solid curve, computed values. Dashed curve, Murakami and Hegemier (Ref. 14). Symbols, Tauchert and Guzelsu (Ref. 1).

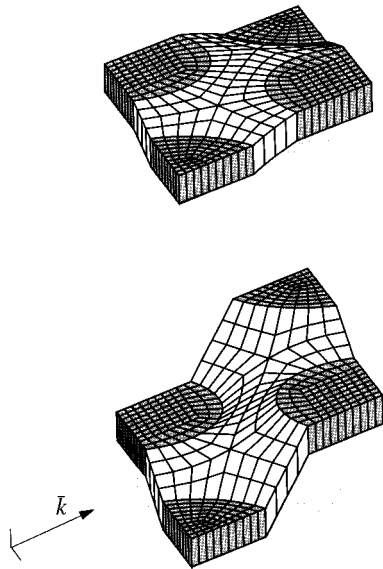


FIG. 7. An example of output from post-processing. The first mode (SV) for the wave reflect case at a frequency of 2 MHz.

case, i.e., the wave vector is directed along the fibers. Figure 6 shows a comparison for the wave reflect case, i.e., the wave vector is directed normal to the fibers.

A minor complication with ABAQUS is that the program does not include the mass matrix in Eq. (19) when asked to compute the constraint forces from the eigenmodes. Therefore Eq. (32) could not be used and the differentiation according to Eq. (24) had to be done numerically. Since the material is symmetric with respect to the direction of the wave vector in the two cases considered, the group velocity and the wave vector have the same direction. The group velocity is then calculated according to

$$c_{gi} = \frac{\partial \omega}{\partial k} n_i, \quad (33)$$

where k is the magnitude of the wave vector and n_i are the direction cosines of the wave vector. The derivation was done numerically by the central difference scheme.

Figure 7 shows an example of the output that may be obtained from a post-processor. The first eigenmode for the wave reflect case and a frequency of 2 MHz is showed. The shading, corresponding to a light source directly above the model, has been added for clarity.

III. DISCUSSION AND CONCLUSIONS

The good agreement between computed values and the exact solution (Fig. 3) in the laminate example certifies that the method presented will work for more complicated geometries as well.

TABLE II. Properties of the boron/epoxy fibrous composite.

	E -modulus E	Poisson's ratio ν	Mass density ρ	Volume fraction D
Boron	379.2 GPa	0.18	2682 kg/m ³	0.54
Epoxy	5.033 GPa	0.40	1261 kg/m ³	0.46

The results for the fibrous composite are shown in Figs. 5 and 6. The two lowest wave guide modes are shown in Fig. 5. The lowest mode corresponds to a shear wave and the other mode is a longitudinal wave. The model of Murakami and Hegemier is quite successful in predicting the behavior up to about 6 MHz, after which the model overestimates the group velocities. The experimental values lie closer to the computed group velocities, at least for the shear wave mode. In Fig. 6 the three lowest wave reflect modes are shown. The two lowest modes correspond to shear waves and the third mode is a longitudinal wave. The agreement between the model of Murakami and Hegemier and the presented computation is not as good as in the wave guide case. In fact, the model of Murakami and Hegemier and the computed values do not agree in the static limit (i.e., for $k=0$, which corresponds to zero frequency). Also, the model of Murakami and Hegemier predicts that the lowest mode is a horizontally polarized shear wave (SH mode) and that the next mode is a vertically polarized shear wave (SV mode). The computations, however, show that it is the other way around. Figure 7 shows the first eigenmode for the wave reflect case; as can be seen this is an SV mode. The experiments do not fit the computations as nicely in the wave reflect case as in the wave guide case, but the qualitative behavior is approximately the same. Tauchert and Guzelsu state that the lowest experimental group velocities were traveling SH waves, and the computed SH -wave group velocities lie closest to those points. The discrepancy between computed and experimental values could partly be due to the fact that the fibrous composite used by Tauchert and Guzelsu was not transversely isotropic, but rather it was a tetragonal material. It is notable that the model of Murakami and Hegemier in this case also overestimates the group velocities. It seems that the model by Murakami and Hegemier is more successful in predicting the behavior of the material for waves in the fiber direction than the behavior for waves normal to the fibers.

Based on the agreement between computations and theory for the laminate and the reasonable results for the fibrous composite, it is concluded that the method presented is useful for computations of dispersion relations for periodic materials. It should also work for other types of periodic structures such as plates and pipes with stiffeners.

ACKNOWLEDGMENTS

Financial support from the Swedish Research Council for Engineering Sciences (TFR) is gratefully acknowledged.

¹T. R. Tauchert and A. N. Guzelsu, "An experimental study of dispersion of stress waves in a fiber-reinforced composite," *J. Appl. Mech.* **39**, 98–102 (1972).

²C. W. Robinson and G. W. Leppelmeier, "Experimental verification of dispersion relations for layered composites," *J. Appl. Mech.* **41**, 89–91 (1974).

³H. J. Sutherland and R. Lingle, "Geometric dispersion of acoustic waves by a fibrous composite," *J. Compos. Mater.* **6**, 490–502 (1972).

⁴V. K. Kinra and V. Dayal, "Acoustic methods of evaluating elastic properties or, will the real Young's modulus please stand up?," in *Manual on Experimental Methods for Mechanical Testing of Composites*, edited by R. L. Pendleton and M. E. Tuttle (Elsevier Applied Science, London, 1989), Sec. VA, pp. 97–103.

- ⁵R. M. Christensen, *Mechanics of Composite Materials* (Krieger, Malabar, FL, 1991), p. 59.
- ⁶F. J. Sabina, V. P. Smyshlyaev, and J. R. Willis, "Self-consistent analysis of waves in a matrix-inclusion composite—I. Aligned spheroidal inclusions," *J. Mech. Phys. Solids* **41**, 1573–1588 (1993).
- ⁷V. P. Smyshlyaev, J. R. Willis, and F. J. Sabina, "Self-consistent analysis of waves in a matrix-inclusion composite—II. Randomly oriented spheroidal inclusions," *J. Mech. Phys. Solids* **41**, 1589–1598 (1993).
- ⁸R. Yang and A. K. Mal, "Multiple scattering of elastic waves in a fiber-reinforced composite," *J. Mech. Phys. Solids* **42**, 1945–1968 (1994).
- ⁹A. I. Beltzer and N. Brauner, "SH waves of an arbitrary frequency in random fibrous composites via the $K-K$ relations," *J. Mech. Phys. Solids* **33**, 471–487 (1985).
- ¹⁰A. I. Beltzer and N. Brauner, "The dynamic response of random composites by causal differential method," *Mech. Mater.* **6**, 337–345 (1987).
- ¹¹E. Sanchez-Palencia and A. Zaouie, *Homogenization Techniques for Composite Media*, Lecture Notes in Physics No. 272 (Springer-Verlag, Berlin, 1986).
- ¹²V. Z. Parton and B. A. Kudryavtsev, *Engineering Mechanics of Composite Structures* (CRC, Boca Raton, 1993).
- ¹³H. Murakami, A. Maewal, and G. A. Hegemier, "A mixture theory with a director for linear elastodynamics of periodically laminated media," *Int. J. Solids Struct.* **17**, 155–173 (1981).
- ¹⁴H. Murakami and G. A. Hegemier, "A mixture model for unidirectionally fiber-reinforced composites," *J. Appl. Mech.* **53**, 765–773 (1986).
- ¹⁵C. Sve, "Time-harmonic waves traveling obliquely in a periodic laminated medium," *J. Appl. Mech.* **38**, 477–482 (1971).
- ¹⁶H. Murakami, A. Maewal, and G. A. Hegemier, "Mixture theory for longitudinal wave propagation in unidirectional composites with cylindrical fibers of arbitrary cross section—II," *Int. J. Solids Struct.* **15**, 335–357 (1979).
- ¹⁷T. J. Delph, G. Hermann, and R. K. Kaul, "Harmonic wave propagation in a periodically layered, infinite elastic body: Plane strain, analytical results¹," *J. Appl. Mech.* **46**, 113–119 (1979).
- ¹⁸T. J. Delph, G. Hermann, and R. K. Kaul, "Harmonic wave propagation in a periodically layered, infinite elastic body: Plane strain, numerical results²," *J. Appl. Mech.* **47**, 531–537 (1980).
- ¹⁹S. B. Dong and R. B. Nelson, "On natural vibrations and waves in laminated orthotropic plates," *J. Appl. Mech.* **39**, 739–745 (1972).
- ²⁰A. H. Shah and S. K. Datta, "Harmonic waves in a periodically laminated medium," *Int. J. Solids Struct.* **18**, 397–410 (1982).
- ²¹S. K. Datta, A. H. Shah, R. L. Bratton, and T. Chakraborty, "Wave propagation in laminated composite plates," *J. Acoust. Soc. Am.* **83**, 2020–2026 (1988).
- ²²S. Minagawa and S. Nemat-Nasser, "On harmonic waves in layered composites," *J. Appl. Mech.* **44**, 689–695 (1977).
- ²³S. Minagawa, S. Nemat-Nasser, and M. Yamada, "Finite element analysis of harmonic waves in layered and fiber-reinforced composites," *Int. J. Numer. Methods Eng.* **17**, 1335–1353 (1981).
- ²⁴S. Minagawa, S. Nemat-Nasser, and M. Yamada, "Dispersion of waves in two-dimensional layered, fiber-reinforced, and other elastic composites," *Comput. Struct.* **19**, 119–128 (1984).
- ²⁵T. Naciri, P. Navi, and A. Ehrlacher, "Harmonic wave propagation in viscoelastic heterogeneous materials. Part I: Dispersion and damping relations," *Mech. Mater.* **18**, 313–333 (1994).
- ²⁶R. B. Nelson and P. Navi, "Harmonic wave propagation in composite materials," *J. Acoust. Soc. Am.* **57**, 773–781 (1975).
- ²⁷R. M. Orris and M. Petyt, "A finite element study of harmonic wave propagation in periodic structures," *J. Sound Vib.* **33**, 223–236 (1974).
- ²⁸P. Langlet, A.-C. Hladky-Hennion, and J.-N. Decarpigny, "Analysis of the propagation of plane acoustic waves in passive periodic materials using the finite element method," *J. Acoust. Soc. Am.* **98**, 2792–2800 (1995).
- ²⁹L. Brillouin, *Wave Propagation in Periodic Structures* (Dover, New York, 1953).
- ³⁰R. A. Kline, *Nondestructive Characterization of Composite Media* (Technomic, Lancaster, 1992).
- ³¹*ABAQUS User's Manual version 5.4* (Hibbit, Karlsson, and Sorensen, Inc., Pawtucket, RI, 1994).

Acoustical properties of irregular and fractal cavities

B. Sapoval, O. Haeberlé, and S. Russ

Laboratoire de Physique de la Matière Condensée, Ecole Polytechnique, C.N.R.S., 91128 Palaiseau Cédex, France

(Received 4 December 1996; accepted for publication 23 May 1997)

Acoustical properties of irregular cavities described by fractal shapes are investigated numerically. Geometrical irregularity has three effects. First, the low-frequency modal density is enhanced. Second, many of the modes are found to be localized at the cavity boundary. Third, the acoustical losses, computed in a boundary layer approximation, are increased proportionally to the perimeter area of the resonator and a mathematical fractal cavity should be infinitely damped. We show that localization contributes to increase the losses. The same considerations should apply to acoustical waveguides with irregular cross section. © 1997 Acoustical Society of America. [S0001-4966(97)00210-5]

PACS numbers: 43.20.Ks [ANN]

INTRODUCTION

Geometrical irregularities appear in many natural and artificial systems and their vibrational properties are of general interest. How trees respond to wind, and how sea waves depend on the topography or geometrical structure of the coasts and breakwaters are largely unanswered questions. The emergence of fractal geometry has been a significant breakthrough in the description of strong geometrical irregularity and its associated physical properties.^{1,2} The fractal language permits discussion of this question in a well-defined and documented geometrical framework. Not only does fractal geometry permit a description of strong statistical irregularity, but it also allows consideration of the deterministic fractals as simple models for extreme geometrical disorder. When the physical properties of the objects that we consider are due to the hierarchical character of their geometry, then their physical properties can be studied on deterministic fractal objects.² This is, for example, the case for self-similar electrodes where the study of deterministic systems is readily applicable to random self-similar structures.³

The three main properties of resonators are their spectrum or modal distribution, the spatial distribution of the modes (which may exhibit localization or confinement effects), and their damping. Current empirical knowledge about waves and resonators indicates that a perturbation of a resonator geometry may strongly modify the quality factor of resonances. It has already been shown in the case of “mass fractals” vibrations (the so-called fractons modes) that geometrical irregularity has a strong effect on damping.⁴

We address here the same general question for acoustical cavities: Do the geometrical irregularities play a role in the losses and why? We believe that the study of fractal resonators can help to understand the acoustical properties of irregular cavities in general, with possible application to room acoustics, acoustical waveguides, and anechoic chambers. The problem of the asymptotic (high-frequency) density of states in fractal resonators has already been studied from a mathematical point of view.⁵⁻⁹

Experimental observation and numerical investigation of the low-frequency vibrations of fractal drums are reported in

Refs. 10 and 11. The drum geometries were generated by iterative transformation of a square initiator, as shown in Fig. 1. The figure shows the contour of prefractals at generation $\nu=0$, $\nu=1$, and $\nu=2$. Systems in which the perimeter is only fractal, like a fractal drum or a fractal cavity, are called “surface fractals” and their vibrations are called “fractinos.” In the case of the fractal drum, the vibrations obey the Dirichlet boundary condition and are named Dirichlet fractinos.^{10,11}

Eigenmodes of 2-D prefractal resonators using Neuman boundary conditions, i.e., Neumann fractinos, have also been studied recently.^{12,13} This renders possible the study of acoustic modal density and damping in the 3-D prefractal cavities shown in Fig. 1. This is the purpose of the present work.

We show on two specific examples that the low-frequency modal distribution is strongly modified and that the damping is increased by a factor which depends of the degree of irregularity of the boundary. We also show that the localization effects found by Russ *et al.* contribute even more to increase the damping. The losses are computed from the spatial distribution of the modes as we recall below.

I. QUALITY FACTOR AND AMPLITUDE DISTRIBUTION

The quality factor Q_N of a resonator for a mode N is the ratio of the stored energy to the losses per cycle W_N

$$Q_N = 2\pi E_N / W_N. \quad (1)$$

The quality factor characterizes the ability of the resonator to accumulate reactive energy for a given power input. It also determines the life time $Q_N \omega_N^{-1}$ of the oscillation when no power source is present.

In this work we restrict to linear acoustics and consider the limit of “very” weak losses so that the amplitude distribution is well-approximated by the zero-loss cavity modes.¹⁴⁻¹⁶ We consider an eigenmode N at frequency ω_N with a pressure distribution:

$$p_N(x, y, z, t) = p_0 V^{1/2} \Psi_N(x, y, z) \cos(\omega_N t). \quad (2)$$

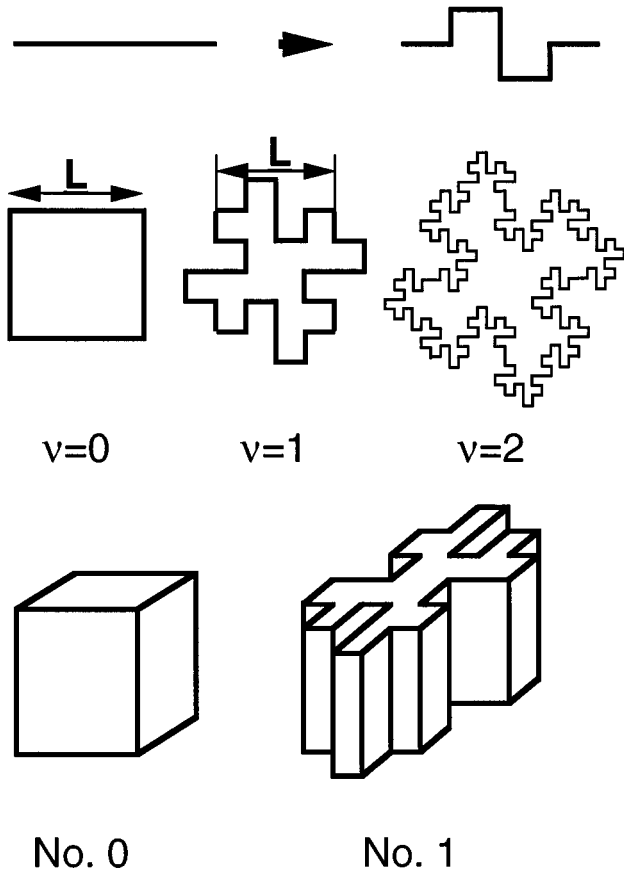


FIG. 1. System geometry. Top: Generator of the fractal geometry. Middle: Cross sections of the prefactal cavities under study. The area is conserved through the iteration process. Bottom: prefactal cavities of generation 0 (cubic cavity) and 1.

Here p_0 is the peak acoustic pressure and V is the volume of the cavity. Calling c the sound velocity, the pressure obeys the Helmholtz equation $\Delta P = (1/c^2) \partial^2 P / \partial t^2$ with the Neumann boundary conditions $\partial P / \partial n = 0$. This condition corresponds to a perfectly reflecting surface with no phase change. Eigenmodes $\Psi_N(x, y, z)$ satisfy the eigenvalue equation $\Delta \Psi_N = -(\omega_N^2/c^2) \Psi_N$. We normalize $\Psi_N(x, y, z)$ in the volume V by

$$\int \int \int_V dv \Psi_N^2(x, y, z) = 1. \quad (3)$$

The maximum elastic energy or kinetic energy is

$$E_N = p_0^2 V \int \int \int_V dv (c^2 \rho)^{-1} \Psi_N^2(x, y, z) = V p_0^2 / c^2 \rho, \quad (4)$$

where ρ is the density of the gas.

Acoustical losses in a rigid cavity are due to heat conduction and viscous dissipation. In the bulk, these losses are small at audio frequencies and are neglected here.¹⁴⁻¹⁶ Energy dissipation takes place at the cavity walls on a small boundary layer with a thickness of order 10^{-4} cm.^{15,17} To calculate the losses, it is convenient to replace the rigid walls by walls with a small admittance and to consider that there are no losses in the fluid. We are restricted here to prefRACTALS in which the smaller flat element (smaller geometrical cutoff) is larger than this thickness.¹⁸ Our goal is to identify the

influence of the geometrical irregularity; we consider that our walls present a small but finite specific admittance $\epsilon(\omega)$. This admittance could be that of the real fluid boundary layer, or more simply, the admittance of a suitable sound absorbing material of small thickness covering the lateral cavity walls.

The energy dissipation is the total outflow of energy from the boundary. In the case of weak losses, the power L_N dissipated at the cavity boundaries can be expressed as a function of the zero-loss amplitude distribution by

$$L_N = V(p_0^2/\rho c) \int \int_S ds |\Psi_N^2(x, y, z)| \text{Re } \epsilon(\omega_N). \quad (5)$$

The quality factor of the mode N is given by

$$1/Q_N = [\text{Re } \epsilon(\omega_N)](c/\omega_N) \int \int_S ds |\Psi_N^2(x, y, z)|. \quad (6)$$

It can then be written $Q_N = 2\pi(\Lambda_N/\lambda_N)/[\text{Re } \epsilon(\omega_N)]$, where λ_N is the wavelength and

$$1/\Lambda_N = \int \int_S ds |\Psi_N^2(x, y, z)|. \quad (7)$$

Then, the higher the amplitude on the boundary, the lower the value of the length Λ_N and the lower the quality factor. Because our purpose is to study the dependence of the damping on the geometry, we have to know the amplitude distribution to compute this integral. This paper is organized as follows: We first recall briefly the numerical method.^{4,12} We then discuss the low-frequency modal density, the localization effects, and finally the effect of geometry on damping.

II. SOLUTION OF HELMHOLTZ EQUATION

As we work on cylindrical cavities with constant irregular cross sections, the variable z can be separated and the eigenfunctions takes the form

$$\Psi_N(x, y, z) = (2/L_z)^{1/2} \cos(m\pi z/L_z) \Psi_n(x, y), \quad (8)$$

with $m=0, 1, 2, \dots$ [for $m=0$, $\Psi_N(x, y, z) = L_z^{-1/2} \Psi_n(x, y)$]. The function $\Psi_n(x, y)$ satisfies the two-dimensional eigenvalue equation $\Delta \Psi_n = -(\omega_n^2/c^2) \Psi_n$ and is normalized over the cross section. The eigenfrequencies ω_N are given by

$$\omega_N^2 = \omega_n^2 + (m\pi c/L_z)^2. \quad (9)$$

Our numerical method to compute $\Psi_n(x, y)$ and ω_n^2 is to consider, instead of the Helmholtz equation, the time-dependent Fourier or diffusion equation:

$$D \Delta \Psi = \partial \Psi / \partial t. \quad (10)$$

In the Helmholtz equation, the variable is the acoustical pressure, i.e., a positive or negative departure for the normal fluid pressure. In Eq. (10), Ψ represents a concentration of diffusing particles, or a departure to a constant concentration, which in our case can also be either positive or negative. Equivalently, Eq. (10) is the Fourier heat equation and the

variable Ψ could represent positive or negative variations of the temperature around a constant value.

The general time-dependent solution of this equation is a combination of *real* exponentials of the form $\Psi = \sum_n c_n \Psi_n(x, y) \exp(-t/\tau_n)$, where τ_n satisfies an equivalent eigenvalue equation $\Delta \Psi_n = -(D\tau_n)^{-1} \Psi_n$ with the same boundary condition. In the diffusional approach, the Neumann boundary condition $\partial \Psi / \partial n = 0$ means that diffusing particles are reflected at the boundary so there exists no net flux across the surface. Here it corresponds to the fact that the gas velocity is null on the walls.

The method is then to numerically compute the time-dependent solution of Eq. (10): Starting with an arbitrary initial function $z_0(x, y, t=0)$ the system will converge naturally to a function proportional to $\exp(-t/\tau_0) \Psi_0(x, y)$ yielding the first eigenstate $\Psi_0(x, y)$, the first eigenvalue $1/\tau_0$, and ω_0 through the correspondence $\omega_0^2/c^2 = 1/D\tau_0$. To compute the next state, one starts with a new trial function which is orthogonal to $\Psi_0(x, y)$. This new distribution converges with a time constant τ_1 to the next eigenfunction with non-zero initial weight, namely $\Psi_1(x, y)$. The procedure is then iterated and the states are obtained sequentially, by orthogonalization of the $(n+1)$ th initial distribution to the n previously computed eigenfunctions, thus converging to the $(n+1)$ th mode. The numerical implementation uses a finite difference method on a discretized system. It is discussed in detail in Refs. 4 and 12. One can find in these papers a discussion of the effects of the finite mesh size, of the convergence problems, and of roundoff errors on final precision.

III. MODAL DENSITY AND LEVEL SPACING

Two quantities play a dominant role in resonators studies: the density of states or modal density and the level spacing.¹⁴⁻¹⁶ Here we deal with the cavities obtained by ‘‘fractalization’’ of the cross section of a cube with side L .

The computation of the low-frequency modes for the 2-D systems shown in Fig. 1 is presented in Ref. 12. To obtain the eigenvalues ω_N^2 of the 3-D cavity, we have to combine the 2-D values ω_n^2 with the vertical modes using Eq. (9). We call $\omega_{n,\max}^2$ the largest eigenvalue that we have computed for a 2-D system. Some combinations of ω_n^2 with $(m\pi c/L_z)^2$ can give $\omega_N^2 \geq \omega_{n,\max}^2$. The 3-D modal density can therefore be exactly computed only for $\omega_N^2 \leq \omega_{n,\max}^2$. With 234, 240, and 214 computed states for systems 0, 1, and 2, we obtain, respectively, the first 2652, 2704, and 2329 modes of the corresponding cavities.

The vibrating modes of a cube of side L are labeled by the number $\mu, \mu',$ and μ'' of half-wavelengths in the x, y, z directions [with $\mu, \mu', \mu'' = 0, 1, 2, \dots$, and eigenvalues $\omega_{\mu,\mu',\mu''}^2 = (\pi^2 c^2/L^2)(\mu^2 + \mu'^2 + \mu''^2)$]. We use in the following a reduced frequency $\Omega_N = \Omega_{n,m} = \omega_{n,m}/\omega_{1,0,0}$, where $\omega_{1,0,0} = \pi c/L$ is the fundamental frequency of the cubic cavity. For the cube we then have $\Omega_{\mu,\mu',\mu''}^2 = (\mu^2 + \mu'^2 + \mu''^2)$.

The numerical results for the integrated modal density for the three cavities (with the same volume L^3) are shown in Fig. 2. They are to be compared with the high-frequency

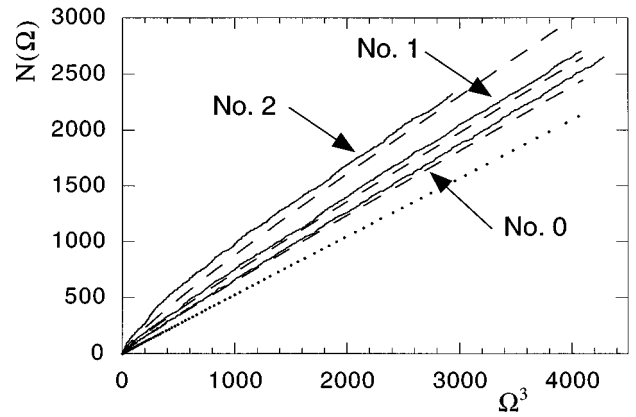


FIG. 2. Integrated modal density for cavities 0, 1, and 2. The dotted line represents the Weyl leading term. Dashed lines represent the Weyl approximation of Eq. (11).

Weyl approximation $N(\omega) = (1/6\pi^2)V(\omega/c)^3 + (1/16\pi) \times S(\omega/c)^2$, which writes, with our reduced frequency units, as

$$N(\Omega) = (\pi/6)\Omega^3 + (\pi/16)(S/L^2)\Omega^2, \quad (11)$$

where S is the total area of the cavity.¹⁹ For cavities 0, 1, and 2 the value of S is, respectively, equal to $6L^2$, $10L^2$, and $18L^2$.

In Fig. 2 the dotted line represents the Weyl leading term $(\pi/6)\Omega^3$ and the dashed lines represent Eq. (11) for the three cavities. The low-frequency modal density is notably increased by the irregularity. The high-frequency Weyl approximation still gives a good estimation of the modal density. Besides the net increase of the modal density due to increased fractalization one observes oscillations.^{9,12,13} These oscillations are due to the existence of a number of degenerate or quasi-degenerate states in our particular deterministic 2-D systems as explained in Ref. 12. These oscillations should not exist in irregular cavities where the feature sizes along the frontier are different or random.

The level spacing is modified in two ways. First, the increase in the modal density reduces the level spacing. Second, as discussed in Ref. 12, the pseudo-chaotic behavior of the 2-D systems induces a partial level repulsion. (This effect could be partially smeared out in 3-D.) These two facts should be reinforced by an increased irregularity.

IV. LOSSES IN PREFRACTAL CAVITIES

In order to selectively study the influence of the geometry on the losses, we consider in the following that the lower and upper surfaces of the cavities have infinite impedance. The losses are then restricted to the lateral surfaces.

Two different situations occur, depending on the nature of the modes, whether trivial modes or higher-order modes. For the trivial modes which correspond to the state $n=0$ of the 2-D problem for which $\Psi_{n=0}(x, y) = 1/L$, integral (7) increases proportionally to the perimeter. These modes are then damped proportionally to the length of the perimeter of an horizontal cross section. Then a prefractal of generation ν presents losses which are 2^ν times larger than the cubic cavity, at least for the lower fractal generations. In our simpli-

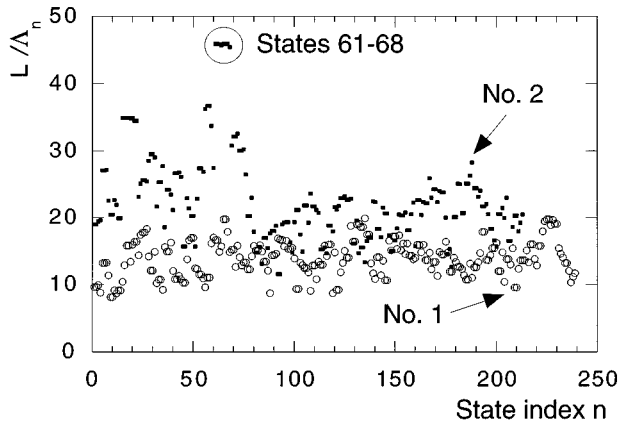


FIG. 3. Power dissipation, as measured by L/Λ_N , for the modes with $m=0$ of the three cavities in a boundary layer approximation. The dissipation is roughly proportional to the length of the perimeter. Some modes exhibit very high losses. For a cubic cavity, the losses take two different values. If $\mu=0, \mu' \neq 0$ (or $\mu \neq 0, \mu' = 0$), $L/\Lambda_N=6$. If $\mu \neq 0, \mu' \neq 0$, $L/\Lambda_N=8$.

fied framework a mathematical fractal would present infinite losses for all these modes as far as our model for the damping still holds. Although somewhat trivial, this statement is important and confirms the influence of fractal geometry on damping. Really, for high enough generation, the smaller cutoff would become smaller than the boundary layer and the problem has to be reconsidered.

More interesting are the higher-order modes ($n \neq 0$) which are of two types: those with $m=0$ and those with $m \neq 0$. If $m=0$ the integral in Eq. (7) factorizes as $ds=Ldl$, where dl is the differential element along the perimeter of a horizontal cross section of the cavity. For these modes the integral for the losses takes the form

$$1/\Lambda_N = \int_{\text{perimeter}} dl |\Psi_n^2(x,y)|. \quad (12)$$

If $m \neq 0$, the integral in Eq. (7) factorizes as $ds=(L/2)dl$ and the losses are simply smaller by a factor of 2 than those obtained from Eq. (12). The integral in Eq. (12) is the quantity that we actually compute from the knowledge of the amplitude distribution of the 2-D Neumann fractinos.

The results are shown in Fig. 3. For prefractal cavities the results indicate that the power dissipation [for constant $\epsilon(\omega)$] is increased by the irregularity of the frontier in a manner which is roughly proportional to the length of the perimeter, *as for the trivial modes*. For a few states, the prefractal systems exhibit still higher losses; for example, see states 61–68 of cavity No. 2. The higher losses for these particular states are due, as shown below, to the localization of these states in small regions near the cavity walls.

V. RELATION BETWEEN LOCALIZATION AND LOSSES

In this section we discuss why the confinement of a vibration in a restricted part of the cavity near the boundary increases the damping. The localization characterizes the irregular distribution of the vibration amplitude and was studied in Ref. 12. It was found that a number of modes were confined at the boundary, the amplitude the inner part of the

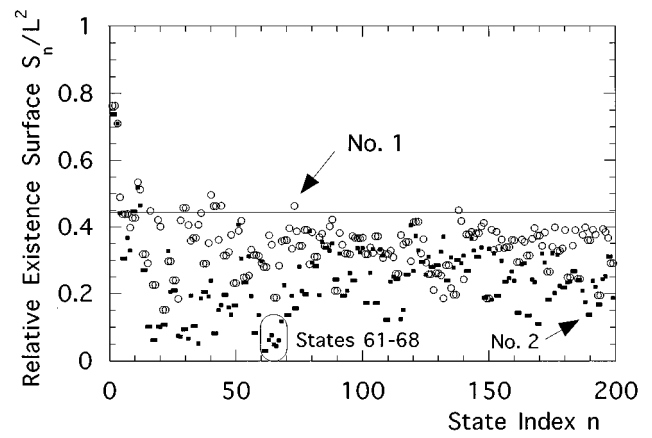


FIG. 4. Relative existence surface S_n/L^2 for the modes ($n \neq 0, m=0$). The localization surface decreases with the fractal generation. Some modes are strongly localized, e.g., modes 61–68 of cavity No. 2. The horizontal line at $S_n/L^2=4/9$ corresponds to the modes of the square.

resonators being small. To characterize mathematically the localization or the confinement of each mode Ψ_n , we compute the “existence surface” S_n defined by Thouless as²⁰

$$S_n = \left[\int dx dy |\Psi_n|^4 \right]^{-1}. \quad (13)$$

If we find that S_n is significantly smaller than the surface L^2 of the cross section, we say that this particular mode is “localized.” Note that for the delocalized cosine functions of the square system, the value of the relative occupation surface is $S_n/L^2=4/9 \approx 0.44$ for all modes.

The values of the relative existence surface S_n/L^2 for our geometries are shown in Fig. 4. Apart from the very first states, the existence surface is only a fraction of the total surface of the resonator. Most important, the tendency to localization is increased by the irregularity of the frontier. For generation 1 the average $\langle S_n/L^2 \rangle$ over the first 200 lower states was found to be equal to 0.35. For generation 2, the average $\langle S_n/L^2 \rangle$ over the 200 states that we have computed is equal to 0.24. The highest degree of localization for this system is equal to 0.031 for the degenerated modes $n=61,62$. One should note that our systems have a rotation degeneracy which has the effect of increasing the existence volume. Without any symmetry the localization surface would be approximately four times smaller.

In Fig. 5 we show the amplitude distribution of a delocalized ($n=4$) and of a localized mode ($n=16$). The spatial location of confined modes is linked to the Neumann boundary condition for which the boundary region is free to vibrate. Eigenmodes can then have a maximum amplitude at the boundary. The confinement is a weak localization effect which does not occur for all states. When the fractal character of the frontier increases, i.e., from one prefractal generation to the next, we find more and more of these localized states. This is an important property of the Neumann modes.¹² Qualitatively, the more irregular and winding the boundary, the more localized the Neumann fractinos. We expect a similar behavior for systems which are irregular in the three spatial directions.

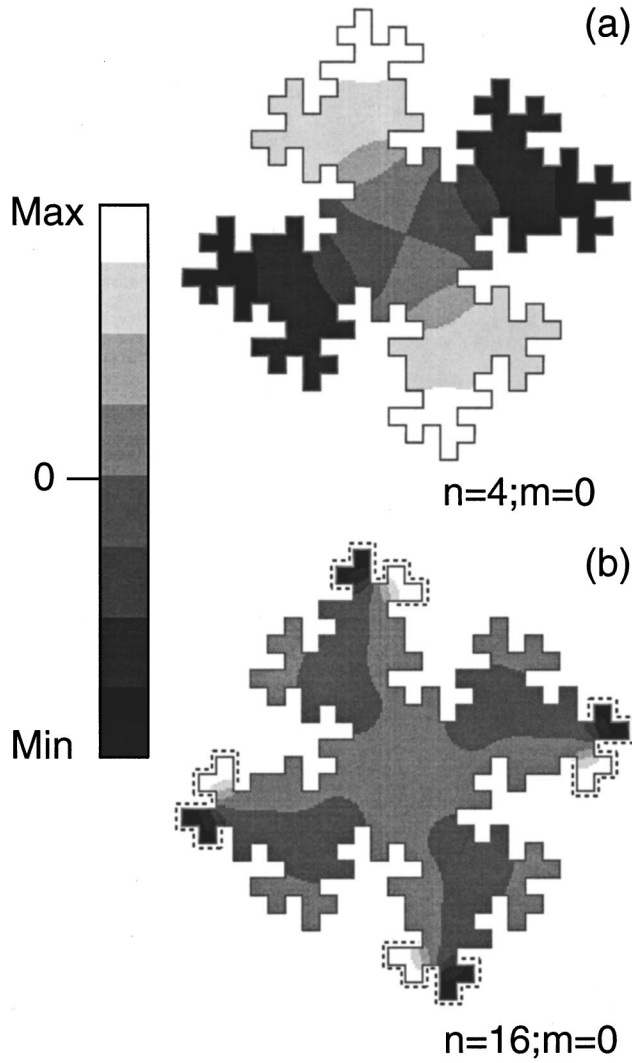


FIG. 5. Two particular modes of the prefractal cavity No. 2. (a) Mode $n=4$, $m=0$; (b) mode $n=16$, $m=0$. The amplitudes are indicated by different gray levels. Black and white regions stand for extremum positive and negative pressures. The gray tones stand for low pressures. Mode (a) is an example of delocalized state, while mode (b) is an example of localized state. Localization occurs at the cavity boundary. The dashed line indicates the perimeter L_p of the zone where the mode is confined. It is also the region where the energy is dissipated.

The effect of localization is to enhance locally the amplitude of the vibration at the cavity walls in the region where the energy is dissipated. There exists a correlative increase of the integral in Eq. (12). If, in a very crude approximation, one considers the mode as constant over its existence surface and zero outside, its amplitude is of order $S_n^{-1/2}$. Integral (12) gives a value

$$\Lambda_N^{-1} \cong S_n^{-1} L_p, \quad (14)$$

where L_p is the *perimeter* of the zone where the states really exist.

Consider for instance mode $n=16$, shown in Fig. 5(b). Its existence volume is approximately given by the surface of the black and white regions: $S_n \cong 4 \times 8 (L/16)^2 = L^2/8$. The perimeter of the zone where the amplitude is large, as indicated by the dashed contour in the figure, is of order $L_0 \cong 4 \times 15 (L/16)$ and from Eq. (14) $L/\Lambda_N \cong 30$. For this mode the

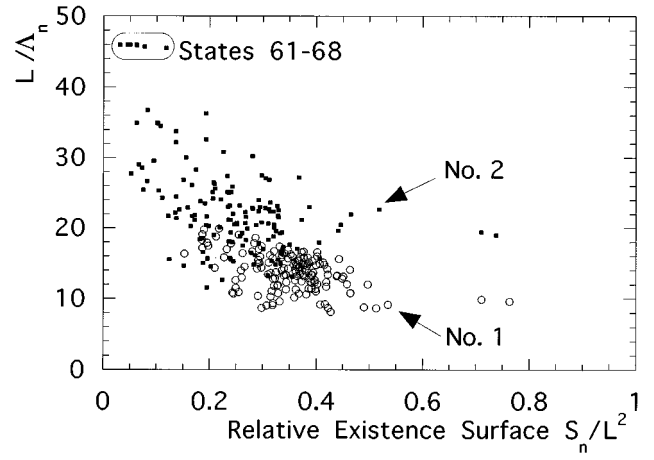


FIG. 6. Dissipation versus localization. The losses increase from one prefractal generation to the next, while the localization volume decreases. States 61–68 of cavity No. 2 which are strongly localized have the largest losses.

numerical value is $L/\Lambda_N = 35$, in good agreement with our crude approximation. This approximation also applies to the strongly localized states 61–68 of system No. 2. These states, which are discussed in Ref. 12, have the highest losses.

The power dissipation as a function of the relative existence surface is shown in Fig. 6. In spite of a strong dispersion, the global trend is indeed an increase of the losses with irregularity and localization.

Equation (14) is of extreme importance because it shows that for a given localized mode, if one locally increases the perimeter, the losses are increased correspondingly. It means that a mathematical fractal would also exhibit infinite damping for these higher-order modes (with the same restrictions than above).

The quality factor for a mode N can be written in our reduced units:

$$Q_N = \pi(\Omega_N \Lambda_N / L) / [\text{Re } \epsilon(\omega_N)]. \quad (15)$$

We have plotted in Fig. 7 the numerical values of the factor

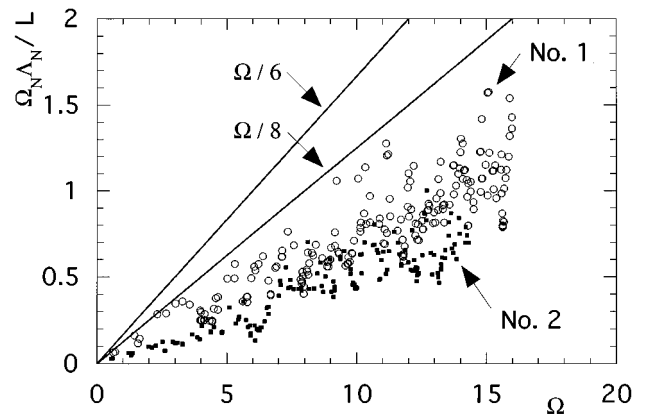


FIG. 7. Quality factor, measured by $\Omega_N \Lambda_N / L$, of the low-frequency modes with $m=0$ as a function of the reduced frequency Ω . For the cube the values of $\Omega_N \Lambda_N / L$ are equal to $\Omega_N/6$ for the modes $\mu=0$, $\mu' \neq 0$ (or $\mu \neq 0$, $\mu' = 0$) and are equal to $\Omega_N/8$ if $\mu \neq 0$, $\mu' \neq 0$. This is indicated by the two lines. The higher the geometrical irregularity, the lower the quality factors.

$\Omega_N \Lambda_N / L$ as a function of the reduced frequency Ω_N for our three cavities. One observes that for all frequencies the irregular cavities present lower quality factors than the cube. Despite the dispersion, increasing the irregularity induces a diminution of the quality factor.

VI. CONCLUSION

We have studied numerically the modal density, the localization, and the losses of acoustical modes in cavities with prefractal shapes. The modal density is enhanced by the irregularity of the boundary. Consequently, the level spacing decreases and becomes more regular. Acoustical losses have been studied in a boundary layer model and have been found to increase with irregularity. As far as our simplified model still applies, a mathematical fractal cavity would present an infinite damping. We have established a simple correspondence between localization and losses. These results confirm in a well-established physical frame the suggestion that fractal resonators present specific damping properties. Note that self-affine geometries¹ could even be more efficient than self-similar geometries in increasing the resonator perimeter, therefore the damping.

The same physical effects should appear in the propagation of sound waves in acoustical waveguides. Neglecting the anisotropy effects, the attenuation length for the acoustic energy of a propagating wave is of order $\Lambda_N / \text{Re}(\epsilon)$. Therefore, the data in Fig. 3 can be used to estimate the attenuation in fractal waveguides. Because of the localization, it should be possible to propagate higher-order localized modes in different regions of such an irregular waveguide with a small interference between these modes. Some of these effects could also exist in electromagnetic waveguides.

Further studies are needed to understand the influence of fractal geometry on ray acoustics which corresponds to the high-frequency limit of our problem.

Several of these results may be of interest for room acoustics. An increased low-frequency modal density could be favorable. On the other hand, localization may have negative consequences. Although our results on damping were obtained in the weak losses case, they can be considered a rationale to better understand the dependence of properties of anechoic chambers on geometry.

ACKNOWLEDGMENTS

One of us (SR) has benefited from the E. E. C. program ‘‘Human Capital and Mobility.’’ The computation was per-

formed at the ‘‘Institut du développement et des ressources en informatique scientifique’’ (IDRIS) in Orsay, France.

- ¹B. B. Mandelbrot, *The Fractal Geometry of Nature* (Freeman, San Francisco, 1982).
- ²B. Sapoval, *Fractals* (Aditech, Paris, 1990); *Universalités et Fractales* (Flammarion, Paris, 1997).
- ³B. Sapoval, ‘‘General formulation of Laplacian transfer across irregular surfaces,’’ *Phys. Rev. Lett.* **73**, 3314–3316 (1994).
- ⁴S. Russ and B. Sapoval, ‘‘Anomalous viscous damping of vibrations of fractal percolation clusters,’’ *Phys. Rev. Lett.* **73**, 1570–1573 (1994). For a review on fractons, see T. Nayama, K. Yakubo, and R. Orbach, ‘‘Dynamical properties of fractal networks: scaling, numerical simulations, and physical realizations,’’ *Rev. Mod. Phys.* **66**, 381–443 (1994).
- ⁵M. V. Berry, ‘‘Distribution of modes in fractal resonators,’’ in *Structural Stability in Physics*, edited by W. Guttinger and H. Elkeimer (Springer-Verlag, Berlin, 1979), pp. 51–53.
- ⁶M. L. Lapidus, ‘‘Fractal drum, inverse spectral problems for elliptic operators and a partial resolution of the Weyl-Berry conjecture,’’ *Trans. Am. Math. Soc.* **325**, 465–529 (1991), and references therein.
- ⁷J. Brossard and R. Carmona, ‘‘Can one hear the dimension of a fractal,’’ *Commun. Math. Phys.* **104**, 103–122 (1986).
- ⁸M. L. Lapidus and C. Pomerance, ‘‘The Riemann zeta-function and the one dimensional Weyl-Berry conjecture for fractal drums,’’ *Proc. London Math. Soc.* **3**, 41–69 (1993).
- ⁹J. Fleckinger, M. Levitin, and D. Vassiliev, ‘‘Heat equation on the triadic von Koch snowflake: Asymptotic and numerical analysis,’’ *Proc. London Math. Soc.* **71**, 372–396 (1995).
- ¹⁰B. Sapoval and Th. Gobron, ‘‘Vibrations of strongly irregular or fractal resonators,’’ *Phys. Rev. E* **47**, 3013–3024 (1993).
- ¹¹B. Sapoval, Th. Gobron, and A. Margolina, ‘‘Vibrations of fractal drums,’’ *Phys. Rev. Lett.* **67**, 2974–2977 (1991).
- ¹²S. Russ, B. Sapoval, and O. Haeberlé, *Phys. Rev. E* **55**, 1413 (1997).
- ¹³Y. Hobiki, K. Yakubo, and T. Nakayama, ‘‘Spectral characteristics in resonators with fractal boundaries,’’ *Phys. Rev. E* **54**, 1997–2004 (1996).
- ¹⁴P. M. Morse and K. Uno Ingard, *Theoretical Acoustics* (Princeton U. P., Princeton, 1968).
- ¹⁵A. D. Pierce, *Acoustics: An Introduction to Its Physical Principles and Applications* (McGraw Hill, New York, 1981).
- ¹⁶M. Bruneau, *Introduction aux théories de l’acoustique* (Université du Maine éditeur, Le Mans, 1983).
- ¹⁷M. Bruneau, C. Garing, and H. Leblond, ‘‘Quality factor and boundary-layer attenuation of low order modes in acoustic cavities,’’ *J. Phys. (Paris)* **46**, 1079–1085 (1985).
- ¹⁸D. L. Koch, ‘‘Attenuation of compressional sound waves in the presence of a fractal boundary,’’ *Phys. Fluids* **30**, 2922–2927 (1987).
- ¹⁹H. P. Baltes and E. R. Hilf, *Spectra of Finite Systems* (BI Wissenschaftsverlag, Vienna, 1976).
- ²⁰D. J. Thouless, ‘‘Electrons in disordered systems and the theory of localization,’’ *Phys. Rep.* **13**, 93–142 (1974).

Helmholtz equation-least-squares method for reconstructing the acoustic pressure field

Zhaoxi Wang^{a)} and Sean F. Wu

Department of Mechanical Engineering, Wayne State University, Detroit, Michigan 48202

(Received 15 August 1995; revised 27 April 1997; accepted 15 May 1997)

A method using spherical wave expansion theory to reconstruct acoustic pressure field from a vibrating object is developed. The radiated acoustic pressures are obtained by means of an expansion of independent functions generated by the Gram-Schmidt orthonormalization with respect to the particular solutions to the Helmholtz equation on the vibrating surface under consideration. The coefficients associated with these independent functions are determined by requiring the assumed form of solution to satisfy the pressure boundary condition at the measurement points. The errors incurred in this process are minimized by the least-squares method. Once these coefficients are specified, the acoustic pressure at any point, including the source surface, is completely determined. In this paper, this method is used to reconstruct the surface acoustic pressures based on the measured acoustic pressure signals in the field. It is shown that this method can be applied to both separable and nonseparable geometries, and the solutions thus obtained are unique. However, the convergence may be worse for an elongated object subject to high-frequency excitations. © 1997 Acoustical Society of America. [S0001-4966(97)00410-4]

PACS numbers: 43.20.Tb, 43.20.Rz, 43.50.Yw [JEG]

INTRODUCTION

In engineering practice, it is often required to diagnose noise sources of vibrating machines so as to come up with better designs to reduce resulting noise radiation. Problems of such are categorized by Turchin *et al.* (1971) as the “inverse problem” which deals with problems of finding unknown sources based on the known consequences. In the case of an inverse acoustic radiation problem, it is to determine the acoustic quantities on the source surface based on measured acoustic pressure signals in the field.

As in all inverse problems, one major difficulty in the inverse acoustic radiation problem is associated with the ill-posedness. By definition (Hadamard, 1923), a problem is well-posed if the solution exists, is unique, and depends continuously on the data; otherwise it is ill-posed. Under most circumstances, an ill-posed problem is very sensitive to the formulations used, and solutions thus obtained do not depend continuously on the auxiliary data. As a result, any slight error in the measured data may result in an enormous reconstruction of the acoustic quantities on the surface.

The inverse problems have been the subject of extensive studies for the past few decades (Landweber, 1951; Twomay, 1963; Franklin, 1970) and have been documented in detail by many people (Ghosh Roy, 1991; Lamm, 1993). For a recent summary of the inverse acoustic scattering problems, readers are referred to a book by Colton and Kress (1992). The present paper is mainly concerned with an inverse acoustic radiation problem, namely, reconstruction of the acoustic field on the surface of a vibrating structure from measured acoustic pressure signals in the field.

An early approach to reconstruction of the acoustic field

on the surface of a planar source is through near-field acoustic holography (NAH) together with a two-dimensional fast Fourier transformation (FFT) algorithm (Williams *et al.*, 1980; Maynard *et al.*, 1985; Veronesi and Maynard, 1987). This approach is extended, called the generalized near-field acoustic holography (GENAH), to cylindrical sources by Williams and Dardy (1987), and further to nonseparable geometries by Borgiotti *et al.* (1990). In order to take into account the evanescent field, the hologram surface on which measurements are taken must be very close to the source surface, within one-half wavelength. (Loyau and Pascal, 1988). Sarkissian (1990, 1991, 1992) developed an algorithm based on an expansion of the surface field in terms of a set of real functions for both near- and far-field acoustic holography.

In order to reconstruct the acoustic field on an irregularly shaped surface, the boundary element method (BEM)-based Kirchhoff integral theory is used to generate a transformation matrix that correlates the field acoustic quantities to the surface ones (Veronesi and Maynard, 1989; Kim and Lee, 1990; Ciskowski and Brebbia, 1991; Bai, 1992). However, the matrix thus obtained is ill-conditioned, and singular value decomposition (SVD) is used to filter out the evanescent waves and to regularize the matrix. Chao (1987) used an implicit least-squares method to approximate reconstruction of the surface acoustic field by minimizing the errors associated with the integral equation approach. Gardner and Bernhard (1988) applied this integral formulation approach to an inverse acoustic radiation problem inside a cavity. Numerical examples indicate that the reconstruction error in the interior problem has the same order of magnitude as that in the exterior problem.

Generally speaking, the BEM-based Kirchhoff integral formulation is a natural approach to reconstruct the acoustic field on the surface of an irregularly shaped object. The main

^{a)}Current address: NVH Laboratory, Chrysler Corporation, 800 Chrysler Dr., Auburn Hills, MI 48326.

advantage of this approach is the reduction of the dimensions of the problem by one, thus improving the efficiency of numerical computations.

However, this approach has several inherent drawbacks resulting from transforming the wave equation into the Fredholm integral equation of the first and second kinds, respectively. The first drawback is associated with the well-known nonuniqueness of the surface Kirchhoff integral equation, and the second is with ill-conditioning of the transformation matrix which makes the inverse acoustic radiation problem an ill-posed one. The first drawback can be overcome by using the CHIEF method (Schenck, 1968), provided that the overdetermined points are properly selected. The second drawback is less straightforward to deal with than the first one.

To show the existence of ill-conditioning difficulty, we consider a general Fredholm integral equation of the first kind

$$\int_a^b K(x,y)f(y)dy = g(x), \quad a \leq x \leq b, \quad (1)$$

where $K(x,y)$ is an arbitrary, integrable kernel, $g(x)$ is given, and $f(y)$ is the sought function. Phillips (1962) has shown that there is no successful way of solving $f(y)$ for an arbitrary kernel $K(x,y)$ when $g(x)$ is specified with only modest accuracy. The reason for that is quite simple: While Eq. (1) can yield $g(x)$ for a given $K(x,y)$ and $f(y)$, its inverse may not be bounded. This can be shown as follows. Let $f(y)$ be the solution to Eq. (1) and add to it a fluctuation $f_m = \sin(my)$. Substituting $f(y)$ into Eq. (1) then yields

$$\int_a^b K(x,y)\sin(my)dy = g_m(x), \quad a \leq x \leq b. \quad (2)$$

Since for any integrable kernel, the function $g_m(x) \equiv \int_a^b K(x,y)\sin(my)dy \rightarrow 0$ as $m \rightarrow \infty$. Hence an infinitesimal change $g_m(x) \neq 0$ in $g(x)$ will cause a finite change f_m in $f(y)$. Also, we expect that $g_m(x) \rightarrow 0$ as $m \rightarrow \infty$ faster for a flat smooth kernel than for a sharply peaked one. Hence the success in solving $f(y)$ for a given $g(x)$ depends to a large extent on the accuracy of $g(x)$ and the shape of $K(x,y)$.

Because of the presence of this inherent ill-posedness in the Kirchhoff integral formulation, any slight error in the measurements may lead to an erroneous result in the reconstruction. Since all measurements will inevitably involve certain uncertainties due either to random fluctuations or to the effect of rapid decay of evanescent waves, this ill-posedness can be a real threat to the success of the inverse acoustic radiation problem. SVD can be used to truncate the order of a matrix and regularize it, thus reducing the reconstruction error. Even with the regularization, the accuracy of reconstruction is still limited to the near field (Kim and Lee, 1990). Moreover, how to handle small singular values in SVD is still a problem open to investigation (Veronesi and Maynard, 1989).

The last but not the least drawback of the BEM-based Kirchhoff integral formulation approach is due to the fact that a large number of measurements must be made in order to uniquely determine the acoustic pressures specified on the

surface nodes. Consequently, the effectiveness of this method can be severely hindered when hundreds of (or even more) discretized nodes must be used to describe the surface acoustic pressure distribution, which is not uncommon in practice. The best way to overcome these problems is to develop a new method that is free of both nonuniqueness and ill-posedness difficulties, and requires much less number of measurement points in reconstruction of the surface acoustic pressure field. The present paper attempts to accomplish such a goal.

In this paper, reconstruction of the acoustic field is done by directly solving the Helmholtz equation (Wang *et al.*, 1995). The acoustic pressure is expanded in terms of a set of independent functions generated by the Gram-Schmidt orthonormalization with respect to the particular solutions to the Helmholtz equation on the particular vibrating surface under consideration. The coefficients associated with these independent functions are determined by requiring the assumed form of solution to satisfy pressure boundary condition at the measurement points. The errors incurred in this process are minimized by the least-squares method. Once these coefficients are specified, the acoustic pressure anywhere, including the source surface, is completely determined. Since the number of expansion terms determines that of measurements, which is usually much smaller than that of discretized nodes on a surface, reconstruction of the acoustic pressure field can be done efficiently. Moreover, solutions thus obtained are always unique.

I. BOUNDARY VALUE PROBLEMS

The acoustic pressure radiated from a vibrating object into an unbounded fluid medium satisfies the wave equation, whose Fourier transformation is known as the reduced wave equation or Helmholtz equation,

$$\nabla^2 p + k^2 p = 0, \quad (3)$$

where p represents the complex amplitude of the acoustic pressure and $k = \omega/c$ is the wave number. At the interface with the surface of the vibrating object, p satisfies one of three types, or their combinations of boundary conditions

Dirichlet problem: $p(\mathbf{x}_B) = g(\mathbf{x}_B)$,

Neumann problem: $\frac{\partial p(\mathbf{x}_B)}{\partial n} = g(\mathbf{x}_B)$, (4)

Mixed or Robin problem:

$$a(\mathbf{x}_B)p(\mathbf{x}_B) + b(\mathbf{x}_B)\frac{\partial p(\mathbf{x}_B)}{\partial n} = g(\mathbf{x}_B),$$

where $\mathbf{x}_B \in \partial B$, a , b , and g are specified, and $\partial/\partial n$ represents the normal derivative on the boundary ∂B .

Solutions to Eq. (3) subject to boundary conditions (4) can be approximated by a linear combination of the independent functions ψ^* (Wang *et al.*, 1995)

$$p^* = \rho c \sum_{i=1}^N C_i \psi_i^*, \quad (5)$$

where ρ and c are the density and speed of sound of the fluid medium, respectively. The independent functions ψ_i^* can be

selected in such a way that they satisfy any one of the following three conditions (Birkhoff and Lynch, 1984):

- (i) ψ_i^* satisfy the differential equation, but not the boundary condition;
- (ii) ψ_i^* do not satisfy the differential equation, but ψ_1^* satisfies the boundary conditions and $\psi_2^*, \psi_3^*, \dots$ satisfy the homogenous boundary conditions; or
- (iii) ψ_i^* satisfy neither the differential equation nor the boundary conditions.

For a differential equation in multiple dimensions,

$$\mathcal{L}[p(\mathbf{x})] = 0, \quad \mathbf{x} \in B, \quad (6)$$

subject to the boundary condition with an operator \mathcal{A} ,

$$\mathcal{A}[p(\mathbf{x}_B)] = \mathcal{G}(\mathbf{x}_B), \quad \mathbf{x}_B \in \partial B, \quad (7)$$

we can select the independent functions ψ_i^* that satisfy any one of the following three integrals (Lieberstein, 1960),

$$(iv) \quad I = \int_{\partial B} \mathcal{W}_1(\mathbf{x}_B) \{ \mathcal{G}(\mathbf{x}_B) - \mathcal{A}[p^*(\mathbf{x}_B)] \}^2 dS,$$

$$(v) \quad I = \int_B \mathcal{W}_1(\mathbf{x}) \mathcal{L}^2[p^*(\mathbf{x})] dV, \quad (8)$$

$$(vi) \quad I = \int_B \mathcal{W}_2(\mathbf{x}) \mathcal{L}^2[p^*(\mathbf{x})] dV + \int_{\partial B} \mathcal{W}_3(\mathbf{x}_B) \times \{ \mathcal{G}(\mathbf{x}_B) - \mathcal{A}[p^*(\mathbf{x}_B)] \}^2 dS,$$

and then seek the values of the coefficients C_i which render the integrals in Eq. (8) minimum. Here \mathcal{W}_i , $i = 1$, to 3, are the weighting functions, and dV and dS are integration elements in the region B and on the boundary ∂B , respectively. Once the coefficients C_i are determined, the acoustic pressure anywhere can be approximated by Eq. (5).

In this paper, we focus our attention on the Helmholtz equation (3) subject to the boundary condition (4), and select the independent functions ψ_i^* that satisfy the condition (i).

II. ORTHONORMALIZATION OF ψ_i^*

The independent functions ψ_i^* in Eq. (5) can be derived from the spherical wave functions through an orthonormalization process. To this end, let us rewrite Eq. (5) in spherical coordinates

$$\begin{aligned} \frac{1}{r^2} \frac{\partial}{\partial r} \left(r^2 \frac{\partial p}{\partial r} \right) + \frac{1}{r^2 \sin \theta} \frac{\partial}{\partial \theta} \left(\sin \theta \frac{\partial p}{\partial \theta} \right) \\ + \frac{1}{r^2 \sin^2 \theta} \frac{\partial^2 p}{\partial \phi^2} + k^2 p = 0, \end{aligned} \quad (9)$$

subject to the Dirichlet boundary condition, Eq. (4), and the Sommerfeld's radiation condition at infinity,

$$\lim_{r \rightarrow \infty} \left[r \left(\frac{\partial p}{\partial r} - ikp \right) \right] = 0. \quad (10)$$

Accordingly, the approximate solution to Eq. (9) can be written in the form of Eq. (5), with ψ_i^* being generated by a linear combination of the particular solutions to the Helmholtz equation ψ_i (Vekua, 1953),

$$\psi_{m,n}(r, \theta, \phi) = h_m(kr) P_{n,m}(\cos \theta) \begin{cases} \cos m\phi \\ \sin m\phi \end{cases}, \quad (11)$$

where $h_m(kr)$ and $P_{n,m}$ denote the spherical Hankel function and the Legendre polynomial, respectively. The former corresponds to an outgoing wave, appropriate for situations where acoustic energy is radiated outward into an unbounded medium. The amplitude of $h_m(kr)$ tends to infinity at $r=0$. However, this does not preclude using it for the present purpose since no physical source has zero radius. Moreover, the point $r=0$ is excluded from $h_m(kr)$ because we are concerned with regions external to the source surface.

For an interior boundary value problem where r may be zero, we can replace $h_m(z)$ by the spherical Bessel function $\mathcal{J}_m(z)$ as its real part, and the spherical Neumann function $\mathcal{N}_m(z)$ as its imaginary part (Morse and Ingard, 1968),

$$h_m(z) = \mathcal{J}_m(z) + i\mathcal{N}_m(z). \quad (12)$$

Since $\mathcal{J}_m(z)$ are well-defined as $z \rightarrow 0$, whereas $\mathcal{N}_m(z)$ are not, and since $\mathcal{N}_m(z)$ bear no physical meaning as $z \rightarrow 0$, we can discard $\mathcal{N}_m(z)$ in Eq. (12) and only retain $\mathcal{J}_m(z)$ as the particular solution to the Helmholtz equation.

The functions ψ_i given by Eq. (11) are readily applicable to a spherical source, but may not be ideal for irregularly shaped geometries, especially for those that contain sharp edges. However, in engineering applications true sharp edges are rare. They are often rounded. Moreover, the radiated acoustic pressure from a finite, irregularly shaped source obeys the spherical spreading law in the far field. Hence Eq. (11) may be used as a first approximation.

The independent function ψ_i^* can now be generated by the Gram-Schmidt orthonormalization with respect to ψ_i (Pinsky, 1991),

$$\begin{aligned} \chi_1 &= \psi_1, & \psi_1^* &= \chi_1 / \|\chi_1\|, \\ \chi_2 &= \psi_2 - (\psi_2, \psi_1^*) \psi_1^*, & \psi_2^* &= \chi_2 / \|\chi_2\|, \\ &\vdots & &\vdots \\ \chi_{n+1} &= \psi_{n+1} - \sum_{i=1}^n (\psi_{n+1}, \psi_i^*) \psi_i^*, & \psi_{n+1}^* &= \chi_{n+1} / \|\chi_{n+1}\|, \end{aligned} \quad (13)$$

where the inner products are taken over the source boundary ∂B ,

$$(\psi_i, \psi_j^*) = \int_{\partial B} \psi_i \psi_j^* dS. \quad (14)$$

The independent functions ψ_i^* thus obtained are now orthonormal on the particular source surface ∂B under consideration,

$$(\psi_i^*, \psi_j^*) = \delta_{ij}, \quad (15)$$

where δ_{ij} is the Kronecker delta. Also, they are uniformly convergent because ψ_i consist of a uniformly convergent series of Legendre functions (Bergman, 1960).

III. THE HELMHOLTZ EQUATION-LEAST-SQUARES (HELS) METHOD

Once ψ_i^* are generated, the formulation for reconstructing the acoustic field can be derived. This process is referred here as the Helmholtz equation-least-squares (HELS)

method, because it solves the Helmholtz equation directly, and the errors incurred in this process are minimized by the least-squares method.

Consider a closed, smooth, and impermeable surface ∂B immersed in an unbounded fluid medium B . Assume that the surface vibrates at a constant angular frequency ω . There are no other sources in the medium except the vibrating surface under consideration.

Given the source location, geometric shape, and pressure boundary conditions at the measurement points in the field

$$p(\mathbf{x}_S) = p_0(\mathbf{x}_S), \quad (16)$$

we wish to reconstruct the acoustic pressure on the source surface.

The first step in solving this problem is to express p^* as a sum of independent functions ψ_i^* , Eq. (5). Here the independent functions ψ_i^* are generated from a complete set of particular solutions ψ_i , given by Eq. (11), through the Gram-Schmidt orthonormalization, Eq. (13). The inner products in the orthonormalization process are taken over the entire source boundary ∂B .

Next, the coefficients C_i associated with the independent functions ψ_i^* are determined by requiring the assumed form of solution, Eq. (5), to satisfy the boundary conditions at the measurement points, Eq. (16). Suppose that an N -term expansion in Eq. (5) is used, and that M measurements are taken, where $M \geq N$. Then we can form M -simultaneous algebraic equations for N unknowns

$$\begin{bmatrix} \psi_{11}^* & \psi_{12}^* & \cdots & \psi_{1N}^* \\ \psi_{21}^* & \psi_{22}^* & \cdots & \psi_{2N}^* \\ \vdots & \vdots & \ddots & \vdots \\ \psi_{N1}^* & \psi_{N2}^* & \cdots & \psi_{NN}^* \\ \vdots & \vdots & \ddots & \vdots \\ \psi_{M1}^* & \psi_{M2}^* & \cdots & \psi_{MN}^* \end{bmatrix} \begin{Bmatrix} C_1 \\ C_2 \\ \vdots \\ C_N \end{Bmatrix} = \begin{Bmatrix} p_{01} \\ p_{02} \\ \vdots \\ p_{0N} \\ \vdots \\ p_{0M} \end{Bmatrix}. \quad (17)$$

If the measured quantities p_0 are exact, then the approximate solution p^* converges to the true value as $N \rightarrow \infty$ (Davis and Rabinowitz, 1961). However, in reality the measurements always contain certain uncertainties due either to random fluctuations or to the effect of rapid decay of the evanescent waves. Hence, the approximate solution will not converge to the true one. Nevertheless, the error involved in the approximate solution can be minimized by the least-squares method

$$I = \sum_{m=1}^M \left(\rho c \sum_{n=1}^N C_n \psi_{mn}^* - p_{0m} \right)^2. \quad (18)$$

Substituting the left-hand side of Eq. (17) into (18) and taking the derivatives of the resultant equation with respect to each individual coefficient C_i , we obtain

$$\begin{aligned} \frac{\partial I}{\partial C_i} &= \frac{\partial}{\partial C_i} \left[\sum_{m=1}^M \left(\rho c \sum_{n=1}^N C_n \psi_{mn}^* - p_{0m} \right)^2 \right] \\ &= \sum_{m=1}^M 2 \left(\rho c \sum_{n=1}^N C_n \psi_{mn}^* - p_{0m} \right) \end{aligned}$$

$$\begin{aligned} &\times \frac{\partial}{\partial C_i} \left(\rho c \sum_{n=1}^N C_n \psi_{mn}^* \right) \\ &= 2 \left(\rho c \sum_{m=1}^N \psi_{mi}^* \sum_{n=1}^N C_n \psi_{mn}^* - \sum_{m=1}^M p_{0m} \psi_{mi}^* \right) \\ &= 0, \quad i = 1, 2, \dots, N. \end{aligned} \quad (19)$$

Equation (17) can be written in a matrix form

$$[\mathcal{T}]\{C\} = \{\mathcal{B}\}, \quad (20)$$

where $[\mathcal{T}]$ represents the transformation matrix that correlates the field measurements to the acoustic field on the source surface, and $[\mathcal{B}]$ contains the information of the boundary condition. The elements of $[\mathcal{T}]$ and $[\mathcal{B}]$ are given by

$$\mathcal{T}_{mi} = \rho c \sum_{n=1}^N \psi_{nm}^* \psi_{ni}^*, \quad \mathcal{B}_m = \sum_{n=1}^N p_{0n} \psi_{nm}^*. \quad (21)$$

Note that the transformation matrix $[\mathcal{T}]$ is nonsingular. Hence the coefficients $\{C\}$ can be solved by inverting the matrix $[\mathcal{T}]$

$$\{C\} = (\rho c)^{-1} [\mathcal{T}]^{-1} \{\mathcal{B}\}, \quad (22)$$

where $[\mathcal{T}]^{-1} = ([\psi_{mn}^*]^T [\psi_{mn}^*])^{-1} [\psi_{mn}^*]^T$ is called the pseudoinverse; here $[\psi_{mn}^*]$ represent a matrix of the form of that on the left-hand side of Eq. (17), and a superscript T stands for a transposition. It can be shown that the condition number of the pseudoinverse is much smaller than that of a direct inverse (Stewart, 1973), hence the system of Eqs. (22) is stable and the accuracy of numerical results for $\{C\}$ is high.

In deriving Eq. (22) no restrictions have been imposed on the measurement points. They can be taken at any point in the field as long as they do not overlap each other.

Once the coefficients C_i are solved, the surface acoustic pressures can be reconstructed by Eq. (5). In fact, one can use Eq. (5) to reconstruct acoustic pressures anywhere external to the vibrating surface.

It is emphasized that the HELS method is free of the nonuniqueness difficulty, because it solves the Helmholtz equation directly. Hence the reconstructed surface acoustic pressures are always unique, even at the characteristic frequencies that correspond to the related interior boundary value problem. Numerical examples that illustrate the uniqueness of solutions thus obtained are given in the next section.

IV. NUMERICAL EXAMPLES

In this section, we show numerical examples of reconstructing acoustic pressures radiated from sources with separable and nonseparable coordinates. In all cases, a surface velocity distribution is preselected, and the acoustic pressures on the source surface and in the field are calculated either analytically or numerically. The field acoustic pressures thus obtained are taken as the input to reconstruct the surface acoustic pressures, which are subsequently compared with the predetermined ones on the surface.

TABLE I. Comparison of the coefficients C_i for a dilating sphere at $ka=10$.

C_i	Calculated values	Exact values
C_0	(-6.2171E+00, -7.7690E+00)	(-6.2171E+00, -7.7690E+00)
C_1	(-2.7756E-17, -2.4980E-16)	(0.0, 0.0)
C_2	(-2.7470E-08, -2.5161E-08)	(0.0, 0.0)
C_3	(-1.6653E-15, +3.5527E-15)	(0.0, 0.0)
C_4	(-2.5862E-08, +3.8174E-08)	(0.0, 0.0)
C_5	(+0.0000E+00, -2.4425E-15)	(0.0, 0.0)
C_6	(-6.6451E-09, +2.8785E-08)	(0.0, 0.0)
C_7	(-4.4409E-16, -6.6613E-16)	(0.0, 0.0)

A. Sources with separable geometries

The examples concerned with sources of separable geometries include a dilating sphere, an oscillating sphere, and a partially vibrating sphere. In what follows, we first consider the case of a dilating sphere. The complex amplitude of the radiated acoustic pressure from a dilating sphere is given by (Pierce, 1981)

$$p = -\frac{ik\rho c a^2 V_S}{r(1-ika)} e^{ik(r-a)}, \quad (23)$$

where V_S is the amplitude of the surface velocity and a is the radius of the sphere.

The approximated acoustic pressure is given by Eq. (5). The independent functions ψ_i^* are generated by the Gram-Schmidt orthonormalization, Eqs. (13) and (14), with respect to the particular solutions ψ_i given by Eq. (11). Since in this case, ϕ_i are already orthogonal to the spherical surface, we can directly set $\psi_i^* = \psi_i$. The coefficients C_i associated with ψ_i^* are determined by requiring p^* to satisfy the pressure boundary condition at the measurement points.

As an example, we select eight measurement points on a hypothetical, concentric spherical surface at $r=2a$, $\phi=0$, and θ varying from 0° to 180° at a uniform interval. In this way we generate an 8×8 square matrix for eight coefficients C_i , $i=1$ to 8.

Table I shows the comparison of the calculated values of C_i and the exact ones for a dilating sphere at $ka=10$ and $V_S=1$ (m/s). Excellent agreements are obtained for all ka values tested. However, for brevity, we only display one case at $ka=10$. Table I indicates that we only need one term expansion to approximate the surface acoustic pressure p . In other words, the acoustic pressure on the surface of a dilating sphere can be reconstructed, theoretically, by taking one measurement in the field.

Next, we consider the case of an oscillating sphere. The complex amplitude of the radiated acoustic pressure in this case is given by (Pierce, 1981)

$$p = -\frac{ka(kr+i)\rho c V_S \cos \theta}{2-(ka)^2-i2(ka)} \left(\frac{r}{r}\right)^2 e^{ik(r-a)}, \quad (24)$$

where $\cos \theta = \mathbf{n} \cdot \mathbf{e}_R$; here \mathbf{n} is the unit normal on the surface and \mathbf{e}_R is the unit normal in the direction of wave propagation from the source to the receiver.

To reconstruct the acoustic field on the surface of an oscillating sphere, we take eight measurements as before. Table II shows the comparison of the calculated values of these eight coefficients C_i and the exact ones at $ka=10$ and $V_S=1$ (m/s). In this case, the surface acoustic pressure can be reconstructed, theoretically, by two measurements in the field.

The third example concerns reconstruction of acoustic pressures on the surface of a partially vibrating sphere. Assume that the normal component of the surface velocity is constant over certain portion of the sphere and zero elsewhere, namely,

$$V_S(\theta) = \begin{cases} V_0, & 0 \leq |\theta| < \theta_0, \\ 0, & \text{elsewhere,} \end{cases} \quad (25)$$

where $2\theta_0$ is the vertex angle of the vibrating surface. The analytic solution for the radiated acoustic pressure is given by Morse and Ingard (1986) in terms of a series expansion. The accuracy of the result in this case depends on the vertex angle $2\theta_0$ and the dimensionless wave number ka . The larger the values of $2\theta_0$ and ka are, the more terms in the expansion are needed.

Once again, we follow the same procedures as described above and take 20 measurements along the generator of a hypothetical, concentric spherical surface at $r=2a$, $\phi=0^\circ$,

TABLE II. Comparison of the coefficients C_i for an oscillating sphere at $ka=10$.

C_i	Calculated values	Exact values
C_0	(+4.4409E-15, +5.5511E-15)	(0.0, 0.0)
C_1	(+7.1320E+00, -7.0067E+00)	(+7.1320E+00, -7.0067E+00)
C_2	(+3.5527E-15, +3.1086E-15)	(0.0, 0.0)
C_3	(+1.0109E-08, -8.7505E-09)	(0.0, 0.0)
C_4	(-4.4409E-16, +4.4409E-16)	(0.0, 0.0)
C_5	(-4.4525E-08, -5.0069E-09)	(0.0, 0.0)
C_6	(-9.7700E-15, -7.7716E-16)	(0.0, 0.0)
C_7	(-3.4523E-08, +1.9789E-08)	(0.0, 0.0)

TABLE III. Comparison of the coefficients C_i for a partially vibrating sphere at $ka = 10$.

C_i	Calculated values	Exact values
C_0	$(-8.1898E-01, -1.0234E+00)$	$(-8.1898E-01, -1.0234E+00)$
C_1	$(+2.4530E+00, -2.4099E+00)$	$(+2.4530E+00, -2.4099E+00)$
C_2	$(+3.5591E+00, +2.3817E+00)$	$(+3.5591E+00, +2.3817E+00)$
C_3	$(-9.8444E-01, +3.4257E+00)$	$(-9.8444E-01, +3.4257E+00)$
C_4	$(-1.6067E+00, +2.2611E-01)$	$(-1.6067E+00, +2.2611E-01)$
C_5	$(+4.5386E-01, +5.6590E-01)$	$(+4.5387E-01, +5.6590E-01)$
C_6	$(-5.7752E-01, +2.4517E+00)$	$(-5.7752E-01, +2.4517E+00)$
C_7	$(-2.5308E+00, +1.6501E+00)$	$(-2.5308E+00, +1.6501E+00)$
C_8	$(-2.0104E+00, -9.2546E-03)$	$(-2.0104E+00, -9.2546E-03)$
C_9	$(+9.7806E-02, +3.4960E-02)$	$(+9.7806E-02, +3.4960E-02)$
C_{10}	$(+1.8322E+00, +6.8817E-01)$	$(+1.8322E+00, +6.8817E-01)$
C_{11}	$(+1.7385E+00, +2.9943E-01)$	$(+1.7385E+00, +2.9943E+00)$
C_{12}	$(+6.4298E-01, +3.1096E-01)$	$(+6.4298E+00, +3.1096E-01)$
C_{13}	$(+5.5858E-02, +5.7644E-04)$	$(+5.5858E-02, +5.7659E-04)$
C_{14}	$(-7.0895E-02, -1.2725E-04)$	$(-7.0896E-02, -1.2734E-04)$
C_{15}	$(-4.4168E-02, -1.1148E-05)$	$(-4.4168E-02, -1.1525E-05)$
C_{16}	$(-1.3358E-02, +9.5407E-08)$	$(-1.3358E-02, -4.2970E-07)$
C_{17}	$(-7.3130E-04, +3.0780E-07)$	$(-7.3095E-04, -2.1416E-09)$
C_{18}	$(+9.3511E-04, +1.9361E-09)$	$(+9.3546E-04, +3.3577E-10)$
C_{19}	$(+1.7850E-04, -8.4724E-08)$	$(+1.7866E-04, +2.4008E-11)$

and θ varying from 0° to 180° . Table III depicts the comparison of the reconstructed values of C_i and the analytic ones given by Morse and Ingard (1986) for $2\theta_0 = 45^\circ$, $ka = 10$, and $V_0 = 1$ (m/s). Results show that the convergence is essentially achieved with 13 expansion terms or equivalently, 13 measurements in the field.

B. Sources with nonseparable coordinates

Spherical sources as discussed above have separable geometries for which analytical solutions for the radiated acoustic pressures can be obtained by using the method of separation of variables. To examine the feasibility of applying the HELS method to sources of nonseparable geometries, we consider a finite cylinder with two spherical endcaps for which there exist no closed-form solutions.

To demonstrate the use of the HELS method, we first select a velocity distribution V_S on the source surface and then solve the surface acoustic pressure p_S by using the BEM-based Kirchhoff integral formulation (Wang, 1995),

$$\{p_S\} = ([A] - 2\pi[I])^{-1}[B]\{V_S\}, \quad (26)$$

where $[I]$ is an identity matrix and the elements of the matrices $[A]$ and $[B]$ are given by

$$A_{mj}^\alpha = \int_{S_m} N_\alpha(\xi) \frac{\partial R_j(\xi)}{\partial n_j(\xi)} \frac{(ikR_j(\xi) - 1)e^{ikR_j(\xi)}}{R_j^2(\xi)} J(\xi) d\xi, \quad (27a)$$

$$B_{mj}^\alpha = \int_{S_m} N_\alpha(\xi) \frac{ik\rho c e^{ikR_j(\xi)}}{R_j(\xi)} J(\xi) d\xi, \quad (27b)$$

where $J(\xi)$ is the Jacobian of the transformation from global to local coordinates, S_m is the area of the m th segment divided on the surface, $R_j(\xi)$ is the distance from the j th node to every point on the m th area segment, and $N_\alpha(\xi)$ are the second-order shape functions of the local coordinates $(\xi) \equiv (\xi_1, \xi_2)$ (Wang, 1995).

As a first example, we consider a short cylinder with a half-length to radius aspect ratio $b/a = 0.5$, where $a = 1$ (m). The cylinder is assumed to dilate uniformly in all directions. In solving the surface acoustic pressure using Eq. (26), we divide the surface into 216 quadrilateral segments with 753 nodes. Once the surface acoustic pressure at each node is determined, the field acoustic pressure can be calculated by the Kirchhoff integral formulation (Wang, 1995)

$$4\pi\{p\} = [A]\{p_S\} - [B]\{V_S\}. \quad (28)$$

In this case, we set the field points to lie along a line parallel to the generator of the cylinder at a distance of 0.1 (m) away from the surface (Fig. 1). The field acoustic pressures thus obtained are taken as input to reconstruct the surface acoustic pressure using the HELS method, which in turn are compared with those given by Eq. (26).

Since there exist no closed-form solution to the Helmholtz equation for a finite cylinder, we use the particular

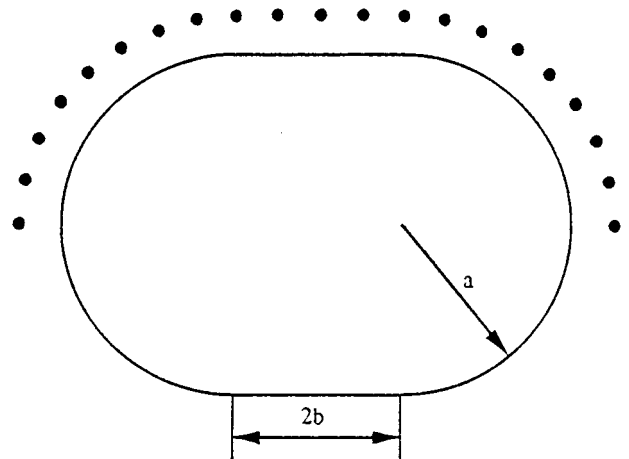


FIG. 1. Locations of measurement points with respect to a cylinder with two spherical endcaps.

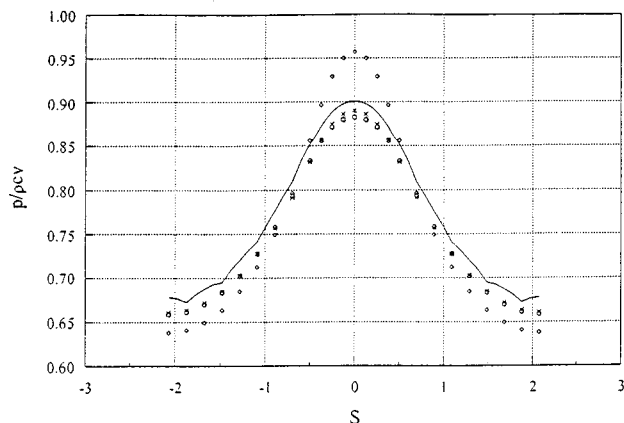


FIG. 2. Comparison of dimensionless acoustic pressures on the surface of a vibrating cylinder with two spherical endcaps at $b/a=0.5$ and $ka=1$. —: Eq. (26); \diamond : Eq. (5) with $N=2$; \circ : Eq. (5) with $N=3$; \times : Eq. (5) with $N=5$.

solutions ψ_i for a spherical surface. This approximation is acceptable because in the far field the radiated acoustic pressure obeys the spherical spreading law. The independent functions ψ_i^* are orthonormalized with respect to the cylindrical surface. The inner products in Eq. (13) are taken with respect to the entire cylindrical surface, and the surface integrals are carried out using Gaussian quadratures with nine interior points. The coefficients C_i associated with the independent functions ψ_i are determined by Eq. (22), and the surface acoustic pressures are reconstructed by Eq. (5).

Figure 2 shows the comparison of the reconstructed acoustic pressure distribution on the surface of a dilating cylinder using the HELS method and those using BEM at $ka=1$. The acoustic pressures are nondimensionalized with respect to $\rho c V_S$ and are plotted against the generator S . Here $S=0$ corresponds to the center of the cylinder wall, $S=\pm 0.5$ (m) represents the edges where the cylinder and two spherical endcaps meet, and $S=\pm 2.07$ (m) represents centers of two spherical endcaps, respectively.

Numerical results demonstrate that the acoustic pressure on the surface can be reconstructed successfully using the HELS method with only a few measurements (see Fig. 2). Here a \diamond denotes reconstruction of surface acoustic pressures with a two-term expansion or equivalently, two measurements in the field, a \circ represents a three-term expansion, and a \times indicates a five-term expansion. The accuracy of reconstruction increases with the number of expansion terms. With $N=5$, the maximum relative error in reconstruction is already less than 5%.

The approximate solution given by Eq. (5) also allows one to predict the radiated acoustic pressure in the field. Figure 3 depicts the comparison of BEM results using Eq. (28) and those using Eq. (5) over a circle of radius $r=4$ (m). The agreement between the two is excellent. The radiation pattern in this case resembles that of a dilating sphere except for extra radiation from the cylinder side wall.

The second example deals with the same cylinder, but oscillating back and forth along the z axis at $ka=1$. In reconstructing the surface acoustic pressures, we follow the same procedures as described above. Figure 4 shows the

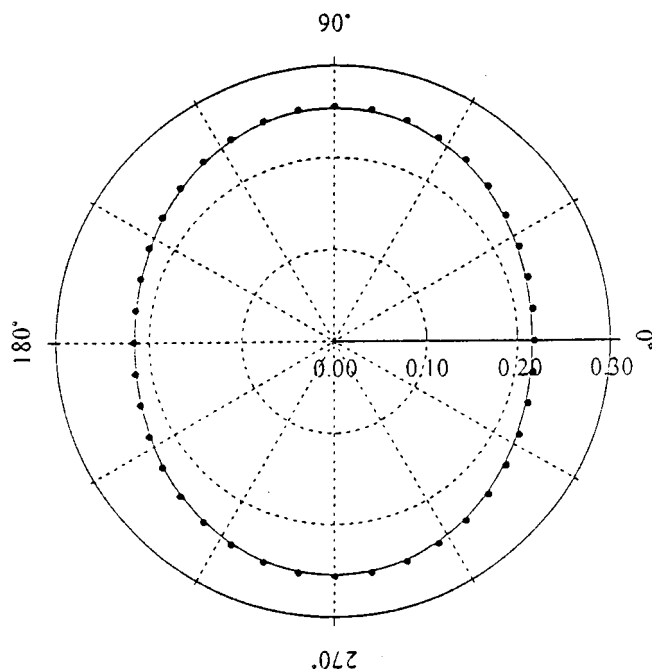


FIG. 3. Comparison of dimensionless acoustic pressures from a vibrating cylinder with two spherical endcaps at $b/a=0.5$, $ka=1$, and $r=4$ (m). —: Eq. (28); \bullet : Eq. (5) with $N=5$.

comparison of the reconstructed surface acoustic pressures using the HELS method and those using BEM. Here a \diamond depicts the results of the HELS method with a four-term expansion or equivalently, four measurements in the field, a \circ stands for a six-term expansion, and a \times implies an eight-term expansion. The maximum relative error with an eight-term expansion is less than 5%.

Figure 5 shows the comparison of the BEM results for the field acoustic pressure and the reconstructed ones using an eight-term expansion along a circle of radius $r=4$ (m). The radiation pattern resembles that of an oscillating sphere.

The third example is concerned with a partially vibrating cylinder. Assume that a small portion on one endcap of the

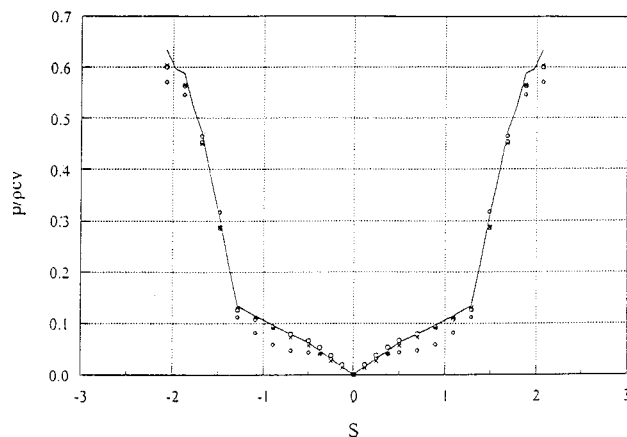


FIG. 4. Comparison of dimensionless acoustic pressures on the surface of an oscillating cylinder with two spherical endcaps at $b/a=0.5$ and $ka=1$. —: Eq. (26); \diamond : Eq. (5) with $N=4$; \circ : Eq. (5) with $N=6$; \times : Eq. (5) with $N=8$.

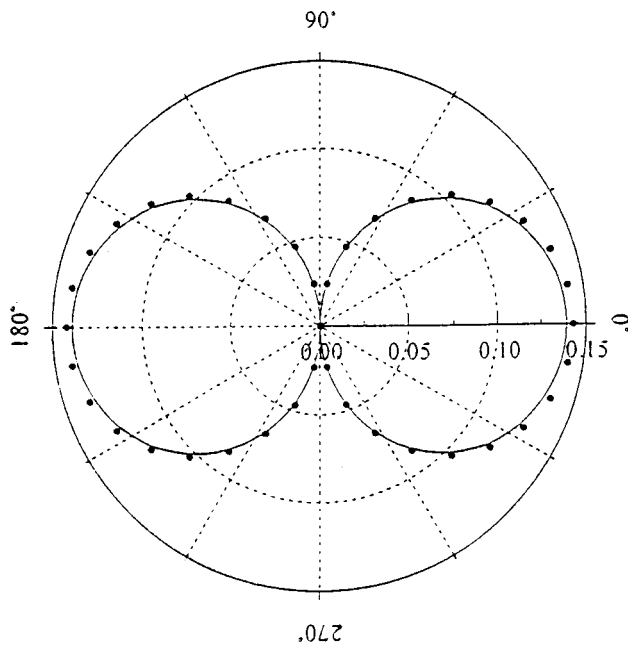


FIG. 5. Comparison of dimensionless acoustic pressures from an oscillating cylinder with two spherical endcaps at $b/a=0.5$, $ka=1$, and $r=4$ (m). —: Eq. (28); ●: Eq. (5) with $N=8$.

cylinder (with a vertex angle of $2\theta_0=60^\circ$) is vibrating at a constant frequency and amplitude, and the rest surface is motionless. Accordingly, the normal component of the surface velocity can be written as

$$V_s(\theta) = \begin{cases} V_0, & 0 \leq |\theta| < 30^\circ, \\ 0, & \text{elsewhere.} \end{cases} \quad (29)$$

Figure 6 demonstrates the comparison of the calculated dimensionless surface acoustic pressures and the reconstructed ones along the surface generator S . A \diamond represents the results of the HELS method with a 10-term expansion, a \circ implies a 14-term expansion, and a \times describes an 18-term expansion. The maximum error with an 18-term expansion is less than 12%.

Figure 7 illustrates the comparison of reconstructed field

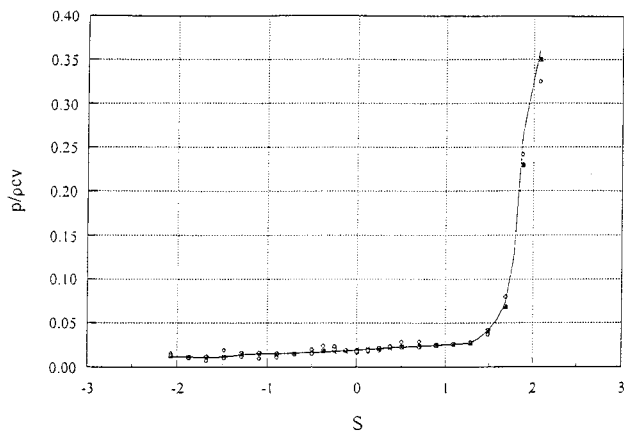


FIG. 6. Comparison of dimensionless acoustic pressures on the surface of a partially vibrating cylinder at $b/a=0.5$ and $ka=1$. —: Eq. (26); \diamond : Eq. (5) with $N=10$; \circ : Eq. (5) with $N=14$; \times : Eq. (5) with $N=16$.

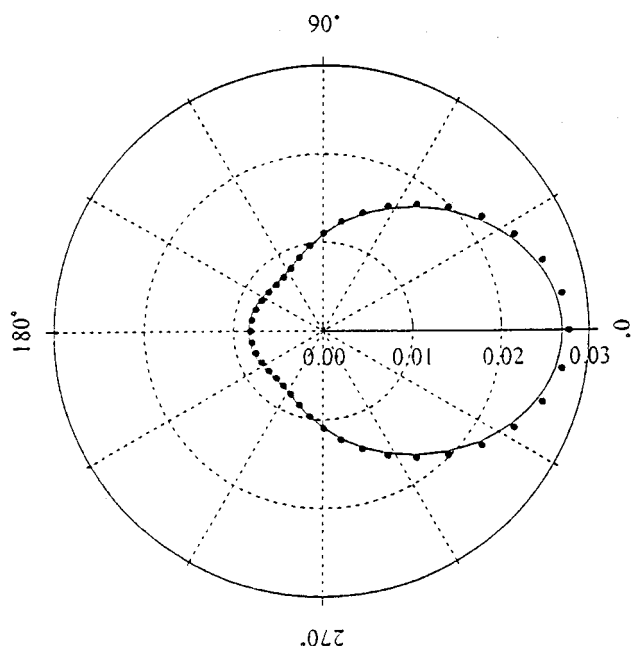


FIG. 7. Comparison of dimensionless acoustic pressures from a partially vibrating cylinder at $b/a=0.5$, $ka=1$, and $r=4$ (m). —: Eq. (28); ●: Eq. (5) with $N=16$.

acoustic pressures using an 18-term expansion and the BEM results over a circle of radius $r=4$ (m). The radiation pattern in this case resembles that of a vibrating piston set in a sphere (Morse and Ingard, 1986).

C. Elongated cylinders subject to higher-frequency excitations

In the preceding section, we consider reconstruction of acoustic pressure fields for a relatively short cylinder vibrating at low frequencies. In engineering practice, we often encounter arbitrarily shaped bodies vibrating at high frequencies. Under these conditions, the convergence of the HELS method may worsen. This is because the HELS method is based on an expansion of the spheroidal functions, which works best for a spherical surface or for a chunky body whose representative spatial aspect ratio $x:y:z$ is close to 1:1:1. For an arbitrarily shaped body, other expansions based on the prolate spheroids, oblate spheroids, and ellipsoidal functions should be used (Burnett, 1994). In a separate paper (Wu and Yu, 1997), the HELS method is generalized and ellipsoidal functions are used in the expansion to reconstruct acoustic pressure fields for an arbitrarily shaped vibrating object.

In this section, we examine the performance of Eq. (5) on reconstructing the acoustic pressures on the surface of a cylinder as the increase of the aspect ratio b/a and the dimensionless frequency ka . Note that if we were to use BEM as before to generate the benchmark results, we must increase the number of discretization points on the cylindrical surface, thus increasing the matrix size and increasing cubically the computational time. Another complication associated with BEM is its inherent nonuniqueness difficulty. As the frequency increases, the characteristic frequencies for

the corresponding interior boundary value problem become closer to each other, and the effect of nonuniqueness difficulties on the resulting numerical computations becomes more prominent. Although this nonuniqueness can be overcome by using the CHIEF method (Schenck, 1968), the overall computational time would increase further and its accuracy would be affected. To circumvent these difficulties, we make use of point sources whose acoustic pressures are well-defined.

As an example, we consider the case of a cylinder with $b/a=2$ and reconstruct the surface acoustic pressures in the following manner. First, we place a monopole at the point that coincides with the center of the cylinder, and calculate the radiated acoustic pressure and the corresponding particle velocity normal to a hypothetical surface identical to that of the cylinder under consideration. Next, we place the cylinder in position and take the acoustic pressure and normal component of the surface velocity thus obtained as the quantities specified on a vibrating cylinder. Once this is done, the field acoustic pressures can be calculated by using Eq. (28). In this example, we choose the field points to lie on a hypothetical, concentric cylindrical surface at a distance of one radius away from the cylinder. The field acoustic pressures thus calculated are used to reconstruct the acoustic pressures on the cylinder surface, which are subsequently compared with those of a monopole.

Figure 8 depicts the comparison of the reconstructed surface acoustic pressures using 15 expansion terms, or 15 measurements, and the exact ones under $ka=1$. Figure 9 illustrates the case of the same cylinder, except the acoustic pressures are generated by a dipole located at the center of the cylinder. In either case, the agreement is almost perfect.

Next, we consider an elongated cylinder with $b/a=10$ subject to a higher-frequency excitation, $ka=5$. To complicate the problem, we use three monopoles located at $z = -0.5a$, 0.0 , and $0.5a$ along the cylinder axis, and push measurement points further to a hypothetical, concentric cylindrical surface at two radii away. Figure 10 depicts that the surface acoustic pressures in this case can be reconstructed

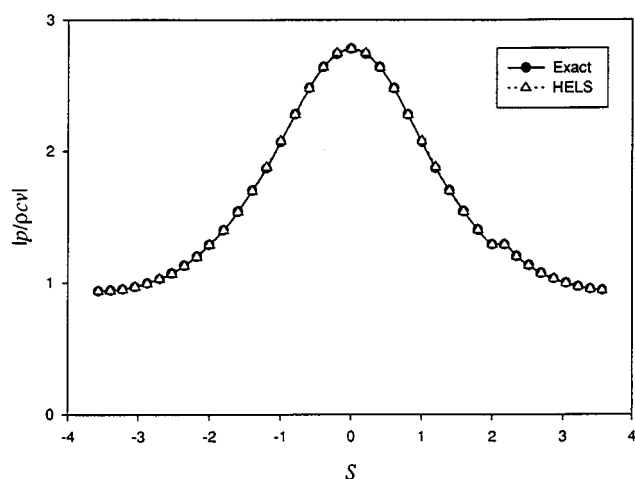


FIG. 8. Comparison of dimensionless acoustic pressures on the surface of a cylinder with two spherical endcaps at $b/a=2$ and $ka=1$. ●: Monopole; ○: Eq. (5) with $N=15$.

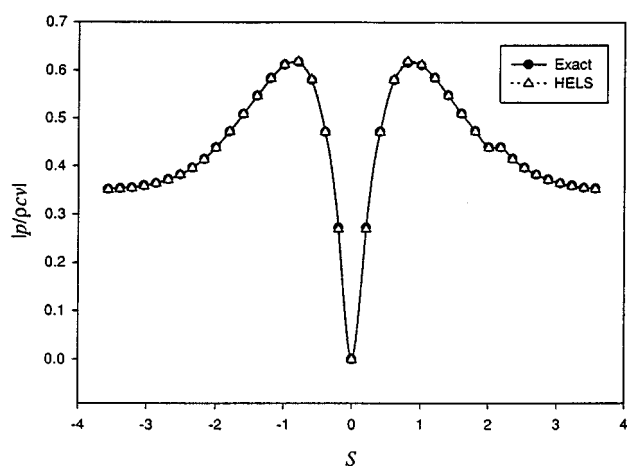


FIG. 9. Comparison of dimensionless acoustic pressures on the surface of a cylinder with two spherical endcaps at $b/a=2$ and $ka=1$. ●: Dipole; ○: Eq. (5) with $N=15$.

successfully with 25 expansion terms, or 25 measurements in the field.

D. Uniqueness of the solutions

In the preceding sections, we have shown that acoustic pressures can be reconstructed by the HELS method with a relatively small number of expansion terms, which is equal to that of the measurements in the field. Since the number of expansion terms in the HELS method is in general much smaller than that of the discretized nodes associated with the BEM-based Kirchhoff integral formulation, numerical computations of the former are much more efficient than those of the latter.

Another advantage of the HELS method is that solutions thus obtained are always unique. This is because the HELS method solves the Helmholtz equation directly, hence it is immune to the nonuniqueness difficulty inherent in the Kirchhoff integral formulation.

In what follows, we consider two examples, namely, a dilating sphere and an oscillating sphere, for which the ana-

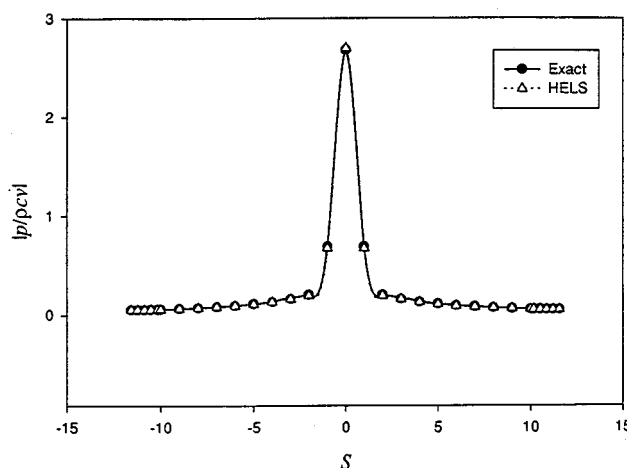


FIG. 10. Comparison of dimensionless acoustic pressures on the surface of a cylinder with two spherical endcaps at $b/a=10$ and $ka=5$. ●: 3 Monopoles; ○: Eq. (5) with $N=25$.

TABLE IV. Comparison of the coefficients C_i for a dilating sphere at $ka=3.1416$.

C_i	Calculated values	Exact values
C_0	$(-0.9080E+00, -5.8526E+00)$	$(-0.9080E+00, -5.8526E+00)$
C_1	$(-1.4302E-15, +6.4614E-16)$	(0.0, 0.0)
C_2	$(+4.3998E-14, -1.0568E-14)$	(0.0, 0.0)
C_3	$(+7.9895E-16, -1.0969E-16)$	(0.0, 0.0)
C_4	$(-7.9683E-15, +1.0615E-15)$	(0.0, 0.0)

lytic solutions are well-known. The characteristic frequencies of the related interior boundary value problem for a dilating sphere can be determined by the roots of the spherical Bessel function of the first kind and order zero, $ka = n\pi$, where n is an integer, while that for an oscillating sphere are given by the roots of the spherical Bessel function of the first kind and order one, $ka=4.493\,409, 7.725\,233, \dots$.

Here we use Eqs. (23) and (24) to calculate the field acoustic pressures on a hypothetical spherical surface at one radius away from the sphere, and take them as input to reconstruct the surface acoustic pressures. For brevity, we only show the results of the acoustic pressures with the excitation frequency close to one of the characteristic frequencies in each case.

Tables IV and V depict comparisons of the reconstructed values of the coefficients C_i associated with five expansion terms and the exact ones at $ka=3.1416$ for a dilating sphere, and $ka=4.4934$ for an oscillating sphere, respectively. In both cases, the results of the HELS method are unique and agree perfectly with the exact ones.

E. Sensitivity analysis

In engineering practice, all measurements are prone to errors due either to system errors or to random fluctuations. Although these errors can be reduced by calibration or by taking more averages, the resulting data are nonetheless not error free. In this section, we examine the robustness of the HELS method by artificially introducing certain bias and random errors in the input, and then compare the resulting reconstruction with the known values. Here bias errors are introduced by multiplying the correct acoustic pressures by a constant, for example, 1.05 for a 5% bias error. Similarly, random errors are introduced by multiplying the known values by a random number sequence scaled to plus or minus a nominal error. For example, a 5% random error is generated by a random number sequence between 0.95 and 1.05.

The first two examples of the sensitivity analysis are concerned with a dilating sphere and an oscillating sphere. Since in these cases the closed-form solutions are available,

the bias and random errors are generated by multiplying the exact values of the field acoustic pressures by some preselected constants or random number sequences.

Figures 11 and 12 show the relative errors in reconstruction of surface acoustic pressures for a dilating sphere and an oscillating sphere at $ka=1$ with erroneous input data, respectively. In these figures, the horizontal axes represent the generator of the spherical surface with the polar angle θ varying from 0° to 180° , and the vertical axes are the relatively errors with respect to the exact value. The solid lines denote relative errors in reconstruction due to 5% bias errors, and the dashed lines represent those due to 10% bias errors in the input. Numerical results show that the same magnitudes of the bias errors are transferred to reconstruction without amplification. This is to be expected because Eq. (5) is linear.

Also shown in Figs. 11 and 12 are the relative errors in reconstruction of the surface acoustic pressures due to 5% random errors in the input, indicated by a \circ , and 10% random errors, indicated by a \diamond , respectively. Numerical results show that the average levels of relative errors in reconstruction are actually lower than those in the input. This is because the random errors have been effectively reduced by the least-squares method. The largest relative error, about 13.8%, is seen around $\theta=90^\circ$ for an oscillating sphere. This is because the amplitude of the acoustic pressure is very close to zero there, hence any round-off error in the computations could lead to a large error in the final results.

Next, we perform a sensitivity analysis on sources of nonseparable coordinates. As before, we consider a vibrating cylinder, an oscillating cylinder, and a partially vibrating cylinder with two spherical endcaps. Because of lack of the analytical solutions, the acoustic pressures are calculated numerically using Eq. (28), which are not exact to begin with.

In what follows, we first examine relative errors in reconstruction due to these inherent numerical errors in the input data. Here the relative errors are defined as the ratio of the absolute value of the difference between the numerical results obtained by using Eqs. (5) and (26) to that of Eq. (26). The solid lines in Figs. 13–15 demonstrate the relative

TABLE V. Comparison of the coefficients C_i for an oscillating sphere at $ka=4.4934$.

C_i	Calculated values	Exact values
C_0	$(-1.2115E-08, -1.4381E-08)$	(0.0, 0.0)
C_1	$(-1.0484E+00, -4.3433E+00)$	$(-1.0484E+00, -4.3433E+00)$
C_2	$(+5.5696E-09, -4.7809E-08)$	(0.0, 0.0)
C_3	$(-5.2786E-07, -6.2351E-07)$	(0.0, 0.0)
C_4	$(-3.2456E-09, +9.9318E-09)$	(0.0, 0.0)

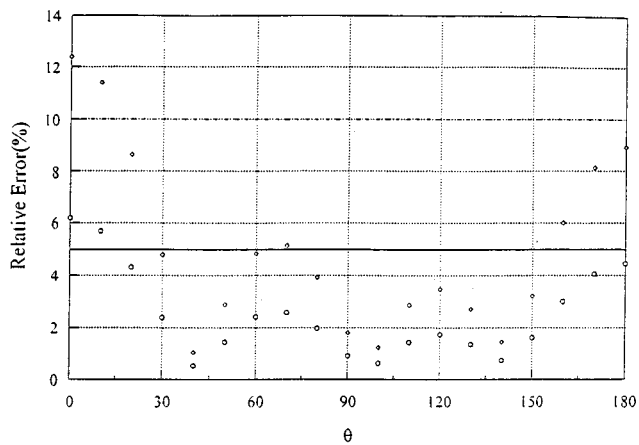


FIG. 11. Relative errors in reconstruction of surface pressures for a dilating sphere subject to either bias or random errors in the input at $ka=1$. —: 5% bias errors; —: 10% bias errors; ○: 5% random errors; ◇: 10% random errors.

errors of the reconstructed surface acoustic pressures of a vibrating cylinder, an oscillating cylinder, and a partially vibrating cylinder, respectively. The average levels of the relative errors are less than 2% for a vibrating cylinder (see Fig. 13), 5% for an oscillating cylinder (see Fig. 14), and 7% for a partially vibrating cylinder (see Fig. 15). The largest error occurs around $\theta=90^\circ$ for an oscillating cylinder for the same reason as that of an oscillating sphere. These inherent numerical errors can be further reduced by increasing the number of segments discretized on the cylindrical surface and the number of internal points in the Gaussian quadratures.

Now we introduce the bias errors to the input data and use them to reconstruct surface acoustic pressures. The dashed and dotted lines in Figs. 13–15 represent the relative errors in reconstruction of surface acoustic pressures for a vibrating cylinder, an oscillating cylinder, and a partially vibrating cylinder due to 5% and 10% bias errors in the input, respectively. The average levels of the relative errors in reconstruction are 6% for a vibrating cylinder, 8% for an os-

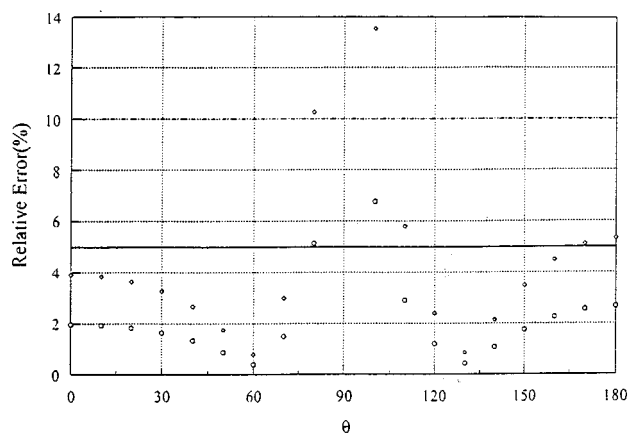


FIG. 12. Relative errors in reconstruction of surface pressures for an oscillating sphere subject to either bias or random errors in the input at $ka=1$. —: 5% bias errors; —: 10% bias errors; ○: 5% random errors; ◇: 10% random errors.

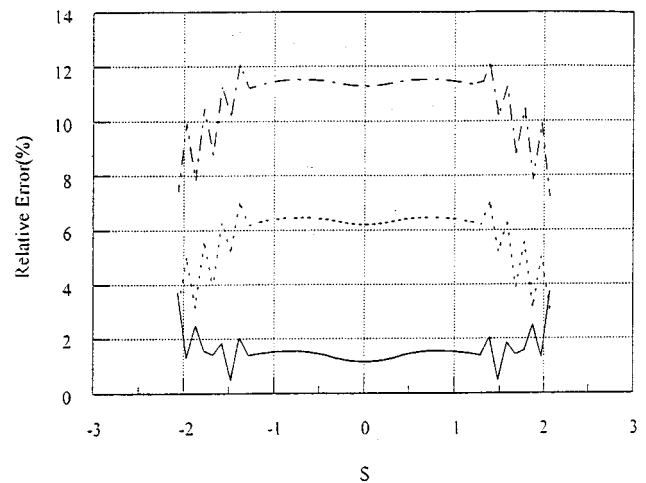


FIG. 13. Relative errors in reconstruction of surface pressures for a vibrating cylinder with two spherical endcaps at $b/a=0.5$ and $ka=1$. —: Inherent errors; —: inherent plus 5% bias errors; ···: inherent plus 10% bias errors.

cillating cylinder, and 10% for a partially vibrating cylinder when 5% random errors are introduced into the input. While the average levels of the relative errors in reconstruction are 12% for a vibrating cylinder, 13% for an oscillating cylinder, and 13% for a partially vibrating cylinder when 10% random errors are introduced into the input. Note that these relative errors are caused by a combined effect of the inherent numerical errors and bias errors in the input. Once again, the bias errors are passed to the final results almost uniformly. This is evidenced in the similarities of the relative error patterns with and without the presence of bias errors.

Next, we introduce random errors into the input data. Figures 16–18 demonstrate the relative errors in reconstruction of surface acoustic pressures due to 5% and 10% random errors, respectively. The average levels of the relative errors in reconstruction are 2% for a vibrating cylinder, 5% for an oscillating cylinder, and 5% for a partially vibrating

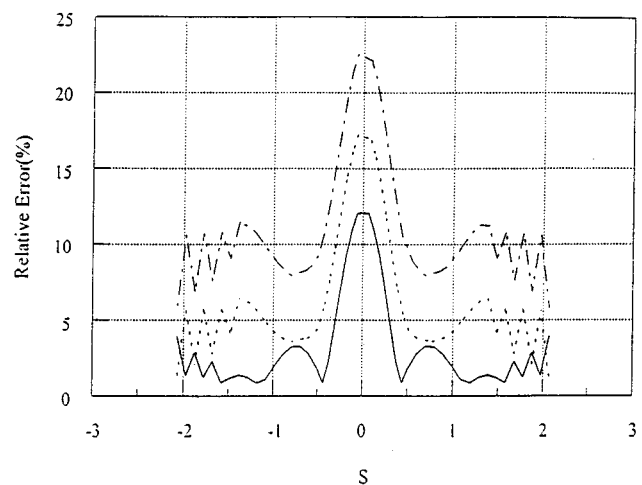


FIG. 14. Relative errors in reconstruction of surface pressures for an oscillating cylinder with two spherical endcaps at $b/a=0.5$ and $ka=1$. —: Inherent errors; —: inherent plus 5% bias errors; ···: inherent plus 10% bias errors.

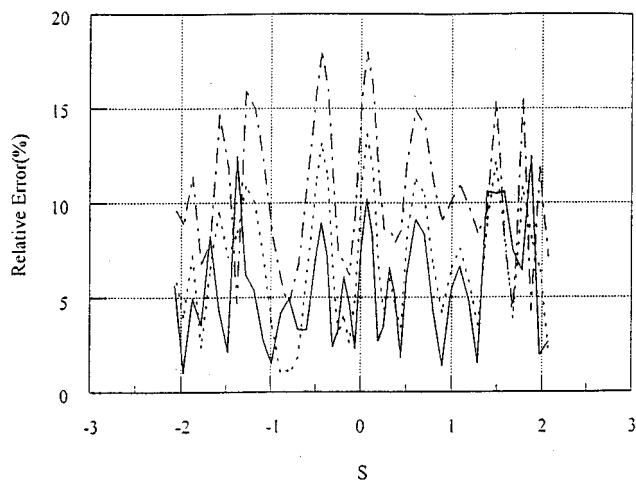


FIG. 15. Relative errors in reconstruction of surface pressures for a partially vibrating cylinder with two spherical endcaps at $b/a=0.5$ and $ka=1$. —: Inherent errors; ---: inherent plus 5% bias errors; - · - · -: inherent plus 10% bias errors.

cylinder when 5% random errors are introduced into the input. The average levels of the relative errors in reconstruction are 10% for a vibrating cylinder, 11% for an oscillating cylinder, and 12% for a partially vibrating cylinder when 10% random errors are introduced into the input. These relative errors are the results of a combined effect of the inherent numerical errors and random errors in the input. As in the cases of vibrating spheres, the average levels of the relative errors in reconstruction due to random errors are lower than those due to bias errors. This is because the random errors have been effectively reduced by the least-squares method.

The examples exhibited above demonstrate that the HELS method can tolerate certain degrees of uncertainties in the input. Such a feature can be appealing because in engineering applications all measurements are not exact.

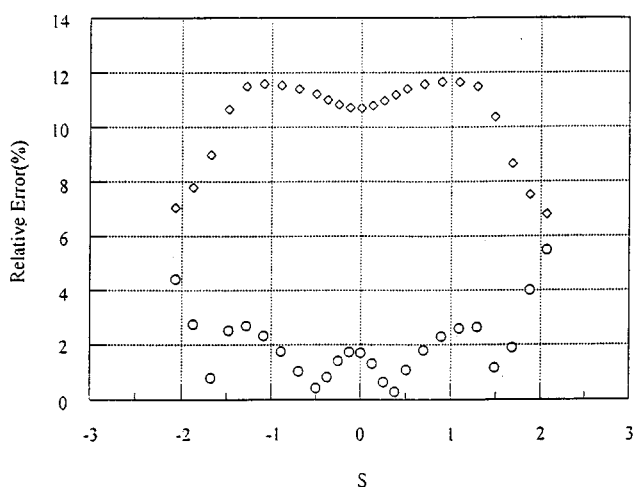


FIG. 16. Relative errors in reconstruction of surface pressures for a vibrating cylinder with two spherical endcaps at $b/a=0.5$ and $ka=1$. ●: Inherent plus 5% random errors; ◇: inherent plus 10% random errors.

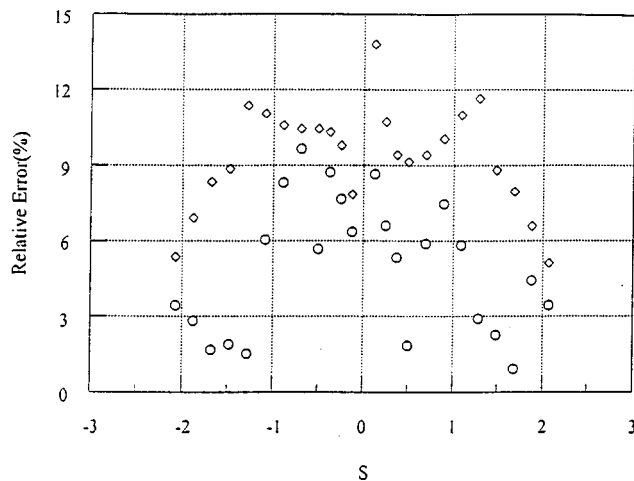


FIG. 17. Relative errors in reconstruction of surface pressures for an oscillating cylinder with two spherical endcaps at $b/a=0.5$ and $ka=1$. ●: Inherent plus 5% random errors; ◇: inherent plus 10% random errors.

V. CONCLUDING REMARKS

The HELS method can be used to reconstruct acoustic pressures on the surfaces of arbitrarily shaped objects based on measured acoustic pressure signals in the field. This method works best for a spherical surface or a chunky object. For an elongated object subject high-frequency excitations, the convergence may be worse and more expansion terms are needed. Since the number of measurements is determined by that of expansion terms, which is in general much smaller than that of the discretized nodes associated with BEM, the efficiency of the HELS method is much higher than that of BEM. Another advantage is that solutions thus obtained are always unique. Moreover, it can tolerate certain degrees of uncertainties in the measured data. These features may make the HELS method a potentially useful diagnosing tool for a vibrating machine.

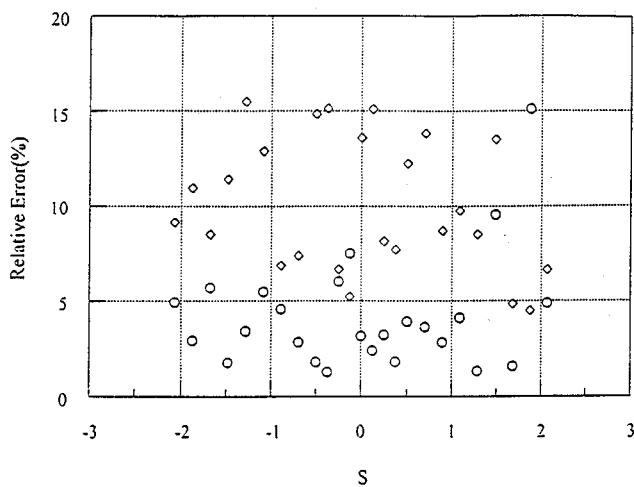


FIG. 18. Relative errors in reconstruction of surface pressures for a partially vibrating cylinder with two spherical endcaps at $b/a=0.5$ and $ka=1$. ○: Inherent plus 5% random errors; ◇: inherent plus 10% random errors.

ACKNOWLEDGMENT

This work was supported by a Rumble Fellowship from Wayne State University.

- Bai, M. R. (1992). "Application of BEM (boundary element method)-based acoustic holography to radiation analysis of sound sources with arbitrarily shaped geometries," *J. Acoust. Soc. Am.* **92**, 533–549.
- Bergman, S. (1960). *Integral Operators in the Theory of Linear Partial Differential Equations* (Springer-Verlag, Berlin), pp. 66–67.
- Birkhoff, G., and Lynch, R. E. (1984). *Numerical Solution of Elliptic Problems* (SIAM, Philadelphia), pp. 258–261.
- Borgiotti, G., Sarkissian, A., Williams, E. G., and Schuetz, L. (1990). "Conformal generalized near-field acoustic holography for axisymmetric geometries," *J. Acoust. Soc. Am.* **88**, 199–209.
- Burnett, D. S. (1994). "A three-dimensional acoustic infinite element based on a prolate spheroidal multipole expansion," *J. Acoust. Soc. Am.* **96**, 2798–2816.
- Chao, Y.-C. (1987). "An implicit least-square method for the inverse problem of acoustic radiation," *J. Acoust. Soc. Am.* **81**, 1288–1292.
- Ciskowski, R. D., and Brebbia, C. A. (1991). *Boundary Element Methods in Acoustics* (Computational Mechanics Publications, Southampton; Elsevier Applied Science, London).
- Colton, D., and Kress, R. (1992). *Inverse Acoustic and Electromagnetic Scattering Theory* (Springer-Verlag, Berlin).
- Davis, P. J., and Rabinowitz, P. (1961). "Advances in orthonormalizing computation," *Adv. Comput.* **2**, 55–133.
- Franklin, J. N. (1970). "Well-posed stochastic extensions of ill-posed linear problems," *J. Math. Anal. Appl.* **31**, 682–716.
- Gardner, B. K., and Bernhard, R. J. (1988). "A noise source identification technique using an inverse Helmholtz integral equation method," *Trans. ASME, J. Vib. Acoust. Stress* **110**, 84–90.
- Ghosh Roy, D. N. (1991). *Methods of Inverse Problems in Physics* (CRC, Boca Raton), pp. 468–469.
- Hadamard, J. (1923). *Lectures on Cauchy's Problem in Linear Partial Differential Equations* (Yale U.P., New Haven).
- Kim, G.-T., and Lee, B.-T. (1990). "3-D sound source reconstruction and field reproduction using the Helmholtz integral equation," *J. Sound Vib.* **136**, 245–261.
- Lamm, P. K. (1993). "Inverse problems and ill-posedness," in *Inverse Problems in Engineering: Theory and Practice*, edited by N. Zabaras, K. A. Woodbury, and M. Raynaud (The American Society of Mechanical Engineers, New York), pp. 1–10.
- Landweber, L. (1951). "An iteration formula for Fredholm integral equations of the first kind," *Am. J. Math.* **73**, 615–624.
- Liberstein, H. M. (1960). "A continuous method in numerical analysis applied to examples from a new class of boundary value problems," *Mathematical Research Center Technical Summary Report*, **175** (University of Wisconsin, Madison, WI).
- Loyau, T., and Pascal, J.-C. (1988). "Broadband acoustic holography reconstruction from acoustic intensity measurements. I: Principle of the method," *J. Acoust. Soc. Am.* **84**, 1744–1750.
- Maynard, J. D., Williams, E. G., and Lee, Y. (1985). "Near-field acoustic holography: I. Theory of generalized holography and the development of NAH," *J. Acoust. Soc. Am.* **78**, 1395–1413.
- Morse, P. M., and Ingard, K. U. (1968). *Theoretical Acoustics* (McGraw-Hill, New York), pp. 332–366.
- Nehari, Z. (1956). "On the numerical solution of the Dirichlet Problem," in *Proceedings of Conference on Differential Equations* (University of Maryland, College Park, MD), pp. 157–178.
- Pierce, A. D. (1981). *Acoustics: An Introduction to Its Physical Principles and Applications* (McGraw-Hill, New York), pp. 153–157.
- Phillips, D. L. (1962). "A technique for the numerical solution of certain integral equations of the first kind," *J. Assoc. Comput. Mach.* **9**, 84–97.
- Pinsky, M. A. (1991). *Partial Differential Equations and Boundary-Value Problems with Applications* (McGraw-Hill, New York), 18 pp.
- Sarkissian, A. (1990). "Near-field acoustic holography for an axisymmetric geometry: A new formulation," *J. Acoust. Soc. Am.* **88**, 961–966.
- Sarkissian, A. (1991). "Acoustic radiation from finite structures," *J. Acoust. Soc. Am.* **90**, 574–578.
- Sarkissian, A. (1992). "Reconstruction of the acoustic field on radiating structures," *J. Acoust. Soc. Am.* **92**, 825–830.
- Schenck, H. A. (1968). "Improved integral formulation for acoustic radiation problems," *J. Acoust. Soc. Am.* **44**, 41–58.
- Stewart, G. W. (1973). *Introduction to Matrix Computations* (Academic, New York), pp. 184–230.
- Turchin, V. F., Kozlov, V. P., and Malkevich, M. S. (1971). "The use of mathematical-statistics methods in the solution of incorrectly posed problems," *Soviet Physics Uspekhi*, **13**, 681–703.
- Twomay, S. (1963). "On the numerical solution of Fredholm integral equations of the first kind by the inversion of the linear system produced by quadrature," *J. Assoc. Comput. Mach.* **10**, 97–101.
- Vekua, I. N. (1953). "On completeness of a system of metaharmonic functions," *Dokl. Akad. Nauk SSSR* **90**, 715–718.
- Veronesi, W. A., and Maynard, J. D. (1987). "Near-field acoustic holography (NAH): II. Holographic reconstruction algorithms and computer implementation," *J. Acoust. Soc. Am.* **81**, 1307–1322.
- Veronesi, W. A., and Maynard, J. D. (1989). "Digital holographic reconstruction of sources with arbitrarily shaped surfaces," *J. Acoust. Soc. Am.* **85**, 588–598.
- Wang, Z. (1995). "Helmholtz Equation-Least Squares (HELs) Method for Inverse Acoustic Radiation Problems," Ph.D. dissertation, Wayne State University, Detroit.
- Wang, Z., Wu, S. F., and Su, S. (1995). "An innovation in inverse acoustic radiation problems," in *Target Identification and Inverse Problems in Acoustics*, edited by R. J. Nagem, G. C. Gaunard, and M. C. Hastings, *Proceedings of the ASME Noise Control and Acoustics Division, NCA-Vol. 21*, pp. 127–136.
- Williams, E. G., and Dardy, H. D. (1987). "Generalized nearfield acoustic holography for cylindrical geometry: Theory and experiment," *J. Acoust. Soc. Am.* **81**, 389–407.
- Williams, E. G., Houston, B. H., and Bucaro, J. A. (1989). "Broadband nearfield acoustical holography for vibrating cylinders," *J. Acoust. Soc. Am.* **86**, 674–679.
- Williams, E. G., Maynard, J. D., and Skudrzyk, E. (1980). "Sound source reconstruction using a microphone array," *J. Acoust. Soc. Am.* **68**, 340–344.
- Wu, S. F., and Yu, Jingyou (1997). "A generalized Helmholtz equation-least-squares (HELs) method for reconstructing acoustic pressure fields," under preparation.

Measurements of newly defined intensimetric quantities and their physical interpretation

Domenico Stanzial and Nicola Prodi

CIARM c/o C.N.R.-Cemoter Acoustics Department via Canal Bianco 28, I-44044 Cassana, Ferrara, Italy

(Received 26 November 1996; revised 9 June 1997; accepted 16 June 1997)

This paper deals with the measurement and physical interpretation of the quantities \mathbf{a} and \mathbf{r} introduced in a previous paper [D. Stanzial, N. Prodi, and G. Schiffrer, "Reactive intensity for general fields and energy polarization," J. Acoust. Soc. Am. **99**, 1868–1876 (1996)]. The quantity \mathbf{a} , which has the same time dependence as the squared acoustic pressure and the same direction as the time averaged sound intensity (\mathbf{j}), will be called here "radiating" intensity, while \mathbf{r} which has zero average, will be called "oscillating" intensity. A coherent picture of the energy transfer process in steady sound fields based on the decomposition $\mathbf{j} = \mathbf{a} + \mathbf{r}$ of the instantaneous sound intensity will be sketched and discussed. Furthermore, a direct experimental comparison between \mathbf{a} and \mathbf{r} and the real and imaginary parts of the complex intensity is presented for some field conditions. © 1997 Acoustical Society of America. [S0001-4966(97)00510-9]

PACS numbers: 43.20.Ye, 43.20.Rz, 43.58.Fm [JEG]

INTRODUCTION

Since the advent of instrumentation devoted to the measure of acoustic intensity, it has been possible to represent the energy transfer process within sound fields by the use of experimentally measured intensity maps. A former noticeable result in this respect was due to Waterhouse and Yates,¹ whose description of the energy transfer process was developed on the concept of "energy streamlines": that is, lines along which all the energy in the field did flow. These lines are tangent to the average acoustic intensity at every point inside the sound field.

An early criticism to this picture came from Mann *et al.*² who started their analysis from the decomposition of instantaneous intensity \mathbf{j} into active and reactive parts and investigated, for a pure-tone field, how the decomposition affected the energy transfer process description. Even if the term containing the reactive intensity time averages to zero, they rightly concluded that both the active and reactive intensities contribute to the actual energy flux. Another topic of their contribution was the introduction of "sources" for reactive intensity, which are formally related to the Lagrangian of the field, but whose physical significance is still an unresolved problem.³

The definition of complex intensity for general fields as found in Ref. 4 leads to the conclusion that, since the time average of reactive intensity is not vanishing, then in order to consider all the contributions to the energy transfer process, it is necessary to also include, together with the active intensity vector field, the flow of energy along the "paths" of averaged reactive intensity. In other words, the generalization of the point of view of Mann *et al.* is that a time average picture of the energy transfer process is only achieved by means of two vector fields.

All the above-mentioned interpretations present a critical aspect: the decomposition of instantaneous intensity \mathbf{j} . Once the mathematical properties of the decomposition are well-defined, then a consequent picture of the energy transfer process can be developed accordingly.

A new contribution to this matter was presented in recent years in Refs. 5 and 6 where the general decomposition $\mathbf{j} = \mathbf{a} + \mathbf{r}$ has been introduced for stationary fields. In Refs. 5 and 6 \mathbf{a} and \mathbf{r} have been called "instantaneous active" and "reactive" intensity. Here, these quantities will be called respectively *radiating* and *oscillating* instantaneous intensity, in order to avoid confusion with the real and imaginary parts of the complex intensity.⁴ The mathematical features of such decomposition will be summarized below; here we simply note that the time averaged value of radiating intensity equals the active intensity, while the time averaged value of oscillating intensity is zero by definition.

On the basis of this decomposition, a framework will be developed which gives both a time average and a time-dependent interpretation of the energy transfer process within general stationary fields. In the time average framework only one vector field (averaged radiating intensity) can be detected, which is tangent to streamlines of energy. But, different from Waterhouse's first intuition, not all of the energy actually flows along these streamlines. In fact, there is also energy which is transferred by the oscillating part of intensity, which cannot contribute to the net flow because it must oscillate due to the vanishing of time average value of \mathbf{r} . Furthermore, within the proposed picture of energy transfer, plane progressive waves are considered as ideal guides for energy radiation and, conversely, standing waves as sound fields where energy is locally oscillating.

The utility of building up such a framework for the description of the time averaged energy transfer process is evident. On the basis of this picture, for instance, practically all the intensity maps so far collected in the more disparate sectors of applied acoustics should be easily reinterpreted: The only lack affecting this kind of sound field visualization can be filled by adding to the intensity maps a suitable measure telling how much energy oscillates around every measuring point.

In this paper the above outlined framework for the energy transfer process is sketched and newly defined instanta-

neous and time averaged intensimetric quantities are introduced and their measures are reported. A comparison of these quantities with the active and reactive intensities known from literature is then accomplished and their different behavior is analyzed to some extent.

I. DEFINITIONS OF INSTANTANEOUS INTENSITIES

A. Definition of new intensimetric quantities

The behavior of the instantaneous intensity vector \mathbf{j} : $= p\mathbf{v}$ can be understood by analyzing the time dependence of pressure p and velocity \mathbf{v} of the air particle at the measurement point. If pressure and velocity have the same time dependence, their values cross the respective zero reference line at the same instant and thus the two quantities yield values with the same algebraic sign. Then the components of their product are positive and its time average is nonvanishing. This occurrence means that a nonzero *time averaged* momentum is transmitted to the confining air particles in such a way that energy flux streamlines are built-up all over the sound field. On the other hand, when pressure and velocity do not cross the zero line at the same instant, a fraction of the sound energy does not flow along the mean streamline passing through the given point and oscillates locally.

These two fundamental features of energy transfer mechanism are instantaneously described by the novel intensimetric quantities \mathbf{a} and \mathbf{r} introduced in Ref. 5.

Part \mathbf{a} is responsible for energy propagation along the streamlines and can be called *radiating intensity*; in formulas it reads:

$$\mathbf{a}(\mathbf{x}, t) := \frac{p^2 \langle p\mathbf{v} \rangle}{\langle p^2 \rangle}, \quad (1)$$

where $\langle \cdot \rangle$ stands for the stationary time averaging procedure. The time averaged radiating intensity coincides with the well-known active intensity

$$\mathbf{A}(\mathbf{x}) := \langle \mathbf{a} \rangle = \langle p\mathbf{v} \rangle.$$

Putting aside mathematical details it can be now noted that the complement to instantaneous intensity which is achieved by a simple vector subtraction:

$$\mathbf{r}(\mathbf{x}, t) := \mathbf{j}(\mathbf{x}, t) - \mathbf{a}(\mathbf{x}, t) = \frac{\langle p^2 \rangle p\mathbf{v} - p^2 \langle p\mathbf{v} \rangle}{\langle p^2 \rangle} \quad (2)$$

averages to zero by definition, i.e., $\langle \mathbf{r} \rangle = 0$.

The vector quantity \mathbf{r} which, differently from \mathbf{a} , must change its orientation at a fixed point, can be called *oscillating intensity*. Since the first-order statistical moment (time average) of the vector \mathbf{r} always vanishes, a nontrivial measure of the average properties of \mathbf{r} has to be obtained by the calculation of the first nonvanishing higher-order moment which, in this case, is the second-order one. The suitable mathematical entity to consider, in order to describe the second-order statistical properties of a vector, is thus the second-order tensor $\mathcal{R} = \sqrt{2} \langle \mathbf{r} \otimes \mathbf{r} \rangle$. This tensor summarizes the most important time averaged spatial informations concerning oscillations of energy. In Ref. 6 a thorough exposition of the tensor formalism can be found.

For the aim of this paper we shall only consider the scalar value

$$R := \sqrt{2 \langle \mathbf{r}^2 \rangle}, \quad (3)$$

which is directly obtained as the trace of the former tensor.

B. Alternative definitions

Mathematically speaking, the definition of radiating intensity consists in a multiplication of each component of active intensity by a normalized scalar function $p^2 / \langle p^2 \rangle$ which clearly has the same time dependence as the instantaneous squared pressure. Since both pressure and the three components of velocity are solutions of the wave equation, there is no physically sensible reason to prefer pressure to the velocity components in the definition given above. Hence, instead of squared pressure, one may equally pursue an alternative normalization based on the square of the three components of velocity. This procedure involves the multiplication of each component of active intensity by a normalization scalar function derived from the respective squared velocity component. On this basis a pair of alternative definitions can be introduced for radiating and oscillating intensities, which will be indicated by \mathbf{a}' and \mathbf{r}' :

$$\mathbf{a}'(\mathbf{x}, t) := \begin{pmatrix} a'_x \\ a'_y \\ a'_z \end{pmatrix}; \quad a'_i := \frac{v_i^2 \langle p v_i \rangle}{\langle v_i^2 \rangle}; \quad i = x, y, z, \quad (4)$$

$$\mathbf{r}'(\mathbf{x}, t) := \mathbf{j}(\mathbf{x}, t) - \mathbf{a}'(\mathbf{x}, t). \quad (5)$$

A few remarks have to be made, as this alternative definitions might seem to produce results different from those obtained by the definitions given in the previous section. In fact, it clearly appears that, starting from the same $p(t)$ and $\mathbf{v}(t)$, the two formulations will yield different time histories of both radiating and oscillating intensity. Nevertheless, it can be shown that the time average properties of the two pairs \mathbf{a} , \mathbf{a}' and \mathbf{r} , \mathbf{r}' coincide, no matter the sound field. In other words the following relations hold:

$$\langle \mathbf{a} \rangle = \langle \mathbf{a}' \rangle = \langle p\mathbf{v} \rangle = \mathbf{A}, \quad (6)$$

$$\sqrt{2 \langle \mathbf{r}^2 \rangle} = \sqrt{2 \langle \mathbf{r}'^2 \rangle} = R. \quad (7)$$

We will support this statement with experimental results in a following section.

Given that \mathbf{a} , \mathbf{a}' and \mathbf{r} , \mathbf{r}' present the same behavior to second statistical order, it can be stated that the two alternative definitions fit the same proposed picture.

C. Definition of active and reactive intensities

As reported in Ref. 4 the definitions of active $\mathbf{I}(t)$ and reactive $\mathbf{J}(t)$ instantaneous intensities in a narrow-band field are, respectively, the real and imaginary part of the complex intensity $\mathbf{I}_c(t)$, which is introduced by the implementation of an Hilbert transformation process, here denoted by a caret:

$$\mathbf{I}_c(t) := \frac{1}{2} [p(t) + i\hat{p}(t)] [\mathbf{v}(t) - i\hat{\mathbf{v}}(t)],$$

$$\mathbf{I}(t) := \text{Re}\{\mathbf{I}_c(t)\} = \frac{1}{2} [p(t)\mathbf{v}(t) + \hat{p}(t)\hat{\mathbf{v}}(t)], \quad (8)$$

$$\mathbf{J}(t) := \text{Im}\{\mathbf{I}_c(t)\} = \frac{1}{2} [\hat{p}(t)\mathbf{v}(t) - p(t)\hat{\mathbf{v}}(t)]. \quad (9)$$

The time average values of the above quantities can be easily calculated and are generally referred to by omitting the explicit time dependence:

$$\mathbf{I} = \langle p \mathbf{v} \rangle, \quad \mathbf{J} = \langle p \hat{\mathbf{v}} \rangle. \quad (10)$$

The instantaneous active intensity averages to the well-known active intensity and, in this respect, \mathbf{I} and Eq. (6) give the same time average description of energy flux.

Moreover, according to (10), the time average of the instantaneous reactive intensity in a general sound field is nonvanishing. The most remarkable difference between \mathbf{J} and the time averaged oscillating intensity, R , Eq. (7) is then evident: while R is a scalar quantity, the reactive intensity \mathbf{J} is a vector quantity.

II. DISCUSSION

First of all, it must be remarked that summarizing the time averaged properties of oscillating intensity by a scalar quantity provides exactly the suitable measure of that part of energy which does not contribute to the net flow. Since oscillating intensity has no average energy streamlines, what one can do is to characterize the total amount of oscillations of energy by the root mean square value R , although neglecting the spatial distribution of such oscillations. A forward step in the analysis shall involve the tensor formalism, which can tell exactly the average magnitude of oscillations of energy along every given direction. On the other hand, the vector field (1) [as well as the alternative field (4)] always has direction and orientation coinciding with that of the active intensity, the modulus being equal only when time averaged. So the averaged streamlines of this quantity coincide with those of active intensity. This leads to the conjecture that the energy transfer within any general stationary sound field can be exhaustively described by the time averaged properties of the radiating and oscillating intensities.

The relationship between the newly defined quantities and active and reactive intensities is also of interest. The equality of the averaged values \mathbf{A} and \mathbf{I} in any sound field has been already stressed. Regarding the oscillating intensity it can be proved (see Ref. 6) that the direction along which oscillations of energy occur coincides with that of \mathbf{J} in a monochromatic field, but this coincidence gets lost in general fields. This fact has also been briefly investigated experimentally. Furthermore the time histories of the paired quantities (1) and (8) as well as those of (2) and (9) have been experimentally obtained, and their comparison will be reported in the next section.

III. EXPERIMENTAL RESULTS

Intensimetric measurements have been carried out in order to experimentally illustrate the newly defined quantities, to check the frame for the energy transfer process based on them, and to relate them with active and reactive intensities known from the literature.

All the measurements were taken along a single Cartesian component coinciding with the axis of a sound intensity probe, Brüel & Kjær 3591 (with 50-mm spacer). The probe supplied two pressure signals to an FFT Brüel & Kjær 2032

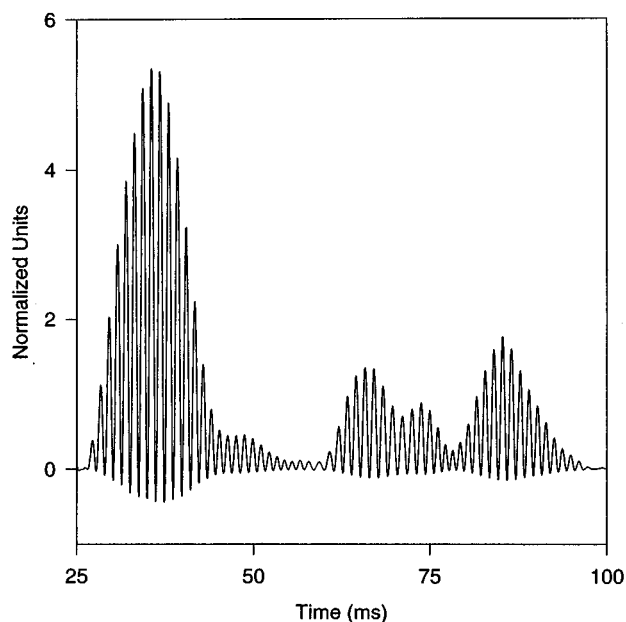


FIG. 1. Instantaneous intensity measured inside an anechoic room. Stimulus is $\frac{1}{3}$ octave band filter noise with center frequency of 400 Hz and the distance between the loudspeaker and the facing probe is 1 m.

analyzer where they were captured and digitally converted. Then they were passed, via an HP-IB port, to a Hewlett-Packard 9817 computer for subsequent processing. The program running on the computer first implemented Euler's equation to get the time history of the velocity in the mid point between microphones and then, exploiting suitable algorithms, gave both the time histories and average values of the acoustic quantities introduced in Sec. I. The test signals were delivered by a small loudspeaker mounted in an enclosed cabinet.

The scale normalization for time-dependent intensimetric measurements was accomplished by dividing each time history by the root-mean square of instantaneous intensity (obtained with the same raw data), whereas measures of pressure and velocity were normalized by the root mean square of pressure.

The first set of measurements was carried out in a large anechoic room with the probe facing the loudspeaker at a distance of 1 m. The test signal was noise in a third octave band centered at 400 Hz. In Fig. 1 the instantaneous intensity is reported as reference: We note that a kind of amplitude modulation seems to characterize the plot, showing also a fundamental of twice the center frequency of the band. Figure 2 presents the temporal evolution of Eqs. (1) and (8) for this field. As expected by the given definition, radiating intensity cannot change its sign along the plot as it must always be equal to that of its average \mathbf{A} . The quantity $\mathbf{I}(t)$ behaves like a sort of running time average of \mathbf{a} .

Similarly, in Fig. 3 quantities (2) and (9) are shown. The instantaneous reactive intensity $\mathbf{J}(t)$ appears to be the envelope signal of \mathbf{r} , whose mean value is clearly zero as it oscillates around the zero line.

The two comparisons of the coupled alternative definitions (1) with (4) and (2) with (5) are shown respectively in Figs. 4 and 5. For both radiating and oscillating instanta-

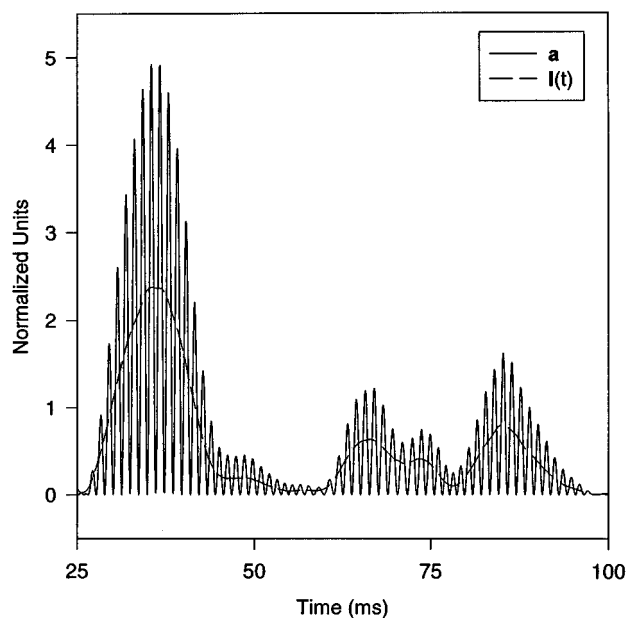


FIG. 2. Comparison of radiating and active instantaneous intensities in the same field conditions as Fig. 1.

neous fluxes, the two formulations give in this case a substantially equivalent time-dependent picture.

Next, measures have been taken in a reverberation room ($V=245 \text{ m}^3$, $RT \approx 4 \text{ s}$) and are here presented in Figs. 6–11. Figure 6 refers to a pure tone at 800 Hz as stimulus, with a distance between the probe and loudspeaker of 1 m. In this case the relationships detected above, that is $I(t)$ being a running time average of a and $J(t)$ acting as the envelope signal of r , are confirmed. It is also worth noting the sign of $J(t)$, which is negative even if the probe is facing the speaker.

In the same room conditions, the stimulus was changed

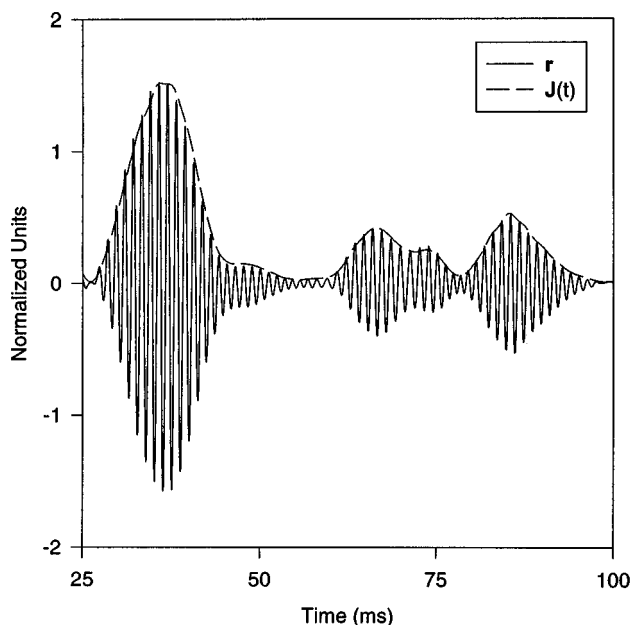


FIG. 3. Comparison of oscillating and reactive instantaneous intensities in the same field conditions as Fig. 1.

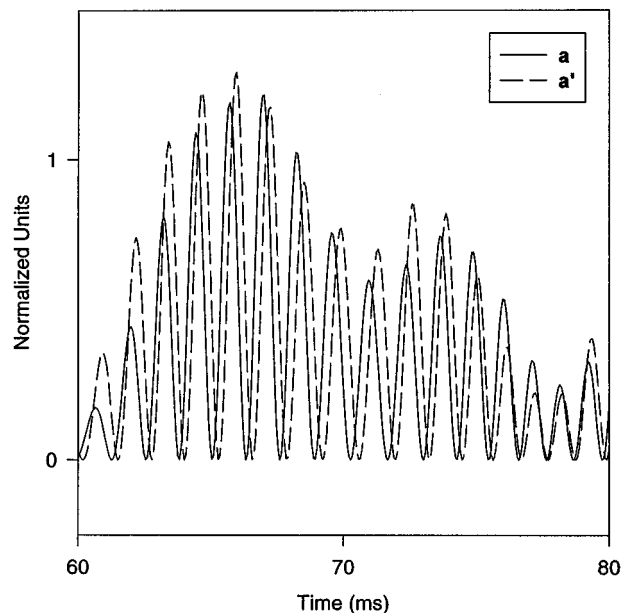


FIG. 4. Comparison of radiating intensity with its alternative definition in the same field conditions as Fig. 1.

to a random noise in the third octave band centered at 630 Hz and the related measures are shown in Figs. 7–11. Figure 7 provides an interesting example of “cooperation” between pressure and normalized velocity (namely $\rho c \mathbf{v}$, where ρ is the equilibrium air density and c is the speed of sound): The zones where the two variables have the same time dependence supply exclusively radiating contribution to instantaneous intensity, whereas the rest gives an oscillating contribution. A link of this kind can be checked by considering Figs. 8 and 9 where the plots of a and $I(t)$ and of r and $J(t)$ are shown, respectively. In the present field conditions neither of the two relations of running the time average and the

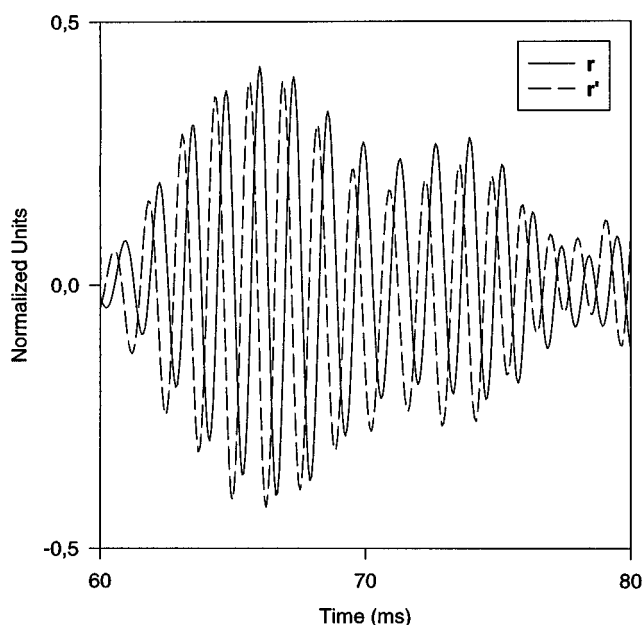


FIG. 5. Comparison of oscillating intensity with its alternative definition in the same field conditions as Fig. 1.

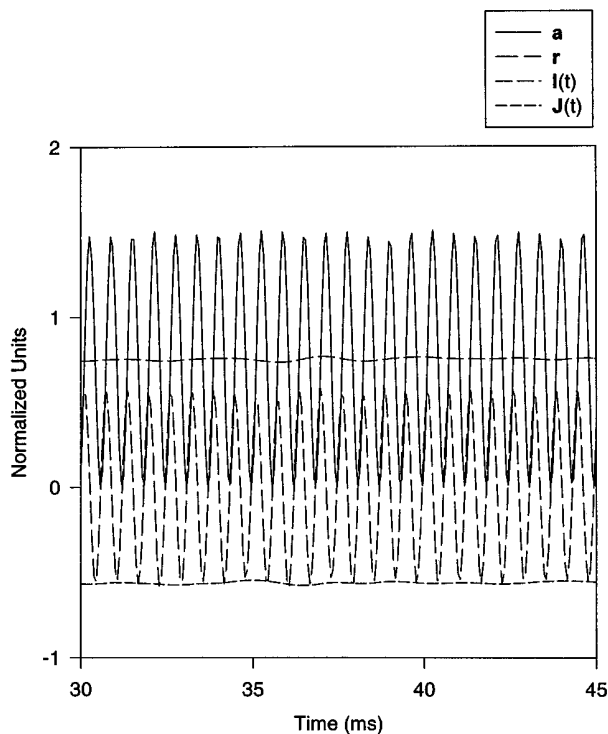


FIG. 6. Intensity quantities measured inside a reverberation room. Stimulus is a pure tone of 800 Hz and the distance between the loudspeaker and the facing probe is 1 m.

envelope signal between the newly defined quantities and the active and reactive instantaneous intensities encountered above is valid. Hence it is not possible to establish a straightforward connection linking the new intensimetric quantities

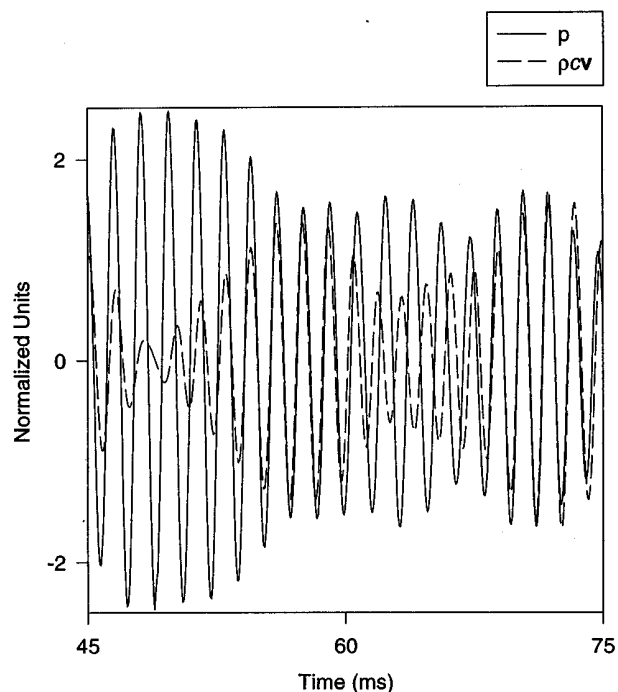


FIG. 7. Time histories comparison of pressure and normalized velocity inside a reverberation room. Stimulus is $\frac{1}{3}$ octave band filter noise with center frequency of 630 Hz and the distance between the loudspeaker and the facing probe is 1 m.

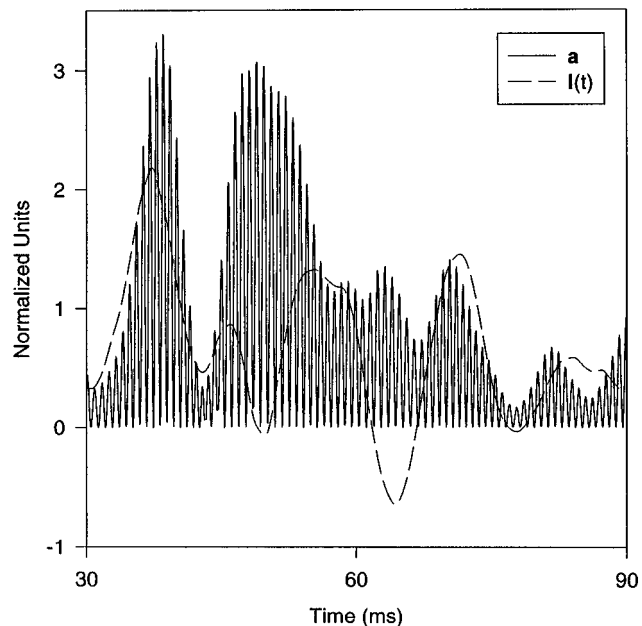


FIG. 8. Comparison of radiating and active instantaneous intensities in the same field conditions as Fig. 7.

to the real and imaginary parts of the complex intensity.

In Figs. 10 and 11 the alternative definitions a' and r' are characterized by a time-dependent picture which is completely different from that of a and r .

In addition to the time dependence of the above mentioned quantities, their spatial dependence was investigated through measurements of their time average values in different points inside test fields.

The measures were taken along the loudspeaker axis at various distances inside the anechoic room and each time average measurement at a fixed point was repeated 20 times and statistically analyzed. The loudspeaker was fed with a

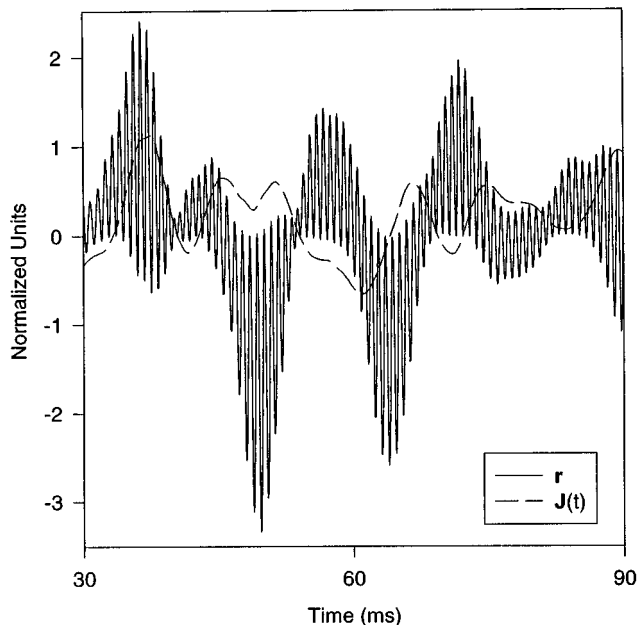


FIG. 9. Comparison of oscillating and reactive instantaneous intensities in the same field conditions as Fig. 7.

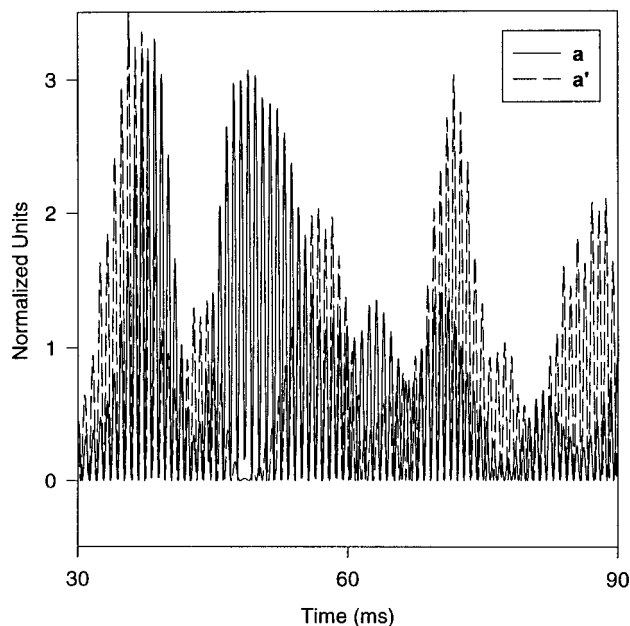


FIG. 10. Comparison of radiating intensity with its alternative definition in the same field conditions as Fig. 7.

third octave band filtered noise centered at 400 Hz. Figure 12 reports the comparison of the averages of the different definitions of radiating and oscillating intensities. Their respective values coincide within errors, thus validating Eqs. (6) and (7). Incidentally one can interpret the intersection point between radiating and oscillating intensity, occurring at about 25 cm from the loudspeaker, as the physical separation between the near field and the far field. In the near field there is a predominant effect of energy locally confined, whereas the far field is characterized by the stronger radiation of energy.

Then a second loudspeaker was added facing the previ-

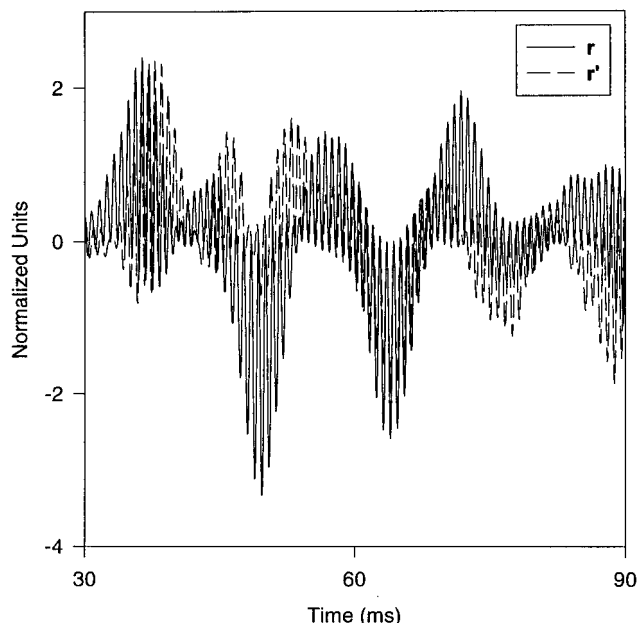


FIG. 11. Comparison of oscillating intensity with its alternative definition in the same field conditions as Fig. 7.

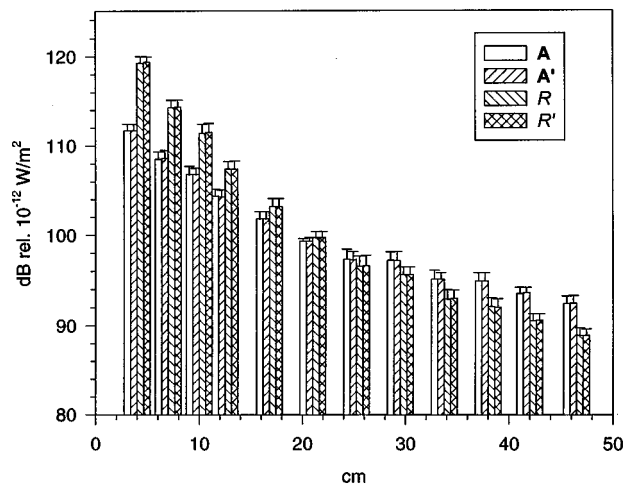


FIG. 12. Averaged intensimetric quantities measured in the region in front of a loudspeaker inside an anechoic room. Stimulus is $\frac{1}{3}$ octave band filter noise with center frequency of 400 Hz.

ous one at a distance of 1.1 m and measures were taken along the line connecting the two. The loudspeaker on the right was fed with a pure tone of 385 Hz while the left one with an equal amplitude pure tone of 415 Hz. The choice of rather close frequency signals (both within the third octave band centered in 400 Hz) was intended to study the field in a quasi-interference condition. Figure 13 shows the time independent R and the modulus of reactive intensity $|J|$ for this bichromatic superposition field. The two quantities behave in a completely different manner in the region of interest: R tells us that at the points close to the center a great amount of

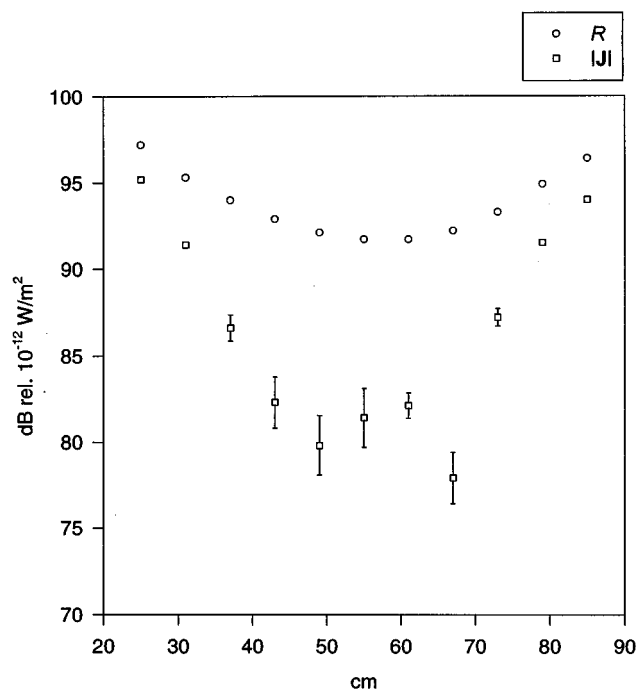


FIG. 13. Comparison of averaged oscillating intensity with the modulus of averaged reactive intensity in the region between two loudspeakers which are 1.1 m apart inside an anechoic room. The loudspeaker on the right is fed with a pure tone of 385 Hz and that on the left with a pure tone of 415 Hz with equal amplitude.

energy is indeed locally confined, just as it happens in the near field of a single loudspeaker. This result is consistent with the interpretation of progressive and standing wave fields within the proposed picture of the sound energy transfer. In detail, the more the condition of equal frequency is approached, the more the field in the region of interest resembles a standing wave pattern, which is agreed to be an acoustic field with all the energy trapped locally. The quantity $|J|$ shows instead much lower values at the same points because the contributions coming from the two sources add vectorially with opposite signs.

IV. CONCLUSIONS

New definitions of instantaneous intensimetric quantities in general stationary fields called radiating and oscillating intensities have been presented and measured for some sound field conditions.

It has been experimentally shown that, although two alternative different time-dependent definitions are possible, they both have the same properties to the second statistical order.

The introduction of radiating and oscillating intensities allows the time average energy transfer process within general stationary fields to be described just in terms of the active intensity maps plus a scalar field accounting for energy which does not contribute to the net flow.

The comparison between instantaneous active and reactive intensity and the newly introduced quantities has shown that there is no straightforward general relationship between them, even if a kind of functional relation appears in some of

the tested fields. At last, although the time average of the radiating intensity coincides with that of the instantaneous active intensity, the average properties of oscillating and reactive intensity are substantially different in a general (non-monochromatic) field.

ACKNOWLEDGMENTS

The measurements presented in the paper have been taken at the Acoustics Laboratory of the Technical University of Denmark under the supervision of Professor Finn Jacobsen. The authors are grateful to Professor Jacobsen both for his support and for the fruitful discussions on intensimetric quantities. The authors wish to thank Professor G. Schiffrer of the Physics Department of University of Ferrara for the critical reading of the manuscript. This work has been supported by a grant from the "Ferrara Ricerche" research pool and by a grant from the National Research Council of Italy within the program "Short term fellowship."

¹R. V. Waterhouse and T. W. Yates, "Energy streamlines for an extended sound source," in *Proc. 2nd International Congress on Acoustic Intensity*, pp. 129–135, Senlis, France, 23–26 September 1985, CETIM.

²J. Adin Mann III, J. Tichy, and A. J. Romano, "Instantaneous and time-averaged energy transfer in acoustic fields," *J. Acoust. Soc. Am.* **82**, 17–30 (1987).

³F. J. Fahy, *Sound Intensity* (Elsevier Applied Science, London, 1989), 1st ed., Chap. 4, p. 67.

⁴F. Jacobsen, "A note on instantaneous and time-averaged active and reactive sound intensity," *J. Sound Vib.* **147**, 489–496 (1991).

⁵G. Schiffrer and D. Stanzial, "Energetic properties of acoustic fields," *J. Acoust. Soc. Am.* **96**, 3645–3653 (1994).

⁶D. Stanzial, N. Prodi, and G. Schiffrer, "Reactive acoustic intensity for general fields and energy polarization," **99**, 1868–1876 (1996).

Analytical solutions for outdoor sound propagation in the presence of wind

Kai Ming Li and Qiang Wang

Engineering Mechanics Department, Faculty of Technology, The Open University, Milton Keynes MK7 6AA, United Kingdom

(Received 6 March 1996; revised 14 February 1997; accepted 28 May 1997)

A theoretical analysis for the sound field due to a point monopole source in a fluid, layered atmospheric environment is described. The analysis has included explicitly the effect of fluid motion in the three-dimensional wave equation. The atmospheric environment is assumed to have sound-speed and vector wind-velocity profiles that either increase or decrease monotonically with height. In addition, the atmosphere is assumed to be vertically stratified. In such an environment, the solution can be expressed analytically in terms of Airy functions but the forms of solution are different for the situations of upward and downward refraction. Some sound-speed and wind-velocity profiles are amenable to exact analyses. Two notable examples are (i) a windless environment with a linear sound-speed profile; and (ii) a medium with a linear wind shear layer and a constant sound speed. These two profiles are studied analytically and compared numerically with other computational schemes. The validity of a heuristic approximation, which replaces the vector wind-velocity profile with an effective sound-speed profile, is also investigated numerically. © 1997 Acoustical Society of America. [S0001-4966(97)05309-5]

PACS numbers: 43.28.Fp, 43.20.Bi [LCS]

INTRODUCTION

For many years there has been sustained interest in the theory of sound propagation in the atmosphere both for civilian and military applications. Particularly, in the last decade, there is considerable interest in many countries for the development of different numerical and analytical models to predict sound transmission loss over a long horizontal distance. The result of this intensive research has led to significant advancements in the field. Much of the details have been summarized recently in an excellent paper¹ in which benchmark cases are established for checking new models and computational codes. However, refraction by the wind gradients as well as temperature gradients have not usually been considered in these prior studies. To address the effect of wind gradients, a useful heuristic approximation is to replace the separate wind and temperature profiles with an effective sound-speed profile.²⁻⁵ However, the main purpose of this paper is to develop an integral and rigorous scheme that includes explicitly a wind velocity profile without resorting to the use of an effective sound-speed profile.

There have been many attempts to model the effect of the vector wind on the sound field because the sound transmission loss in a given direction depends on the wind vector in that direction. In the past, this problem has been tackled by the ray approximation (for example, Refs. 6-8), the high-frequency asymptotic approximation,^{9,10} and the fast-field program (FFP).^{11,12} In this paper, we report an alternative approach to calculate the effect of wind on sound propagation outdoors which involves the evaluation of an inverse Fourier integral by the calculus of residues.¹³ This method has been used in obtaining analytical solutions for a stationary stratified medium.¹⁴ The solution is often referred to as the residue series solution in an upward refracting medium,^{2,5,15} and the normal mode solution in a downward

refracting medium.¹⁶ This paper offers a generalization to the previous results. Also the previous theory is extended to include explicitly vector wind velocity profiles. Similar to those prior studies, the effects of atmospheric absorption and turbulence are ignored because we are primarily concerned with the development of an alternative method for predicting sound propagation outdoors in the presence of wind. The method described in this paper is complementary to the other numerical schemes, see Ref. 1 for the review.

The layout of this paper is as follows. In Sec. I, we discuss the formulation of the problem. Section II considers the residue series solution for the case of an upward refracting medium and in Sec. III we study the case of a downward refracting medium that leads to the normal-mode solution. In Secs. II and III, we demonstrate that the derived expressions can be reduced to previous results in the special case of a bilinear profile.^{2,15,16} We also describe a practical numerical scheme for tracking the poles of the residue series and normal-mode solution. The validation of the current scheme is described in Sec. IV in which numerical results are compared with two benchmark cases. In addition, we give analytic results for two profiles that leads to closed-form expressions for the sound field. These profiles are

- (i) a windless environment with a linear sound-speed profile; and
- (ii) a medium with a linear wind shear layer and a constant sound speed.

Finally we offer some concluding remarks in Sec. V.

I. FORMULATION OF THE PROBLEM

Let a monopole source of strength Q_s be situated at $(0,0,z_s)$ in a moving stratified medium. We assume that the medium properties, such as the mean velocity of air $\mathbf{u}(z)$ and density of air $\rho(z)$, only depend on the vertical distance z .

The angular frequency of the source is ω_s and the time-dependent factor $\exp(-i\omega_s t)$ is understood. In this paper we ignore the effect of gravity and assume that the acoustic wavelength is much smaller than the characteristic length scale for the medium. Also the effects of turbulence and the absorption of sound in the atmosphere are ignored in the calculations. Making use of the continuity and momentum equations,¹⁷ and the method of Fourier transformation, it is possible to show that the acoustic pressure can be expressed in an integral form.⁹

It is convenient to split the wind velocity $\mathbf{u}(z)$ into two components $[\mathbf{u}=(\mathbf{u}_r, u_z)]$ in the horizontal and vertical directions, respectively. The horizontal velocity \mathbf{u}_r can further be resolved into two components (u_x, u_y) along the x and y axes. In order to simplify the analysis, we ignore the vertical flow velocity, i.e., $u_z=0$, because it is usually small in comparison with the horizontal component in an atmospheric environment.

Introduce a Fourier transform pair for the acoustic pressure, $p(x, y, z)$ and $P(k_x, k_y; z)$, such that

$$p = \frac{1}{(2\pi)^2} \int_{-\infty}^{\infty} \int_{-\infty}^{\infty} P e^{i(k_x x + k_y y)} dk_x dk_y \quad (1)$$

and

$$P = \int_{-\infty}^{\infty} \int_{-\infty}^{\infty} p e^{-i(k_x x + k_y y)} dx dy. \quad (2)$$

Similarly, we can define an analogous transform pair for the velocity potential with the notations of $\phi \equiv \phi(x, y, z)$ and $\Phi \equiv \Phi(k_x, k_y; z)$, respectively. Then, the height-dependent part of the Green's function for the velocity potential can be determined by⁹

$$\frac{1}{\rho} \frac{d}{dz} \left(\rho \frac{d\Phi}{dz} \right) + [(\omega_m/c)^2 - k_x^2 - k_y^2] \Phi = Q_s \delta(z - z_s), \quad (3)$$

where Q_s is the source strength. Further, in the transformed space, the velocity potential and acoustic pressure are related according to

$$P = i\rho\omega_m\Phi, \quad (4)$$

where

$$\omega_m(k_x, k_y; z) = \omega_s - k_x u_x - k_y u_y. \quad (5)$$

The variable ω_m in Eq. (5) may be interpreted as the convected angular frequency representing the frequency that would be measured in a local frame of reference moving with the same velocity as the wind. For mathematical convenience, we introduce a modified velocity potential in the transformed space $\tilde{\Phi}$ such that

$$\Phi = -i\tilde{\Phi}/\sqrt{\rho^*(z)}, \quad (6)$$

where $\rho^*(z)$ is the dimensionless density which is obtained by dividing the air density by a reference value ρ_s [the density of air at source height, $\rho_s \equiv \rho(z_s)$]. It is obvious that $\tilde{\Phi}$ is not only proportional to Φ but is also dependent on the density of air. Both variables, Φ and $\tilde{\Phi}$, have the same physical dimension. It is straightforward to show, by substituting Eq.

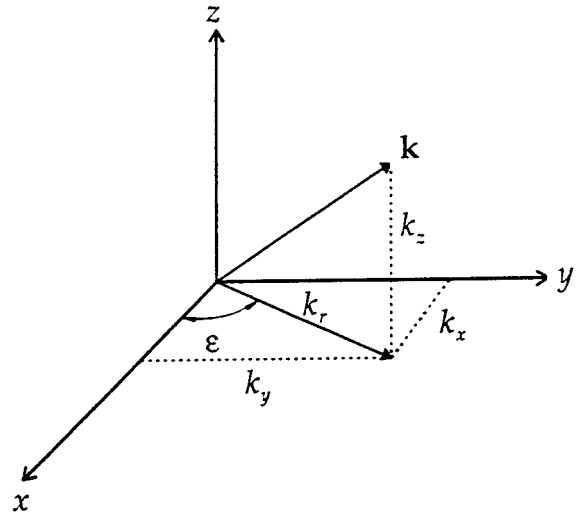


FIG. 1. The spatial position of the propagation vector \mathbf{k} and its components.

(6) into Eq. (4), that P can be expressed in terms of $\tilde{\Phi}$ as

$$P = \sqrt{\rho_s \rho} \omega_m \tilde{\Phi}. \quad (7)$$

Substitution of Eq. (6) into Eq. (3) leads to

$$\frac{d^2 \tilde{\Phi}}{dz^2} + k_z^2(k_x, k_y; z) \tilde{\Phi} = 2\pi i \sqrt{\rho^*} Q_s \delta(z - z_s) \delta(\omega - \omega_s), \quad (8)$$

where

$$k_z(k_x, k_y; z) = + \sqrt{(\omega_m/c)^2 - k_x^2 - k_y^2 + [-(\rho''/2\rho) + (\rho'/2\rho)^2]}, \quad (9)$$

ρ' and ρ'' are the first- and second-order derivatives with respect to the height z . In view of the fact that the variation in the mean density is usually small in a normal atmospheric condition, we can ignore the terms involving ρ'' and ρ'^2 in Eq. (9). Hence in our subsequent analysis, we approximate k_z by

$$k_z(k_x, k_y; z) = + \sqrt{(\omega_m/c)^2 - k_x^2 - k_y^2}. \quad (10)$$

We may interpret k_x , k_y , and k_z as the wave numbers in the x , y , and z axes respectively, see Fig. 1. It is important to note that the positive root of k_z is chosen so that a finite and bounded solution for the acoustic pressure may be obtained. With some tedious analysis, we can show that Eq. (8) is equivalent to those given in the previous publications.^{9,18}

The analysis can be simplified considerably if we use a cylindrical polar coordinate system such that k_x and k_y are given by

$$k_x = k_r \cos \epsilon, \quad k_y = k_r \sin \epsilon, \quad \text{and} \quad k_r^2 = k_x^2 + k_y^2, \quad (11)$$

where ϵ is the azimuthal angle measured from the positive x axis, see Fig. 1. Using the same coordinate system, we can express the wind velocity as

$$u_x = u \cos \psi_w \quad \text{and} \quad u_y = u \sin \psi_w, \quad (12)$$

where u and ψ_w are, respectively, the magnitude and direction of wind.

Making use of Eqs. (5), (11), and (12), the convected angular frequency ω_m can be expressed in the cylindrical polar coordinate system as

$$\omega_m(k_r, \epsilon; z) = \{k_0 n - k_r M \cos(\epsilon - \psi_w)\} c, \quad (13)$$

where k_0 is ω_s/c_0 , $M(z)$ is the mach number for the wind defined as $M(z) = u(z)/c(z)$, the index of refraction in the absence of wind n is defined as

$$n(z) = \frac{k(z)}{k_0}, \quad (14)$$

$c_0 \equiv c(0)$ and $k_0 \equiv k(0)$. Hereafter, the parameter ϵ in the argument of, for example, $\omega_m(k_r, \epsilon; z)$ will be omitted for simplicity. It follows from Eqs. (10) and (13) that the vertical wave number becomes

$$k_z(k_r; z) = +\sqrt{\kappa^2(k_r; z) - k_r^2}, \quad (15)$$

where

$$\kappa(k_r; z) = \omega_m/c = k_0 n - k_r M \cos(\epsilon - \psi_w) \quad (16)$$

which serves to define the wave number in a moving stratified medium. Here we remark that the effective sound speed is given by²

$$\bar{c}(z) = c(z) + \mathbf{u} \cdot \mathbf{r}.$$

The use of the effective sound-speed profile implies that the ‘‘convected wave number’’ is approximated by

$$\frac{\omega_m}{c} \approx \frac{\omega}{c(z) + \mathbf{u} \cdot \mathbf{r}}.$$

This simplification invariably imposes an additional approximation to the problem. In the following analysis, we separate the contributions due to $c(z)$ and $\mathbf{u} \cdot \mathbf{r}$ because, as suggested in Eq. (5) that, this is the ‘‘exact’’ representation of the problem.

To simplify our subsequent analysis, we restrict the problem such that there is only one turning point at $z = z_t$ for a given k_r in Eq. (15). The turning point corresponds to the situation where $k_z(k_r; z_t) = 0$. In terms of ray theory, the turning point represents the point where the slope of a ray path is zero. It is important to note that the solutions for the transformed pressure P are different for an upward refracting medium and for a downward refracting medium because of the requirement of the Sommerfeld radiation condition.^{15,16} We shall address these two different cases separately in the following sections.

II. AN UPWARD REFRACTING MEDIUM

A. The integral solution

We can now apply the turning point theory¹⁹ to obtain an approximate solution for $\tilde{\Phi}$. A pair of linearly independent solutions for Eq. (8) is given by

$$\tilde{\Phi} = \begin{cases} C_1 (\xi/k_z^2)^{1/4} \text{Ai}(-\xi) \\ C_2 (\xi/k_z^2)^{1/4} \text{Ai}(-\xi e^{i2\pi/3}), \end{cases} \quad (17)$$

where $\text{Ai}()$ is the Airy function and C_1 and C_2 are constants to be determined from the boundary conditions. In Eq. (17), the parameter, $\xi(k_r; z)$, is determined by

$$\xi(k_r; z) = \begin{cases} \left[\frac{3}{2} \int_{z_t}^z k_z(k_r; z) dz \right]^{2/3}, & \text{if } z > z_t, \\ -\left[\frac{3}{2} \int_z^{z_t} [-k_z^2(k_r; z)]^{1/2} dz \right]^{2/3}, & \text{if } z < z_t, \end{cases} \quad (18)$$

where it may be regarded as a dimensionless scale factor that characterizes the variations of wind and temperature gradients in the medium.

The stipulated boundary conditions are, namely, the Sommerfeld radiation condition, the continuity of pressure at the source plane, the discontinuity of particle velocity at the source plane, and the impedance boundary condition

$$\frac{\partial P}{\partial z} + ik_0 \beta P = 0, \quad (19)$$

where β is the normalized specific admittance of the impedance plane. For simplicity we assume the source strength, Q_s , to be $-i/\rho_s \omega_s$ so that the sound pressure in a homogeneous medium can be reduced to the well-known form $\exp(ik_0 R_1)/4\pi R_1$, where R_1 is the geometrical distance between the source and receiver. Denoting $z_> = \max(z_s, z)$ and $z_< = \min(z_s, z)$, substituting Eq. (17) into Eq. (8), applying the boundary conditions, and making use of Eq. (7), we can obtain an approximate solution for the transformed pressure P as

$$P = 2\pi \sqrt{\frac{\rho}{\rho_s}} \frac{\omega_m(k_r; z)}{\omega_m(k_r; z_s)} \left[\frac{\xi_< \xi_>}{k_<^2 k_>^2} \right]^{1/4} e^{i\pi/6} \text{Ai}(-\xi_> e^{i2\pi/3}) \times \{\text{Ai}(-\xi_<) - \Gamma \text{Ai}(-\xi_< e^{i2\pi/3})\}, \quad (20)$$

where the subscripts $<$ and $>$ denote the variables to be evaluated at heights $z_<$ and $z_>$, respectively. In other words, $\xi_< = \xi(k_r; z_<)$, $\xi_> = \xi(k_r; z_>)$, $k_< = k_z(k_r; z_<)$, and $k_> = k_z(k_r; z_>)$. In Eq. (20), the reflection factor Γ is given by

$$\Gamma = \frac{\text{Ai}'(-\xi_0) - q \text{Ai}(-\xi_0)}{e^{i2\pi/3} \text{Ai}'(-\xi_0 e^{i2\pi/3}) - q \text{Ai}(-\xi_0 e^{i2\pi/3})}, \quad (21)$$

where $\text{Ai}'()$ denotes the derivative of the Airy function with respect to its argument and the subscript 0 represents the parameters to be evaluated at $z=0$. The scaled and nondimensionalized admittance q is related to β by

$$q = ik_0 \beta l, \quad (22)$$

where

$$l = \frac{1}{d\xi/dz} \Big|_{z=0} \equiv \sqrt{\xi_0/(k_0^2 - k_r^2)}, \quad (23)$$

may be regarded as the creeping wave layer thickness.¹⁵ We remark that the solution for the transformed pressure, cf. Eq. (20), can be reduced to a form similar to that given by Ostashev.²⁰

Assuming the receiver position to be (r, ψ_r) in the cylindrical polar coordinate system and substituting Eq. (20) into Eq. (1), we can rewrite the integral expression for the acoustic pressure as

$$p = \frac{e^{i\pi/6}}{2\pi} \int_0^\infty \int_{-\pi}^\pi \sqrt{\frac{\rho}{\rho_s}} \frac{\omega_m(k_r; z)}{\omega_m(k_r; z_s)} \left[\frac{\xi_{<} \xi_{>}}{k_{<}^2 k_{>}^2} \right]^{1/4} \\ \times \{ \text{Ai}(-\xi_{<}) - \Gamma \text{Ai}(-\xi_{<} e^{i2\pi/3}) \} \\ \times \text{Ai}(-\xi_{>} e^{i2\pi/3}) k_r e^{ik_r r \cos(\epsilon - \psi_r)} d\epsilon dk_r. \quad (24)$$

The integral with respect to the azimuthal angle ϵ can be evaluated asymptotically.¹² Alternatively, the same result may also be obtained by invoking the discrete/continuous Fourier transform pair for the azimuthal angle.¹¹ The sound

field can then be reduced to a onefold Fourier integral as follows:

$$p \approx \frac{e^{i\pi/6}}{\sqrt{2i\pi r}} \int_0^\infty \sqrt{\frac{\rho}{\rho_s}} \frac{\omega_m(k_r; z)}{\omega_m(k_r; z_s)} \left[\frac{\xi_{<} \xi_{>}}{k_{<}^2 k_{>}^2} \right]^{1/4} \{ \text{Ai}(-\xi_{<}) \\ - \Gamma \text{Ai}(-\xi_{<} e^{i2\pi/3}) \} \text{Ai}(-\xi_{>} e^{i2\pi/3}) \sqrt{k_r} e^{ik_r r} dk_r, \quad (25)$$

where the dimensionless scale factor $\xi(k_r; z)$ is obtained by substituting Eqs. (15) and (16) into (18) to yield

$$\xi(k_r; z) = \begin{cases} \left[\frac{3}{2} \int_{z_t}^z \sqrt{[k_0 n(z) - k_r M_e(z)]^2 - k_r^2} dz \right]^{2/3}, & \text{if } z > z_t, \\ - \left[\frac{3}{2} \int_z^{z_t} \sqrt{k_r^2 - [k_0 n(z) - k_r M_e(z)]^2} dz \right]^{2/3}, & \text{if } z < z_t, \end{cases} \quad (26)$$

where

$$M_e(z) = M(z) \cos(\psi_r - \psi_w),$$

which is the effective Mach number and it is proportional to the magnitude of wind vector resolved in the direction of propagation. We note that the azimuthal angles of all the corresponding variables in the right side of Eq. (25) are to be evaluated at the stationary point (where $\epsilon = \psi_r$) as a result of approximating the integral by the method of stationary phase.¹² Further, it is evident from Eq. (26) that the effect of wind can be ignored in the crosswind situation because the effective Mach number M_e is zero.

B. Representation of the solution as a sum of residues series

We have developed an integral representation, cf. Eq. (25), for the sound field in a upward refracting medium in the last section. The integral may be estimated by the method of steepest descents²¹ to give the total sound field. However, the method of steepest descents is inappropriate in the shadow zone because there will be no stationary points in this region. Consequently, we seek an alternative approach by using the residue series representation. The details of the method are described elsewhere.^{2,14} In summary, the total sound field can be approximated by summing the contribution of the poles in the first quadrant of the complex k_r plane for the integrand in Eq. (25). The Airy functions are entire functions so that the only singularities of the integrand in the complex k_r plane are poles where the denominator of the reflection factor vanishes, see Eq. (21). This condition implies that

$$e^{i2\pi/3} \text{Ai}'(-\xi_0 e^{i2\pi/3}) - q \text{Ai}(-\xi_0 e^{i2\pi/3}) = 0. \quad (27)$$

The above equation may be regarded as the dispersion equation²⁰ and it is used to determine the horizontal wave numbers k_r that give contributions to the total sound field.

Suppose that the zeros of Eq. (27) are given by $k_r = K_n$ for $n = 1, 2, 3, \dots$. Then, from Eq. (25), the total sound field can be written in the residue series representation as

$$p \approx \frac{e^{i\pi/4}}{\sqrt{2\pi r}} \sqrt{\frac{\rho}{\rho_s}} \sum_n \frac{\omega_m(K_n; z)}{\omega_m(K_n; z_s)} \left[\frac{\bar{\xi}_{<} \bar{\xi}_{>}}{\bar{k}_{<}^2 \bar{k}_{>}^2} \right]^{1/4} \\ \times \frac{\sqrt{K_n} \text{Ai}(-\bar{\xi}_{>} e^{i2\pi/3}) \text{Ai}(-\bar{\xi}_{<} e^{i2\pi/3}) e^{iK_n r}}{[(\bar{\xi}_0 + q_n^2) \partial \bar{\xi}_0 / \partial K_n - \partial q_n / \partial K_n] [\text{Ai}(-\bar{\xi}_0 e^{i2\pi/3})]^2}, \quad (28)$$

where $\bar{\xi}_0 \equiv \xi(K_n; 0)$, $\bar{\xi}_{<} \equiv \xi(K_n; z_{<})$, $\bar{\xi}_{>} \equiv \xi(K_n; z_{>})$, $\bar{k}_{<} \equiv k_z(K_n; z_{<})$, $\bar{k}_{>} \equiv k_z(K_n; z_{>})$, and the nondimensionalized admittance q_n can be determined from Eq. (22) to give

$$q_n = ik_0 \beta l_n, \quad (29)$$

where l_n is the creeping wave layer thickness for each pole K_n . It follows from Eq. (23) that the creeping wave layer thickness is given by

$$l_n = \sqrt{\xi_0 / (k_0^2 - K_n^2)}. \quad (30)$$

Note that it is straightforward to determine $\partial \bar{\xi}_0 / \partial K_n$ and $\partial q_n / \partial K_n$ from Eqs. (22), (23), and (26). The details will not be given here. The total sound field can now be calculated by summing the residue series given in Eq. (28) provided that we know the profiles of wind velocity and sound speed. In general, there are no closed-form analytic solutions for most profiles. Numerical methods may be used to find $\bar{\xi}(z)$, $\partial \bar{\xi}_0 / \partial K_n$ and $\partial q_n / \partial K_n$ for arbitrary wind velocity and sound-speed profiles.

If the sound-speed gradient assumes the form of the so-called bilinear profile [i.e., $n^2(z) = 1 + 2z/R_c$, where R_c is the radius of curvature of the ray initially propagating horizontally from the source], then one may obtain a much simplified expression for the total sound field. With these approximations, it is possible to show that the dimensionless

scale factor, the creeping wave layer thickness, nondimensionalized admittance, and $\partial \bar{\xi}_0 / \partial K_n$ are given, respectively, by

$$\bar{\xi}(z) \equiv \xi(K_n; z) = (k_0^2 - K_n^2) l_n^2 + z / l_n, \quad (31a)$$

$$l_n = (R_c / 2k_0^2)^{1/3}, \quad (31b)$$

$$q_n = ik_0 \beta (R_c / 2k_0^2)^{1/3}, \quad (31c)$$

and

$$\frac{\partial \bar{\xi}_0}{\partial K_n} = -2K_n \left(\frac{R_c}{2k_0^2} \right)^{2/3}. \quad (31d)$$

In this special case, the thickness of each creeping wave layer l_n is constant for all poles. Consequently, the dimensionless scale factor $\bar{\xi}(z)$ is independent of K_n which implies that $\partial q_n / \partial K_n$ vanishes for all n . Hence the total sound field can be reduced to

$$p \approx \frac{-(R_c / 2k_0^2)^{1/3} e^{i\pi/4}}{\sqrt{8\pi r}} \sqrt{\frac{\rho}{\rho_s}} \times \sum_n \frac{\text{Ai}(-\bar{\xi}_> e^{i2\pi/3}) \text{Ai}(-\bar{\xi}_< e^{i2\pi/3}) e^{iK_n r}}{\sqrt{K_n} (\bar{\xi}_0 + q_n^2) [\text{Ai}(-\bar{\xi}_0 e^{i2\pi/3})]^2}, \quad (32)$$

and this expression is analogous to Eq. (9-5.18) of Ref. 2. It is reassuring to start from a more general situation that leads to the previous expression in the special case.

C. Method for finding eigenvalues

In the last section, we have derived an approximate expression for the total sound field in an upward refracting medium. The solution depends critically on the successful tracking of poles that contribute to give the total sound field. It is noted that Eq. (27) is the eigenvalue function equation and its roots K_n are eigenvalues (referred as poles in the last section). Generally speaking, it is difficult, if not impossible, to determine a closed-form analytic expression for K_n even for the situation of a bilinear profile. An efficient numerical scheme is required for finding the eigenvalues from Eq. (27) for arbitrary wind velocity and sound-speed profiles. To facilitate the determination of K_n , it is convenient to write an error function for the dispersion equation as

$$\Delta_1(b_n) = e^{i2\pi/3} \text{Ai}'(b_n) - q_n \text{Ai}(b_n). \quad (33)$$

Moreover, it is useful to introduce an extra error function such that

$$\Delta_2(k_r) = \xi_0 + b_n e^{-i2\pi/3}, \quad (34)$$

where ξ_0 can be determined from Eq. (26) by noting ξ_0

$\equiv \xi(k_r, 0)$. The location of the pole at $k_r = K_n$ can then be found by minimizing the magnitude of error functions $|\Delta_1|$ and $|\Delta_2|$.

Extending the numerical scheme described by Raspet *et al.*,¹⁵ we can determine the eigenvalues for arbitrary phase and magnitude of β from Eqs. (33) and (34). The scheme starts by assuming a constant value for q_n . We can find b_n from Eq. (33) by setting $\Delta_1 = 0$ as b_n is the only unknown variable in the equation. The root can be found by the standard Newton-Raphson method.²² Substituting this value of b_n into Eq. (34) and setting $\Delta_2 = 0$, we can then find the root K_n by the Newton-Raphson method with k_0 as the initial "guess." This completes a cycle of two independent iterative processes for the determination of the b_n and K_n , respectively. A new value of q_n can now be determined through the use of Eqs. (29) and (30) with K_n given by the previous iteration. This new value of q_n can then be used to determine a new K_n in the next cycle. The process can be used repeatedly until q_n and K_n converge to the required accuracy.

It should be noted that a starting value for b_n is required in the first iterative cycle. For an arbitrary phase and magnitude of β , it is found necessary to start q_n at zero and to increase it at a step of the order of 0.01. The solutions for b_n and K_n obtained from the previous q_n are used as the initial values in the iterative cycle for the next q_n . This procedure ensures the successful locations of all zeros. Examples of this numerical scheme and the sound field computations in the refractive shadow zone will be given in Sec. IV.

III. A DOWNWARD REFRACTING MEDIUM

A. Analytical expression for the sound field

The solution for a downward refracting medium differs from that for an upward refracting medium. However, the technique of finding the solutions for both cases is essentially the same. The details of the analysis will not be repeated but the solution and major points are outlined as follows. The total sound pressure can be approximated by a onefold inverse Fourier integral as

$$p \approx \frac{e^{i\pi/6}}{\sqrt{2i\pi r}} \int_0^\infty \sqrt{\frac{\rho}{\rho_s} \frac{\omega_m(k_r; z)}{\omega_m(k_r; z_s)}} \left[\frac{\xi_{<} \xi_{>}}{k_{<}^2 k_{>}^2} \right]^{1/4} \{ \text{Ai}(-\xi_{<} e^{i2\pi/3}) - \Gamma \text{Ai}(-\xi_{<}) \} \text{Ai}(-\xi_{>}) \sqrt{k_r} e^{ik_r r} dk_r. \quad (35)$$

The integral solution for the downward refracting medium is very similar to that for the upward refracting medium, cf. Eqs. (25) and (35), except that the dimensionless scale factor $\xi(z; k_r)$ and the reflection factor Γ are defined differently as

$$\xi(k_r; z) = \begin{cases} \left[\frac{3}{2} \int_z^{z_t} \{ [k_0 n(z) - k_r M_e(z)]^2 - k_r^2 \}^{1/2} dz \right]^{2/3}, & \text{if } z_t > z, \\ - \left[\frac{3}{2} \int_{z_t}^z \{ k_r^2 - [k_0 n(z) - k_r M_e(z)]^2 \}^{1/2} dz \right]^{2/3}, & \text{if } z_t < z, \end{cases} \quad (36)$$

$$\Gamma = \frac{e^{i2\pi/3} \text{Ai}'(-\xi_0 e^{i2\pi/3}) + q \text{Ai}(-\xi_0 e^{i2\pi/3})}{\text{Ai}'(-\xi_0) + q \text{Ai}(-\xi_0)}. \quad (37)$$

Again, M_e represents the effective Mach number which is proportional to the magnitude of wind resolved in the direction of propagation, i.e., $M_e = M \cos(\psi_r - \psi_w)$. The other variables in Eq. (35) are defined in the analogous form as those for the upward refracting medium.

In a downward refracting medium, the approximate sound field can be calculated in a similar manner as in the case of an upward refracting medium. The solution is well-known and is called the normal-mode solution. Essentially we sum the contributions from the poles in the first quadrant of the complex k_r plane for the integrand in Eq. (35). The condition for a pole is

$$\text{Ai}'(-\xi_0) + q_n \text{Ai}(-\xi_0) = 0, \quad (38)$$

which is obtained by equating the denominator of the reflection factor, see Eq. (37), to zero. Evaluation of the residue at each pole K_n leads to an approximation expression for the sound field in the downward refracting medium as follows:

$$p \approx \frac{e^{i\pi/4}}{\sqrt{2\pi r}} \sqrt{\frac{\rho}{\rho_s}} \sum_n \frac{\omega_m(K_n; z)}{\omega_m(K_n; z_s)} \left[\frac{\bar{\xi}_< \bar{\xi}_>}{\bar{k}^2 \bar{k}_>^2} \right]^{1/4} \times \frac{\sqrt{K_n} \text{Ai}(-\bar{\xi}_>) \text{Ai}(-\bar{\xi}_<) e^{iK_n r}}{[(\bar{\xi}_0 + q_n^2) \partial \bar{\xi}_0 / \partial K_n + \partial q_n / \partial K_n] [\text{Ai}(-\bar{\xi}_0)]^2}, \quad (39)$$

where the overbars denote the variables to be evaluated at the pole K_n .

Assuming a stationary medium [$M_e = 0$] and a bilinear sound-speed profile where $n(z) = 1 - z/R_c$, we can show that the dimensionless scale factor is

$$\bar{\xi}(z) \equiv \xi(K_n; z) = (k_0^2 - K_n^2) l_n^2 - z/l_n, \quad (40)$$

with l_n given by Eq. (31b). In the downward refracting medium, l_n is known as the wave layer thickness¹⁶ whereas it is known as the creeping wave layer thickness in the upward refracting medium.¹⁵ Both parameters are defined analogously and are used to characterize the vertical scale of the solution. Note also that there is a sign difference in the term z/l_n , cf. Eqs. (31a) and (40), between the upward and downward refracting medium. Using the same method as described in Sec. II, it is straightforward to show that Eq. (39) can be reduced, in this special case, to

$$p \approx \frac{-(R_c/2k_0^2)^{1/3} e^{i\pi/4}}{\sqrt{8\pi r}} \sqrt{\frac{\rho}{\rho_s}} \times \sum_n \frac{\text{Ai}(-\bar{\xi}_>) \text{Ai}(-\bar{\xi}_<) e^{iK_n r}}{\sqrt{K_n} (\bar{\xi}_0 + q_n^2) [\text{Ai}(-\bar{\xi}_0)]^2}, \quad (41)$$

which is equivalent to the expression given by Raspet *et al.*¹⁶ [their Eq. (8)].

B. Method for finding eigenvalues

For the downward refraction medium, Eq. (38) is the required eigenvalue equation. The determination of eigenvalues (or poles) can be achieved by a similar numerical method

as described earlier for the case of an upward refracting medium. To summarize, we introduce the following error functions:

$$\Delta_1(\tau_n) = \text{Ai}'(\tau_n) + q_n \text{Ai}(\tau_n), \quad (42)$$

and

$$\Delta_2(K_n) = \bar{\xi}_0 + \tau_n, \quad (43)$$

where $\bar{\xi}[\equiv \xi(K_n; 0)]$ is given by Eq. (36). By using the same method as detailed in Sec. II C, we can solve numerically for K_n by minimizing $|\Delta_1|$ and $|\Delta_2|$.

Due to the large number of modes required for the downward refracting medium, it is found necessary to use an alternative scheme in finding K_n for a given q_n . A scheme similar to those developed by Raspet *et al.*¹⁶ can be used and the details will not be repeated here.

IV. EXAMPLE CALCULATIONS AND COMPARISONS

In this section we present numerical calculations that (a) validate the numerical schemes as detailed in Secs. II and III, and (b) compare the difference in predicting sound transmission loss between the use of effective sound-speed profile and the use of vector wind velocity. To validate our numerical schemes, we compare the present results with benchmark cases,¹ in particular, their cases (ii) and (iii). These two cases correspond to idealized situations where the sound speed either increases or decreases linearly with height at a constant gradient of 0.1 s^{-1} . The effects of wind are ignored in all benchmark cases. In our calculations, the transmission loss (TL) is defined as

$$\text{TL} = 20 \log(p/p_0), \quad (44)$$

where p_0 is the reference sound pressure at a distance of 1 m from the source in the absence of any reflecting boundary.

In these idealized situations, one can rewrite the index of refraction n [cf. Eq. (14)] as

$$n(z) = 1 + a_T z, \quad (45)$$

where a_T is the normalized sound-speed gradient which is obtained by dividing the sound-speed gradient by the sound velocity at the surface. A positive a_T represents the propagation of sound in a downward refracting medium and a negative a_T represents the situation of an upward refracting medium. The normalized sound velocity gradient is the reciprocal of the radius of curvature of the ray path R_c that is used in Secs. II and III. By using the same parameters as the benchmark cases, the magnitude of the normalized sound velocity gradient is $2.915 \times 10^{-4} \text{ m}^{-1}$. This value is used in our first numerical examples.

Substituting Eq. (45) into Eq. (26) [or Eq. (36) as appropriate], noting that the effective Mach number M_e is zero, and integrating the expression with respect to z , one may obtain a closed-form analytic expression for the dimensionless scale factor

$$\bar{\xi}(z) = \left\{ \left(\frac{3}{2a_T} \right) \left[k_0 \ln \left(\frac{k_0 + \sqrt{k_0^2 - K_n^2(1 + a_T z)^2}}{K_n(1 + a_T z)} \right) - \sqrt{k_0^2 - K_n^2(1 + a_T z)^2} \right] \right\}^{2/3}. \quad (46)$$

The resulting expression is the same for the upward and downward refracting medium. With the use of Eq. (46), it is possible to derive analytic expressions for $\partial \bar{\xi}_0 / \partial K_n$ and $\partial q_n / \partial K_n$, respectively, as

$$\frac{\partial \bar{\xi}_0}{\partial K_n} = - \left(\frac{1}{a_T K_n} \right) \sqrt{\frac{k_0^2 - K_n^2}{\bar{\xi}}}, \quad (47)$$

and

$$\frac{\partial q_n}{\partial K_n} = \frac{ik_0 \beta}{\bar{\xi}_0} \left[K_n \left(\frac{\bar{\xi}_0}{k_0^2 - K_n^2} \right)^{3/2} - \frac{1}{2a_T K_n} \right]. \quad (48)$$

These expressions are required for the computation of the sound pressure in Eqs. (32) and (39), respectively. Although the numerical values for $\bar{\xi}_0$, $\partial \bar{\xi}_0 / \partial K_n$, and $\partial q_n / \partial K_n$ may be obtained straightforwardly by numerical integration,²² there is a significant reduction in the computational time if one uses these closed-form analytic expressions. We use these closed-form expressions in the following numerical examples.

To achieve our second objective, we consider a wind shear layer with constant density. The index of refraction is constant and the effective wind velocity varies linearly with height, such that the effective Mach number is given by

$$M_e(z) = a_w z, \quad (49)$$

where a_w is the normalized wind velocity gradient. It is obtained by dividing the wind velocity gradient by the sound speed at the surface and, like the normalized sound-speed gradient, it has units m^{-1} . In a heuristic approximation, the vector wind velocity gradient is customarily replaced by an effective sound-speed gradient. Effectively, one can then replace a_T with a_w and predict the transmission loss by using the same approach as above. However, we wish to use the ‘‘exact’’ formulation to compute the sound pressure in the following numerical examples. In this situation, $\bar{\xi}(z)$, $\partial \bar{\xi}_0 / \partial K_n$, and $\partial q_n / \partial K_n$ can also be determined analytically as

$$\bar{\xi}(z) = \left(\frac{3}{4a_w K_n} \right)^{2/3} \{ (k_0 - a_w K_n z) \sqrt{(k_0 - a_w K_n z)^2 - K_n^2} - K_n^2 \ln[(k_0 - a_w K_n z) + \sqrt{(k_0 - a_w K_n z)^2 - K_n^2}] / K_n \}^{2/3}, \quad (50)$$

$$\frac{\partial \bar{\xi}_0}{\partial K_n} = \frac{k_0 \sqrt{k_0^2 - K_n^2} + K_n^2 \ln[(k_0 + \sqrt{k_0^2 - K_n^2}) / K_n]}{2a_w \sqrt{\bar{\xi}_0} K_n^2}, \quad (51)$$

$$\frac{\partial q_n}{\partial K_n} = ik_0 \beta \left(\frac{1}{2\bar{\xi}_0} \frac{\partial \bar{\xi}_0}{\partial K_n} + \frac{K_n}{k_0^2 - K_n^2} \right) \sqrt{\frac{k_0^2 - K_n^2}{\bar{\xi}_0}}. \quad (52)$$

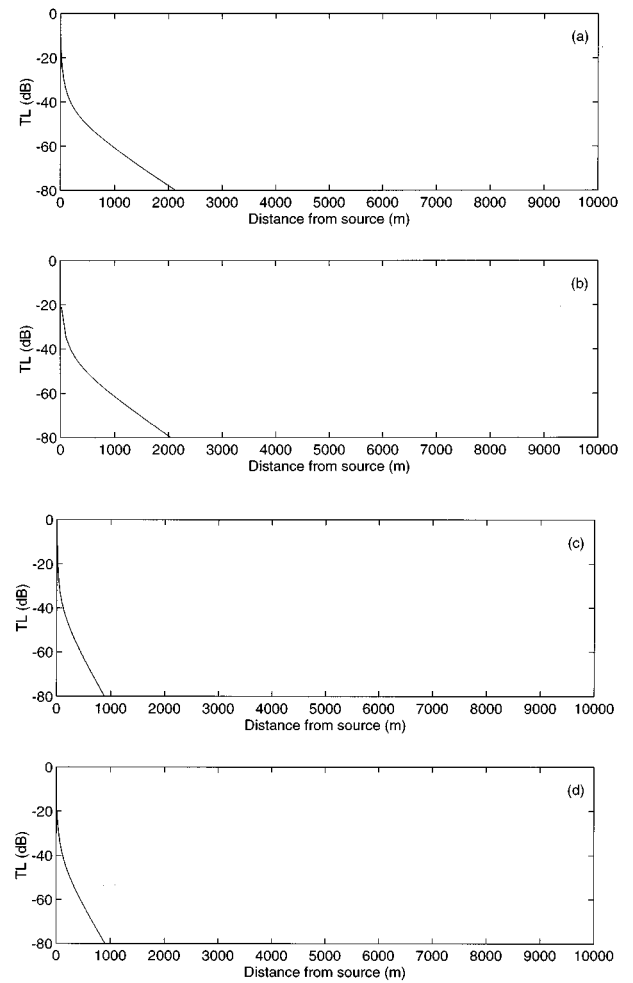


FIG. 2. The predicted transmission loss in an upward refracting medium with a linear sound-speed profile (solid line), and a linear wind velocity gradient (dotted lines). Both models assume a constant gradient of -0.1 s^{-1} . The predicted results obtained from the two models are indistinguishable. The frequency of the source is (a) 10 Hz and (c) 100 Hz. These are to be compared with the benchmark results (see Fig. 13 of Ref. 1) reproduced in (b) and (d) for information.

Again, these closed-form analytical expressions significantly reduce the overall computational time in calculating the sound field.

We choose the benchmark cases (ii) and (iii) as our first examples in order to validate the present numerical schemes. In the benchmark cases, a four parameter model²³ is used to characterize the ground impedance. Using the same parameters as in Ref. 1, the real and imaginary parts of the ground specific normalized impedance ($1/\beta$) are (38.79, 38.41) and (12.81, 11.62) at 10 and 100 Hz, respectively. Similar numerical results are expected for 1000 Hz and, consequently, they are not shown here. Figure 2(a) and (c) display the plots of transmission loss versus distance for 10 and 100 Hz respectively, in an upward refracting medium. This situation corresponds to the benchmark case (iii). The solid line is the prediction for a stratified medium with a linear sound-speed profile while the dotted line is that for a linear wind velocity gradient. The solid and dotted lines coincide in the upward refracting medium. The benchmark results are reproduced in Fig. 2(b) and (d) for the purpose of comparisons. In Fig. 3(a)

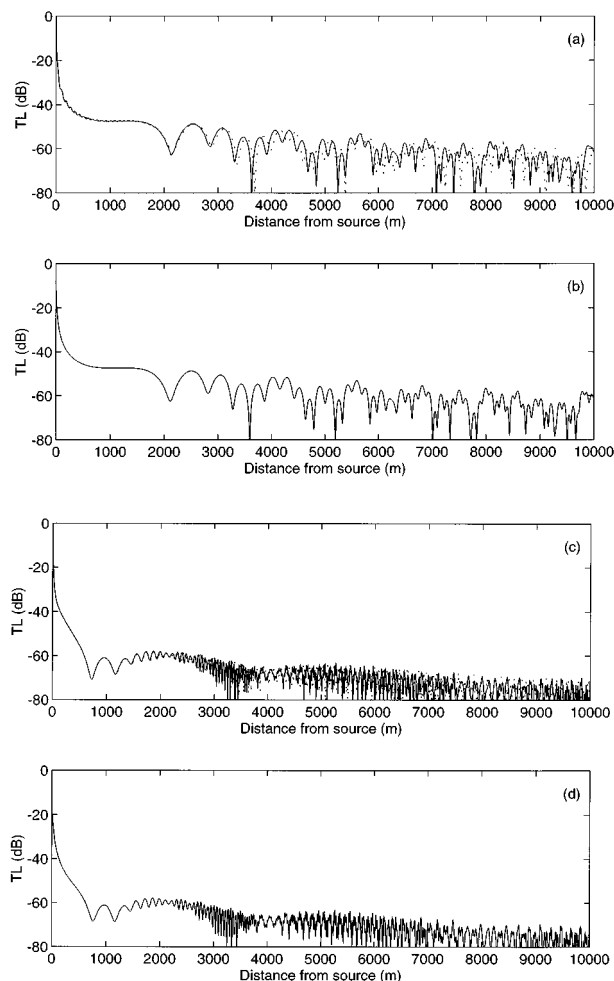


FIG. 3. The predicted transmission loss in a downward refracting medium with a linear sound-speed profile (solid line) and a linear wind velocity gradient (dotted lines). Both models assume a constant gradient of 0.1 s^{-1} . The frequency of the source is (a) 10 Hz and (c) 100 Hz. These are to be compared with the benchmark results (see Fig. 12 of Ref. 1) reproduced in (b) and (d) for information.

and (c) we show the plots for the downward refracting medium that correspond to the benchmark case (ii). Again, the solid and dotted lines represent the predictions for a linear sound-speed profile and a linear wind velocity gradient, respectively. We also display the corresponding benchmark results in Fig. 3(b) and (d) for information.

We can see from Figs. 2 and 3 that there are, generally, good agreements between our calculations and the benchmark results (Figs. 13 and 12 of Ref. 1) for a medium with a constant sound-speed gradient. The source and receiver heights are 5 and 1 m, respectively. Numerical discrepancies at close ranges are expected because a branch-line integral, which results in continuous spectra, is ignored in the present analysis.²⁴ Its inclusion is beyond the scope of the present paper. In an upward refracting medium, there is little difference in the TL predictions by using sound-speed or wind velocity gradients. In Fig. 2, these two predictions agree to within less than 0.5 dB and the solid and dotted lines coincide in the plots. Also we have tried to use a very high gradient ($\sim 10 \text{ m s}^{-1}$ per m) in other calculations. Again, there are no appreciable differences in the predictions and

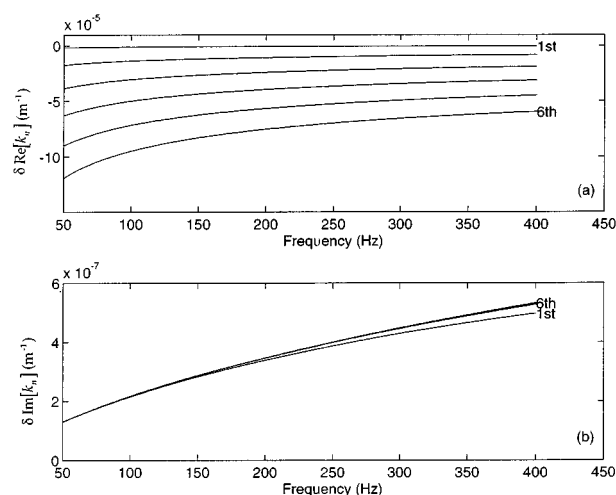


FIG. 4. The difference in the locations of the first six poles by using a wind velocity gradient and an effective sound-speed gradient. (a) Real part and (b) imaginary part of the difference in K_n predicted by the two models.

these numerical results have not been shown. It is obvious that there are no significant errors by using an effective sound-speed profile in the case of an upward refracting medium. However, this is not the case for the downward refracting medium. Although the sound-pressure levels are close for both situations, there is an obvious shift in the interference pattern especially at long ranges and at high frequencies, see Fig. 3(c).

This phenomenon may be explained conveniently in terms of mode theory by considering the following numerical example. In these examples, we compare our results with those calculated by a FFP formulation.¹² In the calculations, the wind velocity increases linearly with height from 0 m s^{-1} at the ground to 20 m s^{-1} at 200 m above the ground. A half space is set at 200 m with the wind velocity at 20 m s^{-1} . The source–receiver geometry and the ground impedance are the same as the benchmark cases.

To explain the phenomenon, it is advantageous to plot the difference in the prediction of the pole locations $\delta(K_n)$ versus frequency for the first six poles, see Fig. 4. The use of effective sound-speed profiles underpredicts the real part of K_n and overpredicts the imaginary of K_n . Nevertheless there are close agreements between the use of wind velocity gradients explicitly and the heuristic approach. However, the agreement becomes worse at higher-order modes and at high wind velocity gradients.

In Fig. 5(a), we plot transmission loss versus horizontal range with the source frequency of 10 Hz. To model a realistic atmosphere, the wind and sound-speed profiles are truncated at about 200 m.¹⁶ The truncated gradients imply that there are only three dominant modes of propagation. These few trapped modes are evident in Fig. 5(a) because of its relatively “clean” interference pattern. The predictions of the transmission loss by both methods agree closely up to a range of about 4000 m. However, there is a general shift of the interference pattern as the range increases. Figure 5(b) displays the transmission loss versus horizontal range at the source frequency of 100 Hz. The interference patterns are much more intricate because there are 27 trapped modes of

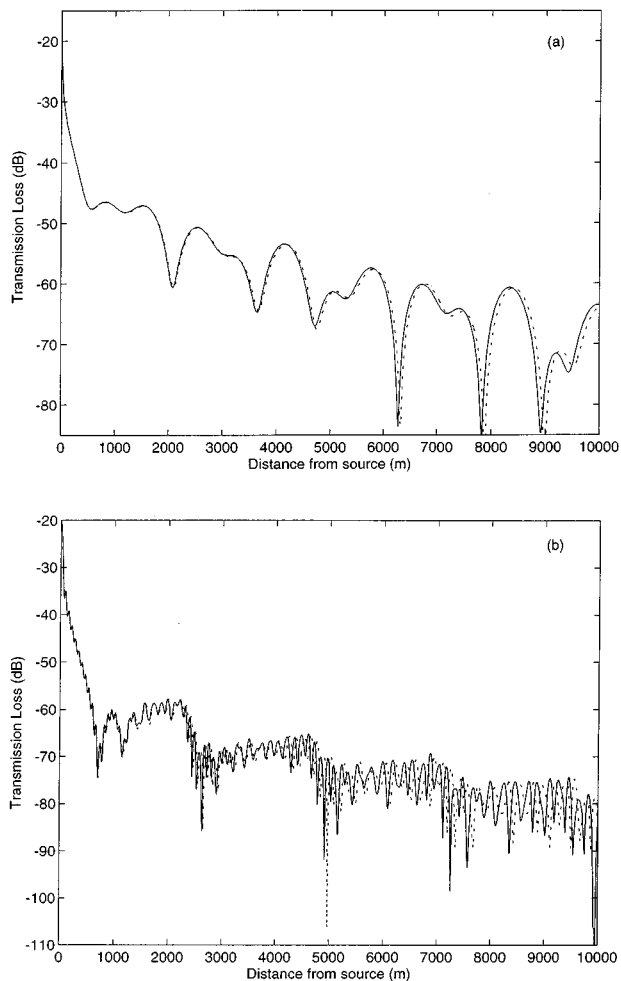


FIG. 5. The predicted transmission loss in a downward refracting medium with a linear wind velocity gradient (dotted lines) and its corresponding effective sound-speed profile. The wind velocity increases linearly with height from 0 m s^{-1} at the ground to 20 m s^{-1} at the height of 200 m. A half space is assumed for the height higher than 200 m. All other parameters are the same as in Fig. 3. The frequency of the source is (a) 10 Hz and (b) 100 Hz. These are to be compared with the predictions in Figs. 5 and 6 of Ref. 12.

propagation at 100 Hz. A shift of the interference pattern is noticeable at about 1500 m. Nevertheless our predicted results agree well with that given in Figs. 5 and 6 of Ref. 12. Finally, we show in Fig. 6 the predicted transmission loss versus frequency. In this example, we use a simple two parameter model²³ for ground impedance for convenience and the parameter values are $100\,000 \text{ Pa s m}^{-2}$ and 100 m^{-1} , respectively. These parameter values, equal to the effective flow resistivity and exponential decay constant for porosity, correspond to a typical outdoor ground surface.²³ Calculations are presented at a source height of 5.0 m, receiver height of 1.0 m, and range of 3000 m. It is not particularly surprising to find that the use of effective sound-speed gradient becomes increasingly inadequate at high frequencies. In this example, 20 modes are used for all frequencies. The gradient of the profiles is 0.1 s^{-1} and it is truncated at 65.7 m for 400 Hz.

Finally, we emphasize that the combined effects of wind velocity and sound-speed gradients can be incorporated in

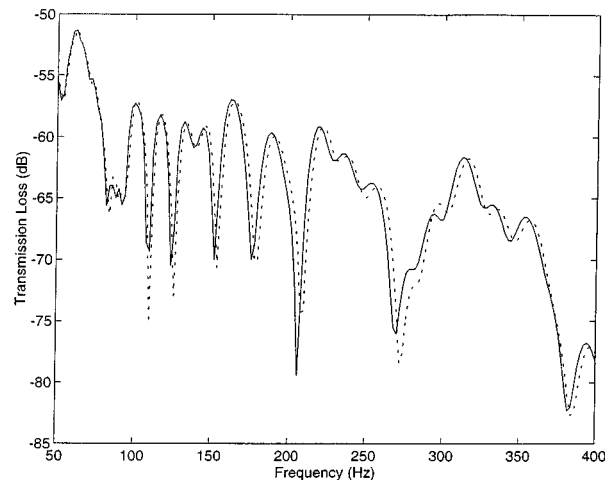


FIG. 6. The predicted transmission loss versus frequency. The source and receiver heights are 5 and 1 m and the range is 3000 m. Two parameter impedance model, with the parameter values of $100\,000 \text{ Pa s m}^{-2}$ and 100 m^{-1} , is used to calculate the ground impedance. The dotted line is the prediction for a wind velocity gradient and the solid line is the corresponding prediction for an effective sound-speed gradient.

the present method as long as the dimensional scale factor $\bar{\xi}(z)$ is a monotonic function of z . Without further approximations, there are usually no simple analytic expressions for most wind velocity and sound-speed profiles. However, it is fairly straightforward to compute $\bar{\xi}(z)$ and its associated variables by numerical integration at the expense of a relatively higher computational cost. Numerical examples for a combined profile are not included in this paper because these results tend to confirm earlier findings,¹² i.e., an effective sound-speed profile is adequate for most upwind situations but it is relatively less satisfactory for the down-wind situation especially at long ranges and at high frequencies.

V. SUMMARY

We have examined the propagation of sound outdoors in the presence of temperature and wind gradients. The present approach is in contrast to the conventional approach in which the effect of wind is included in the analysis by use of an effective sound-speed gradient. Our analysis starts from a set of fundamental hydrodynamic equations where the effect of fluid motion is included explicitly. Analytical expressions have been derived for a stratified medium with either upward refraction or downward refraction with arbitrary vector wind and temperature profiles. In addition, the present analyses are valid when the wind and sound speeds either decrease or increase monotonically with the vertical height above an impedance ground.

In an upward refracting medium, it has been demonstrated that the use of effective gradients is sufficiently accurate in predicting the transmission loss in most practical ranges of interest. In a downward refracting medium, we have shown that the use of effective sound-speed profiles is adequate for predicting the sound field at short distances and at low frequencies. This is due to the fact that the use of effective sound-speed profiles introduces a small but finite “error” in the phase of all propagating modes. The phase errors in the propagating modes increase with range and fre-

quency which implies the heuristic approximation of using an effective sound-speed profile is inadequate at long range and at high frequencies.

ACKNOWLEDGMENTS

We thank the Associate Editor, Lou Sutherland, and two anonymous reviewers for their helpful comments. Q.W. is supported by an Open University Research Studentship. The initial part of the work was conducted while K.M.L. was a Visiting Scholar at the National Center for Physical Acoustics, University of Mississippi. The work was supported in part by the EPSRC, UK through Grant Ref. No. GR/J42052.

- ¹K. Attenborough, S. Taherzadeh, H. E. Bass, X. Di, R. Raspet, G. R. Becker, A. Güdesen, A. Chrestman, G. A. Daigle, A. L'Espérance, Y. Gabillet, K. Gilbert, Y. L. Li, M. J. White, P. Naz, J. M. Noble, and H. A. J. M. van Hoof, "Benchmark cases for outdoor sound propagation models," *J. Acoust. Soc. Am.* **97**, 173–191 (1995).
- ²A. D. Pierce, *Acoustics, An Introduction to its Physical Principles and Applications* (Acoustical Society of America, 1989), 2nd printing.
- ³A. L'Espérance, J. Nicolas, D. K. Wilson, D. W. Thomson, Y. Gabillet, and G. A. Daigle, "Sound propagation in the atmospheric surface layer. Comparison of experiments with FFP predictions," *Appl. Acoust.* **40**, 325–346 (1993).
- ⁴Y. L. Li, S. J. Franke, and C. H. Liu, "Numerical implementation of an adaptive fast-field program for sound propagation in layered media using the chirp z -transform," *J. Acoust. Soc. Am.* **89**, 2068–2075 (1991).
- ⁵M. West, F. Walkden, and R. A. Sack, "The acoustic shadow produced by wind speed and temperature gradients close to the ground," *Appl. Acoust.* **27**, 239–260 (1989).
- ⁶R. J. Thompson, "Ray-acoustic intensity in a moving medium," *J. Acoust. Soc. Am.* **55**, 729–732 (1974).
- ⁷P. Ugincius, "Ray acoustics and Fermat's principle in a moving inhomogeneous medium," *J. Acoust. Soc. Am.* **51**, 1759–1763 (1972).
- ⁸J. S. Lamancusa and P. A. Daroux, "Ray tracing in a moving medium with two-dimensional sound-speed variation and application to sound propagation over terrain discontinuities," *J. Acoust. Soc. Am.* **93**, 1716–1726 (1993).
- ⁹K. M. Li, "A high-frequency approximation of sound propagation in a stratified moving atmosphere above a porous ground surface," *J. Acoust. Soc. Am.* **95**, 1840–1852 (1994).
- ¹⁰V. E. Ostashev, "High-frequency acoustics field of a point source lying above an impedance surface in a stratified moving medium," *Izv. Atmos. Oceanic Phys.* **23**, 370–377 (1987).
- ¹¹D. K. Wilson, "Sound field computations in a stratified, moving medium," *J. Acoust. Soc. Am.* **94**, 400–407 (1993).
- ¹²Y. L. Li, M. J. White, and S. J. Franke, "New fast field programs for anisotropic sound propagation through an atmosphere with a wind velocity profile," *J. Acoust. Soc. Am.* **95**, 718–726 (1994).
- ¹³P. M. Morse and H. Feshbach, *Methods of Theoretical Physics* (McGraw-Hill, New York, 1953), Vol. 1, pp. 408–410.
- ¹⁴B. D. Seckler and J. B. Keller, "Asymptotic theory of diffraction in inhomogeneous media," *J. Acoust. Soc. Am.* **31**, 206–216 (1959).
- ¹⁵R. Raspet, G. E. Baird, and W. Wu, "The relationship between upward refraction above a complex impedance plane and the spherical wave evaluation for a homogeneous medium," *J. Acoust. Soc. Am.* **89**, 107–114 (1991).
- ¹⁶R. Raspet, G. E. Baird, and W. Wu, "Normal mode solution for low frequency sound propagation in a downward refracting atmosphere above a complex impedance plane," *J. Acoust. Soc. Am.* **91**, 1341–1352 (1992).
- ¹⁷A. D. Pierce, "Wave equation for sound in fluids with unsteady inhomogeneous flow," *J. Acoust. Soc. Am.* **87**, 2292–2299 (1990).
- ¹⁸L. Nijs and C. P. A. Wapenaar, "The influence of wind and temperature gradients on sound propagation, calculated with the two-way wave equation," *J. Acoust. Soc. Am.* **87**, 1987–1998 (1990).
- ¹⁹F. W. J. Olver, *Asymptotics and Special Functions* (Academic, New York, 1974). [Also see L. B. Felsen and N. Marcuvitz, *Radiation and scattering of waves* (IEEE, New York, 1994), pp. 339–341. Note that a pair of linearly independent solutions, $Ai(\xi)$ and $Bi(\xi)$, is usually used but we find it to be more convenient to use the pair of solutions given in Eq. (17).]
- ²⁰V. E. Ostashev, "Waveguide propagation of a high-frequency acoustic field in a stratified moving medium near an impedance boundary," *Izv. Atmos. Oceanic Phys.* **22**, 936–941 (1986).
- ²¹K. M. Li, "Propagation of sound above an impedance plane in a downward refracting atmosphere," *J. Acoust. Soc. Am.* **99**, 746–754 (1996).
- ²²W. H. Press, S. A. Teukolsky, W. T. Vetterling, and B. P. Flannery, *Numerical Recipes in FORTRAN: The Art of Scientific Computing* (Cambridge U.P., Cambridge, England, 1992), 2nd ed.
- ²³K. Attenborough, "Ground parameter information for propagation model," *J. Acoust. Soc. Am.* **92**, 418–427 (1992).
- ²⁴D. C. Strickler, "Normal-mode program with both discrete and branch line contributions," *J. Acoust. Soc. Am.* **61**, 856–861 (1974).
- ²⁵K. M. Li, K. Attenborough, and N. W. Heap, "Source height determination by ground effect inversion in the presence of a sound velocity," *J. Sound Vib.* **145**, 111–128 (1991).

The sound field of an arbitrarily oriented quadrupole near ground surfaces

Kai Ming Li and Shahram Taherzadeh

Engineering Mechanics Discipline, Faculty of Technology, The Open University, Milton Keynes MK7 6AA, United Kingdom

(Received 16 January 1996; revised 31 May 1997; accepted 30 June 1997)

The sound field due to an arbitrarily oriented quadrupole above an impedance ground is investigated. To simplify the analysis, the atmospheric and topographical effects on sound propagation are ignored. Two different methods are developed to calculate the sound field. First, an asymptotic method is used to derive a close-form analytic solution. Second, a fast field program (quad-FFP) has been developed for numerical computations of the sound field. It is found that numerical results from both methods agree well. In a recent development, it has been shown that the analytic solution of the sound field due to an arbitrarily oriented dipole can be written in the classical form similar to that due to a monopole. However, it is *not* possible to write the solution in such a form for the case of an arbitrarily oriented quadrupole, but rather the total sound pressure is augmented by two extra terms which are particularly important at a small separation between the source and receiver. © 1997 Acoustical Society of America. [S0001-4966(97)03710-7]

PACS numbers: 43.28.Fp, 43.28.Hr, 43.28.Ra, 43.50.Nm [LCS]

INTRODUCTION

The purpose of this paper is to examine the sound field due to an arbitrarily oriented quadrupole above a ground surface of finite impedance. We wish to investigate the interactions between a jet noise source and ground surfaces of finite impedance. Here, we restrict attention to an idealized case where the jet noise source is represented by a simple quadrupole. We can then model the problem as the analysis of the sound field due to an arbitrarily oriented quadrupole above an infinite plane at $z=0$. The normalized specific admittance of the infinite plane is denoted by β . We investigate the effect of a flat impedance plane in a homogeneous atmosphere on the directivity of a quadrupole noise source and study the ground effect on the predicted spectrum.

We remark that the propagation of sound outdoors due to a monopole source is well known.¹ More recently, Li *et al.*² have developed an asymptotic theory for the propagation of sound due to a dipole and their theory was confirmed by indoor experimental measurements. The outcome of their study is that the sound field due to a dipole can be written in a form similar to the classical formula for a monopole. This paper reports a continuation of that study; the sound field due to an arbitrarily oriented quadrupole above an absorbing ground is investigated. Will the sound field still preserve the same form?

Apart from an application to the jet noise, the present theory can also be applied to noise control and source identification,³ especially to the situation where the noise sources are adjacent to an impedance surface. The theory provides a numerically efficient and accurate method to calculate the sound field due to a quadrupole near an impedance plane.

In the following sections, a general method will be presented for an analytical solution of the sound field due to an arbitrarily oriented quadrupole above an impedance plane. Furthermore, a numerical scheme based on the fast field for-

mulation has been developed recently.⁴ We shall validate the analytical solution by comparing analytical results with the numerical scheme and also with the asymptotic solution given by Generalov.⁵ In addition, we also compare the analytical solutions with the predictions due to two adjacent out-of-phase dipoles in the near field such that $R < 3\lambda$ where R is the source/receiver separation and λ the wavelength.

I. FORMULATION

A quadrupole source $\Gamma_2(\mathbf{r}_s)$ Pa m⁻² situated at $\mathbf{r}_s \equiv (0,0,z_s)$ above a flat ground is shown in Fig. 1. It is convenient to represent the quadrupole by a pair of closely spaced dipoles such that

$$\Gamma_2(\mathbf{r}_s) = \Gamma_1(\mathbf{r}_s + \mathbf{m}\Delta) - \Gamma_1(\mathbf{r}_s - \mathbf{m}\Delta) \text{ as } \Delta \rightarrow 0, \quad (1)$$

where $\Gamma_1(\mathbf{r}_s)$ represents the dipole term, Δ is the separation between the two closely spaced dipoles, and $\mathbf{m} \equiv (m_x, m_y, m_z)$ is the direction cosines which characterizes the orientation of the quadrupole axis. It follows from the analysis of Li *et al.*² that

$$\begin{aligned} \Gamma_1(\mathbf{r}_s) &= S_1 \left\{ l_x \frac{\partial}{\partial x} \delta(\mathbf{r} - \mathbf{r}_s) + l_y \frac{\partial}{\partial y} \delta(\mathbf{r} - \mathbf{r}_s) + l_z \frac{\partial}{\partial z} \delta(\mathbf{r} - \mathbf{r}_s) \right\}, \end{aligned} \quad (2)$$

where S_1 Pa m² is the dipole source strength, $\mathbf{l} \equiv (l_x, l_y, l_z)$ is the corresponding orientation of the dipole axis, and $\mathbf{r} \equiv (x, y, z)$ are the field points in the analysis. After some tedious calculations, we can show

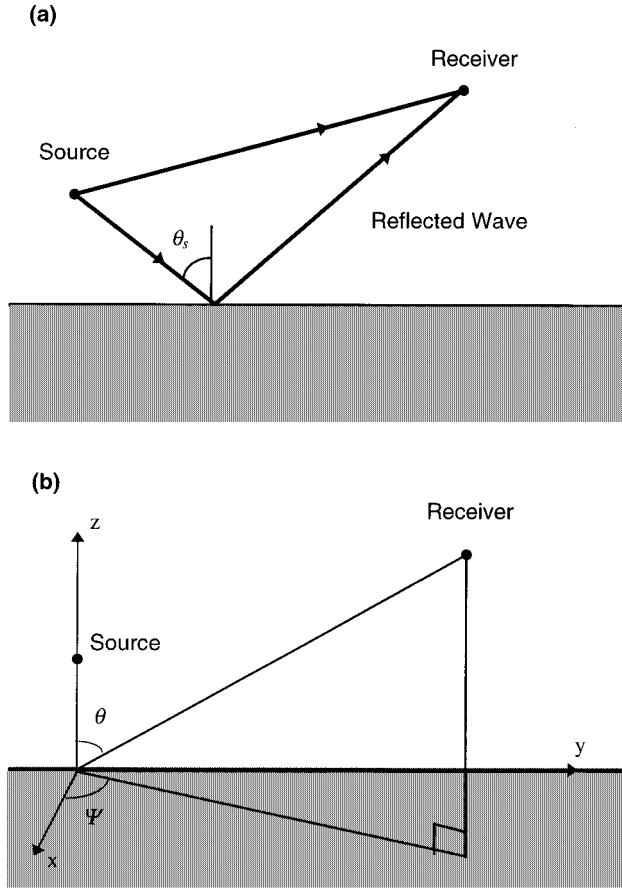


FIG. 1. (a) Source/receiver geometry. (b) Polar and azimuthal angles used in the far-field approximation.

$$\begin{aligned} \Gamma_2(\mathbf{r}_s) = S_2 \left\{ l_x m_x \frac{\partial^2}{\partial x^2} \delta(\mathbf{r} - \mathbf{r}_s) + l_y m_y \frac{\partial^2}{\partial y^2} \delta(\mathbf{r} - \mathbf{r}_s) \right. \\ \left. + l_z m_z \frac{\partial^2}{\partial z^2} \delta(\mathbf{r} - \mathbf{r}_s) + (l_x m_y + l_y m_x) \frac{\partial^2}{\partial x \partial y} \right. \\ \left. \times \delta(\mathbf{r} - \mathbf{r}_s) + (l_y m_z + l_z m_y) \frac{\partial^2}{\partial y \partial z} \delta(\mathbf{r} - \mathbf{r}_s) \right. \\ \left. + (l_z m_x + l_x m_z) \frac{\partial^2}{\partial z \partial x} \delta(\mathbf{r} - \mathbf{r}_s) \right\}. \end{aligned} \quad (3)$$

Alternatively, the quadrupole term can be written in a more compact form⁶ as

$$\Gamma_2 = S_2 (\mathbf{l} \cdot \nabla) (\mathbf{m} \cdot \nabla) \{ \delta(\mathbf{r} - \mathbf{r}_s) \}, \quad (4)$$

where $\nabla \equiv (\partial/\partial x, \partial/\partial y, \partial/\partial z)$ and $S_2 = 2S_1 \Delta$ is the quadrupole source strength which has units of Pa m³. Here, the orientation of the dipole axis, \mathbf{l} , is sometimes known as the dipole-moment-amplitude vector.⁶ The direction cosines, \mathbf{m} may then be regarded as the vector which characterizes the direction of the pair of equal but opposite dipole-moment amplitude vectors.

Using Eq. (3) as the source term, we can find the sound field, $p(\mathbf{r})$, due to a quadrupole by solving the inhomogeneous Helmholtz equation

$$\nabla^2 p + k^2 p = \Gamma_2(\mathbf{r}_s), \quad (5)$$

subject to the impedance boundary condition at $z=0$, i.e.,

$$\frac{\partial p}{\partial z} + ik\beta p = 0, \quad (6)$$

where β is the normalized specific admittance of the ground surface.

The posed problem can be solved readily by use of the method of Fourier transformation. Introduce a Fourier transform pair

$$\hat{p}(k_x, k_y, z) = \int_{-\infty}^{\infty} \int_{-\infty}^{\infty} p(x, y, z) e^{-i(k_x x + k_y y)} dx dy \quad (7)$$

and

$$\begin{aligned} p(x, y, z) = \frac{1}{4\pi^2} \\ \times \int_{-\infty}^{\infty} \int_{-\infty}^{\infty} \hat{p}(k_x, k_y, z) e^{i(k_x x + k_y y)} dk_x dk_y. \end{aligned} \quad (8)$$

Then Eqs. (5) and (6) can be transformed to

$$\begin{aligned} \frac{d^2 \hat{p}}{dz^2} + k_z^2 \hat{p} = -S_2 \left\{ l_x m_x \frac{\partial^2}{\partial x^2} \delta(\mathbf{r} - \mathbf{r}_s) \right. \\ \left. + l_x m_x \frac{\partial^2}{\partial y^2} \delta(\mathbf{r} - \mathbf{r}_s) + l_z m_z \frac{\partial^2}{\partial z^2} \delta(\mathbf{r} - \mathbf{r}_s) \right. \\ \left. + (l_x m_y + l_y m_x) \frac{\partial^2}{\partial x \partial y} \delta(\mathbf{r} - \mathbf{r}_s) \right. \\ \left. + (l_y m_z + l_z m_y) \frac{\partial^2}{\partial y \partial z} \delta(\mathbf{r} - \mathbf{r}_s) \right. \\ \left. + (l_z m_x + l_x m_z) \frac{\partial^2}{\partial z \partial x} \delta(\mathbf{r} - \mathbf{r}_s) \right\} \end{aligned} \quad (9)$$

and

$$\frac{\partial \hat{p}}{\partial z} + ik\beta \hat{p} = 0 \quad \text{on } z=0. \quad (10)$$

It is straightforward to find the solution for \hat{p} as

$$\hat{p} = \hat{\Gamma}_2^- e^{ik_z|z-z_s|} + \hat{\Gamma}_2^+ V e^{ik_z(z+z_s)} \quad (11)$$

where

$$\begin{aligned} \hat{\Gamma}_2^\pm = (-iS_2/2k_z) \{ (l_x k_x + l_y k_y) (m_x k_x + m_y k_y) + l_z k_z k_z^2 \\ + \text{sign}(z_s \pm z) k_z [(l_x m_z + l_z m_x) k_x \\ + (l_y m_z + l_z m_y) k_y] \}, \end{aligned} \quad (12)$$

$$V = \frac{k_z - k\beta}{k_z + k\beta}, \quad (13)$$

and

$$k_z = +\sqrt{k^2 - k_x^2 - k_y^2}. \quad (14)$$

The positive root of k_z is chosen in Eq. (14) in order to satisfy the Sommerfeld radiation condition.

Substitution of Eq. (11) into Eq. (8) leads to an integral expression for the total sound field as

$$p(x, y, z) = \frac{1}{4\pi^2} \int_{-\infty}^{\infty} \int_{-\infty}^{\infty} [\hat{\Gamma}_2^- e^{ik_z|z-z_s|} + \hat{\Gamma}_2^+ V e^{ik_z(z+z_s)}] \times e^{i(k_x x + k_y y)} dk_x dk_y. \quad (15)$$

The evaluation of the integral can be simplified considerably by using polar coordinates such that (k_x, k_y) become (k_r, ξ) and (x, y) become (r, ψ_s) . Furthermore, the direction cosines **l** and **m** can be expressed in terms of the polar coordinates as

$$l_x = \sin \gamma \cos \psi_l, \quad l_y = \sin \gamma_l \sin \psi_l, \quad (16)$$

$$\text{and } l_z = \cos \gamma_l,$$

$$m_x = \sin \gamma_m \cos \psi_m, \quad m_y = \sin \gamma_m \sin \psi_m, \quad (17)$$

$$\text{and } m_z = \cos \gamma_m,$$

where γ and ψ are the polar and azimuthal angles, respectively (see Fig. 1). The subscripts, l and m , denote the corresponding variables for the dipole and quadrupole axes, respectively. The exact evaluation of the integral given in Eq. (15) is difficult, if not impossible, but the integral can be evaluated asymptotically for large kr . We shall derive the asymptotic solution of the total sound field in the next section.

II. ASYMPTOTIC ANALYSIS

In a previous work,² we showed that a dipole can be split into its horizontal-dipole and vertical-dipole components. Using the same idea, we can handle the quadrupole components in a rather similar manner. Introducing the polar coordinates, we can rewrite Eq. (12) as

$$\begin{aligned} \hat{\Gamma}_2^\pm = & (-iS_2/2k_z) \{ k_r^2 \sin \gamma_l \sin \gamma_m \cos (\xi - \psi_l) \\ & \times \cos (\xi - \psi_m) + k_z^2 \cos \gamma_l \cos \gamma_m + \text{sign}(z_s \pm z) \\ & \times k_z [k_r \sin \gamma_l \cos \gamma_m \cos (\xi - \psi_l) \\ & + k_r \cos \gamma_l \sin \gamma_m \cos (\xi - \psi_m)] \}. \end{aligned} \quad (18)$$

Substituting Eq. (18) into Eq. (15), we can show that the total sound field can be split into four components, according to the orientations of the dipole-moment amplitude vector and quadrupole axis, as follows:

$$p = p_{hh} + p_{hv} + p_{vh} + p_{vv}, \quad (19)$$

where

$$\begin{aligned} p_{hh} = & \frac{-iS_2 \sin \gamma_l \sin \gamma_m}{4\pi^2} \\ & \times \int_0^\infty \int_0^{2\pi} \frac{k_r^3 \Lambda^+ \cos (\xi - \psi_l) \cos (\xi - \psi_m) e^{ik_r r \cos (\xi - \psi_s)}}{2k_z} \\ & \times d\xi dk_r, \end{aligned} \quad (20)$$

$$\begin{aligned} p_{hv} = & \frac{-iS_2 \cos \gamma_l \sin \gamma_m}{4\pi^2} \\ & \times \int_0^\infty \int_0^{2\pi} \frac{k_r^2 \Lambda^- \cos (\xi - \psi_l) e^{ik_r r \cos (\xi - \psi_s)}}{2} d\xi dk_r, \end{aligned} \quad (21)$$

$$\begin{aligned} p_{vh} = & \frac{-iS_2 \sin \gamma_l \cos \gamma_m}{4\pi^2} \\ & \times \int_0^\infty \int_0^{2\pi} \frac{k_r^2 \Lambda^- \cos (\xi - \psi_m) e^{ik_r r \cos (\xi - \psi_s)}}{2} d\xi dk_r, \end{aligned} \quad (22)$$

$$\begin{aligned} p_{vv} = & \frac{-iS_2 \cos \gamma_l \cos \gamma_m}{4\pi^2} \\ & \times \int_0^\infty \int_0^{2\pi} \frac{k_r k_z \Lambda^+ e^{ik_r r \cos (\xi - \psi_s)}}{2} \times d\xi dk_r, \end{aligned} \quad (23)$$

$$\Lambda^\pm = \text{sign}(z_s \pm z) e^{ik_z|z-z_s|} + V e^{ik_z(z+z_s)}, \quad (24)$$

i.e.,

$$\Lambda^+ = e^{ik_z|z-z_s|} + V e^{ik_z(z+z_s)}$$

and

$$\Lambda^- = \text{sign}(z_s - z) e^{ik_z|z-z_s|} + V e^{ik_z(z+z_s)}.$$

Here in Eq. (19), the index “ hh ” (horizontal, horizontal) means that the horizontal components of the dipole and quadrupole. The index “ hv ” (horizontal, vertical) means that the horizontal component of the dipole and the vertical component of the quadrupole, and so on.

Denoting the n th-order Bessel function by $J_n(z)$ and making use of the following identities,⁷

$$J_n(z) = \frac{i^{-n}}{2\pi} \int_0^{2\pi} \cos(n\psi) e^{iz \cos \psi} d\psi \quad \text{and} \quad (25)$$

$$\int_0^{2\pi} \sin(n\psi) e^{iz \cos \psi} d\psi = 0,$$

we can evaluate the integral over ξ in Eqs. (20)–(23) to yield

$$\begin{aligned} p_{hh} = & \frac{-iS_2 \sin \gamma_l \sin \gamma_m}{4\pi} \left\{ \cos(\psi_s - \psi_l) \cos(\psi_s - \psi_m) \right. \\ & \times \int_0^\infty \frac{k_r^3 \Lambda^+ [J_0(k_r r) - J_2(k_r r)]}{2k_z} dk_r \\ & + \sin(\psi_s - \psi_l) \sin(\psi_s - \psi_m) \\ & \times \left. \int_0^\infty \frac{k_r^3 \Lambda^+ [J_0(k_r r) + J_2(k_r r)]}{2k_z} dk_r \right\}, \end{aligned} \quad (26)$$

$$\begin{aligned} p_{hv} = & \frac{-iS_2 \cos \gamma_l \sin \gamma_m \cos(\psi_s - \psi_l)}{4\pi} \\ & \times \int_0^\infty k_r^2 \Lambda^- J_1(k_r r) dk_r, \end{aligned} \quad (27)$$

$$\begin{aligned} p_{vh} = & \frac{-iS_2 \sin \gamma_l \cos \gamma_m \cos(\psi_s - \psi_m)}{4\pi} \\ & \times \int_0^\infty k_r^2 \Lambda^- J_1(k_r r) dk_r, \end{aligned} \quad (28)$$

$$p_{vv} = \frac{-iS_2 \cos \gamma_l \cos \gamma_m}{4\pi} \int_0^\infty k_r k_z \Lambda^+ J_0(k_r r) dk_r. \quad (29)$$

Next we may recast Eqs. (26)–(29) in a more convenient form by noting

$$\Lambda^\pm = \text{sign}(z_s \pm z) e^{ik_z|z-z_s|} + e^{ik_z(z+z_s)} + B, \quad (30)$$

where

$$B = \frac{-2k\beta}{k_z + k\beta} e^{ik_z(z+z_s)}. \quad (31)$$

The first and second terms of Eq. (30) can be regarded as the direct source and its corresponding image source in an unbounded medium. The parameter B of Eq. (30) may be regarded as a correction factor known as the boundary wave term² and it is used to account for the finite impedance of the ground surface. In the case of a rigid plane, we have $\beta=0$ and, hence, the boundary wave term vanishes. This implies that the sound field is composed of that due to the direct source and its image, as one would expect in this special case of a hard ground.

Substituting Eqs. (26)–(29) into Eq. (19), we can obtain the sound field due to an arbitrarily oriented quadrupole above an impedance ground. It follows from Eqs. (30) and (31) that the total sound field is composed of a direct wave P_1 , an “image” wave P_2 , and a boundary wave P_3 .² The quantity P_1 corresponds to a sum of the direct wave terms for p_{hh} , p_{hv} , p_{vh} , and p_{vv} [cf. Eqs. (26)–(29)] and, similarly, for P_2 and P_3 .

The solutions for P_1 and P_2 are well known because they correspond to the sound field due to a quadrupole source and its image in an unbounded medium. They are given, respectively, by⁶

$$P_1 = (\mathbf{l} \cdot \nabla)(\mathbf{m} \cdot \nabla) \left[\frac{S_2 e^{ikR_1}}{4\pi R_1} \right], \quad (32a)$$

and

$$P_2 = (\mathbf{l} \cdot \nabla)(\mathbf{m} \cdot \nabla) \left[\frac{S_2 e^{ikR_2}}{4\pi R_2} \right], \quad (32b)$$

where R_1 and R_2 are the distances of the direct and reflected waves. It is tedious but straightforward to expand Eqs. (32a) and (32b) to give

$$P_1 = \frac{S_2}{4\pi} \{ [3(1 - ikR_1) - k^2 R_1^2] (\mathbf{l} \cdot \hat{\mathbf{R}}_1)(\mathbf{m} \cdot \hat{\mathbf{R}}_1) - (1 - ikR_1)(\mathbf{l} \cdot \mathbf{m}) \} \frac{e^{ikR_1}}{R_1^3} \quad (33a)$$

and

$$P_2 = \frac{S_2}{4\pi} \{ [3(1 - ikR_2) - k^2 R_2^2] (\mathbf{l} \cdot \hat{\mathbf{R}}_2)(\mathbf{m} \cdot \hat{\mathbf{R}}_2) - (1 - ikR_2)(\mathbf{l} \cdot \mathbf{m}) \} \frac{e^{ikR_2}}{R_2^3}, \quad (33b)$$

where $\hat{\mathbf{R}}_1$ and $\hat{\mathbf{R}}_2$ are the corresponding unit vectors pointing radially outward from the source to the receiver. In the

spherical polar coordinates, $\hat{\mathbf{R}}_1$ and $\hat{\mathbf{R}}_2$ are given by

$$\hat{\mathbf{R}}_1 \equiv (\sin \phi_s \cos \psi_s, \sin \phi_s \sin \psi_s, \cos \phi_s) \quad (34)$$

and

$$\hat{\mathbf{R}}_2 \equiv (\sin \theta_s \cos \psi_s, \sin \theta_s \sin \psi_s, \cos \theta_s), \quad (35)$$

where the angles ϕ_s and θ_s are the polar angles and ψ_s is the azimuthal angle of the lines joining the source and the image source to receiver. The sound pressures for the direct and reflected waves given in Eqs. (33a) and (33b) agree with that derived by Hu and Bolton.⁸

The remaining integrals for the boundary wave can be evaluated by the double saddle point method to yield uniform asymptotic expressions.^{2,9} In this paper, we describe briefly the asymptotic method and give the results of the analysis as follows.

Using the relation⁷ $J_n(k_r r) = \frac{1}{2} \{ H_n^{(1)}(k_r r) - H_n^{(1)}(-k_r r) \}$ and the polar coordinates, we can rewrite the boundary wave P_3 as

$$P_3 = B_{hh} + B_{hv} + B_{vh} + B_{vv}, \quad (36)$$

where

$$B_{hh} = \frac{iS_2 k^3 \beta \sin \gamma_l \sin \gamma_m \cos(\psi_s - \psi_l) \cos(\psi_s - \psi_m)}{4\pi} \times \int_{-\pi/2+i\infty}^{\pi/2-i\infty} \Xi_1(\mu) e^{ikR_2 \cos(\mu - \theta_s)} d\mu + \frac{iS_2 k^3 \beta \sin \gamma_l \sin \gamma_m \sin(\psi_s - \psi_l) \sin(\psi_s - \psi_m)}{4\pi} \times \int_{-\pi/2+i\infty}^{\pi/2-i\infty} \Xi_2(\mu) e^{ikR_2 \cos(\mu - \theta_s)} d\mu, \quad (37a)$$

$$B_{hv} = \frac{S_2 k^3 \beta \sin \gamma_l \cos \gamma_m \cos(\psi_s - \psi_l)}{4\pi} \times \int_{-\pi/2+i\infty}^{\pi/2-i\infty} \Xi_3(\mu) e^{ikR_2 \cos(\mu - \theta_s)} d\mu, \quad (37b)$$

$$B_{vh} = \frac{S_2 k^3 \beta \cos \gamma_l \sin \gamma_m \cos(\psi_s - \psi_m)}{4\pi} \times \int_{-\pi/2+i\infty}^{\pi/2-i\infty} \Xi_3(\mu) e^{ikR_2 \cos(\mu - \theta_s)} d\mu, \quad (37c)$$

$$B_{vv} = \frac{iS_2 k^3 \beta \cos \gamma_l \cos \gamma_m}{4\pi} \times \int_{-\pi/2+i\infty}^{\pi/2-i\infty} \Xi_4(\mu) e^{ikR_2 \cos(\mu - \theta_s)} d\mu, \quad (37d)$$

$$\Xi_1(\mu) = \left\{ \frac{1 - \beta^2}{\cos \mu + \beta} - (\cos \mu - \beta) \right\} \frac{\sin \mu}{2} \{ H_0^{(1)}(kr \sin \mu) - H_2^{(1)}(kr \sin \mu) \} e^{-ikr \sin \mu}, \quad (38a)$$

$$\Xi_2(\mu) = \left\{ \frac{1-\beta^2}{\cos \mu + \beta} - (\cos \mu - \beta) \right\} \frac{\sin \mu}{2} \{H_0^{(1)}(kr \sin \mu) + H_2^{(1)}(kr \sin \mu)\} e^{-ikr \sin \mu}, \quad (38b)$$

$$\Xi_3(\mu) = \left\{ 1 - \frac{\beta}{\cos \mu + \beta} \right\} \sin^2 \mu \{H_1^{(1)}(kr \sin \mu) e^{-ikr \sin \mu}\}, \quad (38c)$$

$$\Xi_4(\mu) = \left\{ \frac{\beta^2}{\cos \mu + \beta} + (\cos \mu - \beta) \right\} \times \sin \mu \{H_0^{(1)}(kr \sin \mu) e^{-ikr \sin \mu}\}, \quad (38d)$$

and μ is the polar angle measured from the negative z axis and $H_n^{(1)}(z)$ is the n th-order Hankel function. To approximate the integrals, we express the Hankel function and its asymptotic expansion as¹⁰

$$H_n^{(1)}(z) e^{-iz} = \frac{(-1)^n}{\pi z} \times \frac{4^{1-n}}{(2n-1) \cdots 5 \times 3 \times 1} \times \int_0^\infty y^{2n} e^{-y^2/2} (4iz - y^2)^{n-1/2} dy \quad (39a)$$

and

$$H_n^{(1)}(z) e^{-iz} \approx (-i)^n \left(\frac{2}{i\pi z} \right)^{1/2} \left\{ 1 - \left(\frac{4n^2-1}{8iz} \right) + \cdots \right\}, \quad (39b)$$

where $n \geq 1$.

Uniform asymptotic expressions for Eqs. (37a)–(37d) can then be obtained by the method of pole subtraction to give

$$B_{hh} = \frac{-S_2 k^2 \sin \gamma_l \sin \gamma_m \cos(\psi_s - \psi_l) \cos(\psi_s - \psi_m)}{4\pi} \times \{2\beta(\cos \theta_s - \beta) + (1 - \beta^2)(1 - R_p)\} \times i\pi^{1/2} w e^{-w^2} \operatorname{erfc}(-iw) \frac{e^{ikR_2}}{R_2}, \quad (40a)$$

$$B_{hv} = \frac{S_2 k^2 \beta \sin \gamma_l \cos \gamma_m \cos(\psi_s - \psi_l)}{4\pi} \times \{2 \sin \theta_s + \sqrt{1 - \beta^2}(1 - R_p) i\pi^{1/2} w e^{-w^2} \operatorname{erfc}(-iw)\}, \quad (40b)$$

$$B_{vh} = \frac{S_2 k^2 \beta \cos \gamma_l \sin \gamma_m \cos(\psi_s - \psi_m)}{4\pi} \times \{2 \sin \theta_s + \sqrt{1 - \beta^2}(1 - R_p) i\pi^{1/2} w e^{-w^2} \operatorname{erfc}(-iw)\}, \quad (40c)$$

and

$$B_{vv} = \frac{S_2 k^2 \beta \cos \gamma_l \cos \gamma_m}{4\pi} \{2(\cos \theta_s - \beta) - \beta(1 - R_p) i\pi^{1/2} w e^{-w^2} \operatorname{erfc}(-iw)\} \frac{e^{ikR_2}}{R_2}. \quad (40d)$$

Summing the contribution due to the quadrupole source [cf. Eq. (33a)], its corresponding image source [cf. Eq. (33b)], and the boundary wave [Eqs. (36), (37a)–(37d)], the sound field can be expressed in an asymptotic form as

$$p \approx \frac{-S_2 k^2}{4\pi} \left\{ (\mathbf{l} \cdot \hat{\mathbf{R}}_1)(\mathbf{m} \cdot \hat{\mathbf{R}}_1) \frac{e^{ikR_1}}{R_1} + [(\mathbf{l} \cdot \hat{\mathbf{R}}_2)(\mathbf{m} \cdot \hat{\mathbf{R}}_2) R_p + (\mathbf{l} \cdot \hat{\mathbf{R}}_s)(\mathbf{m} \cdot \hat{\mathbf{R}}_s)(1 - R_p) F(w)] \frac{e^{ikR_2}}{R_2} \right\} + \frac{S_2}{4\pi} \times [(\mathbf{l} \cdot \mathbf{m}) - 3(\mathbf{l} \cdot \hat{\mathbf{R}}_1)(\mathbf{m} \cdot \hat{\mathbf{R}}_1)] \times \frac{ikR_1 - 1}{R_1^2} \times \frac{e^{ikR_1}}{R_1} + \frac{S_2}{4\pi} \times [(\mathbf{l} \cdot \mathbf{m}) - 3(\mathbf{l} \cdot \hat{\mathbf{R}}_2)(\mathbf{m} \cdot \hat{\mathbf{R}}_2)] \times \frac{ikR_2 - 1}{R_2^2} \times \frac{e^{ikR_2}}{R_2}, \quad (41)$$

where

$$R_p = \frac{\cos \theta_s - \beta}{\cos \theta_s + \beta}, \quad (42)$$

$$F(w) = 1 + i\pi^{1/2} w e^{-w^2} \operatorname{erfc}(-iw), \quad (43)$$

$$w = +(\frac{1}{2} ikR_2)^{1/2} (\beta + \cos \theta_s). \quad (44)$$

The quantity $\hat{\mathbf{R}}_s \equiv (\sin \mu_p, \cos \Psi_s, \sin \mu_p \sin \Psi_s, \cos \mu_p)$ may be regarded as the unit vector which characterizes the direction of the pole in the complex μ_p plane. The complex angle, μ_p , is determined by $\cos \mu_p + \beta = 0$, which implies that

$$\cos \mu_p = -\beta \quad \text{and} \quad \sin \mu_p = \sqrt{1 - \beta^2}. \quad (45)$$

The quantities R_1 and R_2 are the distances from the source to the receiver and image receiver, and $\hat{\mathbf{R}}_1$ and $\hat{\mathbf{R}}_2$ are the corresponding unit vectors pointing radially outward from the quadrupole center toward the observation points. In Eq. (16), the terms w and $F(w)$ are known as the numerical distance and the boundary loss factor, respectively, and the positive root of w is chosen that leads to an accurate computation of $F(w)$.¹¹

Although it is convenient to introduce the horizontal and vertical components in the asymptotic analysis, a quadrupole source is customarily⁶ classified as two basic types. They are, namely, a longitudinal quadrupole, for which \mathbf{l} and \mathbf{m} are parallel, and a lateral quadrupole, for which \mathbf{l} and \mathbf{m} are perpendicular (see Fig. 2). Consequently, we restrict our calculations to these two basic types in the following section.

III. NUMERICAL RESULTS AND INTERPRETATIONS

The sound field due to an arbitrarily oriented quadrupole can be calculated by using the asymptotic expression given in Eq. (41). However, as a validation of the asymptotic theory, we also develop the fast field program (quad-FFP) to predict the sound field. We remark that an arbitrarily oriented dipole is used as the source in an earlier study.¹² It is fairly straightforward to extend the FFP formulation for the case of an arbitrarily oriented quadrupole by noting Eqs. (19)–(23). The details of the numerical scheme is described in Ref. 4 and will not be repeated here for brevity.

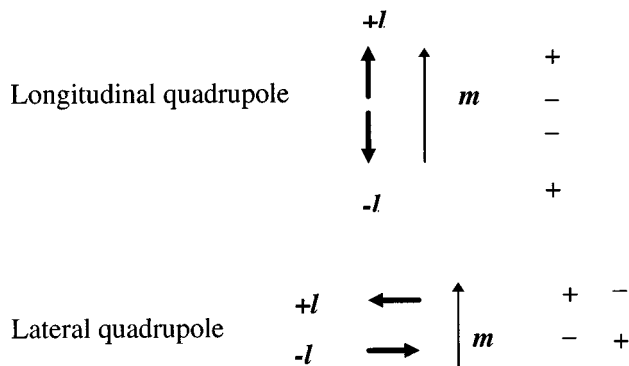


FIG. 2. The two basic types of quadrupole, a longitudinal quadrupole and a lateral quadrupole. The direction of arrows indicate the orientation of the dipole axis (l) and the quadrupole axis (m).

In the following calculations a two-parameter model¹³ for the specific admittance is used. This model assumes a rigid porous ground in which the porosity decreases with depth in an exponential form. It is given by

$$\frac{1}{\beta} = \frac{l+i}{\sqrt{\pi\gamma\rho}} \sqrt{\frac{\sigma_e}{f}} + \frac{ic}{4\gamma\pi} \frac{\alpha_e}{f}, \quad (46)$$

where γ is the adiabatic constant of air, c is the speed of sound in air, ρ is the density of air, and f is the frequency of sound. The two adjustable parameters are the effective flow resistivity of the surface, σ_e , and the rate of decrease of porosity with depth, α_e . This model has been used with tolerable success to fit excess attenuation data taken indoors and outdoors. Substituting values for the constant parameters, we arrive at the following expression for the normalized specific admittance, β , of the ground:

$$\beta = \frac{1}{0.436\sqrt{\sigma_e/f} + i[0.436\sqrt{\sigma_e/f} + 19.48(\alpha_e/f)]}. \quad (47)$$

The parameter values for σ_e and α_e are assumed to be 100 kPa s m⁻² and 50 m⁻¹ in all calculations. These chosen parameters are typical values that are used to model outdoor ground surfaces.

First, we show the comparison of the predictions of our asymptotic solution with numerical results obtained by quad-FFP. Figures 3 and 4 are predictions for the sound field due to a longitudinal quadrupole and a lateral quadrupole. The axis of the longitudinal quadrupole is aligned such that it is perpendicular to the ground surface. It may be called a vertical longitudinal quadrupole. Also the lateral quadrupole is assumed to have $\gamma_m = \pi/2$ and $\gamma_l = 0$ in the following calculations. Numerical results are presented for two frequencies, 1000 and 100 Hz. All three solutions agree to within 0.5 dB except for a very short distance where the horizontal separation is of the order of source or receiver height. As a further check on the accuracy of the solutions, we have also computed the sound field for a source consisting two adjacent out-of-phase dipoles and also the asymptotic solution derived by Generalov.⁵ Again these solutions agree well with our calculations shown in Figs. 3 and 4. We have tried different

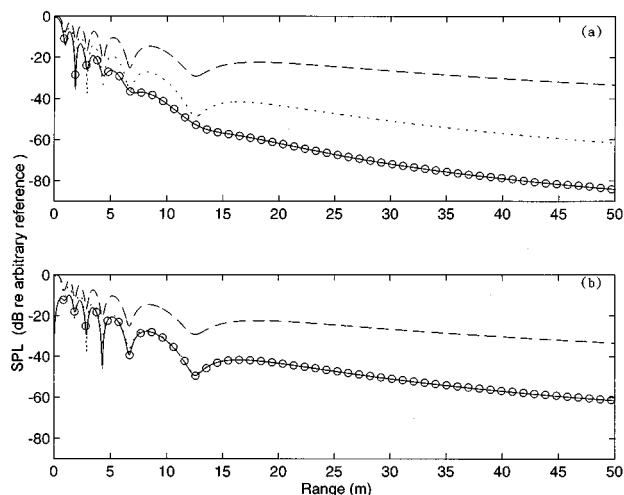


FIG. 3. (a) Sound field, as a function of range, of a vertical longitudinal quadrupole (solid line), a vertical dipole (dotted line), and a monopole (dashed line). The circles represent result of quad-FFP, which is in excellent agreement with the analytical approximation (solid line). Source height: 2.5 m, receiver height: 1.2 m, and source frequency: 1000 Hz. (b) Same as (a) above but for a lateral quadrupole (solid line). The dotted line represents the vertical dipole and the dashed line that of the monopole. The circles again represent results of the quad-FFP.

source/receiver geometries and different source orientations and frequencies. The agreements between the different solutions are generally excellent and their numerical results have not been shown for brevity. These numerical comparisons validate the asymptotic theory derived in Sec. I.

In addition, we have also shown the corresponding sound pressure levels for a monopole (dashed line) and a vertical dipole (dotted line) in Figs. 3 and 4. The details of the numerical predictions of the sound field due to a dipole source are given in Ref. 2. In the far field, the sound pressure level for a longitudinal quadrupole decays at a rate of roughly 18 dB per doubling of distance as a result of destructive interference of two out-of-phase dipoles aligned perpendicularly to the ground surface. However, it is not the case for the sound field due to a lateral quadrupole [see Figs. 3(b)

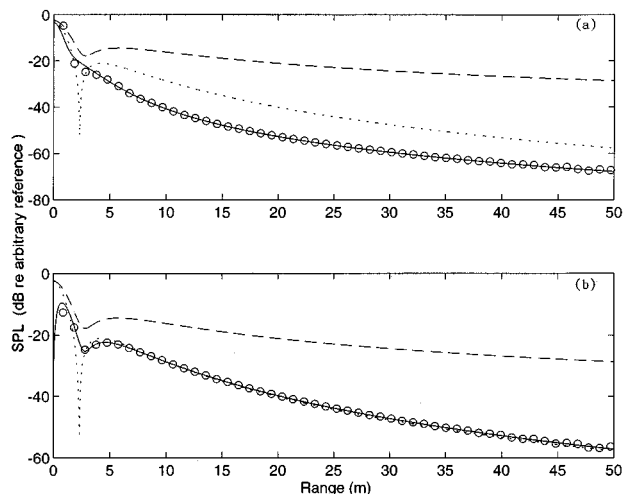


FIG. 4. Captions are same as Fig. 3 but the source frequency is 100 Hz.

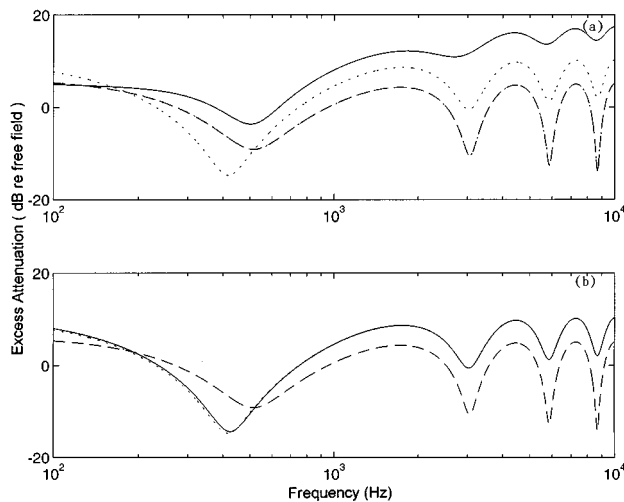


FIG. 5. (a) The excess attenuation spectra for a vertical longitudinal quadrupole (solid line), a vertical dipole (dotted line), and a monopole (dashed line). Source height: 2.5 m, receiver height: 1.2 m, and range: 50 m. (b) Same as (a) above but for a lateral quadrupole with $\gamma_m = \pi/2$, $\gamma_l = 0$, and $\psi_m = \psi_l = 0$ (solid line). The dotted line and dashed line represents the vertical dipole and monopole, respectively. The lateral quadrupole and the vertical dipole spectra are almost coincident within the thickness of the line.

and 4(b)]. The sound pressure level for a lateral quadrupole decays nearly at the same rate as that due to a vertical dipole in the far field. The decrease in the sound pressure level is roughly 12 dB per doubling of distance, as one would expect for a vertical dipole. The main difference in the sound field between a vertical dipole and a lateral quadrupole lies in the near field. This is largely due to the interference effect of the out-of-phase monopoles in close proximity for dipoles and lateral quadrupoles.

Although the asymptotic solution given by Generalov yields similar numerical results,¹⁴ the formula derived in the last section [see Eq. (41)] is more desirable. That is because our equation is expressed in a more recognizable and compact form for the ease of interpretation. It is somewhat difficult to interpret the physical significance of each term in Generalov's solution.

A close examination of Eq. (41) reveals that the asymptotic solution for a quadrupole can no longer be expressed in the classical form similar to that of a monopole. We may interpret the solution as one for which the sound field consists of a monopole (the terms in curly bracket) augmented by two "pseudo-dipoles" at the respective positions of the source and image source. We also note that the contribution due to the monopole term consists of three terms: a direct wave, a reflected wave, and a ground wave. On the other hand, there are no corresponding ground wave terms for the pseudo-dipoles. Moreover, unlike a dipole, the sound pressure level due to the pseudo-dipole decays more rapidly (proportional to $1/R^3$) whereas the level decays as $1/R^2$ for a dipole. Hence, these pseudo-dipole terms are only significant at the near field. We also note that the sound field is dominated by the monopole term in the far field because its level decays as $1/R$.

Figures 5 and 6 show the predicted excess attenuation spectra for a vertical longitudinal quadrupole and a lateral

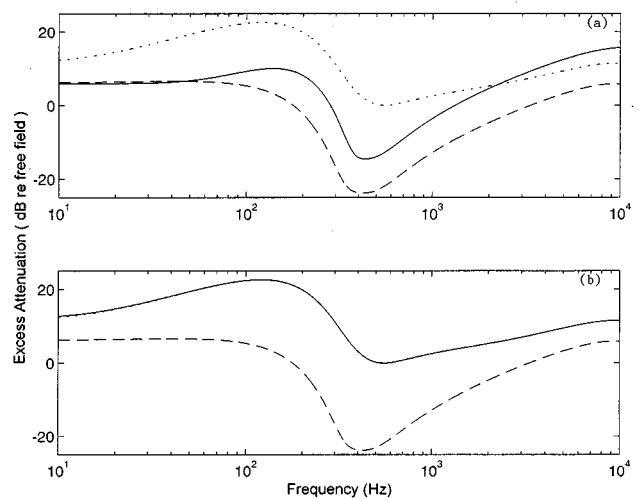


FIG. 6. Captions are same as Fig. 5 but for range of 320 m.

quadrupole. Again, the corresponding spectra due to a vertical dipole and monopole are also shown in the figures for comparison. We define the excess attenuation in decibels as the total sound field relative to the direct field due to the corresponding source. The amplitude of the field of a quadrupole source is a function of frequency [see Eq. (33a)], unlike that of a monopole which is simply $1/R$. This implies that the extra path length of the image wave (i.e., $R_2 - R_1$) becomes significant at high frequencies and the excess attenuation spectrum tends to large positive values. This feature, which is more prominent at smaller incident angles, is therefore not related to the impedance of the boundary, but rather to the fact that the amplitude of the quadrupole field is dependent on the frequency.

In Fig. 5, the source and receiver heights are 2.5 and 1.2 m, respectively, and the separation is 50.0 m. As mentioned in Ref. 2, the predicted excess attenuation for a vertical dipole shows greater interference effects as compared with that due to a monopole [the dotted and dashed lines in Fig. 5(a)]. Furthermore, the frequencies of the subsequent interference dips are about the same for the monopole, vertical dipole, and longitudinal quadrupole, but the interference effects are much less significant for the longitudinal quadrupole. The predicted spectra for a lateral quadrupole, a vertical dipole, and a monopole are shown in Fig. 5(b). At this source/receiver geometry, there is little difference in the predicted spectra between a lateral quadrupole and a vertical dipole.

Figure 6(a) shows prediction of attenuation spectra with a vertical longitudinal quadrupole (solid line), a vertical dipole (dotted line), and a monopole (dashed line) source with the source and receiver heights but the range is 320 m. It can be seen, in this near-grazing geometry, that the predicted excess attenuation due to the longitudinal quadrupole is lower than that due to a vertical dipole, but it is still higher than that due to a monopole. In Fig. 6(b), we show the predicted attenuation, for the same source/receiver geometry, for a lateral quadrupole (solid line), a vertical dipole (dotted line), and a monopole (dashed line). There is not much difference in the predicted excess attenuation between a lateral

quadrupole and a vertical dipole, and these predictions are different from that due to a monopole.

IV. CONCLUDING REMARKS

The sound field due to an arbitrarily oriented quadrupole has been derived and the solution can be expressed in a closed form. The analytic solution has been validated by comparing the numerical results with a computationally intensive numerical scheme. The numerical scheme is based on the well-known fast field program (FFP) and the corresponding Green's function has been modified for an arbitrarily oriented quadrupole.

The predicted excess attenuation for a longitudinal quadrupole is less in comparison with that due to a vertical dipole. However, it is still higher than that due to a monopole. On the other hand, the predicted excess attenuation for a lateral quadrupole is comparable with that due to a vertical dipole.

ACKNOWLEDGMENT

This work was supported by the EPSRC (UK) through grant ref. No. GR/J42052.

- ¹K. Attenborough, "Review of ground effects on outdoor sound propagation from continuous broadband sources," *Appl. Acoust.* **24**, 289–319 (1988).
- ²K. M. Li, S. Taherzadeh, and K. Attenborough, "Sound propagation from a dipole source near an impedance plane," *J. Acoust. Soc. Am.* **101**,

3343–3352 (1997). [Note: There is a typographical error in this paper. The square bracket in Eq. (21b) should read as

$$\left[\frac{1 - ikR_2}{R_2^2} \right].$$

- ³J. S. Bolton, B. K. Gardner, and T. A. Beauvilain, "Sound cancellation by the use of secondary multipoles," *J. Acoust. Soc. Am.* **98**, 2343–2362 (1995).
- ⁴S. Taherzadeh, "Sound propagation in inhomogeneous media," PhD. Thesis, Faculty of Technology, The Open University, 1996.
- ⁵A. V. Generalov, "Sound field of a multipole source of order N near a locally reacting surface," *Sov. Phys. Acoust.* **33**, 492–496 (1987).
- ⁶A. D. Pierce, *Acoustics: An Introduction to Its Physical Principles and Applications* (Acoustical Society of America, New York, 1989), pp. 165–171.
- ⁷M. Abramowitz and I. A. Stegun, *Handbook of Mathematical Functions with Formulas, Graphs, and Mathematical Tables* (Dover, New York, 1972).
- ⁸Z. Hu and J. S. Bolton, "Sound propagation from an arbitrarily oriented multi-pole placed near a plane, finite impedance surface," *J. Sound Vib.* **170**, 637–666 (1994).
- ⁹C. F. Chien and W. W. Soroka, "Sound propagation along an impedance plane," *J. Sound Vib.* **81**, 413–424 (1975).
- ¹⁰G. N. Watson, *A Treatise on the Theory of Bessel Functions* (Cambridge U.P., Cambridge, 1944), pp. 196–198. (The given formula is obtained by substituting $u = y^2/2$ and $\nu = n$ where $n \geq 1$.)
- ¹¹M. R. Stinson, "A note of the use of an approximate formula to predict sound fields above an impedance plane due to a point source," *J. Acoust. Soc. Am.* **98**, 1810–1814 (1995).
- ¹²S. Taherzadeh and K. Attenborough, "Sound propagation from dipole and monopole sources in a stratified fluid above a layered poro-elastic solid," *Computational Acoustics and its Environmental Applications*, edited by C. A. Brebbia (Computational Mechanics Publications, Southampton, 1995), pp. 45–54.
- ¹³K. Attenborough, "Ground parameter information for propagation modelling," *J. Acoust. Soc. Am.* **92**, 418–427 (1992).
- ¹⁴We wish to point out that Generalov's approximate solutions [his Eqs. (13)–(15)] for $|w| \gg 1$ do not yield accurate numerical results. Nevertheless, his "exact" solutions [Eqs. (7)–(10) of Ref. 5] agree with the numerical results of our asymptotic solution and quad-FFP.

Further evidence that the sound-speed algorithm of Del Grosso is more accurate than that of Chen and Millero

Christopher S. Meinen and D. Randolph Watts

Graduate School of Oceanography, University of Rhode Island, Narragansett, Rhode Island 02882

(Received 9 December 1996; revised 13 March 1997; accepted 8 July 1997)

Estimates of the bottom depth of the ocean at 11 sites were determined by combining round-trip acoustic travel time measurements made by inverted echo sounders on the ocean bottom with sound-speed profiles determined from simultaneously measured temperature and salinity profiles. These depths were converted into pressures and were compared to independently measured bottom pressures to determine the accuracy of the algorithms used to calculate the sound-speed profile. The sound-speed algorithms tested were those derived by Del Grosso [J. Acoust. Soc. Am. **56**, 1084–1091 (1974)] and by Chen and Millero [J. Acoust. Soc. Am. **62**, 1129–1135 (1977)], as well as the corrected version of Chen and Millero's algorithm recently published by Millero and Li [J. Acoust. Soc. Am. **95**, 2757–2759 (1994)]. The results of this study agree with the results from recent acoustic tomography experiments which indicate that the algorithm of Del Grosso for the speed of sound in seawater is more accurate than the currently accepted standard algorithm of Chen and Millero. Del Grosso's algorithm also produces more accurate results than those from the Millero and Li correction to the Chen and Millero algorithm. © 1997 Acoustical Society of America. [S0001-4966(97)05610-5]

PACS numbers: 43.30.Es [SAC-B]

INTRODUCTION

The algorithm of Chen and Millero¹ for sound speed in seawater is the internationally accepted standard for use with hydrographic data,² however, recent acoustic tomography work by Spiesberger and Metzger,³ Dushaw *et al.*,⁴ and Spiesberger,⁵ has indicated that the sound-speed algorithm presented in Del Grosso⁶ is more accurate. The two algorithms calculate about the same sound-speed profile in the upper 1000 dbars, but Del Grosso's algorithm calculates speeds that are slower by about 0.8 m s^{-1} at depths of 5000 dbars. (The unit for pressure used here is the decibar, or dbar for short, which is equal to 10^4 Pascals. Oceanographers commonly report pressure in dbars rather than the SI units of Pascals because $1 \text{ dbar} \approx 1 \text{ m}$ of depth in the ocean.) Recently, a correction to the Chen and Millero algorithm for low temperatures and high pressures was published by Millero and Li.⁷ This correction reduces the difference between the two algorithms, but the corrected algorithm also consistently predicts higher sound speeds in the deep water than Del Grosso's algorithm. This study provides further evidence to support Del Grosso's algorithm by comparing pressures measured by pressure sensors to pressures estimated from acoustic travel time measurements made by inverted echo sounders.

I. DATA

Inverted echo sounders (IESs) are instruments moored about one meter off the ocean bottom that measure the time for 10-kHz pulses to travel the round-trip distance to the ocean surface and back.^{8,9} PIES are IESs that are also equipped with pressure sensors from Paroscientific Inc., which are based on oscillating quartz crystals to which tension is applied via a Bourdon tube.¹⁰

If the sound-speed profile through the water column above the PIES is known concurrently with the travel time measurement, it is possible to combine this information to derive an estimate of the bottom depth. Full-water-column CTD (conductivity–temperature–depth) profiles obtained near each PIES site allowed for the calculation of sound-speed profiles as functions of temperature, salinity, and pressure using any of the three sound-speed algorithms.

This study was based upon 11 PIES records which have one or more full-water-column CTD profiles taken at the PIES site during the period of deployment. Four of the PIES were located in a line across the North Atlantic current at pressures of 3300–4900,¹¹ six were in a line across the Kuroshio at pressures of 450–1100,¹² and the final PIES was located near Hawaii at a pressure of about 4800 dbars.¹³

II. METHODS

The travel time measurement, τ , was used to estimate the bottom pressure in the following manner. The round-trip travel time is given by

$$\tau = 2 \int_{-H}^0 \frac{1}{c} dz, \quad (1)$$

where H is the depth of the acoustic transducer and c is the sound speed. Defining

$$\left\langle \frac{1}{c} \right\rangle = \frac{1}{H} \int_{-H}^0 \frac{1}{c} dz, \quad (2)$$

Eq. (1) can be rearranged to give

$$H = \frac{\tau}{2\langle 1/c \rangle}. \quad (3)$$

Sound-speed profiles were calculated from the CTD data using both the Del Grosso (hereafter DG74) and Chen and Millero (hereafter CM77) algorithms as well as the corrected Chen and Millero algorithm (hereafter ML94). These sound-speed profiles were then substituted into Eqs. (2) and (3) along with the concurrent travel times measured by the PIES to calculate the depths (in meters) of the PIES using each of the three sound-speed algorithms. These depths were then converted into pressures by making use of the equation described in Fofonoff and Millard.² They give the following equation for converting from pressure to depth,

$$z = \frac{C_1 p + C_2 p^2 + C_3 p^3 + C_4 p^4}{g(\phi) + \frac{1}{2} \gamma' p} + \frac{\Delta D}{9.8},$$

where $C_1 = 9.72659$, $C_2 = -2.2512E-05$, $C_3 = 2.279E-10$, $C_4 = -1.82E-15$, $\gamma' = 2.184E-06 \text{ m s}^{-2} \text{ dbar}^{-1}$, p is the pressure, and ΔD is the dynamic height anomaly measured from pressure p to the surface. This equation was inverted using an iterative method which resulted in pressures that are accurate to 0.1 dbars. These calculated pressures (in dbars) can be compared to the pressures measured by the pressure sensor located on the PIES. (There are a number of constant offsets that are inherent to the measurements of these instruments which must be accounted for as part of this procedure, as presented in the Appendix.)

III. ERRORS IN THE MEASURED AND CALCULATED PRESSURES

Before presenting the results of this comparison, a discussion of the errors involved in both the measurement of pressure and the calculation of pressure is in order. All errors quoted throughout this paper are at the one standard deviation level except where otherwise noted. Paroscientific states that the absolute accuracy of the pressure sensor measurement is 0.01% of full scale, about 0.5 dbars for instruments designed for up to 4500-m depths.¹⁴ These Paroscientific pressure sensors have historically had problems with long-term drifts while deployed. However, recent work in the Gulf Stream has indicated that these drifts can be removed quite accurately.¹⁰ The linear drifts in the pressure sensors used here were all below 0.3 dbar per year and most of them were less than 0.05 dbars per year. The travel time measurement of the PIES is accurate to 1 ms,⁹ which is equivalent to an error in the calculated pressure of 0.75 dbars.

The largest source of error in the calculation results from the spatial offset between the PIES site and the location where the CTD is taken, which introduces random scatter due to the variation of the sound-speed profile caused by lateral gradients and internal waves and tides during the several hours involved in the CTD measurement. These errors are difficult to quantify; however, based on the maximum oceanic thermocline slope and the amplitude of tidal and higher frequency variability observed the combined error estimate is between 0.25 (at a CTD–PIES distance of 0 km) and 2.5 dbars (at a CTD–PIES distance of 3 km). The specific CTD–PIES distances and errors are accounted for in the results section. Finally, errors in the sound-speed equations will also contribute to errors in the calculated pressure.

TABLE I. Calculated pressures compared to the pressure measured by the bottom pressure sensors. The locations of the instruments are noted. For sites where multiple CTDs were taken, the mean result from all of the casts is shown. Number of CTDs taken at each site is noted. For the shallow sites in the Kuroshio, the ML94 correction to the CM77 algorithm was not used, as the correction is for low temperature and high pressure only.

Measured pressure	DG74 (dbars)	CM77 (dbars)	ML94 (dbars)	Number of CTD casts at site	Location
3313.3	3314.3	3315.2	3314.6	3	North Atlantic Current
3944.8	3945.3	3946.4	3945.6	2	
4814.0	4816.1	4817.6	4816.5	1	
4978.2	4977.9	4979.4	4978.3	2	
4812.4	4814.4	4815.9	4814.8	9	Hawaii
495.1	496.7	496.7	N/A	1	Kuroshio
1098.1	1097.6	1097.7	N/A	1	
1100.9	1100.9	1101.1	N/A	1	
540.0	538.9	538.9	N/A	1	
495.2	496.1	496.1	N/A	1	
531.9	531.4	531.4	N/A	1	

DG74 and ML94 both quote an accuracy of 0.05 m s^{-1} , which translates to a maximum potential error in the calculated pressure of about 0.2 dbars. CM77 quotes an accuracy of 0.2 m s^{-1} , resulting in a maximum potential error of about 0.8 dbars in the calculated pressure.

IV. RESULTS

Table I lists the measured pressures at the 11 PIES sites, together with the mean of the calculated pressures from all CTDs at each site, using CM77, ML94, and DG74. (ML94 was not used to calculate pressures at the shallow sites from the Kuroshio because the correction is for low temperatures and high pressures.) At the shallow (400–1000 m) sites from the Kuroshio, the agreement between the calculated pressures and the measured pressures is generally quite good, and there is little difference between the pressures calculated using DG74 and CM77. This is to be expected since DG74 and CM77 give very similar sound-speed profiles above 1000 dbars. Figure 1(A) shows that instruments located at shallow depths have calculated pressures about equal to the measured pressures, within the range of the scatter. Because of the good agreement between the calculated and measured pressures at these sites, the rest of this discussion will focus on the differences found at the deep sites.

A. Relative differences between algorithms

At depths greater than 3000 m the calculated pressures are consistently higher than the measured pressures. Figures 1B–D show that for these sites the pressures calculated using DG74 are about 1–1.5 dbars closer to the measured pressures than those calculated by CM77. The pressures calculated using ML94 are 0.3–0.4 dbars larger than those from DG74. These differences are significant because the only dissimilarities between the different methods of calculation are the sound-speed algorithms used. The above-quoted sound-speed algorithm accuracies explain a difference of $\sqrt{0.8^2 + 0.2^2} = 0.82$ dbars between DG74 and CM77 and

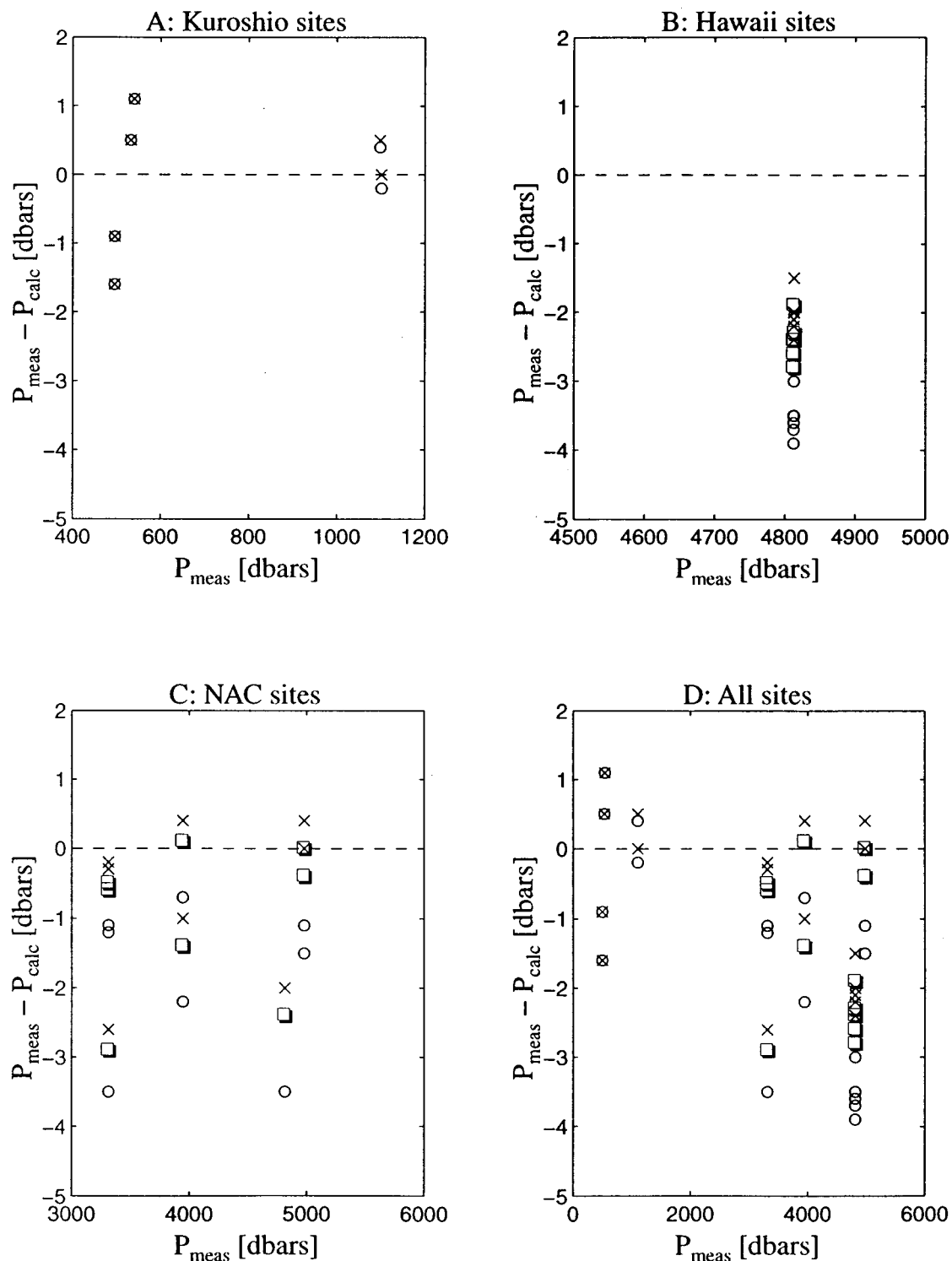


FIG. 1. Pressure difference ($P_{\text{measured}} - P_{\text{calculated}}$) plotted vs P_{measured} , where pressures calculated using DG74 are denoted by crosses, pressures calculated using CM77 are denoted by circles, and pressures calculated using ML94 are denoted by open boxes. Panel A shows the sites from the Kuroshio, panel B shows the site near Hawaii, panel C shows the sites in the North Atlantic Current, and panel D shows all of the sites together. Results from all CTDs are shown. Dashed line denotes zero error.

$\sqrt{0.2^2 + 0.2^2} = 0.28$ dbars between DG74 and ML94. Thus for an individual PIES and CTD pair, the differences between pressures calculated using DG74 and CM77 or DG74 and ML94 would not be significant at the two standard deviation level. It is important to realize, however, that these offsets

are appearing in the mean of 17 different CTD and PIES combinations, and thus it is necessary to consider the standard deviation of the mean. Conservatively, it can be said that there are at least five degrees of freedom, one for each independent PIES site, so the standard deviation of the

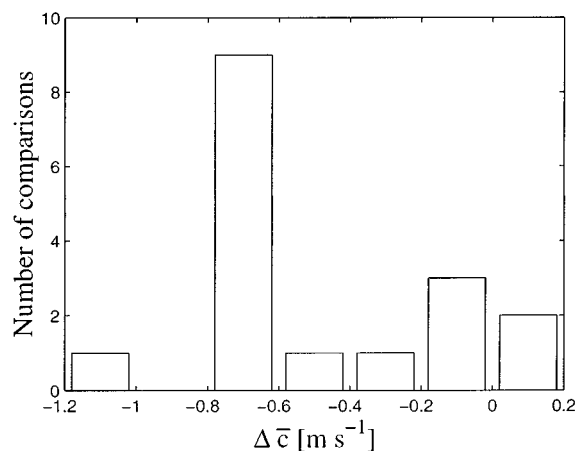


FIG. 2. Histogram of the change in the vertically averaged sound speed that would be necessary to make the calculated pressures (using DG74) at the deep (3000–5000 m) sites equal to the measured pressures.

mean offset between DG74 and CM77 is 0.37, and it is 0.13 dbars between DG74 and ML94. Thus even at the two standard deviation level there are statistically significant differences between the pressures calculated using DG74 and those calculated using CM77 and ML94.

B. Absolute differences between measured and calculated pressures

The mean differences between the measured pressures at the deep sites and those calculated at the same sites using DG74, CM77, and ML94 are 1.4, 2.7, and 1.7 dbars, respectively. The total error (one standard deviation level) estimated for the calculations, due mainly to the spatial offset between the CTD sites and the PIES sites, which have a mean separation of 1.5 km, is 1.5 dbars for the pressure calculations using DG74 and ML94, it is 1.6 dbars for the pressure calculation using CM77. The corresponding standard deviation of the means, once again assuming five degrees of freedom, is about 0.7 dbars for all three algorithms. Thus the differences between the measured pressures and those calculated using DG74 are (barely) not statistically significant at two-standard deviations of the mean, whereas the differences from the pressures calculated using CM77 are nearly twice the size of the 95% errors, and those calculated using ML94 are more than 20% larger than can be accounted for by two standard deviations of the mean. These results indicate that DG74 calculates more accurate sound speeds in the deep ocean than both CM77 and its recently updated version, ML94.

Note, however, that even the pressures calculated by DG74 at the deep North Atlantic Current and Hawaii sites are consistently greater than the measured pressures. The amount by which the vertically averaged sound speed [from Eq. (2)] would need to change to eliminate the difference between measured and calculated pressure can be estimated by rearranging Eq. (3) to give $\Delta c/c \approx \Delta H/H \approx \Delta p/p$. Figure 2 demonstrates that for nearly all of the sites at depths greater than 3000 dbars, the vertical mean sound-speed needs to be reduced to bring the calculated pressures in line with

the measured pressures. This observation is consistent with the results of Spiesberger and Metzger,³ who found that DG74 calculated speeds that were 0.22 m s^{-1} too fast at a depth of 3 km. Including the correction from Spiesberger and Metzger³ in DG74 decreases the calculated pressures by about 0.2–0.4 dbars for the deeper PIES sites (the effect on the shallow Kuroshio sites is negligible). In a later paper Spiesberger⁵ questioned his proposed correction by explaining that the offsets he noted could have been due to his model parameters rather than a problem with the DG74 algorithm. Essentially he enlarged his error bars to indicate that he had insufficient information to determine definitively whether DG74 was predicting speeds that were too fast in the deep water. The results of this study indicate that a correction of the same sign and of somewhat larger magnitude than that recommended by Spiesberger and Metzger³ would give better agreement between the calculated and measured pressures. A decrease in the vertically averaged sound speed of about 0.5 m s^{-1} would reduce the mean of the observed offsets between the directly measured pressures and the calculated pressures to zero. It is important to note, however, that the pressures calculated using DG74 are not statistically different than the measured pressures based on our estimate of the errors involved in this calculation, so these results cannot definitively state that DG74 is calculating speeds that are too fast. However, since two completely different types of experiments, Spiesberger's modeling of acoustic tomography data and this study's comparison of measured pressures to acoustically determined pressures, have both found that DG74 consistently results in deep sound speeds that are too fast, it seems likely that sound speeds calculated at depths greater than 1000 dbars are still too high.

V. CONCLUSIONS

This study involved data from three separate experiments: one in the Kuroshio during 1991–92, the second off Hawaii in 1991–92, and the third in the North Atlantic Current from 1993–95. By directly measuring bottom pressure and comparing it with calculated bottom depth and pressure from travel times measured by inverted echo sounders and sound speed calculated from coinciding full-water-column CTDs, this study has provided additional evidence that Del Grosso's⁶ sound-speed algorithm is more accurate than that of Chen and Millero.¹ Del Grosso's algorithm provides more accurate velocities at depths even when the recently published correction⁷ for low temperatures and high pressures for Chen and Millero's algorithm is used. The results also suggest that even Del Grosso's sound-speed algorithm may be calculating speeds that are slightly too fast in water deeper than 1000 dbars. Further measurements would be required to confirm this hypothesis. Nevertheless, Del Grosso's algorithm is accurate enough to calculate bottom depths and pressures to within about 1 m and 1 dbar in 5000 dbars.

ACKNOWLEDGMENTS

The authors would like to express their sincere appreciation to Karen Tracey for her assistance in processing these data. Dr. Allyn Clarke and his colleagues at the Bedford Institute of Oceanography in Halifax, Nova Scotia provided some of the CTD profiles taken at the sites in the North Atlantic Current. Dr. Mark Wimbush at the University of Rhode Island kindly provided all of the Kuroshio data. Dr. Steve Chiswell of the New Zealand Oceanographic Institute provided the data from Hawaii. Mr. Richard Wearn at Paroscientific Inc. provided a considerable amount of information concerning the accuracy of the pressure sensors. Dr. John Spiesberger at Pennsylvania State University and Dr. Nicholas Fofonoff at the Woods Hole Oceanographic Institute also provided helpful suggestions. The authors would also like to thank the reviewers, who made a number of very helpful suggestions. This project was funded under NOAA Grant No. NA56GP0134.

APPENDIX: INHERENT OFFSETS IN THE PIES

Both the travel time and pressure measurements made by the PIES are subject to some constant offsets which are compensated for here. There is a fixed 3-ms internal response delay in the IES, which must be subtracted from the measured travel time to avoid overestimating the depth of the IES. The pressure sensors measure absolute pressure, rather than gauge pressure, so the atmospheric pressure must be removed from the measured pressure, because the PIES measures the acoustic travel time relative to the sea surface. Since variations of atmospheric pressure are on the order of a tenth of a decibar, it is sufficient to subtract the annual mean regional value of atmospheric pressure (10.2, 10.2, and 10.1 dbars for, respectively, the North Atlantic Current, Hawaii, and Kuroshio regions). Last, the pressure sensor on the PIES

is located 0.58 m below the acoustic transducer, so for comparison to the pressure estimated from the travel time, the corresponding small hydrostatic offset (0.60 dbars) was subtracted from the measured pressure.

¹C.-T. Chen and F. J. Millero, "Speed of sound in seawater at high pressures," *J. Acoust. Soc. Am.* **62**, 1129–1135 (1977).

²N. P. Fofonoff and R. C. Millard, "Algorithms for computation of fundamental properties of seawater," UNESCO Technical Papers in Marine Science, No. 44 (1983).

³J. L. Spiesberger and K. Metzger, "A new algorithm for sound speed in seawater," *J. Acoust. Soc. Am.* **89**, 2677–2688 (1991).

⁴B. D. Dushaw, P. F. Worcester, B. D. Cornuelle, and B. M. Howe, "On equations for the speed of sound in seawater," *J. Acoust. Soc. Am.* **93**, 255–275 (1993).

⁵J. L. Spiesberger, "Is Del Grosso's sound-speed algorithm correct?," *J. Acoust. Soc. Am.* **93**, 2235–2237 (1993).

⁶V. A. Del Grosso, "New equation for the speed of sound in natural waters (with comparisons to other equations)," *J. Acoust. Soc. Am.* **56**, 1084–1091 (1974).

⁷F. J. Millero and X. Li, "Comments on 'On equations for the speed of sound in seawater'," *J. Acoust. Soc. Am.* **95**, 2757–2759 (1994).

⁸D. R. Watts and H. T. Rossby, "Measuring dynamic heights with Inverted Echo Sounders: Results from MODE," *J. Phys. Oceanogr.* **7**(3), 345–358 (1977).

⁹G. F. Chaplin and D. R. Watts, "Inverted Echo Sounder development," *Proc. Oceans*, 249–253 (1984).

¹⁰D. R. Watts and H. Kontoyiannis, "Deep-ocean bottom pressure measurement: Drift removal and performance," *J. Atmos. Oceanic Technol.* **7**(2), 296–306 (1990).

¹¹K. L. Tracey, C. S. Meinen, and D. R. Watts, "North Atlantic Current inverted echo sounder data report for August 1993–July 1995," Technical Report 7, Graduate School of Oceanography, University of Rhode Island, Narragansett, Rhode Island, 1996.

¹²C. James, M. Wimbush, and H. Ichikawa, "East China Sea, Kuroshio 1991–2 Data Report," Technical Report 3, Graduate School of Oceanography, University of Rhode Island, Narragansett, Rhode Island, 1994.

¹³S. M. Chiswell, "Using an array of Inverted Echo Sounders to measure dynamic height and geostrophic current in the North Pacific subtropical gyre," *J. Atmos. Oceanic Technol.* **11**(5), 1420–1424 (1994).

¹⁴R. B. Wearn, 1996 (personal communication).

A comparison of quasi-continuous wave and broadband travel time techniques in the prediction of long-range reverberation

Kevin B. Smith and Erick B. Cushman

Department of Physics, Code PH/Sk, Naval Postgraduate School, Monterey, California 93940

(Received 24 November 1996; accepted for publication 11 April 1997)

Previous work has shown that the general structure of deep ocean reverberation can be reasonably modeled using single-frequency propagation techniques. Recent results indicate that secondary, multipath influences can affect reverberation levels significantly. Primarily, these influences are observed in shadow regions of the primary, direct path ensonification. Temporal separation of these paths is required in order to distinguish these effects. This suggests that regions of the reverberation signal may not be well predicted by single-frequency quasi-cw (continuous wave) methods. In this paper, a quasi-cw method of predicting long-range reverberation is compared to an exact, two-way travel time technique. Each model assumes a simple, constant plane-wave scattering strength, thereby emphasizing the influence of propagation. Results from both models are compared to measured reverberation data from an ONR-SRP bottom reverberation experiment conducted near the Mid-Atlantic Ridge. It is shown that the single-frequency method underestimates reverberation levels on the backside of large ridge structures which act as shadow zones for all propagation paths. Returns from multipaths, however, begin to fill in these regions in time and may explain the lack of such dramatic signal drop-outs from measured data. © 1997 Acoustical Society of America. [S0001-4966(97)02710-0]

PACS numbers: 43.30.-k, 43.30.Gv [JHM]

INTRODUCTION

In 1993, the Office of Naval Research sponsored one of several experiments under a special research program, hereafter referred to as the ONR-ARSRP, to study low-frequency, long-range acoustic reverberation in the deep ocean. The focus of this work is the bottom reverberation and, specifically, the influence of complex multipath propagation on the measured returns. Two full-wave methods for modeling the observed reverberation based fundamentally on forward propagation have shown reasonable agreement with data. The primary difference between the two models is the temporal separation of multipath influences. In this paper, we will show quantitatively the significance of these secondary multipaths on long-range reverberation and discuss the shortcomings of models which do not treat this properly.

Several investigators have shown reasonably good agreement between the dominant observed returns and high levels of seafloor ensonification (low transmission loss) computed from two-way, full-wave continuous wave (cw) transmission loss models (e.g., Makris and Berkson, 1994; Smith *et al.*, 1996). However, Smith *et al.* also found that secondary multipaths contributed significantly to the forward field as measured by a near bottom vertical array roughly 30 km away from the source. A recent algorithm developed to compute exact, two-way travel times of broadband pulses using parabolic equation (PE) modeling techniques (Smith, 1996a) has been employed to determine the influence of these multipaths on the reverberation. These results will be compared to the measured data and contrasted with the predictions of the quasi-cw method.

Throughout the analysis, we will refer back to some of

the data collected during the 1993 summer acoustics cruise. The data used here will be described in Sec. I. In Sec. II, a brief description of the quasi-cw model will be given and the two-way travel time method will be defined. The results from these models will be compared and contrasted with each other and the measured reverberation in Sec. III. We summarize our results in Sec. IV and suggest other mechanisms we have neglected here which could provide a better match with the data. The significance of multipaths in other reverberation-limited scenarios will also be suggested.

I. MEASURED REVERBERATION

The major bottom reverberation experiment of the ONR-ARSRP was carried out in July 1993 (ONR-ARSRP 1993 Cruise Report). Three ships participated in the experiment—the R/V CORY CHOUEST, the R/V ALLIANCE, and the R/V KNORR. The CORY deployed a vertical line source array and a horizontal line receive array. In this work, we will examine only one of the monostatic returns from the CORY transmitting a 200- to 255-Hz LFM chirp. The results are typical and should be considered more generally applicable to other similar reverberation measurements. Both the CORY and the ALLIANCE made water column temperature and conductivity measurements. Conventional CTD casts to full ocean depth made by the ALLIANCE were used to provide sound-speed profiles in the region. In addition, a large-scale reconnaissance survey was carried out in July–August 1992 on the R/V EWING where HMR1 sidescan sonar data and Hydrosweep 15-kHz multibeam bathymetry data were collected (Tucholke *et al.*, 1993). The area covered was approximately

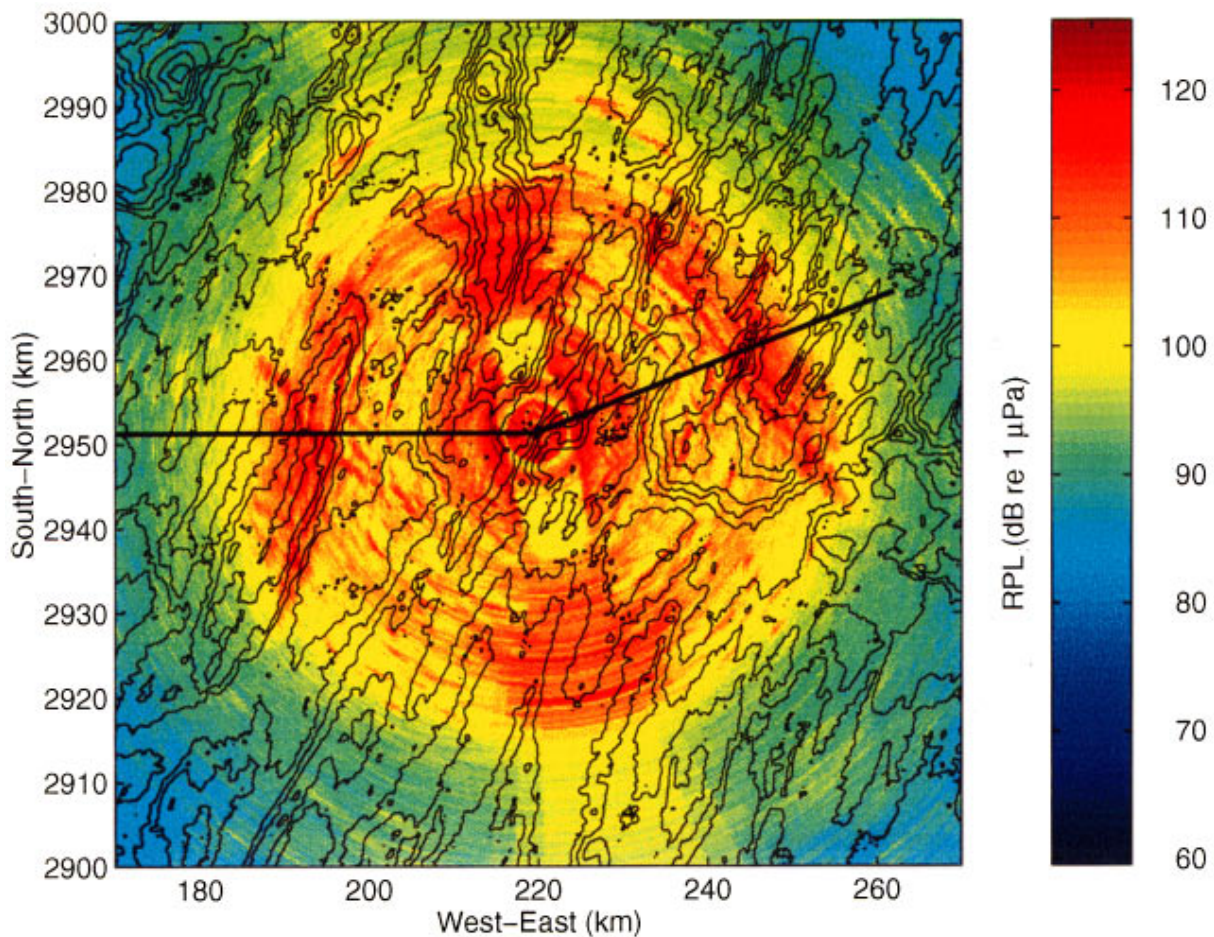


FIG. 1. Measured monostatic reverberation levels from segment #414 of the ONR-ARSRP main acoustics cruise. Bathymetry is contoured at 200 m increments. Radial lines indicate right-left ambiguous directions of beam #72.

200 km in the north-south direction and 400 km in the east-west direction. The data set used for this work was gridded at 200 m×200 m.

Measured reverberation returns from segment #414 (refer to cruise report) have been mapped to local bathymetry and show good correlation with major bathymetric features as displayed in Fig. 1. (Because this work focuses on the reverberation structure and not absolute levels, many reverberation levels are unnormalized.) For this work, we shall focus on beam #72 which contains reverberation data from the CORY towards the west in the direction of a large ridge. Note that the right-left ambiguity inherent in the processing also includes in this signal reverberation structures from the northeast. Data from this beam is plotted in Fig. 2. It is important to note that the “range” of the signal as indicated was computed from a simple, linear time/range conversion, i.e.,

$$r = \frac{c_0 t}{2}, \quad (1)$$

where $c_0 = 1485$ m/s was found to produce a good correlation with bathymetric features. Other approaches may attempt to account for the path curvature in this conversion. However, the important aspect of these approaches is the one-to-one correspondence of the reverberation return with a single region of the seafloor, i.e., only a single, dominant (or

primary) interaction with the bottom is assumed to generate the observed return at any specific time. Throughout this work, we shall continue to report results as a function of range. When appropriate, we will comment on the errors or inadequacies of this approach.

II. NUMERICAL METHODS FOR PREDICTING REVERBERATION STRUCTURE

For all of the numerical work presented here, versions of the University of Miami Parabolic Equation (UMPE) model (Smith and Tappert, 1993) were employed to predict acoustic propagation. Only transmissions along beam #72 were computed for comparison with the reverberation signal described in the previous section, both with and without the right-left ambiguity included. Bathymetry along the radials was extracted from the gridded database. A single sound-speed profile taken from a deep CTD cast in this region of the experiment is used throughout.

A. Quasi-cw approach

The quasi-cw method used to predict reverberation levels is based on Tappert’s PEREV model (1993). In essence, this model can be defined in terms of the standard active, monostatic SONAR equation (Urlick, 1975), i.e.,

$$RL = SL - TL_S - TL_R + BR + 10 \log A, \quad (2)$$

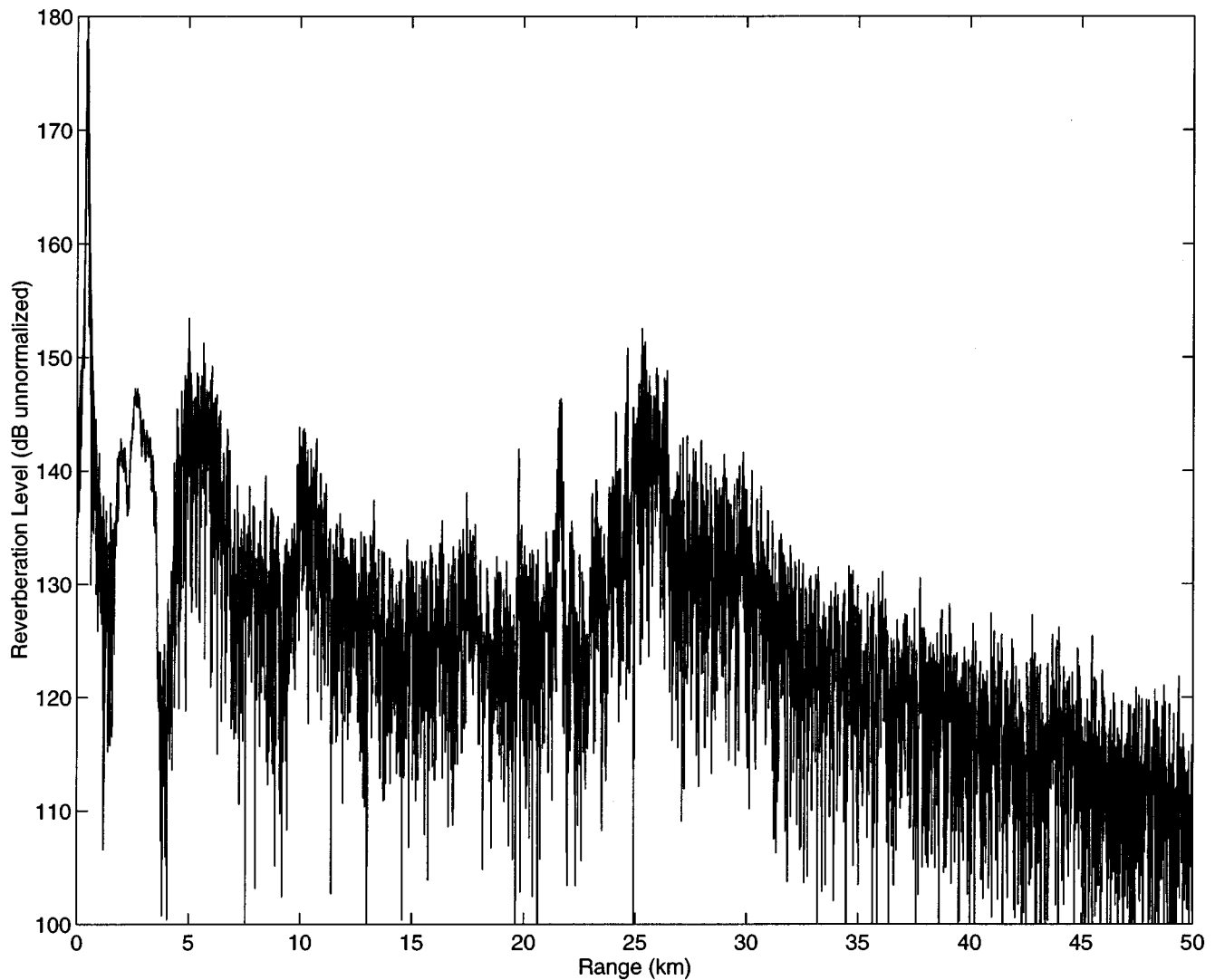


FIG. 2. Reverberation data from segment #414 extracted along beam #72, nearly due west and slightly northeast of the source position in Fig. 1.

where RL is the reverberation level, SL is the source level, BR is the back-reflection coefficient of the PEREV model, and A is the area of the patch ensonified by the convolution of the source pulse width and receiver beam width defined by

$$A = r \frac{c_0 \Delta t}{2} \Delta \phi_R, \quad (3)$$

where r , c_0 , Δt , and $\Delta \phi_R$ are the range to the patch, the reference sound speed, the source pulse width, and the receiver beam width, respectively. The $TL_{S,R}$ terms refer to the two-way transmission loss and contain all of the information on the propagation between the source/receiver position and the scattering patch on the bottom. As stated previously, we are primarily concerned here with the influence of propagation on the reverberation signal. Therefore, we fix the value of BR and assume a statistically homogeneous scattering region. The only other parameters varying in Eq. (2) are then the transmission loss and the ensonification area, the latter of which is only changing by $10 \log r$ along the radial.

The UMPE model computes solutions of the PE field function $\psi(r, z)$ which is defined in terms of the acoustic pressure by

$$p(r, z) = \frac{P_0 R_0}{\sqrt{r}} \psi(r, z) e^{ik_0 r}, \quad (4)$$

where P_0 is the source pressure measured at the reference distance $R_0 = 1$ m. The predicted reverberation signal is then, within a constant factor,

$$RL_{\text{pred}}(r) = \text{const} + 10 \log(|\psi_S(r, z_b(r))|^2) + 10 \log(|\psi_R(r, z_b(r))|^2) - 10 \log r, \quad (5)$$

where $z_b(r)$ is the depth of the bottom, and the influence of the two-way azimuthal spreading and the area of ensonification have been combined into the last term. Note that since this is a cw calculation, no time/range conversion is necessary. In addition, azimuthal coupling is neglected. The influence of azimuthal coupling in this region has been previously investigated (Smith, 1996b) and is not expected to alter the conclusions of this work.

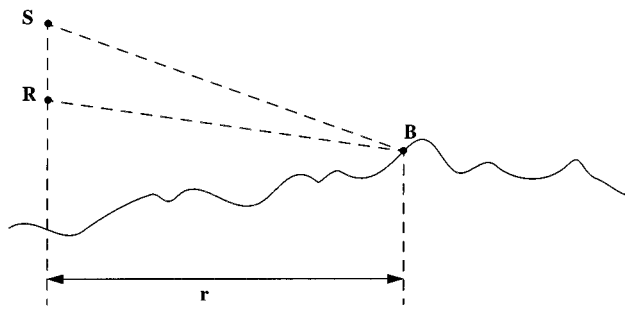


FIG. 3. Depiction of two-way return from a single scattering point. Two-way travel time is the convolution of one-way travel times along each path.

B. Computing exact two-way travel times

To compute one-way travel times with a cw PE model, one merely computes solutions for a spectrum of frequencies and Fourier synthesizes the results. For example, with a spectrum defined over the frequency band $f = f_C \pm \text{BW}/2$,

where f_C is the center frequency and BW is the bandwidth, the arrival time structure of the pressure field at any point $\mathbf{x} = (r, z)$ can be computed from

$$p(\mathbf{x}, t') = \frac{P_0 R_0}{\sqrt{r}} \psi(\mathbf{x}, t')$$

$$= \frac{P_0 R_0}{\sqrt{r}} e^{-i2\pi f_C t'} \int_{-\text{BW}/2}^{\text{BW}/2} \psi(\mathbf{x}, f' + f_C) \times e^{-i2\pi f' t'} df', \quad (6)$$

where $t' = t - r/c_0$ is the central reduced time at range r and $f' = f - f_C$ is the basebanded frequency.

To compute two-way travel times from seafloor reverberation, it is helpful to consider the arrival at a point on the bottom from both the source and receiver, separately, as depicted in Fig. 3. If the time-domain structure of the arrival at point B on the bottom due to a source at S is $\psi_{SB}(r, t')$ and

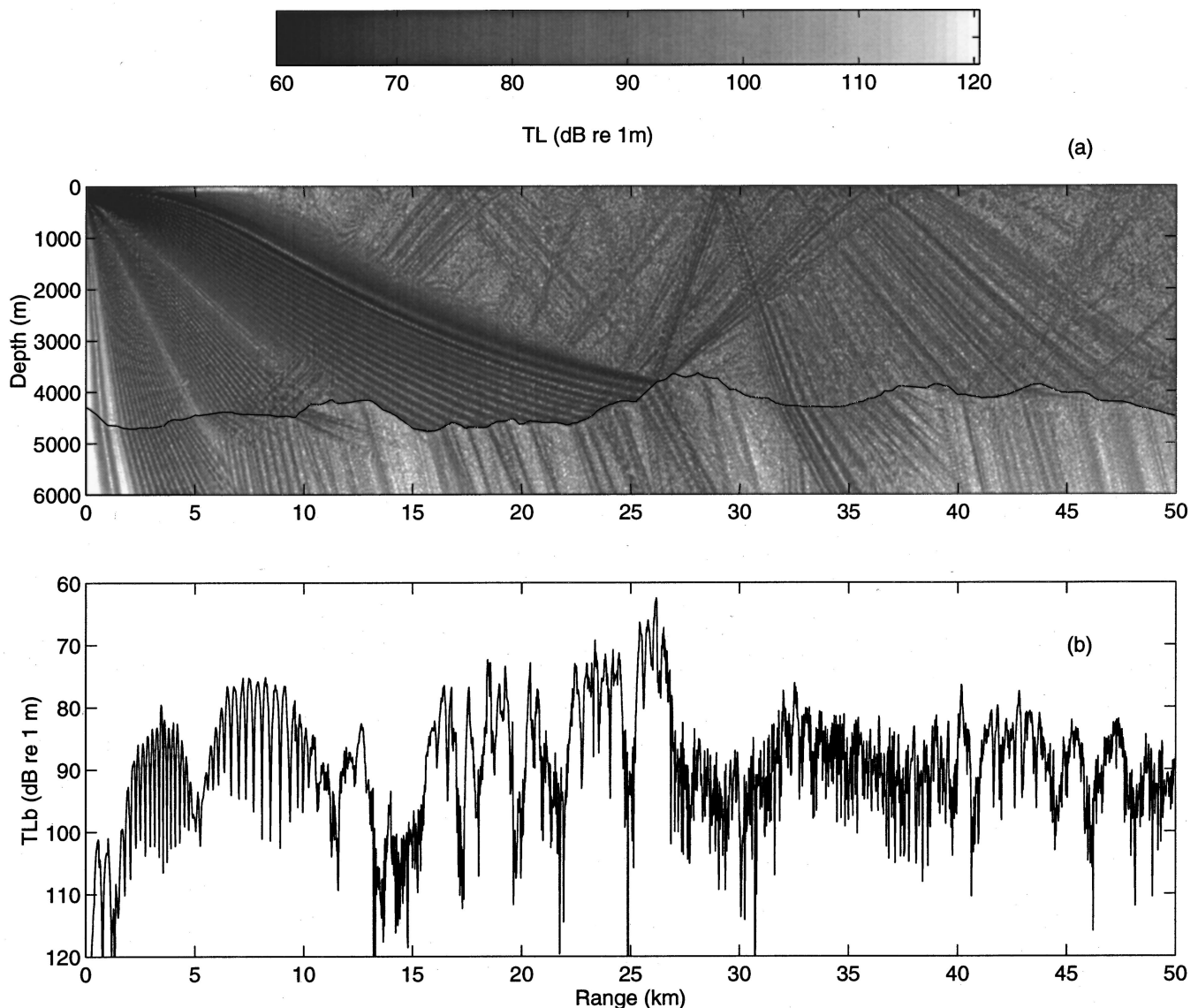


FIG. 4. Transmission loss prediction along the east-west track of beam #72: (a) the cw TL field for 227.5-Hz vertical array source and (b) the corresponding total TL extracted at the bottom interface depth.

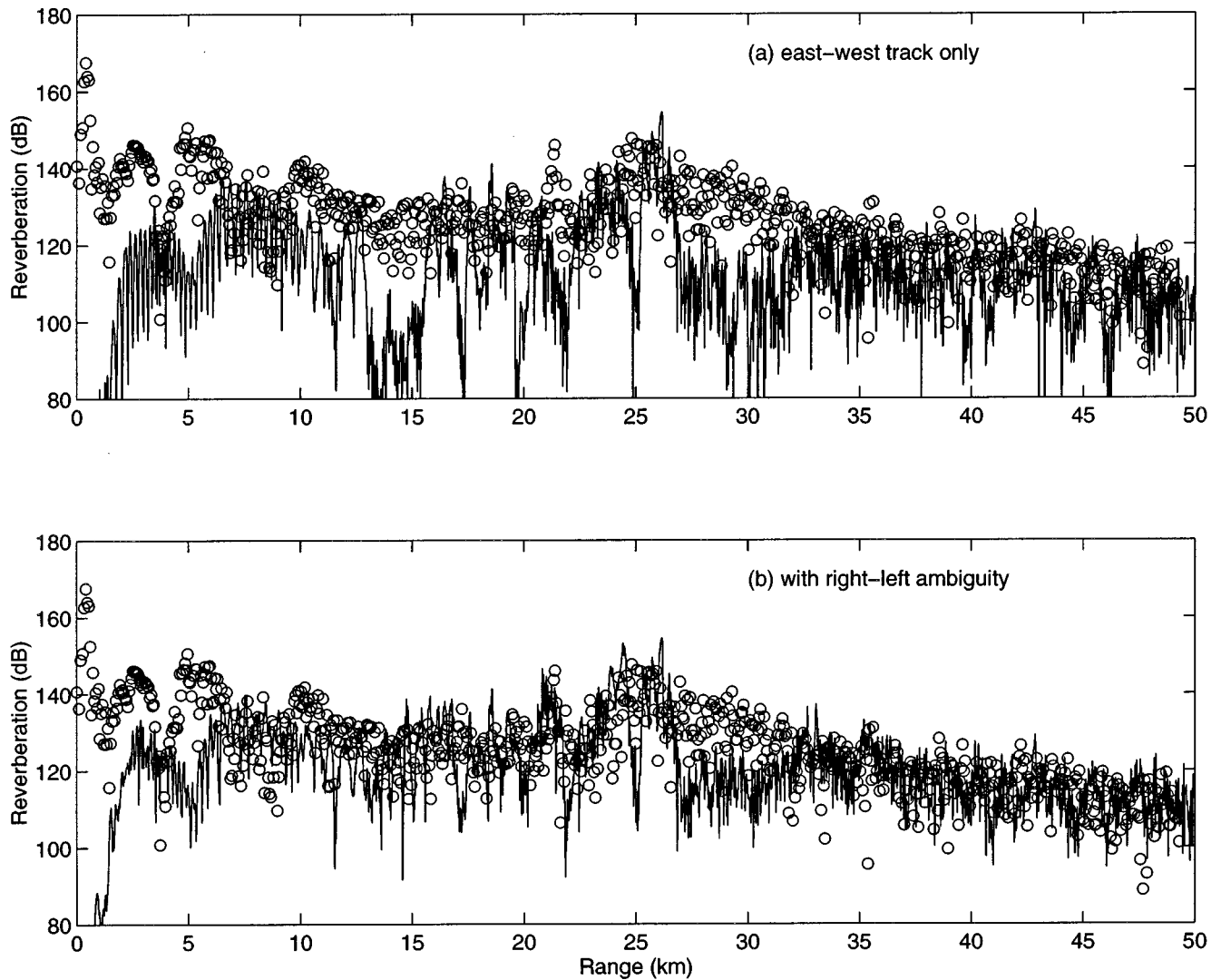


FIG. 5. A comparison of measured reverberation data (circles) and predicted reverberation (solid line) using the cw approach both (a) without and (b) with right-left ambiguity included.

the (reciprocal) time-domain structure of the arrival at point B due to a receiver at R is $\psi_{RB}(r, t')$, then the two-way time-domain arrival at the receiver location R due to a source transmission at S scattering from the bottom at point B (neglecting absolute scattering strength) is the convolution

$$\psi_{2\text{-way}}(r, T) = \int \psi_{SB}(r, t') \psi_{RB}(r, T - t') dt' \quad (7)$$

(where T is still a reduced time variable) or, in the frequency domain, the product

$$\psi_{2\text{-way}}(r, f) = \psi_{SB}(r, f) \psi_{RB}(r, f). \quad (8)$$

The complete two-way transmission loss travel time structure can then be computed by simply combining all the returns from each point along the bottom, i.e.,

$$\begin{aligned} \psi_{2\text{-way}}(T) = & \psi_{2\text{-way}}(r, T) + \psi_{2\text{-way}}\left(r + \Delta r, T + \frac{2\Delta r}{c_0}\right) \\ & + \psi_{2\text{-way}}\left(r + 2\Delta r, T + \frac{4\Delta r}{c_0}\right) + \cdots, \end{aligned} \quad (9)$$

where Δr and c_0 are the range step and reference sound speed, respectively, used in the PE calculation of the propagation. Note that the time window from one range step will overlap with another and this summation must be done coherently. Furthermore, the use of reduced time T is accommodated by adjusting it at each range step by $2\Delta r/c_0$.

As before, the predicted reverberation is defined as proportional to the two-way transmission loss and the influence of the receiver beam pattern. Writing this in terms of the corresponding two-way travel time pressure field,

$$\text{RL}_{\text{pred}}(T) = \text{const} + 10 \log(|p_{2\text{-way}}(T)|^2) + 10 \log r(T), \quad (10)$$

we see that in order to correctly account for the effect of the area term, we may write

$$\text{RL}_{\text{pred}}(T) = \text{const} + 10 \log(|p'_{2\text{-way}}(T)|^2). \quad (11)$$

From Eqs. (6) and (9), we have

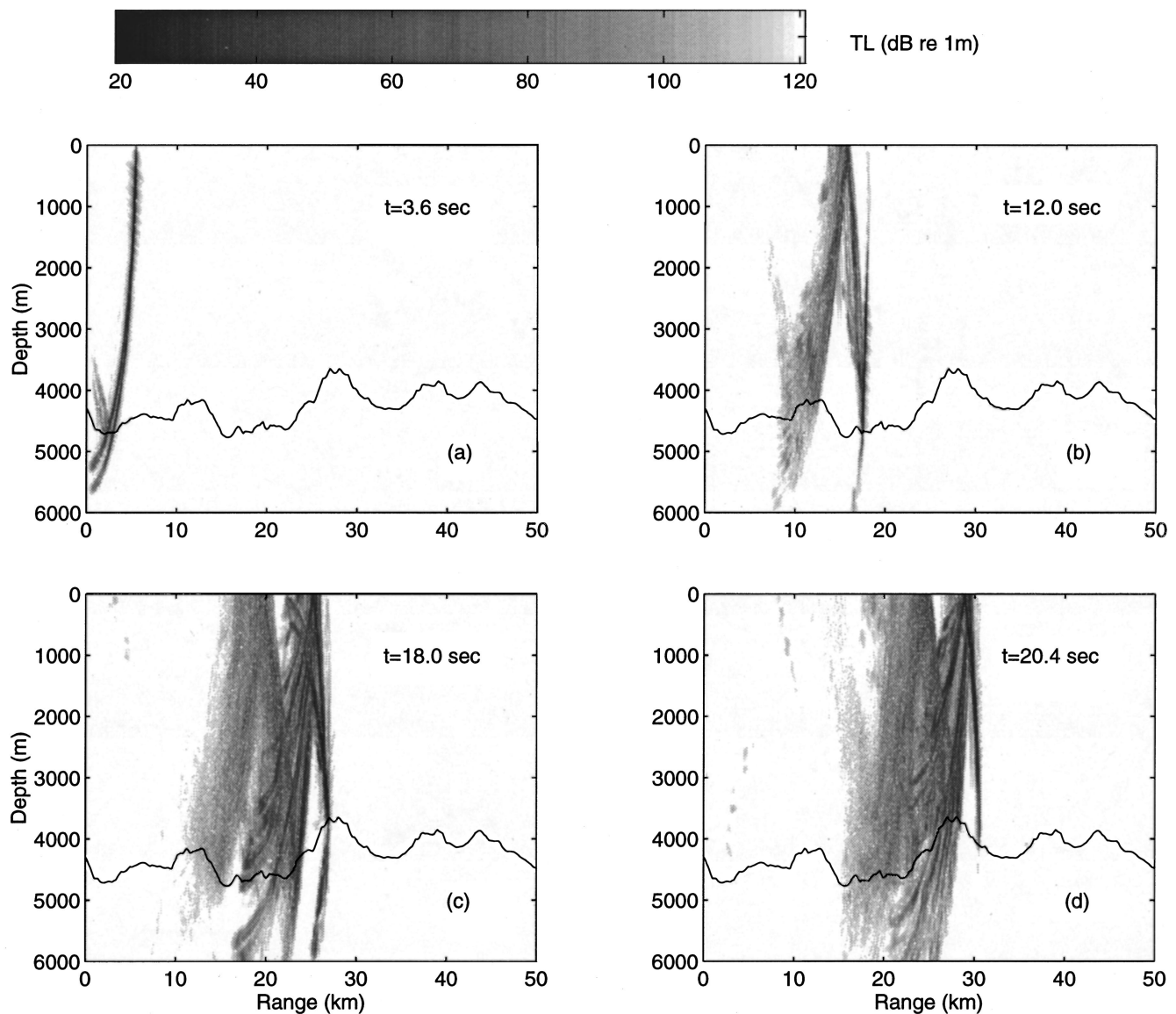


FIG. 6. Time domain animation of acoustic propagation along the east-west track of beam #72. (Taken from Smith *et al.*, 1996.)

$$p'_{2\text{-way}}(T) \propto \frac{\psi_{2\text{-way}}(r, T)}{r^{1/2}} + \frac{\psi_{2\text{-way}}(r + \Delta r, T + 2\Delta r/c_0)}{(r + \Delta r)^{1/2}} + \frac{\psi_{2\text{-way}}(r + 2\Delta r, T + 4\Delta r/c_0)}{(r + 2\Delta r)^{1/2}} + \dots, \quad (12)$$

where the constant of proportionality has been absorbed into the first term of Eq. (11). Once this reverberation time series is computed, times are converted to ranges using the simple, linear conversion defined previously.

III. INTERCOMPARISON OF MODELS AND DATA

In Fig. 4, the cw transmission loss field is plotted along the east-west track for the center frequency of the LFM chirp, 227.5 Hz. The transmission loss extracted at the depth of the bottom interface is also shown. The bottom composition used here is modeled as a homogeneous medium with sound speed $c_b = 1800$ m/s, density $\rho_b = 2$ g/cm³, and attenuation $\alpha_b = 0.025$ dB/m/kHz. The rationale behind this choice of parameters is given below. As expected, high levels of

enisonification (low TL) occur at ranges less than 1/2 convergence zone (CZ) where the bottom has a slope facing in the direction of the source. Increases in TL are observed on the backside of ridge structures where the slope faces away from the source in cw shadow zones. A clear example of this is in the vicinity of 29 km, just past the dominant ridge along this track, where TL increases rapidly from 70 to 100 dB *re*: 1 m.

After combining the results from both the source and receiver and rescaling this two-way TL data to the level of the extracted reverberation data [including the area term in Eq. (5)], the cw prediction can be compared to measurements as shown in Fig. 5. Figure 5(a) shows the comparison of the measured data with the cw prediction along only the east-west radial. Figure 5(b) shows the results when the right-left ambiguity is treated by combining cw results from the two appropriate radials. While there is definite improvement when we account for the right-left ambiguity, there still appear to be significant regions where the reverberation is underestimated, particularly in the cw shadow zone near 27–30 km. Note that the comparison is not expected to agree at

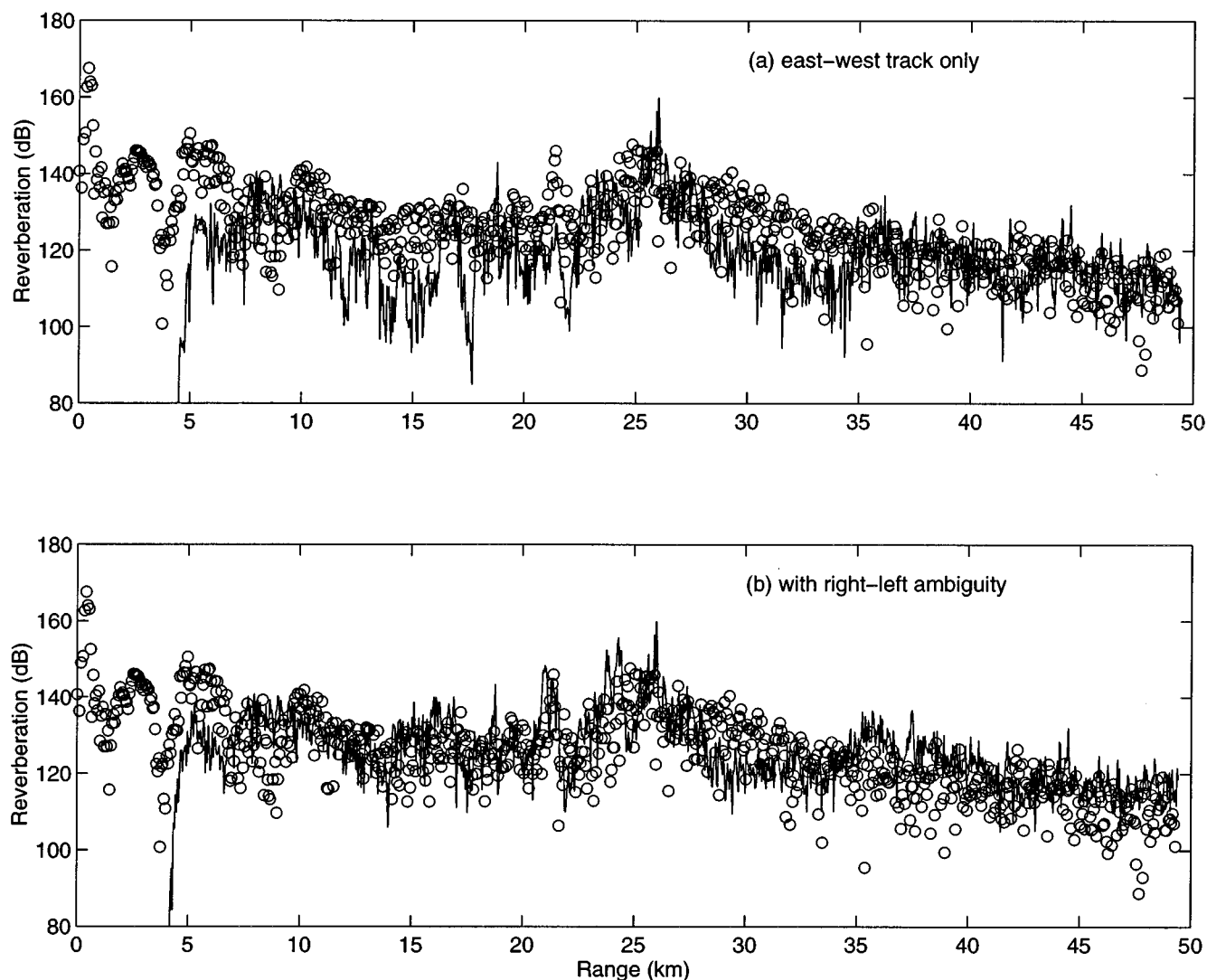


FIG. 7. A comparison of measured reverberation data (circles) and predicted reverberation (solid line) using the two-way travel time approach both (a) without and (b) with right-left ambiguity included.

ranges ≤ 10 km due to both the simple time/range conversion and the numerical tapering of the PE source beyond roughly $\pm 45^\circ$.

In Fig. 6 (taken from Smith *et al.*, 1996), time snapshots of the pulse propagation from the source are shown exhibiting the time-spreading nature of the multipath propagation. For these calculations, a $66\frac{2}{3}$ -Hz bandwidth pulse with a Hamming window centered at 227.5 Hz has been used. The temporal resolution of this pulse is nearly the same as the LFM chirp data. In Fig. 6(d), the influence of the secondary multipaths can be inferred as energy strikes the dominant ridge structure at a time when the primary, direct path energy is in a shadow zone. These interactions may then be expected to fill in some of the missing reverberation energy of the cw prediction. Further discussions on the effects of such multipaths and the calculations of these time snapshots can be found in Smith *et al.* (1996).

A comparison of the measured data and this two-way travel time prediction is displayed in Fig. 7 with and without the influence of the right-left ambiguity. Again, the addition of the right-left ambiguity does seem to produce an im-

provement in the comparison. Furthermore, we see that some of the cw shadow zone has been filled in with energy from the time-delayed secondary multipaths.

A direct comparison of the cw approach and two-way travel time method is shown in Figs. 8 and 9. There are several issues worth noting here. First, we see that the multipaths which fill in some of the cw shadow zone would have been mapped to incorrect ranges, i.e., to the backside of the ridge at ~ 27 – 28 km, nearly 2 km from their true interaction range, as seen in the expanded view of Fig. 9(a). The differences in predicted reverberation levels is also significant, as much as 30 dB. Other features are also observed to be mapped incorrectly by roughly 2 km, most notably a pair of returns which appear at roughly 32.5 and 33 km in the cw calculation but are mapped to roughly 35 and 35.5 km in the two-way travel time calculation. Furthermore, these returns appear more spread in time (and range) presumably due to the inherent multipath nature of the incident field beyond the ridge at $\sim 1/2$ CZ (refer to Fig. 4). However, despite these differences, we note that the majority of the remaining levels agree quite well, indicating that quasi-cw approaches can be

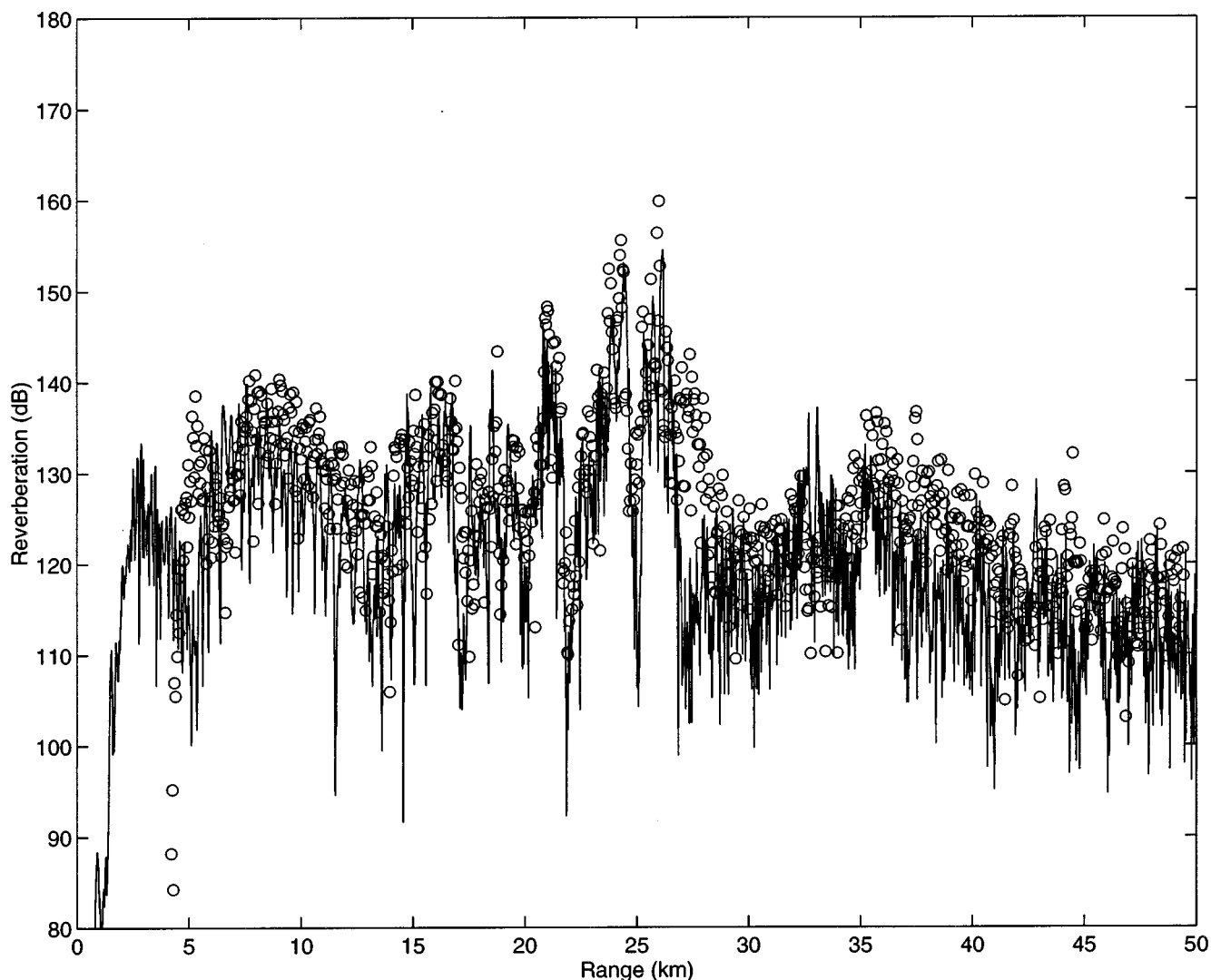


FIG. 8. Comparison of reverberation prediction techniques: cw approach (solid line) and two-way travel time technique (circles).

very accurate away from direct path shadow zones.

Finally, we consider the remaining differences between the measured data and the two-way travel time predictions as compared in Fig. 7(b). It is apparent that, even with multipath spreading, we have still not accounted for all of the observed reverberation energy. Several parameters were varied in the course of this study in an attempt to account for this missing energy such as bottom sound speed and sound-speed gradient, bottom density, bottom attenuation, and random small-scale interface roughness. The choice of parameters used here seemed to produce a better match than other choices (although the parameter search was not intended to be conclusive). It is interesting to note that the choice of sound speed and density are significantly larger than typical values observed in the upper portion of local bottom sediments, i.e., $c_{\text{sed}} \approx 1525$ m/s and $\rho_{\text{sed}} \approx 1.6$ g/cm³ (Bowles, 1994) while the attenuation used is more representative of (if not smaller than) the soft oozes covering much of the area with varying thickness. No attempt was made in this study to combine both bottom types in a realistic fashion. However, this would not change the general nature of the multipath propagation or the conclusions of this work.

IV. SUMMARY

We have shown how both a cw approach and two-way travel time technique to predict long-range reverberation structure compare with measured data. The goal of this work was to contrast the two methods and highlight limitations of the cw approach, specifically those due to multipath effects. The influence of these multipath structures must also be considered in any direct path reverberation model.

As anticipated, the weaker multipath energy does not contribute noticeably at ranges less than the range of the first bottom-limited path. In this region, reverberation is dominated by the primary direct paths. Beyond this range, multipath influences dominate and can produce returns which are more diffuse than may be expected from the associated scattering region due to the nature of the multipath spreading. The most significant influence, however, is in the cw shadow zones where the multipath influence fills in the associated time-domain regions and can account for differences in the predicted reverberation by as much as 30 dB.

Overall, these results do suggest that quasi-cw approaches can be very effective in the prediction of long-

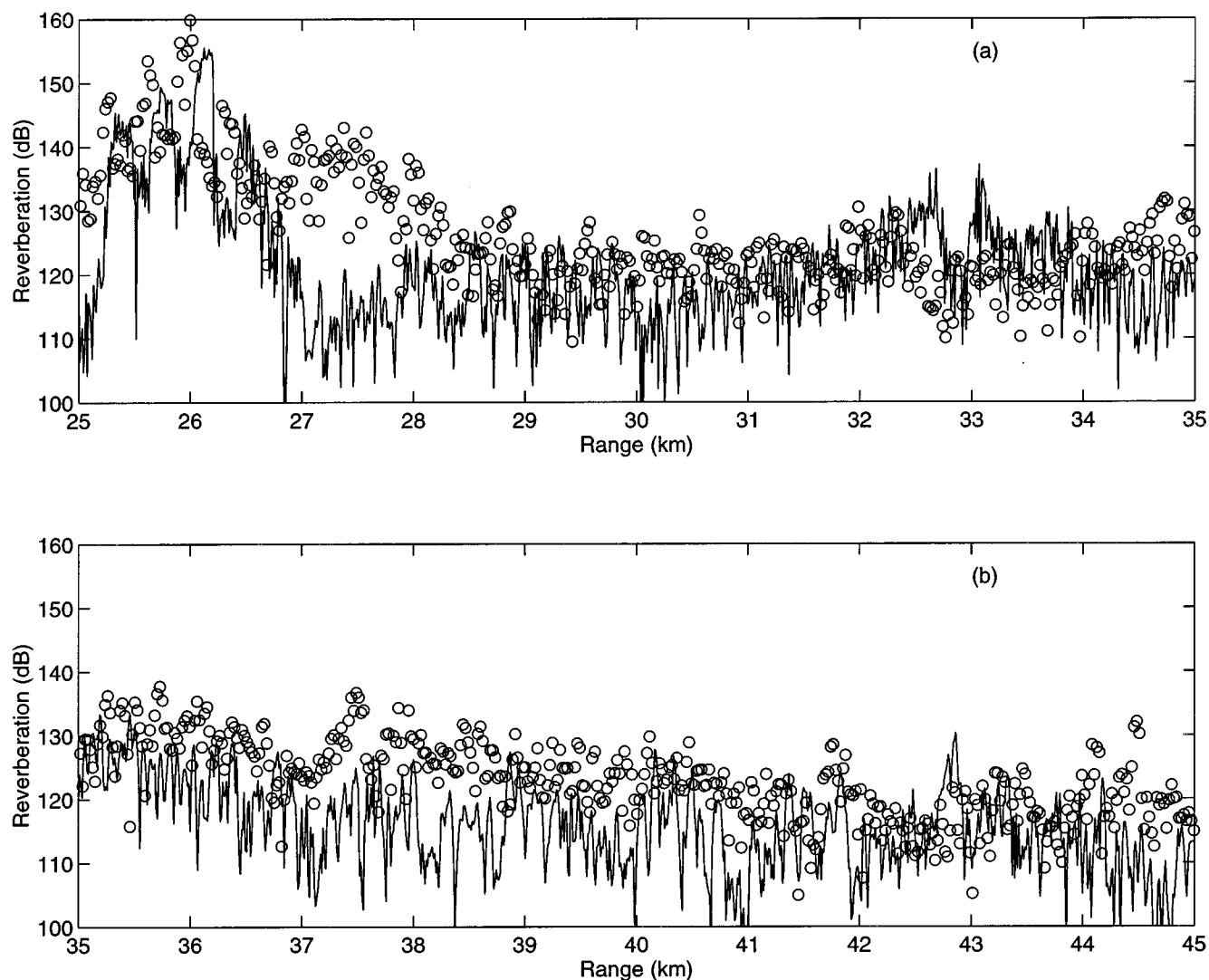


FIG. 9. Expanded view of model comparison in Fig. 8.

range reverberation. In practice, such an approach would generally involve smoothing both the data and the predicted signal, thereby reducing the significance of the diffuse nature of multipath returns. However, significant dropouts of 20–30 dB over several kilometers may not be accounted for by simply smoothing the data. The evaluation of reverberation returns in cw shadow zones should then be considered cautiously. Accurate predictions in these limited regions may require broadband analysis similar to that described here to account for multipath spreading.

ACKNOWLEDGMENTS

This work was supported by the Office of Naval Research, Code 321OA, under Grant No. N0001496WR30025. The authors wish to thank Dr. Fred Tappert for many useful discussions.

Bowles, F. A. (1994). "A Geoacoustic Model for Fine-Grained, Unconsolidated Calcareous Sediments (ARSRP Natural Laboratory)," Naval Research Laboratory, Stennis Space Center, NRL Report.

Makris, N. C., and Berkson, J. M. (1994). "Long-range backscatter from the Mid-Atlantic Ridge," *J. Acoust. Soc. Am.* **95**, 1865–1881.

Office of Naval Research (1993). ARSRP Initial Report, *Acoustics Experiment, R/V Cory Chouest*, 5–26 July 1993.

Smith, K. B. (1996a). "Bottom interactions of pulse propagation and corresponding real-time reverberation," *J. Acoust. Soc. Am.* **99**, 2552.

Smith, K. B. (1996b). "Modeling the effects of azimuthal coupling on acoustic propagation in the presence of 3-dimensional, rough ocean interfaces using the parabolic approximation," Special Issue of *Theoretical and Computational Acoustics*, edited by D. Lee, Y.-H. Pao, M. H. Shultz, and Y.-C. Teng (World Scientific, Singapore), pp. 115–131.

Smith, K. B., and Tappert, F. D. (1993). "UMPE: The University of Miami Parabolic Equation Model, Version 1.1," MPL Technical Memorandum 432.

Smith, K. B., Hodgkiss, W. S., and Tappert, F. D. (1996). "Propagation and analysis issues in the prediction of long-range reverberation," *J. Acoust. Soc. Am.* **99**, 1387–1404.

Tappert, F. D. (1993). "Physics of the PE Reverb Model," ONR-ARSRP Symposium, La Jolla, CA, 23–25 March 1993.

Tucholke, B. E., Kleinrock, M. C., and Stewart, W. K. (1993). "Geological and Geophysical Characteristics of the Acoustic Reverberation Corridor and their Relevance to the Conduct of the G&G Fine-Scale Surveys," ONR-ARSRP Symposium, La Jolla, CA, 23–25 March 1993.

Urick, R. J. (1975). *Principles of Underwater Sound* (McGraw-Hill, New York), p. 219.

The perfectly matched layer for acoustic waves in absorptive media

Qing-Huo Liu and Jianping Tao

Klipsch School of Electrical and Computer Engineering, New Mexico State University, Las Cruces, New Mexico 88003

(Received 24 March 1997; revised 8 July 1997; accepted 9 July 1997)

The perfectly matched layer (PML) was first introduced by Berenger as a material absorbing boundary condition (ABC) for electromagnetic waves. It was first proven by Chew and Liu that a fictitious elastic PML half-space also exists in solids, which completely absorbs elastic waves, in spite of the coupling between compressional and shear waves. The PML absorbing boundary condition provides much higher absorption than other previous ABCs in finite-difference methods. In this work, a method is presented to extend the perfectly matched layer to simulating acoustic wave propagation in absorptive media. This nonphysical material is used at the computational edge of a finite-difference time-domain (FDTD) algorithm as an ABC to truncate unbounded media. Two aspects of the acoustic PML are distinct: (a) For a perfectly matched layer in an intrinsically absorptive medium, an additional term involving the time-integrated pressure field has to be introduced to account for the coupling between the loss from the PML and the normal absorptive loss; (b) In contrast to the full elastodynamic problem, the acoustic PML requires a splitting only on the pressure field, but not on the particle velocity field. The FDTD algorithm is validated by analytical solutions and other numerical results for two- and three-dimensional problems. Unlike the previous ABCs, the PML ABC effectively absorbs outgoing waves at the computational edge even when a dipping interface intersects the outer boundary. © 1997 Acoustical Society of America. [S0001-4966(97)05710-X]

PACS numbers: 43.30.Es, 43.30.Ky, 43.20.Bi, 43.30.Ma [SAC-B]

INTRODUCTION

Absorbing boundary conditions (ABCs) are important in numerical simulations of acoustic wave propagation in unbounded inhomogeneous media with partial-differential equation methods. These artificial boundary conditions are used in finite-difference or finite-element methods to eliminate the reflections from the outer boundary of the computational domain. Considerable efforts have been made in the development of various ABCs. Cerjan *et al.*¹ and Levander² use lossy materials near the computational edge to attenuate outgoing waves. However, since there is always a reflection between layers with different absorption coefficients, this ABC requires a substantial number of layers with a tapered profile of absorption in order not to produce noticeable reflections to the computational domain. Various other absorbing boundary conditions have been proposed to extrapolate the wave field at the boundary from the interior fields. Examples of such ABCs are those of Clayton and Engquist,³ Lindman,⁴ Randall,⁵ Liao,⁶ Higdon,⁷ and Peng and Toksöz.⁸ These ABCs, although successful in many applications, provide only limited absorption to waves within a specific range of incidence angles and frequencies. Furthermore, none of these ABCs can be applied to problems where a dipping interface intersects the outer boundary.

Recently, Berenger introduced a highly effective ABC based on the perfectly matched layer (PML) for electromagnetics.⁹ In the continuous limit, it is proven that a PML interface between a regular medium and such a fictitious perfectly matched medium completely absorbs incident waves from the regular medium, regardless of its incidence

angle and frequency.^{9,10} This new fictitious material has since been used extensively in the finite-difference time-domain (FDTD) simulations of electromagnetic waves. Chew and Liu^{11–13} first proved that such a perfectly matched layer also exists for elastic waves in spite of the coupling of transverse (S) and longitudinal (P) waves at an elastic interface. This new ABC has been implemented for two- and three-dimensional problems.^{11–13} Hastings *et al.* have independently implemented the PML ABC for two-dimensional elastic problems using potentials.¹⁴ Because of the use of potentials, however, the PML ABC in Ref. 14 unfortunately limits the applicability of the ABC to a homogeneous boundary. In contrast, the PML ABC developed by Chew and Liu^{11–13} is applicable to a boundary truncating any inhomogeneous medium.

Most previous effort on PML applications, however, has been concentrated on lossless media.^{9–14} For many applications, attenuation of acoustic waves due to the intrinsic loss is an important factor to characterize. In this work, the PML ABC is extended to scalar acoustic waves in absorptive media. The formulation is based on that in Refs. 11–13 and is analogous to that for electromagnetic waves in conductive media.¹⁵ For acoustic waves in absorptive media, the implementation of PML has to be modified to account for the coupling of loss from a PML and that from the regular absorption loss. One interesting aspect about the PML for acoustic waves is that, unlike the PML for elastic waves, the velocity field components need not be split. The PML ABC is implemented for two- and three-dimensional problems, and the numerical results are validated by analytical solu-

tions as well as FDTD results using Liao's absorbing boundary condition.⁶

I. FORMULATION

Consider a linear inhomogeneous, absorptive medium with space-dependent density $\rho(\mathbf{r})$, sound speed $c(\mathbf{r})$, and absorption coefficient $\gamma(\mathbf{r})$. The pressure field $p(\mathbf{r}, t)$ and particle velocity $\mathbf{v}(\mathbf{r}, t)$ field satisfy the basic Newton's law of motion and equation of continuity

$$\rho \frac{\partial \mathbf{v}(\mathbf{r}, t)}{\partial t} = -\nabla p, \quad (1a)$$

$$\frac{\partial p}{\partial t} + \gamma(\mathbf{r})c^2(\mathbf{r})p(\mathbf{r}, t) = -\rho(\mathbf{r})c^2(\mathbf{r})\nabla \cdot \mathbf{v}(\mathbf{r}, t) + f_s(\mathbf{r}, t), \quad (1b)$$

where $f_s(\mathbf{r}, t)$ is the volume source density of pressure injection rate (Pa/s). In Eq. (1b), the absorption coefficient $\gamma(\mathbf{r})$ is used to characterize the absorptive loss in the medium. This absorption coefficient can be related to the attenuation coefficient $\alpha(\mathbf{r}, \omega)$ by using the complex wave number $k(\mathbf{r}, \omega) = \sqrt{\omega^2/c^2 + i\omega\gamma} = \omega/c'(\mathbf{r}, \omega) + i\alpha(\mathbf{r}, \omega)$, where $c'(\mathbf{r}, \omega)$ is the dispersive wave velocity.

Before proceeding, we briefly discuss the implication of the acoustic medium dispersion properties on the causality of the wave field. For absorptive media, in general both $c(\omega)$ and $\gamma(\omega)$ in Eq. (1b) are frequency dependent in order for the wave field to remain causal. Mathematically, the dispersion relations for $c(\omega)$ and $\gamma(\omega)$ have to satisfy the following Kramers-Kronig relations:¹⁶

$$\frac{1}{c^2(\omega)} - \frac{1}{c^2(\infty)} = \frac{1}{\pi} \text{P.V.} \int_{-\infty}^{\infty} \frac{\gamma(\omega')/\omega'}{\omega' - \omega} d\omega', \quad (2a)$$

$$\frac{\gamma(\omega)}{\omega} = -\frac{1}{\pi} \text{P.V.} \int_{-\infty}^{\infty} \frac{1/c^2(\omega') - 1/c^2(\infty)}{\omega' - \omega} d\omega', \quad (2b)$$

where $c(\infty)$ is the value of $c(\omega)$ as the frequency approaches infinity, and P.V. stands for principal value integral. It can be concluded from Eqs. (2a) and (2b) that for an absorptive medium (i.e., $\gamma \neq 0$), $c(\omega)$ and $\gamma(\omega)$ have to vary as functions of frequency over the infinite range ($-\infty < \omega < \infty$). This, however, does not exclude the possibility of frequency-independent c and γ over a *finite* range of frequency, say $\omega_{\min} \leq \omega \leq \omega_{\max}$. Indeed, one can find many experimental measurements of such cases (for example, Ref. 17). For simplicity, therefore, in this work the acoustic medium is assumed dispersionless so that c and γ are independent of frequency over the bandwidth of interest. The following algorithm, however, can be readily modified to model dispersive media.

In the traditional finite-difference simulation of acoustic waves, Eqs. (1a) and (1b) are combined to obtain the following second-order partial-differential equation for the pressure field:

$$\rho \nabla \cdot \rho^{-1} \nabla p - \frac{1}{c^2} \frac{\partial^2 p}{\partial t^2} - \gamma \frac{\partial p}{\partial t} = -\frac{1}{c^2} \frac{\partial f_s}{\partial t}. \quad (3)$$

In the explicit second-order finite-difference schemes, solving Eq. (3) is more efficient than directly solving Eqs. (1a) and (1b). This is because only pressure fields at the two earlier time steps are needed in Eq. (3) to update the pressure at the next time step, while Eqs. (1a) and (1b) require four scalar variables (three velocity components and one pressure field) to update the wave field. With Eq. (3), various absorbing boundary conditions¹⁻⁸ can be applied to truncate the unbounded medium in the finite-difference time-domain method.

A. Stretched coordinates for absorptive media

In this work, the perfectly matched layer (PML) will be used as an ABC. In order to introduce the PML for acoustic waves in absorptive media, the first-order equations in (1a) and (1b) will be modified using the stretched coordinates as proposed for electromagnetic waves and elastic waves.¹⁰⁻¹³ In the frequency domain, if the complex coordinate-stretching variable is chosen as

$$e_\eta = a_\eta + i \frac{\omega}{\omega_\eta} \quad (\eta = x, y, z), \quad (4)$$

the operator ∇_e expressed in terms of the complex coordinate-stretching variables is

$$\nabla_e = \sum_{\eta=x,y,z} \hat{\eta} \frac{1}{e_\eta} \frac{\partial}{\partial \eta}$$

Then by replacing ∇ with ∇_e , the first-order Eqs. (1a) and (1b) are modified in stretched coordinates as

$$-i\omega\rho\mathbf{v}(\mathbf{r}, \omega) = -\sum_{\eta=x,y,z} \hat{\eta} \frac{1}{e_\eta} \frac{\partial p(\mathbf{r}, \omega)}{\partial \eta}, \quad (5)$$

$$\begin{aligned} -i\omega p(\mathbf{r}, \omega) + \gamma(\mathbf{r})c^2(\mathbf{r})p(\mathbf{r}, \omega) \\ = -\rho(\mathbf{r})c^2(\mathbf{r}) \sum_{\eta=x,y,z} \frac{1}{e_\eta} \frac{\partial v_\eta(\mathbf{r}, \omega)}{\partial \eta} + f_s(\mathbf{r}, \omega), \end{aligned} \quad (6)$$

where a time dependence of $e^{-i\omega t}$ is implied. In Eq. (4), for a PML region, the real part a_η is a scaling factor, and the imaginary part ω_η represents a loss in the PML. In a regular non-PML region, one has $a_\eta = 1$ and $\omega_\eta = 0$.

The addition of the real part a_η in (4) as an independent variable is to accelerate the attenuation to evanescent waves as well as waves in lossy media. This can be easily understood by considering plane waves e^{ikx} propagating in x direction with a complex wave number $k = k' + ik''$. Using $x = x'(a_x + i\omega_x/\omega)$, we have in the stretched coordinates,

$$e^{ikx} = e^{i(a_x k' - (\omega_x/\omega)k'')x'} e^{-(a_x k'' + (\omega_x/\omega)k')x'}, \quad (7)$$

which implies that the extra variable a_x provides an additional freedom to attenuate waves in lossy media further. The proof of zero reflections for a PML interface follows that in Refs. 11-13.

B. Splitting of equations in time domain

For time-domain simulations, the frequency-domain Eqs. (5) and (6) are inverse Fourier transformed into the time domain. By splitting the pressure field p and the source f_s into

$$p = \sum_{\eta=x,y,z} p^{(\eta)}, \quad f_s = \sum_{\eta=x,y,z} f_s^{(\eta)}, \quad (8)$$

and using (4), Eqs. (5) and (6) can be rewritten as

$$(-i\omega a_\eta + \omega_\eta)\rho v_\eta = -\frac{\partial p}{\partial \eta}, \quad (9)$$

$$\left[-i\omega a_\eta + (a_\eta \gamma c^2 + \omega_\eta) + \frac{i\omega_\eta \gamma c^2}{\omega} \right] p^{(\eta)} = -\rho c^2 \frac{\partial v_\eta}{\partial \eta} + \left(a_\eta + \frac{i\omega_\eta}{\omega} \right) f_s^{(\eta)}. \quad (10)$$

Inverse Fourier transforming the above two equations yields the time-domain equations

$$a_\eta \rho \frac{\partial v_\eta}{\partial t} + \omega_\eta \rho v_\eta = -\frac{\partial p}{\partial \eta}, \quad (11)$$

$$a_\eta \frac{\partial p^{(\eta)}}{\partial t} + (a_\eta \gamma c^2 + \omega_\eta) p^{(\eta)} + \omega_\eta \gamma c^2 \int_{-\infty}^t p^{(\eta)}(\mathbf{r}, t') dt' = -\rho c^2 \frac{\partial v_\eta}{\partial \eta} + a_\eta f_s^{(\eta)}(\mathbf{r}, t) + \omega_\eta \int_{-\infty}^t f_s^{(\eta)}(\mathbf{r}, t') dt'. \quad (12)$$

From the above derivation, it is worthwhile to note the following important difference between an acoustic PML and an elastic PML: In the acoustic PML, there is no need to split the particle velocity \mathbf{v} into $\mathbf{v}^{(\eta)}$ as in the elastic PML. This is simply because the second-rank stress tensor in the elastic case collapses into a zero-rank tensor (i.e., a scalar pressure field) in the acoustic case. Equations (11) and (12) consist of a total of six scalar equations. In addition, the third term in (12) requires three additional variables for each cell. Therefore, the memory requirement in the PML region is 4.5 times that required by a regular acoustic medium with the same dimension. This extra memory requirement in the boundary PML region is offset by the effectiveness of PML in absorbing the outgoing waves. Note also that with the introduction of PML, there is an additional term involving the time-integrated pressure field in Eq. (12). This term represents the coupling of the loss in PML with the regular absorption loss. The split equations (11) and (12) can then be solved by the following FDTD method.

II. FINITE-DIFFERENCE IMPLEMENTATION

In view of the computer memory requirement in the PML region, the computational domain may be partitioned into a regular interior region and the boundary PML region, as shown in Fig. 1, to save memory. In the interior region, only the pressure field is used in a centered grid to discretize the second-order equation (3). In the boundary region consisting of several PMLs, both the pressure and the particle velocity fields are used in a staggered grid, as shown in Fig.

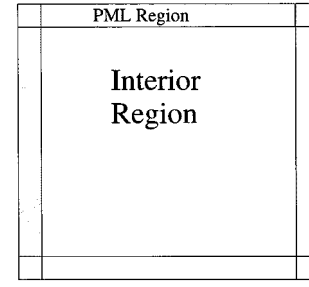


FIG. 1. Computational domain with an interior region and a PML boundary region. The second-order partial differential equation for p may be used for the interior region, while the first-order split equations are used for the PML region.

2 for a unit cell, to discretize the first-order equations (11) and (12). Alternatively, on a parallel computer, in terms of data structure it may be more advantageous to use the first-order equations (11) and (12) throughout the whole computational domain, and simply let $a_\eta = 1$, $\omega_\eta = 0$ for the interior region.

The staggered grid in Fig. 2 is a reduced one from the full elastic staggered grid.¹⁸ In this staggered grid, the pressure field p is located at the cell center, while the velocity field components are located at the cell's face centers. The unbounded medium is truncated into a finite computational domain with a total of $N_x \times N_y \times N_z$ cells. If the finite-difference cell size is Δx , Δy , and Δz in x , y , and z directions, respectively, the pressure field and velocity field components are discretized as

$$p^{(\eta)}(j_x, j_y, j_z, n) \equiv p^{(\eta)}[(j_x + \frac{1}{2})\Delta x, (j_y + \frac{1}{2})\Delta y, (j_z + \frac{1}{2})\Delta z, n\Delta t], \quad (13a)$$

$$v_x(j'_x, j_y, j_z, n) \equiv v_x[j'_x \Delta x, (j_y + \frac{1}{2})\Delta y, (j_z + \frac{1}{2})\Delta z, (n + \frac{1}{2})\Delta t], \quad (13b)$$

$$v_y(j_x, j'_y, j_z, n) \equiv v_y[(j_x + \frac{1}{2})\Delta x, j'_y \Delta y, (j_z + \frac{1}{2})\Delta z, (n + \frac{1}{2})\Delta t], \quad (13c)$$

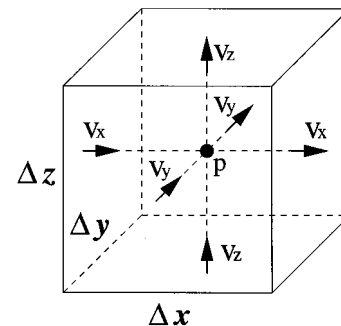


FIG. 2. The relative locations of field components in a unit cell of the staggered grid for the PML region.

$$v_z(j_x, j_y, j'_z, n) \equiv v_z[(j_x + \frac{1}{2})\Delta x, (j_y + \frac{1}{2})\Delta y, j'_z\Delta z, (n + \frac{1}{2})\Delta t], \quad (13d)$$

where n is an integer, $j_\eta = 0, \dots, N_\eta - 1$, and $j'_\eta = 0, \dots, N_\eta$. The central differencing is used for both the spatial and temporal derivatives. Furthermore, the second and third terms on the left-hand side of Eq. (12) require the averaging of their values at $t = n\Delta t$ and $t = (n+1)\Delta t$, since p is not evaluated at $t = (n+1/2)\Delta t$. This averaging has the same second-order accuracy as the central differencing used for the first term on the left-hand side of (12), and therefore does not degrade the overall accuracy in the discretization.

With this discretization, Eq. (11) becomes a time-stepping equation. For example, the time-stepping equation for v_x is

$$v_x(j'_x, j_y, j_z, n) = f_{1x}v_x(j'_x, j_y, j_z, n-1) + f_{2x}[p(j'_x, j_y, j_z, n) - p(j'_x - 1, j_y, j_z, n)], \quad (14)$$

where

$$f_{1\eta} = \frac{a_\eta/\Delta t - \omega_\eta/2}{a_\eta/\Delta t + \omega_\eta/2}, \quad f_{2\eta} = -\frac{1}{(a_\eta/\Delta t + \omega_\eta/2)\rho\Delta\eta}. \quad (15)$$

For the pressure field $p^{(x)}$, Eq. (12) becomes

$$p^{(x)}(j_x, j_y, j_z, n+1) = f_{3x}p^{(x)}(j_x, j_y, j_z, n) + f_{4x}p_I^{(x)}(j_x, j_y, j_z, n) + f_{5x}[v_x(j_x+1, j_y, j_z, n) - v_x(j_x, j_y, j_z, n)] + f_{6x}f_s(j_x, j_y, j_z, n + \frac{1}{2}), \quad (16)$$

where

$$f_{3\eta} = \frac{a_\eta/\Delta t - (a_\eta\gamma c^2 + \omega_\eta)/2}{D_{\eta v}}, \quad f_{4\eta} = -\frac{\omega_\eta\gamma c^2\Delta t}{D_{\eta v}}, \quad (17)$$

$$f_{5\eta} = -\frac{\rho c^2}{D_{\eta v}}, \quad f_{6\eta} = \frac{1}{D_{\eta v}}, \quad (18)$$

$$p_I^{(\eta)}(j_x, j_y, j_z, n) = \frac{1}{2}p^{(\eta)}(j_x, j_y, j_z, 0) + \sum_{l=1}^n p^{(\eta)}(j_x, j_y, j_z, l), \quad (19)$$

and $D_{\eta v} = a_\eta/\Delta t + (a_\eta\gamma c^2 + \omega_\eta)/2 + \omega_\eta\gamma c^2\Delta t/2$. Similar expressions can be derived for the other field components. In Eq. (16), the source f_s is assumed to be located at a regular non-PML region. Otherwise, a time-integrated source term should be added as in the last term on the right-hand side of Eq. (12). It should be noted that the material parameters in Eqs. (15), (17), and (18) must be properly averaged in order to arrive at a higher accuracy.¹⁸

Equations (14) and (16) constitute a leapfrog system for v_η and $p^{(\eta)}$ ($\eta = x, y, z$). Given a particular source excitation $f_s(\mathbf{r}, t)$, this time-stepping system provides the wave field solutions for the entire grid. The absorption of outgoing

waves is achieved by the PML region, which consists of several (typically 10) cells of PML materials with a quadratically or linearly tapered profile to increase the attenuation toward the outer boundary. For example, near the boundary $x=0$, ω_x for the $M=10$ cells of the PML region is chosen as

$$\omega_x(j_x) = \frac{(M-1/2-j_x)^p}{(M-1/2)^p} \omega_{x,\max} \quad (j_x = 0, \dots, M-1), \quad (20)$$

where $\omega_{x,\max}$ is the value at the center of the first cell. At the outer boundary, the normal component of the velocity is forced to zero. This rigid boundary condition does not give rise to reflections into the interior region because of the PML region. It is found that the quadratic profile ($p=2$) gives a better absorption than the linear profile ($p=1$).

III. NUMERICAL RESULTS

We have implemented the FDTD algorithm with the perfectly matched layers as the absorbing boundary condition for two and three dimensions. Unlike the continuous case, some reflection will occur at the discretized PML interface. This reflection is proportional to the contrast in the coordinate-stretching variables. Therefore, to minimize the reflection from the PML layers, we choose a linear profile for the PML coordinate-stretching variables. Typically we use 10 cells of perfectly matched layers at the computational edge.

In the following examples, a monopole source is used to excite the acoustic wave field. The time function $f_s(t)$ of the source is the first derivative of the Blackman-Harris window function.^{15,18} The central frequency of this time function is chosen as $f_c = 2$ kHz.

A. A 2-D homogeneous absorptive medium

The first simple testing case for the FDTD algorithm is a homogeneous medium with $\rho = 1200$ kg/m³, $c = 1500$ m/s, $\gamma = 2 \times 10^{-3}$ s/m² in two dimensions. The monopole line source is located at $(x, y) = (1.1, 1.1)$ m, and the pressure field p is calculated at 18 locations $x_i = 1.0 + (i-1) \times 0.05$, $y_i = 1.15$ m ($i = 1, \dots, 18$). The 2-D FDTD program is used to model a problem with $N_x \times N_y = 88 \times 88$ cells with 12 perfectly matched layers on each side of the computational domain. The cell size is $\Delta x = \Delta y = 0.025$ m. To verify the numerical results, an analytical solution is obtained by inverse Fourier transforming the following frequency-domain solution

$$p(\mathbf{r}, \omega) = \frac{\omega}{4c^2} H_0^{(1)}(kr) F_s(\omega), \quad (21)$$

where $F_s(\omega)$ is the Fourier transform of $f_s(t)$ and $k = \sqrt{\omega^2/c^2 + i\omega\gamma}$.

The 2-D FDTD results are compared with the analytical solutions in Fig. 3(a) for the array. Note that the results are normalized with respect to the peak value of the field at the third receiver (nearest receiver to the source). Figure 3(b) shows more clearly the comparison with analytical solution

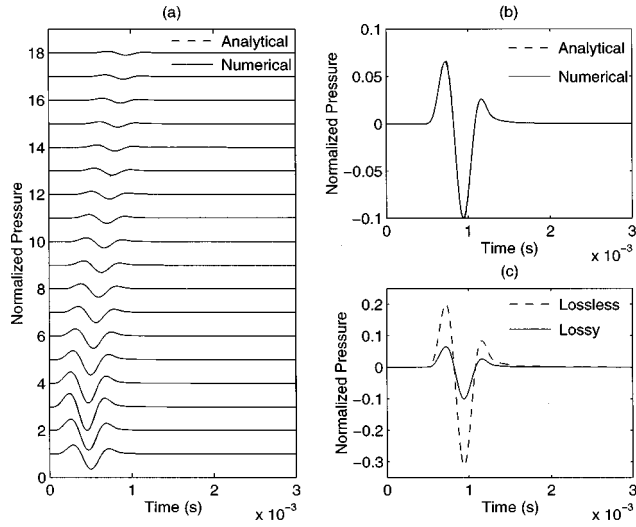


FIG. 3. FDTD results and analytical solutions for a monopole line source in a 2-D homogeneous medium. (a) Pressure waveforms at 18 receiver locations for a lossy medium ($\gamma = 2 \times 10^{-3}$ s/m²). (b) The results of (a) at the 18th receiver. (c) FDTD results for the lossy ($\gamma = 2 \times 10^{-3}$ s/m²) and lossless media at the 18th receiver location.

for the 18th receiver. Excellent agreement is observed between the numerical and analytical results. In Fig. 3(c), the pressure field at the 18th receiver is compared with that for the case where the absorption loss is zero (also obtained by the FDTD program). It shows that the absorption introduces an attenuation of about 9.84 dB to the peak value of the wave field at this location.

From the above results, it is seen that the PML ABC provides an effective attenuation to the outgoing waves since no reflections are observable from the wave forms in Fig. 3. In order to characterize the performance of the PML ABC quantitatively, snapshots are shown in Fig. 4 for the case without absorption loss in the interior medium. With a time step of $\Delta t = 5 \mu\text{s}$, the direct wave from the source has already reached outside the computational domain after the time step $n = 300$ shown in Fig. 4(e). Since the relative maximum amplitudes of Fig. 4(a)–(i) with respect to (b) is -4.56 , 0 , -8.06 , -10.13 , -25.58 , -43.97 , -52.95 , -55.59 , and -63.40 dB, respectively, the amplitude of the reflected wave is estimated to be in the order of -50 dB with respect to Fig. 4(b). The maximum field amplitude (normalized with respect to $n = 120$) as a function of the time steps is shown in Fig. 5(a). The horizontal slice of the pressure field (absolute value) through the source location is shown for these time steps in Fig. 5(b)–(d). As noted from these slices, the symmetry of the wave field is exactly preserved in the finite-difference program.

B. An absorptive cylinder in an absorptive background medium

This tests the two-dimensional program with an absorptive circular cylinder in an absorptive background medium. The monopole line source is located at the center of the cylinder at $(x, y) = (1.1, 1.1)$ m as for Fig. 3. The receiver locations are also the same. The cylinder (radius $a = 0.4$ m) with $\rho_1 = 1200$ kg/m³, $c_1 = 1500$ m/s, $\gamma_1 = 2 \times 10^{-3}$ s/m² is

surrounded by a background medium with $\rho_2 = 1000$ kg/m³, $c_2 = 1000$ m/s, $\gamma_2 = 0.05$ s/m². The discretization is the same as for the last case. The analytical solution for the pressure field is given by

$$p(\mathbf{r}, \omega) = \begin{cases} \frac{\omega}{4c_1^2} [H_0^{(1)}(k_1 r) + R J_0(k_1 r)] F_s(\omega), & r \leq a \\ \frac{\omega}{4c_1^2} T H_0^{(1)}(k_2 r) F_s(\omega), & r \geq a, \end{cases} \quad (22)$$

where (ρ_1, c_1, γ_1) and (ρ_2, c_2, γ_2) are, respectively, the medium parameters inside and outside the cylinder, and $k_j = \sqrt{\omega^2/c_j^2 + i\omega\gamma_j}$ for $j = 1, 2$. The reflection and transmission coefficients are given by

$$R = -\frac{k_2 \rho_1 H_0^{(1)}(k_1 a) H_0^{(1)'}(k_2 a) - k_1 \rho_2 H_0^{(1)'}(k_1 a) H_0^{(1)}(k_2 a)}{D_c(\omega)}, \quad (23)$$

$$T = -\frac{2i\rho_2/\pi a}{D_c(\omega)}, \quad (24)$$

where

$$D_c(\omega) = k_2 \rho_1 J_0(k_1 a) H_0^{(1)'}(k_2 a) - k_1 \rho_2 J_0'(k_1 a) H_0^{(1)}(k_2 a) \quad (25)$$

is the denominator of (23) and (24).

With the configuration of the measurement system, the 1st through 11th receivers measure the incident and reflected waves since they are located within the cylinder, while the 12th through 18th receivers measure the transmitted wave since they are outside the cylinder. The numerical results are compared with analytical solutions for the first 11 receivers in Fig. 6(a), and for the last 7 receivers in Fig. 6(b). Note that the field is normalized with respect to the field at the third receiver, the nearest one from the source. In order to show the transmitted wave clearly, Fig. 6(b) is magnified by a factor of 20. Excellent agreement is observed for fields both inside and outside the cylinder.

In order to see the effect of the absorption loss to the wave field, the above medium is also modeled without loss (i.e., $\gamma_1 = \gamma_2 = 0$). The numerical and analytical results for the lossless medium are shown in Fig. 7(a) and (b) for the field inside and outside the cylinder. The field is again normalized with respect to the field at the third receiver (the normalization factor is about 1.106 times that in Fig. 6). Note that a much larger transmitted field is observed since Fig. 7(b) is now only magnified by a factor of 3.

C. A 3-D homogeneous absorptive medium

Similarly, the 3-D FDTD program was validated first for a monopole point source in a three-dimensional homogeneous medium. The example under investigation is exactly the same as for Fig. 3 except that this is for a monopole point source at $(x, y, z) = (1.1, 1.1, 1.1)$ m, and the pressure field p is calculated at 18 locations $x_i = 1.0 + (i-1) \times 0.05, y_i$

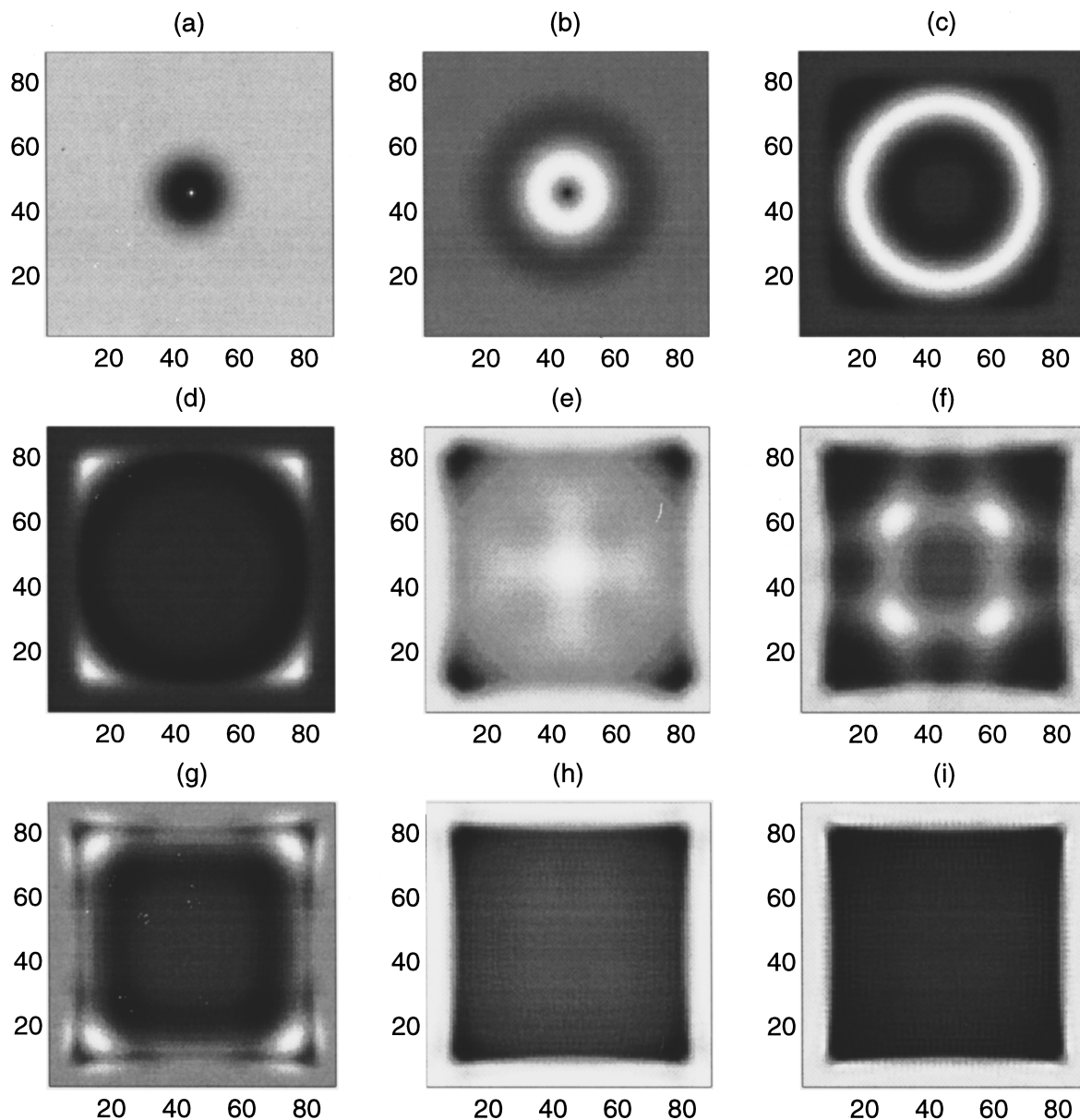


FIG. 4. From (a) to (i), the FDTD snapshots for the lossless medium in Fig. 3(c) at time steps $n=60, 120, 180, 240, 300, 360, 420, 480$, and 540 . The time-step increment is $\Delta t=5 \mu\text{s}$. The relative maximum amplitudes of (a) to (i) with respect to (b) is $-4.56, 0, -8.06, -10.13, -25.58, -43.97, -52.95, -55.59$, and -63.40 dB, respectively.

$= 1.15$, $z_i = 1.1$ m ($i=1, \dots, 18$). The 3-D FDTD program is used to model a problem with $N_x \times N_y \times N_z = 88 \times 88 \times 88$ cells with 12 perfectly matched layers on each side of the computational domain. The discretization is $\Delta x = \Delta y = \Delta z = 0.025$ m and $\Delta t = 5 \mu\text{s}$. The analytical solution in the frequency domain is

$$p(\mathbf{r}, \omega) = -\frac{i\omega}{4\pi c^2 r} e^{ikr} F_s(\omega). \quad (26)$$

The comparison between the 3-D FDTD results and analytical solutions is shown in Fig. 8 for the last 11 receivers. As for the 2-D FDTD results, the 3-D numerical results agree well with the analytical solutions. As expected, in contrast to the 2-D case in Fig. 3, the waveforms in Fig. 8 have exactly the same symmetric shape as the derivative of the source time function $f'_s(t)$. In the 2-D case, the waveforms become

skewed because of the insonification of the infinitely long line source.

D. An absorptive sphere in an absorptive background medium

Another special case where analytical solutions are available is a monopole point source in an absorptive sphere. The monopole source is located at the center of the sphere (radius $a = 0.4$ m) with $\rho_1 = 1200$ kg/m³, $c_1 = 1500$ m/s, $\gamma_1 = 2 \times 10^{-3}$ s/m² surrounded by a background medium with $\rho_2 = 1000$ kg/m³, $c_2 = 1000$ m/s, $\gamma_2 = 0.05$ s/m². The locations of the source and receivers, as well as the discretization, are the same as for Fig. 8. The analytical solution for the pressure field is given by

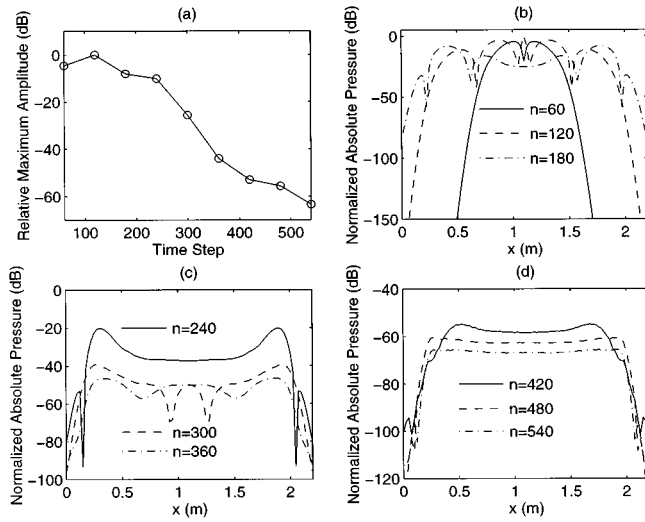


FIG. 5. (a) Corresponding to Fig. 4, the maximum field amplitude as a function of time steps. Horizontal slice of the field (absolute value) through the source location for (b) $n=60, 120, 180$; (c) $n=240, 300, 360$; (d) $n=420, 480, 540$. The field is normalized with respect to the maximum of the field at $n=120$.

$$p(\mathbf{r}, \omega) = \begin{cases} \frac{\omega k_1}{4\pi c_1^2} [h_0^{(1)}(k_1 r) + R j_0(k_1 r)] F_s(\omega), & r \leq a, \\ \frac{\omega k_2}{4\pi c_1^2} T h_0^{(1)}(k_2 r) F_s(\omega), & r \geq a, \end{cases} \quad (27)$$

where (ρ_1, c_1, γ_1) and (ρ_2, c_2, γ_2) are, respectively, the medium parameters inside and outside the sphere, and $k_j = \sqrt{\omega^2/c_j^2 + i\omega\gamma_j}$ for $j=1, 2$. The reflection and transmission coefficients are given by

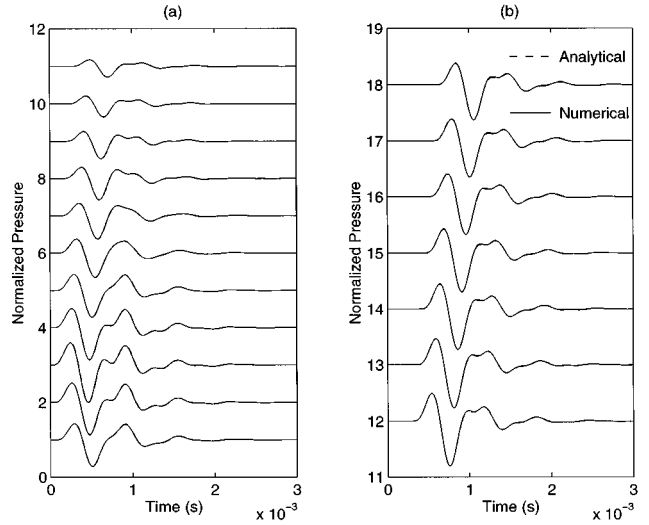


FIG. 7. Same as Fig. 6 except for a lossless cylinder in a lossless background medium (i.e., $\gamma_1 = \gamma_2 = 0$). The results for (b) are magnified by a factor of 3.

$$R = - \frac{k_2 \rho_1 h_0^{(1)}(k_1 a) h_0^{(1)'}(k_2 a) - k_1 \rho_2 h_0^{(1)'}(k_1 a) h_0^{(1)}(k_2 a)}{D_s(\omega)} \quad (28)$$

$$T = \frac{i \rho_2 / k_2 a^2}{D_s(\omega)}, \quad (29)$$

where

$$D_s(\omega) = k_2 \rho_1 j_0(k_1 a) h_0^{(1)'}(k_2 a) - k_1 \rho_2 j_0'(k_1 a) h_0^{(1)}(k_2 a). \quad (30)$$

Figure 9(a) shows the excellent agreement between the numerical and analytical results both inside and outside the

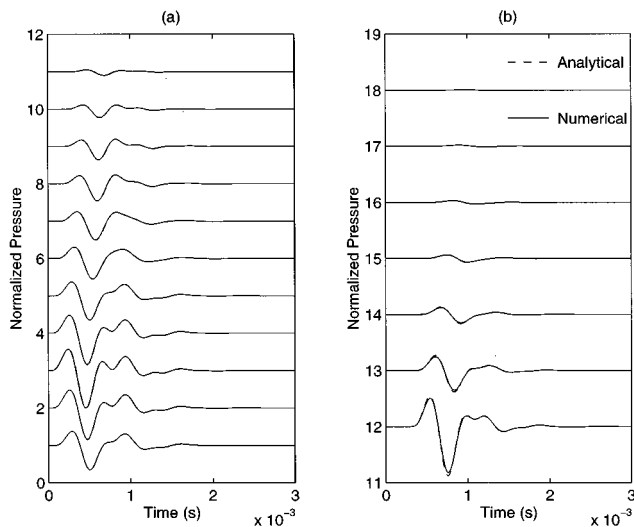


FIG. 6. A monopole line source at the center of an absorptive circular cylinder (radius 0.4 m) in an absorptive medium. The normalized pressure field (with respect to the third receiver) (a) inside the cylinder for the first through 11th receivers, and (b) outside the cylinder for the 12th through 18th receivers. The results for (b) are magnified by a factor of 20.

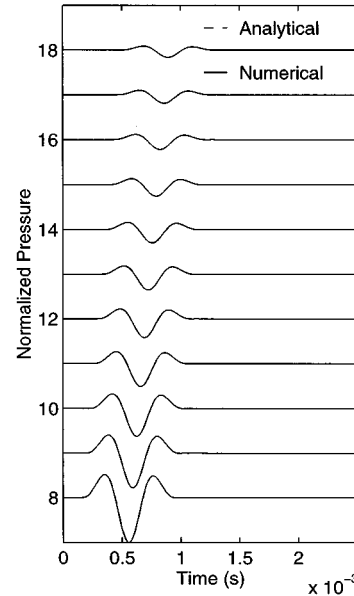


FIG. 8. A monopole point source in an homogeneous absorptive medium with $\rho = 1200 \text{ kg/m}^3$, $c = 1500 \text{ m/s}$, $\gamma = 2 \times 10^{-3} \text{ s/m}^2$. The source is located at $(x, y, z) = (1.1, 1.1, 1.1) \text{ m}$, and the receivers are at $x_i = 1.0 + (i-1) \times 0.05$, $y_i = 1.15$, $z_i = 1.1 \text{ m}$ ($i=8, \dots, 18$).

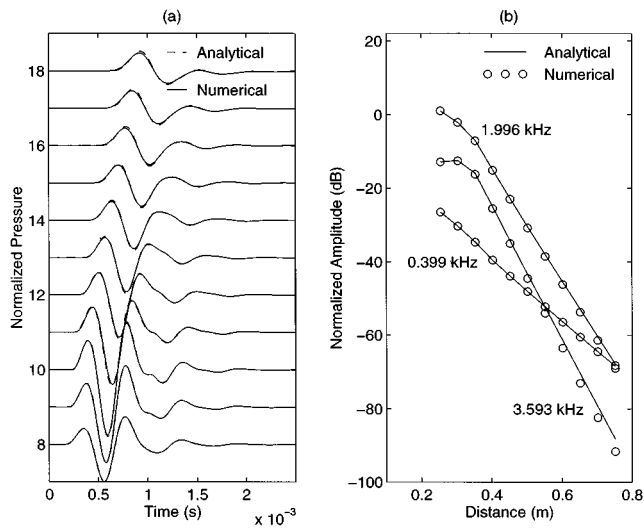


FIG. 9. A monopole point source at the center of an absorptive sphere (radius 0.4 m, $\rho_1 = 1200 \text{ kg/m}^3$, $c_1 = 1500 \text{ m/s}$, $\gamma_1 = 2 \times 10^{-3} \text{ s/m}^2$) in a homogeneous absorptive medium with $\rho_2 = 1000 \text{ kg/m}^3$, $c_2 = 1000 \text{ m/s}$, $\gamma_2 = 0.05 \text{ s/m}^2$. The locations of the source and receivers are the same as in Fig. 8. (a) Transient waveforms, (b) spectral amplitude as a function of receiver distance for $f = 0.399, 1.996, \text{ and } 3.593 \text{ kHz}$.

sphere for the last 11 receivers. To demonstrate that the field calculated by the FDTD method indeed has a correct attenuation, we perform a Fourier transform on the transient waveforms in Fig. 9(a). The spectral amplitude of the pressure field is plotted for three frequencies (low end, center, and high end of the source frequency band) in Fig. 9(b) as a function of the receiver distance from the source, and normalized with respect to the amplitude near the central frequency (1.996 kHz). Overall, the numerical results agree well with analytical solutions. At the high end of the frequency band (3.593 kHz), the error becomes larger. This is typical of FDTD methods, since with a finite cell size ($\Delta x, \Delta y, \Delta z$), both the geometry representation and the spatial derivatives give rise to a larger error at high frequency. The error can be further reduced by refining the cell size.

E. Comparison with Liao's ABC

One important application of this algorithm is in simulations of acoustic wave propagation in underwater environments. Typically the ocean surface and sea floor have to be incorporated in the model. Unfortunately, most existing absorbing boundary conditions cannot be used for such applications if these interfaces have a dip. Under the special case where the interfaces intersect with the computational boundary perpendicularly, Liao's ABC can be used to simulate the wave propagation in FDTD methods. In this example, we compare the FDTD results using PML ABC with those of Liao's ABC^{6,18} for an acoustic measurement in a flat ocean. The three (from top to bottom $j = 1, 2, 3$) layers have the following properties: $\rho_j = 1000, 1200, 2200 \text{ kg/m}^3$; $c_j = 1000, 1500, 2500 \text{ m/s}$. These layers extend to the full range in the y direction. Two rectangular cylinders ($\rho = 2000 \text{ kg/m}^3$, $c = 2000 \text{ m/s}$) are in the second layer and extend from $y = 0.7$ to $y = 0.9 \text{ m}$. The medium is lossless. The x - z cross section at $y = 0.8 \text{ m}$ is shown in Fig. 10(a). A monopole

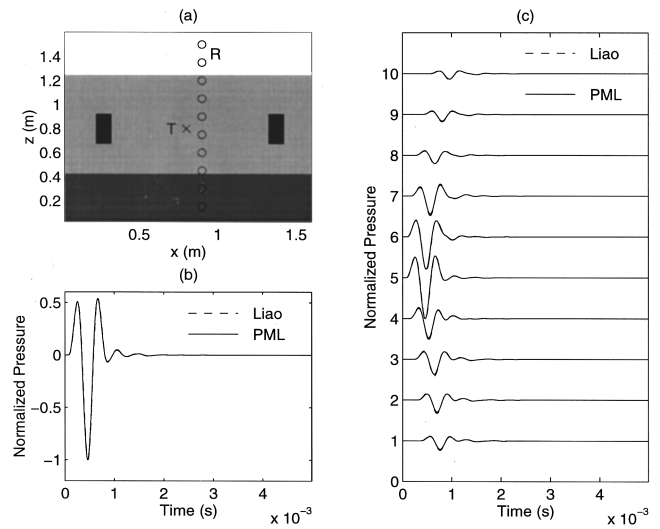


FIG. 10. Comparison of PML ABC and Liao's ABC for acoustic wave propagation in a three-layer medium with rectangular blocks. (a) Configuration. Pressure field at the fifth receiver (b) and at the array receivers (c).

source is located at $(x, y, z) = (0.8, 0.8, 0.8) \text{ m}$, and an array of 10 receivers is located vertically at $x_j = 0.9$, $y_j = 0.8$, and $z_j = 0.15j \text{ m}$ ($j = 1, \dots, 10$).

We compare the 3-D FDTD results using PML ABC with those using Liao's ABC, as shown in Fig. 10(b) for the fifth receiver. Figure 10(c) shows the total pressure field at the receiver array. It is seen that the agreement is excellent. In contrast to the PML ABC, the Liao's ABC, however, requires a double precision in order to be stable.

F. A dipping interface in underwater acoustic measurements

Dipping interfaces are often encountered and are therefore very important for underwater acoustic measurements. Unfortunately, previous absorbing boundary conditions cannot model these dipping interfaces since all of them require at least homogeneity in the direction perpendicular to the truncating boundary. The PML absorbing boundary condition, therefore, offers an unparalleled advantage over other ABC's for these problems.

We illustrate such applications of PML's for a dipping layer shown in Fig. 11(a). The configuration for the three layers is the same as in Fig. 10(a), except that the bottom layer is dipping. In addition, the two rectangular cylinders are replaced by two spheres (radii 0.2 m) located at the same centers. The monopole point source is located at the center of the left sphere, while an array of 31 receivers is located at the top interface. For this problem with a dipping interface, the FDTD algorithm with PML ABC is stable, whereas with Liao's ABC, the algorithm becomes unstable as soon as the waves propagate to the boundary. Figure 11(b) shows the pressure field measured at the 16th receiver, while Fig. 11(c) shows the array waveforms.

G. A large two-dimensional problem

Finally, a large two-dimensional problem is investigated for underwater acoustics as an example of applications. The

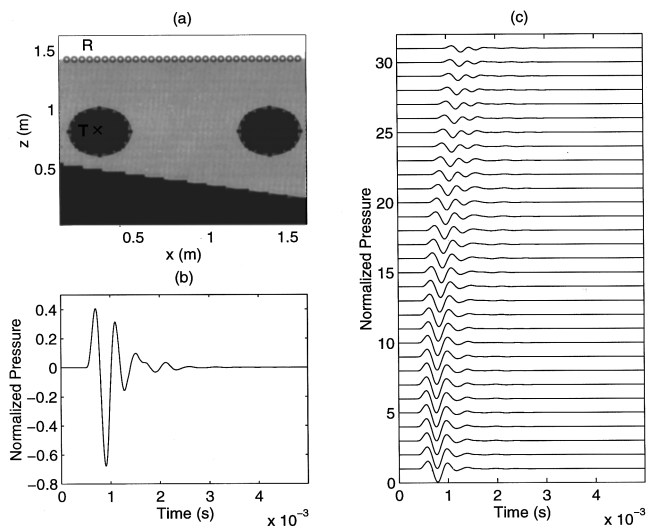


FIG. 11. Simulation of acoustic wave propagation using a 3-D FDTD program with PML ABC for a three-layer medium with two spheres. (a) Configuration. Pressure field at the 16th receiver (b) and at the array receivers (c).

geometry shown in Fig. 12(a) describes a problem with three layers (a top air layer, sea water, and the dipping sea floor). Acoustic wave propagation in such a medium with a wedge is a common problem important to many applications in shallow-water acoustics. In this example, the air–ocean interface is simulated as a soft boundary in order to reduce the number of unknowns in the problem. (The acoustic wavelength in the air is substantially shorter than in water and the sea floor. The full problem, including the wave propagation in the air, requires about 25 and 125 times more unknowns than using this treatment with soft boundary for 2-D and 3-D, respectively.) Therefore, the top air layer need not be included in the computational domain, even though it is shown in the figure. The sea water has parameters $\rho_1 = 1000 \text{ kg/m}^3$, $c_1 = 1500 \text{ m/s}$, $\gamma_1 = 10^{-4} \text{ s/m}^2$. The dipping sea floor has parameters $\rho_2 = 2200 \text{ kg/m}^3$, $c_2 = 2500 \text{ m/s}$, $\gamma_2 = 0 \text{ s/m}^2$. Within the seawater there are several objects (a large rectangular block of size $30 \times 7.5 \text{ m}^2$, seven small circular cylinders of radii 1.5 m, and a larger circular cylinder of radius 10 m) all with $\rho_3 = 2000 \text{ kg/m}^3$, $c_3 = 2000 \text{ m/s}$, $\gamma_3 = 0 \text{ s/m}^2$. A monopole line source is located right below

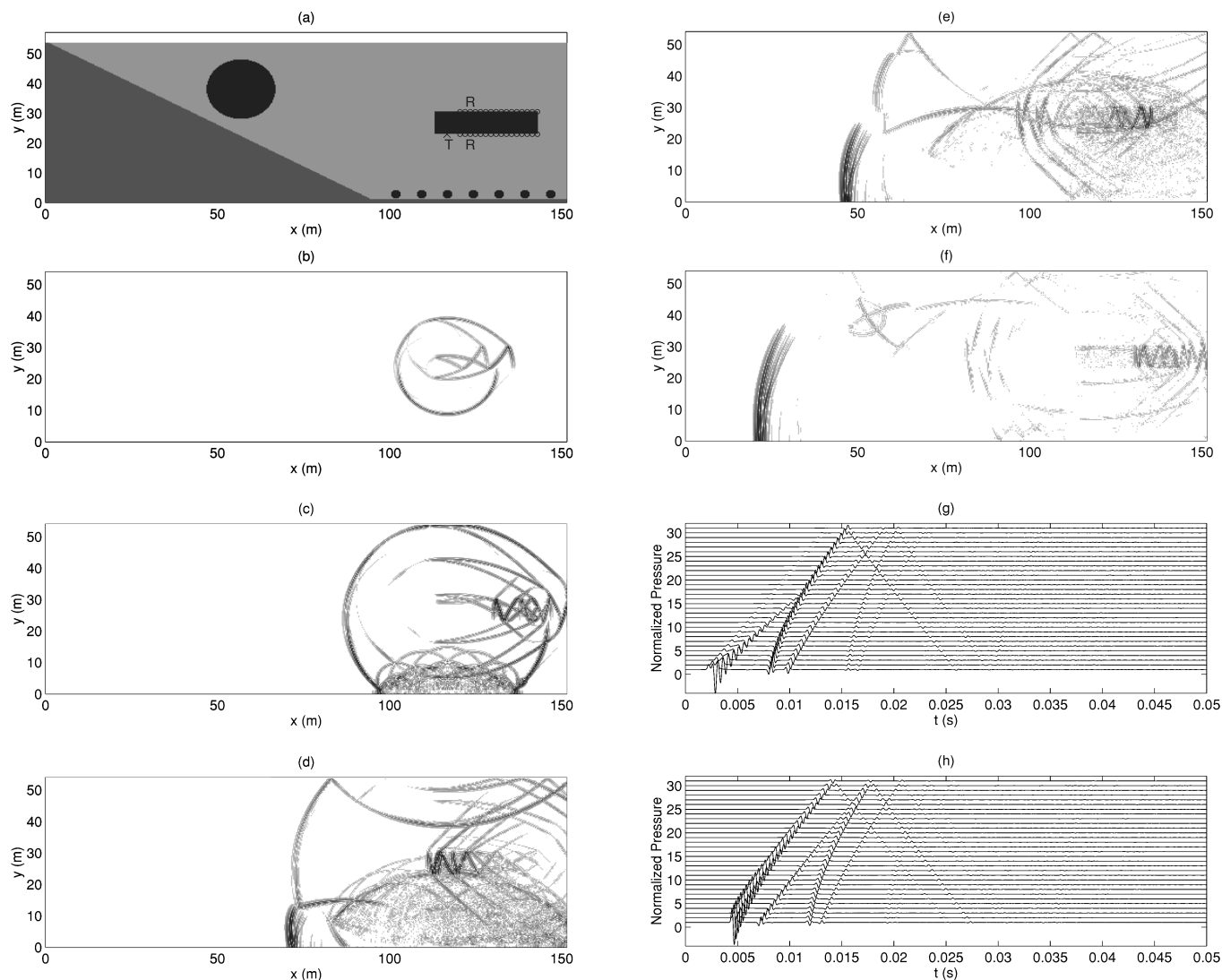


FIG. 12. 2-D simulation of a large problem in shallow water. (a) Geometry. From (b) to (f), snapshots of the absolute value of pressure field at time steps $n = 1000, 2000, 3000, 4000,$ and 5000 , respectively (time-step size $\Delta t = 10 \mu\text{s}$). Pressure waveforms at the bottom (g) and top (h) receiver arrays.

the rectangular block, while two arrays of receivers are mounted below and above the rectangular object, as shown in the figure.

At the highest frequency (5 kHz, or roughly 2.5 times the central frequency of the source time function), this large problem is of dimension $505.5\lambda \times 180.5\lambda$ in terms of the smallest wavelength in the water ($\lambda = 0.3$ m). The problem is discretized into 4044×1444 cells (or 23.36 million unknown scalar field variables) with $\Delta x = \Delta y = 0.0375$ m, and the time-step size is $\Delta t = 10 \mu\text{s}$.

The 2-D FDTD program is used to simulate the acoustic wave propagation in this medium. Figure 12(b)–(f) displays the snapshots at time steps $n = 1000, 2000, 3000, 4000$, and 5000 , respectively. Note that in order to increase the contrast in the figures, we display the absolute value of pressure field. Very complex wave interactions with the medium are observed even at the early time. The source generates a wave inside the rectangular object which creates multiple reflections. Because of the faster sound speed inside this object than the ambient medium, these multiple reflections leak out energy continuously. The waves at the circular objects on the bottom surface form an interesting interference pattern. Shown in Fig. 12(g) and (h) are the pressure waveforms at the bottom and top receiver arrays. A striking difference between these two sets of waveforms is the presence of the head waves along the bottom surface of the rectangular object which are recorded at the bottom receiver array. From Fig. 12(g), it is observed that these head waves (i.e., the first arrivals) propagate with a speed of the sound speed of the rectangular object. The fast decaying direct wave is also present on the bottom receiver array.

It is again worthwhile to emphasize that, given the discontinuities intersecting the computational edge, other absorbing boundary conditions cannot be used to simulate this complex medium because of the numerical instability. With the PML absorbing boundary condition, the 2-D and 3-D FDTD programs remain stable even with a single precision. These computer programs for absorptive media can be used to answer many interesting questions regarding the wave propagation in complex media.

H. A note on computational performance

The FDTD programs were implemented on supercomputers with parallel processors (IBM SP2 and HP SPP-2000 Exemplar) as well as SUN Ultra 1 Station. Because of the intention for parallel computers, the programs were written to treat the PML and interior regions (see Fig. 1) in the same way, that is, the interior region is treated as a PML region with $e_\eta = 1$. In this way the boundary layers do not require a separate code. Of course, if the programs are intended for serial computers, then it will be more efficient to treat the interior region differently from the PML region so that the total memory requirement is slightly less. On an IBM SP2 single processor, the memory requirement for the above large 2-D problem (with 23.36 million unknowns) is about 390 Mbytes, and the CPU time is 6.17 s per time step. This is considered quite efficient given that only nominal optimization has been done on the programs. Further reduction in

the memory and CPU requirement is possible if the finite-difference coefficients are saved only for distinct regions.

IV. CONCLUSIONS

The perfectly matched layer (PML) absorbing boundary condition is applied to simulate acoustic waves in absorptive media. Within the boundary region of the computational domain, perfectly matched layers are used to attenuate outgoing acoustic waves. In contrast to elastic waves, the PML for scalar acoustic waves does not require a splitting in the velocity field components because the second-rank stress tensor collapses to a zero-rank tensor (i.e., a scalar) in the acoustic case. When there is an intrinsic attenuation, an additional term involving the time-integrated pressure field has to be introduced to account for the coupling between the loss from the PML and the normal absorption. This new absorbing boundary condition is stable even when a dipping interface intersects the computational edge, and is thus very useful in simulations of underwater acoustic waves. The PML absorbing boundary condition is implemented for two and three dimensions, and the computer programs have been validated by analytical solutions and other numerical results with Liao's absorbing boundary condition. This algorithm is ideal for parallel computation since the same code can be used for the inner computational domain and for the outer boundary. The extension to viscoelastic waves can be formulated similarly and is the subject of future studies.

ACKNOWLEDGMENTS

This work was supported by a Presidential Early Career Award for Scientists and Engineers (PECASE) through the Environmental Protection Agency and by Sandia National Laboratories under the SURP program.

- ¹C. Cerjan, D. Kosloff, R. Kosloff, and M. Reshef, "A nonreflecting boundary condition for discrete acoustic and elastic wave equations," *Geophysics* **50**, 705–708 (1985).
- ²A. R. Levander, "Use of the telegraph equation to improve absorbing boundary efficiency for fourth-order acoustic wave finite difference schemes," *Bull. Seismol. Soc. Am.* **75**(6), 1847–1852 (1985).
- ³R. Clayton and B. Engquist, "Absorbing boundary conditions for acoustic and elastic wave equations," *Bull. Seismol. Soc. Am.* **67**, 1529–1540 (1997).
- ⁴E. L. Lindman, "Free-space boundary conditions for the time dependent wave equation," *J. Comput. Phys.* **18**, 66–78 (1975).
- ⁵C. J. Randall, "Absorbing boundary condition for the elastic wave equation: Velocity-stress formulation," *Geophysics* **54**, 1141–1152 (1989).
- ⁶Z. P. Liao, H. L. Wong, B. P. Yang, and Y. F. Yuan, "A transmitting boundary for transient wave analysis," *Sci. Sinica A* **27**, 1063–1076 (1984).
- ⁷R. L. Higdon, "Numerical absorbing boundary conditions for the wave equation," *Math. Comput.* **49**, 65–90 (1987).
- ⁸C. Peng and M. N. Toksöz, "An optimal absorbing boundary condition for finite difference modeling of acoustic and elastic wave propagation," *J. Acoust. Soc. Am.* **95**, 733–745 (1994).
- ⁹J.-P. Berenger, "A perfectly matched layer for the absorption of electromagnetic waves," *J. Comput. Phys.* **114**, 185–200 (1994).
- ¹⁰W. C. Chew and W. H. Weedon, "A 3D perfectly matched medium from modified Maxwell's equations with stretched coordinates," *Microw. Opt. Technol. Lett.* **7**, 599–604 (1994).
- ¹¹W. C. Chew and Q. H. Liu, "Perfectly matched layers for elastodynamics: A new absorbing boundary condition" Schlumberger–Doll Research Technical Report, August 1995.

- ¹²W. C. Chew and Q. H. Liu, "Using perfectly matched layers for elastodynamics," in *Proceedings of the IEEE Antennas Propagation Society International Symposium* (IEEE, New York, 1996), Vol. 1, pp. 366–369.
- ¹³W. C. Chew and Q. H. Liu, "Perfectly matched layers for elastodynamics: A new absorbing boundary condition," *J. Comput. Acoust.* **4**(4), 72–79 (1996).
- ¹⁴F. D. Hastings, J. B. Schneider, and S. L. Broschat, "Application of the perfectly matched layer (PML) absorbing boundary condition to elastic wave propagation," *J. Acoust. Soc. Am.* **100**, 3061–3069 (1996).
- ¹⁵Q. H. Liu, "An FDTD algorithm with perfectly matched layers for conductive media," *Microw. Opt. Technol. Lett.* **14**(2), 134–137 (1997).
- ¹⁶H. A. Kramers, *Atti Congr. Internaz. Fisici*, Como, Italy, Sept. 1927.
- ¹⁷Q. H. Liu and C. Chang, "Compressional head waves in attenuative formations: Forward modeling and inversion," *Geophysics* **61**(6), 1908–1920 (1996).
- ¹⁸Q. H. Liu, F. Daube, C. Randall, E. Schoen, H. Liu, and P. Lee, "A three-dimensional finite difference simulation of sonic logging," *J. Acoust. Soc. Am.* **100**, 72–79 (1996).

Modulations of detectable pulse response time spread in shallow water resulting from a combination of sound-speed variability and bottom loss

Charles L. Monjo

Applied Measurement Systems Incorporated, One Oakwood Boulevard, Hollywood, Florida 33020

Hien Nguyen and Harry A. Deferrari

*Division of Applied Marine Physics, Rosenstiel School of Marine and Atmospheric Science,
University of Miami, 4600 Rickenbacker Causeway, Miami, Florida 33149-1098*

(Received 31 October 1995; revised 25 March 1997; accepted 1 July 1997)

Reciprocal transmission tomography experiments in the Florida Straits have yielded a month-long time history of reciprocal pulse responses over three ranges approximately 22 km in length and 250 m in depth. A transmitted pulse of 8.75 ms in duration is spread out approximately 150 ms. The detectable time spread, or pulse width, is observed to vary by as much as 120 ms over time scales on the order of days. In a previous paper a strong correlation was reported between the sound-speed gradient at mid-depth and the total pulse width. A plausible explanation that changes in the sound-speed profile shape was causing the ray arrivals to focus and defocus in time was set forth as a hypothesis for this study, to be examined with range-dependent ray and PE models. The models predict a different and unexpected relation. Variations in the sound-speed profile from the average profile shape to a more convex profile increase the bottom grazing angle to the early arrivals. This results in an attenuation of the early arriving portion of the pulse below ambient noise and therefore an apparent narrowing of the pulse. Likewise, changes in the sound-speed profile from the average profile shape to a linear profile, produce smaller bottom grazing angles for the fastest arrivals, less loss, and an overall wider appearing pulse. © 1997 Acoustical Society of America.
[S0001-4966(97)02910-X]

PACS numbers: 43.30.Cq, 43.30.Pc [SAC-B]

INTRODUCTION

Variability of transmissions in shallow water, bottom-limited areas is not well understood, nor do many quality data sets exist to study the problem systematically. As the focus of the underwater acoustics community turns to shallow water regions, understanding variability of broadband transmissions is necessary before active ASW (detection, match-field processing) or environmental parametrization (inversion of oceanographic and geoacoustic parameters) can be accomplished efficiently. By contrast, the study of refracted-refracted (RR) paths in the deep ocean ($\lambda \ll \text{depth}$) is well advanced.¹⁻³ Perturbations to the sound-speed field are small ($dC/C = 0.0001$)⁴ and resolvable time replicas of the transmitted signal are observed. These paths and their variability can be identified with acoustic ray or normal mode models.⁵⁻⁷ The source of the deep ocean path travel time variability is internal waves and theories utilizing a Garret/Munk⁸ internal wave spectrum can effectively predict 90% of the acoustic fluctuations.

Variability of transmissions in very shallow water ($\lambda \gg \text{depth}$) can also be predicted with some confidence, even though no resolvable time replicas of the transmitted signal are observed. In this case only a few acoustic normal modes are generated and variability occurs due to the interference of a few known mode shapes.^{9,10} The variability of received signals can be understood without resolving the individual ray paths.

The bottom-limited case ($\lambda < \text{depth}$) however, is far

more complicated. At frequencies used by tomographers, hundreds of significant modes are generated. No resolvable replicas of the transmitted signal are observed. The discrete set of predicted ray paths overlap in time and phase interference effects would appear to dominate. In coastal regions such as the Straits of Florida, perturbations to the sound-speed field are large ($dC/C > 0.005$)^{4,11} because the thermocline encompasses the entire water column, and current processes related to bathymetry and coastal boundaries (internal waves, Kelvin and Rossby waves) come into play.

Therefore, the set of ray paths changes, due to the coming and going of new paths, none of which can be resolved in time. Furthermore, large sound-speed fluctuations over time cause significant changes in the bottom attenuation to a particular ray path, as the path samples different spots on the ocean bottom at different angles. The geoacoustic properties of most coastal areas and the range dependence of those properties are not well known. Thus the fluctuation of pulse response amplitude in shallow water, bottom-limited areas is dominated by several unknowable factors.

Acoustic measurements in the Florida Straits provided the impetus for the study reported here. Pulse responses were measured nearly continuously during August 1983 as part of a three point reciprocal transmission experiment. This experiment and its results were reported previously,¹² therefore only a short overview of the experiment and its data will be given here.

The Florida Straits is a shallow water, bottom-limited

area, where there were no resolvable replicas of the transmitted signal observed in the data. Yet a large degree of pulse width variability is observed over both short time scales (on the order of tens of minutes) and long time scales (on the order of days). We define pulse width here as the duration of the detectable multipath time spread above the noise floor.

The thrust of this study is to explain the long time scale pulse width variability. If pulse width variability can be better understood, then various environmental parameters such as bottom loss curves, sound speed, and current profiles can eventually be inferred by inversion, without resolvable replicas of the transmitted signal.

In this study, range-dependent ray and PE models are used to predict pulse response patterns for the entire month of August. The complex PE results are beamformed, and bottom grazing angles are computed from both ray and PE results. The predictions are compared to data and the relation of pulse width to bottom grazing angle is investigated. The sound-speed profile shape is shown to change the bottom grazing angle of the faster arrivals along the pulse. The relation between profile shape and pulse width is drawn.

Five sections follow. In Sec. I a brief overview of the experiment, data, and acoustic setting are presented. In Sec. II model inputs are discussed. In Sec. III the average propagation in the channel is explained and a simple analytical model for the bottom loss effect is presented. In Sec. IV month long ray and PE results are presented and compared to data. Section V includes discussion and conclusions.

I. ACOUSTIC EXPERIMENT AND DATA

A. Setting

The acoustic data were collected in the Florida Straits in an attempt to measure the heat flux through the straits by means of tomographic inversion.¹² The three transceivers were deployed 38 m off the bottom, near 27 deg north (Fig. 1). The experiment was conducted on the western side of the Straits in a depth of approximately 250 m. This study is concerned with the north-south leg of the experiment only. The moorings were 21.11 km apart. The bathymetry has a slight slope and the sound-speed profile is relatively range independent (Fig. 2).

B. Oceanographic setting

The oceanography of the area can only be described as highly complex. The Florida Current is a typical western boundary current and flows northward through the straits at extremely high velocities (200–400 cm/s at the surface). In Fig. 3 the yearly average U component (northward) of flow is shown. The warm, high-speed, surface waters originate in the southern Caribbean.¹³ The cold bottom waters are derived mostly from Antarctic intermediate water.¹⁴ The dynamics of these water masses as they pass through the Florida Straits are very complicated.

The Florida Current has a well-defined, high-speed core which meanders across the Straits in an east-west direction. Both the speed and direction of the current are highly variable with periodicities ranging from 3 to 21 days.^{15,16} The dynamics of the surface water can result in the migration of

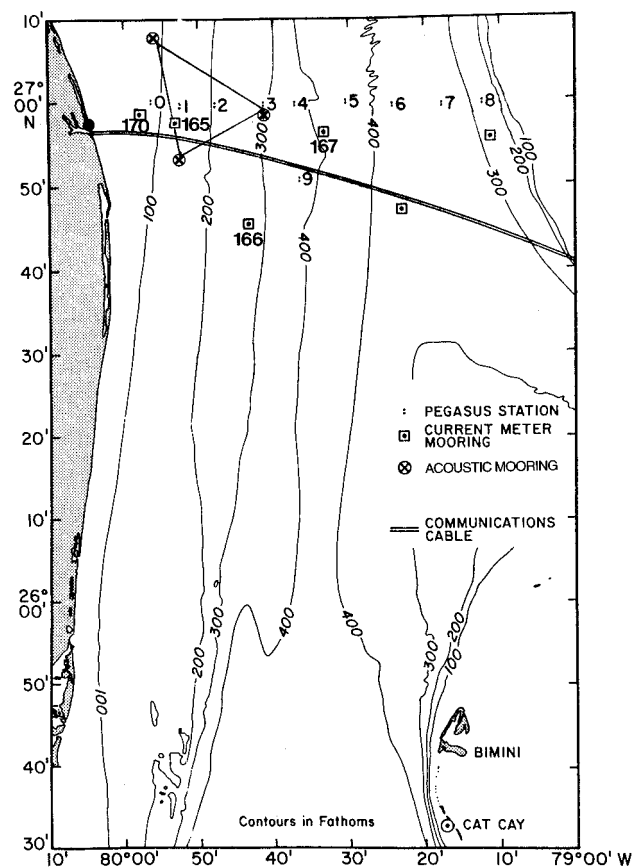


FIG. 1. Locations of acoustic reciprocal transmission moorings and other environmental measurement systems of the subtropical Atlantic climate study (STACS). PEGASUS stations were visited several times a month, and current, temperature, and salinity were measured with a free-fall instrument. Current meter moorings measured current speed and direction and temperature at four or more depths in the water column. Hourly measurements were taken continuously for over two years. Transport was also measured using the electropotential method and a telegraph cable between West Palm Beach and West End. The geometry of the August acoustic experiment is shown (small triangle).

cold bottom water up and down the western slope of the Straits.¹⁷ Thus both bottom and surface temperatures are highly variable in space and time. The near-linear shape of the average sound-speed profile seen in Fig. 2 is constantly changing due to the dynamics of the Florida Current.

The oceanographic data were collected as part of the Sub-Tropical Atlantic Climate Study (STACS).^{18–21} STACS is an ongoing investigation of the Florida Current and collected extensive data during the years of 1982, 1983, and 1984. The sound-speed and current profiles during the August experiment were measured with a PEGASUS²² profiler at stations 0–8 along 27 deg north (Fig. 1). The PEGASUS profiler is a free-falling acoustic Doppler current and temperature profiler with an accuracy of 3.0 cm/s and 0.2 °C.²³ Temperature and current time series at several depths were also collected with Andraa and Niskin current/temperature meters at mooring sites M170, M165, M166, and M167 (Figs. 1 and 3). These instruments both have accuracies of 2.0 cm/s and 0.1 °C.²⁴ Mooring M165 lays directly in the path of transmission for the north-south leg of the experiment (Fig. 2). The north-south leg shows the least amount of

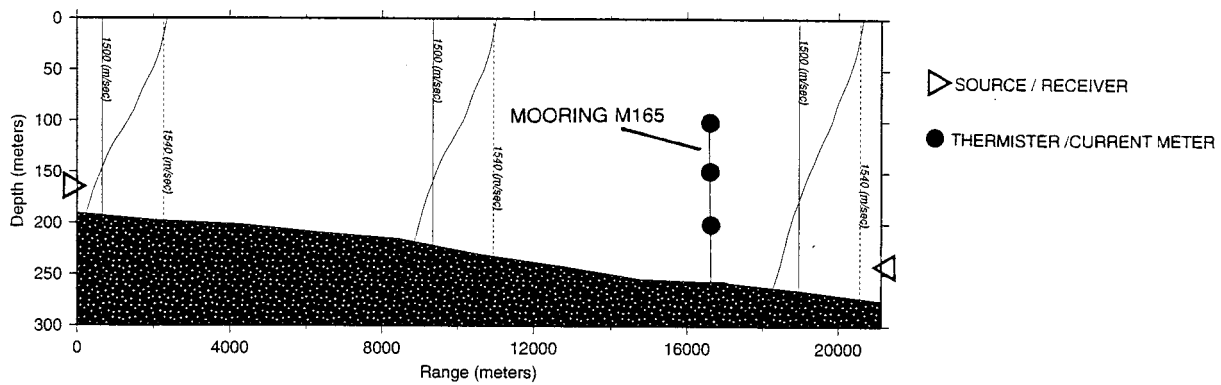


FIG. 2. Geometry of the north/south leg of the acoustic experiment. Source and receiver were mounted 38 m off the bottom. The average sound-speed profile is near linear and downward refracting. Mooring M165 was directly in the path of transmission in about 260 m of water with thermistors at 100, 102, 153, and 202 m depths.

range dependence in the sound-speed profile, as compared to east-west legs. Thus mooring M165 data are a reliable history of the mid-channel sound-speed variation during the acoustic experiment.

C. Geoacoustic setting

Geoacoustic inputs to the models used here were obtained from the literature of past studies (cores, refraction lines, and surface sediment samples) performed within 15 km of the acoustic experiment. These studies give a reliable estimate of the average geoacoustic features along the acoustic track. The geoacoustic input to the models are not range dependent (except for bathymetry). Indeed, true range-dependent geoacoustic inputs (every 200 m to a depth of 1 km) are not directly measurable quantities due to cost and technological constraints. At present, we are forced to estimate the average geoacoustic features of the channel.

The sediment at the experiment site is 25–100 m thick,^{25,26} composed of partially lithified, medium sand or silty sand, made up of approximately 85% carbonate materials, with a grain size in the 100–300 μm range.²⁷ Porosity is in the 0.30–0.50 range and density in the 1.7–2.0 g/cm^3 range.^{28,29} Compressional sound speed at the sediment surface is ~ 1540 – 1560 m/s with a compressional attenuation in the vicinity of 0.4 dB/ λ .³⁰ Shear velocity is low in the 100–300 m/s range at the sediment surface.³¹ The basement is hard limestone with a compressional sound speed in the range of 1800–2200 m/s, a density of ~ 2.1 g/cm^3 , and a compressional attenuation of ~ 0.3 dB/ λ .^{26,29,30}

D. Acoustic data

The acoustic data consist of six sets of pulse responses, sampled every 12 min for a 32-day period beginning 1200 GMT, July 30, 1983. One mooring would transmit an LMPRS³² (linear-maximal pseudo-random sequence) having a single digit duration of a four cycle pulse at 459.5588 Hz, while the other two moorings recorded the incoming transmission. After 4 min, the second mooring transmitted while

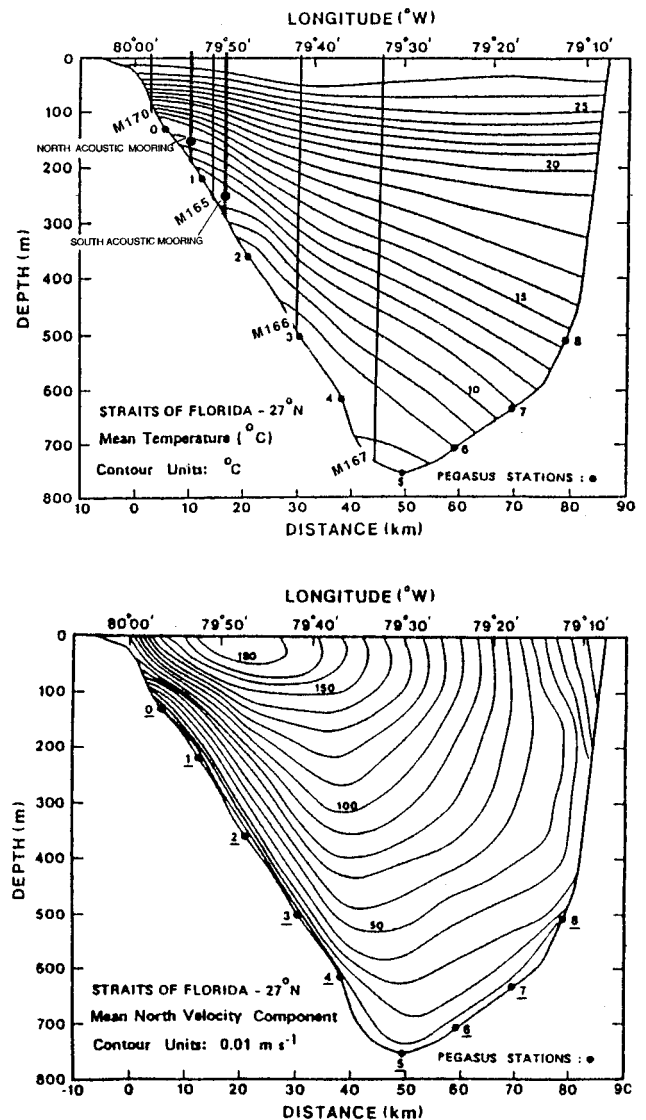


FIG. 3. Average structure of the northern component of current and temperature fields computed from PEGASUS data along 27 deg north. Location of acoustic and current meter moorings are superimposed on the temperature field plot.

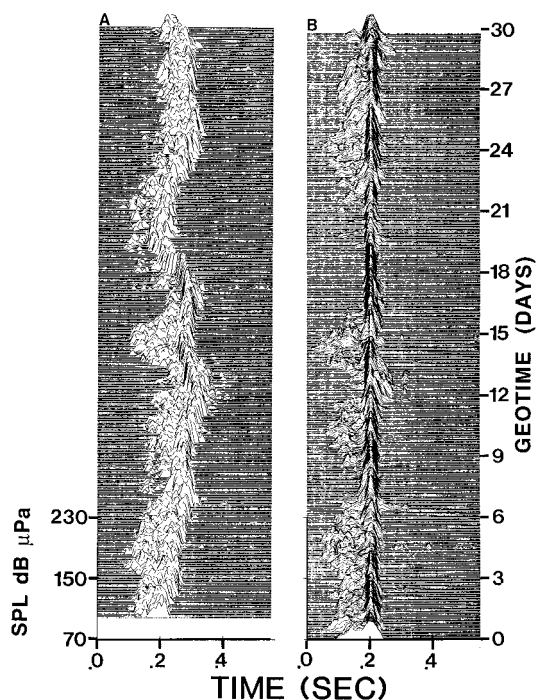


FIG. 4. Thirty-day time history of reciprocal pulse responses for the north-south leg. Each record plotted is an average pulse response over 12 h. The time series on the right has been aligned along the late main peak.

the other two recorded. Finally, the third transceiver would transmit, thus ending one complete cycle. The cycle was repeated every 12 min. This “sing around” results in six sets of pulse responses, pertaining to transmission paths in both directions on all three sides of the triangle. A more detailed explanation of the experiment design was published previously.¹²

The north-to-south data are shown in Fig. 4(a). In Fig. 4(b) the data have been aligned along the late main peak. The pulses in Fig. 4(b) have been averaged over 12 h. The average pulse width is approximately 120 ms. The signals all exhibit a clump of high intensity, slow energy (late main peak) preceded by a broader plateau of lower intensity energy. Pulse width changes dramatically over fairly short time scales (on the order of 1 day). On several occasions the pulse width drops down to approximately 50 ms (days 7.5, 12, 16.5) when just two days prior, pulse width was approximately 200 ms (days 5.5, 10, and 14.5).

There is also a large degree of short time scale, pulse-to-pulse variability. This short time scale variability is not the focus of this study. The short time scale variability is most likely due to internal waves which vary the phasing of arrivals from pulse-to-pulse (12-min sample period). The variability of interest here is the longer time scale variability (on the order of days). The 12-h averaging of the pulse responses in Fig. 4(b) effectively removes the short time scale variations. The pulse width variation over the longer time scales was thought to be caused by temperature profile shape variation which focused and defocused the multipath arrivals in time.

In Fig. 5 we compare the acoustic data with temperature/sound-speed time series collected at mooring M165. Moor-

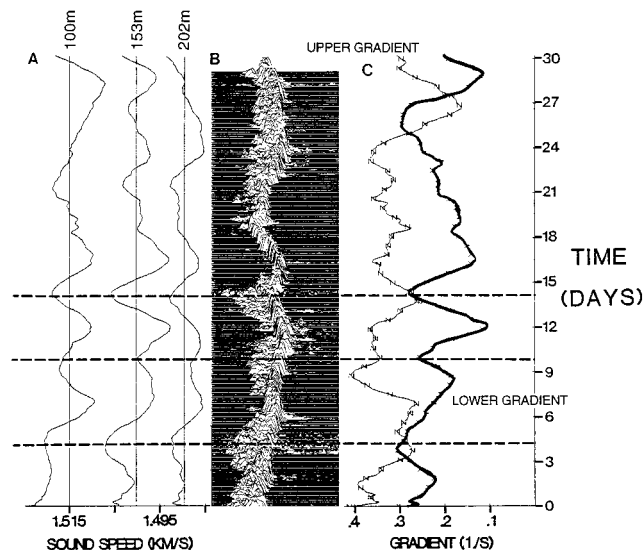


FIG. 5. Comparison of thermistor data and acoustic data. (a) 15-h low-pass time series of sound speed from mooring M165. (b) 1-h averaged pulse response data. (c) Sound-speed gradient between time series from (a). Dashed lines show the locations of positive sound-speed anomalies.

ing M165 had time series at 100, 102, 153, and 202 m. The time series at 102 m has been left out for clarity. On the left is the low passed (15-h) sound speed at 100, 153, and 202 m in a total depth of 253 m. In the center is the acoustic data and on the right is the sound-speed gradient from the time series plotted on the left.

It is clear that the pulse width variation is remarkably similar to the soundspeed variation, especially over the first 18 days of the experiment. During this initial 18-day period one can also see the good correlation in depth of the sound speed time series (correlation coefficient > 0.81). The correlation coefficient³³ (cc) between two time series x and y of length N is defined here as

$$\frac{C_{xy}}{\sigma_x \sigma_y}, \quad (1)$$

where

$$C_{xy} = \frac{1}{N} \sum_{i=1}^N (x_i - \mu_x)(y_i - \mu_y), \quad (2)$$

μ_x = average value of x , μ_y = average value of y , and σ_x = standard deviation of x , σ_y = standard deviation of y . During the initial 18-day period the sound-speed field can be characterized as barotropic. During the latter 12 days of the experiment, the correlation in depth of the sound-speed time series is far lower ($cc < 0.50$) and can be characterized as baroclinic.

During the barotropic period there is also remarkable correlation between the soundspeed variation at the upper depths and pulse width variability ($cc = 0.765, 0.735$, and 0.474 for the 101-m, 153-m, and 202-m time series). The sound-speed time series are dominated by a series of alternating positive and negative temperature/sound-speed anomalies, most likely due to east and west meanders of the Florida Current. The pulse width variation does not align

perfectly with the oceanography at all depths and at all times nor would we expect it to. One must remember that the acoustic measurement is an integrated measurement of the temperature field along the entire acoustic track, while the temperature measurement is a point measurement from one location along the acoustic track. Surely the \pm temperature anomalies collected at mooring M165 occurred at different depths and times along the acoustic track. The fact that the correlations are as high as they are indicates the channel is not highly range dependent.

The positive sound-speed anomalies in Fig. 5 are indicated by the broad dotted lines to help illustrate the relation between pulse width and sound-speed anomaly. Wider pulses are associated with positive sound-speed anomalies (days 4, 10, and 14). During these events the gradient time series converge, i.e., the sound-speed profile approaches linearity. Shorter pulses are associated with negative sound speed anomalies (days 1.5, 8, 12, and 16.5). During these events the gradient time series diverge (except for day 8), i.e., the sound-speed profile becomes more convex. Again we would not expect perfect alignment between an integrated measurement and a point measurement (especially gradient between two fixed depths). The gradient time series are shown to give an intuitive feel for how profile shape is changing.

After day 18, the pulse width is more uniform and lower correlation between pulse width variation and the sound-speed variability is apparent ($cc=0.117, 0.157, -0.501$ for 101, 153, 202 m, respectively). During this period the channel sound-speed time series are far less correlated, and this degrades the dependence between pulse width and sound-speed variation. Our initial hypothesis was that the linear profile spread the arrivals in time and that the convex profile focused the arrivals in time during the first 18 days of the experiment. To support this, sound-speed time series at the surface and bottom of the channel for the entire month were needed.

II. MODEL INPUTS

To model the month long acoustic record, sound-speed profiles along the acoustic track for the entire month were needed. These data were not available; only the PEGASUS profiles and fixed mooring time series as discussed in Sec. I B. Mooring M165, however, is directly in the path of the acoustic transmission and yields a reliable history of the mid-channel sound-speed variation for the entire month of August. The time series of the sound-speed variation at the surface and channel bottom were calculated with a multi-step, high-order interpolation process using empirical orthogonal function (EOF) analysis. EOF analysis decomposes the temperature variation of the channel into a set of depth-dependent variational modes. A description of the process follows.

First, PEGASUS profiles for stations 0, 1, 2, 3, and 4 (Fig. 1) were gathered from the months of July, August, and September for 1982, 1983, and 1984. In all, at least 30 profiles were found at each station. Summer months were used because no surface duct was present and such a profile shape is more easily represented using just a few EOFs. The first

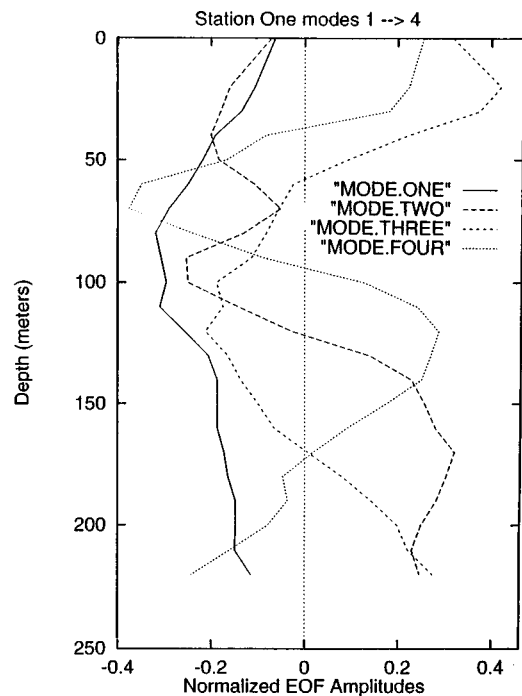


FIG. 6. First four modes computed using EOF analysis of PEGASUS temperature profiles from station one. The first three modes represent over 94% of the temperature variability.

eight EOF modes, in depth, were computed at each PEGASUS station. The first three EOF modes from station one (Fig. 6) represent over 94% of the temperature variation as computed by the EOF analysis mode density routine. These variational modes are functions of depth and will be referred to as EOF modes.

The EOF modes were then used to compute hourly temperature profiles at the thermistor mooring sites. Temperature is related to the EOF modes by

$$T(z_j) = \sum_{i=1}^M a_i \Phi_i(z_j), \quad (3)$$

where $T(z_j)$ is the temperature at depth z_j , $\Phi_i(z_j)$ is the EOF mode value, of mode i at depth z_j , and a_i is the mode coefficient of mode Φ_i . To compute temperature one must first solve for the mode coefficients by inversion of the matrix equation

$$\Phi \mathbf{a} = \mathbf{T}, \quad (4)$$

where Φ are the known EOF mode depth function values at a particular set of depths, \mathbf{T} are the known temperatures at the same depths, \mathbf{a} is the set of desired mode coefficients, and boldfaced type indicates a matrix.

The temperature computation using the EOF modes was initially checked by reconstruction of the input profiles used to compute the EOF modes. By selecting four interior temperatures from a single profile, and using just three EOF modes, Eq. (4) is inverted using the well-known least-squares inversion scheme³⁴

$$\mathbf{a}_{\text{est}} = [\Phi^T \Phi]^{-1} \Phi^T \mathbf{T}, \quad (5)$$

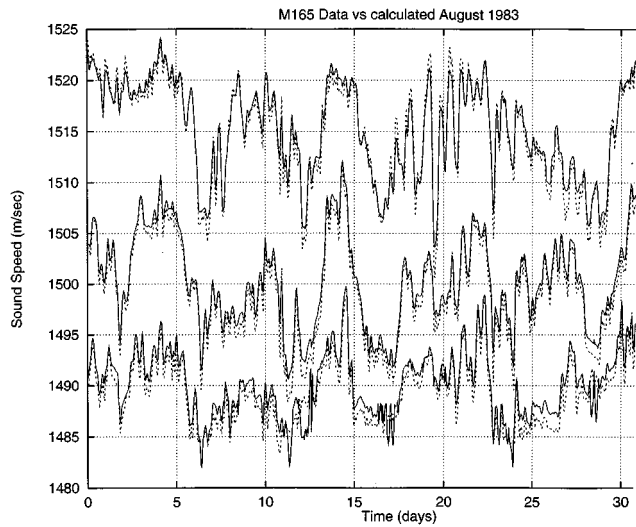


FIG. 7. Comparison of computed sound-speed time series and measured sound-speed time series at mooring M165. The solid line is the sound-speed time series computed using the truncated EOF expansion. The time series have not been smoothed.

where Φ^T indicates the transpose of the EOF mode function matrix Φ , and \mathbf{a}_{est} are the estimated mode coefficient values. The entire profile over the complete channel depth is then reconstructed using Eq. (3) (the truncated EOF expansion).

The exact same procedure can be done at the thermistor mooring sites, but now \mathbf{T} is the set of measured temperatures from the thermistor mooring, and Φ are the known EOF mode functions values at the thermistor depths computed from the PEGASUS profiles. A set of mode coefficients is then solved by inversion [Eq. (5)] for each hourly measurement by the thermistor mooring. A temperature profile for the entire water column can then be computed using Eq. (3). The least-squares inversion procedure computes the set of mode coefficients such that the difference between observed and computed temperature at the thermistor depths is minimized. This interpolation procedure using EOF analysis has been used in the oceanographic and acoustic communities since the 1970's.^{35,36}

To check the validity of the procedure, the computed time series at the thermistor depths is compared to the mooring data. The computed time series match the data nearly perfectly, as shown in Fig. 7. This does not mean the computed time series at the surface or bottom is correctly estimated in all instances of the 30-day experiment using just 3 or 4 EOF modes. If the actual profile shape becomes more complicated, such as a surface duct (i.e., more energy in EOF modes 5, 6, and 7), then the EOF procedure becomes less accurate. We are restricted to use only as many EOFs as there are measured temperature time series available.

The result of this procedure was a set of time series every 10 m at mooring sites M170, M165, M166, and M167. As mentioned earlier, mooring M165 was directly in the path of acoustic transmission. Sound-speed profiles along the acoustic track were calculated with the result at mooring M165, using the upslope (M170) and downslope (M166 and M167) results for range dependence. The sound-speed time

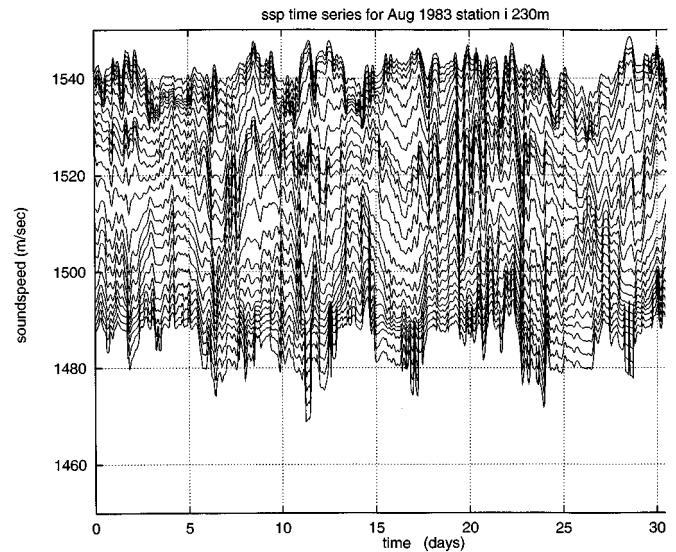


FIG. 8. Time series of sound speed every 10 m at an intermediate location between acoustic moorings. The time series were computed using the time series from mooring M165 and the EOF mode functions derived from the PEGASUS profiles.

series from one location along the acoustic track are shown in Fig. 8.

Unfortunately mooring M170 had just three sensors and M165 had only four sensors, thus only 3/4 EOFs could be used to compute the sound-speed profiles. Even though the EOF procedure recreates the mooring data quite well, that does not mean the surface and bottom time series are as valid. As mentioned earlier, the channel becomes less barotropic during the later part of August, and three or four EOFs may indeed not be enough to validly represent the sound-speed profile at its endpoints. However, the results from the acoustic modeling for the first 18 days of August using the EOF computed inputs are encouraging.

To compare measured and calculated pulse widths (error calculation and correlation coefficients) the pulse width time series are first low-pass filtered (12 h) to remove the short time scale pulse-to-pulse variability. The average absolute difference (average error) between the measured pulse width and the computed pulse width is only 19.8 ms (~ 2 transmitted pulse lengths). Average error for future reference is defined as

$$\frac{1}{N} \sum_{i=1}^N |\text{pwm}_i - \text{pwc}_i|, \quad (6)$$

where N is the number of pulses calculated, pwm is the measured pulse width of an individual sample, and pwc is the calculated pulse width in ms. Average percentage error over the same time period is only 18% defined here as

$$\frac{100}{N} \sum_{i=1}^N \frac{|\text{pwm}_i - \text{pwc}_i|}{\text{pwm}_i}. \quad (7)$$

The correlation coefficient between measured and calculated pulse width is over 0.75. We are confident that the EOF procedure has reconstructed reliable sound-speed time series over the first 18 days of the experiment.

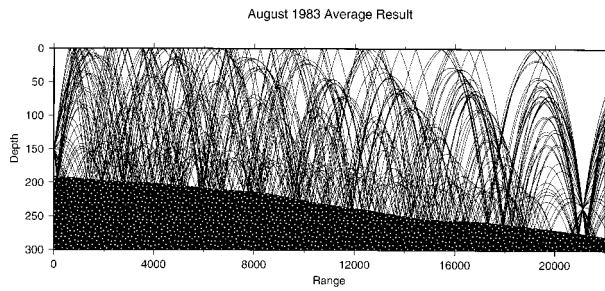


FIG. 9. Ray paths computed with the MEDUSA model for the average profile shown in Fig. 2.

III. PROPAGATION AND BOTTOM LOSS MODELS

A. Average result

A single ray result explains the general features of the propagation environment and pulse responses from the acoustic data. In Fig. 9 the eigenray paths, computed using the MEDUSA³⁷ model for an average sound-speed profile, are presented. A detailed explanation of the acoustic propagation in the Florida Straits is presented in previous papers,¹² thus only a brief explanation will be presented here.

The pulse is made up of refracted bottom reflected (RBR) and surface reflected bottom reflected (SRBR) paths. Due to the slanted bottom, some paths begin as SRBR paths in shallow water and as the channel widens the path becomes a surface grazing RBR path. These paths are designated as mixed arrivals.

The pulse responses seen in the data have a low intensity plateau followed by a high intensity peak. The fastest paths in the pulse response are surface grazing RBR paths and mixed arrivals with only seven turns/surface hits. These paths are the steepest energy observed in the data, thus they are subject to the most bottom loss, the most spreading loss, and have the longest path lengths. The surface grazing energy is followed by RBR paths that turn deeper and deeper in the channel (8–11 turns). These paths make up the early low intensity plateau.

RBR paths that turn 12–19 times turn right at, or near, the receiver depth, and tend to have the same travel time. Those paths nearest the bottom are the flattest energy observed in the data, with the least bottom loss, least spreading loss, and the shortest path lengths. Thus a slow, high intensity peak is formed, as seen in the data (late main peak). The relationships between travel time, transmission loss, and propagation angles are very well-documented in the Jacobson JASA article from 1964³⁸ and the MEDUSA results presented here concur with Jacobson's analytical results.

The SRBR paths with large bottom grazing angles, large path lengths, and the most spreading loss of the eigenray set are not observed in the data. The SRBR paths have bottom grazing angles well past critical and bottom loss accounts for most of the overall loss. The bottom grazing angles of RBR paths are generally less than critical. These angles vary with sound-speed profile shape and result in pulse width variability above the noise floor. A simple one-layer model can explain the bottom loss due to profile shape changes.

TABLE I. Bottom grazing angles computed using Eq. (9), for a single layer, linear gradient model. Angles for RBR paths with 6–9 turns are shown for various gradients from the measured gradient time series of mooring M165.

Range/ <i>N</i>	Range=21 110.0 m				
	Minimum gradient 0.102	$\mu + \sigma$ 0.205	Average gradient 0.249	$\mu - \sigma$ 0.293	Maximum gradient 0.338
<i>N</i> = 6	6.89	13.59	16.40	19.13	21.75
<i>N</i> = 7	5.91	11.71	14.16	16.55	18.87
<i>N</i> = 8	5.18	10.28	12.45	14.58	16.65
<i>N</i> = 9	4.61	9.15	11.10	13.02	14.89

B. Bottom loss model

A simple analytical model can explain the relationship between profile shape and the bottom grazing angle of arrivals along the pulse. Due to the fixed geometry of the experiment, the bottom grazing angles of RBR paths are defined by the cycle distance of each particular arrival. The steep, fastest RBR arrivals turn near the surface, 6–9 times, with cycle distances of 21.11 km/6–9. The flatter, slower RBR arrivals turn nearer the receiver depth and turn 10–19 times. As long as the sound speed of the profile is linearly decreasing with depth, this relation holds true.³⁸ Cycle distance reflects the relative position (travel time) of an arrival along the pulse.

For a simple one layer constant gradient model, the cycle distance *R* is defined by Eq. (8):

$$R = \frac{2}{g} c_s \tan(\theta_s), \quad (8)$$

where c_s is the sound speed at the source depth, *g* is the channel gradient, and θ_s is the launch angle. For a source and receiver on the bottom, θ_s is the bottom grazing angle and c_s is the sound speed at the channel bottom. Solving for θ the relationship between gradient and bottom grazing angle is evident:

$$\theta = \tan^{-1} \left(\frac{Rg}{2c_s} \right). \quad (9)$$

For a fixed cycle distance *R*, small changes in gradient ($\pm 0.05/s$) can shift theta dramatically (± 4.0 deg) while changes in c_s (profile translations) have only a minor effect.

The data from M165 can be used to give some quantitative bounds to the degree of bottom grazing angle change that occurred during the experiment. The mid-channel sound-speed gradient (between 100 m and 202 m) has an average of 0.249/s with a standard deviation of 0.044/s. Extreme maximum and minimum values were 0.338/s and 0.102/s. Bottom grazing angles computed for cycle distances of 21 110.0/6, 21 110.0/7, 21 110.0/8, and 21 110.0/9 are shown in Table I and show the relationship between channel gradient and bottom grazing angle. Stronger/weaker gradients cause ray paths with fixed cycle distances to turn higher/lower in the channel with larger/smaller bottom grazing angles. The sound-speed profile, however, is far better approximated by a two-layer gradient model.

To interpret a two-layer model correctly, one must first understand how profile shape varies over time. In Fig. 10(a), the depth averaged channel gradient is plotted versus the depth averaged sound-speed anomaly from the first 18 days

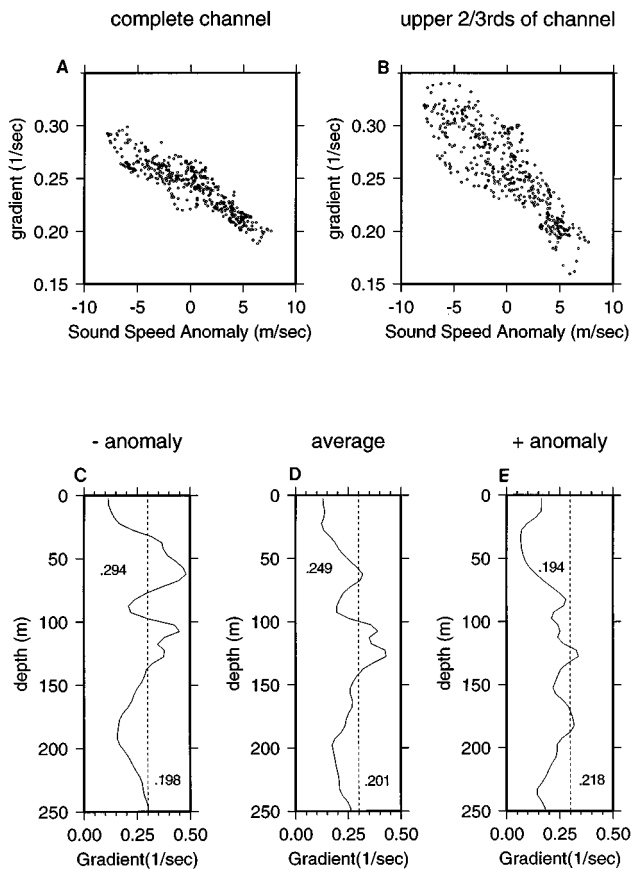


FIG. 10. Relationship between channel gradient and sound-speed anomaly over the first 18 days of August 1983. (a), (b) Negative/positive sound-speed anomalies cause stronger/weaker sound-speed gradients in the upper two-thirds of the channel. (c), (e) Gradient profiles typical of \pm anomalies >4 m/s. (d) The gradient profile for average profiles (zero sound-speed anomaly). Depth averaged gradient for lower third and upper two-thirds of gradient profile are shown next to profiles.

of the experiment. Figure 10(b) shows a similar result computed for the upper two-thirds of the channel. Negative anomalies cause stronger channel gradients and positive anomalies cause weaker channel gradients, especially in the upper two-thirds of the channel. During the last 12 days of the experiment, this relationship still holds true, but not to the extent as is clearly defined in Fig. 10(a) and (b).

With negative anomalies, the sound-speed profile becomes more convex. Strong sound-speed gradients ($>0.40/s$) occur in the upper two-thirds of the channel and weaker than average sound-speed gradients occur in the lower third of the channel. The gradient profile corresponding to negative sound-speed anomalies, stronger than -4 m/s, is shown in Fig. 10(c). To describe the profile as “more convex” is of course an oversimplification of the actual oceanographic processes involved. For the purpose of our bottom loss model, “more convex” is meant to describe how the gradient in the upper two-thirds of the channel strengthens, while the gradient in the lower third of the channel weakens during negative sound-speed anomalies.

With positive sound-speed anomalies the profile becomes almost linear (slightly concave) and weaker gradients in the upper two-thirds of the channel are formed ($<0.1/s$)

TABLE II. Bottom grazing angles are computed using Eq. (10) for a two-layer, linear gradient model. Values for g_2 and g_1 appear at the top of each column where g_2 is the gradient in the upper two-thirds of the channel and g_1 is the gradient in the lower third of the channel. g_2 and g_1 are computed from the calculated oceanography.

Range/N	Range=21 110.0 m			$\leftarrow g_2/g_1$
	Concave profile 0.175/0.255	Average profile 0.249/0.181	Convex profile 0.323/0.107	
$N=6$	12.98	15.58	19.00	
$N=7$	11.63	13.13	15.70	
$N=8$	10.70	11.14	12.85	
$N=9$	10.10	9.29	9.87	

along with slightly stronger gradients in the lower third of the channel [Fig. 10(e)]. The gradient variation in the upper two-thirds of the channel is in fact close to 180-deg out-of-phase with the gradient variation in the lower third of the channel ($cc = -0.71$ for the first 18 days and -0.65 overall). This same effect is also evident in the measured gradient time series from Fig. 5(c) ($cc = -0.55$ for the first 18 days and -0.45 overall). Therefore the change in profile shape over time can be characterized as varying between strongly convex during negative sound-speed anomalies, and slightly concave during positive anomalies.

We can extend our model to two gradient layers using Eq. (10) to show³⁹ the same relationship exists between channel gradient and bottom grazing angle for a two-layer model;

$$\tan(\theta_b) = 1/(1-f^2) \times \{d \pm f[d^2 + ((1-f^2) \times (1-k^2))]^{1/2}\}. \quad (10)$$

d is defined as $g_1 R/2c_1$, f is defined as $(g_1/g_2) - 1.0$, and k is defined as c_2/c_1 , where g_1 and g_2 are the gradients in the lower third and upper two-thirds of the channel, c_1 is the sound speed at the bottom of the channel, and c_2 is the sound speed at the layer interface. In this case we use the calculated oceanography to compute average and standard deviation of the gradients g_1 ($\mu = 0.181/s$, $\sigma = 0.0368/s$) and g_2 ($\mu = 0.249$, $\sigma = 0.0371$). In Table II the bottom grazing angles for the average profile and profiles 2 s.d. toward convex and two s.d. toward concave are computed. Again the same effect is observed as in the one-layer model.

The fastest arrivals integrate the upper two-thirds of the channel and a stronger gradient there causes steeper bottom grazing angles and more bottom loss. A weaker gradient in the upper two-thirds of the channel causes smaller bottom grazing angles and less bottom loss. Surface grazing arrivals travel through the entire upper two-thirds of the channel and are most affected by the process described here.

Late main peak arrivals integrate just the lower third of the channel and are affected only by gradient changes in the lower third of the channel. Notice in Table II, for $N=9$ and a concave profile, bottom grazing angle is increased due to the strong gradient in the lower third of the channel.

The cycle distances in Tables I and II represent the family of arrivals that integrate the upper two-thirds of the channel and make up the front end of the pulse. In each case, the bottom grazing angles for above average gradient strength,

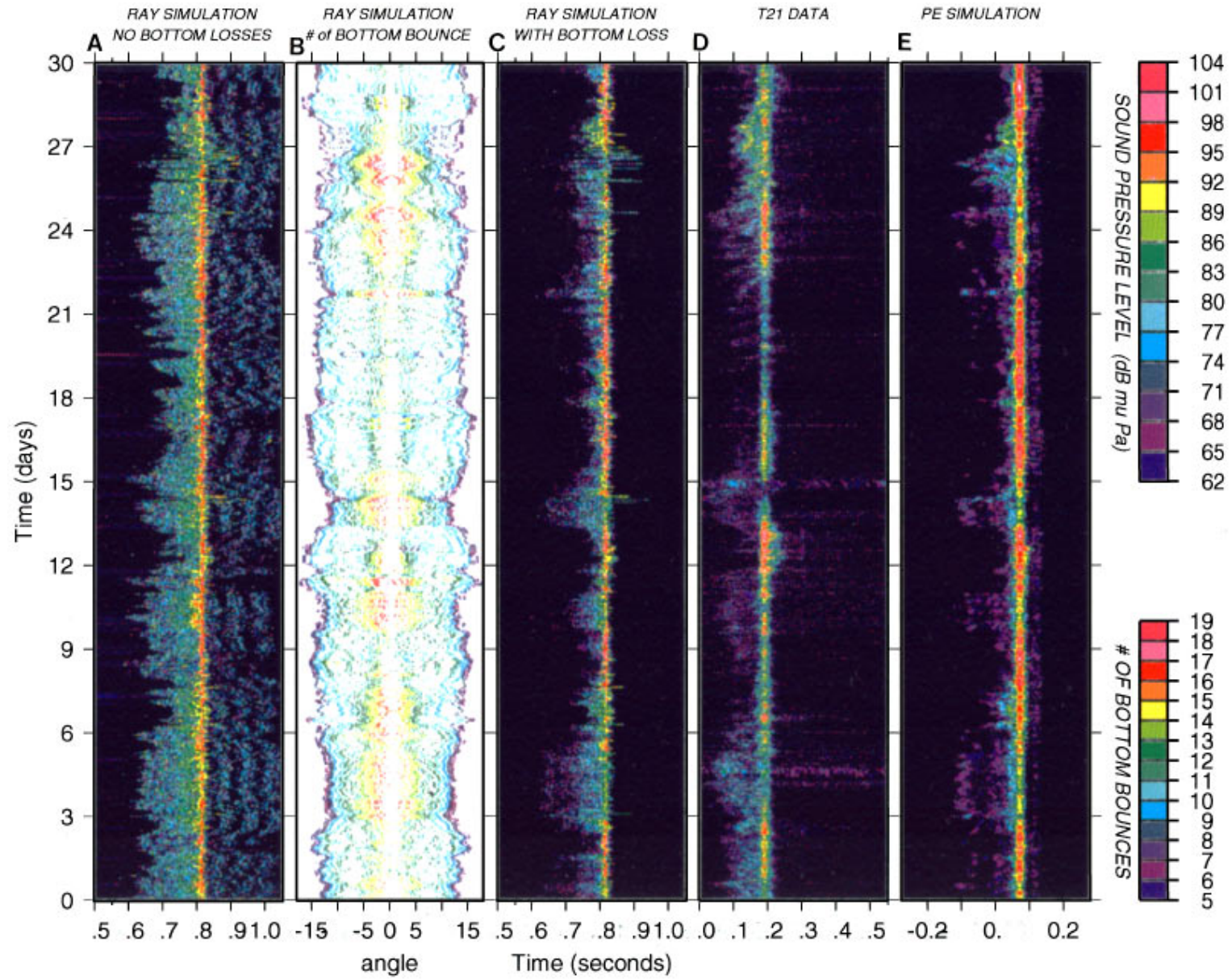


FIG. 11. Comparison of modeling results to the acoustic data. Figure shows computed hourly pulse responses for the entire month of August, against the observed pulse responses collected every 12 mins. (a) Ray results with no bottom loss. (b) Number of bottom interactions for all eigenrays excluding SRBR arrivals. (c) Ray results with angle-dependent bottom loss. (d) Acoustic pulse data. (e) UMPE results using the same inputs as the ray results. The color scale in result (a) is shifted 20 dB to account for the lack of bottom losses.

TABLE III. Pulse width statistics from data and model simulations. Model simulations with bottom loss agree with data.

Pulse width time series	Average pulse width (ms)	s.d.	Ratio μ/σ
	μ	σ	
Measured	117.4	41.9	0.36
MEDUSA no bottom loss	155.1	30.1	0.194
MEDUSA with bottom loss	129.2	36.3	0.28
UMPE	123.4	37.5	0.30

approach or exceed 15 deg, which is near the critical angle for this area (~ 15.25 deg). The stronger gradient increases the bottom grazing angle of faster RBR arrivals and thus higher bottom loss (and a smaller appearing pulse width) is observed.

Flatter arrivals (late main peak energy) integrate just the lower third of the channel and no information about the channel below 202 m is available from mooring M165. However, bottom grazing angles for flat arrivals are generally less than 9 deg, using Eq. (9) with $g=0.20/s$ and $N=10-16$. These angles are considerably smaller compared to critical and bottom loss variability due to a change in bottom grazing angles is unlikely. However, there is considerable modulation of the amplitude of the late main peak. We turn to range-dependent acoustic models to extend our model to a more realistic environment.

IV. MONTH LONG RESULT

Hourly pulse responses for the entire month of August were computed with both MEDUSA and UMPE models⁴⁰ using the calculated oceanography as input. In Fig. 11(a)–(e) the 30-day data and calculated pulse responses are displayed in a color contour plot, to compare both pulse widths and late main peak amplitudes. The pulses have been aligned along their late main peaks to emphasize pulse width variability. Figure 11(b) shows bottom interaction information from the MEDUSA result. The statistics and related errors of the model results are tabulated in Tables III and IV, to aid in the comparison to data.

In Fig. 11(a) and (c), pulse responses predicted by the MEDUSA model are displayed. Pulse responses are computed from travel times, boundary attenuations, and phase changes due to caustics and bottom interactions in the same way as in Ref. 12 [Eqs. (7)–(11)]. Thus the constructive and destructive interference along the pulse is accounted for to the extent that a simple ray model is capable of doing so.

In Fig. 11(a) bottom loss is not included in the pulse response computation. Transmission loss (TL) and surface losses have been accounted for, along with phase changes due to caustics. This result does not match the measured data [Fig. 11(c)]. Sound-pressure levels are too high and even SRBR arrivals are predicted above the noise floor. The predicted average pulse width is too large, the standard deviation is far too small, and the errors are very high (Tables

TABLE IV. Pulse width time series correlations and errors. Model simulations with bottom loss have smaller errors and higher correlation to measured pulse width time series. Results over the first 18 days are far superior to results over the latter 12 days. AE: Average error (ms). APE: Average percentage error. CC: Correlation coefficient.

Model result	First 18 days			Last 12 days			30 days overall		
	AE	APE	CC	AE	APE	CC	AE	APE	CC
MEDUSA no bottom losses	38.5	38.3	0.582	44.5	57.7	0.24	40.6	45.9	0.45
MEDUSA with bottom losses	20.5	19.07	0.761	31.45	42.2	0.35	25.0	28.5	0.62
UMPE	19.8	18.0	0.757	25.90	32.6	0.597	23.8	34.2	0.717

III and IV). Pulse width variation computed by MEDUSA without bottom loss does not match the data.

When bottom losses are included [Fig. 11(c)] the results are improved dramatically. The MEDUSA model keeps track of grazing angle and sound speed on the channel bottom for each bottom interaction. Bottom loss is determined using bottom loss curves computed by the SAFARI program,⁴¹ Fig. 12. SRBR arrivals are now attenuated below the noise level, and pulse width statistics are greatly improved (Tables III and IV). The correlation coefficient between measured and predicted pulse width over the first 18 days is high (0.761). Error is greatly reduced, especially for the first 18 days. Over the final 12 days, the errors increase and correlation is lower but overall results are generally good. Including bottom losses improves the ray model prediction for pulse width.

The PE results [Fig. 11(e) and Tables III and IV], verify the ray results and are in fact a better match to data in some instances. Errors for the first 18 days are smaller and overall results are improved as well (Tables III and IV). In some way the PE result does not degrade in the final 12 days to the extent seen in the ray result. We would expect a full wave model such as UMPE to predict the pulse responses more

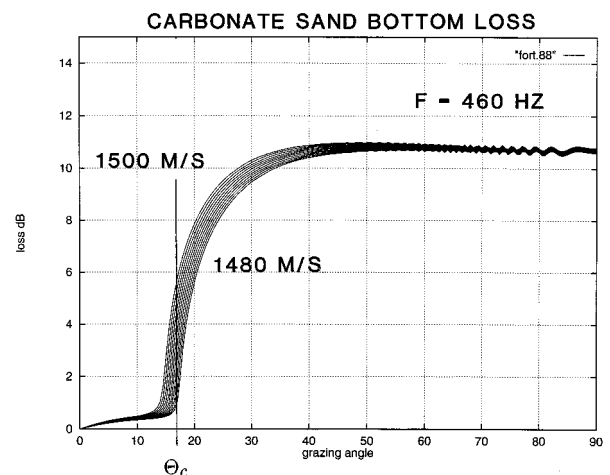


FIG. 12. Bottom loss curves computed with the SAFARI model for different ocean soundspeeds. Sound speed at the ocean bottom is varied to show the large change in loss to a bottom interaction near the critical angle.

precisely than the frequency independent ray model. Full wave models are not dependent on travel times to compute the phasing of the multipath arrivals. Models which include angle-dependent bottom losses improve the prediction of the pulse width variation.

The prediction of late main peak amplitude variability is also improved by including bottom losses. In the data [Fig. 11(d)] the late main peak amplitude is seen to fade in and out and changes of 30 dB over time scales of a few days is common (days 12–17). Furthermore, larger/smaller pulse widths correlate with lower/higher late main peak amplitudes, especially during the initial eighteen days. In the MEDUSA prediction without bottom losses [Fig. 11(a)] the late main peak amplitude is quite uniform over time, with less variability than the observed late main peak. When bottom losses are included, amplitude fades on the order of 6–10 dB are observed in the ray prediction [Fig. 11(c)]. The correlation between wider pulses and lower late main peak amplitudes is now correctly predicted. Somehow bottom losses appear to modulate both pulse width and to a much lesser extent late main peak amplitude.

The variation of the amplitude of the late main peak in the PE result matches the MEDUSA result quite well ($cc=0.845$). However, the predicted amplitude fades are not as strong as the observed amplitude fades. Both ray and PE results show the correspondence between wide/short pulses and weaker/stronger late main peaks [Fig. 11(c) and (e)]. This correspondence seems to also occur in the data [days 4.5, 14, 12, and 17, Fig. 11(d)]. The larger observed amplitude fades imply that processes other than bottom loss dominate late main peak amplitude variability.

Both models, which include bottom losses, predict the pulse variability seen in the data far better than without bottom losses. Agreement between model and measured pulse width is very good over the first 18 days when the channel is more barotropic. Bottom losses in some way seem to be controlling pulse width variability and perhaps late main peak amplitude. Next bottom grazing angles are considered as a possible mechanism.

In Fig. 11(b) MEDUSA results for the number of bottom interactions (excluding SRBR) are plotted as a function of average bottom grazing angle and time. The eigenrays have been separated into rays with positive and negative launch angles for clarity. The figure shows the angular structure of the propagation over the course of the 30-day experiment. The grazing angle of arrivals with six, seven, and eight bottom interactions (surface grazing arrivals) is seen to vary much like the pulse width in Fig. 11(c). Wider pulses are associated to smaller bottom grazing angles and thinner pulses are associated to larger bottom grazing angles. For example, during days 12–17 the bottom grazing angle of arrivals with seven bottom bounces is ~ 17 deg, decreases to ~ 11 deg at day 14, and increases back to 16 deg by day 17. Pulse width has a corresponding change from 40 ms, to 200 ms, and back down to 50 ms. Figure 11(b) and (c) are both MEDUSA results which explains the near-perfect correspondence between pulse width and bottom grazing angle. In Fig. 13, model generated grazing angles are compared to pulse

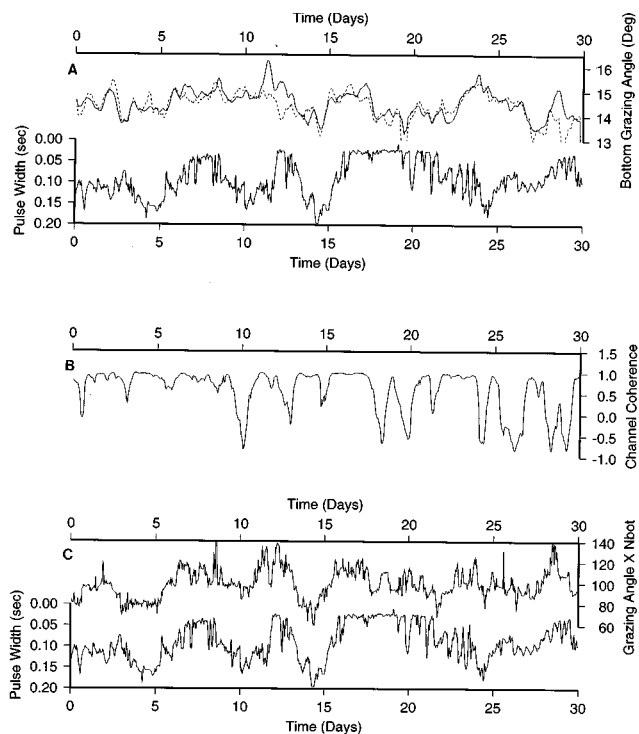


FIG. 13. Comparison of overall pulse width from data, to steep bottom grazing angles computed from ray and PE models. (a) Smoothed ray and PE angles versus pulse width in seconds. The solid line is the MEDUSA result, the dotted line the UMPE result. (b) 12-h "channel coherence" computed from mooring M165 thermistor time series. (c) Normalized steep bottom grazing angles (angle \times bottom bounces) versus pulse width in seconds. Agreement between time series is good if channel coherence is high.

width data to give a more quantitative idea of the association between pulse width and grazing angle.

Arrival angles and bottom grazing angles are outputs of the ray model. The broadband PE results at multiple depths were beamformed and the arrival angle of incoming energy along a pulse at the receiver depth was calculated. Bottom grazing angles could then be inferred using Snell's law. In Fig. 13(a), the average bottom grazing angle of all fast paths (front 25 ms of pulse) for both ray and PE predictions is plotted against pulse width. This allows us to compare grazing angle results from both models to the data. The PE and ray predictions for grazing angle differ in some instances (near day 11) because during extremely high bottom loss (high grazing angle) the beamform of the PE result cannot resolve angles for arrivals with very high attenuation. This degrades the correlation between the two model generated time series. The correlation coefficient between the two time series is 0.77 and average error is less than 0.27 deg with an average percentage error of less than 2%. The PE grazing angle time series serves to verify the ray result.

At first glance the measured pulse width time series, plotted below the grazing angle time series, does not correlate with the grazing angle time series to a high degree. Again the time series are 12-h low passed to remove short time scale variability. For the first 18 days there is only partial correlation between the time series, $cc = -0.42$; after day 18 the correlation is even lower and out-of-phase ($cc = +0.33$) and overall (30 day) the correlation coefficient is

-0.04. We would expect large negative correlation between pulse width (0.0–200 ms) and bottom grazing angle (17–13 deg) if there were some dependence between the two time series.

For a better indication of the total bottom loss to the steep arrivals, bottom grazing angle is multiplied by the number of bottom bounces and replotted against pulse width in Fig. 13(c). Now only the ray angles are plotted. The correlation between curves is improved (correlation = -0.74 for first 18 days, -0.17 for the last 12 days, and -0.55 overall), which indicates that the average number of bottom interactions in the front 25 ms of the pulse varies with time and must be accounted for. The time series in Fig. 13(c) is a far better indicator of steep arrival bottom loss than the time series in Fig. 13(a) because the number of bottom interactions has been included. Clearly pulse width varies with steep arrival bottom loss especially during the first 18 days. The cause for the lower correlation between curves over the latter 12 days is still uncertain.

The lower correlation between curves in Fig. 13(c) during the latter 12 days of the experiment may be a consequence of the more complex oceanography during that period. In Fig. 13(b) a time series of the “lower channel coherence” is generated by computing a running 12-h correlation coefficient between the lower two thermistors from M165. This time series is intended to show the relative complexity of the temperature profile with time. A large correlation coefficient shows the temperature time series are in phase and a simple sound-speed profile exists. A lower correlation coefficient shows the temperature time series are less in phase and a more complex sound speed profile exists. During the last 12 days the correlation drops as the normally barotropic temperature field becomes unstable (more baroclinic). This less barotropic oceanography may cause the lower correlation between pulse width and bottom loss over the latter 12 days of the experiment. Phase interference effects may dominate when the channel is baroclinic.

When the sound-speed profile becomes highly distorted, phasing of the arrivals may control pulse width variability. The pattern of the incoming eigenrays is changed. Normally, for a simple near linear profile, steep arrivals are separated from flat arrivals in time. If the sound-speed profile becomes highly distorted (layer of near-zero gradient) the steep and flat arrivals can overlap in time. Phase interactions occur between flat and steep arrivals which are normally separated by travel time. Destructive/consecutive interference may dominate pulse width variability in these cases. However, the occurrences of zero gradient layers is rare. The sound-speed profile does have sustained periods of thick, weak gradient layers in the latter 12 days of the experiment, and a zero gradient layer is approached on several occasions (Fig. 8 isotherms come together for days 19–24 in the lower third of the channel).

Another possibility is that the lower correlation between pulse width and bottom grazing angle over the final 12 days is due to a less accurate calculation of the actual sound-speed profile. For the last 12 days the sound-speed profile shape is more complicated and four EOFs are not sufficient to accurately describe the profile. In this case while the EOF proce-

dures is reliable mid-channel (Fig. 7), the important interpolated surface and bottom sound speeds may not be accurate. Problems in the calculated oceanography near the bottom is also made evident by the poor prediction of late main peak amplitude during the last 12 days.

The lower correlation between pulse width and bottom loss in the later 12 days may also be due to the degradation of the sound-speed anomaly versus channel gradient relationship. In Fig. 10 this relationship is clearly defined for the first 18 days. After day 18 the relationship becomes less defined and the data clouds have smaller slopes. The slope change will affect the magnitude of pulse width variation. Recall the correlation between the measured pulse width and measured sound speed at 100 and 153 m degrades from ~ 0.75 in the first 18 days to ~ 0.15 in the final 12 days. This implies that some process independent of the EOF analysis is causing the lower correlation between pulse width and bottom loss. As discussed earlier the correlation between measured sound speed time series (at 100, 153, and 202 m) also degrades from ~ 0.80 in the first 18 days down to ~ 0.45 in the final 12 days. It is clear the sound-speed field during the final 12 days is more random than during the initial 18 days. Whether this is the cause for the loss of correlation between pulse width and steep path bottom loss is not clear.

For the first 18 days of the experiment, however, pulse width variability depends on bottom loss variability. To understand how the bottom losses can change over such short time scales one must consider the shape of the angle-dependent bottom loss curve. Figure 12 shows typical bottom loss curves for a carbonate sand bottom as computed by the SAFARI model using the geoacoustic parameters discussed in Sec. 1C. The leftmost curve has an ocean bottom sound speed of 1500 m/s, the rightmost curve 1480 m/s. The critical angles lie somewhere in the steepest region of the curves at approximately 15.5 deg. Surface grazing paths predicted by ray and PE models have a bottom grazing angles around 15.5 deg. Clearly a small change in angle, near 15 deg, can cause large bottom loss variations.

The mechanism controlling bottom loss is twofold. First, for paths with bottom grazing angles near 15.5 deg, sound-speed variation at the ocean bottom will shift the bottom interaction back and forth through the critical angle. For surface grazing paths, loss can increase by as much as 4.0 dB per bounce for a sound-speed change of 20 m/s (Fig. 8, days 11–15).

Second, profile shape (i.e., a gradient change in the upper two-thirds of the channel) can either change the angle of bottom interaction for a particular ray path (fixed cycle distance), or a new/old path can be added/lost. The addition/loss of a path, however, is a smaller effect on pulse width than the change in bottom grazing angle [Fig. 11(b)]. As the gradient between source and surface increases, rays with fixed cycle distances (for example, seven turns at 21.11 km) turn higher in the water column and have steeper interaction angles with the bottom. If the gradient becomes strong enough, the seven RBR turn path may be lost altogether (becomes SRBR or mixed). For weaker gradients above the source/receiver, the rays turn deeper in the water column and have flatter interaction angles. In this case a six turn, surface grazing RBR

path may be created. As the profile shape changes, the bottom grazing angle of ray paths with fixed cycle distances can be shifted by as much as 5 deg [from 11 to 16 deg for 7 turn paths; days 12–14, Fig. 11(b)]. Such a change can increase bottom loss by 4.0 dB per bounce. While there is a high degree of bottom loss variability for RBR paths with bottom grazing angles near critical (front end of pulse), bottom loss variability decreases along the pulse as bottom grazing angles get smaller, and the slope of the bottom loss curve becomes flatter.

For ray paths that make up the late main peak (5–8 deg bottom grazing angle) the slope of the bottom loss curve is flat. Even changes in bottom grazing angle on the order of 2–3 deg should have only a slight effect on late main peak amplitude. However, in the model simulations [Fig. 11(c)] amplitude variations of 3.0–6.0 dB are formed if bottom losses are included.

Still, variations of the predicted late main peak amplitude can be explained in part by bottom loss. In this case the 3–6 dB change in intensity of the late main peak is caused not by variation in bottom grazing angle, but by the gain or loss of paths due to gradient changes in the lower third of the channel. The MEDUSA result [Fig. 11(b) and (c)] suggests that weaker/stronger late main peak amplitude occurs when the set of eigenrays in the late main peak includes paths with a larger/smaller number of bottom interactions caused by a stronger/weaker gradient in the lower third of the channel. Higher intensity late main peaks are made up from deep turning paths with 10–14 bottom bounces [weaker gradient in the lower third of the channel; Figs. 5(c) and 11(b)], while lower intensity late main peaks are made up from deep turning paths with 15–20 bottom bounces (stronger gradient in the lower third of the channel). At these low angles ten extra bottom bounces can account for a total of 4.0–6.0 dB more bottom loss. This could account for part of the late main peak amplitude variation seen in the data in some instances [days 12–17, Fig. 11(c)].

However, the observed amplitude variation of the late main peak is dominated by some other process not related to bottom loss. Somehow amplitude variations on the order of 30 dB are realized. This could be the result of destructive/constructive interference occurring among the 15 plus arrivals which make up the late main peak.

Sound-speed gradient changes affect the amplitude of both the steeper eigenrays in the broad early plateau of the pulse, and to a lesser degree the flatter eigenrays in the late main peak. The amplitude of the steep eigenrays is modulated by variation of the bottom grazing angle near critical due to gradient changes in the upper two-thirds of the channel. The amplitude of the late main peak is modulated in part by variation of the number of bottom interactions due to gradient changes in the lower third of the channel.

V. DISCUSSION AND CONCLUSIONS

Variation of bottom-limited shallow water transmissions is controlled by many factors, but bottom loss appears to be a dominant effect on pulse width. In coastal areas where the geology is such that the critical angle is near the angle of bottom interaction, this effect will dominate. It is not neces-

sary for the interactions to pass back and forth through the critical angle, just that the interactions approach the critical angle with a sufficient number of bottom interactions. Bottom loss can also affect the amplitude of the late main peak significantly, provided the bottom is somewhat lossy for bottom interactions far below critical. In this case the number of bottom interactions can change by as much as 10 with a gradient change in the lower channel, and an extra 3–6 dB bottom loss can be realized.

Bottom loss to both steep and flat arrivals is varied by soundspeed gradient changes in the channel. The angular structure of the propagation is altered by the ocean medium. In this study, range-dependent models were used, thus mode theory has not been addressed. Yet the bottom loss effects discussed here can be explained in terms of modes.

The amplitude of modes in shallow water channels are dominated by two main effects. The first effect is attributed to the randomness of the medium (internal waves) and range dependence (profile shape over range) which cause mode coupling. In this case, the mode amplitudes tend to equilibrate. The second effect is attributed to the preferential sediment penetration by the higher angle modes. In this case the higher angle modes tend to become completely attenuated by the bottom (i.e., mode stripping). These two effects are in competition.⁴² Mode coupling allows low mode energies to be shifted into higher modes, which are subsequently stripped away by bottom loss. An energy sink exists which facilitates attenuation to all angles of propagation. Conversely, medium changes (profile shape) can modulate the degree-of-mode stripping to the higher modes, which in turn modulates how much energy is lost from the low modes (i.e., the sink intensity is modulated). We can also speculate that profile shape variation can modulate the degree of mode coupling between low angle and high angle modes.

In this study the 12-h averaging has removed the effects due to internal waves. Mode coupling still occurs due to the range dependence of the sound speed field. The pulse width modulation observed here can be explained in terms of a modulation of the degree-of-mode stripping to the higher modes. The late main peak modulation might be explained in terms of a modulation of the degree-of-mode coupling between low angle and high angle modes.

In the case of thinner appearing pulses (convex profile), stronger gradients in the upper channel cause the higher modes to become better coupled to the bottom (i.e., a shift in angle up to more SRBR-type propagation). At the same time the weaker gradients in the lower channel cause a shift down in angle and the lowest modes become less coupled to the bottom. As the surface grazing modes shift up in angle and the deep turning modes shift down in angle, mode coupling between the two may decrease. Thus a short pulse width is observed with a more intense late main peak amplitude.

In the case of wider appearing pulses, weaker gradients in the upper channel cause the higher modes to decouple from the bottom (i.e., a shift in angle down away from SRBR-type propagation). At the same time the stronger gradients in the lower channel cause a shift up in angle and the lowest modes become better coupled to the bottom. As the surface grazing modes shift down in angle and the deep turn-

ing modes shift up in angle, mode coupling between the two may increase. Thus a large pulse width is observed with a less intense late main peak amplitude.

In both cases modulation of the energy sink (i.e., degree-of-mode stripping) is the dominant effect on pulse width. In the latter 12 days of the experiment, however, mode stripping may not be the dominant effect. During this period increased range dependence of the medium may dominate and mode energies would be equilibrated. A more uniform pulse width would be realized. We can only speculate as to mechanism behind the modulation of the late main peak intensity.

During the latter 12 days of the experiment, pulse width variability appears to be less affected by angle-dependent bottom loss. The sound-speed field becomes far more complicated and range dependent. This can degrade the relationship between sound-speed anomaly and channel gradient, degrade the accuracy of the EOF analysis, or simply make the phasing of eigenray arrivals the dominant effect controlling pulse width. We believe the lower correlation between pulse width and bottom loss is most likely due to a combination of the first two effects and not destructive interference effects.

In conclusion, we have identified a deterministic and predictable feature of shallow water, bottom-limited propagation which at first appeared random and unknowable. Gradient variations in the channel change the angular makeup of the propagation and bottom loss for the steeper paths is varied. For a single hydrophone experiment such as this one, it may in fact be possible to use pulse width to predict the soundspeed profile by inversion. If the geoacoustic properties are known and a fixed bottom loss curve is assumed, then pulse width is a measure of the degree-of-bottom loss to the steeper arrivals (i.e., the angle of bottom interaction; i.e., the effective gradient between source and surface). If a vertical hydrophone array is used, then the angles of propagation can be determined directly from a beamform of the data, which would yield sound-speed gradients and sound speeds through inversion. Of course some time expansion/contraction of the pulse is occurring and phasing of the arrivals may dominate when the channel is baroclinic. These factors must be quantified before an inversion could be attempted.

ACKNOWLEDGMENTS

This research was supported by the Office of Naval Research through the Ocean Acoustics Program. The Acoustic moorings were designed Niel Williams. Our thanks to Fred Tappert and Kevin Smith for supplying the UMPE model. We thank D. S. Ko for supplying the EOF analysis code. We thank the SACLANT Undersea Research Center for supplying the SAFARI model. The oceanographic data were supplied by Fritz Schott, Tom Lee, and Peter Vertes.

¹H. A. DeFerrari, R. I. Davis, H. B. Nguyen, R. F. Tusting, and N. J. Williams, "Measurements of transmission fluctuations at three ranges for refracted paths through the deep ocean," *J. Acoust. Soc. Am.* **74**, 1448–1463 (1983).

²R. P. Porter and R. C. Spindel, "Low frequency acoustic fluctuations and internal gravity waves in the ocean," *J. Acoust. Soc. Am.* **61**, 943–958 (1977).

³W. H. Munk and F. Zachariasen, "Sound propagation through a fluctuat-

ing stratified ocean: Theory and observations," *J. Acoust. Soc. Am.* **59**, 818–838 (1976).

⁴S. M. Flatte, *Sound Transmission Through a Fluctuating Ocean* (Cambridge U. P., Cambridge, 1979), p. 45.

⁵D. F. Gorden, "Multipath interference nulls in long-range, low frequency, acoustic propagation by normal modes," *J. Acoust. Soc. Am.* **67**, 106–120 (1980).

⁶L. Boden, J. B. Bowlin, and J. L. Spiesberger, "Time domain analysis of normal mode, parabolic and ray solutions to the wave equation," *J. Acoust. Soc. Am.* **90**, 954–958 (1991).

⁷J. L. Spiesberger, E. Terray, and K. Prada, "Successful ray modeling of acoustic multipaths over a 3000 km section of the pacific," *J. Acoust. Soc. Am.* **95**, 3654–3657 (1994).

⁸C. J. R. Garrett and W. H. Munk, "Space-time scales of internal waves," *Geophys. Fluid Dyn.* **2**, 225–264 (1972).

⁹I. Tolstoy and C. S. Clay, *Ocean Acoustics: Theory and Experiment in Underwater Sound* (McGraw-Hill, New York, 1966), Chap. 4.

¹⁰R. H. Ferris, "Comparison of measured and calculated normal mode amplitude functions for acoustic waves in shallow water," *J. Acoust. Soc. Am.* **52**, 981–988 (1972).

¹¹K. D. Leaman, R. L. Molinari, and P. S. Vertes, "Structure and variability of the Florida Current at 27 °N: April 1982–July 1984," *J. Phys. Oceanogr.* **17**, 565–583 (1987).

¹²H. A. DeFerrari and H. B. Nguyen, "Acoustic reciprocal transmission experiments, Florida Straits," *J. Acoust. Soc. Am.* **79**, 299–315 (1986).

¹³M. P. Wennkens, "Water mass properties of the Straits of Florida and related waters," *Bull. Mater. Sci.* **9**, 1–52 (1959).

¹⁴H. Stommel, *The Gulf Stream* (University of California, Berkeley, CA, 1965), pp. 242–245.

¹⁵W. E. Johns and F. Schott, "Meandering and transport variations of the Florida Current," *J. Phys. Oceanogr.* **17**, 1128–1147 (1987).

¹⁶F. A. Schott, T. N. Lee, and R. Zantopp, "Variability of structure and transport of the Florida Current in the period range of days to seasonal," *J. Phys. Oceanogr.* **18**, 1209–1230 (1988).

¹⁷D. A. Brooks and C. N. K. Mooers, "Wind forced continental shelf waves in the Florida Current," *J. Geophys. Res.* **82**, 2569–2576 (1977).

¹⁸R. L. Molinari, W. D. Wilson, and K. Leaman, "Volume and heat transports of the Florida Current: April 1982 through August 1983," *Science* **227**, 295–297 (1985).

¹⁹T. N. Lee, F. A. Schott, and R. Zantopp, "Florida Current: Low frequency variability as observed with moored current meters during April 1982 to June 1983," *Science* **227**, 298–301 (1985).

²⁰J. C. Larsen and T. B. Sanford, "Florida Current volume transports from voltage measurements," *Science* **227**, 302–303 (1985).

²¹F. Schott and R. Zantopp, "Florida Current: Seasonal and interannual variability," *Science* **227**, 308–311 (1985).

²²P. Spain, D. Dorson, and H. T. Rossby, "Pegasus: A simple, acoustically tracked velocity profiler," *Deep-Sea Res.* **28**, 1553–1554 (1981).

²³K. Leaman (personal communication).

²⁴B. Johns (personal communication).

²⁵Ocean Drilling Program Log, "Site 626: Straits of Florida," pp. 49–90 (1986).

²⁶R. E. Sheridan, J. T. Crosby, G. M. Bryan, and P. L. Stoffa, "Stratigraphy and structure of southern Blake plateau, northern Florida Straits, and northern Bahama Platform from multichannel seismic reflection data," *Am. Assoc. Pet. Geol. Bull.* **65**, 2571–2593 (1981).

²⁷J. D. Gassaway, "Mineral and chemical composition of sediments from the Straits of Florida," *J. Sed. Pet.* **40**, 1136–1146 (1970).

²⁸D. S. Gorsline, "Bottom sediments of the Atlantic shelf and slope off the southern United States," *J. Geology* **71**, 422–440 (1963).

²⁹R. E. Sheridan, C. L. Drake, J. E. Nafe, and J. Hannon, "Seismic-refraction study of continental margin east of Florida," *Bull. Am. Assoc. Pet. Geol.* **50**, 1972–1991 (1966).

³⁰E. L. Hamilton, "Geoacoustic modeling of the seafloor," *J. Acoust. Soc. Am.* **68**, 1313–1340 (1980).

³¹T. Yamamoto, A. Turgut, M. Schulkin, and R. Bennett, "Geoacoustic properties of the seabed sediment critical to acoustic reverberation at 50 to 500 Hz: A preliminary data set," TR-91-001, RSMAS, University of Miami (1991).

³²J. L. Stewart, W. B. Allen, R. M. Zarnowitz, and M. K. Brandon, "Pseudorandom signal-correlation methods of underwater acoustic research I: Principles," *J. Acoust. Soc. Am.* **37**, 1079–1090 (1965).

³³J. S. Bendat and A. G. Piersol, *Random Data: Analysis and Measurement Procedures* (Wiley-Interscience, New York, 1971), p. 62.

- ³⁴W. Menke, *Geophysical Data Analysis: Discrete Inverse Theory* (Academic, New York, 1984), p. 41.
- ³⁵R. W. Preisendorfer, F. W. Zwiers, and T. P. Barnett, Foundations of principal component selection rules. SIO Ref. Ser. 81-4., Scripps Institute of Oceanography (1981).
- ³⁶L. R. LeBlanc and F. H. Middleton, "An underwater sound velocity data model," J. Acoust. Soc. Am. **67**, 2055–2062 (1980).
- ³⁷T. L. Foreman, Ray Modeling Methods for Range Dependent Ocean Environments, Rep. ARL-TR-83-41, Applied Research Laboratories, University of Texas at Austin (1983).
- ³⁸M. J. Jacobson, "Analysis of spreading loss for refracted/reflected rays in constant-velocity-gradient media," J. Acoust. Soc. Am. **36**, 2298–2304 (1964).
- ³⁹H. A. Deferrari, "Time-varying multipath interference of broadband signals over a 7-NM range in the Florida Straits," J. Acoust. Soc. Am. **53**, 162–180 (1973).
- ⁴⁰K. B. Smith and F. D. Tappert, "UMPE: The University of Miami Parabolic Equation Model, Version 1.0," MPL Technical Memorandum 432 (May 1993).
- ⁴¹H. Schmidt, SAFARI: Seismo-Acoustic Fast Field Algorithm for Range Independent Environments, Rep. SR-113, SACLANT Undersea Research Center, La Spezia, Italy (1988).
- ⁴²D. B. Creamer, "Scintillating shallow-water waveguides," J. Acoust. Soc. Am. **99**, 1–14 (1996).

Far-field acoustic holography onto cylindrical surfaces using pressure measured on semicircles

Andrew N. Norris

Department of Mechanical and Aerospace Engineering, Rutgers University, Piscataway, New Jersey 08855-0909

(Received 25 April 1997; revised 7 July 1997; accepted 8 July 1997)

A simple formula was recently proposed by Williams [J. Acoust. Soc. Am. **99**, 2022–2032 (1996)] for imaging pressure and velocity on a vibrating circular cylindrical shell using the far-field pressure measured along a meridional semicircle. The method is examined and some new results are obtained. The procedure is generalized to handle cylindrical surfaces of noncircular but convex cross section. It is demonstrated that Williams' formula predicts a supersonic surface intensity which gives the same meridional energy flux as the exact radiated far-field pressure. A modification of Williams' formula is suggested which uses pressure data from several neighboring semicircles, although complete spherical coverage is not required. The modified imaging formula is based upon the first two terms in an asymptotic expansion in the dimensionless wave number. The leading-order term yields the original formula, and the second term results in a boundary layer type of correction in the circumferential direction. Numerical examples are presented which compare the exact supersonic acoustic intensity on a cylinder with that from the original and the modified formula. These indicate that the circumferential on-surface resolution is significantly enhanced by combining data from neighboring semicircles, even when the total far-field spherical coverage is small.

© 1997 Acoustical Society of America. [S0001-4966(97)05110-2]

PACS numbers: 43.30.Jx, 43.20.Rz, 43.40.Rj, 43.35.Sx [SAC-B]

INTRODUCTION

Acoustic holography provides a powerful tool for visualizing and understanding the vibration on a structure using pressure measured in the near or far field. Near-field data is preferred, in the sense that it includes information about the evanescent, subsonic pressure field which does not radiate to the far field. The theory and practice of near-field acoustic imaging has developed considerably in the past decade, beginning with Williams *et al.*¹ who presented the details for the specific case of the circular cylindrical geometry, including the necessary wave-number filtering. Veronesi and Maynard² subsequently described a method for reconstructing data on nonseparable surfaces using singular value decomposition. Borgiotti *et al.*³ discussed numerical applications of the SVD technique for surfaces conforming to a nonseparable closed surface, and they provided accuracy estimates based on the dynamic range of the data.

Far-field acoustic holography for cylindrical and nonseparable surfaces has received less attention. This may be ascribed to the loss in information caused by the radiation process: short wavelength or subsonic surface data does not radiate, and one is left with the filtered supersonic data. Sarkissian⁴ proposed a general scheme for reconstructing surface velocity on arbitrary surfaces from far-field data. The method relies upon impedance eigenfunctions for the surface, which form a complete and orthogonal basis for the far-field radiation pattern. This functional basis is also related to the singular value decomposition of the impedance operator.⁵ However, except for separable surfaces, the set of basis functions must be determined numerically, with increasing difficulty at higher frequencies. Furthermore, the radiation operator which maps surface data to a far-field radiation

pattern is a compact operator, and its inversion is an ill-posed process, implying that far-field reconstruction of surface data is itself an ill-posed problem.

Recently, Williams⁶ showed that a very simple but approximate technique yields surprisingly accurate imaging. The method is specifically for circular cylindrical surfaces, and uses far-field pressure data measured on meridional semicircles to image the surface pressure and velocity in the same plane. Williams provided an extensive comparison of the exact and approximate images, using simulated data and near-field versus far-field experimental data. He also showed that the imaging formula can be derived from the exact equations for the circular cylindrical geometry. Overall, the accuracy is remarkable over a wide frequency range ($ka = 0.3$ – 16.0). The only limitation is that the surface data should be bandlimited in the circumferential, or azimuthal, direction, roughly $n \leq ka/3$.⁶ However, the numerical and experimental comparisons are surprisingly good even for a point drive on the cylinder.

In this paper we will examine the imaging formula from a slightly different perspective. It will be demonstrated that the formula is a simple consequence of a high-frequency approximation. This is implicit in Williams' analysis also, but here we show how the high-frequency nature of the approximation makes it equally applicable to cylinders of arbitrary nonseparable cross section. As with many high-frequency approximations, this one also proves to be accurate for frequencies such that ka is not large, even of order unity. The approach taken here is based upon the Helmholtz surface integral, which allows us to find the leading-order asymptotic approximation for the far-field pattern function. This is derived in the next section, followed by

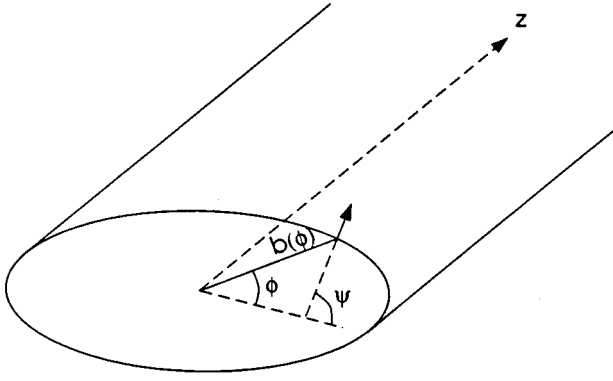


FIG. 1. The cylinder cross section and geometrical parameters.

a discussion of energy conservation. An improvement, based upon the next term in the asymptotic series, is presented in Sec. II for the specific case of a circular cylinder. The new scheme uses data from neighboring circles to give improved circumferential accuracy. Finally, the method is illustrated by examples and alternative numerical implementations are discussed.

I. THE SIMPLE IMAGING FORMULA

A. Derivation

We will work primarily with cylindrical polar coordinates $\mathbf{x}=(\rho, z, \phi)$ but also use spherical polar coordinates $\mathbf{x}=(r, \theta, \phi)$ where $r^2=\rho^2+z^2$ and $z=r \cos \theta$. The acoustic pressure is assumed to radiate from sources on or within a cylinder of constant cross section C defined by the radius $\rho=b(\phi)$ and sufficiently long in the z direction that end effects may be ignored, see Fig. 1. We assume that the cylinder cross section is convex and smooth. The far-field pattern function F is defined by

$$p(r, \theta, \phi) = \frac{e^{ikr}}{r} F(\theta, \phi) + O\left(\frac{1}{r^2}\right), \quad r \rightarrow \infty, \quad (1)$$

where $e^{-i\omega t}$ dependence is assumed. Our objective is to image the acoustic field on the cylindrical surface using F . It is well known that only those components of the surface pressure and velocity which are supersonic can radiate to the far field.⁷ Let $f(b(\phi), z, \phi)$ represent a quantity on the surface $\rho=b(\phi)$, such as pressure or velocity. It may be partitioned into supersonic and subsonic parts, $f^{(s)}(z, \phi)$ and $f^{(c)}(z, \phi)$, respectively, such that $f=f^{(s)}+f^{(c)}$ and

$$f^{(s)}(z, \phi) = \int_{-\infty}^{\infty} dz' f(b(\phi), z', \phi) \frac{\sin[k(z-z')]}{\pi(z-z')}. \quad (2)$$

The supersonic surface pressure and normal velocity on $\rho=b(\phi)$ are defined in the same way as $p^{(s)}(z, \phi)$ and $v^{(s)}(z, \phi)$, respectively. The basic formula that we will derive is for $\hat{p}^{(s)}$, which approximates $p^{(s)}$ (the hat denotes an approximant of a quantity)

$$\begin{aligned} \hat{p}^{(s)}(z, \phi) &= e^{i\pi/4} \sqrt{\frac{k}{2\pi a(\phi)}} \int_0^\pi d\theta \sqrt{\sin \theta} \\ &\times e^{ik(b(\phi)\sin \theta + z \cos \theta)} F(\theta, \psi(\phi)). \end{aligned} \quad (3)$$

Here $a(\phi)$ is the radius of curvature at the position ϕ , and the $\psi(\phi)$ is the angle for the normal, see Fig. 1. Let $l(\phi)$ denote the arclength on the curve defining the cross section, i.e., $dl/d\phi = \sqrt{b^2 + (db/d\phi)^2}$, then

$$a(\phi) = \frac{dl}{d\psi}, \quad \psi(\phi) = \phi - \tan^{-1}\left(\frac{1}{b} \frac{db}{d\phi}\right). \quad (4)$$

Equation (3) reproduces Williams' formula [Eq. (17) of Ref. 6] for the special case of a circular cylinder ($b \equiv a = \text{constant}$). Williams also obtained a simple formula for the supersonic radial velocity on the circular cylinder [Eq. (18) of Ref. 6]. The analogous result for the general cross section is

$$\begin{aligned} \hat{v}^{(s)}(z, \phi) &= \frac{e^{i\pi/4}}{\rho_f c} \sqrt{\frac{k}{2\pi a(\phi)}} \int_0^\pi d\theta (\sin \theta)^{3/2} \\ &\times e^{ik(b(\phi)\sin \theta + z \cos \theta)} F(\theta, \psi(\phi)), \end{aligned} \quad (5)$$

where ρ_f is the fluid density and $c = \omega/k$ the acoustic wave speed.

Williams⁶ derived his formulas for the circular cylinder using an exact representation for the supersonic fields in terms of the far-field pressure. Here we present an alternative derivation which does not rely upon an azimuthal modal expansion explicitly. We start with the Helmholtz integral formula of the radiated acoustic pressure in terms of the pressure and normal velocity on the cylindrical surface,

$$\begin{aligned} p(\rho, z, \phi) &= \int_C dl \int_{-\infty}^{\infty} dz' \left[p(b(\phi'), z', \phi') \right. \\ &\times \frac{\partial g}{\partial n}(\rho, z, \phi; b(\phi'), z', \phi') \\ &\left. - i\omega \rho_f v(b(\phi'), z', \phi') g(\rho, z, \phi; b(\phi'), z', \phi') \right], \end{aligned} \quad (6)$$

where $g(\rho, z, \phi; \rho', z', \phi') = (4\pi R)^{-1} e^{ikR}$, $R = |\mathbf{x} - \mathbf{x}'|$. This implies that the far-field form function has the exact representation

$$\begin{aligned} F(\theta, \phi) &= \frac{-ik}{4\pi} \int_C dl \int_{-\infty}^{\infty} dz' e^{-ik(z' \cos \theta + b(\phi') \sin \theta \cos(\phi - \phi'))} \\ &\times [\rho_f c v(b(\phi'), z', \phi') + \sin \theta \cos(\phi \\ &- \psi(\phi')) p(b(\phi'), z', \phi')]. \end{aligned} \quad (7)$$

By transforming in z , we obtain

$$\begin{aligned} F(\theta, \phi) &= \frac{-ik}{4\pi} \int_C dl e^{-ikb(\phi') \sin \theta \cos(\phi - \phi')} \\ &\times [\rho_f c V(k \cos \theta, \phi') + \sin \theta \cos(\phi \\ &- \psi(\phi')) P(k \cos \theta, \phi')], \end{aligned} \quad (8)$$

where the transforms are

$$\begin{pmatrix} P(k_z, \phi) \\ V(k_z, \phi) \end{pmatrix} = \int_{-\infty}^{\infty} dz e^{-ik_z z} \begin{pmatrix} p(b(\phi), z, \phi) \\ v(b(\phi), z, \phi) \end{pmatrix}. \quad (9)$$

The supersonic surface fields can also be expressed in terms of the z transforms as

$$\begin{pmatrix} p^{(s)}(z, \phi) \\ v^{(s)}(z, \phi) \end{pmatrix} = \frac{k}{2\pi} \int_0^\pi d\theta \times \sin \theta e^{ikz \cos \theta} \begin{pmatrix} P(k \cos \theta, \phi) \\ V(k \cos \theta, \phi) \end{pmatrix}, \quad (10)$$

since Eqs. (9) and (10) are together equivalent to Eq. (2). Our objective is to derive approximations to $P(k \cos \theta, \phi)$ and $V(k \cos \theta, \phi)$. With this in mind we make two assumptions. (i) First, we assume the normal velocity and pressure are related by a ‘‘cylindrical wave’’ approximation, which is most easily expressed in terms of the transformed variables as

$$\hat{V}(k \cos \theta, \phi) = \frac{\sin \theta}{\rho_f c} \hat{P}(k \cos \theta, \phi) \left\{ 1 - \frac{1}{2ika(\phi) \sin \theta} + O\left(\frac{1}{(ka \sin \theta)^2}\right) \right\}. \quad (11)$$

This may be justified by the high-frequency approximation for the z -transformed pressure $P(\rho_n, k_z, \phi)$ near the surface, where ρ_n is the distance from C in the normal direction,

$$P(\rho_n, k_z, \phi) = P(k_z, \phi) e^{i\sqrt{k^2 - k_z^2} \rho_n} \times \sqrt{\frac{a(\phi)}{a(\phi) + \rho_n}} \left[1 + O\left(\frac{1}{ka}\right) \right]. \quad (12)$$

Thus using $V(\rho_n, k_z, \phi) = (i\omega\rho_f)^{-1} \partial P / \partial \rho_n$, and evaluating on the surface ($\rho_n = 0$), we get Eq. (11). This approximation is justified further for the circular cylinder in the Appendix. (ii) Second, we assume that we may perform asymptotic expansions in the large parameter $ka \sin \theta \gg 1$. This was already implicit in the cylindrical wave approximation of Eq. (11).

Equations (3) and (5) can now be derived. First, substituting from Eq. (11) into the exact formula (8) and retaining only the leading order term, we have

$$\hat{F}(\theta, \phi) = \frac{-ik}{4\pi} \int_C dl e^{-ikb(\phi') \sin \theta \cos(\phi - \phi')} [1 + \cos(\phi - \psi(\phi'))] \sin \theta P(k \cos \theta, \phi'). \quad (13)$$

We now apply the stationary phase approximation to this integral, based upon the assumption that $ka \sin \theta \gg 1$. There are two points at which the phase is stationary, given by the implicit relations $\psi(\phi') = \phi$ and $\psi(\phi') = \phi + \pi$. However, the integrand vanishes at the latter point and we get zero contribution there. The remaining stationary phase point gives

$$\hat{F}(\theta, \psi(\phi)) = e^{-i\pi/4} e^{-ikb(\phi) \sin \theta} \times \sqrt{\frac{ka(\phi) \sin \theta}{2\pi}} P(k \cos \theta, \phi), \quad (14)$$

or

$$\hat{P}(k \cos \theta, \phi) = e^{i\pi/4} e^{ikb(\phi) \sin \theta} \times \sqrt{\frac{2\pi}{ka(\phi) \sin \theta}} F(\theta, \psi(\phi)). \quad (15)$$

Substituting from Eq. (15) into Eq. (10) yields the imaging formula (3). The velocity formula (5) follows in the same way using the leading-order term of the cylindrical wave approximation (11).

B. Conservation of radiated energy

The flux of energy across the cylindrical surface at a point is defined as the time averaged power flow:

$$I(z, \phi) = \frac{1}{2} \text{Re}[p(b(\phi), z, \phi) v^*(b(\phi), z, \phi)], \quad (16)$$

and the supersonic acoustic intensity is defined as the contribution from the supersonic components:

$$I^{(s)}(z, \phi) = \frac{1}{2} \text{Re}[p^{(s)}(z, \phi) v^{(s)*}(z, \phi)]. \quad (17)$$

Similarly, one can define a subsonic flux, $I^{(c)}(z, \phi)$, using the subsonic surface fields $p^{(c)}(z, \phi)$ and $v^{(c)}(z, \phi)$. Note that $I(z, \phi) \neq I^{(s)}(z, \phi) + I^{(c)}(z, \phi)$ in general. However, by the definition of the supersonic component, Eq. (2), it follows that

$$\int_{-\infty}^{\infty} dz f^{(s)}(z, \phi) g^{(c)}(z, \phi) = 0 \quad (18)$$

for any surface fields f and g , and hence

$$\int_{-\infty}^{\infty} dz I(z, \phi) = \int_{-\infty}^{\infty} dz I^{(s)}(z, \phi) + \int_{-\infty}^{\infty} dz I^{(c)}(z, \phi). \quad (19)$$

Assuming that all sources lie on or within the surface implies that the total subsonic flux is zero, and hence

$$\int_C dl \int_{-\infty}^{\infty} dz I(z, \phi) = \int_C dl \int_{-\infty}^{\infty} dz I^{(s)}(z, \phi) = \Pi(\omega), \quad (20)$$

where $\Pi(\omega)$ is the total energy radiated to the far field,

$$\Pi(\omega) = \frac{1}{2\rho_f c} \int_0^{2\pi} d\phi \int_0^\pi d\theta \sin \theta |F(\theta, \phi)|^2. \quad (21)$$

We now demonstrate that the imaging formulas have the useful property that they conserve energy. Replacing $p^{(s)}$ and $v^{(s)}$ by the integral expressions of Eq. (10), then integrating in the axial coordinate z and using known properties of the Dirac delta function, we obtain the identity

$$\int_{-\infty}^{\infty} dz I^{(s)}(z, \phi) = \frac{k}{4\pi} \int_0^\pi d\theta \sin \theta \text{Re}[P(k \cos \theta, \phi) \times V^*(k \cos \theta, \phi)]. \quad (22)$$

As a first approximation, the cylindrical wave, or local impedance condition, of Eq. (11) combined with Eq. (22) implies

$$\int_{-\infty}^{\infty} dz I^{(s)}(z, \phi) = \frac{k}{4\pi\rho_f c} \int_0^{\pi} d\theta \sin^2 \theta |P(k \cos \theta, \phi)|^2 \times \left[1 + O\left(\frac{1}{(ka)^2}\right) \right]. \quad (23)$$

If we now substitute the leading-order approximation for $P(k \cos \theta, \phi)$ from Eq. (15), we obtain

$$\int_{-\infty}^{\infty} dz \hat{I}^{(s)}(z, \phi) = \frac{1}{2a(\phi)\rho_f c} \int_0^{\pi} d\theta \sin \theta |F(\theta, \psi(\phi))|^2. \quad (24)$$

Hence using the relation $dl = a d\psi$ [see Eq. (4)], we see that the surface energy flux of the approximate imaged field,

$$a(\phi) \int_{-\infty}^{\infty} dz \hat{I}^{(s)}(z, \phi), \quad (25)$$

exactly equals the differential power radiated per unit azimuthal angle in the far field in the direction $\psi(\phi)$. Thus we have energy conservation for each meridional patch of width dl and of infinite length, $-\infty < z < \infty$. According to Eq. (19), the exact supersonic flux corresponding to (25) is not necessarily the same as the net flux from the patch. The identity only holds for the entire surface. However, the cylindrical wave approximation implies that each patch radiates independently of all others. In this regard, we note that Sarkissian⁸ introduced the idea of far-field eigenfunctions, which have a one-to-one relation with the on-surface eigenfunctions of the real part of the impedance operator. According to the present level of approximation, the patches and the velocity on them represent orthogonal subspaces of these eigenfunctions.

The following is a simple consequence of the preceding analysis,

$$\int_C dl \int_{-\infty}^{\infty} dz \hat{I}^{(s)}(z, \phi) = \Pi(\omega). \quad (26)$$

In summary, Williams' formulas and their generalization to arbitrary cross-sections predict a supersonic acoustic intensity which gives the same local energy flux on a longitudinal patch as the differential far-field intensity, and the same global energy flux as the exact radiated pressure. In this sense the imaging formulas are energy preserving.

II. AN ASYMPTOTIC CORRECTION FOR THE CIRCULAR CYLINDER

A. Analysis

The preceding analysis showed that Williams' formula is based upon the leading-order asymptotic approximation of the exact integral (8) for F . In order to improve upon this result we now explore the possibility of extending the formula by retaining the subsequent term in the asymptotic expansion. For simplicity, we restrict the analysis to the circular cylinder ($b = a$) but use the same methodology as before,

based upon the Helmholtz integral. The case of variable $b(\phi)$ can be treated similarly. The Appendix summarizes the same analysis using the explicit circular functions.

Here, the asymptotic parameter turns out to be $ka \sin \theta$, which may not be large if θ is near 0 or π . However, we will proceed by ignoring these limiting values, and start by considering the integral

$$f(\phi) = \int_0^{2\pi} d\phi' g(\phi') e^{-ika \sin \theta \cos(\phi - \phi')}, \quad (27)$$

where $g(\phi)$ is assumed to be reasonably smooth. Our objective is to obtain the two leading-order terms in the asymptotic expansion of $f(\phi)$. The integral (27) can be put into a form suitable for asymptotic approximation by introducing the dimensionless large parameter $\lambda = 2\sqrt{ka \sin \theta}$, so that with a change of variable

$$f(\phi) = \frac{2}{\lambda} e^{-i\lambda^2/4} \int_{-\lambda}^{\lambda} dx \frac{e^{ix^2/2}}{\sqrt{1-x^2/\lambda^2}} g\left[\phi + 2 \sin^{-1}\left(\frac{x}{\lambda}\right)\right]. \quad (28)$$

Expanding the integrand about $x=0$ in terms of inverse powers of λ gives

$$\begin{aligned} f(\phi) &= \frac{2}{\lambda} e^{-i\lambda^2/4} \int_{-\lambda}^{\lambda} dx e^{ix^2/2} \left\{ g(\phi) + 2\frac{x}{\lambda} g'(\phi) \right. \\ &\quad \left. + \frac{x^2}{2\lambda^2} [g(\phi) + 4g''(\phi)] + O(\lambda^{-3}) \right\} \\ &= \frac{2}{\lambda} e^{-i\lambda^2/4} \left\{ K_{\lambda}(1)g(\phi) - \frac{i}{\lambda^2} K'_{\lambda}(1)[g(\phi) \right. \\ &\quad \left. + 4g''(\phi)] + O(\lambda^{-3}) \right\}, \end{aligned} \quad (29)$$

where

$$K_{\lambda}(\alpha) = \int_{-\lambda}^{\lambda} dx e^{i\alpha x^2/2}. \quad (30)$$

The function $K_{\lambda}(\alpha)$ may be expressed in terms of known functions, but for our purposes it suffices to take the large λ limit, $K_{\infty}(\alpha) = e^{i\pi/4} \sqrt{2\pi/\alpha}$, so that

$$\begin{aligned} f(\phi) &= e^{i(\pi/4 - ka \sin \theta)} \sqrt{\frac{2\pi}{ka \sin \theta}} \left\{ g(\phi) - \frac{1}{2ika \sin \theta} \right. \\ &\quad \left. \times \left[g''(\phi) + \frac{1}{4} g(\phi) \right] + O\left(\frac{1}{(ka \sin \theta)^{3/2}}\right) \right\}. \end{aligned} \quad (31)$$

Equation (8) for F involves two distinct integrals for the integrands V and P , and Eq. (31) can be applied to each integral separately. However, we would like to obtain an expression for F which contains only one of the two integrands. This can be achieved to within the desired asymptotic accuracy by using the cylindrical wave approximation of Eq. (11). Substituting from (11) into the integral (8) and using the asymptotic approximation (31) we obtain

$$\begin{aligned}\hat{F}(\theta, \phi) = & e^{-i(ka \sin \theta + \pi/4)} \sqrt{\frac{ka \sin \theta}{2\pi}} \left[P(k \cos \theta, \phi) \right. \\ & - \frac{1}{2ika \sin \theta} \left(P_{,\phi\phi}(k \cos \theta, \phi) \right. \\ & \left. + \frac{1}{4} P(k \cos \theta, \phi) \right) + O\left(\frac{1}{(ka \sin \theta)^{3/2}}\right) \Big].\end{aligned}\quad (32)$$

This is the first-order correction of the leading-order approximation of Eq. (14). It is interesting to note that there is still no contribution to the far field from the stationary phase point at $\phi + \pi$. That is, the approximation (32) is still local, although it now involves the second derivative of the surface pressure transform.

B. Discussion and examples

Equation (32) was derived as an asymptotic correction of the leading-order term, and as such, we may formally invert it as

$$\begin{aligned}\hat{P}(k \cos \theta, \phi) = & e^{i\pi/4} e^{ika \sin \theta} \sqrt{\frac{2\pi}{ka \sin \theta}} \\ & \times \left[\left(1 + \frac{1}{8ika \sin \theta} \right) F(\theta, \phi) \right. \\ & + \frac{1}{2ika \sin \theta} F_{,\phi\phi}(\theta, \phi) \\ & \left. + O\left(\frac{1}{(ka \sin \theta)^{3/2}}\right) \right].\end{aligned}\quad (33)$$

This gives the following approximation for the supersonic surface pressure,

$$\begin{aligned}\hat{p}^{(s)}(z, \phi) = & e^{i\pi/4} \sqrt{\frac{k}{2\pi a}} \int_0^\pi \frac{d\theta}{\sqrt{\sin \theta}} e^{ik(a \sin \theta + z \cos \theta)} \\ & \times \left[\left(\sin \theta + \frac{1}{8ika} \right) F(\theta, \phi) + \frac{F_{,\phi\phi}(\theta, \phi)}{2ika} \right].\end{aligned}\quad (34)$$

The corresponding approximation for the supersonic surface velocity is, from (11) and (33),

$$\begin{aligned}\hat{v}^{(s)}(z, \phi) = & \frac{e^{i\pi/4}}{\rho_f c} \sqrt{\frac{k}{2\pi a}} \int_0^\pi d\theta \sqrt{\sin \theta} e^{ik(a \sin \theta + z \cos \theta)} \\ & \times \left[\left(\sin \theta - \frac{3}{8ika} \right) F(\theta, \phi) + \frac{F_{,\phi\phi}(\theta, \phi)}{2ika} \right].\end{aligned}\quad (35)$$

We will test the accuracy of the imaging formulas for a monopole at $(\rho, z, \phi) = (\rho', 0, 0)$, $\rho' < a$, for which

$$F(\theta, \phi) = e^{-ik\rho' \sin \theta \cos \phi}.\quad (36)$$

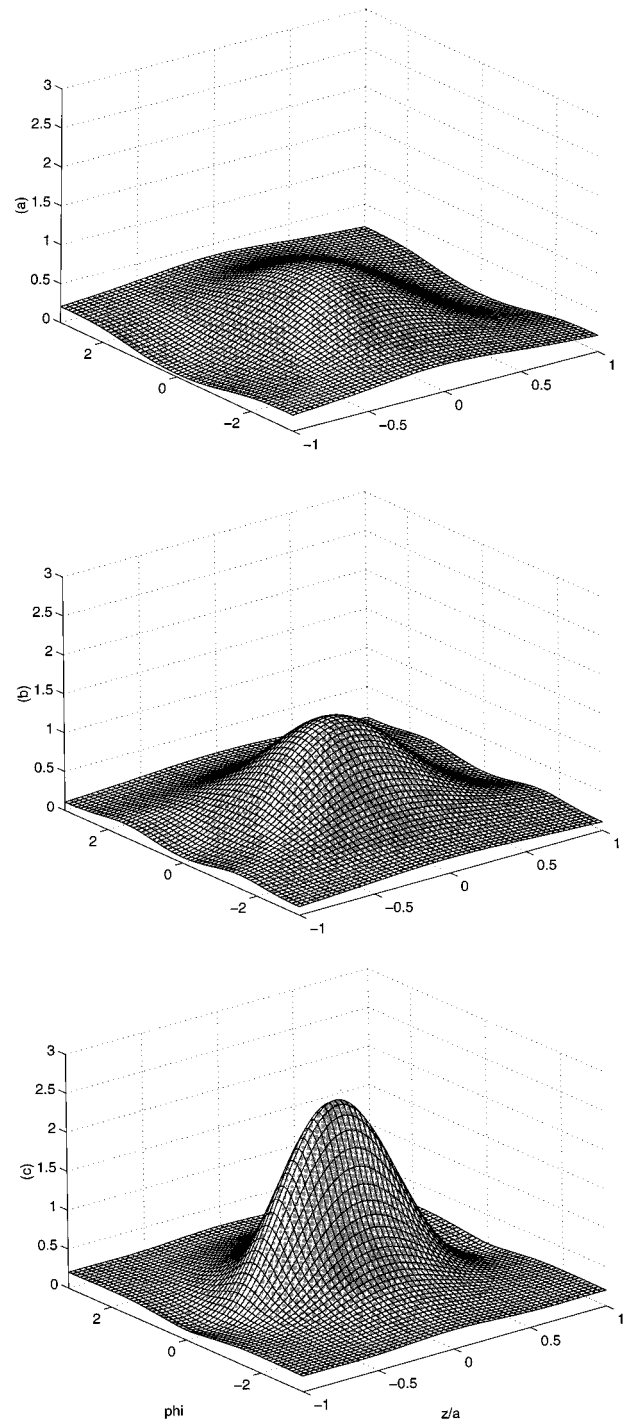


FIG. 2. The supersonic acoustic intensity for $\rho' = 0.5a$ and $ka = 3$, computed using (a) the simple formulas of Eqs. (3) and (5), (b) Eqs. (34) and (35), and (c) the exact result.

The exact supersonic surface pressure can be obtained using the identity (A11). Figures 2 and 3 compare the predicted supersonic acoustic intensity according to the simple formulas of Williams, Eqs. (3) and (5), and the “improved” versions (34) and (35), with the exact supersonic acoustic intensity for a source at $\rho' = a/2$ for $ka = 3$. The amplitudes of the approximations are lower near the center of the image ($z = \phi = 0$) than the exact intensity, but the “improved” imaging formula does appear to give better resolution.

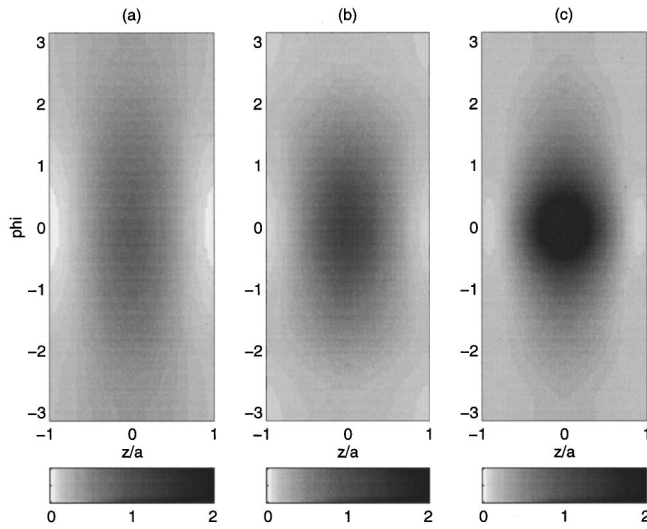


FIG. 3. The same data as shown in Fig. 2, i.e., $\rho' = 0.5a$ and $ka = 3$. (a)–(c) correspond to the same items in Fig. 2.

Before presenting the bad news regarding the “improved” imaging formulas, (34) and (35), we note that the low values of the maximum amplitude of the imaged intensity can be expected from the simple nature of the algorithm. Thus as the monopole source approaches the surface ($\rho' \rightarrow a$) both the pressure and the velocity on the surface become singular, but the simple imaging relation predicts finite values. In fact, using Eqs. (3), (5), and (36) with $\rho' = a$, it gives

$$\begin{aligned} \hat{I}^{(s)}(0,0) &= \frac{k}{4\pi a \rho_f c} \int_0^\pi d\theta (\sin \theta)^{1/2} \int_0^\pi d\theta' (\sin \theta')^{3/2} \\ &= \frac{k}{3a \rho_f c} \quad \text{for } \rho' = a. \end{aligned} \quad (37)$$

Hence the ratio of the imaged to the true intensity is

$$\frac{\hat{I}^{(s)}(0,0)}{I^{(s)}(0,0)} = \frac{2k}{3a} (a - \rho')^2 \quad \text{as } \rho' \rightarrow a. \quad (38)$$

This is consistent with numerical simulations by Williams⁶ who found that the imaged intensity is generally well below the actual supersonic acoustic intensity in magnitude, although it gives the correct overall pattern or image. The result (38), combined with the conservation of energy for the simple imaging algorithm implies that the energy not imaged at the “hot spot” must be redistributed elsewhere on the surface. It is clear from the numerical examples, such as Fig. 2, that the energy redistribution does not occur within a distance of one acoustic wavelength. We can only infer that the approximate formula leads to an enhanced “background” imaged intensity.

Figures 4 and 5 show the comparison of the imaging formulas at higher frequencies using gray scale mosaics similar to Fig. 3. These figures illustrate a serious problem with the “improved” approximation of Eqs. (34) and (35): The second derivatives of F with respect to ϕ tend to dominate and make the correction far larger than the leading-order approximation. This results in the dumbbell appearance of

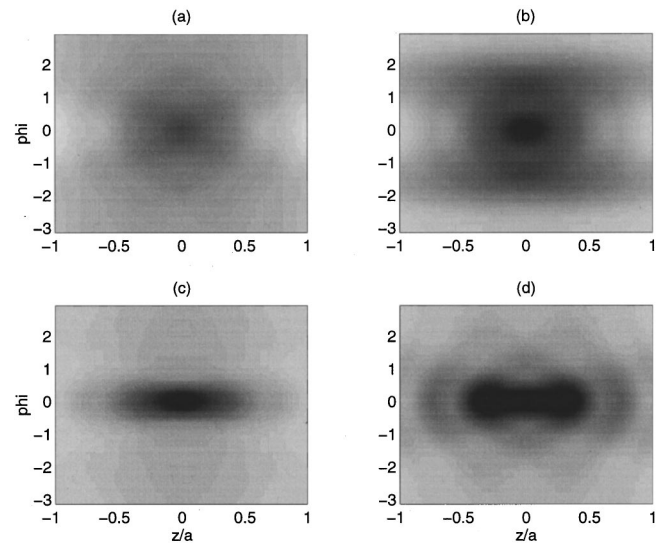


FIG. 4. The approximate, “improved approximate,” and exact supersonic acoustic intensity, (a), (b), and (d), respectively, for $\rho' = 0.5a$ and $ka = 9$. The data in (c) were obtained by solving Eq. (39) by finite differences.

Fig. 5(b), for instance, which is clearly unrepresentative of the actual intensity. The problem with the derivatives of F can be avoided as follows. Ignoring the smaller-order terms, (32) can be written as

$$\hat{P} - \mu^{-2} \hat{P}_{,\phi\phi} = \hat{P}^{(0)}(k \cos \theta, \phi), \quad (39)$$

where

$$\begin{aligned} \hat{P}^{(0)}(k \cos \theta, \phi) &= e^{i(ka \sin \theta + \pi/4)} \sqrt{\frac{2\pi}{ka \sin \theta}} \\ &\times \left(1 - \frac{1}{8ika \sin \theta} \right)^{-1} F(\theta, \phi) \end{aligned} \quad (40)$$

and

$$\mu^2 = -\frac{1}{4} + 2ika \sin \theta. \quad (41)$$

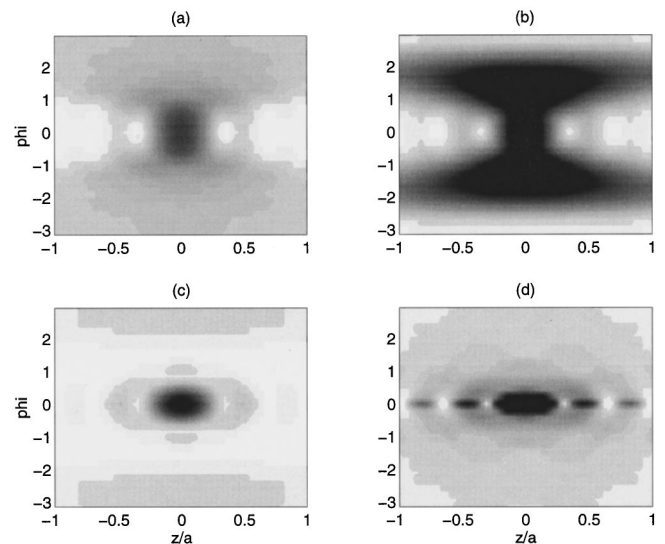


FIG. 5. The same as in Fig. 4 but for $\rho' = 0.9a$ and $ka = 9$.

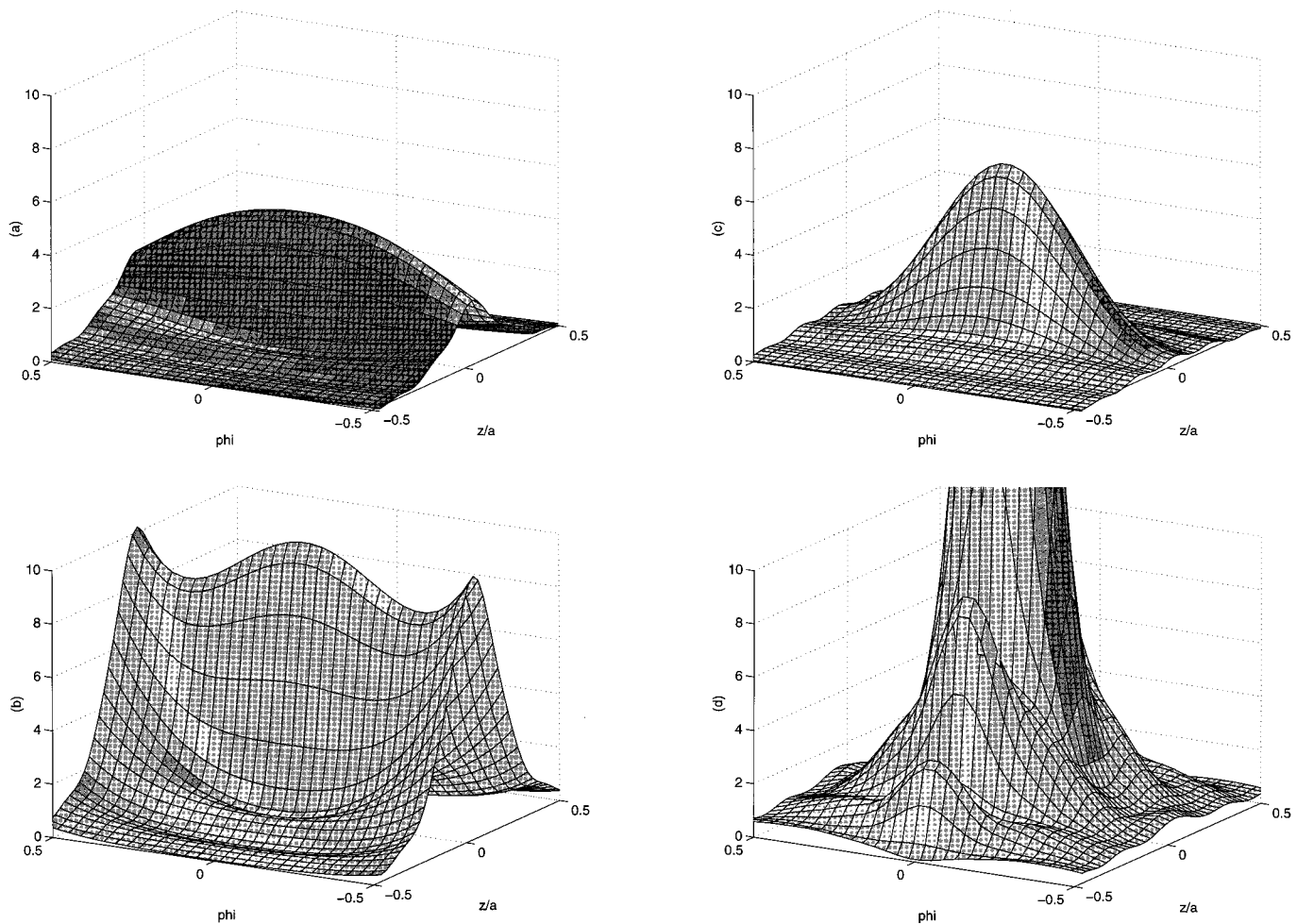


FIG. 6. The approximate, "improved approximate," finite difference solution, and the exact supersonic acoustic intensity, (a), (b), (c), and (d), respectively, for $\rho' = 0.9a$ and $ka = 18$. The difference scheme uses 30 equally spaced points on $-\pi/6 \leq \phi \leq \pi/6$.

Apart from the factor $[1 - 1/(8ika \sin \theta)]^{-1}$, which is close to unity in general, the function $\hat{P}^{(0)}(k \cos \theta, \phi)$ is exactly the leading-order approximation of Eq. (15), or Williams' formula. The images in Figs. 4(c) and 5(c) were obtained by solving Eq. (39) on a grid of 30 equally spaced ϕ points using finite differences as described below. The improved resolution illustrates that the second derivatives of F mentioned previously are indeed the culprit for the poor images in Figs. 4(b) and 5(b), and that a naive inversion of the basic formula (32) can lead to significant error.

The price paid by solving Eq. (39) is that the imaging formula is no longer strictly local. One can argue that if we are using all the data for $-\pi \leq \phi \leq \pi$ then we may as well use the exact modal algorithm (see the Appendix). However, the second-order equation (39) can be solved, in principle, on any interval by several methods: Green's functions, finite differences, etc. We will assume for simplicity that the far-field data is obtained on a set of semicircles evenly spaced in ϕ , say $\phi_j = \phi_1 + (j-1)\Delta\phi$, $j = 1, 2, \dots, M$, where $\Delta\phi$ is the azimuthal spacing. Let $\hat{P}_j = \hat{P}(k \cos \theta, \phi_j)$ and $\hat{P}_j^{(0)} = \hat{P}^{(0)} \times (k \cos \theta, \phi_j)$, then Eq. (39) is approximated by the central difference scheme

$$\hat{P}_j - \frac{1}{\mu^2(\Delta\phi)^2} [\hat{P}_{j+1} - 2\hat{P}_j + \hat{P}_{j-1}] = \hat{P}_j^{(0)}, \quad j = 1, 2, \dots, M. \quad (42)$$

The results shown in Figs. 4(c) and 5(c) for $-\pi \leq \phi \leq \pi$ were obtained using this scheme combined with periodic end conditions, which imply $\phi_0 = \phi_M$ and $\phi_{M+1} = \phi_1$. The results in Figs. 6(c), 7(c), and 8(b) were computed for the sector $-\pi/6 \leq \phi \leq \pi/6$ using similar periodicity conditions to evaluate the scheme at the end points. Other end conditions were tested and it was found that the numerical solutions were not sensitive to the precise form of the conditions used.

The results of Figs. 6(c), 7(c), and 8(b) indicate that better circumferential resolution can be expected if the simple differencing algorithm is adopted. The improvement in the resolution is quite remarkable even with very few semicircles of data, only seven in Fig. 8(b). Some understanding of the effect of using Eq. (39) can be obtained by noting that at high frequencies the real part of μ is large and positive, implying that the second derivative term in (39) acts as a singular perturbation, analogous to a boundary layer

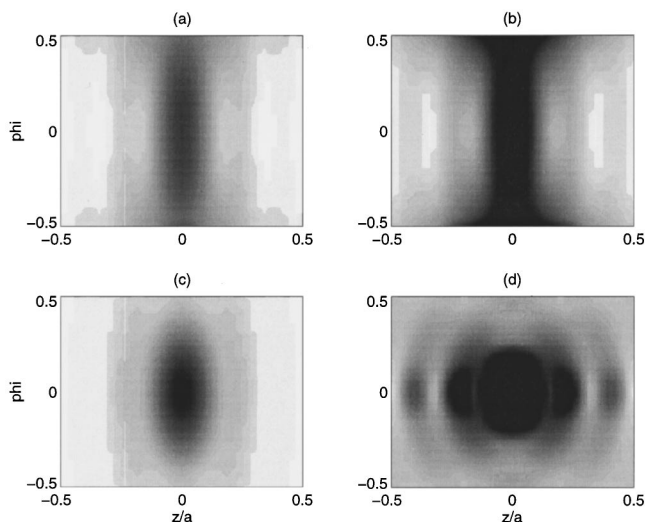


FIG. 7. The results of Fig. 6 depicted by gray scale mosaic.

effect. By ignoring the fact that the range of ϕ is finite, and replacing the domain by the full line, with zero boundary conditions at $\pm\infty$, we may write the solution to (39) as

$$\hat{P}(k \cos \theta, \phi) = \frac{\mu}{2} \int_{-\infty}^{\infty} d\phi' e^{-\mu|\phi-\phi'|} \hat{P}^{(0)}(k \cos \theta, \phi'). \quad (43)$$

Integrating by parts yields

$$\begin{aligned} \hat{P}(k \cos \theta, \phi) &= \hat{P}^{(0)}(k \cos \theta, \phi) \\ &+ \frac{1}{2} \int_0^{\infty} d\phi' e^{-\mu\phi'} [\hat{P}_{,\phi}^{(0)}(k \cos \theta, \\ &\phi + \phi') - \hat{P}_{,\phi}^{(0)}(k \cos \theta, \phi - \phi')]. \quad (44) \end{aligned}$$

This form clearly shows the leading-order term $\hat{P}^{(0)}$, and the boundary layer correction, within a region of azimuthal thickness $1/\text{Re}\mu = O(1/\sqrt{ka \sin \theta})$.

III. CONCLUSION

The imaging formula of Williams is practical and very useful because it provides a simple means to map the far-field pressure back to a cylindrical surface. The power of the method is that it is local, and does not require full circumferential coverage. Data from each semi-circular scan is back projected independently. In this paper we have seen that the same formula can be generalized to cylinders of arbitrary cross section, with the main results being Eqs. (3) and (5). The cross section need not be a separable surface. In fact, the derivation relies upon a local, high-frequency approximation which illustrates that the formula is really the leading order of an asymptotic approximation. We also obtained the first two terms in the asymptotic series for the special case of a circular cylinder. One can, in principle, continue the asymptotic series for arbitrary cross section.

The two-term approximation can be interpreted in two ways. By the nature of its derivation it gives the surface pressure transform P as the solution of a differential equation, Eq. (32). This can be formally solved, in the spirit of

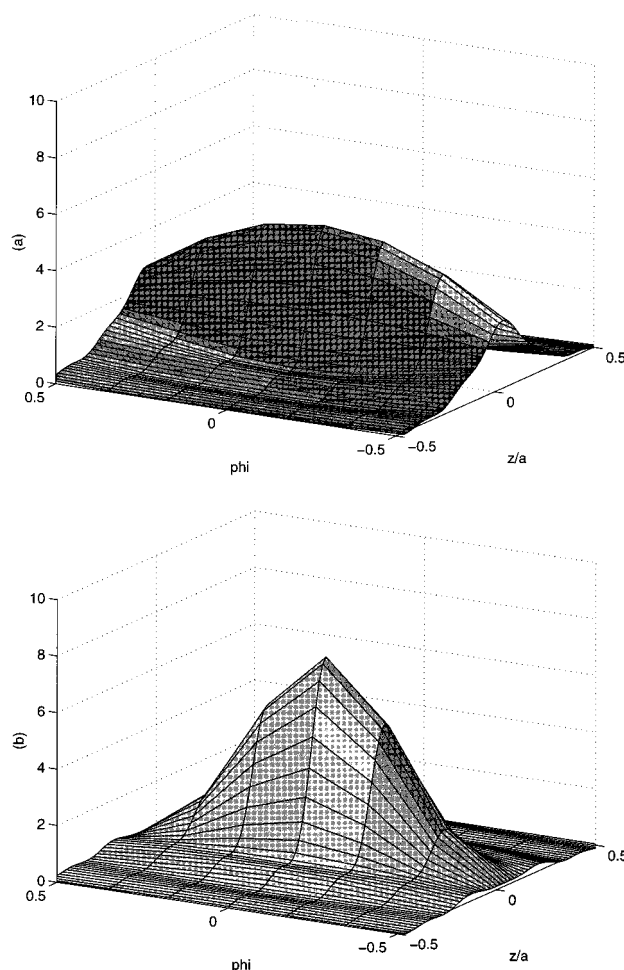


FIG. 8. The approximate, (a), and finite difference solution, (b), for the same parameters as Fig. 6, except that only seven equally spaced ϕ points are used.

the asymptotic approximation, yielding a direct and local imaging formula, Eq. (33), which introduces a correction to Williams' formula. However, as the numerical examples illustrate, this "improved" scheme is actually worse than the original, and the cause of the problem lies with the second-order derivatives with respect to ϕ , which is also related with the ill-posed nature of the inverse problem (see the Appendix). The proper interpretation of the asymptotic correction is as a nonlocal effect, which must be solved as such. One approach is to use finite differences for sets of several neighboring semicircles. The numerical examples for a monopole near the surface indicate that even with very few semicircles one can gain significant resolution in the circumferential direction, as compared with the simple local imaging formula.

ACKNOWLEDGMENTS

My thanks to Earl Williams for comments. This work was supported by the Office of Naval Research.

APPENDIX: THE CIRCULAR CYLINDER

The special case of constant $b(\phi) = a$ is considered here. It may be easily shown, using modal expansions for instance, that the z -transformed surface velocity can be expressed in terms of the surface pressure as

$$V(k \cos \theta, \phi) = \frac{\sin \theta}{\rho_f c} \int_0^{2\pi} d\phi' G(\theta, \phi - \phi') P(k \cos \theta, \phi'), \quad (\text{A1})$$

where

$$G(\theta, \phi - \phi') = \sum_{n=-\infty}^{\infty} -i \frac{H_n^{(1)'}(ka \sin \theta)}{H_n^{(1)}(ka \sin \theta)} e^{in(\phi - \phi')}. \quad (\text{A2})$$

Assuming that $ka \sin \theta \gg 1$ we can use the following asymptotic approximation for the Hankel functions,

$$H_n^{(1)}(x) = (-i)^{n+1} e^{i(x + \pi/4)} \sqrt{\frac{2}{\pi x}} \left[1 + i \frac{(4n^2 - 1)}{8x} + \dots \right]. \quad (\text{A3})$$

By retaining the first two terms in the expansion of $-iH_n^{(1)'}(y)/H_n^{(1)}(y)$ for $y \gg |n|$, we obtain

$$\hat{G}(\theta, \phi - \phi') = \delta(\phi - \phi') \left(1 - \frac{1}{8ika \sin \theta} \right) + \dots \quad (\text{A4})$$

Equations (A1) and (A4) together imply Eq. (11) for the special case of the circular cylinder.

Substituting from (A1) into the Helmholtz integral (8) and using standard identities for Bessel and Hankel functions, we obtain the exact relationship between the far-field form function and the surface pressure transform,

$$F(\theta, \phi) = \frac{1}{2\pi} \int_0^{2\pi} d\phi' P(k \cos \theta, \phi') \times \sum_{n=-\infty}^{\infty} \frac{e^{in(\phi - \phi')}}{\pi(i)^{n+1} H_n^{(1)}(ka \sin \theta)}. \quad (\text{A5})$$

This derivation is related to, and motivated by, that of Williams.⁶ The distinction is that Williams essentially obtained $P(k \cos \theta, \phi)$ directly. There is a slight complication with his approach, which is based upon the fact that the near-to-far-field radiation operator is compact. In order to appreciate this difficulty, define the functions $L_N^{(\pm 1)}(\phi - \phi', \theta)$ as

$$L_N^{(\pm 1)}(\phi - \phi', \theta) = \sum_{n=-N}^N [\pi(i)^{n+1} H_n^{(1)} \times (ka \sin \theta)]^{\mp 1} e^{in(\phi - \phi')}, \quad (\text{A6})$$

then Eq. (A5) is equivalent to

$$F(\theta, \phi) = \frac{1}{2\pi} \int_0^{2\pi} d\phi' P(k \cos \theta, \phi') L^{(1)}(\phi - \phi', \theta), \quad (\text{A7})$$

where $L^{(1)} = \lim_{N \rightarrow \infty} L_N^{(1)}$. It follows from the small argument or large order form of the Hankel functions, $H_n^{(1)}(x) = (-1/\pi)(2/x)^n (n-1)! + \dots$, that the function $L^{(1)}(\phi - \phi', \theta)$ is convergent and well defined. We note in passing that the precise form function requires the infinite sum, in general, and is not defined by the integral using the truncated version $L_N^{(1)}$, where N is approximately $ka \sin \theta$. As a counter example, consider a set of m monopoles, equally spaced azimuthally at $\phi_j = 2\pi j/m$ with amplitudes $e^{im\phi_j}$, j

$= 1, 2, \dots, m$. For large m the dominant contribution to $F(\theta, \phi)$ comes from $n = m$, which would not be picked up if we used the truncated form of $L^{(1)}$.

Let $F_N(\theta, \phi)$ be the function obtained using the truncated function $L_N^{(1)}$ in the integral in Eq. (A7) instead of $L^{(1)}$. The same function is obtained by using the $2N+1$ modal expansion of $P(k \cos \theta, \phi')$, say $P_N(k \cos \theta, \phi')$, as the integrand in Eq. (A7), i.e.,

$$\begin{aligned} F_N(\theta, \phi) &= \frac{1}{2\pi} \int_0^{2\pi} d\phi' P(k \cos \theta, \phi') L_N^{(1)}(\phi - \phi', \theta) \\ &= \frac{1}{2\pi} \int_0^{2\pi} d\phi' P_N(k \cos \theta, \phi') L_N^{(1)}(\phi - \phi', \theta) \\ &= \frac{1}{2\pi} \int_0^{2\pi} d\phi' P_N(k \cos \theta, \phi') L^{(1)}(\phi - \phi', \theta), \end{aligned} \quad (\text{A8})$$

and conversely,

$$P_N(k \cos \theta, \phi) = \frac{1}{2\pi} \int_0^{2\pi} d\phi' F_N(\theta, \phi') L_N^{(-1)}(\phi - \phi', \theta). \quad (\text{A9})$$

However, we cannot take the limit of $N \rightarrow \infty$ in this equation, because, although $P_N \rightarrow P$ and $F_N \rightarrow F$, the limit of $L_N^{(-1)}$ as $N \rightarrow \infty$ does not converge at any point, and hence it is not a well-defined function. In summary, any m -mode limited form of $F(\theta, \phi)$ can be inverted to give the corresponding m -mode form of $P(k \cos \theta, \phi)$. The inversion process is stable for $m \leq N$, where $N \approx ka \sin \theta$, and is unstable for larger m , even though the dominant contribution to F could be from modes with $m > N$. The lack of an explicit integral formula for $P(k \cos \theta, \phi)$ is a consequence of the fact that the integral operator in Eq. (A7) is compact, and as such, has no inverse. The ill-posedness of this type of inverse problem is common, and methods exist to regularize the problem.⁹

If $ka \sin \theta \gg N \gg 1$, then the following approximations can be obtained from (A3),

$$\begin{aligned} L_N^{(\pm 1)}(\phi - \phi', \theta) &= 2\pi e^{\pm i(ka \sin \theta + \pi/4)} \\ &\times \left[\frac{2\pi}{ka \sin \theta} \right]^{\pm 1/2} \left[\delta(\phi - \phi') \left(1 \right. \right. \\ &\left. \left. \pm \frac{1}{8ika \sin \theta} \right) \pm \frac{\delta'(\phi - \phi')}{2ika \sin \theta} + \dots \right]. \end{aligned} \quad (\text{A10})$$

We have also used the approximation $\sin(\lambda x)/(\pi x) \approx \delta(x)$ for sufficiently large λ . The approximations of Eq. (32) for F in terms of P follows from Eq. (A7) combined with Eq. (A10) for $L_N^{(1)}$ in the limit $N \rightarrow \infty$. However, as remarked above, we cannot take the same limit for $L_N^{(-1)}$, although formally doing so yields Eq. (33) from Eqs. (A10) and (A9).

Finally, we note that the numerical examples use the following representation for a monopole located at $(\rho, z, \phi) = (\rho', 0, 0)$, $\rho' \leq a$,

$$p^{(s)}(z, \phi) = \frac{ik}{2} \int_0^\pi d\theta \sin \theta e^{ikz \cos \theta} \sum_{n=-\infty}^{\infty} e^{in\phi} H_n^{(1)} \times (ka \sin \theta) J_n(k\rho' \sin \theta). \quad (\text{A11})$$

¹E. G. Williams, H. D. Dardy, and K. B. Washburn, "Generalized nearfield acoustic holography for cylindrical geometry: Theory and experiment," J. Acoust. Soc. Am. **81**, 389–504 (1987).

²W. A. Veronesi and J. D. Maynard, "Digital holographic reconstruction of sources with arbitrarily shaped surfaces," J. Acoust. Soc. Am. **85**, 588–598 (1988).

³G. Borgiotti, A. Sarkissian, E. G. Williams, and L. Schuetz, "Conformal generalized near-field acoustic holography for axisymmetric geometries," J. Acoust. Soc. Am. **88**, 199–209 (1990).

⁴A. Sarkissian, "Reconstruction of the surface acoustic field on radiating structures," J. Acoust. Soc. Am. **92**, 825–830 (1992).

⁵D. M. Photiadis, "The relationship of singular value decomposition to wave-vector filtering in sound radiation problems," J. Acoust. Soc. Am. **88**, 1152–1159 (1990).

⁶E. G. Williams, "Imaging the sources on a cylindrical shell from far-field pressure measured on a semicircle," J. Acoust. Soc. Am. **99**, 2022–2032 (1996).

⁷E. G. Williams, "Supersonic acoustic intensity," J. Acoust. Soc. Am. **97**, 121–127 (1995).

⁸A. Sarkissian, "Acoustic radiation from finite structures," J. Acoust. Soc. Am. **90**, 574–578 (1991).

⁹D. L. Colton and R. Kress, *Integral Equation Methods in Scattering Theory* (Wiley, New York, 1993).

Stoneley wave excitation by a bounded beam at the down-step of a thin layer on a substrate

R. Briers,^{a)} O. Leroy, and G. Shkerdin^{b)}

Interdisciplinary Research Center, K. U. Leuven Campus Kortrijk, B-8500 Kortrijk, Belgium

(Received 15 January 1997; accepted for publication 30 May 1997)

The mode conversion of a bulk wave into a Stoneley wave at the downward step of a thin layer partially covering a solid substrate is studied. An analytical expression for the amplitude of the excited Stoneley wave is derived by applying mode theory. The excitation amplitude has two pronounced maxima: at grazing and at Rayleigh angle incidence of the bulk wave. The latter maximum is almost independent of the material characteristics of the thin layer. © 1997 Acoustical Society of America. [S0001-4966(97)06209-7]

PACS numbers: 43.35.Pt [HEB]

INTRODUCTION

Most ultrasonic techniques to evaluate materials are based on the measurements of the transmitted and reflected ultrasonic amplitude.¹⁻³ A detailed overview of propagation and scattering of surface waves in structures with surface inhomogeneities is given by Gulyaev *et al.*⁴ In the past Chamuel⁵ studied experimentally the generation of Stoneley waves by a point source at topographic features like a down-step. In the present paper the interaction of a bounded bulk wave with the down-step of a thin layer on a substrate is analyzed theoretically, and particular attention is focused on the amplitude of the Stoneley wave generated along the liquid/substrate interface. The effect of Stoneley wave excitation at the down-step allows the evaluation of the thickness of the thin layer even if the medium constants of the layer are not known.

In Sec. I of this paper the set of radiation modes for a liquid/thin layer/solid structure, needed for the mode expansions of the displacement fields, will be constructed. In Sec. II an analytical expression for the amplitude of the excited Stoneley wave is derived by making use of the method of successive approximations.⁶ The method was introduced earlier when studying the generation of a Stoneley wave by a bounded beam at the end of a fluid-loaded thick plate. Finally, Sec. III presents examples of numerical computations for different configurations.

I. RADIATION MODES FOR A LIQUID/THIN LAYER/SOLID STRUCTURE

A fluid-loaded solid substrate is partially covered by a layer of thickness d . A Gaussian beam is incident at the down-step of the layer, which is located in the plane $z=0$ (see Fig. 1). The substrate has density ρ_1 , dilatational velocity v_d , and shear velocity v_s ; the medium constants of the layer and the liquid are ρ_2 , v_{d1} , v_{s1} , respectively, ρ , v . The

displacement field $\mathbf{u}_1^{\text{tot}}$ in the liquid/layer/solid structure (structure 1) and the displacement field $\mathbf{u}_2^{\text{tot}}$ in the liquid/solid structure (structure 2) can be expanded as⁷

$$\mathbf{u}_1^{\text{tot}}(y, z) = C_1^s \mathbf{u}_1^s(y, z) + \int [C_a^i(k_{y,1}) + C_a^r(k_{y,1})] \mathbf{u}_1^a(k_{y,1}; y, z) dk_{y,1}, \quad (1)$$

$$\mathbf{u}_2^{\text{tot}}(y, z) = C_2^s \mathbf{u}_2^s(y, z) + \int C_a^t(k_{y,2}) \mathbf{u}_2^a(k_{y,2}; y, z) dk_{y,2}. \quad (2)$$

In Eqs. (1) and (2) C_a^i , C_a^r , and C_a^t are the expansion coefficients of, respectively, the incident Gaussian beam and the reflected and transmitted scattered bulk waves, while C_1^s and C_2^s are the expansion coefficients of, respectively, the reflected and transmitted mode-converted Stoneley waves; $k_{y,i}$ is defined as

$$k_{y,i}^2 = k^2 - k_{z,i}^2, \quad i = 1, 2, \quad (3)$$

with $k_{z,i}$ the z component of the wave vector in the liquid of structure i and k the wave number of the liquid. The orthogonal set of modes $\{\mathbf{u}_2^a, \mathbf{u}_2^s\}$ in which the waves in the liquid/solid structure are expanded has been derived in a previous paper.⁸ The *type a* radiation modes (\mathbf{u}_2^a) originate from plane waves incident from the liquid at an angle θ (measured from the y axis) within the range $\arcsin(v/v_s) \leq \theta \leq \pi/2$. The displacement field of the corresponding *type a* radiation modes (\mathbf{u}_1^a) for a liquid/thin layer/solid structure (needed for the expansions of the incident and reflected bulk waves) are calculated as follows.

In the liquid, *type a* radiation modes are represented by the displacement field

$$u_{y,1}^a = C k_{y,1} [-\exp(-ik_{y,1}y) + R \exp(ik_{y,1}y)] \times \exp[i(k_{z,1} - \omega t)], \quad (4)$$

$$u_{z,1}^a = C k_{z,1} [\exp(-ik_{y,1}y) + R \exp(ik_{y,1}y)] \times \exp[i(k_{z,1} - \omega t)], \quad (5)$$

while in the substrate the field takes the form

^{a)}Postdoctoral Fellow of the Flemish Institute for the Encouragement of the Scientific and Technological Research in Industry (I.W.T.).

^{b)}Permanent address: Institute of Radioengineering and Electronics, Russian Academy of Sciences, Moscow, Russia.

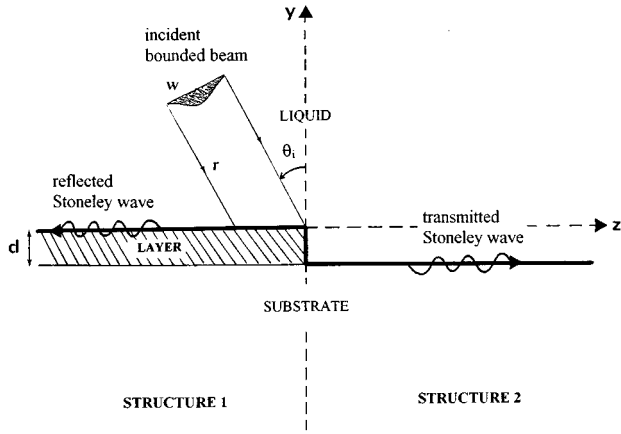


FIG. 1. Geometrical configuration of the two-dimensional diffraction problem.

$$u_{y,1}^a = C[-Dk_{dy,1} \exp(-ik_{dy,1}y) + Sk_{z,1} \times \exp(-ik_{sy,1}y)] \exp[i(k_{z,1} - \omega t)], \quad (6)$$

$$u_{z,1}^a = C[Dk_{z,1} \exp(-ik_{dy,1}y) + Sk_{sy,1} \times \exp(-ik_{sy,1}y)] \exp[i(k_{z,1} - \omega t)], \quad (7)$$

in which

$$k_{sy,1}^2 = k_s^2 - k_{z,1}^2, \quad k_{dy,1}^2 = k_d^2 - k_{z,1}^2. \quad (8)$$

Here, R , D , and S are the unknown reflection and transmission coefficients; C is an arbitrary amplitude; k_d and k_s are the wave numbers of dilatational and shear waves in the substrate; and ω is the circular frequency. In the layer the displacement field is a superposition of two dilatational and two shear waves. The localization length d_l of a type a radiation mode is the smallest for grazing incidence ($\theta \approx \pi/2$) when $d_l \approx 1/k$. Therefore, a layer can be considered a thin one when $d_l \ll d$, or equivalently, when $kd \ll 1$. In this approximation the generalized boundary conditions⁸ at the liquid/layer and layer/substrate interfaces may be used. These boundary conditions restrain only variations of the displacement vector and of the stress tensor components which are linear in the layer thickness d , resulting in a system of three linear equations in the unknown coefficients R , D , and S . Substitution of the solution of this system in Eqs. (4)–(7), gives for the displacement field in the liquid

$$u_{y,1}^a = i \frac{k_{y,1}}{k^2} \sin(k_{y,1}y - \varphi_1), \quad (9)$$

$$u_{z,1}^a = \frac{k_{z,1}}{k^2} \cos(k_{y,1}y - \varphi_1), \quad (10)$$

and for the displacement field in the substrate

$$u_{y,1}^a = -i \frac{k_{y,1}}{k^2} \sin \varphi_1 \left[\left(1 - \frac{2k_{z,1}^2}{k_s^2} \right) (1 + d\alpha) \exp(k_{dy,1}y) + \frac{2k_{z,1}^2}{k_s^2} (1 + d\beta) \exp(k_{sy,1}y) \right], \quad (11)$$

$$u_{z,1}^a = \frac{k_{y,1}}{k^2} \sin \varphi_1 \left[\frac{k_{z,1}}{k_{dy,1}} \left(1 - \frac{2k_{z,1}^2}{k_s^2} \right) (1 + d\alpha) \exp(k_{dy,1}y) + \frac{2k_{z,1}k_{sy,1}}{k_s^2} (1 + d\beta) \exp(k_{sy,1}y) \right]. \quad (12)$$

The phase φ_1 is defined as

$$\varphi_1 = \arccos \frac{B}{\sqrt{A^2 + B^2}} \quad (13)$$

with

$$A = k_{dy,1}k_s^4 + dk_s^6 P_1, \quad (14)$$

$$B = 4 \frac{\rho_1}{\rho} k_{y,1}k_{z,1}^2 \left[-k_{dy,1}k_{sy,1} + \left(k_{z,1} - \frac{k_s^2}{2k_{z,1}} \right)^2 \right] + dk_s^5 k_{y,1}P_2. \quad (15)$$

The expressions for α and β in Eqs. (11) and (12) are

$$\alpha = k_{dy,1} - \frac{k_s^2}{k_{dy,1}} P_1 + \frac{k_{sy,1}}{2k_{z,1}^2 - k_s^2} \left[(2k_{z,1}^2 - k_{s1}^2) \times \left(\frac{\rho_2 v_{s1}^2}{\rho_1 v_s^2} + \frac{2k_{z,1}^2(1 - \rho_2 v_{s1}^2/\rho_1 v_s^2)}{k_{s1}^2} \right) - \frac{4k_{z,1}^2(k_{z,1}^2 - k_{d1}^2)(1 - \rho_2 v_{s1}^2/\rho_1 v_s^2)}{k_{s1}^2} \right], \quad (16)$$

$$\beta = k_{sy,1} - \frac{k_s^2}{k_{dy,1}} P_1 + \frac{1}{2k_{dy,1}} \left[(2k_{z,1}^2 - k_{s1}^2) \times \left(\frac{\rho_2 v_{s1}^2}{\rho_1 v_s^2} + \frac{2k_{z,1}^2(1 - \rho_2 v_{s1}^2/\rho_1 v_s^2)}{k_{s1}^2} \right) - \frac{4k_{z,1}^2(k_{z,1}^2 - k_{d1}^2)(1 - \rho_2 v_{s1}^2/\rho_1 v_s^2)}{k_{s1}^2} - \frac{\rho_2 v_{s1}^2}{\rho_1 v_s^2} \frac{\rho_1}{\rho_2} (2k_{d1}^2 - k_{s1}^2) \right]. \quad (17)$$

In Eqs. (14)–(17) P_1 and P_2 are abbreviations for

$$P_1 = \frac{1}{k_s^4} \left[(k_{z,1}^2 - k_{dy,1}k_{sy,1}) \left(2k_{z,1}^2 - k_{s1}^2 - \frac{2k_{z,1}^2(2k_{d1}^2 - k_{s1}^2)}{k_{s1}^2} \right) \frac{\rho_2 v_{s1}^2}{\rho_1 v_s^2} + 2k_{z,1}^2 \left(1 - \frac{2k_{d1}^2}{k_{s1}^2} \right) \times (k_s^2 - 2k_{z,1}^2 + 2k_{dy,1}k_{sy,1}) - \frac{\rho_1}{\rho_2} \frac{k_{d1}^2}{k_s^2} (k_s^2 - 2k_{z,1}^2)^2 + 4 \frac{\rho_1}{\rho_2} \frac{k_{dy,1}k_{sy,1}k_{z,1}^2 k_{d1}^2}{k_s^2} \right], \quad (18)$$

$$P_2 = \frac{1}{k_s^3} \left[-\frac{\rho_1}{\rho} k_{sy,1} \left(2k_{z,1}^2 - k_{s1}^2 - \frac{2k_{z,1}^2(2k_{d1}^2 - k_{s1}^2)}{k_{s1}^2} \right) \times \frac{\rho_2 v_{s1}^2}{\rho_1 v_s^2} + \frac{\rho_2}{\rho} k_{s1}^2 k_{dy,1} \right]. \quad (19)$$

The value of C was chosen as $1/k^2$, and k_{d1} and k_{s1} are the wave numbers of dilatational and shear waves in the layer. The displacement field (9)–(12) contains the medium constants of the thin layer. When these medium constants are equal to those of the substrate, one finds

$$\alpha=0, \quad \beta=0, \quad \varphi_1=\varphi_0=\arccos \frac{B_0}{\sqrt{A_0^2+B_0^2}}, \quad (20)$$

with A_0 and B_0 the values of A and B for $d=0$, and the expressions (9)–(12) are the same as those for *type a* radiation modes for a liquid/solid structure.⁷ Also, in mode expansion (1), the displacement field (\mathbf{u}_1^s) of a Stoneley eigenmode for a liquid/thin layer/substrate structure appears. Therefore, we refer to a previous paper.⁸

II. EXPRESSION FOR THE EXPANSION COEFFICIENT OF THE TRANSMITTED STONELEY WAVE

From the boundary conditions along the plane $z=0$, and on the basis of the orthogonality relations between radiation modes and eigenmodes that belong to the same structure, a system of four integral equations in the four unknowns C_a^r , C_a^t , C_1^s , and C_2^s can be constructed. The system of integral equations is formally the same as the one that was derived to study the Stoneley wave excitation by a liquid wedge,⁷ although the values of the overlap integrals K_{ij}^{mn} and I_{ij}^{mn} ($i, j = 1, 2$; $m, n = a, s$) are different.

To solve the system of integral equations we apply the method of successive approximations.⁶ In a zeroth-order approximation the waves reflected at the down-step of the thin layer are neglected ($C_a^r=0$; $C_1^s=0$), which simplifies the calculation of the amplitudes of the transmitted waves (in structure 2). The zeroth-order approximation for the transmitted Stoneley wave amplitude C_2^s and transmitted bulk wave amplitude C_a^t are given by

$$C_2^s = \frac{1}{2I_{22}^{ss}} \int_0^k C_a^i(k_{y,1}) (I_{12}^{as} + K_{12}^{as}) dk_{y,1} \quad (21)$$

$$C_a^t(k_{y,2}) = \frac{1}{I_{22}^{aa}(k_{y,2})} \int_0^k C_a^i(k_{y,1}) K_{12}^{aa}(k_{y,1}, k_{y,2}) dk_{y,1}. \quad (22)$$

A first-order approximation for the amplitudes of the reflected waves is then derived from the system of integral equations whereby the zeroth-order approximation for the transmitted waves is used. The first-order approximation for the reflected Stoneley wave amplitude C_1^s takes the form

$$C_1^s = \frac{1}{I_{11}^{ss}} \left(\int_0^\infty C_a^t(k_{y,2}) K_{21}^{as}(k_{y,2}) dk_{y,2} + C_2^s K_{21}^{ss} \right). \quad (23)$$

In this paper we are interested in the dependence of the amplitude of the transmitted Stoneley wave on the medium constants—on the width and angle of incidence of the bounded beam. Calculations performed for a liquid wedge structure have already shown that the amplitude of the reflected Stoneley wave is smaller than the amplitude of the transmitted Stoneley wave. Only near Rayleigh angle incidence of the bulk wave can both amplitudes become of the same order.⁷

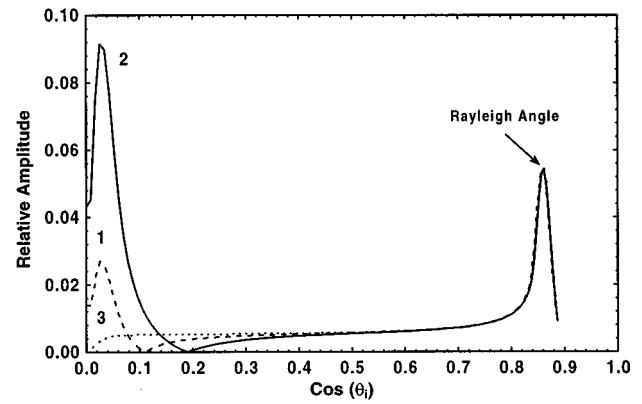


FIG. 2. Relative amplitude $|u_{z,2}^{\text{ston}}/u_0(y=0, z=0)|$ of the transmitted Stoneley wave generated by a 4-MHz Gaussian beam ($w=5$ mm, $r=15$ cm) incident from water as a function of the angle of incidence. The substrate is a steel sample and the thin layer consists of (1) copper, (2) Pyrex glass, (3) steel.

Evaluating the overlap integrals I_{12}^{as} , K_{12}^{as} , and I_{22}^{ss} by using the derived expressions for the displacement field and stress tensor of *type a* radiation modes for a liquid/thin layer/solid and of a Stoneley eigenmode for a liquid/solid structure, C_2^s finally becomes

$$C_2^s = \frac{\rho_1}{\rho} \frac{k_{y,2}^s}{k^2} \int_0^k C_a^i(k_{y,1}) \left[K(k_{y,1}) + \frac{k_{z,1}}{k_{z,2}} I(k_{y,1}) \right] dk_{y,1}, \quad (24)$$

in which the detailed expressions for the functions K and I are presented in the appendix; $k_{y,2}^s$ and $k_{z,2}^s$ are the wave vector components of a Stoneley eigenmode for a liquid/solid structure.

III. EXAMPLES OF NUMERICAL COMPUTATIONS

Figure 2 shows the angular dependence of the amplitude of the Stoneley wave generated by a Gaussian beam incident from water at the down-step of different thin layer/solid structures. The medium constants are given in Table I. The value of kd was fixed at 0.1 (at 4-MHz frequency this corresponds to a layer thickness of $5.8 \mu\text{m}$). Generally two maxima appear: a first one at almost grazing incidence and a second one at Rayleigh angle incidence. The first maximum is determined by the medium constants of the layer and only exists if these constants are different from the substrate medium constants. The same kind of maximum was found for liquid wedge structures.⁷ The second maximum is connected with the existence of the down-step itself. The value of this maximum is almost independent of the material characteristics of the layer. Figure 3 shows that the maximum value at

TABLE I. Values of medium constants used in the calculations.

Medium	Dilatational velocity v_d [m/s]	Shear velocity v_s [m/s]	Density ρ [kg/m ³]	Rayleigh angle
Steel	5720	3160	7800	30°
Brass	4282	2244	8100	44°
Pyrex glass	5570	3440	2230	27°
Water	1460	...	1000	

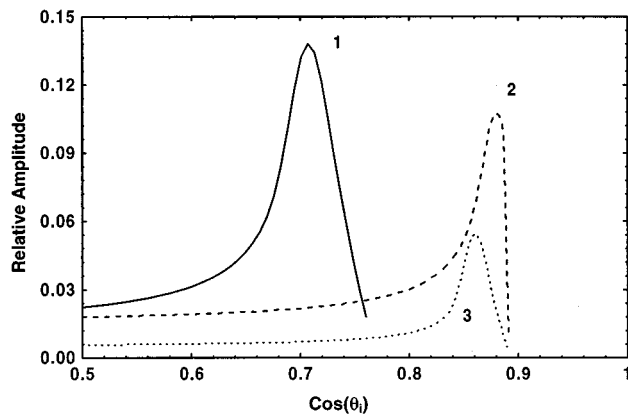


FIG. 3. Relative amplitude $|u_{z,2}^{\text{ston}}/u_0(y=0, z=0)|$ of the transmitted Stoneley wave generated by a 4-MHz Gaussian beam ($w=5$ mm, $r=15$ cm) incident from water near the Rayleigh angle. The medium constants of the thin layer are the same as those of the substrate: (1) copper, (2) Pyrex glass, (3) steel.

Rayleigh angle incidence is affected by the medium constants of the liquid and of the solid substrate. From Fig. 4 the minimum beamwidth required for the strongest Stoneley wave excitation at Rayleigh angle incidence can be predicted. Figure 5 illustrates that the excitation amplitude of the Stoneley wave is proportional to the layer thickness as well as to the frequency.

We remark that only when the bounded beam is incident from the liquid/layer/solid structure is a pronounced maximum found at Rayleigh angle incidence. A leaky Rayleigh wave is generated, resulting in an important concentration of bulk wave energy in the solid as well as in the layer. In this case the layer region ($-d \leq y \leq 0$) gives an important contribution to the overlap integrals K_{12}^{as} and I_{12}^{as} (describing the interaction between the leaky Rayleigh wave field in structure 1 and the Stoneley wave field in structure 2, which is mainly localized in the liquid). When the bounded beam is incident from the liquid/solid structure the contribution of the layer region to the proper overlap integrals is quite small, since the excited Stoneley wave in the liquid/layer/solid

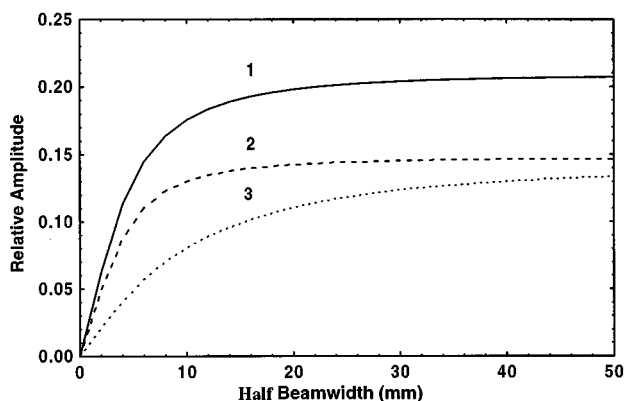


FIG. 4. Relative amplitude $|u_{z,2}^{\text{ston}}/u_0(y=0, z=0)|$ of the transmitted Stoneley wave generated by a 4-MHz Gaussian beam ($r=15$ cm) incident from water at the Rayleigh angle as a function of the beamwidth. The medium constants of the thin layer are the same as those of the substrate: (1) copper, (2) Pyrex glass, (3) steel.

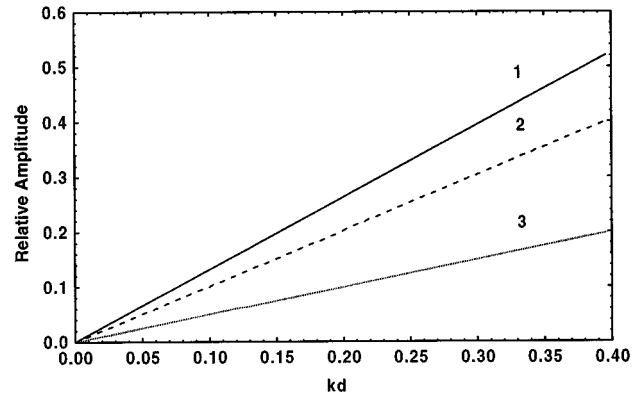


FIG. 5. Relative amplitude $|u_{z,2}^{\text{ston}}/u_0(y=0, z=0)|$ of the transmitted Stoneley wave generated by a 4-MHz Gaussian beam ($r=15$ cm) incident from water at the Rayleigh angle as a function of the shift h of the central axis of the beam (see also Fig. 1). The substrate is a steel sample and the thin layer consists of (1) copper, (2) Pyrex glass, (3) steel.

structure is mainly localized in the liquid. No maximum for the amplitude of the Stoneley wave excited in structure 1 is found at Rayleigh angle incidence.

The effect of Stoneley wave excitation by a bulk wave at the down-step of a layer can give information about the latter. In particular, the layer thickness can be found from measurements of the maximum Stoneley wave amplitude at Rayleigh angle incidence, since this value is independent of the material characteristics of the layer. To measure this amplitude the acousto-optic technique⁹ could be used, which is very sensitive even to weak ultrasound. From the maximum Stoneley wave amplitude at grazing incidence, information about the layer medium constants can be extracted.

IV. CONCLUSIONS

Mode theory was applied to solve the diffraction problem of a bulk wave at the downward step of a thin layer ($kd \ll 1$) on a substrate. The amplitude of the Stoneley wave excited along the liquid/substrate interface has a maximum at grazing and at Rayleigh angle incidence of the Gaussian beam. The Stoneley wave amplitude is proportional to the layer thickness and to frequency. The maximum at grazing incidence is affected by the material constants of the layer in contrast to the maximum at Rayleigh angle incidence. The latter maximum allows the evaluation of the thin layer thickness if the medium characteristics of the layer are not known.

ACKNOWLEDGMENT

The authors would like to thank the Research Council of the K. U. Leuven for the fellowship awarded to Professor G. N. Shkerdin, which enabled us to write this paper.

APPENDIX

The quantities I and K in Eq. (24) are given by

$$I = \frac{\rho}{\rho_1} I_1 + \frac{dk_{y,1}}{k} \frac{\rho}{\rho_1} C(k_{y,1}) \sin \varphi_1 - \frac{2k_{y,1}k_{y,2}^s}{k_s^6} \sin \varphi_1 I_2 \quad (\text{A1})$$

$$K = \frac{\rho}{\rho_1} I_1 + \frac{dk_{y,1}}{k} C_1(k_{y,1}) \sin \varphi_1 - \frac{2k_{y,1}k_{y,2}^s}{k_s^6} \sin \varphi_1 K_1, \quad C_1(k_{y,1}) = \left(1 - \frac{2k_{z,1}^2}{k_s^2}\right) \frac{k_s^2 + 2k_{dy,1}^2}{k_s^2 k_{dy,1}} k + \frac{4kk_{z,1}^2 k_{sy,1}}{k_s^4} \quad (\text{A2})$$

where

$$C(k_{y,1}) = \frac{k}{k_{dy,1}} \left(1 - \frac{2k_{z,1}^2}{k_s^2}\right) + \frac{2kk_{sy,1}}{k_s^2} \quad (\text{A3}) \quad I_1 = (1 - k_{y,2}^s d) \frac{k_{y,2}^s \cos \varphi_1 + k_{y,1} \sin \varphi_1}{(k_{y,2}^s)^2 + (k_{y,1})^2} \quad (\text{A5})$$

$$I_2 = (k_s^2 - 2k_{z,1}^2) \left[(k_s^2 - 2(k_{z,2}^s)^2) \left(\frac{1 + d\alpha_1}{k_{dy,2}^s + k_{dy,1}} - \frac{1 + d\beta_1}{k_{sy,1} + k_{dy,2}^s} \right) + 2(k_{z,2}^s)^2 \left(\frac{1 + d\alpha_1}{k_{dy,1} + k_{sy,2}^s} - \frac{1 + d\beta_1}{k_{sy,2}^s + k_{sy,1}} \right) \right] \\ + (k_s^2 - 2(k_{z,2}^s)^2) \frac{k_s^2 + 2(k_{dy,2}^s)^2}{2k_{dy,2}^s k_{dy,1}} \left(\frac{(k_s^2 - 2k_{z,1}^2)(1 + d\alpha_1)}{k_{dy,2}^s + k_{dy,1}} + \frac{2k_{dy,1}k_{sy,1}(1 + d\beta_1)}{k_{sy,1} + k_{dy,2}^s} \right) \\ + \frac{2(k_{z,2}^s)^2 k_{sy,2}^s}{k_{dy,1}} \left(\frac{(k_s^2 - 2k_{z,1}^2)(1 + d\alpha_1)}{k_{dy,1} + k_{sy,2}^s} + \frac{2k_{sy,1}k_{dy,1}(1 + d\beta_1)}{k_{sy,2}^s + k_{sy,1}} \right), \quad (\text{A6})$$

$$K_1 = (2(k_{z,2}^s)^2 - k_s^2)(k_{dy,2}^s - k_{sy,2}^s) \left(\frac{(k_s^2 - 2k_{z,1}^2)(1 + d\alpha_1)}{(k_{dy,1} + k_{dy,2}^s)(k_{dy,1} + k_{sy,2}^s)} + \frac{2k_{z,1}^2(1 + d\beta_1)}{(k_{sy,1} + k_{dy,2}^s)(k_{sy,1} + k_{sy,2}^s)} \right) \\ + (k_s^2 - 2k_{z,1}^2) \frac{k_s^2 + 2k_{dy,1}^2}{2k_{dy,1}k_{dy,2}^s} (1 + d\alpha_1) \left(\frac{k_s^2 - 2(k_{z,2}^s)^2}{k_{dy,2}^s + k_{dy,1}} + \frac{2k_{dy,2}^s k_{sy,2}^s}{k_{dy,1} + k_{sy,2}^s} \right) + \frac{2k_{z,1}^2 k_{sy,1}}{k_{dy,2}^s} (1 + d\beta_1) \\ \times \left(\frac{k_s^2 - 2(k_{z,2}^s)^2}{k_{dy,2}^s + k_{sy,1}} + \frac{2k_{dy,2}^s k_{sy,2}^s}{k_{sy,1} + k_{sy,2}^s} \right) \quad (\text{A7})$$

with $\alpha_1 = \alpha - k_{dy,1}$, $\beta_1 = \beta - k_{sy,1}$, $k_{dy,2}^s = [(k_{z,2}^s)^2 - k_d^2]^{1/2}$, $k_{sy,2}^s = [(k_{z,2}^s)^2 - k_s^2]^{1/2}$.

¹V. Dayal, "An automated simultaneous measurement of thickness and wave velocity by ultrasound," *Exp. Mech.*, 197–202 (1992).

²R. Dong and L. Adler, "Measurements of reflection and transmission coefficients of Rayleigh waves from cracks," *J. Acoust. Soc. Am.* **76**, 1761–1763 (1994).

³M. Bashyam, "Thickness compensation technique for ultrasonic evaluations of composite materials," *Mater. Eval.*, 1360–1364 (1990).

⁴Yu. V. Gulyaev and V. P. Plesskii, "Propagation of acoustic surface waves in periodic structures," *Sov. Phys. Usp.* **32**, 51–74 (1989).

⁵J. R. Chamuel, "Ultrasonic studies of transient seismo-acoustic waves in bounded solids and liquid/solid interfaces," *Sonoquest Report No. JRC-34-91*, 23–26 (1991), National Technical Information Document No. AD-A243441.

⁶R. Briers, O. Leroy, and G. N. Shkerdin, "Conversion of a Stoneley wave at the extremity of a fluid loaded plate," *J. Acoust. Soc. Am.* **101**, 1347–1357 (1997).

⁷R. Briers, O. Leroy, and G. N. Shkerdin, "A fundamental study of the excitation of a Stoneley wave at a liquid–solid interface: Rayleigh angle and Gaussian beam incidence," *J. Acoust. Soc. Am.* **95**, 1967–1976 (1994).

⁸R. Briers, O. Leroy, and G. N. Shkerdin, "Influence of an inclusion on the phase of a Stoneley wave," *J. Acoust. Soc. Am.* **101**, 1358–1365 (1997).

⁹W. Wevers, S. Devolder, O. Leroy, and P. De Meester, "Thin layer thickness measurements based on the acousto-optic technique," *Appl. Phys. Lett.* **68**, 1732–1734 (1996).

Spectral statistics in damped systems: Diffuse field decay curvature for materials characterization

John Burkhardt

Department of Engineering, Purdue University at Fort Wayne, 2101 Coliseum Boulevard East, Fort Wayne, Indiana 46805-1499

(Received 10 October 1996; accepted for publication 4 June 1997)

A new nondestructive technique is proposed which exploits the unique decay characteristics of diffuse fields in nonproportionally damped systems. A power-law decay model is derived and advanced as the basis for the inverse estimation of both the strength and spatial extent of the dissipative region in nonproportionally damped systems. In materials where mechanical damage results in increased internal friction, a common effect in many engineering metals, this technique is proposed as a nondestructive technique for characterizing such damage. The results of numerical experiments on nonproportionally damped acoustic systems are presented which support the proposed technique. © 1997 Acoustical Society of America. [S0001-4966(97)06009-8]

PACS numbers: 43.35.Zc, 43.55.Br [HEB]

INTRODUCTION

It has long been recognized that the level of internal friction in a material is sensitive to the amount of damage present in its internal structure. This relationship has been extensively explored in polycrystalline materials, where the interaction of ultrasonic waves with dislocations, point defects, and other microstructural characteristics are known to result in dissipation. As a result, experimental measurements of internal friction are often proposed as a tool for the characterization of microstructural damage.

Traditionally, internal friction has been determined experimentally from measurements of ultrasonic attenuation using pulse-echo techniques.¹ Difficulties arise with this technique, however, because measured attenuations have possible contributions from both internal scattering and geometric effects, in addition to internal friction. To avoid the difficulties inherent in attenuation measurements, the decay of diffuse ultrasonic fields has been suggested as a method of measuring levels of internal friction in material samples.^{2,3}

Diffuse fields occur at late times, after many transits across the specimen, and result in wave fields which are postulated to be completely incoherent and uniformly distributed throughout the sample. Under these conditions the decay of the diffuse field results entirely from internal friction in the specimen, and is unaffected by scattering and geometric effects. Therefore, measurements of diffuse decays provide a direct measure of internal friction in a material sample and, as a result, are typically easier to perform and are often considerably more accurate.³

Recent attempts to characterize material properties using diffuse field decays have applied simple exponential decay models which assume proportional damping.^{3,4} The assumption of proportional damping is often justified in solids because many sources of internal friction are well described by a viscoelastic model⁵ and are often distributed uniformly throughout the material sample.

In many systems of practical interest, however, internal damage such as plastic or fatigue damage, and therefore internal friction, is not uniformly distributed throughout the

samples' volume, resulting in nonproportional damping. In these instances the exponential decay model fails, and nonexponential decays are expected. Evidence of nonexponential diffuse decays have been observed in polycrystals³ as well as reverberation rooms.^{6,7}

A theoretical model describing the nonexponential decay of diffuse fields has been derived by appealing to a statistical description of the decay process and is presented in the Theory section of this paper. The experimental use and range of application of the proposed technique is then discussed briefly in Sec. II. Additionally, the validity of the derived decay model and its utility for the estimation of the internal friction characteristics of nonproportionally damped systems has been tested through numerical simulations; these findings are presented in the Numerical Experiments section.

I. THEORY

Central to the characterization of nonexponential decays is an accurate understanding of how modal decay rates vary in systems with nonuniformly distributed internal friction. Recently, Burkhardt and Weaver have answered this question by exploiting statistical concepts to characterize the decay rates of viscously damped diffuse fields.⁸ A similar approach was originally presented by Schroeder;⁹ however, small differences between Schroeder's deviations and those of Burkhardt and Weaver result in subtle, but important, differences in the parametrization of nonexponential decays.⁸

The general approach is to treat modal vectors, u , as uncorrelated, random Gaussian speckle fields. Considering the i th modal vector, u_i , in a system described by a viscous dissipation operator, C , and mass operator, M , the i th modal amplitude decay rate, β_i , can be expressed as

$$\beta_i = \frac{1}{2} \frac{u_i \cdot C u_i}{u_i \cdot M u_i}. \quad (1)$$

If the viscous dissipation strength, c , is constant, but not necessarily uniform, an expression for the expected statistical distribution of modal decay rates, $p(\beta)$, can be derived,⁸

$$p(\beta) = \frac{\beta^{B/2-1} e^{-\beta(mN/c)}}{(c/mN)^{B/2} \Gamma(B/2)}. \quad (2)$$

The probability density function, $p(\beta)$, is characterized by two independent parameters

$$\frac{c}{mN} \quad \text{and} \quad \frac{B}{2}, \quad (3)$$

described in terms of, c , the viscous damping factor, m , the system's mass density, and B and N , the number of "damped sites" and the "total number of sites" in the system, respectively. In continuous systems the number of sites is related to the number of dimensions in which the system resides, d , its extent, D , the extent of the dissipation, D_d , and the wavelength of the excitation, λ ,⁹

$$B \approx \frac{D_d}{(\lambda/2)^d}, \quad N \approx \frac{D}{(\lambda/2)^d}. \quad (4)$$

With an expression for the probability density function of decay rates in diffuse systems available, Eq. (2), the ensemble average energy decay of a diffuse field, $d(t)$, composed of a collection of modes with decay rates drawn from the derived distribution, can be calculated. Assuming the total energy, E_0 , is equally distributed among the modes,

$$d(t) = E_0 \int_0^\infty p(\beta) e^{-2\beta t} d\beta = E_0 \left[1 + \left(\frac{2c}{mN} \right) t \right]^{-B/2}, \quad (5)$$

a power-law description for the nonexponential decay process is recovered. If time is nondimensionalized by the mean energy decay rate $\tau = 2\langle\beta\rangle t$, the energy decay can be written as

$$d(\tau) = E_0 \left[1 + \left(\frac{2}{B} \right) \tau \right]^{-B/2}, \quad (6)$$

resulting in an expression for the nonexponential decay of diffuse fields completely characterized by the number of damped site, B . The energy decay can also be written in terms of decibels relative to the initial energy level:

$$L(t) = -2.17B \ln \left[1 + \left(\frac{2}{B} \right) \tau \right] \text{ dB}. \quad (7)$$

Now, with an expression for the nonexponential decay process, it is possible to exploit its form to determine the two free parameters, B and $2c/mN$, from an observed energy decay. The parameters can be determined in one of two ways, either through a nonlinear curve fit of Eq. (5) or by a linear regression analysis of

$$-\left[\frac{d}{d\tau} \{ \ln[d(t)] \} \right]^{-1} = \frac{2}{B} + \left(\frac{2c}{mN} \right) t, \quad (8)$$

which follows directly from Eq. (5). A similar relation can also be derived from Eq. (7). Determination of the two free parameters provides an immediate estimate of both the intensity of the internal friction through the parameter, c , and its spatial extent through the parameter, B . It should be noted that the derived decays are for the total energy field, which is rarely available. However, if the wave field is sufficiently

diffuse, a local measurement of energy density should be representative of the entire energy field.

II. APPLICATION

Practical application of diffuse field decay curvature for the characterization of internal friction, and, ultimately damage, has limitations on application, as do other experimental techniques. General limitations on diffuse ultrasonic methods have already been discussed by Weaver,¹⁰ and include sufficient modal density and reverberance. Additionally, diffuse field decay curvature techniques would also be limited to systems in which signal duration was sufficient to manifest curvature. On short time scales all energy decays will appear exponential. It is necessary to observe the signal over a time scale in which the difference in the decay rates of the individual modes, which may be small, becomes significant. Practically speaking, the curvature will become evident when the slope of the logarithm of the energy decay is significantly different from its initial slope.

Consider the slope of the logarithm of decay, Eq. (6), normalized by its slope at time zero:

$$\mu(\tau) = \frac{\frac{d}{d\tau} \{ \ln[d(\tau)] \}}{\frac{d}{d\tau} \{ \ln[d(0)] \}} = \left[1 + \left(\frac{2}{B} \right) \tau \right]^{-1}. \quad (9)$$

Now define the "half-life" of the signal, $\tau_{1/2}$, as the time required for the slope of the logarithm of decay to fall to half its original value:

$$\mu(\tau_{1/2}) = 1/2 \Rightarrow \tau_{1/2} = B/2, \quad (10)$$

where B is the number of "damped sites" and $B/2$ is, not unexpectedly, the inverse of the normalized variance of the decay rates derived from Eq. (2) (Ref. 8). Therefore, for the curvature to become evident, approximately $B/2$ factors of e in signal duration are required. Equivalently, using Eq. (7), 1.51B dB of dynamic range would be required to observe a similar change in slope. It is important to note that the required dynamic range required for a successful experiment is a function of both the wavelength of the excitation used in the experiment and the size of the damaged area being probed as related through the parameter, B .

III. NUMERICAL EXPERIMENTS

As a test of the proposed concept, numerical experiments were performed. To avoid the complications associated with a simulation of elastic waves, a simpler, acoustic system was considered. Specifically, the dynamics of viscously damped finite membranes with fixed, irregularly shaped boundaries were simulated using a central finite difference scheme. Following a narrow band excitation, the energy density at a single location in the membrane was recorded as a function of time. The viscous damper strength and its area in the membrane were then estimated by fitting the predicted ensemble averaged decay, Eq. (5), to the recorded energy density for the two free parameters [Eq. (3)].

All of the simulations performed considered a square, discrete membrane model with 301 degrees of freedom per

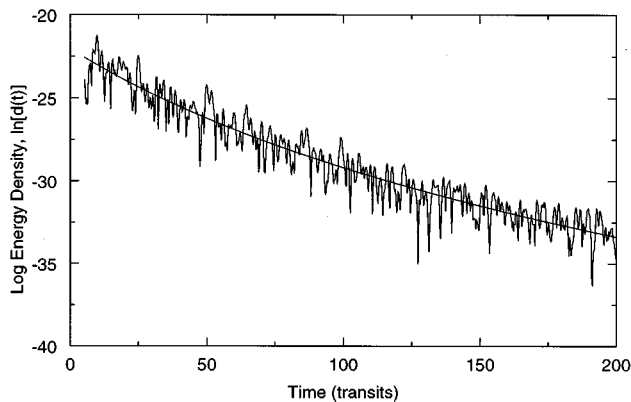


FIG. 1. Logarithmic energy density versus time. $\ln[d(t)]$ vs t . Observed parameters: $\bar{B}=20.6$, $\bar{c}=2.0$.

side before the addition of boundary disorder. Boundary disorder was included by randomly fixing between 0 and 3 degrees of freedom perpendicularly into the mesh at each boundary node, while holding the total number of degrees of freedom fixed at 88 000. The random value was chosen from a uniform distribution, resulting in an average roughness of $1\frac{1}{2}$ deg of freedom. Internal friction was included by viscously damping a square patch of nodes at the center of the mesh. For convenience the viscous damper strength was held constant at 2.0. Additionally, no configuration averaging was performed; all results presented are for individual membranes subjected to single-tone burst excitations.

Because the effect of the damped area on the diffuse decay is directly impacted by the wavelength of the response, Eq. (4), narrow-band Gaussian tone bursts were used to minimize the effect of wavelength dispersion. The half-width of the Gaussian pulse envelope was held constant at 0.5 s, while the underlying harmonic signal was either 20 or 30 Hz. This combination resulted in excitation wavelengths covering approximately 21 ± 0.34 nodes at 20 Hz or 14 ± 0.15 nodes at 30 Hz, respectively. Accordingly, the effects of wavelength dispersion are expected to have a minimal impact on the results.

The number of modes contributing to the system's response was also estimated from the bandwidth of the excitation and the modal density of the membrane. It was estimated that approximately 13 and 19 modes were contributing to the system's response at 20 and 30 Hz, respectively. Such few modes contributing to the system's response is far from ideal and is a result of computational limitations. The small number of modes does not, however, invalidate any of the simulations results. The primary effect was to increase the variability of observed energy decays between nominally identical systems differing only in boundary roughness.

Damped areas and viscous damper strengths estimated from recorded energy density decays were regularly predicted to within 15%. As anticipated, however, the accuracy of these estimates showed fluctuations from system to system in comparison with the specified characteristics of the simulated systems. Figure 1 shows a typical logarithmic energy density decay from a single sample location which pro-

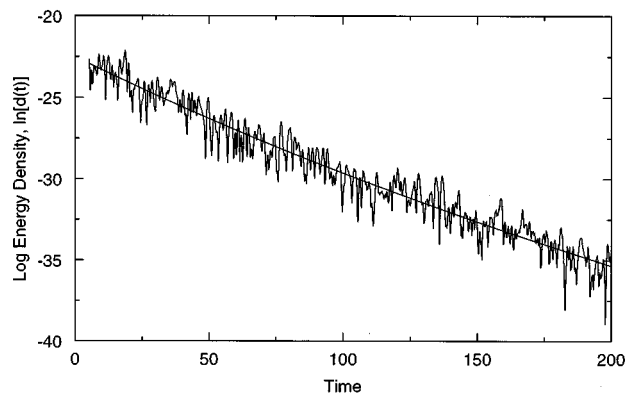


FIG. 2. Logarithmic energy density versus time. $\ln[d(t)]$ vs t . Observed parameters: $\bar{B}=57.7$, $\bar{c}=0.56$.

duced accurate predictions. This simulation was performed at 20 Hz with a 45×45 damped rectangle placed at the center of the system. These parameters result in a theoretical prediction of approximately 18.4 damped sites, $B=18.4$, and, fixed by the simulation, a viscous damper strength of 2.0. Using the Minpack routine LMDIF1, a nonlinear curve fit was performed on the observed decay, yielding estimates for the number of damped sites, $\bar{B}=20.6$, and the viscous damper strength, $\bar{c}=2.0$. This fit shows very good agreement with the estimation of the total damped area and an exact match for the viscous damper strength. Linear curve fits using Eq. (8) were found to be unreliable as a result of the required data inversion, which resulted in data points very far from the mean value of the signal.

While the decay record of Fig. 1 and others like it yielded reasonable predictions for the dissipation parameters of their respective systems, several other simulations proved to differ significantly from the theoretical predictions outlined previously. To illustrate this point the energy density decay from a system nominally identical to the system of Fig. 1, differing only in boundary disorder, is shown in Fig. 2. This decay, when fitted, was found to estimate the number of damped sites at 57.7, $\bar{B}=57.7$, and the viscous damper strength at 0.56, $\bar{c}=0.56$. The large fluctuations in parameter estimation can be attributed to the small number of modes which contribute to the system's response. The possibility of other sources for the fluctuations, such as spatial variation, can be discounted by considering the total energy decay for the same system (Fig. 3). A curve fit of the total energy decay provides estimates of the number of damped sites, $\bar{B}=49.3$, and the viscous damper strength, $\bar{c}=0.66$, very similar to those determined from a single measurement position. Because of this similarity it is reasonable to assume that the observed fluctuations in the decay characteristics of the different systems is due largely to the small sample of modes involved in the system's responses. This result is not unexpected because the modal decay rates contributing to the system's energy density are identical at all locations. As a result, spatial averaging does not increase the number of decay rates sampled from the theoretical ensemble. In agreement with this argument, configuration averaging, which would increase the number of decay rates sampled from the ensemble,

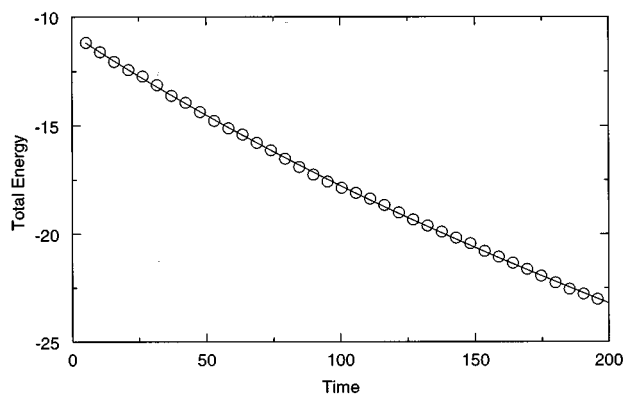


FIG. 3. Logarithm total energy versus time. $\ln[d(t)]$ vs t . \circ Total energy, — curve fit. Observed parameters: $\bar{B}=49.3$, $\bar{c}=0.66$.

was observed to notably increase the accuracy of the parameters' predictions.

IV. CONCLUSIONS

A theoretical model for the nonexponential decay of diffuse fields has been derived and shown to be a useful tool for the determination of both the strength and relative extent of a viscous dissipation mechanism in nonproportionally damped systems. The accuracy of the estimated parameters depends critically upon the characteristics of the system under consideration and the experiment performed to determine them. In general, for accurate estimates the system should be lightly damped, possess considerable disorder, and have a high modal density.

Future work will concentrate on experimentally testing the proposed nondestructive evaluation tool for locating and characterizing damage in engineering materials.

- ¹E. P. Papadakis, "Ultrasonic velocity and attenuation measurement methods with scientific and industrial applications," in *Physical Acoustics*, edited by W. P. Mason and R. N. Thurston (Academic, New York, 1979), Vol. XII, pp. 277–374.
- ²H. Willems, "A new method for the measurement of ultrasonic absorption in polycrystalline material," in *Review of Progress in Quantitative Nondestructive Evaluation*, edited by D. O. Thompson and D. E. Chimenti (Plenum, New York, 1987), Vol. 6A, pp. 473–481.
- ³R. L. Weaver, "Diffuse field decay rates for material characterization," in *Solid Mechanics Research for Quantitative Nondestructive Evaluation*, edited by J. D. Achenbach and Y. Rajapakse (Martinus Nijhoff, 1987), pp. 425–433.
- ⁴M. Paul, B. Haberer, and W. Arnold, "Materials characterization at high temperatures using laser ultrasound," *Mater. Sci. Eng. A* **168**, 87–92 (1993).
- ⁵A. V. Bhatia, *Ultrasonic Absorption* (Oxford U.P., London, 1967).
- ⁶K. Bodlund, "Monotonic curvature of low frequency decay records in reverberation chambers," *J. Sound Vib.* **73**, 19–29 (1987).
- ⁷F. Kawakami and K. Yamiguchi, "A systematic study of power-law decays in reverberation rooms," *J. Acoust. Soc. Am.* **80**, 543–554 (1986).
- ⁸J. A. Burkhardt and R. L. Weaver, "Spectral statistics in damped systems: Part I, Modal decay rate statistics," *J. Acoust. Soc. Am.* **100**, 320–326 (1996).
- ⁹M. R. Schroeder, "Some new results in reverberation theory," in 5th International Congress on Acoustics, Liege G31, 1–4, 1965.
- ¹⁰R. L. Weaver, "Diffuse waves for material NDE," in *Acousto-Ultrasonics*, edited by J. C. Duke, Jr. (Plenum, New York, 1988), pp. 35–44.

A liquid wedge as generating technique for Lamb and Rayleigh waves

R. Briers,^{a)} O. Leroy, and G. Shkerdin^{b)}

Interdisciplinary Research Center, K.U.L. Campus Kortrijk, B-8500 Kortrijk, Belgium

(Received 15 January 1997; accepted for publication 30 May 1997)

A model is developed to describe the excitation of Lamb and Rayleigh waves by a Gaussian beam incident on a liquid/air/solid corner. Analytical expressions for the displacement fields of the generated modes are derived by applying a mode theory that accounts for the contribution of the reflected waves. Numerical computations illustrate the optimum conditions under which the strongest stimulation of Lamb and Rayleigh waves may be expected. © 1997 Acoustical Society of America. [S0001-4966(97)05809-8]

PACS numbers: 43.35.Pt [HEB]

INTRODUCTION

Lamb and Rayleigh waves are of great interest for the detection of material imperfections as well as for the characterization of layered structures.¹⁻⁵ An overview of the advantages of these modes in nondestructive testing and monitoring applications is given by Viktorov.⁶ Many techniques for the generation of Lamb and Rayleigh waves are reported in literature: For instance the use of interdigital,⁷ air-coupled,⁸ or electromagnetic acoustic transducers⁹ and the laser ultrasonic technique.¹⁰

In the liquid wedge method, the acoustic coupling between the source and the solid sample is provided by a liquid. This noncontact method of excitation is very simple in that no special preparation of the solid is required, and it produces repeatable surface wave power levels since no variable contact layers need to be applied to the sample.

Mode theory has already been applied to study the excitation of Stoneley waves by the liquid wedge technique in which two different liquids overlie a solid sample.¹¹ For the generation of Lamb and Rayleigh waves the liquid wedge configuration now consists of a solid sample that is partially immersed in a single liquid. A Gaussian ultrasonic beam is incident at the liquid/air/solid junction. The amplitudes of the generated modes are the solutions of a system of coupled integral equations. The procedure to construct this system is quite similar to the one used for the investigation of Stoneley wave excitation by a liquid wedge. However, to solve the system of coupled integral equations other approximations are used, and the so-called method of successive approximations¹² is applied. In this paper the attention is mainly focused on the parameters (beamwidth, distance of observation, lateral shift, ...) that affect the excitation amplitude of Lamb and Rayleigh waves. The influence of wave reflection and radiation is taken into account in the model.

I. GENERATION OF LAMB WAVES

A. Theoretical model for the excitation problem

The liquid wedge configuration for the generation of Lamb waves in a plate with free boundaries is shown in Fig. 1. A plate of thickness $2d$ is partially immersed in a liquid. A Gaussian beam with half-beamwidth w is incident at an angle θ_i on the liquid/air/solid corner (the point "P"). The resulting displacement fields in u_1^{tot} and u_2^{tot} in, respectively, the region $z < 0$ (structure 1) and $z > 0$ (structure 2) can be expressed by the mode expansions¹¹

$$u_1^{\text{tot}}(y, z) = \int_0^{+\infty} \sum_m \{ [C_{r_m}^i(k_{y,1}) + C_{r_m}^r(k_{y,1})] \times u_1^{r_m}(k_{y,1}; y, z) \} dk_{y,1} + \sum_m C_{s_m}^r u_1^{s_m}(y, z), \quad (1)$$

$$u_2^{\text{tot}}(y, z) = \sum_n [C_{s_n}^t u_2^{s_n}(y, z) + C_{a_n}^t u_2^{a_n}(y, z)], \quad (2)$$

from which the corresponding stress tensor components T_{ij}^{tot} and $T_{ij,2}^{\text{tot}}$ ($i, j = y, z$) can be derived; $k_{y,1}$ is the y component of the wave vector in the liquid; $C_{r_m}^i$ is the (known) expansion coefficient of the incident acoustic beam; $C_{r_m}^r$ and $C_{s_m}^r$ are, respectively, the unknown symmetrical ($m = s$) or anti-symmetrical ($m = a$) expansion coefficients of the scattered bulk wave and the mode-converted Stoneley wave, while $C_{s_n}^t$ and $C_{a_n}^t$ represent, respectively, the unknown expansion coefficients of the n th symmetrical and antisymmetrical Lamb wave that is excited in the free plate. The expressions for the orthogonal set of acoustic modes $\{u_1^{r_m}, u_1^{s_m}\}$ were derived in Ref. 12. Those for the orthogonal set of acoustic modes $\{u_2^{s_n}, u_2^{a_n}\}$ are summarized in the Appendix.

From the boundary conditions along the plane $z = 0$ it follows that¹²

^{a)}Postdoctoral fellow of the Flemish Institute for the Encouragement of the Scientific and Technological Research in Industry (I.W.T.).

^{b)}Permanent address: Institute of Radioengineering and Electronics, Russian Academy of Sciences, Moscow, Russia.

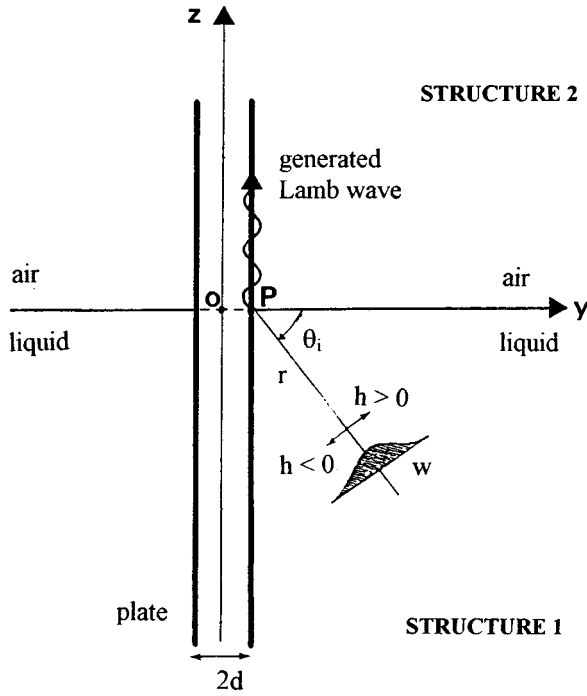


FIG. 1. Geometry of the liquid wedge configuration for the generation of Lamb waves.

$$\int_{-\infty}^{+\infty} [T_{zz,1}^{\text{tot}} u_{z,1}^{r_m*}(k'_{y,1}) - T_{yz,1}^{r_m*}(k'_{y,1}) u_{y,1}^{\text{tot}}] \\ = \int_{-\infty}^{+\infty} [T_{zz,2}^{\text{tot}} u_{z,1}^{r_m*}(k'_{y,1}) - T_{yz,1}^{r_m*}(k'_{y,1}) u_{y,2}^{\text{tot}}], \quad (3)$$

in which $u_{z,1}^{r_m}$ and $T_{yz,1}^{r_m}$ are the components of a fixed radiation mode belonging to the liquid/plate/liquid structure. The asterisk stands for the complex conjugate.

Making use of the orthogonality relations¹¹ that exist among the acoustic modes leads to the integral equation

$$[C_{r_m}^i(k_{y,1}) + C_{r_m}^r(k_{y,1})] \mathcal{H}_{11}^{r_m r_m} = \sum_n C_{m_n}^t K_{21}^{m_n r_m}(k_{y,1}), \quad (4)$$

with $\mathcal{H}_{11}^{r_m r_m}$ defined by the value of the overlap integral¹¹ $K_{11}^{r_m r_m} = \mathcal{H}_{11}^{r_m r_m} \delta(k_{y,1} - k'_{y,1})$.

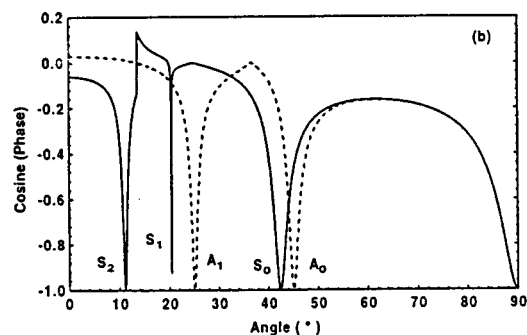
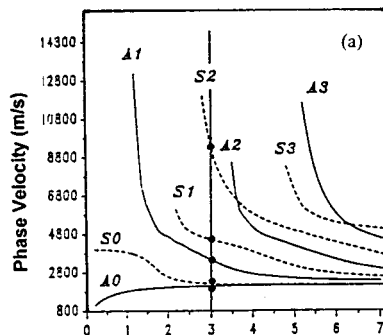


FIG. 3. (a) Lamb wave dispersion curves for a brass plate. (b) Angle dependence of the phase for symmetrical (solid line) and antisymmetrical (dashed line) radiation modes in the case of a water-loaded brass plate ($2d = 1$ mm, 3-MHz frequency).

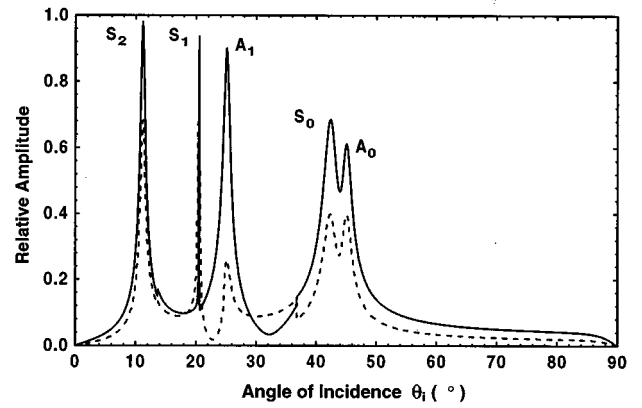


FIG. 2. Displacement amplitudes $|u_{y,2}^{\text{tot}}/u_0(y=d)|$ (solid line) and $|(u_{z,2}^{\text{tot}}/u_0) \times (y=d)|$ (dashed line) for a 1-mm-thick brass plate, caused by a 3-MHz homogeneous plane wave incident from water. Distance of observation is $z = 0.5$ cm.

Putting in Eq. (4) the coefficient $C_{m_n}^t$ equal to zero results in a zeroth-order approximation for the coefficient $C_{r_m}^i$. A first-order approximation for the coefficient $C_{m_n}^t$ of the n th symmetrical ($m=s$) or antisymmetrical ($m=a$) excited Lamb wave in the free plate is then found by working out Eq. (3) with the displacement and stress tensor components of a fixed Lamb eigenmode supported by the free plate. Substituting in this first-order approximation the zeroth order approximation for the scattered bulk wave ($C_{r_m}^i$) gives

$$C_{m_n}^t = \frac{1}{K_{22}^{m_n m_n}} \int_0^k \sum_m C_{r_m}^i(k_{y,1}) I_{12}^{r_m m_n}(k_{y,1}) dk_{y,1} \\ + \sum_n C_{s_m}^r (K_{12}^{s_m m_n} - I_{12}^{s_m m_n}). \quad (5)$$

Since the length over which a Stoneley wave penetrates into the plate near a Lamb angle is smaller than the length over which a radiation mode penetrates into the plate, the overlap integrals $K_{12}^{s_m m_n}$ and $I_{12}^{s_m m_n}$ may be neglected in comparison with the overlap integral $I_{12}^{r_m m_n}$. The integrals $I_{12}^{r_m m_n}$ and $K_{22}^{m_n m_n}$ can be calculated analytically, resulting in the following expression for the coefficient $C_{m_n}^t$:

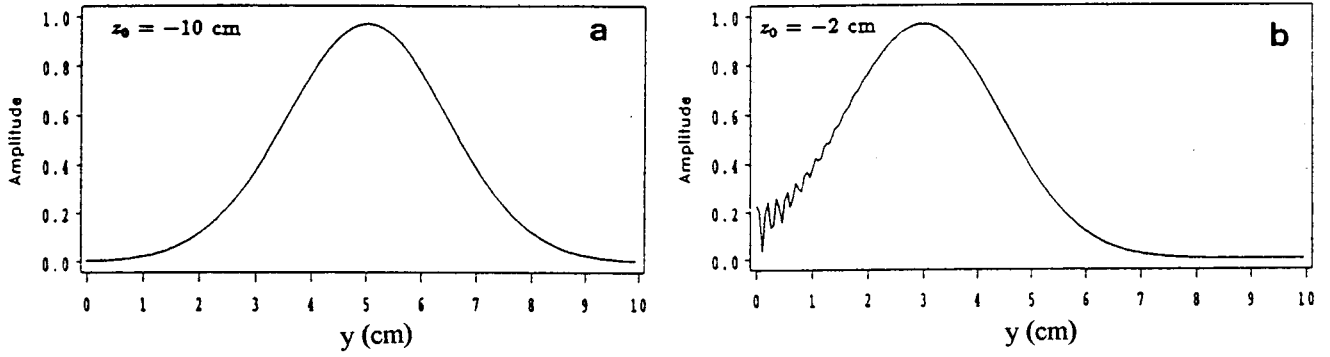


FIG. 4. (a) Description of a 3-MHz Gaussian beam ($\theta_i = 75^\circ$, $w = 1$ cm) in a vertical plane $z_0 = -10$ cm in terms of radiation modes for a water/brass/water structure. (b) Amplitude distribution of the incident Gaussian beam (after some propagation) in the vertical plane $z_0 = -2$ cm.

$$C_{m_n}^t = [k^2 k_{z,2}^{m_n} k_{dy,2}^{m_n} f_m(k_{dy,2}^{m_n} d) \beta^{m_n}(k_{y,2}^{m_n})]^{-1} \int_0^k C_{r_m}^i(k_{y,1}) \times \cos[\varphi_m(k_{y,1})] \beta^{m_n}(k_{z,1}) k_{z,1} k_{y,1} dk_{y,1}. \quad (6)$$

In Eq. (6), $k_{z,1} = (k^2 - k_{y,1}^2)^{1/2}$ with k the wave number of the liquid; $f_m = \tan$ if $m = s$ and $f_m = \cotan$ if $m = a$; φ_m is the phase¹² of a radiation mode characterized by the wave vector component $k_{y,1}$. The function β^{m_n} is given by

$$\begin{aligned} \beta^{m_n}(k_{z,1}) = & (2k_{z,1}^2 - k_s^2) k_{dy,2}^{m_n} f_m(k_{dy,2}^{m_n} d) \left[\frac{2(k_{z,2}^{m_n})^2 - k_s^2}{k_s^2 g_m(k_{dy,2}^{m_n} d)} (F_1^- \mp F_1^+ - F_2^- \pm F_2^+) - \frac{2(k_{z,2}^{m_n})^2}{k_s^2 g_m(k_{sy,2}^{m_n} d)} (F_3^- \mp F_3^+ - F_4^- \pm F_4^+) \right] \\ & + \frac{(2(k_{z,2}^{m_n})^2 - k_s^2)^2}{2k_{dy,1}} \left\{ \frac{k_s^2 - 2(k_{dy,2}^{m_n})^2}{[2(k_{z,2}^{m_n})^2 - k_s^2][1 - g_m(k_{dy,2}^{m_n} d)]^{1/2}} \left[\frac{2k_{z,1}^2 - k_s^2}{k_s^2} (F_1^- \pm F_1^+) + \frac{2k_{dy,1} k_{sy,1}}{k_s^2} (F_2^- \pm F_2^+) \right] \right. \\ & \left. - \frac{1}{[1 - g_m(k_{sy,2}^{m_n} d)]^{1/2}} \left[\frac{2k_{z,1}^2 - k_s^2}{k_s^2} (F_3^- \pm F_3^+) + \frac{2k_{dy,1} k_{sy,1}}{k_s^2} (F_4^- \pm F_4^+) \right] \right\}, \end{aligned} \quad (7)$$

in which F_i^\pm ($i = 1, \dots, 4$) are abbreviations for

$$F_1^\pm = \frac{\sin[(k_{dy,1} \pm k_{dy,2}^{m_n})d]}{g_m(k_{dy,1}d)(k_{dy,1} \pm k_{dy,2}^{m_n})}, \quad (8)$$

$$F_2^\pm = \frac{\sin[(k_{sy,1} \pm k_{dy,2}^{m_n})d]}{g_m(k_{sy,1}d)(k_{sy,1} \pm k_{dy,2}^{m_n})}, \quad (9)$$

$$F_3^\pm = \frac{\sin[(k_{dy,1} \pm k_{sy,2}^{m_n})d]}{g_m(k_{dy,1}d)(k_{dy,1} \pm k_{sy,2}^{m_n})}, \quad (10)$$

$$F_4^\pm = \frac{\sin[(k_{sy,1} \pm k_{sy,2}^{m_n})d]}{g_m(k_{sy,1}d)(k_{sy,1} \pm k_{sy,2}^{m_n})}, \quad (11)$$

and with $g_m = \sin$ if $m = s$ and $g_m = \cos$ if $m = a$; $k_{dy,1} = (k_d^2 - k_{z,1}^2)^{1/2}$, $k_{sy,1} = (k_s^2 - k_{z,1}^2)^{1/2}$, k_d and k_s being, respectively, the longitudinal and transverse wave number in the plate.

B. Examples of numerical computations

The total deformation, due to the excitation of Lamb waves, of the part of the plate situated in air can now be calculated by substituting the coefficients (6) into the mode expansion (2). The coefficients $C_{m_n}^t$ depend on the amplitude distribution of the incident bulk wave $[C_{r_m}^i(k_{y,1})]$. For a water-loaded brass plate of 1-mm thickness, Fig. 2 shows the relative displacement amplitudes of the upperface caused by a 3-MHz incident homogeneous plane wave with amplitude u_0 . For an incident homogeneous plane wave, $C_{r_m}^i(k_{y,1})$ is proportional to the Dirac function.¹¹ At this point we must remark that near the water/air/brass corner, local Lamb modes also are generated, which interfere. This interference obstructs the observation of the propagating Lamb waves. The maximum distance over which the local modes exist is equal to $1/|k_z^{m_n}|$, with $k_z^{m_n}$ the z component of the lowest local Lamb mode, which can be calculated from the characteristic equation (A1). As can be seen from Fig. 3(a), five propagating Lamb modes exist at the frequency–thickness

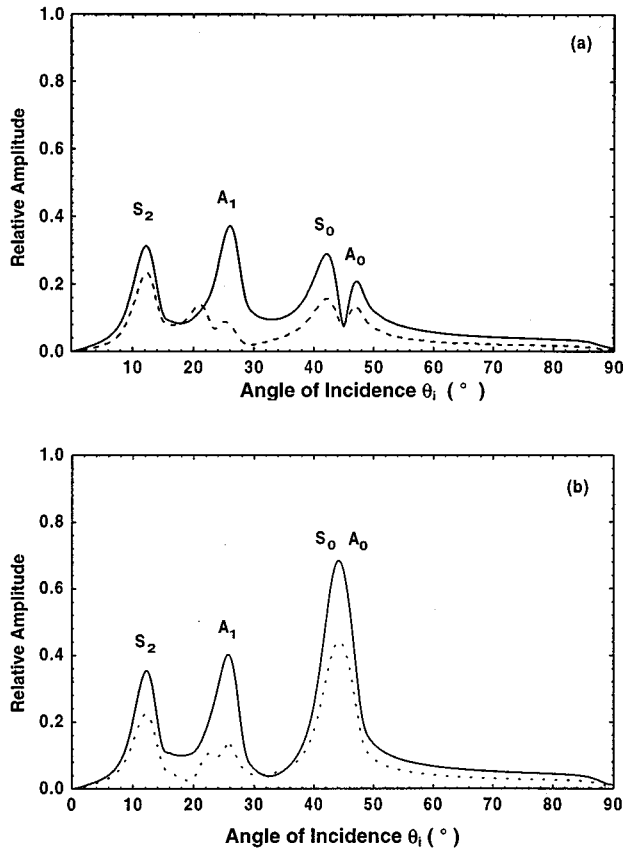


FIG. 5. The same as in Fig. 2 but for a Gaussian beam with half-beamwidth $w=0.5$ cm incident from a distance $r=15$ cm. Distances of observation: (a) $z=0.5$ cm, (b) $z=1$ cm.

combination considered. In Fig. 2 the distance of observation z is 0.5 cm, at which the five propagating Lamb modes are well separated from the local ones. Each maximum in Fig. 2 occurs at the Lamb angle $\theta_i = \arcsin(v_{\text{liquid}}/v_{\text{Lamb}})$, in which the velocity for each particular Lamb mode can be found from the dispersion curves presented in Fig. 3(a) (S_2 at 11° , S_1 at 21° , A_1 at 25° , S_0 at 42.5° , A_0 at 45°). Note that the values of these maxima do not depend on the distance of observation z . Indeed, in the case of an incident homogeneous plane wave, the total normal displacement, (2), for instance, takes the form

$$\frac{u_{y,2}^{\text{tot}}}{u_0}(y=d, z) = -k_y^i k_z^i k^{-1} \left\{ \sum_{m,n} \frac{\cos[\varphi_m(k_y^i)]}{k_{z,2}^{m_n}} \frac{\beta^{m_n}(k_z^i)}{\beta^{m_n}(k_{z,2}^{m_n})} \exp(ik_{z,2}^{m_n} z) \right\}. \quad (12)$$

If now the angle of incidence $\theta_i = \theta_{m_n}$ (and thus $k_z^i = k \sin \theta_i \approx k_{z,2}^{m_n}$, $k_y^i = k \cos \theta_i$) with θ_{m_n} the exact Lamb angle of the n th symmetrical ($m=s$) or n th antisymmetrical ($m=a$) mode, the value of $\cos \varphi_m$ tends to minus one [see Fig. 3(b)], and only the term containing the factor $\exp(ik_{z,2}^{m_n} z)$ remains in expression (12). Taking the modulus of this term results in the very simple z -independent relation

$$\left| \frac{u_{y,2}^{\text{tot}}}{u_0}(y=d) \right| \approx \cos \theta_{m_n}. \quad (13)$$

For angles of incidence between the exact Lamb angles, several terms in expression (12) give a contribution, and as a result the relative displacement amplitude is now dependent on the distance of observation z .

Figure 4 shows the description of a Gaussian beam in terms of radiation modes¹² for a water/brass/water structure. The amplitude distribution after some propagation is shown as well. It is important to mention that our description takes into account the distortions that the bounded beam undergoes from reflections on the solid while propagating closer to its surface. The distortions from the air/liquid interface are taken into account later when expressing the boundary conditions along this interface. In Fig. 5(a) and (b), results are presented for a 3-MHz Gaussian beam of half-width $w=0.5$ cm and incident from a distance $r=15$ cm. The planes of observation are, respectively, $z=0.5$ and $z=1$ cm. Comparing the figures we see that now even at the Lamb angles, the values of the maxima for the displacement amplitude are z dependent (at $z=1$ cm, the A_0 and S_0 modes even interfere constructively). This is due to the fact that an incident bounded beam can generate different Lamb modes at once which interfere with each other. Depending on the beam-width, several radiation modes in the spectrum of the incident bounded beam can be in resonance with different Lamb

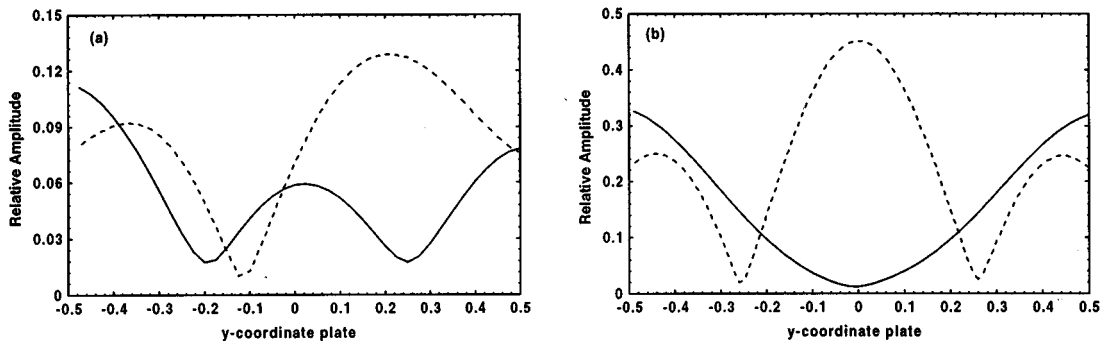


FIG. 6. Displacement amplitudes $|u_{y,2}^{\text{tot}}/u_0|$ (solid line) and $|u_{z,2}^{\text{tot}}/u_0|$ (dashed line) inside a water-loaded brass plate of 1-mm thickness, caused by a 3-MHz Gaussian beam ($w=0.5$, $r=15$ cm) incident at (a) 20.5° and (b) 11.15° (S_2 modus).

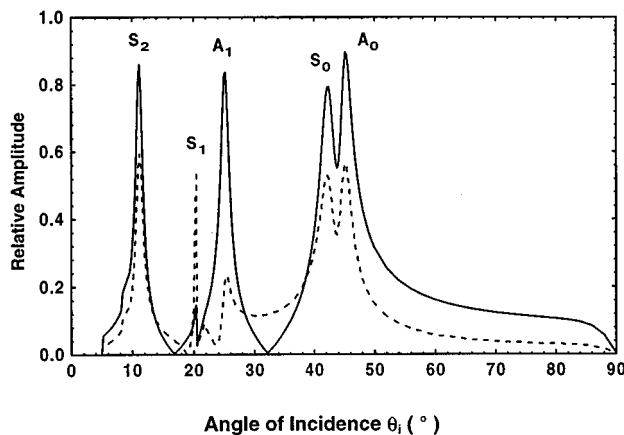


FIG. 7. The same as in Fig. 5(a) but for a Gaussian beam with half-beamwidth $w=5$ cm and incident from a distance $r=30$ cm.

modes. It means that a pure Lamb mode can only be stimulated by a bounded beam for which the angle of divergence is smaller than the resonance width of the particular Lamb mode considered. In Fig. 5 the maximum for the y component of the displacement amplitude of the S_1 mode is missing. A beam of halfwidth $w=0.5$ cm cannot excite this Lamb mode. This is confirmed if we look to the displacement amplitude distribution inside the brass plate [Fig. 6(a)]. As illustrated in Fig. 2(b), the S_1 -modus has a very narrow resonance width and therefore can only be excited by a very wide beam, as shown in Fig. 7. Figure 8 presents the minimum beamwidth required for the strongest excitation of specific Lamb modes. Finally, in Fig. 9 the displacement amplitude of the upper-face of the plate was considered at a distance $z=1.98$ cm. The values of the maxima for the modes A_0 and S_0 are exactly the same as the ones presented in Fig. 3, where $z=0.5$ cm. This is because both modes are observed after a propagation length that corresponds to their so-called “beating-length” (image planes), which is defined as

$$\frac{2\pi}{|k_{z,2}^{a_0} - k_{z,2}^{s_0}|} = 1.48 \text{ cm.} \quad (14)$$

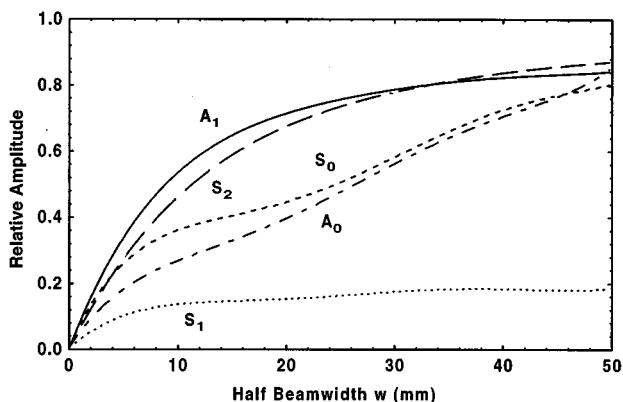


FIG. 8. Displacement amplitude $|(u_{y,2}^{\text{tot}}/u_0)(y=d)|$ of the propagating Lamb modes for a 1-mm-thick water-loaded brass plate, caused by a 3-MHz Gaussian beam, as a function of the half-beamwidth w . The plane of observation is $z=0.5$ cm.

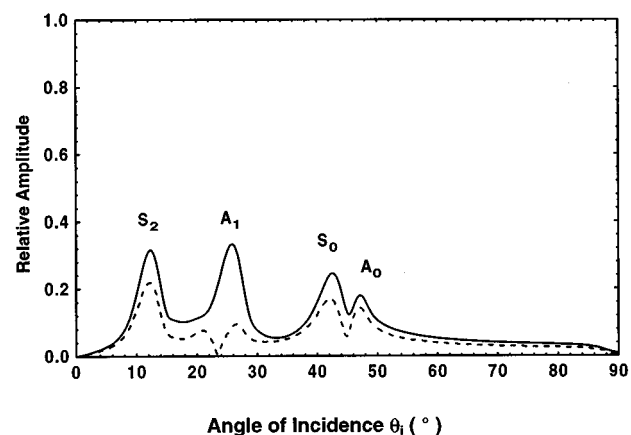


FIG. 9. The same as in Fig. 5(a) but the distance of observation is $z=1.98$ cm.

II. GENERATION OF RAYLEIGH WAVES

A. Theoretical model for the excitation problem

For Rayleigh wave generation the region $y<0$ in Fig. 1 is occupied by a solid half space. Now, the liquid wedge configuration consists of a liquid/solid structure and an air/solid structure. The procedure used earlier¹¹ to investigate the generation of a Stoneley wave by a liquid wedge can be repeated. However, other boundary conditions along the plane $z=0$ have to be taken into account and the resulting acoustic field in the air/solid structure, being a superposition of a scattered bulk wave and a mode-converted Rayleigh wave, has to be expanded in terms of the complete and orthogonal set of acoustic modes for an air/solid structure.¹³

The first-order approximation for the expansion coefficient C_r^i of the generated Rayleigh wave takes the form

$$C_r^i = \frac{1}{K_{22}^{rr}} \int_0^\xi C_a^i(k_{y,1}) I_{12}^{ar}(k_{y,1}) dk_{y,1} + C_s^r (K_{12}^{sr} - I_{12}^{sr}), \quad (15)$$

in which the upperbound of integration ξ is defined by

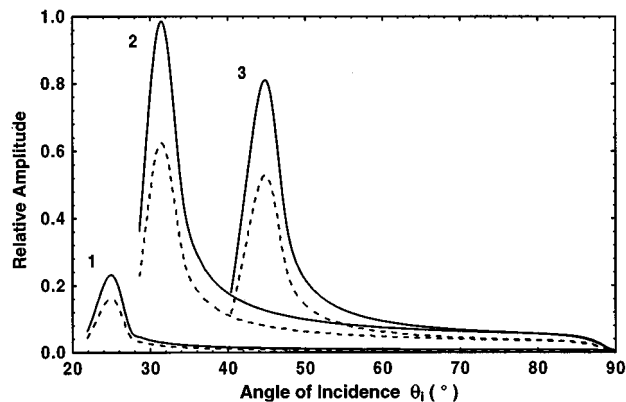


FIG. 10. Displacement amplitudes $|(u_y^{\text{ray}}/u_0)(y=0, z=0)|$ (solid line) and $|(u_z^{\text{ray}}/u_0)(y=0, z=0)|$ (dashed line) of the Rayleigh wave generated by a 3-MHz Gaussian beam ($w=0.5$ cm) incident from water at a distance $r=15$ cm: (1) tungsten, (2) aluminum, (3) brass.

TABLE I. Values of medium constants and the corresponding Rayleigh angle.

Medium	Longitudinal velocity v [m/s]	Transverse velocity v [m/s]	Density ρ [kg/m ³]	Rayleigh angle (deg)
Brass	4342	2288	8100	44
Aluminum	6350	3100	2800	31
Tungsten	6660	3980	15 000	24
Water	1480	...	1000	...

$$\xi = (k^2 - k_s^2)^{1/2}. \quad (16)$$

The Stoneley wave localization length in the solid half-space near the Rayleigh angle is smaller than the one of *type a* radiation modes,¹¹ so that the overlap integrals K_{12}^{sr} and I_{12}^{sr} may be neglected in comparison with the overlap integral I_{12}^{ar} . Working out analytically the integrals K_{12}^{sr} and I_{12}^{sr} on the basis of the displacement and stress tensor fields for a Rayleigh mode and for *type a* radiation modes, C_r^t becomes

$$C_r^t = -[k^2 k_{z,2}^r \beta(k_{z,2}^r)]^{-1} \int_0^\xi C_a^i(k_{y,1}) \sin[\varphi(k_{y,1})]$$

$$\begin{aligned} \beta(k_{z,1}) = & \frac{(k_s^2 - 2(k_{z,2}^r)^2)}{k_{dy,1} k_{dy,2}^r} \left[(k_s^2 - 2k_{z,1}^2) \left(\frac{k_s^2 + 2(k_{dy,2}^r)^2}{k_{dy,1} + k_{dy,2}^r} + \frac{k_s^2 - 2(k_{z,2}^r)^2}{k_{dy,1} + k_{sy,2}^r} \right) + \frac{2k_{dy,1} k_{sy,1}}{k_s^2} \left(\frac{k_s^2 + 2(k_{dy,2}^r)^2}{k_{sy,1} + k_{dy,2}^r} + \frac{k_s^2 - 2(k_{z,2}^r)^2}{k_{sy,1} + k_{sy,2}^r} \right) \right] \\ & + 4 \frac{(k_{z,2}^r)^2}{k_s^2} (2k_{z,1}^2 - k_s^2) (k_{dy,1} - k_{sy,1}) \left[\frac{\frac{k_s^2}{2(k_{z,2}^r)^2} - 1}{(k_{sy,1} + k_{dy,2}^r)(k_{dy,1} + k_{dy,2}^r)} + \frac{1}{(k_{sy,1} + k_{sy,2}^r)(k_{dy,1} + k_{sy,2}^r)} \right] \end{aligned} \quad (18)$$

with

$$(k_{dy,2}^r)^2 = (k_{z,2}^r)^2 - k_s^2, \quad (k_{sy,2}^r)^2 = (k_{z,2}^r)^2 - k_s^2. \quad (19)$$

B. Examples of numerical computations

Figure 10 presents the amplitude of the Rayleigh wave generated along the air/solid interface by a Gaussian beam

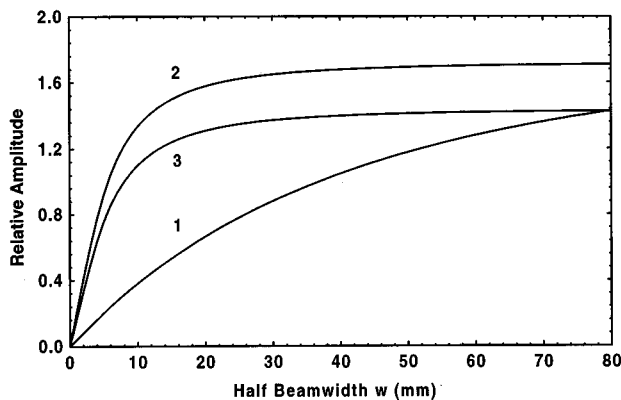


FIG. 11. Displacement amplitude $|(u_y^{\text{ray}}/u_0)(y=0, z=0)|$ as a function of the half-beamwidth w of the incident Gaussian beam for the same parameters and materials as in Fig. 10.

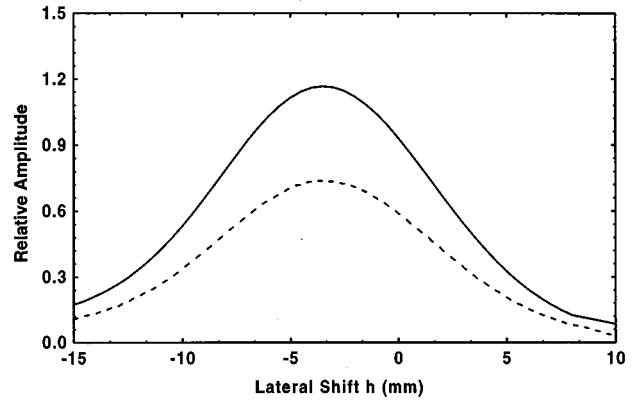


FIG. 12. Displacement amplitudes $|(u_y^{\text{ray}}/u_0)|$ (solid line) and $|(u_z^{\text{ray}}/u_0)|$ (dashed line) as a function of the lateral shift h of the incident Gaussian beam ($w=0.5$, $r=15$ cm, 3-MHz frequency) for a water-loaded brass solid.

$$\times \beta(k_{z,1}) k_{z,1} k_{y,1} dk_{y,1}. \quad (17)$$

In Eq. (17) $k_{z,2}^r$ is the z component of the Rayleigh mode and can be found as the real root of the corresponding characteristic equation; $\varphi(k_{y,1})$ is the phase¹¹ of a *type a* radiation mode. The function $\beta(k_{z,1})$ is defined as

incident from water. Three solid samples were considered: tungsten, aluminum, and brass (see Table I). The strongest excitation is obtained at the Rayleigh angle of the water/solid structure and, as shown in Fig. 11, the values of the maxima are strongly dependent on the finite beamwidth we introduced. In the limit of an incident homogeneous plane wave ($w \rightarrow \infty$), the normal displacement amplitude now follows the simple relation [compare with Eq. (13)]:

$$|(u_y^{\text{ray}}/u_0)(y=0, z=0)| = 2 \cos \theta_r. \quad (20)$$

An increasing beamwidth results in a more narrow spectrum of incident radiation modes. At a particular beamwidth all incident radiation modes are in resonance with the Rayleigh eigenmode, and the Rayleigh wave amplitude will not increase anymore: the angle of divergence of the incident bounded beam is less than the resonance width of the Rayleigh eigenmode. In Fig. 12, the dependence of the Rayleigh wave amplitude on a lateral shift of the incident beam over a distance h is shown. A greater amplitude can be realized moving the bounded beam to the left ($h < 0$) over a distance approximately equal to its half beamwidth w . We also remark that a shift to the right ($h > 0$) results in a more rapidly

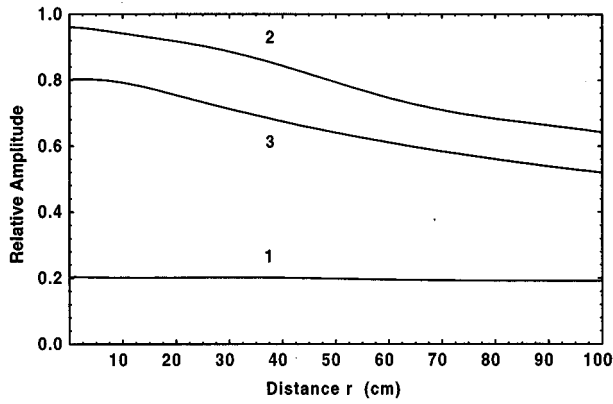


FIG. 13. Displacement amplitude $|(u_y^{ray}/u_0)(y=0, z=0)|$ as a function of the distance r between the Gaussian beam and the liquid/air/solid corner for the same parameters and materials as in Fig. 10.

decreasing amplitude than a shift to the left. This effect can be attributed to the Schoch displacement.^{14,15} At Rayleigh angle incidence the reflected beam is shifted to the right, partially neutralizing the left shift of the incident beam. The same effect was found for Lamb wave generation. Finally, in Fig. 13, the dependence of the source–corner distance r on the Rayleigh wave amplitude is illustrated. Once the distance r is greater than the diffraction length of the incident bounded beam, the Rayleigh wave amplitude begins slightly to decrease.

III. CONCLUSION

Mode theory is used to model the liquid wedge method for the generation of Lamb and Rayleigh waves in which a bounded (Gaussian) beam is incident on a liquid/air/solid corner. In this theoretical model the contributions from reflected waves is taken into account. Applying a method of successive approximations, analytical expressions for the determination of the amplitude of the mode-converted Lamb and Rayleigh waves have been derived. The dependence of this amplitude on several parameters was investigated: the angle of incidence, the distance of observation, the beam-width, the source–corner distance, etc. from which the optimum conditions for the strongest stimulation of Lamb and Rayleigh waves by the liquid wedge technique can be predicted.

ACKNOWLEDGMENTS

The authors would like to thank the Research Council of the K. U. Leuven for the fellowship awarded to Professor G. N. Shkerdin which enabled us to write this paper. We also had very fruitful discussions with Professor M. Breazeale during our meetings covered by a NATO grant.

APPENDIX

The complete and orthogonal set of acoustic modes for an air/plate/air structure only consists of a discrete spectrum of guided propagating modes (with a real value of k_z) and local or nonpropagating modes (with a pure imaginary value

of k_z), i.e., the symmetrical and antisymmetrical Lamb waves. The characteristic equation for (propagating or local) Lamb waves is given by

$$(k_s^2 - 2k_z^{m_n})^2 + 4k_{sy}^{m_n}k_{dy}^{m_n}(k_z^{m_n})^2 \frac{f_m(k_{dy}^{m_n}d)}{f_m(k_{sy}^{m_n}d)} = 0. \quad (A1)$$

The wave vector components $k_z^{m_n}$, $k_{dy}^{m_n}$, and $k_{sy}^{m_n}$ of the n th Lamb wave are related by

$$(k_{dy}^{m_n})^2 = k_d^2 - (k_z^{m_n})^2 \quad (A2)$$

$$(k_{sy}^{m_n})^2 = k_s^2 - (k_z^{m_n})^2, \quad (A3)$$

while the displacement field is given by {we suppress the factor $\exp[i(k_z^{m_n}z - \omega t)]$ }

$$u_y^{m_n} = A_{sm} k_{dy}^{sm} f_m(k_{dy}^{sm}d) \left[\frac{2(k_z^{sm})^2 - k_s^2}{k_s^2} \frac{g_m(k_{dy}^{sm}y)}{g_m(k_{dy}^{sm}d)} - \frac{2(k_z^{m_n})^2}{k_s^2} \frac{g_m(k_{sy}^{m_n}y)}{g_m(k_{sy}^{m_n}d)} \right] \quad (A4)$$

$$u_z^{m_n} = \mp i A_{m_n} k_z^{m_n} \left[\frac{2(k_z^{m_n})^2 - k_s^2}{k_s^2} \frac{g_m(k_{dy}^{m_n}y)}{g_m(k_{dy}^{m_n}d)} + \frac{2k_{dy}^{m_n}k_{sy}^{m_n}}{k_s^2} \frac{f_m(k_{dy}^{sm}d)}{f_m(k_{sy}^{sm}d)} \frac{g_m(k_{sy}^{m_n}y)}{g_m(k_{sy}^{m_n}d)} \right]. \quad (A5)$$

In this paper the arbitrary amplitude A_{m_n} was chosen to be equal to $1/k_s^2$.

- ¹D. N. Alleyne and P. Cawley, "The interaction of Lamb waves with defects," IEEE Trans. Ultrason. Ferroelectr. Freq. Control **39**, 381–397 (1992).
- ²R. Dong and L. Adler, "Measurements of reflection and transmission coefficients of Rayleigh waves from cracks," J. Acoust. Soc. Am. **76**, 1761–1763 (1994).
- ³S. I. Rokhlin, "Lamb wave interaction with lap-shear adhesive joint: Theory and experiment," J. Acoust. Soc. Am. **89**, 2758–2765 (1991).
- ⁴A. H. Nayfeh and D. E. Chimenti, "Propagation of guided waves in fluid-coupled plates of fiber-reinforced composites," J. Acoust. Soc. Am. **83**, 1736–1743 (1988).
- ⁵T. L. Mansfield, "Lamb wave inspection of aluminum sheet," Mater. Eval. **33**, 535–541 (1990).
- ⁶I. A. Viktorov, *Rayleigh and Lamb Waves* (Plenum, New York, 1967).
- ⁷Y. Jin and S. G. Joshi, "Coupling of interdigital transducer to ultrasonic Lamb waves," Appl. Phys. Lett. **58**, 1830–1832 (1991).
- ⁸W. M. D. Wright, D. W. Schindel, and D. W. Hutchins, "Studies of laser-generated ultrasound using a micromachined silicon electrostatic transducer in air," J. Acoust. Soc. Am. **95**, 2567–2575 (1994).
- ⁹R. B. Thompson, G. A. Alers, and M. A. Tennison, "Application of direct electromagnetic Lamb wave generation to gas pipeline inspection," Proc. IEEE Ultrasonic Symposium, New York, 91–94 (1972).
- ¹⁰D. A. Hutchins, "Ultrasonic generation by pulsed lasers," in *Physical Acoustics*, edited by W. P. Mason and R. N. Thurston (Academic, New York, 1988), Vol. 18.
- ¹¹R. Briers, O. Leroy, G. N. Shkerdin, and Yu. V. Gulyaev, "Mode theory as a framework for the investigation of the generation of a Stoneley wave at a liquid/solid interface," J. Acoust. Soc. Am. **95**, 1953–1966 (1994).
- ¹²R. Briers, O. Leroy, and G. N. Shkerdin, "Conversion of a Stoneley wave at the extremity of a fluid loaded plate," J. Acoust. Soc. Am. **101**, 1347–1357 (1997).

- ¹³O. Leroy and G. Shkerdin, "The mode method in the theory of acoustic wave diffraction on division boundaries between different structures," *Proc. Physical Acoustics: Fundamentals and Applications*, edited by O. Leroy and M. Breazeale (Plenum, New York, 1991), pp. 451–455.
- ¹⁴M. A. Breazeale, L. Adler, and G. W. Scott, "Interaction of ultrasonic waves incident at the Rayleigh angle onto a liquid–solid interface," *J. Appl. Phys.* **48**, 530–536 (1977).
- ¹⁵T. J. Plona, L. E. Pitts, and W. G. Mayer, "Ultrasonic bounded beam reflection and transmission effects at a liquid/solid plate/liquid interface," *J. Acoust. Soc. Am.* **59**, 1324–1328 (1976).

Finite difference predictions of P -SV wave propagation inside submerged solids. I. Liquid–solid interface conditions

Girish Dahake and S. M. Gracewski

*Department of Mechanical Engineering and The Center for Biomedical Ultrasound,
University of Rochester, Rochester, New York 14627*

(Received 16 September 1996; accepted for publication 18 June 1997)

A finite difference scheme has been developed to analyze internal strains in submerged elastic solids of irregular geometry subjected to ultrasonic wave sources that simulate a clinical lithotripter. In part I of this paper, the finite difference formulation that accounts for arbitrary liquid–solid interfaces is presented and sample numerical results are discussed. Two different methods for discretizing the liquid–solid interface conditions are developed. The first treats the interface conditions explicitly. The second integrates the heterogeneous wave equations across the interface using the divergence theorem. Both schemes account for varying grid sizes and give similar results for a test problem consisting of a radially diverging source incident on the rectangular solid. The time sequence obtained numerically for strain at the center of a rectangular solid matches well with the experimental results [S. M. Gracewski *et al.*, *J. Acoust. Soc. Am.* **94**, 652–661 (1993)] in terms of the arrival times and the relative amplitudes of the peaks. In addition, strain contours are plotted to visualize the propagation of P (longitudinal) and S (shear vertical) waves inside a circular solid. The reflection from the concave back surface of the circular solid has a focusing effect with the subsequent formation of focal zones, known as caustics, where peak strains occur. In part II of this paper, the finite difference scheme is used to study the effects of geometry changes on the internal stresses and caustics predicted in model stones subjected to lithotripter pulses. © 1997 Acoustical Society of America. [S0001-4966(97)03010-5]

PACS numbers: 43.35.Wa, 43.80.Sh [HEB]

INTRODUCTION

There is a debate regarding the relative contributions of direct stress waves and cavitation to gallstone and kidney stone destruction during clinical lithotripsy *in vivo*.^{1–8} To clarify the role that direct stress waves play in the fragmentation process, knowledge of the evolution of the stress fields inside concretions subjected to lithotripter shock waves is needed. A better understanding of stone fragmentation mechanisms can provide a basis for improved lithotripter design. Stone damage is presumed to occur at the locations where the stresses exceed the ultimate strength of the material. At least two stress wave phenomena occur that increase internal tensile stresses and therefore enhance the likelihood of initiation of fragmentation inside concretions. First, the back surface of a concretion in a liquid (or when surrounded by biological tissue) acts as a pressure release surface, generating a reflected tensile wave that initiates fracture by spalling.⁹ Second, the concave back surface of a concretion focuses the internally reflected waves. Linear ray theory describes the formation of caustics, which are surfaces where infinite stresses are predicted for shock wave front propagation due to this focusing.

Ray tracing can be used to determine locations of shock wave fronts and caustics and the pressure amplitude immediately behind a shock front.^{10,11} Further insight into the fracture process would be obtained if the strain fields within stones of arbitrary geometry subjected to stress wave pulses could be solved analytically. However, analytical solutions are available only for a few wave propagation problems with

simple geometries. Numerical approximations are therefore used for problems involving irregular geometries and interfaces.

The finite difference–time domain (FD–TD) method is one of the approximate methods widely applied in research on elastic and acoustic wave propagation problems. With finite difference methods, it is possible to obtain solutions to some problems for which other methods like the ray methods and perturbation methods fail either partially or completely.¹² In Ref. 13, it is shown that the finite difference method provides a fineness in detail difficult to obtain by alternate numerical procedures like reflectivity methods, ray methods, or perturbation methods. Based on the elastic wave equation without physical approximations, finite difference techniques not only yield reliable arrival times for the various waves, but also account for surface and head waves and the variation in signal amplitude due to elastic impedance variations.

Propagation of waves across discontinuities in impedance has been extensively researched.^{14–20} The first-order velocity-stress finite difference formulation can be successfully used for P - S wave propagation in heterogeneous media including horizontally layered homogeneous media.¹⁴ However, interface conditions for a wide variety of geometries can more easily be incorporated into the second-order equation-of-motion in terms of displacement^{15–20} without increasing the numerical memory allocation requirements. The finite difference scheme presented in Ref. 16 approximates the elastic wave equation for vertically inhomogeneous media that includes interface conditions for horizontal inter-

faces. This scheme accounts for continuity conditions explicitly at planar elastic interfaces and eliminates the use of fictitious lines of grid points,¹⁵ to account for the continuity at the interface. A formulation for boundary conditions that can account for irregular geometries is presented in Ref. 18, however, the method is involved and requires knowledge of the location and slope of the interface prior to coding.

Liquid–solid interfaces are particularly challenging for finite difference codes because the zero shear stress in the liquid allows for a discontinuity in the tangential displacement across the interface. Very few schemes give results that are both convergent and correct.¹⁷ In Ref. 19, results are obtained and compared for an acoustic half-space over an elastic half-space and for an acoustic half-space separated from an elastic half-space by an elastic layer with constant velocity and density gradients. These schemes work, however, only for planar interfaces. The use of the divergence theorem to handle the physics required at interfaces for acoustic and elastic wave propagation in heterogeneous media easily incorporates irregular interfaces.²⁰ A solution for a planar liquid–solid interface and an irregular solid–solid interface is presented in Ref. 20. The displacement formulation for the 2-D elastic wave equation²⁰ gives stable results for step discontinuities, including a liquid layer over an elastic half-space.

In this paper, wave fields in acoustic and elastic media with regular and irregular geometries generated by a 2-D radially diverging pressure pulse source are analyzed using FD–TD techniques. All calculations are in rectangular Cartesian coordinates. Every grid point at a liquid–solid boundary is considered an interface point and the displacement components are calculated for such points using the appropriate interface conditions. The calculations incorporate unequal grid sizes and can handle wave propagation in solids with irregular geometries.

Finite difference calculations are performed on solid cylinders of rectangular or circular cross section, subject to a line source in a surrounding liquid. The planar interfaces of the rectangular cylinders are modeled using two finite difference schemes outlined in Appendices A and B based on techniques described in Refs. 19 and 20, respectively. The first uses the boundary conditions at the liquid–solid interface explicitly whereas the second uses the divergence theorem to account for the physical boundary conditions at the liquid–solid interface. The results obtained by implementing the interface conditions in Appendix B compare favorably to those obtained by the formulation given in Appendix A. In addition, the strains obtained along the axis at the center of the cylinder compare favorably with experimental measurements.¹⁰ Since biological stones are typically spherical in shape, we also studied the focusing effect of the concave back surface of the stones by performing numerical calculations within solids of circular cross section. We present strain contours for a circular cylinder, subject to a line source. Nonplanar interfaces, like those of a circular cylinder, are easily incorporated by using the scheme summarized in Appendix B. The waves reflect from the concave back surface of the circular cylinder leading to internal focusing and the subsequent formation of caustics zones.

The finite difference formulation presented in part I of this paper will be used to study the effect of stone geometry on the induced internal strains in an effort to better understand the mechanisms of fragmentation during clinical lithotripsy. The success of lithotripsy in stone fragmentation is not only limited to breaking the stone once, but relies on its ability to efficiently fracture the stone after the initial cracks are generated. In part II of this paper, numerical calculations will be performed on solids with flat cut-away sections at the front and the back surfaces in an effort to understand the effect of stone orientation and geometry on the strains induced inside the stones. Experimental measurements are also obtained by embedding strain gauges at the center and caustic points of spherical concretions.

I. PROBLEM STATEMENT

The objective of this work is to determine the time variation of the stress wave fields in homogeneous isotropic elastic solids, subjected to 2-D radially diverging waves generated by a source in a surrounding homogeneous, inviscid liquid. A two-dimensional plane strain formulation is presented which restricts the solids to right cylinders with axes parallel to a line source. The incident longitudinal (P) wave refracts into the solid producing a longitudinal (P) and a shear (S) wave pair. The P and S waves undergo multiple reflections inside the solid, producing a P and S wave pair at each reflection. The wave fields quickly become complicated for irregular geometries. A finite difference–time domain (FD–TD) approximation is presented to analyze the stress wave propagation in solid cylinders with arbitrary cross sections.

The elastodynamic equation of motion that governs the displacement vector \mathbf{U} in an isotropic homogeneous elastic medium in terms of rectangular Cartesian coordinates x and y and time t is given by²¹

$$\frac{\partial^2 \mathbf{U}}{\partial t^2} = \mathbf{A} \frac{\partial^2 \mathbf{U}}{\partial x^2} + \mathbf{B} \frac{\partial^2 \mathbf{U}}{\partial x \partial y} + \mathbf{C} \frac{\partial^2 \mathbf{U}}{\partial y^2}, \quad (1)$$

where

$$\mathbf{U} = \begin{pmatrix} u \\ v \end{pmatrix}, \quad \mathbf{A} = \begin{pmatrix} \alpha^2 & 0 \\ 0 & \beta^2 \end{pmatrix}, \quad (2)$$

$$\mathbf{B} = \begin{pmatrix} 0 & \alpha^2 - \beta^2 \\ \alpha^2 - \beta^2 & 0 \end{pmatrix}, \quad \mathbf{C} = \begin{pmatrix} \beta^2 & 0 \\ 0 & \alpha^2 \end{pmatrix}.$$

In these expressions, $u(x, y, t)$ and $v(x, y, t)$ are the components of the displacements in the x and y directions, respectively, and α and β are the longitudinal and the shear wave speeds. The wave speeds are related to the Lamé parameters λ and μ by the relationships

$$\alpha = \left(\frac{\lambda + 2\mu}{\rho} \right)^{1/2}, \quad \beta = \left(\frac{\mu}{\rho} \right)^{1/2}, \quad (3)$$

where ρ is the density. Wave propagation in a homogeneous liquid is governed by the acoustic wave equation, and can be formulated in terms of displacements in a form similar to the elastodynamic equation by setting $\beta=0$ in (1), with $\alpha = (B/\rho)^{1/2}$, where B is the Bulk modulus of the liquid.

Appropriate conditions for the liquid–solid interface and initial conditions are needed to complete the problem statement. Continuity of tractions is required along any interface. By denoting the outward unit vector perpendicular to the solid surface by \mathbf{n} , and the unit vector parallel to the solid surface by \mathbf{t} , we can state this requirement in terms of the stress tensor τ

$$\tau^1 \cdot \mathbf{n} = \tau^2 \cdot \mathbf{n}, \quad (4)$$

where the superscripts 1 and 2 represent the liquid and solid, respectively. Because an inviscid liquid cannot support a tangential stress, this stress in the solid at the liquid–solid interface is zero and slip is allowed between the liquid and the solid along the interface. Therefore, only the normal component of the displacement is required to be continuous across the interface. For an arbitrary liquid–solid interface, the complete set of requirements can be stated as

$$\tau_{nn}^1 = \tau_{nn}^2, \quad \tau_{nt}^2 = 0, \quad \mathbf{U}^1 \cdot \mathbf{n} = \mathbf{U}^2 \cdot \mathbf{n}. \quad (5)$$

The initial conditions are defined by the line source in the liquid, with the solid initially at rest.

A displacement based finite difference method is used to approximate the two-dimensional acoustic and elastic wave propagation. The complete finite difference scheme must approximate the equation of motion at every grid point and the interface conditions at the grid points along the liquid–solid interface. Because the tangential displacement is discontinuous across a liquid–solid interface, the finite difference formulation for a liquid–solid interface is fundamentally different from that for the solid–solid interface, which requires the continuity of all displacement components. The results obtained by letting the shear modulus (μ) go to zero in the homogeneous solid–solid interface calculations may be stable but the displacements are incorrect.¹⁹ On the other hand, the heterogeneous finite difference formulation at a liquid–solid interface¹⁹ exhibits instabilities for step discontinuities in wave speeds. Therefore the displacements obtained from solid–solid interface calculations or the heterogeneous formulation cannot be used as a substitute for displacements at a liquid–solid interface. The displacements at liquid–solid interfaces are obtained by explicit incorporation of the conditions stated in (5) into the finite difference formulation for the grid points along the interface.

A finite difference formulation for planar liquid–solid interfaces parallel to the y axis is presented in Appendix A for rectangular Cartesian coordinates. The scheme presented here is of second order in the space and time increments.¹⁶ All first-order space increments occurring in the interface conditions are eliminated from the equations before introduction into the finite difference formulation. An analogous finite difference formulation, for constant grid sizes, correct to second order in the space increment, for a planar liquid–solid interface in cylindrical coordinates is presented in Ref. 20.

Varying the grid sizes for different media reduces the error in the finite difference representation of the equation-of-motion for the model.²² In any finite difference calculation there are two fundamental considerations: stability which affects the possibility of a solution and grid dispersion

which affects the accuracy of the solution. In an explicit finite difference solution numerical stability exists if

$$\Delta t \leq \frac{\min(\Delta x, \Delta y)}{\sqrt{(\alpha^2 + \beta^2)}}. \quad (6)$$

Grid dispersion is minimized when the time increment is equal to the stability limit.²³ The stability limit varies for media with different velocities. The stability limit for wave propagation from one medium to another can be kept constant by selecting different grid sizes for each medium.

A finite difference formulation for arbitrary liquid–solid interfaces is presented in Appendix B for rectangular Cartesian coordinates with varying grid sizes in the x and y directions. This formulation can be used to analyze wave propagation in cylindrical solids with nonplanar boundaries, including a circular cylinder as discussed in this paper. Curved interfaces are analyzed using the physical interface conditions explicitly rather than constructing an interface made of planar boundaries parallel to the grid lines. The wave equations are integrated across the interface²⁰ using the divergence theorem and then discretized to obtain the finite difference equations for the interface grid points. The technique increases the accuracy of the solution without increasing memory allocation requirements.

II. SOURCE CONDITIONS

The Wolf electrohydraulic lithotripter spark source²⁴ used in the experiments described in these two papers produces a 3-D radially diverging compression wave. In this paper, finite difference solutions are restricted to plane strain in rectangular Cartesian coordinates. Therefore, the lithotripter source is simulated by a line source perpendicular to the plane of interest. The numerical source thus appears as a point source in the x - y plane. Wave amplitudes therefore will decay more slowly due to geometrical spreading in the numerical simulations than in the experiment. However, the locations of the wave fronts in the plane of interest will be identical.

The Wolf pressure waveform has a rapid rise (less than a few ns) followed by a slower decay and a duration of less than 1 μ s.²⁴ Due to numerical limitations in modeling the steep shock front, a smooth pulse of duration 0.67 μ s or 1.0 mm in water is used to approximate the pulse generated by the Wolf lithotripter. The radial displacement for the numerical source is given by^{25,26}

$$u_r(t) = \frac{1}{\Delta^2} [f_0(t) - 2.0f_0(t - \Delta) + f_0(t - 2\Delta)], \quad (7)$$

where

$$f_0(t) = \frac{RA}{4.0\alpha^2} \left[\frac{\alpha t}{R} \left[\left(\frac{\alpha t}{R} \right)^2 - 1.0 \right]^{0.5} - \log_e \left\{ \frac{\alpha t}{R} + \left[\left(\frac{\alpha t}{R} \right)^2 - 1.0 \right]^{0.5} \right\} \right] H \left\langle t - \frac{R}{\alpha} \right\rangle. \quad (8)$$

Here, R is the radial distance from the axis, A is a constant (dimensions of area), $H\langle t \rangle$ is the Heaviside unit step function, and Δ is a constant measuring the sharpness of the

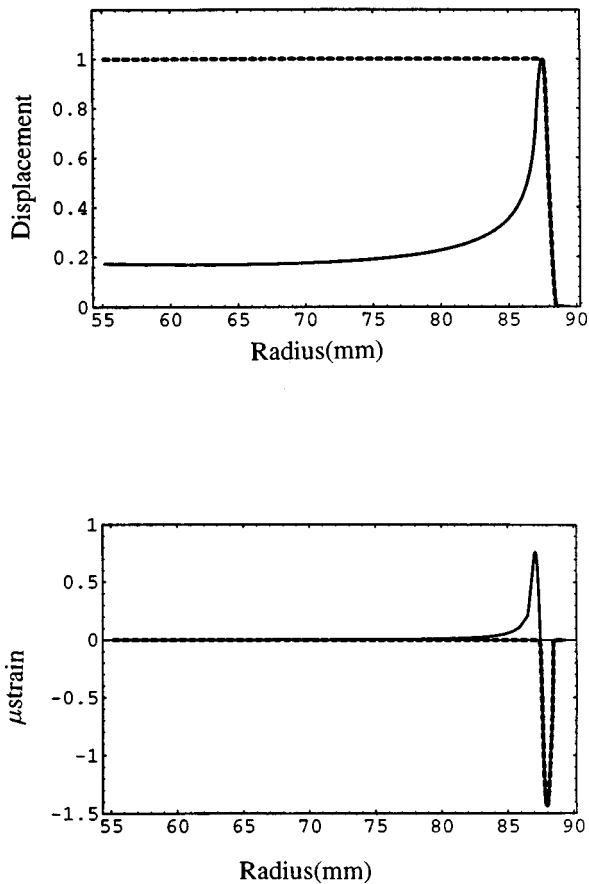


FIG. 1. Wave form of the radially diverging source in the liquid incident on the solid: (a) displacement amplitude; (b) normal strain (ϵ_{xx}) along the plane of symmetry. The dashed curve shows the modified pulse that results in only a compressive strain.

pulse. The expression is obtained by integrating and applying the finite difference method to the source that satisfies the acoustic equation of motion and has the appropriate singularity at the origin. The radially symmetric displacement U in the x - y plane is given by

$$U = \begin{pmatrix} u \\ v \end{pmatrix} = \begin{pmatrix} u_r \cos \theta \\ u_r \sin \theta \end{pmatrix}. \quad (9)$$

The solid curve in Fig. 1(a) shows the displacement versus position for the radially diverging point source given by Eqs. (7)–(9). A pulse emanates from the source at time $t = 0$, causing a variation in stress during a finite time interval, leading to a constant displacement equal to the maximum displacement for each particle in the medium for large time ($t \rightarrow \infty$). This pulse consists of both compressive and tensile strains as shown by the solid curve in Fig. 1(b). The source represented by the solid curve is used to obtain all plots of μ strain versus time presented in the next section. The pulse generated by the Wolf lithotripter is primarily compressive. To approximate the experimental pulse, the numerical source is modified as shown by the dashed curves in Fig. 1. With the modified source, it is easier to indicate mode conversion from compressive to tensile upon reflection in the strain contours. Therefore, the source represented by the dashed curve is used in all pressure contour plots presented in the next section.

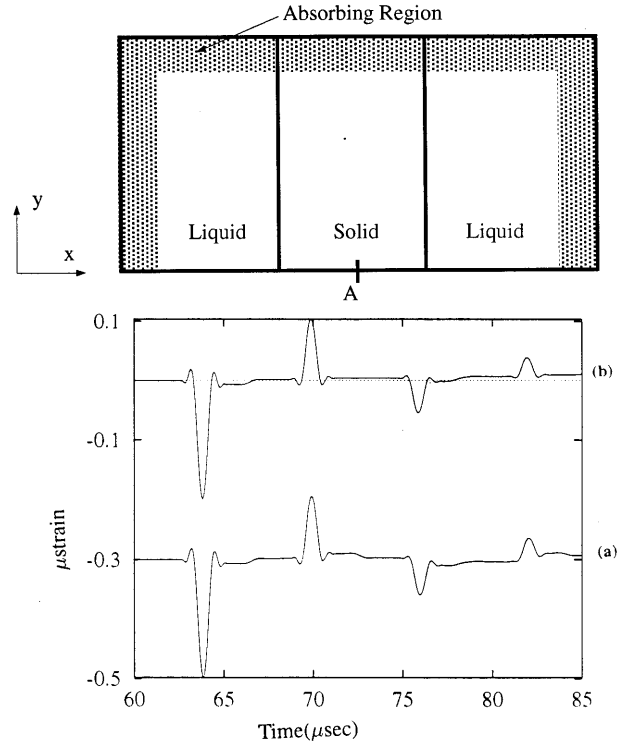


FIG. 2. Time evolution of the normal strain (ϵ_{xx}) at point A for a line source incident on the rectangular cylinder. Trace (a) is obtained by integrating the wave equations across the liquid–solid interface using divergence theorem (Appendix B), whereas trace (b) is obtained by treating the interface conditions explicitly at the liquid–solid interface (Appendix A). Trace (b) is offset vertically so the two curves can be distinguished.

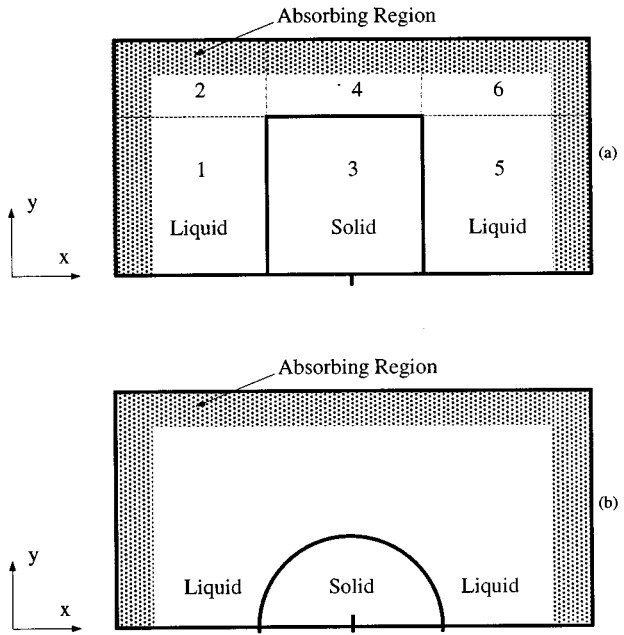


FIG. 3. The computational domains for wave propagation in (a) the rectangular cylinder 3 cm in width and 10.2 cm high and (b) the circular cylinder 2.2 cm in diameter surrounded by a liquid. The dotted region is the absorbing region added to avoid unnecessary reflections from the domain boundaries. Because of the symmetry in the problem only the top half of each cross section is considered for calculations.

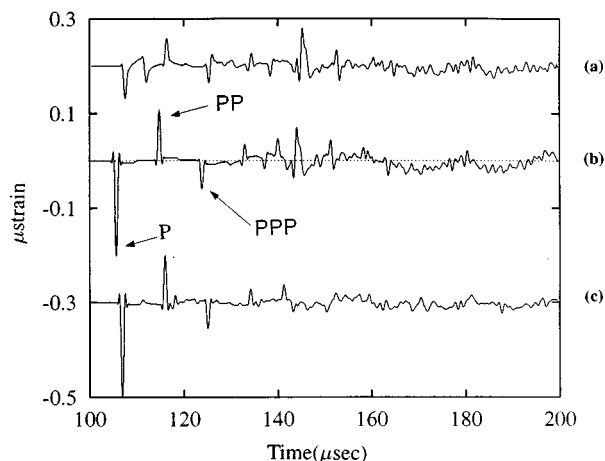


FIG. 4. Strain (ϵ_{xx}) at the center of the rectangular cylinder when the source is 15 cm from the front surface of the cylinder. In trace (b) the initial peaks correspond to the successive reflections from the front and back surface of the cylinder. The signal reflected from the top and the bottom surface arrives after a delay of 38 μs from the time the first pulse reaches the center of the cylinder. In trace (a), a mask is used to block the direct waves propagating along the plane of symmetry. Trace (c) shows the time evolution of strain when a mask is used to block the waves propagating towards the top and the bottom faces of the solid.

III. ABSORBING BOUNDARIES

Artificial absorbing regions along the computational domain boundaries have been introduced to prevent spurious reflections from reaching the regions of interest. This reduces the size of the model and in turn reduces the memory and time requirements for the computations. The technique uses expressions for damping that are based on analogies to shock absorbers. It is successful in reducing the amplitudes of reflected waves to any prespecified value and works effectively for all angles of incidence.²⁷ For the 2-D elastic wave equation a damping term is introduced into Eq. (1) as

$$\frac{\partial^2 \mathbf{U}}{\partial t^2} + 2\mathbf{D}(x,y) \frac{\partial \mathbf{U}}{\partial t} = \mathbf{A} \frac{\partial^2 \mathbf{U}}{\partial x^2} + \mathbf{B} \frac{\partial^2 \mathbf{U}}{\partial x \partial y} + \mathbf{C} \frac{\partial^2 \mathbf{U}}{\partial y^2}, \quad (10)$$

where the damping coefficient $2\mathbf{D}(x,y)$ is nonzero only in the rectangular annulus (absorbing region) as shown in Figs. 2 and 3. A linear damper has been used in all the finite difference calculations in this paper, although some other combinations, e.g., a quadratic or a cubic damper could also be as effective.²⁷ The increase in the number of calculations per time step due to the addition of the absorbing term is compensated by a reduction in the size of the computational domain. The use of an absorbing region around the numerical model has been successful in both elastic and acoustic wave propagation.

IV. NUMERICAL RESULTS AND DISCUSSION

Finite difference methods are applied to analyze the propagation of waves in solid elastic cylinders of rectangular or circular cross section subjected to an explosive line source in the surrounding liquid medium (cross sections are shown in Figs. 2 and 3). The acoustic wave equation is used to compute the displacements in the liquid and the elastic wave equation is used to compute the displacements in the solid.

The displacement components at the interface are calculated using expressions given either in Appendix A or Appendix B for a liquid–solid interface. Because of the symmetry in the problem only the upper half of the cylinder is considered and appropriate symmetry conditions [Eqs. (A26)] are applied along the symmetry plane.

The time evolution of the axial strain is calculated at the center of each cylinder. In addition, principal strain contours are plotted for the 2-D radially diverging source incident on a circular cylinder. In all calculations, the longitudinal wave velocity in the water is 0.15 cm/ μs and the longitudinal and the shear wave velocities in the solid are 0.33 cm/ μs and 0.175 cm/ μs , respectively.

The upper portion of Fig. 2 shows an infinite solid slab of width 2.0 cm in the x direction, subjected to a source located along the plane of symmetry ($y=0$), 9 cm to the left of the front surface of the solid. An absorbing boundary is placed in the computational domain after the source reaches the front surface of the solid, preventing reflections off the domain boundary from reaching the region of interest. This simple geometry is used to compare the interface formulations given in the appendices. The finite difference scheme in Appendix A treats the liquid–solid interface conditions explicitly to compute the displacement components at the interface. It is limited to planar surfaces that are parallel to a coordinate axis. The scheme presented in Appendix B integrates the wave equations across the interface using the divergence theorem. Arbitrary geometries can be handled by this scheme. Normal strains (ϵ_{xx}) calculated at the center of the solid (point A) are nearly identical for the two schemes given in Appendix A and Appendix B. The peaks correspond to the successive P wave reflections from the front and back surface of the solid recorded at point A. Successive reflections alternate between tensile and compressive waves, as expected. At each liquid–solid interface some energy of the wave is lost due to transmission into the surrounding liquid. In addition, the radially diverging wave spreads as it propagates. Therefore the amplitudes of the peaks decay with time.

A rectangular cylinder 3.0 cm in width and 10.2 cm in height is shown in Fig. 3(a). Because of the finite height, the cylinder has three planar interfaces, two normal to the x axis and one normal to the y axis. The two corners at the intersections of these interfaces need special treatment in the numerical model. The computational domain is sampled with grid increments of Δx_1 , Δy_2 in region 1 and 5, Δx_1 , Δy_1 in region 2 and 6, Δx_2 , Δy_2 in region 3, Δx_2 , Δy_1 in region 4. The increments Δx_1 , Δy_1 , Δx_2 , and Δy_2 are, respectively, 0.003 cm, 0.003 cm, 0.0045 cm, and 0.0045 cm. The grid increments are chosen so that the time increment is equal to the stability limit in each of the regions.

In Fig. 4, numerical results are presented that correspond to measured signals obtained from silicon strain gauges implanted in a plaster disk, presented previously in Fig. 9 of Ref. 10. Trace (b) in Fig. 4 shows the strain (ϵ_{xx}) at the center of the rectangular cylinder, shown in Fig. 3(a), generated by a source 15 cm from the front surface. The largest signal is the incident P wave after it refracts into the solid from the liquid. The successive reflections of this P wave from the front and back surfaces of the solid produce the

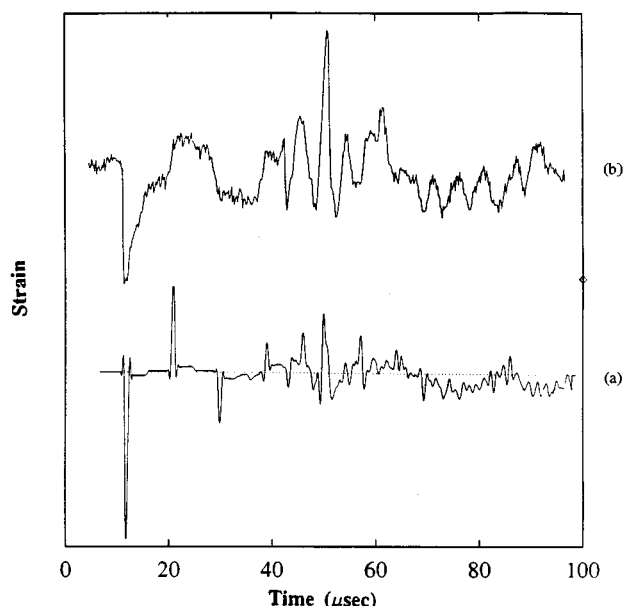


FIG. 5. Comparison of (a) the numerical and (b) the experimental results for a radially diverging source 15 cm from the front surface of a finite solid elastic plate of 3 cm thickness. For the plane strain calculations, the plate has a height of 10.2 cm. For the experiment a 10.2-cm-diam disk was used.

next two signals identified in the figure as *PP* and *PPP*. The signal amplitude decreases after each reflection due to geometric spreading and energy transmission into the liquid. Only after a time delay of about 38 μs does the wave that reflects from the top surface of the solid reach the symmetry plane ($y=0$). The arrival times of the reflections compare well to the experimental results¹⁰ reproduced in Fig. 5. As discussed in Ref. 10, the measured strain gauge signal is smeared because the gauge length is on the order of the wave length. Therefore only arrival times of the various wave fronts are obtained from the experimental measurements. The amplitudes of the waves reflected from the top of the rectangular cross-section are stronger in the experimental trace Fig. 5(b) than those obtained numerically Fig. 5(a), because a two-dimensional plane strain model is used in the numerical calculation, whereas the experimental model is axisymmetric. In the two-dimensional problem, only reflections from the top and the bottom faces contribute to the signal. However, in the experiments, the entire circumference of the disk serves to efficiently reflect and concentrate the waves to the interior and accounts for the increase in the amplitudes of the signal obtained along the axis of symmetry.

To verify the source of the various reflections, masks were placed between the source and the solid, within a few millimeters from its front surface, to partially block the incident wave. The experimental setup and results are presented in Ref. 10. The masks are simulated in the numerical calculations by enforcing zero displacements at the appropriate grid points. First, zero displacements were enforced for $y > 2.1$ cm, 1 mm in front of the solid. This allows the direct wave to propagate from the source to the center of the solid. However, all rays propagating toward the top of the rectangular cross section are blocked. For this mask, trace (c) in

Fig. 4 shows that there are no significant wave arrivals after the direct signal along the axis has decayed. Next, zero displacements were enforced for $y < 0.65$ cm, 1 mm in front of the solid. As shown by trace (a) of Fig. 4, the direct waves are blocked by this mask, but signal reflected from the top face of the rectangular cross section is still evident, arriving at the plane of symmetry after approximately 40 μs . To minimize the contributions from diffracted waves, the axisymmetric masks in the experiments were placed slightly off center.¹⁰ This could not be simulated with the symmetric half-model and therefore contributions from diffraction are evident in the numerical results.

Numerical results are also obtained for a radially diverging source incident on a solid cylinder of circular cross section. The curved interface between the solid and the surrounding liquid is modeled according to the approach in Appendix B, using the computational domain shown in Fig. 3(b). The point source is 9 cm from the front surface of the solid cylinder 2.2 cm in diameter. Only the top half is considered in the calculations because of the inherent symmetry in the problem. The bottom surface of the domain ($y=0$ plane) is therefore a plane of symmetry. The wave pattern that develops inside the circular cylinder is much more complicated than the one obtained for the rectangular cylinder. The incident *P* waves refract at the curved solid surface producing longitudinal and shear wave fronts that propagate inside the cylinder. Along the back interface of the cylinder the wave fronts refract out into the liquid and also reflect back into the solid. The complexity of the resulting wave fronts increases rapidly with time, since with each reflection both a *P* wave and an *S* wave pair are produced. Because of the curvature of the surface the reflected waves are convergent and lead to focusing of the wave fronts.

The time sequence of the maximum strain contours for the wave fields inside the circular cylinder is shown in Fig. 6. The contours are plotted at 1- μs intervals with the first contour 5 μs after the wave refracts into the solid. The refracted field in the solid has a leading *P* wave and a lagging *S* wave front, Fig. 6(a). The amplitude of the *P* wave is maximum on the plane of symmetry. On the other hand, the amplitude of the shear wave varies from zero on the symmetry plane to maximum along the interface. The *P* wave produces a *P* and an *S* wave pair on reflection. The circular geometry focuses the reflected wave fronts from the back and side surfaces, Fig. 6(a)–(e). The *PS* caustic point, for example, is the location of focusing of the refracted *P* wave that is internally reflected as an *S* wave. In Fig. 6(e), focusing at the *PP* caustic appears as the red region along the $y=0$ plane. Figure 6(f)–(g) shows the *PP* wave front diverging into the solid after passing through the caustic point. In Fig. 6(h), the *PP* wave front continues to diverge into the solid while the *PS* wave front converges towards its caustic point along the symmetry plane. The strain along the symmetry plane is maximum at the *PS* caustic point. The *PS* wave after passing through the caustic point diverges into the solid. The *SP* and the *SS* waves also follow behind, and focus at their respective caustic points. These waves then reflect back inside the solid from the front surface as seen in the time sequence shown in Fig. 6(g)–(l).

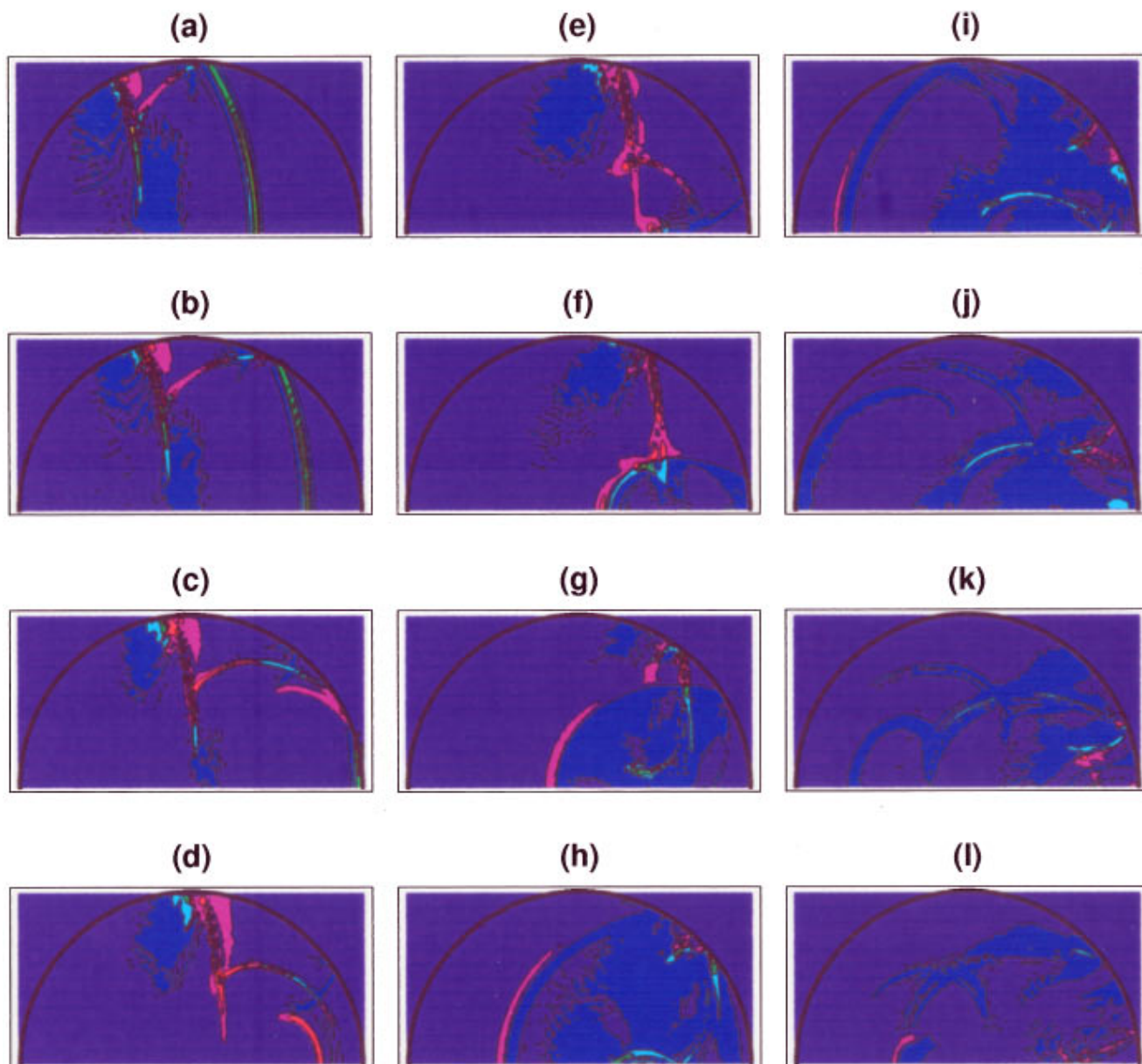


FIG. 6. Principal internal strain contours for a source 9 cm to the left of a solid circular cylinder of diameter 2.2 cm, at 1- μ s intervals: (a) $t = 5 \mu$ s; (b) $t = 6 \mu$ s; (c) $t = 7 \mu$ s; (d) $t = 8 \mu$ s; (e) $t = 9 \mu$ s; (f) $t = 10 \mu$ s; (g) $t = 11 \mu$ s; (h) $t = 12 \mu$ s; (i) $t = 13 \mu$ s; (j) $t = 14 \mu$ s; (k) $t = 15 \mu$ s; (l) $t = 16 \mu$ s. Only the upper half of the solid, outlined in black, is shown because of symmetry. All contour plots in parts I and II of this paper use the same scale and peak compressional to peak tensile strains vary from yellow to green to blue to purple to red and finally to orange.

Figure 7(a)–(e) shows the strain (ϵ_{xx}) calculated at five points along the plane of symmetry of the circular solid: the center and the four caustic points— PP , PS , SP , and SS .¹⁰ These caustic points occur at a distance of 16.2 mm, 14.7 mm, 18.9 mm, and 16.9 mm, respectively, from the front surface of the solid. The successive reflections at the center determined numerically compare well to the experimental results.¹⁰ In addition, at the caustic points, strain pulses of higher amplitude occur at the predicted arrival times of the focused waves at each of the four caustic points, in agreement with ray theory calculations. The magnitude of these focused waves would be even greater for a spherical geometry.

V. SUMMARY

In this paper a finite difference method that explicitly handles liquid–solid interfaces is developed to determine the elastic wave fields inside solids of rectangular and circular cross section subjected to a radially diverging source in the surrounding liquid. The time evolution of strain is plotted for points along the plane of symmetry inside each of the solids. Plots of the reverberant decay of strain inside a solid of rectangular cross section compare well for the two different liquid–solid interface schemes developed here and outlined in Appendices A and B. The time evolution of strain at the center of the rectangular cross section also compares well to experimental results, in terms of arrival times and relative

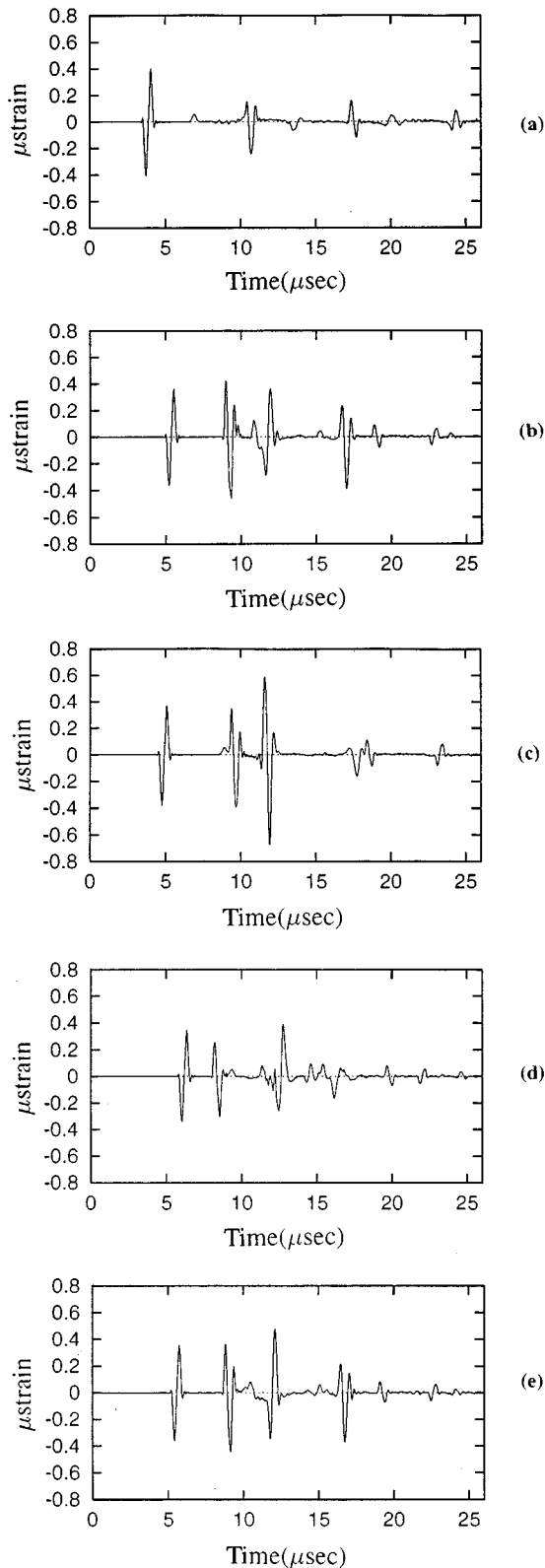


FIG. 7. (a)–(e) The time evolution of strain at points along the plane of symmetry inside a circular cylindrical solid of diameter 2.2 cm subjected to a line source 9 cm to the left of the solid at (a) the center, (b) *PP* caustic point, (c) *PS* caustic point, (d) *SP* caustic point, and (e) *SS* caustic point.

amplitudes of the peaks. In addition, strain contours are shown for a line source incident on a circular cylinder. The concave back surface of the cylinder focuses the wave fronts that subsequently form caustic regions, where the peak

strains occur. The absolute amplitudes of the strains in the numerical and the experimental results differ, because the 2-D Cartesian model cannot account for the additional focusing of an axisymmetric geometry. A better analogue to approximating the strains in actual stones can be obtained by using cylindrical coordinates for the computations. However, the singularity at $r=0$ requires special treatment.

ACKNOWLEDGMENT

This work was supported in part by USPHS Grant No. DK39796.

APPENDIX A: FINITE DIFFERENCE FORMULATION—PLANAR LIQUID–SOLID INTERFACE

A finite difference–time domain (FD–TD) formulation is presented in this appendix for wave propagation in liquid and solid media with a planar liquid–solid interface as shown in Fig. 2. The interface conditions are accounted for explicitly to derive the difference expressions for the displacement of grid points along the liquid–solid interface. For an isotropic, homogeneous, and linearly elastic medium the displacement equations of motion, when restricted to two spatial dimensions (x, y) in rectangular Cartesian coordinates and time (t), reduce to the following form

$$\frac{\partial^2 u_2}{\partial t^2} = \alpha_2^2 \frac{\partial^2 u_2}{\partial x^2} + \beta_2^2 \frac{\partial^2 u_2}{\partial y^2} + (\alpha_2^2 - \beta_2^2) \frac{\partial^2 v_2}{\partial x \partial y}, \quad (\text{A1})$$

$$\frac{\partial^2 v_2}{\partial t^2} = \alpha_2^2 \frac{\partial^2 v_2}{\partial y^2} + \beta_2^2 \frac{\partial^2 v_2}{\partial x^2} + (\alpha_2^2 - \beta_2^2) \frac{\partial^2 u_2}{\partial x \partial y}, \quad (\text{A2})$$

where the subscript 2 refers to the solid. Here, u is the displacement component in x direction and v is the corresponding displacement component in the y direction. The wave equations for displacements in a liquid in Cartesian coordinates are the same as (A1) and (A2) with $\beta=0.0$. The equations of motion in a liquid are

$$\frac{\partial^2 u_1}{\partial t^2} = \alpha_1^2 \frac{\partial^2 u_1}{\partial x^2} + \alpha_1^2 \frac{\partial^2 v_1}{\partial x \partial y}, \quad (\text{A3})$$

$$\frac{\partial^2 v_1}{\partial t^2} = \alpha_1^2 \frac{\partial^2 v_1}{\partial y^2} + \alpha_1^2 \frac{\partial^2 u_1}{\partial x \partial y}, \quad (\text{A4})$$

where the subscript 1 refers to the liquid.

When applying the finite difference method, the region under consideration is discretized using a grid of nodes in the Cartesian coordinate system. The set of displacements at these nodes gives an approximation for the complete displacement wave field.

For a uniform mesh of nodes, we define $x = i\Delta x$ and $y = j\Delta y$, where Δx and Δy are the increments along the x and the y directions, respectively, and $t = l\Delta t$, where Δt is an increment in time and i, j , and l are integers. The notation $u(i, j, l)$ represents the displacement at $u(i\Delta x, j\Delta y, l\Delta t)$. For this derivation, the interface between the liquid and the solid is assumed to be parallel to the y axis along $x = N\Delta x$. By substituting the second-order difference formulations for the derivatives into the governing partial differential equations (A1) and (A2), we obtain a three level explicit finite differ-

ence scheme in time for the interior nodes. The finite difference scheme combines displacements at two time levels to give displacements at a future time. Once the displacement fields at time steps $(l-1)$ and l are determined, the displacement field at the next time step, $(l+1)$ can be calculated from the discretized equations. The displacement fields at time steps 1 and 2 are defined by the initial conditions. Consequently, the displacement field at any time step of interest can be obtained by successive computations starting from the initial conditions.²⁸

The finite difference form of the displacement equations of motion in the solid are given by

$$\begin{aligned}
 u_2(i, j, l+1) &= -u_2(i, j, l-1) + 2.0u_2(i, j, l) \\
 &+ c_{12}(u_2(i+1, j, l) - 2.0u_2(i, j, l) + u_2(i-1, j, l)) \\
 &+ c_{32}(v_2(i+1, j+1, l) - v_2(i-1, j+1, l) \\
 &+ v_2(i-1, j-1, l) - v_2(i+1, j-1, l)) \\
 &+ c_{52}(u_2(i, j+1, l) - 2.0u_2(i, j, l) + u_2(i, j-1, l)), \quad (A5)
 \end{aligned}$$

and

$$\begin{aligned}
 v_2(i, j, l+1) &= -v_2(i, j, l-1) + 2.0v_2(i, j, l) \\
 &+ c_{22}(v_2(i, j+1, l) - 2.0v_2(i, j, l) + v_2(i, j-1, l)) \\
 &+ c_{32}(u_2(i+1, j+1, l) - u_2(i-1, j+1, l) \\
 &+ u_2(i-1, j-1, l) - u_2(i+1, j-1, l)) \\
 &+ c_{42}(v_2(i+1, j, l) - 2.0v_2(i, j, l) + v_2(i-1, j, l)). \quad (A6)
 \end{aligned}$$

For propagation in the liquid the displacement equations of motion are

$$\begin{aligned}
 u_1(i, j, l+1) &= -u_1(i, j, l-1) + 2.0u_1(i, j, l) \\
 &+ c_{11}(u_1(i+1, j, l) - 2.0u_1(i, j, l) + u_1(i-1, j, l)) \\
 &+ c_{61}(v_1(i+1, j+1, l) - v_1(i-1, j+1, l) \\
 &+ v_1(i-1, j-1, l) - v_1(i+1, j-1, l)), \quad (A7)
 \end{aligned}$$

and

$$\begin{aligned}
 v_1(i, j, l+1) &= -v_1(i, j, l-1) + 2.0v_1(i, j, l) \\
 &+ c_{21}(v_1(i, j+1, l) - 2.0v_1(i, j, l) \\
 &+ v_1(i, j-1, l)) + c_{61}(u_1(i+1, j+1, l) \\
 &- u_1(i-1, j+1, l) + u_1(i-1, j-1, l) \\
 &- u_1(i+1, j-1, l)). \quad (A8)
 \end{aligned}$$

The coefficients in these expressions are given by

$$\begin{aligned}
 c_{1k} &= (\alpha_k)^2 \left(\frac{\Delta t}{\Delta x_k} \right)^2, \quad c_{2k} = (\alpha_k)^2 \left(\frac{\Delta t}{\Delta y} \right)^2, \\
 c_{3k} &= ((\alpha_k)^2 - (\beta_k)^2) (\Delta t)^2 \left(\frac{1}{\Delta x_k \Delta y} \right), \\
 c_{4k} &= (\beta_k)^2 \left(\frac{\Delta t}{\Delta x_k} \right)^2, \quad c_{5k} = (\beta_k)^2 \left(\frac{\Delta t}{\Delta y} \right)^2, \\
 c_{6k} &= (\alpha_k)^2 (\Delta t)^2 \left(\frac{1}{\Delta x_k \Delta y} \right),
 \end{aligned}$$

where $k=1$ for propagation in the liquid and 2 for propagation in the solid.

Interface conditions need to be satisfied to complete the finite difference discretization of the computational domain. At the liquid–solid interface along the grid boundary, parallel to the y axis, the interface conditions are

$$\tau_{xx}^1 = \tau_{xx}^2, \quad \tau_{xy}^2 = 0, \quad u_1 = u_2. \quad (A9)$$

In terms of displacements, these interface conditions can be written as

$$\rho_1 \alpha_1^2 \frac{\partial u_1}{\partial x} - \rho_1 \alpha_1^2 \frac{\partial v_1}{\partial y} = \rho_2 \alpha_2^2 \frac{\partial u_2}{\partial x} - \rho_2 (\alpha_2^2 - 2\beta_2^2) \frac{\partial v_2}{\partial y}, \quad (A10)$$

$$\frac{\partial u_2}{\partial y} + \frac{\partial v_2}{\partial x} = 0, \quad (A11)$$

$$u_1 = u_2. \quad (A12)$$

To obtain the final finite difference equations, all of the derivatives in these interface conditions have to be expressed in difference form. The interface conditions at $x = N\Delta x_1$ relate the horizontal and the vertical displacements, $u_1(N, j, l+1)$, $v_1(N, j, l+1)$ in the liquid to $u_2(N, j, l+1)$, $v_2(N, j, l+1)$ in the solid. All the difference approximations at the interface are one sided in the x direction and are centered in the y direction. Since all quantities are continuous in the y direction along the interface, derivatives with respect to y are also continuous. Taking the y derivative of (A10) and (A11) we obtain

$$\begin{aligned}
 \rho_1 \alpha_1^2 \frac{\partial^2 u_1}{\partial x \partial y} - \rho_1 \alpha_1^2 \frac{\partial^2 v_1}{\partial y^2} &= \rho_2 \alpha_2^2 \frac{\partial^2 u_2}{\partial x \partial y} - \rho_2 (\alpha_2^2 \\
 &- 2\beta_2^2) \frac{\partial^2 v_2}{\partial y^2}, \quad (A13)
 \end{aligned}$$

$$\frac{\partial^2 u_2}{\partial y^2} + \frac{\partial^2 v_2}{\partial x \partial y} = 0. \quad (A14)$$

The Taylor series expansion of u_k and v_k , $k=1,2$ at the interface, used to eliminate all the first derivatives from the interface conditions are given to second order by

$$-\Delta x_1 \frac{\partial u_1}{\partial x} + \frac{\Delta x_1^2}{2} \frac{\partial^2 u_1}{\partial x^2} = u_1(N-1, j, l) - u_1(N, j, l), \quad (A15)$$

$$\Delta x_2 \frac{\partial u_2}{\partial x} + \frac{\Delta x_2^2}{2} \frac{\partial^2 u_2}{\partial x^2} = u_2(N+1, j, l) - u_2(N, j, l), \quad (16)$$

$$-\Delta x_1 \frac{\partial v_1}{\partial x} + \frac{\Delta x_1^2}{2} \frac{\partial^2 v_1}{\partial x^2} = v_1(N-1, j, l) - v_1(N, j, l). \quad (A17)$$

$$\Delta x_2 \frac{\partial v_2}{\partial x} + \frac{\Delta x_2^2}{2} \frac{\partial^2 v_2}{\partial x^2} = v_2(N+1, j, l) - v_2(N, j, l). \quad (\text{A18})$$

The mixed derivatives of displacements at the interface are given by

$$\begin{aligned} -2\Delta x_1 \Delta y \frac{\partial^2 u_1}{\partial x \partial y} &= u_1(N-1, j+1, l) - u_1(N-1, j-1, l) \\ &\quad - u_1(N, j+1, l) + u_1(N, j-1, l), \end{aligned} \quad (\text{A19})$$

$$\begin{aligned} -2\Delta x_1 \Delta y \frac{\partial^2 v_1}{\partial x \partial y} &= v_1(N-1, j+1, l) - v_1(N-1, j-1, l) \\ &\quad - v_1(N, j+1, l) + v_1(N, j-1, l), \end{aligned} \quad (\text{A20})$$

$$\begin{aligned} 2\Delta x_2 \Delta y \frac{\partial^2 u_2}{\partial x \partial y} &= u_2(N+1, j+1, l) - u_2(N+1, j-1, l) \\ &\quad - u_2(N, j+1, l) + u_2(N, j-1, l), \end{aligned} \quad (\text{A21})$$

$$\begin{aligned} 2\Delta x_2 \Delta y \frac{\partial^2 v_2}{\partial x \partial y} &= v_2(N+1, j+1, l) - v_2(N+1, j-1, l) \\ &\quad - v_2(N, j+1, l) + v_2(N, j-1, l). \end{aligned} \quad (\text{A22})$$

At the liquid–solid interface, the u displacement component is continuous ($u_1(N, j, l+1) = u_2(N, j, l+1)$) but the v displacement component is discontinuous. Adding (A1) and (A3) and substituting (A10), (A15), (A16), (A20), and (A22) to eliminate all the second-order derivatives in the x direction, we have for the normal displacement u at the interface (where $u_{1,2}$ stands for displacement in either the solid or the liquid along the interface)

$$\begin{aligned} u_{1,2}(N, j, l+1) &= 2.0u_{1,2}(N, j, l) - u_{1,2}(N, j, l-1) + a_1a_2(u_2(N+1, j, l) - u_2(N, j, l)) + a_1a_3(u_1(N-1, j, l) - u_1(N, j, l)) \\ &\quad + a_1a_4(v_2(N, j+1, l) - v_2(N, j-1, l)) - a_1a_5(v_1(N, j+1, l) - v_1(N, j-1, l)) + a_1a_6(u_2(N, j-1, l) \\ &\quad - 2.0u_2(N, j, l) + u_2(N, j+1, l)) - a_1a_7(v_1(N, j+1, l) - v_1(N, j-1, l) + v_1(N-1, j-1, l) \\ &\quad - v_1(N-1, j+1, l)) + a_1a_8(v_2(N+1, j+1, l) - v_2(N+1, j-1, l) + v_2(N, j-1, l) - v_2(N, j+1, l)), \end{aligned} \quad (\text{A23})$$

where

$$\begin{aligned} a_1 &= \left(\frac{(\Delta t)^2}{\rho_1 \Delta x_1 + \rho_2 \Delta x_2} \right), \quad a_2 = \rho_2 (\alpha_2)^2 \left(\frac{1}{\Delta x_2} \right), \quad a_3 = \rho_1 (\alpha_1)^2 \left(\frac{1}{\Delta x_1} \right), \quad a_4 = \rho_2 ((\alpha_2)^2 - 2.0(\beta_2)^2) \left(\frac{1}{\Delta y} \right), \\ a_5 &= \rho_1 (\alpha_1)^2 \left(\frac{1}{\Delta y} \right), \quad a_6 = \rho_2 (\beta_2)^2 \left(\frac{\Delta x_2}{\Delta y} \right) \left(\frac{1}{\Delta y} \right), \quad a_7 = \frac{\rho_1 (\alpha_1)^2}{(2\Delta y)}, \quad a_8 = \rho_2 \frac{((\alpha_2)^2 - (\beta_2)^2)}{(2\Delta y)}. \end{aligned}$$

Similarly for the value of $v_1(N, j, l+1)$ at the interface in the fluid is found using the equation of motion for x in the liquid. Specifically, the tangential displacement in the liquid at the interface is obtained by adding (A4) to the y derivative of (A3) and substituting (A15) to eliminate the second order x derivative at the interface. The result can be expressed as

$$\begin{aligned} v_1(N, j, l+1) &= 2.0v_1(N, j, l) - v_1(N, j, l-1) + b_1(v_1(N, j-1, l) - 2.0v_1(N, j, l) + v_1(N, j+1, l)) + b_2(u_1(N, j+1, l) \\ &\quad - u_1(N, j-1, l) + u_1(N-1, j-1, l) - u_1(N-1, j+1, l)) + b_3(u_1(N, j+1, l-1) - 2.0u_1(N, j+1, l) \\ &\quad + u_1(N, j+1, l+1)) - b_3(u_1(N, j-1, l-1) - 2.0u_1(N, j-1, l) + u_1(N, j-1, l+1)) + b_4(v_1(N-1, j+1, l) \\ &\quad - 2.0v_1(N-1, j, l) + v_1(N-1, j-1, l)) - b_4(v_1(N, j+1, l) - 2.0v_1(N, j, l) + v_1(N, j-1, l)), \end{aligned} \quad (\text{A24})$$

where

$$\begin{aligned} b_1 &= (\alpha_1)^2 \left(\frac{\Delta t}{\Delta y} \right)^2, \quad b_2 = 0.5(\alpha_1)^2 \frac{(\Delta t)^2}{\Delta x_1 \Delta y}, \\ b_3 &= 0.25 \frac{\Delta x_1}{\Delta y}, \quad b_4 = 0.5b_1. \end{aligned}$$

The tangential displacement at the interface in the solid is obtained by substituting (A11), (A18), and (A21) into (A2) and is given by

$$\begin{aligned} v_2(N, j, l+1) &= 2.0v_2(N, j, l) - v_2(N, j, l-1) \\ &\quad + b_5(v_2(N+1, j, l) - v_2(N, j, l)) \\ &\quad + b_6(v_2(N, j-1, l) - 2.0v_2(N, j, l) \\ &\quad + v_2(N, j+1, l)) + b_7(u_2(N+1, j+1, l) \\ &\quad - u_2(N+1, j-1, l) \\ &\quad - u_2(N, j+1, l) + u_2(N, j-1, l)) \\ &\quad + b_8(u_2(N, j+1, l) - u_2(N, j-1, l)), \end{aligned} \quad (\text{A25})$$

where

$$b_5 = 2.0(\alpha_2)^2 \left(\frac{\Delta t}{\Delta x_2} \right)^2, \quad b_6 = (\alpha_2)^2 \left(\frac{\Delta t}{\Delta y} \right)^2,$$

$$b_7 = 0.5 \left(\frac{(\Delta t)^2((\alpha_2)^2 - (\beta_2)^2)}{\Delta x_2 \Delta y} \right),$$

$$b_8 = (\alpha_2)^2 \left(\frac{(\Delta t)^2}{\Delta x_2 \Delta y} \right).$$

The symmetry of the geometry requires computations to be performed only on the region $y > 0$. The symmetry conditions applied along the symmetry plane $y = 0$ are

$$v(i, 0, l) = 0 \quad \text{and} \quad \frac{\partial u}{\partial y}(i, 0, l) = 0. \quad (\text{A26})$$

To compute the displacement u along the symmetry plane $y = 0$, the conditions used are

$$u(i, -1, l) = u(i, 1, l),$$

$$v(i, -1, l) = -v(i, 1, l). \quad (\text{A27})$$

There is no need to introduce an intermediate solution on an imaginary interface in the second-order formulation above.²⁵ The equations of motion along with the boundary conditions are sufficient to determine the interface values of the displacements at subsequent time steps.

APPENDIX B: FINITE DIFFERENCE FORMULATION—CURVED INTERFACE

A finite difference formulation for a curved interface between two isotropic media having different material properties is presented here. The appropriate equation of motion is used for propagation inside the medium and only expressions for the displacements of the grid points located along the interface are derived here. Wave propagation in the liquid

is governed by the acoustic equation and can be formulated in terms of displacements in a form similar to the elastodynamic equations by setting $\mu = 0$.

The 2-D elastic wave equations used to model horizontal u and vertical v displacements in an inhomogeneous isotropic elastic medium without sources are

$$\rho \frac{\partial^2 u}{\partial t^2} = \frac{\partial}{\partial x} \left[(\lambda + 2\mu) \frac{\partial u}{\partial x} + \lambda \frac{\partial v}{\partial y} \right] + \frac{\partial}{\partial y} \left[\mu \left(\frac{\partial u}{\partial y} + \frac{\partial v}{\partial x} \right) \right],$$

$$\rho \frac{\partial^2 v}{\partial t^2} = \frac{\partial}{\partial y} \left[(\lambda + 2\mu) \frac{\partial v}{\partial y} + \lambda \frac{\partial u}{\partial x} \right] + \frac{\partial}{\partial x} \left[\mu \left(\frac{\partial u}{\partial y} + \frac{\partial v}{\partial x} \right) \right], \quad (\text{B1})$$

where λ and μ are the Lamé parameters and ρ is the density. These equations can be written in terms of the divergence of the stresses τ_{xx} , τ_{xy} , τ_{yy} , τ_{yx} :

$$\rho \frac{\partial^2 u}{\partial t^2} = \frac{\partial}{\partial x} (\tau_{xx}) + \frac{\partial}{\partial y} (\tau_{xy}) = \nabla \cdot (\tau_{xx}, \tau_{xy}),$$

$$\rho \frac{\partial^2 v}{\partial t^2} = \frac{\partial}{\partial x} (\tau_{yx}) + \frac{\partial}{\partial y} (\tau_{yy}) = \nabla \cdot (\tau_{yx}, \tau_{yy}), \quad (\text{B2})$$

where $\nabla \cdot$ is the divergence operator. Integrating the above equations over a contour for all grid points adjacent to the interface using the divergence theorem,¹⁶ we obtain expressions for the displacements at any grid point (i, j) along the interface. The following finite difference formulation is valid for varying grid sizes in the x and the y directions and can be applied effectively to an arbitrary interface between two media. The displacement components $u(i, j, l+1)$ and $v(i, j, l+1)$ along the interface are derived from the following expressions:

$$\rho' \frac{\partial^2 u}{\partial t^2}$$

$$= -\mu_{i+1j-1} [u(i, j, l) - u(i, j-1, l)] \frac{x_{i+1} - x_i}{2(y_j - y_{j-1})} - 0.25\mu_{i+1j-1} [v(i+1, j, l) + v(i+1, j-1, l) - v(i, j, l) - v(i, j-1, l)]$$

$$- \mu_{i-1j-1} [u(i, j, l) - u(i, j-1, l)] \frac{x_i - x_{i-1}}{2(y_j - y_{j-1})} - 0.25\mu_{i-1j-1} [v(i, j, l) + v(i, j-1, l) - v(i-1, j, l) - v(i-1, j-1, l)]$$

$$- (\lambda + 2\mu)_{i-1j-1} [u(i, j, l) - u(i-1, j, l)] \frac{y_j - y_{j-1}}{2(x_i - x_{i-1})} - 0.25\lambda_{i-1j-1} [v(i, j, l) + v(i-1, j, l) - v(i, j-1, l) - v(i-1, j-1, l)]$$

$$- (\lambda + 2\mu)_{i-1j+1} [u(i, j, l) - u(i-1, j, l)] \frac{y_{j+1} - y_j}{2(x_i - x_{i-1})} - 0.25\lambda_{i-1j+1} [v(i, j+1, l) + v(i-1, j+1, l) - v(i, j, l) - v(i-1, j, l)]$$

$$+ \mu_{i-1j+1} [u(i, j+1, l) - u(i, j, l)] \frac{x_i - x_{i-1}}{2(y_{j+1} - y_j)} + 0.25\mu_{i-1j+1} [v(i, j, l) + v(i, j+1, l) - v(i-1, j, l) - v(i-1, j+1, l)]$$

$$+ \mu_{i+1j+1} [u(i, j+1, l) - u(i, j, l)] \frac{x_{i+1} - x_i}{2(y_{j+1} - y_j)} + 0.25\mu_{i+1j+1} [v(i+1, j, l) + v(i+1, j+1, l) - v(i, j, l) - v(i, j+1, l)]$$

$$\begin{aligned}
& + (\lambda + 2\mu)_{i+1,j+1} [u(i+1,j,l) - u(i,j,l)] \frac{y_{j+1} - y_j}{2(x_{i+1} - x_i)} - 0.25\lambda_{i+1,j+1} [v(i,j+1,l) + v(i+1,j+1,l) - v(i,j,l) \\
& - v(i+1,j,l)] + (\lambda + 2\mu)_{i+1,j-1} [u(i+1,j,l) - u(i,j,l)] \frac{y_j - y_{j-1}}{2(x_{i+1} - x_i)} + 0.25\lambda_{i+1,j-1} [v(i,j,l) + v(i+1,j,l) \\
& - v(i,j-1,l) - v(i+1,j-1,l)] \equiv R^u(i,j,l), \tag{B3} \\
\rho' \frac{\partial^2 v}{\partial t^2} = & -0.25\lambda_{i+1,j-1} [u(i+1,j,l) + u(i+1,j-1,l) - u(i,j,l) - u(i,j-1,l)] - (\lambda + 2\mu)_{i+1,j-1} [v(i,j,l) - v(i,j-1,l)] \\
& \times \frac{x_{i+1} - x_i}{2(y_j - y_{j-1})} - 0.25\lambda_{i-1,j-1} [u(i,j,l) + u(i,j-1,l) - u(i-1,j,l) - u(i-1,j-1,l)] - (\lambda + 2\mu)_{i-1,j-1} [v(i,j,l) \\
& - v(i,j-1,l)] \frac{x_i - x_{i-1}}{2(y_j - y_{j-1})} - 0.25\mu_{i-1,j-1} [u(i,j,l) + u(i-1,j,l) - u(i,j-1,l) - u(i-1,j-1,l)] \\
& - \mu_{i-1,j-1} [v(i,j,l) - v(i-1,j,l)] \frac{y_j - y_{j-1}}{2(x_i - x_{i-1})} - 0.25\mu_{i-1,j+1} [u(i,j+1,l) + u(i-1,j+1,l) - u(i,j,l) \\
& - u(i-1,j,l)] - \mu_{i-1,j+1} [v(i,j,l) - v(i-1,j,l)] \frac{y_{j+1} - y_j}{2(x_i - x_{i-1})} \\
& + 0.25\lambda_{i-1,j+1} [u(i,j,l) + u(i,j+1,l) - u(i-1,j,l) - u(i-1,j+1,l)] + (\lambda + 2\mu)_{i-1,j+1} [v(i,j+1,l) - v(i,j,l)] \\
& \times \frac{x_i - x_{i-1}}{2(y_{j+1} - y_j)} + 0.25\lambda_{i+1,j+1} [u(i+1,j+1,l) + u(i,j+1,l) - u(i+1,j,l) - u(i,j,l)] \\
& + (\lambda + 2\mu)_{i+1,j+1} [v(i,j+1,l) - v(i,j,l)] \frac{x_{i+1} - x_i}{2(y_{j+1} - y_j)} \\
& - 0.25\mu_{i+1,j+1} [u(i+1,j+1,l) + u(i,j+1,l) - u(i+1,j,l) - u(i,j,l)] + \mu_{i+1,j+1} [v(i+1,j,l) - v(i,j,l)] \\
& \times \frac{y_{j+1} - y_j}{2(x_{i+1} - x_i)} + 0.25\mu_{i+1,j-1} [u(i+1,j,l) + u(i,j,l) - u(i+1,j-1,l) - u(i,j-1,l)] \\
& + \mu_{i+1,j-1} [v(i+1,j,l) - v(i,j,l)] \frac{y_j - y_{j-1}}{2(x_{i+1} - x_i)} \equiv R^w(i,j,l), \tag{B4}
\end{aligned}$$

where $\rho' = (\rho_1 + \rho_2)/2$ at the interface point $(i\Delta x, j\Delta y)$. On replacing the time derivatives by centered differences in (B3) and (B4), we obtain the scheme

$$\begin{aligned}
u(i,j,l+1) &= 2u(i,j,l) - u(i,j,l-1) + \Delta t^2 R^u(i,j,l), \\
v(i,j,l+1) &= 2v(i,j,l) - v(i,j,l-1) + \Delta t^2 R^w(i,j,l). \tag{B5}
\end{aligned}$$

The above scheme can be used for the acoustic case by setting the shear modulus μ to zero. It can be effectively applied to a liquid–solid interface where the interface is approximated appropriately.

¹J. P. Whelan and B. Finlayson, “An experimental model for the systematic investigation of stone fracture by extracorporeal shock wave lithotripsy,” *J. Urol. (Baltimore)* **140**, 395–400 (1988).

²L. A. Crum, “Cavitation microjets as a contributory mechanism for renal calculi disintegration in ESWL,” *J. Urol. (Baltimore)* **140**, 1587–1590 (1988).

³N. Vakil, S. M. Gracewski, and E. C. Everbach, “Relationship of model stone properties to fragmentation mechanisms during lithotripsy,” *J. Lithotripsy Stone Dis.* **3**, 304–310 (1991).

⁴R. Nitsche, V. Schweinsberg, H. Klengel, P. D. Niedmann, and U. R. Fölsch, “Different modes of fragmenting gallstones in extracorporeal shockwave lithotripsy,” *Scand. J. Gastroenterol.* **28**, 229–234 (1993).

⁵W. Sass, M. Bräunlich, H.-P. Dreyer, E. Matura, W. Folberth, H.-G. Priesmeyer, and J. Seifert, “The mechanisms of stone disintegration by shock waves,” *Ultrasound Med. Biol.* **17**, 239–243 (1991).

⁶N. Vakil and E. C. Everbach, “Transient acoustic cavitation in gallstone fragmentation: A study of gallstones fragmented *in vivo*,” *Ultrasound Med. Biol.* **19**, 331–342 (1993).

⁷M. Delius, F. Ueberle, and S. Gambihler, “Destruction of gallstones and model stones by extracorporeal shock waves,” *Ultrasound Med. Biol.* **20**, 251–258 (1994).

⁸M. T. Carnell and D. C. Emmony, “A schlieren study of the interaction between a lithotripter shock wave and a simulated kidney stone,” *Ultrasound Med. Biol.* **21**, 721–724 (1995).

⁹H. Kolsky, *Stress Waves in Solids* (Dover, New York, 1963).

¹⁰S. M. Gracewski, G. Dahake, Z. Ding, S. J. Burns, and E. C. Everbach, “Internal stress wave measurements in solids subjected to lithotripter pulses,” *J. Acoust. Soc. Am.* **94**, 652–661 (1993).

¹¹H. P. Rossmannith and R. E. Knasmillner, “Stress wave focusing induced fracture A photoelastic study,” in *Dynamic Failure of Materials* (Elsevier, New York, 1991), pp. 127–138.

¹²M. Hong and L. J. Bond, “Application of the finite-difference method in seismic source and wave diffraction simulation,” *Geophys. J. R. Astron. Soc.* **87**, 731–752 (1986).

¹³K. R. Kelly, R. W. Ward, S. Treitel, and R. M. Alford, “Synthetic seismograms: A finite-difference approach,” *Geophysics* **41**, 2–27 (1976).

¹⁴J. Virieux, “P-SV wave propagation in heterogeneous media: Velocity-stress finite-difference method,” *Geophysics* **51**, 889–901 (1986).

- ¹⁵Z. Alterman and F. C. Karal, Jr., "Propagation of elastic waves in layered media by finite difference methods," *Bull. Seismol. Soc. Am.* **58**, 367–398 (1968).
- ¹⁶A. Ungar and A. Ilan, "Propagation of elastic waves in vertically inhomogeneous media," *J. Geophys.* **43**, 33–40 (1977).
- ¹⁷R. A. Stephen, "A review of finite-difference methods for seismo-acoustics problems at the seafloor," *Rev. Geophys.* **26**, 445–458 (1988).
- ¹⁸A. Ilan, "Finite difference modeling for *P*-pulse propagation in elastic media with arbitrary polygonal surfaces," *Geophysics* **43**, 41–58 (1977).
- ¹⁹R. A. Stephen, "A comparison of finite difference and reflectivity seismograms for marine models," *Geophys. J. R. Astron. Soc.* **72**, 39–57 (1983).
- ²⁰J. S. Sochacki, J. H. George, R. E. Ewing, and S. B. Smithson, "Interface conditions for acoustic and elastic wave propagation," *Geophysics* **56**, 168–181 (1991).
- ²¹W. Ewing, W. S. Jardetzky, and F. Press, *Elastic Waves in Layered Media* (McGraw-Hill, New York, 1957), p. 76.
- ²²D. M. Boore, "Finite difference methods for seismic waves," in *Methods in Computational Physics* (Academic, New York, 1972), Vol. 11, pp. 1–37.
- ²³R. M. Alford, K. R. Kelly, and D. M. Boore, "Accuracy of finite difference modeling of the acoustic wave equation," *Geophysics* **39**, 834–842 (1974).
- ²⁴D. S. Campbell, H. G. Flynn, D. T. Blackstock, C. Linke, and E. L. Carstensen, "The acoustic fields of the Wolf electrohydraulic lithotripter," *J. Lithotripsy Stone Dis.* **3**, 147–156 (1991).
- ²⁵Z. Alterman and D. Lowenthal, "Computer generated seismograms," in *Methods in Computational Physics* (Academic, New York, 1970), Vol. 12, pp. 35–164.
- ²⁶Z. S. Alterman and J. Aboudi, "Source of finite extent, applied force and couple in an elastic half-space," *Geophys. J. R. Astron. Soc.* **21**, 47–64 (1970).
- ²⁷J. Sochacki, R. Kubichek, J. George, W. R. Fletcher, and S. Smithson, "Absorbing boundary conditions and surface waves," *Geophysics* **52**, 60–71 (1987).
- ²⁸R. J. Blake, L. J. Bond, and A. L. Downie, "Advances in numerical studies of elastic wave propagation and scattering," in *Review of Progress in Quantitative NDE*, edited by D. O. Thomson and D. E. Chimenti (Plenum, New York, 1982), Vol. 1, pp. 157–166.

Finite difference predictions of P -SV wave propagation inside submerged solids. II. Effect of geometry

Girish Dahake and S. M. Gracewski

Department of Mechanical Engineering and The Center for Biomedical Ultrasound,
University of Rochester, Rochester, New York 14627

(Received 16 September 1996; accepted for publication 18 June 1997)

To understand better direct stress wave contributions to stone fragmentation during extracorporeal shock wave lithotripsy (ESWL), the numerical formulation developed in part I is applied to study the time evolution of stress wave fields produced inside submerged isotropic elastic solids having irregular geometries. Cut spheres are used to model stones that have already had an initial fracture. Ellipses are used to approximate other deviations from a spherical geometry. The propagation and focusing of the longitudinal (P) and shear (S) wave fronts are visualized by presenting internal strain contours. Internal strain measurements are obtained from strain gauges embedded inside plaster specimens to confirm the focusing effect obtained from the concave back surfaces of the stones. Fragmentation experiments indicate damage caused by spalling and direct stress wave focusing as well as a front surface pit presumably created by cavitation activity. © 1997 Acoustical Society of America. [S0001-4966(97)03110-X]

PACS numbers: 43.35.Wa, 43.80.Sh [HEB]

INTRODUCTION

There is a debate regarding the relative contributions of direct stress waves and cavitation to gallstone and kidney stone destruction during extracorporeal shock wave lithotripsy (ESWL) *in vivo*.¹⁻⁸ Due to the large patient to patient variations in biological stone strengths and shock wave propagation paths, it is difficult to determine the factors that control the efficacy of stone fragmentation from a series of clinical experiments. Because of the difficulties associated with *in vivo* investigation of stone pulverization mechanisms, numerical models and systematic *in vitro* experiments are being developed to determine factors that govern stone fragmentation. In this paper, we concentrate on determining direct stress wave contributions to stone fragmentation.

In vitro experiments show that many biological stones initially break approximately in half suggesting that internal flaws and stress wave loading may be important in lithotripsy.^{4,9,10} Stone geometry significantly affects the stresses and strains developed within the stone. Concretions with concave surfaces focus the waves that are internally reflected. These reflected waves converge generating large stresses at the caustic points within the stones. Damage is presumed to occur at the locations of the highest induced stresses.

A number of stress wave fragmentation studies have been conducted on perspex spheres, because perspex offers a convenient means of visually identifying internal fracture sites and crack patterns.^{11,12} For an explosive source on the surface of a sphere, three principal regions of damage were observed:

- (i) In the immediate vicinity of the point explosive loadings. Patterns consisted of longitudinal cracks separated by 45° , together with subsurface separation.
- (ii) Near the far end of the sphere. The extent of fracture is about equal to that near the loading region. This type of

fracture, called spalling, is caused by the direct reflection of the compressive pulse as a tensile pulse. Due to the interaction between the incident and reflected pulses, the maximum tensile stress occurs at a distance equal to approximately one-half the pulse width from the back surface of the solid.

(iii) In a region approximately two-thirds the distance along the diameter from the leading edge of the sphere. The four caustics (PP , PS , SS , and SP) are located in this region. The fracture times observed experimentally by high-speed photography correlate well with the calculated arrival times of the wave fronts at the caustic points.

Shock wave experiments have also been carried out on transparent solids of a variety of geometries to observe the fracture patterns generated by the constructive interference between reflected shock waves.¹³⁻¹⁵

In part II of this paper, the finite difference procedure presented in part I is used to study the internal stress wave fields generated within submerged solids of various shapes subjected to a radially diverging source in the surrounding liquid. The 2-D finite difference routine can account for acoustic and elastic wave propagation within homogeneous

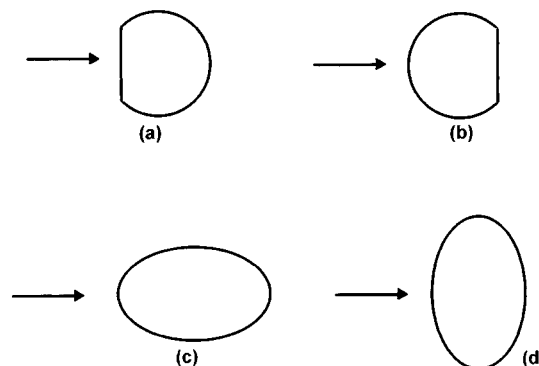


FIG. 1. Variations from circular cross sections considered. Arrows show the direction of the incident wave in the surrounding liquid.

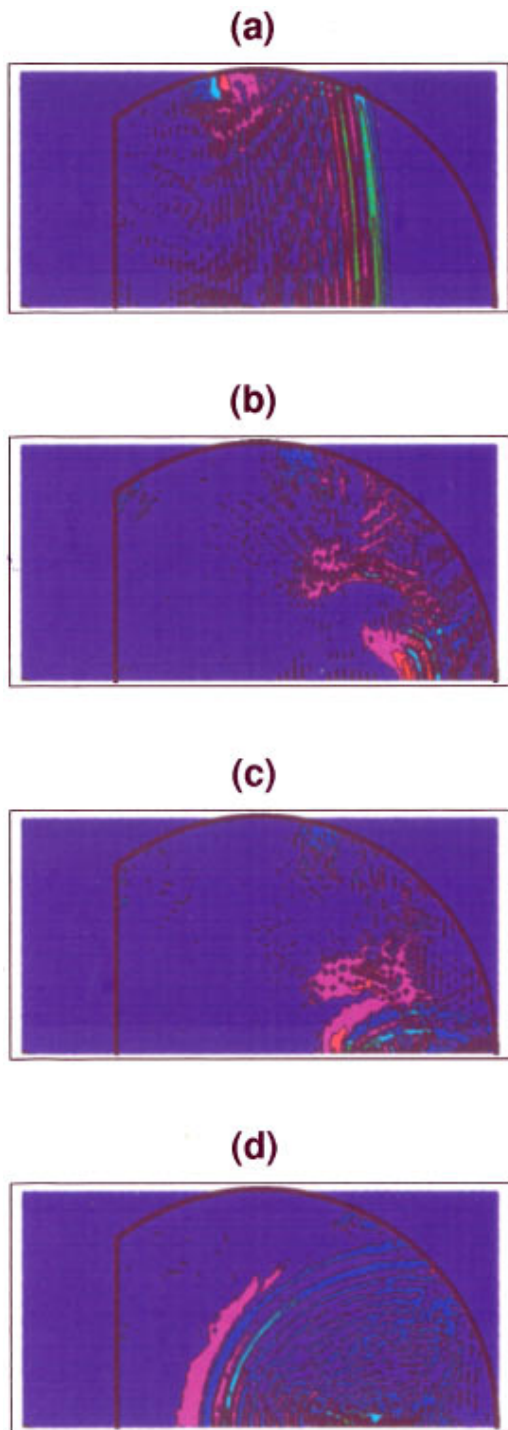


FIG. 2. Time evolution of principal strain contours inside a circular cylinder with a cut face 6.5 mm in front of the center of the circle. Strain contours are plotted at times (a) 4 μ s, (b) 7 μ s, (c) 8 μ s, and (d) 10 μ s after the incident wave first reaches the solid. All contour plots in parts I and II of this paper use the same scale and peak compressional to peak tensile strains vary from yellow to green to blue to purple to red and finally to orange.

liquid and solids, respectively, as well as transmission and reflection at liquid–solid interfaces. To obtain expressions for the grids along a liquid–solid interface of arbitrary shape, the heterogeneous wave equations are integrated across the interface using the divergence theorem. The grid size in both x and y directions is variable to reduce the numerical discretization error. In addition, artificial absorbing regions are

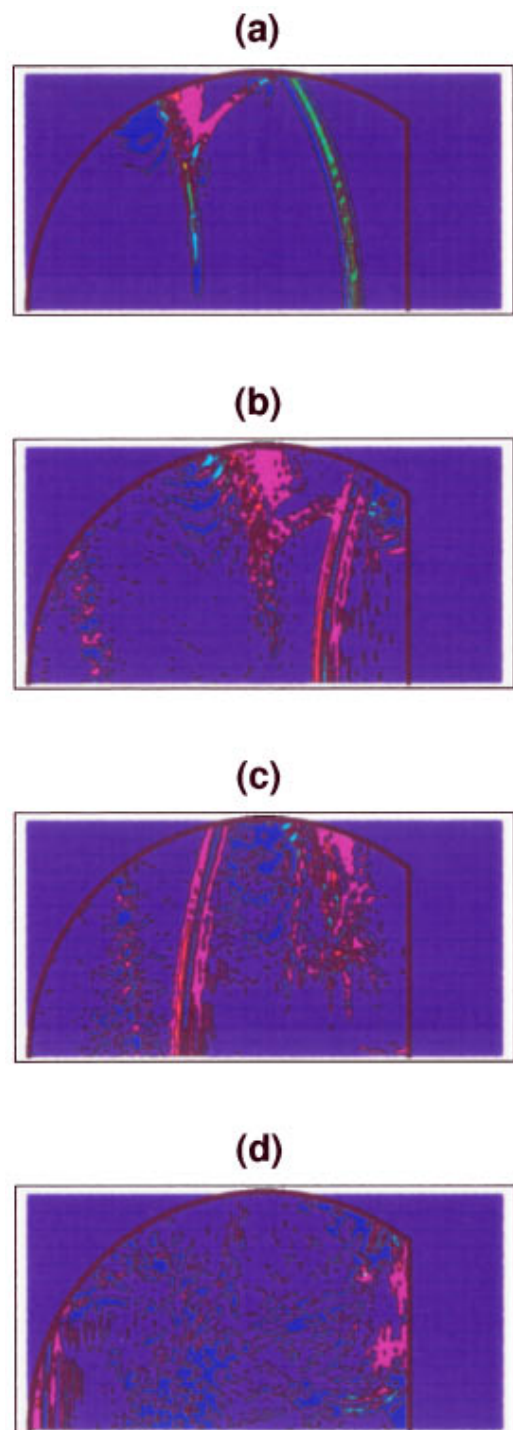


FIG. 3. Time evolution of principal strain contours inside a circular cylinder with a cut face 6.5 mm behind the center of the circle. Strain contours are plotted at times (a) 5 μ s, (b) 7 μ s, (c) 9 μ s, and (d) 11 μ s after the incident wave first reaches the solid. All contour plots in parts I and II of this paper use the same scale and peak compressional to peak tensile strains vary from yellow to green to blue to purple to red and finally to orange.

introduced along the edge of the computational domain to prevent spurious reflections from these boundaries from affecting the accuracy of the solution.

Since gallstones are typically nearly spherical in shape, strain contours and time histories inside a solid of circular cross section subjected to ultrasonic wave sources were presented in part I. The focusing effect of the concave back

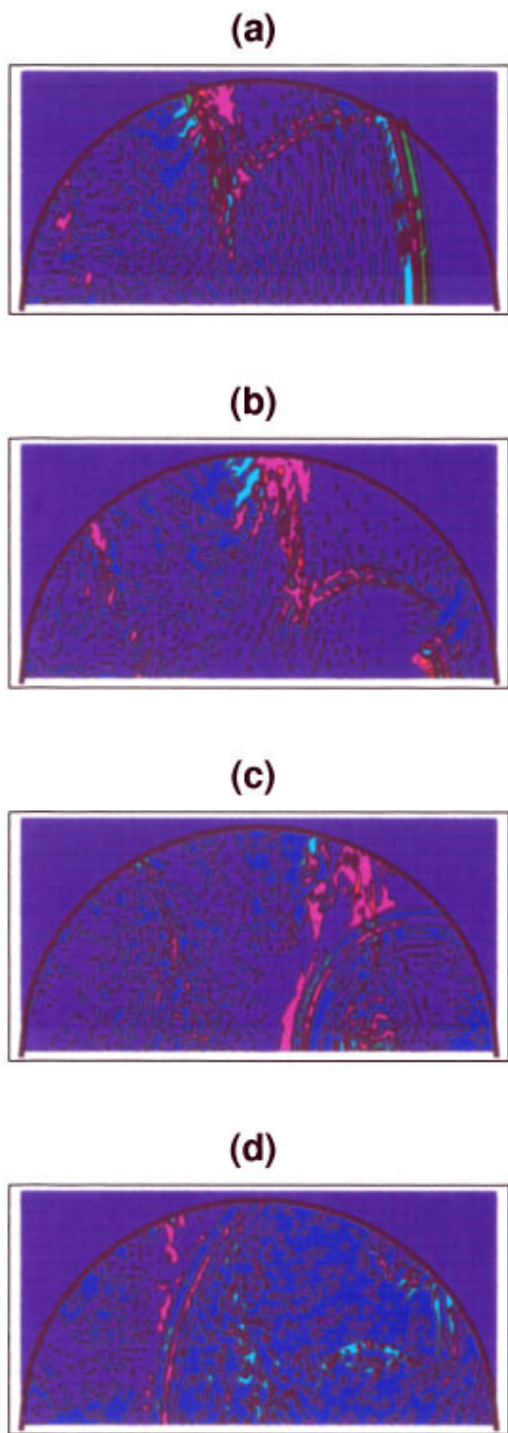


FIG. 4. Time evolution of principal strain contours inside an elliptical cross section when the incident wave is along the major axis. Strain contours are shown at times (a) $6 \mu\text{s}$, (b) $8 \mu\text{s}$, (c) $10 \mu\text{s}$, and (d) $12 \mu\text{s}$ after the incident wave first reaches the solid. All contour plots in parts I and II of this paper use the same scale and peak compressional to peak tensile strains vary from yellow to green to blue to purple to red and finally to orange.

surface produced regions of high stress approximately two-thirds the distance from the front surface. A successful lithotripsy procedure is not only limited to breaking the stone once, but relies on its ability to efficiently fracture the stone after the initial crack breaks it into two or more pieces. The success of lithotripsy depends on the repeated fracture of stones until all pieces are small enough to be discharged

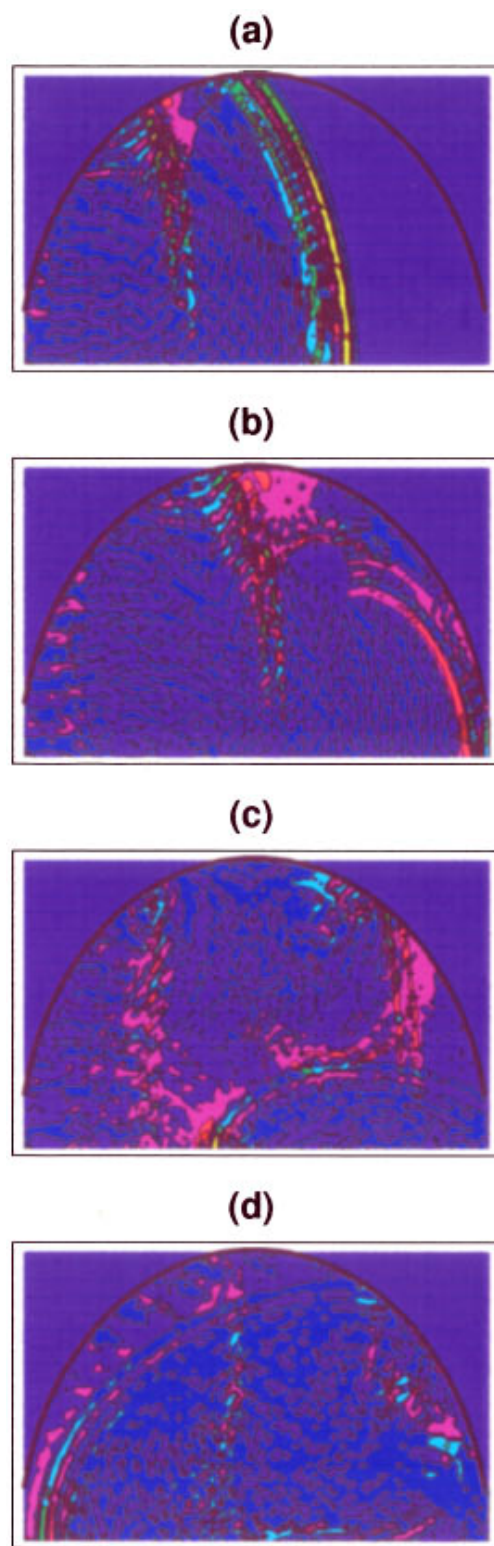


FIG. 5. Time evolution of principal strain contours inside an elliptical cross section when the incident wave is along the minor axis. Strain contours are shown at times (a) $4 \mu\text{s}$, (b) $6 \mu\text{s}$, (c) $9 \mu\text{s}$, and (d) $11 \mu\text{s}$ after the incident wave first reaches the solid. All contour plots in parts I and II of this paper use the same scale and peak compressional to peak tensile strains vary from yellow to green to blue to purple to red and finally to orange.

naturally from the human body. To better understand the subsequent fragmentation of the stones, numerical calculations are performed on circular geometries with regions removed from the front and back. Other variations from the

spherical symmetry are also considered by including ellipsoidal cross sections in the numerical calculations. Strain contours are plotted to visualize the wave front propagation and identify the regions of highest stress.

Experiments are conducted by embedding silicon semiconductor strain gauges inside plaster spheres. Experimental evidence is presented that indicates that there is a focusing effect due to the concave back surface of the stones.

I. NUMERICAL RESULTS

Strain contours and plots of strain versus time at the caustic points are compared for wave propagation inside solids of a variety of cross sections, shown in Fig. 1. These geometries are chosen to model typical deviations from spherical stones that may occur *in vivo*. Solids with flat faces in front and back are used to model partially fragmented stones. The wave source for all numerical calculations is a radially diverging longitudinal (*P*) wave front located in the surrounding liquid 9 cm away from the closest stone surface. Time $t=0$ is defined as the instant the incident wave strikes the front surface of the solid. The longitudinal wave velocity in the water is 0.15 cm/ μ s and the longitudinal and the shear wave velocities in the solid are 0.33 cm/ μ s and 0.175 cm/ μ s, respectively, based on measured values for the plaster used in the experiments.

The time evolution of strain contours for the refracted *P* and *S* waves inside cut circular and elliptical cross sections are shown in Figs. 2–5. Figure 2 shows the strain contours for a 2.2-cm-diam circular cylinder with a cut face in the front, oriented as in Fig. 1(a). The cut face is 6.5 mm from the center. The radius of curvature of the incident *P* wave at the front of the cylinder is large, and consequently the refracted shear (*S*) wave into the solid is weak. The refracted *P* wave front however propagates through the cross section as shown in Fig. 2(a)–(d), producing a *P* and *S* wave front pair on reflection from the back surface. The reflected wave fronts converge on the axis at their respective caustic points. The refracted *S* wave front is much slower and weaker and produces another *P* and *S* wave front pair on reflection from the back surface. Figure 6 shows the strain calculated along the plane of symmetry of the cylinder at the center and the four caustic points, *PP*, *PS*, *SS*, and *SP*. The amplitude of the focused reflected wave at the *PS* caustic is larger than the amplitude of the initially refracted wave, analogous to results for the circular cross section presented in Fig. 4, part I. However, reflected amplitudes are dramatically lower at the *SS* and the *SP* caustic points, as seen in Fig. 6(c) and (e).

Figure 3 shows the strain contours for the *P* wave source incident on a 2.2-cm-diam circular cylinder with a cut face at the back, oriented as in Fig. 1(b). The refracted *P* and the *S* wave fronts diverge into the solid after reflection from the flat surface at the back. Plots of the time evolution of the strain for this cross section is presented in Fig. 7 for the same locations as used for Fig. 6. Even though there is no focusing from the flat back surface, the *SP* wave reflecting from the sides does focus producing a strain with an amplitude of the same order as the incident refracted *P* wave.

In Figs. 4 and 5, principal strain contours are presented for the radially diverging source incident on the major and

minor axes, respectively, of an elliptical cross section with an eccentricity of 1.25 and major axis of 2.2 cm. When the wave is incident along the major axis, the smaller radius of curvature of the back surface concentrates the reflected waves more effectively. For this case, the maximum strain amplitude produced by the reflected waves occurs at the *PS* caustic point and is approximately 1.5 times the amplitude of the incident refracted *P* wave. When the wave is incident along the minor axis, the large radius of curvature of the back surface does not effectively focus the reflected wave energy. In this case, the strain due to the incident refracted *P* wave is the maximum strain at each of the four caustic points.¹⁸

II. EXPERIMENTS

A. Strain gauge measurements

Silicon semi-conductor strain gauges (UFP-500–060, Kulite Semiconductor Products, Inc., Leonia) were embedded inside plaster spheres to measure the internal strains when the spheres were subjected to lithotripter shock wave pulses. Two lithotripters were used to generate the source shock wave pulses. A Wolf model 2137.50 electrohydraulic lithotripter (Richard Wolf GmbH, Postfach 4D, D-7134 Knittlingen, Germany) was used to generate nearly spherically diverging shock wave pulses.^{16,17} The pressure field produced by the radially diverging shock wave source is much simpler than that of focused lithotripter sources. Therefore, the strains within the sphere are easier to interpret and model numerically. In the experiments, the shock source was located 9 cm from the front (closest to the source) surface of the sphere. Therefore, the radius of curvature of the shock wave front was almost an order of magnitude larger than the radius of the 2.2-cm-diam spherical specimen. The shock waves generated by the Wolf lithotripter are predominantly compressive with an amplitude of approximately 1 MPa at 9 cm and a 1- μ s pulse length. A Dasonics Therasonic piezoelectric lithotripter (Dasonics, Inc., Milpitas, CA, USA) was used as the focused wave source. At the focus, the peak positive pressure of approximately 50 MPa was sufficient to conduct fragmentation experiments and produced significant cavitation activity in the surrounding water bath.

The plaster was made from a mixture of 100 parts Ultracal 30 (United States Gypsum Company, Chicago, IL) to 36 parts water by weight. Immediately after mixing, the plaster was poured into 2.2-cm-diam spherical molds and allowed to set. Before each experiment the plaster samples were submerged in degassed water and degassed under a 24-in. Hg vacuum for at least 2 h and then pressurized at 10 atm for approximately 10 min to drive any remaining air bubbles into solution. The longitudinal (*P*) and shear (*S*) wave speeds measured in similarly prepared disk specimens are 3290 ± 40 m/s and 1750 ± 90 m/s, respectively. Details of sample preparation procedure and experimental protocol can be found in Ref. 16.

To embed a strain gauge within a plaster sphere, the gauge was suspended in the mold using a thin Kevlar fiber, before the plaster was added. Gauges are centered at the *PP* caustic point and aligned radially with in the sphere. Dur-

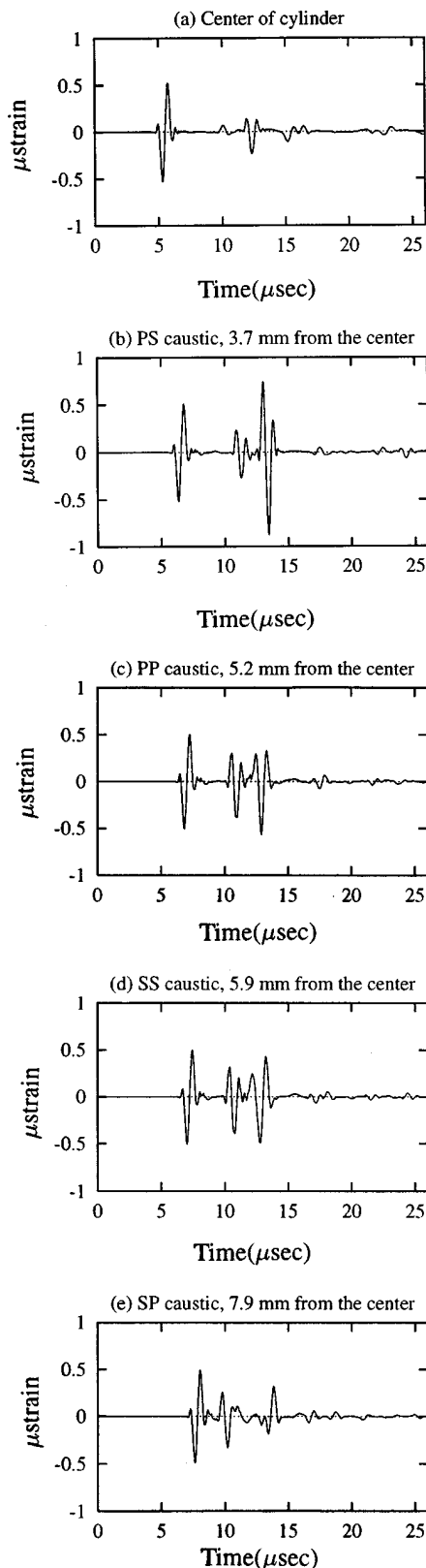


FIG. 6. Strain along the axis inside the circular cylinder with a cut face 6.5 mm in front of the center. The five measurement locations are the center of the circle and the four caustic points located in the back half of the circle.

ing the experiment, the strain gauge is aligned with the shock wave propagation direction, thereby aligning it with a principal direction of strain. The silicon gauges are U shaped with a half-width of 0.2 mm and an effective gauge length of

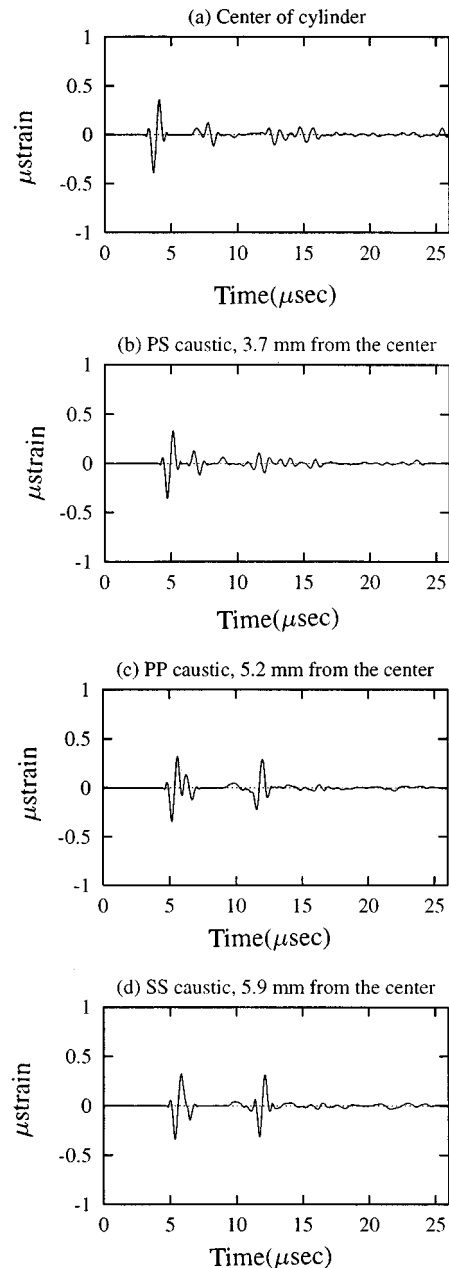


FIG. 7. Strain along the axis inside the circular cylinder with a cut face 6.5 mm behind the center of the circle. The four measurement locations are the same as used for Fig. 6. The SP caustic point lies outside the solid.

0.8 mm. Because the shock wave pulse length is of the same order of magnitude as the gauge length, the gauge essentially integrates the strain along its length and smears out the pulse. However, information about the arrival times, relative magnitudes, and polarity of the strain wave pulses can be obtained from the strain gauges.¹⁶

To verify that stress wave focusing exists within the plaster spheres, a 2.2-cm-diam sphere with a strain gauge centered at the *PP* caustic was subjected to Wolf lithotripter pulses. Figure 8(a) shows a typical strain signal recorded by the strain gauge. The signals had excellent pulse-to-pulse reproducibility and reasonable sphere-to-sphere reproducibility. The initial negative (compressive) strain peak corresponds to the *P* wave that refracts into the solid sphere when the pressure pulse propagating in the liquid reaches the

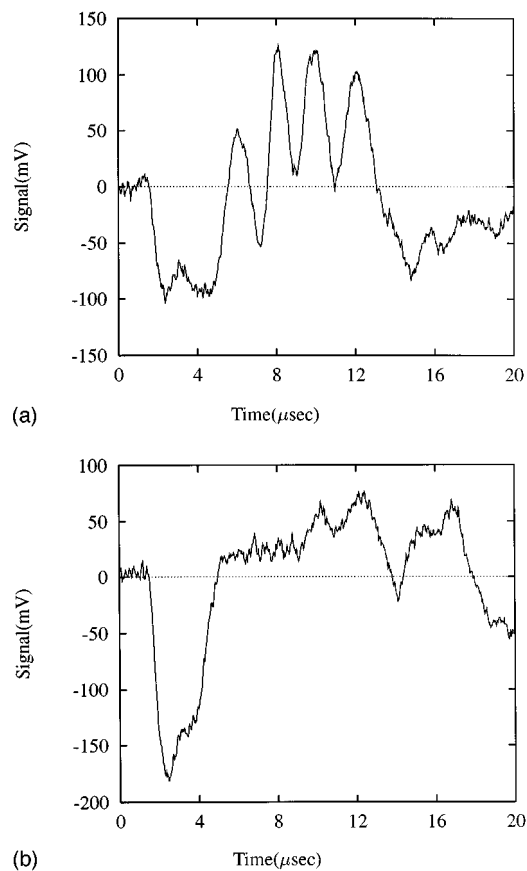


FIG. 8. Strain signal in millivolts recorded by the semiconductor strain gauge inside a sphere subjected to an incident radially diverging wave source 9.0 cm from the front surface. (a) shows the strain at the *PP* caustic point 5.2 mm to the right of the center. (b) shows the strain at a point 5.2 mm to the left of the center.

sphere surface. This incident refracted (*P*) wave produces a tensile and a slower shear wave pulse after reflecting from the pressure release back surface of the sphere. The subsequent positive (tensile) peaks in the strain signal are produced by these reflected waves and the incident refracted shear (*S*) wave. Because of the pulse smearing, it is difficult to make a one-to-one correspondence between the pulses. However, the highest amplitude of these tensile pulses is larger than the incident pulse indicating that reflection from the back surface does indeed produce wave focusing within the sphere. The sphere is then rotated 180° to position the strain gauge at the *PPP* focal point located within the front half of the sphere. The *PPP* wave undergoes two internal reflections from the solid-liquid interface. The energy loss due to transmission to the surrounding liquid during these two internal reflections reduces the pulse amplitude to less than 40% of its original value. Therefore, the amplitude of the *PPP* wave is significantly lower than the *PP* wave when it is focused by reflection from the concave surface of the sphere. The focused signal is therefore of lower amplitude than the incident refracted signal for this case, as shown in Fig. 8(b).

It has been suggested that the violent collapse of a cloud of cavitation bubbles near the surface of the stone may produce internal stresses with magnitudes larger than those produced by the direct shock wave pulse. This is certainly true

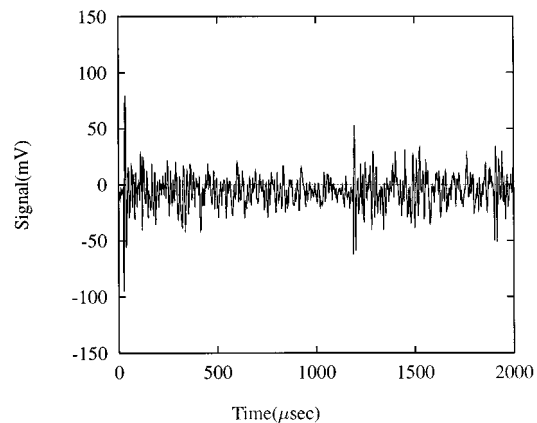


FIG. 9. Strain signal in millivolts recorded by a semiconductor strain gauge inside a sphere at the focus of a Dasonics piezoelectric lithotripter. The oscilloscope trigger delay was set so that the direct shock wave arrival occurs at the beginning of the trace. The shock wave created by the cavitation bubble collapse arrives at the strain gauge approximately 1.2 ms later.

very close to the site of bubble collapse, near the surface of the stone. A strain gauge embedded at the *PP* caustic point, well within a plaster sphere, was used to investigate whether the shock wave generated by cavitation bubble collapse can penetrate to the interior. The instrumented plaster sphere was placed at the focus of the Dasonics lithotripter and subjected to shock wave pulses. A needle hydrophone was used to monitor the pressure field in the liquid near the focal region of the lithotripter. Figure 9 shows that the direct shock wave produces a larger signal (nearly 40% larger) in the strain gauge than the shock wave produced by the cavitation bubble collapse. This is true even though the signal recorded by the hydrophone in the nearby water shows that signal due to the cavitation bubble collapse can be larger than that due to the direct incident wave.

B. Fragmentation studies

Fracture experiments were conducted on plaster spheres placed slightly above the focus of the Dasonics lithotripter. Three regions of damage were consistently observed, similar to those of the perspex spheres subjected to point explosions on their front surfaces.^{11,12} First, a small pit, presumably due to cavitation activity occurred on the front surface, as shown in the left half of Fig. 10. Second, small chips spalled off the back surface as shown in the right half of Fig. 10. Third, the sphere broke into two or more large pieces. In most spheres, a relatively planar crack perpendicular to the wave propagation direction fractured the sphere into two large pieces. This fracture occurred approximately two-thirds the distance along the diameter from the front surface of the sphere. Variations in the exact location of the crack initiation point suggest that preexisting flaws and pores act as nuclei for fracture. The axisymmetric characteristics of the crack suggest that it initiated near the axis of symmetry and propagated outward to the surface of the sphere. In some of the spheres, the back piece of the sphere also broke into three pieces at approximately 120° angles, as shown in the right half of Fig. 10.

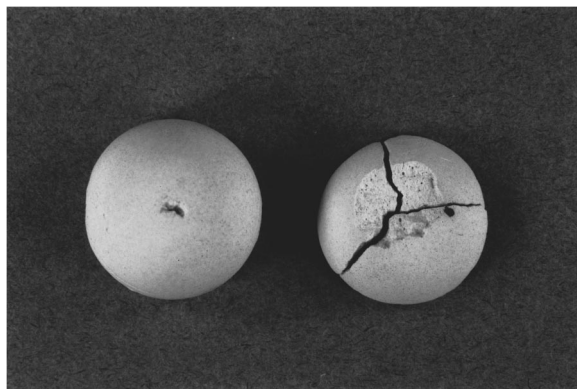


FIG. 10. Photograph of typical damage to a plaster sphere subjected to shock wave pulses at the focus of a Disonics piezoelectric lithotripter. The sphere broke into two pieces along a crack perpendicular to the shock wave propagation direction. The left figure shows the pit on the front surface of the stone presumably created by cavitation. The right figure shows the crater produced by spalling on the back surface of the stone.

To investigate the effect of crack development on internal wave focusing and successive fragmentation of the stones, fracture experiments were also conducted on cut plaster spheres. Flat faces, 6.5 cm from the center of the sphere and perpendicular to the radius, were cut using a diamond saw. Spheres with the flat surface facing the shock wave source broke in almost the same pattern as the complete spheres. It was expected that cut spheres rotated 180° so their flat surface faces away from the source would break less readily because of the reduction in the focusing upon reflection. However, these specimen broke after approximately the same number of shock waves as for the specimens with their flat surface facing the source. Although the numerical calculations previously presented indicate that the focusing is significantly reduced when the flat surface is on the back side of the specimen, it is not totally eliminated. There is still some internal reflection and focusing from the sides of the sphere. To completely eliminate this focusing, some spheres were cut in half and placed at the focus with their flat surface positioned away from the source. These hemi-spheres did not break even after subjecting them to three or more times the average number of shocks that caused fracture in the complete spheres. These experimental results are consistent with the hypothesis that stress wave focusing contributes to fragmentation of stones by lithotripter shock wave pulses.

To verify that cracks initiated internally, spheres and cut spheres subjected to half the number of shock waves typically leading to fracture were sectioned and observed by light microscopy. Internal cracks were observed even when there was no surface indication of fracturing. In Fig. 11, a horizontal crack exists approximately 0.5 cm below and parallel to the planar back surface of a cut sphere. Although it was difficult to photograph the entire length of a crack, the microscope magnification and lighting could be adjusted so that it was easy to follow the crack from one end to the other to verify that it did not initiate at the stone surface.

III. SUMMARY AND DISCUSSION

A 2-D finite difference-time domain (FD-TD) code is used to analyze the time evolution of the strain fields inside

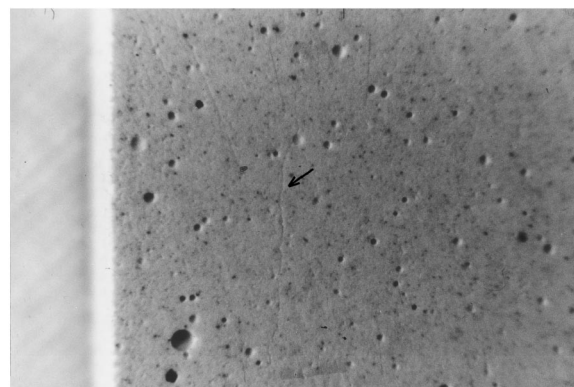


FIG. 11. Photograph of internal crack parallel to the cut face of a plaster sphere.

submerged isotropic elastic solids of various geometries subjected to a wave source in the liquid that simulates a Wolf lithotripter. Waves reflected from the concave back surface of a sphere or circular disk are focused, creating caustic regions within these solids. Imbedded strain gauges have verified that higher strain amplitudes are produced at the caustics due to wave focusing. Cracks are more likely to develop in the regions of high tensile stresses occurring within these caustic regions. Microscopic evaluation of sectioned plaster specimens indicate that cracks do indeed initiate near these caustic regions close to the symmetry axis of the stones. Internal cracks were observed even when the nearby exterior surface of the stones appeared undamaged. These cracks, if subjected to additional shock wave pulses, typically break the spherical plaster stones into two large pieces, with the crack surface perpendicular to the wave propagation direction. The axisymmetric characteristics of these cracks provide additional evidence that the crack initiation occurred near the axis of symmetry of the spheres. The exact location of crack initiation varies slightly, presumably depending on the size distribution of pores and inhomogeneities that serve as crack nuclei within the plaster material.

Although typical kidney stones and gallstones can initially be modeled as nearly spherical in shape, the geometry changes as pieces break away from the stones. To simulate stones after they have broken into two pieces, spheres where the back surface of the sphere has been removed by a planar cut have been used for fragmentation studies. The numerical simulations on cut circular cylinders predict a significant reduction in focusing and internal strain amplitudes. However, waves reflecting from the sides of the cut spheres and disks still do focus internally and produce regions of high strains. Experimentally, internal crack initiation still occurs if the cut is 6.5 mm beyond the center of the sphere. However, spheres cut along the diameter perpendicular to the wave propagation direction did not break even when subjected to three or more times as many shock waves.

Embedded strain gauges were used to compare the amplitudes of the internal strains generated by the direct shock wave and by cavitation bubble collapse. The direct shock wave produced significantly higher internal stresses than did the shock wave generated by the cavitation bubble collapse. Even though bubble collapse can produce higher stresses lo-

cally, the amplitude decays rapidly with distance and does not significantly penetrate to the center of our model stones. Therefore, the internal damage that was observed was most likely caused primarily by the direct stress wave interaction with the stone material.

ACKNOWLEDGMENT

This work was supported in part by USPHS Grant No. DK39796.

- ¹J. P. Whelan and B. Finlayson, "An experimental model for the systematic investigation of stone fracture by extracorporeal shock wave lithotripsy," *J. Urol. (Baltimore)* **140**, 395–400 (1988).
- ²L. A. Crum, "Cavitation microjets as a contributory mechanism for renal calculi disintegration in ESWL," *J. Urol. (Baltimore)* **140**, 1587–1590 (1988).
- ³N. Vakil, S. M. Gracewski, and E. C. Everbach, "Relationship of model stone properties to fragmentation mechanisms during lithotripsy," *J. Lithotripsy Stone Dis.* **3**, 304–310 (1991).
- ⁴R. Nitsche, V. Schweinberg, H. Klengel, P. D. Niedman, and U. R. Fölsch, "Different modes of fragmenting gallstones in extracorporeal shockwave lithotripsy," *Scand. J. Gastroenterol.* **28**, 229–234 (1993).
- ⁵W. Sass, M. Bräunlich, J.-P. Dreyer, E. Matura, W. Folberth, H.-G. Priesmeyer, and J. Seifert, "The mechanisms of stone disintegration by shock waves," *Ultrasound Med. Biol.* **17**, 239–243 (1991).
- ⁶N. Vakil and E. C. Everbach, "Transient acoustic cavitation in gallstone fragmentation: A study of gallstones fragmented *in vivo*," *Ultrasound Med. Biol.* **19**, 331–342 (1993).
- ⁷M. Delius, F. Ueberle, and S. Gambihler, "Destruction of gallstones and model stones by extracorporeal shock waves," *Ultrasound Med. Biol.* **20**, 251–258 (1994).
- ⁸M. T. Carnell and D. C. Emmony, "A schlieren study of the interaction between a lithotripter shock wave and simulated kidney stone," *Ultrasound Med. Biol.* **21**, 721–724 (1995).
- ⁹S. J. Burns, S. M. Gracewski, N. Vakil, and A. R. Basu, "Dynamic failure mechanisms in gallstones using lithotripsy," in *Dynamic Failure of Material* (Elsevier, New York, 1991), pp. 114–126.
- ¹⁰S. J. Schulte and R. L. Baron, "Piezoelectric biliary lithotripsy: An *in vitro* study of factors affecting gallstone fragmentation," *Am. J. Roentgenol.* **155**, 1211–1216 (1990).
- ¹¹J. F. Siva-Gomes, S. T. S. Al-Hassani, and W. Johnson, "A note on times to fracture in solid perspex spheres due to point explosive loading," *Int. J. Mech. Sci.* **19**, 309–314 (1976).
- ¹²E. Lovell, S. T. S. Al-Hassani, and W. Johnson, "Fracture in solid spheres and circular disks due to a 'point' explosive impulse on the surface," *Int. J. Mech. Sci.* **16**, 193–199 (1974).
- ¹³H. Kolsky, *Stress Waves in Solids* (Dover, New York, 1963), Chap. 8.
- ¹⁴H. Kolsky and A. C. Shearman, "Investigation of fractures produced by transient stress waves," *Research* **2**, 384–389 (1949).
- ¹⁵A. G. Mamalis, G. Giouftsidis, and W. Johnson, "Fracturing of paraboloidal-ended perspex rods explosively loaded in air and salt water," *Int. J. Mech. Sci.* **29**, 159–177 (1987).
- ¹⁶S. M. Gracewski, G. Dahake, and Z. Ding, "Internal stress wave measurements in solids subjected to lithotripter pulses," *J. Acoust. Soc. Am.* **94**, 652–661 (1993).
- ¹⁷D. S. Campbell, H. G. Flynn, D. T. Blackstock, C. Linke, and E. L. Carstensen, "The acoustic fields of the Wolf electrohydraulic lithotripter," *J. Lithotripsy Stone Dis.* **3**, 147–156 (1991).
- ¹⁸G. S. Dahake, "Wave propagation problems in solids subjected to plane and radially diverging waves incident in a liquid—A numerical and experimental approach," Ph.D. thesis, University of Rochester (1996).

Solid-liquid interface reconstructions from ultrasonic time-of-flight projection data

Douglas T. Queheillalt and Haydn N. G. Wadley

*Intelligent Processing of Materials Laboratory, School of Engineering and Applied Science,
University of Virginia, Charlottesville, Virginia 22903*

(Received 2 April 1997; accepted for publication 23 June 1997)

The large difference in the ultrasonic velocity of solid and liquid semiconducting materials results in significant ray refraction and pulse time delays during propagation through solid-liquid interfaces. This has led to an interest in the use of ultrasonic time-of-flight (TOF) measurements for deducing the interfacial geometry. A ray-tracing analysis has been used to analyze two-dimensional wave propagation in the diametral plane of model cylindrical solid-liquid interfaces. Ray paths, wavefronts, and TOFs for rays that travel from a source to an arbitrarily positioned receiver on the diametral plane have been calculated and compared to experimentally measured TOF data obtained using a laser generated/optically detected ultrasonic system. Examinations of both the simulations and the experimental results reveals that the interfacial region can be identified from transmission TOF data. When the TOF data collected in the diametral plane were used in conjunction with a nonlinear least-squares reconstruction algorithm, the interface geometry (i.e., axial location and shape) were precisely recovered and the ultrasonic velocities of both solid and liquid phases were obtained with error of less than $\sim 3\%$. © 1997 Acoustical Society of America.

[S0001-4966(97)00710-8]

PACS numbers: 43.35.Yb [HEB]

INTRODUCTION

Many single-crystal semiconductors are grown by variants of a Bridgman technique in which a cylindrical ampoule containing a molten semiconductor is translated through a thermal gradient, resulting in the directional solidification and growth of a single crystal.¹ During this form of crystal growth, the solid-liquid interface shape and velocity (i.e., rate of change of its location) together with the local temperature gradient control the mechanism of solidification (i.e., planar, cellular, or dendritic), the likelihood of secondary grain nucleation/twin formation (i.e., loss of single crystallinity), solute (dopant) segregation, dislocation generation, etc., and therefore determines the resultant crystals' quality.¹⁻⁴ For crystals grown by the vertical variant of the Bridgman (VB) technique, optimum properties are obtained with a low ($\sim 1-5$ mm/h) constant solidification velocity and a planar or near planar (slightly convex toward liquid) interface shape maintained throughout growth.^{5,6} The solidification rate and the interface shape are sensitive functions of the internal temperature gradients (both axial and radial) during solidification which are governed by the heat flux distribution incident upon the ampoule, the latent heat release at the interface, and heat transport (by a combination of conduction, buoyancy surface tension driven convection, and radiation) within the ampoule.⁷⁻⁹ The solid-liquid interface's instantaneous location, growth velocity, and interfacial shape during growth are therefore difficult to predict and optimize, especially for those semiconductor materials with low thermal conductivity (i.e., CdTe alloys).¹⁰ Thus the development of technologies to noninvasively sense the solid-liquid interfacial shape and location (its change with time gives the solidification rate) during VB crystal growth have become

recognized as a key step for developing a better understanding of the growth process and implementing sensor-based process control.

Ultrasonic techniques are of potential interest for this sensing application because of the significant difference in the longitudinal wave velocity between the solid and the liquid phases of many semiconducting materials (Fig. 1).¹¹⁻¹³ Thus severe ray bending and significant time delays occur when ultrasound is propagated through a semiconductor solid-liquid interface. In other material systems, this approach has already been successfully used to recover the interface geometry (location and shape) during, for example, the controlled solidification of polycrystalline aluminum.^{14,15} While single crystal semiconductors are elastically anisotropic, extensive modeling suggests that similar strategies are likely to work in VB geometry solid-liquid bodies, provided point sources and receivers are used, and an anisotropic generalization of Snell's law is incorporated in ray tracing.¹⁶ The advent of laser ultrasonics¹⁷ (i.e., laser generation and interferometric detection¹⁸) offers both the needed ultrasonic point sources/receivers and a noninvasive means for their introduction into the high-temperature environment of crystal growth furnaces.

In previous work¹⁹ we have demonstrated the feasibility of using laser ultrasonics to characterize solid-liquid bodies, similar to those found during VB crystal growth. We have also shown that because of the severe ray bending at the solid-liquid interface, a detailed ray-tracing analysis is necessary in order to reconstruct the interface from ultrasonic time-of-flight (TOF) projection data. A detailed study of ray paths and TOF analysis of ultrasound propagating in the diametral plane of solid-liquid bodies for a coincident source/receiver indicated that data obtained from paths on the dia-

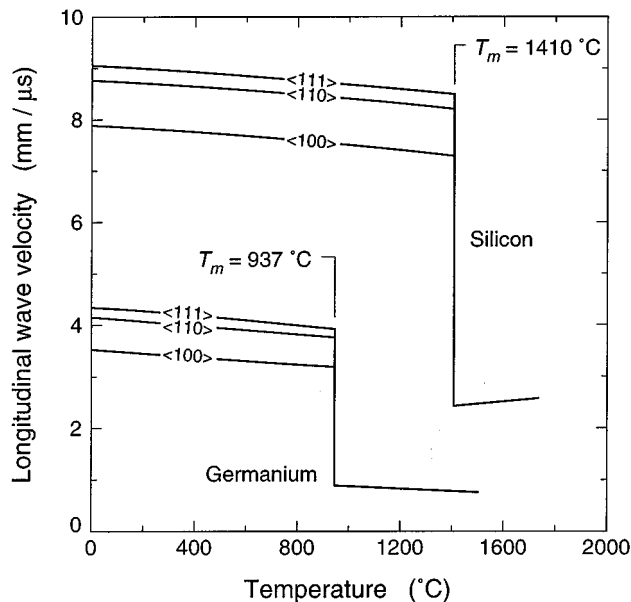


FIG. 1. Temperature and orientation dependencies of the quasi-longitudinal wave velocities for solid and liquid silicon (Si) and germanium (Ge).

metral plane with identical axial positions was insufficient to precisely characterize all interface shapes. Interfaces that curved into the solid (concave interfaces) were shown to be particularly difficult to characterize with this type of data.

Here, we extend the previous work on wave propagation in model solid-liquid bodies to a situation where the receiver is positioned at arbitrary locations relative to the source in the diametral plane. The diametral plane is defined as the sagittal plane through the diameter of the ampoule. A detailed study of ray paths, wavefronts, and the TOF of rays that travel from a source to an arbitrarily positioned receiver is reported. It is shown that the interfacial region can be easily identified from transmission TOF measurements because the velocity of the liquid is much smaller than that of the solid. Also since convex and concave interfaces result in distinctly different TOF data profiles when source and receiver points are axially displaced, the interface location and shape (convex or concave) can be easily determined.

I. EXPERIMENTAL PROCEDURE

A. Model interfaces

A bench-top model with known solid-liquid velocities was constructed from water and solid polymethylmethacrylate (PMMA) contained in a 37.5-mm-radius cylindrical aluminum ampoule; see Fig. 1. Ultrasound was optically generated and laser interferometrically detected on the outer surface of this aluminum ampoule. The interface convexities h [defined such that $h > 0$ corresponds to a convex interface (Fig. 2)] examined here were ± 2 , ± 5 , ± 10 mm and planar ($h = 0$ mm). The water and PMMA had a measured longitudinal wave velocity of 1.497 ± 0.01 mm/ μ s and 2.670 ± 0.01 mm/ μ s at 21 °C, respectively, while the 2024-T6 Al alloy had a measured longitudinal wave velocity of 6.35

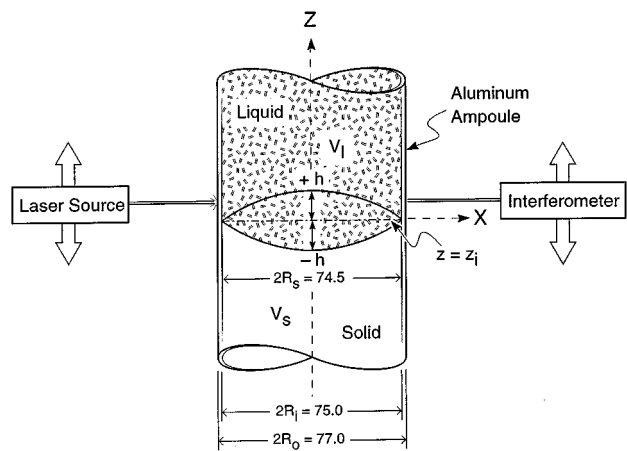


FIG. 2. A schematic of the H₂O/PMMA bench-top model showing the solid-liquid interface position (z_i), interfacial curvature (h), and the velocity fields of the liquid and solid phases (v_l, v_s) (all dimensions in mm).

± 0.01 mm/ μ s and a shear wave velocity of 3.01 ± 0.01 mm/ μ s at 21 °C. All experiments were conducted at 21 ± 2 °C.

B. Laser ultrasonic measurements

A laser ultrasonic sensing system (Fig. 3) was used to acquire TOF data between precisely positioned source and receiver points. The ultrasonic source was a ~ 10 -ns duration Q -switched Nd:YAG laser pulse of 1.064- μ m wavelength. The energy per pulse was 15 mJ and the roughly Gaussian beam of the multimode pulse was focused to an approximate circular spot 0.5 mm in diameter. Thus the resultant source power density was ~ 1500 MW/cm². A glass slide and propylene glycol couplant were used to enhance the acoustic signal strength.¹⁷

The ultrasonic receiver was a heterodyne laser interferometer. It responded to the sample's out-of-plane (normal) surface displacement associated with wavefront arrivals at the receiver point.¹⁸ It was powered by a 1-W single mode argon ion laser (operated at 0.25 W), which produced a continuous Gaussian beam of 514-nm wavelength focused to a circular spot ~ 100 μ m in diameter. The signal from the interferometer was bandpass filtered between 10 kHz and 10 MHz and recorded with a (LeCroy 7200) precision digital oscilloscope at a 2-ns sampling interval using 8-bit analog-to-digital conversion. To improve the signal to noise ratio, each waveform used for TOF measurement was the average of ~ 100 pulses collected at a pulse repetition rate of 20 Hz. A fast photodiode identified the origination time for the ultrasonic signals.

Two sets of computer controlled translation stages were positioned such that the ampoule could be translated along the axial z axis allowing the fixed receiver's position to be located at any point on the diametral plane. Thus the source could be independently translated to acquire a "fan-beam" ultrasonic TOF projection set. Multiple ultrasonic TOF projection scans were acquired for each interface in two sensing configurations. The first configuration positioned the receiver at four positions in the liquid ($z_r = 5, 10, 15$, and 20 mm

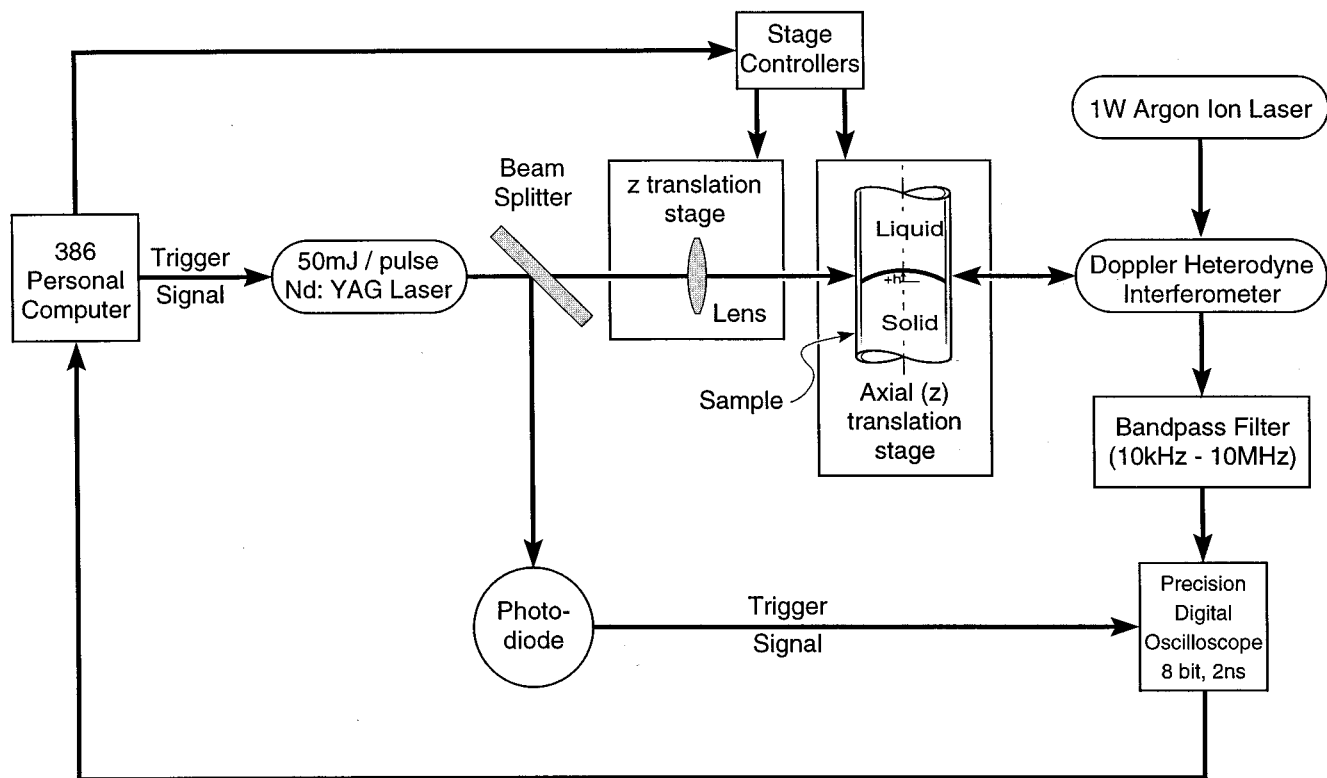


FIG. 3. A schematic of the laser ultrasonic test facility used to evaluate the sensor concepts.

above the outer edge of the interface, z_i). The second position the receiver at four positions in the solid phase ($z_r = -5, -10, -15$, and -20 mm). For each receiver positions, the ultrasonic source was scanned from the liquid phase ($z_s = 40$ mm) to the solid phase ($z_s = -20$ mm) at 1-mm increments to obtain a TOF projection set.

II. RAY PATH AND TIME-OF-FLIGHT ANALYSIS

It is assumed that infinitesimal omnidirectional ultrasonic point sources and receivers were positioned on opposite sides of the diametral plane. When an ultrasonic pulse is generated by the source, it was assumed to propagate in all directions in the diametral plane. One of the directions will usually result in a ray (which may or may not be refracted, depending on the source and receiver's position) whose path reaches the receiver point. Knowledge of this ray path is a necessary first step for understanding ultrasonic propagation through a solid-liquid interface, for predicting a ray's TOF, and, ultimately, for reconstructing the interface location and curvature from TOF projection data.

If the coordinates of the source (x_s, z_s) and receiver (x_r, z_r) points on the diametral plane are prescribed, then determining the ray path between these two points constitutes a boundary-value problem. The solutions of boundary-value problems like this are usually preceded by solutions of initial value problems²⁰ in which initial ray angles at the source point are prescribed and the ray paths are obtained by solving for the refraction angles at the interface. After obtaining the ray paths for an arbitrary set of initial ray angles emanating from the source point, the ray path between the prescribed source/receiver points can be obtained using the

shooting method.²¹ In this approach, an initial ray direction is first arbitrarily chosen, and the distance between the receiver point and the intersection of the ray path with the outer boundary calculated. This procedure is then repeated using a slightly different initial ray angle until the distance is smaller than a prescribed tolerance δ , $\sim 50 \mu\text{m}$. The ray path and wavefront analysis solved the initial value problem, while the boundary-value problems solution was used later for image reconstruction. A further complication arises because acoustic energy can only be transmitted across an interface when the refraction angle is less than $\pi/2$. This could sometimes lead to an incomplete projection data set (i.e., dark zone) with potentially deleterious consequences for some interface reconstruction techniques. It will be shown that this problem can be overcome using this fan beam approach.

The measured time-of-flight, τ_m , for a ray that propagates along a path of length, L_m , is defined by

$$\tau_m = \int_{L_m} \frac{dl}{v}, \quad m = 1, 2, \dots, M, \quad (1)$$

where dl is an infinitesimal element of the path, v is the local ultrasonic velocity ($1/v$ is the local slowness) within the object, and M is the number of different rays. When an ultrasonic ray is incident upon a solid-liquid interface, both reflected and refracted rays propagate on the diametral plane (defined by the incident propagation vector and the normal to the interface at the intersection of the incident ray with the interface).^{22,23} We arrange for the diametral cross-sectional plane on which ultrasonic rays propagate to coincide with the x - z plane in a Cartesian coordinate system (Fig. 2). It is

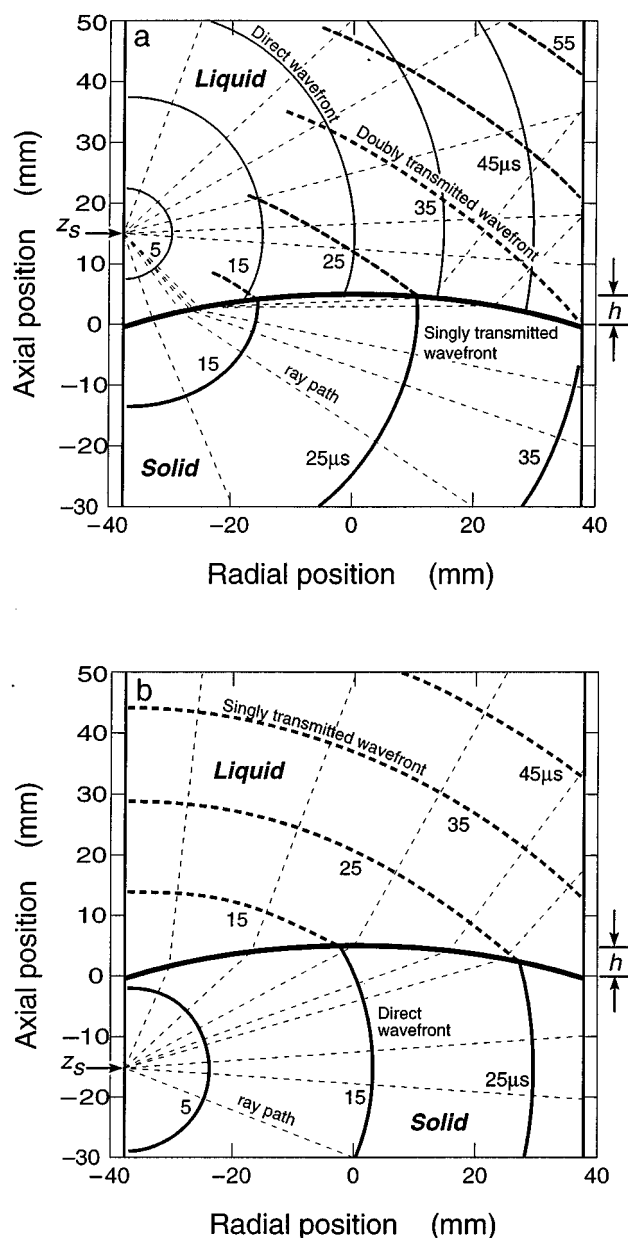


FIG. 4. Ray paths and wavefronts on the diametral plane of a convex interface ($h=5$ mm) for a source located in (a) the liquid ($z_s=15$ mm) and (b) the solid ($z_s=-15$ mm).

assumed that during crystal growth, the thermal gradients are small and axially symmetric resulting in relatively uniform velocities on both sides of the spherically shaped interface, simplifying the computation of τ_m . The detailed procedure for calculating ray paths is similar to that of Ref. 19 and is therefore omitted here.

A. Convex interfaces ($h>0$)

1. Ray paths and wavefronts

An example of the numerically simulated ray paths and wavefronts on the diametral plane for a convex interface ($h=5$ mm) are shown in Fig. 4(a) and (b) for source points located in either the liquid ($z_s=15$ mm) or the solid ($z_s=-15$ mm), respectively. For a source point located above the interface [Fig. 4(a)] ray paths in the liquid are straight

until refracted by the interface during propagation into the solid. Note that some of the rays are refracted at the first liquid–solid interface encountered and are then refracted again at the second solid–liquid interface (doubly transmitted rays). Others are only refracted at the first liquid–solid interface and are termed singly transmitted rays. Both doubly transmitted rays and rays with direct paths may reach the same boundary point. However, these different kinds of rays are experimentally distinguishable because the doubly transmitted rays have different travel times and are weaker because they suffered extra energy losses due to refraction and mode conversion at each interface. When the source was located below the interface [Fig. 4(b)], allowable ray paths are either straight (in the solid) or are refracted only once by the interface.

Wavefronts separate ultrasonically disturbed regions from those that are undisturbed. Thus the TOF of an ultrasonic signal can, in principle, be measured at any receiver point on the sample's periphery that is intersected by a wavefront. The wavefronts at any time after source excitation can be obtained by connecting points along the ray paths with the same travel time. The calculated quasi-longitudinal wavefronts at 10- μ s intervals are shown in Fig. 4(a) and (b). Ray paths and wavefronts for $h=2$ mm and $h=10$ mm interfaces are similar in nature and are not shown.

2. Time-of-flight projections

The most convenient manner in which to present the TOF data is in the form of ultrasonic TOF projections. The TOF projection data for convex interfaces ($h=2, 5$, and 10 mm) are shown in Fig. 5(a)–(d) for a receiver located above the interface at locations $z_r=5, 10, 15$, and 20 mm, respectively. In Fig. 5 the TOF of rays generated below the interface ($z_s<0$) corresponds to singly transmitted rays. When the source is located above the interface ($z_s>0$), two TOF arrivals corresponding to doubly transmitted and direct rays are shown. The experimental TOF projection data of Fig. 5 (the points) are seen to be in good agreement with the numerically simulated data predicted by the ray path model (the curves).

From direct observation of the TOF projection data (Fig. 5) the interface location (z_i) is identified by the transition of direct and doubly transmitted rays to singly transmitted rays at the interface edge ($z_i=0$). Also, the TOF of doubly transmitted rays coincides with that of the singly transmitted rays at $z_i=0$ for each interface convexity, and corresponds to the minimum time-of-flight in the projection data. The TOF projections of direct rays in the liquid are constant for all interface convexities at each receiver location. However, the TOF projections of singly and doubly transmitted rays are shifted to the left (i.e., to shorter TOFs) as the interface convexity h was increased. This can be intuitively explained. As the convexity is increased, the fraction of the total ray path length in the lower velocity liquid decreases, while the fraction in the higher velocity solid increases, resulting in an overall decrease in TOF. Also, it is interesting to note that as the receiver's position was translated further from the interface edge (i.e., as z_r goes from 5 to 10 to 15 to 20 mm) the overall TOF projection for each interface convexity shifts to in-

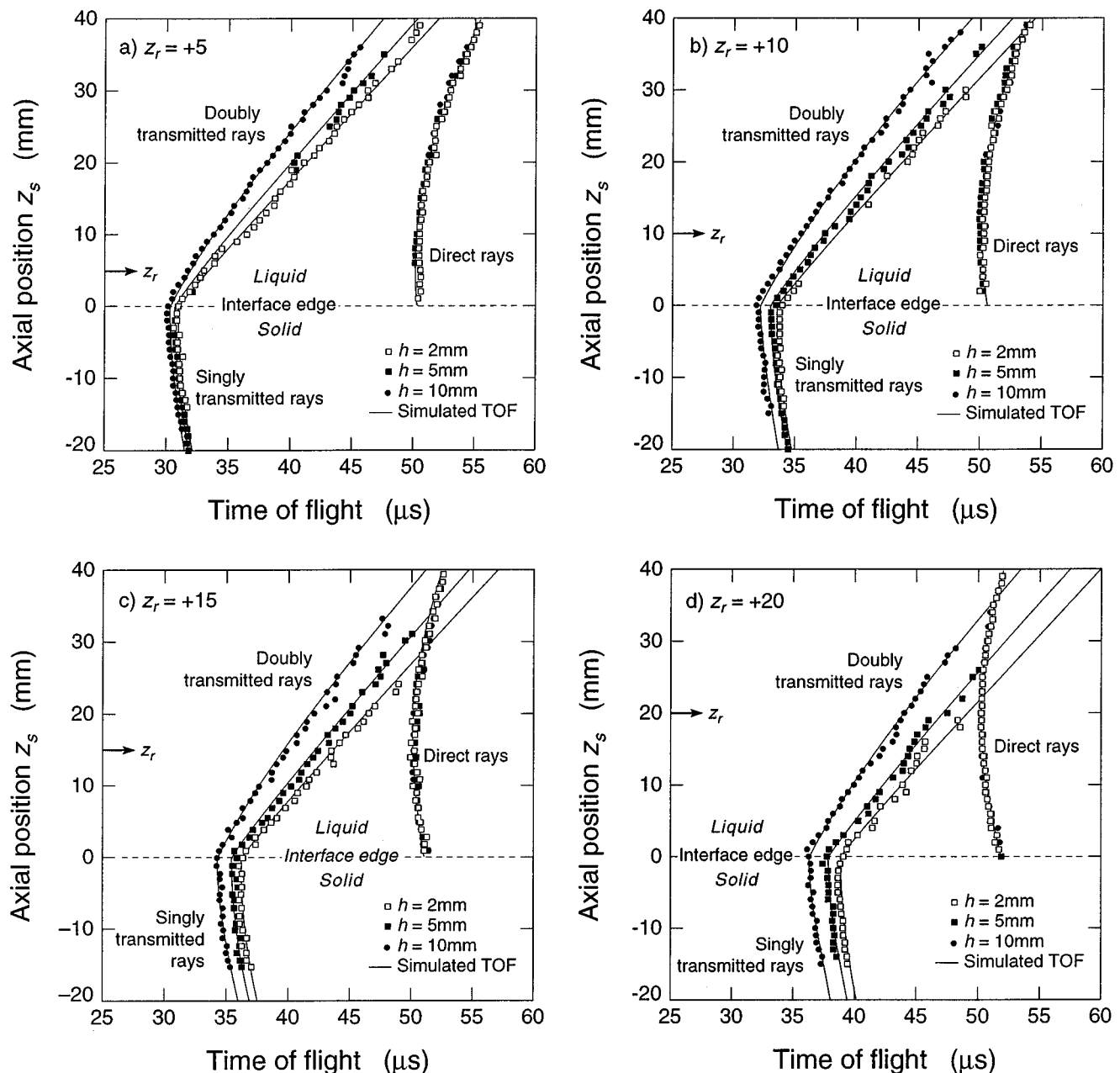


FIG. 5. Ultrasonic time-of-flight projection data of convex interfaces, $h=2$, 5, and 10 mm, for a receiver located in the liquid at axial positions (a) $z_r=5$ mm, (b) $z_r=10$ mm, (c) $z_r=15$ mm, and (d) $z_r=20$ mm.

creased TOF values and the relative time spacing between each interface ($h=2$, 5, and 10 mm) also increases.

The TOF projection data for convex interfaces ($h=2$, 5, and 10 mm) are shown in Fig. 6(a)–(d) for a receiver located below the interface at locations $z_r=-5$, -10 , -15 , and -20 mm, respectively. In Fig. 6 the TOF of rays generated below the interface ($z_s<0$) correspond to direct rays. When the source is located above the interface ($z_s>0$) only singly transmitted rays were observed. Again, the TOF projection data show good agreement between the experimentally determined TOFs and the numerically simulated data predicted by the model.

When the receiver is positioned below the interface (Fig. 6) the interface location is again identified by the transition of singly transmitted rays to direct rays at the interface

edge ($z_i=0$). The TOF of singly transmitted ray paths coincides with that of the direct ray paths at $z_i=0$ for all interface convexities. The TOF projections of direct rays are constant for all interface convexities at each receiver location. However, the TOF of direct rays has a minimum at z_r because the ray path length is the smallest. Similar to before, the TOF data projections of singly transmitted rays are shifted to shorter TOFs as the interface convexity was increased. Again, as the convexity increases the ray travels more in the solid and less in the liquid resulting in shorter TOFs. It is interesting to note that as the receiver's position was axially translated further from the interface (i.e., as z_r goes from -5 to -10 to -15 to -20 mm) the overall TOF increases for each interface convexity. However, this affect

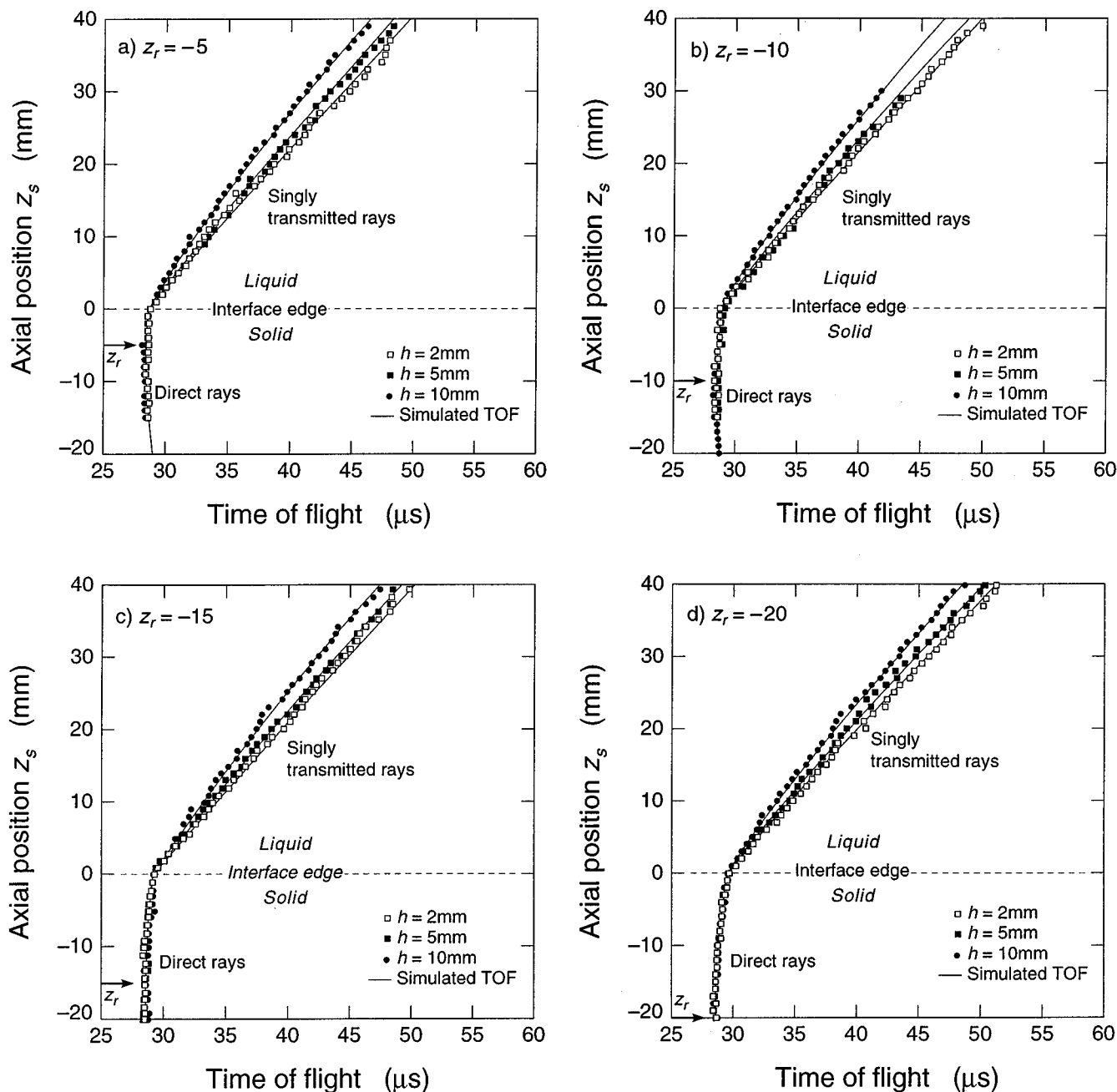


FIG. 6. Ultrasonic time-of-flight projection data of convex interfaces, $h=2, 5$, and 10 mm, for a receiver located in the solid at axial positions (a) $z_r = -5$ mm, (b) $z_r = -10$ mm, (c) $z_r = -15$ mm, and (d) $z_r = -20$ mm.

is not as pronounced when the receiver is located in the solid.

B. Concave interfaces ($h < 0$)

1. Ray paths and wavefronts

Numerically simulated ray paths and wavefronts on the diametral plane for a concave interface ($h = -5$ mm) are shown in Fig. 7(a) and (b) for a source located above the interface ($z_s = 20$ mm) and below the interface ($z_s = -20$ mm), respectively. In Fig. 7(a) ray paths in the liquid are straight, whereas they are bent by the interface during propagation into the solid. Notice that none of the rays are doubly transmitted; they can only be refracted once at the

liquid–solid interface (singly transmitted rays). However, due to the divergent nature of the concave interface, there may be a region of nonpropagation (i.e., dark zone) in which the wavefront does not intersect the outer boundary. The first dark zone on the left ($x < 0$) is due to ray bending caused by the interface, while no rays travel through the second dark zone ($x > 0$) because the refraction angle in the solid is greater than $\pi/2$. It is interesting to note that the second dark zone increases in size as the convexity of the interface becomes increasingly negative (from $h = -5$ mm to $h = -10$ mm) and/or when the source point was translated toward the interface (i.e., as z_s goes from 20 to 15 to 10 to 5 mm). In Fig. 7(b) ray paths are straight (in the solid) or are

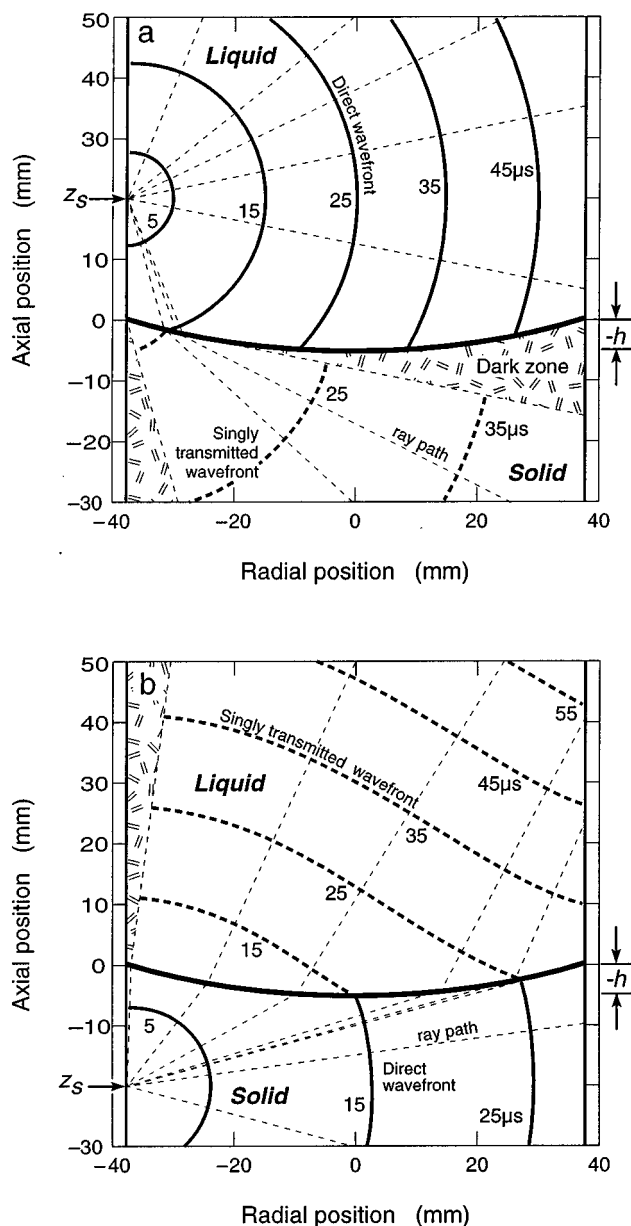


FIG. 7. Ray paths and wavefronts on the diametral plane of a concave interface ($h = -5$ mm) for a source located in (a) the liquid ($z_s = 20$ mm) and (b) the solid ($z_s = -20$ mm).

refracted once by the interface. Again, the first dark zone on the left ($x < 0$) is due to ray bending caused by the interface. No second dark zone ($x > 0$) was observed for the $h = -5$ mm interface. As before, when the convexity was increased negatively (from $h = -5$ mm to $h = -10$ mm) and/or as the source point approached the solid-liquid interface, another dark zone in the liquid ($x > 0$) near the interface edge ($z_i = 0$) was observed. The calculated quasi-longitudinal wavefronts at $10\text{-}\mu\text{s}$ intervals are also shown in Fig. 7(a) and (b). Ray paths and wavefronts for the $h = -2$ mm and $h = -10$ mm interfaces were similar in nature (except for the magnitude of the dark zones) and are not shown here.

2. Time-of-flight projections

The ultrasonic TOF projections for concave ($h = -2$ and -5 mm) interfaces are shown in Fig. 8(a)–(d) for a receiver

located above the interface ($z_r = 5, 10, 15$, and 20 mm), respectively. In Fig. 8 the TOF of rays generated below the interface ($z_s < 0$) corresponds to singly transmitted rays. When the source was located above the interface ($z_s > 0$) only direct rays were observed. The TOF projections for $h = -10$ mm are not shown because the magnitude of the dark zone extended beyond that of the scanned region (i.e., the singly transmitted wavefronts did not intersect the outer boundary in the scanned region, $40\text{ mm} > z_s > -20$ mm). Both TOF projection sets show good agreement between the experimentally determined TOFs and the numerically simulated data predicted by the ray path models.

With the receiver located above the interface (Fig. 8) the interface location may be deduced by the presence of a dark zone just below the interface or by the absence of direct rays below the interface. The TOF projects of direct rays in the liquid are constant for both interface convexities and vary accordingly with the receiver's position. However, the TOF projection of singly transmitted rays is shifted to the right (i.e., longer TOFs) as the interface convexity h was increased. As the negative convexity was increased, the fraction of the total path length of the ray in the lower velocity liquid increased, and the fraction in the higher velocity solid decreased resulting in an overall increase in TOF. Again, it is interesting to note that as the receiver's position was translated further from the interface edge (as z_r goes from 5 to 10 to 15 to 20 mm), the overall TOFs of singly transmitted rays for each interface convexity shifts to increased TOF values. The magnitude of the dark zone increased with increasing convexity (as h goes from -2 to -5 to -10 mm) and the magnitude for each individual interface decreased as the receiver's position was translated further from the interface edge. It also appears that the rate of change in dark zone magnitude with respect to the receiver's position is dependent on the interface convexity.

The ultrasonic TOF projections for concave ($h = -2$ and -5 mm) interfaces are shown in Fig. 9(a)–(d) for a receiver located below the interface ($z_r = -5, -10, -15$, and -20 mm), respectively. In Fig. 9 the TOF of rays generated below the interface ($z_s < 0$) corresponds to direct rays. When the source was located above the interface ($z_s > 0$), only singly transmitted rays were observed. The TOF projection data for the $h = -10$ mm interface convexity are not shown because the dark zone extended beyond that of the scanned region. Both TOF projection sets show good agreement between the experimentally determined TOFs and the numerically simulated data predicted by the ray path models.

When the receiver was located below the interface (Fig. 9) the interface location is identified by the presence of a dark zone just above the interface or by the absence of direct rays above the interface edge ($z_i = 0$). The TOFs for direct rays in the solid are constant for both interface convexities and shift accordingly with the receiver's position. When no dark zone was observed, the TOF of singly transmitted rays coincided with that of direct ray paths at $z_i = 0$ for the interfaces. Again, the TOF data projections of singly transmitted rays are shifted to longer TOFs as the interface convexity h was increased negatively and/or as the receiver's position was translated further from the interface edge. In addition,

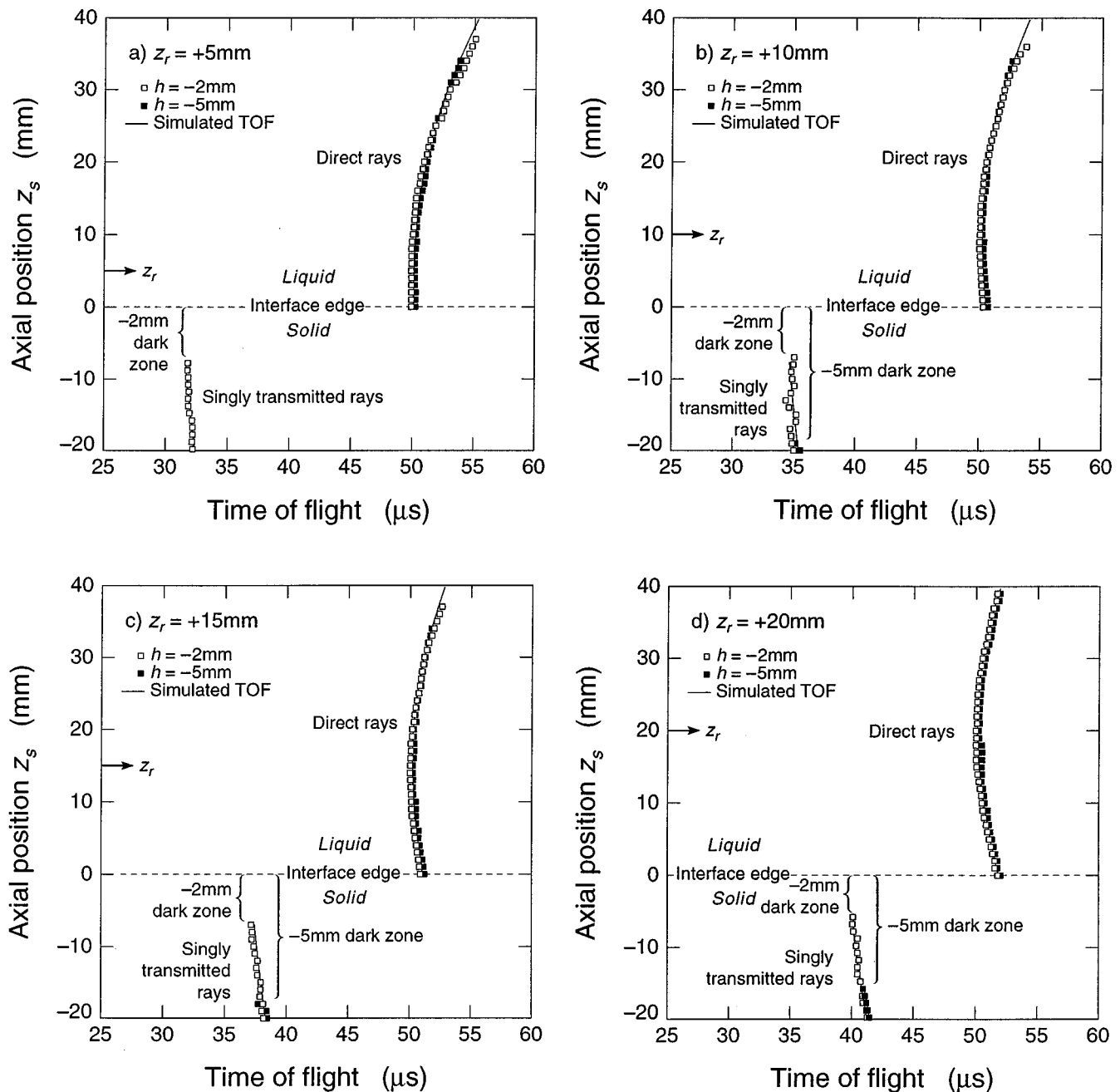


FIG. 8. Ultrasonic time-of-flight projection data of concave interfaces, $h = -2$ and -5 mm, for a receiver located in the liquid at axial positions (a) $z_r = 5$ mm, (b) $z_r = 10$ mm, (c) $z_r = 15$ mm, and (d) $z_r = 20$ mm.

the overall magnitude of the dark zone increased with increasing convexity (as h goes from -2 to -5 to -10 mm) and the magnitude of each individual interface decreased as the receiver's position was translated further from the interface edge.

C. Discussion

An inspection of the ultrasonic TOF projection data reveals that both the magnitude and form of TOF curves are unique for different sensing configurations and interface curvatures. The TOF projection data reveal when a solid-liquid interface exists either by a transition in propagation modes (i.e., doubly transmitted rays to singly transmitted rays or

singly transmitted rays to direct rays) or the observance of dark zones at the interface edge ($z_i = 0$). Determining whether the interface was above or below the receiver point can be done by inspecting the TOF curves. For either convex or concave interfaces, the TOF curves for direct rays will be symmetric about the receiver point and much larger when the receiver is positioned in the slower velocity liquid. Also, if we compare convex and concave interfaces, we find that for a convex interface the TOF of transmitted rays (both singly and doubly) increases with decreasing interface convexity, while for a concave interface the TOF of singly transmitted rays decreases with decreasing interface convexity.

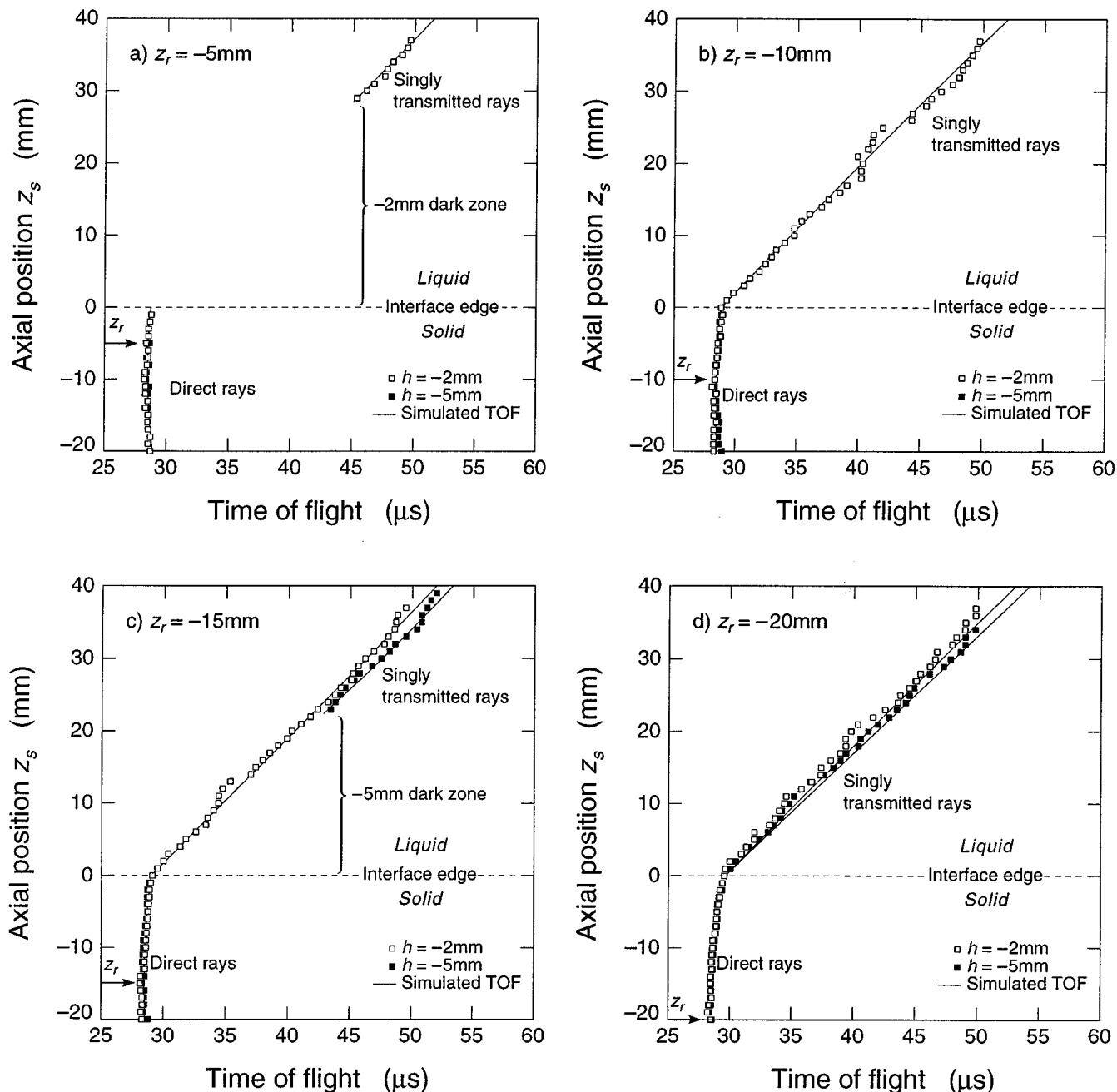


FIG. 9. Ultrasonic time-of-flight projection data of concave interfaces, $h = -2$ and -5 mm, for a receiver located in the solid at axial positions (a) $z_r = -5$ mm, (b) $z_r = -10$ mm, (c) $z_r = -15$ mm, and (d) $z_r = -20$ mm.

III. INTERFACE CURVATURE RECONSTRUCTIONS

A reconstruction method is needed to quantitatively determine the interface location, the interfacial curvature, and velocity fields. There are a variety of techniques available for reconstructing an object image from ultrasonic TOF projection data, including nonlinear least-squares fitting, algebraic reconstruction techniques (ART), and convolution backprojection (CB) methods.^{24,25} Convolution backprojection methods have not been applied to situations where ray bending is significant, and although algebraic reconstruction techniques are beginning to incorporate ray bending,²⁶ both of these procedures require large data sets which are difficult to obtain in the crystal growth environment. Reconstruction ap-

proaches that can be used with limited data and exploit the often significant *a priori* information available are preferable. The crystal grower requires the axial location (z_i) of the interface (its change with time gives the solidification velocity) and its approximate curvature (h). The liquid and solid velocities (v_l, v_s) are also useful since they are related to the local temperature and the crystals crystallographic orientation. In previous work, we used a nonlinear least-squares reconstruction approach and determined that it often provides sufficiently accurate results from relatively limited data sets in minimal computational time.

We assume an interface model of the type shown in Fig. 2, but where h , z_i , v_l , and v_s are all unknown. For the ray

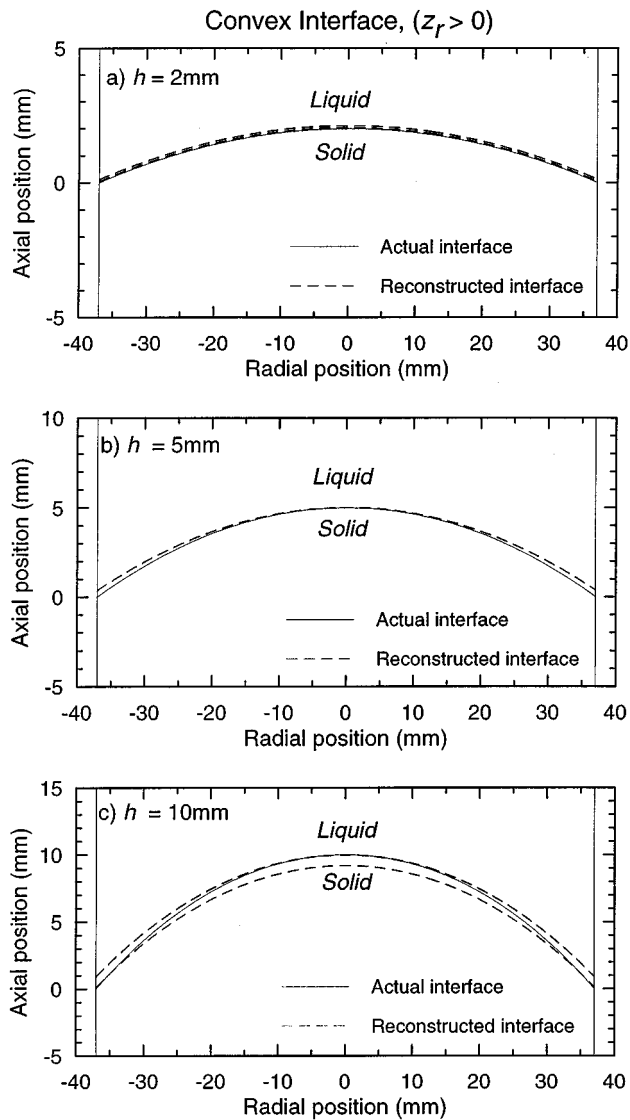


FIG. 10. Nonlinear least-squares interface reconstructions of convex interfaces for all receiver locations above the interface with interface convexities of (a) $h = 2$ mm, (b) $h = 5$ mm, and (c) $h = 10$ mm.

path models, the TOF depends nonlinearly on the interface convexity (h), interface location (z_i), liquid (ν_l), and solid (ν_s) velocities, and the mean-square error given by

$$\chi^2 = \sum_{i=1}^M [\tau_i - \hat{\tau}_i(x_i; h, z_i, \nu_l, \nu_s)]^2, \quad (2)$$

where τ_i are the measured TOFs and $\hat{\tau}_i$ are the numerically simulated TOFs for an initial estimate of the interface parameters. To reconstruct the model unknowns from the ultrasonic TOF projection data, a Levenberg–Marquardt nonlinear least-squares reconstruction method was used.²⁷ The nonlinear least-squares method determines the best-fit parameters (h, z_i, ν_l, ν_s) by minimizing χ^2 .

Using data (~ 30 – 50 rays) for convex interfaces, the reconstructed interface locations and curvatures when the receiver was above the interface are shown in Fig. 10(a)–(c) for $h = 2, 5$, and 10 mm, respectively. The reconstructed parameters obtained when the receiver was below the interface

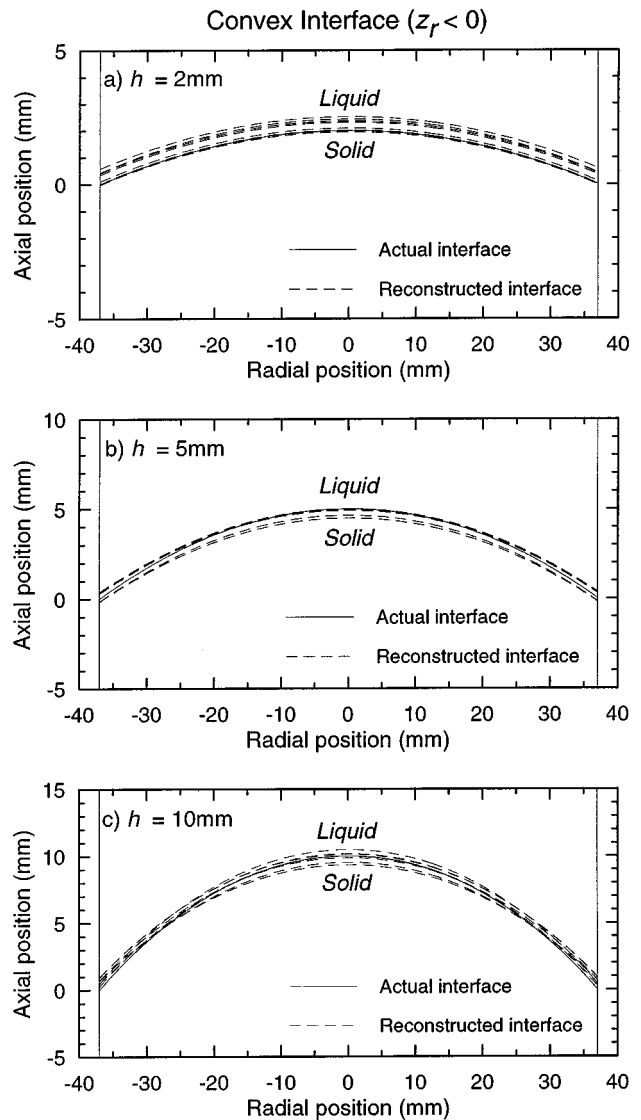


FIG. 11. Nonlinear least-squares interface reconstructions of convex interfaces for all receiver locations below the interface with interface convexities of (a) $h = 2$ mm, (b) $h = 5$ mm, and (c) $h = 10$ mm.

are shown in Fig. 11(a)–(c). Both Figs. 10 and 11 represent eight individual reconstructions each, where some of the reconstructions overlap each other. It is clear that the reconstructed interface locations and curvatures coincide well with those of the actual interfaces. For the reconstructed velocities, the mean liquid velocity was $\nu_l = 1.487$ ($\sigma = 0.040$) and the mean solid velocity was $\nu_s = 2.677$ ($\sigma = 0.037$).

Using concave interface data (~ 10 – 55 rays) the reconstructed interface locations and curvatures when the receiver was above the interface are shown in Fig. 12(a) and (b) for $h = -2$ and -5 mm, respectively. The reconstructed parameters obtained when the receiver was below the interface are shown in Fig. 13(a) and (b). Again, Figs. 12 and 13 represent multiple reconstructions with some overlap in the reconstructed surfaces. The reconstructed interface locations and curvatures coincide well with those of the actual interfaces. For the reconstructed velocities, the mean liquid velocity was $\nu_l = 1.493$ ($\sigma = 0.006$) and the mean solid velocity was $\nu_s = 2.713$ ($\sigma = 0.037$).

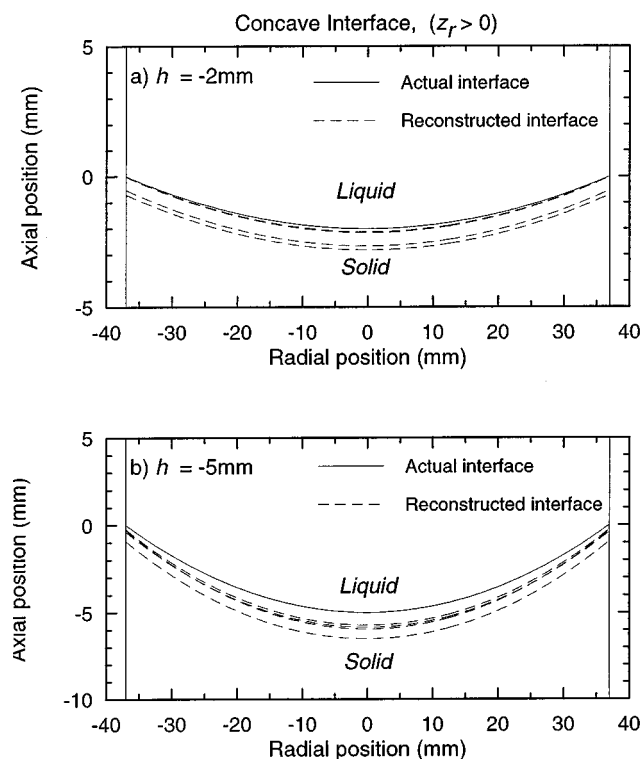


FIG. 12. Nonlinear least-squares interface reconstructions of concave interfaces for all receiver locations above the interface with interface convexities of (a) $h = -2$ mm and (b) $h = -5$ mm.

The reconstructed interface parameters and velocities for all the models (convex and concave) are precisely recovered and the nonlinear least-squares reconstruction algorithm represents a robust approach for interface reconstructions using ultrasonic TOF projection data. Using the boundary-value solutions with free parameters (h , z_i , v_l , v_s) the reconstruction algorithm converged upon the correct interface model (convex or concave), and thus recovered the interface geometry (i.e., solid-liquid interface location, curvature) and velocity fields for all interface convexities from laser ultrasonic TOF projection data collected in the diametral plane.

IV. CONCLUSIONS

An extension of a previously developed laser ultrasonic sensor methodology for sensing the solid-liquid interface location and curvature similar to those encountered during vertical Bridgman growth of CdTe alloys and other semiconducting materials has been conducted. A combination of ray tracing, wavefront, and TOF analysis and experimental testing on model cylindrical solid-liquid interfaces with a laser ultrasonic system was used to improve sensing concepts to determine a solid-liquid interface's location, curvature, and velocity fields from ultrasonic TOF projection data collected in the diametral plane. Because convex and concave solid-liquid interfaces resulted in uniquely different TOF data profiles, the interface shape (convex or concave) was readily determined from the TOF data. When TOF data (~ 10 – 60 rays) collected in the diametral plane was used in conjunction with a nonlinear least-squares reconstruction algorithm,

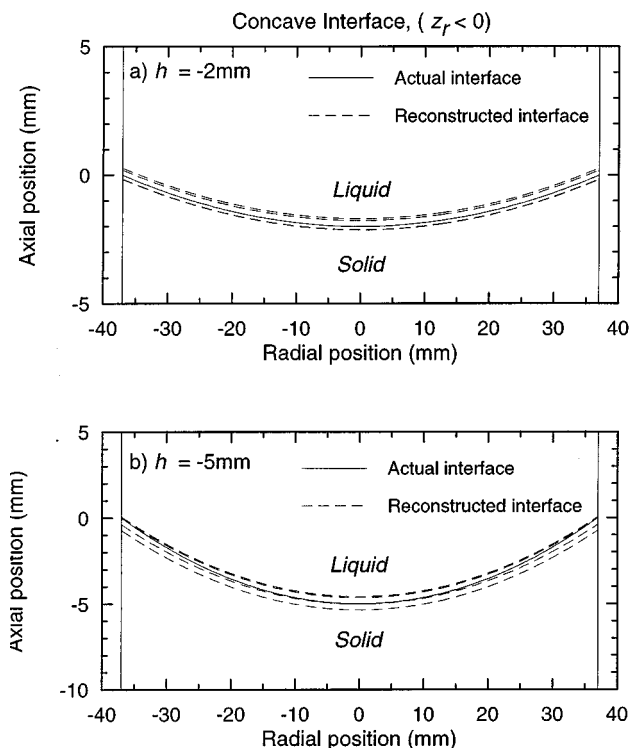


FIG. 13. Nonlinear least-squares interface reconstructions of concave interfaces for all receiver locations below the interface with interface convexities of (a) $h = -2$ mm and (b) $h = -5$ mm.

the interface geometry (i.e., location and curvature) has been successfully reconstructed and the ultrasonic velocities of both solid and liquid obtained. The development and integration of this sensing methodology into semiconducting material growth promises to significantly advance process understanding and design.

ACKNOWLEDGMENTS

We are grateful to Brent Bollong and Art Sochia of Johnson Matthey Electronics for helpful discussions concerning crystal growth. This work has been performed as part of the Infrared Materials Producibility Program (IRMP) managed by Duane Fletcher (JME) that includes Johnson Matthey Electronics, Texas Instruments, II-VI Inc., Loral, the University of Minnesota and the University of Virginia. We are grateful for the many helpful discussions with our colleagues in these organizations. The IRMP consortium work, and our work within it, has been supported by ARPA/CMO under Contract No. MD A972-91-C-0046 monitored by Raymond Balcerak.

¹ *Handbook of Crystal Growth*, Vols. I and II, edited by D. T. Hurler (North Holland, New York, 1993).

² T. Fu and W. R. Wilcox, "Influence of insulation on stability of interface shape and position in the vertical Bridgman-Stockbarger technique," *J. Cryst. Growth* **48**, 416–424 (1980).

³ M. Pfeiffer and M. Muhlberg, "Interface shape observation and calculation in crystal growth of CdTe by the vertical Bridgman method," *J. Cryst. Growth* **118**, 269–276 (1992).

⁴ P. Rudolf and M. Muhlberg, "Basic problems of vertical Bridgman growth of CdTe," *Mater. Sci. Eng. B* **16**, 8–16 (1993).

⁵ S. Sen, W. H. Konkel, S. J. Tighe, L. G. Bland, S. R. Sharma, and R. E. Taylor, "Crystal growth of large-area single-crystal CdTe and CdZnTe by

- the computer-controlled vertical modified-Bridgman process," J. Cryst. Growth **86**, 111–117 (1988).
- ⁶M. Azoulay, S. Rotter, G. Gafni, and M. Roth, "The crystalline quality distribution in CdZnTe single crystal correlated to the interface shape during growth," J. Cryst. Growth **116**, 515–517 (1992).
- ⁷S. Brandon and J. J. Derby, "Internal radiative transport in the vertical Bridgman growth of semitransparent crystals," J. Cryst. Growth **110**, 481–500 (1991).
- ⁸S. Kuppurao, J. J. Derby, and S. Brandon, "Modeling the vertical Bridgman growth of cadmium zinc telluride. I. Quasi-steady analysis of heat-transfer and convection," J. Cryst. Growth **155**, 93–102 (1995).
- ⁹S. Kuppurao, J. J. Derby, and S. Brandon, "Modeling the vertical Bridgman growth of cadmium zinc telluride. II. Transient analysis of zinc segregation," J. Cryst. Growth **155**, 103–111 (1995).
- ¹⁰M. Saitou and A. Hirata, "Ratio of liquid to solid thermal conductivity calculated from the solid–liquid interface shape," J. Cryst. Growth **118**, 365–370 (1992).
- ¹¹R. L. Parker and J. R. Manning, "Application of pulse-echo ultrasonics to locate the solid/liquid interface during solidification and melting," J. Cryst. Growth **79**, 341–353 (1986).
- ¹²C. K. Jen, Ph. de Heering, P. Sutcliffe, and J. F. Bussiere, "Ultrasonic monitoring of the molten zone of single crystal germanium," Mater. Eval. **49**, 701–707 (1991).
- ¹³J. N. Carter, A. Lam, and D. M. Schleich, "Ultrasonic time-of-flight monitoring of the position of the liquid–solid interface during the Bridgman growth of germanium," Rev. Sci. Instrum. **63**, 3472–3476 (1992).
- ¹⁴F. A. Mauer, S. J. Norton, Y. Grinberg, and H. N. G. Wadley, "An ultrasonic method for reconstructing the two dimensional liquid–solid interface during solidifying bodies," Metall. Trans. B **22**, 467–473 (1991).
- ¹⁵S. J. Norton, A. H. Kahn, F. A. Mauer, and H. N. G. Wadley, "Inverse problems in the sensing of materials processing," in *Proceedings of the Symposium on Intelligent Processing of Materials*, edited by H. N. G. Wadley and W. E. Eckart (TMS, Warrendale, 1990), pp. 275–291.
- ¹⁶Y. Lu and H. N. G. Wadley, "Two-dimensional wave propagation in cylindrical single-crystal solid–liquid bodies," J. Acoust. Soc. Am. **98**, 2663–2680 (1995).
- ¹⁷C. B. Scruby and L. E. Drain, *Laser Ultrasonics: Techniques and Applications* (Adam Hilger, New York, 1990).
- ¹⁸J. P. Monchalán, "Optical detection of ultrasound," IEEE Trans. Ultrason. Ferroelectr. Freq. Control **UFFC-33**, 485–499 (1986).
- ¹⁹D. T. Queheillalt, Y. Lu, and H. N. G. Wadley, "Laser ultrasonic studies of solid–liquid interfaces," J. Acoust. Soc. Am. **101**, 843–853 (1997).
- ²⁰H. B. Keller, *Numerical Methods for Two-Point Boundary Value Problems* (Blaisdell, Waltham, MA, 1969).
- ²¹G. E. Forsythe, M. A. Malcolm, and C. B. Moler, *Computer Methods for Mathematical Computations* (Prentice-Hall, Englewood Cliffs, NJ, 1977).
- ²²F. I. Fedorov, *Theory of Elastic Waves* (Plenum, New York, 1968).
- ²³M. J. P. Musgrave, *Crystal Acoustics* (Holden-Day, San Francisco, 1970).
- ²⁴Special Issue on Physical and Computational Aspects of 3-Dimensional Image Reconstruction, IEEE Trans. Nucl. Sci. **NS-21** (1974).
- ²⁵J. F. Greenleaf, S. A. Johnson, S. A. Samayoa, and F. A. Duck, "Algebraic reconstruction of spatial distributions of acoustic absorption within tissue from their two dimensional acoustic projections," Acoust. Holography **5**, 591–603 (1974).
- ²⁶H. N. G. Wadley and G. M. Prabhakar (in preparation).
- ²⁷W. H. Press, B. P. Flannery, S. A. Teukolsky, and W. T. Vetterling, *Numerical Recipes: The Art of Scientific Computing (Fortran)* (Cambridge University, New York, 1990).

A modeling technique for active control design studies with application to spacecraft microvibrations

G. S. Aglietti, S. B. Gabriel, and R. S. Langley

Department of Aeronautics and Astronautics, University of Southampton, Southampton SO17 1BJ, England

E. Rogers

Department of Electronics and Computer Science, University of Southampton, Southampton SO17 1BJ, England

(Received 26 August 1996; revised 15 May 1997; accepted 25 June 1997)

Microvibrations, at frequencies between 1 and 1000 Hz, generated by on board equipment, can propagate throughout a spacecraft structure and affect the performance of sensitive payloads. To investigate strategies to reduce these dynamic disturbances by means of active control systems, realistic yet simple structural models are necessary to represent the dynamics of the electromechanical system. In this paper a modeling technique which meets this requirement is presented, and the resulting mathematical model is used to develop some initial results on active control strategies. Attention is focused on a mass loaded panel subjected to point excitation sources, the objective being to minimize the displacement at an arbitrary output location. Piezoelectric patches acting as sensors and actuators are employed. The equations of motion are derived by using Lagrange's equation with vibration mode shapes as the Ritz functions. The number of sensors/actuators and their location is variable. The set of equations obtained is then transformed into state variables and some initial controller design studies are undertaken. These are based on standard linear systems optimal control theory where the resulting controller is implemented by a state observer. It is demonstrated that the proposed modeling technique is a feasible realistic basis for in-depth controller design/evaluation studies. © 1997 Acoustical Society of America. [S0001-4966(97)02510-1]

PACS numbers: 43.40.Dx, 43.40.Vn [CBB]

INTRODUCTION

Spacecraft microvibrations are defined as very low amplitude disturbances which can occur at any frequency between say 1 and 1000 Hz. Despite the low amplitude of these disturbances they can significantly degrade the performance of sensitive instruments, and there has been a growing interest^{1,2} in the application of both active and passive control techniques to this problem.

These vibrations are produced by the functioning of on board equipment (sources) such as reaction wheels, gyroscopes, thrusters, electric motors, pumps, switches, and all types of mechanisms, and they propagate through the satellite structure (Fig. 1) towards sensitive equipment (receivers) jeopardizing their correct functioning.³

Stability requirements are particularly demanding for microgravity experiments and accurately targeted optical instruments. Among the latter are mirror pointing systems such as those of space telescopes⁴ where small mechanical disturbances produce jitter that causes the blurring of images, and interferometers,⁵ where the optical path difference has to be controlled with an accuracy of nanometers. It is therefore necessary to control the effect of mechanical disturbances on the structure which supports the optical elements. In other equipment such as laser communication systems⁶ the vibrations induce oscillations of the beam that cause problems at the receiving station. Many suspension systems for isolating microgravity experiments have been designed and tested and a great deal of literature is available.⁷

As far as vibration suppression is concerned, a well-established hierarchy of procedures is followed during the development phase of a project. First there is the minimization of the dynamic disturbance along with the isolation of the source. Then, if practical, the isolation of the receiver and eventually modifications in the location of the equipment in order to decrease the source-receiver coupling. If necessary, some elements along the vibration path, such as structural junctions, can be modified in order to filter the transmission at particular frequencies; or stiffeners can be redesigned to reduce the source-receiver coupling. During all the phases of the development, passive damping technology is typically employed to reduce the level of dynamic disturbance, and active control systems are only considered as the last resort to achieve the required performance. It has, however, been demonstrated that for extremely challenging vibration suppression requirements, such as those for satellite based instruments, the only reliable approach is through an integration of passive and active control systems.

The application of active control techniques to microvibrations problems and, in particular, feedback based schemes, requires the availability of simple yet realistic structural models to investigate and compare the performance of possible control schemes. These models ought to include only the bare essentials in their representation of the physical system, meaning that they should include all the necessary elements to produce a realistic simulation of the dynamics of the system, without including excessive structural detail. These conflicting requirements, simplicity and

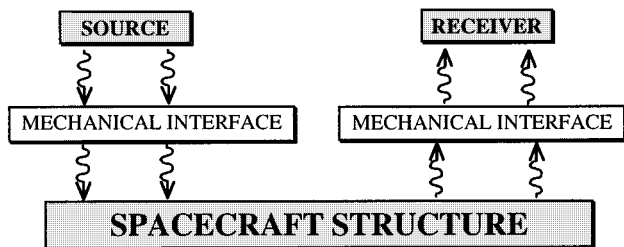


FIG. 1. Microvibration propagation path.

realism, are merged in the modeling technique which is presented in this paper.

The proposed methodology offers an alternative to the finite element method⁸ (FEM), which is perhaps the most common dynamic analysis technique employed in aerospace engineering. The accuracy of the FEM, which is generally very good at low frequencies (say, around a few hundred Hz), decreases as the frequency increases above the first natural frequency of the structure. This problem can be partially overcome by refining the mesh, although this produces large models which are computationally expensive and not particularly suited to active control system design studies.

To put the present approach into context, it is useful to briefly review a number of other modeling techniques which have been employed in place of the FEM for active control studies. In general terms it is possible to classify these techniques into three groups: elastic wave studies, energetic or variational methods, and mechanical impedance based techniques.

Most previous work based on the study of elastic wave propagation has considered one-dimensional structures, such as beams, with feedforward controllers implemented as adaptive filters.^{9–11} The control strategy is usually to cancel or minimize the displacement, or another output such as the velocity, at a certain location by forcing an opposite wave pattern into the structure. However, the use of feedforward controllers assumes a certain knowledge of the input disturbance, which might not be available, and which is not required by feedback controllers such as those proposed here. As far as the structural modeling technique is concerned, the elastic wave approach, which is probably the most appropriate for one-dimensional propagation cases, is not particularly suited to multidimensional structures, such as panels, due to the difficulties in the mathematical modeling.

With regard to energetic methods, such as the one proposed here, Hagood *et al.*¹² present a dynamic model of a beam, with piezoelectric patches, which is derived through the application of Hamilton's principle. Also included in the mathematical model are the dynamics of the passive electric circuit used to "shunt" the piezoelectric material. Also relevant is the work of Tzou^{13,14} who uses Hamilton's principle and the Kirchhoff–Love thin shell assumptions to derive the equations describing the dynamics of a shell with distributed piezoelectric sensors and actuators. In addition, Banks *et al.*¹⁵ have used a variational approach to study in detail the interaction between a structural component and an attached piezoelectric patch. The basic principles outlined in Refs.

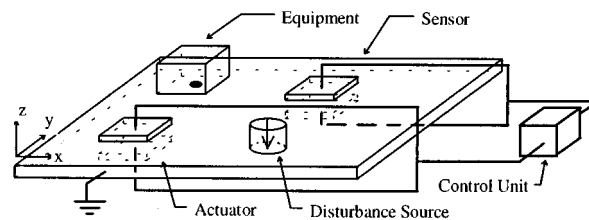


FIG. 2. Model layout.

12–15 are incorporated within the present study.

Mechanical impedance based methods have generally been used to model the effect of piezoelectric actuators on shell-like structures.^{16,17} The interaction between the actuator and the structure is determined by applying equilibrium and compatibility relations at the edges of the patches, so that the actuator's presence is imposed on the underlying structure by a set of line moments/forces acting along the edges of the patch. In contrast, full bonding of the patch is considered in the present modeling approach, so that the compatibility and equilibrium conditions are applied throughout the whole patch/structure surface, which more truly models the case of an ideal adhesive layer.

The modeling technique which is presented in this paper provides an alternative to the methodologies described thus far. Based on the use of the Lagrange–Rayleigh–Ritz procedure, a very compact mathematical model of an electromechanical system composed of a mass loaded panel with piezoelectric patches acting as sensors and actuators is produced. The results of the simulations are verified against a finite element model, and the advantages of accuracy and simplicity previously mentioned are discussed in further detail.

The work has led to some basic results on the use of the proposed model in the design and evaluation of active feedback control strategies. In particular, it is written in standard linear systems state space form and this representation is then used as a basis for controller design based on linear optimal control theory, where the resulting controller is implemented using a state observer. These studies demonstrate that the modeling technique developed here is a valuable addition to the currently available techniques for microvibration based modeling, analysis, and control studies.

I. SYSTEM DESCRIPTION

Equipment on board satellites is very often mounted on light weight panels. This study considers one such mass loaded panel, sketched in Fig. 2, with an active control system applied to minimize the displacements at a certain location. The equipment mounted on the panel is modeled as a set of lumped masses, and the input disturbance as a set of point forces. Sensors and actuators for the active control system are twin patches of piezoelectric material bonded onto the opposite faces of the panel.

The bending vibrations of the panel produce a stretching and shrinking of the patches depending on whether they are on the top or on the bottom of the panel [Fig. 3(a)]. Due to

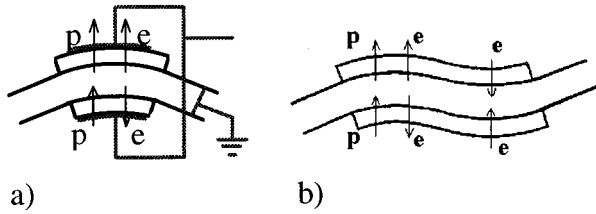


FIG. 3. Patch section view during deformation. (a) Deformation wavelength longer than patch. (b) Deformation wavelength equal or shorter than patch.

the piezoelectric effect, these deformations induce an electric field perpendicular to the panel which is detected by the electrodes.

The outer electrodes of the patches are electrically connected together and the panel, which is grounded, is used as the other electrode for both patches of the pair [Fig. 3(a)]. The same configuration applies to the actuator, but here the electric field is applied externally to produce the contraction or expansion of the patch, which will then produce a curvature of the panel. Note that the effectiveness of the piezoelectric elements, both sensors and actuators, decreases when the wavelength of the deformation becomes smaller than the patch. This is because the signal produced is partially or completely [as in Fig. 3(b)] cancelled by the opposite field generated by the other part of the patch which undergoes an opposite kind of deformation. This limiting factor needs to be considered when attempting to control high frequency vibrations which of course have very short wavelengths. This limit might be raised by decreasing the patch dimensions, but this diminishes the control authority at low frequencies.

To implement the final control scheme, the signal generated by the sensor is fed to the control unit which commands the actuator.

II. MATHEMATICAL MODEL

A. Lagrange's equations

The dynamics of the system is described by Lagrange's equations of motion which take the form

$$\frac{d}{dt} \left(\frac{\partial T}{\partial \dot{q}_i} \right) - \frac{\partial T}{\partial q_i} + \frac{\partial U}{\partial q_i} = Q_i, \quad (1)$$

where T and U are the kinetic and potential energies of the system, and q_i and Q_i are, respectively, the i th generalized coordinate and generalized force. The kinetic energy and potential energy (elastic and electric) are written in the form

$$T = T_{pl} + T_{lm} + T_{pz}, \quad U = U_{pl} + U_{pz}, \quad (2)$$

where T_{pl} , T_{lm} , and T_{pz} are, respectively, the kinetic energy of the panel, lumped masses, and piezoelectric patches, and U_{pl} and U_{pz} are the potential energies stored in the panel and in the piezoelectric patches.

The displacement field (out-of-plane displacement w) is described as a superposition of shape functions $S_{m,n}$ (consisting of the modes of the bare panel), multiplied by the time dependent modal coordinates $\phi_{m,n}$

$$w(x, y, t) = \sum_{m=1}^{N_m} \sum_{n=1}^{N_n} S_{m,n}(x, y) \phi_{m,n}(t) = \mathbf{s}^t \boldsymbol{\phi}, \quad (3)$$

where \mathbf{s} is the vector of the shape functions and $\boldsymbol{\phi}$ is the vector of the modal coordinates. Since the effectiveness of the piezoelectric patches decreases when the wavelength of the deformations to be controlled is equal to or smaller than the patch dimension, the modal base can be reduced to consider the modes with wavelength greater or equal to the patch length only. In addition to this reduced modal base, other shape functions, e.g., the static deformed shapes, could be used.¹² As with all energy methods, a convergence check on the number of trial functions employed is always advisable.

As explained in what follows, the full set of generalized coordinates q_i which appears in Eq. (1) consists of $\boldsymbol{\phi}$ together with the voltages at the piezoelectric patches.

The external excitation consists of N_f point forces F_j acting on the panel at arbitrary locations, and therefore the generalized forces will have the form:

$$Q_i = \sum_{j=1}^{N_f} F_j \frac{\partial w}{\partial f_i} \quad (4a)$$

or

$$\mathbf{Q} = \mathbf{S}_f \mathbf{f}, \quad (4b)$$

where \mathbf{f} is the vector of the forces and \mathbf{S}_f is a matrix containing the modal shape vector \mathbf{s} evaluated at the force locations.

A detailed description of the various terms which appear in Eq. (2) is given in what follows.

B. Kinetic energy

The kinetic energy of the various elements can be calculated directly by integration, using the well-known formula:

$$T = \int \int \int_{\text{Vol}} \frac{1}{2} \rho \dot{w}^2 dx dy dz \quad (5)$$

which, for the transversely vibrating panel, yields

$$T_{pl} = \frac{1}{2} \dot{\boldsymbol{\phi}}^t \mathbf{M}_{pl} \dot{\boldsymbol{\phi}}, \quad (6a)$$

$$\mathbf{M}_{pl} = \int \int \int_{pl} \rho \mathbf{s} \mathbf{s}^t dx dy dz, \quad (6b)$$

where \mathbf{M}_{pl} is the (diagonal) inertia matrix of the bare panel.

The same notation is used to write the kinetic energy of the piezoelectric patches in the form

$$T_{pz} = \frac{1}{2} \dot{\boldsymbol{\phi}}^t \mathbf{M}_{pz} \dot{\boldsymbol{\phi}}, \quad (7a)$$

$$\mathbf{M}_{pz} = \sum_{i=1}^{N_p} \int \int \int_{pz_i} \rho_{pz_i} \mathbf{s} \mathbf{s}^t dx dy dz, \quad (7b)$$

where the index i identifies the N_p patches, over which the integrals are evaluated. In this case the inertia matrix is fully populated, having cross terms which couple the modal coordinates. For the lumped masses the kinetic energy is

$$T_{lm} = \frac{1}{2} \dot{\boldsymbol{\phi}}^t \mathbf{M}_{lm} \dot{\boldsymbol{\phi}}, \quad (8a)$$

$$\mathbf{M}_{lm} = \sum_{i=1}^{N_l} M_{lm_i} \mathbf{s}_{lm_i} \mathbf{s}_{lm_i}^t \quad (8b)$$

with N_l as the total number of masses, and \mathbf{s}_{lm_i} is the shape function vector, evaluated at the lumped mass locations.

C. Potential energy

The potential energy of the system is stored as the elastic energy of the panel and the elastic/electric energy of the piezoelectric patches. The elastic energies are directly calculated from the expression:

$$U = \int \int \int_{Vol} \frac{1}{2} \boldsymbol{\varepsilon}^t \boldsymbol{\sigma} dx dy dz, \quad (9)$$

where $\boldsymbol{\sigma}$ and $\boldsymbol{\varepsilon}$ are the vectors of the stresses and strains and, by assuming a plane stress condition, for the panel we can write:

$$U_{pl} = \frac{1}{2} \boldsymbol{\phi}^t \mathbf{K}_{pl} \boldsymbol{\phi}, \quad (10)$$

where \mathbf{K}_{pl} is the stiffness matrix:

$$\begin{aligned} \mathbf{K}_{pl} = \int \int \int_{pl} \frac{Ez^2}{(1-\nu^2)} & \left(\frac{\partial^2 \mathbf{s}}{\partial x^2} \frac{\partial^2 \mathbf{s}^t}{\partial x^2} + \frac{\partial^2 \mathbf{s}}{\partial y^2} \frac{\partial^2 \mathbf{s}^t}{\partial y^2} \right. \\ & \left. + 2\nu \frac{\partial^2 \mathbf{s}}{\partial x^2} \frac{\partial^2 \mathbf{s}^t}{\partial y^2} + 2(1-\nu) \frac{\partial^2 \mathbf{s}}{\partial x \partial y} \frac{\partial^2 \mathbf{s}^t}{\partial x \partial y} \right) dx dy dz. \end{aligned} \quad (11)$$

For the piezoelectric patches, the potential energy can be expressed as the sum of three energy components

$$U_{pz} = U_{pz}^{elast} + U_{pz}^{elastelect} + U_{pz}^{elect}, \quad (12)$$

where U_{pz}^{elast} is the energy stored due to the elasticity of the material, $U_{pz}^{elastelect}$ represents the further energy due to the voltage driven piezoelectric effect, and U_{pz}^{elect} is the electric energy stored due to the dielectric characteristics of the piezoelectric material.

1. Elastic energy

The computation of the elastic energy requires an appropriate modeling of the stress and strain pattern in the piezoelectric patches. The following assumptions are made: (a) the electrodes attached to the piezoelectric patches have negligible stiffness, (b) the layer of adhesive which connects the patches to the panel is negligibly thin compared to the patch and is able to transfer all the shear strain, (c) the natural boundary conditions at the edges of the patch ($\sigma=0$) are not enforced, and a strain distribution such as the one shown in Fig. 4 is assumed through the thickness of the patch. The last assumption is particularly appropriate due to the geometry of the patch, which is very thin and quite wide.

From the assumptions made, it is possible to write the elastic energy stored in the patches by using the same procedure used for the panel as

$$U_{pz}^{elast} = \frac{1}{2} \boldsymbol{\phi}^t \mathbf{K}_{pz}^{elast} \boldsymbol{\phi}, \quad (13)$$

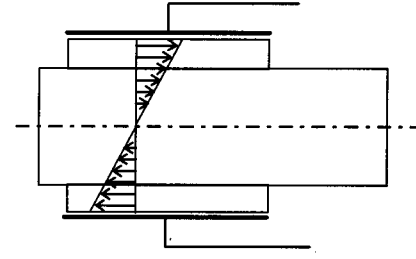


FIG. 4. Assumed strain distribution through the panel/patch assembly.

where

$$\begin{aligned} \mathbf{K}_{pz}^{elast} = \sum_{i=1}^{N_p} \int \int \int_{pz_i} \frac{E_{pz_i} z^2}{(1-\nu_i^2)} & \left(\frac{\partial^2 \mathbf{s}}{\partial x^2} \frac{\partial^2 \mathbf{s}^t}{\partial x^2} + \frac{\partial^2 \mathbf{s}}{\partial y^2} \frac{\partial^2 \mathbf{s}^t}{\partial y^2} \right. \\ & \left. + 2\nu_i \frac{\partial^2 \mathbf{s}}{\partial x^2} \frac{\partial^2 \mathbf{s}^t}{\partial y^2} \right. \\ & \left. + 2(1-\nu_i) \frac{\partial^2 \mathbf{s}}{\partial x \partial y} \frac{\partial^2 \mathbf{s}^t}{\partial x \partial y} \right) dx dy dz \end{aligned} \quad (14)$$

is the stiffness matrix, which is fully populated.

2. Elastoelectric energy

In the piezoelectric patches a further stress is produced when an electric field is applied across the material. Due to this electrically induced stress there will be a further energy, $U_{pz}^{elastelect}$, stored in the system, which can be calculated using the same procedure as used for the elastic energy. By assuming that the patch has a constant thickness h_{pz} which is thin enough to prevent fringe effects and has a voltage v applied at its electrodes, a constant electric field $e = v/h_{pz}$ can be assumed across the patch, and the further stress due to the applied voltage will be

$$\boldsymbol{\sigma}_{elect} = \begin{pmatrix} \sigma_{x_{elect}} \\ \sigma_{y_{elect}} \end{pmatrix} = \frac{E_{pz}}{1-\nu^2} \begin{pmatrix} d_{xz} + \nu d_{yz} \\ d_{yz} + \nu d_{xz} \end{pmatrix} e. \quad (15)$$

Here d_{xz} and d_{yz} are the piezoelectric constants of the material, which is assumed to have poling direction z perpendicular to the panel. Hence $U_{pz}^{elastelect}$, can be written as

$$U_{pz}^{elastelect} = \int \int \int_{pz} \frac{1}{2} \boldsymbol{\sigma}_{elect}^t \boldsymbol{\varepsilon} dx dy dz. \quad (16)$$

Now the electric field in the patch i can be written in the form

$$e_i(t) = \mathbf{v}(t)^t \mathbf{p}_i, \quad (17)$$

where \mathbf{v} is the vector of N_p elements which contains the patch voltages, and \mathbf{p}_i is a vector with $1/h_{pz_i}$ in the position of the i th piezoelectric patch and zeros in all the other positions. By substituting the expressions for electric stress (15) in Eq. (16), and considering $d_{xz} = d_{yz} = d_z$, it is possible to write the elastoelectric potential energy stored in the N_p patches as

$$U_{pz}^{\text{elastelect}} = \mathbf{v}^t \mathbf{K}_{pz}^{\text{elastelect}} \phi \quad (18)$$

with

$$\mathbf{K}_{pz}^{\text{elastelect}} = \sum_{i=1}^{N_p} \int \int \int_{pz_i} \frac{E_{pz_i} d_{z_i} \mathbf{p}_i}{2(1-\nu_i)} \times \left(z \frac{\partial^2 \mathbf{s}^t}{\partial x^2} + z \frac{\partial^2 \mathbf{s}^t}{\partial y^2} \right) dx dy dz. \quad (19)$$

3. Electric energy

The energy stored in the piezoelectric material as electric energy can be expressed as

$$U_{pz}^{\text{elect}} = \int \int \int_{pz} \frac{1}{2} e d dx dy dz, \quad (20)$$

where e is the electrical field (potential difference/length) in the material, which is assumed to have direction perpendicular to the panel, and d is the electrical displacement (charge/area). For each patch d will be given by

$$d_i = \varepsilon_{pz_i} \mathbf{p}_i^t \mathbf{v}, \quad (21)$$

where ε_{pz_i} is the dielectric constant of the piezoelectric material of the i th patch. Therefore the electric energy stored will be

$$U_{pz}^{\text{elect}} = \frac{1}{2} \mathbf{v}^t \mathbf{K}_{pz}^{\text{elect}} \mathbf{v}, \quad (22)$$

$$\mathbf{K}_{pz}^{\text{elect}} = \sum_{i=1}^{N_p} \int \int \int_{pz_i} \varepsilon_{pz_i} \mathbf{p}_i \mathbf{p}_i^t dx dy dz,$$

where the elements of the matrix $\mathbf{K}_{pz}^{\text{elect}}$ are the capacitances of the piezoelectric patches.

D. Electromechanical system dynamic equation

With all the energy expressions available as functions of the generalized coordinates ϕ and \mathbf{v} the application of the Lagrange's equation (1) is quite straightforward, and the resulting equations are

$$(\mathbf{M}_{pl} + \mathbf{M}_{pz} + \mathbf{M}_{lm}) \ddot{\phi} + (\mathbf{K}_{pl} + \mathbf{K}_{pz}^{\text{elast}}) \phi + (\mathbf{K}_{pz}^{\text{elastelect}})^t \mathbf{v} = \mathbf{Q}, \quad (23a)$$

$$\mathbf{K}_{pz}^{\text{elastelect}} \phi + \mathbf{K}_{pz}^{\text{elect}} \mathbf{v} = 0. \quad (23b)$$

Equation (23a) is produced by deriving the energies with respect to the modal coordinates ϕ and Eq. (23b) is produced by deriving the energies with respect to the voltages \mathbf{v} , under the assumption that all modal coordinates and voltages are degrees of freedom of the system. In the case in which all the patches act as actuators, their voltages v_i will be externally driven and therefore Eq. (23b) becomes redundant. Alternatively, if all the patches act as sensors, Eq. (23b) can be used to write an expression for the voltages as a function of the modal coordinates. This expression can then be substituted into Eq. (23a) to produce a complete set of equations in the unknowns ϕ . In the most general case some of the patches act as actuators and others as sensors, and it is therefore necessary to partition the matrix $\mathbf{K}_{pz}^{\text{elastelect}}$ to separate actuator

and sensor contributions. By calling \mathbf{v}_a and \mathbf{v}_s , respectively, the vectors of the voltages at the actuators and at the sensors, and $\mathbf{K}_{pza}^{\text{elastelect}}$ and $\mathbf{K}_{pzs}^{\text{elastelect}}$ the respective partitions of the matrix $\mathbf{K}_{pz}^{\text{elastelect}}$ it is possible to rewrite Eq. (23a) as

$$\mathbf{M} \ddot{\phi} + \mathbf{C}_s \dot{\phi} + (\mathbf{K}^{\text{elas}} + \mathbf{K}_{pzs}) \phi = -(\mathbf{K}_{pza}^{\text{elastelect}})^t \mathbf{v}_a + \mathbf{s}_f^t f, \quad (24)$$

where all the inertia elements are included in the matrix \mathbf{M} and the stiffness due to the elasticity in \mathbf{K}^{elas} . Furthermore

$$\mathbf{K}_{pzs} = -(\mathbf{K}_{pzs}^{\text{elastelect}})^t (\mathbf{K}_{pzs}^{\text{elect}})^{-1} \mathbf{K}_{pzs}^{\text{elastelect}} \quad (25)$$

represents the contribution to the stiffness from the piezoelectric energy stored in the patches acting as sensors, where $\mathbf{K}_{pzs}^{\text{elect}}$ is the partition of $\mathbf{K}_{pz}^{\text{elect}}$ relating to the sensors. In addition, structural damping has been added to the system by including in the equations the damping matrix \mathbf{C}_s .

III. CONTROL SYSTEM

The mathematical model developed in the previous section can be written in state space form to provide a standard mathematical basis for control studies. The model obtained in its final form is

$$\dot{\mathbf{x}} = \mathbf{A} \mathbf{x} + \mathbf{B}_v \mathbf{v}_a + \mathbf{B}_f f, \quad \mathbf{v}_s = \mathbf{C}_v \mathbf{x}, \quad \mathbf{w}_{\text{out}} = \mathbf{C}_w \mathbf{x}, \quad (26)$$

where

$$\mathbf{x} = \begin{pmatrix} \phi \\ \dot{\phi} \end{pmatrix}, \quad \mathbf{A} = \begin{bmatrix} \mathbf{0} & \mathbf{I} \\ -\mathbf{M}^{-1} \mathbf{K} & -\mathbf{M}^{-1} \mathbf{C}_s \end{bmatrix},$$

$$\mathbf{B}_v = \begin{bmatrix} \mathbf{0} \\ \mathbf{M}^{-1} (\mathbf{K}_{pza}^{\text{elastelect}})^t \end{bmatrix}, \quad (27)$$

$$\mathbf{B}_f = \begin{bmatrix} \mathbf{0} \\ \mathbf{M}^{-1} \mathbf{s}_f^t \end{bmatrix}, \quad \mathbf{C}_v = [(-\mathbf{K}_{pzs}^{\text{elect}})^{-1} \quad \mathbf{K}_{pzs}^{\text{elastelect}} \quad \mathbf{0}],$$

$$\mathbf{C}_w = [\mathbf{s}_{\text{out}}^t \quad \mathbf{0}],$$

where \mathbf{K} is the total stiffness matrix which appears in Eq. (24), \mathbf{w}_{out} is the output displacement, and \mathbf{s}_{out} is the vector of the mode shapes evaluated at the output location. Based on this representation, some initial controller design studies based on state feedback design using linear quadratic regulator (LQR) theory (for the background theory see, for example, the text¹⁸ and the relevant cited references), have been undertaken. In particular, the minimization of the performance index:

$$J = \int_0^\infty (\mathbf{w}_{\text{out}}^t \mathbf{Q} \mathbf{w}_{\text{out}} + \mathbf{v}_a^t \mathbf{R} \mathbf{v}_a) dt, \quad (28)$$

where \mathbf{Q} (positive semidefinite) and \mathbf{R} (positive definite) are weighting matrices of compatible dimensions to be selected by the designer, yields the state feedback law:

$$\mathbf{v}_a = \mathbf{G}_{fs} \mathbf{x}, \quad (29)$$

where \mathbf{G}_{fs} is the full-state feedback gain matrix, given by

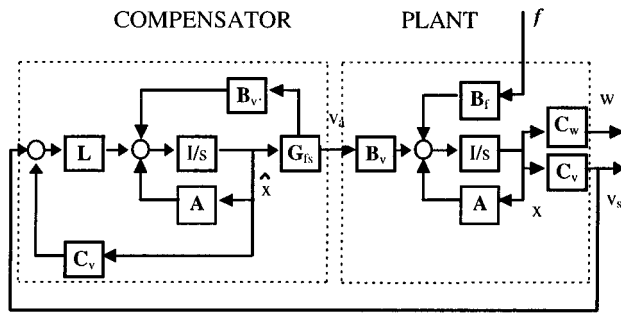


FIG. 5. Block diagram of the actively controlled system.

$$\mathbf{G}_{fs} = \mathbf{R}^{-1} \mathbf{B}_v \mathbf{P}_c \quad (30)$$

where \mathbf{P}_c satisfies the algebraic Riccati equation

$$\mathbf{A}' \mathbf{P}_c + \mathbf{P}_c \mathbf{A} - \mathbf{P}_c \mathbf{B}_v \mathbf{R}^{-1} \mathbf{B}_v' \mathbf{P}_c + \mathbf{C}_w' \mathbf{Q} \mathbf{C}_w = 0. \quad (31)$$

Recognizing that it is not possible to physically measure all entries in the state vector, the state feedback law will actually be implemented as

$$\mathbf{v}_a = \mathbf{G}_{fs} \hat{\mathbf{x}},$$

where the estimated state vector $\hat{\mathbf{x}}$ is generated by the observer

$$\dot{\hat{\mathbf{x}}} = \mathbf{A} \hat{\mathbf{x}} + \mathbf{B} \mathbf{u} + \mathbf{L}(\mathbf{y} - \mathbf{C} \hat{\mathbf{x}}), \quad (32)$$

where \mathbf{L} is the observer gain matrix, and \mathbf{y} is the output vector which is equal to \mathbf{v}_s .

The theory of the observer structure guarantees that: $\lim_{t \rightarrow \infty} (\mathbf{x}(t) - \hat{\mathbf{x}}(t)) = 0$ and combining the plant and observer state models yields

$$\begin{pmatrix} \dot{\mathbf{x}} \\ \dot{\hat{\mathbf{x}}} \end{pmatrix} = \begin{bmatrix} \mathbf{A} & -\mathbf{B}_v \mathbf{G}_{fs} \\ \mathbf{L} \mathbf{C}_v & \mathbf{A} - \mathbf{L} \mathbf{C}_v - \mathbf{B}_v \mathbf{G}_{fs} \end{bmatrix} \begin{pmatrix} \mathbf{x} \\ \hat{\mathbf{x}} \end{pmatrix} + \begin{pmatrix} \mathbf{B}_f \\ \mathbf{0} \end{pmatrix} f. \quad (33)$$

The block diagram of Fig. 5 shows the final form of the feedback control scheme.

The plant represents the real electromechanical system composed of the aluminum panel with the piezoelectric patches, and lumped mass, while the compensator is the active control system, composed of the observer followed by a full-state feedback controller.

IV. EXAMPLE APPLICATION

As an illustrative example, the dynamics of a system composed of a simply supported aluminum panel with a lumped mass mounted on it, and two pairs of piezoelectric patches acting as the sensors and actuators of the control system, has been studied (Fig. 6).

The source of the disturbance is a harmonic point force of one Newton in amplitude acting perpendicular to the panel at $x = 254$ mm, $y = 50.8$ mm.

$$f = F e^{j\omega t} \quad (34)$$

and, for model testing purposes, a harmonic input voltage (1 V) applied to the actuator was considered.

$$\mathbf{v}_a = V e^{j\omega t}. \quad (35)$$

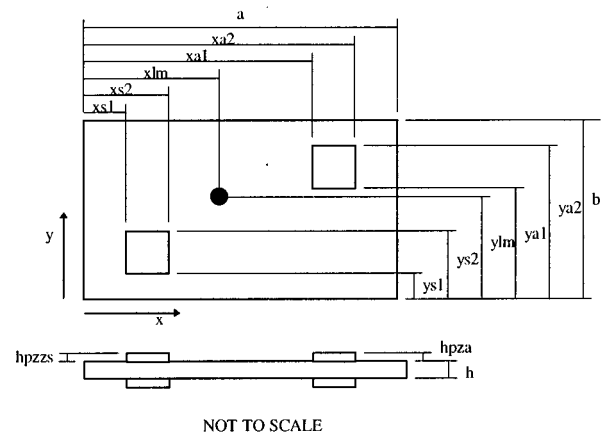


FIG. 6. Plan and side views of the model.

The modal shapes of the bare panel

$$S_{m,n}(x,y) = \sin\left(\frac{m\pi x}{a}\right) \sin\left(\frac{n\pi y}{b}\right) \quad (36)$$

are taken as Ritz functions to model the displacement field. Since the frequency range studied is between 0 and 1 kHz and the piezoelectric patches are taken to be 1/6 of the panel length, the first 36 modal shapes were used as Ritz functions, so that

$$\mathbf{w} = \mathbf{s}' \boldsymbol{\phi} = (s_1 \cdots s_{36}) (\phi_1 \cdots \phi_{36})'. \quad (37)$$

In addition to this reduced modal base, other shape functions, e.g., the static deformed shape generated by a constant input at the actuator, could be used. The configuration of the control system, with only one sensor and one actuator, is such that the vectors \mathbf{v}_a and \mathbf{v}_s reduce to scalars. The basic control objective here is the minimization of the displacements at the center of the panel.

A. Model verification and numerical simulation

The simulation of the dynamics of the system was carried out using MATLAB running on a Sun workstation and the mathematical model was verified by comparing the results with those obtained by modeling the same system with the standard finite element (FE) method (ANSYS code).

The verification of the model was performed by comparing the frequency response at the center of the panel obtained with the Lagrange model with that obtained with the FE model. The FE model, shown in Fig. 7, was made up of 384 eight-noded layered shell elements (Shell91), where in the areas of the piezoelectric patches there were three layers (piezoelectric material upper patch/aluminum/piezoelectric material lower patch) and in the remainder of the panel there was a single layer of aluminum. The total number of nodes was 1233; 49 in x direction and 33 in y direction.

Two different test cases were set up to validate the model.

1. Test case 1: Voltage driven panel

In this test, the driving force is produced by the contractions of the piezoelectric actuator when a sinusoidal voltage of amplitude of 1 V is applied, and due to the linearity of the

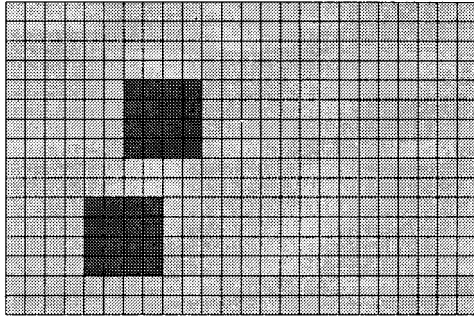


FIG. 7. FEM model used to validate the Lagrange model (the darker squares indicate the position of the piezoelectric patches).

model the results can be scaled up to whatever input voltage is required. In the FEM model the effect of the applied voltage is produced by applying unit moments along the line edges of the piezoelectric patch. The value of the applied moment, which corresponds to the input voltage, is calculated as in Ref. 19 as an extrapolation of the beam case. The frequency response of the panel in the range 50 to 500 Hz is shown in Fig. 8. Note that the discrete frequencies employed in the FEM results have led to truncation of the resonance peaks, a smaller (and more computational expensive) frequency step would fully resolve these peaks.

2. Test case 2: Point force driven panel

In this test a lumped mass of 50 g has been added to the panel at the location reported in Table I and the forcing input is a point force acting perpendicular to the panel at the arbitrarily chosen location $x = 254$ mm, $y = 50.8$ mm. The results of the simulations are shown in Fig. 9.

From the comparison of the results of these tests it can be concluded that the Lagrange model gives a good representation of the dynamics of the system, with a good agreement with the results obtained with FEM, but with a much smaller model.

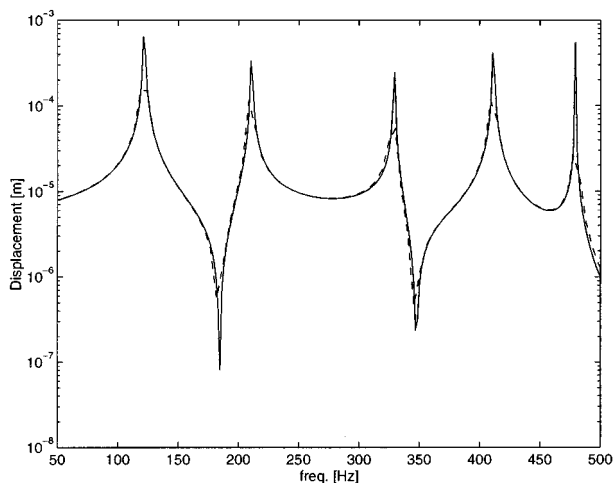


FIG. 8. Test case 1, frequency response to point force input. Solid line—Lagrange model, Dashed line—FEM.

TABLE I. Dimensions and material properties.

Panel	$a = 304.8$ mm	$E = 71e9$ Pa
	$b = 203.2$ mm	$\rho = 2800$ kg/m ³
	$h = 1.52$ mm	$\nu = 0.33$
		$\eta = 0.001^a$
Sensor	$xs1 = 0.8$ mm	$E = 63e9$ Pa
	$xs2 = 101.6$ mm	$\rho = 7650$ kg/m ³
	$ys1 = 25.4$ mm	$\nu = 0.3$
	$ys2 = 76.2$ mm	$d = 1.66e-10$ m/V
	$hpzs = 0.19$ mm	$\epsilon = 1700 \epsilon^0$
Actuator	$xa1 = 76.2$ mm	$E = 63e9$ Pa
	$xa2 = 127$ mm	$\rho = 7650$ kg/m ³
	$ya1 = 101.6$ mm	$\nu = 0.3$
	$ya2 = 152.4$ mm	$d = 1.66e-10$ m/V
	$hpza = 0.19$ mm	$\epsilon = 1700 \epsilon^0$
Lumped mass	$xlm = 50.8$ mm	$Wlm = 50$ g
	$ylm = 152.4$ mm	

^a $\eta = 0$ for the Lagrange/FEM model comparison.

3. Controlled structure simulation

The simulation of the controlled structure has been performed by closing the control loop which commands the actuator with the signal coming from the sensor. The value of the gain matrices \mathbf{L} (which produces the optimal estimate of the states) and \mathbf{G}_{fs} (which is the full-state feedback gain matrix) have been calculated with the routines available in MATLAB. In this case the weighting matrices \mathbf{Q} and \mathbf{R} in the performance index in Eq. (28) are scalars because only one input and one output are present in the system.

Figure 10 shows a comparison of the displacement response at the center of the panel for the structure with and without control in the frequency range up to 1 kHz using $\mathbf{Q} = 10^{13}$ and $\mathbf{R} = 1$, values which have been selected after a small number of design iterations. The continuous line represents the response of the system without the control system applied, while the dotted line represents the response with active control. Also in Fig. 10 the response of the same electromechanical system, when the point force is applied at a

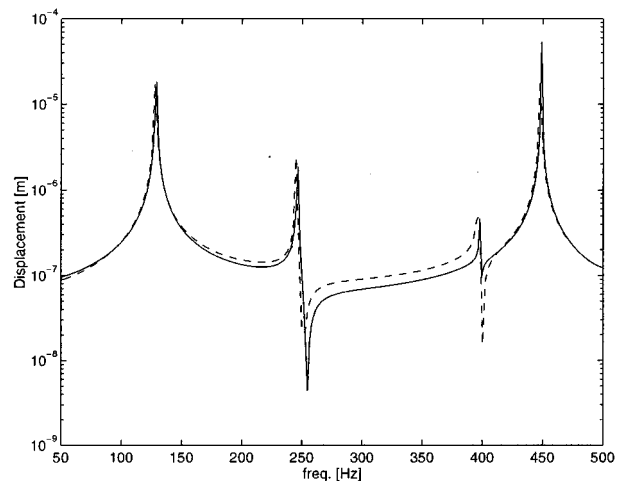


FIG. 9. Test case 2, frequency response to actuator voltage input. Solid line—Lagrange model, Dashed line—FEM.

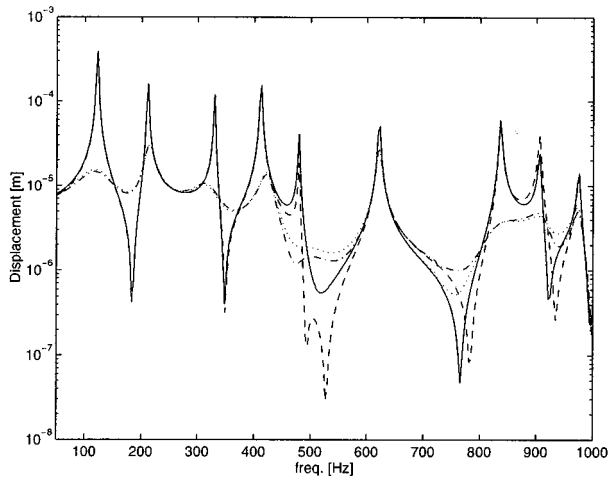


FIG. 10. Frequency response to point force input disturbance. Solid line—Uncontrolled system in nominal configuration, Dotted line—Controlled system in nominal configuration, Dashed line—Uncontrolled system with force offset, Dash-dotted line—Controlled system with force offset.

location 6 mm offset in the x and y directions with respect to the nominal position ($x = 254$ mm, $y = 50.8$ mm) of the force, is shown. This simulation suggests that the system has inherent robustness as evidenced by the fact that the system response is “very similar” to the nominal case. These are only very preliminary observations, however, but they strongly suggest that this area should be fully investigated. The performance potential of the control system can be further highlighted by comparing the deformed shape of the panel with and without a control system, as shown in Fig. 11 for an input frequency of 400 Hz.

Closer inspection of the frequency response of Fig. 10 shows that in the region of the resonance at 620 Hz, no attenuation is produced on the panel. From the curve of the actuator’s signal given in Fig. 12, it is not possible to ascertain the reason for this since the control input at that frequency is very strong. A physical explanation of this phenomena can be obtained by observing the contour plot of the deformed shape of the panel in Fig. 13. It is possible to see

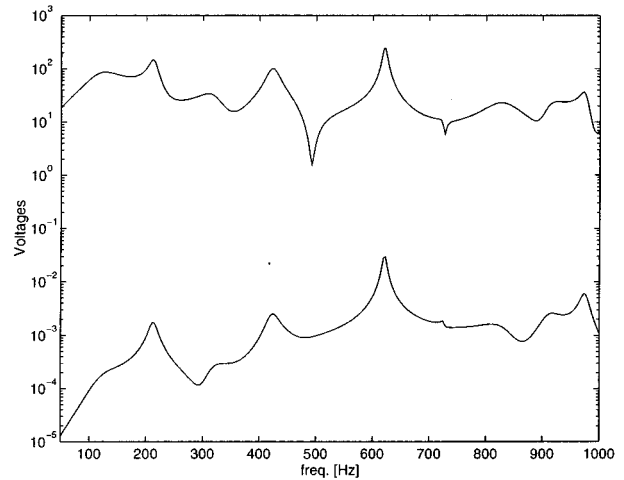
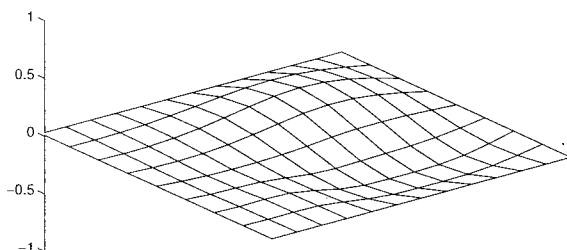


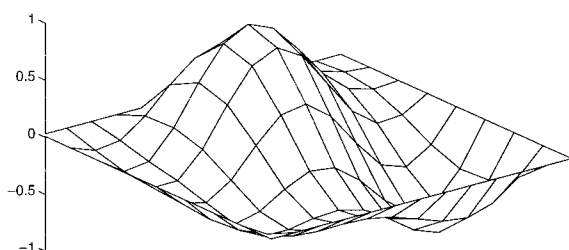
FIG. 12. Control system signals. Upper curve: actuator; lower curve: sensor.

from this plot that the actuator patch is cut through the middle by a nodal line [with $w(x,y) = 0$, $\partial^2 w / \partial x^2 = 0$, $\partial^2 w / \partial y^2 = 0$] and therefore no control is possible over this mode for the reasons explained in Sec. I.

Further development of this basic control scheme is proceeding. One key area arises from the fact that linear quadratic controllers with observers, although optimal for the nominal model, may yield far from satisfactory performance in the real life situations in which the plant differs significantly from the model. In particular, the guaranteed passband robustness properties of full-state feedback based design (see, for example, Anderson and Moore²⁰) can simply disappear with the introduction of a state observer. Consequently, loop transfer recovery techniques are currently under investigation for this application, i.e., is it possible to recover appropriate loop properties for an LQ design by a suitable adjustment to the LQ design process (for the basics see, for example, Anderson and Moore²⁰). Once this work is sufficiently advanced, it will clearly be necessary to compare the effectiveness of feedback control techniques with alternative approaches such as adaptive feed forward and feedback con-



a)



b)

FIG. 11. Deformed shapes of the panel subject to a point force of 1 N and frequency 400 Hz. (a) Response damped by the active control system. (b) Response of the system without control.

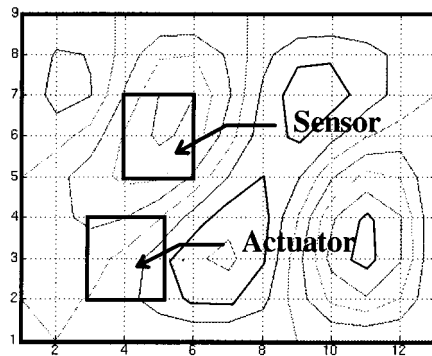


FIG. 13. Deformed shape contour plot at 620 Hz.

control strategies cooperated with the on-line secondary path identification. Only then will definitive conclusions be available as to the advantages and disadvantages of competing methods for microvibrations control, in spacecraft or other applications. Also there is a very strong likelihood that, in at least some cases, the best solution will be a mixture of feedback and feed forward control actions.

V. CONCLUSIONS

Based on the investigations reported here, it can be concluded that the developed modeling strategy provides a simple yet realistic approach for active control design studies. This method can be used to assess the feasibility of various control algorithms, and provides an efficient means of studying the robustness of control systems by considering the effect of structural parameter changes and unmodeled dynamics. Here some highly promising basic control laws have been designed based on linear optimal control theory.

The correctness of the structural model has been tested, with satisfactory results, against a FEM model. The comparison highlighted the accuracy of the results, which have been obtained with a much smaller model. Another advantage of the modeling technique described was the inclusion of electrical degrees of freedom (the voltages at the sensors) directly in the system motion equations.

It is emphasized that the present modeling technique is intended to serve as a tool for the theoretical investigation of active control strategies. For this reason an effort has been made to incorporate the essential physics of a typical system while avoiding the detail and complexity associated with a specific application. A future intention is to consider a structure made of more panels connected along their edges in order to have a more realistic representation of a spacecraft, which could also include a more detailed dynamic representation of equipment boxes. Other techniques, instead of the superposition of bare panel modal shapes, will also be considered to obtain more suitable shape functions which are used to write the system energies.

Currently in-depth development and extensions of the basic feedback based control scheme considered in this paper are underway. The aim of this work is to gain detailed in-

sight into the true potential of feedback control schemes for microvibrations control across a range of application domains. This work has two main aspects, i.e., development and evaluation of feedback control schemes on their own, and in due course, the comparison/evaluation of such schemes against alternative strategies such as those based on feed forward controllers implemented as adaptive filters. Only then will it be feasible to fully assess the benefits of one general approach against the other.

- ¹H. R. Stark and C. Stavrinidis, "ESA microgravity and microdynamics activities—An overview," *Acta Astron.* **34**, 205–221 (1994).
- ²D. I. Jones, "Vibration control in space," *Comput. Control Eng. J.* **5**, 89–95 (1994).
- ³S. J. Dine, D. E. L. Tunbridge, and P. P. Collins, "The vibration environment on a satellite in orbit," IEE Colloquium on "High Accuracy Platform Control in Space" in *Proceedings of the Institution of Electrical Engineers* (IEE, London, 1993).
- ⁴J. Su, C. Huang, F. Austin, and G. Knowles, "Vibration control of an active mirror pointing system," *Proc. SPIE* **1917**, 37–48 (1993).
- ⁵J. W. Melody and H. C. Briggs, "Analysis of structural and optical interactions of the Precision Optical Interferometer," *Proc. SPIE* **1947**, 44–57 (1993).
- ⁶V. A. Skormin and M. A. Tascillo, "A jitter rejection technique in a satellite based laser communication system," in *Proceedings of the 1993 IEEE National Aerospace & Electronics Conference* (IEEE, New York, 1993), pp. 1107–1115.
- ⁷S. A. Collins and A. H. Von Flotow, "Active vibration control for spacecraft," *42nd Congress of the International Astronautical Federation*, IAF Paper 91-289 (1991).
- ⁸O. C. Zienkiewicz, *The Finite Element Method* (McGraw-Hill, London, 1977).
- ⁹S. J. Elliot and L. Billet, "Adaptive control of flexural waves propagating in a beam," *J. Sound Vib.* **163**, 295–310 (1993).
- ¹⁰B. R. Mace, "Active control of flexural vibrations," *J. Sound Vib.* **114**, 253–270 (1987).
- ¹¹K. O. Prakah-Asante and K. C. Craig, "Investigation of modal based and wave-type vibration energy transmission of active control of structures," *Proc. SPIE* **2190**, 295–306 (1994).
- ¹²N. W. Hagood, W. H. Chung, and A. H. Von Flotow, "Modeling of piezoelectric actuator dynamics for active structural control," in *Proceedings of the 31st SDM Conference*, AIAA Paper 90-1097 (1990), pp. 2242–2256.
- ¹³H. S. Tzou, "Damping control of 'smart' piezoelectric shell structures," in *Proceedings of the 4th International Conference on Recent Advances in Structural Dynamics* (University of Southampton, ISVR, UK, 1991), pp. 659–668.
- ¹⁴H. S. Tzou, "Neural sensation and actuation of shells using distributed piezoelectric transducers," in *Proceedings of the 4th International Conference on Recent Advances in Structural Dynamics* (University of Southampton, ISVR, UK, 1991), pp. 668–678.
- ¹⁵H. T. Banks, R. C. Smith, and Yun Wang, "The modeling of piezoceramic patch interactions with shells, panels, and beams," *Q. Appl. Math.* **L111**, 353–381 (1995).
- ¹⁶S. W. Zhou, C. Liang, and C. A. Rogers, "Modeling of distributed piezoelectric actuators integrated in thin cylindrical shells," *J. Acoust. Soc. Am.* **96**, 1605–1612 (1994).
- ¹⁷F. Lalonde, Z. Chaudhry, and C. A. Rogers, "Impedance-based modeling of actuators bonded to shell structures," *Proc. SPIE* **2443**, 396–408 (1995).
- ¹⁸J. M. Maciejowski, *Multivariable Feedback Design* (Addison-Wesley, Reading, MA, 1989), pp. 222–263.
- ¹⁹M. J. Brennan, M. J. Day, S. J. Elliott, and R. J. Pinnington, "Piezoelectric actuators and sensors," in *Proceedings of the IUTAM Symposium on the Active Control of Vibration*, Bath, edited by C. R. Burrows and P. S. Keogh (Mechanical Engineering Publications Ltd., London, 1994), pp. 263–274.
- ²⁰B. D. O. Anderson and J. B. Moore, *Optimal Control Linear Quadratic Methods* (Prentice-Hall, Englewood Cliffs, NJ, 1989).

Vibration of truss structures

Joseph E. Bondaryk

Department of Ocean Engineering, Massachusetts Institute of Technology, Cambridge, Massachusetts 02139

(Received 20 January 1997; revised 9 April 1997; accepted 9 June 1997)

Recent trends in underwater vehicle design suggest the use of trusslike structures to support vibrating machinery. Experimental measurements are used to understand the dynamic behavior of a set of 1:15 model, three-dimensional truss structures over the full scale equivalent frequency range 10–1400 Hz. A cubic truss with all equal struts, a rectangular truss with two strut sizes, and a less practical truss composed of pyramid-shaped cells are considered. In conjunction with experiments, a direct global stiffness matrix numerical model is used to identify fundamental truss processes. The periodic nature of trusses causes them to act as mechanical comb filters in frequency with 3–5 dB per bay of attenuation at nonresonant frequencies. In trusses with long runs of axial struts, energy is carried down the truss axis primarily by compressional resonances. The spacing of the resonant peaks is controlled by strut length. A filtering strategy uses strut length to reduce the overall truss response via destructive interference of the frequency resonance structures of the individual struts. Multiple periodicities and impedance discontinuities at the truss joints cause the resonant peaks at low frequencies to widen. The consequence of this is that trusses with varied strut lengths tend to a low-pass frequency characteristic. This effect is compared to an equivalent applied damping and is shown to achieve up to 6 dB per bay of attenuation at the higher frequencies. © 1997 Acoustical Society of America. [S0001-4966(97)02610-6]

PACS numbers: 43.40.At, 43.40.Cw [CBB]

INTRODUCTION

There is currently interest in the application of trusslike structures to support internal components of ships and underwater vehicles. Just as these provide definite advantages for construction and refit, it is believed that they may provide the opportunity to improve the acoustic characteristics of the vessel as well. By mounting noisy equipment, such as rotating or reciprocating machinery, to a truss structure rather than directly to the hull, the path to the hull is lengthened, providing the opportunity for applied damping. This is illustrated in Fig. 1. Damping could take the form of constrained layers, dynamic absorbers,¹ or fill material inside the truss members themselves.²

Such treatments are greatly enhanced by the intrinsic properties of the truss: scattering of energy between wave types and multipath. A truss structure, by its very nature, is constructed from very many joints and struts. A single joint will typically connect from four to six struts at various angles to one another. Each strut can support at least four propagating wave types: compressional, torsional, and two flexural plus evanescent waves. The connection points scatter an incoming wave type on one strut into all other wave types on all other struts. Multiple joints imply constant scattering of wave types into one another,³ resulting in a sharing of energy and eventual equilibrium.⁴ This energy balance between wave types ensures that damping of any one wave type effectively damps them all. The high interconnectivity of the members implies that an energy packet traveling in the truss will propagate along the same member many times. Such a multipath implies that even a small amount of damping material could potentially be very effective.^{5,6} However, the fundamental dynamic behavior of the truss must be un-

derstood to design practical trusses and devise effective damping mechanisms.

This paper describes a set of experimental and numerical studies made to investigate the basic vibrational properties of undamped, three-dimensional truss structures. In Secs. I and II are described a set of experiments on truss models, whose struts are about 1:15 the size that would be used in actual application. The frequency range of these model studies covers the range 100 Hz to 20 kHz, which corresponds to a full scale equivalent frequency range of about 6–1400 Hz.

The periodic nature of these trusses causes sharp filtering at certain frequencies and has been described for other wave-bearing systems.^{7,8} However, the multiple periodicities at work in the truss and impedance discontinuities at the truss joints cause the resonant peaks at low frequencies to widen significantly.⁹ It is shown that, in principle, the fre-

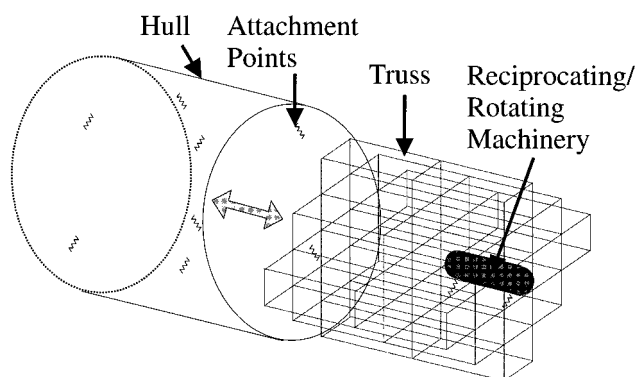


FIG. 1. Application of a truss structure, hull mounting system for machinery.

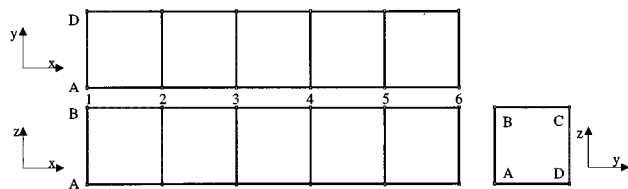


FIG. 2. Plan view, side view, and cross section of *cubic truss*.

quency response of any truss can be approximated by combining the response of the component pieces. The consequence of these two effects suggests that trusses with varied strut lengths tend to a low-pass frequency characteristic.

In Sec. III is described a set of direct global stiffness matrix (DGSM) numerical models made to identify the compressional and flexural contributions in the experimental truss frequency responses. Results show that, in trusses with long runs of axial struts, energy is carried down the axis primarily by the compressional resonances of these struts. A model with random strut lengths shows that the observed low-pass filtering effect can be compared to an equivalent applied damping.

I. EXPERIMENT

A. Truss designs

Several trusses were constructed to explore the effect of member length on the overall dynamics of the truss. These cube-based designs incorporate joints which allow long axial runs in the truss. Also, a pyramid-based design was examined which eliminates this characteristic.

The *cubic truss* is a three-dimensional structure constructed from 1.27×10^{-2} m (0.5 in.) diameter tubes of aluminum 6061 T6, $\rho = 2700 \text{ kg/m}^3$, $E = 70 \times 10^9 \text{ N/m}^2$, $\nu = 0.33$, with wall thickness 1.651×10^{-3} m (0.065 in.). These are close fit into machined joints of the same material and held in place by a conventional 30-minute epoxy. The average joint mass is 5.15×10^{-2} kg.

The *cubic truss* is a line of five cubes as constructed from 24 joints and 44 struts as shown in Fig. 2. All strut members have an average exposed length $l = 0.815$ m. As a whole, the truss is 4.2 m long and weighs approximately 6.9 kg. The joints are labeled with letters A–D indicating transverse location and numbers 1–6 indicating axial location as shown in Fig. 2. A second cubic truss was built identical in design to that in Fig. 2 except with exposed strut length $l = 0.48$ m. This is known as the *short cubic truss*.

The truss shown in Fig. 3 is composed of both long and

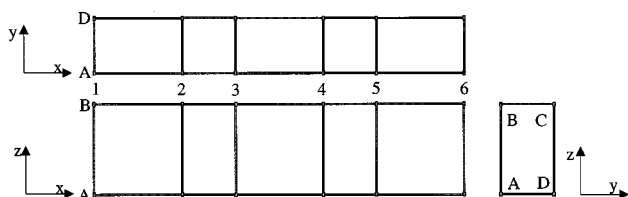


FIG. 3. Plan view, side view, and cross section of *rectangular truss*.

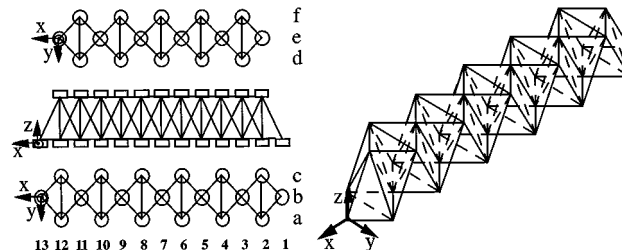


FIG. 4. Top plan view, side view, bottom plan view, and perspective view of *pyramid truss*.

short strut lengths in a rectangular cross section with alternating long and short bays. The long struts have an exposed length $l = 0.815$ m and the short struts have an exposed strut length $l = 0.48$ m. This is known as the *rectangular truss*.

The *pyramid truss* is a fully three-dimensional structure constructed of the same tubing but different machined joints, each of mass 0.12 kg. The *pyramid truss* is a conglomerate of square-based pyramid sections, stiffened by cross bracing, and is shown in Fig. 4. There are only three different strut lengths in the design, 44 of 0.48 m, used in the pyramid bases; 11 of 0.68 m, used as base cross struts; and 54 of 0.815 m, used as the vertical, diagonal members. As a whole, the truss is 4.7 m long and weighs approximately 16 kg. The joints are labeled with letters a–f indicating transverse location and numbers 1–13 indicating axial location as shown in Fig. 4. Note that this truss has no continuous axial members.

B. Experimental setup

All the results discussed in this paper were obtained using the following experimental setup. The truss itself was suspended from a wooden support structure by a set of bungee chords. This provided isolation for frequencies above 10 Hz and was used to approximate a free-free mounting condition. No damping material was added to any of the trusses under investigation. A right-hand rule coordinate system was used with the x axis defined as the major axis of the truss, the y axis defined as is the minor axis of the truss, and the z axis defined opposite to gravity. The truss was excited in the X , Y , or Z direction, using a Brüel & Kjær (B&K) 4810 shaker driven by wideband random noise from a Hewlett–Packard (HP) spectrum analyzer over the frequency range 10 Hz to 25 kHz.

Accelerations were measured at each joint of the truss by 0.5-g Kistler accelerometers, attached with bees wax in the X , Y , or Z direction. Input force and acceleration were also measured with a B&K 8001 impedance head, mounted between the truss and input shaker. Data was acquired by a HP VXI 48-channel acquisition system under the control of the SDRC I-DEAS software package. Narrowband, 8-Hz, autospectra were collected for each channel along with cross-spectra with the input force over the frequency range 8 Hz–20 kHz and averaged over 100 ensembles.

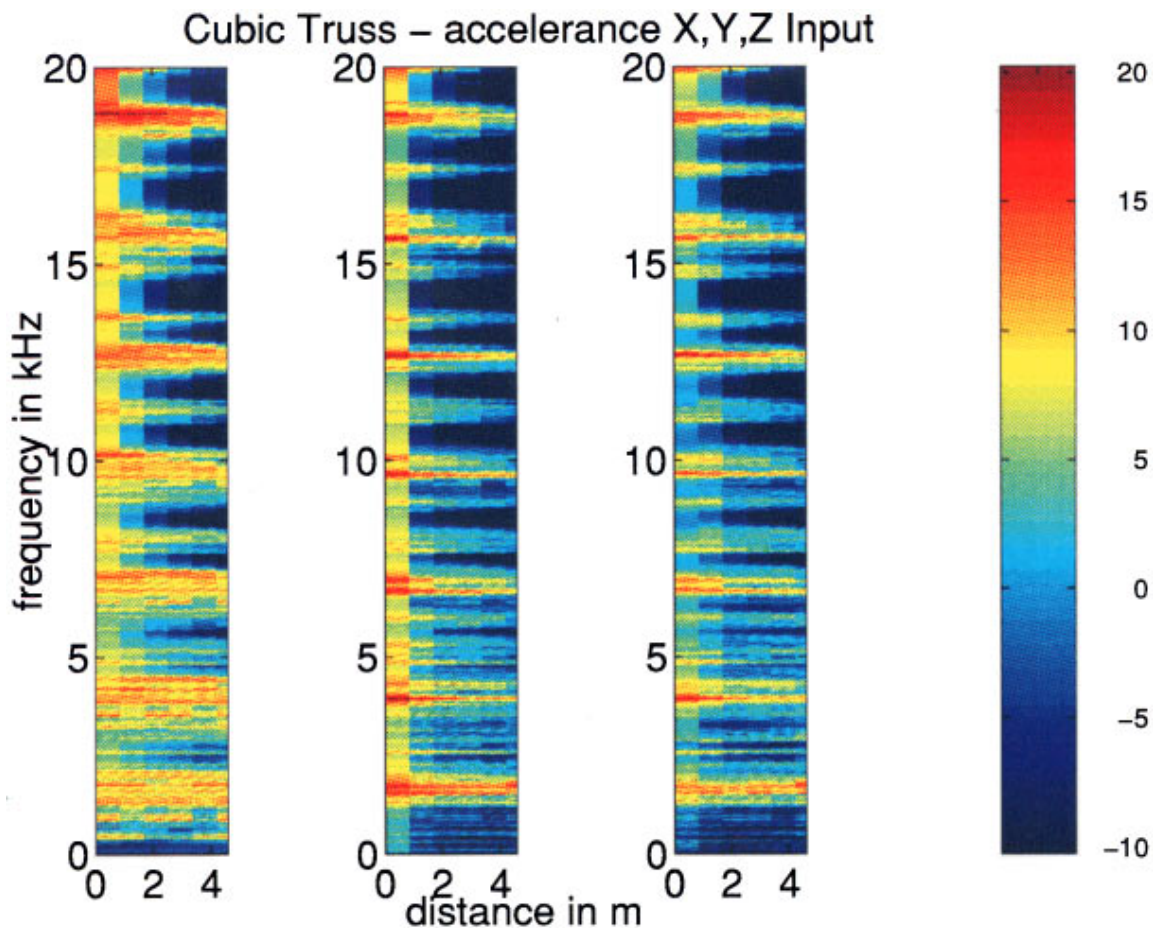


FIG. 5. Accelerance in dB *re*: 1 m/s²/N versus axial distance and frequency for *cubic truss*. Panels represent input force in the X, Y, and Z directions from left to right.

II. EXPERIMENTAL RESULTS

A. Frequency response of the cubic and rectangular trusses

To determine the overall spatial and frequency response of the *cubic truss*, it was forced at joint A1 and the resulting accelerations were measured at each of the 24 joints in three directions. It was found that no particular output direction dominated the response, so results will be presented as a magnitude of the three output directions. Also, except for the forced joint, all joints at the same axial location on the truss respond similarly. Therefore, the results will be averaged over the joint locations and shown as a function of axial location only.

Figure 5 shows the magnitude of the accelerance averaged over joints A–D. Accelerance is defined as acceleration as measured at a truss joint divided by the input force at A1. The color levels are dB *re*: 1 m/s²/N. The *x* axis is axial distance along the truss, where the forcing is at 0 m. The *y* axis is frequency in kHz. The three panels represent input forcing in the X, Y, and Z directions, respectively, from left to right.

There are a number of observations to be made about this data. Regardless of the forcing (or measurement) direction, the frequency response shows a similar characteristic of periodic resonances. The X-directed (axial) force tends to inject power farther into the truss, while the Y and Z (trans-

verse) forces tend to energize the truss cross section local to the source. The X-input resonances are also much wider than the other two. This is due to the direct excitation of wide compressional resonances versus narrow flexural resonances and will be discussed further in the DGSM modeling section. Note that the Y and Z responses are nearly identical, as should be the case for this symmetric truss. There is also a strong decay of accelerance level with axial distance at non-resonant frequencies.

A more quantitative view of the data is shown in Fig. 6. This shows the average attenuation of acceleration in dB per bay in the *cubic truss* versus frequency in 100-Hz bands. The solid line is due to the axially directed X force and the dashed due to the Y force. Notice that there seems to be two distinct processes at work in the truss, creating two sets of overlapping resonances. The first has very little decay and is periodic with regions of resonant transmission at approximately 1, 4, 7, 9, 12.5, 15.5, and 18.5 kHz. The other process which shows a strong decay with frequency and has visible regions of resonant transmission at 5, 8, 11, 13.5, 15, 16, and 17.5 kHz and presumably additional regions in between which are obscured by the regions previously described.

To demonstrate the effect of member length on this resonant structure, the same measurements were made on the *short cubic truss* whose members had a 48-cm exposed

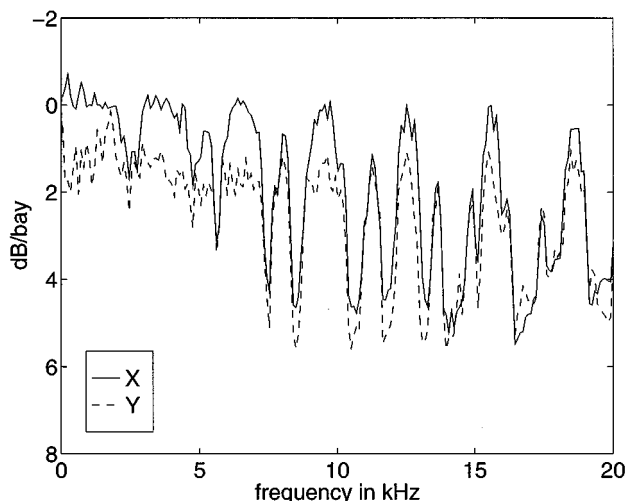


FIG. 6. Average attenuation in *cubic truss*, in dB per bay versus frequency in 100-Hz bands, for input force in the X and Y directions.

length, a factor of 0.6 shorter. As before, the data for this truss are very consistent across measurement direction and joint cross section location. Therefore, only the reduced data will be presented here. Figure 7 shows the average attenuation in the *short cubic truss* in dB per bay versus frequency in 100-Hz bands. The solid line is due to the axially directed X force, dashed is due to the Y force. As before there seem to be two distinct processes at work in this truss. The first has very little decay and is periodic with regions of resonant transmission at approximately 2, 6, 11, and 16 kHz. The other process shows a strong decay with frequency and has visible regions of resonant transmission at 5, 7, 9, 13, 15, 17, and 19 kHz and presumably additional regions in between which are obscured by the above regions. Notice here that the frequency response from 166 Hz to 20 kHz is a scaled version of the low-frequency region of Fig. 6 from 100

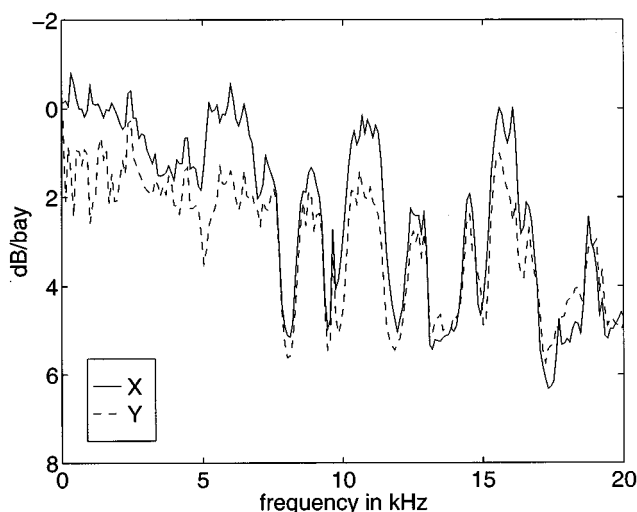


FIG. 7. Average attenuation in *short cubic truss*, in dB per bay versus frequency in 100-Hz bands, for input force in the X and Y directions.

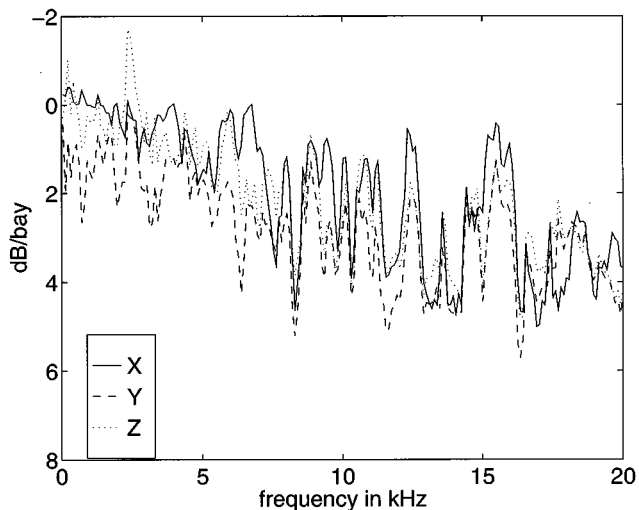


FIG. 8. Average attenuation in *rectangular truss*, in dB per bay versus frequency in 100-Hz bands, for input force in the X, Y, and Z directions.

Hz–12 kHz, which is due to the scaling of the truss by a factor of approximately 0.6.

Each of these trusses has formed a mechanical comb filter over frequency, which is not very surprising given their periodic nature. However, the resonant peaks in this response are undesirable, since a noisy machine vibrating at these frequencies will transmit energy without attenuation through the truss and to the hull. Conversely, the antiresonances of the response are highly desirable, since the truss will block energy transmission to the hull at these frequencies. As the above two trusses demonstrate, the separation between resonances is dependent on the strut length only. This suggests that by cascading struts of varied length, it may be possible to design a truss response that blocks most frequencies.

To demonstrate the value of this technique, the same measurements were made on the *rectangular truss* of Fig. 3. This truss is a mix of the two strut lengths examined above. These data are very consistent across measurement direction and joint cross section location. Therefore, only the reduced data will be presented here. Figure 8 shows the average attenuation in dB per bay in the *rectangular truss* versus frequency in 100-Hz bands. The solid line is due to the axially directed X force, dashed is due to Y, and dotted is due to Z, shown since the truss is no longer Y–Z symmetric. Note that there is no clear set of periodic resonances in the frequency response, since there are now two length scales at work in the truss. More importantly, there is now a clear trend to the attenuation, which rises 3 dB per bay over the 20-kHz bandwidth. This was the reason for mixing different strut lengths.

The frequency response of the *rectangular truss* can be decomposed into a cascade of two “filters,” the response of the *cubic truss* and that of the *short cubic truss*, since it contains both strut lengths. In electronic filter design, cascading filters is equivalent to multiplying their frequency spectra together.¹⁰ Figure 9 demonstrates this idea for the X-directed force only. The X-input attenuation curves from Figs. 6 and 7 were multiplied together and the square root taken. The resulting curve is shown as the dashed line of Fig. 9. The

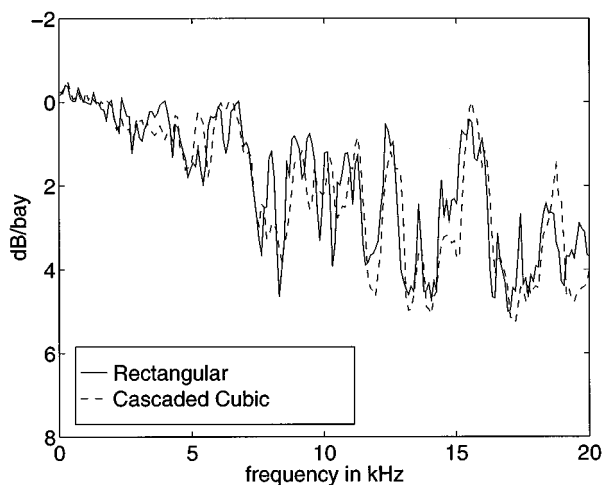


FIG. 9. Average attenuation for X input in dB per bay versus frequency in 100-Hz bands. *Rectangular truss* response (solid) is compared to cascade of *cubic truss* and *short cubic truss* responses (dashed).

solid line is the X -input attenuation from the rectangular truss of Fig. 8. The agreement between these curves is excellent. This shows that the response of any truss can in theory be approximated by combining the response of the component pieces.

The implication of this procedure on the frequency response of trusses is worth comment. These systems tend to have fairly wide low-frequency resonances and fairly sharp high-frequency resonances for reasons that will be addressed in the DGSM modeling section. This means that combining such sections of widely varying size will have the effect of reinforcing the low frequencies and nulling out the high frequencies. This will result in a general low-pass characteristic for the overall response.

B. Frequency response of the pyramid truss

This section explores the response of a truss which eliminates the continuous axial members, such as those that run the length of the *cubic*, *short cubic*, and *rectangular truss* designs. The *pyramid truss* of Fig. 4 is a nonpractical, but fully 3-D structure with three different strut lengths, two of which were used construction of the *rectangular truss*. Notice that the angles between short rods in the X - Y plane are right angles, requiring complete interchange of energy between flexural and compressional waves at these joints. The angles between the long rods in the X - Z plane are approximately 52° . It is therefore possible to couple both compressional and flexural waves all the way down the truss axis through these struts.

To determine the overall spatial and frequency response of the *pyramid truss*, it was forced at joint b1 and the resulting accelerations were measured at each of the central joints in three directions. Auxiliary measurements have shown this set of joints to be representative of all joints in each axial cross section. As observed in the cubic trusses, the data here too are very consistent across measurement direction and cross section. Therefore, only the reduced data will be presented here. Figure 10 shows the average attenuation in the

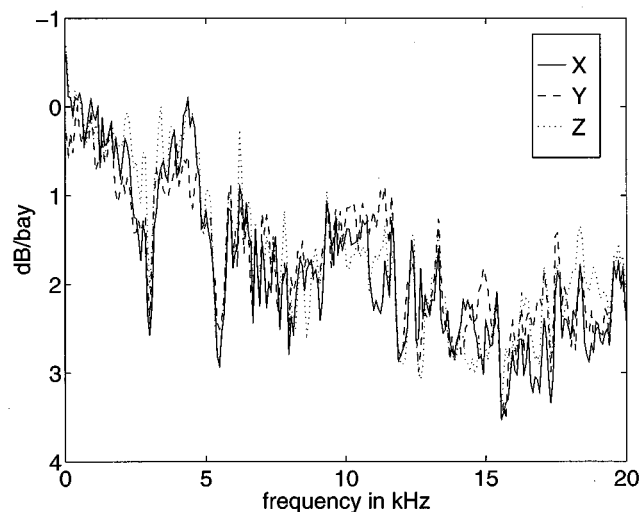


FIG. 10. Average attenuation in *pyramid truss*, in dB per bay versus frequency in 100-Hz bands, for input force in the X , Y , and Z directions.

pyramid truss in dB per bay versus frequency in 100-Hz bands. The solid line is due to the axially directed X force, dashed is for the Y force, and dotted is for the Z force.

The response of this truss is difficult to decompose, since the 45° and 52° angles in the structure thoroughly mix the responses of the various wave types on the various strut lengths and introduce coupling losses. The filtering effect caused by multiple member sizes in the *rectangular truss* is also present here. It is complicated by a similar filtering effect which takes place between the compressional and flexural waves coupled at an angled joint. Notice, however, that there are wide compressional resonances present in the response of the *pyramid truss* for frequencies below 7 kHz where the compressional wavelength is longer than the long struts. These are very reminiscent of those observed on the *cubic truss*. Above 7 kHz, there is an average 2 dB per bay attenuation level. This loss demonstrates the value of eliminating long axial runs in truss design.

III. DGSM MODEL AND RESULTS

The trusses in this paper were modeled by a direct global stiffness matrix method, used previously at MIT by Fricke and Hayner.¹¹ It is similar in nature to other wave propagation methods.^{8,12,13}

The DGSM models the joints as separate elements with 6 degrees of freedom, inertia and rotational inertia in three directions. The struts are modeled as wave-bearing members which can support compressional, torsional, two orthogonal flexural, and two orthogonal evanescent wave types. At each frequency, a stiffness formulation, relating forces and moments to displacements and rotations at the end of each strut, is constructed for each wave type. Each joint/strut interface is modeled as a point connection where displacement, rotation, force, and moment boundary conditions are enforced. A single stiffness matrix, K , for all of the struts in the truss is assembled and inverted. The displacements and rotations, U , at each interface are thus available by applying a force and

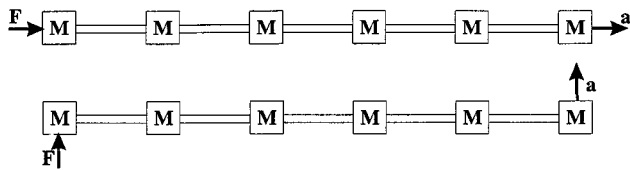


FIG. 11. Compressional rod model (top) and flexural rod model (bottom).

moment vector, F , to this Global matrix via $U = K^{-1}F$. The calculation is then stepped along in frequency to assemble a total truss spatial and frequency response.

A. Mass studies

The DGSM code was run on a simple lineal model to identify the basic resonance structure of the *cubic truss*. First, mass studies were performed to understand the widening of the resonances at low frequency. All models used the nominal aluminum material properties listed in Sec. I A.

The model used was five rods of identical length, $l = 81.5$ cm, laid end to end along the X axis and joined at a joint having varying mass, M . The model was run for no mass, $M = 0$, effectively infinite mass, $M = 1$ kg, and mass equal to the nominal experimental *cubic truss* joint mass, $M = 51.5$ g. First, the model was excited by a force in the X direction, which generated pure compressional waves (see top of Fig. 11). Figure 12 shows the attenuation of axial acceleration in dB per bay versus frequency. The three lines are for the three mass cases listed above. The infinite mass case gives the compressional resonant structure that would be observed for a single rod of length $l = 81.5$ cm. The zero mass case gives the compressional resonant structure that would be observed for a single rod of length $l = 4.075$ m $= 5 \times 0.815$ m. The nominal joint masses modify this structure to something in between the two. In particular, this response looks like the infinite mass case at high frequency with the regions of resonant transmission *extended* in frequency. For an *infinite* periodic system, the start points of these regions are shown in Ref. 9 to correspond to frequency

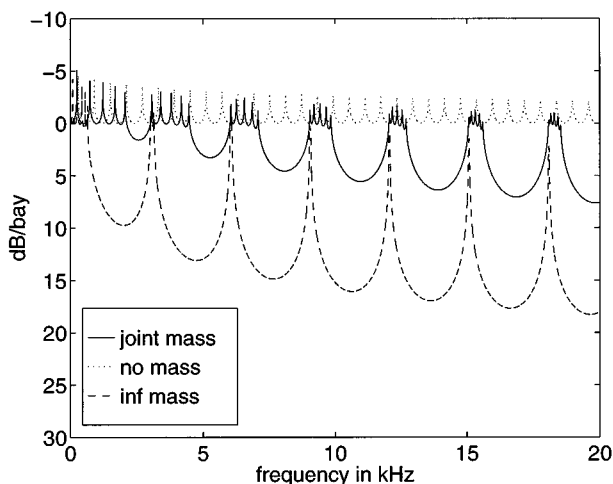


FIG. 12. Mass study on compressional waves in a long rod with masses.

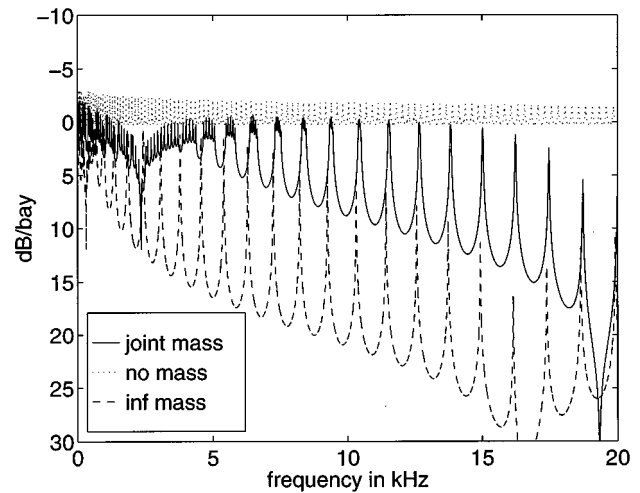


FIG. 13. Mass study on flexural waves in a long rod with masses.

points where $k_l l = n\pi$ for $n = 0, 1, 2, \dots$, where k_l is the compressional wave number and l is the strut length. These frequencies are $f = 3124n$ Hz for this example. It was also shown in this reference that these regions narrow as frequency increases and as the ratio of mass to strut mass increases. This is in perfect agreement with the numerical data of Fig. 12. In addition, in the nominal joint mass case, the transmission regions contain many smaller peak structures, in this case five, equal to the number of rods in the entire structure. This is how the finite nature of the structure is manifested in the response. This numerical data and theory is consistent with data observed on the *cubic truss* (see Fig. 6). Even the five distinct peaks can be seen in the experimental data at low frequencies. At high frequency, the data resolution prevents observation of these separate peaks.

Next, the rod model was excited with a transverse Y force which generated pure flexural waves (see bottom of Fig. 11). Similarly, Fig. 13 shows the attenuation of transverse acceleration in dB per bay versus frequency. The three lines are for the three mass cases listed above. The joint mass case is basically a combination of the infinite and zero mass case. At low frequencies for the two nonzero mass curves, the attenuation shows a large maximum. This is consistent with analysis in Ref. 9 which shows, for an infinite beam with a single mass excited in bending, that this frequency corresponds to a minimum in the flexural wave transmission. This occurs when $\lambda_f \approx \sqrt{\Theta/m}$, where λ_f is the flexural wavelength and m and Θ are the mass and radius of gyration of the blocking mass, respectively. This study shows that the resonant structure of a simple system can be greatly modified by the presence of discontinuities, in this case provided by mass, along its axis.

B. Cubic truss model

The above results for the nominal cubic truss joint mass are shown together on the same graph in Fig. 14. The solid line shows the axial attenuation for an X -directed force and the dashed line shows the transverse attenuation for a Y -directed force. For this symmetric numerical model, only

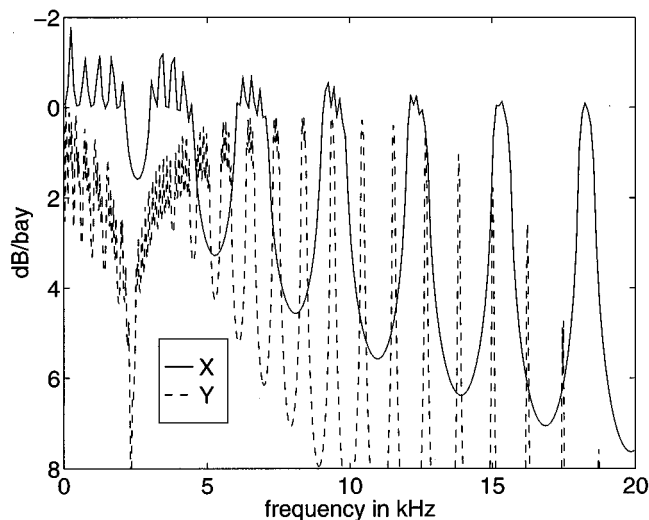


FIG. 14. Attenuation in *DGSM cube truss rod model* in dB per bay versus frequency in 100-Hz bands for input force in the X and Y directions. Model is a rod with six equally spaced masses.

compressional waves are generated by the X-directed force. The resonances in the frequency domain line up with the widely spaced peaks of the response of the *cubic truss* (see Fig. 6). Likewise, only flexural waves are generated by the Y-directed force. The resonances in the frequency domain now line up with the narrowly spaced peaks in the response of the *cubic truss* in Fig. 6. This modeling shows that most of the energy is carried down the truss in the compressional resonant structure and a lesser amount in the flexural resonant structure.

Finally for completeness, the DGSM was used to model the cubic truss in its entirety. The nominal strut and joint locations were entered into the model. A damping factor of $\eta=0.001$ modified the material modulus. The solid line of Fig. 15 shows the DGSM calculation of average attenuation in the cubic truss in dB per bay versus frequency due to an axially directed X force. This plot compares very well with

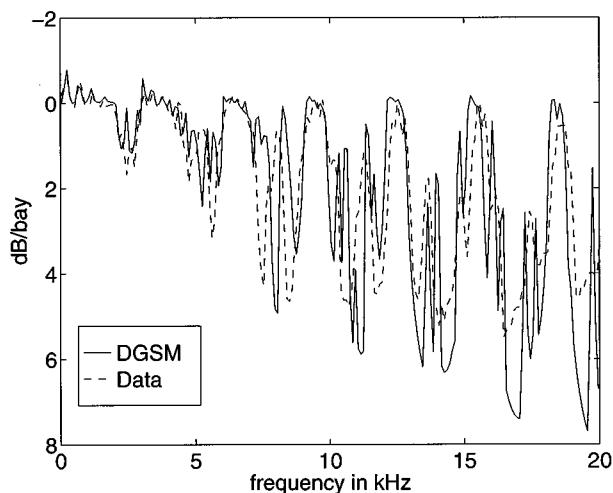


FIG. 15. Average attenuation in *DGSM cube truss model* in dB per bay versus frequency in 100-Hz bands for input force in the X direction. Model of nominal *cubic truss* configuration (solid) versus data (dashed).

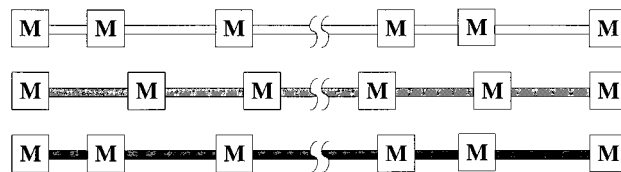


FIG. 16. Models for Fig. 17: 20 random length undamped members with mean length $L=1$ m (top); 20 uniform length damped members, $\eta=0.04$ and $L=1$ m (middle); and 20 random length damped members with mean length $L=1$ m and $\eta=0.04$ (bottom).

the experimental data, shown as the dashed line, and validates the DGSM model.

C. Random length model

In order to extend this idea of filtering by truss member lengths identified in the *rectangular truss*, several numerical studies were made. Figure 16 shows the three cases considered. The top configuration is a lineal truss model made of 20 random length rods joined by the nominal *cubic truss* joint masses, excited in compression. This model is a typical realization of struts chosen from a uniform distribution of lengths from 0–2 m, giving a mean of 1 m. The damping factor is $\eta=0$ in this calculation, so all decay comes from the filtering effect of the struts. The solid black line of Fig. 17 shows the average attenuation in dB per bay versus frequency for this model. Note the general low-pass characteristic. The rise in attenuation of 6 dB per bay over the 20-kHz bandwidth amounts to a significant benefit in terms of vibration reduction.

The random model is compared to the model shown in the middle of Fig. 16, a lineal truss model where all 20 members were the same length with $L=1$ m. The dashed black line of Fig. 17 shows the average attenuation in dB per bay versus frequency for this model. In this case, a constant

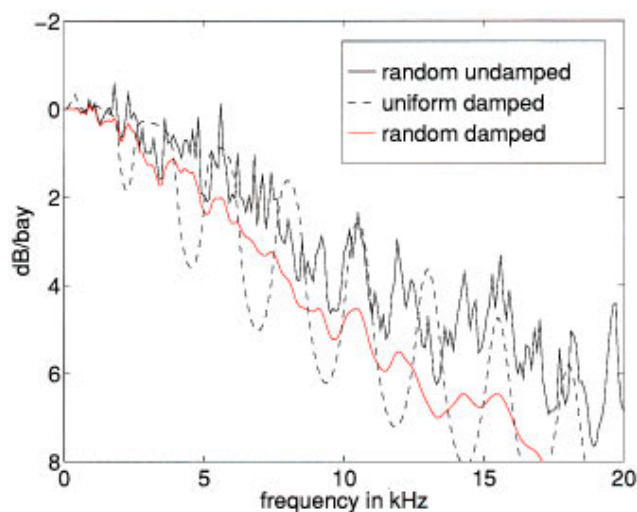


FIG. 17. Attenuation in *DGSM random member model* in dB per bay versus frequency in 100-Hz bands for input force in the X direction: 20 random length undamped members with mean length $L=1$ m (black solid); 20 uniform length damped members, $\eta=0.04$ and $L=1$ m (black dashed); and 20 random length damped members with mean length $L=1$ m and $\eta=0.04$ (red solid).

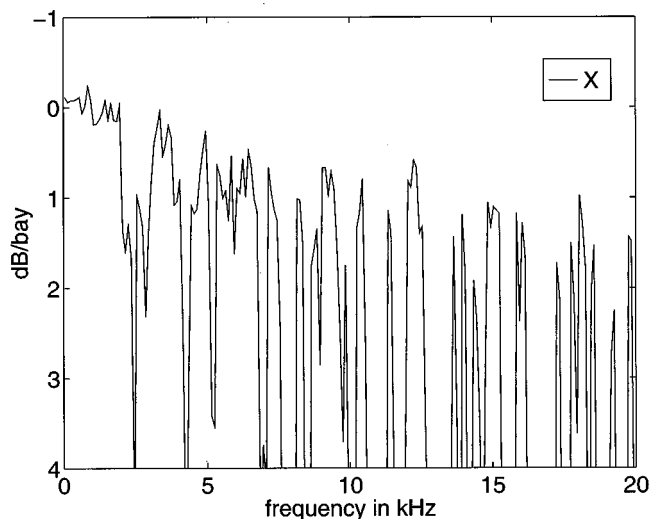


FIG. 18. Attenuation from joint b1 to joint b11 in DGSM model of the pyramid truss, in dB versus frequency in 100-Hz bands for input force in the X direction.

damping factor of $\eta=0.04$ was applied via the material modulus in order to provide equivalent decay versus frequency for the resonant peak structure. This shows that the filtering effect can be as effective as damping and described in damping terms.

The configuration shown in the bottom of Fig. 16 is the same random realization as the first, this time with the additional damping factor of $\eta=0.04$. The solid red line of Fig. 17 shows the average attenuation in dB per bay versus frequency for this model. Notice that the added damping provides only incremental attenuation. This is because additional damping widens resonant peaks and therefore works against the filtering effect.

D. Pyramid truss model

Finally, the DGSM was used to model the pyramid truss in its entirety. The nominal strut and joint locations were entered into the model. A damping factor of $\eta=0.001$ modified the material modulus. Figure 18 shows the attenuation of acceleration from joint b1 to joint b13 in the pyramid truss model versus frequency due to an axially directed X force. This plot should be compared with the experimental data of Fig. 10. The numerical modeling in this case is not as accurate as the modeling of the *cubic truss*, probably due to the fact that the joint/strut interfaces were modeled as point connections and joint eccentricity was not taken into account. This should gravely underestimate the flexural transmission and thus the overall truss response.

IV. CONCLUSIONS

This paper has described a set of experimental and numerical studies made to investigate the basic vibrational properties of undamped, three-dimensional truss structures. The direct global stiffness matrix numerical model was shown to be an effective tool for understanding the spatial and frequency characteristics of truss structures, when used in conjunction with experimental data.

The periodic nature of trusses causes them to act as mechanical comb filters in frequency with 3–5 dB per bay of attenuation at nonresonant frequencies. Numerical analysis of the experimental data showed that, in trusses with long runs of axial struts as are found in most practical truss designs, energy is carried down the truss axis primarily by the compressional resonances of the concatenated axial struts. This mechanism was greatly diminished in the *pyramid truss*, where no such long axial runs existed.

The spacing of the resonant peaks is controlled by the strut lengths within the truss. This suggested a filtering strategy where varying the strut lengths was used to reduce the overall truss response via destructive interference of the frequency resonance structures of the individual struts. This was demonstrated experimentally in the *rectangular truss*. This also showed that, in principle, the frequency response of any truss can be approximated by combining the response of its component pieces. Numerical modeling showed that the multiple periodicities at work in the truss and impedance discontinuities at the truss joints cause the resonant peaks at low frequencies to widen significantly. This causes trusses with varied strut lengths to have a low-pass frequency characteristic. A further study with random strut lengths showed that the observed low-pass filtering effect can be compared to an equivalent applied damping. The 6 dB per bay of attenuation at the highest frequency was seen in this case, which is an impressive number for vibration control.

In summary, trusses can be an effective isolation system, particularly at higher frequencies, where wavelengths are much smaller than the strut members. However, designers should be careful *not* to include axial periodicities when applying truss technology. Damping treatments should be used in conjunction with mixed axial member sizes to maximize truss performance.

ACKNOWLEDGMENTS

I wish to acknowledge the Office of Naval Research and the Advanced Research Program Administration for financial support of this research. I would also like to express my warmest thanks to Professor Ira Dyer of MIT for his personal and technical support.

¹D. Branthonne, "Influence of dynamic absorbers on a three dimensional truss," Master's thesis, Massachusetts Institute of Technology, 1994.

²D. Warwick and D. Feit, "An evaluation of polyethylene beads as a damping treatment for tubular truss structures," CDNSWC Report CDNSWC-SIG-94-146-7250, Oct. 1994.

³R. L. Frink, "Dynamic behavior of multi-legged pinned and rigid structural joints," Master's thesis, Massachusetts Institute of Technology, 1995.

⁴K. Machens and I. Dyer, "Energy partitioning in a truss structure," *Acustica* **1**, 1–2 (1996).

⁵M. R. A. Heath, "Dynamic behavior of a three dimensional aluminum truss in free space," Master's thesis, Massachusetts Institute of Technology, 1994.

⁶J. Park, "Spatial spectral analysis of elastic waves in a three-dimensional truss structure," Master's thesis, Massachusetts Institute of Technology, 1996.

⁷L. Brillouin, *Wave Propagation in Periodic Structures* (Dover, New York, 1946).

⁸D. J. Mead, "A general theory of harmonic wave propagation in linear periodic systems with multiple coupling," *J. Sound Vib.* **27**, 235–260 (1973).

- ⁹L. Cremer, M. Heckl, and E. E. Ungar, *Structure-Borne Sound* (Springer-Verlag, Berlin, 1988), 2nd ed.
- ¹⁰W. M. Siebert, *Circuits, Signals and Systems* (McGraw-Hill, New York, 1986).
- ¹¹J. R. Fricke and M. A. Hayner, "Direct global stiffness matrix method for 3-D truss dynamics," in ASME 15th Biennial Conference on Mechanical Vibration and Noise, September 1995.
- ¹²A. H. von Flotow, "Disturbance propagation in structural networks," *J. Sound Vib.* **106**, 433–450 (1986).
- ¹³Y. Yong and Y. K. Lin, "Dynamic response analysis of truss-type structural networks: A wave propagation approach," *J. Sound Vib.* **156**, 27–45 (1992).

Transmission of sound across a trusslike periodic panel; 2-D analysis

Michael El-Raheb

The Dow Chemical Company, Midland, Michigan 48674

Paul Wagner

1020 Crestview Drive, Pasadena, California 91107

(Received 6 January 1997; accepted for publication 28 May 1997)

Transmission of sound across a 2-D trusslike periodic panel in contact with an acoustic fluid on both its faces is analyzed. Elastic frequency response of the panel made of repeated cells is expressed using transfer matrices of the unit cell, and acoustic pressure of the fluid is expressed using a source boundary element method. Transmission loss (TL) of a panel is computed for two geometries and compared with measurements. These comparisons reveal differences that result from attenuation zones due to periodicity along one axis of the panel and response that is predominantly along the other axis. Conditions under which these differences disappear are explained. A nondimensional parameter, including the ratio of sound speeds in solid and fluid and the ratio of panel length to radius of gyration of the cross-section controls the drop in TL at coincidence, called strength of coincidence. © 1997 Acoustical Society of America. [S0001-4966(97)05609-9]

PACS numbers: 43.40.Rj, 43.40.Dx, 43.55.Rg [CBB]

INTRODUCTION

The refinement of extrusion techniques for light weight transparent materials like polycarbonate has generated an expanding number of new applications requiring translucence, structural integrity, and thermal and sound isolation. Since simple flat sheet cannot meet all of these requirements, a composite panel of cellular construction along one axis, called the periodic axis, and homogeneous along the axis of extrusion has been suggested [see Fig. 1(a)]. This construction raises structural stiffness considerably, and reduces thermal transmission because of the cavity in a cell.

The sound isolation properties of this construction are the subject of this paper. Frequency response of a 2-D model of the trusslike panel with cellular periodicity was the subject of Ref. 1. This reference presents a detailed parametric study of the effects on frequency response from cellular periodicity, panel curvature, imperfection of members in a cell, elimination of the diagonal member, water filling the cell, and damping by constrained visco-elastic layers. The cellular periodicity along one axis of the panel produces propagation and attenuation zones, PZ and AZ, in frequency response. Within the first PZ (PZ1), a 2-D model of a panel strip along the periodic axis displays modes of vibration that include distinctive waviness like the homogeneous plate. As frequency rises, the waviness diminishes and so does response amplitude. A frequency is reached when waviness of the response mode disappears completely, while amplitude continues to fall. This frequency boundary marks the start of AZ1. As frequency rises further, another boundary is reached when waviness reappears, marking the start of PZ2. Boundaries separating PZ and AZ are frequencies where members of a cell resonate. Restricting motions to be along the non-periodic axis only extends PZ1 to infinite frequency. For these modes, it resembles the homogeneous plate.

Reference 2 treated the elastic-acoustic coupling of

complex connected straight and circular thin strips. The analysis adopted transfer matrices to model the elastodynamics of the strip, coupled to acoustic media wetting both surfaces of the strip, and modeled by boundary elements. Comparison of experimental transmission loss, "TL," for a homogeneous flat rectangular panel to that computed for a strip of equal length, thickness, and properties revealed a fundamental relation between frequency response of the plate and strip. Frequency response of a rectangular simply supported homogeneous plate in the x - y plane to a uniformly distributed pressure excitation includes two dominant modes; one with highest wave number along x and lowest wave number along y , and one with lowest wave number along x and highest wave number along y . Each mode closely matches that of a strip of plate along the axis with the highest wave number. This result will explain differences between TL measured across a rectangular panel with periodicity along one axis, and numerical TL of a 2-D strip of that panel along its periodic axis.

When the panel is excited over one face by plane waves at some incidence angle θ from the normal, vibration of the panel produces acoustic pressure over the other face. The ratio of acoustic energy from transmission to that from excitation determines panel transmission loss TL. At normal incidence $\theta=0$, the distribution of incident acoustic pressure over the panel is uniform. At the grazing angle $\theta=\pi/2$, the distribution follows a sinusoidal function with wavelength that of the acoustic field. When wavelengths of acoustic field and vibrating panel coincide, constructive interference magnifies the response amplitude causing TL to fall.

Returning to the 2-D model of the panel strip along its periodic axis, if coincidence frequency occurs within an AZ, then the attenuated response would reduce the drop in TL at coincidence. However, in the panel spanning both axes, response along the nonperiodic axis is not attenuated and forms the dominant part of the response at coincidence,

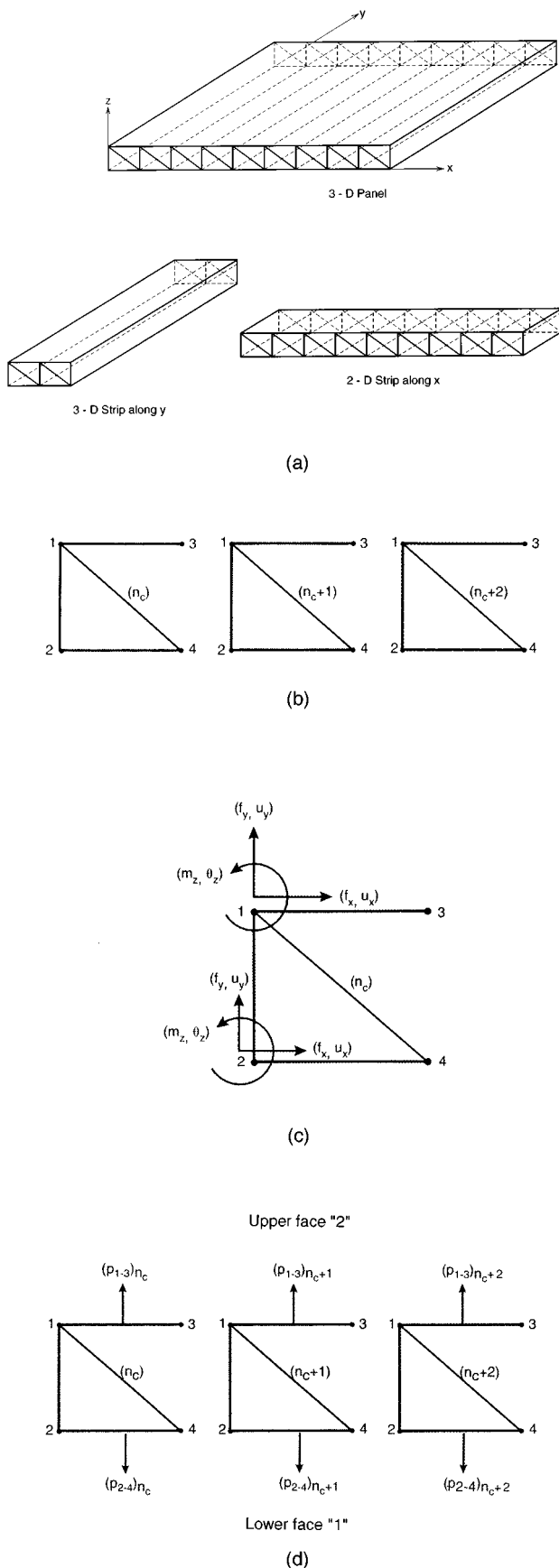


FIG. 1. (a) Panel with cell periodicity along one axis. (b) Corner convention of consecutive cells showing n_c , (n_c+1) , and (n_c+2) disconnected. (c) Cell state vector $S_{c12}(n_c)$ at interface n_c in global coordinates. (d) Acoustic pressure over segments on lower and upper faces of cells.

maintaining the drop in TL. In contrast, if coincidence occurs within a PZ, then the drop in TL is not attenuated, and the 2-D model would not lack this essential feature. However, if coincidence falls within an AZ, an accurate description of sound transmission across the panel requires the superposition of two models; a 2-D model of a panel strip along the periodic axis, and a 3-D model of a panel strip along the other axis. The reason why a 3-D model becomes necessary is given in Sec. II.

To date, no analytical or hybrid methods exist to analyze the coupled elastoacoustic response of composite panels. This class of structures is treated by general purpose computer programs³⁻⁶ which rely on several related computational schemes and differ principally in the simulation of the acoustic field. All programs treat the structural response using finite elements and modal expansion. The displacement vector at the nodal points is expressed as a superposition of eigenfunctions of the undamped structure in vacuum. These modes provide an *a priori* description of the spatial dependence needed to calculate the modal acoustic pressure, its gradient, and modal inner products. Computing these quantities requires the evaluation of multiple integrals which are computationally intensive. Moreover, one limitation of the modal expansion method is high modal density, as is the case for the present panel, restricting the method's utility to frequencies within PZ1. Another limitation is the inadequacy of in-vacuum eigenfunctions to problems where the fluid density is comparable to the structural areal density, or when the material viscoelasticity produces substantial dissipation. These conditions strongly modify resonant frequencies and mode shapes.

This work develops a hybrid method treating the coupled elastoacoustic response of the 2-D trusslike panel with cellular periodicity. The state vector s_c of forces and displacements at two corners of a cell interface is related to s_c at the next interface by the cell transfer matrix T_c according to an analytical solution in the frequency domain of the homogeneous elasto-dynamic equation for each member in the cell (see Ref. 1). This method overcomes the difficulty from high modal density, strong fluid loading, and viscoelastic dissipation since T_c is a frequency-dependent complex matrix accounting for complex valued material properties. The acoustic pressure and its gradient are analyzed using a 2-D Green's function and boundary elements. Since the panel has finite width, a single layer potential over the top and bottom faces of cells in the panel suffice to model the acoustic fields wetting the panel. In contrast, a thin unbaffled strip requires a double layer potential, as explained in Ref. 2. Pressure, assumed constant over a segment formed by the face of a cell, is the sum of influence coefficients multiplied by an unknown source density vector. Concentrated forces from pressure integrated over a segment are assumed to act only at interfaces of cells. Expressing continuity of elastic and acoustic velocities at midpoints of a segment completes the coupling between fluid and panel.

Section I develops the hybrid model of the 2-D panel strip. Section II applies the model to baffled flat panels in which the fluid in contact with the upper face is acoustically isolated from the fluid in contact with the lower face. The

section then compares TL with measured data across rectangular panels with the same construction and material properties. It explains how the difference between measured and computed TL results from attenuation zones due to cell periodicity, response that is predominantly along the nonperiodic axis, and panel size. Section III studies the drop in TL at coincidence, called the strength of coincidence, by introducing the projection function \mathbf{P} which is the integral of the product of incident plane-wave pressure and response mode. The way \mathbf{P} changes with frequency near coincidence leads to a nondimensional parameter $\eta = (l/r_g)/(c_0/c_f)$, where (l/r_g) is the ratio of panel length l to radius of gyration r_g and (c_0/c_f) is the ratio of speeds of sound in solid c_0 and fluid c_f . The strength of coincidence depends on η ; unless η exceeds a threshold, the strength will not be measurable.

I. CONSTRUCTING THE HYBRID METHOD

The hybrid method is made up of three steps. The first step uses transfer matrices of the repeated cell to form the global transfer matrix of the panel relating the ensemble of state vectors at all interfaces of cells to the external excitation, from known point forces and net acoustic pressure, applied at these interfaces. The second step uses influence coefficients to relate the source density applied over each segment to acoustic pressure and its normal gradient. The third step couples the elastic and acoustic fields by requiring continuity of acoustic and elastic velocities at the center of each segment.

A. Analysis of structural response

The 2-D model of a panel strip along its periodic axis is shown in Fig. 1(b). The panel consists of N_c repeated rectangular cells. Cell n_c has four nodes connected by thin members and reinforced by a diagonal along side (1-4) [see Fig. 1(b)]. The two faces of the panel are formed by connecting nodes (1-3) and (2-4) of all cells. Let $\mathbf{S}_{c12}(n_c)$ be the state vector of all forces and displacements along global coordinates at interface (1-2) of cell n_c

$$\mathbf{S}_{c12}(n_c) = \{\mathbf{f}_1, \mathbf{f}_2, \mathbf{g}_1, \mathbf{g}_2\}, \quad (1)$$

$$\mathbf{f} = \{f_x, f_y, m_z\}; \quad \mathbf{g} = \{u_x, u_y, \theta_z\},$$

where forces, moments, displacements, and rotations at corners 1 and 2 are shown in Fig. 1(c). The cell transfer matrix \mathbf{T}_c is defined as

$$\mathbf{S}_{c34}(n_c) = \mathbf{T}_{c12-34}(n_c) \mathbf{S}_{c12}(n_c). \quad (2)$$

Continuity of \mathbf{S}_c at interfaces of cells

$$\mathbf{S}_{c12}(n_c + 1) = \mathbf{S}_{c34}(n_c) \equiv \mathbf{T}_{c12-34}(n_c) \mathbf{S}_{c12}(n_c), \quad (3)$$

combined with constraints at the ends of the panel produces the global tridiagonal transfer matrix \mathbf{T}_G relating the global state vector \mathbf{S}_G of the ensemble of state vectors at all interfaces of cells to the external excitation from known point forces and net acoustic pressure \mathbf{F}_{G0}

$$\mathbf{T}_G \mathbf{S}_G = \mathbf{F}_{G0},$$

$$\mathbf{S}_G = \{\mathbf{S}_{c1}, \mathbf{S}_{c2}, \dots, \mathbf{S}_{cN_c+1}\}^T, \quad (3a)$$

$$\mathbf{F}_{G0} = \{\mathbf{F}_{10}, \mathbf{F}_{20}, \mathbf{0}, \mathbf{F}_{30}, \mathbf{0}, \dots, \mathbf{0}, \mathbf{F}_{N_c+1,0}\}^T,$$

$$\mathbf{T}_G = \begin{bmatrix} -\mathbf{I} & \mathbf{Z}_1 & \mathbf{0} & \mathbf{0} \\ \mathbf{t}_{11}^1 & \mathbf{t}_{12}^1 & -\mathbf{I} & \mathbf{Z}_2 \\ \mathbf{t}_{21}^1 & \mathbf{t}_{22}^1 & \mathbf{0} & -\mathbf{I} & \mathbf{0} & \mathbf{0} \\ \mathbf{0} & \mathbf{0} & \mathbf{t}_{11}^2 & \mathbf{t}_{12}^2 & -\mathbf{I} & \mathbf{Z}_3 \\ & & \mathbf{t}_{21}^2 & \mathbf{t}_{22}^2 & \mathbf{0} & -\mathbf{I} \\ & & & & \vdots & \vdots \\ & & & & & \mathbf{t}_{11}^N & \mathbf{t}_{12}^N & -\mathbf{I} & \mathbf{Z}_N \\ & & & & & \mathbf{t}_{21}^N & \mathbf{t}_{22}^N & \mathbf{0} & \mathbf{I} \\ & & & & & \mathbf{0} & \mathbf{0} & -\mathbf{I} & \mathbf{Z}_{N+1} \end{bmatrix}. \quad (3b)$$

In (3b)

$$\begin{bmatrix} \mathbf{t}_{11}^j & \mathbf{t}_{12}^j \\ \mathbf{t}_{21}^j & \mathbf{t}_{22}^j \end{bmatrix} \equiv \mathbf{T}_{cj}$$

are the four submatrices forming the transfer matrix of the j th cell, \mathbf{T}_{cj} , \mathbf{Z}_j is a (6×6) stiffness matrix connecting the j th interface to a fixed point in space, and \mathbf{I} is the (6×6) unit matrix. Details on the derivation of \mathbf{T}_c and \mathbf{T}_G are included in Ref. 1.

B. Analysis of acoustic response

A source density of constant spatial intensity σ_j is distributed along the j th segment of the 2-D panel made of faces (1-3) or (2-4) of a cell as shown in Fig. 1(d). Acoustic pressure and its normal gradient at the central point of the i th segment with unit normal n_i are given by

$$p_i = \sum_{j=1}^{2N_c} A_{ij} \sigma_j, \quad (4a)$$

$$\frac{\partial p_i}{\partial n_i} = \sum_{j=1}^{2N_c} B_{ij} \sigma_j, \quad (4b)$$

where the sum is over $2N_c$ segments formed by faces (1-3) and (2-4) of all cells, and A_{ij} and B_{ij} are pressure and pressure gradient influence coefficients of the source density over the j th segment. In 2-D,

$$A_{ij} = -\frac{1}{2} \int_0^{s_j} [Y_0(k_f r_{ij}) - iJ_0(k_f r_{ij})] ds, \quad i = \sqrt{-1}, \quad (5a)$$

$$B_{ij} = \frac{k_f}{2} \int_0^{s_j} [Y_1(k_f r_{ij}) - iJ_1(k_f r_{ij})] ds,$$

$$r_{ij} = ((x_i - x_j)^2 + (y_i - y_j)^2)^{1/2}, \quad k_f = \frac{\omega}{c_f}, \quad (5b)$$

where c_f is speed of sound in the acoustic fluid, ω is radian frequency, $s(0 \leq s \leq s_j)$ is an intrinsic coordinate along the j th segment, and J_n , Y_n are Bessel and Neuman functions. As $r \rightarrow 0$, $Y_0(k_f r)$ has a $\ln(r)$ integrable singularity while $Y_1(k_f r)$ has a $(1/r)$ singularity in the form of a Cauchy principal value. Details on the derivation of A_{ij} and B_{ij} are included in Ref. 2.

C. Analysis of coupled response

Let subscripts ‘‘1’’ and ‘‘2’’ refer to quantities on the ‘‘lower’’ and ‘‘upper’’ faces of the panel [see Fig. 1(d)]. Consider an un baffled panel in which the fluid in contact with faces 1 and 2 are connected. Global dynamic equilibrium at all interfaces in the panel is expressed by (3):

$$\mathbf{T}_G \mathbf{S}_G = \mathbf{F}_{G_0} = \bar{\mathbf{p}} + \bar{\mathbf{p}}_0 + \mathbf{F}_0, \quad (6)$$

where $\bar{\mathbf{p}}$ are forces from acoustic pressure on both faces produced by motion of the panel and found by (4a), integrated over segments and acting at interfaces, $\bar{\mathbf{p}}_0$ are known forces from acoustic pressure generated by external acoustic sources, and \mathbf{F}_0 are external point forces. Expressing $\bar{\mathbf{p}}$ in terms of influence coefficients

$$\bar{\mathbf{p}} = \bar{\mathbf{A}}_e \boldsymbol{\sigma}, \quad (7)$$

$\bar{\mathbf{A}}_e$ is the extended pressure influence coefficient matrix where in $\bar{\mathbf{A}}_e(i', j)$ all rows vanish except when

$$i' = 2 + 12(i - 1) \Rightarrow \bar{A}_e(i', j) = A(i, j) \Delta l_i, \quad (7a)$$

$$i' = 5 + 12(i - 1) \Rightarrow \bar{A}_e(i', j) = A(2N_c - i + 1, j) \Delta l_{2N_c - i + 1},$$

where $i = 1, N_c$, and Δl_k is length of the k th segment. The form in (7a) assumes that acoustic elements are ordered as follows [see Fig. 1(d)]:

$$\mathbf{p} = \{(p_{1-3})_1, (p_{1-3})_2, \dots, (p_{1-3})_{N_c}, (p_{2-4})_{N_c}, (p_{2-4})_{N_c-1}, \dots, (p_{2-4})_1\}^T.$$

This means that the ordering of segments is such that pressures on top faces (1-3) of all cells are followed by pressures on bottom faces (2-4) of all cells along the panel strip in a clockwise sense. Substituting (7) in (6) determines \mathbf{S}_G :

$$\mathbf{S}_G = \mathbf{T}_G^{-1} \bar{\mathbf{A}}_e \boldsymbol{\sigma} + \mathbf{S}_0, \quad (8)$$

$$\mathbf{S}_0 = \mathbf{T}_G^{-1} \{\bar{\mathbf{p}}_0 + \mathbf{F}_0\},$$

where \mathbf{S}_0 is a state vector from external acoustic and mechanical excitation. Define \mathbf{M} as

$$\mathbf{M} = \mathbf{T}_G^{-1} \bar{\mathbf{A}}_e, \quad (9)$$

and \mathbf{W} as the reduced version of \mathbf{M} including only rows $8 + 12(i - 1)$ and $12(N_c - i + 1) + 11$; $i = 1, N_c + 1$, which correspond to u_y in \mathbf{S}_c . The reduced (8) takes the form

$$\mathbf{w} = \mathbf{W} \boldsymbol{\sigma} + \mathbf{w}_0, \quad (10)$$

where \mathbf{w}_0 is the reduced vector of \mathbf{S}_0 , including the same rows as \mathbf{W} . Continuity of acoustic and elastic velocities normal to faces requires that

$$\rho_f \omega^2 \mathbf{w} = \frac{\partial \mathbf{p}}{\partial \mathbf{n}}, \quad (11)$$

where ρ_f is the density of acoustic fluid. Invoking (4b) in (11) yields

$$\rho_f \omega^2 \mathbf{w} = \mathbf{B} \boldsymbol{\sigma} + \mathbf{V}_0, \quad (12)$$

where $\mathbf{V}_0 = \partial p_0 / \partial \mathbf{n}$. Eliminating \mathbf{w} from (10) and (12) yields

TABLE I. Panel geometry.

Member	Panel 1		Panel 2	
	l (cm)	h (cm)	l (cm)	h (cm)
(1-3)	1.5	0.1	5.0	0.3
(1-2)	1.62	0.06	4.0	0.2
(2-4)	1.5	0.1	5.0	0.3
(1-4)	2.21	0.03	6.4	0.1

$$\left(\mathbf{W} - \frac{1}{\rho_f \omega^2} \mathbf{B} \right) \boldsymbol{\sigma} = \frac{1}{\rho_f \omega^2} \mathbf{V}_0 - \mathbf{w}_0, \quad (13)$$

which determines $\boldsymbol{\sigma}$, and \mathbf{w} follows from (10). If the panel is flat and baffled then in (13) $\mathbf{B} = \mathbf{I}$, the unit matrix, and \mathbf{A} simplifies to

$$\mathbf{A} = \begin{bmatrix} \mathbf{A}_2 & \mathbf{0} \\ \mathbf{0} & \mathbf{A}_1 \end{bmatrix},$$

where \mathbf{A}_1 and \mathbf{A}_2 are uncoupled pressure influence coefficients on faces 1 and 2 of the panel.

II. RESULTS

The hybrid method is applied to two panels with cell geometries listed in Table I where (l, h) are length and thickness of each member [see Fig. 1(b)]. All panels are made of polycarbonate with material properties

$$E = 2.3 \times 10^9 \text{ Pa}, \quad \rho = 1.2 \text{ g/cm}^3,$$

where (E, ρ) are Young's modulus and mass density. Panel 1 has mass 3.7 kg/m^2 and is 1.5 m long with 100 cells, while panel 2 has mass 10 kg/m^2 and is 1.5 m long with 30 cells. Both panels are simply supported at the ends and include viscoelastic damping in the form of a complex modulus $E_c = E(1 + 0.02i)$. The acoustic fluid is air with $\rho_f = 1.225 \times 10^{-3} \text{ g/cm}^3$ and $c_f = 340 \text{ m/s}$. We define

$$v_{\text{RMS}} = 20 \log_{10} \left[\frac{\omega}{v_{\text{ref}}} \left\{ \frac{1}{N_c + 1} \sum_{j=1}^{N_c+1} |u_{y1}|_j^2 \right\}^{1/2} \right] \quad (14)$$

as the average root mean square velocity along y at corner 1 of all cells normalized by a reference velocity v_{ref} . For illustration, all v_{RMS} plots to follow are calculated for the structure subjected to uniform mechanical excitation without any acoustic coupling. We also define

$$\text{TL}^D = 10 \log_{10} \left| \int_0^{\pi/2} \text{TL}^\theta \cos \theta d\theta \right|, \quad (15)$$

$$\text{TL}^\theta = R_e \int_0^l p v^* ds / (l \cos \theta / \rho_f c_f).$$

Here, TL^D is transmission loss from diffuse sound in dB, TL^θ is the ratio of transmitted to incident acoustic energy, (p, v^*) are acoustic pressure and complex conjugate of acoustic velocity, and l is length of panel. For each panel, frequency response of computed v_{RMS} and TL^D are compared to measured TL^D .

TL was measured experimentally for a rectangular periodic panel with dimensions 1.5 m along the periodic axis and

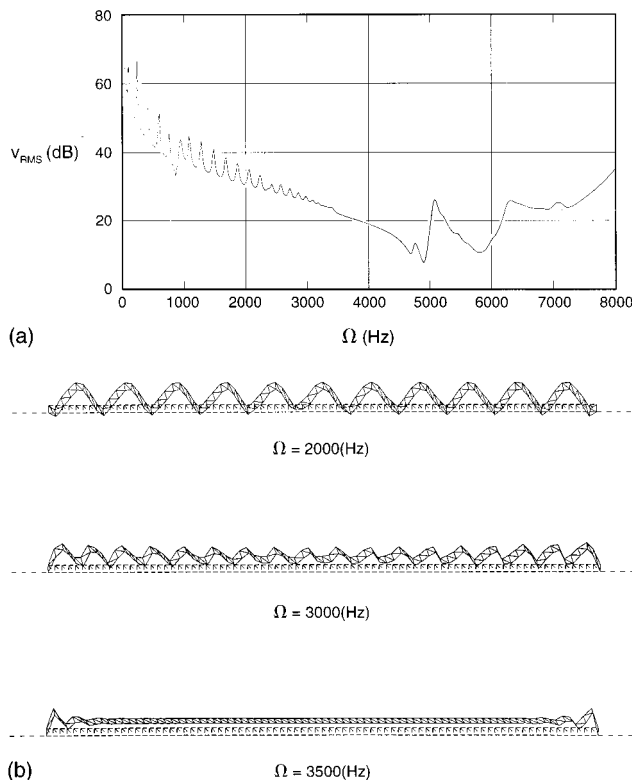


FIG. 2. (a) V_{RMS} (dB) of 2-D panel 1; $l_x = 1.5$ m, 100 cells (1.5×1.62) cm, 3.72 kg/m^2 . (b) Response modes of panel 1 near AZ1.

1.25 m along the nonperiodic axis. The panel was inserted over a window acoustically insulated along its perimeter and separating wall, connecting anechoic receiving and reverberating chambers with volumes 110 m^3 and 215 m^3 , respectively. Measurements were carried out according to ISO 140-3:1995 at the Mook facility of Peutz Consulting Associates in the Netherlands.^{7,8} Instrumentation included B&K sound level meter, Sony TCD-D10 DAT recorder, Jay Bin loudspeakers, Stage Accompany amplifier, and B&K third octave band filter. The sound source simulated a diffuse field. Acoustic velocity levels were measured at four locations with 2-g microphones. The accuracy of measurements was 1 dB.

Figure 2(a) plots v_{RMS} against circular frequency Ω in Hz for panel 1. v_{RMS} diminishes with Ω along an average line with resonant peaks that weaken as AZ1 is approached at 3200 Hz. The AZ is identified by the loss of waviness in response modes as shown in Fig. 2(b). Response reaches a minimum within AZ1 at 4900 Hz followed by a peak at 5100 Hz, marking the start of PZ2. Figure 3 plots TL^D against Ω for panel 1. Computed TL^D exhibits valleys at the same resonant frequencies as v_{RMS} . The peak at 4900 Hz and valley at 5100 Hz correspond to the minimum and maximum response of v_{RMS} and at the same frequencies. Measured TL^D (Ref. 7) follows the same average line as computed TL^D up to 800 Hz. Measured TL^D then bends down reaching a local maximum near 2000 Hz, followed by a dip at coincidence near 4000 Hz. Computed TL^D lacks the coincidence dip at 4000 Hz since this frequency lies within AZ1, which is the interval $3200 \text{ Hz} < \Omega < 5100 \text{ Hz}$. In this interval, response is domi-

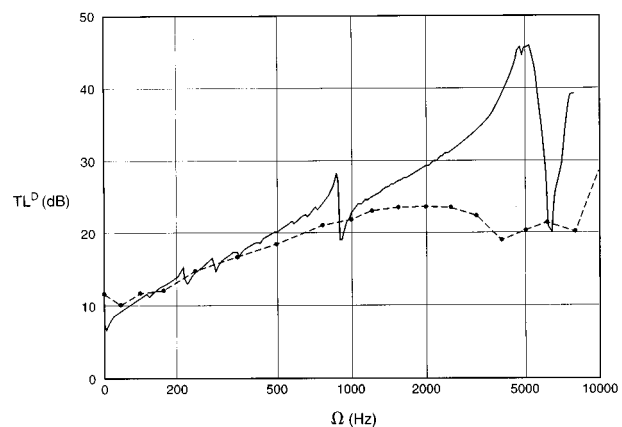


FIG. 3. Calculated and measure TL^D of panel 1; $(l_x, l_y) = (3.6 \times 3.0)$ m, 200 cells (1.5×1.62) cm, 3.5 kg/m^2 ; ——— calculated, ----- measured.

nated by motions along the nonperiodic axis, a feature lacking in the present 2-D model.

It is shown in Ref. 2 that the frequency response of a rectangular simply supported plate to a uniformly distributed pressure excitation includes the following two dominant modes

$$(m_{\text{max}}, 1) \quad \text{and} \quad (m_{\text{min}}, n_{\text{max}}), \quad (16)$$

where (m, n) are wave numbers, n an integer, of the plate response mode along (x, y) defined by

$$w(x, y) \approx \sum_n w_n \sin(k_x x) \sin(k_y y),$$

$$k_x = m\pi/l_x = \sqrt{k^2 - k_y^2}, \quad (17)$$

$$k = \sqrt{\omega/(c_0 r_g)}, \quad k_y = n\pi/l_y,$$

where (l_x, l_y) are lengths of plate along (x, y) , $c_0 = \sqrt{E/\rho(1-\nu^2)}$ is the speed of sound in the material, and $r_g = h/\sqrt{12}$ is radius of gyration of the plate cross section with thickness h . Given an ω , m_{max} is the largest m for $n = 1$ in (17), and m_{min} is the smallest m for the largest $n = n_{\text{max}}$ such that $k_x^2 > 0$ in (17). For a panel with periodicity along x , if mode $(m_{\text{max}}, 1)$ lies within an AZ, $(m_{\text{min}}, n_{\text{max}})$ forms the dominant contribution to TL^D which exhibits the dip at coincidence. Therefore, prediction of TL of the periodic panel near coincidence requires the superposition of two models; a 2-D model of a panel strip along the periodic axis x , and a 3-D model of a panel strip along its other axis.

In order to create conditions where the 2-D model would exhibit a measurable strength of coincidence, it is necessary to shift the boundary of AZ1 to a range of frequencies where it does not overlap coincidence. One way is to raise E of member (1-2) and the diagonal (1-4) of all cells by two orders of magnitude. This raises shear stiffness to such an extent that flexure dominates response allowing the 2-D panel to behave like a homogeneous strip at frequencies comparable to coincidence. Figure 4 plots v_{RMS} against Ω of the modified panel 1. Note that AZ1 now starts at 5200 Hz. Response reaches a minimum at 6100 Hz and peaks at the start of PZ2 at 7300 Hz. Figure 5 plots TL^D against Ω for the

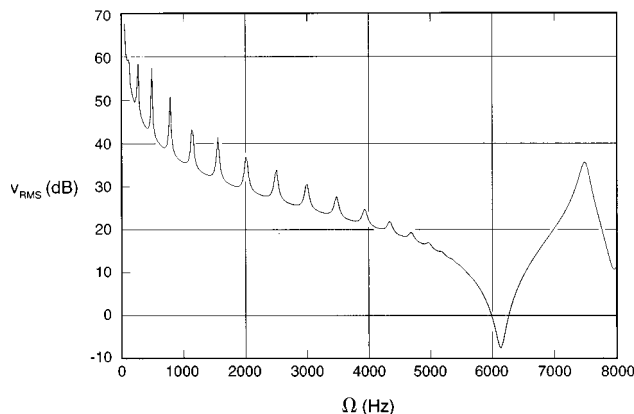


FIG. 4. v_{RMS} (dB) of modified panel 1; $l_x=1.5$ m, 100 cells (1.5×1.62) cm, 3.72 kg/m^2 .

modified panel 1. Now TL^D exhibits a measurable strength of coincidence at 2000 Hz which agrees with the computed coincidence frequency

$$\Omega_c = \frac{1}{2\pi} \frac{c_f^2}{c_0 r_g} = 2039 \text{ Hz}$$

assuming a simplified beamlike model to compute r_g , i.e., $r_g = \sqrt{I_{xx}/A}$, where $I_{xx} = \frac{1}{2} h_{1-3} l_{1-2}^2$ and A = areal density/ ρ . Coincidence is followed by a rise in slope of the TL^D line, a trend which is broken near 5200 Hz when TL^D peaks sharply at 6100 Hz, then falls to a minimum at 7300 Hz. These frequencies correspond to the minimum in AZ1 and the maximum in PZ2 consistent with v_{RMS} shown in Fig. 4. The measured Ω_c at 4000 Hz in Fig. 3 is higher than that of the modified panel 1 at 2000 Hz. This difference is caused by higher flexibility of members (1-3) and (1-4) in the measured panel which reduces the effective r_g along the nonperiodic axis yielding a higher Ω_c . It is the failure of the simplified beamlike approximation of r_g that yields to an Ω_c smaller than that measured by a factor of 2. This leads to the conclusion that a fully 3-D model along the nonperiodic axis is necessary.

Figure 6 plots v_{RMS} against Ω for panel 2. Here AZ1 starts at 1000 Hz and reaches a minimum at 1200 Hz followed by the peak in PZ2 at 1800 Hz. Figure 7 plots TL^D

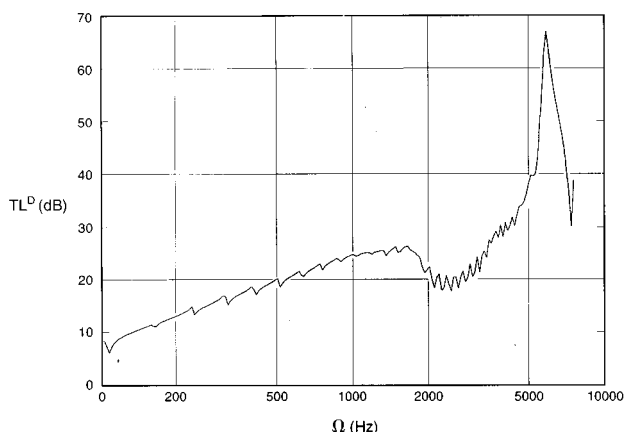


FIG. 5. TL^D of modified panel 1 (diffuse sound); $l_x=1.5$ m, 100 cells (1.5×1.62) cm, 3.72 kg/m^2 .

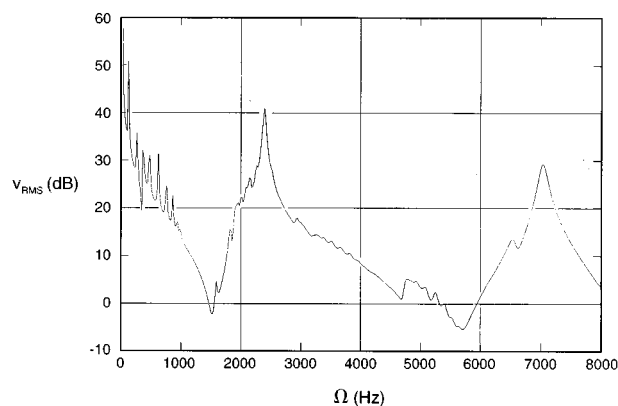


FIG. 6. v_{RMS} (dB) of modified panel 2; $l_x=1.5$ m, 30 cells (5×4) cm, 10 kg/m^2 .

against Ω for panel 2. Computed TL^D peaks at 1200 Hz, falls to a minimum at 1800 Hz, the start of PZ2, then resumes up a steeper line in PZ2. Measured TL^D (Ref. 8) exhibits the expected behavior near coincidence starting at 1000 Hz; bending down of TL^D is followed by a weak dip near 2000 Hz at coincidence, followed by a steeper line past coincidence. The fact that the minimum of the computed TL^D at 2000 Hz lies within PZ2, and the fact that its slope is steeper past coincidence, are consistent with that minimum being the computed coincidence.

Contrasting the weak dip in TL^D at measured coincidence for panel 2 (see Fig. 7) to the stronger dip measured for panel 1 (see Fig. 3) suggests that the two panels differ in some new parameter. Besides dimensions of the unit cell, the two panels differ in size; panel 1 measures 3.6×3.0 m while panel 2 measures 1.5×1.25 m, the first value is along the axis of periodicity. Defining this nondimensional parameter and the threshold needed to attain a measurable strength of coincidence is the subject of the next section.

III. PROJECTION FUNCTION

In the following analysis, the effect on strength of coincidence of panel length and phase velocities in fluid and solid will be evaluated by considering the projection of the acoustic plane wave excitation on the elastic response mode. A homogeneous strip is considered for simplicity, although

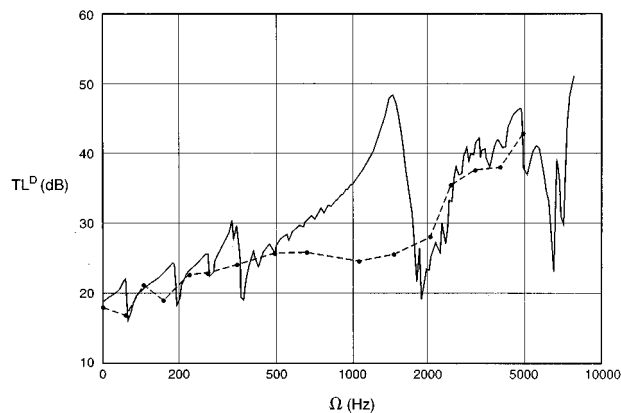


FIG. 7. Calculated and measure TL^D of panel 2; $(l_x, l_y) = (1.5 \times 1.25)$ m, 30 cells (5×4) cm, 10 kg/m^2 ; ——— calculated, ----- measured.

results apply phenomenologically to the periodic panel since the underlying physics is the same. In fact, if the change with frequency of panel radius of gyration is known, then the concept of projection function applies to periodic panels also.

Since coincidence results from the interaction of an incident plane wave with a response mode, the projection of one function onto the other establishes a measure of the drop in TL^D at coincidence. Let P be the projection function defined by

$$P = \int_0^l p_I(x, \omega) \phi(x, \omega) dx, \quad (18)$$

$$p_I(x, \omega) = e^{i\bar{k}_f x}, \quad \bar{k}_f = \frac{\omega}{c_f \sin \theta},$$

$$\phi(x, \omega) = \sin(kx), \quad k = \sqrt{\omega/(c_0 r_g)}.$$

P_I is incident acoustic pressure and ϕ is an approximation to the response mode. Performing the integral in (18) yields

$$P = \frac{\gamma - e^{i\gamma_f}(\gamma \cos \gamma - i\gamma_f \sin \gamma)}{\gamma^2 - \gamma_f^2}, \quad (19)$$

$$\gamma = kl, \quad \gamma_f = \bar{k}_f l.$$

Expressing γ in terms of γ_f reduces (19) to

$$P = \frac{\sqrt{\gamma_f \eta} - e^{i\gamma_f}(\sqrt{\gamma_f \eta} \cos \sqrt{\gamma_f \eta} - i\gamma_f \sin \sqrt{\gamma_f \eta})}{\gamma_f(\eta - \gamma_f)}, \quad (20)$$

$$\eta = (l/r_g)/(c_0/c_f \sin \theta).$$

In (20), P is a function of the single independent variable γ_f and the nondimensional parameter η . At coincidence $\gamma_f = \eta$ and P simplifies to

$$P_c = \lim\{P(\gamma_f, \eta)\} = i(\eta - \sin \eta e^{i\eta})/(2\eta), \quad (21)$$

$$\gamma_f \rightarrow \eta.$$

Define $\mathcal{P} = 10|\log_{10}|P||$ and $\omega^* = \omega/\omega_c$ where $\omega_c = 2\pi\Omega_c$ and Ω_c is coincidence frequency in Hz defined earlier. Figure 8(a) plots \mathcal{P} against ω^* for three values of $\eta = 10, 20, 30$. For $\omega^* < 1$, \mathcal{P} fluctuates about an average line that rises with η . \mathcal{P} then falls to an almost fixed minimum at $\omega^* = 1$. For $\omega^* > 1$, \mathcal{P} increases steeply with ω^* then develops sharp peaks about an average line that increases smoothly with ω^* . The difference

$$\mathcal{P}_r = \max \mathcal{P}(\omega^* < 1) - \mathcal{P}(\omega^* = 1) \quad (22)$$

is a measure of strength of coincidence. For example, a strength of 10 requires $\eta > 23$. Figure 8(b) plots \mathcal{P}_r against η . The steep rise in \mathcal{P}_r near $\eta = 20$ reveals a distinct threshold of η for strong coincidence. For panel 1, $\eta = 113$ consistent with the strong coincidence in Fig. 3, while for panel 2, $\eta = 18.7$ consistent with the weak coincidence in Fig. 7.

IV. CONCLUSION

A hybrid method is developed to analyze transmission of sound across a 2-D trusslike panel with cellular periodicity. Analysis proceeds through elastic response using transfer matrices of the unit cell and through acoustic response using

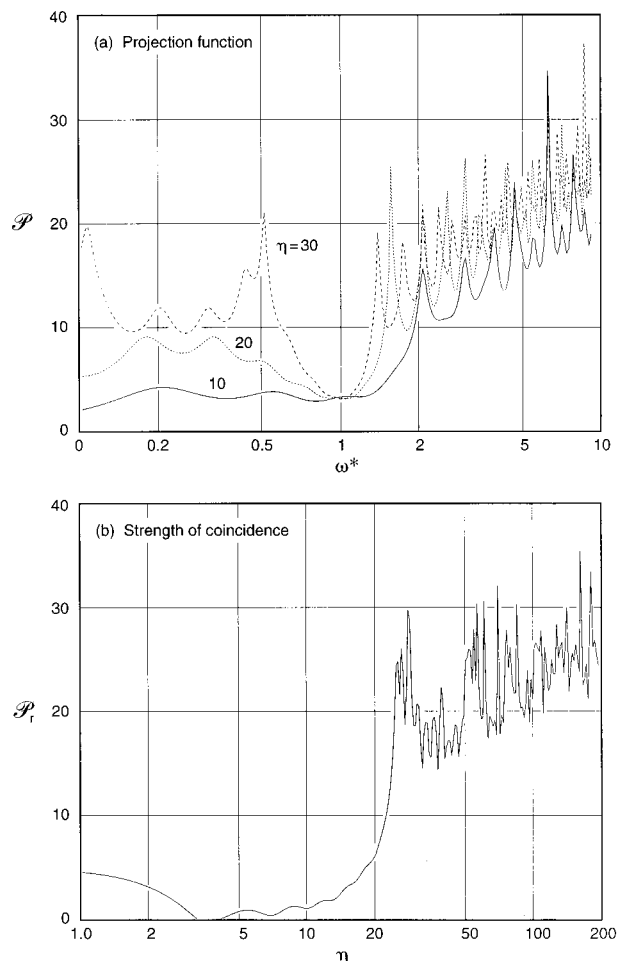


FIG. 8. Projection function and strength of coincidence.

2-D boundary elements. The method succeeds even when modal density is high. Noteworthy results from the simulation of baffled panels are:

- (1) TL computed by the hybrid method agrees with measured TL below AZ1.
- (2) Near coincidence, computed response is attenuated when periodicity produces AZ's that overlap with coincidence. Even with overlap, measured TL includes the distinctive features of coincidence because response is dominated by motions along the nonperiodic axis of the panel.
- (3) A proper simulation of TL across the panel requires the superposition of two models; a 2-D panel strip along the periodic axis, and a 3-D panel strip along the nonperiodic axis.
- (4) A case was constructed where the hybrid model exhibited strong coincidence by raising modulus of interior members of the unit cell shifting the boundary of AZ1 to frequencies above coincidence.
- (5) Except near coincidence, v_{RMS} qualitatively reproduces the TL^D behavior with the prescription that v_{RMS} peaks and valleys become TL^D valleys and peaks.
- (6) A nondimensional parameter η is derived for a homogeneous strip that controls strength of coincidence; unless η exceeds a threshold value, coincidence is weak. If the panel is sufficiently short, the dip at coincidence disappears.

- ¹M. El-Raheb, "Frequency response of trusslike periodic panel; 2-D analysis," J. Acoust. Soc. Am. **101**, 3457–3465 (1997).
- ²M. El-Raheb, "Elasto-acoustics of a two-dimensional thin strip by a hybrid method," J. Acoust. Soc. Am. (in press).
- ³M. A. Hamdi, "Rayon User's Manual," STRACO SA, Compiègne, France (1992).
- ⁴P. Guisset, "SYSNOISE User's Manual," NIT N.V., Leuven, Belgium (1992).
- ⁵F. Sgard and N. Atalla, "GAUSVEM, User's Manual," Version 1, GAUS, Université de Sherbrooke (1992).
- ⁶N. Vlahopoulos *et al.*, "COMET/ACOUSTICS User Document," Automated Analysis, Inc. (July 1994).
- ⁷M. Verkamen, "Laboratory noise measurements on polycarbonate panels," Peutz and Associates consulting firm B. V., Report No. A-456-1 (February 1993).
- ⁸M. Verkamen, "Laboratory measurements of airborne sound insulation according to ISO 140-3:1995 of polycarbonate structural sheet (Calibre 603-3)," Report No. A-688-E (July 1996).

Implementation of an active headset by using the H_∞ robust control theory

Mingsian Bai and Dunjay Lee

Department of Mechanical Engineering, Chiao-Tung University, 1001 Ta-Hsueh Road, Hsin-Chu 30050, Taiwan, Republic of China

(Received 27 August 1996; revised 4 April 1997; accepted 29 May 1997)

This paper presents a methodology for implementing an active headset by using H_∞ robust control theory. The adopted structure is feedback tracking control. Performance, stability, and robustness of the closed-loop system have been taken into account in the design procedure by using a general framework of the H_∞ theory. The resultant controller is realized on the basis of operational amplifier circuitry. Experiments are conducted to test the developed headset. The result shows that the headset achieves broadband attenuation up to approximately 15 dB in the band 200–800 Hz. The design considerations indicated in the experimental result are also addressed. © 1997 Acoustical Society of America. [S0001-4966(97)05709-3]

PACS numbers: 43.50.Ki, 43.38.Si [GAD]

INTRODUCTION

The active noise control (ANC) technique has been an active area in acoustics since Lueg filed his patent.¹ Research efforts have been attempted to put this emerging technology into a great variety of applications, such as headsets, active duct silencers, active noise cancelers in vehicles or aircraft cabins, and so forth.^{2–4} Among the ANC applications, active headsets can be regarded as the most mature and practical from a commercial standpoint.

As opposed to the feedforward control widely used in active duct silencers, feedback control structure is adopted for the design of active headsets. The reason for this is partly because the upstream reference is usually unavailable and partly because the system order is sufficiently low for feedback control to be practical in broadband noise rejection. The conventional design of the controller for active headsets can be dated back to Olson and May,⁵ and also Wheeler.⁶ Their designs were based on classical frequency-domain compensation that relies heavily on heuristically shaping the open-loop frequency response with acceptable margins.

In contrast to the classical compensation, the H_∞ robust control theory based on two Riccati equations (the so-called 1988 approach) is employed in the paper for controller synthesis because it not only provides a unified framework for all control structures, but also yields controllers with guaranteed margins.^{7–12} In addition, the H_∞ theory reveals physical insights into the perturbations and uncertainties of models resulting from system identification, aging of electronic components, environmental changes, nonlinearity, and drifting of acoustic system properties that usually arise in practical applications. These factors might cause deterioration of performance or even of stability. It is then highly desirable to develop an ANC controller capable of accommodating these detrimental effects. To this end, the H_∞ control theory is employed in this study to meet the requirement of robust performance and robust stability optimally in the face of plant uncertainties by choosing proper weighting functions.

The H_∞ controller is realized on the basis of operational

amplifier circuitry to avoid unnecessary time delay that might cause undesired degradation of performance and even stability of the system. Experiments are then conducted to test the developed headset. The result shows that the headset proves to be robust in attenuating broadband noises. The design considerations indicated in the experimental results are also addressed in the conclusion.

1. THEORETICAL BACKGROUND

A. H_∞ robust control theory

A brief review of the H_∞ robust control theory is given in this section. The following derivation contains a fair amount of mathematical definitions and results. Because the H_∞ theories can be found in much control literature,^{7–12} we present only the key ones needed in the development of the ANC algorithm. The rest are mentioned without proof. In addition, since the system model is identified by a parametric procedure in discrete-time domain, we present only the discrete-time H_∞ algorithm.

In modern control theory, all control structures can be described by using a generalized control framework, as depicted in Fig. 1. The framework contains a controller $C(z)$ and an augmented plant $P(z)$. The controlled variable $v(k)$ corresponds to various control objectives $z_1(k)$, $z_2(k)$, and $z_3(k)$, and the extraneous input $w(k)$ consists of the reference $r(k)$, the disturbance $d(k)$, and the noise $n(k)$. The signals $u(k)$ and $e(k)$ are the control input to the plant and the measured output from the plant, respectively. The general input–output relation can be expressed as

$$\begin{bmatrix} V(z) \\ E(z) \end{bmatrix} = \begin{bmatrix} P_{11}(z) & P_{12}(z) \\ P_{21}(z) & P_{22}(z) \end{bmatrix} \begin{bmatrix} W(z) \\ U(z) \end{bmatrix} = P_\gamma(z) \begin{bmatrix} W(z) \\ U(z) \end{bmatrix}, \quad (1)$$

where the submatrices $P_{ij}(z)$, $i, j=1,2$ are compatible partitions of the augmented plant $P_\gamma(z)$ and the symbols are capitalized to represent the Z-transformed variables.

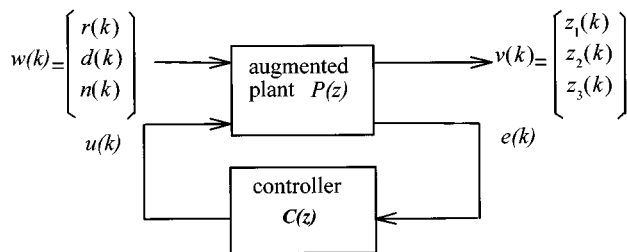


FIG. 1. Generalized control framework.

The rationale of the H_∞ control is to minimize the infinity norm of the transfer function $T_{vw}(z)$ between $v(k)$ and $w(k)$, which can be expressed by the *linear fraction transformation* (LFT) as

$$T_{vw}(z) = \text{LFT}(P_\gamma(z), C(z)) = P_{11}(z) + P_{12}(z)C(z) \\ \times [1 - P_{22}(z)C(z)]^{-1}P_{21}(z). \quad (2)$$

Hence, the mathematical statement of the optimal H_∞ problem reads

$$\min_{C(z)} \|T_{vw}(z)\|_\infty = \min_{C(z)} \sup_{0 \leq \theta < 2\pi} \|T_{vw}(e^{j\theta})\|. \quad (3)$$

However, instead of finding the optimal solution, which is generally very difficult, one is content with the suboptimal solution that can be analytically obtained. This becomes the so-called *standard H_∞ problem*: finding $C(z)$ such that $\|T_{vw}(z)\|_\infty < 1$. Inasmuch as a control problem is cast into the generalized framework, an optimal controller can be synthesized by many H_∞ algorithms. The available algorithms can be divided into two classes: the model matching algorithms (the 1984 approach) and the two Riccati equation algorithms (the 1988 approach). In the study, we use the latter approach, which does not require a chain of factorizations as in the former approach, and thus numerical problems in handling high-order (acoustical) plants can be minimized. Since the computational algorithm contains lengthy algebraic definitions and expressions that are standard in control literature, but are not the emphasis of this paper, we simply refer to Ref. 12 for details.

B. Feedback control structure

In this section, an analysis is carried out for a typical feedback structure (Fig. 2) on the basis of the aforementioned generalized control framework. The symbols $P_1(z)$

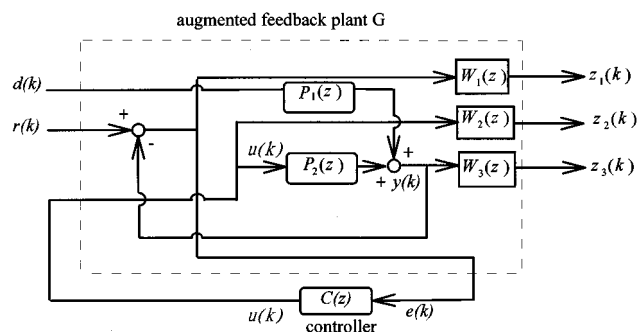
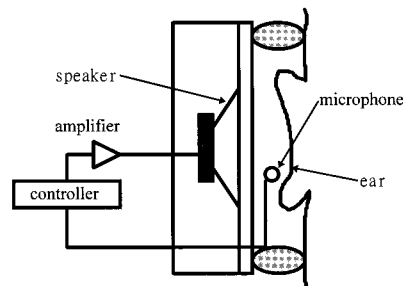
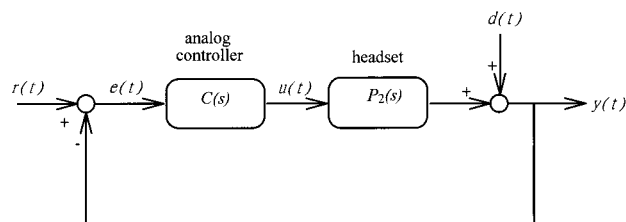


FIG. 2. Feedback ANC structure.



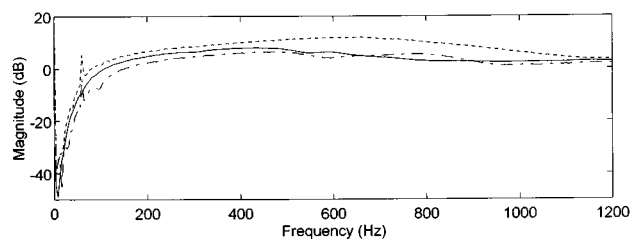
(a)



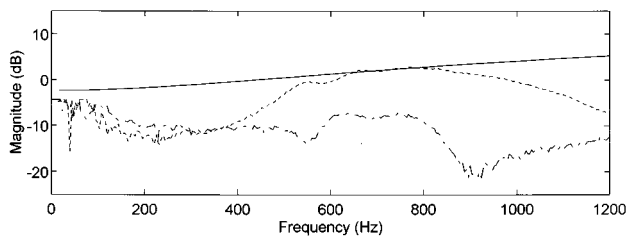
(b)

FIG. 3. The H_∞ active headset system. (a) Experimental setup; (b) block diagram.

and $P_2(z)$ correspond to the primary (disturbance) path and the secondary (control) path, respectively. To find an H_∞ controller, we weight the sensitivity function $\tilde{S}(z)$ by $W_1(z)$, the control input $u(k)$ by $W_2(z)$, and the complementary sensitivity function $\tilde{T}(z)$ with $W_3(z)$, where the sensitivity function and the complementary sensitivity function are defined, respectively, as¹³



(a)



(b)

FIG. 4. Frequency response functions of the headset. (a) Three example headset models (nominal plant —; perturbed plant 1 ---; perturbed plant 2 ...); (b) multiplicative plant perturbations ΔP_1 and ΔP_2 versus the inverse of the weighting function $W_3^{-1}(s)$ [$W_3^{-1}(s)$ —; ΔP_1 ---; ΔP_2 ...].

TABLE I. The plant model of the headset identified by the ARX procedure.

Zeros	Poles
^a -3.0841	$0.6612 \pm 0.3483i$
^a 1.0320	$-0.4426 \pm 0.3324i$
-0.4387	
0.0034	
Gain=0.3921	

^aDenotes nonminimal phase zeros.

$$\tilde{S}(z) = \frac{1}{1 + P_2(z)C(z)} \quad (4)$$

and

$$\tilde{T}(z) = \frac{P_2(z)C(z)}{1 + P_2(z)C(z)}. \quad (5)$$

Note that $\tilde{S}(z) + \tilde{T}(z) = 1$. To achieve disturbance rejection and tracking performance, the nominal performance condition must be satisfied,

$$\|\tilde{S}(z)W_1(z)\|_{\infty} < 1. \quad (6)$$

Note that the notations $W_1(z)$, $W_2(z)$, and $W_3(z)$ denote the Z transform of weighting functions which should not be confused with the extraneous input $w(k)$ in Fig. 1. On the other hand, for system stability against plant perturbations and model uncertainties, the robustness condition derived from the *small-gain theorem*¹⁰ must be satisfied,

$$\|\tilde{T}(z)W_3(z)\|_{\infty} < 1. \quad (7)$$

In common practice of loop shaping, $W_1(z)$ is chosen as a lowpass function and $W_3(z)$ is chosen as a highpass function. It is well-known that the trade-off between $\tilde{S}(z)$ and $\tilde{T}(z)$, in conjunction with the waterbed effect, dictates the performance and robustness of the feedback design. This classical trade-off renders the so-called *mixed sensitivity problem*.¹¹

$$\|\tilde{S}(z)W_1(z) + \tilde{T}(z)W_3(z)\|_{\infty} < 1, \quad (8)$$

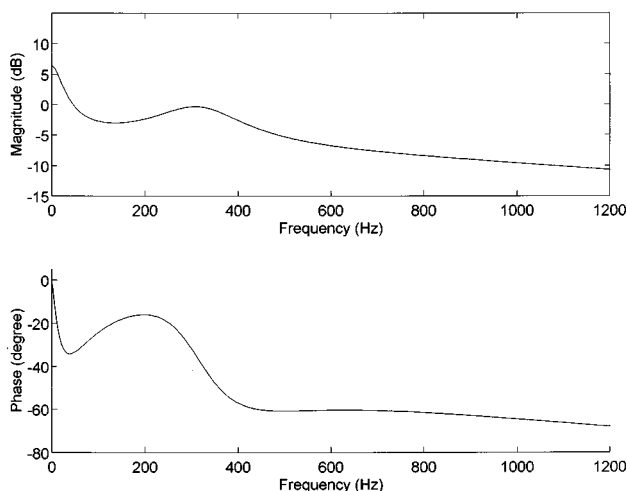


FIG. 5. Frequency response function of the H_{∞} active headset controller. (a) Magnitude (dB); (b) phase (deg).

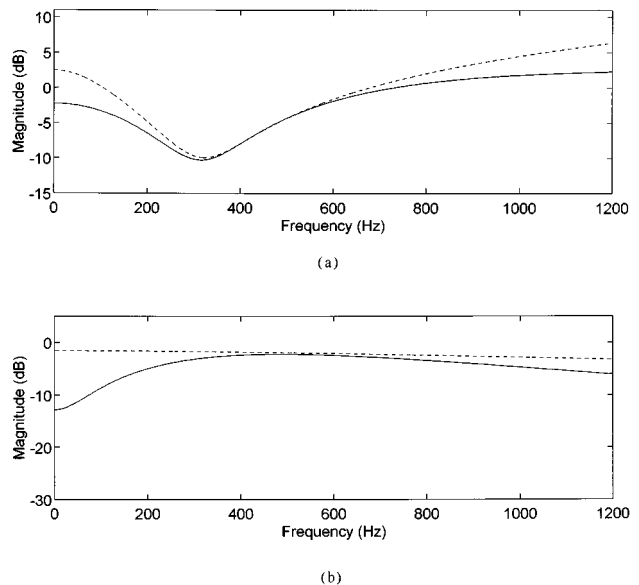


FIG. 6. Loop shaping of the unity feedback control design for the active headset. (a) $W_1^{-1}(s)$ \cdots vs $\tilde{S}(s)$ --- ; (b) $W_3^{-1}(s)$ \cdots vs $\tilde{T}(s)$ --- .

which is also a necessary and sufficient condition for the controller to achieve both nominal performance and robust stability.

In terms of the generalized control framework, the input-output relation of the augmented plant corresponding to the feedback structure is

$$\begin{bmatrix} Z_1(z) \\ Z_2(z) \\ Z_3(z) \\ E(z) \end{bmatrix} = \begin{bmatrix} W_1(z) & -W_1(z)P_2(z) \\ 0 & W_2(z) \\ 0 & W_3(z)P_2(z) \\ 1 & -P_2(z) \end{bmatrix} \begin{bmatrix} D(z) \\ U(z) \end{bmatrix}. \quad (9)$$

Hence it can be shown by LFT that the suboptimal condition of the feedback controller reads

$$\left\| \begin{bmatrix} W_1(z)\tilde{S}(z) \\ W_2(z)\tilde{S}(z)C(z) \\ W_3(z)\tilde{T}(z) \end{bmatrix} \right\|_{\infty} < 1, \quad (10)$$

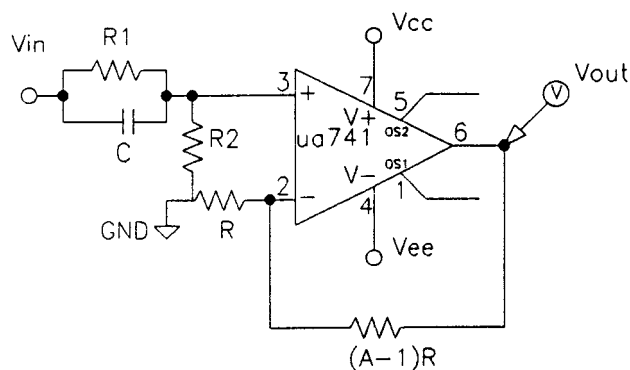
where $\tilde{S}(z)$ and $\tilde{T}(z)$ are defined in Eqs. (4) and (5), and

$$R(z) = \frac{C(z)}{1 + P_2(z)C(z)}. \quad (11)$$

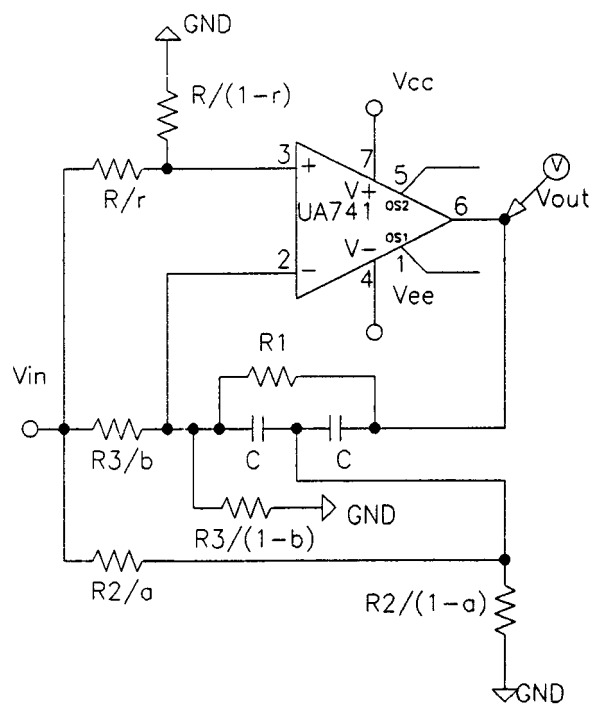
With reference to Eq. (9), the H_{∞} controller can then be found via the synthesis procedure outlined in Ref. 12.

TABLE II. The controller model for the headset obtained by the H_{∞} synthesis procedure.

Poles ($\times 10^4$)	Zeros ($\times 10^5$)
-2.0959	-3.4362
-1.6790	$-0.1327 \pm 0.1302i$
-0.8121	-0.1885
$-0.0592 \pm 0.1973i$	-0.0361
Gain=0.1623	



(a)



(b)

FIG. 7. Templates of operational amplifier circuit. (a) First-order circuit; (b) second-order circuit.

II. EXPERIMENTAL INVESTIGATIONS

Experimental investigations were conducted to verify the practicality of the H_∞ controller synthesis technique. The technique was employed to design an active headset. A headset generally has small acoustical volume, which implies the associated model is usually of low order. This is a desirable property that admits the use of feedback control structure for broadband noise rejection.

The experimental setup and the corresponding block dia-

gram are illustrated in Fig. 3. Note that the primary path, $P_1(z)$, is simply taken as unity in this case. The earcup of the headset is lined with some fiberglass sound-absorbing material to provide appropriate damping for the system. The importance of passive damping, an often overlooked factor in active design, lies not only in high-frequency attenuation but also system robustness against plant uncertainties.¹⁴ With proper damping treatment, the plant can be gain-stabilized even with poorly modeled or unmodeled flexible modes. Another benefit of passive damping is that a lower order of plant model than the lightly damped plants can usually be obtained, so that numerical error can be reduced.

The relative position of the sensor and actuator is another important issue. In the experiment, the sensor (a capacitor microphone) is placed in the close vicinity of the control loudspeaker to form the so-called *collocated control*. In doing so, the waterbed effect, in conjunction with non-minimal phase zeros and time delay, can be alleviated.^{10,13} In what follows, the design procedure will be carried out in terms of performance, stability, and robustness of the closed-loop system.

Prior to controller design, the mathematical model of the plant has to be established via an ARX system identification procedure.¹⁵ In practical situations, the acoustical plant of the headset may differ from person to person. In the experiment, three testees are asked to wear the headset to give three plant models, as shown in Fig. 4(a). One of the models is taken as the nominal and the others are taken as the perturbed plants. This figure gives us the general idea of the size of plant uncertainty. The poles and zeros of the nominal plant are included in Table I. Note that the model is of very low order ($=4$ in this case). The plant uncertainty can be accommodated by choosing a suitable weighting function, W_3 , with sufficient high-frequency roll-off in H_∞ design. The plant uncertainties and the chosen weighting function, W_3 , are illustrated in Fig. 4(b). After the weighting function, W_3 , has been chosen for robustness, we then choose W_1 as a lowpass function for loop-shaping the nominal performance in the closed-loop feedback design.

On the basis of the identified plants, the aforementioned H_∞ synthesis procedure is employed to calculate the optimal controller. The frequency response function of the resultant H_∞ controller is shown in Fig. 5. The weighting functions W_1 and W_3 used for the H_∞ design, and the resultant sensitivity function and the complementary sensitivity function of the unity feedback system, are shown in Fig. 6. Note that the sensitivity functions are bounded by the reciprocals of the weighting functions, as required by the H_∞ design procedure. Taking into consideration the cost of the headset and time delay of common digital systems that might cause undesired degradation of performance and stability, we choose to implement the H_∞ controller by analog filters. Hence, the discrete H_∞ controller is converted into a continuous equivalent by bilinear transform. The transfer function of the resulting analog controller is tabulated in Table II. The H_∞ controller is then implemented by using operational amplifier circuitry. To be more specific, the transfer function of the controller is first converted into a cascade form composed of first- and second-order templates, as shown in Fig. 7. The

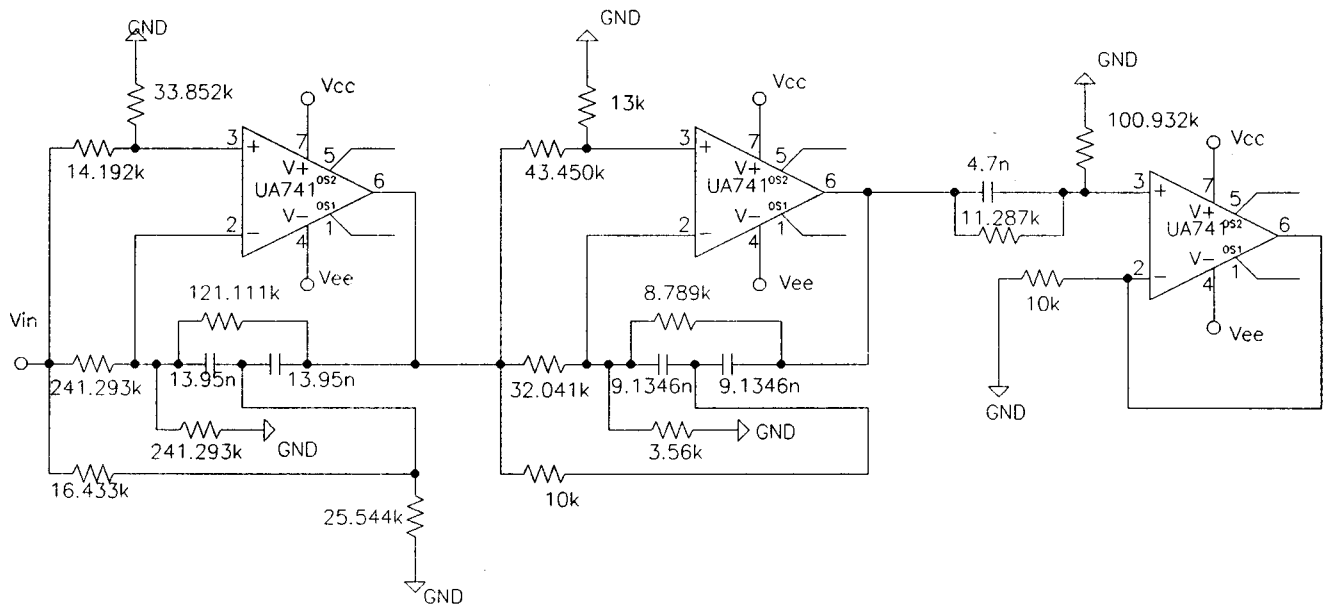


FIG. 8. Electric circuit diagram of the H_∞ active headset controller.

formula for the first- and second-order templates, respectively, are

$$\frac{V_{out}(s)}{V_{in}(s)} = A \frac{s + 1/R_1 C}{s + (1/R_1 C + 1/R_1 C)} \quad (12)$$

and

$$\frac{V_{out}(s)}{V_{in}(s)} = \frac{rs^2 + s\{r[2(G_1 + G_3) + G_2] - aG_2 - 2bG_3\}/C + [rG_2(G_1 + G_3) - bG_2G_3]/C^2}{s^2 + 2(G_1/C)s + (G_1G_2/C^2)}, \quad (13)$$

where $G_i = 1/R_i$, $i = 1, 2, 3$. A general practice is to pair the poles and the zeros in a stage as closed to each other as possible so that the frequency response is equalized. In addition, the gains of all filter stages should be uniformly distributed to minimize noise amplification. A more detailed description of the implementation of analog filters can be found in Ref. 16. According to this procedure, the foregoing fifth-order H_∞ controller is implemented by cascading one first-order stage and two second-order stages

$$C(s) = \frac{0.7046s^2 + 2.4466 \times 10^5 s + 8.7447 \times 10^8}{s^2 + 1.1838 \times 10^3 s + 4.2430 \times 10^6} \times \frac{0.2303s^2 + 6.1131 \times 10^3 s + 7.9584 \times 10^7}{s^2 + 2.4912 \times 10^4 s + 1.3636 \times 10^8} \times \frac{s + 1.8851 \times 10^4}{s + 2.0959 \times 10^4}. \quad (14)$$

Common operational amplifiers such as ua741 or high-impedance field-effect transistor (FET) operational amplifiers TL074 can be used in the implementation of the above transfer function. The resulting circuit diagram is shown in Fig. 8.

Figure 9 shows the open-loop gain before and after the active compensation. Before compensation, although the gain margin is infinite and the gain crossover frequency is

5034 Hz, the phase margin is only 35.80 deg, as shown in Fig. 9(a). Thus, the system is apparently not robust enough to cope with plant perturbations. However, after compensation, the phase margin in Fig. 9(b) is raised to 82.32 deg at the gain crossover frequency 575 Hz, and the gain margin becomes 15.13 dB at the phase crossover frequency 2460 Hz. The robustness is indeed improved by the compensation. In addition, the compensated system also has acceptable gain margin of 15.23 dB and phase crossover frequency of 2460 Hz. Figure 10 shows the experimental results for rejecting a Gaussian white noise by using the headset before and after the active control is activated. From the result, it can be observed that broadband attenuation up to approximately 15 dB has been achieved in the frequency range 200–800 Hz.

In addition to noise rejection, the active headset is also designed for tracking external command signals. In Fig. 11, the closed-loop transfer function between command input and the plant output remains approximately flat within 100–865 Hz, and the phase remains almost linear between 100 and 900 Hz. To test the tracking performance, the headset is used for listening to pop music in a noisy environment. Figure 12 shows the sound received by the embedded microphone, with and without the active control. The result suggests that the active headset indeed produces satisfactory performance of signal tracking in conjunction with noise rejection.

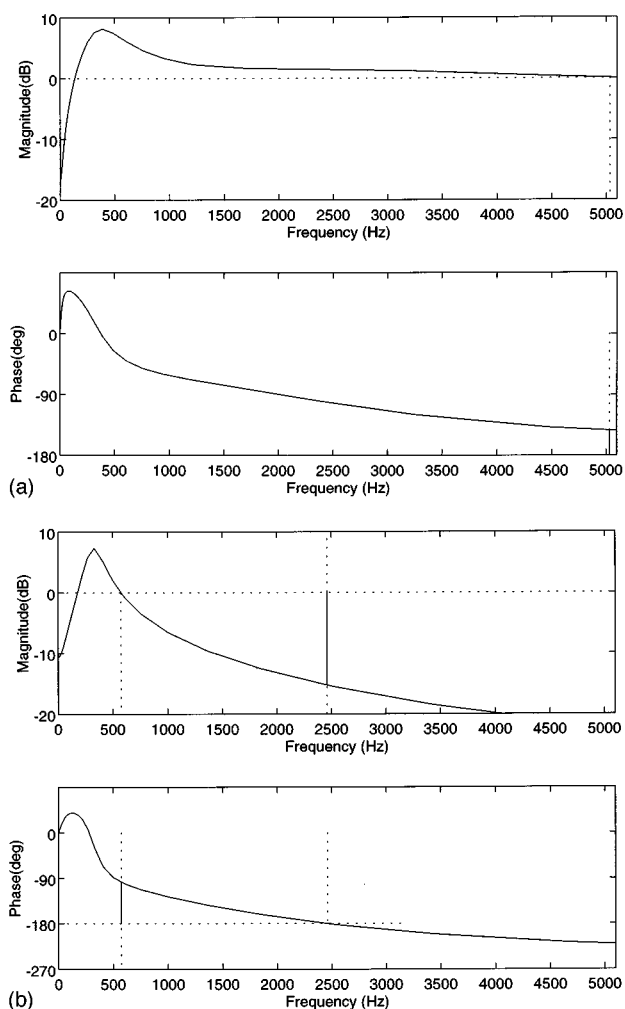


FIG. 9. Open-loop transfer function of the headset with and without the active control. (a) Without active control; (b) with active control.

III. CONCLUSION

An active headset has been implemented by using H_∞ robust control theory. Performance, stability, and robustness of the feedback system have been taken into account in the

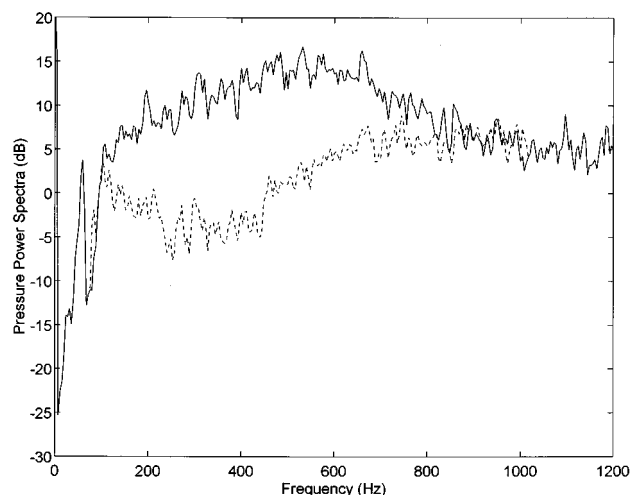


FIG. 10. Sound pressure power spectra in the headset cavity with and without the active control. Active control off —; active control on ...

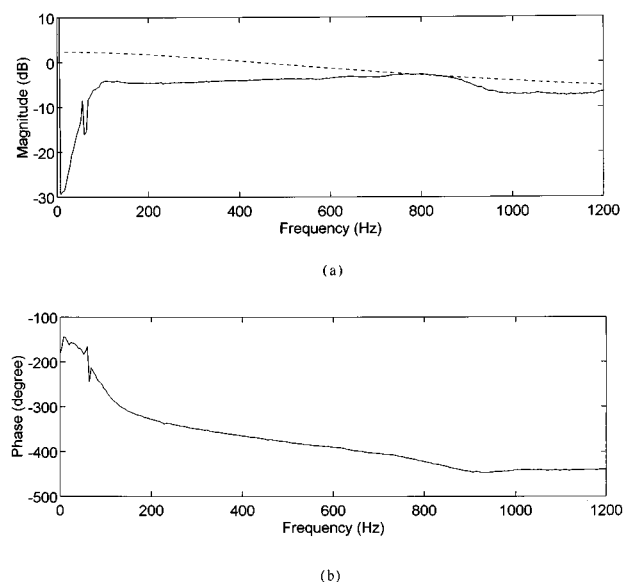


FIG. 11. Transfer function $\tilde{T}(s)$ between the command input and the plant output of the closed-loop system for the active headset. (a) $W_3^{-1}(s)$... vs $\tilde{T}(s)$ —; (b) phase of $\tilde{T}(s)$.

design procedure by using a general framework of the H_∞ theory. Robust margins are satisfied, in addition to nominal performance. This is vital in practical applications, where system uncertainties are present. Because feedback control is used, no reference input is needed, so that the acoustic feedback problem can be avoided. The common impression that feedback control is not suitable for broadband noise attenuation does not apply to this case, in which the plant is of very low order ($=4$). The resultant controller is realized via operational amplifier circuitry. The experimental results show that the active headset is effective in tracking external command signals and rejecting broadband noise.

Some crucial factors, including small acoustical volume, proper passive damping treatment, and collocated arrangement of the microphone and the speaker, must be taken into account in designing the active headset. We should be able to

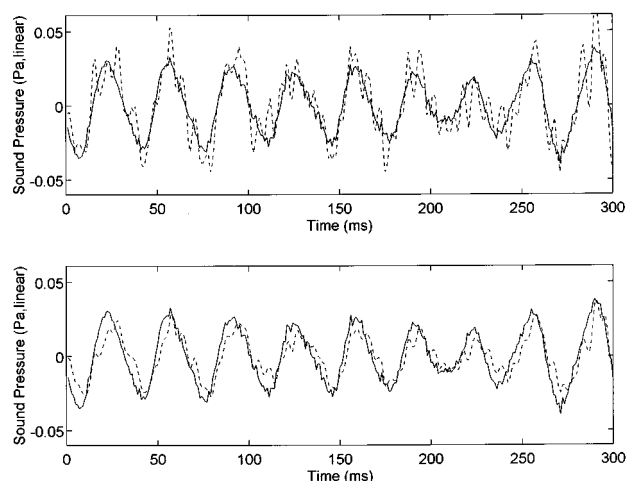


FIG. 12. Tracking performance of the headset to a pop music exposed to white noise environment. (a) Command signal — versus corrupted signal received in the headset without active control ...; (b) command signal — versus signal received in the headset with active control ...

improve the performance of the headset further if the physical configuration is optimized for the active control purpose. This aspect will be explored in future research.

ACKNOWLEDGMENTS

This paper is written in memory of the late Professor Anna Pate, Iowa State University. Special thanks also go to Professors F. B. Yeh and M. C. Tsai for the helpful discussions on the H_∞ control theory. The work was supported by the National Science Council in Taiwan, Republic of China, under the project number NSC 83-0401-E-009-024.

¹P. Lueg, "Process of silencing sound oscillations," US Patent No. 2,043,416 (1936).

²S. J. Elliot and P. A. Nelson, "Active noise control," *Noise News Int.* **2**, 75–98 (1994).

³M. O. Tohki and R. R. Leitch, *Active Noise Control* (Clarendon, Oxford, 1992).

⁴C. R. Fuller and A. H. von Flotow, "Active control of sound and vibration," *IEEE Control Systems Magazine* **15**(6) (December 1995).

⁵H. F. Olson and E. G. May, "Electronic sound absorber," *J. Acoust. Soc. Am.* **25**, 1130–1136 (1953).

⁶P. D. Wheeler, "Voice communication in the cockpit noise

environment—the role of active noise reduction," Ph.D. thesis, University of Southampton, England, 1986.

⁷J. C. Doyle, K. Glover, P. Khargonekar, and B. A. Francis, "State space solution to standard H_2 and H_∞ control problems," *IEEE Trans. Autom. Control*. **34** (8), 832–847 (1989).

⁸P. A. Iglesias and K. Glover, "State-space approach to discrete-time H_∞ control," *Int. J. Control* **54**, 1031–1073 (1991).

⁹I. Yaesh and U. Shaked, "Transfer function approach to the problems on discrete-time systems: H_∞ -optimal linear control and filtering," *IEEE Trans. Autom. Control*. **36**, 1264–1271 (1991).

¹⁰J. C. Doyle, B. A. Francis, and A. R. Tannenbaum, *Feedback Control Theory* (Macmillan, New York, 1992).

¹¹F. B. Yeh and C. D. Yang, *Post Modern Control Theory and Design* (Eurasia, Taiwan, 1992).

¹²M. C. Tsai and C. S. Tsai, "A transfer matrix framework approach to the synthesis of H_∞ controllers," *Int. J. Control* **5**, 155–173 (1995).

¹³G. F. Franklin, J. D. Powell, and A. Emami-Naeini, *Feedback Control of Dynamic Systems* (Addison-Wesley, Reading, MA, 1994).

¹⁴R. Gueler, A. H. von Flotow, and D. W. Vos, "Passive damping for robust feedback control of flexible structures," *J. Guid. Control. Dyn.* **16**(4), 662–667 (1993).

¹⁵L. Jung, *System Identification: Theory for the User* (Prentice-Hall, Englewood Cliffs, NJ, 1987).

¹⁶R. Schaumann, M. S. Ghausi, and K. R. Laker, *Design of Analog Filters* (Prentice-Hall, Englewood Cliffs, NJ, 1990).

Individual differences in susceptibility to the “irrelevant speech effect”

Wolfgang Ellermeier^{a)} and Karin Zimmer

Institut für Psychologie der Universität Regensburg, 93040 Regensburg, Germany

(Received 20 November 1996; revised 4 April 1997; accepted 11 June 1997)

Individual differences in objective effects of noise on performance were analyzed with respect to their distribution, temporal stability, and the precision of measurement to be attained. Seventy-two subjects had to memorize sequences of visually presented digits while being exposed to one of three auditory background conditions which were randomly mixed on a trial-by-trial basis: (1) foreign speech; (2) pink noise; and (3) silence. Individual “irrelevant speech effects,” operationalized by the difference in recall errors under speech and in silence, were normally distributed over a wide range extending from slight facilitation to severe disruption. When 25 subjects repeated the experiment after four weeks, the individual differences were replicated with a reliability of $r_{tt} = 0.45$. Internal consistency, a measure of the precision with which individual effects can be measured in a single session, was moderate ($\alpha = 0.55$). However, both retest, and consistency coefficients are severely attenuated by the use of (sound-minus-silence) difference scores, the reliability of which is bound to be considerably lower than that of the original error scores whenever these are correlated. Given that the original error rates in a specific auditory condition can be determined with reliabilities approaching 0.85, it may be concluded that individual performance decrements due to noise can be reliably measured in the “irrelevant speech” paradigm. Self-report measures of noise susceptibility collected to explore potential sources of the large inter-individual variation exhibited only weak relationships with the objectively measured noise effects: Subjects were quite inaccurate in assessing their individual impairment in the three auditory conditions, and a questionnaire-based measure of general noise sensitivity only accounted for a small portion of the variance in objectively measured performance decrements, although in both cases the predictive relationship was much stronger in female than in male subjects. © 1997 Acoustical Society of America. [S0001-4966(97)00110-0]

PACS numbers: 43.50.Qp, 43.72.Dv [GAD]

INTRODUCTION

In environmental noise research, the need to study individual differences has always been more apparent than in other areas of psychoacoustics. One obvious reason is that much of the survey research concerned with noise evaluation uses correlational statistics. Individual differences on a subjective dimension (e.g., annoyance) are correlated with other subjective (e.g., attitudinal) or objective measures (such as exposure levels) characterizing individuals or groups of respondents. Appreciable individual variation and its reliable measurement are crucial to this research approach.

Therefore, instruments for measuring individual differences in annoyance with various noise sources (Job, 1988; Taylor, 1984, for reviews), in response criteria for reporting distress (Green and Fidell, 1991), or in general noise sensitivity (Weinstein, 1978) have been developed. Nevertheless, a recent review (Staples, 1996) blamed a lack of understanding of individual differences in reaction to noise for costly policy failures in the implementation of noise abatement, or traffic rerouting programs.

In contrast to the questionnaire-based noise evaluation studies thus characterized, research into the objective effects of noise on performance—focusing on the demonstration of

overall effects of experimental manipulations—has shown little concern with individual differences (Jones and Davies, 1984, for an earlier review). There are occasional reports of personality variables such as anxiety or extraversion interacting with noise effects (summarized in Smith and Jones, 1992); analyses of the stability of individual differences, however, turn out to be rather disconcerting. Smith *et al.* (1981), for example, in an experiment, which required subjects to memorize lists of words both in the quiet and under continuous white noise, found quiet-noise differences in recall scores, and in indices of higher-order cognitive processing (“clustering”) to produce correlations as low as $r = 0.05$ between two sessions one week apart. That is, subjects appearing particularly susceptible to noise in the first session were not the same ones as those showing the largest performance decrements in the second session, and the magnitude of the correlation indicated almost nonexistent individual stability of these noise effects.

This inconsistency of performance across sessions may stem in part from the highly variable effects of continuous or intermittent white noise. Generally, these earlier studies show that white noise presented at high sound-pressure levels may either improve, depress, or result in no change in performance. Moreover, those factors that predict such outcomes cannot be articulated with any degree of certainty. Such inconsistency in mean effects suggests (but is by no

^{a)}Electronic mail: wolfgang.ellermeier@psychologie.uni-regensburg.de

means definitive in suggesting) that reliability measures may be poor in such settings.

While the studies thus characterized all employed broadband noise of relatively high level (≥ 80 dB), more recent research, pioneered by Colle and Welsh (1976) as well as by Salamé and Baddeley (1982), found highly replicable overall noise effects (no single instance of improvement has been encountered, for example) when using temporally structured sounds of moderate intensity, and a particular task requiring recall “in the correct order.” The phenomenon referred to has been termed the “irrelevant speech effect” (ISE), since the presentation of auditory material (typically speech) which the subject is told to ignore, and which is of no significance to the task performed, has sizable effects on the serial recall of visually presented items such as letters or digits (for reviews see Jones and Morris, 1992; Jones, 1993; Jones *et al.*, 1996). In recent years, the ISE paradigm has become prototypical for studying moderate-level noise effects in a situation representative of modern office environments. The quickly growing number of studies on the effect have either addressed the cognitive mechanisms involved (e.g., Salamé and Baddeley, 1982; Buchner *et al.*, 1996), or the properties of the auditory distractors producing maximal interference (e.g., Jones and Macken, 1995a; Jones *et al.*, submitted; Ellermeier and Hellbrück, in press); individual differences, however, have not been analyzed to our knowledge, and even the presentation of standard errors seems to be the exception rather than the rule (see however, LeCompte, 1994; Jones and Macken, 1995b).

In our opinion, the need for laboratory studies of individual differences in the susceptibility to noise expressed in a recent review (Staples, 1996) is best addressed by looking at the paradigm characterized above, for which there is ample and consistent evidence of performance disruption. Consequently, the present study was designed to collect data on a fairly large number of subjects ($N=72$) under standard “irrelevant speech” conditions. More specifically, a foreign language (Japanese) was used to elicit the effect unconfounded by semantic content, and a “placebo control” (pink noise) was presented in addition to the quiet baseline, in order to control for unspecific or expectation-based effects due to the mere presence of an acoustical distractor.

The study was conducted with two goals in mind: The primary goal was to assert the presence of individual differences in noise susceptibility in a controlled laboratory experiment, and to show that these can be reliably measured, applying established psychometric methods derived from classical test theory (Nunnally, 1978; Kline, 1993; Lienert and Raatz, 1994). According to this approach, errors in the “irrelevant speech” paradigm are treated much like errors in an intelligence test, the precision and replicability of which is to be determined. A secondary goal was to link behavioral effects to differences in self-reported noise sensitivity in order to explore (a) if subjects are able to assess their susceptibility to a given noise, and (b) if the personal attribute of “noise sensitivity” (Weinstein, 1978) may account for some portion of the variance in error rates observed in the laboratory.

I. GENERAL METHOD

A. Subjects

Seventy-two students at the University of Regensburg (median age 24, range 19–44; 31 male, 41 female) participated as subjects. A random subset of this sample consisting of 25 subjects was asked and agreed to participate in a retest session four weeks later. Hearing problems, knowledge of Japanese, or prior experience in “irrelevant speech” experiments were exclusion criteria for the experiment. All subjects were naive both with respect to the literature on noise effects, and to the specific hypotheses being investigated.

B. Apparatus and stimuli

1. Visual stimuli

The visual material to be memorized consisted of random permutations of the digits 1 through 9, presented sequentially in the center of a colour monitor. The digits were about 2 cm in height and appeared for 800 ms each, with 200-ms pauses between digits.

2. Auditory stimuli

The “irrelevant” auditory materials were recorded and played with 8-bit resolution and an 22-kHz sampling rate using a “Soundblaster-compatible” PC sound card. Two types of auditory materials were used: (1) Japanese speech, and (2) pink noise. The speech sample consisted of a 15-s segment from a lecture given by a male speaker. The noise sample was recorded from a Bruel & Kjaer (type 1405) noise generator. These single tokens of speech and noise were shaped to have smooth onsets and offsets, and to yield A-weighted, energy-equivalent sound-pressure levels, L_{eq} , of 76 dB, as verified by measurements at the headphones using a Cortex Electronic (model MK 1) artificial head system. Due to its continuous and broadband nature, the pink-noise sample appeared louder: The mean computed loudness levels were 44.7 sone for the noise, and 25 sone for the speech sample. The auditory stimuli were presented diotically over headphones (Beyerdynamic DT 550) in a quiet, but not sound-treated laboratory room [ambient A-weighted sound level approximately 40 dB].

C. Procedure

Each trial was initiated by a 2-s visual warning signal (a square of decreasing size cueing the subject to the point of fixation), after which the stream of 9 digits was displayed at a rate of 1 per s. Following a 5-s retention interval, a 3×3 numerical array consisting of the numbers 1 through 9 prompted subjects to enter the correct serial order by sequentially clicking the computer mouse on the digits displayed.

On sound trials, the acoustical background (speech or pink noise) was present both during the encoding and the rehearsal phase, for a total of 14 s. No sound was presented during the self-paced recall period. Subjects were told to ignore the auditory input while quietly rehearsing the number sequence.

In order to be able to measure individual differences unconfounded with practice effects, the auditory conditions

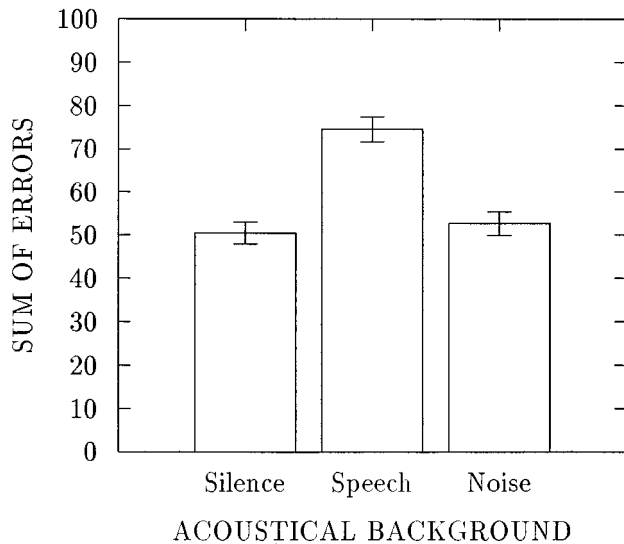


FIG. 1. Effect of “irrelevant speech” compared with two control conditions. The sum of serial recall errors in 20 trials averaged across 72 subjects is plotted along with standard errors of the mean.

were randomly mixed on a trial-by-trial basis. Subjects were run in blocks of 30 trials in which speech, pink noise, and silent conditions occurred with equal frequency. After three trials of practice, they completed two (or three) of these 30-trial blocks, lasting approximately 15 min each.

Twenty-five subjects repeated the experiment four weeks later in order to determine the stability of the effects over time. Furthermore, this subset of our sample was asked to estimate the degree of interference (or potential facilitation) produced by the “irrelevant” sounds by rating them on a bipolar scale ranging from -3 (“will severely hurt my performance”) over zero (no effect) to $+3$ (“will help considerably”). These ratings were obtained after subjects had read the instructions, had heard the two sound samples, but prior to actually performing the serial recall task. The rating procedure was repeated at the end of the first session (with modified wording, where appropriate), in order to assess, whether actual experience with the task changed subjects’ evaluation of sound effects.

In addition, all 72 subjects completed two questionnaires measuring individual noise sensitivity with respect to a wide range of noise sources: (1) A German version of Weinstein’s (1978) noise sensitivity scale, and (2) a newly constructed noise-sensitivity questionnaire currently being evaluated in our laboratory (Zimmer and Ellermeier, submitted).

II. INDIVIDUAL DIFFERENCES IN SUSCEPTIBILITY TO “IRRELEVANT SPEECH”

A. Overall effect of irrelevant sound on performance

In all analyses presented in this paper, serial recall performance was evaluated using the method almost exclusively employed in research on “irrelevant speech” effects: An error was scored whenever the subject failed to report the correct digit in the correct position. The sum of errors in 20 trials computed separately for each auditory condition served as the basic dependent variable, assuming a minimum of

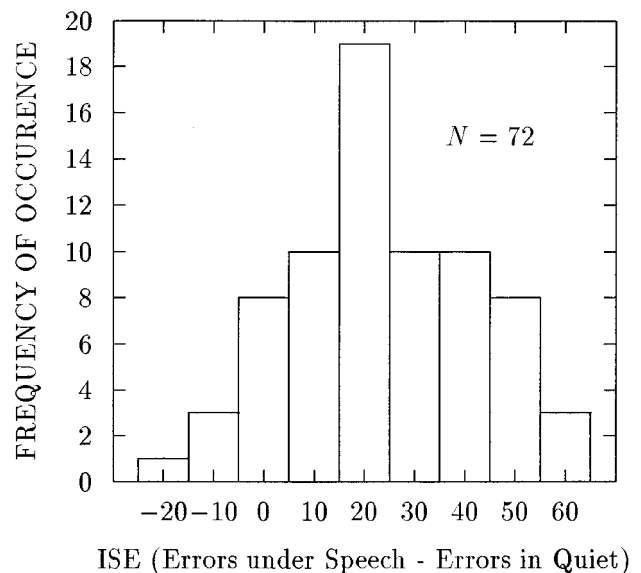


FIG. 2. Distribution of “irrelevant speech effects” (ISEs) obtained from 72 subjects. The abscissa shows how far the error rate under speech exceeds the error rate produced in the quiet baseline.

zero, and a potential maximum of 380 (20 trials \times 9 digits).

Figure 1 shows the mean number of errors obtained with the three “irrelevant” backgrounds. On the average, 50 errors were produced in the quiet condition, 74 while exposed to Japanese speech, and 52 with continuous pink noise, thus yielding a highly significant effect of the auditory background [$F(2,142)=97.16$; $p<0.001$]. As is evident in Fig. 1, this effect is almost entirely due to the increased error rate with speech, the two control conditions (silence and pink noise) do not produce significantly different error rates.

Presenting these overall effects for fairly standard experimental conditions only serves to make the point that the data obtained in the present investigation are entirely consistent with the literature. The effect size, an increase in error rate by about 50%, is somewhat larger than typically reported (Jones *et al.*, 1996), which may be due to the mixed presentation of auditory conditions, and to the fact that an extra retention interval delayed subject’s recall, two measures, which tend to increase “irrelevant speech” effects. The pattern of outcomes as depicted in Fig. 1, namely the lack of impairment under continuous broadband noise, is consistent with current theoretical explanations both in terms of a “filter” passing speechlike information (Salamé and Baddeley, 1982), and in terms of the importance of “changing-state” features of the auditory background (Jones and Macken, 1993; Jones *et al.*, 1996).

B. Distribution of effect sizes

Since the focus of the present investigation is on individual differences, a fundamental question is whether sufficient individual variation is observed in the paradigm under study. That is clearly the case, as is evident in Fig. 2, which shows the distribution of individual effect sizes, operationalized as the difference in errors between the speech and quiet conditions. As would be expected for a difference between two random variables, that distribution is Gaussian, with ap-

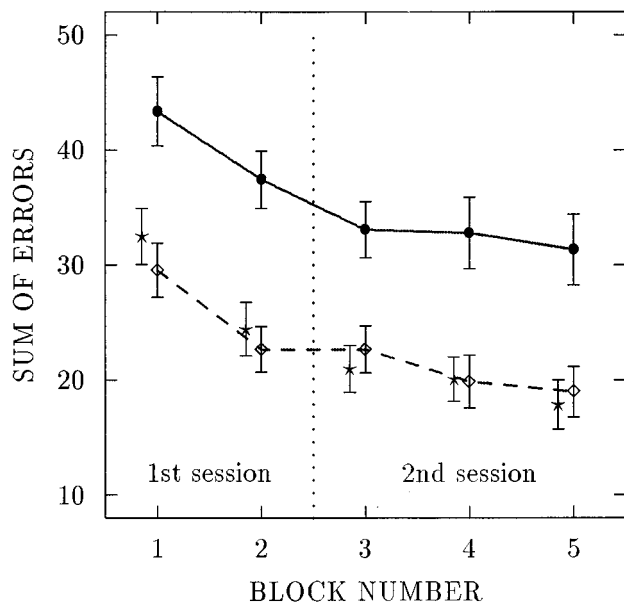


FIG. 3. Practice effects in the irrelevant speech paradigm. The graph shows the total number of errors per 30-trial block, averaged over 25 subjects, and plotted separately for the irrelevant speech condition (closed circles) and for the two control conditions: pink noise (stars), and silence (diamonds). Blocks 1 and 2 were completed in the first session, blocks 3–5 refer to data from the second session collected four weeks later.

parent deviations from a normal distribution being nonsignificant (Kolmogorov–Smirnov goodness of fit test: $z = 0.543$; n.s.).

More importantly, however, the spread of effect sizes is considerable, ranging from a minimum of -18 to a maximum of $+65$, the latter corresponding to a boost in error rate by 329% and the former reflecting an actual *reduction* in errors under speech by 33%. Note that roughly one-eighth of the sample shows no, or negative irrelevant speech effects.

Interestingly, individual effect sizes are in no way related ($r = 0.01$; n.s.) to a subject's memory capacity, which, in order to obtain a measure independent of the magnitude of the ISE, was operationalized as the number of digits recalled in the second control condition (pink noise). Further analyses did not provide any evidence for a systematic nonlinear (e.g., U-shaped) trend as a function of memory capacity either.

III. RELIABILITY OF INDIVIDUAL "IRRELEVANT SPEECH EFFECTS"

The individual scores described in the previous section are meaningful only if they can be reliably measured. The alternative, of course, is that the distribution depicted in Fig. 2 just captures noise in the measurement procedure, not individual differences in susceptibility to the irrelevant speech effect. In order to address this problem, the individual outcomes of the experiment were treated much like scores in a psychometric test, and conventional procedures for determining the reliability of a test were applied.

A. Retest reliability

In order to examine the temporal stability of overall irrelevant speech effects within and across sessions, mean performance is depicted as a function of time in Fig. 3. In all

auditory conditions, error rate drops considerably with practice, as confirmed by a highly significant main effect of block number [$F(4,96) = 15.26$; $p < 0.001$] in a two-factor analysis of variance over the five blocks and three sound conditions. The *differences* in error rates between the sound conditions, however, remain essentially the same, as indicated by the parallel curves in Fig. 3 and by the insignificant [$F(8,129) = 0.86$; n.s.] interaction between block number and sound condition in the analysis of variance. Although subjects learn to memorize more digits, they do not improve in dealing with the "irrelevant sound," a finding which is in line with two other published studies investigating habituation effects within sessions (Jones *et al.*, in press) and over a two-week interval (Hellbrück *et al.*, 1996). For subsequent analyses, it justifies the use of difference scores for measuring noise effects.

Test–retest reliability (r_{tt}) captures the stability of *individual* test scores over time, and is obtained by correlating observations made on a set of subjects on two occasions (cf. Kline, 1993). Since the focus of the present investigation is on the reliability of noise effects, the *difference* in errors between the silence and speech conditions obtained for each of the 25 subjects participating in the retest was correlated with the corresponding difference obtained four weeks later. The test–retest correlation was significant ($r_{tt} = 0.45$; $p < 0.05$) but only of moderate magnitude. Interestingly, retest reliability of the "pink-noise silence" difference was essentially zero ($r_{tt} = -0.09$; n.s.), suggesting that performance rankings in the pink-noise control condition vary randomly over time and do not characterize individuals, a finding which agrees with earlier research employing broadband noise (e.g., Smith *et al.*, 1981).

To conclude, it turns out that the individual differences measured in the irrelevant speech paradigm are replicable over a four week interval. The moderate size of the test–retest correlation may either be due to an actual temporal instability of the attribute measured, or to a low internal consistency of the test. That possibility shall be considered in the next section.

B. Internal consistency

A method of determining the precision of measurement without having to rely on temporal stability is to compute the internal consistency of a test (see Kline, 1993). The α -coefficient (Cronbach, 1951) indicates to what extent the items of a test measure the same variable.

For the purpose of measuring noise effects, an "item" was defined as the difference in errors between two temporally adjacent speech and quiet trials. Thus item scores ranged from -9 (no errors under speech, all nine digits wrong in silence) to $+9$ (all false with speech, no errors in silence). Twenty such item scores were obtained for the 60-trial session completed by all 72 subjects (disregarding the 20 pink-noise trials). Internal consistency turned out to be $\alpha = 0.55$. Naturally, one would expect it to be high, since all trials were generated by the same scheme, but individual trial pairs will exhibit strong random variations, thus attenuating the consistency coefficient.

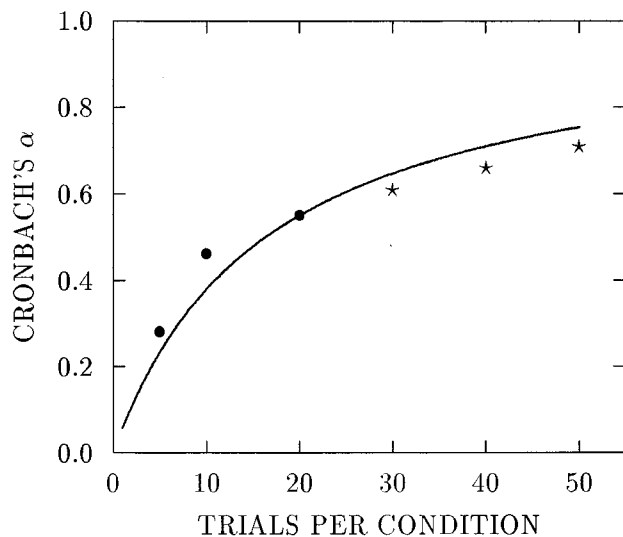


FIG. 4. Reliability of measuring the “irrelevant speech effect” as a function of the number of trials employed in each condition. Cronbach’s α is a measure of the “internal consistency” of test items (here: errors on a speech trials minus errors on a silent trial; see text). Points beyond 20 trials (stars) are based on data from those 25 subjects who participated in the retest; all other points (filled circles) are based on 72 subjects. The solid line is the improvement in “internal consistency” to be expected on the basis of the Spearman–Brown formula; the prediction was made based on the α of 0.55 through which the function passes.

Figure 4 shows how internal consistency grows with the number of speech-silence trial pairs presented to subjects. The solid line represents the theoretical prediction based on the Spearman–Brown formula describing the relationship between test length and reliability (see Nunnally, 1978, Eq. 7-7), and the data points approximate that prediction quite well. Using the Spearman–Brown formula, and extrapolating from the current α of 0.55 (which is our estimate based on the highest number of subjects and trials), we find that 66 trials per condition are needed to arrive at a reliability of 0.80, and 148 trials to reach the reliability of 0.90 considered desirable for intelligence tests, for example.

C. Temporal stability reconsidered

It turns out that much of the seemingly low test–retest reliability observed in the irrelevant speech paradigm may not be due to a temporal instability of the attribute being measured, but rather to the low internal consistency of the speech-silence error differences accumulated in a subject’s score. If that is the case, one may try to estimate the underlying temporal stability of the trait (here, noise susceptibility in an ISE experiment) by correcting for the low internal consistency of the measurement procedure used. The resulting *stability coefficient* (Cureton, 1971; Lienert and Raatz, 1994, Eq. 10.10) is

$$r_{tt}(\text{stab}) = r_{tt(\text{retest})} / \alpha = 0.45 / 0.55 \approx 0.82, \quad (1)$$

which turns out to be fairly high, and much more encouraging than what the (uncorrected) retest coefficient suggests.

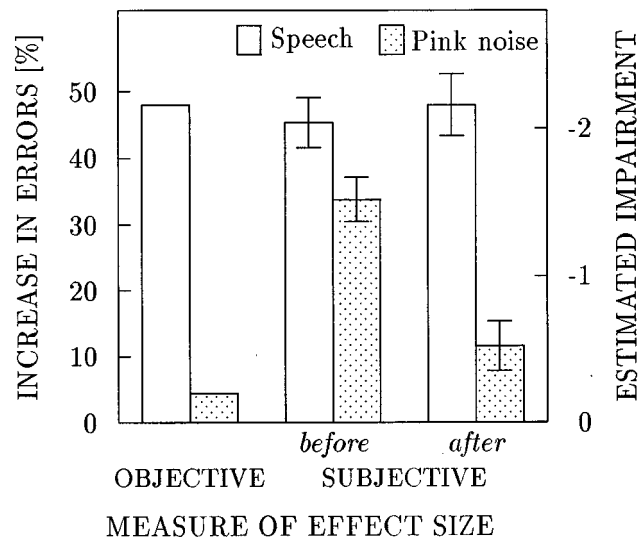


FIG. 5. Comparison of subjective estimates of memory impairment (right axis) under speech and noise (shaded bars) with objective performance decrements in percent (left axis, referring to the left pair of bars). Subjects judged expected (or experienced) effects of the sounds on a scale from -3 to $+3$ before and after performing a serial recall experiment.

IV. SUBJECTIVE ESTIMATES OF NOISE SUSCEPTIBILITY

To address the question of whether subjects can accurately judge the performance decrements they produce in an irrelevant speech experiment, they were presented with the speech and noise samples both before and after actually performing the memory task and were asked to rate the degree to which they thought they would be affected (resp. had been affected) by the sounds.¹

Figure 5 contrasts the objective effects of the two types of auditory materials with the mean subjective estimates of effect sizes given on two occasions. It is striking that before participating in the main experiment, subjects erroneously expect to be almost equally impaired by the speech and noise backgrounds (see the two middle bars in Fig. 5), whereas after experiencing 60 trials, the pattern of retrospectively estimated effect sizes comes much closer to the objective overall performance profile (depicted on the left in Fig. 5). This shift in the ratings shows up as a statistically significant (sound \times time of testing) interaction [$F(1,24) = 20.54$; $p < 0.001$] in the two-way analysis of variance of the subjective estimates. Thus it seems that subjects can quite accurately estimate mean sound effects after participating in the experiment, while working on the assumption that “any sound will hurt” before.

In order to assess how well they predict their own *individual* performance changes due to noise, each subject’s difference in ratings of the two sounds was correlated with the actual difference in errors produced when exposed to the sounds. While the correlation obtained with the *a priori* ratings was nonsignificant ($r = 0.16$), it increased to $r = 0.44$ ($p < 0.05$) after the experiment,² thus paralleling the pattern obtained for predicted mean effects.

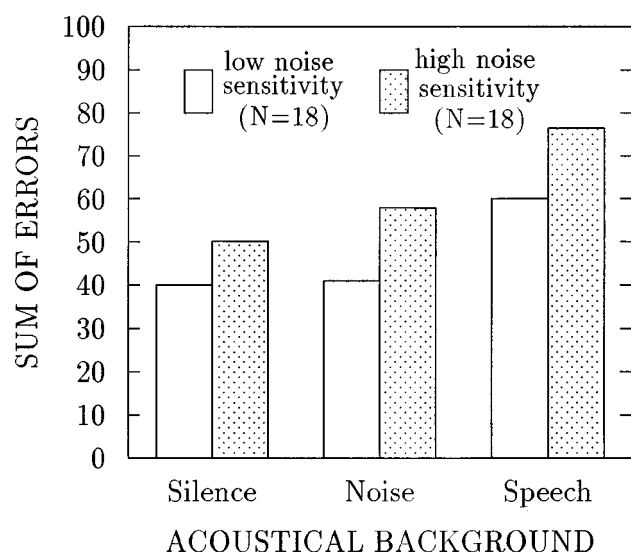


FIG. 6. Serial recall errors of subjects scoring high (upper 25%) and of subjects scoring low (lower 25%) on the noise-sensitivity questionnaire as a function of the auditory condition.

V. RELATIONSHIP BETWEEN GENERAL NOISE SENSITIVITY AND THE “IRRELEVANT SPEECH EFFECT”

Since all subjects completed a 52-item questionnaire consisting of statements about noise in a variety of contexts (Zimmer and Ellermeier, submitted), we were able to explore whether general noise sensitivity (Weinstein, 1978) might account for some portion of the variance in the objectively measured noise effects observed in the “irrelevant speech” paradigm.

For that purpose, the subjects representing the highest and lowest quartile of our sample regarding their total noise sensitivity score were contrasted with respect to the errors made in the “irrelevant speech” task. It turned out that the highly noise-sensitive subjects produced more errors than the insensitive ones across all experimental conditions (see Fig. 6), as confirmed by the significant main effect of noise sensitivity [$F(1,34)=7.24$; $p<0.05$] in a 2×3 (sensitivity groups \times sound conditions) mixed analysis of variance. Planned comparisons indicate that this group difference is statistically significant ($p<0.05$) in the two sound conditions (speech and pink noise), and not significant in silence. The pattern of outcomes depicted in Fig. 6 seems to indicate, however, that noise sensitivity does not affect the error rates in the three experimental conditions differentially, which is reflected in the lack of a significant interaction in the analysis of variance.

The association between noise sensitivity and noise effects is weaker, though, than the comparison of extreme groups suggests. That becomes evident when individual noise-sensitivity scores are correlated with individual “irrelevant speech” effects (a given subject’s difference in errors between the speech and quiet conditions). That correlation is only $r=0.23$ (significant at $p<0.05$, one-tailed test), even after correcting for the ISE’s low reliability.

Interestingly, the correlation observed in the 41 female subjects is much higher ($r=0.39$) than the correlation found

for the 31 male subjects in our sample ($r=0.038$), and that finding holds up when a German version of Weinstein’s (1978) noise-sensitivity scale is substituted for our newly constructed questionnaire. Furthermore, the relationship between the specific impairment ratings discussed in Sec. IV and actual irrelevant speech effects also turned out to be much higher in females ($r=0.46$) than in males ($r=0.08$).

It seems that women are more accurate at judging their own noise sensitivity than are men, at least with regard to the specific effects measured in the present irrelevant speech paradigm. That is true in the absence of any overall gender effects: neither in general noise sensitivity as measured by our questionnaire do women differ significantly from men, nor in the magnitude of the “irrelevant speech effect” (which is 25.4 for females, 22.4 for males).

VI. DISCUSSION

The results of the present study shall be discussed with respect to three related topics: (a) the nature of individual differences in susceptibility to the “irrelevant speech effect”; (b) the potential role of noise sensitivity in accounting for some portion of these individual differences; and (c) subject’s accuracy in judging their own susceptibility to noise.

A. Nature of individual differences in ISEs

The present study establishes that—embedded in the solid overall effects typically found in “irrelevant speech” experiments—there are sizeable individual differences in the magnitude of the effect, which are normally distributed, spanning a range from negative effects (with facilitation due to the speech background) over null results to considerable impairment. Note that whereas in many published studies such differences might be attributable to procedural artefacts (such as the subjects receiving different orders of the “treatments” in a counterbalancing scheme), the present study attempted to minimize potential interactions with practice or fatigue by running all conditions randomly mixed within each block of trials.

What then, are the sources of the variance observed? Basically, we will have to consider (1) “true” individual differences in susceptibility to the effect, (2) measurement error, and (3) temporal instability of the variable of interest. The psychometric indices of test–retest reliability and internal consistency derived from the present data set permit to estimate the contributions of these factors to some extent.

First of all, the fact that a significant test–retest correlation (r_{tt}) was obtained suggests that there is some basic stability of the pattern of outcomes overtime. The moderate correlation of $r_{tt}=0.45$ contrasts sharply with the retest coefficients near 0.05 that Smith *et al.* (1981) obtained for a free-recall task, and with similar insignificant measures reported by Wilkinson (1974), which had suggested a haphazard rank ordering of subjects with respect to effect sizes that cannot be replicated on a second occasion. It appears that the task and sound parameters used in the irrelevant speech paradigm make it more suitable not only for showing overall effects, but also for studying individual differences in response to noise.

The internal consistency coefficient, α , on the other hand, is a measure of reliability unconfounded by temporal changes. It reflects the degree to which individual differences are captured in the same way by the items making up the test. Its magnitude, $\alpha=0.55$, gives a better estimate of the amount of error still present in the data.

By psychometric standards, both retest reliability and internal consistency of the present measurements are disappointingly low. It turns out that this is largely due to the use of (speech-minus-silence) *difference* scores, which on statistical grounds are expected to yield lower correlations than the raw scores they are derived from whenever these raw scores are correlated themselves (see Nunnally, 1978, pp. 246–255; Lienert and Raatz, 1994, pp. 214–218). The following formula (adapted from Eq. 10.53 in Lienert and Raatz, 1994) predicts the reliability of a difference score r_{diff} from the reliabilities of the original scores (r_1, r_2) and their correlation (r_{12}):

$$r_{\text{diff}} = \frac{r_1 + r_2 - 2r_{12}}{2(1 - r_{12})}. \quad (2)$$

Given that in the present experiment recall scores under speech and in silence correlated with $r_{12}=0.69$ and substituting the consistency coefficients for measuring errors in speech ($\alpha=0.84$) and errors in silence ($\alpha=0.85$) for r_1 and r_2 , respectively, then the reliability of speech-silence difference scores is predicted to be $r_{\text{diff}}=0.50$ which is quite close to the value actually obtained (0.55).

The statistical fact that the reliability of difference scores is inversely related to the correlation between the original scores creates a problem for the measurement of noise effects in terms of performance differences between experimental conditions, since that correlation is bound to be high in the irrelevant speech paradigm, given that identical memory tests are compared under two different acoustical backgrounds. In terms of psychometric theory, when working with ISE difference scores, we are not simply addressing the reliability of a “test,” but rather the reproducibility of a “test profile” which is expected to be attenuated considerably.

These considerations suggest that it is only the complement of the reliability ($\alpha=0.85$) of the raw error scores, or a mere 15%, that make up the variance not accounted for. That residual error may be attributed to trial-by-trial fluctuations in memory span, attention, fatigue, and the like, and is to be expected even in highly homogeneous tasks like reacting to the onset of a tone repeatedly, or memorizing digit sequences as in the present experiment.

In the present context, however, we do not want to measure memory span (as reflected in the raw error scores) but rather noise effects (as reflected in a difference between error scores obtained in two conditions). Thus if a research problem requires the measurement of individual differences with a reliability comparable to that of established psychometric personality or performance tests (≥ 0.90), much larger numbers of trials will have to be collected from each subject than is commonly done to determine overall effects in an “irrelevant speech” experiment. Extrapolating from the theoretical curve depicted in Fig. 4 suggests that 148 trials per con-

dition are required to arrive at a reliability of 0.90 which, given that our present 30-trial blocks took approximately 15 min, would add up to almost 3-h running time during which 148 speech and 148 silent trials would have to be intermixed. In practice these numbers may underestimate the number of trials required, as the data points falling short of the curve suggest; on the other hand, the absence of a discontinuity in the reliability estimates made after 20 and 30 trials (see Fig. 4) suggests that it is possible to pool data from sessions widely spaced in time.

B. The role of noise sensitivity

A secondary goal of the present investigation was to explore whether a person’s noise sensitivity as measured by a questionnaire might account for some portion of the variance in objectively measured noise effects. While a comparison of extreme groups (Fig. 6) suggested such an influence, the overall correlation between individual sensitivity scores and ISEs turned out to be rather low ($r=0.23$). Note, however, that noise sensitivity is a very general construct, reflecting many facets of the noise response unrelated to performance, such as sleep disturbances, interference with leisure activities, etc. On the other hand, the irrelevant speech effect very specifically measures the impact of speechlike sounds on the recall of serial order information. Thus relating a very broadly defined personality variable to a fairly narrow behavioral measure, one should not expect the relationship to be very strong. This interpretation is supported by the observation that if only those items judged *a priori* to relate to performance effects of noise are included in the correlation, it slightly increases to $r=0.31$.

It seems that, generally, attempts to relate self-report measures of noise susceptibility to behavior have not been all that successful. Thomas and Jones (1982) found equally low correlations (averaging 0.25 across different experimental conditions) when relating noise annoyance as measured by a questionnaire to the determination of uncomfortable loudness levels in the laboratory, two measures, for which one might expect a much closer intrinsic linkage.

As far as noise sensitivity is concerned, it might prove more promising to explore its relationship to a whole range of objective measures, using a multivariate approach more akin to the broad definition of the concept.

C. Subjective assessment of noise effects

Although self-reported general noise sensitivity did not correlate highly with the actual noise effects, one might expect a closer relationship, if subjects are queried about the specific interactions between task and noise in the experiment proper. It turns out that the subjects are unable to estimate effect sizes on the basis of familiarity with the sounds alone. They improve somewhat after gaining experience with the task. Interestingly, though, they are accurate only in predicting overall effects (see Fig. 5), while failing to predict their own noise susceptibility (as indicated by the low correlation of $r=0.29$ between individual estimates and error rates).

Admittedly, this result might be highly dependent on the specific sounds used in a given experiment. Had we, for example, used a familiar versus an unfamiliar language as irrelevant background conditions, subjects might have predicted differential effects, while the literature suggests equal disruption (e.g., Colle and Welsh, 1976; Salamé and Baddeley, 1982). Nevertheless, a study from our laboratory (Wolski, 1996) using quite different and nonintuitive stimuli (10 varieties of frequency-modulated tones) found a similarly low correlation between estimated and observed effects ($r = 0.23$). The low validity of self-evaluations seems to be a rather general finding: Mabe and West (1982) found a mean correlation of $r = 0.29$ in their meta-analysis of 55 studies relating subject's self-evaluations to objective criteria in a number of different performance domains.

A puzzling observation contributed by the present investigation is that, based on three types of performance estimates (retrospective impairment ratings and two varieties of noise-sensitivity questionnaires), women seem to be far better at predicting their performance under noise than are men. This gender difference might deserve further systematic study.

D. Practical recommendations for measuring noise effects

The present study offers several recommendations of practical importance for the investigation of individual differences in the irrelevant speech paradigm: First of all, a considerably larger number of trials than is typically used in experiments aiming at overall effects is required: 30 trials per condition might be sufficient for measuring individual differences in error rate; several hundred trials should be collected, when differences between errors in quiet and errors under irrelevant sound constitute the variable of interest. Second, conditions should be mixed in order to avoid confounding practice and fatigue effects with the individual outcomes. Third, the difficulty of individual trials should neither be too high (ten digits to memorize) nor too low (six digits), so floor and ceiling effects do not restrict the range of individual outcomes, and thereby attenuate the internal consistency of the task. Finally, as Fig. 3 indicates, spreading data collection over several session (or weeks) does not seem to introduce discontinuities, and might be more appropriate than running long sessions incurring additional problems of attention and fatigue.

VII. CONCLUSIONS

The present analysis of objectively measured noise effects suggests the following conclusions:

- (1) Individual differences in noise susceptibility as measured in the irrelevant speech paradigm exist, and are normally distributed over a considerable range.
- (2) They may be measured reliably, are fairly replicable over time, and do not change even with extensive practice.

- (3) For statistical reasons, however, measurement in terms of noise-minus-quiet performance differences severely constrains the precision with which individual effect sizes may be determined.
- (4) Subjects scoring high on a noise-sensitivity questionnaire produce more errors under noise than do subjects of low noise sensitivity. Nevertheless, individual differences in noise sensitivity only account for a small portion of the variance in objectively measured noise effects.
- (5) Subjective estimates of the impairment produced by a specific noise source are of low criterion validity and are practically useless when subjects did not have a chance to perform under the noise in question.

ACKNOWLEDGMENTS

We would like to thank Maria Klatte for providing us with a program to run the "irrelevant speech" experiment using a PC sound card, and Peter Daniel from Neutrik Cortex Instruments, Regensburg, for helping with equipment calibration and loudness computations. We are grateful to Dylan Jones for his helpful comments on an earlier version of this paper.

¹Obtaining subjective effect size ratings owes much to discussions with Dylan Jones at the occasion of the 7th Oldenburg symposium on psychoacoustics held in August, 1996.

²These correlations—like the ones computed for the questionnaire data presented in the next section—were corrected for measurement error due to the low reliability of the noise effects (see Sec. III B). This "correction for attenuation" (see Nunnally, 1978, p. 237) was applied according to the formula $\hat{r}_{12} = r_{12} / \sqrt{r_{22}}$ (see Lienert and Raatz, 1994, Eq. 11.24), where r_{12} is the "raw" correlation between the two variables, and r_{22} is the reliability of the second variable (here 0.55).

Buchner, A., Irmen, L., and Erdfelder, E. (1996). "On the irrelevance of semantic information for the "irrelevant speech" effect," *Q. J. Exp. Psychol.* **49A**, 765–779.

Colle, H. A., and Welsh, A. (1976). "Acoustic masking in primary memory," *J. Verb. Learn. Verb. Behav.* **15**, 17–32.

Cronbach, L. J. (1951). "Coefficient alpha and the internal structure of tests," *Psychometrika* **16**, 297–334.

Cureton, E. E. (1971). "The stability coefficient," *Educ. Psychol. Measurement* **31**, 45–55.

Ellermeier, W., and Hellbrück, J. (in press). "Is level irrelevant in "irrelevant speech"? Effects of loudness, signal-to-noise ratio, and binaural unmasking," *J. Exp. Psychol.: Human Percept. Perform.*

Green, D. M., and Fidell, S. (1991). "Variability in the criterion for reporting annoyance in community noise surveys," *J. Acoust. Soc. Am.* **89**, 234–243.

Hellbrück, J., Namba, S., and Kuwano, S. (1996). "Irrelevant background speech and human performance: Is there long-term habituation?" *J. Acoust. Soc. Jpn.* **17**, 239–247.

Job, R. F. S. (1988). "Community response to noise: A review of factors influencing the relationship between noise exposure and reaction," *J. Acoust. Soc. Am.* **83**, 991–1001.

Jones, D. M. (1993). "Objects, streams, and threads of auditory attention," in *Attention: Selection, Awareness, and Control. A Tribute to Donald Broadbent*, edited by A. Baddeley and L. Weisskrantz (Clarendon, Oxford).

Jones, D. M., and Davies, D. R. (1984). "Individual and group differences in the response to noise," in *Noise and Society*, edited by D. M. Jones and A. J. Chapman (Wiley, New York), pp. 125–153.

Jones, D. M., and Macken, W. J. (1993). "Irrelevant tones produce an irrelevant speech effect: Implications for phonological coding in short-term memory," *J. Exp. Psychol.: Learn. Memory Cogn.* **19**, 369–381.

- Jones, D. M., and Macken, W. J. (1995a). "Auditory babble and cognitive efficiency: The role of number of voices and their location," *J. Exp. Psychol. Appl.* **1**, 216–226.
- Jones, D. M., and Macken, W. J. (1995b). "Organizational factors in the effect of irrelevant speech: The role of spatial location and timing," *Memory Cognit.* **23**, 192–200.
- Jones, D. M., Bridges, A., Alford, D., Macken, W. J., and Tremblay, S. (submitted). "Mechanisms of auditory attention: the role of distinctiveness in the irrelevant speech effect," submitted to *J. Exp. Psychol.: Learning, Memory, and Cognition*.
- Jones, D. M., and Morris, N. (1992). "Irrelevant speech and cognition," in *Handbook of Human Performance*, edited by D. M. Jones and A. P. Smith (Academic, London), Vol. 1, pp. 29–53.
- Jones, D. M., Beaman, P., and Macken, W. J. (1996). "The object-oriented episodic record model," in *Models of Short-Term Memory*, edited by S. E. Gathercole (Psychology Press, Hove, UK), pp. 209–237.
- Jones, D. M., Macken, W. J., and Mosdell (in press). "The role of habituation in the disruption of recall performance by irrelevant sound," *Br. J. Psychol.*
- Kline, P. (1993). *The Handbook of Psychological Testing* (Routledge, London).
- LeCompte, D. C. (1994). "Extending the irrelevant speech effect beyond serial recall," *J. Exp. Psychol.: Learn. Memory, Cogn.* **20**, 1396–1408.
- Lienert, G. A., and Raatz, U. (1994). *Testaufbau und Testanalyse* [Test construction and test evaluation] 5th ed. (Beltz, Weinheim, Germany).
- Mabe, P. A., and West, S. W. (1982). "Validity of self-evaluation of ability: Review and meta-analysis," *J. Appl. Psychol.* **67**, 280–296.
- Nunnally, J. C. (1978). *Psychometric Theory* (McGraw-Hill, New York), 2nd ed.
- Salamé, P., and Baddeley, A. D. (1982). "Disruption of short-term memory by unattended speech: Implications for the structure of working memory," *J. Verb. Learn. Verb. Behav.* **21**, 150–164.
- Smith, A. P., and Jones, D. M. (1992). "Noise and performance," in *Handbook of Human Performance*, edited by D. M. Jones and A. P. Smith (Academic, London), Vol. 1, pp. 1–28.
- Smith, A. P., Jones, D. M., and Broadbent, D. E. (1981). "The effects of noise on recall of categorized lists," *Br. J. Psychol.* **72**, 299–316.
- Staples, S. L. (1996). "Human response to environmental noise: Psychological research and public policy," *Am. Psychol.* **51**, 143–150.
- Taylor, S. M. (1984). "A path model of aircraft noise annoyance," *J. Sound Vib.* **96**, 243–260.
- Thomas, J. R., and Jones, D. M. (1982). "Individual differences in noise annoyance and the uncomfortable loudness level," *J. Sound Vib.* **82**, 289–304.
- Weinstein, N. D. (1978). "Individual differences in reactions to noise: A longitudinal study in a college dormitory," *J. Appl. Psychol.* **63**, 458–466.
- Wilkinson, R. T. (1974). "Individual differences in response to the environment," *Ergonomics* **17**, 745–756.
- Wolski, U. (1996). "Experimentelle Untersuchung der Wirkung frequenzmodulierten Hintergrundschalls auf die Leistung in einer Gedächtnisaufgabe" ["Effects of frequency-modulated tones on performance in a memory task."] Master's thesis, University of Regensburg, Germany.
- Zimmer, K., and Ellermeier, W. (submitted). "Konstruktion und Evaluation eines Fragebogens zur Erfassung der individuellen Lärmempfindlichkeit" ["Construction and evaluation of a noise sensitivity questionnaire."], submitted to *Diagnostica*.

Use of pseudo-random sequences and a single microphone to measure surface impedance at oblique incidence

Jing-Fang Li

Department of Mechanical Engineering, University of British Columbia, 2324 Main Mall, Vancouver, British Columbia V6T 1Z4, Canada

Murray Hodgson

Occupational Hygiene Program and Department of Mechanical Engineering, University of British Columbia, 3rd Floor, 2206 East Mall, Vancouver, British Columbia V6T 1Z3, Canada

(Received 5 June 1996; revised 11 April 1997; accepted 5 June 1997)

The use of a pseudo-random sequence and a single microphone is suggested for the experimental determination of the acoustical properties (surface impedance, reflection coefficient, etc.) of sound-absorbing materials. An experimental system is developed with which the surface impedance and reflection coefficient at oblique incidence are determined from measurements of the impulse-response function sequentially at two locations close to the surface of the material using a pseudo-random sequence and a single microphone. This technique is validated using the measurement of a residual pressure-intensity index. The advantage of this technique is that it is possible to perform measurements of the surface properties of materials without phase-mismatch errors that occur with two-microphone methods. Models for estimating the surface impedance from plane-wave and spherical-wave hypotheses are reviewed and compared. Measurements of impedance at oblique incidence are carried out on a sheet of glass fiber in an anechoic room, as well as in a semi-reverberant room, and the results are compared. Surface impedances and reflection coefficients are presented as a function of angle of incidence. The proposed experimental system can be used to measure the acoustical properties of materials at oblique angles of incidence and in semi-reverberant environments. © 1997 Acoustical Society of America. [S0001-4966(97)06609-5]

PACS numbers: 43.55.Ev, 43.58.Bh [JDQ]

INTRODUCTION

Sound-absorbing materials are often characterized by their surface acoustical properties: the impedance, the reflection and absorption coefficients, etc. A lot of work has been done on the measurement of the surface impedances and reflection coefficients of materials in a free field or in semi-reverberant environments using two- or single-microphone cross-spectral functions or transfer-function techniques. Lahti¹ applied the intensity technique to measure the surface impedance of materials and of ground surfaces. He showed that the impedance can be determined directly by two-microphone and cross-spectral FFT techniques for measuring sound intensity, both in the laboratory and outdoors. By the same technique Carles *et al.*² described the *in situ* measurement of impedance and reflection coefficient of materials as a function of angle of incidence. By this technique the acoustical properties of materials could be characterized and the refraction angle of the acoustical wave inside the materials estimated. The two-microphone transfer-function technique has been employed for free-field and *in situ* impedance measurements³⁻¹² and for the characterization of porous media using the probe and level-difference techniques.¹³ Using this technique the acoustical pressures at two locations close to the surface of the material are measured using a two-microphone probe. The pressure and the particle velocity at the midpoint between the two locations are calculated by an approximate finite-difference method using the ratio of pressures measured at one location to that at another location.

The acoustical impedance at the midpoint is then the ratio of the pressure to the particle velocity. The surface impedance of the material is calculated using plane-wave^{4,9,11} or spherical-wave hypotheses.^{3,5,6} Investigations^{7,8,14} have been made of the limitations of, and the different sources of errors associated with, the two-microphone transfer-function technique—for example, the influence of the separation distance of the two microphones, the phase-mismatch error, etc. The use of a single microphone for measuring the transfer function in an impedance tube has been shown to eliminate the crucial problem of phase matching of the two microphones.^{15,16} However, the measurement process must be stationary, periodic, and repeatable in order to realize the measurement sequentially at two locations. Recently the acoustical holography technique has been used for measuring reflection coefficients at oblique incidence in an anechoic chamber.¹⁷ The plane-wave reflection coefficient at oblique incidence is obtained from measurements on two parallel planes. However, the precision of this technique used in determination of the properties of materials needs to be further analyzed.

The purpose of this article is to extend the use of pseudo-random sequences and a single microphone to impedance measurements of materials at oblique incidence in a semi-reverberant environment. First a technique for measuring acoustical impedance close to the surface of the material using a pseudo-random sequence and a single microphone is described. Experimental validation of this technique is performed by measuring a residual pressure-intensity index¹⁸ in

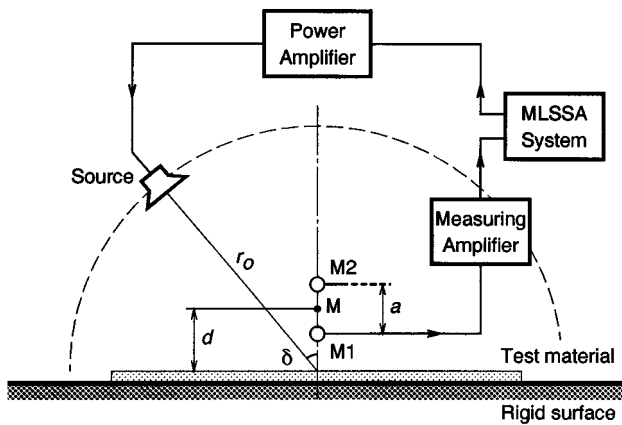


FIG. 1. Experimental configuration and equipment.

the sound field. Different models of wave reflection for estimating the surface impedance of materials from the measured acoustical impedance, including the plane-wave and spherical-wave assumptions, are reviewed. For the spherical-wave assumption, two methods are derived using different ways from that in Refs. 5 and 7. The reason the two methods using the spherical-wave assumption are different is explained. Measurements on glass fiber, both in an anechoic room and in a nonanechoic room, are described. Experimental results for the surface impedance and reflection coefficient of a glass fiber are presented. The experimental results are compared with the values predicted by the Delany and Bazley model.¹⁹ The comparison between the experimental values in the anechoic room and in the semi-reverberant room demonstrates the feasibility of measurements of surface impedance of material using the proposed experimental system involving a pseudo-random sequence and a single microphone.

I. EXPERIMENTAL METHOD

In this section an experimental system for measuring the acoustical properties of materials at oblique incidence is developed. The experimental method involves the measurement of the transfer function between the field point and the excitation signal at two points, using a pseudo-random excitation and a single microphone. The experimental system and the experimental technique are validated by measuring the residual pressure-intensity index.

A. Measurement system

A sketch of the experimental setup is shown in Fig. 1. A loudspeaker source is placed above the surface of the material at a constant distance r_0 from the test surface. M , being at a distance d from the sample of acoustical material, is the midpoint between two locations M_1 and M_2 at which a microphone is placed sequentially for measuring the sound field. δ is the nominal angle of incidence of the source to the surface. The acoustical impedance at midpoint M is expressed by two transfer functions, H_1 and H_2 , measured at M_1 and M_2 using the approximate finite-difference method (the time dependence $e^{-i\omega t}$ is used here):

$$\tilde{Z}_M = \frac{p}{u} = \frac{i\omega\rho a}{2} \frac{H_1 + H_2}{H_1 - H_2}, \quad (1)$$

where ρ is the air density, $\omega = 2\pi f$ is the angular frequency, with f being the frequency, and a is the distance between the two positions M_1 and M_2 .

If the process is stationary, H_1 and H_2 do not have to be determined simultaneously. A single microphone can be used to measure the transfer function sequentially at two locations.^{15,16} A digital pseudo-random signal generated by the maximum length sequence system analyzer (MLSSA)²⁰ was used in these measurements. MLSSA is a single-channel analyzer. However, it can do the work of conventional two-channel analyzers when the excitation signal is controlled. It computes a linear system impulse response by cross correlating the pseudo-random stimulus—a maximum length sequence (MLS)—with the measured system response. Unlike white noise, a MLS is deterministic and periodic, yet retains many desirable characteristics of white noise. The deterministic nature of the MLS means that it can be pre-computed and need not be measured simultaneously with the system response, as required by dual-channel FFT techniques. The periodic nature of the MLS means zero windowing error, as long as the entire period of the sequence is used to make the measurement.

In order to reduce the noise from the system and the environment, the transfer functions for calculating \tilde{Z}_M in Eq. (1) are averaged:

$$\bar{H}_1(\omega) = \sum_{n=1}^N H_{1n}(\omega) \quad \text{and} \quad \bar{H}_2(\omega) = \sum_{n=1}^N H_{2n}(\omega). \quad (2)$$

In the following section the residual pressure-intensity index¹⁸ is used to validate the experimental conditions.

B. Verification of experimental system and method

As for sound intensity, the acoustical impedance determined from two transfer functions is very sensitive to phase errors. In Ref. 14 the biased impedance \hat{Z} is expressed as a function of equivalent phase errors defined in terms of the characteristics of the microphones. In the measurement configuration adopted here, the microphone is oriented parallel to the surface of the material and the measurement is little sensitive to the vent effect in reactive fields. The biased impedance \hat{Z} depends only on the equivalent phase error ϕ_e between the signals measured at two positions.¹⁴

$$\hat{Z} = \frac{Z \pm |Z|^2/K_0}{1 \pm 2 \operatorname{Re}\{Z\}/K_0}, \quad \text{with} \quad K_0 = |p_0|^2/2\rho c |I_0| \approx ka/|\phi_e|. \quad (3)$$

The residual pressure-intensity index is defined as

$$L_{K_0} = L_{p_0} - L_{|I_0|} \\ = 10 \log K_0 \approx 10 \log ka/|\phi_e| \quad (\text{in dB}). \quad (4)$$

As only one channel is used in the impedance measurement, the equivalent phase error here does not include the electronic phase mismatch. However, if the repeatability properties of a system are not perfect (because of noise and non-linear effects, for example), an equivalent phase error will be introduced. This error can be represented as the difference in phases between two average transfer functions, \bar{H}_1 and \bar{H}_2 , which are determined from N time acquisitions without changing the position of the microphone:

$$\phi_e = \text{Arg}\{\bar{H}_1 \bar{H}_2^*\} = \bar{\varphi}_1 - \bar{\varphi}_2, \quad (5)$$

where \bar{H}_1 and \bar{H}_2 are given in Eq. (2). $\bar{\varphi}_1$ and $\bar{\varphi}_2$ are the phases of \bar{H}_1 and \bar{H}_2 , respectively (for $a=0$). It is noted from Eq. (5) that ϕ_e depends on the acquisition number N , and that it decreases with increasing N . As $\bar{\varphi}_1$ and $\bar{\varphi}_2$ are random variables which have Gaussian distributions, it is natural to determine ϕ_e by calculating the standard deviation of the phase of the transfer function φ .

In order to determine experimentally the statistical properties of the phase of the transfer function (i.e., the reproducibility of the measurement system)—for example, the mean value $\bar{\varphi}$ and the variance $\sigma^2[\varphi]$ —a series of transfer functions H_m ($m=1,2,3,\dots,M$) was measured using a single microphone at the same position in the sound field. The configuration of this measurement was the same as shown in Fig. 1. The measurements were done in a semi-reverberant room. The glass fiber sheet was placed on the floor of the room. A microphone was placed 10 cm from the surface of the material. The loudspeaker used in the impedance measurement was driven by a deterministic broadband signal generated by the MLSSA system.

Suppose that the acquisition number M is large enough; then the standard deviation of the phase of the transfer function is estimated by

$$\sigma[\varphi] \approx \sqrt{\frac{1}{M-1} \sum_{m=1}^M (\varphi_m - \bar{\varphi})^2}, \quad (6)$$

where $\bar{\varphi} = \text{Arg}\{\bar{H}\}$ with $\bar{H} = (1/M) \sum_{m=1}^M H_m$. Since φ_1 and φ_2 have Gaussian distributions, the variances of $\bar{\varphi}_1$ and $\bar{\varphi}_2$ determined by two sets of N measurements are

$$\text{Var}[\bar{\varphi}_1] \approx \text{Var}[\bar{\varphi}_2] \approx \frac{\sigma^2[\varphi]}{N}. \quad (7)$$

The variance of $\bar{\varphi}_1 - \bar{\varphi}_2$ is expressed as

$$\text{Var}[\bar{\varphi}_1 - \bar{\varphi}_2] = \text{Var}[\bar{\varphi}_1] + \text{Var}[\bar{\varphi}_2] - 2 \text{Cov}[\bar{\varphi}_1, \bar{\varphi}_2]. \quad (8)$$

Since the two sets of measurements are independent of each other, $\text{Cov}[\bar{\varphi}_1, \bar{\varphi}_2] = 0$, and Eq. (8) becomes

$$\text{Var}[\bar{\varphi}_1 - \bar{\varphi}_2] = \frac{2\sigma^2[\varphi]}{N}. \quad (9)$$

The equivalent phase error can be defined statistically from the variance of $\bar{\varphi}_1 - \bar{\varphi}_2$ by

$$|\phi_e| \approx \sqrt{\frac{2}{N}} \sigma[\varphi]. \quad (10)$$

Substituting Eq. (10) into Eq. (4) yields

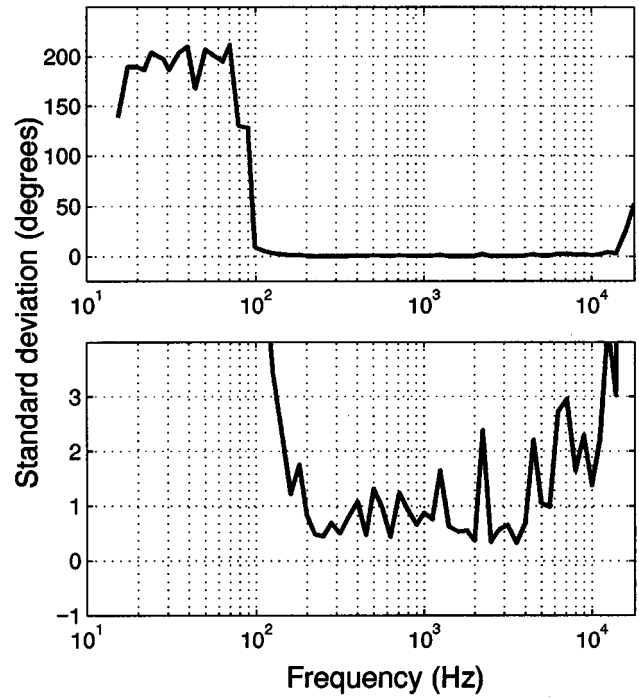


FIG. 2. Standard deviation $\sigma[\varphi]$ (in degrees) of the phase angle of the transfer function estimated using the 150 experimental samples H_m ($m=1,2,3,\dots,150$). The lower graph shows the standard deviation on an expanded scale.

$$\begin{aligned} L_{K_0} &= 10 \log \sqrt{\frac{N}{2} \frac{ka}{\sigma[\varphi]}} \\ &= 10 \log \frac{ka}{\sqrt{2}\sigma[\varphi]} + 5 \log N \quad (\text{in dB}). \end{aligned} \quad (11)$$

Equation (11) shows that the residual pressure-intensity index L_{K_0} is dependent on the standard deviation of the phase of the measured transfer function, the separation distance of the microphones, frequency, and the number of acquisitions.

Figure 2 shows the standard deviation $\sigma[\varphi]$ estimated from 150 measurement samples. It is noted that $\sigma[\varphi] > 25^\circ$ at frequencies $f < 100$ Hz. This means that significant uncertainty occurs at frequencies $f < 100$ Hz. This is because that insufficient energy is generated by the loudspeaker at low frequencies. The residual pressure-intensity index is generally used as a quality indicator of the instruments for the finite-difference approximation in acoustics. The estimated values L_{K_0} were calculated using $\sigma[\varphi]$ in the case of $a = 10$ cm and $a = 0.5$ cm, respectively. The results are presented in Fig. 3, where $N = 32$. It is shown that for $a = 10$ cm, $L_{K_0} > 20$ dB over the frequency range $200 < f < 20\,000$ Hz, whereas when $a = 0.5$ cm, $L_{K_0} > 20$ dB over the frequency range $2000 < f < 20\,000$ Hz.

This verification allows us to obtain the impedance using a single microphone without phase-mismatch errors as in the two-microphone method. With the hypothesis of a Gaussian distribution of φ , the 68% confidence intervals of the measured impedance can be estimated by substituting Eq. (10) into Eq. (3). It also shows that there exists a low-frequency limitation using this technique. In order to reduce

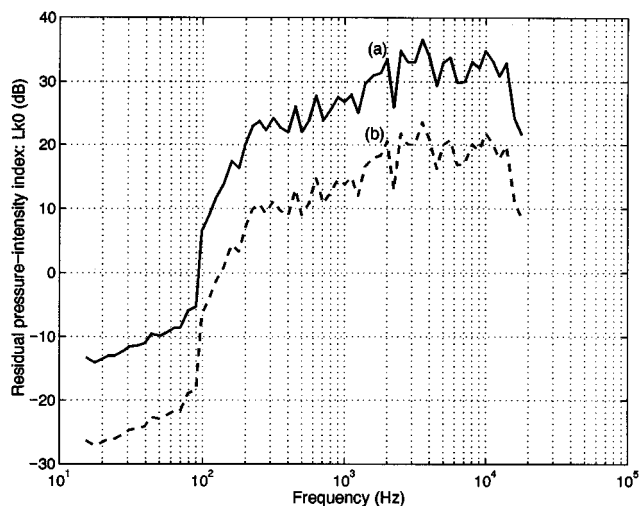


FIG. 3. Residual pressure-intensity index (in dB) for two distances between the two microphone positions: (a) $a = 10$ cm; (b) $b = 0.5$ cm.

the error caused by the system, the separation distance between the two microphone positions should be as large as possible. Unfortunately this will result in a high-frequency limit associated with the finite-difference method. Nevertheless the separation distance of the microphone position should be chosen by considering the system error, as well the error caused by the finite-difference method.

II. REVIEW OF MODELS FOR ESTIMATING THE SURFACE IMPEDANCE OF MATERIALS

The surface impedance of materials can be determined from the acoustical impedance \tilde{Z}_M measured several centimeters above the surface of the material. Two types of wave propagation have been used in the estimation of surface impedance.^{3,5} The first model involves the use of the plane-wave assumption. This model is easily implemented and can give an adequate evaluation of surface impedances when the distance from the source to the surface of the material is greater than 2 m, and when the frequency is greater than 500 Hz.⁹ However, in some cases, the source should be as close as possible to the surface of the material in order to reduce the effects of finite size of test material and to avoid unexpected noise generated by reflections from the ceiling and walls when doing *in situ* measurements. When the source is close to the material, the determination of the surface impedance by the plane-wave assumption can be strongly biased at low frequencies.^{3,9,10} Thus the spherical-wave approximation should be used. There are two methods for estimating the surface impedance of materials using the spherical-wave hypothesis.^{5,6} The first method uses the definition of the acoustical impedance at the sound-field point. The second method uses the pressures at two field points to derive the surface impedance. The objective of this section is to review models for estimating the surface impedance of materials. Expressions for estimating the surface impedance of materials based on plane- and spherical-waves hypotheses are given in terms of the angle of incidence of the excitation signal and of the acoustical impedance of the material. The expressions are derived from the calculation of \tilde{Z}_M

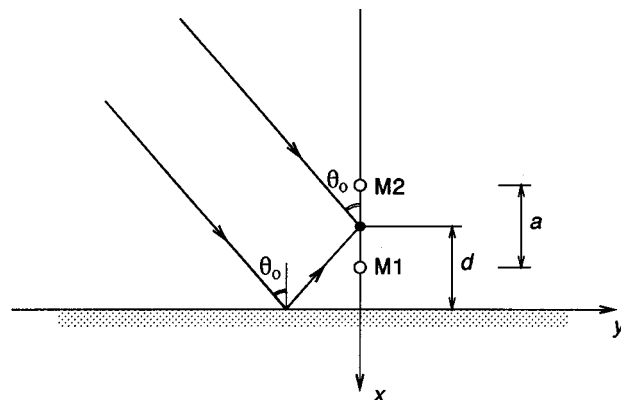


FIG. 4. Coordinate system for the plane-wave model.

$= p_M / u_M$, instead of the p_1 / p_2 ratio.^{3,5,6} As a result, the expressions for estimating the surface impedance are represented by \tilde{Z}_M instead of p_1 / p_2 . However the expressions in this section are equivalent to those in Refs. 5, 3, and 6. The procedure for the derivation of the expression for the spherical-wave surface impedance will allow the relationship between the two methods to be established.²¹

A. Estimation of surface impedance by the plane-wave hypothesis

In the coordinate system shown in Fig. 4 the pressure and the particle velocity are given by (the phase reference point is chosen as the origin of the coordinate system)

$$p = A e^{ik(x \cos \theta_0 + y \sin \theta_0)} + AR(\theta_0) e^{ik(-x \cos \theta_0 + y \sin \theta_0)}, \quad (12a)$$

$$u_x = \frac{1}{i\rho c k} \frac{\partial p}{\partial x} = \frac{A \cos \theta_0}{\rho c} [e^{ik(x \cos \theta_0 + y \sin \theta_0)} - R(\theta_0) e^{ik(-x \cos \theta_0 + y \sin \theta_0)}], \quad (12b)$$

where θ_0 is the angle of incidence of the plane wave. The acoustical impedance is obtained from:

$$Z = \frac{p}{u_x} = \frac{\rho c}{\cos \theta_0} (e^{ikx \cos \theta_0} + R e^{-ikx \cos \theta_0}) \times (e^{ikx \cos \theta_0} - R e^{-ikx \cos \theta_0})^{-1}. \quad (13)$$

By setting $x = 0$ in Eq. (13), the surface impedance becomes:

$$Z_s = \frac{\rho c}{\cos \theta_0} \frac{1 + R(\theta_0)}{1 - R(\theta_0)}. \quad (14)$$

In order to estimate the relationship between the surface impedance and the acoustical impedance at any point above the surface, the reflection coefficient $R(\theta_0)$ is solved from Eq. (13):

$$R(\theta_0) = \frac{\xi e^{ikx \cos \theta_0} - e^{ikx \cos \theta_0}}{\xi e^{-ikx \cos \theta_0} + e^{-ikx \cos \theta_0}}, \quad (15)$$

with $\xi = Z \cos \theta_0 / \rho c$. Taking $x = -d$ and $Z = \tilde{Z}_M$ in Eq. (15), then substituting the result into Eq. (14), one has:

$$Z_s = \frac{\tilde{Z}_M \cos \theta_0 + i\rho c \tan kd \cos \theta_0}{\rho c + i\tilde{Z}_M \cos \theta_0 \tan kd \cos \theta_0} \frac{1}{\cos \theta_0}, \quad (16a)$$

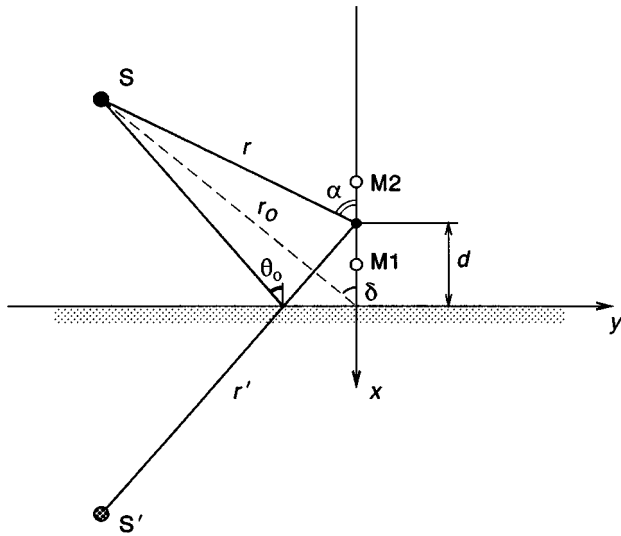


FIG. 5. Coordinate system for the spherical-wave model used for acoustical impedance measurements.

$$R(\theta_0) = \frac{Z_s \cos \theta_0 / \rho c - 1}{Z_s \cos \theta_0 / \rho c + 1}, \quad (16b)$$

where d is the distance from the midpoint between the two measurement locations to the surface of material, and \tilde{Z}_M is the acoustical impedance at the midpoint as given by Eq. (1).

B. Estimation of surface impedance by the spherical-wave hypothesis

Two methods for estimating the surface impedance of materials are derived by use of the spherical-wave assumption. The expression for the spherical pressure at the field point above the material is used in the calculations. Figure 5 shows the configuration for spherical waves. The material is backed by a rigid surface. Thus the pressure at midpoint M is given by the following approximation:

$$p = p_0 \left(\frac{e^{ikr}}{r} + R(\theta_0) \frac{e^{ikr'}}{r'} \right). \quad (17)$$

The spherical-wave approximation can be acceptable within a small distance of the material. Two formulae are derived using the spherical-wave assumption.

1. Use of acoustical impedance measurements

In the first method, the acoustical impedance at the midpoint is calculated using the pressure and particle velocity at this point. The particle velocity in the x direction is obtained by taking the derivative of Eq. (17) with respect to the variable x :

$$u_x = \frac{1}{ik\rho c} \frac{\partial p}{\partial x} = \frac{p_0}{\rho c} \left[\frac{e^{ikr}}{r} \left(1 + \frac{i}{kr} \right) \cos \alpha - R(\theta_0) \frac{e^{ikr'}}{r'} \left(1 + \frac{i}{kr'} \right) \cos \theta_0 \right], \quad (18a)$$

where

$$\cos \alpha = \beta \cos \theta_0, \quad (18b)$$

$$\beta = \frac{\cos \delta - d/r_0}{\cos \delta + d/r_0} \sqrt{\frac{(1 + 2d \cos \delta / r_0 + d^2/r_0^2)}{(1 - 2d \cos \delta / r_0 + d^2/r_0^2)}},$$

$$r = \sqrt{(r_0 \sin \delta)^2 + (r_0 \cos \delta - d)^2}, \quad (18c)$$

$$r' = \sqrt{(r_0 \sin \delta)^2 + (r_0 \cos \delta + d)^2}.$$

r_0 is the distance from the source to the point on the surface of the test material, δ is the nominal angle of incidence shown in Fig. 5, and θ_0 is the effective angle of incidence. The expression for the acoustical impedance at distance d from the surface of the material is obtained from Eqs. (17) and (18):

$$Z_M = \frac{p}{u_x} = \frac{\rho c}{\cos \theta_0} \left[\frac{e^{ikr}}{r} + \frac{R(\theta_0)e^{ikr'}}{r'} \right] \left[\frac{e^{ikr}(1 + i/kr)\beta}{r} - \frac{R(\theta_0)e^{ikr'}(1 + i/kr')}{r'} \right]^{-1}. \quad (19)$$

The surface reflection coefficient is deduced from Eq. (19) in terms of the acoustical impedance at point M :

$$R(\theta_0) = \frac{\beta(1 + i/kr)\tilde{\xi}_M - 1}{(1 + i/kr')\tilde{\xi}_M + 1} \frac{r'}{r} e^{-ik(r-r')}, \quad (20)$$

with $\tilde{\xi}_M = Z_M \cos \theta_0 / \rho c$.

At the surface, $d=0$, $\theta_0 = \delta$, $\beta=1$, and $r=r'=r_0$; the surface impedance can be obtained from Eq. (19):

$$Z_s(\theta_0) = \frac{\rho c}{\cos \theta_0} \frac{1 + R(\theta_0)}{1 - R(\theta_0)} \frac{1}{1 + i/kr_0}. \quad (21)$$

The measurement procedure determines $R(\theta_0)$ from Eq. (20), where Z_M is substituted by the approximation \tilde{Z}_M of Eq. (1) using a finite-difference method which involves two measured impulse-response functions. The relationship between the effective angle of incidence θ_0 and the nominal angle of incidence δ is

$$\theta_0 = \text{Arctan} \frac{\sin \delta}{d/r_0 + \cos \delta}. \quad (22)$$

If the position of the microphone is very close to the surface of the material—i.e., $r \gg d$, $r' \gg d$ —the following approximations hold: $\beta \approx 1$, $\alpha \approx \theta_0 \approx \delta$, $r \approx r_0 - d \cos \theta_0$, $r' \approx r_0 + d \cos \theta_0$. Equation (20) becomes

$$R(\theta_0) \approx \frac{[ik - (r_0 - d \cos \theta_0)^{-1}]\tilde{\xi}_M - ik}{[ik - (r_0 + d \cos \theta_0)^{-1}]\tilde{\xi}_M + ik} \frac{r_0 + d \cos \theta_0}{r_0 - d \cos \theta_0} \times e^{-2ikd \cos \theta_0}, \quad (23)$$

where $\tilde{\xi}_M \approx \tilde{Z}_M \cos \theta_0 / \rho c$.

2. Use of a relationship between pressures at two field positions

The second method uses the pressures at two positions close to the surface of the material to obtain the approximate pressure \tilde{p}_M and particle velocity \tilde{u}_M at the midpoint using the finite-difference method. Then the surface impedance and reflection coefficient are obtained using \tilde{p}_M and \tilde{u}_M .

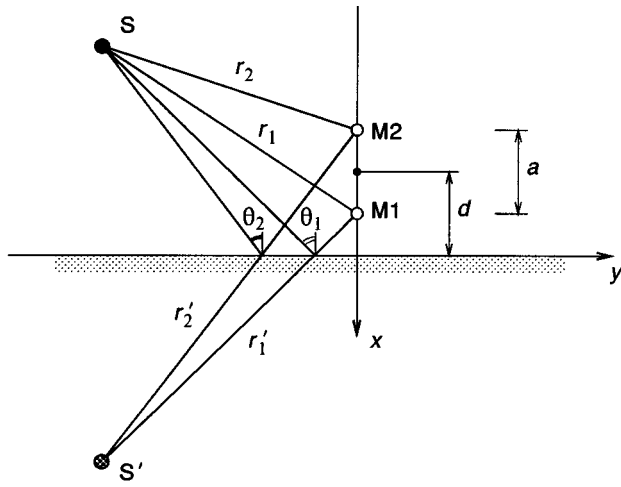


FIG. 6. Coordinate system for the spherical-wave model based on a relationship between the pressures at two field positions.

The cylindrical coordinate system shown in Fig. 6 is used in the calculations which follow. The pressures at points M_1 and M_2 are written as

$$p_1 = p_0 \frac{e^{ikr_1}}{r_1} + p_0 R(\theta_1) \frac{e^{ikr'_1}}{r'_1}, \quad (24a)$$

$$p_2 = p_0 \frac{e^{ikr_2}}{r_2} + p_0 R(\theta_2) \frac{e^{ikr'_2}}{r'_2}. \quad (24b)$$

The pressure at the surface of the material is given by

$$p = p_0 \frac{e^{ikr_0}}{r_0} + p_0 R(\delta) \frac{e^{ikr_0}}{r_0}, \quad (24c)$$

where δ is the nominal angle of incidence shown in Fig. 5, and

$$\theta_1 = \text{Arctan} \frac{\sin \delta}{\cos \delta + (d - a/2)/r_0}, \quad (24d)$$

$$\theta_2 = \text{Arctan} \frac{\sin \delta}{\cos \delta + (d + a/2)/r_0},$$

$$\begin{cases} r_1 = |SM_1| = [(r_0 \sin \delta)^2 + (r_0 \cos \delta + a/2 - d)^2]^{1/2}; \\ r_2 = |SM_2| = [(r_0 \sin \delta)^2 + (r_0 \cos \delta - a/2 - d)^2]^{1/2}; \\ r'_1 = |S'M_1| = [(r_0 \sin \delta)^2 + (r_0 \cos \delta - a/2 + d)^2]^{1/2}; \\ r'_2 = |S'M_2| = [(r_0 \sin \delta)^2 + (r_0 \cos \delta + a/2 + d)^2]^{1/2}. \end{cases} \quad (24e)$$

The impedance at the mid-point between M_1 and M_2 can be obtained using the finite-difference method:

$$\begin{aligned} \tilde{Z}_M &= \tilde{p}_M / \tilde{u}_M \\ \text{with } \tilde{p}_M &= (p_1 + p_2)/2, \quad \tilde{u}_M = (p_1 - p_2)/ipcka. \end{aligned} \quad (25)$$

Substituting Eqs. (24a) and (24b) into Eq. (25) yields:

$$\tilde{Z}_M = \frac{ipcka}{2} \frac{T_1 + T_2 + R(\theta_1)T'_1 + R(\theta_2)T'_2}{T_1 - T_2 + R(\theta_1)T'_1 - R(\theta_2)T'_2}, \quad (26)$$

where $T_1 = e^{ikr_1}/r_1$, $T'_1 = e^{ikr'_1}/r'_1$, for example. For the case where $r_0 \gg a$ and the angle of incidence is not close to 90° , $\theta_1 \approx \theta_2 \approx \theta_0$ and $R(\theta_1) \approx R(\theta_2) \approx R(\theta_0)$ [θ_0 is given in Eq. (22)]. In this case the surface reflection coefficient can be solved out:

$$R(\theta_0) = \frac{-i\omega paA/2 + B\tilde{Z}_M}{C\tilde{Z}_M + i\omega paD/2}, \quad (27)$$

where $A = T_1 + T_2$, $B = T_1 - T_2$, $C = T'_2 - T'_1$, and $D = T'_1 + T'_2$. The surface impedance is obtained by substituting $R(\theta_0)$ into Eq. (21). It should be noted that Eq. (27) is equivalent to the results in Refs. 5 and 6.

Although Eq. (27) and Eq. (20) are both derived using the spherical-wave model, they give different results in estimating the surface impedance Z_s by Eq. (21). The reason is that Eq. (20) is derived from the calculation of the pressure and velocity at midpoint M . Errors will be included in Eq. (20) if Z_M is replaced by \tilde{Z}_M which can be obtained from measurements. On the other hand, Eq. (27) is deduced from the pressures p_1 and p_2 at two positions M_1 and M_2 . Thus \tilde{Z}_M is involved in this expression. It was shown that these two expressions can be made identical over some frequency range by introducing an error-correction function.²¹

III. EXPERIMENTAL PROCEDURE, RESULTS, AND ANALYSIS

This section will present the use the experimental system described in Sec. I for measurements of the acoustical properties of materials. An experimental procedure for measuring the surface impedance is presented. Different models for obtaining the surface impedance as described in the previous section are compared, using the measured data. Then the normalized surface impedance and reflection coefficient are presented as a function of angle of incidence. Measurements in an anechoic room and in a semi-reverberant room are compared.

A. Experimental procedure

A block diagram of the experimental configuration and the main equipment used in the measurements are shown in Fig. 1.

1. Source

The sound source was a loudspeaker enclosed with a wood box driven by the pseudo-random-sequence generator of the MLSSA system. The loudspeaker was supported by a stand which allowed the nominal angle of incidence δ to be changed from normal incidence to 50° . The distance from the source to the surface of the material r_0 could also be varied. In this study three distances $r_0 = 31, 56, 71$ cm are considered. The angles of incidence tested were $\theta_0 = 0^\circ, 10^\circ, 20^\circ, 30^\circ, 40^\circ$, and 50° .

2. Receiver

A $\frac{1}{4}$ in. microphone (Bruel&Kjaer type 4135) was used to measure the pressure in the acoustical field. The microphone was mounted on a support allowing the position relative to the surface of the test sample to be adjusted with a

TABLE I. Measurement-position separation a and the corresponding frequency range f_1-f_2 for the finite-difference method.

a (cm)	10	5	1	0.5
f_1-f_2 (Hz)	300–600	600–1200	1200–5800	5800–14 000

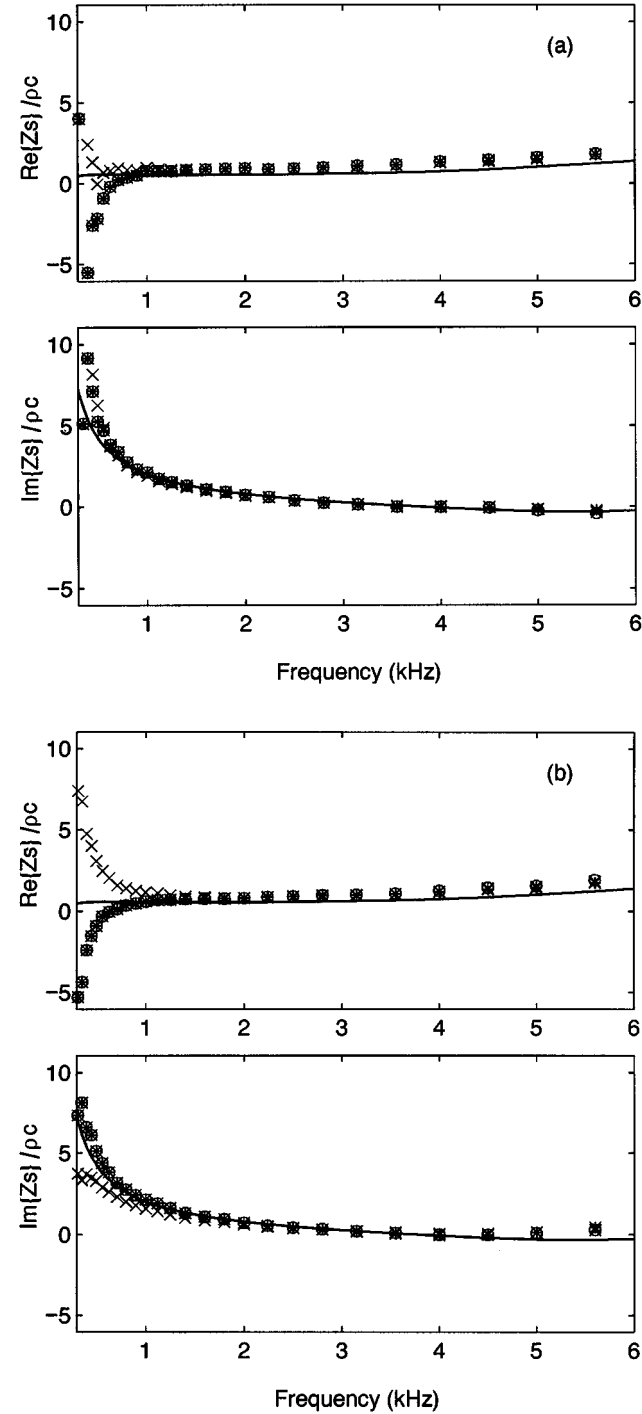


FIG. 7. Real and imaginary parts of the normalized surface impedance of glass fiber at normal incidence for two distances from the source to the surface of material: (a) $r_0=71$ cm; (b) $r_0=31$ cm. (—) predicted values using Delany and Bazley model; (○○○○○○) method 1 by spherical-wave Eq. (20); (*****) method 2 by spherical-wave Eq. (27); (××××××××) plane-wave assumption.

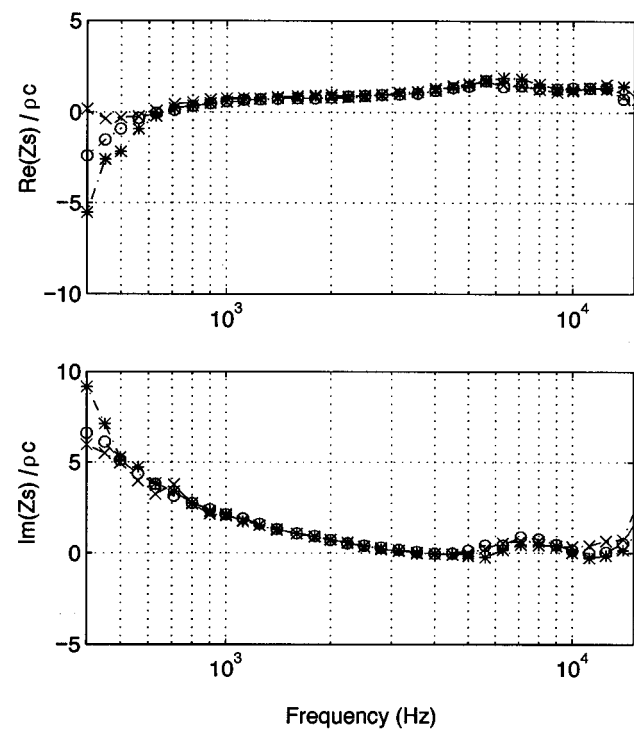


FIG. 8. Normalized surface impedance of glass fiber at normal incidence for three distances r_0 : (*****) $r_0=71$ cm; (××××××××) ($r_0=56$ cm; (○○○○○○○○) $r_0=31$ cm.

precision of 0.025 cm. The first position of the microphone was set at 2 cm from the surface. Measurements were performed at several positions with respect to the surface to allow different a to be obtained. In order to minimize the error caused by the inaccuracies in the positioning of the microphone, a should be as large as possible.⁷ However, large microphone separation distance reduces the high-frequency cutoff. In the situation here, the inaccuracies in the positioning of the microphone are relatively small. This error ϵ can be estimated using Eq. (1):

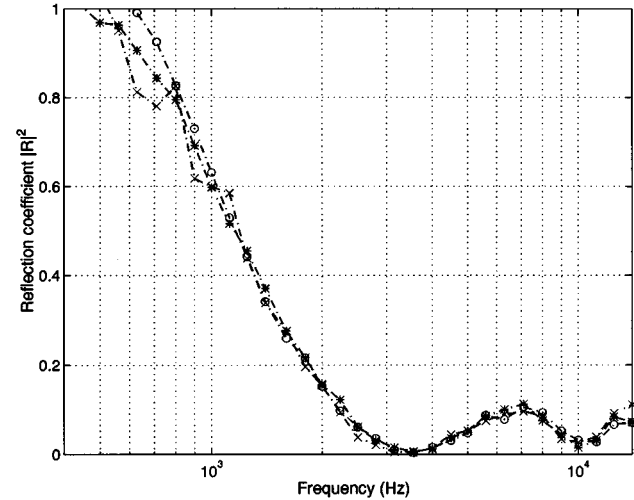


FIG. 9. Amplitude of the surface reflection coefficient of glass fiber at normal incidence for three distances r_0 from the loudspeaker to the surface of the sample: (*****) $r_0=71$ cm; (××××××××) $r_0=56$ cm; (○○○○○○○○) $r_0=31$ cm.

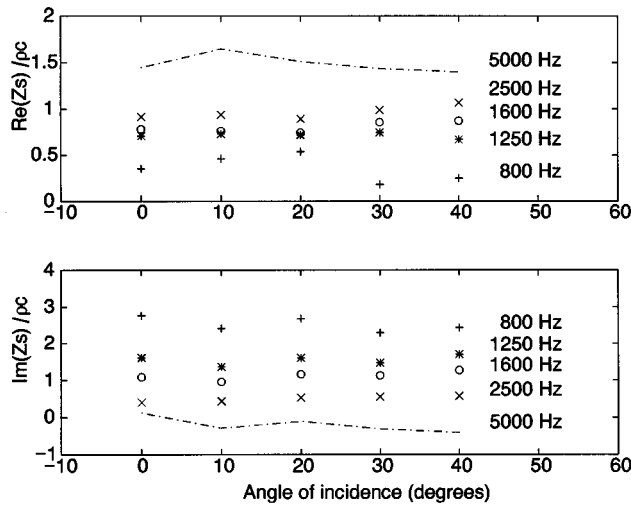


FIG. 10. Normalized surface impedance of glass fiber at oblique incidence at the frequencies indicated.

$$\epsilon = \frac{|\tilde{Z}_M - \tilde{Z}'_M|}{|\tilde{Z}'_M|} = \pm \frac{\Delta a}{a + \Delta a}, \quad (28)$$

where Δa is the inaccuracy in measuring a . For the system used here $\Delta a = \pm 0.05$ cm. If the minimum separation distance $a = 0.5$ cm, then the maximum error caused by inaccuracy of positioning the microphone is $0.9\% \leq \epsilon \leq 1.1\%$. This maximum error occurs at high frequencies $f > 5800$ Hz, when $a = 0.5$ cm is used in the impedance measurements.

3. Test material

An industrial glass fiber was chosen as the test material for the measurements; its size was 1.2×1.2 m², its thickness 2 cm. Its normal flow resistivity was $\sigma \approx 20\,000$ Nsm⁻⁴ obtained experimentally from the pressure difference across a sample of the material subjected to a steady air flow.²² The glass fiber sheet was backed by an acoustically hard, plane boundary. The anisotropic properties¹² are not considered here.

B. Measurements in the anechoic room

1. Comparison of different models

The models described in Sec. II were used to determine surface impedance, and the results were compared. The acoustical impedance \tilde{Z}_M was calculated from the averaged pair of measured transfer functions \bar{H}_1 and \bar{H}_2 using Eq. (2) (the averaging number was 32). The low-frequency limitation ($f_c = 0.25c/a$) caused by the finite-difference method is taken into consideration by choosing different distances a between the two positions for different frequency ranges. The distance from the first microphone position to the surface of the material was 2 cm. The test distances, a , and the corresponding frequency ranges for which results are presented in this section, are given in Table I.

The plane-wave reflection coefficients and surface impedances were calculated from \tilde{Z}_M using Eqs. (15) and (16). Equations (20) and (27), corresponding to method 1 and method 2, were used for calculating the spherical-wave re-

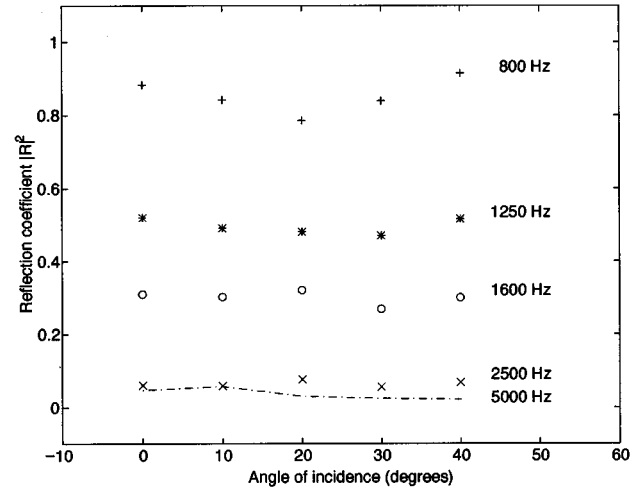


FIG. 11. Amplitude of the surface reflection coefficient of glass fiber at oblique incidence at the frequencies indicated.

flection coefficients. Then the spherical surface impedance was obtained from Eq. (21). Experimental results were compared with the predicted values calculated using the model of the impedance at oblique incidence for a layer of finite thickness backed by a rigid wall.²²

$$Z_s(\theta_0) = iZ_c \frac{1}{\sqrt{1 - k_0^2 \sin^2 \theta_0 / k_c^2}} \times \cotg(k_c \sqrt{1 - k_0^2 \sin^2 \theta_0 / k_c^2} e), \quad (29)$$

where $k_0 = \omega/c$, e is the thickness of the test material. k_c and Z_c are, respectively, the complex wave number and the characteristic impedance in the material, obtained using the Delany and Bazley model:¹⁹

$$k_c = \frac{\omega}{c} [1 + 0.0978X^{-0.700} + i0.189X^{-0.595}], \quad (30a)$$

$$Z_c = \rho c [1 + 0.0571X^{-0.754} + i0.087X^{-0.732}], \quad (30b)$$

where ρ and c are the density of air and the sound speed in air, and X is a dimensionless parameter equal to:

$$X = \rho f / \sigma, \quad \text{with } 0.01 < X < 1.0, \quad (31)$$

$f = \omega/2\pi$ being the frequency.

Measured and predicted values of normalized surface impedance at normal incidence for $\sigma = 20\,000$ Nsm⁻⁴ are presented in Fig. 7(a) for $r_0 = 71$ cm and (b) for $r_0 = 31$ cm, respectively. Note that the plane-wave and spherical-wave estimations and prediction all give similar values in the frequency range 1–4 kHz, especially for the imaginary part of $Z_s/\rho c$. In the case of $r_0 = 31$ cm [Fig. 7(a)], the two methods using the spherical-wave estimations—Eqs. (20) and (27)—give good agreement with prediction. At frequencies above 5 kHz, there are differences between these two methods calculated by Eq. (20) and Eq. (27) although they are both derived from the spherical-wave hypothesis. The reason is that Eq. (20) is derived from the calculation of the pressure p and the normal component of the particle velocity u_x at midpoint M , resulting in $Z_M = p/u_x$. Errors will be included in Eq. (20) if Z_M is replaced by \tilde{Z}_M which can be obtained from measure-

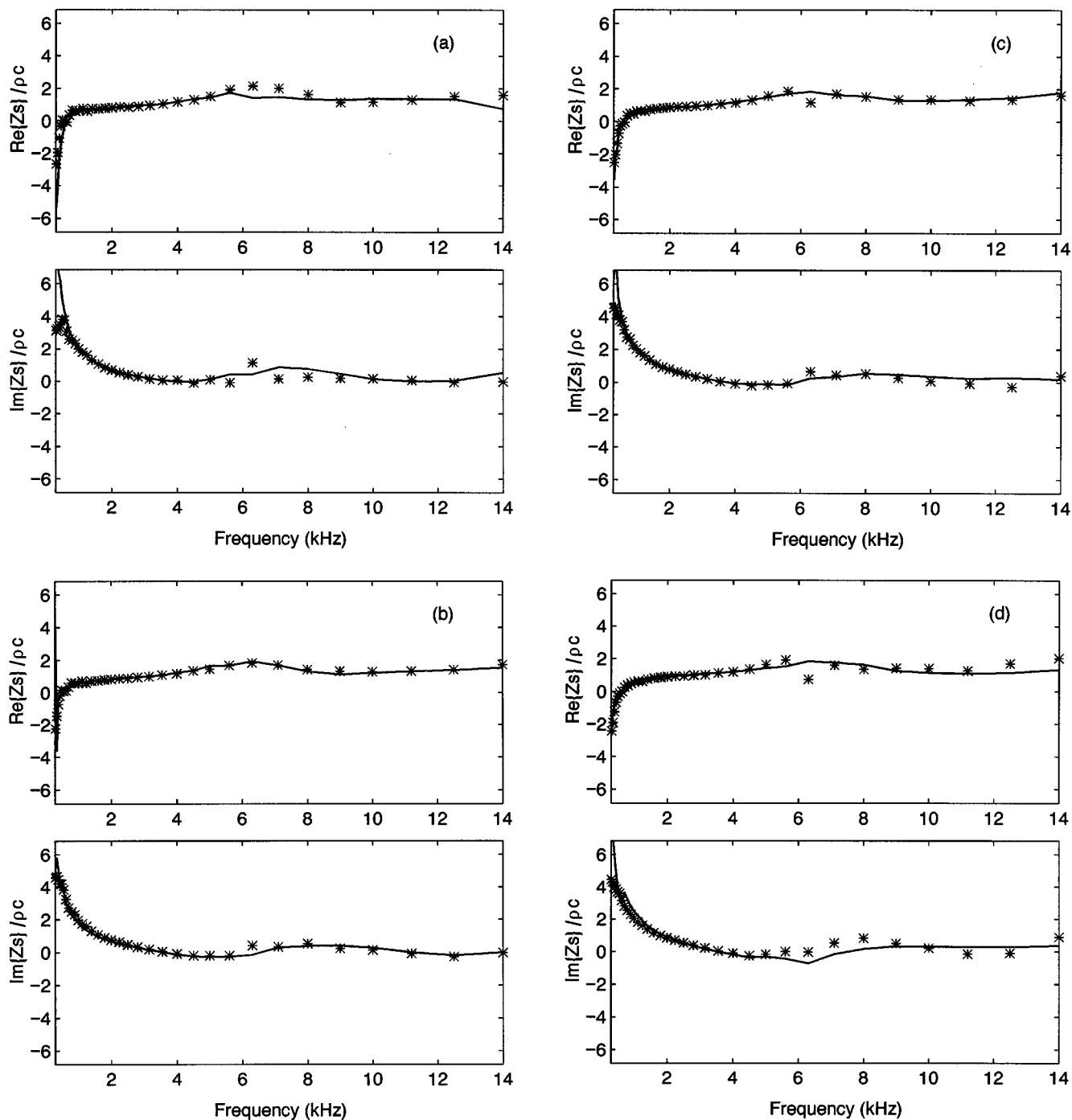


FIG. 12. Comparison of the normalized surface impedance of glass fiber measured in an anechoic room (—) and in a nonanechoic room (*****) for $r_0 = 31$ cm: (a) $\theta_0 = 0^\circ$; (b) $\theta_0 = 10^\circ$; (c) $\theta_0 = 30^\circ$; (d) $\theta_0 = 40^\circ$.

ments. However, Eq. (27) is deduced from the pressures p_1 and p_2 at two positions M_1 and M_2 . Thus \tilde{Z}_M is involved in this expression itself. Thus the error from the finite-difference method is not included in this calculation. As a result, Eq. (27) provides the best agreement with prediction with respect to the real part of $Z_s/\rho c$. However the relationship between these two methods can be established. It was shown that these two expressions can be made identical over some frequency range by introducing an error-correction function.²¹

At frequencies below 1 kHz, there are significant differ-

ences between the calculated and predicted values, especially in the case of plane-wave propagation for which the difference increases with decreasing distance r_0 . At lower frequency, the values from the plane-wave model deviate significantly from the predicted values, especially, when $r_0 = 31$ cm. The results for the spherical-wave model show similar deviations at low frequencies. The results shown in Fig. 7 demonstrate that method 2 using the spherical assumption gives the best estimates of Z_s . In the following work Eqs. (21) and (27) will be used to calculate the surface impedance and reflection coefficient.

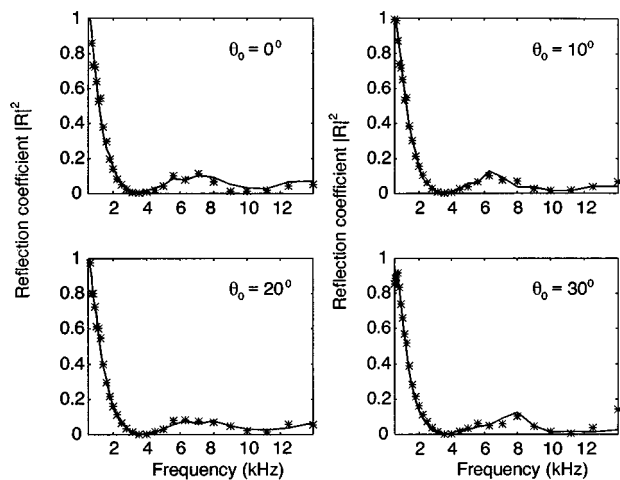


FIG. 13. Comparison of the surface reflection coefficient of glass fiber measured in an anechoic room (—) and in a nonanechoic room (-----) for $r_0 = 31$ cm with the angles of incidence indicated.

2. Effect of source/surface distance r_0

Figure 8 shows measured values of the normalized surface impedance $Z_s/\rho c$ for the glass fiber at normal incidence as a function of frequency for the three distances from the source to the surface of the sample; the corresponding measured surface reflection coefficients are shown in Fig. 9. The results for the three distances r_0 are very similar at low frequencies, but there are small differences above 4000 Hz. This is because of errors resulting from the finite-difference approximation used to calculate \bar{Z}_M by Eq. (2). This error is related to r_0 , as well as to the angle of incidence, and increases with frequency.²¹ Thus it should be corrected for at high frequencies.

3. Variation of Z_s and R_s with incident angle θ_0

An acoustical material can be characterized as extended reaction or local reaction according to whether the surface impedance depends on angle of incidence or not.² Using the experimental system described in Sec. I, measurements were made for different angles of incidence. The loudspeaker was moved around the microphone measurement position which was not changed. In Figs. 10 and 11 the measured normalized surface impedance $Z_s(\theta_0)/\rho c$ and reflection coefficient $R(\theta_0)$ are plotted versus angle of incidence at 800, 1250, 1600, 2000, and 5000 Hz with $r_0 = 31$ cm. From the results it can be seen that the glass fiber is of extended reaction at low frequencies and of more local reaction at high frequencies, as indicated by Eqs. (29) and (30).

C. Measurement in a semi-reverberant room

The same measurements were performed in a semi-reverberant room with dimensions $10 \times 5 \times 3$ m³ and reverberation time of about 1 s. Figures 12 and 13 show the measured normalized surface impedances and reflection coefficients at oblique incidence for $r_0 = 31$ cm in the anechoic and semi-reverberant rooms under the same conditions. For $r_0 = 31$ cm, the surface-reflection coefficients and impedances measured in the semi-reverberant room agree well with those obtained in the anechoic room at frequencies

below 5 kHz. Differences between the two results appear at high frequencies, especially in the case of normal incidence. However, from a practical point of view, these differences can be considered insignificant in comparison with the advantages associated with being able to measure in semi-reverberant environments.

IV. CONCLUSION

A technique using pseudo-random sequences and a single microphone for measurement of the acoustical properties of materials has been developed and validated experimentally by measuring the residual pressure-intensity index L_{K0} . It was shown that this technique has low-frequency limitations because of insufficient energy generated by the measurement system. An experimental system has been developed for determining the acoustical properties of materials at oblique incidence in reverberant acoustical environments based on the measurement of two transfer functions sequentially at two locations using a single microphone. Estimation of the plane-wave and spherical-wave surface impedance and reflection coefficient of materials was reviewed using the measured acoustical impedance at the midpoint. It was noted that there are differences between the two methods which use the spherical-wave assumption. The representations of the two methods using the spherical-wave assumption reveal why the two methods give different result especially at high frequencies. It will be shown elsewhere²¹ that these differences can be eliminated by correction of the errors caused by the finite-difference approximation. The comparison showed that the use of the method two in spherical-wave assumption Eq. (27) gives the best results over a wide frequency range, especially for the reverberant measurement when the distance from the source to the surface of the material must be as small as possible. Measurements were carried out for glass fiber at different angles of incidence. It was shown that the surface impedance of tested glass fiber changed with angle of incidence. The results of experiments in a semi-reverberant room show good agreement with those in an anechoic room for $300 < f < 5000$ Hz. This allows us to conclude that the acoustical properties of materials can be measured in typical reverberant rooms using a pseudo-random sequence and a single microphone.

¹T. Lahti, "Direct measurement of the ground impedance by the intensity technique," FASE 84 Congress Proc. **13-4**, 589-592 (1984).

²C. Carles, D. Abraham, and J.-C. Pascal, "Mesure *in situ* de l'impédance acoustique des matériaux en fonction de l'angle d'incidence," Proceedings of the 2nd International Congress on Acoustic Intensity, Senlis, France, 23-26 Sept. 1985, pp. 97-104.

³J. F. Allard, Y. Champoux, and J. Nicolas, "Pressure variation above a layer of absorbing material and impedance measurement at oblique incidence and low frequencies," J. Acoust. Soc. Am. **86**, 766-770 (1989).

⁴J. F. Allard, R. Bourdier, and A. M. Bruneau, "The measurement of acoustic impedance at oblique incidence with two microphones," J. Sound Vib. **101**, 130-132 (1985).

⁵J. F. Allard and Y. Champoux, "In situ two-microphone technique for the measurement of the acoustic surface impedance of materials," Noise Control Eng. J. **15**, 15-23 (1989).

⁶M. A. Nobile, "Measurement of the spherical wave absorption coefficient at oblique incidence using the two-microphone transfer function method,"

- Inter-Noise 89 Proc. Newport Beach, CA, Dec. 4–6, 1989, pp. 1067–1072.
- ⁷Y. Champoux and A. L'Espérance, "Numerical evaluation of errors associated with the measurement of acoustic impedance in a free field using two microphones and a spectrum analyzer," *J. Acoust. Soc. Am.* **84**, 30–38 (1988).
 - ⁸T. Legouis and J. Nicolas, "Phase gradient method of measuring the acoustic impedance of materials," *J. Acoust. Soc. Am.* **81**, 44–50 (1987).
 - ⁹Y. Champoux, J. Nicolas, and J. F. Allard, "Measurement of acoustic impedance in a free field at low frequencies," *J. Sound Vib.* **125**, 313–323 (1988).
 - ¹⁰J. F. Allard, C. Depollier, and P. Guignouard, "Free field surface impedance measurements of sound-absorbing materials with surface coatings," *Appl. Acoust.* **26**, 199–207 (1989).
 - ¹¹J. F. Allard and B. Sieben, "Measurements of acoustic impedance in a free field with two microphones and a spectrum analyzer," *J. Acoust. Soc. Am.* **77**, 1617–1618 (1985).
 - ¹²J. F. Allard, R. Bourdier, and A. L'Espérance, "Anisotropy effect in glass wool on normal impedance in oblique incidence," *J. Sound Vib.* **114**, 233–238 (1987).
 - ¹³C. Frederickson, J. M. Sabatier, and R. Raspet, "Acoustic characterization of rigid-frame air-filled porous media using both reflection and transmission measurements," *J. Acoust. Soc. Am.* **99**, 1326–1332 (1996).
 - ¹⁴J.-F. Li and J.-C. Pascal, "The influence of microphone vents on measurements of sound intensity and impedance," *J. Acoust. Soc. Am.* **99**, 969–978 (1996).
 - ¹⁵F. J. Fahy, "Rapid method for the measurement of sample acoustic impedance in a standard wave tube," *J. Sound Vib.* **97**, 168–170 (1984).
 - ¹⁶W. T. Chu, "Transfer function technique for impedance and absorption measurements in an impedance tube using a single microphone," *J. Acoust. Soc. Am.* **80**, 555–560 (1986).
 - ¹⁷M. Tamura, "Spatial Fourier transform method of measuring reflexion coefficients at oblique incidence. I: Theory and numerical examples," *J. Acoust. Soc. Am.* **88**, 2259–2264 (1990).
 - ¹⁸F. Jacobsen, "Spatial sampling errors in sound power estimation based upon intensity," *J. Sound Vib.* **145**, 129–140 (1991).
 - ¹⁹M. E. Delany and E. N. Bazley, "Acoustical properties of fibrous absorbent materials," *Appl. Acoust.* **3**, 105–116 (1970).
 - ²⁰D. D. Rife, *Maximum-Length Sequence System Analyser—Reference Manual* (Version 9.0) (DRA Laboratories, Sterling, VA, 1994).
 - ²¹J.-F. Li, M. Hodgson, and J.-C. Pascal, "Errors caused by the finite-difference approximation in the estimation of the surface impedances of materials," *Proc. NoiseCon'96*, Bellevue, WA, June 13–15, 1996, pp. 723–728.
 - ²²J. F. Allard, *Propagation of Sound in Porous Media: Modelling Sound Absorbing Materials* (Chapman & Hall, London, 1995), Chaps. 2 and 3.

A time domain binaural model based on spatial feature extraction for the head-related transfer function

Zhenyang Wu,^{a)} Francis H. Y. Chan,^{b)} and F. K. Lam

Department of Electrical and Electronic Engineering, University of Hong Kong, Pokfulam Road, Hong Kong

Joseph C. K. Chan

Division of Technology, City University of Hong Kong, Tat Chee Ave, Hong Kong

(Received 18 July 1996; revised 9 June 1997; accepted 11 June 1997)

A complex-valued head-related transfer function (HRTF) can be represented as a real-valued head-related impulse response (HRIR). The interaural time and level cues of HRIRs are extracted to derive the binaural model and also to normalize each measured HRIR. Using the Karhunen–Loeve expansion, normalized HRIRs are modeled as a weighted combination of a set of basis functions in a low-dimensional subspace. The basis functions and the space samples of the weights are obtained from the measured HRIR. A simple linear interpolation algorithm is employed to obtain the modeled binaural HRIRs. The modeled HRIRs are nearly identical to the measured HRIRs from an anesthetized live cat. Typical mean-square errors and cross-correlation coefficients between the 1816 measured and modeled HRIRs are 1% and 0.99, respectively. The real-valued operations and linear interpolating in the model are very effective for speeding up the model computation in real-time implementation. This approach has made it possible to simulate real free-field signals at the two eardrums of a cat via earphones and to study the neuronal responses to such a virtual acoustic space (VAR). © 1997 Acoustical Society of America. [S0001-4966(97)02410-7]

PACS numbers: 43.64.Bt, 43.66.Ba, 43.64.Ha, 43.66.Qp [RDF]

INTRODUCTION

Sound arriving at listener's eardrums in a free-field sound signal varies with source direction (Shaw, 1974; Blauert, 1983). A direction-dependent transformation is referred to as a head-related transfer function (HRTF) to acknowledge the primary acoustical importance of head and pinnas. Each HRTF pair obtained in the two ears contains interaural cues in time and level, and spectral cues. The spectral cues of the HRTF are characterized by peaks and notches, some of which vary systematically with changes in sound source direction. New approaches based on the HRTFs have enabled researchers to synthesize directional stimuli for headphone presentation using measured HRTFs (Wightman and Kistler, 1989; Chan *et al.*, 1993; Brugge *et al.*, 1992; Wenzel, 1992). In these approaches, the stimulus waveforms appropriate for the right and left eardrums were computed using the pair of HRTFs corresponding to a sound-source direction and then delivered through compensated headphones. In a physiological study, we need more sophisticated stimuli for earphone presentation to understand how the neural system might use directional cues. Those allow complete and independent control of localization cues in synthesizing virtual auditory signals, that would be difficult to obtain with free-field stimuli, and present virtual auditory space to the subject with continuous spatial resolution.

Functional representations of the HRTFs were proposed by several authors (Batteau, 1967; Genuit, 1986; Chen *et al.*,

1992). They sought a mathematical model or equation that represents the HRTF as a function of frequency and direction, such that the models could provide explicit mathematical relationship between the HRTF and source location. One direction of research, for example, was based on Batteau's pinna-simulating model that saw the HRTF as being synthesized by a delay-and-add system with one direct path and two delayed paths. Functional approaches would reduce the storage requirement and represent the HRTF at an arbitrary direction. However, attempts to describe the HRTF in a simple mathematical equation have been of only limited success. Also, to maintain model accuracy it would be necessary to determine the delay time and the attenuation for the delayed path. Application of the functional model is thus limited to representation of external ear characteristics over whole auditory space.

Low-dimensional and orthogonal representations for sets of HRTFs have been generated by using the Karhunen–Loeve expansion of HRTFs, and employing an essentially identical mathematical operation, Kistler and Wightman (1992) established a model based on principal components analysis and minimum-phase reconstruction. They applied principal components analysis (PCA) to the logarithms of the HRTF magnitudes after the removal of direction-independent and subject-dependent spectral features. From the PCA representation, HRTFs for each direction were reconstructed using phase estimates based on the minimum phase characteristic corresponding to each magnitude function. These studies are available only for the measured directions. More recently, a spatial feature extraction and regularization model for the HRTFs was proposed (Chen *et al.*, 1995). In this model the HRTFs were expressed as weighted

^{a)}Current address: Department of Radio Engineering, Southeast University, Nanjing 210018, People's Republic of China.

^{b)}Electronic mail: fhychan@eee.hku.hk

combinations of a set of complex valued eigentransfer functions. The sample weights are determined by projecting all measured HRTFs onto the eigentransfer functions. A functional representation for weights is obtained by applying a thin plate generalized spline smoothing model to regularize the sample weights. This approach maintains the phase of the spectral components and model accuracy at a whole upper 3/4 sphere but deals with large amounts of complex valued computation in matrix-vector products and two-dimensional splines.

Both the PCA model and the spatial feature extraction and regularization model have focused on the frequency components. The time domain and frequency domain behaviors are related through the Fourier transform and are equivalent in their carrying of directional information. In the time domain, we can describe the HRTF as head-related impulse responses (HRIR). The HRIR, unlike HRTF, is a real-valued time series. The HRIR model need only deal with real valued computation. Using the HRIR model the actual phase information is maintained instead of having to make minimum phase approximations, and the extensive computation with complex-valued eigenfunctions is also avoided. The eardrum stimuli can be obtained by directly convolving the HRIR with the free-field signals in the time domain.

In this paper, a binaural HRIR model for the implementation of virtual acoustic space is developed. In this model the interaural time and level cues are extracted from the measured HRIRs of a cat. The HRIRs are normalized by removing the time differences and level differences. Karhunen-Loeve expansion is used to represent the normalized HRIR in a low-dimensional space. The normalized HRIRs, which contain the spectral cues, are expressed as weighted combinations of a set of basis functions. The basis functions are real-valued eigenvectors that are derived from a covariance matrix of the measured HRIRs. The weights, applied to each basis function and termed real spatial characteristic functions (RSCFs), define the relative contribution of each basis function to the HRIR and are real-valued functions of the spatial location. At an arbitrary spatial location, the estimates of the RSCFs, as well as the estimates of the interaural time and level cues can be obtained by interpolating the RSCFs and the interaural time and level cues at measurement locations. The modeled binaural HRIRs are reconstructed from these estimates. The modeled binaural HRIRs are used to synthesize stimuli that, when presented over earphones, simulate free-field sound signals transmitted to the eardrums of a cat. The work described in this article represents our attempt, through the development of a simple binaural model, to simulate realistic stimuli.

I. MODELING METHODS

The data employed in the evaluation of the model were derived from a detailed set of direction-dependent recordings made near the eardrum of an anesthetized cat by Musicant *et al.* (1990). In that study, the cat was secured in a holder in an experimental chamber with the head oriented. The frontal direction at ear level was defined as 0° azimuth and 0° elevation. The left and right sides at ear level were defined as -90° and $+90^\circ$ azimuth, respectively. The back direction at

ear level was defined as $\mp 180^\circ$ azimuth. Direction on the median plane spanned the range of $\pm 90^\circ$ elevation. The free-field loudspeaker was moved in the spherical coordinate system. The loudspeaker signal was a digitally generated $10\text{-}\mu\text{s}$ rectangular pulse. The output of the preamplifier of the microphone, whether in the free-field or from the ear canal, was sampled by a 12-bit A/D converter at a rate of 160 kHz. Sampling was for a duration of 6.4 ms with a total of 1024 sampling points. Two recordings (left and right ears) were made for each position at which the loudspeaker was located. In this study, the data on a 9° grid are used to develop the model and the whole set of data on a 4.5° grid is used for comparisons with the model.

A. Data preprocessing

The free-field recording and eardrum recordings were contaminated by random noise, echoes, and dc levels that were produced by microphone, reflecting objects, and amplifier, respectively. Data preprocessing eliminates these effects as far as possible. Figure 1(a)–(f) is a depiction of the data preprocessing employed to eliminate the unwanted components of raw recordings. Careful examination of the eardrum recording [Fig. 1(a)] and free-field recording [Fig. 1(b)] reveals that random noise is dominant in the low (< 1.5 kHz) and high (> 30 kHz) frequency regions where the speaker has low responses and these recordings contain one or two echo components following the primary response peak. These unwanted components can cause very large variances in the estimated HRTF [Fig. 1(e)].

A Hamming window and linear phase finite-impulse-response (FIR) filter were chosen to preprocess these recording signals [Fig. 1(c) and (d)]. The distance between the primary response peak and the first echo is about 2.5 ms. So, we selected the window width as 450 sample points, corresponding to a width of about 2.8 ms. The window center is located at the primary response peaks of the recordings. A linear phase FIR filter was used to eliminate the random noise in free-field recording and eardrum recordings. The filter is a bandpass filter with 0.5-dB ripple for 1–30-kHz passband and 65-dB attenuation for 40–80-kHz stop band. The additional delay of the filter output is a constant with no phase distortion in the passband. After filtering, the signal was downsampled by a factor of 2 (to 80 kHz), thereby reducing the number of sampled points to 512.

Differences in propagation path lengths between sound source and eardrum lead to different delays in eardrum recordings. Onset times of each recording were detected. Details of detecting method were described by Chen *et al.* (1995). Each eardrum recording was then shifted backward or forward to a common time origin. Interaural time difference (ITD) is a major cue influencing the identification of the sound source direction. We calculated the ITD by subtracting the onset time of ipsilateral recording from the onset time of contralateral recording at each direction. The ITDs were used as a delay parameter for every reconstructed HRIR in a binaural model.

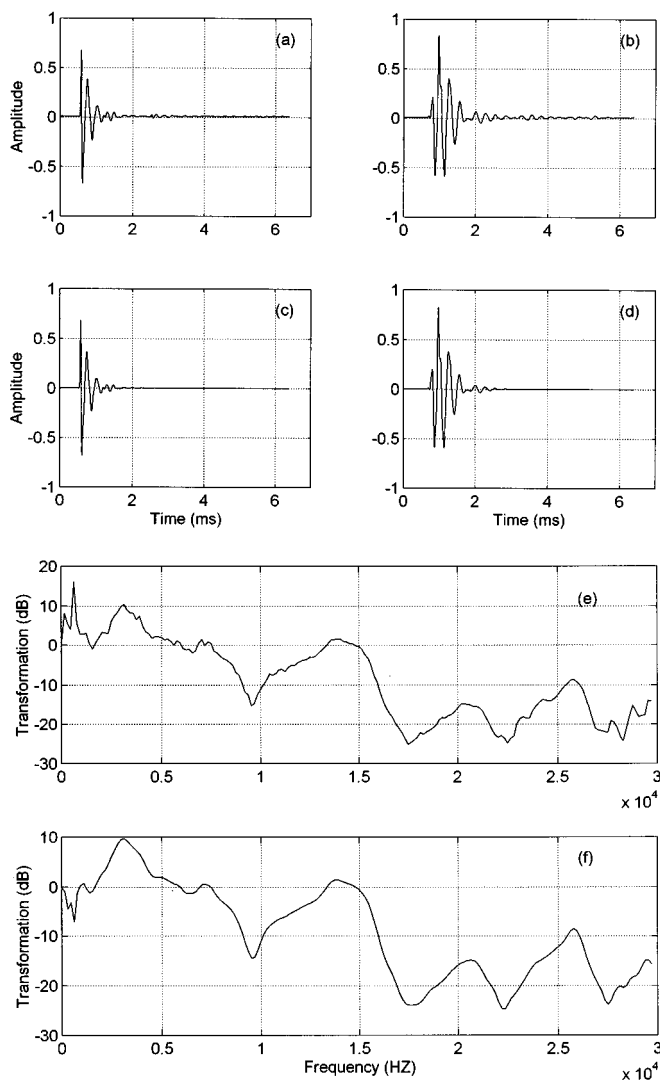


FIG. 1. Comparison between the HRTFs using the raw data in free field (a) and eardrum (b) and preprocessed data (c) and (d). Panel (e) is HRTF relative to (a) and (b); Panel (f) is HRTF relative to (c) and (d). Loudspeaker location was at 18° azimuth and 18° elevation.

B. Estimation and normalization of the HRIR

The HRIR, in most of the HRIR literature, is simply determined from the inverse Fourier transform of HRTF. The estimation of HRIR based on the fast Fourier transform (FFT) method is given by

$$H(\omega) = \frac{Y(\omega) + N(\omega)}{U(\omega)}, \quad (1)$$

where $Y(\omega) + N(\omega)$ and $U(\omega)$ are the Fourier transforms of eardrum recording $y(n) + \eta(n)$ and free-field recording $u(n)$, and $N(\omega)$ is Fourier transform of measurement noise $\eta(n)$. This method is termed empirical transfer function estimation. The estimate error in Eq. (1) is dependent on the measurement noise $\eta(n)$. Least-squares FIR filters could be applied to the HRIR estimation problem (Chen *et al.*, 1995; Wu *et al.*, 1996). The least-squares FIR filters were designed entirely in the time domain based on least-squares error criterion. Wu *et al.* (1996) compared the empirical estimation

with the least-squares FIR filter estimation under different signal-to-noise ratio (SNR) conditions. The conclusion is that the least-squares FIR filter method is much better than the empirical method when the SNR of an eardrum recording is less than 40 dB. The SNR of an eardrum recording is difficult to define precisely because the level gain varies with azimuth and elevation. The maximum level gain difference over the sphere is about 25 dB. Some of the recordings have small peak values, that is only 30 dB above quantization noise of a 12-bit A/D converter. The level is generally low, furthermore, in the high-frequency region (above 15 kHz) where spectral notches occur in the eardrum recordings. For example, the noise peak is approximately 20 dB above the deepest notch at some directions. The improvement obtained with the least-squares FIR filter estimation is evident in this project.

Previous investigators (Hiranaka and Yamasaki, 1983) have reported that a 2-ms interval of time gating was enough to observe the human HRIR. The cat HRIRs have shorter duration because the cat external ear is smaller than the human's. Noting that the maximum cat ITD is about 0.26 ms, the duration of HRIR was selected longer than 2 ms. For the HRIR, the length N equals to the product of the duration (2×10^{-3} s) and the sampling rate (80×10^3 Hz) and is corresponding exactly to the number of coefficients in the least-squares FIR filter $h(n)$ which is used to estimate the unknown HRIR system. The output of the FIR filter, $\hat{y}(n) = h(n) * u(n)$, where the asterisk denotes the convolution, is expected to be an approximation of $y(n)$. When the sum of square errors,

$$\epsilon = \sum_{n=0}^{N-1} [\hat{y}(n) - \{y(n) + \eta(n)\}]^2, \quad (2)$$

is minimized, the FIR filter coefficients $h(n)$, $n=0,1,\dots,N-1$, represent the best estimate of HRIR. This result is termed as least-squares FIR filter (Hakin, 1986).

Due to the "head-shadow effect", each HRIR has different energy which equals to the sum-square of $h(n)$. We define the square root of the energy as the level gain of the HRIR. All HRIRs used in our model were normalized by its level gain. The normalized HRIRs, having the same energy and onset time, would have different spectral characteristics. The normalizing procedures decrease the variances of HRIRs. Interaural level difference (ILD) is another major cue influencing the identification of the sound source direction. The ILD for broadband frequencies is the ratio of the ipsilateral level gain to the contralateral level gain. The ILD at a particular frequency or over a narrow frequency band depends on the ILD for broadband frequencies as well as the binaural HRIRs. The ILD for broadband frequencies was also used as an amplitude parameter for every reconstructed HRIR in a binaural model.

C. Low-dimensional representation of normalized HRIRs and linear interpolation

The low-dimensional representation of log-magnitude HRTFs was reported in (Kistler and Wightman, 1992). The low-dimensional representation of complex valued HRTFs

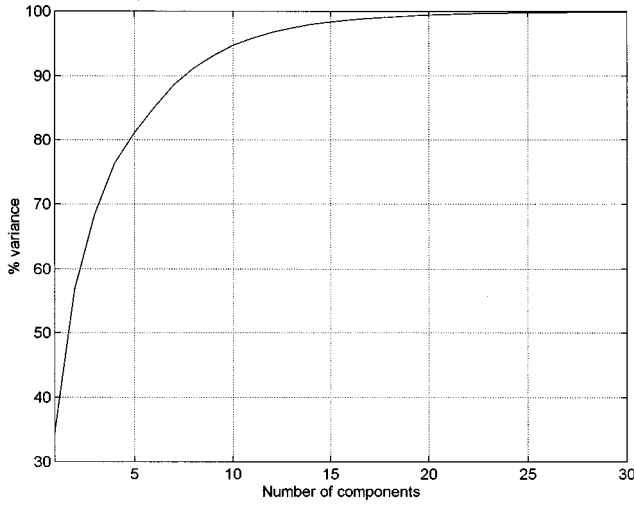


FIG. 2. The percentage of HRIR variation versus the number of components.

was described in detail by Chen *et al.* (1995). A brief description of our procedure for low-dimensional representation of normalized HRIR is given here.

We derived orthonormal basis functions from the normalized HRIRs. Prior to deriving the basis function, the space sample average was subtracted from each normalized HRIR to remove the direction-independent component. The space sample average is defined as

$$\mathbf{h}_{av} = \frac{1}{P} \sum_{j=1}^P \mathbf{h}_j, \quad (3)$$

where vector \mathbf{h}_j with N elements represents the j th normalized HRIR from a set of P eardrum recordings. A time autocovariance matrix was then calculated by

$$\mathbf{R}_h = \frac{1}{P} \sum_{j=1}^P (\mathbf{h}_j - \mathbf{h}_{av})(\mathbf{h}_j - \mathbf{h}_{av})^T \quad (4)$$

which is a real valued matrix. The normalized HRIR on a 9° grid, which corresponds to $p=541$ measured samples, are used to determine the \mathbf{R}_h . The eigenvectors of \mathbf{R}_h were chosen as the columns of an orthonormal transformation matrix $\mathbf{Q} = [\mathbf{q}_1 \ \mathbf{q}_2 \ \cdots \ \mathbf{q}_N]$. For the Karhunen–Loeve expansion, a given normalized HRIR \mathbf{h}_j is represented by

$$\mathbf{h}_j = \mathbf{Q}\mathbf{w}_j + \mathbf{h}_{av} = \sum_{i=1}^N w_{ij}\mathbf{q}_i + \mathbf{h}_{av}, \quad (5)$$

where the weight vector \mathbf{w}_j is a set of orthonormal transform coefficients, given by

$$\mathbf{w}_j = \mathbf{Q}^T(\mathbf{h}_j - \mathbf{h}_{av}). \quad (6)$$

A small set of basis vector, that is discrete basis function, was then selected to represent the normalized HRIRs in a low-dimensional space. The Karhunen–Loeve expansion minimizes the mean-square error (MSE) for a given number of basis vector. Figure 2 shows the percentage of HRIR variation increases as a function of the number of components which are referred to weighted basis vectors. We noted that the first five components (Kistler and Wightman, 1992)

represent 90% of human HRTF magnitude variation while the cat's HRIRs require eight components which account for the same amount of variation in Fig. 2. This is because that phase information is kept in the HRIRs and the HRIRs for the cat have a 30-kHz band width. We chose 20 components in this project, which can represent more than 99.9% of the variation in the normalized HRIRs.

We further define the i th coefficient subset $\{w_{ij}, j = 1, \dots, p\}$ as discrete samples of an underlying continuous function (Chen *et al.*, 1995), termed the i th real spatial characteristic function (RSCF). The RSCFs are functions of spatial coordinates (θ, φ) and are denoted as $w_i(\theta, \varphi)$, $i = 1, 2, \dots, 20$. The normalized HRIR in a continuous space (θ, σ) is represented as

$$\hat{\mathbf{h}}(\theta, \phi) = \sum_{i=1}^{20} \hat{w}_i(\theta, \phi) \mathbf{q}_i + \mathbf{h}_{av}. \quad (7)$$

Using the linear space interpolation algorithm, for the arbitrary direction (θ, φ) over the upper 3/4 sphere (elevation from -36° to 90°), we get the estimates of RSCFs

$$\begin{aligned} \omega_i(\theta, \phi) \approx & \frac{(\theta - \theta_2)(\varphi - \varphi_2)}{A} w_i(\theta_1, \varphi_1) \\ & + \frac{(\theta - \theta_2)(\varphi - \varphi_1)}{A} w_i(\theta_1, \varphi_2) \\ & + \frac{(\theta - \theta_1)(\varphi - \varphi_2)}{A} w_i(\theta_2, \varphi_1) \\ & + \frac{(\theta - \theta_1)(\varphi - \varphi_1)}{A} w_i(\theta_2, \varphi_2), \end{aligned} \quad (8)$$

where $A = 9 \times 9$ is an area of the 9° grid, (θ_1, φ_1) , (θ_1, φ_2) , (θ_2, φ_1) , and (θ_2, φ_2) are the four neighboring measurement locations of (θ, φ) .

II. RESULTS

A. Interaural features

The ITD contour plot is presented in Fig. 3. This figure was constructed by subtracting the onset time of the right (near) ear from that of the left (far) ear for each sound source location. The plots, on a 4.5° grid, were determined through interpolation from the measured samples on a 9° grid. The numbers with a plus sign (+) are the time differences in ms. The maximum time difference, noted by an asterisk (*), is located at 108° azimuth, 0° elevation with 0.2625 ms. All contours are clustered around the maximum point. The minimum contour is located at the median plane (azimuth 0° or 180°) and the top of head (elevation 90°).

Figure 4 is an interaural representation (right minus left in dB) of level gain for broadband frequencies. The plots, on a 4.5° grid, also were determined through interpolation from the measured samples on a 9° grid. The numbers with a plus sign (+) are the level differences in dB. The maximum level difference, noted by an asterisk (*), is located at 72° azimuth, 9° elevation with 14.69 dB. The area up to 3-dB decrements is located in 45° to 95° azimuth and -18° to 20° elevation. Minima, ranging from 140° to 170° azimuth and

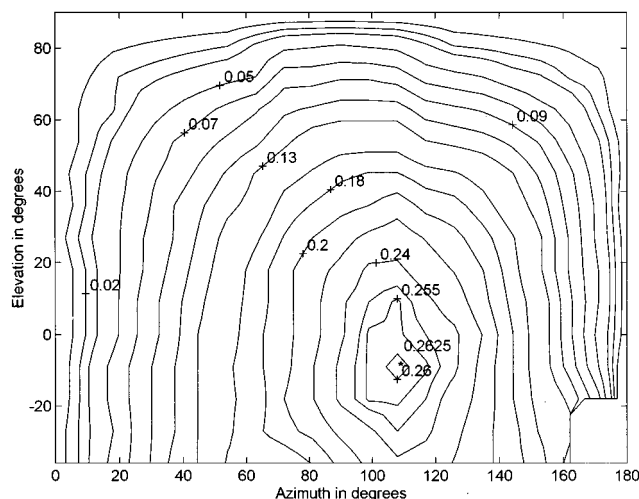


FIG. 3. Contour plot of interaural time difference (ITD) obtained by subtracting the onset time of ipsilateral recording from that of contralateral recording at any specified loudspeaker location.

9° to 60° elevation, are negative ILDs. Those are most likely due to the fact that the lengths of two contralateral diffraction paths around the head are approximately equal in this region and the sounds excite more vibration modes on the left (far) ear. The values of ILD are near 0 dB at directly overhead and at the interaural axis.

B. Characteristics of basis functions and RSCFs

The space-sample average of normalized HRIR and six RSCF basis functions are plotted in Fig. 5. They represent time characteristics of auditory space described by the measured HRIRs. Each basis function is characterized by the number of the peaks and its envelope. Both the space sample average and the first-order basis function have broadband gain over the low- and middle-frequency ranges (up to 14 kHz) and a peak at 3 kHz. They contribute mostly to the first arriving wave that involves the resonances of the ear canal. The second-order basis function, with 40- μ s lag, is very

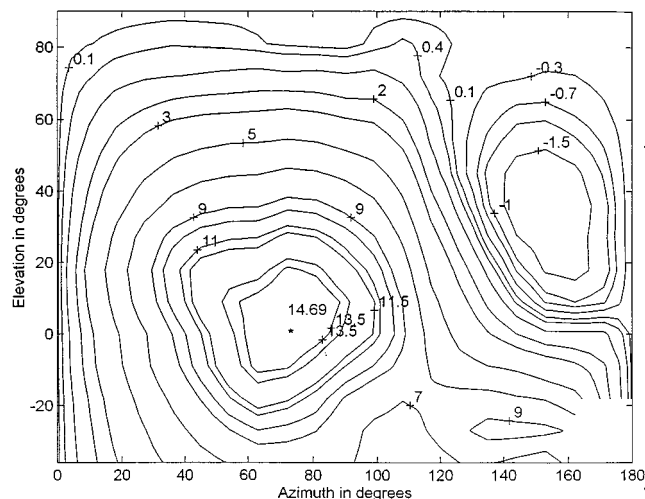


FIG. 4. Contour plot of interaural level difference (ILD) obtained by subtracting the level gain of contralateral recording from that of ipsilateral recording at any specified loudspeaker location.

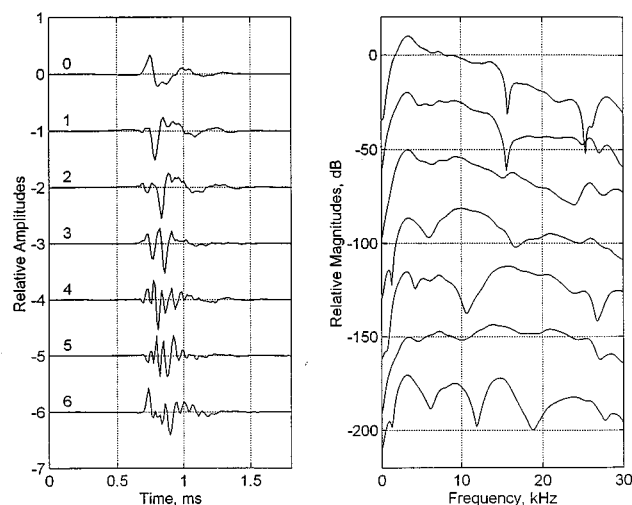


FIG. 5. The mean HRIR (numbered 0) and the first- through sixth-order basis functions (numbered 1–6). The left panel depicts amplitudes in time domain and the right panel magnitudes in frequency domain. The positions of the waveforms and spectra on the ordinate are arbitrary.

similar to the first-order basis function. This basis function seems to represent the second arriving wave produced by reflection or diffraction. It is difficult to directly relate specific basis function features to features in the HRIR waveform. However, more peaks are observed in the higher-order basis functions and they perhaps contribute to the details of high-frequency contents produced by reflection of pinna or diffraction around head.

A contour plot of the first-order RSCF of a cat's left ear is depicted in Fig. 6. The RSCF magnitudes have obvious features that are related to the geometry of the external ear. The maximum peak is 0.6114, noted by an asterisk, at azimuth -54° and elevation 27° of the ipsilateral side. This is the opening direction of the cat's pinna. In general, the values in the first-order RSCF increase with small peaks and notches as the sound source moved from below to the top of the head. For a fixed azimuth, the positive maximum RSCF usually occurs in the region between 45° and 90° elevation. The zero contour in the front ipsilateral side is below the

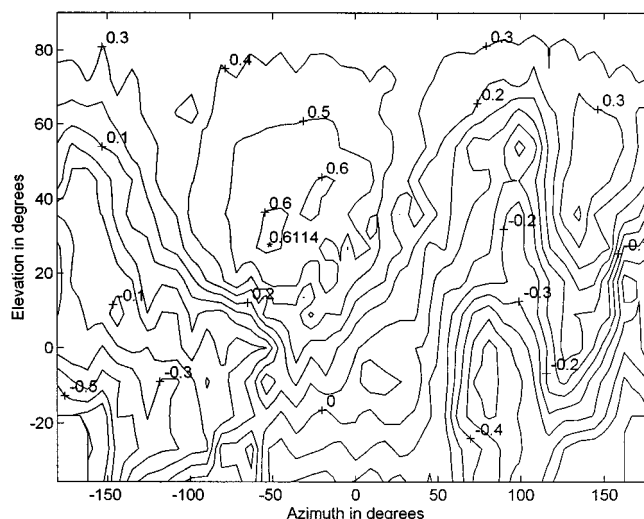


FIG. 6. Contour plot of the first-order RSCF.

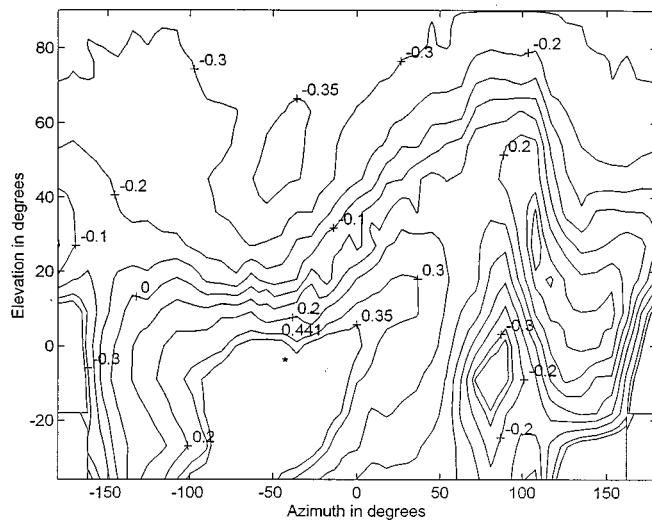


FIG. 7. Contour plot of the second-order RSCF.

equator but then moves up in all other regions. Of interest is that RSCF has positive values in the direct sound regions and minus values in the head shadow regions. The head shadow also effects the low-elevation region of the ipsilateral side, as cat's ears are at the top of their head.

A contour plot of the second-order RSCF is depicted in Fig. 7. In contrast with the first-order RSCF, the maximum peak of the second-order RSCF positions at azimuth -45° and elevation -4.5° in the lower-elevation region. We also observe that both the first-order RSCF and the second-order RSCF have large absolute values in the region of elevation -20° – 0° and azimuth 70° – 100° . The contralateral diffraction in the region contains many low and middle frequencies, according to the characteristics of related basis functions. The complexities of the RSCFs increase and the average absolute magnitudes decrease as the RSCF order increases.

C. Error between the measured and modeled HRIRs

In order to judge the suitability of the model, a comparison was made between measured and modeled HRIRs for the left ear of a cat. The HRIRs on a 9° grid (at 541 directions) were used to determine the model. The MSE and cross-correlation coefficient were examined by comparing the model and measured HRIRs on a 4.5° grid over a total of 1816 locations. The distributions of MSEs and cross-correlation coefficients for all 1816 directions are presented in Fig. 8(a) and (b), respectively. The ranges of MSEs and cross-correlation coefficients for this population are 0.03%–20% and 0.9–0.999, respectively. These indicate that some HRIR pairs are not very similar. However, the MSEs for 62% of 1816 HRIRs are less than 1% and only that for 0.5% of 1816 HRIRs are more than 10%. The mean MSE, 1.32%, is quite small and the mean cross-correlation coefficient, 0.993, is very high. HRIR model's interpolation capabilities are further illustrated in Fig. 8(c) and (d). In the figures, MSEs and cross-correlation coefficients are compared at the directions not used to develop the model. These locations are at the midpoints of those used to develop the model parameters and thus represent likely locations of maximum inter-

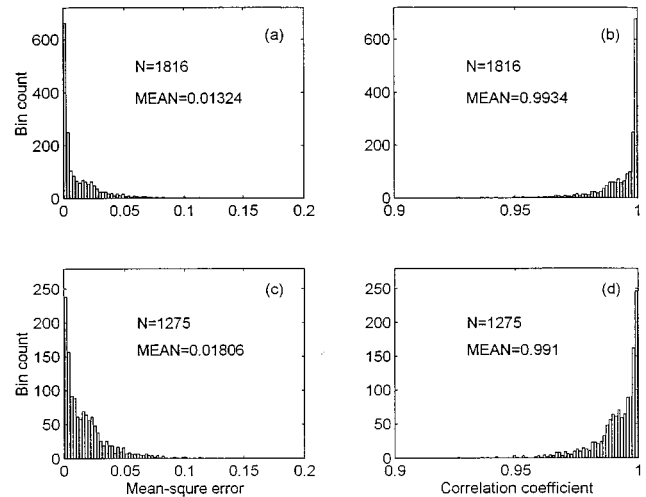


FIG. 8. Distributions of MSE (a) and cross-correlation coefficients (b) for all 1816 directions, and distributions of MSE (c) and cross-correlation coefficients (d) for 1275 directions which are not used to develop the model.

polation error. The mean MSE, 1.8%, is small and the mean cross-correlation coefficient, 0.991, is high for these locations. Those indicate that the interpolation errors are slightly greater than approximation errors. In order to compare with the thin-plate spline algorithm (Chen *et al.*, 1995), the average errors over subregions on the sphere are listed in Table I. Typical average errors are 1% with the range of 0.2%–2.9%. Larger average errors are obtained in the frontal ipsilateral region near the opening direction (at about azimuth -40° and elevation 18° for the left ear). The result is very similar to thin-plate spline algorithm in error distribution except the rear lower elevation area where thin-plate spline algorithm has larger errors. There are two reasons for the error difference in this area. The first is that the preprocessing and least-squares method improve the quality of estimating the HRIRs in this project. The second reason is that the normalizing procedures decrease the variance of HRIRs. Table II lists the average cross-correlation coefficients for different subregions. The distribution of average cross-correlation coefficients is similar to the distribution of average errors. The data in these tables show that the error variances are small enough to maintain the model fidelity. This result suggests that the linear interpolating algorithm can adequately fit the HRIR at any direction over the upper 3/4 sphere.

TABLE I. Average error in 32 subareas.

Azimuth in degrees	Elevation in degrees			
	–36 to 0	0 to 30	30 to 60	60 to 90
–180 to –135	0.7934	1.0015	0.9482	0.6856
–135 to –90	0.4782	0.8931	0.8424	0.2196
–90 to –45	1.5357	1.7152	1.6458	1.2636
–45 to 0	1.2111	2.9081	2.1361	1.4011
0 to 45	1.0788	1.8800	2.2632	0.7944
45 to 90	0.9872	1.0852	1.1176	1.0721
90 to 135	0.4519	0.7684	0.8226	1.1576
135 to 180	0.7602	1.1165	0.5345	0.8938

TABLE II. Average cross-correlation coefficient in 32 subareas.

Azimuth in degrees	Elevation in degrees			
	−36 to 0	0 to 30	30 to 60	60 to 90
−180 to −135	0.9960	0.9950	0.9953	0.9966
−135 to −90	0.9976	0.9955	0.9958	0.9989
−90 to −45	0.9923	0.9916	0.9917	0.9936
−45 to 0	0.9939	0.9855	0.9893	0.9929
0 to 45	0.9945	0.9906	0.9886	0.9960
45 to 90	0.9951	0.9945	0.9944	0.9947
90 to 135	0.9978	0.9962	0.9959	0.9941
135 to 180	0.9962	0.9944	0.9973	0.9955

D. The model implementation in the stimulus delivery system

The general features of our stimulus delivery system have been described elsewhere (Chan, 1993; Rhode, 1976; Chen *et al.*, 1994), so only the essential elements to implement the model are summarized here. Two parallel computers were used in this project. Stimuli for a given direction were synthesized in DEC Alpha. The stimuli were synthesized by compensating the acoustic channels, computing the modeled binaural HRIRs at a given direction, and convolving the HRIR with the compensated sound source. The acoustic volume and ear canal shape vary from subject to subject, and even from time to time for the same subject depending upon the fit of the transducer to the ear. To insure high-fidelity stimulation, the acoustic channels must be compensated. The least-squares FIR filters were used to equalize the acoustic channels that are for the left and right ears, respectively (Chen *et al.*, 1994). The sound source, the length of which could be infinite, is convolved with the pair of the FIR filters to compensate the left and right channels. The binaural HRIRs are modeled by computing the normalized HRIRs from interpolating RSCFs, adding the delays of ITD parameters as well as scaling the amplitudes with the level gain parameters. The compensated signals were convolved with the modeled binaural HRIRs at a 160-kHz sampling rate in real time. The synthesized stimuli were then directly stored on the memory of Micro VAX that presents the stimuli through a specially designed digital stimulus system (Rhode, 1976).

III. SUMMARY AND DISCUSSION

A simplified model for HRIR was developed and has been implemented in a DEC Alpha computer to simulate the sounds to the eardrum of the cat. The model avoids minimum phase approximation by directly representing the impulse response of HRTF. Furthermore, the only operations involved in reconstruction of the HRIR are real multiplication and real addition, which means the cost of computation is low. The linear interpolating algorithm was also used to speedup the model computing. Typical MSEs and cross-correlation coefficients between modeled HRIR and measured HRIR are 1% and 0.995, respectively.

Both the largest MSE and the lowest cross-correlation coefficient occur at interpolated points near the opening direction of the cat's pinna where the HRIRs have strong echoes reflected from the pinna. By checking the HRIRs in this

area, we find that the HRIRs have large amplitude variances. These can be resolved by increasing the space-samples near the opening direction. Also, we can reduce the space-samples in the region of fewer errors to decrease the amount of space-samples. The space-samples, in fact, are not well-distributed in the sphere. There is high sample density in the region of higher elevation.

It is potentially important that measuring precision and estimation quality for HRIR affect the model fidelity. Generally, a broadband test signal is employed to make free-field recordings. Both the spectra of the test signal and transfer function for the acoustic transducer, however, are not flat within the concerned frequency range. This causes low SNR in some frequency ranges where the transducer does not emit much energy. To improve the test signal, new test signals, such as maximum-length sequences or Golay codes, have been used in the transfer function measurements (Gardner and Martin, 1995; Zhou *et al.*, 1992). In this project, we show that the least-squares FIR filter can be employed in the estimation of HRIRs with a high degree of fidelity.

Although our work in this project is restricted to the cat, we believe that our method could be at least a step toward applying the method to virtual acoustic space (VAS) implementation for human beings.

ACKNOWLEDGMENTS

Data used in this paper were collected in the Department of Neurophysiology at the University of Wisconsin-Madison, supported by NIH program project Grant No. NS12732 and by NIH/NRSA institutional fellowship Grant No. NS07026. The authors would like to thank Professor J. E. Hind and Professor J. F. Brugge of that Department, and A. D. Musicant, now at Middle Tennessee State University, for providing the data. Dr. R. Reale tested reconstructed signals in experimental subjects. We would also like to thank Dr. J. Chen for his invaluable suggestions on the manuscript. Computing assistance of R. Kochhar and Zhengran Li are very much appreciated. The present work was supported in part by University of Hong Kong Research Grants and National Natural Science Foundation of China.

- Batteau, D. W. (1967). "The role of the pinna in human localization," *Proc. R. Soc. London, Ser. B* **168**, 158–180.
- Blauert, J. (1983). *Spatial Hearing: The Psychophysics of Human Sound Localization* (MIT, Cambridge, MA).
- Brugge, J. F., Chan, J. C. K., Hind, J. E., Musicant, A. D., Poon, P. W. F., and Reale, R. A. (1992). "Neural coding of virtual acoustic space," *J. Acoust. Soc. Am.* **92**, 2333.
- Chan, J. C. K., Musicant, A. D., and Hind, J. E. (1993). "An insert earphone system for delivery of spectrally shaped signals for physiological studies," *J. Acoust. Soc. Am.* **93**, 1496–1501.
- Chen, J., Van Veen, B. D., and Hecox, K. E. (1992). "External ear transfer function modeling: A beamforming approach," *J. Acoust. Soc. Am.* **92**, 1933–1944.
- Chen, J., Wu, Z., and Reale, R. A. (1994). "Application of least-squares FIR filter to virtual acoustic space," *Hearing Res.* **80**, 153–166.
- Chen, J., Van Veen, B. D., and Hecox, K. E. (1995). "A spatial feature extraction and regularization model for the head-related transfer function," *J. Acoust. Soc. Am.* **97**, 439–452.
- Gardner, W. G., and Martin, K. D. (1995). "HRTF measurements of a KEMAR," *J. Acoust. Soc. Am.* **97**, 3907–3908.

- Genuit, K. (1986). "A description of the human outer ear transfer function by elements of communication theory," Proceedings of 12th International Congress on Acoust. (Toronto, Canada), ADSTR. B6-8.
- Hakin, S. (1986). *Adaptive Filter Theory* (Prentice-Hall, Englewood Cliffs, NJ).
- Hiranaka, Y., and Yamasaki, H. (1983). "Envelope representation of pinna impulse responses relating to three-dimensional localization of sound sources," J. Acoust. Soc. Am. **73**, 291–296.
- Kistler, D. J., and Wightman, F. L. (1992). "A model of head-related transfer functions based on principal components analysis and minimum-phase reconstruction," J. Acoust. Soc. Am. **91**, 1637–1647.
- Musicant, A. D., Chan, J. C., and Hind, J. E. (1990). "Direction-dependent spectral properties of cat external ear: New data and cross-species comparisons," J. Acoust. Soc. Am. **87**, 757–781.
- Rhode, W. S. (1976). "A digital system for auditory neurophysiology research," in *Current Computer Technology in Neurobiology*, edited by P. Brown (Hemisphere, Washington, DC), pp. 543–567.
- Shaw, E. A. G. (1974). "Transformation of sound pressure level from the free field to the eardrum in the horizontal plane," J. Acoust. Soc. Am. **56**, 1848–1861.
- Wenzel, E. M. (1992). "Issues in the development of virtual acoustic environments," J. Acoust. Soc. Am. **92**, 2332(A).
- Wightman, F. L., and Kistler, D. J. (1989). "Headphone simulation of free-field listening: I. Stimulus synthesis," J. Acoust. Soc. Am. **85**, 858–867.
- Wu, Z., Chen, J., and Reale, R. A. (1996). "Measurement and estimation of free field to eardrum transfer function for virtual acoustic space research," Acta Acust. (China) **21**, 84–92.
- Zhou, B., Green, D. M., and Middlebrooks, J. C. (1992). "Characterization of external ear responses using golay codes," J. Acoust. Soc. Am. **92**, 1169–1171.

Influence of contralateral noise on distortion product latency in humans: Is the medial olivocochlear efferent system involved?

Anne Lise Giraud^{a)} and Jocelyne Wable

Laboratoire "Perception et Mécanismes Auditifs," UPRESA CNRS 5020, Pavillon U, Hôpital Edouard Herriot 3, Place d'Arsonval, 69437 Lyon Cedex 03, France

André Chays

Service d'ORL et de Chirurgie Cervico-Faciale, Hôpital Nord. 31, Chemin des Bourrelly, 13915 Marseille Cedex 20, France

Lionel Collet and Sylviane Chéry-Croze

Laboratoire "Perception et Mécanismes Auditifs," UPRESA CNRS 5020, Pavillon U, Hôpital Edouard Herriot 3, Place d'Arsonval, 69437 Lyon Cedex 03, France

(Received 10 July 1996; revised 8 May 1997; accepted 9 May 1997)

To test the hypothesis of temporal modifications of cochlear responses when medial efferents are activated, otoacoustic emission latencies were estimated in 16 normal human subjects, in the presence and absence of a contralateral broadband noise, using measurements of the phase of the $2f_1 - f_2$ distortion product (group latency method). Significant decrease in the latency of lower frequency (0.8–2.7 kHz) emissions was found in the presence of increasing levels of contralateral sound, and this effect disappeared when the primary-tone levels increased to 60 dB SPL. To ensure that effects were not attributable to mechanisms involving middle ear structures, susceptible to activation by contralateral sound, latency measures were performed in seven subjects whose efferents were severed during a vestibular neurotomy and in two subjects with paralyzed stapedial muscle. Results in patients were compared to those obtained in three surgical control patients with intact efferent bundle, and in eight other normal subjects. All the subject groups exhibited a decrease in latency under contralateral sound except the patients with the severed efferent system who showed increased latencies. © 1997 Acoustical Society of America. [S0001-4966(97)02909-3]

PACS numbers: 43.64.Jb, 43.64.Wn [RDF]

INTRODUCTION

The human auditory system includes a cochleo-cochlear feed-back loop, the main element of which is a crossed efferent projection from the medial part of the superior olivary complex (Rasmussen, 1946), known as the crossed olivocochlear bundle. Studies in animals have shown that medial efferent fibers are myelinated cholinergic neurons that synapse directly onto the outer hair cells of the organ of Corti (Eybalin, 1993). These outer hair cells have a motile activity (Brownell *et al.*, 1985; Zenner *et al.*, 1985) which has the effect of selectively amplifying the passive oscillations of the basilar membrane (Ashmore, 1987). Several studies have shown that electrical stimulation of the olivocochlear bundle, at its crossover, (i.e., the floor of the fourth ventricle), decreases auditory nerve response amplitude (Winslow and Sachs, 1987; Guinan and Gifford, 1988). Similar results were obtained by recording the cochlear afferent response during contralateral sound stimulation (Folsom and Owsley, 1987; Warren and Liberman, 1989; Liberman, 1989), and numerous studies have since used this non-invasive means of studying the cochleo-cochlear neural circuit in humans by sound applied in the contralateral ear (Collet *et al.*, 1990; Froehlich *et al.*, 1990; Vuillet *et al.*, 1991). Taken together,

these studies demonstrate that otoacoustic emissions (OAEs), sounds emitted by the cochlea (Kemp, 1978) and assumed to reflect the electromotile-based oscillations of the outer hair cells (Brownell, 1990), are reduced in amplitude by the activation of the cochlear-efferent system which can be presumed to occur under contralateral acoustic stimulation (CAS). Several arguments suggest that medial olivocochlear efferents are involved in this amplitude reduction effect; first, similar effects have been obtained with electrical stimulation of the crossed olivocochlear bundle in animals (Mountain, 1980; Siegel and Kim, 1982); second, in animals, amplitude reduction effects disappeared after sectioning the crossed olivo-cochlear bundle (Rajan, 1988) and, in humans, were greatly reduced by sectioning the vestibular nerve, which is thought to contain the cochlear efferents (Williams *et al.*, 1993, 1994; Giraud *et al.*, 1996a). Finally, Kujawa *et al.* (1993) demonstrated, in guinea pigs, that this amplitude reduction is suppressed by specific antagonists of the medial olivocochlear efferent neurotransmitter.

Although OAEs have been widely used to investigate the olivocochlear efferent system physiology, almost all of these studies have focussed on OAE amplitude. Nevertheless, a few reports have described a phase shift effect on evoked-OAEs with contralateral sound (Ryan *et al.*, 1991; Berlin *et al.*, 1993). In a recent work, we have shown that this phase shift corresponds to an advance of signals re-

^{a)}Electronic mail: a-giraud@cismun.univ-lyon1.fr

corded during a CAS (Giraud *et al.*, 1996b). Such a phase advance effect suggests that CAS may shorten cochlear response latency with possible repercussions on afferent discharges. Latency cannot be directly investigated by click-evoked OAEs, as it is difficult to obtain accurate measures in both the frequency and time domains with such broadband stimuli. Otherwise, direct measures on afferent responses, i.e., latency of wave I of brainstem auditory evoked potentials, require stimulation levels much higher than those used for OAEs. OAE latencies can be measured using the phase gradient method which can be easily applied to distortion product OAEs (DPOAEs). These emissions are recorded during stimulation by two primary tones, f_1 and f_2 , at discrete frequencies which are combinations of f_1 and f_2 , such as $f_1 + f_2$, $f_1 - f_2$, $2f_1 - f_2$, $2f_2 - f_1$, etc. . . . The phase gradient method, used by Kimberley *et al.* (1993) and O'Mahoney and Kemp (1995), consists of measuring variations in the DPOAE phase as one of the primary frequencies is varied. This method provides a useful tool for assessing the "round trip delay," defined as the time between onset of primary tones and detection of DPOAEs in the ear canal, thus comprising both the forward (OAE build-up time) and backward traveling wave delays.

The hypothesis that DPOAE latency could be affected by contralateral broadband noise was tested in a sample of 12 normal hearing subjects, and the changes were analyzed in terms of the influence of stimulus parameters, such as primary frequency, primary intensity and CAS level. An exclusive involvement of the medial efferent system in the acoustic-mediated latency modifications could be controversial, in as much as contralateral sound is thought to elicit the stapedial reflex as well, which could alter emitted responses. To determine the respective contribution of each nervous pathway in the described temporal modifications, we took advantage of two human pathologies. Repeated DPOAE latency measurements, in the presence and absence of contralateral acoustic stimulation, were made in seven vestibular neurotized patients, in whom efferents had been severed, and two Bell's Palsy patients, in whom the stapedial muscle is unfunctional. Our argument was that, if the latency changes were really due to efferent activation, they should appear in subjects with inhibited stapedial reflexes and not appear in de-efferented subjects. Positive effects were also to be expected in the control group of eight other normal hearing subjects and three subjects who had undergone an operation under the same surgical conditions as for neurotomy but in whom the vestibular nerve and efferents had not been severed.

I. METHODS

A. Subjects

This study, which consisted of the recording of the $2f_1 - f_2$ DPOAE in the presence or absence of a contralateral broadband noise, was performed in 28 subjects. This sample was divided into a group of 16 normal subjects (12+8) and a group of 12 pathological subjects. The normal subjects were tested in their right ear and the patients were

tested on their pathological side. All the subjects were volunteers and experiments were carried out with the written-informed consent of subjects.

Healthy subjects answered a questionnaire to ensure that they had no auditory congenital disease in their family and no severe otological disorder following infection, use of ototoxic drugs or exposure to long term noise. The hearing of all the subjects was tested with pure-tone audiometry and tympanometry. A hearing level equal or better than 10 dB HL was required for healthy as well as pathological subjects. All the subjects presented DPOAEs at a low intensity level (50 dB SPL). Lastly, the absence of spontaneous OAEs was assessed to avoid possible interferences with DPOAEs (Wier *et al.*, 1988; O'Mahoney and Kemp, 1995). The relevant characteristics of each group are described in Table I.

The seven neurotized patients, recruited from a population of 140 subjects, who received vestibular neurotomies, were selected based on acoustic criteria described in Table I. The outcome of the vestibular-nerve section was evaluated in three ways prior to inclusion into the study: The patient was questioned to ensure that no vertigo persisted, the video recording of the operation was re-examined before experiments to confirm a complete nerve section has been achieved, and the unilateral vestibular disorder was confirmed by three successive nystagmographic recordings, the last one being completed the day of the DPOAE experiment. These nystagmographic responses, including the spontaneous horizontal optokinetic and bithermal caloric measures, were recorded with a video-based device (Collin ORL, Videonystagmoscope).

B. Surgery

The patients were all operated on by the same surgeon under the same conditions. The retrosigmoid approach was chosen because it gives the best view of the acoustico-facial bundle, with low prevalence of complications. The patient was recumbent and a craniotomy limited to a 1.5 cm trepanation just behind the sigmoid sinus was carried out. The displacement of the cerebellum through drainage of cerebrospinal fluid and positioning of the head gave way to the root of the VIIIth cranial nerve. In the case of vestibular neurotomy, acoustic and vestibular nerves were separated and the vestibular tract was sectioned (Magnan *et al.*, 1991). In the case of hemifacial spasm, the retrosigmoid surgical approach was coupled with an endoscopic procedure. The endoscope allowed the surgeon to recognize the irritative vascular contact from the normal arterial loop. Using an operating microscope the offending artery was carefully mobilized and held away from the nerve with a small Teflon foam pad (Magnan *et al.*, 1994).

C. Auditory screening

Tonal audiometry was performed in a sound-proof room, using a Madsen DAIH audiometer at 0.25, 0.5, 1, 2, 4, and 8 kHz. Tympanometry and acoustic reflex recordings were performed in a separate sound-proof room using an Amplaidd 702 impedancemeter.

TABLE I. Summary of subjects' characteristics.

	Normal subjects	Vestibular neurotomized subjects	Patients operated for hemifacial spasm	Bell's Palsy patients
Sample size	$n=16$ $\begin{cases} 8 \text{ males} \\ 8 \text{ females} \end{cases}$	$n=7$ $\begin{cases} 4 \text{ males} \\ 3 \text{ females} \end{cases}$	$n=3$ $\begin{cases} 1 \text{ male} \\ 2 \text{ females} \end{cases}$	$n=2$ $\begin{cases} 1 \text{ male} \\ 1 \text{ female} \end{cases}$
Age	mean=27.22 years s.d.=3.5	mean=39.14 years s.d.=7.26	male: 64 years females: 31 and 57 years	male: 19 years female: 31 years
Pathology	none	Meniere's disease $n=5$ Acoustic Neuroma $n=1$ Atypical vertigo associated with Klippel-Trenaunay syndrome $n=1$	syndrome attributed to vascular pulsations against the entry zone of the facial nerve (VIIIth)	paralysis of the VIIIth nerve
Relevant characteristics	intact olivocochlear efferent fibers	olivocochlear efferent fibers cut	surgical control subjects	absence of stapedial reflex
Hearing level	equal or better than 10 dB HL	equal or better than 10 dB HL on 5 out of the 6 tested frequencies	equal or better than 10 dB HL	equal or better than 10 dB HL
Acoustic reflex to contralateral broad band noise	reflexes bilaterally present	reflexes bilaterally present	reflexes bilaterally present	reflex present on the healthy side, absent on the paralysed side
Tympanometry	normal	normal	normal	normal
Vestibular Examination	normal	normal on the intact side; pathologic on the operated side	normal	normal

D. Recording of DPOAEs and latency calculation using the phase gradient method

DPOAEs were recorded in a sound-proof room using the Otodynamics ILO92 hardware and software. A probe, composed of a microphone collecting the emissions of the cochlea and two separate stimulus transducers, was inserted into the external ear canal where the primaries, f_1 and f_2 , were acoustically mixed. The primaries were equilevel pure tones whose values were determined in order to obtain an optimal f_2/f_1 ratio, ranging from 1.20 to 1.24 according to the data of Harris *et al.* (1989). The noise reject threshold was set at 8 mPa. Noise values were obtained from 10 adjacent spectral lines around the DPOAE, separated by 12 Hz. The DPOAE was determined to be present if its level was greater than the mean noise plus two standard deviations (s.d.). DPOAE recordings were made using an average of 160 samples, each lasting 81.92 ms. At the end of the sampling, a high precision FFT allowed the measurement of the DPOAE phase. The latency was calculated using the swept- f_2 paradigm in which four phases are measured, with f_1 fixed and f_2 varying by steps ranging from 12 Hz to 48 Hz, according to the f_1 frequency (see Table II). The latency, expressed in ms, is defined as the slope of the linear relation-

ship between the phase and the frequency of the four DPOAEs. We decided to take the latency into account only when the correlation coefficient between the four phase values was above 0.99. If the four points did not belong to the regression line, the measure was re-done. Figure 1 illustrates the phase gradient method.

E. Contralateral acoustic stimulation

The CAS was delivered with a clinical audiometer Amplaid 455 through an earphone (Telephonics TDH 39P, bandwidth 0.05–8 kHz). The CAS was a broadband noise with a flat spectrum between 0.5 and 8 kHz. The subjective perception threshold for this contralateral broadband noise was measured for each subject and found to be below or equal to 15 dB SPL (mean=13.07; s.d.=5.60). The CAS values were chosen to be below the clinically determined acoustic-reflex threshold for broadband noise (mean=91.36 dB SPL; s.d.=11.42).

F. Experimental procedures

Three experiments were carried out in order to characterize the latency modifications induced by a contralateral

TABLE II. Details of the stimulation paramaters used in the four experiments.

Experiment 1: 8 normal subjects Ipsilateral level of primaries=55 dB SPL. Contralateral noise level=35 dB SL						
	$f_1=1001$ Hz	$f_1=1501$ Hz	$f_1=2002$ Hz	$f_1=2502$ Hz	$f_1=3003$ Hz	$f_1=3503$ Hz
Frequency of	$f_2=1196, 1208, 1221, 1233$ Hz	$f_2=1807, 1819, 1831, 1843$ Hz	$f_2=2405, 2429, 2454, 2478$ Hz	$f_2=3003, 3027, 3052, 3076$ Hz	$f_2=3625, 3650, 3674, 3699$ Hz	$f_2=4187, 4236, 4285, 4333$ Hz
Primaries and first	$2f_1 - f_2=787$ Hz	$2f_1 - f_2=1177$ Hz	$2f_1 - f_2=1562$ Hz	$2f_1 - f_2=1964$ Hz	$2f_1 - f_2=2344$ Hz	$2f_1 - f_2=2746$ Hz
DPOAEs	$f_1=4004$ Hz $f_2=4822, 4871, 4919, 4968$ Hz $2f_1 - f_2=3113$ Hz	$f_1=4968$ Hz $f_2=6030, 6079, 6128, 6177$ Hz $2f_1 - f_2=3906$ Hz	$f_1=5505$ Hz $f_2=6641, 6689, 6738, 6787$ Hz $2f_1 - f_2=4296$ Hz	$f_1=6006$ Hz $f_2=7251, 7300, 7349, 7397$ Hz $2f_1 - f_2=4688$ Hz	$f_1=6506$ Hz $f_2=7837, 7886, 7935, 7083$ Hz $2f_1 - f_2=5102$ Hz	
Experiment 2: 8 normal subjects $2f_1 - f_2$ frequency=1177 Hz. Contralateral noise level=35 dB SL						
Primary level	50 dB SPL	55 dB SPL	60 dB SPL	65 dB SPL	70 dB SPL	75 dB SPL
Experiment 3: 8 normal subjects $2f_1 - f_2$ frequency=1177 Hz. Ipsilateral level of primaries=55 dB SL						
CAS level	0 dB SL	10 dB SL	20 dB SL	30 dB SL	40 dB SL	50 dB SL
Experiment 4: 20 subjects comprising 7 vestibular neurotomized patients, 3 patients operated for hemifacial spasm, 2 Bell's Palsy patients and 8 normal subjects $2f_1 - f_2$ frequency=1177 Hz. Ipsilateral level of primaries=55 dB SPL. Contralateral noise level=35 dB SL						

broadband noise. In eight normal subjects, DPOAEs were recorded three times, in each of the stimulation conditions described in Table II, in the presence (CAS condition) and in the absence (no-CAS condition) of contralateral broadband noise. The three latency values were averaged to obtain a final value expressed in ms allowing statistical analysis. An additional experiment was performed in order to compare the

latency modification induced by a contralateral broadband noise, in eight other normal subjects and in patients. The latency was measured 6 times in the CAS and the no-CAS condition at appropriate stimulation levels (see Table II).

G. Statistics

In the three experiments characterizing DPOAE latency, the latency values were averaged between subjects. The effect of CAS, which corresponded to a latency shortening in most cases, is expressed as a percentage of latency reduction. Non-parametrical paired tests (Wilcoxon U-test) were performed between CAS and no-CAS conditions. In experiments in which ipsi and contralateral levels were varied, a one-way ANOVA was used to evaluate the effect of stimulation level. The influence of frequency and primary level on latency was estimated using curve-fitting procedure in both CAS and no-CAS conditions.

Results in pathological subjects are presented individually and averaged for vestibular neurotomized (VNT) and normal subject samples in which the CAS and no-CAS conditions were compared using non-parametric Wilcoxon U-tests.

Probabilities below 0.05 were considered as being statistically significant.

II. RESULTS

A. Influence of DPOAE frequency

Figure 2(a) displays the latency of $2f_1 - f_2$ taken at 11 frequencies ranging from 787 to 5102 Hz, in response to two 55 dB SPL equilevel pure tones. In both CAS and no-CAS conditions, an increase of the DPOAE frequency induced a

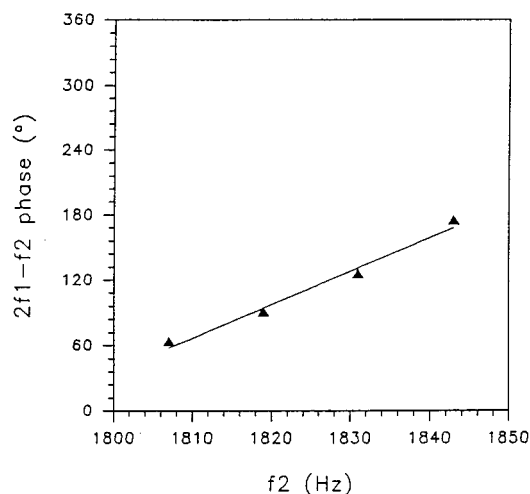


FIG. 1. An example of latency calculation using the swept- f_2 paradigm: The four points correspond to the phase of $2f_1 - f_2$, recorded in one normal subject, in response to $f_1=1501$ Hz and four increasing values of f_2 (separated by 12 Hz). The latency, defined as the slope of the regression line, is the time separating the onset of the primaries and the emission being detected in the ear canal. Because the site of generation of the four DPOAEs is considered to be the same along the basilar membrane, the phase gradient is only related to the increase in frequency and consequently to the duration of the DPOAE travel.

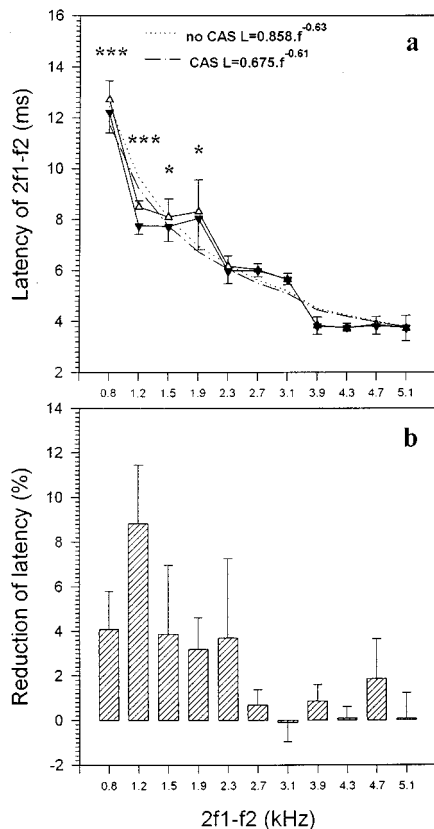


FIG. 2. (a) The latency of $2f_1 - f_2$ was measured for increasing values of $2f_1 - f_2$ in the absence (open triangles) and in the presence (filled triangles) of contralateral broadband noise. Stars indicate a significant latency shortening (** $p < 0.01$; * $p < 0.05$). Vertical bars indicate standard errors. Dotted lines represent the theoretical curves according to the following equations: (....) Latency = $10.70 \cdot f^{-0.63}$; $p < 0.01$. (—) Latency = $10.17 \cdot f^{-0.61}$; $p < 0.01$, with f : Distortion frequency. (b) The modification in latency is represented as a percentage of reduction with standard deviation bars.

decrease in latency. Latency values ranged from 12.5 ms at 787 Hz to 3.5 ms at 5102 Hz and these experimental data can be fitted by the following equation: Latency = $a \cdot (\text{DPOAE Frequency})^b$. Parameters a and b in each of the two conditions are given in Figure 2. Although possible interferences between DPOAEs and spontaneous OAEs were avoided, a great interindividual variability was observed, particularly on low frequencies.

When a 35 dB SL broadband noise was delivered in the contralateral ear, the latency was modified. Both experimental and calculated curves were found to be statistically different in the CAS and no-CAS conditions ($p < 0.01$). This modification took place on low frequencies, particularly between 0.8 and 2 kHz where a very variable latency shortening was point by point significant, and reached about 10% of the latency on the 1177 Hz distortion frequency. As apparent in Figure 2(b), the decreased-latency effect disappeared for the frequencies that were greater than about 2.7 kHz.

According to the distribution of latency modifications, the influence of the stimulation levels was investigated on the 1177 Hz $2f_1 - f_2$ distortion frequency, where the effect was found to be the largest.

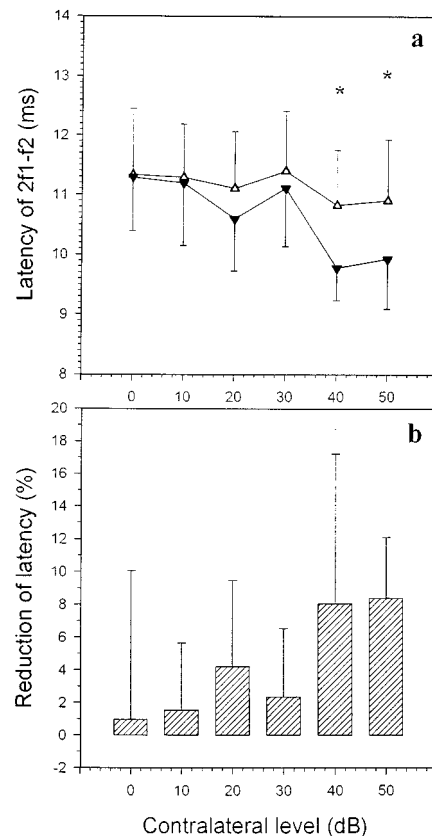


FIG. 3. (a) The latency of $2f_1 - f_2 = 1177$ Hz is represented as a function of the contralateral noise level: in the absence (open triangles) and in the presence (filled triangles) of CAS. Stars indicate significant differences between CAS and no-CAS conditions. Vertical error bars indicate standard deviations. (b) The effect of the contralateral stimulation is expressed as a percentage of latency reduction. The ANOVA was significant ($p < 0.05$). Vertical error bars indicate standard deviations.

B. Influence of the contralateral level

The $2f_1 - f_2$ DPOAEs were recorded in response to 55 dB SPL equilevel pure tones, in order to obtain responses in all the tested subjects. The contralateral level was increased from the individual perceptual threshold (0 dB SL) to 50 dB above. The no-CAS condition corresponded to a test-retest experiment. It can be noted that the mean latency values were strongly reproducible as well as the great standard deviation reflecting a great interindividual variability, as shown in Figure 3(a). On the contrary, latencies from one individual were quite stable during the test-retest. The CAS induced a latency modification, corresponding to a latency shortening reaching 8–10% of the latency at 40 and 50 dB SL. The CAS also induced a slight decrease of the variability particularly on the last two points. The ANOVA was significant ($p < 0.05$) showing an effect of the contralateral level on the latency reduction.

C. Influence of the primary level

The influence of the primary level was investigated at the 1177 Hz distortion frequency with a 35 dB SL contralateral broadband noise. This value was chosen according to previous experimental data (Collet *et al.*, 1990), in order to obtain an obvious effect of CAS as well as to avoid con-

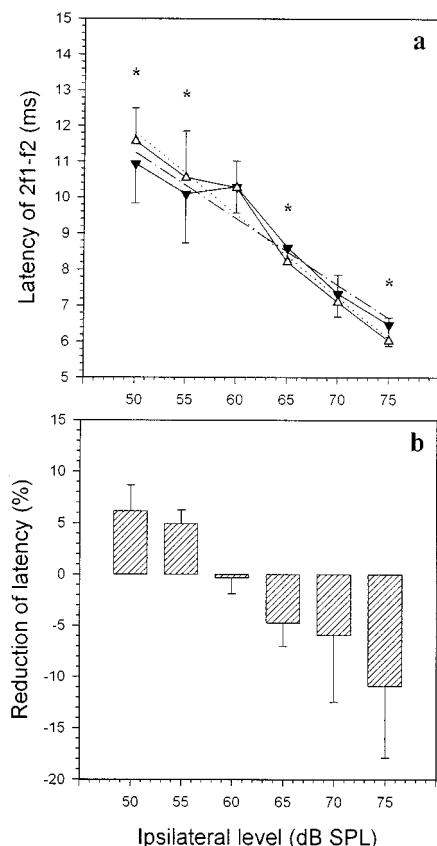


FIG. 4. (a) Latencies for $2f_1 - f_2 = 1177$ Hz is represented as a function of the ipsilateral stimulation level in the absence (open triangles) and in the presence (filled triangles) of CAS with standard error bars. Stars indicate significant differences between CAS and no-CAS conditions. Dotted lines represent linear regressions of the experimental data: (...) $r=0.98$; $p<0.01$ (---) $r=0.97$; $p<0.01$. (b) The effect of the level of primaries is expressed as a percentage of latency reduction. The ANOVA was significant ($p<0.01$). Vertical error bars indicate standard deviations.

founding bone-conduction effects. In both CAS and no-CAS conditions, the latency decreased linearly as the stimulation intensity increased. The regression lines in both conditions are represented in Figure 4(a). Latency ranged from 11.5 ms for low primary levels (50 dB SPL) to 6 ms for high primary levels (75 dB SPL). In this experiment, the contralateral sound did not lead to a latency shortening for all stimulation intensities. At low levels the latency shortening obtained in the two previous experiments was indeed confirmed, but, when the primary level increased, the effect became slighter and slighter before reversing. From 60 to 75 dB SPL, a latency lengthening took place instead reaching 10–15% of the latency; this inversion is obvious in Figure 4(b). The strongly significant ($p<0.001$) ANOVA reflected the effect of the primary intensity variations.

D. Effects of pathologies on CAS-induced latency modifications

In eight normal subjects, individual latency values, corresponding to a test–retest experiment, demonstrated that, despite noticeable interindividual variability, the latency shortening induced by CAS was strongly reproducible. Fig-

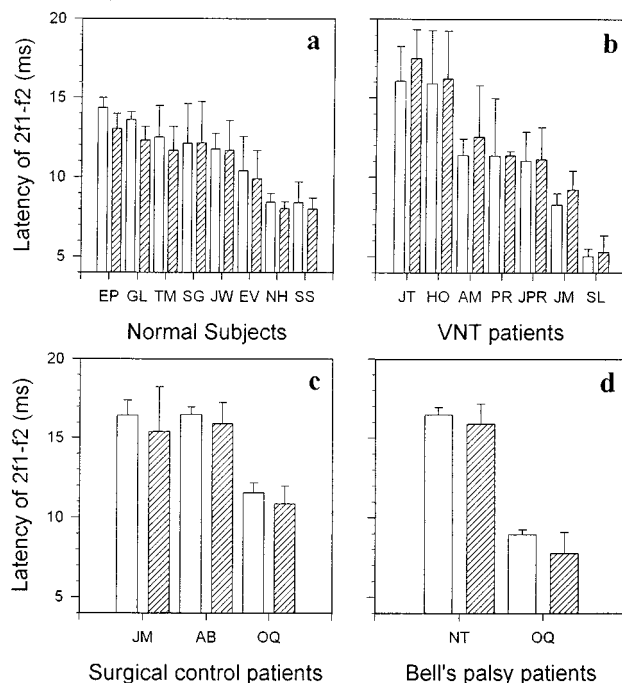


FIG. 5. Individual representation of latencies for $2f_1 - f_2 = 1177$ Hz are represented individually in the absence (white boxes) and in the presence (hatched boxes) of CAS in: (a) normal subjects, (b) vestibular neurotized patients, (c) patients operated for hemifacial spasm, (d) Bell's Palsy patients. Vertical error bars indicate standard deviations.

ure 5 reveals that only one subject (SG) exhibited a latency lengthening in these stimulating conditions. Although the effect was not significant individually, Figure 6(a) shows that the mean values differed significantly ($p<0.05$). In identical experimental conditions, vestibular neurotized patients, in whom the efferents are assumed to be severed, exhibited a systematic latency lengthening. The whole sample presented this effect, which was not significant individually, but, as indicated in Figure 6(b), reached significance on average. In patients who were operated on using the retrosigmoid approach but without any section of the vestibular nerve, the latency shortening was present, exactly as in normal subjects. The same effect occurred in the two Bell's Palsy patients, in whom the stapedial reflex was inhibited.

III. DISCUSSION

A. Latency measured by the phase gradient method

The phase gradient method, based on information coming directly from the cochlea, can be considered a useful non-invasive tool for measuring DPOAE latency in humans. The technique was used by Kimberley (1993) who demonstrated that these latencies differed from those obtained using the N1 component of auditory brainstem potentials (Don and Eggermont, 1978) by only 0.8 ms, which represents the synaptic delay between the inner hair cell and auditory nerve. In the present study, DPOAE latency was found to range from 12.5 ms for $f_2 = 1$ kHz to 3.5 ms for $f_2 = 7$ kHz, which is consistent with latencies found by O'Mahoney (1993) and O'Mahoney and Kemp (1995), indicating round-trip delays

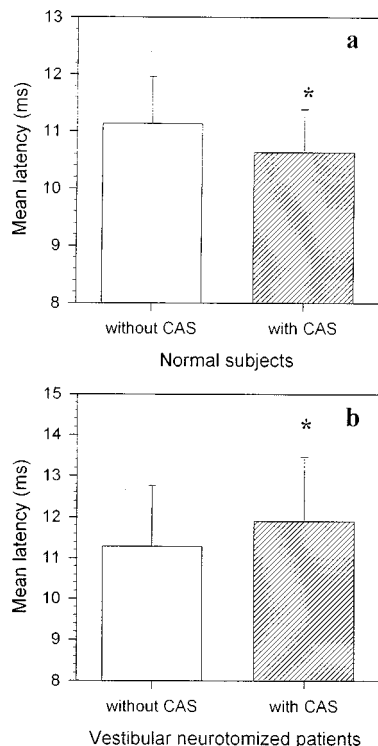


FIG. 6. Mean latency values are represented in (a) normal and (b) vestibular neurotized subject samples in the absence (white boxes) and in the presence (hatched boxes) of CAS, with standard deviation error bars. Stars indicate significant differences between the two conditions ($p < 0.05$).

ranging from 8.5 for $f_2 = 1$ kHz to 3 ms for $f_2 = 7$ kHz in response to higher primary levels than ours ($f_1 = 70$ and $f_2 = 60$ dB SPL). The difference between these results and ours may come from the fact that, in the case of $2f_1 - f_2$, maximum distortion is predictably obtained in the stimulation conditions used by O'Mahoney, i.e., for an $f_1 - f_2$ intensity difference of 10 dB (Hauser and Probst, 1991). Therefore, the difference between our results and those of O'Mahoney and Kemp (1995) can be attributed to stimulus intensity.

As indicated in Figure 2, a non-linear negative relation linked latency and frequency. This is in agreement with the findings of Kimberley *et al.* (1993) using DPOAE latency measurement, and with those of Don and Eggermont (1978), using brainstem evoked responses. The equation proposed by the latter authors, to explain the influence of the characteristic frequency of derived narrow band brainstem evoked responses on the latency of waves I, III and V, was also applicable to our experimental data, with different parameters. The linear relationship between primary level and latency, presented here in Figure 4(a), is also consistent with these previous studies.

B. The influence of CAS on DPOAE latency

CAS was found to modify DPOAE latency significantly in many stimulation conditions. Latency was shortened for the lowest frequencies tested (0.8–2.3 kHz), particularly when the primary intensities were low. This effect disappeared when at least one of the three signals (f_1 , f_2 or

$2f_1 - f_2$) was located around 4 kHz, and reappeared slightly for higher frequencies. Such a frequency distribution of CAS-induced effects on OAEs is now familiar. Veuille *et al.* (1992), with transiently evoked OAEs, and Chéry-Croze *et al.* (1993), with DPOAEs, have described an almost identical distribution of the amplitude reduction effect, and, in a previous study, we found a similar distribution of the CAS-induced phase shift effect (Giraud *et al.*, 1996b). Veuille *et al.* (1992) have suggested that the absence of CAS-induced effects around 4 kHz may reflect a discontinuity in efferent innervation in humans, similar to that observed in anatomical studies in animals (Guinan *et al.*, 1984).

When primary intensity increased, the latency decrease reversed into an increase. This strongly significant inversion suggests the involvement of two antagonist mechanisms, one tending to reduce latency and the other, on the contrary, increasing it. It is noteworthy that this turn-around occurred around 65 dB SPL. In rabbits, this level has been mentioned as the limit between two different DPOAE generation mechanisms (Whitehead *et al.*, 1992). Moreover, Kimberley (1993) has suggested that DPOAEs above 65 dB SPL may reflect the passive cochlear mechanisms involved in stimulus transduction, rather than active micromechanisms. The latency shortening, on the other hand, observed in response to low primary levels, thought to induce DPOAEs of active origin, may result in efferent activation, as efferents are known to be effective mostly at low ipsilateral intensities (Guinan and Gifford, 1988). The passive origin of DPOAEs and the lesser effectiveness of efferents at high stimulation levels would thus be coherent with the hypothesis of an antagonistic mechanism prevailing above 65 dB SPL. A latency reduction proportional to CAS intensity, at low primary levels, is also consistent with such a hypothesis.

CAS-induced latency modifications could result either from changes in the emission generation mechanism, or from changes in traveling wave delay. Direct modification of traveling wave delay could occur if efferents alter the basilar membrane properties, i.e. stiffen the OHC/basilar membrane system and thus accelerate the propagation speed. However, no obvious change in basilar membrane motion has been found under efferent stimulation (Murugasu and Russell, 1996). Concerning possible changes in emission generation mechanisms, three hypotheses can be proposed: (1) Because the efferents are directly connected to the outer hair cells, assumed to be the physiological substrate of DPOAEs, their activation may induce phase changes in outer hair cell oscillations. If such phase changes differentially affected the four phase measures, this would modify the measured latency. (2) Because DPOAE may have more than one source on the basilar membrane (Whitehead *et al.*, 1992), efferent action could easily change the proportion of DPOAEs generated by each source and thereby effectively change the resultant phase and location of the source, and thus the latency. (3) The time taken by the basilar membrane to build up to a peak may be shortened.

C. Structures involved in the modifications of distortion product latency

An involvement of olivocochlear efferent fibers is one hypothesis which could explain the latency reduction induced by CAS at low primary levels, because such latency shortening was present in almost all the normal subjects and absent in all the vestibular neurotomized patients. These findings suggest that integrity of fibers traveling within the vestibular nerve is necessary to a latency reduction effect. Anatomical data from cats (Rasmussen, 1946; Liberman and Brown, 1986) indicate that cochlear efferent fibers travel within the inferior vestibular nerve, which is sectioned in neurotomized patients along with the superior branch. Sectioning both the crossed and uncrossed olivocochlear efferents may suppress the latency shortening effect.

On the other hand, the significant lengthening of latency found in neurotomized patients, almost equal to the shortening found in normal subjects (mean latency lengthening=0.6 ms; mean latency shortening=0.5 ms), raises again the possibility of an antagonistic mechanism elicited by the contralateral sound. The persistence of the latency decrease in surgical control subjects tends to rule out the surgical act itself as a possible explanation for this reversal of effect in neurotomized patients. Although latency shortening seems to be attributable to olivocochlear efferents, lengthening effects are harder to account for. Observations with Bell's Palsy, although the sample was only of two subjects, tend to indicate a behavior similar to that of normal subjects but fail to resolve whether the latency shortening was purely due to efferents or was an effect resulting from antagonistic mechanisms, involving structures other than the stapedial muscle. The reversed effect in neurotomized patients may be mediated by some other crossed pathway, which could be either that which innervates the tensor tympani muscle (not inhibited in Bell's Palsy patients) or an efferent pathway not traveling within the vestibular nerve and by which the central nervous system may also influence cochlear functioning. Burns *et al.* (1993) suggested that the cochlear efferents may act synergistically with middle ear muscles, such as the tensor tympani muscle. At the tested frequencies ($f_2=1820$ Hz; $2f_1-f_2=1177$ Hz), however, middle ear influence on latency is not very important (Moulin and Kemp, 1996). Therefore, the latency lengthening effect cannot be conclusively attributed to the middle ear.

Although the structures underlying latency modifications cannot be determined with certainty, there is evidence for two mechanisms, one of which can be situated with certainty within the cochlea. The predominance of lengthening effects at high ipsilateral intensities may be simultaneously due to three mechanisms: (1) a reduction in efferent effectiveness (Veillet *et al.*, 1991; Moulin *et al.*, 1993); (2) an increase in ipsilateral stapedial pathway effectiveness; and (3) a weak activation of the ipsilateral efferent feedback by high-level primaries, pure tones having been demonstrated to weakly activate olivocochlear efferents (Veillet *et al.*, 1991). Otherwise, in a situation where both efferents and middle ear structures are generally thought to be effective, i.e., at a low primary level (55 dB SPL) and high contralateral level (50 dB SL), the resulting effect, as shown in Figure 3, is a short-

ening of latency. This observation indicates that latency lengthening appears in a situation where the crossed olivocochlear bundle is rendered less effective, i.e., at high primary levels or when the cochlear efferents are severed; in all other experimental conditions, latency shortening may decrease but is never reversed.

D. Functional and perceptual hypothesis

This study highlights CAS-induced modifications of OAE latency mediated mainly by the olivocochlear efferent pathway and to much less extent by middle ear structures. Identical pathways have been shown to be involved in transiently evoked OAE amplitude reduction (Giraud *et al.*, 1995). The evidence of latency shortening confirms the hypothesis suggested by studies of click-evoked OAE phase advance under CAS (Ryan *et al.*, 1991; Berlin *et al.*, 1993; Giraud *et al.*, 1996b). These studies also demonstrated that temporal modifications in evoked emissions are indistinct from amplitude reduction effects occurring under identical conditions.

The identification of temporal modifications in cochlear emissions, attributed to medial olivocochlear fibers, seems consistent with data for afferent response latency, under efferent activation. Liberman (1989), in cats, demonstrated an increase in compound action potential latency in response to weak stimuli in presence of broadband contralateral noise. Sohmer (1965) and Vijay and Dayal (1967) also described, in animals, an increase in N1 latency (60 to 120 μ s) under electrical stimulation of the crossed olivocochlear bundle. In humans, a CAS-linked decrease in N1 latency has been found under particular stimulus conditions (Folsom and Owlesley, 1984; Boezeman *et al.*, 1983). However, no change in auditory nerve fiber response phase was found with efferent stimulation (Gifford and Guinan, 1983), suggesting that OAE alterations are not directly linked to temporal changes in the afferent response. These considerations also suggest that olivocochlear efferents act rather on the emission generation mechanism than on cochlear traveling time. Indeed, any reduction in traveling time should appear in the afferent response latency.

Finally, in spite of amplitude reduction effects on cochlear and efferent responses, interpreted as inhibitory effects of the olivocochlear efferent system, one of the most probable interpretations of the present results would be a facilitation of the OAE generation mechanism, probably by a reduction of the time required by the basilar membrane to build up to a peak. Based on this interpretation, it can be extrapolated that an olivocochlear efferent activation may improve the susceptibility of the OHC/basilar membrane system to follow rapid temporal fluctuations; in other words they may improve the temporal resolution of the cochlear amplifier.

ACKNOWLEDGMENTS

We wish to thank Dr. Annie Moulin, Iain MacGill and the reviewers for constructive criticism of the manuscript.

- Ashmore, J. F. (1987). "A fast motile response in guinea pig outer hair cells: The cellular basis of the cochlear amplifier," *J. Physiol. (London)* **388**, 323–347.
- Berlin, C. I., Hood, L. J., Szabo, P., Ceccola, R. P., Rigby, P., and Jackson, D. F. (1993). "Contralateral suppression of non linear click-evoked otoacoustic emissions," *Hearing Res.* **71**, 1–11.
- Boezeman, E. H. J. F., Kapteyn, T. S., and Snel, A. M. (1983). "Effect of contralateral and ipsilateral masking of acoustic stimulation on the latencies of auditory evoked potentials from cochlea and brainstem," *Electroencephalogr. Clin. Neurophysiol.* **55**, 710–713.
- Brownell, W. E. (1990). "Outer hair cell electromotility and otoacoustic emissions," *Ear Hear.* **11**, 82–92.
- Brownell, W. E., Bader, C. R., Bertrand, D., and de Ribaupierre, Y. (1985). "Evoked mechanical responses of isolated cochlear outer hair cells," *Science* **227**, 194–196.
- Burns, E. M., Harrison, W. A., Bulen, J. C., and Keefe, D. H. (1993). "Voluntary contraction of middle ear muscles: Effects on input impedance, energy reflectance and spontaneous otoacoustic emissions," *Hearing Res.* **67**, 117–127.
- Chéry-Croze, S., Moulin, A., and Collet, L. (1993). "Effect of contralateral sound stimulation on the distortion product $2f_1 - f_2$ in humans: Evidence of a frequency specificity," *Hearing Res.* **68**, 53–58.
- Collet, L., Kemp, D. T., Veuillet, E., Duclaux, R., Moulin, A., and Morgon, A. (1990). "Effect of contralateral auditory stimuli on active cochlear micromechanical properties in human subjects," *Hearing Res.* **43**, 251–262.
- Don, M., and Eggermont, J. J. (1978). "Analysis of the click-evoked brainstem potentials in man using high-pass noise masking," *J. Acoust. Soc. Am.* **63**, 1084–1091.
- Eyblain, M. (1993). "Neurotransmitters and neuromodulators in the mammalian cochlea," *Physiol. Rev.* **73**, 309–373.
- Folsom, R. L., and Owsley, R. M. (1987). "N1 action potentials in humans: Influence of simultaneous contralateral stimulation," *Acta Oto-Laryngol.* **103**, 262–265.
- Froehlich, P., Collet, L., Chanal, J. M., and Morgon, A. (1990). "Variability of the influence of a visual task on the active micromechanical properties of the cochlea," *Brain Res.* **508**, 286–288.
- Giraud, A. L., Chéry-Croze, S., Collet, L., and Chays, A. (1996a). "Evidence of a medial olivocochlear involvement in the contralateral suppression of otoacoustic emissions," *Brain Res.* **705**, 15–23.
- Giraud, A. L., Perrin, E., Chéry-Croze, S., Chays, A., and Collet, L. (1996b). "Contralateral acoustic stimulation induces a phase advance in evoked-otoacoustic emissions in humans," *Hear. Res.* (in press).
- Gifford, M. L., and Guinan, Jr., J. J. (1983). "Effects of crossed-olivocochlear bundle stimulation on cat auditory nerve fiber responses to tones," *J. Acoust. Soc. Am.* **74**, 115–123.
- Guinan, Jr., J. J., and Gifford, M. (1988). "Effect of electrical stimulation of efferent olivo-cochlear neurons on cat auditory fibers. III. Tuning curves and threshold at CF," *Hearing Res.* **37**, 29–46.
- Guinan, Jr., J. J., Warr, W. B., and Norris, B. E. (1984). "Topographic organization of the olivocochlear projections from the lateral and medial zones of the superior olivary complex," *J. Comp. Neurol.* **226**, 21–27.
- Harris, F. L., Lonsbury-Martin, B. B., Stagner, A. C., and Martin, G. K. (1989). "Acoustic distortion product in humans: Systematic changes in amplitude as a function of f_2/f_1 ratio," *J. Acoust. Soc. Am.* **85**, 220–229.
- Hauser, R., and Probst, R. (1991). "The influence of systematic primary-tone level variations L2-L1 on the acoustic distortion product emission $2f_1 - f_2$ in normal human ears," *J. Acoust. Soc. Am.* **89**, 280–286.
- Kemp and Brown (1983). "A comparison of mechanical nonlinearities in the cochlea of man and gerbil from ear canal measurements," in *Physiological Bases and Psychophysics of Hearing*, edited by R. Klinke and R. Hartmann (Springer-Verlag, Berlin), pp. 82–88.
- Kemp, D. T. (1978). "Stimulated acoustic emissions from within the human auditory system," *J. Acoust. Soc. Am.* **64**, 495–496.
- Kimberley, B. P., Brown, D. K., and Eggermont, J. J. (1993). "Measuring human cochlear traveling wave delay using distortion product emission phase responses," *J. Acoust. Soc. Am.* **94**, 1343–1350.
- Kujawa, S. G., Glatke, T. J., Fallon, M., and Bobbin, R. P. (1993). "Contralateral sound suppresses distortion product otoacoustic emissions through cholinergic mechanisms," *Hearing Res.* **68**, 97–106.
- Lieberman, M. C. (1989). "Rapid assessment of sound-evoked olivocochlear feed-back: Suppression of compound action potentials by contralateral sound," *Hearing Res.* **38**, 47–56.
- Lieberman, M. C., and Brown, M. C. (1986). "Physiology and anatomy of single olivocochlear neurons in the cat," *Hearing Res.* **24**, 17–36.
- Magnan, J., Bremond, G., Chays, A., Gignac, D., and Florence, A. (1991). "Vestibular neurotomy by retrosigmoid approach: Technique, indications and results," *Am. J. Otol.* **12**, 101–105.
- Magnan, J., Chays, A., Lepetre, C., Pencroff, E., and Locatelli, P. (1994). "Surgical perspectives of endoscopy of the cerebellopontine angle," *Am. J. Otol.* **15**, 366–370.
- Moulin, A., and Kemp, D. T. (1996). "Multicomponent acoustic distortion product otoacoustic emission phase in humans. I: General characteristics," *J. Acoust. Soc. Am.* **100**, 1618–1639.
- Moulin, A., Collet, L., and Duclaux, R. (1993). "Contralateral auditory stimulation alters acoustic distortion products in humans," *Hearing Res.* **65**, 193–210.
- Mountain, D. C. (1980). "Changes in endolymphatic potential and crossed olivocochlear bundle stimulation alter cochlear mechanics," *Science* **210**, 71–72.
- Murugasu, E., and Russell, I. (1996). "The effect of efferent stimulation on basilar membrane displacement in the basal turn of the guinea pig cochlea," *J. Neurosci.* **16**, 325–332.
- O'Mahoney, C. F. (1993). "Investigating the latency of the $2f_1 - f_2$ distortion product otoacoustic emission in normal and pathological ears using the phase gradient method," Research Report submitted for the degree of Master of Science; University of London.
- O'Mahoney, C. F., and Kemp, D. T. (1995). "Distortion product otoacoustic emission delay measurement in human ears," *J. Acoust. Soc. Am.* **97**, 3721–3735.
- Rajan, R. (1988). "Effect of electrical stimulation of the crossed olivocochlear bundle on temporary threshold shifts in auditory sensitivity. I: Dependence on electrical stimulation parameters," *J. Neurophysiol.* **60**, 549–568.
- Rasmussen, G. L. (1946). "The olivary peduncle and other fiber projections of the superior olivary complex," *J. Comp. Neurol.* **84**, 141–219.
- Ryan, S., Kemp, D. T., and Hinchcliffe, R. (1991). "The influence of CAS on click-evoked otoacoustic emissions in humans," *Br. J. Audiol.* **25**, 391–397.
- Siegel, J. H., and Kim, D. O. (1982). "Efferent neural control of cochlear mechanics: Olivocochlear bundle stimulation affects cochlear biomechanical nonlinearity," *Hearing Res.* **6**, 171–182.
- Sohmer, H. (1965). "The effect of contralateral olivocochlear bundle stimulation on the cochlear potentials evoked by acoustic stimuli of various frequencies and intensities," *Acta Oto-Laryngol.* **60**, 60–70.
- Veuillet, E., Collet, L., and Duclaux, R. (1991). "Effect of CAS on active micromechanical properties in human subjects: Dependence on stimulus variables," *J. Neurophysiol.* **65**, 724–735.
- Veuillet, E., Collet, L., and Morgon, A. (1992). "Differential effect of ear canal pressure and CAS on evoked otoacoustic emissions in humans," *Hearing Res.* **61**, 47–55.
- Vijay, S., and Dayal, M. D. (1968). "The effect of olivocochlear bundle stimulation on latency of action potential," *Laryngoscope* **68**, 1590–1596.
- Warren, E. H., and Lieberman, M. C. (1989). "Effect of contralateral sound on auditory nerve response I. Contribution of cochlear efferents," *Hearing Res.* **37**, 89–104.
- Whitehead, M. L., Lonsbury-Martin, B. L., and Martin, G. K. (1992). "Evidence for two discrete sources of $2f_1 - f_2$ distortion-product otoacoustic emission in rabbits: I. Differential dependence on stimulus parameters," *J. Acoust. Soc. Am.* **91**, 1587–1607.
- Wier, C. C., Pasanen, E. G., and McFadden, D. (1988). "Partial dissociation of spontaneous emissions and distortion products during aspirine use in humans," *J. Acoust. Soc. Am.* **84**, 230–237.
- Williams, E. A., Brookes, G. B., and Prasher, D. K. (1993). "Effect of CAS on otoacoustic emissions following vestibular neurotomy," *Scand. Audiol.* **22**, 197–203.
- Williams, E. A., Brookes, G. B., and Prasher, D. K. (1994). "Effects of olivocochlear bundle section on otoacoustic emissions in humans: Efferent effects in comparison with control subjects," *Acta Oto-Laryngol.* **114**, 121–129.
- Winslow, R. L., and Sachs, M. B. (1987). "Effect of electrical stimulation of the crossed olivocochlear bundle on auditory nerve response to tones in noise," *J. Neurophysiol.* **57**, 1002–1021.
- Zenner, H. P., Zimmermann, U., and Schmitt, U. (1985). "Reversible contraction of isolated mammalian cochlear hair cells," *Hearing Res.* **18**, 127–133.

Effects of electrode configuration on psychophysical strength-duration functions for single biphasic electrical stimuli in cats

David W. Smith

Hearing Research Laboratories, Division of Otolaryngology—Head and Neck Surgery, Box 3550,
Duke University Medical Center, Durham, North Carolina 27710

Charles C. Finley

Hearing Research Laboratories, Division of Otolaryngology—Head and Neck Surgery, Box 3550,
Duke University Medical Center, Durham, North Carolina 27710 and Center for Auditory Prosthesis
Research, Research Triangle Institute, Research Triangle Park, North Carolina 27709

(Received 5 February 1996; revised 12 May 1997; accepted 13 May 1997)

The interface between electrode and neural target tissue is thought to influence certain characteristics of neural and behavioral responses to electrical stimulation of the auditory system. At present, the biophysical properties of this interface are not well understood. Here the effects of biphasic phase duration and electrode configuration on psychophysical threshold in response to electrical stimulation in cats are described. Five cats were trained to respond to acoustic stimuli using food as a reward in an operant reinforcement paradigm. After training, the animals were unilaterally deafened and implanted with a multicontact intracochlear electrode array. Thresholds for single presentations of biphasic current pulses were measured as a function of phase duration and electrode arrangement. Statistical analyses of the data indicated that strength-duration function slopes between 200 and 1600 μ s/phase were significantly different for the different electrode configurations and, overall, were unrelated to the absolute level of the strength-duration function (i.e., were independent of absolute threshold). For all subjects, the slope of this function for intermediate pulse durations was dependent on electrode configuration and most shallow for radial-bipolar configurations (-3.4 dB/doubling), was steepest for monopolar arrangements (-5.9 dB/doubling), and was intermediate for longitudinal-bipolar pairings (-4.4 dB/doubling). Slopes for both shorter and longer phase duration stimuli were not significantly different. The underlying mechanisms for these effects may include, or be a combination of altered electrical field patterns, integrated activity across multiple fibers, and stochastic behavior of individual auditory neurons to electrical stimulation. © 1997 Acoustical Society of America. [S0001-4966(97)02110-3]

PACS numbers: 43.64.Me, 43.66.Cb, 43.66.Gf, 43.66.Ts [RDF]

INTRODUCTION

Clinical investigations in humans and experimental studies in animals have shown that changing the location, orientation, and separation of electrodes within a multielectrode scala tympani implant will, upon stimulation, produce alterations in psychophysical threshold (Pfungst *et al.*, 1995) and in electrically evoked auditory brainstem responses (EABRs) to electrical stimuli (Shepherd *et al.*, 1993). The biophysical bases for these changes are uncertain, since several aspects of the intracochlear electrical field surrounding the target tissue are altered simultaneously when electrode configuration is changed (Finley *et al.*, 1990; Frijns *et al.*, 1995; Girzon, 1987; Suesserman and Spelman, 1993). For a given current level, increasing the separation of the stimulating electrodes both broadens the resulting current field to progressively include more nerve fibers and decreases the extracellular potential gradients that determine current flow patterns across neural membranes. Similarly, placing electrodes closer to the target tissue generally increases stimulus potential levels and steepens the gradients of stimulus fields in the vicinity of target neurons, thus effectively reducing thresholds and focusing stimulation (Beitel *et al.*, 1995; Shepherd *et al.*,

1993). Changes in the orientation of the stimulating contacts (e.g., switching among radially oriented bipolar, longitudinally oriented bipolar, and monopolar configurations) will likely alter the geometry of the electrical field surrounding a neuron and may produce excitation at a different location along the neural membrane (Hartmann *et al.*, 1984; Pfingst *et al.*, 1995; van den Honert and Stypulkowski, 1984).

Absolute behavioral sensitivity is commonly described in terms of psychophysical threshold contours as a function of sinusoidal stimulus frequency or pulsatile phase duration. The shape and slope of the contours are dependent on a number of factors, including nerve survival pattern (Pfingst *et al.*, 1985), central versus peripheral placement of stimulating electrodes (Shannon, 1989) and overall stimulus duration (Pfingst *et al.*, 1995), as well as changes in electrode configuration. Regarding electrode effects, Pfingst (1989) determined that, in the monkey, threshold drops with increases in bipolar contact separation at a rate of 3.9 dB/mm for 100-Hz sinusoids and 1.7 dB/mm for 1.0-kHz sinusoids. Recent studies in cats presented with long duration sinusoidal bursts have shown reduced absolute threshold levels and increased threshold contour slopes as electrode configuration changed

from radial-bipolar to longitudinal-bipolar to monopolar electrode configurations (Smith *et al.*, 1995). Similar studies using sinusoidal stimuli in nonhuman primates reported comparable findings, showing that increasing electrode *separation* from narrow bipolar to monopolar arrangements produces, in most cases, a greater increase in thresholds for low-frequency as compared with high-frequency electrical stimuli (Pfungst *et al.*, 1995). Complicating the nonhuman primate studies, however, are differences in the type of electrode used and variability in positioning of the electrodes within, and around, scala tympani. If, as the extant literature suggests, threshold is sensitive to electrode configuration in the cochlea, then comparisons across subjects are most easily made where the location, orientation and separation of the electrodes has been held relatively constant.

The goal of this study was to determine the effects of biphasic pulse phase duration and different intracochlear electrode configurations on psychophysical thresholds in cats. Studies were carried out in animals implanted with the same multicontact intracochlear electrode array. This array was designed to position the electrode contacts in a relatively constant position, across subjects, with respect to the modiolus. Behavioral strength-duration functions (detection threshold measured as a function of pulse duration) were measured for three different electrode configurations (radial-bipolar, longitudinal-bipolar, and monopolar configurations) in each of five cats.

I. MATERIALS AND METHODS

A. Subjects

Five young-adult male cats, weighing between 3.5 and 4 kg, served as subjects in these studies. The animals were maintained on a calorie-restricted diet to facilitate training and testing procedures that required the use of food as reinforcement in an operant paradigm. In order to reduce the potential for accidental damage to the implant or connector, we initially acclimated the cats to restraint and to acoustic stimulation. After baseline acoustic training, the animals were implanted unilaterally with a multichannel intracochlear electrode array.

The care and use of the animals in these studies was approved by the Duke University Institutional Animal Care and Use Committee.

B. Surgical and implantation procedures

After the initial training and testing period for acoustic stimuli, each animal was implanted, under sterile conditions, with a multichannel scala tympani electrode array. The array was inserted into the scala tympani through a small hole in the round window. The carrier was secured at the round window niche by cementing the electrode's Dacron®/silastic cuff at the promontory with medical-grade cyanoacrylate cement. The implant cable was then routed through a groove made in the lambdoidal ridge to the calvaria, where a second Dacron® tab, containing a bare-wire reference electrode, was cemented to the skull for stress relief. From the second Dacron® tab, the cable was routed under the temporalis

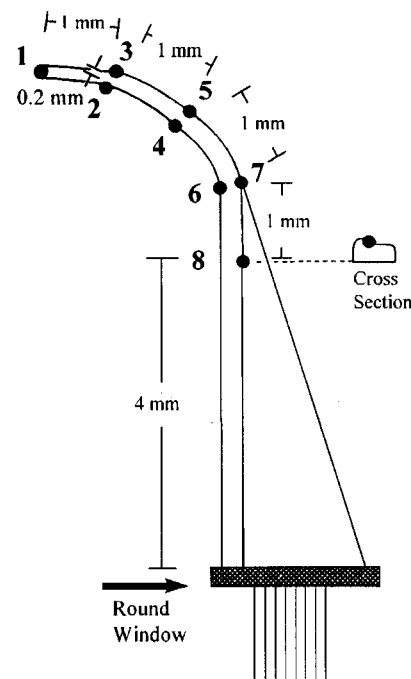


FIG. 1. Schematic diagram of the intracochlear electrode array implanted in cats. The electrode consisted of eight contacts arranged in three bipolar pairs (2–3, 4–5, 6–7) and two single contacts (1, 8). The contacts can be stimulated in any combination. The vertical dashed line along the carrier indicates continuation of the curved portion of the carrier.

muscle to the vertex, directly behind the orbits, where the electrode terminated in a titanium, skull-based connector that was mounted by four titanium screws.

To ensure destruction of all hair cells, thus eliminating the possibility of “electrophonic” activation of the cochlea, we flushed the implanted ear with a 10% neomycin solution at surgery and prior to insertion of the electrode.

A schematic of the electrode array is shown in Fig. 1. The electrodes were fabricated from platinum/iridium wire. The exposed contacts were 225- μ m-diam hemispheres, arranged along the carrier in three radial-bipolar pairs (2–3, 4–5, and 6–7) and two single electrodes (1 and 8). A bare-wire extracochlear reference was placed under the temporalis muscle for monopolar stimulation. The tapered silastic carrier was designed to maintain placement of the radial electrode pairs (2–3, 4–5, and 6–7) at a constant distance relative to the modiolar wall (Loeb *et al.*, 1995). This design was adopted to help reduce the confounding influence of nontapered electrodes, the placement of which becomes progressively eccentric, relative to the modiolus, as the basal turn widens near the round window (cf. Shepherd *et al.*, 1993).

C. Apparatus

All behavioral testing was conducted in sound-attenuating chambers (Industrial Acoustics Company, Bronx, NY). Restrained by a plastic collar in a standing yoke, the animals were allowed freedom of movement sufficient to either stand or sit. A response panel was mounted directly in front of the animal. The panel contained a cue light, which served to indicate experimental conditions to the animal, an insulated microswitch response key, and a feeder tube. A

peristaltic pump outside the chamber delivered pureed cat food through silicon tubing to a small trough attached to the feeder tube.

All stimuli were generated digitally by a PC-based waveform generator and digital-to-analog converter (Tucker-Davis Technologies, Gainesville, FL) and were passed through a programmable attenuator (Tucker-Davis Technologies). The output of the attenuator was directed through a custom ac-coupled, current-controlled stimulus isolator to a cable leading inside the test chamber to a manual switching arrangement. Stimuli were then directed to the subject's percutaneous pedestal by a set of fine, flexible wires that were selected according to the desired electrode stimulus configuration.

D. Electrical stimuli

The stimuli were single presentations of charge-balanced, biphasic current pulses. Stimulus pulse duration ranged from 25 to 10 000 $\mu\text{s}/\text{phase}$. The initial phase of the stimulus was always anodic. For the electrode pairs reported here, the positive phase was always applied to the first electrode of the pair specified (i.e., positive stimulation applied to electrode 1 of pair 1-8, or to the bare-wire temporalis electrode in M-1). Stimulus intensity is expressed in dB *re*: 1 mA peak.

The impedances of the intracochlear electrodes were monitored daily using an electrode impedance meter (BAK, model IMP-1, Germantown, MD). Daily prestimulation impedances typically ranged from 40 to 100 k Ω , and typically dropped by 25%–50% after test session stimulation.

E. Psychophysical procedures/data analysis

More detailed descriptions of the behavioral techniques can be found in Smith *et al.* (1994, 1995). Briefly, the animals were trained to press the response key to the flashing cue light. If the subject maintained contact, the test stimulus was presented following a variable interval; the animal was trained to release the key to indicate signal detection. A correct response was followed by delivery of 0.6 ml of pureed cat food through the feeder tube. Thresholds were determined using a "staircase" or tracking procedure, where stimulus intensity was decreased 1 dB for the subsequent trial following correct detection. Likewise, a miss resulted in a 1 dB increase in stimulus intensity on the next trial. Threshold for a given stimulus condition was defined as the level at which 50% signal detection was reported. Twenty percent of all trials were "catch-trials," where all experimental conditions were identical to test stimulus trials, except the test stimulus was withheld. Data from sessions with more than 20% responses to catch-trials are typically discarded and not used in summary threshold calculations. No such sessions occurred, however, and the response to catch-trial rate averaged 3% in the present studies. Psychophysical data were collected in daily testing sessions lasting typically 1 to 2 h. The behavioral data presented here represent the average of six behavioral thresholds measured on separate days.

F. Data analysis

The slopes of strength-duration functions at each measured phase duration were calculated. For a given phase duration, the slope, expressed as dB/doubling of phase, was the threshold difference in dB between two points along the function at $1/\sqrt{2}$ and $\sqrt{2}$ times the given phase condition. In some instances, these points corresponded exactly to other measured phase duration conditions. In cases where a corresponding measure did not exist, the threshold value at the intermediate point was estimated by assuming a linear, straight-line function of threshold between measured phase duration conditions that spanned the target duration. At the end points of the strength-duration function, the slope was calculated by doubling the threshold difference between the end-point threshold and the threshold at a point either $1/\sqrt{2}$ or $\sqrt{2}$ times the end-point duration, depending on which end of the strength-duration function was being considered.

Summary statistics are based on one-way analysis of variance (ANOVA) for repeated measures across electrode conditions calculated for each stimulus phase duration studied. Assumptions of normality of the data at each duration were tested. When a statistically significant difference was indicated among the electrode condition groups, a pairwise multiple comparison procedure (Student–Newman–Keuls method) was used to identify significant group differences. When assumptions of normality were not met within the relatively small data sample ($n=3$ electrodes \times 5 animals = 15) at each phase duration, a Friedman repeated measures analysis of variance on ranks was used prior to identifying group differences using multiple pairwise comparisons. This occurred at two duration conditions for the slope measures, 800 and 5000 $\mu\text{s}/\text{phase}$. At the two longest phase duration conditions, statistical analyses could not be completed because data were not collected for all animals.

II. RESULTS

Absolute threshold *levels* varied widely, both across and within animals, as a function of phase duration and electrode configuration. The maximum threshold difference across animals and electrode arrangement for a fixed phase duration was 24 dB. For monopolar, longitudinal-bipolar, and radial-bipolar electrode separations, the largest absolute differences across subjects were 8, 13, and 20 dB, respectively. The range of absolute thresholds reported here and elsewhere for cats (Smith *et al.*, 1994, 1995) fell well within the range reported previously for implanted humans (Moon *et al.*, 1993) and monkeys (Pfungst *et al.*, 1991).

Behavioral strength-duration functions are presented in Fig. 2 for subjects F04, F06, F07, F08, and F09. Threshold functions for each animal were determined using radial-bipolar, longitudinal-bipolar, and monopolar electrode configurations. The specific contacts used in a given electrode arrangement for each subject are indicated in the figure legend and should be compared with the schematic (Fig. 1). Thresholds were based on detection of single, biphasic stimuli, the phase durations of which were varied.

For all subjects and all electrode arrangements, thresholds decreased with increases in pulse duration to between

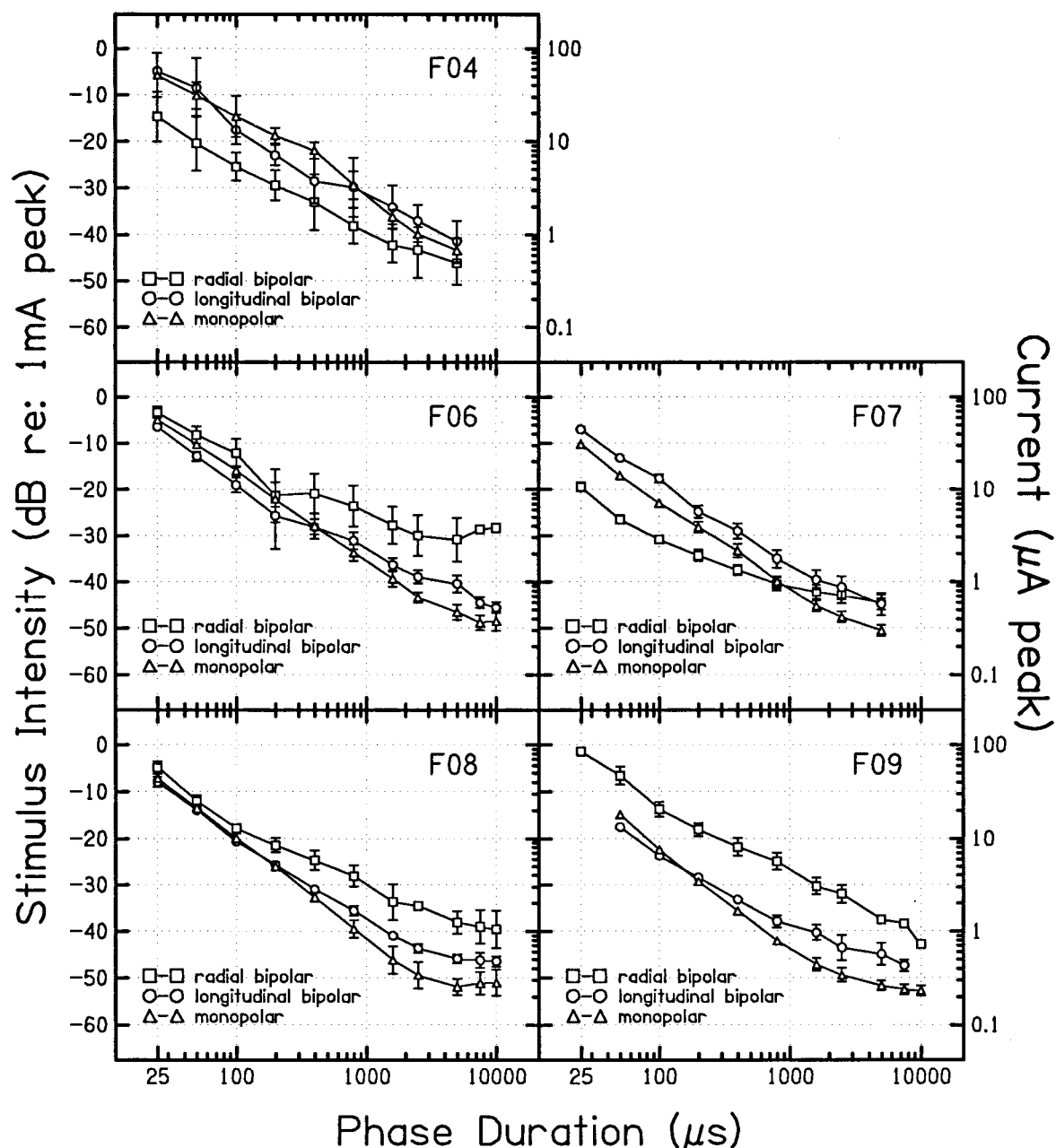


FIG. 2. Behavioral strength-duration functions for electrical stimuli as measured in subjects F04, F06, F07, F08, and F09. In subjects F04, F06, F07, and F08, functions were determined for radial-bipolar (6-7), longitudinal-bipolar (1-8), and monopolar (M-1) electrode configurations. In subject F09 functions were determined for radial-bipolar (4-5), longitudinal-bipolar (4-2), and monopolar (4-M) electrode configurations. Bars, \pm s.d.

approximately 800 and 1200 μ s/phase; in most cases, further increases in phase duration produced shallower or flattened slopes. The phase duration at which the flattening began was variable and was statistically unrelated to either the degree of the flattening or the electrode arrangement.

For subjects F06, F08, and F09, long phase-duration thresholds decreased as a function of electrode separation and orientation (from radial-bipolar to longitudinal-bipolar to monopolar configurations). In all three cases, the intermediate longitudinal-bipolar separation yielded threshold values between the two extreme separations. This pattern was observed regardless of the relative thresholds for the short phase durations seen across electrode separations. For subjects F06 and F08, thresholds for short phase-duration

stimuli varied by less than 4 dB for the three separations tested in these animals, as compared with a maximum of 20 dB for long phase durations for the same electrode arrangements. Subject F09, while similar to F06 and F08 in terms of the ordered and wide separation of threshold functions at long phase durations as a function of electrode arrangement, did not demonstrate the close separation at short phase durations.

In animals F04 and F07, no systematic change in the absolute level of threshold as a function of contact separation was evident. In contrast to the other subjects, F04 and F07 showed, with changes in electrode configuration, as much or more variation in thresholds for short phase-duration stimuli as they did for long phase-duration stimuli.

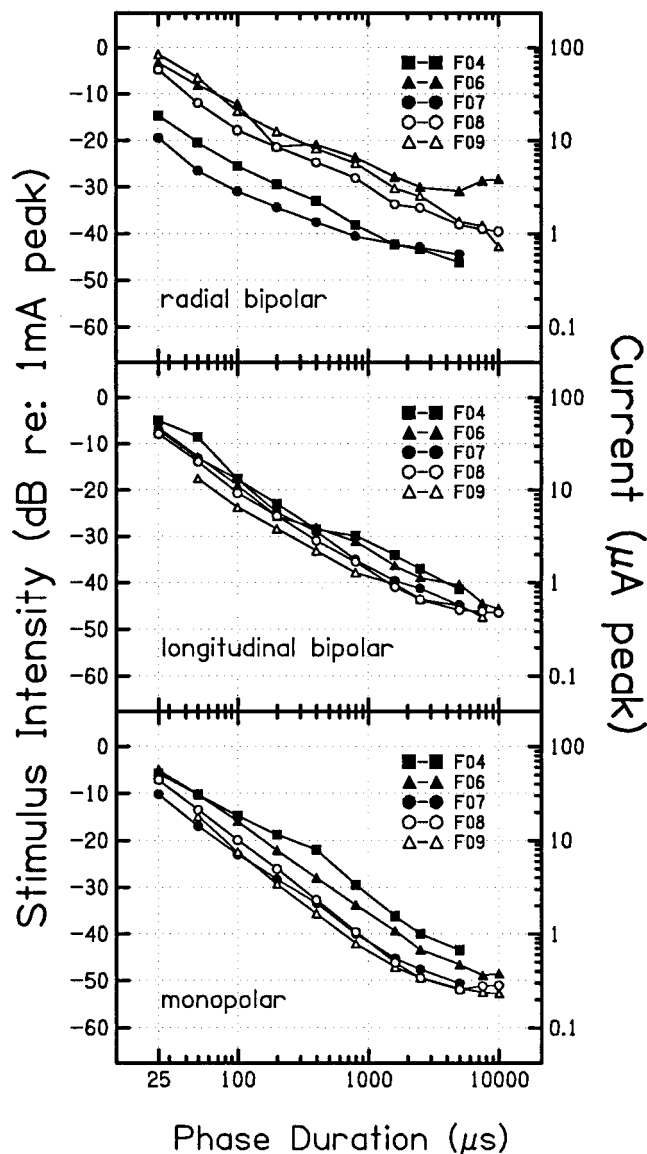


FIG. 3. Comparison of strength-duration functions for radial-bipolar, longitudinal, and monopolar electrode configurations from all subjects. Data are taken from Fig. 2.

To compare directly strength-duration functions for similar electrode configurations and spacings across animals, we plotted the data from Fig. 2 for each electrode configuration, as shown in Fig. 3. Doing so resulted in a series of essentially parallel functions, across subjects, for each electrode configuration. While there is considerable variability in the absolute level of the curves, the slopes of the threshold functions appear relatively similar for each electrode arrangement.

The effects of electrode arrangement on the slope of the strength-duration functions, independent of animal or absolute threshold level, can be observed more precisely by averaging the data of Fig. 3, by electrode configuration, across animals. Figure 4(a) presents the average strength-duration functions for all animals for each electrode arrangement. Although the data in Fig. 4(a) appear to be normalized at the 200 μ s/phase duration condition, they are actually the simple

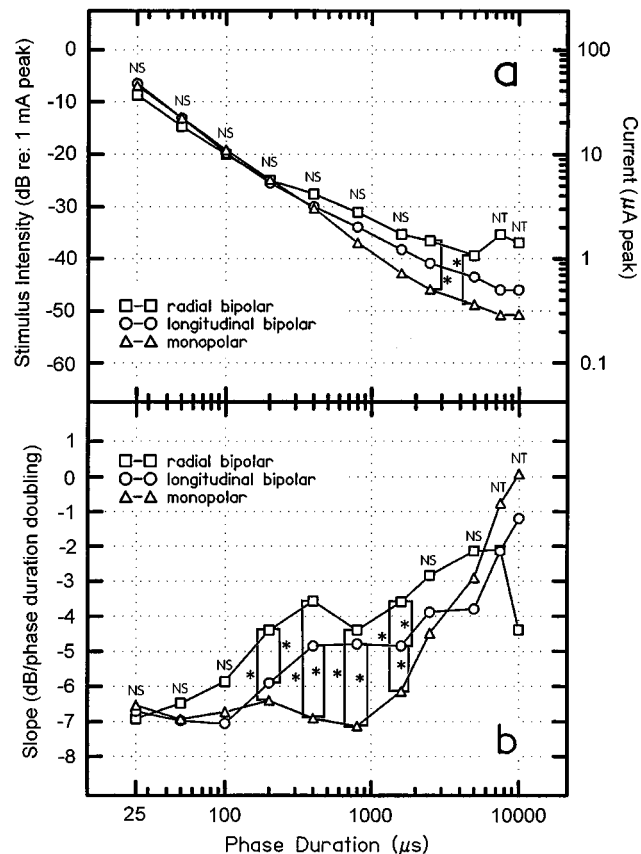


FIG. 4. (a) Strength-duration functions, averaged across all subjects, for radial-bipolar, longitudinal-bipolar, and monopolar electrode configurations. Asterisks indicate comparisons of *absolute level* across electrode configurations that were statistically significant ($p < 0.05$); NS indicates comparisons of *absolute level* across electrode configurations where no statistical difference was found; NT indicates that pairings were not statistically analyzed because an insufficient number of subjects were tested with the long phase duration stimuli (i.e., phase durations $> 5000 \mu$ s; see Figs. 2 and 3). Data are taken from Fig. 3. (b) Strength-duration function slopes, measured from the average functions in (a), as a function of electrode configuration. Slopes were measured at each phase duration. Pairwise comparison of *slope* across the various electrode configurations yielded statistically significant differences (asterisks) at middle phase durations (200–1200 μ s/phase). NS indicates phase durations for which no statistical differences were determined for comparisons of slope across the different electrode configurations; NT indicates phase durations for which comparisons were not made (see above).

averaged threshold functions across the five subjects. With pulse durations greater than 200 μ s/phase, there is a progressive dependence of slope magnitude on electrode separation and orientation. Slopes systematically increase as electrode spacing is increased from radial-bipolar to longitudinal-bipolar to monopolar configurations. For shorter phase durations, little electrode dependent variation occurred.

Figure 4(b) presents the average slopes (dB/doubling of phase duration) of the strength-duration functions for all animals for each electrode arrangement. Again, for shorter pulse durations ($< 100 \mu$ s/phase), slopes are large and not significantly different across electrode configurations. At longer phase durations (200 to 1600 μ s/phase), the slopes vary, depending on electrode configuration, with the radial-bipolar and monopolar conditions having the shallowest and steepest slopes, respectively. At extremely long phase durations

TABLE I. Averaged slopes of strength-duration functions for animals F04, F06, F07, F08 and F09 as a function of electrode configuration. The slope (dB/doubling of phase duration) for each electrode configuration is calculated as the average of the individual slope estimates over the specified range of phase durations. The ranges were selected on the basis of the ranges of phase duration over which statistically significant or nonsignificant differences in slopes were observed as a function of electrode configuration as described in Fig. 4(b).

Animal	Electrode configuration	Slope (dB/doubling of phase duration)		
		50–100 μ s	200–1600 μ s	2500–5000 μ s
F04	radial bipolar (6-7)	–5.0	–3.9	–2.5
	longitudinal bipolar (1-8)	–6.8	–4.0	–4.5
	monopolar (M-1)	–4.4	–5.6	–4.1
F06	radial bipolar (6-7)	–5.5	–3.2	–1.8
	longitudinal bipolar (1-8)	–6.3	–4.0	–3.5
	monopolar (M-1)	–5.7	–5.9	–4.1
F07	radial bipolar (6-7)	–4.8	–2.5	–1.4
	longitudinal bipolar (1-8)	–5.6	–4.9	–3.3
	monopolar (M-1)	–6.0	–5.4	–3.1
F08	radial bipolar (6-7)	–5.6	–3.7	–2.5
	longitudinal bipolar (1-8)	–6.1	–5.0	–2.3
	monopolar (M-1)	–6.3	–6.4	–2.2
F09	radial bipolar (4-5)	–5.9	–3.9	–3.8
	longitudinal bipolar (4-2)	–5.8	–4.2	–3.0
	monopolar (4-M)	–6.9	–4.8	–1.4
Mean	radial bipolar	–5.4	–3.4	–2.1
	longitudinal bipolar	–6.1	–4.4	–3.3
	monopolar	–6.0	–5.9	–3.2

(>2500 μ s/phase), the averaged slope magnitudes tend to merge at smaller values for the longitudinal bipolar and monopolar configurations. The calculated slope for the radial-bipolar configuration abruptly jumped to a higher level, most likely because the group data were averaged over fewer animals.

Results of the statistical analyses for both strength-duration function level and slope across electrode conditions, for each tested stimulus phase duration, are shown in Fig. 4(a) and (b), respectively. Brackets connect data points that are statistically different ($p < 0.05$). At the two longest phase duration conditions, statistical analyses could not be completed because data were not collected for all animals at these conditions (see Fig. 2). These conditions are indicated in Fig. 4 as not tested, but the data points are included to show trends. In the case of strength-duration function levels, significant differences across electrodes are observed only at very long phase durations, and only between radial-bipolar and monopolar conditions. In the case of strength-duration function slopes, no differences across electrodes are seen at short and very long phase durations; however, at intermediate durations, significant electrode effects are observed. In all cases, the radial-bipolar and monopolar conditions are significantly different statistically. In one case (1600 μ s/phase duration), all three electrode configurations are significantly different statistically.

Table I summarizes the slopes measured from the individual functions in Fig. 2. Different aspects of the behavior of the strength-duration functions, in response to changes in electrode configuration, are illustrated by presenting

strength-duration function slopes averaged across phase duration conditions for the ranges of 50–100 μ s/phase, 200–1600 μ s/phase, and 2500–5000 μ s/phase. Ranges were selected on the basis of the distribution of the durations that had statistically different slopes across electrode configurations. For the short phase-duration range (50–100 μ s/phase), the slopes tend to converge at similar steep values. In the intermediate range of 200–1600 μ s/phase pulses, the slope of the strength-duration function increases as contact separation is increased and electrode configuration is changed from radial-bipolar to monopolar. For the longest phase-duration range, the slopes tend to smaller values and are independent of electrode configuration.

III. DISCUSSION

The objective of this study was to describe the effects of electrode configuration and biphasic pulse duration on detection threshold for single-pulse electrical stimuli. Behavioral strength-duration functions were determined for radial-bipolar, longitudinal-bipolar, and monopolar electrode configurations in each animal. The radial-bipolar pairs were closely spaced (200 μ m), whereas the longitudinal pairs, except for subject F09 (1 mm), were widely spaced (4 mm). This study contributes new information regarding behavioral responses to single pulses delivered with radial-bipolar electrodes. Additionally, it compares relative performance across radial-bipolar, longitudinal-bipolar, and monopolar electrode configurations within the same individuals. Previously, we described comparable changes in slopes of threshold func-

tions for single-cycle and long-duration sinusoidal stimuli in cats (Smith *et al.*, 1995). Thus far, all of our psychophysical data in cats have fallen well within the range of data presented in the literature for implanted monkeys (Pfungst *et al.*, 1981) and for humans (Eddington *et al.*, 1978; Moon *et al.*, 1993; Shannon, 1983) in terms of both absolute level and strength-duration function slope.

Two patterns emerge from the present data that suggest further insights into the influence of electrode configuration on strength-duration functions. First, for a given electrode configuration, there is considerable variation in absolute threshold level across animals, independent of the duration of the stimulus phase. Second, the shapes of the strength-duration functions, as defined by their slopes, are remarkably similar across animals for a given electrode configuration, are independent of absolute threshold level, and vary systematically across electrode type, depending on the duration of the stimulus phase.

A. Variation in absolute thresholds

Absolute threshold levels varied widely, both within and across animals, as a function of phase duration and electrode configuration. Assuming fully functional electrodes with intact, well-insulated leads and clean contact surfaces, factors contributing to the determination of absolute threshold may include behavioral factors, placement of the electrodes, relative degrees of current shunting based on electrode design, and variable survival of the target neural population. In order to reduce variation across animals, the experimental protocol was designed to control many of these factors.

The behavioral testing paradigm addressed well the factors related to poor or inconsistent performance of the animals during behavioral testing as indicated by the low standard deviations (s.d.s) of the measured thresholds across sessions and the consistently low (<6%) catch trial (false alarm) rate. As shown in Fig. 2, s.d.s are consistently lower than the absolute differences in thresholds across electrodes for a fixed phase duration, and they are lower than the threshold changes occurring for a given strength-duration function and a fixed electrode condition.

To minimize the effects of variation in electrode placement across animals, we collected all data in animals implanted with the same multicontact electrode array in scala tympani. Variations in electrode placement in the scala tympani have been shown to alter modeled potential fields in the vicinity of the spiral ganglion cells (Finley *et al.*, 1990; Finley, 1991; Frijns *et al.*, 1995) and have altered as well the threshold and growth rates, with stimulus intensity, of experimental electrical auditory brainstem response measures (Shepherd *et al.*, 1993). This array in the present study was designed to maintain a relatively consistent placement of intracochlear electrode contacts near the modiolus and habenua perforata (as scala tympani widens towards the base of the cochlea), independent of gross anatomical variances across individuals. Pending histologic analyses, no verification of contact placement is available in the present study. Nevertheless, all electrode configurations were studied in each animal, thus providing within-animal controls. Elec-

trode and lead integrity was monitored throughout the study by daily electrode impedance measurements.

Other electrode-dependent effects on absolute threshold may be based on direction and degree-of-spread of the stimulus current. Both factors are largely determined by the orientation of the electrode configuration (i.e., radially versus longitudinally oriented bipolar pairs) and the physical spacing between the contacts (i.e., bipolar versus monopolar). As to configuration, radially oriented pairs would be expected to be more effective in stimulating the radially directed cochlear fibers as compared with a longitudinally oriented electrode pair with equal spacing (Ranck, 1975). At the same time, however, the longitudinally oriented pair would possibly recruit more fibers because the current spread along the cochlear partition is broader than that of a radially oriented electrode pair (van den Honert and Stypulkowski, 1987). In the present studies, all but one (F09) of the longitudinally oriented bipolar pairs was selected for spacing that was broad and many times greater than that of the radial-bipolar pair. Consequently, while both electrode orientation and separation change when the bipolar pairs are switched, it is most likely the degree of electrode separation that is the dominant factor influencing threshold.

Contact separation, when increased, reduces thresholds at a given current level by producing broader current fields that recruit progressively more nerve fibers (Finley *et al.*, 1990; Girzon, 1987; van den Honert and Stypulkowski, 1987). In addition, wider contact spacing decreases the degree of direct interelectrode current shunting that contributes strongly to higher thresholds for the closely spaced bipolar condition. In general, when the neural target population is held constant, these effects combine to produce higher thresholds for more closely spaced electrode configurations. This pattern was observed in subjects F06, F08, and F09. It did not hold true, however, for subjects F04 and F07, where the radial-bipolar condition had the lowest thresholds (Fig. 2).

For subjects F04 and F07, electrode placement and geometry may have played a less significant role than did the survival pattern of the target neural tissue. At implantation, the scalae of all animals were perfused with a 10% neomycin solution to ensure destruction of all hair cells and to deafen the animals. Nevertheless, such treatment may create a diverse survival pattern of spiral ganglion cells. Several studies (Leake *et al.*, 1982; Leake and Hradek, 1988; Pfingst *et al.*, 1981; Pfingst and Sutton, 1983) have shown significant variation in the density and distribution of spiral ganglion cell survival following destruction of cochlear receptors in long-term implanted subjects, even among animals deafened using the same ototoxic regimen. A result consistent with the influence of variable neural survival upon thresholds is that comparing absolute strength-duration levels across electrode configurations (Fig. 3) revealed considerably more variability across animals for the radial-bipolar configuration than for either of the two wider arrangements. This may have occurred because fields from closely spaced electrode couplings falloff relatively more rapidly with distance from the stimulating contacts than do more widely spaced pairs. As such, stimulation by the radial-bipolar configurations is more

dependent on activation of local neural populations than are the more widely spaced longitudinal-bipolar and monopolar configurations, and absolute threshold levels for the radial-bipolar arrangement should also be more sensitive to local variations in neural survival. Consequently, we hypothesize that variation in *absolute* threshold for animals using the radial-bipolar configuration (Fig. 3) reflects relative differences, across subjects, in the survival of neural tissue near the stimulating electrodes and in the proximity of the electrodes to the target structures. For the more widely spaced configurations, less sensitivity to survival patterns would be expected.

Confounding interpretation of potential neural survival effects in this study is that, of all test animals, only F09 was tested with radial-bipolar (4–5), longitudinal-bipolar (4–2), and monopolar (4–M) electrode combinations that employed a single electrode (4) common to all three arrangements. The other animals had a single radial pair (6–7), a widely spaced longitudinal pair (1–8), and a monopolar condition (1–M), the electrodes of the latter two arrangements being distant from those of the radial pair. Comparisons of data across these electrode pairings within an animal are potentially more susceptible to the effects of variable neural survival and electrode placement in different regions of the cochlea, as opposed to the F09 case where the same population of neurons in the vicinity of electrode contact (4) are most likely stimulated in each condition. In the case of F09, the expected trend of decreasing threshold from radial to monopolar configurations was observed.

The averaged strength-duration functions across all animals for each electrode condition [Fig. 4(a)] emphasize the degree of absolute threshold variability occurring in this study. Statistically significant differences in absolute thresholds across electrode conditions were observed only for the longest phase duration conditions. These differences were most likely due to temporal and spatial integration of activity across many fibers where monopolar electrodes addressed relatively more target fibers than did the closely spaced, radial-bipolar pairs (Moon *et al.*, 1993; Pfingst *et al.*, 1991; Shannon, 1983).

B. Effects of electrode configuration on strength-duration function slope

The above sources of variation in absolute thresholds notwithstanding, the data from this study show consistent trends in strength-duration function slopes within animals as a function of both electrode configuration and phase duration. Progressively increasing electrode contact separation, from radial-bipolar to longitudinal-bipolar to monopolar couplings, produced an orderly increase in the slope of the strength-duration function (Fig. 4 and Table I) for intermediate-length phase durations (200–1600 μ s/phase). With these changes in configurations, the average slope across animals increased from –3.4 dB (radial-bipolar) to –4.4 dB (longitudinal-bipolar) to –5.9 dB (monopolar) per doubling of phase duration. For both shorter and longer phase-duration conditions, slopes tended to converge, to

steeper slopes for shorter phase durations, and to shallower slopes for longer phase durations, independent of electrode configuration.

Importantly, as described above, the increase in slope with increasing contact separation was *independent* of the absolute level of the thresholds for each electrode coupling. For example, radial-bipolar threshold functions varied in absolute level across animals by as much as 20 dB (Fig. 2), yet no relationship between slope and threshold minima was evident across subjects. Moreover, in subjects F04 and F07, in general, the radial-bipolar configurations produced some of the lowest overall behavioral thresholds over much of the range of phase durations tested, as compared with the wider electrode contact separations in the same animal. These configurations also yielded the *shallowest* measured slopes as compared with the other, wider electrode contact separations in these same animals. The results suggest that the slope of the contour is not a simple function of the absolute level of the threshold minima, but that electrode configuration, *per se*, is a primary determinant of the slope.

Several factors have been postulated to directly contribute to the slopes of psychophysical strength-duration functions. First, and most fundamental, is the responsiveness of single neurons to electrical stimulation, wherein with perfect membrane integration of stimulus charges, strength-duration slopes approach –6.0 dB/doubling of phase duration (Aidley, 1971; McNeil, 1976) for short-duration pulses. For longer duration pulses, slopes are shallower and approach zero due to nonlinear membrane properties as the neuron accommodates to the stimulus. In addition, fibers may behave as leaky integrators (i.e., losing charge as integration occurs) resulting in integration slopes for short and medium duration stimuli that are less than –6 dB/doubling. Such neural behavior has been demonstrated in electrically stimulated auditory fibers (Moxon, 1971; Parkins and Columbo, 1987; van den Honert and Stypulkowski, 1984). In the present data, slopes for short-duration pulses (<200 μ s/phase) approach –6 dB/doubling independent of electrode configuration. Similarly, slopes for very long durations pulses (>1600 μ s/phase) are shallow and are similarly independent of electrode configuration. Both results suggest that these components of strength-duration slope are largely determined by the behavior of the target neurons themselves. It is possible, however, that multiple neurons could be acting as leaky integrators with slopes <6 dB/doubling, but be recruited in a manner to increase the slopes of the threshold curves. The integration of activity across multiple fibers by the central nervous system (Pfingst *et al.*, 1991) can produce slopes well in excess of –6 dB/doubling of phase duration (Moon *et al.*, 1993; Shannon, 1983). Such integration appears to be most effective for longer-duration stimuli and is reduced with poorer nerve survival (Miller *et al.*, 1994; Pfingst *et al.*, 1985).

For intermediate pulse durations (200–1600 μ s/phase), slopes in the present data are dependent on electrode configuration and must involve additional underlying mechanisms. Recently, Pfingst *et al.* (1995) described electrode-dependent, strength-duration slope changes to long-sinusoidal bursts. They observed steeper slopes for

monopolar and widely spaced bipolar configurations as compared with narrowly spaced bipolar stimulation. They discussed two hypotheses that may relate to these phenomena. One is that changes in electrode configuration result in changes in the site of spike initiation; such changes consequently reflect underlying differences in nodal membrane characteristics. The other is that changes in electrode configuration produce differences in the manner and degree of across-fiber integration. The investigators proposed that these mechanisms are not mutually exclusive and may operate simultaneously.

Regarding the across-fiber integration hypothesis, spatial mapping data and model results indicate that increasingly greater numbers of fibers would be recruited for electrode configurations progressing from radial-bipolar to longitudinal-bipolar to monopolar (Finley *et al.*, 1990; Frijns *et al.*, 1995; van den Honert and Stypulkowski, 1987). Assuming that behavioral threshold is defined by some aggregate level of activity from multiple fibers, it follows that threshold could be achieved with a higher level of activity from a few fibers or with a lesser level of activity from more fibers (Pfungst *et al.*, 1991; White *et al.*, 1994). Hence current levels to achieve threshold with monopolar stimulation would be expected to be smaller than those for bipolar stimulation, as is generally observed experimentally. It is important to note, however, that as electrodes are brought closer together, current shunting increases rapidly, which in turn would tend to increase bipolar thresholds, independent of any changes in neural activity. Recent data indicate that when a monopolar electrode is located close to the target neural tissue, very sharp spatial recruitment of neurons can occur that is comparable to that observed with radial-bipolar configurations (Beitel *et al.*, 1995; van den Honert, personal communication). Behavioral thresholds for this monopolar condition, however, do not increase to the level observed for radial-bipolar stimulation (Beitel *et al.*, 1995), although roughly comparable numbers of neurons may be recruited in both cases. In this case, the relatively lower monopolar threshold occurs, perhaps, because there is less current shunting in the monopolar case, independent of changes in neural recruitment. In addition to these effects, Pfingst *et al.* (1995) proposed that electrode-dependent changes in strength-duration functions may also be related to the efficiency of integration, which may be affected by the relative synchrony of firing across fibers. The present data do not directly address this possibility.

Recently, White and colleagues (White *et al.*, 1994) proposed a stochastic, neural-behavioral model of perceptual threshold that combines neural membrane characteristics with across-fiber integration. This model allows examination of a number of interactive factors including the extent of stimulus spread with different electrode configurations, as well as the stochastic threshold behavior, density, and distribution of the surviving target neurons. The model contains a central integrator that counts spikes over neural populations within an integration time window. An essential component of the model is the characterization of individual neural fibers, based on the stochastic behavior of single nodes. Each fiber responds in a manner described by an integrated Gauss-

ian input-output function, linking firing probability with input stimulus level: As experimentally observed (Dynes, 1996; van den Honert, personal communication; Verveen and Derksen, 1968), stimuli with short phase durations elicit steeper input-output functions than do long-duration stimuli. The stimulus for each model fiber is determined both by the field structure (monopolar versus bipolar) and by the stimulus level applied to the electrode. Behavioral threshold for single-pulse stimuli is achieved when the integrator detects X total spikes, independent of the number of sampled fibers.

For the simple case where electrode configuration is held constant, a cochlea with relatively good nerve survival (i.e., more available fibers) should require a lower average discharge probability, and hence a lower stimulus level, to elicit behavioral threshold (i.e., X total spikes) than would a cochlea with poor nerve survival. Similarly, a lower average discharge probability should be required to achieve behavioral threshold with monopolar electrodes because such electrodes presumably stimulate a larger portion of the cochlea, consequently recruiting a larger number of fibers than would closely spaced bipolar electrodes. With the added consideration of the effects of a changing stimulus phase duration, the model predicts strength-duration functions very similar to those described behaviorally in this study. Specifically, strength-duration slopes are steeper for monopolar than for bipolar stimulation because of the combined effects of monopolar electrodes addressing more fibers and the shallower fiber input-output functions for long-duration stimuli (i.e., at low stimulus levels, fibers have higher probabilities of firing with longer stimuli than with shorter stimuli). The general model assumes that the central integrator sums activity over a time window; consequently, additional predictions of how behavioral threshold should change as a function of pulse rate, burst duration, and total number of pulses, in combination with phase duration and electrode configuration, are possible.

In summary, systematic changes in the slope of the strength-duration functions, independent of absolute threshold levels, were observed with electrode choice. The measured slope of the strength-duration functions steepened in an orderly manner with progressive increases in contact separation. The underlying mechanisms involved may include a combination of alteration in electrical field patterns, integration of activity across multiple fibers, and consideration of the stochastic behavior of individual auditory neurons.

ACKNOWLEDGMENTS

The authors gratefully acknowledge Mr. Karl Konrad for his assistance in developing the computer program and hardware necessary to undertake these studies and Ms. Valerie Olszyk for her contribution in running the day-to-day behavioral sessions. We also wish to thank Dr. Gerald Loeb for design and fabrication of the electrode arrays and Dr. Bryan Pfingst and Mr. Franz Weiser for assistance in the design and fabrication of the percutaneous connector pedestal. This research and manuscript have benefitted greatly from the assiduous engineering and analytic support provided by Dr. Chris van den Honert and Dr. Mark White.

Editorial assistance was provided by Ms. Ann Tamariz. This work was supported by Grant No. P01 DC 00036 from the National Institute on Deafness and Other Communication Disorders, National Institutes of Health.

- Aidley, D. J. (1971). *The Physiology of Excitable Cells* (Cambridge U.P., London).
- Beitel, R. E., Snyder, R. L., Schreiner, C. E., and Leake, P. A. (1995). "Psychophysical and neurophysiological thresholds for electrical stimuli of the cochlea in the deaf cat," *Abst. Assn. Res. Otolaryngol.* **18**, 181.
- Dynes, S. B. C. (1996). "Discharge characteristics of auditory nerve fibers for pulsatile electrical stimuli," Ph.D. thesis, Massachusetts Institute of Technology, Cambridge, MA.
- Eddington, D. K., Dobelle, W. H., Brackmann, D. E., Mladejovsky, M. G., and Parkins, J. L. (1978). "Auditory prosthesis research with multiple channel intracochlear stimulation in man," *Ann. Otol. Rhinol. Laryngol.* (St. Louis) (Suppl. 53) **87**, 1–39.
- Finley, C. C. (1991). "Bipolar electrode placement in scala tympani: Effects on neural potential profiles, longitudinal recruitment and activating function," *Abst. Assn. Res. Otolaryngol.* **14**, 52.
- Finley, C. C., Wilson, B., and White, M. W. (1990). "Models of neural responsiveness to electrical stimulation," in *Models of the Electrically Stimulated Cochlea*, edited by J. M. Miller and F. A. Spelman (Springer-Verlag, New York), pp. 55–96.
- Frijns, J. H. M., Deshoo, S. L., and Schoonhoven, R. (1995). "Potential distributions and neural excitation patterns in a rotationally symmetric model of the electrically stimulated cochlea," *Hearing Res.* **87**, 170–186.
- Girzon, G. (1987). "Investigation of current flow in the inner ear during electrical stimulation of intracochlear electrodes," MS thesis, Massachusetts Institute of Technology, Cambridge, MA.
- Hartmann, R., Topp, G., and Klinke, R. (1984). "Discharge patterns of cat primary auditory fibers with electrical stimulation of the cochlea," *Hearing Res.* **13**, 47–62.
- Leake, P. A., and Hradek, B. T. (1988). "Cochlear pathology of long term neomycin induced deafness in cats," *Hearing Res.* **33**, 11–34.
- Leake, P. A., Vivion, M. C., O'Reilly, B. F., and Merzenich, M. M. (1982). "Deaf animal models for studies of a multichannel cochlear prosthesis," *Hearing Res.* **8**, 225–246.
- Loeb, G. E., Peck, R. A., and Smith, D. W. (1995). "Microminiature molding techniques for cochlear electrode arrays," *J. Neurosci. Methods* **63**, 85–92.
- McNeil, D. R. (1976). "Analysis of a model for excitation of myelinated nerve," *IEEE Trans. Biomed. Eng.* **23**, 329–337.
- Miller, C. A., Abbas, P. J., and Robinson, B. K. (1994). "The use of long-duration current pulses to assess nerve survival," *Hearing Res.* **78**, 11–26.
- Moon, A. K., Zwolan, T. A., and Pflugst, B. E. (1993). "Effects of phase duration on detection of electrical stimulation of the human cochlea," *Hearing Res.* **67**, 166–178.
- Moxon, E. C. (1971). "Neural and mechanical responses to electrical stimulation of the cat's inner ear," Ph.D. thesis, Massachusetts Institute of Technology, Cambridge, MA.
- Parkins, C. W., and Colombo, J. (1987). "Auditory-nerve single-neuron thresholds to electrical stimulation from scala tympani electrodes," *Hearing Res.* **31**, 267–286.
- Pflugst, B. E. (1989). "Physical constraints in biophysical/neural models of threshold," in *Cochlear Implants. Models of the Electrically Stimulated Cochlea*, edited by J. M. Miller and F. A. Spelman (Springer-Verlag, New York), pp. 161–183.
- Pflugst, B. E., and Sutton, D. (1983). "Relation of cochlear implant function to histopathology in monkeys," *Ann. (N.Y.) Acad. Sci.* **405**, 224–239.
- Pflugst, B. E., DeHaan, D. R., and Holloway, L. (1991). "Stimulus features affecting psychophysical detection thresholds for electrical stimulation of the cochlea. I: Phase duration and stimulus duration," *J. Acoust. Soc. Am.* **90**, 1857–1866.
- Pflugst, B. E., Glass, I., Spelman, F. A., and Sutton, D. (1985). "Psychophysical studies of cochlear implants in monkeys: Clinical implications," in *Cochlear Implants*, edited by R. A. Schindler and M. M. Merzenich (Raven, New York), pp. 305–321.
- Pflugst, B. E., Morris, D. J., and Miller, A. L. (1995). "Effects of electrode configuration on threshold functions for electrical stimulation of the cochlea," *Hearing Res.* **85**, 76–84.
- Pflugst, B. E., Sutton, D., Miller, J. M., and Bohne, B. A. (1981). "Relation of psychometric data to histopathology in monkeys with cochlear implants," *Acta Oto-Laryngol.* **92**, 1–13.
- Ranck, J. B. (1975). "Which elements are excited in electrical stimulation of the mammalian central nervous system: A review," *Brain Res.* **98**, 417–440.
- Shannon, R. V. (1983). "Multi-channel electrical stimulation of the auditory nerve in man. I. Basic psychophysics," *Hearing Res.* **11**, 157–189.
- Shannon, R. V. (1989). "Threshold functions for electrical stimulation of the human cochlear nucleus," *Hearing Res.* **40**, 173–177.
- Shepherd, R. K., Hatsushika, S., and Clark, G. M. (1993). "Electrical stimulation of the auditory nerve: The effect of electrode position on neural excitation," *Hearing Res.* **66**, 108–120.
- Smith, D. W., Finley, C. C., van den Honert, C., Olszyk, V. B., and Konrad, K. E. M. (1994). "Behavioral and electrophysiological responses to electrical stimulation in the cat. I. Absolute thresholds," *Hearing Res.* **81**, 1–10.
- Smith, D. W., Watt, S., Konrad, K. E. M., and Olszyk, V. B. (1995). "Behavioral auditory thresholds for sinusoidal electrical stimuli in the cat," *J. Acoust. Soc. Am.* **98**, 211–220.
- Suesserman, M. F., and Spelman, F. A. (1993). "Quantitative *in vivo* measurements of inner ear tissue resistivities. I. *In vitro* characterization," *IEEE Trans. Biomed. Eng.* **40**, 1032–47.
- van den Honert, C. (personal communication).
- van den Honert, C., and Stypulkowski, P. H. (1984). "Physiological properties of the electrically stimulated auditory nerve. II. Single fiber recordings," *Hearing Res.* **14**, 225–243.
- van den Honert, C., and Stypulkowski, P. H. (1987). "Single fiber mapping of spatial excitation patterns in the electrically stimulated auditory nerve," *Hearing Res.* **29**, 195–206.
- Verveen, A. A., and Derksen, H. E. (1968). "Fluctuation phenomena in nerve membrane," *Proc. IEEE* **56**, 906–916.
- White, M. W., Finley, C. C., van den Honert, C., Xue, S., and Smith, D. W. (1994). "Stochastic nerve fiber responses explain a wide range of psychophysical behavior," *Abst. Internatl. Coch. Impl., Speech and Hear. Symp.*, Melbourne, Australia (unpublished).

Model calculations of the effects of wide-band inhibitors in the dorsal cochlear nucleus

Michael C. Reed

Department of Mathematics, Duke University, Durham, North Carolina 27708-0320

Jacob J. Blum

Division of Physiology, Department of Cell Biology, Duke University Medical Center, Durham, North Carolina 27710

(Received 21 October 1996; revised 12 June 1997; accepted 13 June 1997)

In two previous papers [Reed and Blum, *J. Acoust. Soc. Am.* **97**, 425–438 (1995), Blum *et al.*, *J. Acoust. Soc. Am.* **98**, 181–191 (1995)] a computational model for signal processing in the dorsal cochlear nucleus (DCN) was developed. In those modelling studies, stellate cells inhibited only type II cells. In this study, the effect of including wide-band inhibitory (WBI) connections from stellate cells to type IV cells, as proposed by Nelken and Young [*J. Neurophysiol.* **71**, 2446–2462 (1994)], is examined. Inclusion of the WBI connections improves the fit to the experimental pure tone response maps for both the “standard” and “non-standard” cells examined by Spirou and Young [*J. Neurophysiol.* **66**, 1750–1768 (1991)]. Thus, these modelling studies support the hypothesis of Nelken and Young [*J. Neurophysiol.* **71**, 2446–2462 (1994)]. The degree of improvement is greatest for cells with prominent upper inhibitory sidebands. The qualitative features of the pure tone response map and the theoretical model allow one to deduce the probable frequency bias of the type II to type IV and stellate to type IV connections. © 1997 Acoustical Society of America. [S0001-4966(97)02310-2]

PACS numbers: 43.64.Qh, 43.64.Bt, 43.64.Fy [RDF]

INTRODUCTION

In two previous papers (Reed and Blum, 1995; Blum *et al.*, 1995), we developed a computational model for signal processing in the dorsal cochlear nucleus (DCN). The purpose of the model was to investigate the hypotheses put forward by Young and co-workers (Young *et al.*, 1988; Young *et al.*, 1992; Spirou and Young, 1991) to explain the observed responses of type II and type IV units to pure tones and broadband and notch noise. In pure tone studies, the output in spikes/s of type II and type IV units was presented in the form of response maps, i.e., as a family of curves, each corresponding to a different amplitude, giving the response of the particular neuron as a function of tone frequency. Eight examples of such response maps for type IV units, taken from Spirou and Young (1991), are presented below (see the first column of Figs. 3 and 4). The response map of an individual type IV unit is quite complex in that the unit shows varying degrees of excitation and inhibition in different regions of the frequency-amplitude plane. These regions vary markedly from unit to unit, although certain consistent features are usually present. Typically, at best frequency (BF), the units are excited by low amplitude tones (best frequency excitatory region: BFER) but inhibited at higher amplitudes. This region of excitation is sometimes isolated and sometimes connected to large regions of excitation stretching to the upper left (higher amplitude and lower frequencies) or to the upper right (higher amplitude and higher frequencies). Sometimes this upper right excitatory region is flanked on the right by another inhibitory region termed the upper inhibitory sideband (UIS) (see panels A1–A4 of Fig. 3, for

example). In all cases there is a central inhibitory region (CIA) near best frequency at higher amplitudes.

Figure 1(A) shows the connectional scheme proposed by Young *et al.* (1988) to explain the BFER and the CIA. Their idea was that an auditory nerve fiber directly excites the type IV cell [connection b in Fig. 1(A)] and a type II cell (connection a) which inhibits the type IV cell (connection e). The type II cell has a higher threshold than the type IV cell so the type IV cell is initially excited at low sound amplitudes but then inhibited at higher amplitudes by the type II cell. In addition, they proposed other cells (marked by “?”) which strongly inhibit type II cells and weakly inhibit type IV cells in order to account for inhibitory sidebands on type II and type IV units.

Previously, we incorporated these general ideas into a mathematical model so that we could test the effect of various hypotheses about cell properties and connectional patterns on the features of the response maps. We note that we refer to the model type II and type IV cells as T2 and T4 cells, respectively, so that it is always clear whether we are referring to experimental data or model results. The model, described in detail in Reed and Blum (1995), initially contained 40 auditory nerve (AN) fibers, 40 T2 cells, and 40 T4 cells. This model did not account very well for the experimental response maps. However, the inclusion of 40 stellate cells (ST), excited by AN fibers and inhibiting only T2 cells, yielded good semiquantitative fits to the four “standard” and four “non-standard” response maps of Spirou and Young (1991). The ST cells correspond to the cells marked with a “?” in Fig. 1(A). In the model, each AN fiber responds to a pure tone according to a simplified tuning curve whose shape depends on the BF of the fiber. The other cells,

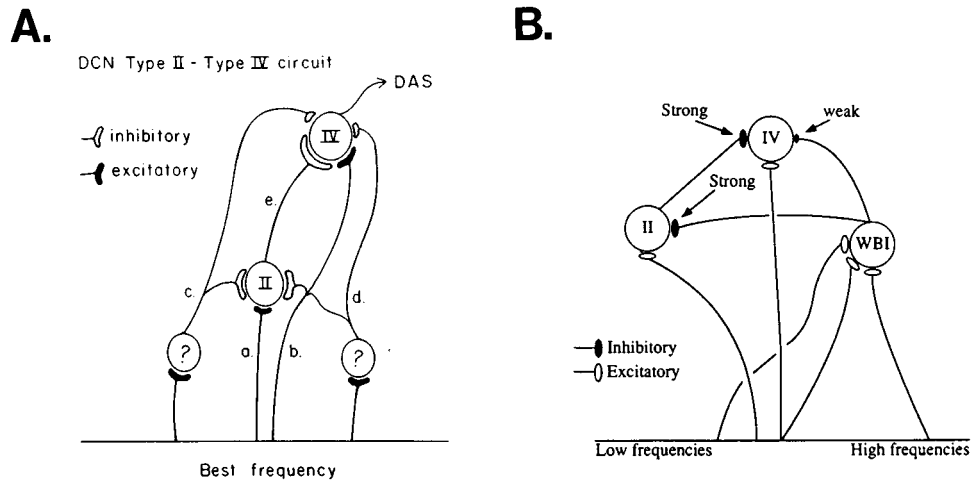


FIG. 1. Panel (A) shows a schematic model of a DCN connective scheme proposed by Young *et al.* (1988). Terminal size indicates the strength of the inhibitory (open areas) or excitatory effect (filled areas). Auditory nerve input is shown arranged (with frequency increasing from left to right) along the basilar membrane. Panel (B) shows the connective scheme proposed more recently by Nelken and Young (1994). Note that the symbols for excitatory and inhibitory connections are opposite to those in Panel (A). The cells labelled “?” in Panel (A) are now called wide-band inhibitors (WBI) as they receive auditory nerve input from a wide frequency band. The other connections are the same except that it is now clearly indicated that the WBI inhibition of type IV cells goes from high to low frequencies and the type II inhibition of type IV cells goes from low to high frequencies. Figures are reproduced with permission.

ST, T2, and T4, have simple input–output relationships that saturate for high excitatory inputs. Although many connective schemes were explored, it was found that three simple variations on the connections between T2 and T4 cells were sufficient to obtain reasonable fits to the data. The three connective schemes used, shown in Fig. 2, are referred to as S5, L3, and R3. In the connective scheme S5, shown in Fig. 2(A), the N th T2 neuron projects to five T4 neurons, $N-2$, $N-1$, N , $N+1$, and $N+2$, with strengths, 0.5, 1, 2, 1, and 0.5, respectively. In the present model, N ranges from 1

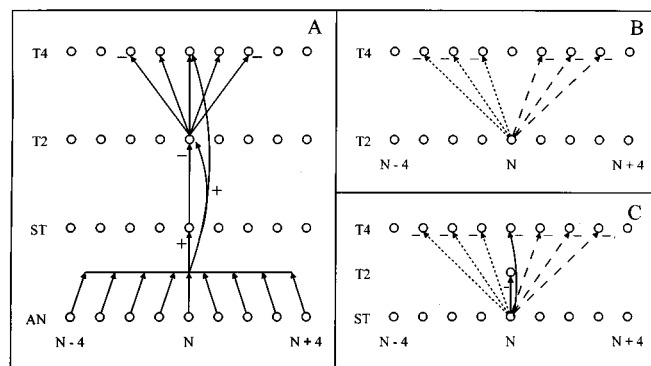


FIG. 2. Panel (A) shows one of the standard connective schemes used in Reed and Blum (1995). The N th T2 cell makes five connections to the T4 cells numbered $N-2$, $N-1$, N , $N+1$, $N+2$, with connective strengths 0.5, 1, 2, 1, and 0.5, respectively. Panel (B) shows two other connective patterns from T2 to T4 cells, three to the left (dotted lines) and three to the right (dashed lines), which are used in some simulations. The strength of each connection is 1.66 so the total inhibition produced by each T2 cell is the same (namely 5) for each of the three T2–T4 connective patterns. Panel (C) shows three stellate connective patterns used in this study. In each of these schemes, the stellate cell inhibits the T2 cell at the same BF. In the “straight-up” pattern the N th stellate cell inhibits the T4 cell at the same BF (solid line). The other two patterns are referred to as three to the left (dotted lines) and three to the right (dashed lines). Strengths of these connections are indicated in the discussions of each individual simulation.

to 40, the higher values of N corresponding to higher frequencies. End effects are handled by ignoring hypothetical inputs from and outputs to neurons to the left and to the right of each row of 40 neurons in the model. These end effects do not affect any of the results shown for T2 or T4 neurons in this paper. In schemes R3 and L3 each T2 neuron projects three to the right (R3) or left (L3) with strength 1.66. This is shown in the dashed and dotted lines of Fig. 2(B). The strength is chosen so that the total inhibitory strength delivered to the T4 cells by each T2 cell is the same in each of the three schemes, namely the T2 output in spikes/s multiplied by 5. The actual connective schemes repeat these patterns uniformly along the frequency axis. We remark that the shapes of the AN tuning curves vary systematically with increasing BF as shown in Figure 3 of Reed and Blum (1995). This variation results in appreciably different response maps for T4 neurons with different BFs even though the connective pattern and cell parameters are uniform across the frequency axis [compare, for example, Figs. 3(B3), 3(B4), and 4(B4)]. Using only these three connective schemes and by choosing T4 neurons with different BFs, we obtained the variety of model response maps shown in the second columns of Figs. 3 and 4. In one case [Fig. 4(B3)] the strength of the T2 to T4 connections was reduced. All other connections and cell properties were held constant.

Although the model response maps obtained in Reed and Blum (1995) captured most of the major qualitative features of the variety of experimental response maps, there was one notable inadequacy. None of the model response maps had the upper inhibitory sideband which is clearly present in some experimental response maps [for example, see Figs. 3(A1), 3(A3), 3(A4), and 4(A2)]. At the time, the source and properties of additional inhibitory inputs was uncertain, so we did not pursue this matter further. Since then, however,

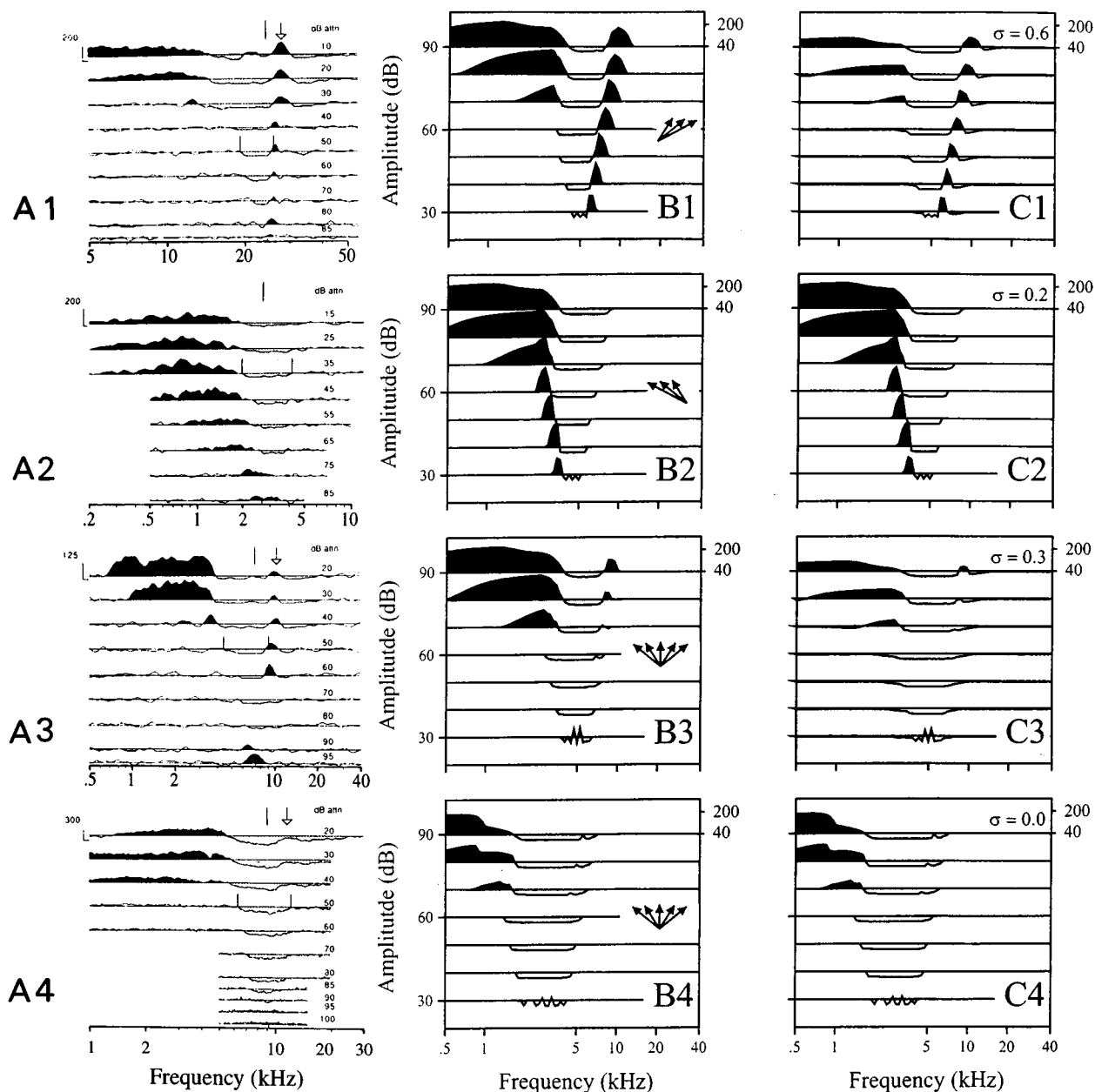


FIG. 3. Panels (A1)–(A4) reproduce the response maps of four “standard” type IV cells from Figure 2 of Spirou and Young (1991). Panels (B1)–(B4) reproduce the simulations from Reed and Blum (1995) that most closely matched the corresponding experimental maps; the insets in column B show schematically the T2–T4 connective pattern used. In those simulations there were no inhibitory connections between the ST and T4 cells. Panels (C1)–(C4) show the identical simulations (all parameters and connections are the same as in the corresponding simulations in column B) except that a single straight-up connection from the ST cells to the T4 cells has been added. In each panel the strength, σ , of the ST to T4 connection is indicated.

Nelken and Young (1994) have performed experiments using more complex sound inputs. They point out that several lines of evidence suggest that the additional inhibition on type IV cells is not caused by type II cells, and they suggest that it arises from direct weak connections from the stellate cells to the type IV cells, as shown in Fig. 1. Recent studies by Winter and Palmer (1995) on the guinea pig cochlear nucleus show that glycinergic stellate cells in the ventral cochlear nucleus (VCN), which are known to project to the DCN (Oertel *et al.*, 1990), have onset firing properties consistent with their being the wide-band inhibitory neurons postulated by Nelken and Young (1994). For our modeling studies, it

does not matter whether the wide-band inhibitory neurons arise within the DCN, in the VCN, or in both nuclei. It was therefore of considerable interest to ascertain whether the inclusion of weak direct connections from the ST cells to the T4 cells in the model would significantly improve the model response maps. Nelken and Young refer to the stellate cells as wide-band inhibitors (WBI) because they appear to receive auditory nerve input from a wide frequency band. Note that this was already included in our original model (see Fig. 2). In this paper we focus primarily on the effect of the WBI on the response maps to pure tones. In a subsequent paper we study the responses to more complex sound inputs.

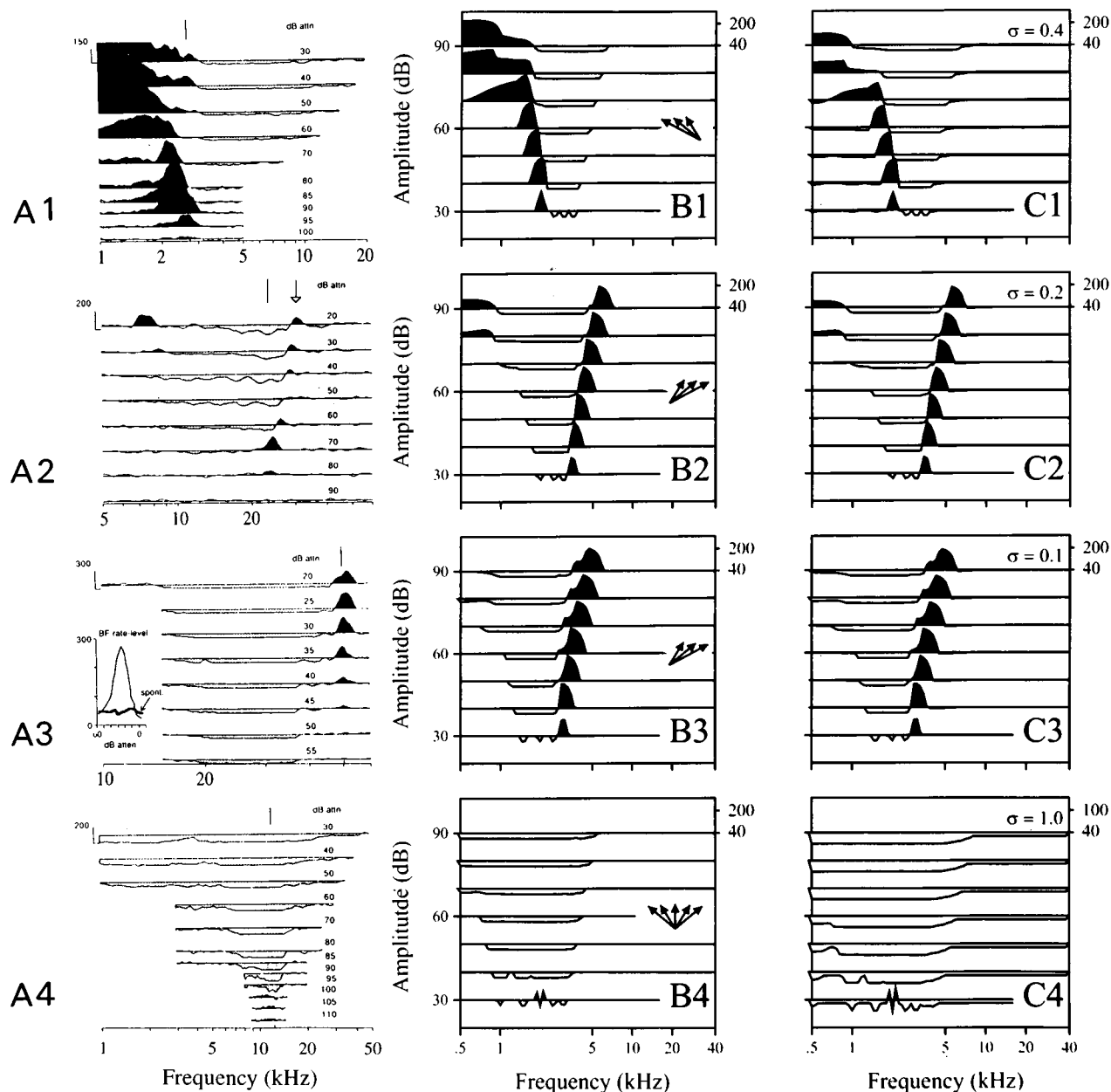


FIG. 4. Panels (A1)–(A4) reproduce the response maps of four “non-standard” type IV cells from Figure 2 of Spirou and Young (1991). Panels (B1)–(B4) reproduce the simulations from Reed and Blum (1995) that most closely matched the corresponding experimental maps; the insets in column B show schematically the T2–T4 connective pattern used. In those simulations there were no inhibitory connections between the ST and T4 cells. Panels (C1)–(C4) show the identical simulations (all parameters and connections are the same as in the corresponding simulations in column B) except that an additional straight-up connection from the ST cells to the T4 cells has been added. In each panel the strength, σ , of the ST to T4 connection is indicated.

I. RESULTS

In order to study the effect of the WBI on response maps, we initially chose the simplest possible connections from the ST to the T4 cells, namely, each ST cell makes a single connection to the T4 cell with the same BF, as shown by the single solid line from ST to T4 in Fig. 2(C). For clarity in the diagram the direct connection from AN to T4 and all the connections to and from the T2 cells have been omitted. The connections from the AN cells are as in Fig. 2(A). The connections from the T2 to T4 cells are one of the three patterns S5, R3, and L3 shown in Fig. 2(A) and (B) and indicated by insets in the B columns of Figs. 3 and 4. The results of these simulations are shown in Figs. 3 and 4. Panels (A1)–(A4) Fig. 3 show the “standard” response maps of type IV units obtained by Spirou and Young (1991). Panels (B1)–(B4) show the corresponding model response maps obtained in our earlier study (Reed and Blum, 1995). Panels (C1)–(C4) show the results of simulations with all connections and parameters the same as the simulations in Panels (B1)–(B4) except that a single “straight-up” WBI connection from the N th ST neuron to the N th T4 neuron has been added. The spikes/s carried by this connection is the ST cell output in spikes/s multiplied by σ , whose value is as indicated in each panel. Note that the maximum value of σ used was 0.6. By comparison, the strength of the T2 to T4 connection is 5. Thus, the inhibition provided by the WBI is

els (A1)–(A4) Fig. 3 show the “standard” response maps of type IV units obtained by Spirou and Young (1991). Panels (B1)–(B4) show the corresponding model response maps obtained in our earlier study (Reed and Blum, 1995). Panels (C1)–(C4) show the results of simulations with all connections and parameters the same as the simulations in Panels (B1)–(B4) except that a single “straight-up” WBI connection from the N th ST neuron to the N th T4 neuron has been added. The spikes/s carried by this connection is the ST cell output in spikes/s multiplied by σ , whose value is as indicated in each panel. Note that the maximum value of σ used was 0.6. By comparison, the strength of the T2 to T4 connection is 5. Thus, the inhibition provided by the WBI is

indeed weak compared to the inhibition provided by the T2 cells. In each case, the value of σ is the value which yielded a model response map most similar (by visual inspection) to the corresponding experimental map. Figure 4 is in the same format for the four “non-standard” type IV units of Spirou and Young (1991).

Panel C1 of Fig. 3 shows that by adding the WBI with strength $\sigma=0.6$ one obtains a strong UIS. Furthermore, the excitatory output in both the left and right excitatory regions is diminished and thus the model response map resembles more closely the experimental response map. In panel (C2) the strength of σ is 0.2. This produces almost no improvement in the response map except for slight widening of the CIA which is barely visible, consistent with absence of a UIS for this type IV unit. The experimental response map (A3) is quite similar to (A1) and, as in that case, the addition of the WBI produces a well-defined UIS and a widening of the CIA on the left and a decrease in the magnitude of excitation. The experimental response map of (A4) is somewhat similar to that of (A2) since it contains no upper right excitatory region, though it does have a suggestion of one as indicated by the decreased inhibition below the open arrowhead. As is the case of (A2), the inclusion of the WBI makes only a very slight improvement.

Comparing panels (B1) and (C1) of Fig. 4, one can see that the addition of the WBI widens the CIA appreciably, thus improving the fit to the experimental data shown in panel (A1). There is no UIS since there is no upper right excitatory region. Panel (A2) shows an experimental response map which has a long upper right excitatory region and a small UIS at high amplitudes as well as a very small upper left excitatory area. Inclusion of the WBI [panel (C2)] resulted in a significant reduction [compared to panel (B2)] in the spike output in the upper left excitatory area and added a small UIS, thus significantly improving the fit. The addition of the WBI in panel (C3) makes almost no improvement of panel (B3). Inclusion of the WBI makes a marked improvement of panel (C4) over panel (B4). The CIA is much wider, as in the experimental data shown in panel (A4).

In the above discussion we have repeatedly said that adding the wide-band inhibitor with a specific value of σ improved the fit. Since the response map contains a large amount of complex data, it was of interest to check whether our qualitative visual estimate of the best value of σ could be substantiated by a more detailed statistical analysis. Although the original numerical data for column A in Figs. 3 and 4 are no longer available, we reconstructed the data by scanning the original figures kindly provided to us by Dr. E. Young. We decided to focus on Fig. A1 which has a large value of the visually estimated σ . Figure 5 shows the mean square deviation of our model predictions from the experimental data for different values of σ , the strength of the connection between the wide-band inhibitor and the corresponding T4 cell. As can be seen, the fit improves markedly as σ increases from 0. The best fit occurs for values near $\sigma = 0.6$ or 0.7 , thus validating our visual estimate. As σ is increased still further, the fit becomes much worse.

We have seen that the addition of the single straight-up WBI connection improves each of the earlier model response

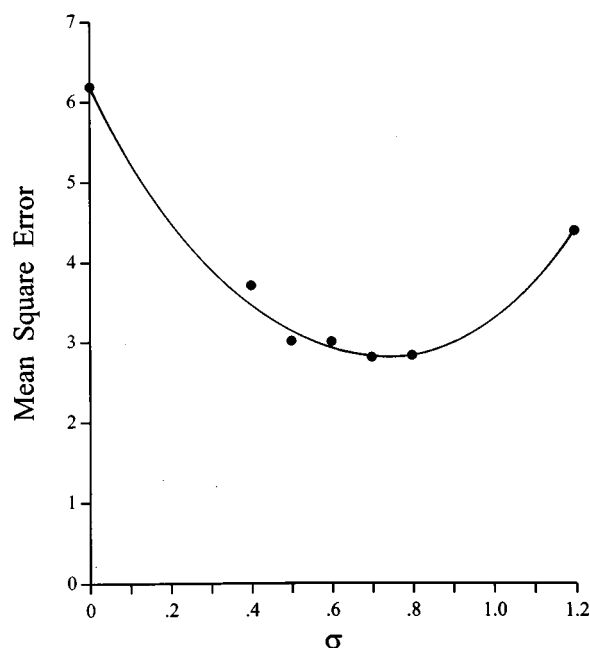


FIG. 5. The points on the graph show the mean-square difference between our model predictions and the experimental data in panel (A1) of Fig. 3 for different values of the strength of the wide-band inhibitory connections (ST to T4).

maps [panels (B1)–(B4) of Figs. 3 and 4], although in some cases the improvement is slight. Since the direction of the T2 to T4 connections had a strong effect on model response maps and since Nelken and Young (1994) suggest that the ST to T4 connections go from higher to lower frequencies, we next examined the effect of ST to T4 connectational patterns that are biased to the right or the left. Figure 6(A) shows the effect of changing the ST to T4 connections from a single straight-up connection to three connections biased to the right (i.e., towards higher frequencies), i.e., as shown by the dashed lines in Fig. 2(C). The strength of each of the three connections is one-third that of the single straight-up connection so that the total inhibition delivered by the stellate cells is unchanged. The three to the right connection decreases the size of the UIS and extends the CIA to the left as compared to panel (C1) of Fig. 3. If, instead, the three connections are biased to the left [i.e., towards lower fre-

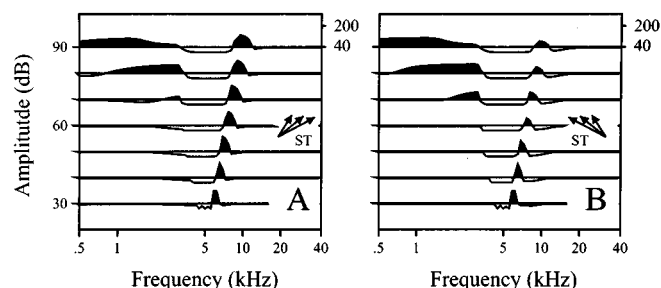


FIG. 6. Panel (A) shows the response map obtained by keeping all parameters and connections the same as in Fig. 3(C1) except that the ST to T4 connections are three to the right (each with strength 0.2) instead of a single connection straight up (with strength 0.6); see Fig. 2(C). Panel (B) is the same except that the ST to T4 connections are three to the left instead of three to the right.

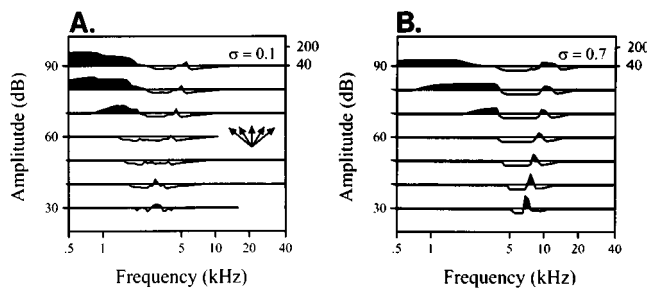


FIG. 7. Panel (A) shows a model response map where the WBI connections from the ST cells to the T4 cells are three to the left as shown by the dotted lines in Fig. 2C with the strength $\sigma = 0.1$ for each connection. The T2 to T4 connections are straight up as shown in Fig. 2(A) and in the inset to this panel. Panel (B) shows a model response map where each WBI connection goes from the $N + 2$ ST cell to the N th T4 cell with the strength $\sigma = 0.7$. The T2 to T4 connections are three to the right as shown by the dashed lines in Fig. 2(B).

quencies, as shown by the dotted lines in Fig. 2(C)], then the UIS is made larger and there is less inhibition on the left of the CIA [Fig. 6(B)]. Comparing Fig. 6(A) and (B) with the experimental data in Fig. 3(A1), we see that biasing to the right makes the fit worse and biasing to the left makes the fit better than using a single straight-up connection. Our modeling results, therefore, support the hypothesis of Nelken and Young (1994) that the ST to T4 connections are biased from higher to lower frequencies. Simulations of left and right bias of the ST to T4 connections in the other cases are not shown because they produce similar effects, i.e., right bias extends the CIA to the left and weakens the UIS, and vice versa for left bias. We have also experimented with greater divergence (for example, five or ten ST to T4 connections) and found no major differences from the above conclusions.

Closer examination of Fig. 6(B) shows that at intermediate sound amplitudes both the width and height of the upper right excitatory response decrease before increasing again at higher sound amplitudes. Note that this is a property of the right upper excitatory band in three of the experimental maps shown, namely, Figs. 3(A1), 3(A3), and 4(A2). This behavior was never seen in any of our previous simulations, so it was decided to investigate this further. Figure 7(A) shows a simulation in which the T2 to T4 connections are straight-up, as shown in Fig. 2(B), but weaker, and the ST to T4 connections are biased three to the left with $\sigma = 0.1$, i.e., total inhibitory strength 0.3. We show the response map of T4 neuron #6. Figure 7(A) matches the experimental data in Fig. 3(A3) in all essential features; in particular, there is a 20-dB gap between the BFER and the upper right excitatory region. Note the successive improvement from Fig. 3, panel (B3), to Fig. 3, panel (C3), to Fig. 7(A). In addition, we tried a simple scheme in which the $N + 2$ stellate cell is connected to the N th T4 cell, consistent with Nelken and Young's suggestion that the stellate to type IV connections go from high to low frequency. The resulting response map is shown in Fig. 7(B). It closely resembles the experimental response map in Figure 2b taken from Young *et al.* (1992). Notice that we have not changed any of the many parameters in the system, but merely changed the direction and strength of the single ST to T4 connection.

II. DISCUSSION

In our previous study (Reed and Blum, 1995) in which there were no inhibitory connections from ST to T4 cells, we were able to obtain model response maps that were qualitatively similar to those obtained experimentally. The only major deficiency was the lack of an upper inhibitory sideband. Inclusion of such connections, as suggested by Nelken and Young, not only produces model response maps with inhibitory sidebands, but also affects the width and strength of the upper and lower excitatory regions in a way that was not possible before. For example, without the ST to T4 connections we never observed the decrease in spike output in the upper excitatory region at intermediate sound amplitudes as shown in Figs. 6(B) and 7. Thus, these model calculations lend strong support to the existence of a wide-band inhibitor as proposed by Nelken and Young (1994).

Nelken and Young (1994) also proposed that the ST to T4 connections go from higher frequencies to lower frequencies. We have found that the direction of the ST to T4 connections has only mild effects on response maps, for example, increasing or decreasing the width of the UIS and CIA. In several cases, however, the choice of high to low frequency connections significantly improved the fit to the experimental maps (see the discussion of Figs. 6 and 7), thus supporting Nelken and Young's suggestion. The effect of the ST to T4 connectional pattern on the responses to more complex sounds than pure tones is presently under investigation.

In contrast to the WBI connections, the T2 to T4 connectional pattern has more dramatic effects on the response maps. As shown by Figs. 3 and 4, T2–T4 connections biased to the right produce a response map with a continuous upper excitatory band [see Figs. 3(C1), 4(C2), and 4(C3)], whereas T2–T4 connections biased to the left produce a response map with a continuous, strong, lower excitatory band [see Figs. 3(C2) and 4(C1)]. Straight-up spreading connections, such as those in Figs. 3(C3), 3(C4), and 4(C4), produce maps with isolated best frequency response areas. These modeling studies, therefore, allow one to examine a response map of a type IV unit and to hypothesize with some confidence the direction of the type II to type IV connectional pattern for that particular type IV unit. Furthermore, depending on the strength and width of the UIS, one can predict (with less certainty) the strength and direction of the ST to T4 connections. Thus, reasonable predictions of the anatomy of the incoming projections can be made based on the response of the type IV unit to pure tones.

Recently Voigt and Davis (1996) and Davis and Voigt (1996) have examined a model isofrequency sheet in the DCN containing a relatively small number of cells. They were able to obtain reasonable fits to experimentally observed cross-correlograms and post stimulus time histograms. Their work is complementary to ours in that it focused on connectional properties and time-averaged temporal behavior within a single isofrequency sheet whereas ours focuses on steady-state behavior and the connections between isofrequency sheets. Thus both projects do not deal with the detailed time course of cell firing (pauses, buildup, chopper, etc.) or response latency (e.g., Godfrey *et al.*, 1975; Kitzes *et al.*, 1978; Kim *et al.*, 1994; Manis,

1990; Waller and Godfrey, 1994; and Feng *et al.*, 1994). The fact that good fits to the data can be obtained in both modeling projects with relatively few cells raises an interesting and important question. The typical size of the DCN of the cat is of the order of 2 mm by 2 mm by 1 mm, i.e., $4 \times 10^9 \mu\text{m}^3$. The size of the most common cells (stellates) is of the order of 5–10 μm in diameter. Choosing the larger diameter yields a cell volume of $10^3 \mu\text{m}^3$. Thus there are of the order of 4×10^6 cells in the DCN. Even if one assumes a much larger cell size to account for the volume occupied by the neuropil, it is clear that there is at least one order of magnitude more cells in the DCN than the 120 cells required for satisfactory qualitative fit to the steady-state tonal response maps. The question is why is it necessary to have so many cells present. The most likely answer is that these cells are involved in temporal processing of complex time-varying auditory inputs as well as somato-sensory inputs (Young *et al.*, 1995).

ACKNOWLEDGMENTS

This research was supported by NSF Grant No. DMS9501404. The authors are grateful to John Davies for the preparation of software and figures and to Dr. E. Young for providing us with response map data.

- Blum, J. J., Reed, M., and Davies, J. M. (1995). "A computational model for signal processing by the dorsal cochlear nucleus. II. Responses to broadband and notch noise," *J. Acoust. Soc. Am.* **98**, 181–191.
- Davis, K. A., and Voigt, H. F. (1996). "Computer simulation of shared input among projection neurons in the dorsal cochlear nucleus," *Biol. Cybern.* **74**, 413–425.
- Feng, J. J., Kuwada, S., Ostpoff, E.-M., Batra, R., and Morest, D. K. (1994). "A physiological and structural study of neuron types in the cochlear nucleus I, intracellular responses to acoustic stimulation and current injection," *J. Comp. Neurol.* **346**, 1–18.
- Godfrey, D. A., Kiang, N. Y. S., and Norris, B. E. (1975). "Single unit

- activity in the dorsal cochlear nucleus of the cat," *J. Comp. Neurol.* **162**, 269–284.
- Kim, D. O., Ghoshal, S., Khant, S. L., and Parham, K. (1994). "A computational model with ionic conductances for the fusiform cell of the dorsal cochlear nucleus," *J. Acoust. Soc. Am.* **96**, 1501–1514.
- Kitzes, L. M., Gibson, M. M., Rose, J. E., and Hind, J. E. (1978). "Initial discharge latency and threshold considerations for some neurons in cochlear nuclear complex of the cat," *J. Neurophysiol.* **41**, 1165–1181.
- Manis, P. B. (1990). "Membrane properties and discharge characteristics of guinea pig dorsal cochlear nucleus neurons studied *in vitro*," *J. Neurosci.* **10**, 2338–2351.
- Nelken, I., and Young, E. D. (1994). "Two separate inhibitory mechanisms shape the responses of dorsal cochlear nucleus Type IV units to narrow-band and wideband stimuli," *J. Neurophysiol.* **71**, 2446–2462.
- Oertel, D., Wu, S. H., Garb, M. W., and Dizack, C. (1990). "Morphology and Physiology of cells in slice preparations of the posteral ventral cochlear nucleus of mice," *J. Comp. Neurol.* **295**, 136–154.
- Reed, M. C., and Blum, J. J. (1995). "A computational model for signal processing by the dorsal cochlear nucleus. I. Response to pure tones," *J. Acoust. Soc. Am.* **97**, 425–438.
- Spirou, G., and Young, E. D. (1991). "Organization of dorsal cochlear nucleus type IV unit response maps and their relationship to activation by bandlimited noise," *J. Neurophysiol.* **66**, 1750–1768.
- Voigt, H. F., and Davis, K. A. (1996). "Computation of neural correlations in dorsal cochlear nucleus," in *Advances in Speech, Hearing, and Language Processing* (JAI, London), Vol. 3, pp. 359–382.
- Waller, H. J., and Godfrey, D. A. (1994). "Functional characteristics of spontaneously active neurons in rat dorsal cochlear nucleus *in vitro*," *J. Neurophysiol.* **71**, 467–478.
- Winter, I. M., and Palmer, A. R., (1995). "Level dependence of cochlear nucleus onset unit responses and facilitation by second tones or broadband noise," *J. Neurophysiol.* **73**, 141–159.
- Young, E. D., Nelken, I., and Conley, R. A. (1995). "Somatosensory effects on neurons in dorsal cochlear nucleus," *J. Neurophysiol.* **73**, 743–765.
- Young, E. D., Spirou, G. A., Rice, J. J., and Voigt, H. F. (1992). "Neural organization and responses to complex stimuli in the dorsal cochlear nucleus," *Philos. Trans. R. Soc. London, Ser. B* **336**, 407–419.
- Young, E. D., Shofner, W., White, J., Robert, J.-M., and Voigt, H. F. (1988). "Response properties of cochlear nucleus neurons in relationship to physiological mechanisms," in *Auditory Function: Neurological Bases of Hearing*, edited by G. Edelman, W. E. Gall, and W. M. Cowan (Wiley, New York), pp. 277–312.

Two-tone rate suppression boundaries of cochlear ganglion neurons in chickens following acoustic trauma

Lin Chen, Patricia G. Trautwein, Nicholas Powers, and Richard J. Salvi^{a)}

Hearing Research Laboratories, 215 Parker Hall, Department of Communicative Disorders and Sciences,
State University of New York at Buffalo, Buffalo, New York 14214

(Received 17 September 1996; revised 21 March 1997; accepted 13 May 1997)

The purpose of the present study was to examine the effects of acoustic trauma and hair cell loss and regeneration on the two-tone rate suppression (TTRS) boundaries of cochlear ganglion neurons in chickens. Chickens were exposed for 48 hours to a 525-Hz, 120-dB SPL tone which destroyed the hair cells and tectorial membrane in a crescent-shaped patch along the abneural side of the basilar papilla. Afterwards, TTRS boundaries were recorded from cochlear ganglion neurons at 0–1, 5, 14, and 28 days postexposure. Acoustic trauma reduced the percentage of neurons with TTRS boundaries below CF (TTRSB) (52.6% to 8.2%) and above CF (TTRSA) (88.4% to 46.6%). In addition, the exposure reduced TTRS boundary slopes, elevated best suppression threshold (BST), and increased the frequency separation between the tips of the TTRS boundaries and CF. All the TTRS measures started to recover by 5 days postexposure and by 14 days and 28 days postexposure, most measures had recovered to normal levels. However, the BST, TTRS slopes, and the frequency separation of TTRSB boundaries from CF were still slightly abnormal near the exposure frequency. In addition, the percentage of neurons with TTRS below CF was reduced significantly. The partial recovery of TTRS boundaries is presumably due to the regeneration of hair cells and the lower honeycomb layer of the tectorial membrane. The residual TTRS deficits observed 28 days postexposure were most closely associated with the missing upper fibrous layer of the tectorial membrane. © 1997 Acoustical Society of America. [S0001-4966(97)02210-8]

PACS numbers: 43.64.Wn, 43.64.Pg, 43.64.Nf, 43.64.Ri [RDF]

INTRODUCTION

As in mammals, the cochlear sensory cells and supporting structures in birds are susceptible to acoustic overstimulation (Saunders and Tilney, 1982; Cotanche *et al.*, 1987; Raphael, 1991). High-level pure tone exposures (115–125 dB SPL) typically destroy hair cells in a crescent-shaped patch along the abneural edge of the basilar papilla (Ryals and Rubel, 1982; Cotanche *et al.*, 1987; Raphael, 1991), a region occupied primarily by short hair cells (SHCs) (Tanaka and Smith, 1978). The sensory cells along the neural edge of the papilla, mainly tall hair cells (THCs), often survive acoustic trauma (Cotanche *et al.*, 1987; Raphael, 1991). Even extremely aggressive exposures (140–150 dB SPL) may not completely destroy THCs on the neural side of the basilar papilla (personal observations). Acoustic overstimulation also destroys the tectorial membrane in a crescent-shaped region along the abneural edge of the basilar papilla, but the damaged region is much broader than the region of hair cell loss (Cotanche, 1987b; Raphael, 1991; Saunders and Salvi, 1995; Saunders *et al.*, 1995; Trautwein *et al.*, 1996). Unlike mammals, most of the damaged structures in the avian cochlea regenerate within a few weeks (Cotanche, 1987a; Corwin and Cotanche, 1988; Ryals and Rubel, 1988). The missing hair cells along the abneural edge of the papilla regenerate and the lower honeycomb layer of the tectorial membrane reforms and reestablishes contact with the stereocilia bundle on newly formed hair cells (Cotanche, 1987b).

However, the upper fibrous layer of the tectorial membrane fails to regenerate (Cotanche, 1987b; Raphael, 1991; Saunders *et al.*, 1995).

Recent studies have provided some insights into the functional recovery of the auditory system that occurs when the hair cells regenerate after acoustic overstimulation. (McFadden and Saunders, 1989; Poje *et al.*, 1995; Saunders and Salvi, 1995; Chen *et al.*, 1996b; Saunders *et al.*, 1996a, 1996b; Trautwein *et al.*, 1996). When most of the hair cells regenerate, the avian auditory system appears to recover almost completely, when assessed using evoked potential, single unit, or behavioral tests (McFadden and Saunders, 1989; Cohen and Saunders, 1993; Saunders and Salvi, 1995; Chen *et al.*, 1996c). The only exception is that some neurons near the exposure frequency have discharge rate-level functions with abnormally steep slopes and higher than normal saturation discharge rates (Saunders *et al.*, 1996a). On the other hand, when auditory function is assessed with distortion product otoacoustic emissions (DPOAE), there appears to be little or no recovery near the exposure frequency (Froyovich *et al.*, 1995; Trautwein *et al.*, 1996). These results suggest that the cochlear nonlinearities may be especially sensitive to cochlear pathology and may not fully recover when the hair cells and tectorial membrane regenerate.

One cochlear nonlinearity which may be especially sensitive to acoustic trauma is two-tone rate suppression (TTRS) seen in cochlear nerve fibers. In mammals, TTRS has been shown to be vulnerable to cochlear pathologies induced by noise exposure (Schmiedt *et al.*, 1980; Salvi *et al.*, 1982; Schmiedt and Schulte, 1992). In fact, TTRS can be compro-

^{a)}Electronic mail: salvi@acsu.buffalo.edu

mised without significant alteration of threshold and frequency selectivity (Robertson and Johnstone, 1981). The loss of TTRS is irreversible in mammals since the hair cell lesions are permanent. Given the results from mammals, one would expect that hair cell loss in birds would result in the loss of TTRS. On the other hand, since the hair cells regenerate in birds (Cotanche, 1987a, 1987b; Corwin and Cotanche, 1988; Ryals and Rubel, 1988; Hashino and Salvi, 1993), it is conceivable that TTRS might recover. However, if the tectorial membrane affects the cochlear nonlinearities, then TTRS might not completely recover due to the absence of the upper layer of the tectorial membrane. The purpose of the present study was to determine the degree to which TTRS in chicken cochlear ganglion neurons was impaired following acoustic trauma and to determine the degree to which TTRS recovered when the hair cells and lower honeycomb layer of the tectorial membrane regenerated.

In a previous paper (Chen *et al.*, 1996a), we described in detail the characteristics of TTRS boundaries in normal adult chickens. In the present study, a group of chickens of the same age were exposed to a traumatizing tone that damaged the hair cells in a crescent patch along the basilar papilla (Saunders and Salvi, 1995; Saunders *et al.*, 1995; Chen *et al.*, 1996b; Trautwein *et al.*, 1996). Afterwards, TTRS boundaries were measured from cochlear ganglion neurons at 0–1, 5, 14, and 28 days postexposure. The data from the sound-exposed animals were then compared to data from normal controls (Chen *et al.*, 1996a).

I. METHOD

A. Subjects and surgical procedures

Twenty-one adult, white leghorn chickens (*Gallus domesticus*, 12–15 weeks old, 1000–1300 g) were exposed to a 525-Hz, 120-dB-SPL pure tone for 48 h. The TTRS boundaries were recorded from a total of 350 cochlear ganglion neurons at 0–1, 5, 14, and 28 days after the termination of exposure. The TTRS boundaries measured from normal animals (20 subjects) in a previous study (Chen *et al.*, 1996a) were used as control data.

The surgical procedures used to record from single cochlear ganglion neurons were exactly the same as those described in a previous paper (Chen *et al.*, 1996a). Chickens were anesthetized with urethane (5.7 ml/kg, 25%, i.m.) and additional anesthetic was given as needed to maintain an areflexive state. Body temperature was maintained at 41 °C using a heating pad coupled to a thermosensor inserted into the pectoralis muscle. The animal was tracheotomized and unilaterally ventilated (1.3–1.8 l/min) with humidified air after making a hole in an abdominal air sac. Spontaneous respiration ceased during unilateral ventilation (Schwartzkopff and Bremond, 1963), thereby reducing body movement and brain pulsation.

The skin and muscle on the dorsal surface of the skull were removed and a metal bar was glued to the skull with cyanoacrylic glue and dental cement. The bar was mounted to a clamp on a magnetic base to stabilize the animal's head during the recordings. The porous bone covering the posterolateral surface of the skull was carefully removed with for-

ceps until the round window was clearly visualized. A silver ball electrode was placed on the round window to record the compound action potential (CAP) which was used to monitor the physiological condition of the cochlea. A small opening, about 1 mm in diameter, was made in scala tympani in the basal region of the cochlea. The cochlear ganglion appeared as a thin, white strip deep within recessus scala tympani. Bird Ringer's solution (0.85 g NaCl, 0.042 g KCl, 0.025 g CaCl₂, to 100 ml H₂O) was injected subcutaneously at intervals of 1–2 h to compensate for fluid loss during the experiment.

Procedures for the use and care of animals in this research were approved by the Institutional Animal Care and Use Committee of State University of New York at Buffalo.

B. TTRS boundary tracking procedure

Action potentials were recorded from single cochlear ganglion neurons with a glass micropipette (4 M potassium acetate, 40–60 MΩ). The pipette was directed toward the cochlear ganglion with a manual micromanipulator and advanced remotely with a Trent Wells microdrive. The output of the electrode was directed to an amplifier (Dagan Cell Explorer, 10×, 3-kHz low-pass filter), audio monitor (Grass AM-8, variable gain, 100–3000-Hz bandpass) and then in parallel to an oscilloscope and the A/D converter on a signal processing board (Loughborough Sound Images, TMS25) in a personal computer. Spike discharges were displayed on the computer monitor and discriminated in software when the amplitude of the spike exceeded the trigger level. Spike arrival times were stored with a resolution of 20 μs.

The stimuli for measuring TTRS were synthesized digitally (100-kHz sampling rate, 16-bit D/A converter) with two signal processing boards (Loughborough Sound Images, TMS25) located in a personal computer. The output from each signal processing board was low-pass filtered at 20 kHz (90 dB roll off from 20 to 24 kHz), and then directed to a computer-controlled attenuator, current amplifier, and sound source (Etymotic ER2) coupled to a brass earpiece which was inserted into the external ear canal. The acoustic stimuli from each channel were calibrated from 100–20 143 Hz (32 points/octave) with a probe tube microphone (Etymotics ER-7C) located 1–2 mm in front of the tympanic membrane. The calibration data were stored on the disk of the computer and used later to adjust the attenuator to obtain the desired SPL.

Our procedure for measuring the tuning curves has been described in detail in several recent reports (Salvi *et al.*, 1992, 1994; Chen *et al.*, 1996a, 1996c). The paradigm used to measure the lower boundaries of the TTRS suppression areas (Holton, 1980; Schmiedt, 1982a; Prijs, 1989; Delgutte, 1990; Chen *et al.*, 1996a) is illustrated in Fig. 1(a). A continuous tone (excitatory tone) was presented 20 dB above the threshold at CF [Fig. 1(a), filled circle] in order to produce a moderate discharge rate. A suppressing tone (50-ms duration, 1-ms rise/fall time, raised cosine gating) was then presented at a frequency well above characteristic frequency (CF) to begin tracking the TTRS boundary above CF (TTRS_a boundary). The suppressing tone was initially presented at a level equal to the threshold at CF and the threshold for TTRS was determined with the following tracking

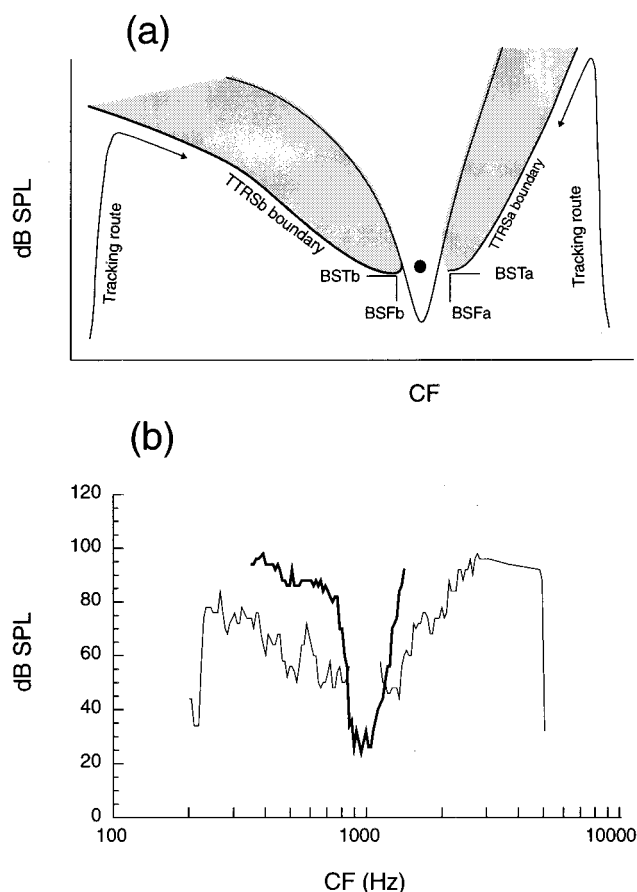


FIG. 1. (a) Schematic showing the tracking procedure for TTRS boundaries. TTRSb: two-tone suppression below CF; TTRSa: two-tone suppression above CF; BSTb: best suppression threshold of TTRSb; BSTa: best suppression threshold of TTRSa; BSFb: best suppression frequency of TTRSb; BSFa: best suppression frequency of TTRSa; (b) Example of TTRS boundaries (thin lines) and a tuning curve (thick line) recorded from a normal chicken.

rule. The computer compared the spike count during the two-tone interval (excitatory tone and suppressing tone) and the one-tone interval (excitatory tone only). If the spike count during the two-tone interval was equal to or greater than that in the single-tone interval, then the level of the suppressing tone was increased by 2 dB. The level of the suppressing tone continued to be increased in 2-dB steps until the spike count during the two-tone interval was less than that in the single-tone interval. That is, the level of the suppressing tone was increased until it was above the suppression threshold. At this point, the level of the suppressing tone was decreased (a reversal) two steps (4 dB) so that the level of the suppressing tone would presumably be below the suppression threshold. The spike counts in the two intervals were again compared and the level of the suppressing tone was increased or decreased by 2 dB according to the rules presented above. In order to achieve threshold at a given frequency, two reversals in a row were required at the same level. After threshold was determined at one frequency, the frequency was decreased by $\frac{1}{32}$ of an octave and testing began again. This procedure continued until the test frequency equaled CF. At this point, the frequency dropped to 100 Hz and the TTRS boundary

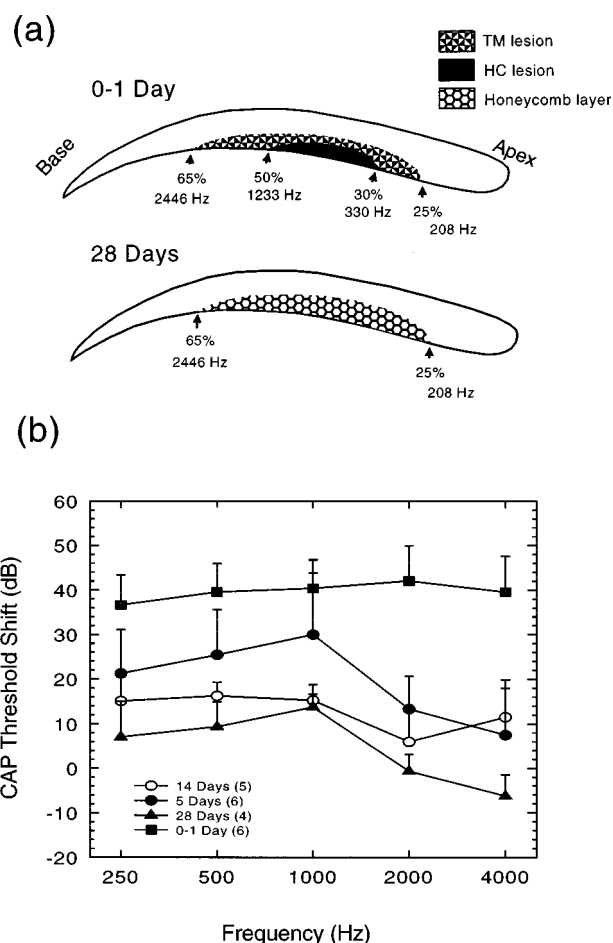


FIG. 2. (a) Schematic showing region of the basilar papilla with hair cell loss and tectorial membrane damage at 0-1 day and 28 days after the 525-Hz tone exposure. See text for source of data. (b) Average CAP threshold shifts and standard deviations of chickens at different times after the 525-Hz tone exposure. Sample size indicated in parenthesis.

below CF (TTRSb boundary) was tracked up to CF in the same fashion.

Figure 1(b) shows an example of a tuning curve and the TTRS boundaries obtained with the procedures described above for a control unit from a normal chicken. The tuning curve from the normal chicken has a narrow, relatively symmetrical V-shaped tip (thick line). The TTRS boundaries can be seen above and below CF. The TTRS boundaries approach the tip of the tuning curve and the lowest threshold for TTRS is approximately 20 dB above the threshold at CF. The TTRS boundaries were measured from 249 control units as described in detail in an earlier publication (Chen *et al.*, 1996a).

II. RESULTS

A. Cochlear damage and CAP threshold shift

Several earlier studies have described the anatomical damage to the chicken cochlea caused by our 525-Hz exposure (Saunders and Salvi, 1995; Saunders *et al.*, 1995; Chen *et al.*, 1996b; Trautwein *et al.*, 1996). In order to put the physiological data into perspective, a brief summary of the anatomical results is presented in Fig. 2(a). Immediately (0-1 day) after the exposure, most of the hair cells were

missing or severely damaged in a crescent-shaped patch along the abneural edge of the papilla extending from approximately 30%–50% of the distance from the apex of the cochlea; this corresponds to frequencies between 330 and 1233 Hz on the chicken's frequency-place map (Chen *et al.*, 1994). The tectorial membrane lesion extended over a much more broader area, from approximately 25%–65% of the distance from the apex of the cochlea; this region corresponds to frequencies between 208 and 2446 Hz.

Figure 2(b) shows the CAP threshold shifts at different times of recovery after the 525-Hz exposure from all chickens used in our TTRS experiment. Immediately (0–1 day) after the exposure, the threshold was elevated by approximately 40 dB across all frequencies. Five days after the exposure, the CAP showed some recovery and the recovery was most pronounced at high frequencies. Additional recovery was observed at 14 days post exposure between 250 and 1000 Hz. Four weeks after the exposure, the CAP threshold shifts were elevated 7–14 dB between 0.25 and 1 kHz, but were within the normal range at higher frequencies.

B. Changes of tuning curves and TTRS boundaries

The TTRS boundaries were tracked in 350 units in the sound-exposed chickens. During the early stages of recovery, TTRS boundaries were absent in some units or the boundaries were truncated to such a degree that it was impossible to obtain accurate quantitative measure of the slope. Thus, the total number of units from which it was possible to obtain quantitative measures of TTRS was less than 350. To illustrate qualitatively how the TTRS boundaries changed over the course of the recovery period, Fig. 3 show the TTRS boundaries (thick lines) and tuning curves (dotted lines) respectively at 0–1, 5, 14, and 28 days following the traumatizing tone exposure. Immediately (0–1 day) after the exposure, the best suppression threshold (BST) of TTRS boundaries was greatly elevated [Fig. 3(a)–(d)] and in some cases it was so high that the boundaries were not able to be measured [e.g., Fig. 3(d)]. The excitatory tuning curves of all the units were extremely broad at this time and CF thresholds were also markedly elevated [Fig. 3(a)–(d)]. Most of the neurons evaluated immediately after the exposure failed to show any evidence of TTRS. In cases where TTRS was present after the exposure, TTRS boundaries were characterized by a wide frequency separation between the best suppression frequency (BSF) and CF, shallow TTRS slopes, and elevated BSTs. Moreover, if a TTRS boundary was present after the exposure, it was almost always located above the CF. After 5 days of exposure, TTRS boundaries were more prevalent and showed signs of recovery [Fig. 3(e)–(h)]. One characteristic of the 5-day postexposure tuning curves is that their low-frequency tails often contained a distinct, low-threshold notch below the tip of the tuning curve. Interestingly, the TTRSb stopped as the TTRS boundary approached the notch [Fig. 3(h)]. The TTRS boundaries were more prevalent and steeper at 14 days postexposure [Fig. 3(i)–(l)]. After 28 days of recovery, TTRS boundaries were nearly normal looking [Fig. 3(m)–(p)] in neurons that expressed TTRSa and TTRBb boundaries. A quantitative description of

the loss and recovery of TTRS boundaries at different times is given below.

C. Occurrence of TTRS boundaries

The TTRS boundaries were often eliminated immediately after acoustic trauma on one side or both sides of the tuning curve. The frequency of occurrence of the boundaries gradually increased as recovery time increased (Fig. 4). In normal chickens ($n=249$ neurons), the occurrence of TTRSb and TTRSa boundaries was 52.6% and 88.4%, respectively (Fig. 4). Immediately (0–1 day) after the exposure, the proportion of neurons with TTRSa dropped to 46.6% and the percentage of neurons with TTRSb dropped to 8.2% (χ^2 test, $p<0.01$). Five days after the exposure, the percentage of the neurons with TTRSa recovered to 70.0% and the percentage of the neurons with TTRSb recovered to 22.9% (χ^2 test, $p<0.01$). At 14 and 28 days postexposure, the percentage of the neurons with TTRSa boundaries was normal (χ^2 test, $p>0.1$). However, the percentage of neurons with TTRSb boundaries was still significantly lower than normal at 14 and 28 days postexposure (χ^2 test, $p<0.05$).

D. Best suppression threshold

The BST is defined as the lowest SPL that resulted in a suppression of the firing rate at frequencies below CF(BSTb) or above CF(BSTa) [Fig. 1(a)]. The effects of acoustic trauma on BSTb is shown in Fig. 5. The maximum and minimum values (dashed line) and median values (solid line) from the control group are plotted in each panel for the purpose of comparison. From 0–1 day through 14 days postexposure, most data points were distributed above the median value for the normal control group. A statistical analysis revealed that the BSTb values at 5 and 14 days postexposure were significantly higher than those of normal chickens (Kolmogorov–Smirnov test, $p<0.05$). A statistical analysis was not performed for chickens 0–1 day postexposure because too few data points were available; however, all BSTb values were above the median at this time. The BSTb values had been improved by 28 days postexposure and were not significantly different from those in normal chickens (Kolmogorov–Smirnov test, $p>0.05$).

The effects of acoustic trauma on BSTa are shown in Fig. 6. Immediately (0–1 day) after the exposure, the BSTa values were significantly elevated (Kolmogorov–Smirnov, $p<0.01$) and most data points were distributed above the median value (solid line) for the control group. The BSTa values improved from 5 to 28 days postexposure. A statistical analysis showed a significant difference in BSTa between normal animals and animals at 5 and 14 days of recovery (Kolmogorov–Smirnov test, $p<0.01$); however, no statistically significant difference between control animals and experimental animals was evident at 28 days of recovery (Kolmogorov–Smirnov test, $p>0.1$). Despite the absence of an overall difference at 28 days postexposure, the neurons with CFs below 300 Hz had BSTa values that were above the median and the lowest BSTa values of units with CFs less than 1000 Hz were not as sensitive as those in normal chickens.

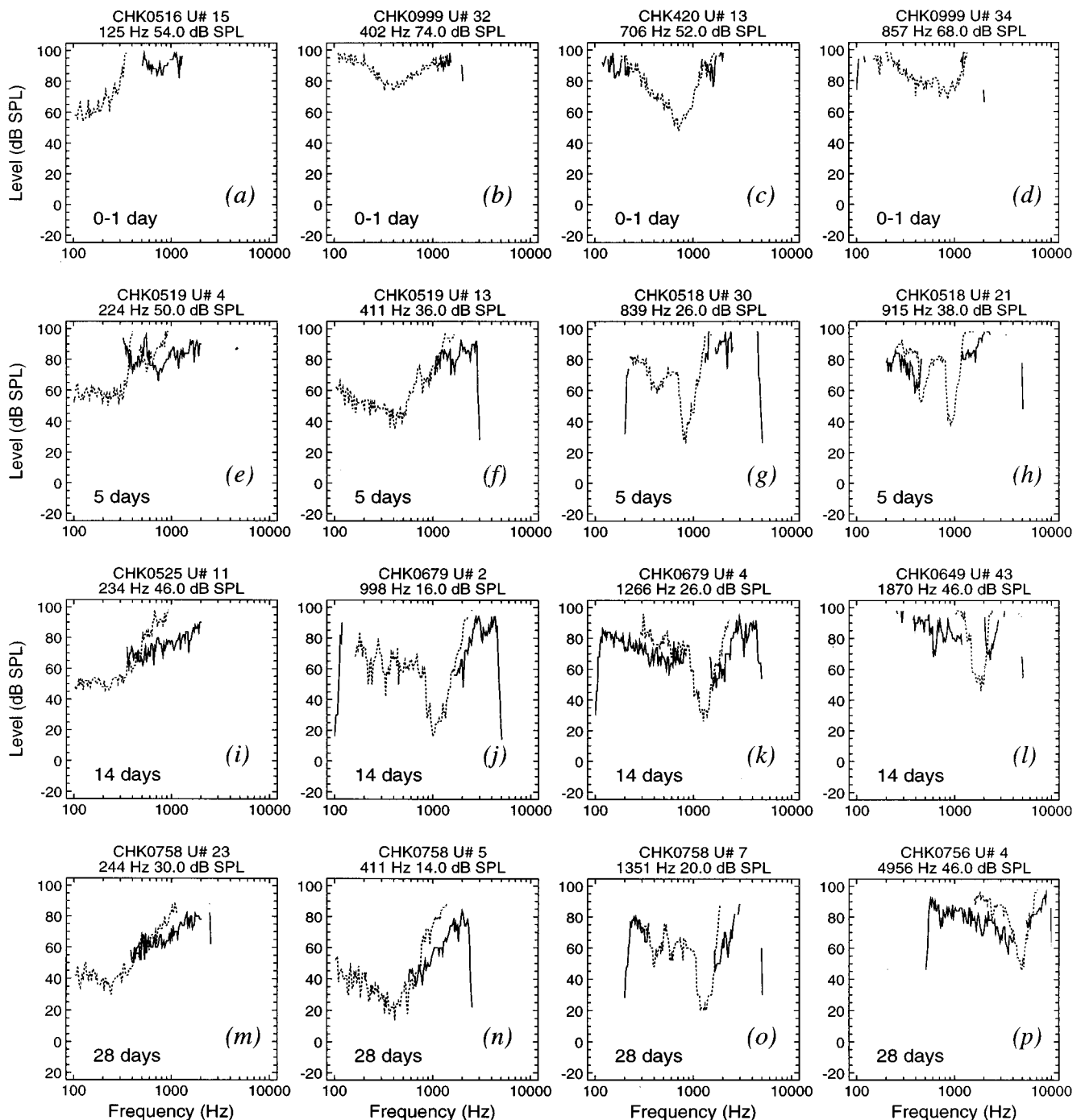


FIG. 3. Examples of TTRS boundaries (solid lines) and tuning curves (dotted lines) measured from different cochlear ganglion neurons in chickens after 0–1, 5, 14, and 28 days of recovery from acoustic trauma. Chicken number, unit number, CF, and unit threshold are indicated above each panel.

E. TTRS boundary slopes

Figure 7 shows the effects of acoustic trauma on TTRSb boundary slopes. Because only a few units had TTRSb boundaries at 0–1 day postexposure, the sample is small and biased towards units that retain suppression below CF. Despite this sampling bias, most of TTRSb slopes were near or above the median. From 5–14 days postexposure, the number of data points increased significantly and most data points were distributed above the median value (solid line) from normal chickens. A statistical analysis showed that the TTRSb boundary slopes were significantly reduced

(Kolmogorov–Smirnov test, $p < 0.05$). At 28 days postexposure, the TTRSb boundary slopes appeared to be slightly shallower than normals; however, a statistical analysis showed that the slopes were not significantly different from those in normal chickens (Kolmogorov–Smirnov test, $p > 0.1$). That is, TTRSb slopes were normal in units that expressed TTRSb boundaries; however, many neurons lacked TTRSb boundaries at 28 days postexposure (Fig. 4).

The consequences of acoustic trauma on TTRSa boundary slopes are illustrated in Fig. 8. From 0–1 day through 14 days postexposure, the slopes of the TTRSa boundaries were

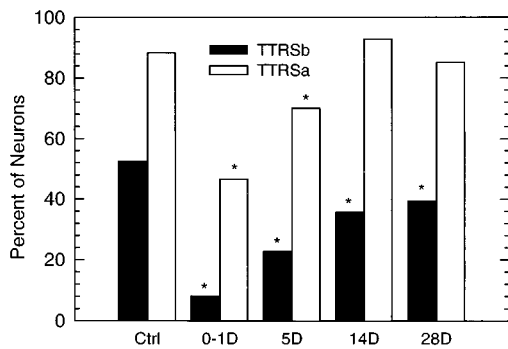


FIG. 4. Percentage of neurons with TTRSb boundaries and TTRSa boundaries in control and exposed chickens. Stars (*) indicate a statistically significant difference between two groups of chickens.

significantly less than the median values (solid line) from normal animals (Kolmogorov–Smirnov test, $p < 0.01$ 0–1 day and 5 days postexposure; $p < 0.05$ 14 days postexposure). Most of the slope values were below the normal median value out to 14 days postexposure. The TTRSa boundary slopes recovered and were not significantly different from those in normal chickens at 28 days postexposure (Kolmogorov–Smirnov test, $p > 0.1$). In addition, the percentage of neurons that expressed TTRSa boundaries was normal (Fig. 4) at this time.

F. Frequency separation of TTRS boundaries from CF

The frequency separations between CF and the tip of the lower TTRS boundary, CF-BSFb, and the frequency separation between the tip of the upper TTRS boundary and CF, BSFa-CF, are plotted against CF for both normal and exposed ears in Figs. 9 and 10, respectively. After the exposure, the separation of the tip of the TTRSb from CF was greater than normal. From 0–1 day to 14 days postexposure,

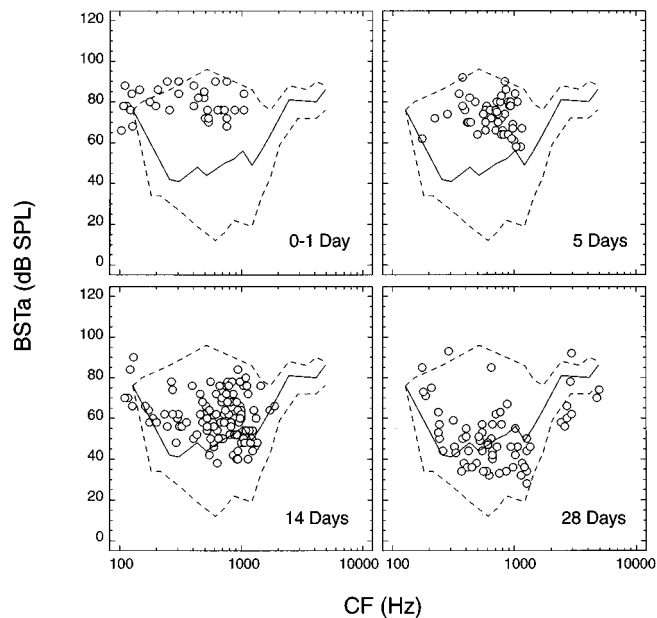


FIG. 6. The BSTa as a function of CF at four recovery times. Dashed lines and solid line in each panel are the minimum, maximum, and median values from control animals ($n = 220$).

most data points were distributed above the median value (solid line) from normal chickens (Kolmogorov–Smirnov test, $p < 0.01$). By 28 days postexposure, the distance of the tip of TTRSb boundary from CF had recovered in units exhibiting TTRSb boundaries and was not significantly different from the values of normal chickens (Kolmogorov–Smirnov test, $p > 0.1$). However, it is important to recall that the percentage of neurons exhibiting TTRSb boundaries was lower than normal at this time (Fig. 4).

Figure 10 shows the effects of acoustic trauma on the

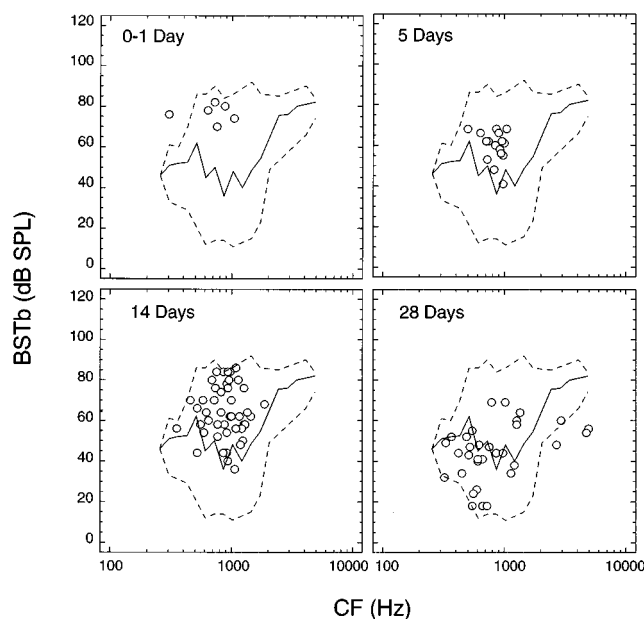


FIG. 5. The BSTb as a function of CF at four recovery times. Dashed lines and solid line in each panel are the minimum, maximum, and median values from control animals ($n = 131$).

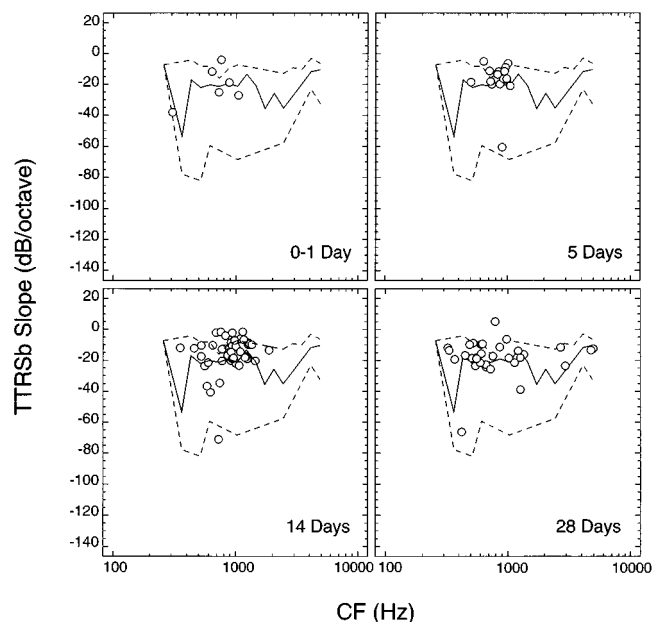


FIG. 7. The TTRSb slope as a function of CF at four recovery times. Dashed lines and solid line in each panel are the minimum, maximum, and median values from control animals ($n = 131$).

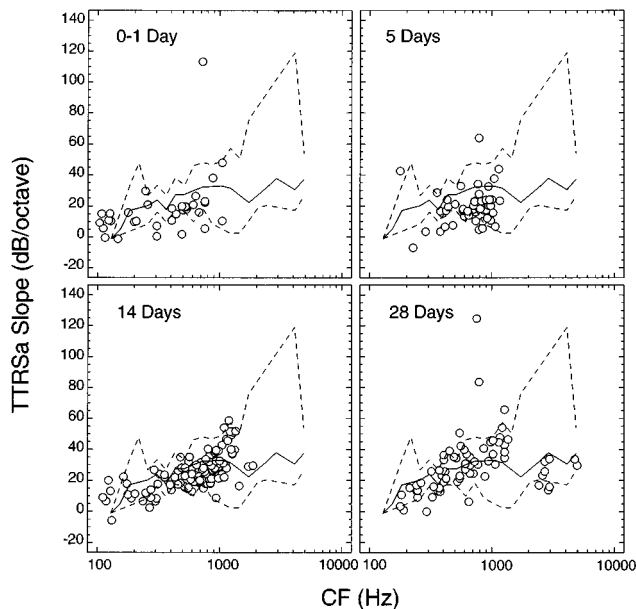


FIG. 8. The TTRSa as a function of CF at four recovery times. Dashed lines and solid line in each panel are the minimum, maximum, and median values from control animals ($n = 220$).

frequency separation of the tip TTRSa from CF. After the exposure, the TTRSa boundary tended to be separated further from the tuning curve tip. The distance of the TTRSa boundary from CF recovered relatively quickly. At 0–1 day and 5 days postexposure, most data points were distributed above the median value (solid line) from normal chickens (Kolmogorov–Smirnov test, $p < 0.01$). However, at 14 and 28 days postexposure, the distance of the TTRSa boundary from CF was not significantly different from that of the control group.

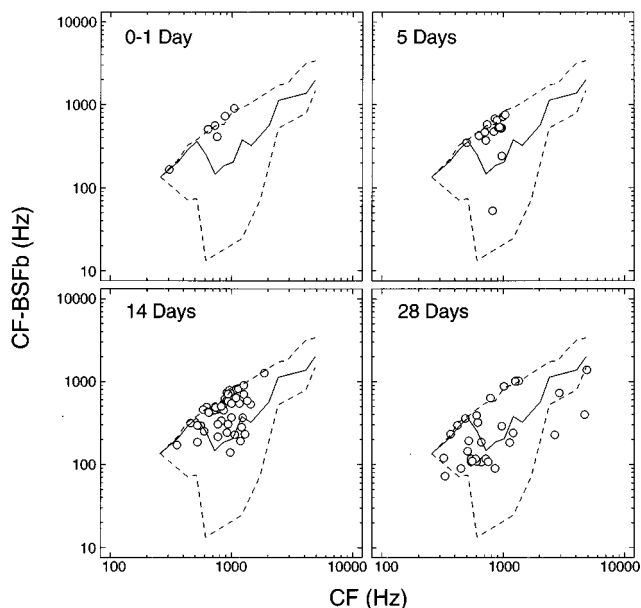


FIG. 9. Frequency separation of TTRSb boundaries from CF (CF-TTRSb) as a function of CF at four recovery times. Dashed lines and solid line in each panel are the minimum, maximum, and median values from control animals ($n = 131$).

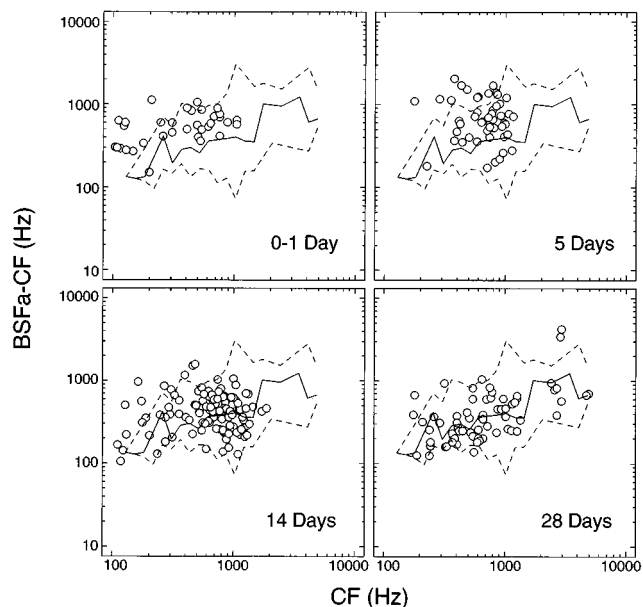


FIG. 10. Frequency separation of TTRSa boundaries from CF (TTRSa-CF) as a function of CF at four recovery times. Dashed lines and solid line in each panel are the minimum, maximum, and median values from control animals ($n = 220$).

An alternative way of describing the relationship between the boundary tip and CF is to compute the ratio of BSFa to CF and CF to BSFb (Prijs, 1989). Larger values of BSFa/CF and CF/BSFb indicate greater frequency separation between CF and the tip of the TTRS boundary. In normal chickens, the median value of BSFa/CF was 1.38 and the median value of CF/BSFb was 1.43 (Fig. 11). Immediately after the exposure, both BSFb and BSFa are widely separated from CF as indicated by the increased values of BSFa/CF and CF/BSFb. Note that CF/BSFb increased much more than BSFa/CF. Most of the improvement in BSFa/CF occurred between 0–1 day and 14 days postexposure while CF/BSFb continued to decrease out to 28 days postexposure. Both BSFa/CF and CF/BSFb were essentially normal at 28 days postexposure.

III. DISCUSSION

The results of the present study show that TTRS in birds is vulnerable to acoustic overstimulation just as it is in mam-

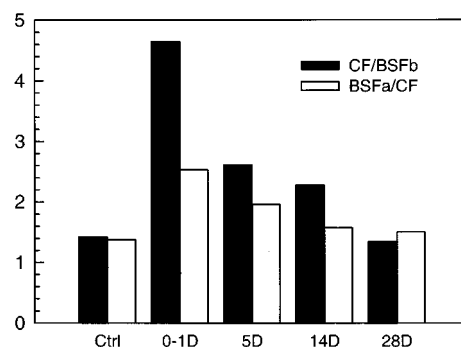


FIG. 11. Recovery of frequency separation of TTRSb boundaries and TTRSa boundaries as indicated by ratios of BSFa/CF and CF/BSFb.

mals (Salvi *et al.*, 1982; Schmiedt, 1982b; Schmiedt and Schulte, 1992). Acoustic trauma: (1) reduced the occurrence of TTRS boundaries (Fig. 4), (2) reduced the TTRS slopes (Figs. 7 and 8), (3) elevated BST (Figs. 5 and 6), and (4) increased the frequency separation between the tips of the boundaries and CF (Figs. 9, 10, and 11). Unlike mammals, TTRS in chickens recovered to a large extent after the hair cells and lower honeycomb layer of the tectorial membrane regenerated. However, the recovery of TTRSb was incomplete. Some neurons regained their TTRSb boundaries while others failed to show evidence of suppression below CF even after 28 days of recovery. We wish to emphasize the bimodal nature of the recovery of TTRSb boundaries and the fact that there was a significant reduction in the number of neurons that expressed TTRSb boundaries after the exposure. On the other hand, if a neuron had a TTRSb boundary, then the quantitative measures of TTRSb were typically normal or only slightly outside the normal range at 28 days postexposure.

A. Relationship between cochlear damage and TTRS

Based upon our earlier intracellular labeling studies (Chen *et al.*, 1994), most if not all of our recordings presumably originate from neurons that contact a single hair cell along the neural edge of the basilar papilla. Our measurements therefore reflect TTRS transmitted through the hair cells along the neural edge of the papilla. The exact source of TTRS is not yet known; however, certain generation sites can be excluded on the basis of the present results. If TTRS originated in or near the hair cells along the neural edge of the papilla, then TTRS should have remained intact after the exposure since there was relatively little damage in this region. Since TTRS was absent in most neurons after the exposure, it seems unlikely that TTRS originates in the hair cells along the neural edge of the papilla. The alternative is that TTRS originates in or near the hair cells along the abneural edge of the papilla and is transmitted to the hair cells along the neural edge. Our traumatizing stimulus caused several prominent cochlear pathologies along the abneural edge of the basilar papilla which could operate alone or in combination to impair TTRS. The following three sections will consider the relationship between the three most prominent cochlear pathologies and the recovery of TTRS.

B. Hair cell damage

At 0–1 day postexposure, most of the hair cells were missing or severely damaged along the abneural edge of the papilla and TTRS was absent or severely impaired at this time. One interpretation of these results is that the hair cell lesion contributes to the loss or impairment of TTRS. However, the hair cell lesion was confined to a crescent-shaped patch that extended 30%–50% of the distance from the apex of the cochlea or 330–1233 Hz on the frequency place map (Chen *et al.*, 1994, 1996b; Saunders and Salvi, 1995; Saunders *et al.*, 1995; Trautwein *et al.*, 1996). Since neurons with CFs outside the damaged area also showed abnormal TTRS; the hair cell lesion cannot fully account for the impairment of TTRS during the early stage of recovery.

After 28 days of recovery, the damaged area was repopulated by new hair cells and many measures of TTRS were within normal limits at this time. While these results suggest that hair cell regeneration may contribute to the recovery of TTRS, some other structural or functional deficits must be contribute to the loss of TTRSb boundaries (Fig. 4). A plausible candidate is the tectorial membrane which is thought to transmit radial shearing forces to the stereocilia bundles on the hair cells lying along the neural edge of the papilla (Saunders *et al.*, 1996a, 1996b).

C. Tectorial membrane damage

The tectorial membrane lesion extends over a much broader segment of the basilar papilla than the region of hair cell loss [Fig. 2(a)]. Previous results indicate that the tectorial membrane lesion extends from approximately 25%–65% of the distance from the apex of the cochlea; this correspond to 208–2446 Hz on the frequency-place map (Saunders and Salvi, 1995; Saunders *et al.*, 1995; Chen *et al.*, 1996b; Trautwein *et al.*, 1996). Because the tectorial membrane lesion is much broader than the region of hair cell loss, it accounts for the loss of TTRS over a much broader range of CFs.

After 28 days of recovery, the hair cells and lower honeycomb layer of the tectorial membrane had regenerated. Although most TTRS measures were within normal limits, many neurons still lacked TTRSb boundaries (Fig. 4). In addition, the maximum TTRSb boundary slopes (Fig. 7), the minimum BSTa values (Fig. 6), and the minimum frequency separation of TTRSb from CF (Fig. 9) were still slightly below normal in neurons with CFs near or slightly above the exposure frequency. These residual losses were most closely associated with the absence of the upper fibrous layer of the tectorial membrane.

D. Tegmentum vasculosum

The endolymphatic potential (EP) has been shown to play an important role in generating cochlear nonlinearities in mammals. Reducing the EP causes a significant reduction in DPOAEs amplitude in gerbils (Mills *et al.*, 1993). A similar reduction of the EP in our chickens could conceivably account for the loss of TTRS. Acoustic trauma has been reported to cause a large decline in the EP of young chicks for a period of several days (Poje *et al.*, 1995). The decline of the EP could be the result of damage to its generator, the tegmentum vasculosum (Ryals *et al.*, 1995). We recently measured the positive EP in adult chickens exposed to the same stimulus used in the present study. Our results showed that the positive EP was unchanged after the exposure, thereby eliminating the EP as a causal factor in the loss of TTRS (Trautwein *et al.*, in press).

E. Species differences

Acoustic exposure tends to damage the abneural edge of the basilar papilla and preferentially destroy SHCs. Since the afferent and efferent innervation pattern and relative location of SHCs are similar to those mammalian OHCs (Tanaka and Smith, 1978; Fischer, 1992), it is tempting to compare the changes in TTRS in mammals with OHC loss with the

present results. Previous results from old gerbils raised in noise have shown that even in the cochlear region with 60% OHC loss, TTRS below CF is always present, but TTRS above CF is absent (Schmiedt and Schulte, 1992). These results suggest that a full complement of OHCs is not essential for TTRS below CF (Schmiedt and Schulte, 1992) and that TTRS above CF is more vulnerable to acoustic trauma. This is opposite to what has been observed in the present study. Specifically, chicken TTRSb boundaries were more vulnerable than TTRSa boundaries. This species difference may be due to different types of cochlear damage or it may be due to different nonlinear generators in birds versus mammals.

F. TTRS and DPOAEs

Although both TTRS and DPOAEs are thought to originate from the nonlinear cochlear mechanics and perhaps share common generators (Rhode and Cooper, 1993), the two types of nonlinearities show drastically different behavior in chickens following acoustic trauma. The TTRS showed considerable recovery following acoustic trauma whereas there was almost no improvement in the DPOAEs near the exposure frequency (Froymovich *et al.*, 1995; Trautwein *et al.*, 1996). The depression in DPOAE amplitude in these earlier studies was most closely linked to the loss of the upper fibrous layer of the tectorial membrane (Trautwein *et al.*, 1996). In mammals, TTRS and DPOAEs are thought to derive from basilar membrane–OHC interactions (Ruggero *et al.*, 1992). The explanation for the relatively good recovery of TTRS and poor recovery of DPOAEs in birds may lie in different generation mechanisms or in different transmission paths for TTRS versus DPOAEs.

ACKNOWLEDGMENT

This research was supported by research grant No. R01DCD01685 from the National Institute on Deafness and Other Communication Disorders, National Institutes of Health.

Chen, L., Salvi, R., and Shero, M. (1994). "Cochlear frequency-place map in adult chickens: Intracellular biocytin labeling," *Hearing Res.* **81**, 130–136.

Chen, L., Salvi, R. J., Trautwein, P. G., and Powers, N. (1996a). "Two-tone rate suppression boundaries of cochlear ganglion neurons in normal chickens," *J. Acoust. Soc. Am.* **100**, 442–450.

Chen, L., Trautwein, P., Shero, M., and Salvi, R. J. (1996b). "Correlation of hair cell regeneration with physiology and psychophysics in adult chickens following acoustic trauma," in *Auditory System Plasticity and Regeneration* (Thieme, Stuttgart), pp. 43–61.

Chen, L., Trautwein, P. G., Shero, M., and Salvi, R. J. (1996c). "Tuning, spontaneous activity and tonotopic map in chicken cochlear ganglion neurons following sound induced hair cell loss and regeneration," *Hearing Res.* **98**, 152–164.

Cohen, Y. E., and Saunders, J. C. (1993). "The effects of sound exposure on the spectral response patterns of the nucleus magnocellularis in the neonatal chick," *Exp. Brain Res.* **95**, 205–213.

Corwin, J. T., and Cotanche, D. A. (1988). "Regeneration of sensory hair cells after acoustic trauma," *Science* **240**, 1772–1774.

Cotanche, D. A. (1987a). "Regeneration of hair cell stereociliary bundles in the chick cochlea following severe acoustic trauma," *Hearing Res.* **30**, 181–196.

Cotanche, D. A. (1987b). "Regeneration of the tectorial membrane in the chick cochlea following severe acoustic trauma," *Hearing Res.* **30**, 197–206.

Cotanche, D. A., Saunders, J. C., and Tilney, L. (1987). "Hair cell damage produced by acoustic trauma in the chick cochlea," *Hearing Res.* **25**, 267–286.

Delgutte, B. (1990). "Two-tone rate suppression in auditory-nerve fibers: Dependence on suppressor frequency and level," *Hearing Res.* **49**, 225–246.

Fischer, F. P. (1992). "Quantitative analysis of the innervation of the chicken basilar papilla," *Hearing Res.* **61**, 167–178.

Froymovich, O., Rebala, V., Salvi, R. J., and Rassael, H. (1995). "Long term effects of acoustic trauma on distortion product otoacoustic emissions in chickens," *J. Acoust. Soc. Am.* **97**, 3021–3029.

Hashino, E., and Salvi, R. J. (1993). "Changing spatial patterns of DNA replication in the noise-damaged chick cochlea," *J. Cell. Sci.* **105**, 23–31.

Holton, T. (1980). "Relations between frequency selectivity and two-tone rate suppression in lizard cochlear-nerve fibers," *Hearing Res.* **2**, 21–38.

McFadden, E. A., and Saunders, J. C. (1989). "Recovery of auditory function following intense sound exposure in the neonatal chick," *Hearing Res.* **41**, 205–216.

Mills, D. M., Norton, S. J., and Rubel, E. W. (1993). "Vulnerability and adaptation of distortion product otoacoustic emissions to endocochlear potential variation," *J. Acoust. Soc. Am.* **94**, 2108–2122.

Poje, C. P., Sewell, D. A., and Saunders, J. C. (1995). "The effects of exposure to intense sounds on the DC endocochlear potential in the chick," *Hearing Res.* **82**, 197–204.

Prijs, V. F. (1989). "Lower boundaries of two-tone suppression regions in the guinea pig," *Hearing Res.* **42**, 73–82.

Raphael, Y. (1991). "Pure-tone overstimulation protects surviving avian hair cells from acoustic trauma," *Hearing Res.* **53**, 173–184.

Rhode, W. S., and Cooper, N. P. (1993). "Two-tone suppression and distortion production on the basilar membrane in the hook region of cat and guinea pig cochleae," *Hearing Res.* **66**, 31–45.

Robertson, D., and Johnstone, B. M. (1981). "Primary auditory neurons: Nonlinear responses altered with changes in sharp tuning," *J. Acoust. Soc. Am.* **69**, 1096–1098.

Ruggero, M. A., Robles, L., Rich, N. C., and Recio, A. (1992). "Basilar membrane responses to two-tone and broadband stimuli," *Philos. Trans. R. Soc. London, Ser. B* **336**, 307–315.

Ryals, B. M., and Rubel, E. W. (1982). "Patterns of hair cell loss in chick basilar papilla after intense auditory stimulation," *Acta Oto-Laryngol.* **93**, 205–210.

Ryals, B. M., and Rubel, E. W. (1988). "Hair cell regeneration after acoustic trauma in adult Coturnix quail," *Science* **240**, 1774–1776.

Ryals, B. M., Stalford, M. D., Lambert, P. R., and Westbrook, E. W. (1995). "Recovery of noise-induced changes in the dark cells of the quail tegmentum vasculosum," *Hearing Res.* **83**, 51–61.

Salvi, R. J., Perry, J., Hamernik, R. P., and Henderson, D. (1982). "Relationship between cochlear pathologies and auditory nerve and behavioral responses following acoustic trauma," in *New Perspectives on Noise-Induced Hearing Loss* (Raven, New York), pp. 165–188.

Salvi, R. J., Saunders, S. S., Hashino, E., and Chen, L. (1994). "Discharge patterns of chicken cochlear ganglion neurons following kanamycin-induced hearing loss and regeneration," *J. Comp. Physiol. A* **174**, 351–369.

Salvi, R., Saunders, S. S., Powers, N. L., and Boettcher, F. A. (1992). "Discharge patterns of cochlear ganglion neurons in the chicken," *J. Comp. Physiol. A* **170**, 227–241.

Saunders, S. S., and Salvi, R. J. (1995). "Pure tone masking patterns in adult chickens after recovery from acoustic trauma," *J. Acoust. Soc. Am.* **98**, 1365–1371.

Saunders, J. C., and Tilney, L. G. (1982). "Species differences in susceptibility to noise exposure," in *New Perspectives on Noise-Induced Hearing Loss* (Raven, New York), pp. 229–248.

Saunders, S. S., Salvi, R. J., and Miller, K. M. (1995). "Recovery of thresholds and temporal integration in adult chickens after high-level 525-Hz pure tone exposure," *J. Acoust. Soc. Am.* **97**, 1150–1164.

Saunders, J. C., Doan, D. E., Poje, C. P., and Fisher, K. A. (1996a). "Cochlear nerve activity after intense sound exposure in neonatal chicks," *J. Neurophysiol.* **76**, 770–787.

Saunders, J. C., Doan, D. E., Cohen, Y. E., Adler, H. J. and Poje, C. P. (1996b). "Recent observations on the recovery of structure and function in the sound damaged chick ear," in *Auditory Plasticity and Regenera-*

- tion: *Basic Science and Clinical Implications* (Thieme, Stuttgart), pp. 62–83.
- Schmiedt, R. A. (1982a). “Boundaries of two-tone rate suppression of cochlear-nerve activity,” *Hearing Res.* **7**, 335–351.
- Schmiedt, R. A. (1982b). “Differential effects of kanamycin and impulse-noise exposure on responses of auditory nerve fibers,” in *New Perspectives on Noise-Induced Hearing Loss* (Raven, New York), pp. 153–164.
- Schmiedt, R. A., and Schulte, B. A. (1992). “Physiologic and histopathologic changes in quiet- and noise-aged gerbil cochleas,” in *Noise-Induced Hearing Loss* (Mosby, St. Louis), pp. 246–256.
- Schmiedt, R. A., Zwislocki, J. J., and Hamernik, R. P. (1980). “Effects of hair cell lesions on responses of cochlear nerve fibers. I. Lesions, tuning curves, two-tone inhibition, and responses to trapezoidal-wave patterns,” *J. Neurophysiol.* **43**, 1367–1389.
- Schwartzkopff, J. J., and Bremond, J. (1963). “Méthode de dérivation des Potentials cochléaires chez l’oiseau,” *J. Physiol. (Paris)* **55**, 495–518.
- Tanaka, K., and Smith, C. A. (1978). “Structure of the chicken’s inner ear: SEM and TEM study,” *Am. J. Anat.* **153**, 251–272.
- Trautwein, P. G., Chen, L., and Salvi, R. J. (in press). “Steady state EP is not responsible for hearing loss in adult chickens following acoustic trauma,” *Hearing Res.*
- Trautwein, P., Salvi, R. J., Miller, K., Shero, M., and Hashino, E. (1996). “Partial recovery of distortion product otoacoustic emissions in chickens following acoustic overstimulation,” *Audiol. Neuro-Otol.* **1**, 86–103.

Multidimensional scaling of complex sounds by school-aged children and adults

Prudence Allen and Cheryl-Ann Bond

University of Western Ontario, Department of Communicative Disorders, 1500 Elborn College, London, Ontario N6G 1H1, Canada

(Received 21 August 1996; revised 7 July 1997; accepted 7 July 1997)

A paired-comparisons procedure was used to evaluate the processing of complex, nonspeech sounds by 7- and 10-year-old children and adults. Stimuli were brief duration and included pure tones, harmonic complexes, and bands of noise. From their similarity ratings, a three-dimensional multidimensional scaling solution was derived. Results suggested that listeners classified the stimuli into clusters based upon periodicity and the number of spectral peaks. Within each cluster, the stimuli were ordered according to frequency. Because individual differences in the overall weightings of features were large, separate solutions were derived for two subgroups of listeners, formed based upon similarities in the pattern of dimension weights obtained in the group analysis. One subgroup, for whom the full group analysis captured a large proportion of the variance in the ratings, included the adults, many of the 10-year-olds, and a few of the 7-year-olds. The solution derived for this subgroup suggested that spectral and temporal information were weighted equally and integrated into all dimension weights. Frequency information was coded but given less weight and was not used for stimulus classification. A second subgroup of listeners included most of the 7-year-old and some of the 10-year-old children. Examination of their data suggested that they relied heavily on an analysis of the signals according to periodicity as was reflected in their temporal fine structure. Also encoded but of lesser importance were aspects of spectral shape and absolute frequency. © 1997 Acoustical Society of America. [S0001-4966(97)05210-7]

PACS numbers: 43.66.Ba, 43.66.Fe, 43.66.Lj [WJ]

INTRODUCTION

To understand how children encode natural sounds it is important to examine not only age-related changes in sensitivity and resolution for the acoustic features that comprise the sounds, but also to examine the processing of the complex sounds themselves. By studying whole sounds we can begin to understand how individual features are weighted and integrated in the formation of auditory images to which meaning can be assigned. One method that can be used to study the perception of complex stimuli is paired comparisons. Individuals are asked to rate the similarity of pairs of stimuli within a set, but are not told which features to consider when making the judgments. From their ratings a multidimensional scaling (MDS) analysis is used to derive a multidimensional space in which the stimuli are represented as points and the axes are assumed to represent psychological attributes of the stimuli. The relative distance between points reflects the perceived similarity of the stimuli. The underlying assumption is that perceived similarity is composed of a weighted combination of perceptual features, each of which corresponds to one or more physical attributes of the stimuli.

When adult listeners are asked to rate the similarity of complex sounds, scaling solutions have shown that both spectral and temporal features are encoded. Howard and Silverman (1976) derived a three-dimensional solution from the similarity ratings of a set of 16 complex sounds that varied along four physical dimensions including fundamental frequency, driving waveform, formant frequency, and the number of formants. Examination of dimensions 1–3 suggested

coding of fundamental frequency, driving waveform, and a combination of formant frequency and number, respectively. Yet the relative weight each listener assigned to the three dimensions varied with their prior listening experience. The musically trained listeners showed higher weights for the dimensions thought to represent the temporal information provided by the fundamental frequency but untrained listeners were equally likely to weight any one of the dimensions as most salient. Similar results were found when Howard (1977) evaluated the two-dimensional space created from similarity ratings of a set of eight sonar recordings. Results suggested that the dimensions corresponded to the shape of the 1/3 octave spectra and the presence of a low-frequency periodicity. Again, musically trained listeners weighted the dimensions corresponding to the low-frequency periodicity most heavily but the musically naive listeners showed higher weights for the dimension corresponding to spectral shape.

Individual differences in feature salience are not limited to comparisons based on musical training. Christensen and Humes (1996) used multidimensional scaling to evaluate the processing of brief tonal complexes varying in harmonicity, spectral shape, and amplitude envelope. Within each acoustic dimension the stimuli were bimodally distributed producing a set of eight sounds from all possible combinations. Similarity ratings of the sounds were used to produce a three-dimensional space within which each dimension appeared to represent one of the three acoustic dimensions. Yet examination of individual dimension weights showed that listeners weighted the dimensions differently. These differences in relative feature salience remained in a subsequent classifica-

tion task in which it was shown that the listeners classified stimuli based on the acoustic feature represented in the dimension they had weighted highest in the scaling task. Thus feature salience varied between individuals and was predictive of classification trends.

Classification is an important skill in the organization of sensory input and it is through the detection of similarities that classes are often formed. Kuhl (1992) argues that the detection of similarities and the formation of stimulus classes is an essential part of children's learning, enabling them to assign meaning to sounds that are often inherently variable. One step in understanding how children organize their auditory world is to examine how they evaluate the similarity of complex stimuli, specifically, which acoustic features are most salient and how feature information is processed and integrated in the perception of unfamiliar sounds. This paper reports a study that therefore evaluated age-related differences in the processing of a set of unfamiliar, nonspeech, complex sounds using a paired comparisons procedure and a multidimensional scaling analysis. Listeners were school-aged children and adults.

I. METHOD

A. Listeners

Listeners were ten 6- to 7-year-old children (mean age = 7 years 2 months; range = 6 years 9 months to 8 years 0 months) and eleven 10- to 11-year-old children (mean age = 10 years 7 months; range = 10 years 0 months to 11 years 6 months) recruited from the London community, and 11 adults (mean age = 26 years 0 months, range = 22 years 6 months to 29 years 6 months) recruited from the student population of the University of Western Ontario. Throughout this paper the groups will be discussed as the 10-year-olds, 7-year-olds, and adults. Adults and parents of children read a letter of information and signed a consent form before any testing was begun. Verbal consent was also obtained from the children themselves. All listeners were paid for their participation. Listeners were required to pass an audiometric screening (20 dB HL at 500, 1000, 2000, and 4000 Hz) in both ears. In addition, children were tested for normal middle ear status using tympanometry. If middle ear problems were suspected on a particular day the child was not tested.

B. Stimuli

The stimulus set (described in Table I) included 17 unfamiliar, complex sounds that varied along several spectral and temporal dimensions thought important for both speech and nonspeech processing including frequency range and bandwidth, pitch, number of peaks in the amplitude spectrum, number of tonal components, and temporal envelope. Within each dimension the acoustic values covered a relatively wide distribution and differed enough so as to be discriminable for all listeners.

Stimuli included three pure tones (250, 1000, and 4000 Hz), six harmonic complexes consisting of the low (2–6), high (12–16), or wide (2–16) harmonics of either a 110- or 200-Hz fundamental, two amplitude-modulated narrow-band noises (produced by modulating 500 and 2000 Hz narrow-

TABLE I. Stimulus codes used in Figs. 2, 5, and 6 and their descriptions.

ID code	Description
T250	Pure tone of 250 Hz
T500FM	Frequency modulated tone: 450–550 Hz at 10 Hz
T1000	Pure tone of 1000 Hz
T2000FM	Frequency modulated tone: 1800–2200 Hz at 10 Hz
T4000	Pure tone of 4000 Hz
C110L	Complex, $F_0 = 110$ Hz, Harmonics 2–6 (220–660)
C110H	Complex, $F_0 = 110$ Hz, Harmonics 12–16 (1320–1760)
C110W	Complex, $F_0 = 110$ Hz, Harmonics 2–16 (220–1760)
C200L	Complex, $F_0 = 200$ Hz, Harmonics 2–6 (400–1200)
C200H	Complex, $F_0 = 200$ Hz, Harmonics 12–16 (2400–3200)
C200W	Complex, $F_0 = 200$ Hz, Harmonics 2–16 (400–3200)
N500	398–630 Hz noise band
N500AM	398–630 Hz noise, AM by 12 dB at 6 Hz
N1000	794–1259 Hz noise band
N2000	1589–2518 Hz noise band
N2000AM	1589–2518 Hz noise band, AM by 12 dB at 6 Hz
NWIDE	500–2000 Hz noise band

band noises by 12 dB at 6 Hz), two frequency-modulated tones (range 450–550 and 1800–2200 Hz, each sinusoidally modulated at 10 Hz), three narrow-band noises (center frequencies of 500, 1000, and 2000 Hz with bandwidths ± 0.1 log units relative to the center frequency), and one wideband noise (500–2000 Hz). All stimuli were 430 ms in duration, including 10-ms cosine squared on and off ramps. The stimuli were computed digitally and converted to analog form by 16-bit digital-to-analog converters (Ariel DSP-16) at a sampling rate of 25 000 Hz, low-pass filtered at 8000 Hz, attenuated and amplified by a custom-made system, and output via TDH-49 circumaural headphones or EAR 3A insert earphones with matched output responses. The overall level of each stimulus was varied randomly with each presentation over a 10 dB range centered at 65 dB HL referenced to the average detection threshold of a group of normal hearing adult listeners.

C. Procedure

The listener's task was to rate the similarity of pairs of stimuli but no information was given to them regarding the features to be used in making judgments. All possible pairs of the stimulus set were judged once, including "like" pairs, for a total of 153 trials, completed in blocks of approximately 25. Listeners completed the experiment in one or two sessions on separate days.

On each trial, two identical pictures appeared on a computer monitor, one at the left-most edge of the screen and the other in a random position between the left picture and the right side of the screen. Two stimuli were then presented sequentially, with random order, one to each ear. Using a computer mouse, listeners moved the right-most picture horizontally to any position between the right side of the screen and the left figure while the left-most picture remained stationary. The two pictures were always presented along the same horizontal plane and were not allowed to move vertically. The similarity of the two stimuli was indicated by the distance the listener placed between the two pictures. More similar sounds resulted in closer placement of the pictures

than did less similar sounds. Distance between the pictures, evaluated as a percentage of the total distance, represented the dissimilarity measure submitted to the MDS analysis. Once the picture had been moved, the stimuli were presented again and the listener had the option to either modify his or her judgment or end the trial if he or she was satisfied with the position of the pictures. Adults performed the experiment alone using both the mouse and keyboard to initiate trials and enter their responses. Children were assisted by an experimenter but otherwise performed the task as the adults.

Before the start of the experiment, listeners were presented with a set of six practice trials to ensure they understood the task. The stimuli for these practice trials included a 530-Hz pure tone, a narrow-band noise (421–667 Hz), and a harmonic complex with a fundamental frequency of 200 Hz and harmonics 2–16. While there are no correct or incorrect answers in a MDS task, the practice data were examined prior to beginning the test trials for obvious response errors and biases, such as a failure to rate “like” pairs as similar or use the full range of the scale. When these errors occurred the listener was reinstructed. Before beginning either the practice or experimental trials listeners were presented with all stimuli in the set, in random order. If the experiment was completed in two sessions the stimuli were also played at the beginning of the second session.

II. RESULTS

Dissimilarity measures were analyzed using the INDSCAL model of ALSCAL which uses an alternating least-squares approach to creating a group stimulus space using Euclidean distances between stimuli. The proportion of the variance (R^2) in the ratings that can be accounted for by the placement of stimuli within the group space, along with the R^2 attributable to each dimension, are reported. The procedure also provides weightings that reflect the importance each individual listener places on the dimensions described by the group space. A multiple regression analysis was used to help identify the primary acoustic correlates of each dimension in the space. Dimension weights for each stimulus were dependent variables in the equation and acoustic features including average frequency, periodicity (coded as the number of components within each critical band), and the number of peaks in the amplitude spectrum were independent variables. Each acoustic parameter was logged prior to the regression analysis.¹

A. Group MDS solution

1. Variance accounted for

A single three-dimensional solution was derived from the similarity ratings of all listeners. A three-dimensional solution was chosen for analysis as it represents the maximum number of dimensions that can be meaningfully described with a stimulus set of the size used in this study. The open symbols of Fig. 1 show the individual proportion of variance accounted for plotted as a function of listener age. Averages for each age group are shown by the filled symbols plotted at the mean of each age group. The horizontal dashed line shows mean R^2 values obtained for fits to random data.² On average, R^2 increased with increasing age although there

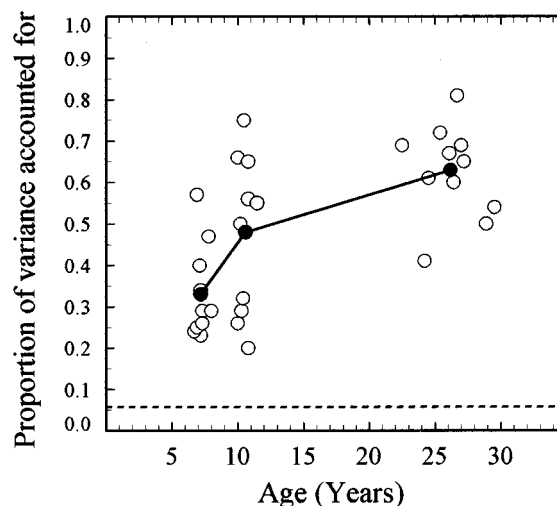


FIG. 1. Proportion of the variance accounted for (R^2) in the three-dimensional multidimensional scaling solution derived from the data of all listeners, plotted as a function of listeners age.

were large individual differences. R^2 was, on average, 64% for the adults, 51% for the 10-year-olds, and 31% for the 7-year-olds. The fits to the simulated random data suggest that although the R^2 was lower for the younger listeners than the older, a significant proportion of the variance was accounted for, arguing for the presence of structure in data from these younger listeners.

2. Derived 3-dimensional space

The three-dimensional space created by the MDS analysis is shown in Fig. 2. Dimensions 1–3 are represented by

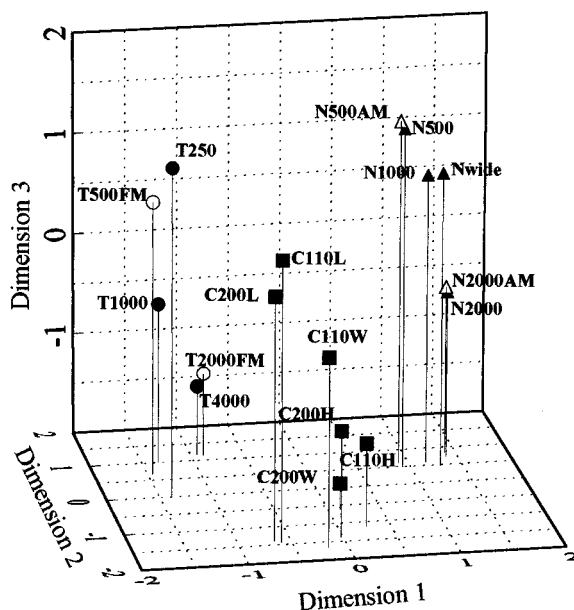


FIG. 2. The three-dimensional space created from the similarity ratings of all 32 listeners. Harmonic complexes are shown by the filled squares. Noise bands are shown by the triangles (filled symbols show steady state and open symbols show amplitude modulated). Tones are represented by the circles (filled symbols for steady state and open for frequency modulated.) Stimuli are described in Table I.

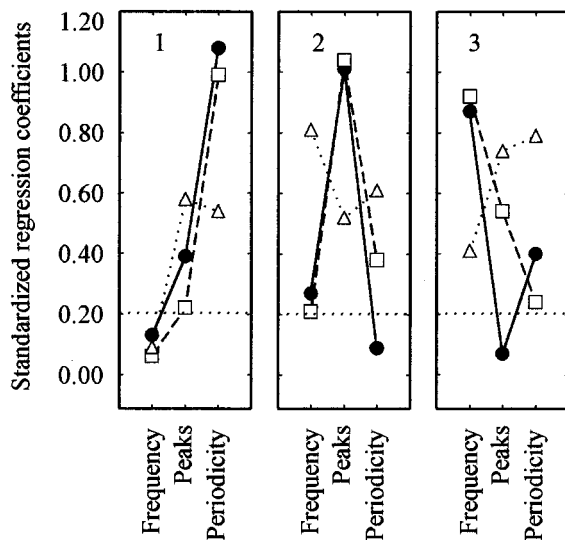


FIG. 3. Absolute values of standardized regression coefficients derived from the multiple regression analysis in which the dimensional weights were dependent variables and the acoustic parameters of periodicity, spectral shape, frequency, and bandwidth were independent variables. Data for dimensions 1–3 are shown in separate panels. Solid symbols show results for the solution derived from the group of 32 listeners. Open symbols show results from the analysis of two subgroups of these listeners, as described in the text. Results for Group 1 and 2 are shown by the open triangles and boxes, respectively.

the x , y , and z axes, respectively. Examination of the projection of the stimuli onto the x/y plane shows three clusters of stimuli. One cluster, with relatively negative dimension 1 weights and positive dimension 2 weights, contains the tones, both steady (filled circles) and frequency modulated (open circles). A second cluster, defined by weights near zero on dimension 1 and negative dimension 2 weights, contains the harmonic complexes (filled squares), including those containing high, low, and wide formant frequencies drawn both from the 110- and the 200-Hz fundamental. A third cluster, defined by positive weights on both dimension 1 and 2, contains the noises, both steady state (filled triangles) and amplitude modulated (open triangles).

The result of the multiple regression analysis of stimulus dimension weights with acoustic parameters is shown by the solid circles in Fig. 3. Results for dimensions 1–3 are shown in separate panels. Plotted are the absolute values of the obtained standardized regression coefficients for each acoustic parameter and each dimension. The absolute value of the coefficients was chosen for display to facilitate visualization of correlation magnitudes. Sign differences merely indicated a positive or negative correlation while it is the strength of the correlation that is most useful for interpretation of the dimensions. The horizontal line at 0.20 on each panel indicates the level above which the coefficients were statistically significant.

Dimension 1 of the three-dimensional (3-D) solution accounted for 19.3% of the variance in the data. The multiple correlation coefficient (R) for dimension 1 weights and acoustic parameters was 0.98. The largest coefficient was observed for periodicity (1.08).³ The very periodic tonal signals and the very aperiodic noises are represented by the

most extreme positions along dimension 1 while the complexes lie between the two. There was also a small contribution of the number of spectral peaks (0.39). Dimension 2 accounted for only slightly less of the variance in the data than did dimension 1, 17.7%. Results of the regression analysis showed an R of 0.98 with the largest coefficient observed for the number of spectral peaks (1.01). The tones and noises with single spectral peaks received positive dimension 2 weights while the multi-peaked complexes received negative weights. There was also a very small contribution of frequency (0.27). Dimension 3 accounted for less variance in the data than was observed for either dimension 1 or 2, 11.6%. The regression analysis produced an R of 0.96 with the largest coefficient obtained for average frequency (0.87). Lower frequency stimuli are placed at positive positions along dimension 3 and stimuli with higher-frequency representations are placed at much more negative values. Periodicity also showed a small but significant (0.40) contribution to dimension 3 weights.

Thus the MDS solution suggested that the listeners may have compared the stimuli by classifying them into one of three groups formed on the basis of similarities in both spectral and temporal features. Most significant in this classification were dimension 1 and 2 weights which correlated most highly with periodicity, as was coded in the number of components per critical band, and the spectral shape of the signals, coded as the number of spectral peaks. A small contribution to the ratings was made by absolute frequency which was reflected largely in its correlation with dimension 3 weights. Coding of frequency appears, from examination of the MDS space, to reflect a continuous rating of average frequency, performed both across and within the clusters formed in the two-dimensional space.

B. Individual differences

As was observed in Fig. 1, the variance accounted for in the MDS solution varied with listener age. This suggests that the group solution provided a better fit to the data of the older listeners than the younger. The pattern of weights in the individual data were therefore examined. Figure 4 shows the individual listener weights for each of the dimensions created in the group space. These weights indicate the extent to which the individual's similarity judgments appeared to rely on the perceptual dimensions described by the group space. The data for the adults, 10- and 7-year-olds are shown by the filled circles, open triangles, and filled squares, respectively. Note that the adults and most of the 10-year-old children showed relatively high weights for all 3 dimensions while the 7-year-olds and some of the 10-year-olds did not.

The MDS solution defines a three-dimensional space that best fits the data of all listeners, extracting features that are in common for the listeners. Our concern was that the two groups of listeners (those with high weights and those with low), while using the same acoustic features to compare the stimuli, may have used the information differently. We therefore performed separate MDS analyses on the data from the two groups of listeners defined by similarities in their patterns of weights in the group solution. A hierarchical cluster analysis was used to assign group membership for the

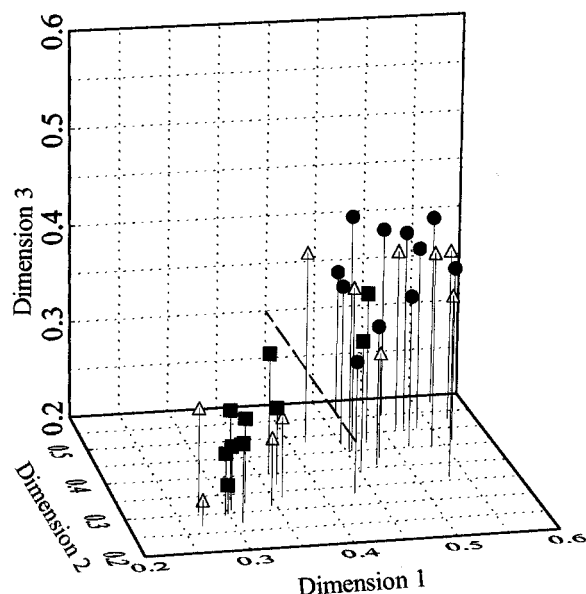


FIG. 4. Relative weight assigned to dimensions 1, 2, and 3 for individual adults (filled circles), 10-year-olds (open triangles), and 7-year-olds (filled squares).

subsequent analyses. Submitted to the analysis were individual weights for dimensions 1–3. The division between groups formed at the level of two clusters is shown by the dashed line in Fig. 4. Group 1 contains predominantly, but not exclusively, the older listeners. These individuals showed relatively strong weights on all 3 dimensions. Group 2 included mostly younger listeners with relatively low-dimension weights for the group solution.

1. Group 1 listeners

Group 1 included the data from all 11 of the adults, seven of the eleven 10-year-olds, and two of the ten 7-year-olds. The derived MDS solution is shown in Fig. 5. Symbols are as stated for Fig. 2. Results of the multiple regression analysis between dimension weights and acoustic parameters are shown by the open triangles in Fig. 3, as reported for the larger group analysis.

The solution accounted for 62.8% of the variance in the ratings and is similar to that for the larger group of listeners. Three clusters of stimuli were formed including the noises, tones, and harmonic complexes. Dimension 1 of the solution accounted for 34.4% of the variance in the ratings. The R for dimension 1 weights and acoustic features was 0.97. The strongest contributions came from the number of spectral peaks (0.58) and periodicity (0.54). Unlike the group solution in which the largest contributor was periodicity, with only a small contribution made by spectral shape, the coefficients for both features and dimension 1 of this subgroup were of relatively equal magnitude. As can be seen in Fig. 5, placement of stimuli along dimension 1 reflects an integration of both features. Lowest values were given to the aperiodic, single-peaked noises, near zero values were assigned to the periodic, single-peaked tones, and positive values were assigned to the periodic, multiple-peaked complexes. Dimension 2 of the solution accounted for much less variance in the

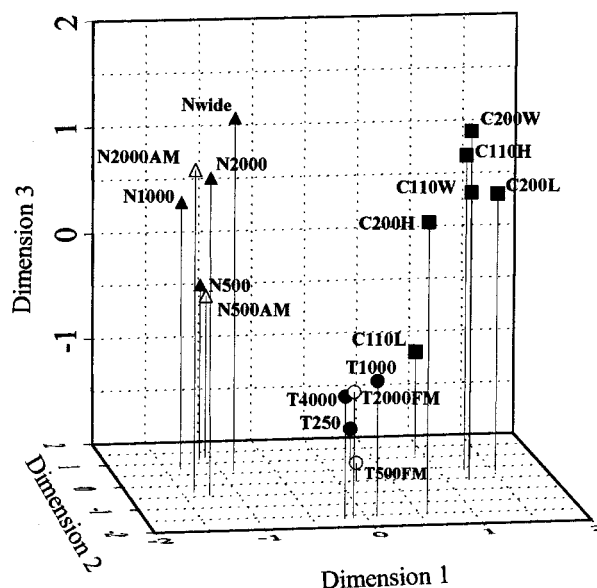


FIG. 5. The three-dimensional space derived for subgroup 1 which included predominantly the older listeners. Symbols are as in Fig. 2.

solution than did dimension 1 (16.7%). Weights correlated strongly with multiple acoustic features, including frequency (0.81), periodicity (0.61), and spectral peaks (0.52). R was 0.93. The correlation with frequency can be seen within each cluster in which stimuli with lower frequencies are given higher weights than are stimuli with higher frequencies. The contribution of periodicity and spectral peaks to dimension weights can be seen in the organization of the clusters themselves along dimension 2. There is a tendency for more negative weights for the more periodic, single-peaked tones, but the noises and complexes, in spite of differences in both number of spectral peaks and periodicity, are generally assigned similar but more positive weights. Dimension 3 accounted for very little variance in the solution (9%). Like dimension 2, it showed significant correlations with the same three parameters, periodicity (0.79), spectral peaks (0.74), and frequency (0.41). R was 0.93. Noises and complexes, despite their differences, are given higher dimension 3 weights than the tones. Within each cluster the stimuli with higher frequency are given more positive weights than those with lower frequency.

Thus the solution shows a strong classification response based primarily on the integration of periodicity and spectral shape information which was reflected in all dimension weights. Dimension 2 and 3 weights also included frequency information.

2. Group 2 listeners

Group 2 included predominantly younger listeners: eight of the ten 7-year-olds, only four of the eleven 10-year-olds, and none of the adults. The solution is shown in Fig. 6 and the results of the multiple regression analysis between weights and acoustic features is shown by the open squares in Fig. 3. The solution accounted for 30.7% of the variance in the data. Similar groups of stimuli were formed within the space as for group 1 listeners but the location and formation

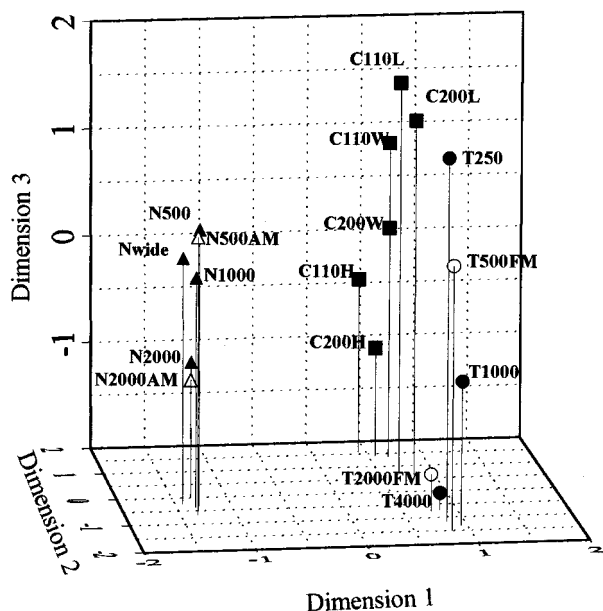


FIG. 6. The three-dimensional space derived for subgroup 2 listeners which included predominantly the younger listeners. Symbols are as in Fig. 2.

of the groups was somewhat different. Also, each dimension accounted for relatively similar amounts of variance in the total solution. This is in contrast to the solution from group 1 in which the contribution of each dimension decreased by approximately half, with progression from dimension 1 to 3.

Dimension 1 accounted for 11.4% of the variance in the data, representing about 1/3 of the total variance accounted for. R for dimension 1 weights and acoustic features was 0.98 with a significant contribution observed only for periodicity (0.99). The aperiodic noises were placed at negative dimension 1 values of very similar magnitude and the stimuli with a more periodic temporal fine structure, the tones and complexes, were placed at very similar positive values. While dimension 1 for the older listeners reflected a parsing of stimuli into three groups, the solution for these younger listeners included only two, failing to separate the tones from the complexes. Along dimension 2, which accounted for roughly the same amount of variance in the data as dimension 1 (10.4%), the stimuli are organized in a more continuous fashion than was observed for the older listeners. The multiple regression showed that the largest contribution to dimension 2 weights was made by the number of spectral peaks in the signals (1.04), but there were very small contributions of periodicity (0.39) and frequency (0.21) as well. There is a tendency for the multiple-peaked complexes to be given more positive weights than the single-peaked noises and tones, yet, within the range occupied by these single peaked stimuli, the weightings differ based on periodicity. Along dimension 3, which accounted for 8.9% of the variance in the data, the stimuli are organized, within clusters, according to average frequency (0.92). Lower-frequency stimuli are given higher dimension 3 weights than are higher-frequency stimuli. The contributions of spectral shape (0.54) and periodicity (0.24) are also significant. Multiple-peaks stimuli tend to have higher weights than single peaked and, on average, the periodic stimuli have higher weights

than the aperiodic but the variance is quite large.

Thus group 2 listeners appeared to form similar clusters of stimuli as were observed in the solution derived for the Group 1 listeners. However, while the clustering was represented fully in dimension 1 weights for the Group 1 listeners who weighted spectral shape and periodicity equally, clustering for the Group 2 listeners required both dimension 1 and 2. These listeners appeared to rely most heavily on periodicity information in making their similarity judgments. Periodicity was a significant contributor to all three dimensions and yet, in the dimension for which periodicity was the most significant contributor, dimension 1, classification was more coarse than that observed for group 1 listeners, reflecting only the encoding of the presence or absence of a periodic temporal fine structure. Spectral shape was a significant contributor to dimensions 2 and 3, and frequency accounted for a small amount of the variance in the data, correlating significantly only with dimension 3, which itself accounted for very little variance in the overall solution.

From these subgroup analyses it can be seen that the solution obtained for the full group of listeners extracted features that were common for both subgroups of listeners. Thus, for example, dimension 1 showed a strong correlation with periodicity reflecting that both subgroups of listeners showed high salience for periodicity information. Yet the large group analysis obscured the observations that for some listeners, particularly the older ones, spectral shape was equally as salient and appeared to be integrated with periodicity information.

III. DISCUSSION

This study evaluated the processing of complex sounds by young children and adults using a multidimensional scaling analysis of similarity ratings for a set of nonspeech sounds that varied both spectrally and temporally. The goal was to describe potential age-related differences in feature salience which may be predictive of how children organize their encoding of unfamiliar sounds.

A. Reliability

Many studies have been reported using multidimensional scaling with older listeners, but its use with children is less common. One question that therefore arises concerns the extent to which children produced reliable estimates of similarity. This is particularly critical given that the proportion of variance in the data accounted for by the MDS solution showed a tendency to decrease with decreasing age. Variance unaccounted for in a solution may arise from inconsistent judgments (e.g., Howard, 1977). Because only single judgments of similarity were obtained for each stimulus pair, the potential for evaluating test-retest reliability in the data was limited. However, inspection of the similarity ratings for "like" pairs and comparisons with fits to random data shed some light on the topic.

All listeners were required to judge the perceived similarity of identical stimulus pairs. These judgments were not used by INDSCAL in deriving the multidimensional space but are useful for evaluating the validity of similarity estimates in instances of equality. For even the youngest listen-

ers, dissimilarity judgments for “like” pairs were at or very close to 0.0, suggesting that all listeners grasped the concept of similarity, in its extreme. Their ability to judge lesser degrees of similarity cannot be evaluated directly as there is no right or wrong answer in a paired comparisons procedure. But the results of a series of Monte Carlo simulations suggested that the proportion of variance accounted for by the solution to the obtained data exceeded that expected for fits to random data. When 100 sets of 32 matrices containing random data were fitted with a 3-D scaling solution, the proportion of variance accounted for was only 0.058, well below that obtained in this study. When the number of matrices was reduced to 20 or 12, as in our group 1 and 2 subgroups, the proportion of variance accounted for in fitting random data remained very low, 0.070 and 0.091, for sets of 20 and 12 matrices, respectively, arguing for the presence of structure in the data. Together, evaluation of ratings for “like” pairs and comparisons with fits to random data suggest that even the younger listeners were producing similarity estimates that reflected some degree of validity.

B. Relative salience of acoustic features

A major question in this study was whether the relative salience of various acoustic features might vary with age and, if so, which features may be most salient to children. An additional question was how would acoustic information be used in the processing of these unfamiliar sounds. Previous studies of complex sound processing with adult listeners suggested that both temporal and spectral features are encoded, with individual differences in relative feature salience (Christensen and Humes, 1996; Howard and Silverman, 1976; Howard, 1977). This study also suggested encoding of spectral and temporal information, not only by adults, but also by children. Yet age-related differences in relative feature weights were not apparent in the solution to the large group of listeners. Instead, the trend was for generally lower weights across all dimensions with decreasing age. But inspection of solutions to subgroups of listeners suggested that listeners of different ages may have used the acoustic information differently in assigning similarity estimates.

1. Temporal features

Periodicity appeared to play an important role in determining listeners’ judgments of similarity for the stimuli used in this experiment. Dimension 1 of the large group solution correlated most significantly with periodicity as was reflected in the number of components per critical band. Placement of stimuli along dimension 1 suggested encoding not only of temporal fine structure, but also envelope fluctuations produced by the combination of multiple tones that were not fully resolved. Listeners are typically able to resolve only the lower three to four harmonics of a stimulus with higher harmonics generally unresolved and therefore producing a roughness sensation which is observable in slow fluctuations of the temporal envelope. Roughness will be perceived whenever component tones fall within 10%–20% of the center frequency of a critical band (e.g., Pickles, 1988). The harmonic complexes used in this study all contained harmonics at least as high as the sixth and multiple components

likely fell within a critical band, producing a roughness sensation that could have been used to differentiate the harmonic complexes from the pure tones. Dimension 1 weights showed a significant correlation with the number of components per critical band, but not with the total number of components overall, suggesting roughness as the relevant cue.

The assessment of both temporal fine structure and envelope fluctuations is likely a first stage in auditory temporal analyses and physiological evidence exists to suggest that these cues are processed separately in the auditory system (Langner, 1992). It is therefore possible that use of these cues may mature independently. Group 2 listeners, who tended to be mostly younger children, separated the signals along dimension 1 according to the presence or absence of a periodic temporal fine structure only while the solution to the larger group separated stimuli according to differences in the temporal envelope as well. These differences may be related to age-related differences in the processing of modulation. Hall and Grose (1994) measured the temporal modulation transfer function in 4- to 10-year-old children and found that while the time constant of the auditory periphery may be mature in children as young as 4 yr, suggesting the potential for encoding the temporal fine structure of a signal, the depth of modulation required for detection was higher in children as old as 9 to 10 yr. It may be that the depth of the envelope fluctuations in the harmonic complexes in this study was either below or very near modulation detection thresholds for the younger listeners potentially reducing the salience of roughness cues.

The very low-frequency modulation produced in the AM noises and FM tones did not appear in the three-dimensional solution for any group of listeners. The modulated signals appeared in the scaling solutions in positions close to the signals from which they had been derived (pure tones for the FM signals, and narrow-band noises for the AM signals). The signals were very brief producing relatively few cycles of modulation which may have reduced salience for this feature. It is possible that higher dimensions, not extracted in these solutions, may have reflected modulation.

2. Spectral features

Spectral information, including both the pattern of energy distribution across frequency and absolute frequency, was also important in the processing of these signals. Spectral shape varied little across the stimulus set and consisted always of relatively flat patterns of excitation in either single- or multiple-frequency regions, providing a rather coarse examination of shape processing. But the solutions from all groups of listeners reflected the differences in shape. The only age-related differences was that older listeners (group 2) integrated spectral shape information equally with periodicity while for younger listeners (group 1) spectral shape was coded in a separate dimension and was not integrated with periodicity. Similarly, absolute frequency information was encoded and represented in dimension 2 weights for the older listeners and in dimension 3 weights for the younger listeners. It therefore was given greater weight by the older listeners than the younger but its relative contribution did not differ across ages. Thus as predicted by the

tonotopic organization of the entire auditory system, spectral information, regarding both spectral shape and absolute frequency, was an important feature in processing for listeners of all ages.

C. Feature integration and classification

The stimulus set used in this study was relatively large and stimuli varied along several dimensions, potentially placing significant demands on the information processing resources of the listeners. One strategy for reducing these demands is to categorize the stimuli based upon an integration of perceptual features (e.g., Sjöberg and Thorslund, 1979; Torgerson, 1965; Tversky, 1977). When stimuli are categorized, the derived space will reflect not only the perceptual encoding of the features as they correlate with the dimensions of the space, but also the more cognitive structure of the formed categories. The placement of stimuli in the 3-D space created in this experiment suggests that our listeners may have used such a categorically based similarity rating. Of interest then are potential age-related differences in category formation that may be suggested by the solutions to the data from the two subgroups of listeners.

The solution to the data from the older listeners of group 1 showed a very tight classification of stimuli according to both spectral and temporal features. This classification is very clear in the projection of stimuli in the 2-D space but can also be observed quite readily in the distribution of stimuli according to dimension 1 weights alone. This, combined with the relatively equal weighting of spectral and temporal cues in all dimensions, may suggest that these older listeners evaluated similarity based on category membership and that those categories were constituted from an integration of information from both spectral and temporal domains. Examination of stimulus weights in higher-order dimensions suggested that within each category the stimuli were ordered according to similarities and differences in absolute frequency but that absolute frequency was not used in the definition of the categories.

Group 2 listeners, who tended to be younger, produced similar data that resulted in a multidimensional space in which the clustering of stimuli was less clear. Dimension 1 did not represent an integration of spectral and temporal information but instead showed the formation of two relatively narrow categories that correlated with temporal fine structure only. Examination of positioning along dimension 2, which correlated with spectral shape, suggested a potentially more continuous evaluation, as did the organization along dimension 3. Thus category formation did not appear to reflect the degree of information integration as was observed for the older listeners.

In a recent study (Allen and Nelles, 1996), preschool and young school-aged children were asked to perform a sample discrimination task in which sequences of tonal components were drawn from one of two distributions that differed in mean frequency. The listener's task was to select the sequence drawn from the distribution with the higher mean frequency. Adults' performance improved as the number of components sampled increased, suggesting that they were able to integrate information to reduce uncertainty. Yet chil-

dren's performance did not begin to improve with increases in the number of components sampled until the children were at least seven years of age. Less adultlike integration of information in the current study by the younger children may be consistent with these findings.

D. Stimulus set effects in feature salience

Many acoustic features were measured as an aide to interpretation of the solutions derived in this study but only a few of them appeared to play a significant role in the similarity ratings. This does not imply that the listeners were insensitive to features that did not correlate with the dimensions in the derived solutions or that the features that were encoded would be important for the processing of all sets of sounds. The stimulus set itself likely exerted a strong influence on the pattern of results. It has been argued that feature salience in a similarity rating task will be influenced by listeners' selective attention to that feature and that attention will be motivated by the potential of the feature to be used for classification (Tversky, 1977; Nosofsky, 1986). Features that show large degrees of differences across the stimulus set or that are distributed categorically will have higher feature salience than features that vary less or are distributed continuously.

In the current stimulus set, the stimuli were distributed categorically according to at least two parameters. In the temporal domain, stimuli either had a periodic fine structure and flat temporal envelope (tones); a periodic fine structure and periodic temporal envelope (complexes); or were aperiodic (noise bands). Spectrally, stimuli had either single (tones and noise bands) or multiple (complexes) peaks. This combination of features therefore provided large amounts of inherent structure in the stimulus set. Thus it is not surprising that both features were highly salient in the resultant solutions. In contrast, frequency varied continuously across the data set, potentially reducing its use in classification and its subsequent salience.

E. Summary

This study used a multidimensional scaling procedure to evaluate the encoding of a set of brief duration, unfamiliar, complex sounds by school-aged children and adults. Stimuli were pure tones, both steady state and frequency modulated, noise bands, both steady state and amplitude modulated, and harmonic complexes that varied in fundamental frequency and number and location of harmonics. Results showed that listeners of different ages attended to similar acoustic features but that their use of these features varied with age. Adults and many children, mostly older, appeared to classify stimuli based on analysis of temporal and spectral structure, coded within dimension 1 weights. Dimensions 2 and 3 continued with that encoding and included information regarding absolute frequency as well. Younger children were more likely to classify the stimuli based upon temporal fine structure, encoding that information in dimension 1 weights. Information regarding spectral shape and frequency were encoded and reflected in dimension 2 and 3 weights but was not used for classification.

ACKNOWLEDGMENTS

The authors would like to express their sincere thanks to James Nelles and Carolyn Spriet who assisted in data collection, Janik Joire for technical support, and the listeners who participated in the study. We would also like to thank the National Science and Engineering Research Council and the Atkinson Charitable Foundation for financial support and Dr. Lincoln Gray, Dr. Doris Kistler, and Dr. Frederic Wightman for their comments on an earlier version of this manuscript.

¹Several other acoustic measures were made including bandwidth, high- and low-frequency cutoff, modulation rate, and total number of frequency components. Parameters that were highly correlated with one another or that showed no significant contribution to dimension weights were excluded from the final analysis.

²A Monte Carlo simulation was run in which 100 3-D MDS solutions were derived for sets of 32 matrices that contained random data. The mean and standard deviation in obtained *R*-squared values were 0.058 and 0.006, respectively.

³Suppression effects (see Cohen and Cohen, 1975) were sometimes observed in the multiple regression because the bivariate correlation between periodicity and spectral peaks was nonzero (-0.481). This resulted in coefficients that were greater than 1 for the variable with the higher bivariate correlation with the dimension weight. However, in no instance did the suppression alter the overall pattern of results.

- Allen, P., and Nelles, J. (1996). "Information integration in children," *J. Acoust. Soc. Am.* **100**, 1043–1051.
- Christensen, L. A., and Humes, L. E. (1996). "Identification of multidimensional complex sounds having parallel dimension structure," *J. Acoust. Soc. Am.* **99**, 2307–2315.
- Cohen, J., and Cohen, J. (1975). *Applied Multiple Regression/Correlation Analysis for the Behavioral Sciences* (Erlbaum, Hillsdale, NJ).
- Hall, J. W., and Grose, J. H. (1994). "Development of temporal resolution in children as measured by the temporal modulation transfer function," *J. Acoust. Soc. Am.* **96**, 150–154.
- Howard, J. H. (1977). "Psychophysical structure of eight complex underwater sounds," *J. Acoust. Soc. Am.* **62**, 149–156.
- Howard, J. H., and Silverman, E. B. (1976). "A multidimensional scaling analysis of 16 complex sounds," *Percept. Psychophys.* **19**, 193–200.
- Kuhl, P. (1992). "Psychoacoustics and speech perception: Internal standards, perceptual anchors, and prototypes," in *Developmental Psychoacoustics*, edited by L. Werner and E. Rubel (American Psychological Association, Washington, DC), pp. 293–332.
- Langner, G. (1992). "Periodicity coding in the auditory system," *Hearing Res.* **60**, 115–142.
- Nosofsky, R. M. (1986). "Attention, similarity, and the identification-categorization relationship," *J. Exp. Psychol.: General* **115**, 39–57.
- Pickles, J. O. (1988). *An Introduction to the Physiology of Hearing* (Academic, New York).
- Sjöberg, L., and Thorslund, C. (1979). "A classificatory theory of similarity," *Psychol. Res.* **40**, 223–247.
- Torgerson, W. S. (1965). "Multidimensional scaling of similarity," *Psychometrika* **30**, 379–393.
- Tversky, A. (1977). "Features of similarity," *Psychol. Rev.* **84**, 327–352.

Discrimination of changes in the spectral shape of noise bands

Niek J. Versfeld

Institute for Perception Research, P.O. Box 513, 5600 MB Eindhoven, The Netherlands

(Received 31 January 1996; revised 24 June 1997; accepted 30 June 1997)

Discrimination experiments were performed for a change in the spectral shape of noise bands. The subject's task was to discriminate noise bands with a positive spectral slope from those with a negative spectral slope. Thresholds were measured at several bandwidths and center frequencies, as well as for several noise samples. Experiments were performed while roving the overall intensity. At a fixed center frequency of 1 kHz, sensitivity was best for bandwidths of 3–6 semitones (ST). At larger bandwidths, thresholds increased only slowly. At a fixed bandwidth of 1 ST, threshold hardly changed as a function of the center frequency. At a fixed bandwidth of 58 Hz, threshold was lowest near 500–1000 Hz. Model calculations show that the EWAIF model [Feth, *Percept. Psychophys.* **15**, 375–378 (1974)] can account for the present results if the signal's bandwidth does not exceed 1 ST. The IWAIF model [Anantharaman *et al.*, *J. Acoust. Soc. Am.* **94**, 723–729 (1993)] can account for the present results only if the signal's bandwidth is smaller than 1 ST but larger than about 25 Hz. Results obtained with broadband signals could be described only qualitatively with the multichannel model [Durlach *et al.*, *J. Acoust. Soc. Am.* **80**, 63–72 (1986)]. Then, the model needs the assumption that either the output of the different frequency bands cannot be optimally combined, or that only two bands are used in the discrimination process. The present results are compared with those obtained with two-tone complexes measured under identical conditions [Versfeld and Houtsma, *J. Acoust. Soc. Am.* **98**, 807–816 (1995)]. © 1997 Acoustical Society of America. [S0001-4966(97)04110-6]

PACS numbers: 43.66.Ba, 43.66.Fe [JWH]

INTRODUCTION

According to the concept of the critical band, the degree to which broadband signals can be discriminated (or are rated dissimilar) is related solely to the sum of differences in activity across a number of frequency bands (Plomp, 1976; Florentine and Buus, 1981). In this view frequency bands that remain unaltered upon switching from one signal to another do not contribute in the discrimination process. However, over the last decade many experiments have been reported clearly showing that the mere presence of energy in frequency bands remote from a target band may contribute to the detectability of a change in that target band. Thus, it was argued, the auditory system is able to make across-band comparisons and discriminates on the basis of a change in the spectral shape. The processing of the signal in this particular manner is often referred to as “profile analysis” (see Green, 1988, for a review).

Up to now most profile-analysis experiments have been performed with tonal stimuli; only a few papers address spectral-shape discrimination with noiselike stimuli (e.g., Farrar *et al.*, 1987; Moore *et al.*, 1989). To our knowledge, no papers exist that discuss the relation between tonal and noiselike stimuli. The present paper is an attempt to do so, and reports on experiments with noiselike stimuli. The results are compared with those presented in an earlier paper (Versfeld and Houtsma, 1995) containing data obtained with two-tone complexes, measured under identical conditions, and in one experiment even utilizing the same subjects.

Three experiments are reported, all dealing with the discriminability between two noise bands that are identical except for the sign of their spectral slope. These types of signal

have been chosen not only because they are closely related to the two-tone complexes and multitone complexes in previous experiments (Versfeld and Houtsma, 1991, 1995), but also because the results may be relevant for speech research since some speaker characteristics seem to be related to the spectral slope of speech sounds (Li and Pastore, 1995).

In the first experiment, discriminability for a change in the spectral slope is measured at several bandwidths; in the second experiment, the influence of different noise samples on threshold is investigated; in the last experiment, threshold is measured at several center frequencies where the bandwidth has been kept fixed to either 1 semitone (ST) or 58 Hz. Similarities and differences between the present data set and the one in Versfeld and Houtsma (1995) will be discussed in terms of models that have been used previously in describing profile-analysis data.

I. GENERAL PROCEDURE

A. Stimuli

Noise bands were generated digitally (at 16 bits resolution and a sample frequency of 10 kHz) by summation of sinusoids, spaced 1 Hz apart, of the appropriate amplitude and starting phase. For each experimental condition, that is, fixed bandwidth and center frequency, the starting phase was chosen randomly once, and subsequently preserved from trial to trial. The spectral slope was linear on a log-amplitude, log-frequency scale, and its magnitude was expressed as the level difference ΔL between the two spectral edges. The signal bandwidth was expressed in semitones (ST). As an example, the spectrum of a noise band with a bandwidth of 24 ST and a (positive) spectral slope of 8 dB/

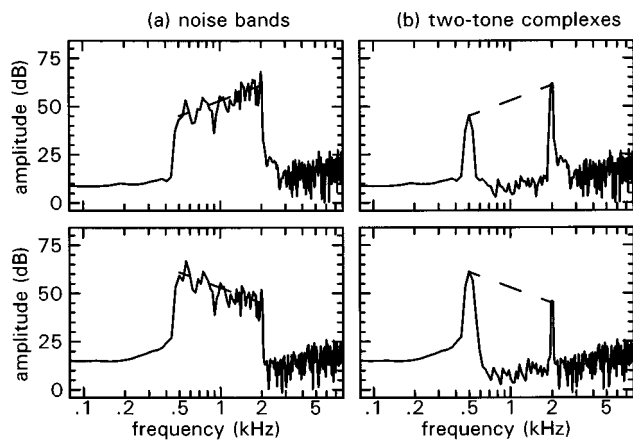


FIG. 1. Example of the amplitude spectra of stimuli similar to those used in the experiments: (a) noise bands and (b) two-tone complexes. All stimuli have a bandwidth of 24 ST ($f_1 = 500$ Hz, $f_2 = 2000$ Hz) and a level difference ΔL of 16 dB. The dashed lines indicate the imposed spectral slopes.

oct is plotted in the upper panel of Fig. 1(a). The lower panel of Fig. 1(a) displays the same noise band but with a negative spectral slope. The dashed line indicates the imposed spectral slope. Thus, the level difference ΔL between the edge components was 16 dB. Because the starting phase was kept fixed, departures from the imposed spectral slope were the same for both spectra (which is clearly illustrated in Fig. 1). Consequently, the difference between the two spectral shapes always is a straight line with a slope equal to twice the imposed spectral slope. In other words, the spectral change was well defined.

The two panels in Fig. 1(b) display the spectrum of a two-tone complex, also with a bandwidth of 24 ST and a level difference ΔL of 16 dB. Versfeld and Houtsma (1995) reported experiments with these two-tone signals, and results reported in the present paper will be compared with theirs.

B. Procedure

The experimental procedure used throughout the experiments reported in this paper was identical to that adopted by Versfeld and Houtsma (1995). For that reason, the general procedure is described here only briefly.

In an adaptive, three-interval oddity task, the subject's task was to discriminate a noise band with a positive spectral slope from a noise band with a negative spectral slope [see Fig. 1(a)], by indicating which interval out of three contained the stimulus with the odd spectral slope. The magnitude of the spectral slope was varied adaptively and the adaptive rules were chosen such that most trials were conducted near the 70.7%-correct point on the psychometric function. For the present paradigm, the level difference ΔL to obtain this percentage of correct responses corresponds to a sensitivity d' of 2.13 (Versfeld *et al.*, 1996). In order to facilitate comparison with data in the literature, thresholds ΔL reported in the present paper correspond to $d' = 1$. A linear relationship between d' and ΔL was assumed, i.e., $d' \propto \Delta L$. Then, reported thresholds are obtained simply by dividing the originally obtained thresholds by 2.13. According to Versfeld

et al. (1996), a sensitivity $d' = 1$ corresponds to a 44.7% correct score.

Each of the three sound bursts in one trial lasted 400 ms (including a 20-ms linear onset and a 20-ms linear offset ramp). The bursts were separated by 100-ms silent intervals. There was no response-time limit, and visual feedback was provided after each response.

The absolute threshold for the stimulus (with a flat spectral envelope) was determined for each subject and each bandwidth in advance. In the actual experiment, the subjects were prevented from using loudness cues by randomly varying the overall level of *each sound burst* between 30 and 50 dB sensation level. It was verified both by measurements and computer simulations that, with the 20-dB roving level, discrimination thresholds based on loudness cues only could not produce thresholds lower than about 7 dB. Under practically all conditions the obtained thresholds were lower, indicating that loudness cues were indeed not utilized.

II. EXPERIMENT I: EFFECT OF BANDWIDTH

A. Stimuli and subjects

Stimuli were noise bands centered at 1 kHz, that is, the center frequency f_c , defined as the geometric mean of the two edge frequencies, was kept fixed at 1 kHz. The bandwidth was set at 0.5, 1, 2, 3, 6, 12, or 24 ST.

Six subjects (five university students, who were paid for their services, and the author) participated in this experiment. Some of them were experienced listeners. Before the actual data collection of a condition, subjects were trained until the threshold had stabilized. Next, per subject and per condition 750 trial responses were collected, resulting in a standard error of the threshold estimate of 3.6%.

B. Results

The results of experiment I are displayed in Fig. 2, where thresholds ΔL (dB) have been plotted as filled symbols as a function of the bandwidth (ST). The data have been averaged across subjects, and bars indicate the standard deviation between subjects. The data for the individual subjects can be found in Table I.

For all subjects discriminability was best at a bandwidth of 3–6 ST. Starting from the minimum, threshold only slowly increases with increasing bandwidth. With decreasing bandwidth, however, threshold below 1 ST shows a sharp upturn.

With narrow-band signals subjects reported that the perceptual cue was a change in pitch. With increasing bandwidth the pitch cue gradually changed into a timbre cue: noise bands with a positive spectral slope were perceived as sounding sharper (as opposed to dull) than bands with a negative slope. The reported percept is consistent with the findings of von Bismarck (1974), who studied the verbal attributes of steady-state signals with different spectral shapes.

Both threshold behavior and reported perceptual cues suggest that, around a bandwidth of 3 ST, a transition occurs. Since 3 ST is about the width of the critical band, it might be that for bandwidths smaller than 3 ST, within-channel cues

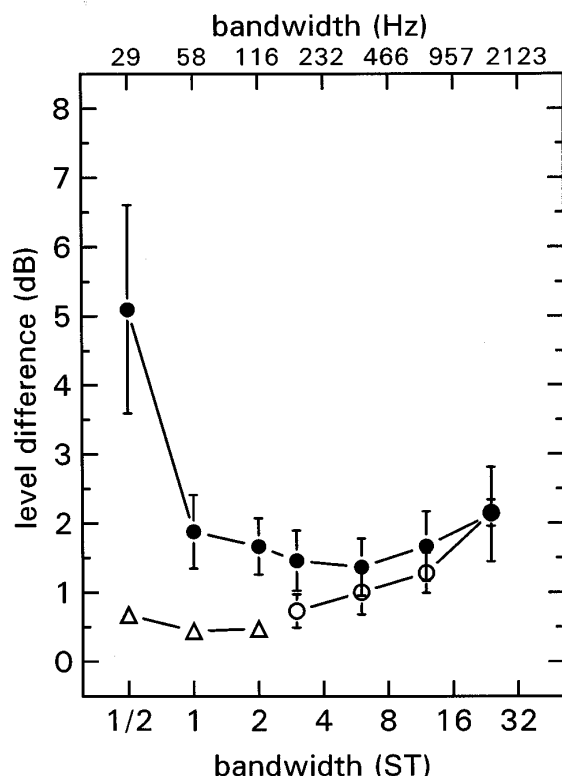


FIG. 2. Results of experiment I. Thresholds ΔL (dB) are plotted as a function of bandwidth (ST). Results are averaged across subjects. Filled and open symbols indicate thresholds obtained with noise bands and two-tone complexes, respectively. Error bars indicate the standard deviation between subjects. The signal bandwidth expressed in Hertz is given at the top of the figure.

dominate in the discrimination process, whereas across-channel cues dominate for larger bandwidths.

The open circles in Fig. 2 are the averaged data of experiment I of Versfeld and Houtsma (1995), who, for four subjects, measured thresholds ΔL for a relative change in the amplitudes of two-tone complexes [see Fig. 1(b)]. Error bars

indicate the standard deviation between subjects. The triangles denote thresholds for the same type of two-tone complexes and were taken from Versfeld (1993). These data have been collected under very similar conditions to the present experiment. Only one subject (the author) participated, but the data are in good agreement with earlier results of Versfeld and Houtsma (1991). With two-tone complexes, too, a minimum occurs, although this is not too apparent from Fig. 2. The results of Versfeld and Houtsma (1991) and Versfeld (1993) show that this minimum is near 1 ST, and thus is situated at a smaller bandwidth than with noise bands. With two-tone complexes, too, threshold increases sharply with decreasing bandwidth. The upturn, however, starts at bandwidths below 0.5 ST (cf. Versfeld and Houtsma, 1991). Except for a bandwidth of 24 ST, thresholds for two-tone complexes are smaller than those for noise bands.

III. EXPERIMENT II: EFFECT OF NOISE SAMPLE

Since in the previous experiment the starting phase was preserved from trial to trial, in other words, only one noise sample per bandwidth was taken, no information was obtained on the variability of the threshold as a function of the noise sample. To get an impression of the variability, in this experiment thresholds for different noise samples were measured.

A. Stimuli

Stimuli were noise bands centered at 1 kHz and had a bandwidth of 1 ST. Five noise samples were taken at random and labeled A–E. They differed from each other only with respect to the starting phase of the components. Sample A was used in experiment I. Thresholds were measured using six subjects (those who participated in experiment I). At least 450 trials were taken per subject and per condition, resulting in a standard error of the threshold of 4.5% or less.

TABLE I. Results of experiment I. Thresholds ΔL (dB), ΔE_{WAIF} (Hz), and ΔI_{WAIF} (Hz) for several bandwidths (ST).

Bandwidth	Subject 1			Subject 2			Subject 3			Subject 4		
	ΔL	ΔE_{WAIF}	ΔI_{WAIF}	ΔL	ΔE_{WAIF}	ΔI_{WAIF}	ΔL	ΔE_{WAIF}	ΔI_{WAIF}	ΔL	ΔE_{WAIF}	ΔI_{WAIF}
0.5	5.87	6.18	6.32	4.99	5.34	5.41	4.18	4.59	4.56	7.35	7.47	7.78
1	1.74	5.52	3.85	1.58	4.94	3.49	2.21	7.15	4.88	2.31	7.47	5.10
2	1.58	8.94	6.99	1.48	8.39	6.55	1.73	9.75	7.65	2.08	11.55	9.19
3	1.48	10.29	9.83	1.15	7.53	7.64	1.53	10.67	10.16	1.92	13.32	12.73
6	1.27	18.17	16.88	1.26	17.98	16.75	1.60	22.68	21.25	1.27	18.20	16.88
12	1.59	47.14	42.38	1.79	52.43	47.68	1.87	54.75	49.80	1.34	40.21	35.74
24	2.13	109.21	114.91	2.17	111.37	117.05	2.48	127.31	133.65	1.67	86.38	90.20
Bandwidth	Subject 5			Subject 6			Average					
	ΔL	ΔE_{WAIF}	ΔI_{WAIF}	ΔL	ΔE_{WAIF}	ΔI_{WAIF}	ΔL	ΔE_{WAIF}	ΔI_{WAIF}			
0.5	2.90	3.32	3.19	5.29	5.62	5.72	5.10	5.42	5.53			
1	1.01	2.77	2.24	2.42	7.83	5.34	1.88	5.95	4.15			
2	1.01	5.66	4.47	2.11	11.68	9.32	1.66	9.33	7.34			
3	0.78	5.51	5.19	1.89	13.11	12.53	1.40	10.1	9.30			
6	0.77	11.12	10.25	2.01	28.47	26.67	1.36	19.4	18.08			
12	0.98	29.61	26.15	2.44	70.82	64.85	1.67	49.2	44.50			
24	1.16	61.74	62.72	3.15	160.86	169.32	2.13	109.0	114.91			

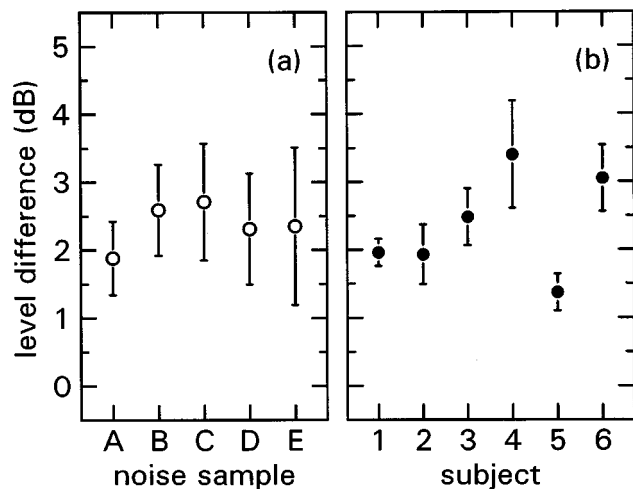


FIG. 3. Results of experiment II. Thresholds ΔL (dB) are plotted for (a) the noise samples A–E and (b) the six subjects #1–#6. Error bars indicate the standard deviation between subjects (a) and noise samples (b).

B. Results

Figure 3 displays the results of experiment II, where thresholds have been plotted as a function of the five noise samples [Fig. 3(a)], and as a function of the six subjects [Fig. 3(b)]. The individual data are given in Table II. Error bars denote the standard deviations between subjects [Fig. 3(a)] or between samples [Fig. 3(b)].

Standard deviations in Fig. 3(a) are about equal. For all subjects thresholds for sample A were lower than those for samples B–D. Similarly, thresholds for sample D were lower than those for sample C. Standard deviations in Fig. 3(b) are generally much smaller than those in Fig. 3(a) and roughly increase with increasing threshold. This clearly indicates that the variance in the data is caused mainly by between-subject differences: for a single subject, thresholds for the five noise samples are very similar. A 6 (subjects) \times 5 (samples) analy-

sis of variance (ANOVA) confirmed this: the differences between subjects accounted for 72% of the total variance (which is highly significant: $F[5,20]=19.2$, $p<0.0001$), whereas the differences between the noise samples accounted for only 8% of the total variance (which is also significant: $F[4,20]=4.1$, $p<0.05$). There was no significant interaction between subject and noise sample.

In conclusion, the results show that between-subject variability is much larger than between-sample variability, the latter being small enough to ensure that the shape of the threshold curve in Fig. 2 is preserved.

IV. EXPERIMENT III: EFFECT OF CENTER FREQUENCY

The results of experiment I showed that the use of noise bands instead of two-tone complexes (i.e., addition of frequency components) increased threshold and caused a shift in the bandwidth for which a minimum is reached from 1 to 3–6 ST. In experiment III it is investigated how threshold for a change in the sign of the spectral slope of noise bands behaves when it is measured as a function of center frequency f_c . The obtained results can be compared to those obtained by Versfeld and Houtsma (1995) with two-tone complexes.

A. Stimuli

In complete analogy with Versfeld and Houtsma (1995), the bandwidth was fixed at 58 Hz for one condition, whereas it was fixed at 1 ST in the other condition. Center frequencies for both conditions were 125, 250, 500, 1000, 2000, and 4000 Hz. At $f_c=1$ kHz a bandwidth of 58 Hz corresponds to a bandwidth of 1 ST. Yet, at this center frequency thresholds were measured for two different noise samples, both different from those used in experiments I and II.

Two subjects participated. They had also participated in the two previous experiments [subjects #2 and #5 (the au-

TABLE II. Results of experiment II. Thresholds ΔL (dB), ΔE_{WAIF} (Hz), and ΔI_{WAIF} (Hz) for several noise samples.

Sample	Subject 1			Subject 2			Subject 3			Subject 4		
	ΔL	ΔE_{WAIF}	ΔI_{WAIF}	ΔL	ΔE_{WAIF}	ΔI_{WAIF}	ΔL	ΔE_{WAIF}	ΔI_{WAIF}	ΔL	ΔE_{WAIF}	ΔI_{WAIF}
A	1.74	5.52	3.85	1.58	4.94	3.49	2.21	7.15	4.88	2.31	7.47	5.10
B	2.27	5.49	5.01	2.47	5.95	5.45	2.59	6.01	5.71	3.68	8.51	8.06
C	1.99	3.69	4.40	2.33	4.28	5.14	3.07	5.63	6.75	3.51	6.45	7.70
D	1.93	3.84	4.26	1.76	3.52	3.89	2.58	5.03	5.69	3.06	5.85	6.73
E	1.86	4.15	4.11	1.51	3.41	3.34	1.97	4.37	4.35	4.45	9.69	9.70
Average	1.96	4.54	4.33	1.93	4.42	4.26	2.48	5.64	5.48	3.40	7.59	7.46
s.d.	0.20	0.90	0.43	0.44	1.06	0.97	0.42	1.05	0.91	0.79	1.55	1.70
Sample	Subject 5			Subject 6			Average					
	ΔL	ΔE_{WAIF}	ΔI_{WAIF}	ΔL	ΔE_{WAIF}	ΔI_{WAIF}	ΔL	ΔE_{WAIF}	ΔI_{WAIF}			
A	1.01	2.77	2.24	2.42	7.83	5.34	1.88	5.95	4.15			
B	1.65	3.95	3.65	2.87	6.84	6.32	2.59	6.13	5.71			
C	1.61	3.02	3.56	3.72	6.83	8.15	2.71	4.98	5.97			
D	1.22	2.49	2.70	3.34	6.32	7.33	2.31	4.51	5.10			
E	1.38	3.13	3.05	2.92	6.35	6.42	2.35	5.18	5.18			
Average	1.37	3.07	3.04	3.05	6.83	6.71	2.37	5.35	5.22			
s.d.	0.27	0.55	0.59	0.49	0.61	1.07	0.32	0.68	0.70			

thor) in experiments I and II], as well as in the experiments with two-tone complexes (Versfeld and Houtsma, 1995). Although the number of subjects is small, results from previous experiments show that their behavior is similar to that of the other subjects in the group. Their performance, however, is somewhat better, which is probably due to greater experience. Per subject and per condition 600 trials were taken, resulting in a standard error of the threshold estimate of about 4%.

B. Results

Figure 4 displays, with filled symbols, the individual thresholds for two subjects for noise bands with a 58-Hz [Fig. 4(a)] or a 1-ST [Fig. 4(b)] bandwidth. Different symbols indicate the different subjects (subject #2 is indicated with circles; #5 with triangles). Also plotted (with open symbols) are thresholds for changes in the amplitude of two-tone complexes, as obtained by Versfeld and Houtsma (1995). The secondary axis at the top of the figure indicates the corresponding bandwidth of the noise band in semitones [if the bandwidth was kept fixed at 58 Hz, Fig. 4(a)], or in Hertz [if the bandwidth was 1 ST, Fig. 4(b)]. As noted before, the stimuli in the two conditions at $f_c = 1$ kHz had the same bandwidth, but were different samples. Nevertheless, thresholds are very similar [cf. thresholds at $f_c = 1$ kHz in Fig. 4(a) with those at $f_c = 1$ kHz in Fig. 4(b)]. They are also close to those obtained in experiment II. This supports the conclusion of experiment II that, at least for these two subjects, threshold hardly depends on noise sample.

With noise bands, threshold for the 58-Hz condition [Fig. 4(a)] decreases at first as center frequency increases. At 500 Hz, a minimum of about 1.2 dB is reached. Further increase of the center frequency causes the threshold to increase, with a sharp upturn between 2000 and 4000 Hz. Thresholds for two-tone complexes show a similar trend, albeit that their absolute values are smaller and that the location of the minimum is situated near 1 kHz. Furthermore, it appears that subject #2 is able to maintain low thresholds even at 4 kHz. For both the noise bands and the two-tone complexes, the largest between-subject difference is situated at $f_c = 4$ kHz.

Threshold for noise bands in the 1-ST condition [Fig. 4(b)] seems to be independent of center frequency for subject #2. Threshold behavior for subject #5 tends to show a bowl-like shape. The same is the case for the thresholds obtained with two-tone complexes. The between-subject differences are strikingly similar for thresholds obtained with noise bands and two-tone complexes, which is visible in both panels of Fig. 4.

V. MODEL PREDICTIONS

So far, no model has been successful in accounting for all profile-analysis data. Instead, the belief is that discriminability is based on different perceptual cues, or a combination of more cues (Richards and Nekrich, 1993), depending on the type of spectral change and on the signal's bandwidth. The use of a specific cue even can be manipulated by the instruction to the subject (Southworth and Berg, 1995). A

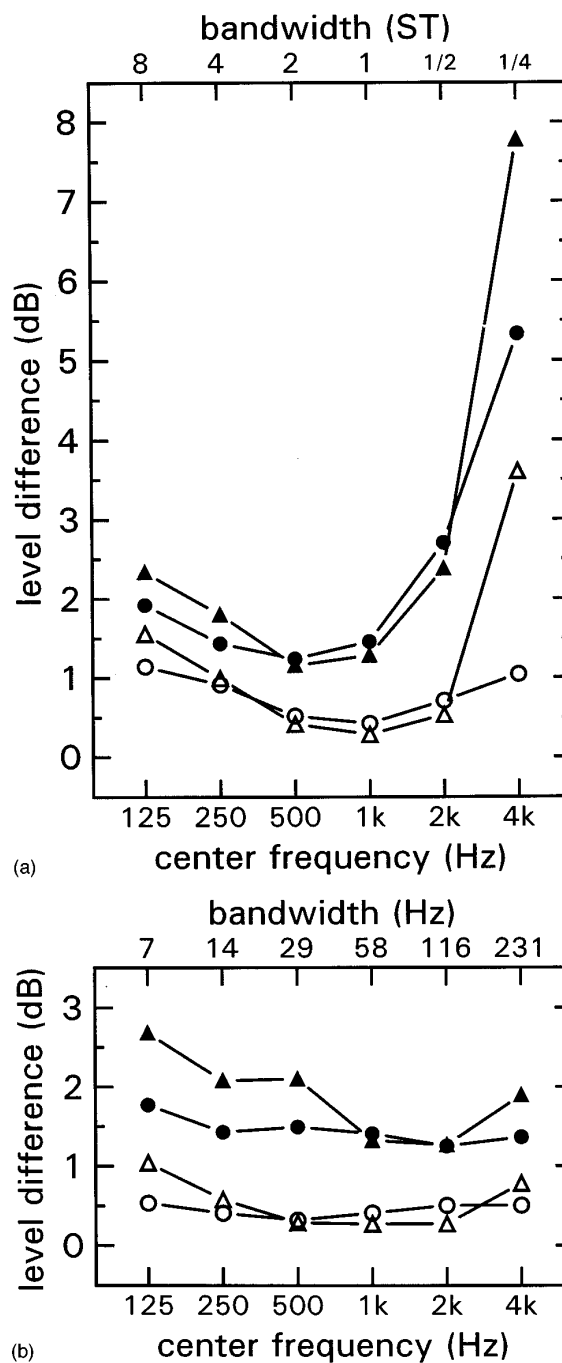


FIG. 4. Results of experiment III. Thresholds ΔL (dB) for signals with a bandwidth of 58 Hz (a) and 1 ST (b) are plotted as a function of center frequency. Filled and open symbols indicate thresholds obtained with noise bands and two-tone complexes, respectively. Different symbols indicate the individual subjects.

change in pitch may be the perceptual cue if the spectral shape changes in an asymmetrical manner (Green *et al.*, 1992), which is, for example, the case with the stimuli in the present experiment. A change in some of the characteristics of the temporal envelope may also provide the listener with a potential cue (Richards, 1992; Kidd, Jr. *et al.*, 1993). Lastly, if the signal's bandwidth is large enough in comparison with the critical bandwidth, changes in the spectral envelope can be detected by comparing the output of the different bands in a relative fashion—profile analysis in the true sense of the

word. Whether one or more of these cues could potentially be utilized by the subjects in the present experiment, and whether this behavior can be described with a model, will be discussed in this section.

A. Pitch cues

As noted earlier, subjects reported using pitch cues when discriminating between a (narrow) noise band with a positive and one with a negative spectral slope. A model that might describe the data is the EWAIF model (Feth, 1974). Another model, closely related to the EWAIF model is the IWAIF model (Anantharaman *et al.*, 1993; Dai, 1993).

1. The EWAIF model

The EWAIF model states that a change in the spectral shape is perceived as a change in pitch. The mapping of the signal's spectrum onto the pitch axis is done by calculation of the envelope-weighted average of the instantaneous frequency, or EWAIF,

$$\text{EWAIF} = \frac{\int_0^T E(t) f(t) dt}{\int_0^T E(t) dt}. \quad (1)$$

In this equation $E(t)$ and $f(t)$ are the (temporal) envelope function and the instantaneous frequency, respectively. Averaging is done over some time interval T . The EWAIF is expressed in Hertz. If, for two signals, the difference in the associated values for EWAIF increases, the discriminability between these two signals increases. Feth (1974) proposed the EWAIF model to describe threshold behavior of complementary pairs of two-tone complexes, similar to those depicted in Fig. 1(b). The model could account for thresholds obtained with narrow-band signals, i.e., signals that fell within one critical band. In order for the auditory system to calculate some quantity like EWAIF, the instantaneous frequency and the temporal envelope need to be extracted from the signal as a whole, thus it is to be assumed that the model breaks down as soon as the signal bandwidth exceeds the critical bandwidth. Just this assumption led Feth and O'Malley (1977) to make use of two-tone complexes to measure the width of the critical band.

For all bandwidths, noise samples and values of ΔL used in experiments I–III the instantaneous frequency and envelope function were extracted from the sampled waveform by means of a discrete Hilbert transformation (Feth and Stover, 1987; Kidd, Jr. *et al.*, 1991). $E(t)$ and $f(t)$ were calculated for the noise-band pairs with a positive and negative spectral slope and were subsequently used to calculate ΔEWAIF , the difference in EWAIF between a noise band with a positive slope and one with a negative slope. The integration time T was set to 400 ms, the duration of the stimulus. The relation between ΔEWAIF and ΔL is plotted in Fig. 5(a) as solid lines for the bandwidths used in experiment I, and in Fig. 5(b) for the five noise samples from experiment II. Note that the ordinate in panel (a) is logarithmic, whereas (for clarity) it is linear in panel (b). Figure 5 shows that for narrow-bandwidth signals, relationships are not entirely monotonic. This probably is due to errors intro-

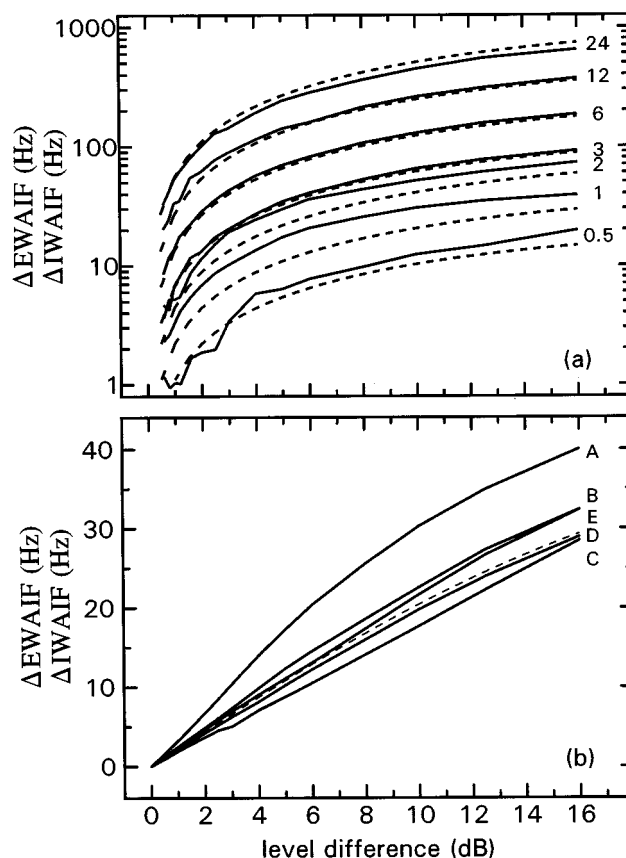


FIG. 5. Relationship between ΔL and ΔEWAIF (solid lines) or ΔIWAIF (dashed lines). (a) Relationship for the different bandwidths used in experiment I. (b) Relationship for the different noise samples used in experiment II. Note that the ordinate in panel (a) is logarithmic, whereas it is linear in panel (b).

duced by the calculation of the instantaneous frequency, involving a differentiation which is a highly noise-sensitive process (cf. Anantharaman *et al.*, 1993). The functions for the different bandwidths are, apart from the irregularities, rather similar and seem to lie parallel. Indeed, if ΔEWAIF is normalized with respect to the stimulus bandwidth (i.e., $\Delta\text{EWAIF}/[f_2 - f_1]$), the different curves practically coincide. Relationships between ΔL and ΔEWAIF were also determined for the stimuli from experiment III, but they are not shown in a figure, because they hardly provide additional information (as will be shown below).

With the aid of Fig. 5, thresholds ΔL were next converted to thresholds ΔEWAIF . Tables I–III yield, for the individual subjects, thresholds ΔL (dB) and the corresponding ΔEWAIF thresholds (Hz) for experiments I–III, respectively.

Since ΔEWAIF is a measure for discriminability, it is expected to be constant at threshold. The values in Table I for experiment I show that this might be true for bandwidths of 0.5 and 1 ST, but certainly not for larger bandwidths: ΔEWAIF rapidly increases with increasing bandwidth.

The EWAIF model is phase dependent and might therefore account for the differences in threshold with experiment II. Ideally, ΔEWAIF for the five noise samples should be the same for the individual subject. The calculations presented in Table II show that this seems not to be the case. An ANOVA

TABLE III. Results of experiment III. Thresholds ΔL (dB), Δ_{EWAIF} (Hz), Δ_{IWAIF} (Hz), and ΔF (Hz) as a function of center frequency f_c (Hz), for Subjects #2 and #5. Stimulus bandwidth was either 58 Hz or 1 ST.

Bandwidth	f_c	Subject #2				Subject #5			
		ΔL	Δ_{EWAIF}	Δ_{IWAIF}	ΔF	ΔL	Δ_{EWAIF}	Δ_{IWAIF}	ΔF
58 Hz	125	1.92	3.94	4.25	1.04	2.33	4.74	5.14	1.82
58 Hz	250	1.43	3.08	3.17	2.05	1.80	4.11	3.98	2.06
58 Hz	500	1.24	4.12	2.75	1.39	1.16	3.88	2.57	1.22
58 Hz	1000	1.45	3.27	3.21	2.49	1.28	2.87	2.83	1.72
58 Hz	2000	2.70	5.85	5.95	4.29	2.38	5.10	5.25	3.75
58 Hz	4000	5.33	10.23	11.53	7.43	7.78	13.44	16.39	15.87
1 ST	125	1.77	1.07	0.49	1.04	2.68	1.47	0.74	1.82
1 ST	250	1.43	1.37	0.79	2.05	2.08	1.97	1.15	2.06
1 ST	500	1.49	1.56	1.65	1.39	2.10	2.27	2.32	1.22
1 ST	1000	1.41	3.44	3.12	2.49	1.32	3.24	2.92	1.72
1 ST	2000	1.25	4.64	5.53	4.29	1.27	4.69	5.62	3.75
1 ST	4000	1.36	12.47	12.04	7.43	1.89	17.28	16.71	15.87

shows that the differences between the noise samples hardly decrease upon converting thresholds ΔL to Δ_{EWAIF} : the different samples still account for 7.6% of the variance ($F[4,20]=4.1$, $p<0.05$), whereas the between-subject variability does not decrease significantly, indicating that the differences between the thresholds of the different samples cannot be explained in terms of differences in EWAIF.

Table III yields, for two subjects, the thresholds Δ_{EWAIF} for noise bands as a function of the center frequency f_c obtained from the results of experiment III. Thresholds were measured for a bandwidth of 58 Hz or 1 ST. It can be shown that in calculating the difference in EWAIF between two signals, all terms containing f_c are cancelled out. Thus, two pairs of noise bands that differ with respect to center frequency but have the same bandwidth if expressed in Hertz, and the same starting phase, have identical values for Δ_{EWAIF} . The ΔL greatly varies with center frequency [cf. Fig. 4(a)], thus Δ_{EWAIF} also greatly varies with center frequency. Because spectral changes are transformed to pitch changes, it is likely that Δ_{EWAIF} varies as a function of center frequency in much the same way as does the pure-tone frequency difference limen, ΔF . Consequently, $\Delta_{EWAIF}/\Delta F$ rather than Δ_{EWAIF} is expected to be constant at threshold. Versfeld and Houtsma (1995) measured such pure-tone jnd's for the present two subjects (#2 and #5). Thresholds ΔF , based on 600 trials, are given in Table III. Figure 6(a) displays, with filled symbols, and for the two individual subjects, the ratio $\Delta_{EWAIF}/\Delta F$ for noise bands with a 58-Hz bandwidth as a function of the center frequency f_c . The two subjects are indicated with different symbols. Figure 6(b) does the same for 1-ST bandwidth noise bands. The standard error is about 6%. Open symbols in Fig. 6 represent model calculations with two-tone complexes for the same two subjects. If the perceived change in pitch, described by the change in EWAIF, was the discrimination cue, this ratio should be close to unity. Figure 6(b) shows that, on average, this is true for the noise bands in the 1-ST condition. For the noise bands with a bandwidth of 58 Hz [Fig. 6(a)], the ratio $\Delta_{EWAIF}/\Delta F$ is systematically larger than unity for center frequencies below 1000 Hz but is otherwise similar to ratios of the 1-ST condition. Values for $\Delta_{EWAIF}/\Delta F$ are systemati-

cally larger for two-tone complexes than for noise bands, despite the fact that thresholds ΔL are much smaller for two-tone complexes than for noise bands. Two phenomena may account for these results. First, since the EWAIF model is a within-channel model, it might be that the pitch cue cannot be used in full because the signals are partially resolved by the auditory periphery (which is true for the 58-Hz signals at the lowest center frequencies in terms of equivalent rectangular bandwidths). Second, signals like noise bands or even two-tone complexes are more complex than pure tones, and may need a greater pitch difference to obtain threshold. This may cause the systematic increase in the value of $\Delta_{EWAIF}/\Delta F$.

A perhaps more direct test of the EWAIF model, that is, minus the assumption that Δ_{EWAIF} is coupled to ΔF , is to calculate at each center frequency the ratio Δ_{EWAIF} (58 Hz)/ Δ_{EWAIF} (1 ST), which ideally should be unity. For noise bands, this ratio has been plotted with filled symbols as a function of the center frequency in Fig. 7(a). The open symbols were obtained with two-tone complexes. The different

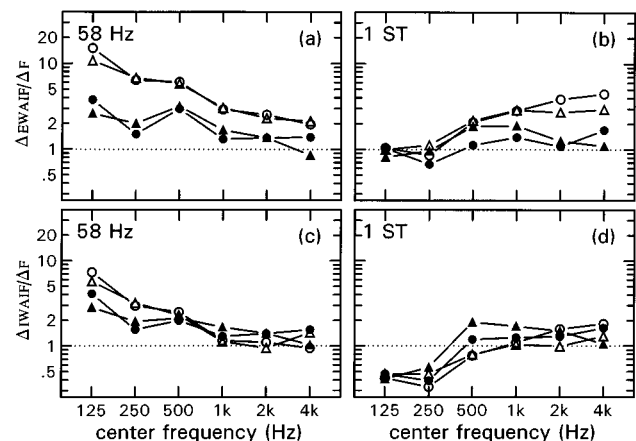


FIG. 6. Ratio $\Delta_{EWAIF}/\Delta F$ (a),(b) and $\Delta_{IWAIF}/\Delta F$ (c),(d) at threshold as a function of center frequency for the results of experiment III. Signal bandwidth was 58 Hz (a),(c) or 1 ST (b),(d). Filled and open symbols indicate results obtained with noise bands and two-tone complexes, respectively. The individual subjects are indicated by different symbols.

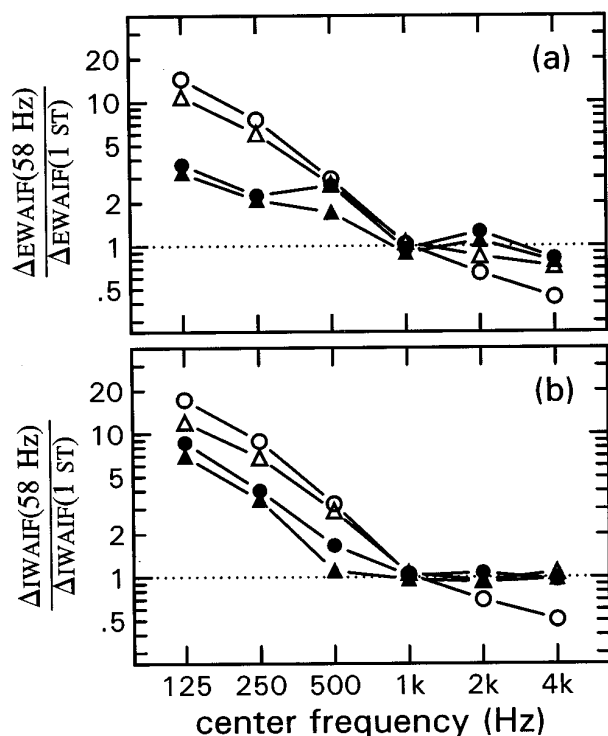


FIG. 7. Ratio $\Delta\text{EWAIF}(58\text{ Hz})/\Delta\text{EWAIF}(1\text{ ST})$ (a) and $\Delta\text{IWAIF}(58\text{ Hz})/\Delta\text{IWAIF}(1\text{ ST})$ (b) at threshold as a function of center frequency for the results of experiment III. Filled and open symbols indicate results obtained with noise bands and two-tone complexes, respectively. The individual subjects are indicated by different symbols.

symbols indicate the two subjects. Figure 7(a) shows that, especially for center frequencies below 1000 Hz, the ratio $\Delta\text{EWAIF}(58\text{ Hz})/\Delta\text{EWAIF}(1\text{ ST})$, deviates from unity for both noise bands and two-tone complexes.

The results in Figs. 6(a), 6(b), and 7(a) thus indicate that the EWAIF model can account for the data obtained with two-tone complexes and noise bands if the signal's bandwidth is smaller than about 1 ST, that is, the EWAIF model can probably account for the results only if the signal's bandwidth is small in comparison with the critical bandwidth, i.e., only if the signal is completely unresolved. The relative complexity of the noise bands and two-tone complexes in comparison with the pure tones probably does play a role, causing the ratio $\Delta\text{EWAIF}/\Delta F$ to be systematically larger than unity.

2. The IWAIF model

A model closely related to, and in fact derived from, the EWAIF model is the so-called IWAIF model (acronym for intensity-weighted average of the instantaneous frequency; Anantharaman *et al.*, 1993; Dai, 1993). The IWAIF of a signal is given by

$$\text{IWAIF} = \frac{\int_0^T E^2(t) f(t) dt}{\int_0^T E^2(t) dt}. \quad (2)$$

Anantharaman *et al.* (1993) have shown that the IWAIF is in fact equal to

$$\text{IWAIF} = \frac{\int_0^\infty |S(f)|^2 f df}{\int_0^\infty |S(f)|^2 df}, \quad (3)$$

where $S(f)$ is the Fourier transform of the (time) signal. Thus, IWAIF represents the "center of gravity" of the energy spectral density function. Although the EWAIF and the IWAIF models in origin are closely related, Eq. (3) shows that neither instantaneous frequency nor envelope function are required to determine IWAIF, thus in principle obviating the restriction that it can be applied only to signals that cannot be resolved by the auditory system. Moreover, the EWAIF model operates in the temporal domain, whereas the IWAIF model can be viewed as one operating in the spectral domain. Also, the EWAIF model is phase sensitive, whereas the IWAIF model essentially is not. Thus, although the EWAIF and the IWAIF model calculations probably will resemble each other, the interpretation can be essentially different.

Departing from Eq. (3), the difference in IWAIF between a noise band with a positive and a negative spectral slope can be derived analytically, and can be written as (see the Appendix)

$$\Delta\text{IWAIF} = \frac{1+m}{2+m} \left[\frac{f_2^2 \alpha^2 - f_1^2}{f_2 \alpha^2 - f_1} \right] - \frac{1-m}{2-m} \left[\frac{f_2^2 - \alpha^2 f_1^2}{f_2 - \alpha^2 f_1} \right], \quad (4)$$

where $\alpha = 10^{\Delta L/20}$, $m = 2 \ln(\alpha)/\ln(f_2/f_1)$ (where the logarithm has base e), f_1 and f_2 are the lower and upper frequency component of the signal, respectively, α represents the amplitude ratio of the two edge components of the noise bands, and m is simply related to the spectral slope S (in dB/oct) by $S \approx 3m$. One property of Eq. (4) is that ΔIWAIF (just like ΔEWAIF) does not depend on the absolute frequencies, but rather on the frequency difference $f_2 - f_1$, and thus is independent of center frequency. Moreover, it can be shown that $\Delta\text{IWAIF}/(f_2 - f_1)$ is virtually independent of the signal bandwidths used in the present experiments. Thus, for the present noise bands $\Delta\text{IWAIF}/(f_2 - f_1)$ is only dependent on ΔL .

Again, the relationship between ΔL and ΔIWAIF has been calculated for the noise samples of the experiments, using Eq. (4). Their relationship is represented in Fig. 5 by dashed lines. Figure 5(a) shows that the shape of the functions is similar for the EWAIF model and the IWAIF model, but their relative position is sometimes different. Figure 5(b) shows only one curve for the IWAIF model (or stated differently: the five curves coincide), since the model is phase independent.

Thresholds ΔIWAIF for noise bands were determined, and are given in Tables I–III for experiments I–III, respectively. The calculations using the data of experiment I show that ΔIWAIF decreases with decreasing bandwidth but levels off at a bandwidth of about 1 ST. With narrower bandwidths, ΔIWAIF seems to increase again. Computations further indicate that the IWAIF model cannot account for the differences in threshold for the various noise samples in experiment II, simply because the model is phase independent. An ANOVA shows that the different samples still account for 8.1% of the variance ($F[4,20] = 4.2$, $p < 0.05$).

Figure 6(c) and (d) displays the ratio $\Delta I_{W A I F} / \Delta F$ for the 58-Hz condition and the 1-ST condition of experiment III, respectively. Again, open and filled symbols denote calculations with two-tone complexes and noise bands, respectively. The figures show that for low center frequencies none of the four conditions yields ratios that correspond to the frequency difference limen. For center frequencies of 500 Hz and above, the ratios obtained with noise bands are slightly higher than unity. Thus, the change in the center of gravity needs to be somewhat larger than the change in frequency of a pure tone. The reason for this is similar to that mentioned with the EWAIF model. The finding that ratios $\Delta I_{W A I F} / \Delta F$ are remote from unity in Fig. 6(d) at the lower center frequencies may be due to the extremely narrow signal bandwidths of these conditions (7 or 14 Hz). The fluctuations in the signal then are very slow, resulting in an unstable center of gravity, hence a poor estimate of the IWAIF. Figure 7(b) shows the ratio $\Delta I_{W A I F}$ (58 Hz)/ $\Delta I_{W A I F}$ (1 ST) for the two subjects. With noise bands, this ratio is very close to unity for conditions at higher center frequencies.

In conclusion, the results seem to indicate that the IWAIF model does well at narrow bandwidths (up to 1 ST), but only if the signal's bandwidth is large enough to ensure a stable estimate of the IWAIF.

B. Models acting on the temporal envelope

Several investigators have found that with narrow-band stimuli a change in the temporal envelope caused by a change in the spectral profile can be a valid cue (Richards, 1992; Berg *et al.*, 1992; Kidd, Jr. *et al.*, 1993; Green *et al.*, 1992). The PSE model proposed by Green *et al.* (1992) seems to be particularly successful. In this model differences in the power spectrum of the (temporal) envelope (PSE) between the two stimulus alternatives are used to predict threshold behavior.

One special property of the two-tone complexes used by Versfeld and Houtsma (1995) was that the temporal envelope was identical for both stimulus alternatives. This means that no envelope cues could be used. There is reason to believe that, with the noise bands of the present experiment, envelope cues play a very minor role. First of all, our subjects reported that they utilized pitch as a cue, not "roughness" or "smoothness" (verbal attributes that are typical for describing differences in the temporal envelope). Second, previous research (Green *et al.*, 1992) has shown that changes in the temporal envelope are mainly utilized when the spectral change is symmetric, that is, when it does not produce a shift in the "center of gravity" of the power spectrum, hence causing pitch cues to be weak or even absent. (An example of such a symmetric change is an increment in amplitude in the middle component of a linearly spaced multitone complex.) The present noise bands do not satisfy this condition. Third, it can be shown that the power spectrum of the temporal envelope of two noise bands with opposite spectral slopes are identical, but only if the spectral slope is linear on a linear-amplitude, linear-frequency scale. With the present stimuli this is approximately true for shallow spectral slopes. This does not mean that there cannot be any envelope cues, but indicates that the PSE model is bound to fail, since

it will predict no differences in PSE between the two stimulus alternatives. Last, the temporal envelope for signal pairs is identical not only for $\Delta L = 0$, but also for very large values of ΔL , since the signals then reduce to a sinusoid with frequency equal to either f_1 or f_2 : the temporal envelope is flat in both cases.

Yet, to verify a possible effect of change in the temporal envelope the PSE was calculated for the signals of the present experiment, and relations were determined between ΔL and ΔPSE (as described by Kidd *et al.*, 1993) for each of the experimental conditions. The calculations mostly resulted in capricious functions, indicating that the differences in PSE between the two stimulus alternatives were very small and probably due to discretisation errors. More importantly, ΔPSE was not constant at threshold.

In retrospect, we could have avoided temporal-envelope cues by using noise bands with a linear spectral slope on a linear-frequency and linear-amplitude scale. In that case, it can be shown that the power spectrum of the envelope remains unaltered when changing from a positive to a negative spectral slope. However, at the time we thought a slope in dB/oct to be perceptually more relevant.

C. Multichannel models

In multichannel models as developed by Plomp (1976), Durlach *et al.* (1986), and Ito (1990), a broadband signal is filtered by a set of (nonoverlapping) bandpass filters. The amount of activity is measured in each band. Thus the output of the model is a crude spectral representation of the signal. The frequency bands are usually identified with critical bands. Thus, if the entire signal falls well within a critical band (as is the case with most of the stimuli from experiments II and III), the model is reduced to a single-channel model, which can only register differences in overall level. Since the overall level was varied randomly between and within trials, a single-channel model will fail to describe the data for narrow-band signals. It therefore seems sensible to apply a multichannel model only to those results of experiment I that were obtained with broadband signals. Though the theoretical background of the multichannel model is fairly straightforward, a precise quantitative implementation is difficult since assumptions have to be made about, for instance, the auditory filter shape. Also, only few data points from experiment I can be used to fit the model. Nevertheless, some qualitative statements can be made. If the output of the different critical bands can be compared (correlated) with one another [which is an essential feature in the model of Durlach *et al.* (1986)], thresholds are not or only slightly influenced by a roving overall level, and the listener is able to achieve the low thresholds of experiment I. If the output of the different bands could be perfectly compared, one would expect an ever-decreasing threshold with increasing bandwidth, since widening of the bandwidth, while keeping the level difference fixed, results in a large spectral change. (In the log-amplitude, log-frequency domain, the spectral difference between two noise bands with opposite slopes is a straight line with a slope twice the imposed spectral slope, hence the difference is linearly related to the bandwidth.) The results, however, show that the opposite is true. This

indicates, in terms of the model, that the capability of across-channel comparison is not perfect. It is possible that the ability to compare the output of different channels decreases as bands become more remote [a phenomenon similar to that observed with two-tone complexes (Versfeld, 1993)]. Also, it may be that not all, but only a limited number of channels are monitored. This possibility is discussed below.

VI. DISCUSSION

Noise bands with spectral slopes that change in sign can be discriminated while a roving intensity level is present. Changes are best perceived when the signal's bandwidth is about 3 ST. The presence of such a minimum suggests that probably more than one discrimination mechanism exists. Subjects report that, with the present signals, changes in the spectral shape of narrow-band stimuli are detected by pitch shifts, whereas spectral-shape differences in broadband stimuli are discriminated by comparison of timbre (dullness versus sharpness). Details of the noise sample seem to have little influence on threshold.

Although mere differences in the temporal envelope may provide the listener with a cue, it has been made plausible that for the current set of conditions these cues are unreliable and probably even absent.

Calculations with the EWAIF and the IWAIF model indicate, first of all, that these models cannot account for the present results if the relative bandwidth of the noise bands exceeds the value of 1 ST. In other words: the signals need to be well within the critical bandwidth. The EWAIF model as proposed by Feth (1974) can account for all data if the signal's bandwidth is 1 ST or less, but the IWAIF model fails to account with conditions at lower center frequencies. A possible explanation for this failure is that the auditory system has difficulties in estimating the center of gravity (i.e., calculating IWAIF) with these slowly fluctuating signals, since they are only 7 and 14 Hz wide at center frequencies of 125 and 250 Hz, respectively. This also explains the slight increase in Δ IWAIF for the 0.5-ST results in experiment I (29-Hz bandwidth). Multichannel EWAIF or IWAIF models (where EWAIF or IWAIF is calculated after the signal has been filtered into separate frequency channels) may account for signals with bandwidths that are larger than 1 ST (Anantharaman *et al.*, 1991).

In conclusion, the EWAIF model can account for the present results if the signal is well within the critical bandwidth and its bandwidth does not exceed 1 ST. This restriction holds also for the IWAIF model. Additionally, the IWAIF model can account for the data only if the signal's bandwidth is larger than about 20–30 Hz.

Threshold shifts due to different phase relations (experiment II) could not be explained by the EWAIF or the IWAIF model. The ANOVAs showed that the different noise samples gave a just-significant effect, so phase probably does play only a minor role in discrimination. This conclusion is supported by Dai *et al.* (1996), who showed that their pitch matches to narrow-band complex signals could be accounted for by the (phase-independent) IWAIF model much better than by the EWAIF model. Of course, one can never rule out the possibility that the signals are filtered in the auditory

system [both with respect to the amplitude (Berg *et al.*, 1992) and phase], such that the EWAIF or IWAIF of the resulting signal indeed can explain the obtained thresholds.

The choice of stimuli in the present experiments was based on earlier experiments with two-tone complexes (Versfeld and Houtsma, 1995). In addition to the results of the present experiments, Figs. 2, 4, 6, and 7 also display the (calculations based on) results obtained with two-tone complexes. Threshold behavior for the two stimulus types show differences with respect to absolute values (thresholds are always higher for noise bands than for two-tone complexes), and the position of the minimum (about 3 ST for noise bands and 1 ST for two-tone complexes). On the other hand, the between-subject differences for noise bands and two-tone complexes (cf. Fig. 4) are strikingly similar. In the following the relationship between the two stimulus types is discussed.

The multichannel model of Durlach *et al.* (1986) can only be applied to signals with a bandwidth that exceeds the critical band. Then, it can qualitatively account for the results of experiment I, but only if some kind of nonoptimal processing takes place. Figure 2 showed that for bandwidths beyond about 3 ST, threshold increases for both noise bands and two-tone complexes. Although these data points provide scarce evidence, it seems that *mainly two regions of the spectrum* are used in the decision process. This idea, already proposed by Bernstein *et al.* (1987), is in fact a very simple but interesting version of the multichannel model. With a roving intensity level the minimum number of channels which have to be observed in order to detect a change in the spectral shape is two. With two-tone complexes it is obvious that only two channels are involved. With large-bandwidth noise bands most information is present at the edges of the noise band. It is possible that only the information in the edge bands is used. Alternatively, the higher thresholds for noise bands, as well as the shift in the position of the minimum (3–6 ST for noise bands and 1 ST for two-tone complexes) suggests that, with noise bands, not the edges, but rather some intermediate bands are monitored. Unfortunately, the present data cannot give conclusive evidence for this hypothesis.

In the literature, Bernstein *et al.* (1987) reported several experiments where the threshold for detecting an increase in amplitude of only one component in a 21-component spectrum was compared with thresholds for detecting broadband spectral changes (e.g., flat versus tilted spectra). They found that thresholds obtained with broadband changes could not be predicted by the single-component thresholds unless it was assumed that only two regions of the spectrum were used in the discrimination process. In profile-analysis experiments it was found in general that complex changes give poorer thresholds than would be expected from optimum combination of thresholds obtained with single-component changes in the same multitone spectrum and (Green and Kidd, Jr., 1983; Green *et al.*, 1987; Richards *et al.*, 1989; Berg and Green, 1992).

Farrar *et al.* (1987) studied the discriminability of different speechlike noise spectra, embedded in long-term averaged speech noise. In an attempt to predict their results with a simple multichannel model they found rather large values

for the internal noise variance, indicating poor performance. Inspection of their Figure 6 indicates that only two regions are used, viz., those containing the spectral peaks. The same variance was assumed for all bands in their multichannel model. Had it been possible to let the internal noise variance vary across bands, they probably would have found a small variance in two bands and large variances in the other bands, indicating that only two regions of the spectra were used.

The ability of the auditory system to detect a peak or a notch in an otherwise flat spectrum has been studied to some extent in the literature (Moore *et al.*, 1989; Schacknow and Raab, 1976). A simple multichannel model predicts that threshold should decrease as the bandwidth of the peak or notch increases. The results, however, showed only a slight dependence or even none at all. This again suggests that only two regions of the spectrum are used. One region is then situated at the peak (notch), the other at the nonchanging part of the spectrum.

It seems that the discrimination of complex spectral changes can be explained qualitatively by assuming that only two regions are used. It has to be kept in mind, however, that all experiments reported are discrimination experiments where only two stimulus alternatives had to be compared. It is very well possible that, in experiments where, for instance, a set of spectra have to be discriminated or identified, observation of more than two spectral regions will be involved. This is true for example, for experiments where different timbres (Plomp, 1976) or vowels (Pols *et al.*, 1969) have to be judged for dissimilarity. In that case, the whole spectrum has to be monitored and not just the two regions containing most of the information that is relevant for discrimination.

ACKNOWLEDGMENTS

This work has been supported by the Netherlands Organization for the Advancement of Pure Research (NWO) through the PSYCHON foundation, Grant No. 560-262-034. Some of the results have been presented previously in Versfeld (1992). The author is very grateful to Adrian Houtsma for all his support, and is indebted to Dik Hermes and Armin Kohlrausch for their comments on earlier versions of this manuscript. Two anonymous reviewers are acknowledged for their very constructive remarks. The author once again thanks Theo de Jong for his indispensable technical assistance.

APPENDIX: DERIVATION OF ΔIWAIF FOR NOISE BANDS WITH OPPOSITE SPECTRAL SLOPES

The amplitude spectrum $L_P(f)$ of a noise band with a positive spectral slope, edge frequencies f_1 and f_2 , and levels L and $L + \Delta L$ at the two spectral edges [cf. Fig. 1(a)] is given by

$$L_P(f) = L + S \log_2 \left(\frac{f}{f_1} \right), \quad (\text{A1})$$

where S is the spectral slope expressed in dB/oct. Similarly, the amplitude spectrum $L_N(f)$ of a noise band with a negative spectral slope is given by

$$L_N(f) = L + \Delta L - S \log_2 \left(\frac{f}{f_1} \right). \quad (\text{A2})$$

Conversion of Eqs. (A1) and (A2) to a linear amplitude scale yields

$$A_P(f) = A_0 10^{L_P(f)/20} = A \left(\frac{f}{f_1} \right)^{m/2}, \quad (\text{A3})$$

$$A_N(f) = A_0 10^{L_N(f)/20} = A \alpha \left(\frac{f}{f_1} \right)^{-m/2}, \quad (\text{A4})$$

where A_0 is a reference amplitude, $A = A_0 10^{L/20}$, $\alpha = (A + \Delta A)/A$, and $m = S/(10 \log_{10}(2)) = 2 \log_e(\alpha)/\log_e(f_2/f_1)$.

For a noise band with a positive spectral slope, Eq. (3) in the main text can be written as (cf. Anantharaman *et al.*, 1993)

$$\text{IWAIF}_P = \frac{\int_{f_1}^{f_2} A_P^2(f) f df}{\int_{f_1}^{f_2} A_P^2(f) df}. \quad (\text{A5})$$

Substituting the expression for $A_P(f)$, given in Eq. (A3), into Eq. (A5) yields, after calculating the integral and doing some rearranging, an expression for IWAIF_P :

$$\text{IWAIF}_P = \frac{1+m}{2+m} \left[\frac{f_2^2(f_2/f_1)^m - f_1^2}{f_2(f_2/f_1)^m - f_1} \right]. \quad (\text{A6})$$

Similarly, IWAIF_N is given by

$$\text{IWAIF}_N = \frac{1-m}{2-m} \left[\frac{f_2^2 - f_1^2(f_2/f_1)^m}{f_2 - f_1(f_2/f_1)^m} \right]. \quad (\text{A7})$$

By using the equality $\alpha^2 = (f_2/f_1)^m$, the expression for $\Delta\text{IWAIF} = \text{IWAIF}_P - \text{IWAIF}_N$ can be written as

$$\Delta\text{IWAIF} = \frac{1+m}{2+m} \left[\frac{f_2^2 \alpha^2 - f_1^2}{f_2 \alpha^2 - f_1} \right] - \frac{1-m}{2-m} \left[\frac{f_2^2 - f_1^2 \alpha^2}{f_2 - f_1 \alpha^2} \right], \quad (\text{A8})$$

which is Eq. (4) in the main text.

- Anantharaman, J. N., Krishnamurthy, A. K., and Feth, L. L. (1991). "Auditory processing of complex signals using the multichannel EWAIF," *J. Acoust. Soc. Am.* **89**, 1938–1939.
- Anantharaman, J. N., Krishnamurthy, A. K., and Feth, L. L. (1993). "Intensity-weighted average of instantaneous frequency as a model for frequency discrimination," *J. Acoust. Soc. Am.* **94**, 723–729.
- Berg, B. G., and Green, D. M. (1992). "Discrimination of complex spectra: Spectral weights and performance efficiency," in *Auditory Physiology and Perception*, edited by Y. Cazals, L. Demany, and K. Horner (Pergamon, Oxford), pp. 373–379.
- Berg, B. G., Nguyen, Q. T., and Green, D. M. (1992). "Discrimination of narrow-band spectra. I: Spectral weights and pitch cues," *J. Acoust. Soc. Am.* **92**, 1911–1918.
- Bernstein, L. R., and Green, D. M. (1987). "Detection of simple and complex spectral changes of spectral shape," *J. Acoust. Soc. Am.* **82**, 1587–1592.
- Dai, H. (1993). "On the pitch of two-tone complexes," *J. Acoust. Soc. Am.* **94**, 730–734.
- Dai, H., Nguyen, Q., Kidd, Jr., G., Feth, L. L., and Green, D. M. (1996). "Phase independence of pitch produced by narrow-band sounds," *J. Acoust. Soc. Am.* **100**, 2349–2351.
- Durlach, N. I., Braida, L. D., and Ito, Y. (1986). "Towards a model for discrimination of broadband signals," *J. Acoust. Soc. Am.* **80**, 63–72.

- Farrar, C. L., Reed, C. M., Ito, Y., Durlach, N. I., Delhorne, L. A., Zurek, P. M., and Braida, L. D. (1987). "Spectral shape discrimination. I. Results from normal-hearing listeners for stationary broadband noises," *J. Acoust. Soc. Am.* **81**, 1085–1092.
- Feth, L. L. (1974). "Frequency discrimination of complex periodic tones," *Percept. Psychophys.* **15**, 375–379.
- Feth, L. L., and O'Malley, H. (1977). "Two-tone auditory spectral resolution," *J. Acoust. Soc. Am.* **62**, 940–947.
- Feth, L. L., and Stover, L. J. (1987). "Demodulation processes in auditory perception," in *Auditory Processing of Complex Sounds*, edited by W. A. Yost and C. S. Watson (Erlbaum, Hillsdale, NJ), pp. 76–86.
- Florentine, M., and Buus, S. (1981). "An excitation-pattern model for intensity discrimination," *J. Acoust. Soc. Am.* **70**, 1646–1654.
- Green, D. M. (1988). *Profile Analysis* (Oxford U.P., New York).
- Green, D. M., and Kidd, Jr., G. (1983). "Further studies of auditory profile analysis," *J. Acoust. Soc. Am.* **73**, 1260–1265.
- Green, D. M., Berg, B. G., Dai, H., Eddins, D. A., Onsan, Z., and Nguyen, Q. (1992). "Spectral shape discrimination of narrow-band sounds," *J. Acoust. Soc. Am.* **92**, 2586–2597.
- Green, D. M., Onsan, Z. A., and Forrest, T. G. (1987). "Frequency effects in profile analysis and detecting complex spectral changes," *J. Acoust. Soc. Am.* **81**, 692–699.
- Ito, Y. (1990). "Auditory discrimination of power spectra for roving two-tone stimuli," Ph.D. thesis, Massachusetts Institute of Technology.
- Kidd, Jr., G., Mason, C. R., Uchanski, R. M., Brantley, M. A., and Shah, P. (1991). "Evaluation of simple models of auditory profile analysis using random reference spectra," *J. Acoust. Soc. Am.* **90**, 1340–1354.
- Kidd, Jr., G., Uchanski, R. M., Mason, C. R., and Deliwala, P. S. (1993). "Discriminability of narrow-band sounds in the absence of level cues," *J. Acoust. Soc. Am.* **93**, 1028–1037.
- Li, X., and Pastore, R. E. (1995). "Perceptual constancy of a global spectral property: Spectral slope discrimination," *J. Acoust. Soc. Am.* **98**, 1956–1968.
- Moore, B. C. J., Oldfield, S. R., and Dooley, G. J. (1989). "Detection and discrimination of spectral peaks and notches at 1 and 8 kHz," *J. Acoust. Soc. Am.* **46**, 458–467.
- Plomp, R. (1976). *Aspects of Tone Sensation* (Academic, London).
- Pols, L. C. W., van der Kamp, L. J. Th., and Plomp, R. (1969). "Perceptual and physical space of vowel sounds," *J. Acoust. Soc. Am.* **46**, 458–467.
- Richards, V. M. (1992). "The detectability of a tone added to narrow bands of equal-energy noise," *J. Acoust. Soc. Am.* **91**, 3424–2435.
- Richards, V. M., and Nekrich, R. D. (1993). "The incorporation of level and level-invariant cues for the detection of a tone added to noise," *J. Acoust. Soc. Am.* **94**, 2560–2574.
- Richards, V. M., Onsan, Z. A., and Green, D. M. (1989). "Auditory profile analysis: Potential pitch cues," *Hearing Res.* **39**, 27–36.
- Schacknow, P. N., and Raab, D. H. (1976). "Noise-intensity discrimination: Effects of bandwidth conditions and mode of masker presentation," *J. Acoust. Soc. Am.* **60**, 893–905.
- Southworth, C., and Berg, B. G. (1995). "Multiple cues for the discrimination of narrow-band sounds," *J. Acoust. Soc. Am.* **98**, 2486–2492.
- Versfeld, N. J. (1992). "On the perception of spectral changes in noise bands," in *The Auditory Processing of Speech*, edited by M. E. H. Schouten (Mouton de Gruyter, Berlin), pp. 219–227.
- Versfeld, N. J. (1993). "Profile-analysis models applied to two-tone complexes," in *Contributions to Psychological Acoustics*, edited by A. Schick (BIS, Oldenburg), pp. 269–285.
- Versfeld, N. J., and Houtsma, A. J. M. (1991). "Perception of spectral changes in multi-tone complexes," *Q. J. Exp. Psychol.* **43A**, 459–479.
- Versfeld, N. J., and Houtsma, A. J. M. (1995). "Discrimination of changes in the spectral shape of two-tone complexes," *J. Acoust. Soc. Am.* **98**, 807–816.
- Versfeld, N. J., Dai, H., and Green, D. M. (1996). "The optimum decision rules for the oddity task," *Percept. Psychophys.* **58**, 10–21.
- von Bismarck, G. (1974). "Sharpness as an attribute of the timbre of steady sounds," *Acustica* **30**, 159–172.

Coherence masking protection in brief noise complexes: Effects of temporal patterns

Peter C. Gordon^{a)}

Department of Psychology, The University of North Carolina at Chapel Hill, CB# 3270, Davie Hall, Chapel Hill, North Carolina 27599-3270

(Received 25 April 1996; revised 2 November 1996; accepted 2 May 1997)

Three experiments examined listeners' thresholds for classifying the pitch of a target signal in a masking noise when it was presented alone as compared to when it was presented with a "cosignal." The target signal was a narrow band of noise centered on either 375 or 625 Hz and the masker was noise low-pass filtered at 1000 Hz. The cosignal provided no information about the pitch of the target signal but could potentially combine with it to form an auditory object; it was spectrally well separated from the target signal, consisting of a band of noise ranging from 2200 to 2900 Hz. Experiment 1 showed that identification thresholds were lower when the target signal was paired with the cosignal than when it was presented alone if the onsets and offsets of the target signal and cosignal were temporally synchronous. This is an instance of "coherence masking protection," a phenomenon that has previously been established in the perception of vowels [P. C. Gordon, *Percept. Psychophys.* **59**, 232–242 (1997)]. The effect disappears when the cosignal leads and lags the target signal by short durations, a finding that also matches that observed previously with vowels. The finding that temporal relations between the components of a stimulus have similar effects on the perception of nonspeech noise complexes and speech sounds suggests that speech perception makes use of general auditory mechanisms for perceptual integration of this sort. Experiments 2 and 3 examine further the role of temporal relations between the onsets and offsets of the target signal and the cosignal in producing coherence masking protection. The results show that either onset synchrony or offset synchrony is sufficient to produce the effect when the cosignal is of greater duration than the target signal, but that only onset synchrony produces the effect when the target signal has greater duration than the cosignal. This pattern indicates that the target signal and cosignal do not contribute equally to the formation of auditory objects. © 1997 Acoustical Society of America. [S0001-4966(97)03609-6]

PACS numbers: 43.66.Dc, 43.66.Mk [RHD]

INTRODUCTION

Hypotheses about the processes underlying phonetic perception have frequently been tested and refined by comparing the perception of speech stimuli to the perception of nonspeech stimuli that mimic some properties of speech sounds (e.g., Liberman *et al.*, 1967; Mann and Liberman, 1983; Pisoni, 1977; Remez, 1980). Such comparisons have been made in order to determine whether characteristics of phonetic perception must be explained by speech-specific processes or whether they can be explained in terms of the operation of general auditory mechanisms. The rationale is that if phonetic perception differs from nonphonetic perception an appeal to specialized mechanisms is warranted, but a finding that phonetic and nonphonetic perception are very similar is most parsimoniously explained by appeal to general auditory mechanisms. The present paper applies this rationale to the integration of acoustic information in phonetic perception as it is shown by the phenomenon of coherence masking protection (Gordon, 1997).

Gordon (1997) demonstrated coherence masking protection (CMP) in speech sounds using a paradigm in which identification thresholds for speech sounds in noise were

compared to identification thresholds for the acoustic information that distinguished the speech sounds when it was isolated from the remainder of the speech sound. Under certain conditions, identification thresholds were lower for the speech sounds than for the distinctive information alone, indicating that being part of a coherent speech object protected the distinctive information from masking. More specifically, Gordon (1997) had listeners classify a stimulus as /t/ (as in "bit") or /ε/ (as in "bet"), a distinction that can be minimally cued by the frequency of the first formant. When the signals were presented in a low-pass masking noise, identification thresholds for the vowels were lower than identification thresholds for the acoustic energy underlying the first formant even though that energy provided the only basis for distinguishing the vowels.

Development of the CMP paradigm was motivated in part by findings obtained in the comodulation masking release (CMR) paradigm (Hall *et al.*, 1984; Hall and Grose, 1988, 1990). In that paradigm, changes in detection thresholds for simple signals are studied as a function of the addition of energy bands to the masker at frequencies that are widely separated from the signal. When the amplitude modulation of the added energy bands has the same envelope as the on-signal masking band, thresholds are reduced. No effect on thresholds is observed when the envelopes of the

^{a)}Electronic mail: pcg@gibbs.oit.unc.edu

added energy bands differ from that of the on-signal masker. The CMR paradigm provides a way of studying how factors promoting auditory coherence in a masker can release a signal from masking (Hall and Grose, 1990). CMP builds on this logic by examining how coherence within a signal may protect a signal from masking (Gordon, 1997).

Gordon (1997) studied CMP in steady-state vowels. As Darwin (1981) has noted, there are two salient acoustic bases for coherence in such stimuli: synchrony of the onsets and offsets of the formants and the relation of the harmonics to a common fundamental. Research using techniques developed by Darwin (Darwin, 1984a, 1984b; Darwin and Gardner, 1986; Roberts and Moore, 1990, 1991) has shown that both of these factors play a role in determining whether acoustic energy contributes to the phonetic identification of sounds presented at suprathreshold levels. Gordon (1997) focused on synchrony of formants as a basis for the threshold-level coherence measured by CMP. Vowel sounds were created in which the harmonic structure at low frequencies was eliminated and the distinctive first formant was simulated by a narrow band of noise. CMP was observed with these stimuli if the higher formants and first formant were coterminous, but not when the higher formant began in advance and ended after the first formant. This result showed that synchrony of onsets and offsets was a sufficient basis for CMP in vowel sounds, even in the absence of a harmonic basis for coherence. The current experiments examine whether different types of synchrony provide a basis for CMP in nonspeech sounds. This serves two goals: to provide a basis for comparing perceptual integration in speech and nonspeech stimuli, and to understand better how synchrony of changes in energy across different parts of the spectrum influences the creation of auditory objects.

I. EXPERIMENT 1. CMP WITH SYNCHRONOUS COSIGNALS VERSUS FRINGING COSIGNALS

The nonspeech stimuli in the present experiment were designed to mimic some of the central properties of the stimuli used in the third experiment of Gordon (1997). That experiment studied identification of the vowels /I/ and /ε/ that were constructed by combining a distinctive first formant consisting of a narrow band of noise with higher formants produced by the Klatt synthesizer. The noise-band first formant was 50 Hz wide and was centered on 375 Hz for /I/ and 625 Hz for /ε/. The higher formants were identical for the two vowels; in particular, F_2 was set at 2200 Hz and F_3 was set at 2900 Hz. Identification thresholds in low-pass noise were determined for three types of targets. In the *synchronous-formants* condition, the higher formants and the noise band both had a duration of 40 ms and were gated on and off together. In the *fringing-formants* condition, the higher formants had a duration of 120 ms while the noise band had a duration of 40 ms; the higher formants began 40 ms before the noiseband and ended 40 ms after it. In the *no-formants* condition, only the noise band was presented. In the two conditions in which higher formants were presented, listeners identified the target stimulus as one of the two vowels (/I/ vs /ε/). In the no-formants condition, listeners identified the noise band as a low- or high-pitched sound. Identifi-

cation thresholds were lowest in the synchronous-formants condition; they did not differ significantly in the fringing- and no-formants conditions.

Nonspeech analogs of the synchronous-formants and fringing-formants conditions were created by replacing the formants with a bandlimited white noise that ranged from 2200 Hz to 2900 Hz; this bandlimited noise will be referred to as the *cosignal*. The cosignal was constructed so that it had energy in the frequency range of the second and third formants of the stimuli used by Gordon (1997). The cosignal did not prompt a phonetic percept in the judgment of the author. Listeners in the experiment were not told to identify the stimuli as speech, and none reported hearing them as such. Accordingly, if a speech-specific mechanism were responsible for integrating the higher formants with the first formant in the Gordon (1997) experiments, then integration of the cosignal with the first formant would not necessarily be expected in the current experiments. Alternatively, if general auditory mechanisms were responsible for the integration observed by Gordon (1997), then integration of the cosignal with the first formant would be expected in the current experiments.

The cosignal differed from the higher-formant stimulus in that it had a flat spectrum in the range of the second and third formants while the higher-formant stimulus contained two prominences in this range. Further, the higher-formant stimulus had a harmonic progression built on a fundamental of 125 Hz that began at 1200 Hz (due to the high-pass filtering that was used to eliminate information about the first formant) and extended to 4700 Hz (the cutoff of the anti-aliasing filter). These differences meant that while the formant stimuli had a pitch related to the fundamental of 125 Hz and a timbre reflecting the prominences of the formants, the cosignal sounded like a moderately high-frequency noise. For the higher-formant stimulus used by Gordon (1997), combination with the noise-band first formant produced a clear impression of a vowel, the identity of which was determined by the frequency of the target signal. For the cosignal used in the current study, this combination created the impression of a noise with a tone in it; the pitch of the tone was determined by the frequency of the target signal.

The current experiment examined identification thresholds for the target signals when they were paired with a synchronous cosignal, a fringing cosignal, or no cosignal, thereby matching the temporal patterns used by Gordon (1997) with the higher-formant stimulus.

A. METHOD

1. Subjects

Twelve subjects participated in a single session that lasted approximately an hour and a half. They were recruited with posted notices and were paid at a rate of \$6/h. for their participation. To be included in the experiment, subjects had to meet a criterion of average identification thresholds of 64 dB SPL in the first six runs of the experiment. All subjects tested met this criterion.

2. Stimuli

Two 50-Hz-wide bands of noise, one centered on 375 Hz and the other on 625 Hz served as the target signals in the task. The noisebands were made by passing a broadband (0–2000 Hz), constant spectrum-level noise through a digital filter (IHR Universal) with extremely sharp spectral skirts and a noise floor over 70 dB down. The sampling rate of the filter was 2500 Hz and the output was low-pass filtered at 1250 and recorded onto digital audio tape.¹ Playback of the tape was then redigitized at 10 kHz using a Kay Elemetrics CSL system. The noises were edited into 40-ms stimuli with 5-ms linear onset and offset ramps. Nine different 40-ms stimuli were made from each noise so that the fluctuations present in the narrow bands of noise would not be the same in each stimulus presentation; the starting level of the signal was 69 dB SPL. The cosignal consisted of a bandpass noise between 2200 and 2900 Hz; its starting level was 62 dB SPL and it began and ended with 5-ms linear ramps. The masking noise consisted of a 600-ms noise low-pass filtered at 1000 Hz, and it was presented at approximately 62 dB SPL. In the synchronous-cosignal condition, both the signal and cosignal began 420 ms into the masker. In the fringing-cosignal condition, the cosignal began 380 ms into the masker (ending 120 ms later), and the signal began 420 ms into the masker. In the no-cosignal condition, the 40-ms noise band began 420 ms into the masker.

3. Procedure and design

On each trial, a single stimulus consisting of a target signal and accompanying cosignal was presented in the masking noise; subjects were asked to identify it as a low-pitched or high-pitched sound by pressing the appropriate key. A one-up, three-down adaptive tracking procedure was used to determine listeners' thresholds. Both the level of the signal and cosignal were adjusted during tracking. After incorrect responses, a visual error message was presented to the subject. No overt message was presented after correct responses. The step size of the signal and cosignal adjustment was 8 dB for the first 2 reversals, 4 dB for the next 2 reversals, and 2 dB for the final 12 reversals in a run. The average signal level of the last eight reversals was taken as the threshold for the run. Subjects performed 18 runs, rotating through the conditions in the order: synchronous cosignal, fringing cosignal, and no cosignal. After every group of three runs, subjects were shown their identification threshold averaged over the preceding three runs and were encouraged to try as hard as possible to reduce this threshold in the remainder of the testing. This feedback served to increase subjects' motivation and to provide them with a way of tracking their performance without giving them information on their performance in the different experimental conditions. The first two runs in each condition were considered practice and were not included in the analysis.

B. Results

Table I shows the mean signal level at threshold in the three experimental conditions for individual subjects as well as the overall means and standard deviations. Analysis of

TABLE I. Results of experiment 1. Mean signal level (dB SPL) at identification threshold for target signals with synchronous cosignals, fringing cosignals, and no cosignals.

Subject number	Synchronous cosignal	Fringing cosignal	No cosignal
1	54.6	55.6	57.9
2	57.4	57.9	55.0
3	60.3	63.4	57.5
4	54.4	57.7	57.9
5	54.1	57.0	56.8
6	58.5	60.7	61.3
7	52.3	57.2	56.0
8	59.0	60.7	59.3
9	56.1	58.7	60.8
10	55.1	58.7	60.0
11	58.9	63.7	61.9
12	53.4	56.1	58.2
Mean	56.2 (2.6)	58.9 (2.6)	58.6 (2.2)

variance showed that performance in the three conditions differed significantly, $F(2,22) = 18.4$, $p < 0.001$. Identification thresholds were lower in the synchronous-cosignal condition than in both the fringing-cosignal condition [$t(11) = 4.73$, $p < 0.001$] and the no-cosignal condition, $t(11) = 4.28$, $p < 0.002$. Identification thresholds did not differ significantly in the fringing-cosignal and no-cosignal conditions, $t(11) = 0.44$, $p > 0.25$.

C. Discussion

The results showed a significant CMP; identification thresholds were lower in the synchronous cosignal condition than in the no-cosignal condition, indicating that the identification of the target signal was facilitated by the presence of the cosignal which of itself provided no information about the frequency of the target signal. No CMP was observed for the fringing-cosignal condition, as shown by the lack of difference between that condition and the no-cosignal condition. This pattern of results for nonspeech stimuli exactly parallels the findings of Gordon (1997) for vowel stimuli with matched temporal patterns. In both cases, CMP was observed only when the high-frequency energy was synchronous with the distinctive signal. The finding of parallel results for speech and nonspeech stimuli is most parsimoniously explained by the idea that coherence of the sort that provides protection from masking derives from general processes of auditory perception that apply across domains.

II. EXPERIMENT 2: CMP WITH TEMPORALLY LEADING OR LAGGING COSIGNALS

The results of the first experiment demonstrate that the temporal relation between the target signal and the cosignal affects CMP. CMP is observed when their onsets and offsets are simultaneous but it is not observed when the cosignal leads and lags the target signal by 40 ms. Gordon (1997) employed temporal leads and lags of 40 ms in his study of CMP in speech sounds because studies by Darwin and his colleagues have shown that perceptual integration of acoustic components for purposes of phonetic and pitch perception is

influenced considerably by asynchrony of this magnitude (Darwin, 1984a, 1984b; Darwin and Sutherland, 1984; Hukin and Darwin, 1995; Roberts and Moore, 1991), though these findings have been obtained with signals of longer duration than have been studied in the CMP paradigm. This research has further shown that having asynchronous onsets disrupts perceptual integration to a greater degree than having asynchronous offsets. The current experiment examines the role of onset and offset synchrony in the perceptual integration process underlying CMP. It explores whether CMP occurs for *onset-synchronous* stimuli in which the target signal and cosignal begin at the same time but the cosignal extends 40 ms past the offset of the target signal, and whether it occurs for *offset-synchronous* stimuli in which the target signal and cosignal end at the same time but the cosignal begins 40 ms before the target signal. The stimuli in these conditions examine separately the two sources of asynchrony in the fringing stimuli used in the previous experiment.

A. Method

1. Subjects

Fifteen subjects from the same population as the previous study participated in the experiment. None of them had participated in the previous study. Three subjects failed to meet the criterion for inclusion in the study and were dismissed after the first six runs.

2. Stimuli, procedure, and design

The signals, cosignals, and masking noise were the same as in the previous experiment, except that the cosignals were shortened to 80 ms. In the onset-synchronous cosignal condition, both the signal and cosignal began 420 ms into the masker; the signal ended 40 ms later and the cosignal ended 80 ms later. In the offset-synchronous cosignal condition, the cosignal began 380 ms into the masker, the signal began 40 ms later. Both ended 460 ms into the masker. The procedure and design were the same as in the preceding experiment.

B. Results

Table II shows the mean signal level at threshold in the three experimental conditions for individual subjects as well as the overall means and standard deviations. Analysis of variance showed that performance in the three conditions differed significantly, $F(2,22)=11.5$, $p<0.001$. Identification thresholds were higher in the no-cosignal condition than in both the onset-synchronous cosignal condition [$t(11)=4.43$, $p<0.002$] and the offset-synchronous cosignal condition, $t(11)=3.81$, $p<0.005$. Identification thresholds did not differ significantly in the onset-synchronous cosignal and offset-synchronous cosignal conditions, $t(11)=0.61$, $p>0.25$.

C. Discussion

Significant CMPs were observed for both onset-synchronous and offset-synchronous stimuli. This indicates that synchrony either at the beginning or the end of a target

TABLE II. Results of experiment 2. Mean signal level (dB SPL) at identification threshold for target signals with onset-synchronous cosignals, offset-synchronous cosignals, and no cosignals. Target signals are 40 ms and cosignals are 80 ms.

Subject number	Onset-synchronous cosignal	Offset-synchronous cosignal	No cosignal
1	54.2	56.0	57.5
2	56.2	57.0	57.5
3	56.4	57.1	59.4
4	55.4	54.8	58.0
5	57.0	58.1	60.3
6	53.1	55.4	58.6
7	56.0	55.8	65.4
8	57.2	56.8	57.3
9	58.1	58.3	59.6
10	58.1	56.8	57.3
11	55.9	55.3	60.2
12	55.7	56.8	57.0
Mean	56.1 (1.4)	56.5 (1.1)	59.0 (2.3)

signal embedded in a cosignal can provide a sufficient basis for perceptual integration but that neither onset-synchrony nor offset-synchrony is a necessary condition. The results of experiment 1 showed that perceptual integration of the sort underlying CMP does not occur when neither the onsets nor offsets of the target signal and cosignal are synchronous. With respect to the previous literature, this pattern offers one insight and creates one discrepancy.

The insight concerns the question of whether the effect of asynchronous onsets observed in studies of phonetic classification can be attributed to perceptual grouping or whether it results from perceptual adaptation (e.g., Darwin and Sutherland, 1984; Roberts and Moore, 1991). Previous studies of onset asynchrony have examined vowel (and pitch) identification in which an “extraneous sound” begins simultaneously with or in advance of some acoustic complex to be identified. The effect of the extraneous sound on identification of the complex typically decreases when the sound begins in advance of the complex. This finding can be explained by a perceptual grouping mechanism that integrates synchronous acoustic energy across the spectrum. Such a grouping mechanism receives independent support from studies of the effect of onset synchrony in auditory streaming (Bregman and Pinker, 1978). However, perceptual adaptation provides an alternative explanation of the effect of onset asynchrony in vowel and pitch identification. On this account, the early portion of the extraneous sound produces perceptual adaptation that reduces the contribution of the later portion of the extraneous sound to identification of the acoustic complex to which it is added. Perceptual adaptation has a well-established physiological basis (Kiang *et al.*, 1965) and it has been demonstrated in vowel identification studies through the phonetic classification of auditory afterimages (Summerfield *et al.*, 1984). Accordingly, perceptual grouping and perceptual adaptation constitute rival, though nonexclusive, accounts of why onset asynchrony reduces the contribution of an extraneous sound to the identification of an acoustic complex.

Perceptual adaptation cannot be the basis of CMP be-

cause the paradigm involves comparison of exactly the same target signal, with and without a cosignal. The addition of the spectrally distant cosignal would not affect perceptual adaptation in the spectral region of the target signal. The results of the present experiment show CMP for the onset-synchronous (but offset-asynchronous) stimuli, while the fringing stimuli of the preceding experiment (in which neither onsets nor offsets were synchronous) did not show CMP. As noted above, this indicates that onset-synchrony is a sufficient acoustic basis for the kind of perceptual grouping that underlies the CMP effect. Therefore, the present results demonstrate that simultaneous onsets can form the basis for at least one kind of perceptual integration.

The discrepancy created by the current findings is that onset synchrony and offset synchrony produced CMP effects of indistinguishable magnitude whereas previous research using identification paradigms has shown that disrupting onset synchrony caused a greater decrease in the contribution of the extraneous sound than did disrupting offset synchrony (e.g., Darwin, 1984a; Roberts and Moore, 1991). Before addressing this discrepancy at a conceptual level, an important difference should be noted in the arrangement of the parts of the stimulus in the current experiment as compared to earlier research that has looked at the role of asynchrony in perceptual integration.

III. EXPERIMENT 3: CMP WITH TEMPORALLY LEADING OR LAGGING TARGET SIGNALS

The temporal patterns within the stimuli used in experiment 2 were chosen to change single dimensions of the fringing stimuli used in experiment 1. As such, asynchrony was created by having the duration of the high-frequency cosignal exceed that of the distinctive, lower-frequency target signal. Previous research has taken the opposite tack and has used distinctive signals of greater duration than the acoustic complexes into which they were to be integrated (e.g., Darwin, 1984a; Roberts and Moore, 1991). The present study takes this latter approach: Onset asynchrony (with offset synchrony) is created by having the onset of the target signal lead the onset of the cosignal by 40 ms. Offset asynchrony (with onset synchrony) is created by having the offset of the target signal lag the offset of the cosignal by 40 ms. Identification thresholds for both of these conditions were compared to those for identifying the target signal alone.

A. Method

1. Subjects

Fifteen subjects from the same population as the previous study participated in the experiment. None of them had participated in either of the previous studies. Three subjects failed to meet the criterion for inclusion and were dismissed after the first six runs.

2. Stimuli, procedure, and design

The signals were the same as in the previous two experiments, except that they were 80 ms in duration (including onset and offset ramps) as opposed to the 40 ms used previously. The cosignals were the same as before, except they

TABLE III. Results of experiment 3. Mean signal level (dB SPL) at identification threshold for target signals with onset-synchronous cosignals, offset-synchronous cosignals, and no cosignals. Target signals are 80 ms and cosignals are 40 ms.

Subject number	Onset-synchronous cosignal	Offset-synchronous cosignal	No cosignal
1	52.1	54.9	54.9
2	55.5	55.2	56.7
3	51.2	52.6	54.7
4	53.5	55.6	53.4
5	56.6	57.2	57.0
6	52.0	54.3	54.9
7	52.8	53.3	55.3
8	51.5	54.3	52.5
9	52.6	55.0	53.7
10	52.8	54.6	55.6
11	52.6	55.0	53.9
12	55.8	57.4	54.0
Mean	53.2 (1.8)	55.0 (1.4)	54.7 (1.3)

were now 40 ms in duration. In the onset-synchronous cosignal condition, both the signal and cosignal began 420 ms into the masker; the cosignal ended 40 ms later and the signal ended 80 ms later. In the offset-synchronous cosignal condition, the signal began 380 ms into the masker, the cosignal began 40 ms later. Both ended 460 ms into the masker. The procedure and design were the same as in the preceding two experiments.

B. Results

Table III shows the mean signal level at threshold in the three experimental conditions for individual subjects as well as the overall means and standard deviations. Analysis of variance showed that performance in the three conditions differed significantly, $F(2,22)=9.6$, $p<0.005$. Identification thresholds were lower in the onset-synchronous cosignal condition than in both the offset-synchronous cosignal condition [$t(11)=4.04$, $p<0.001$] and the no-cosignal condition, $t(11)=3.5$, $p<0.01$. Identification thresholds did not differ significantly in the offset-synchronous cosignal and no-cosignal conditions, $t(11)=0.54$, $p>0.25$.

C. Discussion

The results of the experiment show that onset synchrony makes a greater contribution to CMP than does offset synchrony. A significant CMP effect was observed when the target signal and cosignal were onset synchronous but offset asynchronous. No CMP effect was observed when the target signal and cosignal were offset synchronous but onset asynchronous. This finding is consistent with previous research showing that onset asynchrony causes a greater reduction in perceptual integration than does offset asynchrony (e.g., Darwin, 1984a; Roberts and Moore, 1991). This shows that synchrony of onsets and offsets has a consistent effect on perceptual integration as studied by identification of both suprathreshold and threshold-level complex sounds.

The present finding concerning the relative importance of onset and offset synchrony differs from the pattern found

in experiment 2. It appears that perceptual integration of the target signal into the cosignal depends not only on synchrony of onsets and offsets, but also on whether the target signal leads the cosignal, or the cosignal leads the target signal; the former disrupts CMP while the latter does not. This difference indicates that the target signal and cosignal do not contribute symmetrically to perceptual integration as measured in the CMP paradigm, in that a leading target signal is perceptually segregated from the cosignal while a leading cosignal is not perceptually segregated from the target signal. This asymmetry could be due to a number of factors: (1) The target signal conveys the distinctive information necessary to perform the identification, so listeners likely focus more attention in the frequency region of the target signal than in that of the cosignal. (2) The target signal is close to its masked threshold, but the cosignal is not. (3) The target signal has a narrow bandwidth and is at a relatively low frequency, while the cosignal has a broader bandwidth and is at a higher frequency. Additional studies are required to determine the extent to which any of these factors are responsible for the asymmetry in the roles of the target signal and cosignal in producing CMP.

IV. GENERAL DISCUSSION

The results of the three experiments show that identification thresholds for masked noise bands can be reduced by the addition of acoustic energy that is spectrally well separated from the target signal, a phenomenon that has been dubbed “coherence masking protection” (CMP) in studies of speech perception (Gordon, 1997). Experiment 1 showed that CMP in nonspeech stimuli was influenced by the temporal arrangement of the components of the sound in a manner that closely matched that observed with speech stimuli. The results of experiments 2 and 3 tease apart the contribution of the synchrony of stimulus onsets and offsets to CMP. Below, the implications of these results are discussed with respect to two issues: specialized versus general processes in speech perception and possible mechanisms underlying CMP.

A. Specialized versus general processes in speech perception

Gordon (1997) demonstrated CMP in the perception of vowels and showed that it could be disrupted by certain asynchronies between the first formant and higher formants. This finding could be attributed either to specialized mechanisms for phonetic perception that exploit temporal regularities inherent in the production of speech or to general mechanisms of auditory perception that exploit temporal regularities that are often characteristic of events in the world. Experiment 1 of the current paper showed that CMP in the perception of nonspeech sounds was influenced by the temporal relations between low-frequency and high-frequency energy in a manner that exactly matched that observed for the temporal relation between the first formant and higher formants in experiment 3 of Gordon (1997). While it is possible that different mechanisms underlie the effect in speech and nonspeech sounds, the more parsimonious explanation is that CMP in speech sounds (and nonspeech sounds)

emerges from the operation of general mechanisms of perceptual integration that can be applied to sounds irrespective of their origin.

The contention that phonetic perception uses specialized mechanisms arose early in the study of speech perception (Liberman, 1982 for a review), and has continued to have ardent supporters (e.g., Remez *et al.*, 1994). Over the last 15 years, a critical arena in which this contention has been debated is the integration of acoustic energy into coherent percepts. Support for the view that speech makes use of specialized mechanisms for perceptual integration has been claimed based on the phenomenon of duplex perception (e.g., Liberman *et al.*, 1981; Whalen and Liberman, 1987; cf. Bailey and Herrmann, 1993) and on the ability to recognize sine-wave replicas of speech (Remez *et al.*, 1994). Support for the view that speech makes use of general mechanisms for perceptual integration has come from studies showing that the phonetic contribution of acoustic energy is strongly influenced by factors (synchrony, harmonic relations and streaming) that contribute to perceptual integration in nonspeech sounds (Ciocca and Bregman, 1989; Darwin, 1984a), and by studies showing nonspeech stimuli can show duplex perception (Fowler and Rosenblum, 1990). Bregman (1990) has presented a two-stage model of perceptual integration of acoustic energy in speech perception; the first stage uses general processes of auditory segregation while the second stage uses speech-specific schemas.

CMP is an effect on the identification thresholds of fairly simple masked signals. Historically, detection thresholds for simple masked signals formed the basis of the critical-band model and were assumed to reflect very early stages of auditory processing, in part because of the simplicity of the tasks and in part because of the match between psychoacoustic data and recordings in the peripheral nervous system (Moore, 1993). Phenomena such as comodulation masking release (CMR; Hall *et al.*, 1984) have shown that the critical-band model cannot account completely for psychoacoustic data on masked thresholds. To some extent this means that effects on masked thresholds cannot necessarily be attributed to early stages of perceptual processing based on the relationship between psychoacoustic and neurophysiological data. However, there is still good reason for believing that effects such as CMR and CMP emerge from basic processes of perceptual organization and not from strategic decision processes. In these paradigms, listeners are presented with a simple task in which they are given considerable practice with feedback, features that could be expected to optimize strategic decision processes. However, performance is improved by the addition of acoustic energy that does not in a straightforward way increase the signal-to-noise ratio in the spectral region of the target signal, but which does provide a basis for perceptual reorganization of the stimulus. This suggests that CMP should be attributed to an early stage of perceptual processing like the first stage of perceptual segregation/integration proposed by Bregman (1990).

B. Mechanisms of CMP

Gordon (1997) discusses two distinct models of the CMP phenomenon, both based on ideas developed in the CMR literature. The results of experiments 2 and 3 of the current paper provide challenges to both these models.

The first model elaborated by Gordon (1997), called “peak listening,” is based on “listening in the valleys” or “dip listening” accounts of CMR (Buus, 1985) which state that listeners use changes in energy of the comodulated flanking bands to locate energy minima in the on-signal masking band, thus finding the optimal signal-to-masker ratio. In the peak-listening model of CMP, the clearly audible cosignal (or higher formants) are seen as marking the temporal location of the target signal (or first formant) in the masking noise, thereby indicating the temporal location of the optimal signal-to-masker ratio. Because a fringing cosignal marks the target signal but no CMP is observed, Gordon (1997) considered a modified peak-listening model in which the signal-to-masker ratio is averaged over the interval in which the cosignal is present. With fringing cosignals, this interval includes time when the target signal is not on, thereby eliminating the CMP effect. However, this modified peak-listening model is challenged by the present results. The onset-synchronous and offset-synchronous stimuli of experiment 2 produced CMPs of 2.9 and 2.4 dB, respectively, while the synchronous stimuli of experiment 1 produced a CMP of 2.4 dB. The onset-synchronous and offset-synchronous stimuli include intervals in which the cosignal is on but the target is off; therefore, computing signal-to-masker ratios over the interval of the cosignal should be less effective than it would be with synchronous cosignals. Thus the finding in experiment 2 that CMP occurs for onset-synchronous and offset-synchronous stimuli appears to undercut the modified peak-listening model.

The second model elaborated by Gordon (1997) involves two processes, both of which build on prominent constructs in the study of the perception of complex sounds. The first is auditory grouping as it has been related to CMR (Hall and Grose, 1990) and the second is comparative perceptual evaluation, as it has been developed in profile analysis (Green, 1988). The auditory grouping process responds to the simultaneous energy changes at the frequencies of the target signal and cosignal that occur when the onset and offset of the signals occur at the same time. Given the very brief signals (40 and 80 ms) used in the present experiments, these energy changes occur at a rate where substantial CMR is observed with periodic modulation of masking bands (Hall and Haggard, 1983). Because the CMR paradigm involves comodulation over a relatively long interval, the masking bands could group auditorily based on many instances of simultaneous changes in energy. In contrast, such grouping in CMP could only be based on the simultaneous energy changes that occur due to the onsets or offsets of the target signal and cosignal. The perceptual comparison process is engaged by the perceptually coherent object and enables listeners to be more sensitive to the identification of the target signal because the cosignal provides a concurrent perceptual basis for estimating the expected energy level at the frequencies of the target signal. No audible comparative basis is

available when there is no cosignal, the target signal must be identified by comparing energy at the two target-signal frequencies or by comparing energy at those frequencies to the memory of the energy level earlier in the masker. The combination of the target signal and the cosignal into a coherent perceptual object could potentially allow listeners to identify the stimulus based on timbre, the distribution of energy across the spectrum, as well as on pitch.

The results of experiments 2 and 3 suggest that auditory grouping as measured by CMP can be based on synchrony of specific energy changes in different parts of the spectrum. Experiment 2 shows this for both the onset and offset of energy. Experiment 3 shows that auditory grouping can be based on the synchrony of onsets, but shows that synchrony of offsets is not sufficient to produce grouping if the onset of the target signal precedes that of the cosignal. The contrast between the results of experiments 2 and 3 indicates that the target signal and cosignal do not contribute in an equivalent manner to the formation of an auditory object. The discussion of experiment 3 indicates several factors—attentional focus, masking, frequency, and bandwidth of the signals—that might explain this difference. Exploration of these factors may provide further insight into the processes that integrate acoustic energy into coherent auditory objects.

ACKNOWLEDGMENTS

The research reported in this paper was supported by grants from the Stephenson Faculty Fund and by the University Research Council of the University of North Carolina at Chapel Hill. I would like to thank Tom Carrell, John Grose, Joe Hall, and Bob Peters for helpful discussions of this research. I would also like to thank Tim Fiscus and Shelley Poovey for assistance in testing subjects. Direct correspondence to Peter C. Gordon, Department of Psychology, University of North Carolina at Chapel Hill, Chapel Hill, NC 27599-3270.

¹My thanks to John Grose for making the noise bands.

- Bailey, P. J., and Herrman, P. (1993). “A reexamination of duplex perception evoked by intensity differences,” *Percept. Psychophys.* **54**, 20–32.
- Bregman, A. S. (1990). *Auditory Scene Analysis* (MIT, Cambridge, MA).
- Bregman, A. S., and Pinker, S. (1978). “Auditory streaming and the building of timbre,” *Can. J. Psychol.* **32**, 19–31.
- Buus, S. (1985). “Release from masking caused by envelope fluctuations,” *J. Acoust. Soc. Am.* **78**, 1958–1965.
- Ciocca, V., and Bregman, A. S. (1989). “The effects of auditory streaming on duplex perception,” *Percept. Psychophys.* **46**, 39–48.
- Darwin, C. J. (1981). “Perceptual grouping of speech components differing in fundamental frequency and onset-time,” *Q. J. Exp. Psychol.* **33A**, 185–207.
- Darwin, C. J. (1984a). “Auditory processing and speech perception,” in *Attention and Performance X: Control of Language Processes*, edited by H. Bouma and D. G. Bouwhuis (Erlbaum, Hillsdale, NJ), pp. 197–210.
- Darwin, C. J. (1984b). “Perceiving vowels in the presence of another sound: Constraints on formant perception,” *J. Acoust. Soc. Am.* **76**, 1636–1647.
- Darwin, C. J., and Gardner, R. B. (1986). “Mistuning a harmonic of a vowel: Grouping and phase effects on vowel quality,” *J. Acoust. Soc. Am.* **79**, 838–845.
- Darwin, C. J., and Sutherland, N. S. (1984). “Grouping frequency components of vowels: When is a harmonic not a harmonic?” *Q. J. Exp. Psychol.* **36A**, 193–208.

- Fowler, C. A., and Rosenblum, L. D. (1990). "Duplex perception: A comparison of monosyllables and slamming doors," *J. Exp. Psychol: Human Perception and Performance* **16**, 742–754.
- Gordon, P. C. (1997). "Coherence masking protection in speech sounds: The role of formant synchrony," *Percept. Psychophys.* **59**, 232–242.
- Green, D. M. (1988). *Profile Analysis: Auditory Intensity Discrimination* (Oxford U.P., New York).
- Hall, J. W., III, and Grose, J. H. (1988). "Comodulation masking release: Evidence for multiple cues," *J. Acoust. Soc. Am.* **84**, 1669–1675.
- Hall, J. W., III, and Grose, J. H. (1990). "Comodulation masking release and auditory grouping," *J. Acoust. Soc. Am.* **88**, 119–125.
- Hall, J. W., III, and Haggard, M. P. (1983). "Co-modulation—A principle for auditory pattern analysis in speech," *Proceedings of the 11th ICA* **4**, 69–71.
- Hall, J. W., III, Haggard, M. P., and Fernandes, M. A. (1984). "Detection in noise by spectrotemporal pattern analysis," *J. Acoust. Soc. Am.* **76**, 50–56.
- Hukin, R. W., and Darwin, C. J. (1995). "Comparison of the effect of onset asynchrony on auditory grouping in pitch matching and vowel identification," *Percept. Psychophys.* **57**, 191–196.
- Kiang, N. Y.-S., Watanabe, T., Thomas, E. C., and Clark, L. F. (1965). *Discharge Patterns of Single Fibers in the Cat's Auditory Nerve* (MIT, Cambridge, MA).
- Liberman, A. M. (1982). "On finding that speech is special," *Am. Psychol.* **37**, 148–167.
- Liberman, A. M., and Mattingly, I. G. (1989). "A specialization for speech perception," *Science* **243**, 489–494.
- Liberman, A. M., Isenberg, D., and Rackerd, B. (1981). "Duplex perception for stop consonants: Evidence for a phonetic mode," *Percept. Psychophys.* **30**, 133–143.
- Liberman, A. M., Cooper, F. S., Shankweiler, D. P., and Studdert-Kennedy, M. (1967). "Perception of the speech code," *Psychol. Rev.* **74**, 431–460.
- Mann, V. A., and Liberman, A. M. (1983). "Some differences between phonetic and auditory modes of perception," *Cognition* **14**, 211–235.
- Moore, B. C. J. (1993). "Frequency analysis and pitch perception" in *Human Psychophysics*, edited by W. A. Yost, A. N. Popper, and R. R. Fay (Springer-Verlag, New York).
- Pisoni, D. B. (1977). "Identification and discrimination of the relative onset time of two component tones: Implications for voicing perception in stops," *J. Acoust. Soc. Am.* **61**, 1352–1361.
- Remez, R. E. (1980). "Susceptibility of a stop consonant to adaptation on a speech-nonspeech continuum: Further evidence against feature detectors in speech perception," *Percept. Psychophys.* **27**, 17–23.
- Remez, R. E., Rubin, P. E., Berns, S. M., Pardo, J. S., and Lang, J. M. (1994). "On the perceptual organization of speech," *Psychol. Rev.* **101**, 129–156.
- Roberts, B., and Moore, B. C. J. (1990). "The influence of extraneous sounds on the perceptual estimation of first-formant frequency in vowels," *J. Acoust. Soc. Am.* **88**, 2571–2583.
- Roberts, B., and Moore, B. C. J. (1991). "The influence of extraneous sounds on the perceptual estimation of first-formant frequency in vowels under conditions of asynchrony," *J. Acoust. Soc. Am.* **89**, 2922–2932.
- Summerfield, Q., Haggard, M. P., Foster, J., and Gray, S. (1984). "Perceiving vowels from uniform spectra: phonetic exploration of an auditory after-effect," *Percept. Psychophys.* **35**, 203–213.
- Whalen, D. H., and Liberman, A. M. (1987). "Speech perception takes precedence over nonspeech perception," *Science* **237**, 169–171.

The role of spread excitation and suppression in simultaneous masking

Brian C. J. Moore and Deborah A. Vickers

Department of Experimental Psychology, University of Cambridge, Downing Street, Cambridge CB2 3EB, England

(Received 6 February 1997; accepted for publication 23 June 1997)

This experiment was intended to clarify the relative role of spread of excitation and suppression in simultaneous masking, for masker frequencies just below and well below the signal frequency. The experiment had two stages. In stage 1, growth-of-masking functions were measured in simultaneous masking for a 2200-Hz sinusoidal signal and a sinusoidal masker with frequency of either 1800 Hz or 500 Hz. Straight lines fitted to these data were used to determine masker levels that would give 10, 20, and 30 dB of masking. In stage 2, thresholds for detecting a brief 2200-Hz signal were measured using forward masking. It was reasoned that the threshold of the signal would give an indication of the amount of excitation evoked by the masker in the frequency region of the signal. Three forward maskers were used: (1) a 2200-Hz sinusoid at 10, 20, or 30 dB sensation level (SL); (2) a 2200-Hz sinusoid at the same levels as in (1) together with a sinusoid with frequency 500 or 1800 Hz at a level just sufficient to mask the 2200-Hz sinusoid. We refer to this as the “combined masker,” (3) a 500-Hz or 1800-Hz sinusoid at the same levels as in (2) above. The 1800-Hz combined masker produced slightly less forward masking than the 2200-Hz masker (1), which might be explained in terms of suppression or as perceptual cueing. Both the 1800-Hz combined masker and the 1800-Hz component alone (3) gave significant amounts of forward masking (up to 18 dB), indicating that these maskers produced substantial excitation at 2200 Hz. This is consistent with the idea that the simultaneous masking of the 2200-Hz component in stage 1 was produced by spread of excitation rather than by suppression. The 500-Hz combined masker produced much less forward masking than the 2200-Hz component alone, indicating strong suppression of the 2200-Hz component of the combined masker by the 500-Hz component. However, both the 500-Hz combined masker and the 500-Hz component alone produced some forward masking. This is not consistent with the idea that masking of the 2200-Hz component in stage 1 (simultaneous masking) was produced solely by suppression. © 1997 Acoustical Society of America. [S0001-4966(97)01710-4]

PACS numbers: 43.66.Dc, 43.66.Mk, 43.66.Ba [JWH]

INTRODUCTION

Traditionally, the simultaneous masking of a narrow-band signal by a masker with a different center frequency has been assumed to be caused by spread of the excitation produced by the masker to the “place” corresponding to the signal frequency (Wegel and Lane, 1924; Fletcher, 1940; Zwicker, 1970; Zwicker and Fastl, 1990). However, an alternative possibility is that the signal is suppressed by the masker (Wightman *et al.*, 1977; Weber, 1983; Pickles, 1984; Delgutte, 1988, 1990). A masker may suppress the response to a signal that is remote in frequency without itself producing excitatory activity at the signal place (Hind *et al.*, 1967; Sachs and Kiang, 1968). These are not the only ways in which masking might occur, but they are often considered as the two most likely possibilities, and henceforth we will restrict the discussion to these two mechanisms. Further, we will assume that the properties of simultaneous masking are largely determined by peripheral processes—spread of excitation and suppression—rather than by central processes.

Moore and Glasberg (1982b) carried out a psychoacoustical study to investigate the roles of spread of excitation and suppression in simultaneous masking. They performed a two-stage experiment. In stage 1, they measured psychoacoustical tuning curves (PTCs) in simultaneous masking, us-

ing a 1-kHz sinusoidal signal at 12 or 22 dB SPL, and a variable narrow-band noise masker. A noise was used in preference to a sinusoid, in order to minimize the use of beats as a cue. The second stage of the experiment involved measuring thresholds in *forward* masking for a 1-kHz sinusoidal signal. The idea was that the threshold of the signal would be related to the excitation evoked by the masker(s) at the place corresponding to 1 kHz. One of the maskers consisted of a 1-kHz sinusoid at 12 or 22 dB SPL together with a narrow-band noise at the level corresponding to the masked threshold determined in stage 1, i.e., the 1-kHz component of the masker was at its simultaneous masked threshold. They reasoned that if simultaneous masking is caused entirely by suppression, then there should be negligible excitation at the 1-kHz place; in fact, the excitation should be equivalent to that produced by a tone at absolute threshold. Hence, there should be negligible forward masking. In fact, in most cases, the results showed a significant amount of forward masking, when the narrow-band noise was both below and above 1 kHz. Moore and Glasberg concluded that their results were not consistent with an explanation based entirely on suppressive masking. They argued instead that simultaneous masking was caused by “swamping” of the signal excitation by that of the masker (spread of excitation).

Weber (1983) carried out a very similar experiment to that of Moore and Glasberg (1982b). He found that forward masking did not consistently reveal suppression produced by the off-frequency masker. He concluded that the data were consistent with an explanation of simultaneous masking involving only excitatory interactions between the masker and the signal.

Pickles (1984) carried out a neurophysiological study to assess the relative roles of suppression and spread of excitation in simultaneous masking. He adjusted the levels of variable sinusoidal maskers so that a fixed signal at the characteristic frequency (CF) of a single neuron would be at masked threshold (using similar criteria to those used in behavioral experiments). He then compared the discharge rate with that obtained when the signal alone was presented at a level corresponding to the absolute threshold in quiet. For most frequencies of the variable masker, Pickles found that the discharge rates at masked threshold were higher than those at absolute threshold. He concluded that simultaneous masking resulted mainly from spread of excitation rather than from suppression.

Delgutte (1990) came to a rather different conclusion. He measured masked thresholds for single neurons using a method similar to one often used to measure behavioral thresholds. This was done both for simultaneous masking, and for a nonsimultaneous situation analogous to the pulsation threshold technique used in psychophysics (Houtgast, 1972, 1974). The nonsimultaneous technique allowed estimation of the excitation evoked by the masker at the signal frequency. For a 1-kHz masker at 40 dB SPL, thresholds were similar for the simultaneous and nonsimultaneous situations, consistent with the idea that the simultaneous masking was produced mainly by spread of excitation. However, when the masker level was increased to 60 or 80 dB SPL, simultaneous thresholds were well above nonsimultaneous thresholds when the signal frequency was above 1 kHz. Delgutte concluded that, in general, simultaneous masking had both excitatory and suppressive components. However, for high masker levels, and for signal frequencies well above the masker frequency, suppressive masking appeared to be dominant.

There is not necessarily a discrepancy between the physiological results of Delgutte and the psychoacoustical results of Moore and Glasberg (1982b) and of Weber (1983), since the psychoacoustical studies did not use masker frequencies well below the signal frequency; the lowest masker frequency was 600 Hz (for a signal frequency of 1000 Hz). In this paper we describe an experiment similar to that of Moore and Glasberg (1982b), but extending it by including a masker frequency well below the signal frequency, and by using a wider range of signal levels. The aim of the experiment was to clarify the relative role of spread of excitation and suppression in simultaneous masking, for masker frequencies just below and well below the signal frequency.

I. EXPERIMENT

A. Design

The experiment had two stages. In stage 1, growth-of-masking functions in simultaneous masking were determined

for a 2200-Hz sinusoidal signal and a sinusoidal masker with a frequency of either 1800 Hz or 500 Hz. When the masker frequency was 1800 Hz, an additional narrow-band noise was added to mask the $2f_1-f_2$ combination tone; see below for details. According to the findings of Delgutte (1988, 1990), the dominant mechanism of masking should be spread of excitation for the 1800-Hz masker and suppression for the 500-Hz masker. The signal and masker frequencies were chosen so that beats between the signal and masker would not provide a salient detection cue; even for the 1800-Hz masker, the beat rate of 400 Hz would be too high for the beats to play a major role. The growth-of-masking functions were fitted with straight lines and these fitted lines were used to predict the masker levels required to give 10, 20, and 30 dB of masking. We chose to measure growth-of-masking functions rather than measuring the masker levels required to mask signals at 10, 20, and 30 dB sensation level (SL) in order to increase the accuracy of the estimates; each estimated masker level was based on several data points rather than just one.

In stage 2, thresholds for detecting a brief 2200-Hz signal were measured using forward masking. It was reasoned that the threshold of the signal would give an indication of the amount of excitation evoked by the masker in the frequency region of the signal. Three different forward maskers were used:

- (1) A 2200-Hz sinusoid at 10, 20, or 30 dB SL.
- (2) a 2200-Hz sinusoid at the same levels as in (1) together with a sinusoid with frequency 500 or 1800 Hz at a level just sufficient to mask the 2200-Hz sinusoid. These levels were determined in stage 1, as described above. In other words, the forward masker had two components, and the 2200-Hz component was itself at masked threshold. We refer to this as the "combined masker." It was reasoned that if the 2200-Hz component of the combined masker was mainly masked by spread of excitation, then the combined masker would produce significant excitation at 2200 Hz. Therefore, there would be significant forward masking of a 2200-Hz signal. If, on the other hand, the 2200-Hz component of the combined masker was mainly masked by suppression, then the combined masker should produce little excitation at 2200 Hz. Therefore, there should be little or no forward masking of the 2200-Hz signal.
- (3) A 500-Hz or 1800-Hz sinusoid at the same levels as in (2) above. By comparing the forward-masked thresholds for maskers (2) and (3) we could get some idea of the excitation evoked by the 2200-Hz component of the combined masker.

B. Stimuli

The sinusoidal stimuli were derived from Farnell DSG1 signal generators. A trial consisted of two observation intervals, marked by lights, separated by a silent interval of 500 ms. The masker was presented in both intervals. It had a steady state duration of 200 ms, and raised-cosine rise/fall times of 10 ms. The signal was presented randomly in either the first or the second interval. In stage 1, it was presented

synchronously with one of the masker bursts. In stage 2 (forward masking), the signal had a 10-ms steady state duration and 5-ms raised-cosine rise/fall times, and it was presented immediately after the masker (0-ms delay at the 0-voltage points).

Stimulus timing was controlled by a Texas Instruments 990/4 computer system. Two analogue multipliers (AD 534L) in series were used as gates, giving an on-off ratio exceeding 100 dB. The signal level was varied using a Charybdis model D programmable attenuator. Levels of the individual masker components were controlled either by a second Charybdis attenuator, or by manual attenuators (Hatfield 2125). The stimuli were passed through a final manual attenuator to one earphone of a Sennheiser HD414 headset.

In stage 1, it was found that a combination tone produced by the interaction of the 2200-Hz signal and the 1800-Hz masker could sometimes be heard. To mask this, a narrow-band noise was added to the 1800-Hz masker (and gated with the masker), centered at the combination tone frequency (1400 Hz). The noise was generated by passing white noise (Hewlett Packard 3722A) through two Kemo VBF8/03 filters in series, each with two sections, one set to low pass and one set to high pass. The cutoff frequency for all sections was 1400 Hz. The overall noise level was 20 dB below the level of the 1800-Hz masker. The noise was used both in stage 1 and in stage 2.

C. Procedure

An adaptive two-interval two-alternative forced-choice method was used. A three-down one-up rule was used to estimate the signal level corresponding to the 79.4% correct point on the psychometric function. The signal level was changed in 5-dB steps up to the first four turnpoints and in 2-dB steps thereafter. Twelve turnpoints were obtained and threshold was taken as the mean of the levels at the last eight turnpoints. At least two threshold estimates were obtained for each condition. If the estimates covered a range of more than 2 dB, at least one additional estimate was obtained and all estimates were averaged. The standard deviation of the final estimate ranged from 0.9 to 2.5 dB. The standard error was always less than 1.5 dB. Observation intervals were marked by lights on the response box, and feedback was provided by a light indicating the correct interval. Absolute thresholds were estimated using the same procedure. Subjects were tested individually in a double-walled sound attenuating chamber.

D. Subjects

Four subjects were tested, all with normal hearing; absolute thresholds were better than 20 dB HL at all audiometric frequencies. One subject was author DV. The other subjects were paid for participating. Absolute thresholds for the 2200-Hz signal for a steady state duration of 200 ms were 8, 7, 4, and 5 dB SPL for subjects JP, RB, DV, and MR, respectively. Subjects were given at least 10-h practice, covering all conditions, before formal data collection began.

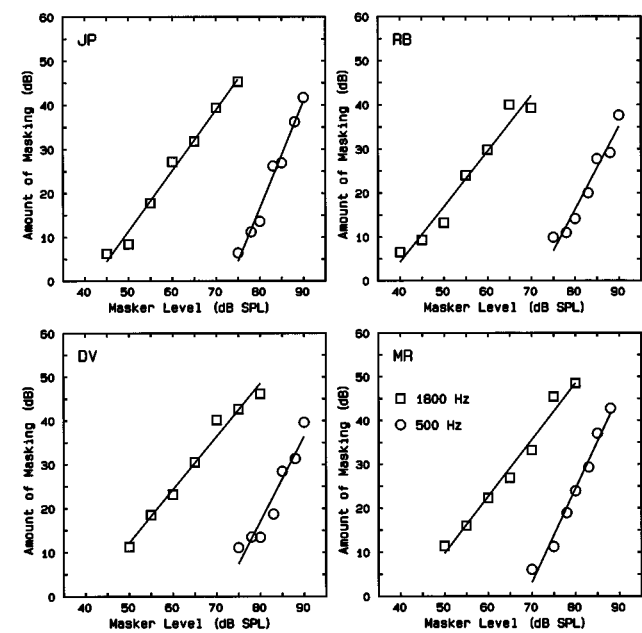


FIG. 1. Results of stage 1, showing growth-of-masking functions in simultaneous masking for a 2200-Hz signal and either an 1800-Hz masker (squares) or a 500-Hz masker (circles). Best-fitting straight lines are also shown. Each panel shows results for one subject.

II. RESULTS

A. Stage 1

The results of stage 1 are shown in Fig. 1. The amount of simultaneous masking of the 2200-Hz signal is plotted as a function of masker level, for the 1800-Hz masker (squares) and the 500-Hz masker (circles). Recall that the results for the former were obtained in the presence of a narrow-band noise designed to mask the combination tone $2f_1-f_2$. The figure also shows the straight lines fitted to the data. Each of these lines accounted for more than 92% of the variance in the data. The slopes of the lines for the 1800-Hz masker are slightly greater than 1, being 1.37, 1.26, 1.21, and 1.29 for JP, RB, DV, and MR, respectively. The slopes are markedly greater for the 500-Hz masker, being 2.42, 1.88, 1.93, and 2.13 for JP, RB, DV, and MR, respectively. The increase in slope with decreasing masker frequency is consistent with earlier work (Wegel and Lane, 1924; Ehmer, 1959; Zwicker and Fastl, 1990).

The fitted lines were used to determine levels of the 1800-Hz and 500-Hz maskers that would be required to give 10, 20, and 30 dB of masking of the 2200-Hz signal. These levels, which are given in Table I for each subject, were used in stage 2, as described below. Note that the 500-Hz masker

TABLE I. Masker levels in dB SPL used in stage 2 for each subject and each masker frequency.

Subject	Masker frequency, Hz		
	500	1800	2200
JP	77, 81, 86	45, 54, 62	18, 28, 38
RB	77, 82, 87	45, 53, 61	17, 27, 37
DV	76, 82, 87	48, 57, 65	14, 24, 34
MR	73, 78, 83	50, 58, 66	15, 25, 35

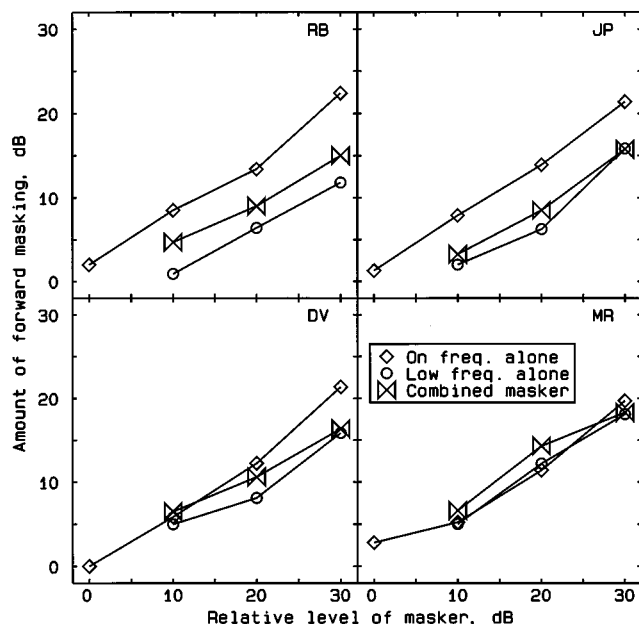


FIG. 2. Results of stage 2 for the 1800-Hz masker, showing the amount of forward masking of a 2200-Hz signal as a function of relative masker level; see text for details. The masker was either a 2200-Hz sinusoid (diamonds), an 1800-Hz sinusoid (circles), or a combination of the two ("bowtie" symbols).

had relatively high absolute levels and also levels well above those of the 2200-Hz masker. Thus in the combined masker, the conditions would be expected to produce strong suppression of the 2200-Hz component by the 500-Hz component (Houtgast, 1974; Shannon, 1976; Duifhuis, 1980). The 1800-Hz masker had lower levels, which would not be expected to lead to strong suppression of the 2200-Hz component of the combined masker. For example, Shannon (1976) showed that a low-frequency component in a two-tone complex produced very little suppression (as revealed by unmasking in a forward-masking situation) unless the absolute level of that component was at or above 70 dB SPL. Duifhuis (1980) came to a similar conclusion using the pulsation-threshold technique. The highest level used for our 1800-Hz masker was 66 dB SPL.

B. Stage 2: Explanation of relative level

Figure 2 shows the results for stage 2 for the 1800-Hz masker, while Fig. 3 shows results for the 500-Hz masker. The amount of forward masking of the 2200-Hz signal is plotted as a function of the "relative level" of the masker. The term "relative level" requires some explanation. In the case of the on-frequency masker alone (2200 Hz—diamonds), it refers to the level of the masker above its own absolute threshold. For example, for subject RB the absolute threshold for the 2200-Hz 200-ms tone was 7 dB SPL, so the 2200-Hz masker was presented at levels of 7, 17, 27, and 37 dB SPL; these are referred to as relative levels of 0, 10, 20, and 30 dB, respectively. In the case of the low-frequency masker alone (500 Hz or 1800 Hz), "relative level" refers to the level of that masker required to simultaneously mask a 2200-Hz signal presented at the relative level specified. For example, for subject RB, the levels of the 1800-Hz masker

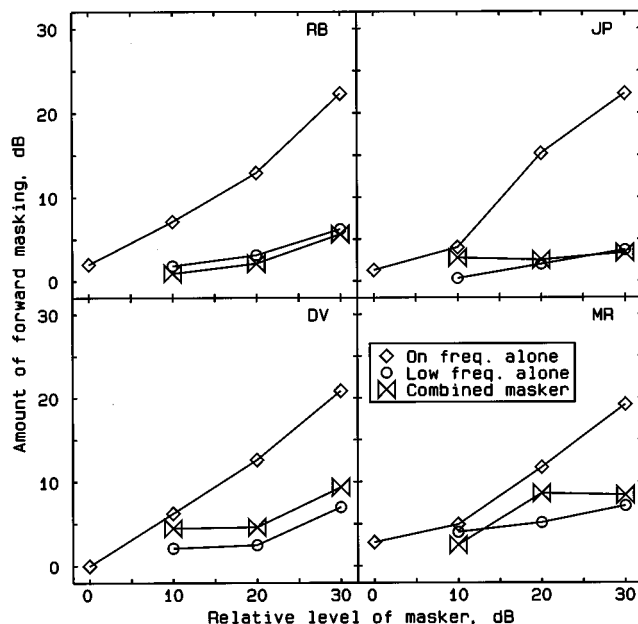


FIG. 3. As Fig. 2, but for a masker frequency of 500 Hz.

required to simultaneously mask the 2200-Hz signal at 17, 27, and 37 dB SPL were 45, 53, and 61 dB SPL, so these were the three masker levels used in stage 2. In the case of the combined masker (500 Hz plus 2200 Hz or 1800 Hz plus 2200 Hz), "relative level" refers to appropriate combinations of the levels of the individual maskers. For example, for subject RB, the 2200-Hz 17-dB masker was paired with the 1800-Hz 45-dB masker, and the 2200-Hz 37-dB masker was paired with the 1800-Hz 61-dB masker.

C. Stage 2: On-frequency masker alone

The results for the on-frequency masker alone are shown by diamonds. These are not exactly the same in Figs. 2 and 3, as all conditions for Fig. 2 (some of which used the 1800-Hz masker) were run with a narrow-band noise centered at 1400 Hz, whereas this noise was absent for Fig. 3. However, the results are always very similar for the two cases. This is as expected, since the noise centered at 1400 Hz would produce a negligible amount of masking compared to the 2200-Hz masker. The amount of masking increases with increasing masker level, reaching about 20 dB for the relative masker level of 30 dB.

D. Stage 2: Effect of adding the 1800-Hz masker

Consider now the effect of adding the 1800-Hz masker to the 2200-Hz masker (Fig. 2, "bowtie" symbols). For two subjects, JP and RB, this produced a reduction in forward masking for all masker levels. For subject DV, a reduction occurred only for the highest masker level and for MR, there was no reduction, or even a slight increase. The reduction might have been caused by suppression of the 2200-Hz component of the masker by the 1800-Hz component. Alternatively, it may have been caused by the introduction of an extra perceptual cue. When a signal in forward masking has the same frequency as a masker, it may be "confused" with

the masker, or heard as a continuation of the masker. The addition of an extra component to the masker at a different frequency may help to reduce this confusion, thereby reducing the signal threshold (Terry and Moore, 1977; Moore, 1980, 1981; Moore and Glasberg, 1982a; Neff, 1985, 1986).

We believe that “cueing” is the most likely cause of the threshold reductions that occurred for some subjects with addition of the 1800-Hz masker, for the following reasons. First, physiological data suggest that suppression of a given tone by a tone lower in frequency is weak or absent except when the suppressor level is rather high (Sachs and Kiang, 1968; Javel, 1981; Delgutte, 1988, 1990). Psycho-physical data lead to the same conclusion (Houtgast, 1974; Shannon, 1976; Duifhuis, 1980); suppression is weak or absent when the absolute level of a low-frequency suppressor is below about 70 dB SPL. For the conditions of our experiment, the 1800-Hz masker was always at a low to moderate level. For example, for subject JP, who showed the largest threshold reductions, the level of the 1800-Hz component of the combined masker ranged from 46 to 62 dB SPL. For the lowest masker level, adding the 1800-Hz component (at 46 dB SPL) to the 2200-Hz component (at 18 dB SPL) produced a threshold reduction similar to that produced by reducing the level of the 2200-Hz masker (alone) by 10 dB. It seems implausible that a low-frequency suppressor with a level of 46 dB SPL could produce suppression equivalent to a 10-dB reduction in level.

For all subjects, the combined masker produced a significant amount of forward masking, which reached 15–18 dB for the highest masker level. This indicates that the combined masker produced significant excitation in the frequency region of the signal. Hence, it seems likely that the simultaneous masking of the 2200-Hz signal by the 1800-Hz masker (as measured in stage 1) was produced by spread of excitation rather than by suppression.

The 1800-Hz masker alone (circles) produced amounts of forward masking that were similar to but, in 9 cases out of 12, slightly below those for the combined masker. This indicates that the 1800-Hz masker produced significant excitation in the frequency region of the 2200-Hz signal. The fact that the combined masker generally produced slightly more forward masking than the 1800-Hz masker alone suggests that the excitation evoked by the 1800-Hz component of the masker at 2200-Hz was comparable to the excitation evoked by the 2200-Hz component of the masker. Again, this suggests that the simultaneous masking of the 2200-Hz signal, as measured in stage 1, was mediated by spread of excitation rather than by suppression.

E. Stage 2: Effect of adding the 500-Hz masker

Consider now the effect of adding the 500-Hz masker to the 2200-Hz masker (Fig. 3, “bowtie” symbols). This produced very substantial reductions in forward masking, in comparison to that produced by the 2200-Hz masker alone. Part of the reductions might be attributed to perceptual cueing, as described earlier for the 1800-Hz combined masker. However, there is no obvious reason why the added tone should provide a more effective cue when its frequency is 500 Hz rather than 1800 Hz. The fact that the threshold

reductions were much larger for the 500-Hz combined masker than for the 1800-Hz combined masker suggests that suppression played a substantial role for the former.

For subject JP, the combined masker produced only a very small amount of forward masking. Even for the highest masker level, the amount of forward masking was only 3 dB. The amount of forward masking was comparable to the 1.8 dB produced by a 2200-Hz forward masker at its own absolute threshold (the left-most diamond in Fig. 3). Also, the 500-Hz masker alone produced only a very small amount of forward masking. This indicates that the combined masker and the 500-Hz masker alone produced negligible excitation in the frequency region of the 2200-Hz signal and suggests that the simultaneous masking of the 2200-Hz signal, as measured in stage 1, was mediated primarily by suppression rather than by spread of excitation.

The other subjects show slightly larger amounts of forward masking for the combined masker, ranging up to about 9 dB. The 500-Hz masker alone produced similar amounts of forward masking to the combined masker. These results indicate that the combined masker, and the 500-Hz masker alone, did produce small amounts of excitation in the frequency region of the 2200-Hz signal. The maximum amounts of forward masking are similar to those produced by a 2200-Hz masker at 5–15 dB above its own absolute threshold. These results are inconsistent with the idea that the simultaneous masking of the 2200-Hz signal, as measured in stage 1, was mediated *purely* by suppression.

III. DISCUSSION

The results showed clear differences between the masking produced by the 1800-Hz combined masker and the 500-Hz combined masker; the latter produced much less forward masking. This is consistent with the idea that the 500-Hz component of the combined masker produced strong suppression of the 2200-Hz component. The 500-Hz combined masker did produce *some* forward masking of the 2200-Hz signal, indicating that the combined masker produced some excitation in the frequency region of the signal. The amount of forward masking produced by the 500-Hz combined masker was usually greater than the forward masking produced by a 2200-Hz masker at its own absolute threshold. This means that the excitation evoked by the combined masker in the frequency region of the signal was at a suprathreshold level. This in turn implies that the masking of the 2200-Hz signal in simultaneous masking, as measured in stage 1, was not mediated purely by suppression. If this were the case, the signal would have been suppressed to a level equivalent to the absolute threshold level, and would have produced a negligible amount of forward masking.

The results are consistent with the idea that simultaneous masking might result from a *combination* of suppression and spread of excitation (Delgutte, 1990; Beveridge and Carlyon, 1996). It is known that when a masker produces only a small amount of masking, the masked threshold is usually greater than would be predicted from a simple summation of the effective power of the masker and the power of the assumed internal noise that gives rise to the absolute threshold (Humes and Jesteadt, 1989). If the 500-Hz masker

suppressed the signal so that its effective level was close to the absolute threshold, then the ratio of signal excitation to masker excitation in the frequency region of the signal would need to be higher to reach threshold than if no suppression occurred (and the overall level were higher). Hence the suppression would influence the masking of the signal, but spread of excitation to the frequency region of the signal would also be involved.

As pointed out by Delgutte (1990, 1996), the evidence indicating that strong suppression can occur for masker frequencies well below the signal frequency has important implications for the interpretation of masking patterns. These are plots of the threshold (or amount of masking) of a signal as a function of signal frequency in the presence of a masker with fixed frequency and level. In early work, it was thought that the signal threshold might be directly related to the amount of excitation evoked by the masker at the characteristic frequency (CF) or place corresponding to the signal frequency (Wegel and Lane, 1924; Fletcher and Munson, 1937; Egan and Hake, 1950; Zwicker, 1956). The present results, and the earlier work of Delgutte (1990), indicate that the signal threshold may seriously overestimate the excitation produced by the masker at the signal frequency when the masker is much lower in frequency than the signal. Put another way, the high-frequency sides of excitation patterns may be more restricted, and have steeper slopes, than indicated by masking patterns.

Excitation patterns form the basis of several perceptual models, including models of loudness perception (Zwicker and Scharf, 1965; Moore and Glasberg, 1996) and models for the detection of frequency and amplitude modulation (Zwicker, 1952; Zwicker and Fastl, 1990). If the excitation patterns on which those models are based are too broad, then the models themselves must be inaccurate. In this context, it is of interest that Moore and Sek (1994) showed that an excitation-pattern model could account for thresholds for the detection of amplitude modulation, frequency modulation, and mixtures of the two, but only if they assumed sharper excitation patterns than specified by Zwicker and co-workers or by Glasberg and Moore (1990).

IV. CONCLUSIONS

This experiment used forward masking as a tool for determining the amount of excitation evoked by a masker in the frequency region of the signal. The results lead to the following conclusions:

- (1) In simultaneous masking, when the masker frequency (1800 Hz) is just below the signal frequency (2200 Hz), the dominant mechanism of masking is spread of the excitation evoked by the masker to the signal frequency.
- (2) In simultaneous masking, when the masker frequency (500 Hz) is well below the signal frequency, there is strong suppression of the signal by the masker. However, the amount of excitation evoked by the masker and the masker-plus-signal in the frequency region of the signal remains at a suprathreshold level. Therefore, the masking of the signal cannot be explained solely in terms of suppression. Probably, the signal threshold is determined both by suppression and by spread of excitation.

ACKNOWLEDGMENTS

This work was supported by the Medical Research Council (UK). We thank Brian Glasberg for writing the computer programs to run the experiment, and Tom Baer, Larry Humes, and a friendly but anonymous reviewer for helpful comments on an earlier version of this paper.

- Beveridge, H. A., and Carlyon, R. P. (1996). "Effects of aspirin on human psychophysical tuning curves in forward and simultaneous masking," *Hearing Res.* **99**, 110–118.
- Delgutte, B. (1988). "Physiological mechanisms of masking," in *Basic Issues in Hearing*, edited by H. Duifhuis, J. W. Horst, and H. P. Wit (Academic, London).
- Delgutte, B. (1990). "Physiological mechanisms of psychophysical masking: Observations from auditory-nerve fibers," *J. Acoust. Soc. Am.* **87**, 791–809.
- Delgutte, B. (1996). "Physiological models for basic auditory percepts," in *Auditory Computation*, edited by H. L. Hawkins, T. A. McMullen, A. N. Popper, and R. R. Fay (Springer, New York).
- Duifhuis, H. (1980). "Level effects in psychophysical two-tone suppression," *J. Acoust. Soc. Am.* **67**, 914–927.
- Egan, J. P., and Hake, H. W. (1950). "On the masking pattern of a simple auditory stimulus," *J. Acoust. Soc. Am.* **22**, 622–630.
- Ehmer, R. H. (1959). "Masking patterns of tones," *J. Acoust. Soc. Am.* **31**, 1115–1120.
- Fletcher, H. (1940). "Auditory patterns," *Rev. Mod. Phys.* **12**, 47–65.
- Fletcher, H., and Munson, W. A. (1937). "Relation between loudness and masking," *J. Acoust. Soc. Am.* **9**, 1–10.
- Glasberg, B. R., and Moore, B. C. J. (1990). "Derivation of auditory filter shapes from notched-noise data," *Hearing Res.* **47**, 103–138.
- Hind, J. E., Rose, J. E., Brugge, J. F., and Anderson, D. J. (1967). "Coding of information pertaining to paired low-frequency tones in single auditory nerve fibres of the squirrel monkey," *J. Neurophysiol.* **30**, 794–816.
- Houtgast, T. (1972). "Psychophysical evidence for lateral inhibition in hearing," *J. Acoust. Soc. Am.* **51**, 1885–1894.
- Houtgast, T. (1974). "Lateral suppression in hearing," Ph.D. thesis, Free University of Amsterdam.
- Humes, L. E., and Jesteadt, W. (1989). "Models of the additivity of masking," *J. Acoust. Soc. Am.* **85**, 1285–1294.
- Javel, E. (1981). "Suppression of auditory nerve responses: I. Temporal analysis, intensity effects and suppression contours," *J. Acoust. Soc. Am.* **69**, 1735–1745.
- Moore, B. C. J. (1980). "Detection cues in forward masking," in *Psychophysical, Physiological and Behavioral Studies in Hearing*, edited by G. van den Brink and F. A. Bilsen (Delft University Press, Delft).
- Moore, B. C. J. (1981). "Interactions of masker bandwidth with signal duration and delay in forward masking," *J. Acoust. Soc. Am.* **70**, 62–68.
- Moore, B. C. J., and Glasberg, B. R. (1982a). "Contralateral and ipsilateral cueing in forward masking," *J. Acoust. Soc. Am.* **71**, 942–945.
- Moore, B. C. J., and Glasberg, B. R. (1982b). "Interpreting the role of suppression in psychophysical tuning curves," *J. Acoust. Soc. Am.* **72**, 1374–1379.
- Moore, B. C. J., and Glasberg, B. R. (1996). "A revision of Zwicker's loudness model," *Acustica—Acta Acustica* **82**, 335–345.
- Moore, B. C. J., and Sek, A. (1994). "Effects of carrier frequency and background noise on the detection of mixed modulation," *J. Acoust. Soc. Am.* **96**, 741–751.
- Neff, D. L. (1985). "Stimulus parameters governing confusion effects in forward masking," *J. Acoust. Soc. Am.* **78**, 1966–1976.
- Neff, D. L. (1986). "Confusion effects with sinusoidal and narrow-band-noise forward maskers," *J. Acoust. Soc. Am.* **79**, 1519–1529.
- Pickles, J. O. (1984). "Frequency threshold curves and simultaneous masking functions in single fibers of the guinea pig auditory nerve," *Hearing Res.* **14**, 245–256.
- Sachs, M. B., and Kiang, N. Y. S. (1968). "Two-tone inhibition in auditory nerve fibers," *J. Acoust. Soc. Am.* **43**, 1120–1128.
- Shannon, R. V. (1976). "Two-tone unmasking and suppression in a forward masking situation," *J. Acoust. Soc. Am.* **59**, 1460–1470.
- Terry, M., and Moore, B. C. J. (1977). "Suppression effects in forward masking," *J. Acoust. Soc. Am.* **62**, 781–784.
- Weber, D. L. (1983). "Do off-frequency simultaneous maskers suppress the signal?" *J. Acoust. Soc. Am.* **73**, 887–893.

- Wegel, R. L., and Lane, C. E. (1924). "The auditory masking of one sound by another and its probable relation to the dynamics of the inner ear," *Phys. Rev.* **23**, 266–285.
- Wightman, F. L., McGee, T., and Kramer, M. (1977). "Factors influencing frequency selectivity in normal and hearing-impaired listeners," in *Psychophysics and Physiology of Hearing*, edited by E. F. Evans and J. P. Wilson (Academic, London).
- Zwicker, E. (1952). "Die Grenzen der Hörbarkeit der Amplitudenmodulation und der Frequenzmodulation eines tones," *Acustica* **2**, 125–133.
- Zwicker, E. (1956). "Die elementaren Grundlagen zur Bestimmung der Informationskapazität des Gehörs," *Acustica* **6**, 356–381.
- Zwicker, E. (1970). "Masking and psychological excitation as consequences of the ear's frequency analysis," in *Frequency Analysis and Periodicity Detection in Hearing*, edited by R. Plomp and G. F. Smoorenburg (Sijthoff, Leiden).
- Zwicker, E., and Fastl, H. (1990). *Psychoacoustics—Facts and Models* (Springer-Verlag, Berlin).
- Zwicker, E., and Scharf, B. (1965). "A model of loudness summation," *Psychol. Rev.* **72**, 3–26.

A probe-signal study of auditory discrimination of complex tones

Nicholas I. Hill^{a)} and Peter J. Bailey

Department of Psychology, University of York, York YO1 5DD, United Kingdom

Philip Hodgson

Department of Experimental Psychology, University of Oxford, Oxford OX1 3UD, United Kingdom

(Received 18 September 1995; revised 19 September 1996; accepted 23 January 1997)

The present experiments used an analogue of the probe-signal method of Greenberg and Larkin [J. Acoust. Soc. Am. **44**, 1513–1523 (1968)] to investigate the extent to which listeners direct attention to a particular spectral region when discriminating complex tones. The listeners' task was to discriminate between two seven-component complex tones on the basis of an increment in the level of a single component. On two-thirds of trials the increment was achieved by adding a fixed *primary signal* to one component of the complex. The primary-signal trials were relatively easy and were intended to cue listeners to attend to the component to which the primary was added. On the remaining trials a smaller *probe signal* was added either to the cued component, or to one of three other components. The results of the first experiment, in which the complex tones had a flat spectrum, showed significantly better performance for probe signals applied to the cued component compared to the other three components. To control for the possibility that the observed pattern of results was due to the use of timbral cues, a second experiment was conducted in which the spectral profile of the tones was randomized between trials. The results for the second experiment were similar to those of the first experiment and are consistent with the idea that listeners were focusing attention on the spectral region defined by the primary signal. © 1997 Acoustical Society of America. [S0001-4966(97)03909-X]

PACS numbers: 43.66.Fe, 43.66.Lj [RHD]

INTRODUCTION

In a pioneering study of the frequency selectivity of the auditory periphery, Greenberg and Larkin (1968) measured the detection rate in noise for an infrequently presented sinusoidal target (the probe) as a function of its spectral separation from a frequently presented sinusoidal target (the primary). The intended purpose of the primary-signal trials was to direct and maintain the listeners' attention to a particular frequency region so that the consequences of focused attention for sensitivity at unattended frequencies could be explored. Consistent with a bandpass-filter model of frequency selectivity, detection performance for the probes was found to decrease from about 80% correct for probes close in frequency to the primary, down to 50% (chance) for probes differing in frequency from the primary by more than 15%–20%. However, as discussed by Greenberg and Larkin, the observed pattern of results may reflect changes in response bias rather than a genuine shift in sensitivity. For example, observers may require more sensory evidence before concluding that a signal was presented if the probability of such a signal having been presented was relatively low. Similarly, observers may have deliberately disregarded distant probes because they were led to believe that they would only ever be presented with the primary signal, and may therefore have treated the unexpected signal as an irrelevant artifact. The

plausibility of this heard-but-not-heeded account of the Greenberg and Larkin data is enhanced by the fact that no feedback was provided to their subjects.

The extent to which the pattern of results reported by Greenberg and Larkin (1968) was due to a genuine shift in sensitivity as opposed to some kind of response bias was investigated in a series of experiments by Scharf *et al.* (1987). In one group of experiments they employed narrow-band complex signals as probes, thereby ensuring a timbre difference between the probes and the pure-tone primary even when they occupied the same spectral region. If the decrease in detection performance for distant probes observed by Greenberg and Larkin was simply due to the fact that they were perceptually distinct from the primary, then detection performance for the complex probes ought to be poor regardless of their spectral content. However, Scharf *et al.* found that the detection rate for a complex probe centered on the primary was significantly better than that for either a sinusoidal or complex probe presented in an unexpected frequency region, even when feedback was provided. In a different experiment in the same series, Scharf *et al.* found that informing observers about the presence of the probes led to a small improvement in detection performance for probes close to the primary, but had no effect on detection performance for more distant probes. Taken together, the above results provide strong support for the idea that directing attention to a particular frequency region can lead to a reduction in an observers' sensitivity to energy in non-attended regions.

The studies of both Greenberg and Larkin (1968) and

^{a)}Electronic mail: nihl@york.ac.uk

Scharf *et al.* (1987) were concerned with the allocation of attention to a single-frequency region. However, several studies have been reported which suggest that observers can attend selectively to two or more frequency regions simultaneously (e.g., Macmillan and Schwartz, 1975; Buus *et al.*, 1986; Schlauch and Hafter, 1991). Schlauch and Hafter (1991) used a modified version of the probe-signal technique in which the frequency of the primary was varied randomly across trials so as to remove any cumulative memory effects. Observers were encouraged to attend to the frequency region encompassing the primary by means of an auditory pre-cue comprising either one, two, or four components depending on the condition. In the single-component cue condition, the frequency of the cue always corresponded to that of the primary, whereas in the complex cue conditions the frequency of the primary matched that of one of the components of the cue. For both the two-component and four-component cue conditions probe detection rates decreased systematically with increasing frequency separation from the most proximal component of the cue. This result is consistent with the idea that observers were monitoring the output of filters centered on each of the cue components.

Given the evidence that observers can attend selectively to one or more spectral regions, resulting in reduced sensitivity elsewhere, the question arises as to the extent to which the allocation of attention can be controlled strategically by the observer, as opposed to being driven by the spectral characteristics of the cue. Of relevance to this issue is a probe-signal study reported by Hafter *et al.* (1993) in which again the frequency of the primary was varied randomly across trials. They demonstrated that cuing effects could be observed both in an "iconic cue" condition, that is, when the frequency of the primary matched that of an auditory pre-cue, and also in a "relative cue" condition in which the frequency of the primary was set to 1.5 times that of the cue. In the latter case, detection performance was consistently better for probes close to the cued frequency than it was for a probe having the same frequency as the cue. This latter result suggests that some degree of endogenous control of attention is possible.

By contrast with Hafter *et al.*'s study which suggested that attention could be directed independently of the cuing stimulus, Dai and Buus (1991) report a result which suggests that stimulus-driven attentional allocation can interfere with attempts to listen selectively. In their study, Dai and Buus found that when a noise masker was gated on 300 ms ahead of the target rather than being presented continuously, the selectivity usually observed in probe-signal detection studies was much less apparent. One explanation put forward to account for the broadening in the detectability pattern was that listeners' attention may be automatically directed towards frequency regions where there is a sudden change in the level of excitation. If this is the case, then the result of Hafter *et al.* (1993) may indicate that their listeners were able to redirect attention during the 300-ms interval between the offset of the cue and the first observation interval.

The suggestion that observers engaged in detection tasks can modulate dynamically their relative sensitivity to energy in a particular spectral region raises the possibility that such

strategies may be employed in more general listening situations. For example, continuous speech typically provides unfolding information about the identity of upcoming segments which could be exploited by the auditory system to direct attention to critical spectrotemporal regions (Watson and Foyle, 1985). Furthermore, the ability to attend selectively to a number of discrete frequency regions simultaneously may play a role in the auditory system's ability to segregate concurrent sounds (Woods and Colburn, 1992). For example, by identifying the principal periodicities present in a signal, and directing attention towards the subset of active channels corresponding to approximate integer multiples of one of these principal periodicities, segregation of harmonic sounds may be achieved (e.g., Assmann and Summerfield, 1990).

The objective of the present research was to examine whether, when discriminating between complex tones, listeners direct their attention to the spectral region most likely to contain the discriminating information. The two experiments employed an analogue of the probe-signal procedure in which the signal was an increment in the level of a single component of a seven-component complex. Attention was directed towards a particular component by adding a primary signal to that component on the majority of trials. The level of the primary signal was 8 dB above threshold (defined as the level corresponding to 79% correct). On the remaining trials a threshold probe signal was added to either the cued component or to one of three other components. Several features of the present task distinguish it from previous applications of the probe-signal technique. For example, when detecting signals in noise the cue associated with detection is a tonal percept with a specific pitch. In the present case the cue is a characteristic change in some overall perceptual attribute of the complex. Furthermore, the use of stimuli with constant spectral profile means that listeners could use within-interval, across-channel cues rather than comparing energy in a particular region across intervals. Finally, the results of Dai and Buus (1991) suggest that attention may be directed automatically towards frequency regions where there is a sudden change in the level of excitation. In the present task all components of the stimulus begin at the same time and therefore any automatic focusing of attention towards regions where there is a sudden change in energy would limit the extent to which listeners can attend selectively to a single component.

I. EXPERIMENT 1

A. Listeners

The four listeners (two male) were aged between 20 and 26 yr, had normal pure-tone thresholds over the range of frequencies used in this experiment, and reported no history of hearing problems. Listeners were unaware of the objectives of the experiment and were paid.

B. Stimuli and equipment

The stimuli were complex tones comprising seven logarithmically spaced components at frequencies of 200, 270, 365, 492, 664, 897, and 1211 Hz. The components were gated synchronously in sine-phase, and had a total duration

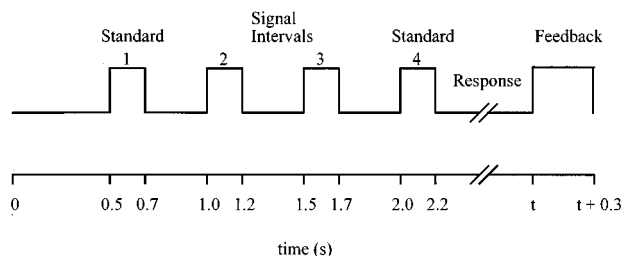


FIG. 1. Schematic representation of the structure and time course of a single trial. The standard was presented in each of intervals 1–4, with the signal added to the standard during either interval 2 or 3 with equal probability. Listeners were given an unlimited time in which to respond.

of 200 ms including 10-ms cosine-squared onset and offset ramps. Each component of the standard was presented at 40 dB SPL. Stimuli were synthesized using a sampling rate of 10 kHz and were converted to voltages using 16-bit digital-to-analog converters (Data Translation DT2823). The stimuli were then low-pass filtered at 3.5 kHz and suitably attenuated before being presented monaurally to the listeners' right ear over Sennheiser HD414 headphones. Listeners were run individually in a single-walled, sound-attenuating chamber. Stimulus generation and experimental control were achieved using custom software running on an IBM-compatible PC.

C. Procedure

Listeners were required to discriminate between the standard and standard-plus-signal, where the signal was an increment in the amplitude of one of components three through six. Discrimination performance was measured using a four-interval, two-alternative, forced-choice procedure with the signal added to the standard during either interval two or three with equal probability (see Fig. 1). Each trial began with a 500-ms pause followed by the four stimulus presentation intervals each separated by silent intervals of 300 ms. Listeners were given an unlimited time in which to indicate their response, following which they were presented with visual feedback for 300 ms. The next trial began immediately after the termination of feedback.

Prior to the main experiment each listener was run on a series of calibration sessions to determine the amount by which a component in the complex had to be incremented to give 79% correct discrimination performance. Thresholds were determined for components three, four, five, and six using a three-down, one-up adaptive procedure. Each threshold was based on at least eight runs of the adaptive procedure with typically three runs of each condition completed per 1-h session. The intensity increments corresponding to these thresholds are given in Table I. The main experiment assessed the extent to which listeners were able to attend selectively to a particular frequency component using a variant of the probe-signal method. Specifically, listeners were encouraged to direct attention to a particular component by adding a primary signal to that component on two-thirds of the trials within a given block. The level of the primary signal relative to that of the signal corresponding to 79% correct was +8 dB. On each of the remaining trials, a probe

TABLE I. Increment in intensity corresponding to the addition of a probe signal to components three, four, five, and six, respectively. Increment magnitudes were determined using a three-down, one-up adaptive procedure which targeted the level corresponding to 79% correct.

Listener	Probe-signal intensity increment (dB)			
	3	4	5	6
AK	1.3	1.3	2.8	2.2
CMP	1.3	1.7	0.8	0.8
RJS	1.8	2.2	2.0	1.3
CT	1.4	2.2	2.5	1.8

signal was added randomly to one of components three through six with equal probability. The level of each probe was set to correspond to 79% correct. The primary- and probe-signal trials were interleaved pseudorandomly with the restrictions that (a) each contiguous group of three trials included one presentation of a probe signal, and (b) probe signals were never presented on successive trials. Listeners were simply instructed to identify the odd stimulus, and were not informed about the presence of probe signals.

Each listener was run on two conditions with the ordering of the conditions counterbalanced. In the *primary-3* condition, the primary signal was added to component three (365 Hz) while in the *primary-6* condition the primary signal was added to component six (897 Hz). Data were collected over four sessions run on different days with sessions one and two devoted to one of the conditions, and sessions three and four devoted to the other. Listeners AK and CMP were presented first with the primary-3 condition, while listeners RJS and CT were presented first with the primary-6 condition. Each session lasted approximately 1 h, and comprised a practice block of 40 trials, followed by 12 blocks of 60 trials. Only the primary signal was presented during the practice block.

D. Results and discussion

Figure 2 shows the percentage of correct discrimination responses for each listener and condition. The columns represent performance for probe signals added to components three, four, five, and six, respectively. Open columns denote performance in the primary-3 condition, while the shaded columns denote performance in the primary-6 condition. The error bars associated with each column indicate 95% confidence intervals. The dashes above the component-3 and component-6 markers denote performance for the primary signals added to components three and six, respectively. Each column is based on 120 trials, and each dash on 960 trials.

For all listeners, the performance associated with the primary signals exceeded that associated with the probes, only listener RJS failed to achieve more than 90% correct for both stimuli. In the case of the probe signals, performance was best when the frequency of the probe matched that of the primary, although for RJS the difference between components four and six in the primary-6 condition failed to reach significance (two-tailed test for proportion). Given that the levels of the probe signals were set to give discrimination

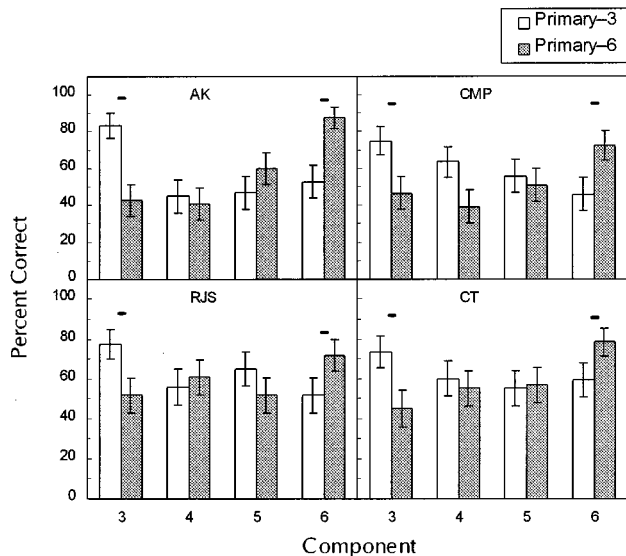


FIG. 2. Percent correct discrimination responses for each listener and condition in experiment 1. The columns show performance for probe signals added to components three, four, five, and six, respectively. Open columns denote performance in the primary-3 condition, shaded columns that in the primary-6 condition. Error bars denote 95% confidence intervals. The two dashes in each panel show discrimination performance associated with the primary signals.

performance of approximately 79%, the fact that listeners generally performed better when the frequency of the probe matched that of the primary is consistent with the idea that they were focusing attention on a spectral region encompassing the primary.

The effect of the primary-signal frequency is further illustrated by comparing the performance for probe signals added to components three and six across the two conditions. For the probe added to component three, performance of all listeners was significantly better when the primary was also added to component three than when added to component six. A complementary result holds for the probe added to component six with performance for all listeners being better when the primary signal was also added to component six (two-tailed test for proportion, $p < 0.05$).

In traditional probe-signal detection studies the pattern of performance for the probe shows a steady decline as the frequency separation between the probe and primary is increased. In the present data performance is generally poor whenever the frequency of the probe and primary differ. There are at least two factors that contribute to the observed pattern. First, the frequency ratio between successive components of the complex is 1.35. The data of traditional probe-signal studies also show probe performance around chance level at similar frequency separations (e.g., Greenberg and Larkin, 1968; Dai *et al.*, 1991). Second, the probe signals in the present experiment were set at a level corresponding to 79% correct discrimination. This contrasts with a value approaching 90% correct in most previous probe-signal studies. The use of a four-interval procedure with feedback makes it unlikely that listeners were simply ignoring probes at unexpected frequencies.

While the results of experiment 1 are consistent with the

hypothesis that listeners were attending selectively across frequency, they are also consistent with what one would predict had listeners been selecting the target on the basis of its spectral profile. In particular, if listeners had been selecting the complex whose timbre matched most closely that of the standard-plus-primary, then on trials in which the probe differed in frequency from the primary, the timbre of the standard would be heard as a better match to the standard-plus-primary than would the standard-plus-probe. The fact that discrimination performance for the probe signal added to component four dips below chance for listeners AK and CMP adds some support for this hypothesis.

The idea that observers may perform auditory discriminations of complex sound spectra by reference to a representation of timbre in long-term memory is supported by a number of findings. For example, Green *et al.* (1983) found that signal threshold in a profile analysis task was only marginally affected by increases in interstimulus interval from 300 to 8000 ms. Similarly, Kidd *et al.* (1986) showed that signal thresholds increased significantly when the spectral profile of the standard was varied between 50-trial blocks.

While the present experiment did not require listeners to use the spectral profile of the stimuli as a cue, the sensitivity of listeners to perturbations of spectral profile means that the possibility that they did so cannot be discounted. For this reason a second experiment was conducted in which the levels of the individual components were randomized across trials. The results of a study by Kidd *et al.* (1988) suggest that this should promote the use of across-interval rather than within-interval comparisons.

II. EXPERIMENT 2

This experiment was identical to experiment 1 except that the level of each component was randomized across trials. Accordingly, any difference in performance between probes is likely to reflect differences in the distribution of attention across frequency rather than the degree of timbral similarity between the standard-plus-probe and standard-plus-primary.

A. Listeners

The four listeners (one male) were aged between 20 and 28 yr, had normal pure-tone thresholds over the range of frequencies used in this experiment, and reported no history of hearing problems. Listeners MW, CT, and IJ were unaware of the objectives of the experiment, although listener CT had previously participated in experiment 1. These listeners were paid and listener NIH was the first author.

B. Procedure

The procedure was identical to that employed in experiment 1 except that the level of each component was varied randomly across (but not within) trials. These levels were selected independently from the range 35 to 45 dB SPL and had a uniform distribution. Listeners MW and CT were presented first with the primary-3 condition, while listeners NIH and IJ were presented first with the primary-6 condition. The

TABLE II. Increment in intensity corresponding to the addition of a probe signal to components three, four, five, and six, respectively. Increment magnitudes were determined using a three-down, one-up adaptive procedure which targeted the level corresponding to 79% correct.

Listener	Probe-signal intensity increment (dB)			
	3	4	5	6
MW	2.5	2.6	2.4	2.5
CT	2.8	2.9	4.2	2.9
NIH	2.2	2.3	2.4	1.7
IJ	2.4	2.3	2.6	2.3

intensity increments corresponding to threshold were again determined using a three-down, one-up procedure and are given in Table II.

C. Results and discussion

Figure 3 shows the percentage of correct discrimination responses for each listener and condition. The columns represent performance for probe signals added to components three, four, five, and six, respectively. Open columns denote performance in the primary-3 condition, while the shaded columns denote performance in the primary-6 condition. The error bars associated with each column indicate 95% confidence intervals. The dashes above the component-3 and component-6 markers denote performance for the primary signals added to components three and six, respectively. Each column is based on 120 trials, and each dash on 960 trials.

The pattern of results associated with the probe-signals is similar to that obtained in experiment 1 with discrimination performance again being best when the frequency of the

probe matched that of the primary. There does, however, appear to be a greater effect on components immediately adjacent the primary than was observed in experiment 1. The difference in performance between components three and four in the primary-3 condition was not significant for listeners CT and NIH, nor was the difference between components five and six for listener IJ in the primary-6 condition (two-tailed test for proportion). The pattern of results for listener NIH, the first author, suggests that awareness that probe-signals could differ in frequency from the primary does not significantly influence listening strategy.

The effect of primary-signal frequency is comparable to that observed in experiment 1 with once again all listeners performing significantly better when the frequency of the probe-signal matched that of the primary (two-tailed test for proportion, $p < 0.05$). The results therefore add further support to the idea that subjects were attending selectively to a frequency region encompassing the primary signal.

III. GENERAL DISCUSSION

The present experiments extended the traditional probe-signal method pioneered by Greenberg and Larkin (1968) to a task involving the discrimination of complex tones. The results of experiment 1 showed that the accuracy with which listeners correctly identified an increment in the level of a single component of a multitone complex was affected by the probability of that component being incremented. In particular, discrimination performance was significantly better when the incremented component had a high probability of carrying the signal, rather than when its probability of being incremented was relatively low. This result is consistent with the idea that listeners were attending selectively to the spectral region most likely to contain the discriminating information. The second experiment replicated these findings using an identical procedure but with the profile of the standard varied randomly from trial to trial. It therefore appears unlikely that listeners were identifying the target by comparing its profile with that of a stored template in memory. The results of both experiments are broadly analogous with those obtained from traditional probe-signal detection tasks and suggest that listeners may also deploy attention strategically when discriminating complex tones.

Further evidence that attentional factors may influence the processing of auditory stimuli can be inferred from the results of a binaural interference experiment reported recently by Buell and Trahiotis (1994). They measured the threshold for detecting the presence of an interaural temporal disparity (ITD) applied to a narrow band of an otherwise diotic broadband noise. The center frequency of the target band was either 300, 1200, 2400, or 4800 Hz. Trial-by-trial randomization of the center frequency of the target band resulted in significantly higher thresholds than were obtained when the target band was fixed within a block. One interpretation of this result is that listeners performed better in the fixed-target condition because they were able to direct attention selectively towards the spectral region containing the critical information. Based on these findings we are currently planning further experiments to investigate whether results similar to those reported in experiments 1 and 2 are observed

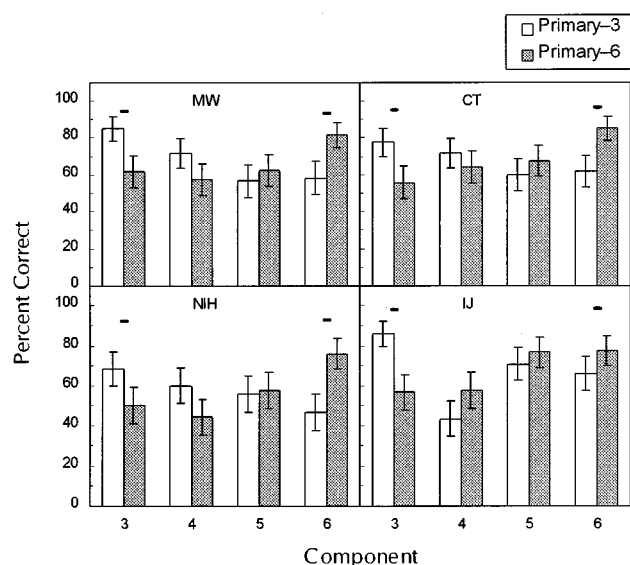


FIG. 3. Percent correct discrimination responses for each listener and condition in experiment 2. The columns show performance for probe signals added to components three, four, five, and six, respectively. Open columns denote performance in the primary-3 condition, shaded columns that in the primary-6 condition. Error bars denote 95% confidence intervals. The two dashes in each panel show discrimination performance associated with the primary signals.

when the cue for discrimination is an interaural delay rather than an intensity increment. The advantage of using ITDs is that subjects cannot perform the discrimination on the basis of timbral cues.

While there is a growing body of evidence supporting the idea that attention can be allocated to specific spectral regions, the mechanism by which attention may influence the processing of complex sounds is unclear. One possibility is that listeners may be able to attenuate the contribution of selected frequency channels at a relatively early stage in the auditory pathway, such that information in critical spectral regions makes a greater relative contribution to subsequent processing stages and hence to the resultant percept. Evidence supporting this idea comes from a probe-signal detection study by Dai *et al.* (1991) in which it was shown that the effective attenuation of probes outside the attended band was approximately 7 dB, and was independent of the frequency separation. The goal of the present experiments has been to indicate that attentional factors may play a wider role in auditory perception than simply facilitating the detection of weak sounds in noise. The extent to which attention is employed in the processing of natural sounds, and the means by which it operates are subjects for future research.

ACKNOWLEDGMENT

Financial support was provided by the U.K. Medical Research Council through Project Grant No. G9306195N.

Assmann, P. F., and Summerfield, Q. (1990). "Modeling the perception of concurrent vowels: Vowels with different fundamental frequencies," *J. Acoust. Soc. Am.* **88**, 680–697.

- Buell, T. N., and Trahiotis, C. (1994). "Detection of interaural delay in bands of noise: Effects of spectral interference combined with spectral uncertainty," *J. Acoust. Soc. Am.* **95**, 3568–3573.
- Buus, S., Schorer, E., Florentine, M., and Zwicker, E. (1986). "Decision rules in the detection of simple and complex tones," *J. Acoust. Soc. Am.* **80**, 1646–1657.
- Dai, H., and Buus, S. (1991). "Effect of gating the masker on frequency-selective listening," *J. Acoust. Soc. Am.* **89**, 1816–1818.
- Dai, H., Scharf, B., and Buus, S. (1991). "Effective attenuation of signals in noise under focused attention," *J. Acoust. Soc. Am.* **89**, 2837–2842.
- Green, D. M., Kidd, Jr., G., and Picardi, M. C. (1983). "Successive versus simultaneous comparison in auditory intensity discrimination," *J. Acoust. Soc. Am.* **73**, 639–643.
- Greenberg, G. Z., and Larkin, W. D. (1968). "Frequency-response characteristic of auditory observers detecting signals of a single frequency in noise: The probe-signal method," *J. Acoust. Soc. Am.* **44**, 1513–1523.
- Haftner, E. R., Schlauch, R. S., and Tang, J. (1993). "Attending to auditory filters that were not stimulated directly," *J. Acoust. Soc. Am.* **94**, 743–747.
- Kidd, Jr., G., Mason, C. R., and Green, D. M. (1986). "Auditory profile analysis of irregular sound spectra," *J. Acoust. Soc. Am.* **79**, 1045–1053.
- Kidd, Jr., G., Mason, C. R., and Hanna, T. E. (1988). "Evidence for sensory-trace comparisons in spectral shape discrimination," *J. Acoust. Soc. Am.* **84**, 144–149.
- Macmillan, N. A., and Schwartz, M. (1975). "A probe-signal investigation of uncertain-frequency detection," *J. Acoust. Soc. Am.* **58**, 1051–1058.
- Scharf, B., Quigley, S., Aoki, C., Peachey, N., and Reeves, A. (1987). "Focused auditory attention and frequency selectivity," *Percept. Psychophys.* **42**, 215–223.
- Schlauch, R. S., and Haftner, E. R. (1991). "Listening bandwidths and frequency uncertainty in pure-tone signal detection," *J. Acoust. Soc. Am.* **90**, 1332–1339.
- Watson, C. S., and Foyle, D. C. (1985). "Central factors in the discrimination and identification of complex sounds," *J. Acoust. Soc. Am.* **78**, 375–380.
- Woods, W. S., and Colburn, H. S. (1992). "Test of a model of auditory object formation using intensity and interaural time difference discrimination," *J. Acoust. Soc. Am.* **91**, 2894–2902.

Identification of multidimensional stimuli containing speech cues and the effects of training

Laurel A. Christensen

Department of Communication Disorders and Kresge Hearing Research Laboratory, Louisiana State University Medical Center, 1900 Gravier Street, New Orleans, Louisiana 70112

Larry E. Humes

Audiology Research Laboratory, Department of Speech and Hearing Sciences, Indiana University, Bloomington, Indiana 47405

(Received 5 November 1996; accepted for publication 23 June 1997)

The purpose of this study was to determine how listeners with normal hearing make use of cues from multiple, independent stimulus dimensions when classifying synthesized stimuli containing acoustic cues found in speech. Listeners classified synthesized stimuli that differed on three independent and discriminable dimensions. The three dimensions of the stimuli included: (1) the fricative spectrum center frequency; (2) the slope of the frequency transition; and (3) the duration of the temporal gap. Each of the three dimensions could take on one of three possible values. Twenty-seven stimuli were synthesized using all possible combinations of the values on the three dimensions. Multidimensional scaling of paired-comparison similarity judgments confirmed the existence of three perceptual dimensions. Listeners were then trained to classify three exemplar stimuli as "circle," "triangle," and "square," respectively. Following this training, subjects classified all 27 stimuli as "circle," "triangle," and "square." From this it was determined how each listener's attention was distributed among the dimensions. Results indicated the listeners did not pay equal attention to the three stimulus dimensions. In addition, it was demonstrated that it was possible to train a listener to attend to a dimension that was not previously used to classify the stimuli. © 1997 Acoustical Society of America. [S0001-4966(97)01810-9]

PACS numbers: 43.66.Fe, 43.66.Lj, 43.66.Mk, 43.71.An [JWH]

INTRODUCTION

Acoustic changes along several dimensions, including frequency, amplitude, and time, are critical for changing perception of a speech signal from one phoneme to another. The acoustic elements responsible for perceptual changes have been the topic of considerable research. Experiments using speech synthesis and waveform editing have verified the existence of multiple perceptual cues and have shown that listeners are able to make many acoustic-phonetic distinctions after redundant cues have been removed (Cooper *et al.*, 1952; Delattre *et al.*, 1952). Thus the listener does not need all of the redundant information in natural speech to make a phonetic decision. It is not clear, however, how a listener uses the information or cues available to make these distinctions. In other words, when several perceptual cues are available to a listener, does the listener use all the information or does the listener focus primarily on one or two cues for signaling a distinction? The research described in this paper will focus on how listeners with normal hearing make use of multiple cues to classify stimuli. This question becomes even more interesting when it is discussed with respect to the speech understanding abilities of listeners with hearing impairment.

Listeners with sensorineural hearing impairment have difficulty understanding speech. The inaudibility of the speech signal has been found to be the primary factor underlying these speech-understanding deficits in both young and elderly listeners (e.g., Dirks *et al.*, 1986; Dubno and Dirks,

1989; Humes and Christopherson, 1991; Humes and Roberts, 1990; Humes *et al.*, 1994). However, hearing loss cannot account for all of the variance in speech-recognition performance. It could be hypothesized that the remaining variance is due to the differential weighing of acoustic cues by listeners. That is, an individual primarily relying on spectral cues to make acoustic-phonetic distinctions in speech may have more trouble understanding speech following a hearing loss than an individual primarily relying on temporal cues. Before this hypothesis regarding listeners with hearing impairment can be evaluated, the way in which listeners with normal hearing use redundant cues to make acoustic-phonetic decisions must be determined.

The relative importance of cues that signal the same acoustic-phonetic distinction have been examined in trading-relations studies. Repp and his colleagues (1978) discussed the consequences of articulating an intervocal stop consonant. The cues he defined included rising and falling transitions, a period of attenuation of sound, bursts, and a delayed *F1* onset. However, Repp indicated that despite the apparent diversity of cues, they are integrated into the percept of a phoneme. Within this wide array of cues, trading relations exist among several cues. That is, one cue can be exchanged for another without a change in the percept. The ability to use a variety of acoustic cues for one perceptual entity makes the cues equivalent. It has also been shown that when the perceptual utility of one cue is attenuated, another cue may take on primary importance in signaling the contrast. From this finding, it is assumed the perceptual cues are phoneti-

cally equivalent. That is, by strengthening the value of one cue, the weakening of another can be offset. This is called a phonetic trading relation (Repp, 1982).

Evidence that listeners may use the available redundant cues differently for making an acoustic–phonetic distinction comes from three lines of study: (1) the use of acoustic cues in nonspeech stimuli; (2) the development of perceptual abilities in children; and (3) the use of acoustic cues by listeners with impaired hearing. These studies indicate that listeners not only need a reduced set of available cues to make a distinction, but also that different listeners may use different cues to make acoustic–phonetic distinctions. That is, different listeners may weight certain cues more heavily than other cues as suggested by Nittrouer's developmental weighing shift hypothesis (Nittrouer, 1992).

Research using nonspeech stimuli has explored the ability of listeners to categorize complex sounds based on information in multiple, independent stimulus dimensions. Kidd and Watson (1987) and Christensen and Humes (1996) had listeners classify complex sounds. The goal of both studies was to determine the degree to which listeners allocated attention to each of three independent dimensions. Results of both experiments indicate that subjects did not use stimulus information available in multiple dimensions equally to categorize complex sound pulse stimuli. In the Christensen and Humes (1996) study, perceptual weights for each of the three stimulus dimensions were calculated using a mathematical model, the generalized context model (GCM; Nosofsky, 1986). These weights indicated that most listeners placed the majority of their attention on one or two stimulus dimensions to classify the stimuli. Furthermore, it was observed that not all listeners preferred the same dimension. Finally, Christensen and Humes (1996) demonstrated that it was possible to train a listener to use a dimension other than the one initially used to classify the stimuli.

There is evidence that children may use the cues available for making acoustic–phonetic distinctions in speech differently than adults. Developmental changes have been evidenced in studies that have shown the auditory perceptual abilities of children are not equivalent to the perceptual abilities of adults (e.g., Elliott, 1986; Elliott and Hammer, 1988; Elliott and Katz, 1980; Sussman, 1993). Normally developing children require a larger acoustic difference to discriminate certain speech sounds than adults (Elliott *et al.*, 1986; Sussman and Carney, 1989). Morrongiello, Best, and colleagues (Morrongiello *et al.*, 1984; Best *et al.*, 1981) suggest that children weigh transition information more heavily than adults when differentiating “say” and “stay” along a continuum. Walley and Carrell (1983) also found that children and adults relied more heavily on formant transitions than on short-term spectral cues for identification of consonants in consonant–vowel tokens. In another study, Nittrouer and Studdert-Kennedy (1987) examined the development of children's sensitivity to acoustic consequences of coarticulation using fricatives synthesized along a continuum that varied on fricative spectrum, vowel context, and vocalic transition. Results of their study indicated that children weighted formant transition information more heavily than fricative spectrum information when identifying these stimuli. Nittrouer (1992)

concluded that young children rely more on dynamic cues in the speech signal and less on static cues. Reliance on static cues develops as children learn the detail of syllabic production. Sussman and Carney (1989) studied the effects of transition length on the perception of stop consonants and compared these effects to adults. Results of their study indicated that children's ability to discriminate formant transitions developed over time and had not yet reached full adult values even at 10 years of age. In one additional study, Jerger and colleagues (1993) explored the auditory (voice) and linguistic (word) dimensions of speech processing rather than acoustic–phonetic dimensions used in the previously discussed studies. Results indicated speech processing differences when comparing adults and children who were required to attend selectively to the voice dimension while ignoring the word dimension or vice versa. Children between 3 and 6 years of age required significantly more time to process the word dimension when compared to adults. These results suggest a developmental improvement for processing linguistic information and that children require more information than adults to identify words.

For a listener with impaired hearing, a perceptual cue may be altered by the hearing loss and the listener may need to use other cues to signal the phoneme. For example, cues in the temporal domain may be used instead of spectral cues. There is evidence that listeners with impaired hearing may use the perceptual cues available in the speech signal different than listeners with normal hearing. Lindholm and colleagues (1988) looked at acoustic cues for identification of stop consonant place of articulation. Listeners with normal hearing and with mild-to-moderate hearing impairment identified 18 CV syllables comprising all possible combinations of three factors (formant transition, spectral tilt, and abruptness of frequency change) that correspond to /b/, /d/, and /g/ in the /æ/ environment. Results indicated that listeners with normal hearing relied on formant transitions to identify place of articulation, while listeners with hearing loss relied more on spectra tilt and abruptness of frequency change. Thus it was concluded that listeners with hearing impairment rely more heavily on temporal cues and cues to gross spectral shape. Summers and Leek (1992) also found evidence that listeners with hearing impairment compensated for spectral distortion produced by their hearing loss by placing greater perceptual weight on temporal cues when identifying vowels.

In summary, there are multiple cues available to a listener to make acoustic–phonetic distinctions in speech. Research on trading relations shows that not all cues may be of equal importance in signaling distinctions and that not all perceptual cues need to be available to make a distinction. Research focused on the classification of multidimensional nonspeech sounds, the perceptual development of children, and the use of perceptual cues by listeners with hearing impairment indicates that cues may be weighted differently by different individuals. The exact way in which listeners with normal hearing make use of multiple, perceptual cues to make acoustic–phonetic distinctions has not been determined.

The research described here focused on how listeners

with normal hearing make use of cues from multiple, independent stimulus dimensions to classify synthesized stimuli containing acoustic cues found in speech. The signals used in this research were speechlike in that they contain cues important for making acoustic–phonetic distinctions in speech. Real speech was not used in this study to avoid the use of these familiar, over learned signals. It was assumed that listeners would have a long developed bias toward certain cues in the acoustic–phonetic pattern of real speech. One goal of this research was to determine if listeners attended equally to all dimensions of multidimensional stimuli. If attention among dimensions was found to be unequal, a final goal of this research was to determine if listeners can be trained to use previously unused cues to classify the stimuli.

I. GENERAL METHOD

A. Subjects

Nineteen subjects with normal hearing between the ages of 20 and 35 years ($M=24.9$ y) participated in this series of experiments. Criteria for normal hearing included pure-tone air-conduction thresholds of less than 20 dB HL (ANSI, 1989) from 500 to 4000 Hz and normal tympanograms in the test ear. All testing in the experiment was completed monaurally with the test ear selected arbitrarily.

B. Stimuli/Apparatus

Twenty-seven, four-formant stimuli were developed using the synthesizer software (KLSYN88a) University Synthesizer Package from Sensimetric Corporation (1990). This software is based on the work of Klatt and Klatt (1990). The stimuli consisted of two 100-ms samples of frication noise, separated by a period of silence or temporal gap. The second burst of frication noise differed from the first by having a formant transition change in slope (frequency) throughout the final 100-ms of frication noise (see Fig. 1 for schematics of three of the stimuli). Thus the stimuli consisted of three sequentially presented dimensions including: (1) the center frequency of the fricative spectrum (cue available at stimulus onset); (2) the duration of the temporal gap between the two bursts of frication noise, which also varied the total duration of the stimuli (cue available at middle and end of the stimulus); and (3) the slope of the frequency transition (cue available in final portion of the stimulus). Each of the stimulus dimensions, fricative spectrum center frequency, duration of the temporal gap, and the slope of the frequency transition could take on one of three possible values. Twenty-seven sounds were synthesized by combining all possible values of the three stimulus dimensions.

The three dimensions chosen to compose the stimuli were selected because of their importance in making acoustic–phonetic distinctions in natural speech. Examples of these cues in natural speech are numerous. The spectra (center frequency) of frication noise and bursts serve as a cue for fricative, affricate, and stop consonant identification (Behrens and Blumstein, 1988; Harris, 1958; Heinz and Stevens, 1961). Duration or temporal gap cues are used to help determine vowel identification (Peterson and Lehiste, 1960). In addition, one cue used for stop consonant identification is the

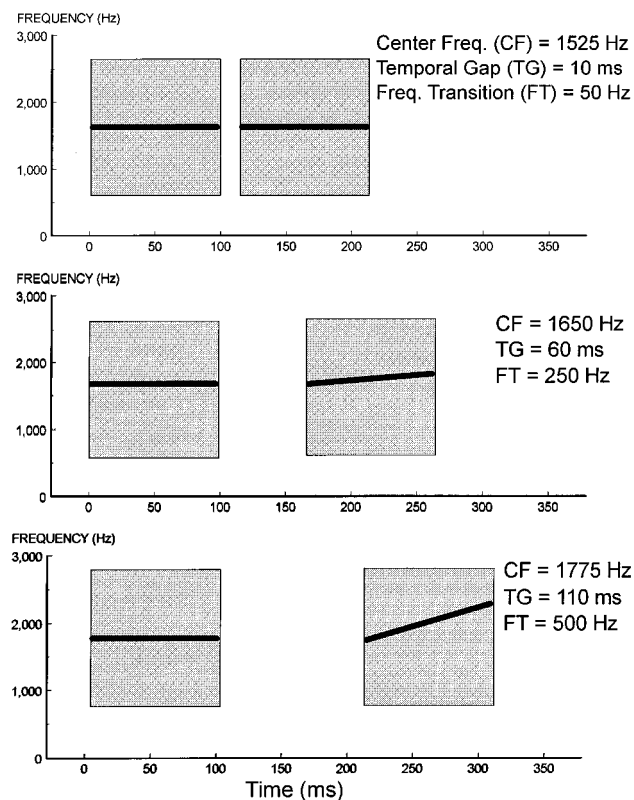


FIG. 1. Schematics of the three exemplar stimuli synthesized for these experiments. The top graph consists of the stimulus with the two, 100-ms fricative noise spectrum portions centered at 1525 Hz with bandwidths of 2000 Hz (represented by the open boxes), a gap of 10 ms between noise spectra, and a 50-Hz transition in the final 100 ms of frication noise (represented by the shaded bar in the second 100-ms frication portion). The middle graph represents the stimulus with the frication noise portions centered at 1650 Hz, a gap of 60 ms, and a 250-Hz transition. The bottom graph represents the stimulus with the frication noise portions centered at 1775 Hz, a gap of 110 ms, and a 500-Hz transition.

silence prior to the release of the burst (Van Tassel *et al.*, 1987). Finally, diphthongs, liquids, glides, nasals, and stop consonants all use frequency transition information to signal their identification (e.g., falling or rising, fast or slow) (O'Connor *et al.*, 1957; Fujimura, 1962; Mermelstein, 1977; Repp, 1986; Cooper *et al.*, 1952).

The stimuli were synthesized using four band-pass resonators ($F3$ – $F6$). Resonators, $F0$, $F1$, and $F2$, were set to 0 dB and were not used to synthesize the stimuli. The bandwidths of each resonator were adjusted so that the overall bandwidth of each stimulus would be 2000 Hz. This was accomplished by adjusting the synthesizer values for formant frequencies $F3$, $F4$, $F5$, bandwidths $B3$, $B4$, and $B5$, and amplitudes of frication excited in each formant ($A3F$, $A4F$, and $A5F$). A final narrow-band-pass filter was developed using $F6$, $B6$, and $A6F$. This resonator served as a prominence at the center frequency of the frication noise. The slope of this filter was varied during the final 100 ms of the sounds to create the frequency transition dimension. The synthesizer parameter values for the final stimuli are shown in the Appendix.

Discrimination testing using a standard two-alternative forced-choice paradigm compared the lowest value along each dimension to the middle value and the middle value

along each dimension to the highest value. Discrimination of the extreme values along a stimulus dimension was assumed to be greater than that measured for two adjacent values along the same dimension. Three stimuli were presented on each trial with the first stimulus being the “standard” for that trial and either the second or third stimulus differing from the standard. Subjects determined which of the last two stimuli was different from the first stimulus, the standard. For each of the three values along dimension A, there were nine possible combinations of values along the other two independent dimensions. Thus discrimination can be performed in nine different “contexts.” The stimuli were recorded so that there were 108 discriminations of each dimension across all 9 contexts. That is, there were 12 discriminations of each stimulus value for each of the 9 contexts. Results verified three-dimensional stimuli with values on each dimension that were on average 85% discriminable. The discrimination percent correct values were arcsine transformed and submitted to analysis of variance. Results of the ANOVA were not significant [$F(2,23)=0.63$, $p>0.05$] indicating that differences in the discriminability of the three dimensions did not reach conventional levels of statistical significance.

Schematics of three of the synthesized stimuli can be seen in Fig. 1. These three stimuli, termed the exemplar stimuli, include the stimulus with the smallest or lowest values on the three dimensions as shown in the top graph (1525-Hz fricative-spectrum center frequency, 10-ms temporal gap, and 50-Hz frequency transition). The stimulus with the middle values on each of the three dimensions is shown in the middle graph (1650-Hz fricative-spectrum center frequency, 60-ms temporal gap, and 250-Hz frequency transition). Finally, the stimulus with the largest or highest values on the three dimensions is shown in the bottom graph (1775-Hz fricative-spectrum center frequency, 110-ms temporal gap, and 500-Hz frequency transition). Thus the three values on each of the three dimensions include: (1) fricative spectrum center frequency (1525 Hz, 1650 Hz, and 1775 Hz); (2) temporal gap (10 ms, 60 ms, 110 ms); and (3) frequency transition (50 Hz, 250 Hz, 500 Hz).

C. Materials/Procedures

The stimuli for these experiments were presented via computer (IBM-PC compatible, 80486). The stimuli were output from a 16-bit digital-to-analog converter (Tucker-Davis Technologies, QDA1) at a sampling rate of 10 kHz and routed to an audiometer (Grason-Stadler, model 162). Stimuli were not low-pass filtered upon playback because no voicing source was used. Spectral analysis (Spectral Dynamics, SD 380) of the transducer output in a 2-cc coupler confirmed that no aliasing was occurring acoustically at the output of the earphones. The output of the audiometer was sent to 12 matched pairs of ER-3A insert earphones. Materials were presented at 75 dB SPL. The stimulus utilized for calibration was a noise centered at 1650 Hz with a 2000-Hz bandwidth. Acoustic calibration was accomplished with an HA-2 2-cc coupler as recommended by Frank and Richards (1991). Responses were collected from up to 12 subjects using 80286-based IBM-compatible personal computers in-

terfaced to the 80486 computer via a 16-port serial interface board. All testing was completed in a large acoustically treated room with noise levels low enough to permit threshold measurements with headphones to within 15 dB of audiometric zero from 250 Hz to 8000 Hz (ANSI, 1991). Subjects in these experiments participated in two 2-h sessions each week for 6 weeks. Subjects were paid for their participation.

II. EXPERIMENTS

A. Experiment 1: Similarity judgments

1. Method

For this experiment, subjects were required to rate similarities of all 351 possible pairs of the 27 stimuli. Both orderings of the pairs were presented to balance the order of presentation of the stimuli. The pairs were randomly presented and subjects rated the similarity between the pairs on a nine-point rating scale. A nine-point scale is used extensively to collect proximity data (e.g., Wish, 1971; Wish *et al.*, 1970). A rating of one indicated the two sounds were “very similar” while a rating of nine indicated the two sounds were “very different.” Pairs were presented with 1 s between the members of each pair. Subjects were given instructions to listen to the two stimuli and rate them on the nine-point scale. No practice similarities were given. Subjects responded using the number pad on their computer and the next pair of stimuli was not presented until a response was registered from every subject.

2. Results and discussion

From the similarity judgments, one mean triangular stimulus-response matrix was calculated for the entire group of subjects. This matrix was then submitted to multidimensional scaling (MDS) analysis using an alternating least squares scaling method (ALSCAL) and a standard euclidean model. The best-fit coordinate space from the MDS was three dimensional in nature with a stress value of 0.093 and an r^2 value of 0.913. Figure 2 shows the three-dimensional solution following axes rotation. The axes were rotated from the original solution to make interpretation easier. Rotation is permitted because the configuration is based on distance between points and these distances do not change when the configuration is rotated (Kruskal and Wish, 1989).

From Fig. 2 it can be seen that each of the perceptual dimensions in the solution mapped directly to a corresponding stimulus dimension, as indicated by the axis labels in this figure. Each of the three plots in this figure shows a different two-dimensional view of the three-dimensional solution. In the top panel in this figure, for example, the perceptual space is mapped in a plot of the temporal gap dimension by the center frequency dimension. The legend in the right-hand portion of Fig. 2 indicates the stimulus values along each of the three dimensions for each of the 27 stimuli. Notice that, in all three of the two-dimensional plots, the perceptual space can be partitioned by the stimulus values along each dimension. For example, in the top two two-dimensional plots, stimuli S1–S9, all having short 10-ms temporal gaps, are mapped to the extreme right of the perceptual space,

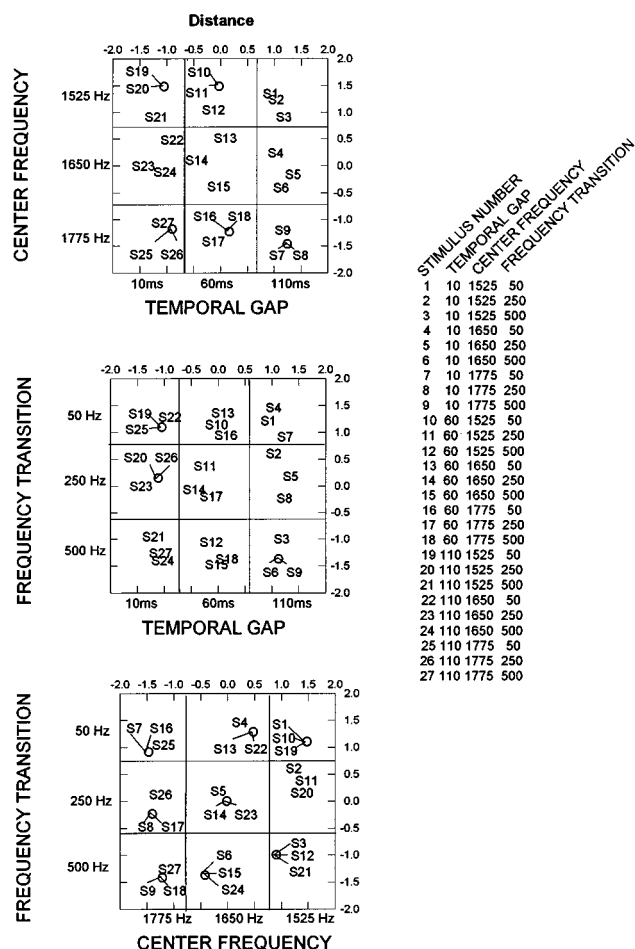


FIG. 2. Two-dimensional plots of the MDS solution for the 27 speechlike stimuli from experiment 1. Each plot graphs the relative distance of all 27 stimuli by two dimensions. Each plot can be partitioned by the stimulus values on each of the dimensions. The stimuli are labeled S1 to S27 on the graphs and their corresponding values on the three dimensions can be seen in the legend. Overlapping stimuli are represented by open circles with lines to label the stimuli.

while stimuli S19–S27, all having long 110-ms temporal gaps are mapped to the extreme left. Comparable partitions of the perceptual space are apparent for the other two-dimensional plots. In general, Fig. 2 demonstrates the good correspondence between the stimulus parameters and the perceptual space.

Individual subject weights on each dimension of the MDS solution derived above were calculated by holding the rotated coordinate space fixed and applying a zero iteration individual scaling (INDSCAL) solution (Kruskal and Wish, 1989). Figure 3 is a graph of the individual subject weights derived from INDSCAL. In the graph, the 19 subjects are represented along the abscissa, while weight is represented along the ordinate. The weight for each dimension is plotted for each listener. The first 11 listeners placed the greatest weight on the center frequency dimension. Listeners 12–15 placed greatest weight on the temporal gap dimension. Finally, listeners 16–19 placed greatest weight on the frequency transition dimension. Thus the weights calculated for the individual listeners indicated that listeners were not attending equally to the three stimulus dimensions and different listeners placed greatest weight on different dimensions.

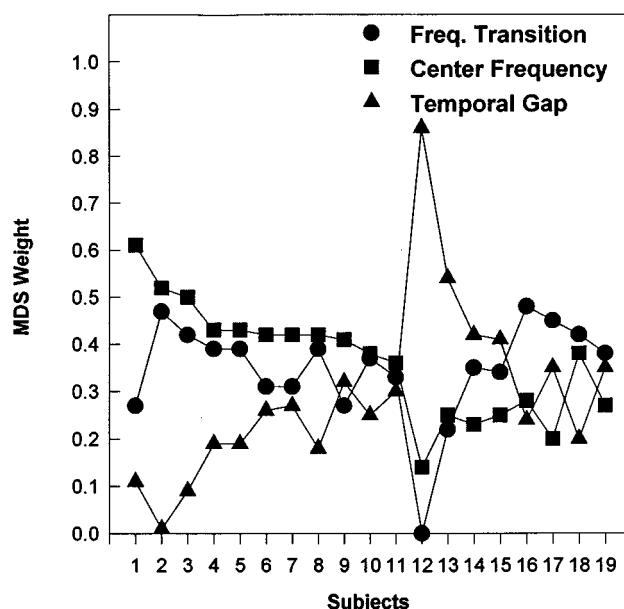


FIG. 3. Individual weights for each subject derived from the MDS solution. Plotted on the abscissa is the individual subject. The symbols represent each dimension.

This experiment confirmed that subjects were perceiving these stimuli along three perceptual dimensions that corresponded to the stimulus dimensions being manipulated. In the next experiment, subjects were trained to label three exemplar stimuli and then asked to classify all of the stimuli on the basis of this training.

B. Experiment 2: Exemplar training

1. Method

The purpose of this experiment was to train the subjects to label three exemplar stimuli. These three exemplar stimuli contained the smallest (termed the “circle” stimulus), middle (termed the “triangle” stimulus), and largest (termed the “square” stimulus) values on the three stimulus dimensions, respectively. (See Fig. 1 for schematics of the three exemplar stimuli.) More specifically, the “circle” stimulus consisted of the smallest or lowest values on each of the three dimensions, or a fricative spectrum center frequency of 1525 Hz, a temporal gap of 10 ms, and a frequency transition of 50 Hz. The “triangle” stimulus consisted of the middle values on each of the three dimensions, or a fricative spectrum center frequency of 1650 Hz, a temporal gap of 60 ms, and a frequency transition of 250 Hz. Finally, the “square” stimulus consisted of all the largest or highest values on the three dimensions, or a fricative spectrum center frequency of 1775 Hz, a temporal gap of 110 ms, and a frequency transition of 500 Hz. Following the similarity judgments described in the previous experiment, 18 subjects were trained to label three exemplar stimuli as “circle,” “triangle,” and “square.” (One subject dropped out of the experiment after the similarity judgments.) To familiarize the subjects with the exemplar stimuli and associate them with their corre-

sponding label, subjects first listened to ten presentations of each stimulus, beginning with ten “circles” and ending with ten “squares.” As each stimulus was presented, the subject’s computer screen displayed the name of the stimulus being played. Subjects were required to press the return key following the presentation of each stimulus and the next stimulus was presented after every subject had pressed return. Following these blocked presentations of the exemplar stimuli, all three stimuli were played in sequence, with the three-stimulus sequences repeated ten times. Sequences were played with 500 ms between stimuli. Specifically, the subjects were presented with ten “circle-triangle-square” stimulus sequences in succession. Again, as each stimulus was presented, the computer screen displayed the name of each stimulus and each subject was required to press the return key after each sequence presentation. Stimuli were played out in sequence so that listeners could compare the exemplar stimuli.

Following this familiarization, subjects were presented these three exemplar stimuli, 20 times each, in a random order and asked to identify or label each as “circle,” “triangle,” or “square.” After the subject selected “circle,” “triangle,” or “square” using the keyboard, they were given feedback as to the correct answer. Subjects were required to perform with an accuracy of 90% or better to continue on to the classification portion of this experiment. Fifteen subjects achieved 90% accuracy after only one training session of 60 trials. Three subjects required two, 60-trial training sessions to achieve 90% accuracy.

After subjects were able to label the three exemplar stimuli with 90% accuracy, subjects were presented all 27 stimuli 80 times each and asked to classify each one as either a “circle,” “triangle,” or “square.” Subjects were given no other instructions. Subjects were presented these stimuli in twenty blocks of 108 presentations (four presentations of each of the 27 stimuli). After ever 5 blocks of 108 trials, subjects were retested to determine if the 90% identification of the exemplar stimuli was maintained. A total of 60 stimuli were used for each of these measurements. Identification accuracy of the exemplar stimuli was maintained throughout the testing.

2. Results and discussion

The results of the exemplar training indicated most subjects placed the majority of attention on the frequency transition dimension; however, the distribution of weights was different for individual subjects. To further illustrate this point, the data from two subjects are plotted in Fig. 4. Subjects KG and RT were chosen because they represent the subject that places the least and most attention on the frequency transition dimension, respectively. These plots display the percentage of time each stimulus was classified as “circle,” “triangle,” or “square” as a function of frequency transition value. Stimuli are arranged along the abscissa in this figure according to their values on the frequency transition dimension. Thus the first 9 stimuli all have a frequency transition value of 50 Hz, the second 9 have a frequency transition value of 250 Hz, and the last 9 stimuli all have a frequency transition value of 500 Hz. In the lower

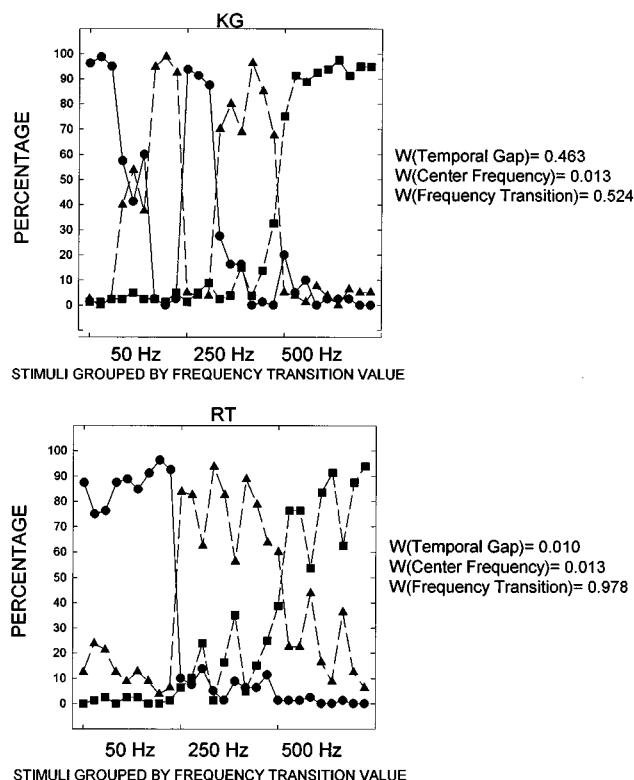


FIG. 4. Results of the exemplar training in experiment 2 for two subjects—KG (top) and RT (bottom). In this figure, the percentage of time each stimulus was labeled as a circle, triangle, or square is shown. Plotted along the abscissa are the stimuli arranged by values on the transition dimension. Thus the first 9 stimuli have a transition of 50 Hz, followed by 9 with a transition value of 250 Hz, and finally 9 with a transition value of 500 Hz. The derived GCM weights are plotted beside each graph.

plot, subject RT, classified the first 9 stimuli, all with a value of 50 Hz on the frequency transition dimension, as “circle” the majority of the time. That is, regardless of the stimulus values along the other two dimensions (temporal gap and fricative spectrum center frequency), when the frequency transition equaled 50 Hz, subject RT labeled the stimulus a “circle.” In addition, stimuli with the values of 250 Hz and 500 Hz on the frequency transition dimension were being classified the majority of the time as “triangle” and “square,” respectively. In other words, this subject attended to the frequency transition dimension in order to classify the stimuli.

The generalized context model (GCM; Nosofsky, 1986) was used to calculate the perceived dimension weights for each subject. The GCM is an exemplar based approach to model performance in identification tasks. The GCM is based on the assumption that categorization of a stimulus will be determined by how similar it is to exemplar members of each category. Therefore, the GCM assumes that people will store individual exemplars in memory, and make classification decisions on the basis of the similarity comparisons with the stored exemplars. The GCM is used in conjunction with the MDS solution and can predict performance in categorization experiments involving the same set of stimuli scaled in the MDS solution (Nosofsky, 1992). In the GCM,

similarity among stimuli is determined by the distances between the stimuli in the MDS space and can be modified on the basis of selective attention. The exemplar stimuli are represented by the greatest distance within the psychological space. In other words, the exemplar stimuli are farthest apart in the psychological space. The similarity of all other stimuli to the exemplar stimuli is determined by the selective attention a listener places on each dimension. The GCM states that given the presentation of a stimulus, the likelihood that it will be placed in a certain category J is found by summing the weighted similarity of stimulus i (from the MDS solution) to all exemplars of category J , and then multiplying by the response bias for category J . This strength is then divided by the sum of strengths for all categories to determine the conditional probability with which stimulus i is classified in category J :

$$P(R_J/S_i) = b_J \sum_{j \in C_J} M_j \eta_{ij} / \sum_K b_K \sum_{k \in C_K} M_k \eta_{ik}, \quad (1)$$

where b_J is the category J response bias; M_j is an exemplar-strength term; and η_{ij} is the similarity between exemplars i and j . To calculate the similarities, first the distance between exemplar i and j (d_{ij}) is calculated based on the individual difference scaling solution. The distance between i and j in a multidimensional psychological space is given by

$$d_{ij} = \left[\sum w_m |x_{im} - x_{jm}|^r \right]^{1/r}, \quad (2)$$

where x_{im} is the psychological value of exemplar i on dimension m ; the value of r defines the distance metric (e.g., $r=1$, city block; $r=2$, Euclidean); and w_m ($0 \leq w_m, \sum w_m = 1$) is the attention-weight given to dimension m . This distance (d_{ij}) is converted to a similarity measure by the function

$$\eta_{ij} = \exp(-c \cdot d_{ij}^p), \quad (3)$$

where c is a general sensitivity parameter; and the value of p defines the similarity gradient (e.g., $p=1$, exponential; $p=2$, Gaussian). The GCM assigns a weight ranging from 0 to 1.0 to each dimension for each individual subject with the sum of the weights of all the dimensions equal to 1.0. The GCM model has an advantage over other similar exemplar-based models of categorization in that the GCM can represent context-dependent changes in similarity. That is, it is assumed that similarities will change given the paradigms used to do the categorization. [For a full review and derivation of the GCM see Nosofsky (1986, 1992).]

The GCM weights calculated for the two subjects in Fig. 4 are listed to the right of the plots. These weights indicated that subject RT attended most to the frequency transition dimension (0.978). KG, in contrast, distributes attention primarily between the frequency transition and the temporal gap dimension.

Consider the results for subject KG plotted in the top of Fig. 4. For subject KG, it can be seen that all 9 stimuli with a frequency transition value of 500 Hz were being classified as “square” 70%–100% of the time. This subject appeared to be using the frequency transition dimension to classify the stimuli with the 500-Hz frequency transition. For

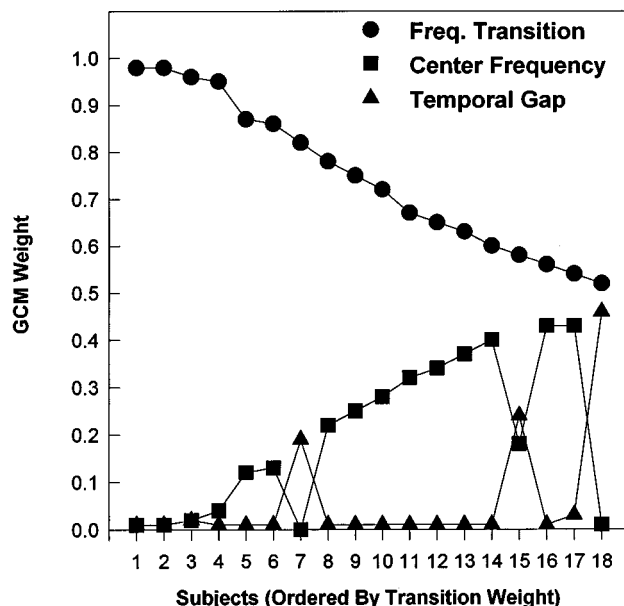


FIG. 5. GCM weights for each dimension are plotted for each subject following the exemplar training in experiment 2.

the frequency transition values of 50 and 250 Hz, however, it is not as clear how the subject classified the stimuli. If this subject was only using the frequency transitions for classification, the stimuli with the 50-Hz frequency transition values would have been classified as “circle” the majority of the time, while the stimuli with the 250-Hz frequency transition values would have been classified as “triangle” the majority of the time. As can be seen from the graph, this subject did not always label the stimuli according to the frequency transition values. The weights derived from the GCM model indicated that this subject used a combination of two dimensions to classify the stimuli. This subject had a GCM weight of 0.524 on the frequency transition dimensions and a weight of 0.463 on the temporal gap dimension. The fricative-spectrum dimension was not given much weight by this subject.

Figure 5 shows the distribution of the weights on the three dimensions for all of the subjects. As can be seen from this figure, the frequency transition dimension received the most attention, while the temporal gap dimension was seldom weighted very heavily.

Having established that classification performance for these stimuli reflected individual differences in “preferred” dimensions, the next experiment examined the ability to train listeners to attend to other stimulus dimensions. In particular, since the temporal gap dimension was not preferred by many subjects, all subjects were trained to attend to this dimension.

C. Experiment 3: Temporal gap training

1. Method

The purpose of this experiment was to train the subjects to focus their attention on the temporal gap dimension. In this experiment, 16 subjects from the previous 2 experiments were trained on a subset of the 27 stimuli. (An additional 2

of the original 19 subjects had dropped out of the study after the completion of experiment 2.) Specifically, subjects were taught to label stimuli 1, 2, 4, 7, and 8 as “circle” (10-ms temporal gap), stimuli 10, 11, 14, 16, and 17 as “triangle” (60-ms temporal gap), and stimuli 19, 20, 21, 22, 24, 26, and 27 as “square” (110-ms temporal gap). Stimuli 3, 5, 6, 9, 12, 13, 15, 18, 23, and 25 were not trained and were used as test stimuli to assess the generalization of training to non-trained stimuli. The stimuli chosen for the training stimuli were selected on the basis of their perceptual distance from one another in the MDS solution. The stimuli chosen for training stimuli contain every possible combination of the values on the center frequency and frequency transition dimensions. For this to occur, two additional stimuli were selected to train in the “square” category.

Subjects listened to 15 repetitions of the “circle” and “triangle” stimuli and 24 repetitions of the “square” stimuli. This training was of similar format to the previous experiment. However, in the previous experiment, there was only one “circle” stimulus, one “triangle” stimulus, and one “square” stimulus. In this experiment, there were several of each stimulus category (“circle,” “triangle,” and “square”). Each sequence of training stimuli was a different random ordering of either the “circle,” “triangle,” or “square” stimuli. Following this familiarization, subjects then listened to a three-stimulus sequence of “circle”-“triangle”-“square” thirteen times (randomly sampling different examples of the training stimuli in each category).

Subjects were then presented all seventeen of the training stimuli, eight times each, in a random order. Subjects were asked to respond after each stimulus presentation as to whether they heard a “circle,” a “triangle,” or a “square.” Immediate trial-to-trial feedback was provided. Subjects were required to obtain performance accuracy of 80% on this testing to continue with the experiment. A performance criterion of 80% identification accuracy was used in this experiment, rather than the 90% criterion in previous experiments, because very few subjects could reach the 90% criterion after 6 training sessions of 136 trials. However, the 80% criterion has been used by many investigators as indicative of good identification performance (Nitttrouer and Studdert-Kennedy, 1987; Sussman, 1993). Subjects achieved 80% at different learning rates. Three subjects, for example, achieved performance of 80% or better after only one training session of 136 trials. However, most subjects required from two to six training sessions of 136 trials each to achieve a performance level of 80% correct. One subject could not obtain the required 80% accuracy after extensive training and did not continue with the rest of the experiment.

When 15 subjects had attained an accuracy of 80%, they were once again presented with all 27 stimuli 80 times each. Subjects were presented the stimuli in 20 blocks of 108 stimulus presentations. After every 5 blocks, the subjects were retested with 136 trials of the training stimuli to determine if the performance level of 80% correct was maintained. Identification accuracy of the training stimuli was maintained throughout testing. Subjects were simply instructed to classify these stimuli on the basis of what they learned from the training trials.

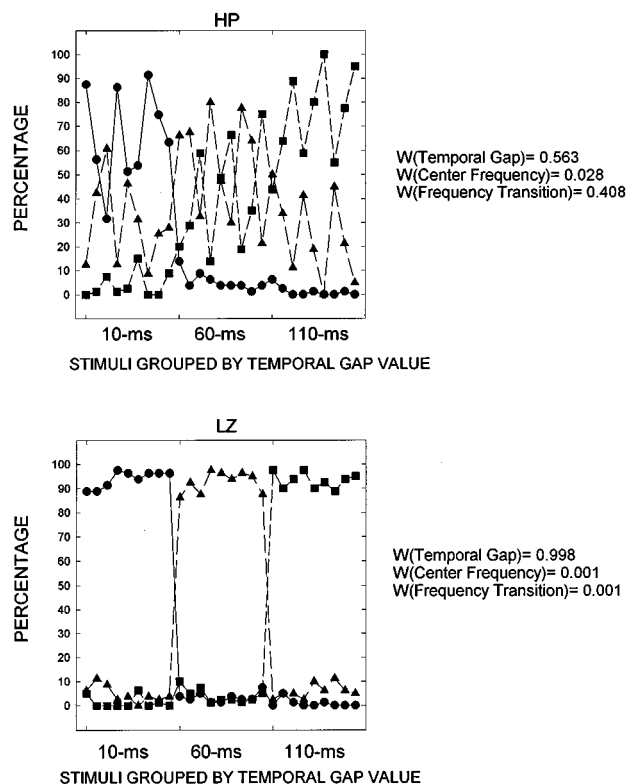


FIG. 6. Results of the temporal gap training in experiment 3 for two subjects—HP (top) and LZ (bottom). In this figure, the percentage of time each stimulus was labeled as a circle, triangle, or square is shown. Plotted along the abscissa are the stimuli arranged by values on the gap dimension. Thus the first 9 stimuli have a gap of 10 ms, followed by 9 with a gap of 60 ms, and finally 9 with a gap of 110 ms. The derived GCM weights are plotted beside each graph.

2. Results and discussion

Figure 6 show the results of the temporal gap training for two subjects. These two subjects, HP and LZ, represent the two subjects that attained the least and most GCM weight on the temporal gap dimension, respectively. The plots in this figure are plotted with the temporal gap value varying along the abscissa. That is, the first 9 stimuli have a temporal gap value of 10 ms, the next 9 a temporal gap value of 60 ms, and the final 9 a temporal gap value of 110 ms. The data in the lower plot are from a subject with a GCM weight on the temporal gap dimension of 0.998. As can be seen from this graph, this subject labeled the stimuli with temporal gaps of 10 ms, 60 ms, and 110 ms, as “circle,” “triangle,” and “square,” respectively, 80%–100% of the time, regardless of the stimulus values for the other two dimensions. The top plot shows a subject with a GCM weights on the temporal gap dimension of 0.563. This subject did not learn to place all attention to the temporal gap dimension, however, the GCM weight of 0.563 does represent the most weight on any of the three dimensions.

Figure 7 shows the GCM weights for all of the subjects following temporal gap training. Results are ordered from the subjects placing the most weight on the temporal gap dimension to those placing the least weight on this dimension. As can be seen from this figure, the temporal gap dimension is now most heavily weighted by the subjects.

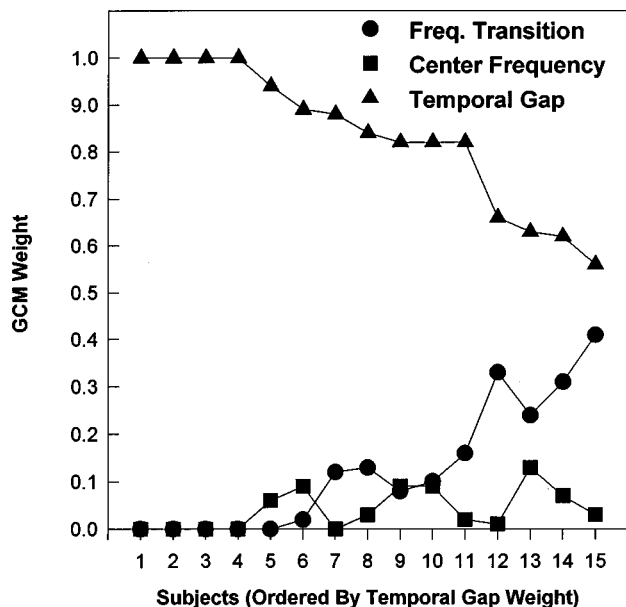


FIG. 7. GCM weights for each dimension are plotted for each subject following the temporal gap training in experiment 3.

When comparing this figure to Fig. 5, it is obvious that subjects have shifted their perceptual weights toward the temporal gap dimension. Recall that after the initial exemplar training, the majority of the subjects placed the greatest weight on frequency transition.

To further verify the shift in attention to the temporal gap dimension, a paired sample t -test was performed on the GCM weights derived for the temporal gap dimension following the initial exemplar training and the weights derived following training to the temporal gap dimension. The mean GCM on the temporal gap dimension prior to training on this dimension was 0.07, whereas the mean GCM weight following training to this dimension was 0.83. The two-tailed paired sample t -test was significant at the 0.01 level ($t = -17.57$, $df = 14$).

In this experiment, subjects were able to shift their attention to the temporal gap dimension following training on this dimension. Given their ability to shift their attention to the temporal gap dimension, in the next experiment the subjects were trained on the frequency transition dimension to determine if attention could easily be shifted to another dimension.

D. Experiment 4: Frequency transition training

1. Method

The goal of this experiment was to determine if the subjects could be retrained to attend to a new dimension (frequency transition). Ten subjects from the previous experiment returned to participate in this experiment. These subjects were trained in this experiment to label a new set of stimuli as “circle,” “triangle,” or “square.” In this experiment, stimuli 1, 4, 7, 13, and 16 were trained to be labeled as “circle” (50-Hz frequency transition), stimuli 2, 5, 8, 11, and 14 as “triangle” (250-Hz frequency transition), and stimuli 3, 6, 9, 12, 15, 21, 24, and 27 as “square” (500-Hz

frequency transition). The “circle,” “triangle,” and “square” stimuli consistently differ in their frequency transition values of 50 Hz, 250 Hz, and 500 Hz, respectively. Stimuli 10, 17, 18, 19, 20, 22, 23, 25, and 26 were reserved for use as testing stimuli to examine the generalization of training. Subjects were trained on these stimuli as in the preceding temporal gap-training experiment and subjects were again tested until performance of 80% accuracy in labeling the training stimuli was attained. Eight of the ten subjects were able to perform to criterion with only one training session of 144 trials. Two subjects required longer training and reached only levels of 73% and 77% after 4 training sessions consisting of a total of 576 trials. Nonetheless, these subjects did complete the final part of the experiment even with their reduced performance levels because they were close to the desired performance criterion and the number of subjects participating in the experiment had already been reduced considerably due to attrition.

Following training, the subjects were again presented all 27 stimuli 40 times each. The stimuli were presented in 10 blocks of 108 trials and the subjects were retested after 5 blocks to see if 80% identification accuracy of the training stimuli was maintained (73% and 77% for two subjects as noted). Identification accuracy of the training stimuli was maintained throughout the testing.

2. Results and discussion

Figure 8 shows examples of two subjects with the least and most weight on the frequency transition dimension. The graphs in this figure are plotted with the frequency transition value along the abscissa. That is, the first 9 stimuli have a frequency transition value of 50 Hz, the next 9 a frequency transition value of 250 Hz, and the final 9 a frequency transition value of 500 Hz. The data in the lower plot are from a subject with a GCM weight on the frequency transition dimension of 0.990. As can be seen from this graph, this subject categorized the stimuli with frequency transitions of 50, 250, and 500 Hz as “circle,” “triangle,” and “square,” respectively, the majority of the time. The upper plot shows a listener with a GCM weight of 0.437 on the frequency transition dimension. This listener did not learn to place all attention on the frequency transition dimension following training. The GCM weights for all subjects are plotted in Fig. 9. As can be seen here, the highest weights are now placed on the frequency transition dimension.

Again, to further verify the shift in attention to the frequency transition dimension, a paired sample t -test was performed on the GCM weights derived for the frequency transition dimension following the temporal gap training and the GCM weights derived following training to the frequency transition dimension. The mean GCM on the frequency transition dimension prior to training on this dimension was 0.09 whereas the mean GCM weight following training to this dimension was 0.87. The paired sample t -test was significant at the 0.01 level ($t = -12.05$, $df = 9$).

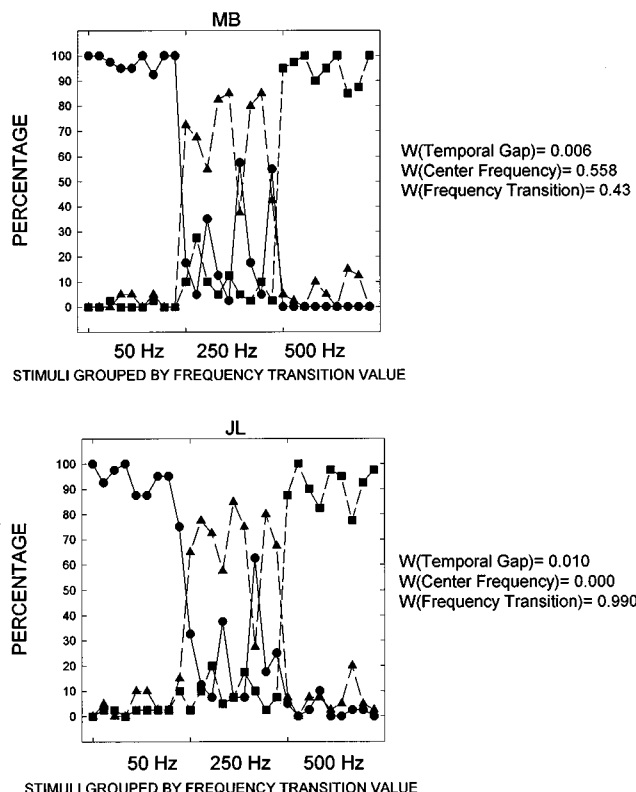


FIG. 8. Results of the frequency transition training in experiment 4 for two subjects—MB (top) and JL (bottom). In this figure, the percentage of time each stimulus was labeled as a circle, triangle, or square is shown. Plotted along the abscissa are the stimuli arranged by values on the transition dimension. Thus the first 9 stimuli have a transition value of 50 Hz, followed by 9 with a transition value of 250 Hz, and finally 9 with a transition value of 500 Hz. The derived GCM weights are plotted beside each graph.

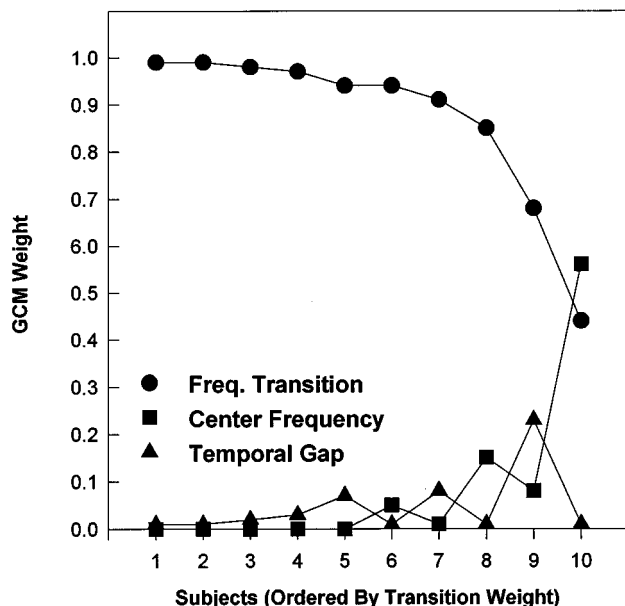


FIG. 9. GCM weights for each dimension are plotted for each subject following the frequency transition training in experiment 4.

III. GENERAL DISCUSSION

The purpose of the current investigation was to determine how listeners with normal hearing make use of cues from multiple, independent stimulus dimensions to classify stimuli containing acoustic cues found in speech. Results of these four experiments indicated that most subjects did not equally use stimulus information available in multiple dimensions to classify the synthesized stimuli. Rather, subjects allocated their attention to one or two particular stimulus dimensions and used this information to classify the stimuli. This was evident both from the MDS INDSCAL weights (experiment 1) and the weights derived from the GCM (experiment 2). In addition, it was demonstrated (experiments 3 and 4) that it was possible to train individuals to use a dimension other than the one initially used to classify the stimuli. The results of this experiment were in agreement with those of Kidd and Watson (1987) and Christensen and Humes (1996) for nonspeech complex sound-pulse stimuli.

The results of experiment 2 indicated that most subjects placed the majority of attention on the frequency transition dimension. This finding may be due to the sequential (serial) nature of the cues in this experiment. The order of occurrence of the dimensions in these stimuli was (1) fricative spectrum center frequency; (2) the duration of the temporal gap; and finally (3) the slope of the frequency transition. The preference for the transition cue could be due to it being the last dimension heard in the stimuli. This dimension would be the most recent in the listener's minds and would be the last to fade away or decay from storage. In a previous experiment (Christensen and Humes, 1996) dimensions were parallel in nature and a preference to one particular dimension was not seen. An experiment that puts transition in a different order would need to be done to determine if the serial nature of the stimuli accounts for the frequency transition dimension to be given the majority of attention.

The results of experiments 1 and 2 indicate that preferences for dimensions were not always maintained from the similarity judgments (experiment 1) to classification (experiment 2). This is evidenced by comparing Figs. 3 and 5. Experiment 1 using MDS analyses of similarity judgments indicated that the primary dimension attended to by most subjects was the center frequency dimension. However, three subjects primarily attended to temporal gap and four subjects primarily attended to frequency transition. The secondary dimension for most subjects was the frequency transition dimension. While the center frequency dimension was the primary dimension for most subjects, the highest weight assigned this dimension was 0.62. Experiment 2 using the GCM weights found that all subjects placed the majority of their perceptual weight on the frequency transition dimension. The secondary dimension for the majority of subjects was the center frequency dimension. Only three of the listeners attended secondarily to the temporal gap dimension. Although all subjects did attend primarily to frequency transition, individual listeners weighted this dimension differently. GCM weights ranged from approximately 0.54 to 0.98 on this dimension. Agreement between the primary and secondary dimensions for the GCM and MDS occurred for 9 of the 18 subjects. That is, the top two weighted dimensions by

each model were the same for 9 of the 18 subjects. However, for only 4 of the 18 subjects did the dimension assigned the most weight agree for the two methods. The lack of agreement between the two methods is likely due to the nature of the tasks used to derive the two sets of weights. Specifically, MDS utilizes similarity judgments where there are no right or wrong answers, while the GCM weights were derived after subjects were trained on exemplar stimuli. A similarity judgment only requires a listener to rate similarity, while the other experiments that used the GCM required a listener to actually label or classify the stimuli into a group. Thus the decision process for the subject changes in the two tasks and probably accounts for the discrepancy.

In experiment 3, subjects were trained to attend to the gap dimension. As stated previously, subjects achieved 80% accuracy at different learning rates. Three subjects attained the 80% accuracy after one training session of 136 trials. A closer look at the GCM weights of these subjects following the original training indicated that two of these subjects were already attending to the gap dimension with GCM weights of 0.24 and 0.46, respectively. Only one other subject placed substantial weight (0.19) on the gap dimension following exemplar training, this subject was able to achieve 80% accuracy in only two training sessions of 136 trials. Thus it was easier for listeners that naturally attended to the gap dimension to learn to attend exclusively to that dimension.

One final consideration regarding the individual differences in training and classification is the relationship between the percent correct on the training sessions and the GCM weight given to the trained dimension following classification. It might be assumed that the harder it was to train a subject, the less attention they would give the trained dimension during classification. This assumption was not found to be true. For example, two subjects were not able to meet the 80% criterion in experiment 4, but did complete the classification portion of the experiment. These two subjects had GCM weights on frequency transition (the trained dimension) of 0.97 and 0.94. Four of the ten subjects had lower GCM weights of the frequency transition dimension and these four subjects were able to meet the criterion of 80% in the training sessions.

The purpose of this research was to examine the way in which listeners use multiple cues to classify stimuli. Listeners learn to process real speech efficiently after extensive training during infancy and early childhood. For the purposes of these experiments, novel stimuli containing acoustic cues found in speech were selected over actual speech to avoid the familiarity of the over learned speech signal. In a previously mentioned study (Christensen and Humes, 1996), we looked at the classification of complex sound pulses that differed along three independent dimensions. The use of the current stimuli containing speech cues represents an attempt to use stimuli more like speech without moving to the actual speech stimulus. This use of stimuli containing speech cues over real speech, however, limits the generalization of the results to real speech. It is not known if listeners will use multiple dimensions exactly the same way in real speech. Future research will focus on this question.

Although the current investigation does not utilize real-speech, the results may be applicable to listeners' use of multiple cues in making acoustic-phonetic distinctions in speech. In particular, the acoustic-phonetic patterns of speech contain multiple, redundant cues for making acoustic-phonetic distinctions. It may be that the multidimensional speech signal is processed in much the same way as the multidimensional stimuli used in these experiments. That is, listeners may pay particular attention to one available cue, even though more cues which signal an acoustic-phonetic distinction exist. The results of the current investigation that listeners differentially weight acoustic cues when making acoustic-phonetic distinctions are supported by the results of other research. As mentioned previously, research studying the development of perceptual abilities in children, the use of acoustic cues by listeners with hearing impairment, and the use of acoustic cues in nonspeech stimuli also support this finding.

As previously stated, it could be hypothesized that the use of cues contributes to the variability found among speech recognition scores of listeners with hearing impairment. For example, consider the differences in the use of cues by listeners with hearing impairment and listeners with normal hearing when identifying stop consonants found by Lindholm and colleagues (1988). Listeners with hearing impairment tended to use temporal cues while listeners with normal hearing tended to use spectral cues. Listeners with hearing impairment may be demonstrating the ability to learn to use information in the speech signal that was previously redundant and not used to make an identification. That is, listeners with hearing impairment may have used formant transitions for stop-consonant identification until this information became inaudible or distorted due to the development of a peripheral hearing loss. After the onset of the hearing loss, listeners with hearing impairment may have learned to shift their attention to cues that were more readily available to them, such as temporal cues and gross spectral shape cues. It is not known how this learning may take place or if all listeners have learned to shift their attention. This difference in learning may account for some of the variance in speech recognition not accounted for by the inaudibility of the speech signal. This hypothesis is supported in the literature previously discussed on trading relations (Repp, 1982).

Future research needs to examine how a peripheral hearing loss affects the use of acoustic cues by listeners. This could be accomplished by simulating a hearing loss, using filtering or spectrally shaped masking noise, in listeners with normal hearing to determine how the inaudibility of the signal affects the use of cues or dimensions in multidimensional stimuli and eventually in real speech. In addition, it would need to be determined if listeners could be trained to use temporal cues instead of spectral cues in order to facilitate classification. Answers to these questions may help to further determine the nature of the speech understanding problems experienced by listeners with hearing impairment. Moreover,

rehabilitative strategies for listeners with hearing impairment with speech-recognition deficits could be a final product of future research.

ACKNOWLEDGMENTS

This work supported by the National Institute of Aging and the Air Force Office of Scientific Research. We thank

Rob Nosofsky for the contribution of his mathematical models which strengthen the findings of this research. In addition, we thank Diane Kewley-Port, Charles Watson, and Gary Kidd for invaluable advice and help with the development of the stimuli used in this project. Finally, we thank Gary Kidd and three anonymous reviewers for their helpful comments on previous versions of this manuscript.

APPENDIX: KLATT SYNTHESIZER PARAMETER VALUES FOR FINAL SPEECH-LIKE STIMULI

	Parameter	Description	Value
Configuration parameters			
1.	DU	duration of utterance	230-ms–10-ms gap 280-ms–60-ms gap 330-ms–110-ms gap
2.	UI	update interval	5-ms
3.	SR	sampling rate	10 000 samples/sec
4.	NF	number of formants	5
5.	SS	source switch	2
6.	RS	random seed	8
7.	SB	same noise burst	1
8.	CP	cascade/parallel	1
9.	OS	Output waveform selector	0
10.	GV	gain for voicing	0
11.	GH	gain for aspiration	0
12.	GF	gain for friction	80
Variable parameters			
13.	<i>F0</i>	fundamental frequency	OFF
14.	<i>AV</i>	amplitude of voicing	0
15.	<i>OQ</i>	open quotient	50
16.	<i>SQ</i>	speed quotient	20
17.	<i>TL</i>	spectral tilt	0
18.	<i>FL</i>	flutter variable	0
19.	<i>DI</i>	diplophonia	0
20.	<i>AH</i>	amplitude of aspiration	0
21.	<i>AF</i>	amplitude of friction	60
(This parameter was set to 0 at 100 ms for the length of the gap.)			
22.	<i>F1</i>	frequency of 1st formant	OFF
23.	<i>F2</i>	frequency of 2nd formant	OFF
24.	<i>F3</i>	frequency of 3rd formant	725 Hz-1525 Center 850 Hz-1625 Center 975 Hz-1775 Center
25.	<i>F4</i>	frequency of 4th formant	1525 Hz 1650 Hz 1775 Hz
26.	<i>F5</i>	frequency of 5th formant	2325 Hz-1525 Center 2450 Hz-1650 Center 2575 Hz-1775 Center
27.	<i>F6</i>	frequency of 6th formant	1525 Hz 1650 Hz 1775 Hz
(This parameter varied over the final 100 ms of the sound to create the transitions.)			
28.	<i>B1</i>	bandwidth of the 1st formant	OFF
29.	<i>B2</i>	bandwidth of the 2nd formant	OFF
30.	<i>B3</i>	bandwidth of the 3rd formant	450 Hz
31.	<i>B4</i>	bandwidth of the 4th formant	600 Hz
32.	<i>B5</i>	bandwidth of the 5th formant	450 Hz
33.	<i>B6</i>	bandwidth of the 6th formant	100 Hz
34.	<i>DFI</i>	change in <i>F1</i>	0
35.	<i>DBI</i>	change in <i>B1</i>	0

36.	FNP	frequency of nasal pole	280 Hz
37.	BNP	bandwidth of nasal pole	90 Hz
38.	FNZ	frequency of nasal zero	280 Hz
39.	BNZ	bandwidth of nasal zero	280 Hz
40.	FTP	frequency of tracheal pole	2150 Hz
41.	BTP	bandwidth of tracheal pole	180 Hz
42.	FTZ	frequency of tracheal zero	2150 Hz
43.	BTZ	bandwidth of tracheal zero	180 Hz
44.	A2F	amplitude of friction F2	0
45.	A3F	amplitude of friction F3	50 dB
46.	A4F	amplitude of friction F4	50 dB
47.	A5F	amplitude of friction F5	50 dB
48.	A6F	amplitude of friction F6	60 dB
49.	AB	amplitude of friction bypass	0
50.	B2F	bandwidth of friction F2	OFF
51.	B3F	bandwidth of friction F3	450 Hz
52.	B4F	bandwidth of friction F4	600 Hz
53.	B5F	bandwidth of friction F5	450 Hz
54.	B6F	bandwidth of friction F6	100 Hz
55.	ANV	amplitude of voicing-nasal	0
56.	A1V	amplitude of voicing F1	0
57.	A2V	amplitude of voicing F2	0
58.	A3V	amplitude of voicing F3	0
59.	A4V	amplitude of voicing F4	0
60.	ATV	amplitude of voicing-tracheal	0

- ANSI (1989). ANSI-S3.6-1989, "Specifications for audiometers" (American National Standards Institute, New York).
- ANSI (1991). ANSI-S3.1-1991, "Maximum permissible ambient noise levels for audiometric test rooms" (American National Standards Institute, New York).
- Behrens, S., and Blumstein, S. (1988). "On the role of the amplitude of the fricative noise in the perception of place of articulation on voiceless fricatives consonants," J. Acoust. Soc. Am. **84**, 861–867.
- Best, C. T., Morriongiello, B., and Robson, R. (1981). "Perceptual equivalence of acoustic cues in speech and nonspeech perception," Percept. Psychophys. **29**, 191–211.
- Christensen, L. A., and Humes, L. E. (1996). "Identification of multidimensional complex sounds having parallel dimension structure," J. Acoust. Soc. Am. **99**, 2307–2315.
- Cooper, F. S., Delattre, P. C., Liberman, A. M., Borst, J. M., and Gerstman, L. J. (1952). "Some experiments on the perception of synthetic speech sounds," J. Acoust. Soc. Am. **24**, 597–606.
- Delattre, P., Liberman, A. M., Cooper, F. S., and Gerstman, L. J. (1952). "An experimental study of the acoustic determinants of vowel color: Observations on one- and two-formant vowels synthesized from spectrographic patterns," Word **8**, 195–210.
- Dirks, D. D., Bell, T. S., Rossman, R. N., and Kincaid, G. E. (1986). "Articulation index predictions of contextually dependent words," J. Acoust. Soc. Am. **80**, 82–92.
- Dubno, J. R., and Dirks, D. D. (1989). "Auditory filter characteristics and consonant recognition for hearing-impaired listeners," J. Acoust. Soc. Am. **85**, 1666–1675.
- Elliott, L. L. (1986). "Discrimination and response bias for CV syllables differing in voice onset time among children and adults," J. Acoust. Soc. Am. **80**, 1250–1255.
- Elliott, L. L., and Hammer, M. A. (1988). "Longitudinal changes in auditory discrimination in normal children and children with language-learning problems," J. Speech Hear. Res. **53**, 467–474.
- Elliott, L. L., and Katz, D. R. (1980). "Children's pure-tone detection," J. Acoust. Soc. Am. **67**, 343–344.
- Elliott, L. L., Busse, L., Partridge, R., Rupert, J., and DeGraaf, R. (1986). "Adult and child discrimination of CV syllables differing in voice onset time," Child Dev. **57**, 628–635.
- Frank, T., and Richards, W. D. (1991). "Hearing aid coupler output level variability and coupler correction levels for insert earphones," Ear Hear. **12**, 221–227.
- Fujimura, O. (1962). "Analysis of nasal consonants," J. Acoust. Soc. Am. **34**, 1865–1875.
- Harris, K. S. (1958). "Cues for the discrimination of American English fricatives in spoken syllables," Lang. Speech **1**, 1–7.
- Heinz, J. M., and Stevens, K. N. (1961). "On the properties of voiceless fricative consonants," J. Acoust. Soc. Am. **33**, 589–596.
- Humes, L. E., and Christopherson, L. A. (1991). "Speech identification difficulties of hearing-impaired elderly persons: The contributions of auditory-processing deficits," J. Speech Hear. Res. **34**, 686–693.
- Humes, L. E., and Roberts, L. (1990). "Speech-recognition difficulties of the hearing-impaired elderly: The contributions of audibility," J. Speech Hear. Res. **33**, 726–735.
- Humes, L. E., Watson, B. U., Christensen, L. A., Cokely, C. G., Halling, D. C., and Lee, L. (1994). "Factors associated with individual differences in clinical measures of speech recognition among the elderly," J. Speech Hear. Res. **37**, 465–474.
- Jerger, S., Pirozzolo, F., Jerger, J., Elizondo, R., Desai, S., Wright, E., and Reynosa, R. (1993). "Developmental trends in the interaction between auditory and linguistic processing," Percept. Psychophys. **54**, 310–320.
- Kidd, G. R., and Watson, C. S. (1987). "Perception of multidimensional complex sounds," J. Acoust. Soc. Am. Suppl. 1 **81**, S33.
- Klatt, D. H., and Klatt, L. C. (1990). "Analysis, synthesis, and perception of voice quality variations among female and male talkers," J. Acoust. Soc. Am. **87**, 820–857.
- Kruskal, J. B., and Wish, M. (1989). *Multidimensional Scaling* (Sage, Newbury Park).
- Lindholm, J. M., Dorman, M., Taylor, B. E., and Hannley, M. T. (1988). "Stimulus factors influencing the identification of voiced stop consonants by normal-hearing and hearing-impaired adults," J. Acoust. Soc. Am. **83**, 1608–1614.
- Mermelstein, P. (1977). "On detecting nasals in continuous speech," J. Acoust. Soc. Am. **67**, 581–587.
- Morriongiello, B., Robson, R., Best, C., and Clifton, R. (1984). "Trading relations in the perception of speech by 5-year-old children," J. Exp. Child Psychol. **37**, 231–250.
- Nittrouer, S. (1992). "Age-related differences in perceptual effects of formant transitions within syllables and across syllable boundaries," J. Phon. **20**, 351–382.
- Nittrouer, S., and Studdert-Kennedy, M. (1987). "The role of coarticulatory effects in the perception of fricatives by children and adults," J. Speech Hear. Res. **30**, 319–329.

- Nosofsky, R. M. (1986). "Attention, similarity, and the identification-categorization relationship," *J. Exp. Psychol.* **115**, 39–57.
- Nosofsky, R. M. (1992). "Similarity scaling and cognitive process models," *Annu. Rev. Psychol.* **43**, 25–53.
- O'Connor, J. D., Gerstman, L. J., Liberman, A. M., Delattre, P. C., and Cooper, F. S. (1957). "Acoustic cues for the perception of initial /w,y,r,l/ in English," *Word* **13**, 24–43.
- Peterson, H. E., and Lehiste, I. (1960). "Duration of syllable nuclei in English," *J. Acoust. Soc. Am.* **32**, 693–703.
- Repp, B. H. (1982). "Phonetic trading relations and context effects: New experimental evidence for a speech mode of perception," *Psychol. Bull.* **92**, 81–110.
- Repp, B. H. (1986). "Perception of the [m]–[n] distinction in CV syllables," *J. Acoust. Soc. Am.* **79**, 1987–1999.
- Repp, B. H., Liberman, A. M., Eccardt, T., and Pesetsky, D. (1978). "Perceptual integration of acoustic cues for stop, fricative, and affricate manner," *J. Exp. Psychol.* **4**, 621–637.
- Summers, W. V., and Leek, M. R. (1992). "The role of spectral and temporal cues in vowel identification by listeners with impaired hearing," *J. Speech Hear. Res.* **35**, 1189–1199.
- Sussman, J. E. (1993). "Auditory processing in children's speech perception: Results of selective adaptation and discrimination tasks," *J. Speech Hear. Res.* **36**, 380–395.
- Sussman, J. E., and Carney, A. E. (1989). "Effects of transition length on the perception of stop consonants by children and adults," *J. Speech Hear. Res.* **32**, 151–160.
- University Synthesizer Package [Computer Software] (1990). Sensimetrics Corporation, Cambridge, MA.
- Van Tassel, D., Soli, S., Kirby, V., and Widin, G. (1987). "Speech waveform envelope cues for consonant recognition," *J. Acoust. Soc. Am.* **82**, 1152–1161.
- Walley, A. C., and Carrell, T. D. (1983). "Onset spectra and formant transitions in the adult's and child's perception of articulation in stop consonants," *J. Acoust. Soc. Am.* **73**, 1011–1022.
- Wish, M. (1971). "Individual differences in perceptions and preferences among nations," in *Attitude Research Reaches New Heights*, edited by C. W. King and D. Tigert (American Marketing Association, Chicago).
- Wish, M., Deutsch, M., and Biener, L. (1972). "Differences in perceived similarity of nations," in *Multidimensional Scaling: Theory and Applications in the Behavioral Sciences, Vol. 2*, edited by A. K. Romney, R. N. Shepard, and S. Nerlove (Seminar, New York).

Auditory profile analysis: Is there perceptual constancy for spectral shape for stimuli roved in frequency?

Hedwig Gockel^{a)} and Hans Colonius

Graduate Programme "Psychoacoustics," FB 5, Department of Cognitive Psychology, Carl von Ossietzky University of Oldenburg, D-26111 Oldenburg, Germany

(Received 24 March 1997; revised 10 July 1997; accepted 10 July 1997)

The ability to discriminate between two spectral shapes was investigated using a one-interval, two-alternative forced choice procedure. Each stimulus consisted of seven components equally spaced on a logarithmic frequency scale (frequency ratio of 1.2 between adjacent components). The two spectral shapes were produced by first generating a complex each of whose components was equally loud (when heard in isolation) and then increasing the level of either the third or the fifth component by a certain amount. To render pitch an unusable cue, the center frequencies of the stimuli were randomly varied between presentations (maintaining the ratio between adjacent components) over a range of about three octaves (279–2074 Hz). The data indicate that listeners were not able to distinguish between the two types of profiles even for very large increments in level of the third and the fifth components. The results suggest that there is no perceptual constancy for this type of spectral shape for stimuli roved over a sufficiently large frequency range. The spectral shape cannot be perceived independently of stimulus frequency. The results are related to the multi-channel model applied in profile analysis tasks. © 1997 Acoustical Society of America. [S0001-4966(97)05310-1]

PACS numbers: 43.66.Jh, 43.66.Hg, 43.66.Fe [WJ]

INTRODUCTION

Since the early 1980s, "profile analysis," as a new approach to studying spectral shape discrimination, has triggered a vast amount of research. In profile analysis experiments the observer has to discriminate between a standard complex spectrum and a signal-plus-standard spectrum. The standard stimulus typically consists of n components of equal level, equally spaced on a logarithmic frequency scale. In the signal-plus-standard spectrum one component is incremented in level. The overall level of the stimulus is varied randomly for each presentation to prevent subjects from basing their judgment on sequential level differences. For stimuli whose individual components are all separated by at least one critical band, an explanation in terms of a simultaneous comparison of output levels measured in different frequency channels (multi-channel model) is still the most favoured one (see, e.g., Green, 1992). In several studies, the observers' empirical weighting patterns for the frequency components involved have been investigated (see, e.g., Berg and Green, 1990; Green and Berg, 1991). This weighting pattern reflects the relative contribution of the different frequency channels in the across-channel level comparison process which the listener is assumed to perform.

A number of previous studies have investigated the sensitivity of listeners to changes in spectral shape when the spectrum of the standard was not flat. For example, Green and Kidd (1983) employed standard spectra, where the single component of the standard to which the signal was added (pedestal) ranged from -18 to $+24$ dB in level *re*: the non-

signal components. The data showed no substantial decrease in performance for pedestal levels within a range of -6 to $+12$ dB of the standard level. Thus, the authors argued that "once the spectrum of the background is encoded, the stimulus is compared with the long-term memory store of the spectrum and slight variations are detectable." Similar conclusions have been drawn from experiments using "alternating" spectra (successive frequency components alternated between two amplitudes) or "tilted" spectra (Bernstein and Green, 1988). These experiments indicated that standard spectra may deviate to a certain extent from a flat spectrum (3- to 9-dB depth of alternation when detecting an increment in a single component; spectral tilt by as much as 6 dB/oct when detecting a change in spectral tilt) before discrimination performance is severely reduced. These investigators noted that "listeners are able to equalize modest irregularities in the spectrum of the background and to detect deviations from this standard spectrum."

The present experiment investigated the ability to discriminate between two other types of nonflat spectra, namely, two different "single-peaked" profiles. To render pitch an invalid cue, a large frequency-roving range was introduced, keeping the frequency ratio between components constant. Thus, the question addressed was: "Is there perceptual constancy of spectral shape for stimuli roved in frequency?," or, expressed within the theoretical framework of the multi-channel model: "Can listeners develop appropriate weighting functions with respect to relative signal position within a tone complex or is the development of appropriate weights restricted to absolute frequency?" The specific stimuli (single peaked) were chosen because they evoked a well-defined pitch cue (for unroved stimuli).

Richards *et al.* (1989) reported a study related to this

^{a)}Present address: MRC Applied Psychology Unit, 15 Chaucer Rd., Cambridge CB2 2EF, England. Electronic mail: hedwig.gockel@mrc-apu.cam.ac.uk

TABLE I. Frequencies of components used in the seven-tone complexes.

No.	1	2	3	4	5	6	7	8	9	10	11	12	13	14	15	16	17	18
f (Hz)	162	194	233	279	335	402	482	579	694	833	1000	1200	1440	1728	2074	2488	2986	3583

one. In a “standard” profile analysis task (discrimination between a flat standard spectrum and a spectrum where the center component was incremented in level) they randomly varied the center frequencies of the stimuli (by varying the sample rate) for each presentation over a 1-oct range (500–1000 Hz). They found thresholds (defined as the ratio of the signal amplitude to the amplitude of each component of the standard, in decibels) to be increased by about 30%, but performance remained above the best that could occur if sequential level cues were used. Thus, for a frequency-roving range smaller than the present one, discrimination between two spectral shapes was still possible. Their aim was to determine whether discrimination of spectral shape is mediated by changes in pitch that are concomitant with changes in spectral shape. In their study, the possible pitch cue was defined as the difference in pitch between standard and signal-plus-standard stimulus calculated according to the envelop weighted average instantaneous frequency (EWAIF) model (Feth and Stover, 1987), and the roving range was chosen so as to make that cue unreliable. However, one could think of another more local pitch cue (as opposed to the global EWAIF value) such as an increase in pitch strength in a certain frequency region. The effectiveness of such a local pitch cue might not have been overcome by a 1-oct roving range. In the study of Richards *et al.* the difference between center frequencies of the two stimuli presented in a trial had a triangular distribution with a mean equal to zero. The difference between center frequencies would be less than 147 Hz on 50% of trials and less than 231 Hz on 71% of trials. If, for example, subjects listened for an increase in pitch strength within a frequency range of ± 1 critical bandwidth around the average frequency of the incremented component (750 Hz), then a pitch cue would have been available on a substantial proportion of trials.

In the present study, the possible pitch cue was defined as the difference in pitch between the two components which might have been incremented in level, and the roving range was chosen so as to make this cue unreliable. Thus, an increase in pitch strength in a certain frequency region was rendered an unreliable cue, and the only cue which might be used by subjects to discriminate between the two different “single-peaked” profiles was spectral shape.

I. GENERAL METHOD

A. Stimuli and equipment

Each stimulus was derived from a complex of seven sinusoids, each of which would have equal loudness if presented alone (see below for details). The first stimulus type (I3) was produced by incrementing the amplitude of the third component. The second stimulus type (I5) was produced by incrementing the amplitude of the fifth component. Adjacent components were equally spaced on a logarithmic frequency scale and had a frequency ratio of 1.2. To prevent absolute

frequency from being a useful cue in discriminating between the two different profile types, the center frequency of the stimuli was randomly varied between each presentation over a range of nearly 3 oct, maintaining the frequency ratio between components. Frequency roving was done in discrete steps with a frequency ratio of 1.44 (i.e. 1.2 squared) as step size. For one subject, stimuli with center frequencies from 279–1728 Hz were used, while for the other two subjects stimuli with center frequencies from 335–2074 Hz were used¹ (see Table I for the frequencies of the components).

The calculated probability of correctly discriminating the profiles based solely on a pitch cue (related to the frequency of the incremented component) is about 0.58 for the present stimulus set. The crude assumption underlying this calculation is that subjects are perfectly able to discriminate between frequencies of the incremented components. So, this probability (which corresponds to a d' value of 0.40 assuming zero bias) is an upper limit for the proportion of correct responses if discrimination is based on such a local pitch cue alone.

Because of the large frequency rove range employed, it was necessary to take account of the fact that equal loudness contours of sinusoids are not flat. Therefore, before starting the experiment proper, equal loudness contours were determined over the frequency range used for each subject. A one-up one-down procedure was used to determine the level of each component required to give equal loudness to the 1000-Hz component with a level of 49 dB SPL. In the main experiment, then, the 1000-Hz component had a level of 49 dB SPL, while the levels of the other components were those required to give equal loudness (before the increment was added in phase either to the third or the fifth component of this “flat profile”). There was no variation in overall level in this experiment.

The starting phases of all components were fixed (zero phase). The duration of all stimuli was 1000 ms, including 40-ms rise/fall times shaped by a hanning window. The stimuli were generated digitally (Sun ELC), played by a 16-bit digital-to-analog converter (D/A) at a sampling rate of 44 100 Hz and low-pass filtered at 20 kHz (ninth-order elliptic filter; 0.3-dB pass band ripple; –80-dB stop band attenuation). The stimuli were presented monaurally over the left ear piece of a Beyer DT 990 Pro headphone. Subjects were individually seated in a double-walled (IAC) sound-insulated chamber, and responded via a PC keyboard. Brief instructions (in addition to a more detailed paper version) and feedback were presented using a PC monitor which was located outside the booth in front of its window. The PC, which was connected to the Sun, served only as an input–output terminal. A light emitting diode (LED), fixed at the bottom front of the monitor’s frame, indicated the beginning of a new trial. The LEDs were controlled by a signal generated on the Sun and played by the second channel of the D/A converter to ensure precise timing.

B. Procedure

A one-interval procedure was used to measure subjects' ability to distinguish between the two types of profiles. Preliminary experiments, using the 2I-2AFC procedure which is usually applied in profile analysis experiments, showed that the difference in perceived overall pitch between profile stimuli randomly roved over such a large frequency range was rather striking. Therefore, a one-interval procedure was considered to be easier because it would remove at least the rapid succession of this dominant impression. As a result, a more subtle cue (e.g., "component dominance" and its relative pitch within a tone complex) might gain more influence on the percept. Besides this, Kidd *et al.* (1986) noted that their "own preliminary work indicates that auditory profile analysis may operate effectively in a one-interval paradigm." The negligible effect of the interstimulus interval on performance reported by Green *et al.* (1983) supports this conclusion. The two stimulus types I3 and I5 were presented with equal probability and pseudorandomly. Following each presentation of a stimulus, subjects were asked to indicate its type. Following each response, feedback was provided. Five different increment sizes, $-5, 0, 5, 10,$ and 15 dB (expressed as the signal-to-standard ratio in decibels), were tested in a *blocked* design in order to minimize variability of the percept. Increment sizes were selected following some informal pilot experiments. They were determined so that, even for the smallest increment size, subjects could easily discriminate between (1) stimuli of the same center frequency but of different type (I3 vs I5) and (2) stimuli with identical absolute increment frequency but different center frequencies. Within each session, each condition (size of increment) was tested in a pseudorandom order. One session consisted of five blocks, each with 96 trials of a fixed increment size. The total duration of a single session was about 70 min, including rest times. Each subject was tested in at least 20 sessions, with a total of 9600 trials. At the beginning of each session, each stimulus was presented once, together with a number (3 or 5 presented on the screen) to indicate its type.

C. Subjects

The three subjects ranged in age from 22–32 years and had normal hearing as measured by conventional audiometry. Stimuli were delivered monaurally to the better ear of each subject (cw: right ear; hg, tm: left ear). All subjects were highly trained in profile analysis tasks. They all participated in a "classical" profile analysis experiment (without frequency roving; 2I-2AFC task) and showed very good performance for stimuli with center frequencies over the frequency range from 279–2074 Hz (tested in a blocked design for the different center frequencies).

II. RESULTS

Data given refer exclusively to the last ten sessions, when performance had stabilized (actually, only one subject showed a small effect of practice). Figure 1 shows values of d' and corresponding 95% confidence intervals as a function of increment size (confidence intervals were calculated following Macmillan and Creelman, 1991). All values for d'

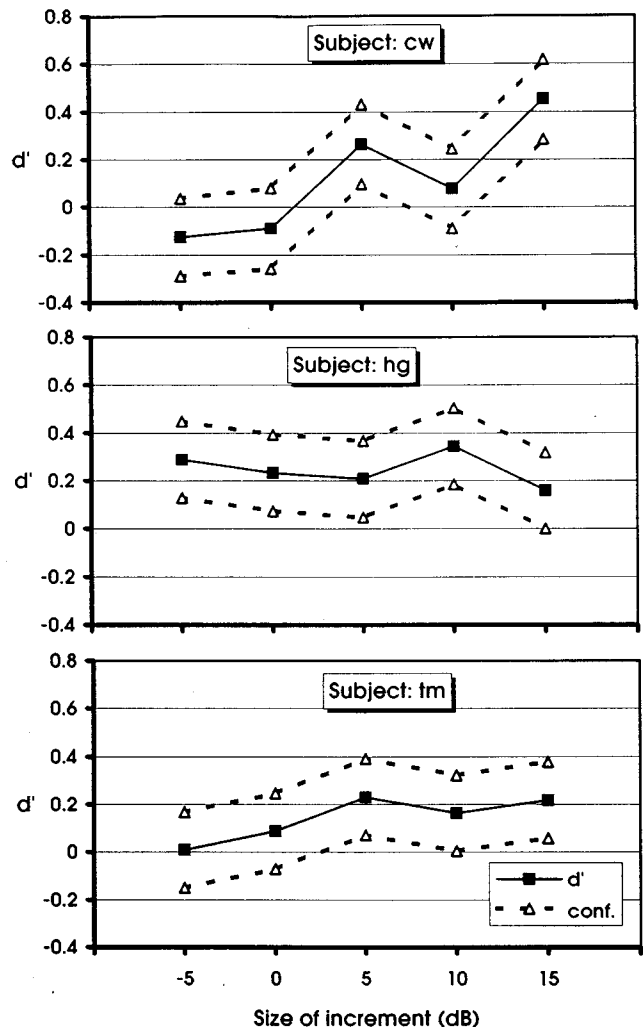


FIG. 1. Sensitivity index d' and corresponding 95% confidence intervals for the profile identification task as a function of increment size. Each panel gives results for a single subject. Each data point is based on 960 trials.

are rather low. They do not exceed a value of 0.45. Two subjects (cw and tm) show d' values significantly different from zero for increment sizes of $+5$ dB and $+15$ dB. The third subject (hg) produced values significantly different from zero for nearly all increment sizes, with maximum performance for increment sizes of -5 dB and $+10$ dB.

Although the d' values are rather low, they, nevertheless, indicate levels of performance better than chance for the identification task. Hence, one might assume that identification of profile type is difficult, but possible. On the other hand, as noted above, the d' value for an observer who makes optimum use of a local pitch cue based on the absolute frequency of the incremented component (categorizes stimuli with increments in the lower half of the presented frequency range as I3 and stimuli with increments in the upper half of the presented frequency range as I5) would be 0.4 and none of the observed d' values is significantly larger than this. Thus, subjects could have used the absolute frequency of the incremented component as a cue. However, a closer look at performance levels as a function of the center frequency of the profile stimuli reveals that both conclusions

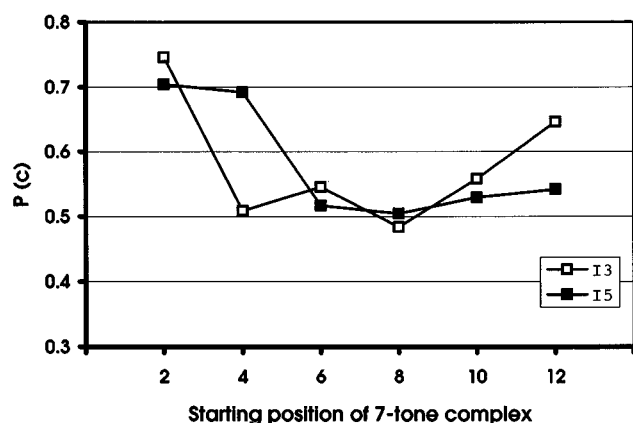


FIG. 2. Plot of $P(c)$ as a function of nominal starting position of the presented stimulus (subject: cw; size of increment: 15 dB). The higher the nominal starting position, the higher the lowest frequency component in the presented seven-tone complex (ranging from 194–1200 Hz). Each curve corresponds to one type of profile. Each data point is based on 80 trials.

would be wrong. To clarify this point, we first concentrate on the data of subject cw for an increment size of 15 dB. For this subject and condition, the calculated d' reached its maximum value of 0.45. Figure 2 shows the proportion correct, $P(c)$, as a function of the nominal starting position of the stimulus. Nominal starting positions correspond to the frequency of the lowest component in the seven-tone complex; see the numbers and frequencies in Table I. The higher the nominal starting position, the higher the frequency of the first component in the seven-tone complex (ranging from 194–1200 Hz). Each curve corresponds to one type of profile. Each data point is based on 80 trials. To facilitate comparison of data resulting from presentation of the two stimulus types, the raw $P(c)$ values are corrected for response bias. The correction procedure employed is equivalent to shifting the two curves in opposite directions by the same amount for all data points. The amount of shift (here 0.17) is determined by the observed overall probability (for an increment size of 15 dB) of responding “I5” minus 0.5, since an unbiased observer responds “I5” on half of the trials. These corrected data show that the probability of correct identification of stimulus type is about 0.5 (guessing rate) for stimuli located around the central part of the total frequency rove range employed (starting positions 6 and 8). Higher performance levels are observed (if at all) only for stimuli located at/near the edges of the total frequency rove range employed.

This response pattern corresponds to the edge effect which is well known from experiments investigating “absolute identification” ability (see, e.g., Pollack, 1952; Garner, 1953; Braida and Durlach, 1972; Lippmann *et al.*, 1976). In the absolute identification paradigm there are as many response categories as there are different stimuli employed, and the subjects’ task is to “name” each stimulus appropriately. Because of the similarity between the pattern of the present data and the edge effect described above, and because type-identification ability was essentially zero for the mid-frequency range, it seems likely that correct responses above chance level were due to absolute identification of stimuli instead of identification of correct stimulus type. The

response pattern also indicates that the stimuli were not simply categorized as I3 or I5 according to the absolute frequency of the incremented component. Here $P(c)$ for the I5 category is relatively high for low-frequency stimuli and $P(c)$ for the I3 category is relatively high for high-frequency stimuli. In addition, the relatively good performance for both the I3 and I5 stimuli at starting position 2 demonstrates that the two stimuli were easy to discriminate.

A similar response pattern was found for all subjects in conditions where the observed d' value was significantly different from zero. For no subject and no increment magnitude were values of $P(c)$ consistently above chance level for all starting positions. Thus, the type of stimulus independent of its frequency location was not identified. Rather, it is likely that some individual sounds were memorized and identified.

III. DISCUSSION

In summary, the data show that even after extensive training, subjects were unable to identify which type of profile was presented. Incrementing the level of the third or the fifth component in a seven-tone complex did not provide distinguishable percepts, when the center frequencies of the stimuli were randomly varied over a range of 3 oct. Since the same subjects showed quite high performance levels in a “classical” experiment on profile analysis for all center frequencies used and for similar stimuli, the reason for this inability is probably the large frequency rove range employed. One might argue that the single-interval procedure led to poorer performance than a two-interval procedure would have done. However, as mentioned above, in pilot experiments using a two-interval task subjects reported that the striking differences in overall pitch associated with the rove prevented them from hearing subtle differences. This, together with the reported negligible effect of the interstimulus interval (Green *et al.*, 1983), makes it quite unlikely that better performance would be obtained using a two-interval procedure.

In contrast to the present results, Richards *et al.* (1989) found that roving the center frequency of the stimuli only slightly impaired the ability to detect an increment in the level of a single component. The relatively small effect in their experiment can probably be attributed to the relatively small rove range used in comparison to the present one. The rove range employed in their study may not have been sufficient to eliminate a local pitch cue. Another difference between the two studies was that one of the stimuli of Richards *et al.* had a flat spectrum. We cannot rule out the possibility that discrimination between a flat and an incremented profile would result in better performance than observed in the present study, even if the stimuli were roved over a 3-oct range. However, this difference between stimuli probably was not the important factor in determining the different pattern of results, since it has been demonstrated (as mentioned in the Introduction) that standard spectra may deviate to a certain extent from a flat spectrum before discrimination performance is severely reduced (Bernstein and Green, 1988).

In general, such an investigation has to cope with two opposing requirements: (1) the size of the frequency rove range should be large enough to render a pitch cue almost

unusable and (2) components should be resolvable over the whole frequency range used (for simple evaluation in terms of the multi-channel model), or, expressed somewhat less restrictively, the global shape of the internal representation of the spectrum (i.e., the excitation pattern) should be maintained over the whole frequency range used. The frequency range used in the present experiment was chosen so as to satisfy these two requirements. Thus, the only available cue was spectral shape. However, listeners did not seem to be able to develop an appropriate weighting pattern (cf. Durlach *et al.*, 1986) with respect to relative signal position within a tone complex. Hence, it is concluded that this type of spectral shape cannot be perceived independently of stimulus frequency.

Takeuchi and Braida (1995) reported a similar finding but with respect to amplitude envelope pattern. They investigated listeners' ability to compare amplitude envelope patterns whose center frequencies were randomly varied over a range of about 4 oct. Although performance was above chance level, it markedly decreased when the center frequencies were different for the target and comparison signal. Thus, Takeuchi and Braida concluded that the amplitude envelopes of signals do not appear to be perceived independently of the signal itself. However, the perception of spectral shape is probably even more strongly linked to signal frequency than the perception of amplitude envelope pattern.

It should be noted that the present results are compatible with the finding of Gockel (1996, 1997) that subjects are able to identify the frequency of the incremented component. This ability might provide a local pitch cue in profile analysis tasks which would have been destroyed by the present randomization of center frequencies over such a large frequency range.

ACKNOWLEDGMENTS

This research was supported by the Deutsche Forschungsgemeinschaft through a research grant in the Graduate Programme "Psychoacoustics." The authors wish to thank Brian Moore, Nicholas Hill, and an anonymous reviewer for helpful comments on a previous version of this manuscript.

¹If subjects had learned the task (which they did not), it was intended then to present subjects with the complementary set of stimuli without feedback. Transfer of discrimination ability to the same task with unknown stimuli would indicate the ability to judge profile spectra with respect to the relative position of an increment, independent of absolute location of the complex on the frequency scale. If, on the other hand, they had reached a certain performance level during training due to identification of individual stimuli, then one would expect performance with unknown stimuli to be poor.

- Berg, B. G., and Green, D. M. (1990). "Spectral weights in profile listening," *J. Acoust. Soc. Am.* **88**, 758–766.
- Bernstein, L. R., and Green, D. M. (1988). "Detection of changes in spectral shape: Uniform vs. non-uniform background spectra," *Hearing Res.* **32**, 157–166.
- Braida, L. D., and Durlach, N. I. (1972). "Intensity perception. II. Resolution in one-interval paradigms," *J. Acoust. Soc. Am.* **51**, 483–502.
- Durlach, N. I., Braida, L. D., and Ito, Y. (1986). "Towards a model for discrimination of broadband signals," *J. Acoust. Soc. Am.* **80**, 63–72.
- Feth, L. L., and Stover, L. J. (1987). "Demodulation processes in auditory perception," in *Auditory Processing of Complex Sounds*, edited by W. A. Yost and C. S. Watson (Erlbaum, Hillsdale, NJ), pp. 76–86.
- Garner, W. R. (1953). "An informational analysis of absolute judgements of loudness," *J. Exp. Psychol.* **46**, 373–380.
- Gockel, H. (1996). "Auditory discrimination of spectral shape—Cues and limits in perception," Ph.D. thesis, Universität Oldenburg.
- Gockel, H. (1997). "On possible cues in profile analysis: Identification of the incremented component," submitted to *J. Acoust. Soc. Am.*
- Green, D. M. (1992). "The number of components in profile analysis tasks," *J. Acoust. Soc. Am.* **91**, 1616–1623.
- Green, D. M., and Berg, B. G. (1991). "Spectral weights and the profile bowl," *Q. J. Exp. Psychol. A* **43**, 449–458.
- Green, D. M., and Kidd, Jr., G. (1983). "Further studies of auditory profile analysis," *J. Acoust. Soc. Am.* **73**, 1260–1265.
- Green, D. M., Kidd, Jr., G., and Picardi, M. C. (1983). "Successive versus simultaneous comparison in auditory intensity discrimination," *J. Acoust. Soc. Am.* **73**, 639–643.
- Kidd, Jr., G., Mason, C. R., and Green, D. M. (1986). "Auditory profile analysis of irregular sound spectra," *J. Acoust. Soc. Am.* **79**, 1045–1053.
- Lippmann, R. P., Braida, L. D., and Durlach, N. I. (1976). "Intensity perception. V. Effect of payoff matrix on absolute identification," *J. Acoust. Soc. Am.* **59**, 129–134.
- Macmillan, N. A., and Creelman, C. D. (1991). *Detection Theory: A User's Guide* (Cambridge U.P., Cambridge).
- Pollack, I. (1952). "The information of elementary auditory displays," *J. Acoust. Soc. Am.* **24**, 745–749.
- Richards, V. M., Onsan, Z. A., and Green, D. M. (1989). "Auditory profile analysis: Potential pitch cues," *Hearing Res.* **39**, 27–36.
- Takeuchi, A. H., and Braida, L. D. (1995). "Effect of frequency transposition on the discrimination of amplitude envelope patterns," *J. Acoust. Soc. Am.* **97**, 453–460.

Perceptual segregation of a harmonic from a vowel by interaural time difference and frequency proximity

C. J. Darwin and R. W. Hukin

Experimental Psychology, University of Sussex, Brighton BN1 9QG, England

(Received 17 January 1997; accepted for publication 20 June 1997)

The five experiments reported here examine the conditions under which sounds differing in their interaural time difference (ITD) are segregated for the purposes of perceiving a vowel's identity. Experiment 1 confirms previous findings that (i) a difference in ITD provides only a very weak cue for segregating a vowel's 500-Hz harmonic from the remainder of an isolated vowel; (ii) embedding the harmonic in a series of 500-Hz tones produces some segregation, which is enhanced if the harmonic and the tones differ in ITD from the rest of the vowel; and (iii) when these latter sounds are presented in the same block as isolated vowels, they facilitate segregation of the harmonic by ITD in the isolated vowels. The subsequent experiments show that this last effect, across-trial facilitation, is only produced by sounds which cue both the frequency and the ITD of the harmonic; either alone is insufficient. We also show that: (i) a single cue tone at the frequency of the harmonic is sufficient to facilitate the use of ITD in grouping; (ii) sequential organization by frequency proximity dominates over sequential organization by ITD when simultaneous sound sources are present; and (iii) the effectiveness of a cue tone can be abolished by capturing it into a synchronous harmonic complex. The experiments clarify the conditions under which ITDs contribute to the segregation of simultaneous sounds. © 1997 Acoustical Society of America.

[S0001-4966(97)01610-X]

PACS numbers: 43.66.Mk, 43.66.Pn, 43.66.Qp, 43.71.Es [JWH]

INTRODUCTION

This paper addresses the relationship between two different grouping cues: common frequency and interaural time difference (ITD). It is well-established that rapidly played tones that are similar in frequency will be more likely to form a single coherent stream or melody than will tones that are very different in frequency (Bregman and Campbell, 1971; van Noorden, 1975). Such coherence allows a pure tone that is part of a complex to be perceptually removed by a precursor tonal sequence with a consequent change in the complex's timbre (Bregman and Pinker, 1978), vowel quality (Darwin *et al.*, 1989), or pitch (Darwin *et al.*, 1995). Frequency proximity thus helps to define a sound source across time.

An alternative way to define a sound source across time is to exploit the fact that a sound source tends to come from a particular direction. Evidence for auditory grouping according to direction is more varied. Although, the identification of speech (Cherry and Taylor, 1954), or a tune (Deutsch, 1979) is severely disturbed by alternating the signal between the ears, the disturbance is reduced by adding another sound to the opposite ear (Schubert and Parker, 1956; Deutsch, 1979)—a finding which diminishes the usefulness of sequential grouping by common direction when multiple sound sources are present. A well-known example where grouping by frequency-proximity dominates over grouping by lateral position is in the opening bars of the last movement of Tchaikovsky's Sixth Symphony (Deutsch, 1982). Here the notes of the melody and of the accompanying "second violin" part alternate between the first and second violins (who would originally have sat on the conductor's left and right).

Recently, attention has been paid to the use in auditory

grouping of specific cues to direction. In particular, Culling and Summerfield (1995) have demonstrated, somewhat counterintuitively, that interaural time differences (ITDs) cannot be used by the auditory system to segregate simultaneous sounds. They presented listeners with two simultaneous "whispered" vowels each of whose first two formants were represented by a pair of noise bands. They found that although listeners could use a common interaural level difference (ILD) to group together formants for vowel identification, they were unable to use a common ITD. Listeners were no better at identifying the vowel they heard on the left when the noise bands of the target vowel had a different ITD ($+390\ \mu\text{s}$) from those of the other vowel ($-390\ \mu\text{s}$) than when all four noise bands had the same ITD. The finding is the more surprising since low-frequency ITDs are the dominant cue for lateralizing complex sounds in azimuth (Wightman and Kistler, 1992).

The generality of the conclusion that listeners are unable to use ITDs to segregate simultaneous sounds was questioned by Hukin and Darwin (1995). They examined the effectiveness of an ITD difference in segregating the 500-Hz fourth harmonic of a vowel from the remaining harmonics. They measured the extent of the segregation through the shift in the phoneme boundary between the vowels /i/ and /ε/ along a first-formant continuum (Darwin and Sutherland, 1984). This paradigm relies on the fact that the distinction between /i/ and /ε/ can be cued by a change in first formant frequency (F_1). Listeners can readily label sounds along a continuum differing in F_1 as either /i/ or /ε/; their phoneme boundary is then established at the 50% identification point. In our previous experiments this boundary normally occurs at an F_1 of around 450 Hz. The perceived frequency of the

first formant itself depends on the relative amplitude of nearby harmonics (Darwin and Gardner, 1985), so that if the amplitude of a harmonic close to the first-formant frequency is changed, the corresponding change in the perceived $F1$ can be detected by a shift in the /i/-/ε/ phoneme boundary. The technique is sensitive to changes of around 1 dB in the level of harmonics close to $F1$. If the 500-Hz harmonic makes a reduced contribution to the vowel quality as a result of experimental manipulations, then the phoneme boundary should shift to higher nominal $F1$ values.

In partial support of Culling and Summerfield's conclusion that segregation of simultaneous sounds is not determined by ITD differences, Hukin and Darwin (1995) found that an ITD difference of $\pm 666 \mu\text{s}$ between the 500-Hz component and the rest of the vowel gave a far smaller shift in the phoneme boundary than did an infinite ILD difference. The difference in ILD gave a shift in the phoneme boundary that was equivalent to a physical reduction in the level of the 500-Hz component of over 8 dB, whereas the ITD gave a reduction of about 2 dB. However, they did find that differences in ITD promoted segregation under slightly different stimulus conditions.

The conditions were derived from an earlier experiment (Darwin *et al.*, 1989) on grouping by frequency proximity which had shown that embedding a vowel in a short sequence of 500-Hz tones reduced the contribution of the 500-Hz harmonic to the vowel (measured as described above by a shift in the phoneme boundary). We will refer to this effect as within-trial segregation by tonal context. Hukin and Darwin (1995) showed that this segregation was greater when all the 500-Hz tones (surrounding tones and the harmonic of the vowel) were given a different ITD from the rest of the vowel ($\pm 666 \mu\text{s}$). We will refer to this latter effect as within-trial segregation by ITD.

Hukin and Darwin also showed that when a block of trials contained trials that did contain the tone sequence mixed together with the original stimuli (that did not contain a tone sequence), then the latter sounds did show some segregation due to ITD (although recall that they showed no segregation when presented separately). We will refer to this effect as across-trial facilitation of segregation by ITD.

In the present paper we first replicate the experiment of Hukin and Darwin, using a group of subjects who will be used for all the experiments. We then show (experiments 2 and 3) that across-trial facilitation of segregation by ITD requires that the cue provides information about both the tonal quality and the lateral position of the harmonic that is to be segregated; neither is sufficient alone. That such across-trial facilitation can be produced by trials with only a single cue tone is shown in experiment 4. This experiment also demonstrates the important result that within-trial segregation by ITD depends only on the ITD of the cue tone, not on the ITD of the segregated harmonic. Experiment 5 shows that none of the above effects occur when the cue is itself grouped into a separate complex.

I. EXPERIMENT 1: TONE SEQUENCE AND ITD

The first experiment replicated the first experiment of Hukin and Darwin (1995). The replication was made for two

reasons, first to ensure that the within-trial segregation by ITD and the across-trial facilitation of segregation by ITD that Hukin and Darwin reported were robust, and second to allow data from the same subjects to be compared across the remaining experiments.

A. Method

The method used in these experiments was the same as that used by Hukin and Darwin (1995). The contribution that the 500-Hz component of a vowel makes to its categorization as either /i/ or /ε/ was estimated from the phoneme boundary along an $F1$ continuum. Physical or perceptual removal of the 500-Hz component from the vowel gives a shift in the phoneme boundary to higher nominal formant frequencies. In order to provide some calibration of the size of the effect, different continua had different physical gains of the 500-Hz component, in addition to those introduced by varying the $F1$ frequency.

The original vowel continuum contained six sounds whose first formant frequency varied between 379 and 500 Hz to give a percept that changed from /i/ at low values of $F1$ to /ε/ at high values. The second- and third-formant frequencies were fixed at 2100 and 2900 Hz, respectively. The bandwidths of the three formants were kept constant at 90, 110, and 170 Hz. All sounds were synthesized on a fundamental frequency of 125 Hz and at a level such that the 500-Hz component of the member of the basic (0-dB gain) continuum with an $F1$ of 500 Hz was 60 dB SPL. The duration of the vowels was 56 ms (including 16-ms raised-cosine on- and off-ramps).

From this basic continuum were derived four sets of experimental continua in which the amplitude of the 500-Hz component was either 0 dB, +3 dB, +6 dB, or +9 dB relative to that in the basic continuum. Each condition in the following experiments thus consists of 24 different stimuli: 6 $F1$ values \times 4 gains of the 500-Hz component. In all conditions, the vowel components other than the 500 Hz were all presented binaurally with an ITD that led on the left ear (ITD = +666 μs). The 500-Hz component was presented with either the same ITD as the other vowel components (condition L), or an ITD that led on the right ear (condition R: ITD = -666 μs) to give a total of eight vowel continua. These two sets of four continua constituted the two uncued conditions.

Two further, cued conditions (LL, RR) were made by preceding each vowel with four, and following it with two, 500-Hz cue tones identical (including in level) to its 500-Hz component and with the same ITD of $\pm 666 \mu\text{s}$. The cue tones were separated from each other and the vowel by 160 ms. The various conditions are illustrated in Fig. 1.

Subjects listened to the stimuli under two different modes of presentation. With blocked presentation the L and R conditions were given in one block of trials, and the LL and RR conditions in a separate block. With mixed presentation all four conditions were randomized together. With each mode of presentation subjects identified ten tokens of each stimulus in a pseudo-random order within blocks.

The sounds were synthesized by harmonic summation in real time with 16-bit resolution and at a sample rate of 44.1

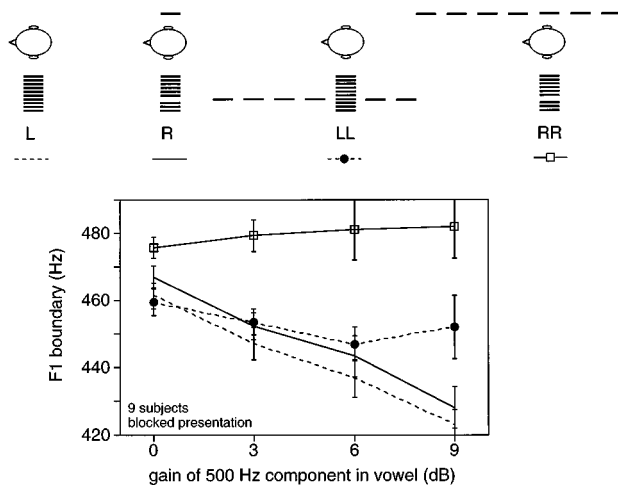


FIG. 1. Phoneme boundaries (with standard errors across subjects) along an /i/-/ε/ continuum, with different additional gains on the 500-Hz component of the vowel for blocked presentation in experiment 1. With blocked presentation, the uncued conditions (L,R) are presented in one block, and the cued (LL,RR) in a separate block.

kHz using custom software (Russell and Darwin, 1991) on a Digidesign Protocols board attached to an Apple Macintosh IIfx, which also controlled the experiment. The vowel spectral envelopes were calculated using source and transfer functions taken from the Klatt synthesizer in serial mode (Klatt, 1980). The outputs of the Protocols interface were connected to Tucker-Davis PA3 programmable attenuators which were used to set the overall level for the experiment. Subjects listened over Sennheiser HD414 headphones in a double-skinned IAC booth.

Subjects were told that they would hear a vowel in their left ear which could be either /i/ as in “pit,” or /ε/ as in “pet,” and that they might also hear a tone in either ear, which they were to ignore. They signalled their response on each trial using the “i” and “e” keys on the Mac keyboard. Each trial followed 500 ms after the response to the previous one.

The same nine subjects took part in each experiment, all of whom had previous experience of similar vowel identification experiments. All were native speakers of British English with normal pure-tone thresholds over the range of frequencies of interest in this experiment. Two subjects had contributed data to experiment 2 of Hukin and Darwin (1995). Phoneme boundaries were estimated for each subject’s data in each continuum using an automatically fitted rescaled tanh function.¹ All curve fits were checked by eye. Analysis of variance was carried out on these phoneme boundaries with SuperANOVA (Abacus Concepts, Inc.) using the Greenhouse-Geisser adjustment for correlation among repeated measures.

B. Results and discussion

Figures 1 and 2 show the mean phoneme boundaries and their standard errors across subjects. The results closely replicated the results of experiment 2 of Hukin and Darwin (1995). As expected, for both modes of presentation, pho-

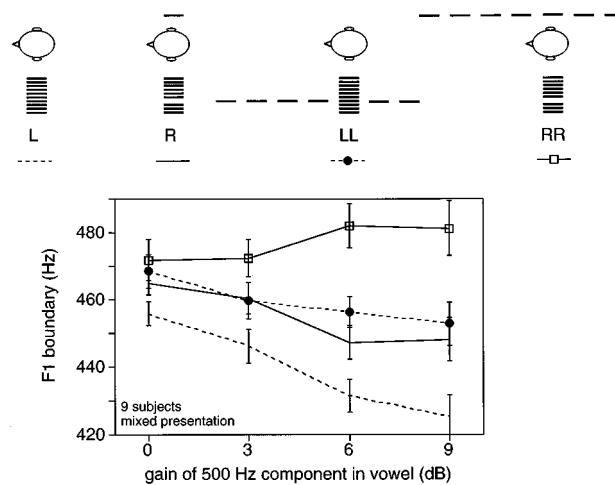


FIG. 2. Phoneme boundaries for mixed presentation in experiment 1.

neme boundaries in the L condition move to lower frequencies as the gain of the 500-Hz component increased, thus demonstrating the sensitivity of the paradigm to physical changes in the level of that component. An increase in the frequency of the phoneme boundary corresponds to a decrease in the effective level of the 500-Hz component.

1. Blocked presentation

Giving the 500-Hz component of the vowel a different ITD has no significant effect on the phoneme boundary (Condition L vs R: $F_{1,8}=3.8$, $p>0.05$). This result supports Culling and Summerfield’s (1995) conclusion that a difference in ITD is an ineffective cue for segregation. As also found previously by Hukin and Darwin (1995), a tonal context produces two effects. First, it is effective at perceptually removing the 500-Hz harmonic from the vowel: the LL condition has significantly higher ($F_{1,8}=5.8$, $p<0.05$) and flatter—across changes in gain—($F_{3,24}=6.0$, $p<0.005$) phoneme boundaries than does the L condition (within-trial segregation by tonal context). Second, it allows ITD to produce additional segregation: The RR condition has much higher ($F_{1,8}=29.4$, $p<0.001$) phoneme boundaries than the LL condition (within-trial segregation by ITD).

2. Mixed presentation

The results for the L, LL, and RR condition are very similar with mixed and with blocked presentation. But, as found in the Hukin and Darwin’s earlier experiment, the results for the R condition are different. Putting the L and R conditions in the same block of trials as the LL and RR conditions leads to the R condition having a significantly higher phoneme boundary than the L condition ($F_{1,8}=13.9$, $p<0.01$). This increase in the boundary in the R compared to the L condition is larger with mixed than with blocked presentation ($F_{1,8}=8.5$, $p<0.02$)—across-trial facilitation of segregation by ITD.

This experiment has replicated the three results reported in experiment 2 of Hukin and Darwin (1995). First, giving the 500-Hz component of a vowel a different ITD from the

remaining components leads to no significant segregation of that component as measured by a shift in phoneme boundary. Second, embedding the vowel in a sequence of 500-Hz tones leads to some segregation of the 500-Hz harmonic (within-trial segregation by tonal context) which is substantially increased when all the 500-Hz tones are given a different ITD from the rest of the vowel (within-trial segregation by ITD). Third, mixing trials that contain the tone sequence with those that do not increases the segregation by ITD of the 500-Hz component from the vowel on trials without a tonal sequence: across-trial facilitation of segregation by ITD.

The following two experiments examine what aspect of the mixed presentation is responsible for inducing increased segregation by ITD in the R condition. Experiment 2 asks whether exposure to only the frequency of the 500-Hz tone is sufficient; experiment 3 asks whether exposure to the location of an additional, contralateral sound source is sufficient.

II. EXPERIMENT 2: FREQUENCY ONLY

This experiment asks whether the across-trial facilitation of segregation by ITD found by Hukin and Darwin (1995) and replicated in experiment 1 can be produced when subjects only have knowledge of the frequency of the to-be-segregated tone, rather than knowledge of both its frequency and its ITD.

These experiments found that a difference in ITD between the 500-Hz harmonic of a vowel and the remainder of the vowel was much more effective at removing that harmonic from the calculation of vowel quality in blocks of trials which also contained vowels embedded in a 500-Hz tone sequence that shared the harmonic's distinct ITD. The tone sequence on some trials thus shared both the frequency and the ITD of the to-be-segregated tone. Can a similar across-trial effect be obtained when the tone sequence only gives frequency, but not ITD information about the to-be-segregated tone? To answer this question experiment 2 repeats the mixed block part of experiment 1, but omits the condition in which the tone sequence has an ITD that leads on the right ear.

A. Stimuli

The experiment used mixed presentation of the L, R, and LL conditions of experiment 1. These three conditions were presented in a single mixed block of 720 trials (10 replications of 6 sounds from each continuum \times 4 levels of the 500-Hz component \times 3 conditions) to the same nine subjects of experiment 1.

B. Results and discussion

The mean phoneme boundaries and their standard errors are shown in Fig. 3. Replicating the previously found within-trial segregating effect of a tone sequence, phoneme boundaries are significantly higher ($F_{1,8}=11.1$, $p<0.02$) and flatter ($F_{3,24}=9.7$, $p<0.001$) in the presence of the tone sequence (condition LL) than without it (condition L). However, there is no evidence that the frequency information present in the tone sequence produces an across-trial facilitation of segregation by ITD. If there were, we would expect the R condi-

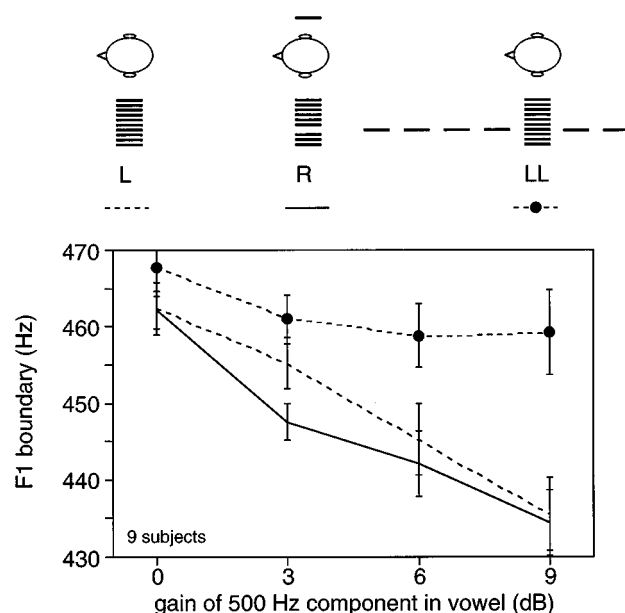


FIG. 3. Phoneme boundaries in experiment 2. The experiment used mixed presentation of a subset of conditions from experiment 1.

tion to have higher phoneme boundaries than the L, which it does not. Facilitation of segregation is significantly smaller here ($F_{1,8}=22.7$, $p<0.002$) than that found in the previous experiment when both frequency and ITD information was available from the tonal context. So, making subjects aware that there is a separate sound source present at 500-Hz during the same block of trials is not sufficient to induce segregation of the 500-Hz tone by ITD in the R condition. The conditions necessary for across-trial induction of segregation by ITD must therefore include some information about the location (or the ITD) of the additional sound source.

Is any sound with the same ITD a sufficient cue to give across-trial facilitation of segregation? The following experiment asks whether a narrow-band noise centered around the frequency of the tone can give such across-trial facilitation. Experiment 3 also asks whether such a narrow-band noise can produce the within-trial segregation either by context or by ITD found with tone sequences.

III. EXPERIMENT 3: NARROW-BAND NOISE

A. Method

The experiment was identical in design to experiment 1 except that the 500-Hz six-tone sequence used in the LL and RR conditions of experiment 1 was replaced by a similar sequence of six narrow-band noises. The noise was centered around 500 Hz with a bandwidth of 70 Hz. It consisted of harmonics 47–54 of a flat amplitude, random-phase signal with a fundamental of 10 Hz. The level of the noise in the 0-dB conditions was such that, when passed through a (fourth-order) gammatone filter centered on 500 Hz, it had the same energy as that of the 500-Hz component of a vowel in the original continuum with $F1=500$ Hz. Its level was incremented in steps of 3 dB with the level of the 500-Hz component of the vowel. The narrow-band noise thus pro-

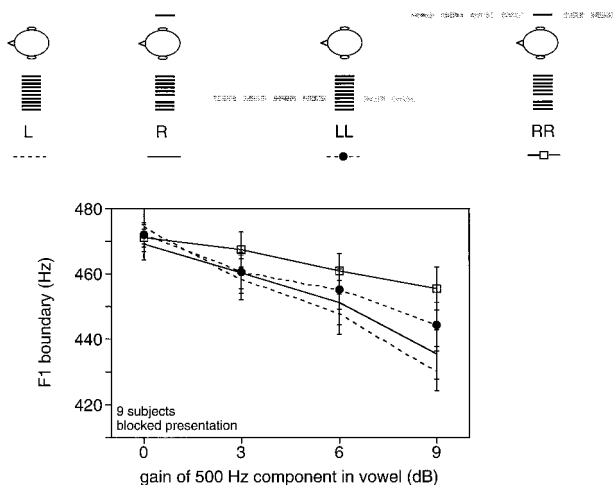


FIG. 4. Phoneme boundaries for blocked presentation in experiment 3. The experiment was similar to experiment 1 but used narrow-band noise as the cue.

vides similar energy in the auditory channel responding to a 500-Hz tone, but is different in timbre, and so is less likely to stream with the 500-Hz component of the vowel. The same nine subjects took the experiment.

B. Results

1. Blocked presentation

The phoneme boundaries for blocked presentation are shown in Fig. 4. As found in experiment 1, giving the 500-Hz component of the vowel a different ITD again has no significant effect on the phoneme boundary: The R condition's boundaries are not significantly higher ($F_{1,8}=0.3$, $p>0.5$) or flatter ($F_{3,24}=1.2$, $p>0.3$) than the L condition's. However, unlike experiment 1, a change in ITD also has no effect when the vowel is put in a sequence of narrow-band noise bursts: The RR condition is neither higher ($F_{1,8}=1.0$,

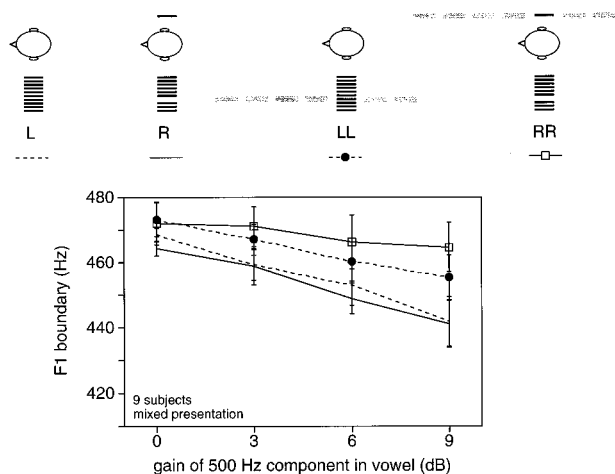


FIG. 5. Phoneme boundaries for mixed presentation in experiment 3. The experiment was similar to experiment 1 but used narrow-band noise as the cue.

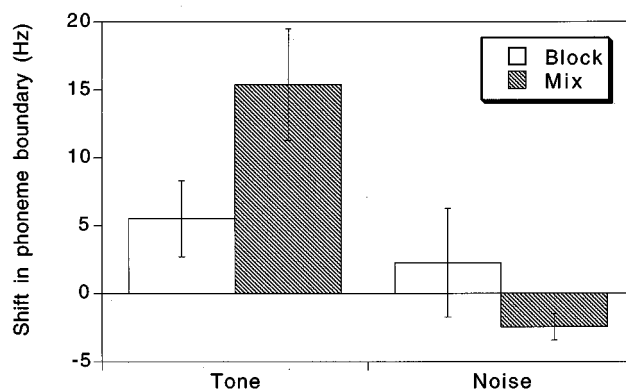


FIG. 6. Comparison of across-trial facilitation of segregation by ITD produced with mixed presentation by tone sequences in experiment 1 and narrow-band noise sequences in experiment 3. Each bar represents the difference in phoneme boundary between the R and L conditions averaged across the four levels of the 500-Hz component. The extent of across-trial facilitation is given by the difference between the mixed and the blocked conditions for each type of cue sequence.

$p>0.3$) nor flatter ($F_{3,24}=1.8$, $p>0.1$) than the LL. The sequence of noise bursts thus produces no within-trial segregation by ITD.

2. Mixed presentation

The pattern of results with mixed presentation is very similar to that found with blocked presentation (Fig. 5). Although the difference in phoneme boundary between the L and R conditions is marginally significant ($F_{1,8}=6.3$, $p<0.05$), the size of the effect is small and it is in the opposite direction to that expected if segregation were occurring. A sequence of noise bursts leading on the opposite ear thus does not produce any across-trial facilitation of segregation by ITD. The tonal sequence in experiment 1 produces significantly more across-trial facilitation (averaging across level of the 500-Hz component) than does the noise sequence in experiment 3 ($F_{1,8}=18.04$, $p<0.005$), as illustrated in Figs. 6.

The noise sequence flattens the phoneme boundary function slightly: The LL condition gives flatter phoneme boundaries than the L ($F_{3,24}=4.8$, $p<0.02$). Overall, the noise context produces smaller changes in the phoneme boundaries than did the tonal context of experiment 1 ($F_{1,8}=8.7$, $p<0.02$). Since the small change produced by the noise context (although not that produced by the tonal context) is independent of ITD, it could be the result of peripheral adaptation to the 500-Hz noise band reducing the response to the 500-Hz harmonic of the vowel.

In summary, a sequence of 500-Hz narrow-band noise bursts is much less effective than a tone sequence at producing either within-trial or across-trial effects of ITD on grouping. Taking experiments 2 and 3 together, subjects need very specific information about the nature of an additional sound source before they show across-trial facilitation of segregation by ITD: Information about both the ITD and the specific tonal quality of the sound is necessary.

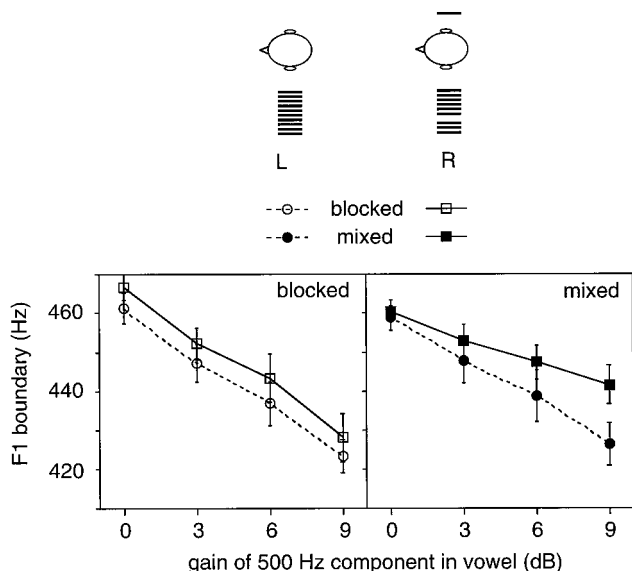


FIG. 7. Phoneme boundaries in the uncued conditions of experiment 4 with blocked and mixed presentation. The experiment was similar to experiment 1 but used a single tone as the cue.

IV. EXPERIMENT 4: SINGLE CUE

Experiment 4 differed from experiment 1 in two ways. First, the tonal context used was a single 500-Hz precursor tone rather than multiple tones. A single cue tone, although providing less sequential grouping than four tones, extends the generality of the effects that we have found. Second, conditions were included to investigate the interaction between grouping by frequency proximity and by ITD. In particular, the precursor 500-Hz tone was played with an ITD favoring one ear, while the 500-Hz harmonic of the vowel was played with an ITD favoring either the same or the opposite ear. Deutsch (1979) found that sequential grouping by frequency dominated over the ear of presentation for the identification of tunes whose notes alternated between the ears only when each note of the tune was accompanied by a drone note to the opposite ear. If a similar dominance of sequential grouping by frequency proximity over ITD occurs for our stimuli, then the extent to which the 500-Hz component is removed from the vowel should depend less on its location than on that of the precursor tone.

A. Method

The L and R conditions were identical to those of experiment 1. Four further, cued conditions (LL, LR, RL, RR) were made by preceding the vowel with a single 500-Hz precursor “cue” tone identical to its 500-Hz component but with an ITD of $\pm 666 \mu\text{s}$ that was independent of the ITD of the 500-Hz tone in the vowel. The first letter in the condition name refers to the leading ear for the cue tone, the second to the leading ear for the 500-Hz harmonic of the vowel. The cue tone ended 160 ms before the onset of the vowel. The various conditions are illustrated in Figs. 7 and 8.

The experiment was run in three blocks: one with ten repetitions of just the two uncued conditions (blocked L and R), and two mixed blocks, each with five repetitions of all

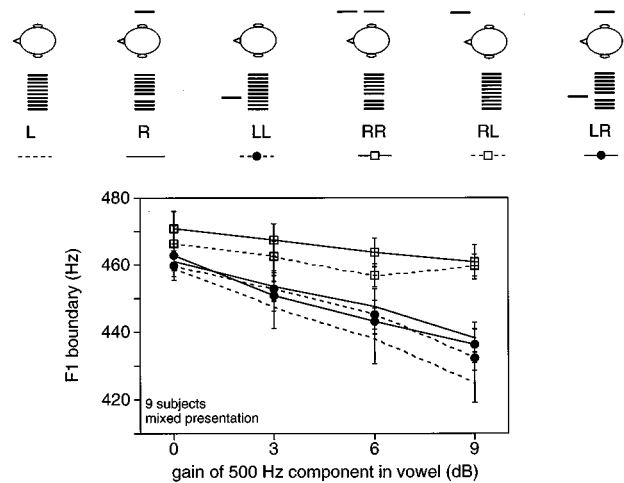


FIG. 8. Phoneme boundaries in the mixed conditions of experiment 4. The experiment was similar to experiment 1 but used a single tone as the cue.

six conditions (mixed L, R, LL, RL, LR, and RR). Each mixed block thus had 720 trials (5 replications \times 6 F_1 values \times 4 levels of the 500-Hz component \times 2 lateralizations of the 500-Hz component \times 3 types of cue tone: no cue tone, $\pm 666 \mu\text{s}$). The trials within each block were presented in different, pseudo-random orders.

B. Results and discussion

If the present cueing paradigm with a single precursor tone were as effective as experiment 1 was with four preceding and two following tones, we would expect to find: (i) within-trial segregation by tonal context (LL and RR conditions giving higher-frequency boundaries than L and R, respectively); (ii) within-trial segregation by ITD (RR condition giving higher-frequency boundaries than L); (iii) across-trial facilitation of segregation by ITD (R condition giving a greater increase in boundary frequency over the L condition with mixed than with blocked presentation).

In addition, the experiment asked whether sequential grouping by frequency can overrule grouping by ITD. The experiment included two conditions where the 500-Hz cue tone and the 500-Hz harmonic of the vowel had opposite ITDs (conditions LR and RL). If the cue tone can, by virtue of its proximity in frequency to the vowel harmonic, segregate the harmonic from the vowel regardless of their relative ITDs, then we might find (iv) similar, high phoneme boundaries in the RR and RL conditions on the one hand, and lower boundaries in the LL and LR conditions on the other.

All four effects were found in the present experiment, although, as found previously (Darwin *et al.*, 1989), the single cue tone produced weaker segregation than did a longer sequence.

1. Uncued conditions

Looking first at the results from the block of trials which consisted only of the uncued conditions (Fig. 7), we find, as expected from previous experiments, that giving the 500-Hz component of the vowel a different ITD has no effect on the phoneme boundaries: With blocked presentation condition R is no different from condition L ($F_{1,8} = 3.8$, $p > 0.05$).

Looking now at the results from the uncued conditions with mixed rather than blocked presentation, the R condition has significant higher boundaries than the L ($F_{1,8}=6.7$, $p<0.05$), a difference which increases with the gain of the 500-Hz component ($F_{3,24}=5.6$, $p<0.01$). Moreover, this relative increase is significantly bigger with mixed than with blocked presentation ($F_{3,24}=3.7$, $p<0.05$). These differences replicate with a single cue tone the across-trial facilitation of segregation by ITD from experiment 1 in which cues to the frequency and location of a separate sound source from other trials in the same experimental block allow the segregating effect of a difference in ITD to emerge.

2. Cued conditions

Figure 8 shows the results for mixed presentation. The within-trial segregation by tonal context produced by a single cue tone when all sounds have the same ITD is weak: the LL condition is not significantly different overall from the L condition ($F_{1,8}=2.0$, $p>0.01$). However, more specific *post hoc* contrasts (based on the expected pattern of results from earlier experiments) within this main effect show that the two higher gains of the LL condition have a higher boundary than those of the L condition (+6 dB: $p<0.02$; +9 dB: $p<0.002$). Overall weak segregation from a single preceding tone is compatible with the earlier finding (Darwin *et al.*, 1989) that the extent to which a harmonic is segregated from a vowel increases as the number of preceding tones increases up to four.

Preceding the vowel by a single cue tone having the same level and ITD as the 500-Hz component of the vowel, but a different ITD from the rest of the sounds, produces substantial changes in the frequencies of the phoneme boundaries. The phoneme boundaries are at a higher frequency for the RR condition than for the R ($F_{1,8}=18.2$, $p<0.005$). Moreover, the increase in boundary frequency is greater for the RR condition than for the LL condition ($F_{1,8}=11.1$, $p<0.02$). This last result extends to a single precursor tone the result of our previous paper (Hukin and Darwin, 1995) that differences in ITD produce within-trial segregation by ITD, enhancing the segregating effect of a tonal context on the harmonic of a vowel.

However, there is an additional, novel feature of the results of this experiment: The shift in the phoneme boundary in the cue tone conditions relative to the uncued conditions is determined more by the ITD of the cue tone ($F_{1,8}=16.5$, $p<0.005$), than by the ITD of the harmonic in the vowel ($F_{1,8}=5.6$, $p<0.05$). As a measure of the dominance of the cue tone's ITD over the harmonic's ITD, the RL condition has significantly higher ($F_{1,8}=10.8$, $p<0.02$) and flatter ($F_{3,24}=4.1$, $p<0.05$) phoneme boundaries than the LR condition.

The likely explanation for this last result is that sequential grouping by frequency proximity exerts a dominant influence in causing the two 500-Hz tones to group together (perhaps with the apparent location of the second being attributed to that of the first, cue tone). This dominance of the cue tone's location is likely to depend on the fact that the cue tone is presented alone (and so has a clear location), while the harmonic of the vowel is presented simultaneously with

other harmonically related sounds and so has a more labile subjective location (cf. Hill and Darwin, 1996).

The irrelevance of the ITD of the 500-Hz harmonic to the extent to which it is segregated from the vowel by a cue tone reinforces Culling and Summerfield's conclusion that ITD is a very poor segregating cue for simultaneous sounds. Differences in ITD can however influence the segregating power (via frequency proximity) of isolated sounds presented at different times.

In summary, experiment 4 has shown:

- (i) within-trial segregation by tonal context. A single cue tone at the frequency of the 500-Hz component of a vowel can produce some segregation of that component from a vowel when all sounds have the same ITD. This effect is only significant at higher levels of the 500-Hz component;
- (ii) within-trial segregation by ITD. When the cue tone has a different ITD ($-666\ \mu\text{s}$) from the other sounds ($+666\ \mu\text{s}$), segregation of the 500-Hz harmonic from the vowel is substantial. An important new finding is that this segregation occurs regardless of the ITD of the 500-Hz harmonic;
- (iii) across-trial facilitation of segregation by ITD. For the uncued conditions with mixed presentation (including trials with the single cue tone present in the same block of trials), there is significantly more segregation by ITD than with blocked presentation.

V. EXPERIMENT 5: COMPLEX SINGLE CUE

Experiment 5 acts as a control experiment for the results of experiment 4 being due to purely local effects around 500 Hz. The explanations that we have offered for the segregating effects of a tonal context have been based on principles of perceptual organisation. These principles are further invoked in experiment 2 to construct conditions where there should be no grouping by frequency proximity and so no tendency for the cue tone to segregate the 500-Hz harmonic from the vowel.

In this experiment we add four higher harmonics of 166.7 Hz synchronously to the 500-Hz cue tone. The 500-Hz cue tone should then form part of a single 166.7-Hz complex and not therefore be free to form a separate perceptual group with the 500-Hz harmonic of the vowel. A similar manipulation has been used to regroup the leading portion of a component of a complex to prevent it being removed, by virtue of its onset time, from the calculation of vowel quality (Darwin and Sutherland, 1984), pitch (Ciocca and Darwin, 1993), or profile analysis (Hill and Bailey, 1997). If the effects that we have found in the first experiment are due to mechanisms that are purely local to 500 Hz, then we would expect them also to appear in this experiment. If they are due to perceptual grouping, then they all should disappear.

A. Method

The experiment was similar to the mixed part of experiment 1, and used the same subjects. In addition to the cue tone, all conditions also contained a tonal complex that was simultaneous with the cue tone, but could be presented with

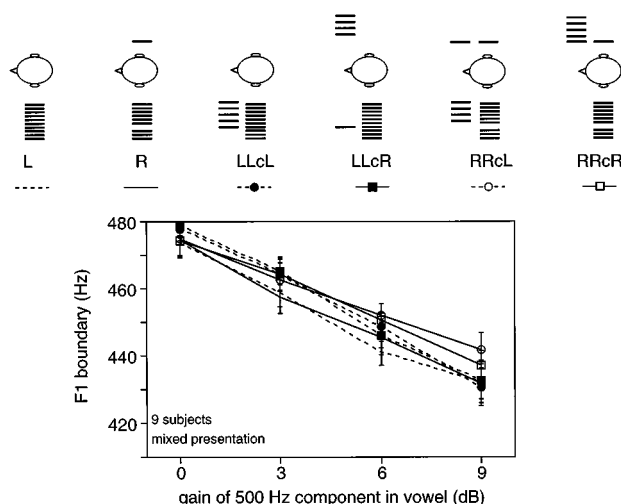


FIG. 9. Phoneme boundaries in experiment 5. The experiment was similar to experiment 4 but used a complex tone as the cue.

the same or different ITDs. The additional complex consisted of the fourth through seventh harmonics of 166.7 Hz. The amplitude of the 500-Hz cue tone which constituted the third harmonic of the complex's harmonic series was the same as in the previous experiment (i.e., identical to that of the 500-Hz harmonic that it preceded), but the amplitude of the higher harmonics fell at -6 dB/oct. The various conditions are shown diagrammatically in Fig. 9. The 500-Hz cue tone always had the same ITD as the 500-Hz harmonic of the vowel. This ITD could be either $\pm 666 \mu\text{s}$. The ITD of the additional complex was also $\pm 666 \mu\text{s}$ but varied independently to give four different conditions.

B. Results and discussion

Phoneme boundaries for the two uncued and the four cued conditions are shown in Fig. 9. There are no differences in phoneme boundary across the different conditions ($F_{5,40} = 2.4$, $p > 0.1$). Adding a complex that is harmonically related to the cue tone has prevented it from producing any segregation of the 500-Hz harmonic from the vowel. The segregation found in the first experiment is thus unlikely to be due to processes that are local to 500 Hz. Rather, it is more likely to be due to mechanisms of perceptual organisation which, in the cued conditions of experiment 1, recognize the 500-Hz cue tone as a separate sound source with a distinct location. This source is able to capture the 500-Hz harmonic of the vowel, by the principle of frequency proximity. But experiment 5 has shown that the 500-Hz cue tone loses this ability when it is itself part of a separate harmonic complex.

Capture of the 500-Hz cue tone by the complex occurs regardless of their relative ITDs. For example, there is no significant difference between the uncued L condition and the LLcR condition where, although the cue tone has the same ITD as the complete vowel, the additional complex has the opposite ITD. Here the shared onset, offset, and harmonic relations between the cue tone and the complex over-

ride the difference in ITD. This result is another example of the weakness of the grouping exerted by differences in ITD in simultaneous sounds.

It is also clear that there is no across-trial facilitation of segregation by ITD in this experiment. As found in experiment 3, this across-trial facilitation cannot be induced simply by having interspersed trials that have any sound presented with a different ITD. The present experiment has also shown that it is not sufficient to have the cue tone physically present with the appropriate ITD if it is being perceptually integrated into a different percept.

VI. SUMMARY

The present experiments have confirmed previous results showing that in blocks of trials where only the harmonics of a vowel are all present simultaneously, there is no significant segregation of a single harmonic by ITD (experiments 1, 2, and 4).

They have also clarified the conditions under which some perceptual segregation by ITD can occur for simultaneous sounds. Some segregation by ITD (on uncued trials) does occur if other trials are present in the same block in which multiple cue tones (experiment 1) or a single cue tone (experiment 4) are present before the vowel, sharing the harmonic's frequency *and* ITD (experiments 2 and 3). This across-trial facilitation of segregation by ITD is abolished if the cue tone itself forms part of a separate complex tone (experiment 5).

The experiments have also clarified the conditions under which precursor events can segregate a harmonic from a vowel:

- a single 500-Hz cue tone is more effective at removing the 500-Hz harmonic from a vowel when the cue tone has a different ITD from the vowel than when it has the same ITD. However, this segregation is not influenced by the ITD of the harmonic in the vowel (experiment 4);
- a single 500-Hz cue tone is *not* effective at removing the 500-Hz harmonic from a vowel when the cue tone is itself captured in a simultaneous harmonic complex (experiment 5). The extent of this capture is itself unaffected by the relative ITDs of the cue and captor tones.

There are two overall conclusions from these experiments. The first confirms Culling and Summerfield's contention that grouping of purely simultaneous sounds by ITD is weak. An individual harmonic cannot be segregated from a vowel on the basis of a difference in ITD unless the listener already has clear evidence for a separate sound source. This evidence must be quite specific: The sound source that induces across-trial segregation by ITD needs to share the ITD and specific tonal quality of the to-be-segregated harmonic; neither narrow-band noise with an appropriate ITD, nor a 500-Hz tone with an inappropriate ITD suffice. The weakness of grouping by simultaneous ITD, when the listener has no such additional evidence for an extra sound source, sits well with experiments that have demonstrated that listeners can integrate ITD across simultaneously present frequencies

that form a single perceptual group (Trahiotis and Stern, 1989; Hill and Darwin, 1996). Such across-frequency integration of ITD may help to maintain a stable lateral position for auditory objects in environments where ITDs are disturbed by echoes and reverberation (Woods and Colburn, 1992). However, the present experiments have shown that the auditory system does have the flexibility to perform segregation by ITD when there is independent evidence of an appropriate additional sound source.

The second conclusion is that sequential grouping by frequency proximity dominates ITD when multiple sounds are present. The single cue tone in experiment 4 was more effective at segregating the harmonic when the cue tone had a different ITD from the vowel; but this effect was barely influenced by the ITD of the harmonic itself. It is likely that this dominance of frequency proximity over ITD acts only over a short timespan, whereas the across-trial facilitation discussed in the previous paragraph is longer term.

An important restriction on grouping by frequency proximity is that it is itself influenced by perceptual grouping. When the cue tone is itself captured, it is ineffective at segregating out the harmonic from the vowel. This restriction has obvious practical advantages, preventing inappropriate segregation when there is an accidental coincidence of frequencies in adjacent sounds. That such capturing itself does not depend on the relative ITDs of the cue tone and its captor harmonics confirms the first conclusion: Grouping of purely simultaneous sounds by ITD is weak.

ACKNOWLEDGMENTS

This research was supported by MRC Grant No. G9505738N. Comments from Dr. Peter Bailey and an anonymous reviewer improved the paper.

¹The rescaled tanh function $1/(1 + e^{-s(a-x)})$, where a is the boundary and s the slope parameter provided a sufficiently good fit and allowed convenient boundary estimation using the general curve fit function of the "Kaleidagraph v.3.0.1" program (Abelbeck Software) with a and s as free parameters. All curve fits were checked by eye.

Bregman, A. S., and Campbell, J. (1971). "Primary auditory stream segregation and perception of order in rapid sequences of tones," *J. Exp. Psychol.* **89**, 244–249.

Bregman, A. S., and Pinker, S. (1978). "Auditory streaming and the building of timbre," *Can. J. Psychol.* **32**, 19–31.

Cherry, E. C., and Taylor, W. K. (1954). "Some further experiments upon the recognition of speech, with one and with two ears," *J. Acoust. Soc. Am.* **26**, 554–559.

Ciocca, V., and Darwin, C. J. (1993). "Effects of onset asynchrony on pitch perception: adaptation or grouping?," *J. Acoust. Soc. Am.* **93**, 2870–2878.

Culling, J. F., and Summerfield, Q. (1995). "Perceptual separation of concurrent speech sounds: Absence of across-frequency grouping by common interaural delay," *J. Acoust. Soc. Am.* **98**, 785–797.

Darwin, C. J., and Gardner, R. B. (1985). "Which harmonics contribute to the estimation of the first formant?," *Speech Commun.* **4**, 231–5.

Darwin, C. J., and Sutherland, N. S. (1984). "Grouping frequency components of vowels: When is a harmonic not a harmonic?," *Q. J. Exp. Psychol.* **36A**, 193–208.

Darwin, C. J., Hukin, R. W., and Al-Khatib, B. Y. (1995). "Grouping in pitch perception: evidence for sequential constraints," *J. Acoust. Soc. Am.* **98**, 880–885.

Darwin, C. J., Pattison, H., and Gardner, R. B. (1989). "Vowel quality changes produced by surrounding tone sequences," *Percept. Psychophys.* **45**, 333–342.

Deutsch, D. (1979). "Binaural integration of melodic patterns," *Percept. Psychophys.* **25**, 399–405.

Deutsch, D. (1982). "Grouping mechanisms in music," in *The Psychology of Music*, edited by D. Deutsch (Academic, New York), pp. 99–134.

Hill, N. I., and Bailey, P. J. (1997). "Profile analysis with an asynchronous target: evidence for auditory grouping," *J. Acoust. Soc. Am.* **102**, 477–481.

Hill, N. I., and Darwin, C. J. (1996). "Lateralisation of a perturbed harmonic: Effects of onset asynchrony and mistuning," *J. Acoust. Soc. Am.* **100**, 2352–2364.

Hukin, R. W., and Darwin, C. J. (1995). "Effects of contralateral presentation and of interaural time differences in segregating a harmonic from a vowel," *J. Acoust. Soc. Am.* **98**, 1380–1387.

Klatt, D. H. (1980). "Software for a cascade/parallel formant synthesizer," *J. Acoust. Soc. Am.* **67**, 971–995.

Russell, P., and Darwin, C. J. (1991). "Real-time synthesis of complex sounds on a Mac II with 56001 DSP chip," *Br. J. Audiol.* **25**, 59–60.

Schubert, E. D., and Parker, C. D. (1956). "Addition to Cherry's findings on switching speech between the two ears," *J. Acoust. Soc. Am.* **27**, 792–794.

Trahiotis, C., and Stern, R. M. (1989). "Lateralization of bands of noise: Effects of bandwidth and differences of interaural time and phase," *J. Acoust. Soc. Am.* **86**, 1285–1293.

van Noorden, L. P. A. S. (1975). "Temporal coherence in the perception of tone sequences," Eindhoven University of Technology, Ph.D. dissertation.

Wightman, F. L., and Kistler, D. J. (1992). "The dominant role of low-frequency interaural time differences in sound localization," *J. Acoust. Soc. Am.* **91**, 1648–1661.

Woods, W. A., and Colburn, S. (1992). "Test of a model of auditory object formation using intensity and interaural time difference discriminations," *J. Acoust. Soc. Am.* **91**, 2894–2902.

The effect of head rotations on vertical plane sound localization

Stephen Perrett and William Noble

Department of Psychology, University of New England, Armidale, NSW 2351, Australia

(Received 28 December 1996; revised 27 May 1997; accepted 28 May 1997)

Current understanding gives predominant weight to stationary cues for auditory localization. Two experiments were conducted to investigate the possible existence of a dynamic cue. The first experiment involved localization of concealed sources in the upper median vertical plane (MVP) and showed, as expected, that elevation was not detectable with motionless listening when high-frequency energy was absent or when normal pinna function was distorted. Elevation under such conditions did become detectable with horizontal head rotations, provided low-frequency energy was present in the signal. This indicates that the basis of the dynamic cue is variation in the rate of transformation of low-frequency interaural time/phase differences. The second experiment involved localization of sources arrayed throughout upper and lower regions of the MVP and in the left lateral vertical plane (LVP); it showed that upper hemisphere sources can be distinguished somewhat from those in the lower hemisphere, even in motionless listening conditions, but more so with rotation. The greatest benefit for localization from rotation of the head appears to be gained for sources positioned in the front MVP. © 1997 Acoustical Society of America.

[S0001-4966(97)06109-2]

PACS numbers: 43.66.Mk, 43.66.Nm, 43.66.Pn, 43.66.Qp [RHD]

INTRODUCTION

The following experiments demonstrate that a critical source of information for vertical plane sound localization is provided by rotations of the head in the horizontal plane. This shows that the auditory system is tuned to dynamic as well as stationary features of audible signals for this aspect of its functioning.

It is well-established that static cues allow fairly proficient localization of sounds. Information for horizontal (left–right) location is generated by interaural difference cues, the most significant being differences in low-frequency ongoing time/phase (Wightman and Kistler, 1992). The information furnished by interaural cues is ambiguous in terms of vertical and front–back localization. There is zero interaural time/phase difference throughout the median vertical plane (MVP), therefore there is no information on that basis concerning vertical and front–back displacement. Fairly accurate spatial discrimination is possible despite this, provided the sound contains a distribution of audible energy above about 4 kHz (Hebrank and Wright, 1974; Noble *et al.*, 1994), thus allowing interaction with the directionally different filtering properties of the pinnae (Shaw, 1982).

A wholly different mechanism for detecting the whereabouts of sounds, including their vertical and front–back displacement, was earlier proposed by Wallach (1939, 1940), as part of a general hypothesis about localization based on the operation of dynamic cues. Wallach argued that rotating the interaural axis through the horizontal plane would eliminate front–back ambiguity due to the contrasting alteration in interaural differences for sources initially behind versus those in front of that axis. Moreover, the rate of change in interaural differences due to head rotation is greatest for a sound at the horizon (level with the interaural axis). For a sound directly overhead or directly below, there is no change with any amount of such rotation. For sounds at intermediate el-

evations the rate declines systematically, for the same head rotation, as the degree of elevation increases above or below the horizon. Thus in theory, rotation of the head could allow discrimination of front from back locations, and also the degree of vertical displacement of the sound from the horizon. The only remaining ambiguity would be the direction of that vertical displacement, whose resolution, in Wallach's argument, would require a further head movement (tilting from shoulder to shoulder).

Wallach (1939, 1940) examined the effect of horizontal rotations of the interaural axis in conjunction with a head-mounted switching mechanism that allowed a bank of horizontally arrayed loudspeakers to be successively activated. The angular separation of the sound sources relative to the angular displacement of the head could be varied so as to manipulate the pattern of change in interaural differences. Thereby, different elevations of apparently single sources in the MVP could be simulated. Results did indicate a perception of virtual vertical displacement.

It may be argued that this experimental arrangement introduced conditions remote from ordinary listening, leaving the question of the effectiveness of head movement without a clear answer. Subsequent studies of movement, in relation to sound sources that were actually displaced vertically (Thurlow and Runge, 1967; Thurlow and Mergener, 1970), offered only limited support for Wallach's hypothesis. As a result, the view has emerged that the status of head movement is uncertain for identifying the whereabouts of sounds (Middlebrooks and Green, 1991). The evident role for the pinnae, alone or in combination with interaural differences, in offering accurate stationary cues throughout all regions of auditory space (Butler *et al.*, 1990), including the disambiguation of sources forward and rearward of the interaural axis (Muscant and Butler, 1984), has helped to diminish the presumed importance of a dynamic "Wallach cue."

Wallach's hypothesis about elevation may not have been subjected to appropriate forms of subsequent experimental test (Perrett and Noble, in press). This is because either the signal used offered too rich a set of stationary cues (as was the case in a study by Pollack and Rose, 1967), or the spatial range of vertically displaced sources was too limited (in the case of Thurlow and Runge, 1967). Perrett and Noble (in press) used a 2-kHz low-pass noise, thus excluding the contribution of the pinnae, and concealed sound sources arrayed throughout the left lateral vertical plane (LVP) and the left horizontal plane (HP). It was found that a single 45° leftward rotation of the head was generally as effective as free-head movement in judging the elevation of those sources, and that both types of movement were more effective than motionless listening. Furthermore, in the absence of pinna cues, even very slight head movement served to disambiguate front from rear sources, while motionless listening was associated with substantial front-back confusion.

That experiment offered significant if partial support for Wallach's hypothesis. In the first experiment reported here, a particular examination is made of the region of auditory space, the MVP, in which Wallach simulated source elevations with his experimental technique.

I. EXPERIMENT 1

In the first experiment, front-back discrimination and the accuracy of elevation judgement were tested using sources positioned in the upper MVP, under both motionless and repeated 60° head-rotation conditions about a vertical axis, with broadband, low-pass, and high-pass noise, and with normal and distorted pinna function.

A. Method

Ten female and six male students (average age 26 years), with no previous experience in such experiments, and reporting no abnormalities of hearing, were tested using a series of seven different signals, in four different listening conditions, giving 28 experimental conditions per listener. The signals used were broadband (white) noise—constant sound-pressure level across all frequencies from 0.25 to 18 kHz—and various low- and high-pass noises, filtering providing a rejection slope of approximately 90 dB/octave. For half the sample, the order of signal presentation was: 1-, 2-, and 4-kHz low-pass noise; broadband noise; 1-, 2-, and 4-kHz high-pass noise. The reverse order was used for the other half of the sample. Signals were inverse filtered to compensate for the transfer function of each loudspeaker, and were presented at a nominal level of 60 dBA, with random variation, in 0.375-dB steps, over a range of ± 3 dB, from trial to trial. Each signal was ramped on and off over 90 ms, with total signal duration of 3 s. Signals were produced from each of seven loudspeakers placed in a hemispherical circumference of 1.25-m radius, at 30° intervals, in the upper MVP, from 0° elevation directly in front, through 90° (overhead) to 0° directly behind. In each condition, the loudspeakers were activated in a random order across seven trials. Testing occurred with the listener seated in the interior of a 1.2-m-

radius closed spherical screen. The screen was acoustically transparent, whilst visually obscuring the whereabouts of all sources. The technical features of the test facility, signal generation, signal filtering and delivery, are described in Perrett and Noble (in press).

The four listening conditions were: (1) normal, motionless listening; (2) normal, rotation listening; (3) distorted (short open tubes affecting pinna function), motionless listening; (4) distorted, rotation listening. In all conditions, listeners wore an unobtrusive head harness which held a laser light pointer, and the receiver component of a Polhemus Isotrak-II head tracker. In normal listening there was no encumbrance of the outer ears. In motionless conditions, while the sound was on, the listener kept the light of the laser pointer aimed at a dot created by a light emitting diode (LED) backprojected onto the spherical screen at 0° elevation and azimuth. In distorted listening the listener wore tapered open plastic tubes, 3 cm in length, inserted in their ear canals to achieve a snug but comfortable fit. The tubes had the effect of excluding the directional filtering architecture of the pinnae (Fisher and Freedman, 1968; Freedman and Fisher, 1968), thus distorting any high-frequency component of the signal (Musicant and Butler, 1984). In rotation, after initially facing the LED dot at 0°, the listener, in response to signal onset, oscillated their head, moving the laser light back and forth between two other LED dots back projected onto the screen at +30° and -30° azimuth in the front HP. With a signal duration of 3 s, all listeners achieved at least two complete ($\sim 60^\circ$) oscillations. The orders of the four listening conditions (normal, motionless; distorted, motionless; normal, rotation; distorted, rotation) were counterbalanced within the two overall orders of signals; thus each person went through the seven-signal series four times, starting with either motionless or rotation conditions, and either normal or distorted (tubes) conditions.

At the beginning of each trial, the listener lined up the laser light with the dot at 0°. When ready, they pushed a handheld button, which began head-tracker recording; within 1–2 s after that, the sound began, and the listener moved or remained still as the condition required. All testing was under TV surveillance, and listeners were able to comply readily with all instructed conditions. Following the offset of the sound, the listener moved freely until the laser was aimed at the judged location of the sound. When thus aimed, a second button-push switched off head-tracker data collection, and the head-tracker coordinates captured at that moment gave the measure of perceived location. Prior to the start of each listening condition, listeners were provided with practice trials involving signals presented from an eighth loudspeaker situated directly to their left. Practice trials were repeated until listeners demonstrated they understood what they were required to do. No feedback on localization accuracy was given during practice or at any other time during the experiment.

B. Results

1. Front-back discrimination

Front/back errors were recorded whenever a listener chose an apparent source position in the opposite hemi-

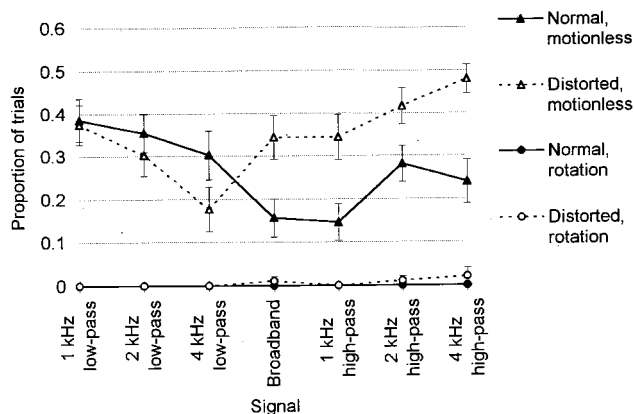


FIG. 1. Front-back errors for seven types of noise under four different listening conditions (error bars indicate ± 1 standard error of the mean).

sphere, front or back, to where the sound had originated (the source directly overhead was not included in this analysis). Figure 1 shows the proportion of front-back errors occurring in each of the conditions. The general outcome is clear. With every type of signal, the motionless condition produced front-back confusion for a substantial proportion of trials, whereas the rotation conditions produced virtually none. The varying pattern of front-back errors, as a function of signal type, merits further analysis.

A nonparametric test (Wilcoxon matched-pairs signed ranks) was used for the front-back error analysis. On aver-

age, 27% of all motionless trials in normal listening conditions and 35% of all motionless trials with tubes inserted in the ear canals, resulted in front-back errors. As expected (Musicant and Butler, 1984), an increase in the number of front-back errors due to distortion of pinna function became apparent when the signal contained high-frequency acoustic energy. The addition of tubes had no significant effect on motionless listening with the low-pass signals. Compared with normal motionless listening, the distorted(tubes)-motionless condition produced significantly greater proportions of front-back errors for broadband noise ($p < 0.01$), 1-kHz high-pass noise ($p < 0.01$), 2-kHz high-pass noise ($p < 0.05$), and 4-kHz high-pass noise ($p < 0.01$). In rotation conditions, no front-back errors occurred for normal listening, while only 0.6% of distorted listening trials resulted in front-back errors. For each signal, whether listening was distorted by tubes or not, motionless trials produced significantly more front-back errors than rotation ($p < 0.01$).

2. Elevation judgment

a. Apparent elevation. Figure 2 displays the average apparent elevation from the horizon of each of the sound sources under each of the four listening conditions, ignoring all other types and components of error. Crosses (X) indicate actual sound source elevation.

The three low-pass signals produced similar results. Listening while motionless afforded little or no perception of

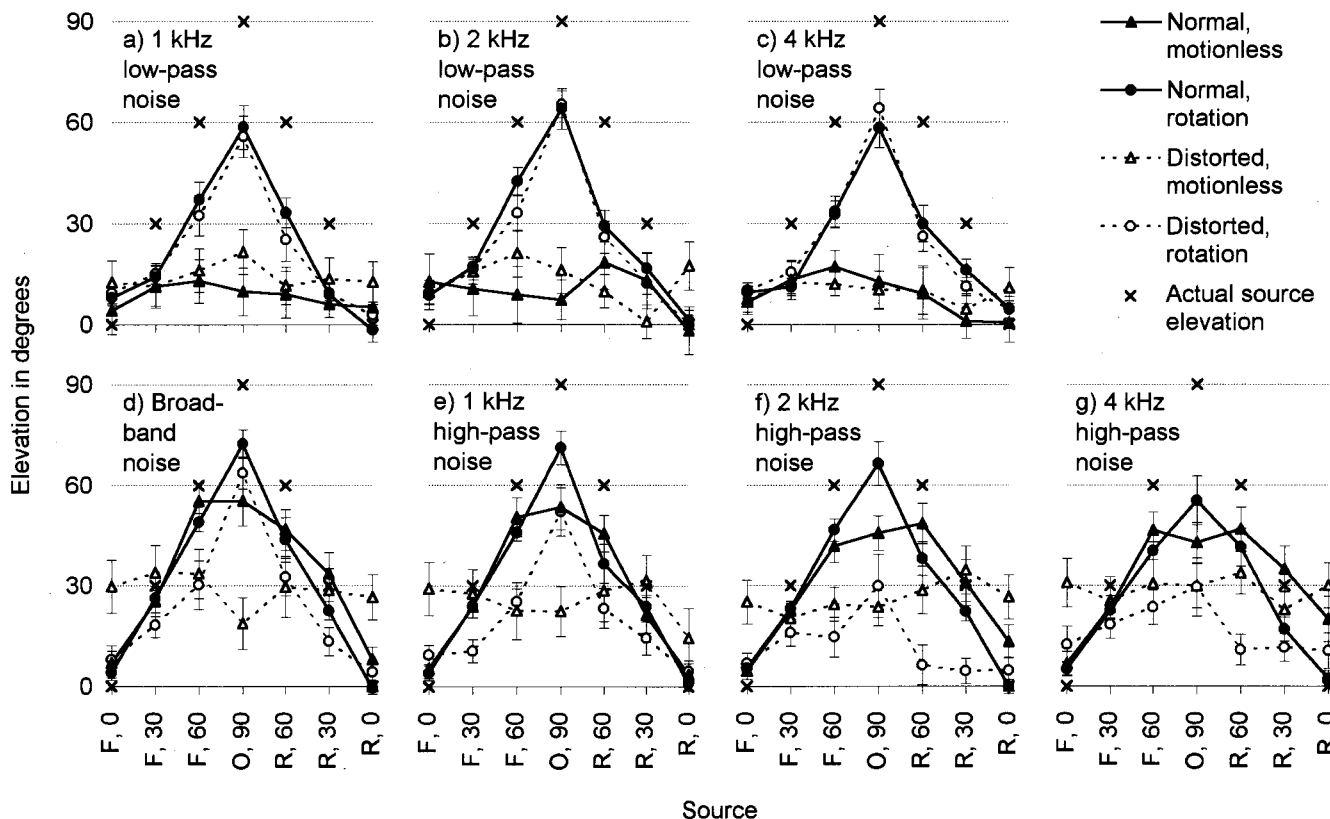


FIG. 2. Apparent elevation angle of seven types of noise under four different listening conditions. Actual source positions are at 0°, +30°, +60° elevation, forward (F, 0, etc.); rearward (R, 60, etc.); and at +90°, overhead (O). Actual elevations are indicated by crosses (X).

TABLE I. Mean absolute elevation error, in degrees, for seven different signals under four different listening conditions. Standard deviations in parentheses.

Signal	Pinna function	Rotation	Motionless
1-kHz low pass	Normal	20.3 (7.8)	39.3 (9.9)
	Distorted	22.4 (7.7)	36.0 (9.9)
2-kHz low pass	Normal	18.2 (7.5)	41.3 (13.9)
	Distorted	20.1 (5.3)	35.4 (9.1)
4-kHz low pass	Normal	20.9 (7.5)	36.7 (12.2)
	Distorted	20.2 (7.4)	36.5 (10.2)
Broadband	Normal	11.1 (7.7)	17.9 (10.4)
	Distorted	19.5 (8.1)	36.2 (9.0)
1-kHz high pass	Normal	12.6 (6.5)	17.1 (9.3)
	Distorted	24.3 (11.4)	36.7 (9.8)
2-kHz high pass	Normal	13.5 (7.2)	14.4 (5.7)
	Distorted	32.0 (13.2)	33.5 (6.6)
4-kHz high pass	Normal	16.8 (7.0)	22.3 (8.9)
	Distorted	30.7 (12.1)	32.6 (8.0)

the true elevation of the sound sources in the MVP. By contrast, rotation did provide such information, with individual source elevations being accurately judged. As expected, the presence of tubes made no obvious difference with low-pass signals, in either the motionless or rotation conditions. The failure of listeners to derive any noticeable advantage from normal over distorted pinna function confirms that the effect of rotation did not implicate the pinnae.

A broadband noise changed the response pattern, such that normal, motionless listening was associated with more accurate elevation detection, whereas distortion in motionless listening, as expected, disrupted the vertical plane response. Rotation nonetheless served to restore vertical plane discrimination, despite the distorting effect of tubes on pinna cues, although the most accurate response pattern occurred under rotation conditions with normal pinna function.

The foregoing picture is clarified by the further changes in response pattern that arose when an increasing proportion of low-frequency energy was removed from the signal. Now, rotation could not compensate for a distorted high-frequency signal, the collapse in performance under rotation-plus-distortion being particularly noticeable between the 1- and 2-kHz high-pass conditions. There was also a slight decrement in normal conditions with an increasingly high-frequency cutoff.

b. Absolute elevation error. For the purpose of statistical analysis of response patterns, we used absolute elevation error averaged across all seven source locations. All major effects observed in the apparent elevation data were confirmed by this analysis. The data for each type of signal were analysed separately using a two factor, repeated measures ANOVA (movement: rotation versus motionless×pinna: normal versus distorted). Table I shows the mean values. Again the three low-pass signals yielded similar results. Unexpectedly, the movement×pinna interaction effect was found significant ($p=0.01$) for the 2-kHz signal, but not

significant for the 1- or 4-kHz signal. *Post hoc* analysis of the 2-kHz low-pass data, using Tukey's HSD, revealed that under motionless conditions, absolute elevation error was significantly less when participants listened with tubes than when they listened normally ($p<0.05$). As expected, the main effect for pinna was not significant for all three low-pass signals. The main effect for movement was significant ($p<0.001$) for these signals, with rotation producing less error than motionless listening.

With a broadband signal the movement×pinna interaction effect was significant ($p=0.006$). *Post hoc* testing revealed that normal listening produced significantly more accurate elevation judgment than distorted listening in either motionless ($p<0.01$) or rotation conditions ($p<0.01$). Rotation produced significantly greater accuracy than motionless listening in both the distorted ($p<0.01$) and the normal conditions ($p<0.05$). Indeed the distorted, rotation listening condition was not significantly different from the normal, motionless listening condition. The main effect for movement was significant ($p<0.001$).

The 1-kHz high-pass noise analysis reveals a similar set of results to that for the broadband signal, although due to somewhat more error in the distorted rotation condition, the pinna×movement interaction was not significant. The main effect for movement was significant ($p=0.001$), with rotation producing more accurate elevation judgments than motionless listening. The main effect for pinna was also significant ($p<0.001$), with normal pinna function producing more accurate elevation judgment than distorted pinna function.

Results for the 2-kHz and 4-kHz high-pass signals did not show any effect for rotation. The movement×pinna interaction effects for these signals were not significant. The main effects for movement were also not significant, confirming that when signals do not provide acoustic energy below 2 kHz, the rotation cue fails. Both signals produced significant main effects for pinna ($p<0.001$), there being greater accuracy with normal than with distorted pinna function.

C. Discussion

The main elements of these findings do not require extensive interpretation. In the absence of pinnae transforms, horizontal head rotations can allow MVP localization that is just as proficient as when pinna cues are available. Even with a distorted pinna cue, head rotation can permit such proficiency, provided there is audible low-frequency energy in the signal. We consider the implication of that finding in Sec. III.

A feature of the results obtained for rotation conditions, which merits comment here, is that listeners attributed virtually all sound sources, at least for locations in front of them, to positions at and above the horizon. The rotational Wallach cue, as recruited here, would not be expected to enable a distinction of whether any given elevation of a low-pass sound was upward or downward from the horizon. In Wallach's argument, a second head movement, so as to rotate the interaural axis relative to the horizon, would be required.

In the Perrett and Noble (in press) study, which included sources arrayed vertically throughout the LVP (i.e., above and below the HP), there were clear signs, in the rotation and even the motionless conditions, that listeners could discriminate between sources above and below the HP, suggesting they may have recruited other spectral cues, perhaps related to the shoulders and torso (Kuhn, 1987) to help disambiguate sources above and below the HP. It was also apparent, however, that elevated sources coinciding with the MVP, i.e., those directly above and below, were not well-discriminated in either condition. We determined on a second experiment in the present study which included sources throughout the MVP. This allowed us to test whether the up-down confusion extends throughout the MVP, as would be expected from a strict reading of Wallach's theory.

The results from the first experiment revealed a somewhat more impressive effect for rotation than was evident in the LVP data of the study by Perrett and Noble (in press). It is not clear whether the difference was due to the rotation cue being more useful for MVP localization than for LVP localization, or due to procedural differences, such as the use of a single 45° head rotation in the earlier study, compared with the repeated 60° oscillations used in the first experiment in the present study. We decided, therefore, to include LVP sources in the second experiment, to determine if head rotation assists accuracy in elevation judgment differently, depending on whether sources are in the MVP or LVP.

II. EXPERIMENT 2

In the second experiment, localization of low-pass noise was tested under motionless and rotation conditions with sources positioned throughout the MVP and the left LVP. Head rotation in this experiment was the repeated 60° oscillations employed in the first experiment.

A. Method

The second experiment involved 22 people (9 female, 13 male students; average age 37 years), reporting normal hearing function. None had prior experience in auditory localization experiments. The sounds, 2-kHz low-pass noise, were presented from each of 17 loudspeakers positioned, as shown in Fig. 3, at 30° intervals, throughout the entire MVP, and at 30° intervals through the left LVP (extending from directly overhead, through directly left on the interaural axis to directly below). Each loudspeaker was selected once in a random sequence, resulting in 17 trials in each of four blocks (two motionless blocks and two rotation blocks). The number of trials was kept low because we wanted to sample unpracticed responses, so that our findings would represent, as closely as possible, listeners' real sensitivity to localization cues in novel situations. To compensate for the low number of trials per listener, the number of participants (22) was relatively high for an experiment of this kind. To control for possible practice and order effects, block orders were counterbalanced between and within subjects. The sequence of blocks was motionless-rotation-rotation-motionless for half the listeners and rotation-motionless-motionless-

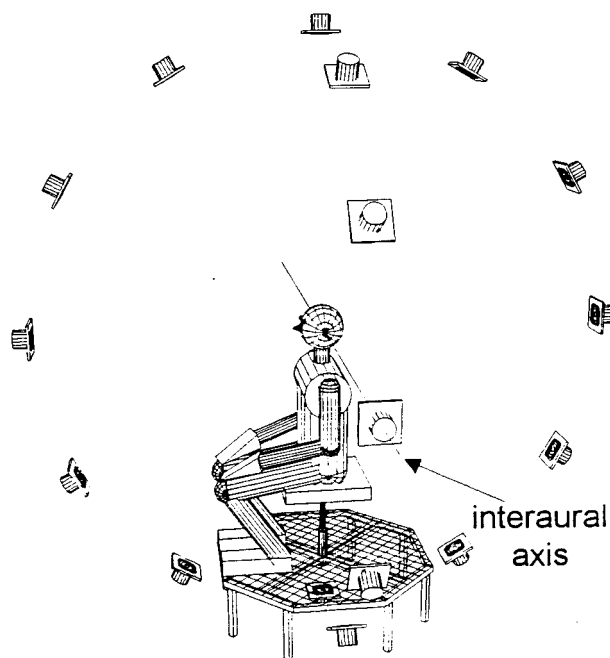


FIG. 3. Loudspeaker positions used in the second experiment (screen not shown). Displayed is the complete circle of loudspeakers lying in the median vertical plane, and the semicircle lying in the left lateral vertical plane.

rotation for the others. To acquaint and reacquaint listeners with the required movements, three practice trials involving the loudspeakers directly in front, directly behind and directly left were provided before the first, second and fourth blocks. All other technical and procedural details were the same as for the first experiment.

B. Results

1. Front-back errors

In the motionless listening condition 35% of trials resulted in front-back errors; in the rotation condition 0.4% of trials resulted in front-back errors: results confirming those from the first experiment.

2. Elevation judgment

a. Apparent elevation. Figure 4 displays the average apparent elevation from the HP of each of the sound sources under rotation and motionless conditions. Figure 4(a) shows performance for sources in the LVP, and Fig. 4(b) for sources in the MVP. The symbol "×" indicates the actual elevation of sources at and above the HP and the symbol "+" indicates sources below.

It is evident that rotation provides an advantage over motionless listening for judging the elevation of upper hemisphere sources. Comparison of the upper MVP data points with those of the first experiment suggests slightly poorer performance in experiment 2; this was due to responses to the loudspeaker directly overhead, performance at other locations being identical with that of the first experiment. Rotation can also be seen to have produced substantially greater

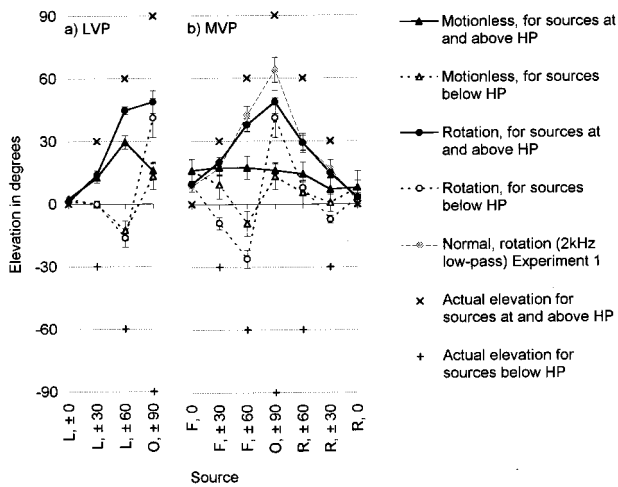


FIG. 4. Apparent elevation angle for LVP and MVP sources under rotation and motionless listening conditions. Actual source positions are at 0° , $\pm 30^\circ$, $\pm 60^\circ$ elevation, leftward (L, 0, etc.); forward (F, 0, etc.); rearward (R, 60, etc.), and at $\pm 90^\circ$ overhead and below (O). The symbol “ \times ” indicates the actual elevation of sources at and above the HP; the symbol “+” indicates sources below.

accuracy for some sources in the lower MVP, but it failed to deliver any benefit for MVP sources that were directly below (-90°) or rearward at -60° elevation.

Rotation appears not to have provided any advantage for judging the elevation of lower LVP sources [Fig. 4(a)]. Generally, listeners were able to discriminate fairly well between sources above and below the HP, in the LVP and the front MVP, in both the motionless and rotation conditions.¹ Back MVP sources, below the horizon, were localized inaccurately in both rotation and motionless conditions, but listeners distinguished upper sources from lower sources more clearly in the rotation condition than in the motionless condition. The regions of greatest benefit from rotation were the front MVP and upper back MVP.

b. Comparing experiments and the effects of test order and practice. The absolute elevation error data for the first experiment were compared with those for the corresponding sources in the upper MVP of the second (see upper section of Table II). From a repeated measures ANOVA with one

TABLE II. Mean absolute elevation error across experiments and test orders (standard deviations in parentheses).

Experiment		Rotation	Motionless
1		18.2 (7.5)	41.3 (13.9)
		20.1 (6.7)	36.9 (9.6)
Both experiments		19.3 (7.0)	38.7 (11.6)
Blocks	Test order group	Rotation	Motionless
1–2	Rotation first	33.1 (6.5)	40.5 (4.9)
	Motionless first	30.6 (3.8)	42.8 (7.2)
	Both groups	31.9 (5.3)	41.6 (6.1)
3–4	Rotation first	31.1 (6.8)	39.9 (4.9)
	Motionless first	28.9 (5.0)	39.0 (4.4)
	Both groups	30.0 (6.0)	39.5 (4.5)

TABLE III. Apparent elevation and benefit from rotation for three different regions and two hemispheres. Standard deviations in parentheses.

Region	Hemisphere	Rotation	Motionless	Benefit
LVP	Upper	28.9 (10.7)	21.3 (13.9)	8.7 (7.4)
	Lower	-8.2 (13.0)	-6.4 (13.8)	1.8 (9.4)
				* 5.3 (4.9)
Front MVP	Upper	29.3 (7.1)	17.3 (18.3)	16.2 (13.7)
	Lower	-19.9 (15.8)	-2.7 (24.6)	21.2 (17.1)
				* 18.7 (11.1)
Back MVP	Upper	22.0 (11.9)	10.6 (24.9)	16.5 (20.5)
	Lower	-4.1 (9.5)	1.0 (21.4)	4.5 (16.4)
				* 10.5 (9.0)

*Mean benefit for upper and lower sources combined.

within-subjects factor (movement: rotation versus motionless) \times one between-subjects factor (experiment: experiment 1 versus experiment 2) there was no significant interaction for movement \times experiment and no significant main effect for experiment. The main effect for movement was significant ($p < 0.001$), with rotation, as expected, producing significantly less absolute elevation error than motionless listening. These outcomes indicate that the inclusion of the additional sources below the HP and in the LVP did not have a significant impact on upper MVP elevation judgment generally.

The overall absolute elevation error data for the second experiment were analyzed to check for possible order or practice effects to determine whether these factors had a significant impact on listeners' response patterns. A repeated measures ANOVA was conducted, with two within-subjects factors (practice: blocks 1–2 versus blocks 3–4; \times movement: motionless versus rotation) and one between-subjects factor (order: motionless first versus rotation first). The relevant means are reported in the lower section of Table II. No significant interaction effects were observed. The main effect for order of conditions was also not significant. The main effect for practice was significant ($p = 0.028$) with the mean absolute elevation error being slightly but significantly greater at times 1–2 than at times 3–4. As expected, the main effect for movement was significant ($p < 0.001$).

c. Distinguishing sources above from below. To test for the ability to distinguish sources above the HP from those below, two two-factor, repeated measures ANOVAs (hemisphere: upper versus lower hemisphere \times region: front MVP versus LVP versus back MVP) were conducted on the apparent elevation data. One ANOVA was on the rotation listening condition and the other on the motionless listening condition. Data for sources in the HP and those directly overhead and directly below were not included. Means are shown in the third and fourth columns of Table III. Significant hemisphere \times region interaction effects were observed for both the rotation ($p < 0.001$) and motionless ($p = 0.005$) conditions. For rotation listening (third column of Table III), *post hoc* tests showed significant differences ($p < 0.01$) between upper and lower sources in each spatial region (front and back MVP, LVP). For motionless listening (fourth col-

umn of Table III), *post hoc* comparisons revealed significant differences between upper and lower sources for the front MVP ($p < 0.01$) and the LVP ($p < 0.01$), but not for the back MVP.

d. Region of greatest benefit from rotation. To determine if the benefit from head rotation, in judging elevation more accurately, is dependent on the position of the source, a “benefit-from-rotation” variable was derived. This was done by subtracting the absolute elevation error for rotation trials from that for motionless trials. Again, a two-factor, repeated measures ANOVA (hemisphere: upper versus lower hemisphere \times region: front MVP versus LVP versus back MVP) was conducted, this time on the benefit from rotation data. As before, data for HP sources, and for those directly overhead and directly below were excluded. Means are shown in the rightmost column of Table III. The hemisphere \times region interaction effect was significant ($p = 0.005$). *Post hoc* testing revealed that the benefit from rotation was not significantly different across regions of the upper hemisphere. Across regions in the lower hemisphere, significantly more benefit was obtained from rotation with sources in the front MVP than with those in either the LVP ($p < 0.01$) or the back MVP ($p < 0.01$). Benefit from rotation was not significantly different between upper and lower hemisphere sources when each region was considered separately. The main effect for hemisphere was also not significant. The main effect for region was significant ($p < 0.001$). *Post hoc* testing showed that greater benefit was gained from rotation for front MVP sources than for LVP sources ($p < 0.01$). No other differences between regions reached levels of significance.

III. GENERAL DISCUSSION

The findings about the efficacy of head rotation with low-pass sounds reported in the first experiment were replicated in the second experiment, in which signals from sources throughout the whole MVP were used. As we have found in previous experiments (Perrett and Noble, 1995; *in press*), listeners tend to hear low-pass signals as lying toward the horizon. It was observed that listeners clearly distinguished frontal sources above the horizon from those below in rotation conditions, and to some extent even in motionless conditions. An involvement of the shoulders and torso (Kuhn, 1987) may account for the ability to make this distinction. Such an explanation is, of course, outside of Wallach’s hypotheses. The principal finding from the first experiment is that the dynamic cue to source elevation requires acoustic energy below 2 kHz. When only high-frequency energy is provided, distortion of input cannot be remedied by head rotations, suggesting the transformation of interaural level differences is not a strong counter cue. By contrast, when low-frequency energy is provided along with such distorted high-frequency input (broadband or 1-kHz high-pass signals, tubes inserted in the ear canals), rotation serves to overcome the distortion effect. Taken with the finding that the elevation of low-pass signals is detectable under rotation conditions, this strongly indicates that the dynamic

“Wallach cue” relies on variations in the rate of change of interaural time/phase, as a function of elevation from the horizon.

There were considerable intra- and inter-individual variations in performance, particularly for sources well above and directly overhead, which accounts for the less than perfect average results obtained.² The decline in performance above about 60° in motionless conditions for a broadband signal confirms our earlier observation (Perrett and Noble, 1995), and, as we argued then, the apparently more accurate result reported by Butler and Humanski (1992) is explained by the fact that response choices were constrained in their study. With unconstrained response choices, as in our previous and present studies, an “overshoot” phenomenon occurs for sources at and close to the zenith under motionless conditions, depressing the average apparent elevation. There is also the following geometric point, that applies across all conditions. For a source directly overhead, judged elevation can only be 90° or less; for sources closer to the horizon, judgments can fall above or below the actual source, resulting in an average apparent elevation that looks more accurate. The important point to remember is the finding of overall differences in apparent elevation under different listening and signal conditions.

The results of the second experiment demonstrate that head rotation assists judgement of elevation more for some spatial regions than for others. The only sources in the MVP for which rotation failed to deliver any benefit were those directly below (−90°) or rearward at −60° elevation. The direct path of the sound from the source at −90° to the ears, would have been obstructed by the listener’s seat, hence disrupting any potential cue. Sounds from the source at −60° behind, will interact similarly with the obscuring surface of the listener’s back. Benefit from rotation was also found to be greater for sources in the front MVP than for those in the LVP. These outcomes suggest that the rotation cue to elevation is most useful when listeners are oriented such that the source lies roughly in their front MVP. Indeed, if rotation occurs, listeners are more able to achieve such an orientation, as indicated by the virtual elimination of front–back confusion. In normal circumstances, auditory localization involves the visual system. Once oriented in the general direction of an unseen source, visual scanning is likely, involving horizontal rotations of the head. The findings of the present study strongly suggest that such head rotations afford listeners useful auditory information concerning the elevation of a sound source, provided the sound includes low-frequency acoustic energy.

IV. CONCLUSION

The significance of the present findings lies in the clear demonstration of the efficacy of the rotational “Wallach cue” in detecting elevation. The spatial hearing function of the auditory system operates with dynamic as well as static features of input signals. Sounds in the everyday environment come as a mix of broadband, narrow band, low pass, and high pass, and movement is an inherent feature of how humans and other animals subsist. The results here show

how detection of the location of audible events can occur across those various sorts of input, due to the multiple forms of information for spatial position.

ACKNOWLEDGMENT

The work reported here has been supported by grants from the Australian Research Council.

¹Listeners generally superimposed a very slight tilting of the head from shoulder to shoulder during head rotation in the horizontal plane. In theory (Wallach, 1939, 1940) this could serve to distinguish sources above the horizon from those below. Listeners were still able to tell when sources lay above or below the horizon in motionless conditions, suggesting that slight head tilts were not the only feasible source of such information.

²In rotation conditions, listeners were free to repeatedly rotate over the 60° range throughout the 3-s duration of the signal, hence there was some variation between individuals and trials. Inspection of a sample of video records showed no consistent links between rate (hence number) of rotations and performance accuracy.

Butler, R. A., and Humanski, R. A. (1992). "Localization of sound in the vertical plane with and without high-frequency spectral cues," *Percept. Psychophys.* **51**, 182–186.

Butler, R. A., Humanski, R. A., and Musicant, A. D. (1990). "Binaural and monaural localization of sound in two-dimensional space," *Perception* **19**, 241–256.

Fisher, H. G., and Freedman, S. J. (1968). "The role of the pinna in auditory localization," *J. Aud. Res.* **8**, 15–26.

Freedman, A. J., and Fisher, H. G. (1968). "The role of the pinna in auditory localization," in *The Neuropsychology of Spatially Oriented Behavior*, edited by S. J. Freedman (The Dorsey Press, Homewood, Illinois).

Hebrank, J., and Wright, D. (1974). "Spectral cues used in the localization of sound sources on the median plane," *J. Acoust. Soc. Am.* **56**, 1829–1834.

Kuhn, G. F. (1987). "Physical acoustics and measurements pertaining to directional hearing," in *Directional Hearing*, edited by W. A. Yost and G. Goorevitch (Springer-Verlag, New York).

Middlebrooks, J. C., and Green, D. M. (1991). "Sound localization by human listeners," *Annu. Rev. Psychol.* **42**, 135–159.

Musicant, A. D., and Butler, R. A. (1984). "The influence of pinnae-based spectral cues on sound localization," *J. Acoust. Soc. Am.* **75**, 1195–1200.

Noble, W., Byrne, D., and LePage, B. (1994). "Effects on sound localization of configuration and type of hearing impairment," *J. Acoust. Soc. Am.* **95**, 992–1005.

Perrett, S., and Noble, W. (1995). "Available response choices affect localization of sound," *Percept. Psychophys.* **57**, 150–158.

Perrett, S., and Noble, W. (in press). "The contribution of head motion cues to localization of low-pass noise," *Percept. Psychophys.*

Pollack, I., and Rose, M. (1967). "Effect of head movement on the localization of sounds in the equatorial plane," *Percept. Psychophys.* **2**, 591–596.

Shaw, E. A. G. (1982). "External ear response and sound localization," in *Localization of Sound: Theory and Applications*, edited by R. W. Gatehouse (Amphora, Groton, CT).

Thurlow, W. R., and Mergener, J. R. (1970). "Effect of stimulus duration on localization of direction of noise stimuli," *J. Speech Hear. Res.* **13**, 826–838.

Thurlow, W. R., and Runge, P. S. (1967). "Effect of induced head movements on localization of direction of sounds," *J. Acoust. Soc. Am.* **42**, 480–488.

Wallach, H. (1939). "On sound localization," *J. Acoust. Soc. Am.* **10**, 270–274.

Wallach, H. (1940). "The role of head movements and vestibular and visual cues in sound localization," *J. Exp. Psychol.* **27**, 339–368.

Wightman, F. L., and Kistler, D. J. (1992). "The dominant role of low-frequency interaural time differences in sound localization," *J. Acoust. Soc. Am.* **91**, 1648–1661.

Dichotic beats of mistuned consonances

M. Patrick Feeney

School of Hearing and Speech Sciences, Ohio University, Athens, Ohio 45701

(Received 12 September 1995; revised 5 January 1997; accepted 3 July 1997)

The beats of mistuned consonances (BMCs) result from the presentation of two sinusoids at frequencies slightly mistuned from a ratio of small integers. Several studies have suggested that the source of dichotic BMCs is an interaction within a binaural critical band. In one case the mechanism has been explained as an aural harmonic of the low-frequency tone (f_1) creating binaural beats with the high-frequency tone (f_2). The other explanation involves a binaural cross correlation between the excitation pattern of f_1 and the contralateral f_2 occurring within the binaural critical band centered at f_2 . This study examined the detection of dichotic BMCs for the octave and fifth. In one experiment with the octave, narrow-band noise centered at f_2 was presented to one ear along with f_1 . The other ear was presented with f_2 . The noise was used to prevent interactions in the binaural critical band centered at f_2 . Dichotic BMCs were still detected under these conditions, suggesting that binaural interaction within a critical band does not explain the effect. Localization effects were also observed under this masking condition for phase reversals of tuned dichotic octave stimuli. These findings suggest a new theory of dichotic BMCs as a between-channel phase effect. The modified weighted-image model of localization [Stern and Trahiotis, in *Auditory Physiology and Perception*, edited by Y. Cazals, L. Demany, and K. Horner (Pergamon, Oxford, 1992), pp. 547–554] was used to provide an explanation of the between-channel mechanism. © 1997 Acoustical Society of America. [S0001-4966(97)05410-6]

PACS numbers: 43.66.Nm, 43.66.Pn, 43.66.Rq [RHD]

INTRODUCTION

The beats of mistuned consonances (BMCs) result from the monaural presentation of two sinusoids separated by at least a minor third in frequency and spaced at a slightly mistuned ratio of small integers (e.g., the mistuned fifth: 200 and 302 Hz where the frequency ratio is mistuned from 2:3). Of the frequency ratios resulting in BMCs, the mistuned octave yields the most prominent beats, and beat strength declines with increasing complexity of the frequency ratio (Plomp, 1967). Three main theories have been proposed to explain monaural BMCs: (1) The interaction of aurally generated combination tones and the stimulus components (Helmholtz, 1954); (2) the interaction of the second or higher aural harmonics of the lower-frequency sinusoid with the higher-frequency sinusoid or its harmonics (Lamore, 1977b, 1979; Ayres, 1982; Ayres and Clack, 1984a, 1984b); and (3) the perception of phase-induced changes in the waveform of the signal at some place on the basilar membrane where the excitation patterns of the two sinusoids overlap (Goldstein, 1965; Plomp, 1967; Filip, 1970; Lamore, 1975, 1977a). All three of these theories involve a within-frequency-channel (i.e., critical band) mechanism.

The phenomenon of dichotic BMCs was first described by Thompson (1881) who reported that “the beats of the lower notes did not seem to be mere maxima and minima of loudness; they were heard as a moving of the lower tone backward and forward from the ear to the back of the head” (p. 354). Thurlow and Bernstein (1957) reported that two subjects heard dichotic BMCs for sinusoids at a ratio of 1: n if both tones were below 1000 Hz. They also reported that the phenomenon was accompanied by a sense of stimulus movement across the head. Observations were also made for

the mistuned fifth which produced weaker beats. Dichotic beats for the ratio 1: n were reported to persist at stimulus levels as low as 30 dB SPL, suggesting that acoustic cross-over effects were not a likely source of the phenomenon. Results similar to those of Thurlow and Bernstein (1957) were reported by Tobias (1963) for the mistuned octave.

There is one report of dichotic BMCs in the physiological literature. Yin *et al.* (1987) measured responses from neurons in the central nucleus of the inferior colliculus (IC) of the cat in response to dichotic sinusoids ($f_1, f_2; f_2 > f_1$) mistuned from a ratio of small integers. The stimulus frequencies ranged from 150–2000 Hz. Period histograms from these neurons were obtained using a period of 1 s. The histograms were found to have cyclic maxima at the expected beat rate of mistuned consonances. Although the stimulus frequency limit for the effect was not systematically tested, the cyclic pattern in the period histograms was not observed for values of f_2 above about 1600 Hz. The responses were found to be cyclic in 22 of 27 neurons that were also sensitive to interaural time differences of noise bursts.

Yin *et al.* (1987) suggested that the responses of these IC neurons were due to a cross-correlation process in the brain stem similar to that suggested for the localization of low-frequency sounds by Jeffress (1948). They noted that the “binaural interactive effects over disparate frequency bands...are considerably wider than those normally thought to be possible in binaural critical band estimates from psychoacoustics” (p. 579). However, Yin *et al.* pointed to a behavioral study by Thurlow and Elfner (1959) in which similar binaural effects over a wide frequency range were reported. In that study, subjects noted changes in the lateralization of a

low-frequency pure tone presented to one ear in the presence of a second tone of a different frequency presented to the other ear. Each tone was presented at a level of 30 dB sensation level (SL). Subjects were also asked to report the detection of beats. Lateralization/beat effects were reported for some of their subjects for frequency ratios of $f_2:f_1$ as high as 9:1.

Several studies have suggested that dichotic BMCs were not the result of a binaural process between f_1 and f_2 as suggested by Yin *et al.* (1987). Demany and Semal (1988) reported that two subjects failed to hear dichotic beats for the mistuned octave when the sinusoids were presented at levels of 45–50 dB SPL and with values of f_1 ranging from of 180–900 Hz. This led them to suggest that the stimulus used in previous studies of dichotic BMCs may have been contaminated by harmonic distortion which led to the perception of beats.

Ayres and Clack (1984b) suggested that phase effects for the dichotic octave were the result of the binaural interaction between an aural harmonic of f_1 and the f_2 component. They presented a continuous high-level 400-Hz tone to one ear and a series of four 800-Hz tone bursts at 10 dB SPL to the other ear. The phase of the 800-Hz tone was reversed (180°) on either the second or fourth tone burst. The level of the 400-Hz tone was varied to construct psychometric functions for the detection of the phase change. Four of nine subjects achieved better than chance performance when the level of the 400-Hz tone exceeded about 65 dB SPL or greater. A lateral shift in perceived internal location of the 800-Hz tone bursts was a cue commonly used by the subjects. Ayres and Clack (1984b) suggested two alternative explanations for these results: (1) listeners could detect phase changes in a pair of dichotic sinusoids an octave apart, or (2) subjects were detecting the phase difference between the 800-Hz probe in one ear and an aural harmonic of the 400-Hz tone in the other ear. The first hypothesis is essentially “frozen” binaural BMCs (a fixed phase relationship rather than a running phase change caused by mistuning). Ayres and Clack (1984b) chose to test the second hypothesis by attempting to cancel the proposed aural harmonic at 800 Hz in the ear with the 400-Hz tone. If the aural harmonic was responsible for the detection of the phase difference between the 400- and 800-Hz sinusoids, the cancellation of the harmonic should cause scores to fall to chance. Ayres and Clack used a tone-on-tone masking procedure (Clack, 1977) to calculate the intensity and phase of the aural harmonic of the 400-Hz tone. Cancellation of the aural harmonic at 800 Hz caused detection of phase changes in the contralateral 800-Hz tone to decrease. This prompted Ayres and Clack to support the aural harmonic hypothesis to explain dichotic octave phase effects. However, in 6 of 11 cases of supposed aural harmonic cancellation, subjects still detected phase changes better than expected by chance.

Ayres (1981) presented an explanation for dichotic BMCs as a binaural process using a modification of the Jeffress–Colburn cross-correlation model of localization (Colburn, 1977; Jeffress, 1948). Ayres assumed that the f_2 place on the basilar membrane would be stimulated by the excitation pattern of f_1 . In this case f_1 and f_2 would serve as

inputs to the binaural correlator in the channel centered on f_2 . Ayres suggested that for the dichotic octave: “Since alternative positive peaks of $2f$ coincide with peaks of f (at some delay depending on the phase of the acoustic signals), the display, when averaged over several cycles, will show a maximum, just as it does when given a single binaural tone at $2f$ ” (p. 101). In the case of the mistuned dichotic fifth, this model predicts poorer performance because the inputs to the binaural correlator at the f_2 place would be f_1 and $1.5f_1$. In this case the output of the binaural correlator at f_2 would have two separate maxima which Ayres suggested would cause the listener to have a less-well-defined spatial location for the stimuli making detection of phase changes more difficult.

Both the aural harmonic hypothesis (Ayres and Clack, 1984b) and the modified binaural correlator model (Ayres, 1981) of dichotic BMCs depend on the presence of input to the central auditory system of a signal originating at the f_2 channel from the ear with the f_1 stimulus. In the case of the aural harmonic hypothesis, the frequency of the stimulus at the f_2 channel for the dichotic octave is $2f_1$. In the case of the dichotic fifth the aural harmonic hypothesis predicts that listeners would not hear beats because the aural harmonic at $2f_1$ is remote from f_2 which is at $1.5f_1$. However, binaural beats might be heard between higher aural harmonics of the two sinusoids. The modified binaural correlator model simply requires that the excitation pattern of f_1 extends to the f_2 place. Thus, this model could explain dichotic BMCs regardless of the frequency ratio. Moreover, the correlator model predicts that detection for dichotic octave BMCs would be stronger than for the dichotic fifth as described above.

A test of both the aural harmonic and modified binaural correlator theories of dichotic BMCs could be made by introducing masking noise to the ear with the f_1 component in the frequency region of f_2 . This could mask either the aural harmonic of f_1 or the excitation pattern from f_1 at the f_2 place. If the listener could still detect beats, or fixed phase changes in tuned consonances, it would suggest that neither of these explanations was sufficient to account for the presence of dichotic BMCs. This is the approach taken in the present study. Detection of dichotic BMCs for the octave and fifth were first examined in quiet. Then narrow-band noise was used to mask excitation at the f_2 place in the ear with the f_1 component. Several experiments were conducted to rule out other bases of detection of the mistuning such as frequency discrimination or acoustic crossover. Lateralization effects caused by a phase change in f_2 for the tuned octave were also examined.

I. EXPERIMENT 1. DETECTION OF DICHOTIC BMCs

A. Method

1. Subjects

Four subjects participated in this experiment.¹ Two females aged 18 and 25 years (subjects 1 and 2, respectively) and one male aged 19 years (subject 3) were students who were paid for their participation in the study. The fourth subject was the author, age 44 years. Subjects 1 and 2 had 8 and 14 years of musical training, respectively. Subjects 3 and 4 had no formal music training. None of the subjects were

possessors of absolute pitch. All subjects had audiometric thresholds of 15 dB HL or lower in the frequency region of the stimuli used in this study.

2. Apparatus

Sinusoids were computer generated with a sampling rate of 15 672 Hz and played out through a 12-bit D–A (digital-to-analog) converter. The signal duration was 2 s with a computer-generated 20-ms rise–fall time shaped by a \cos^2 time function. All sinusoids were generated with a 0° starting phase.

The experiment was controlled by a microprocessor interfaced with the signal delivery and subject response equipment. The outputs of each channel of the D–A converter were separately low-pass filtered at 8 kHz and routed to separate digital attenuators. The attenuated signals were separately amplified and then delivered to the two ears of the subject via Etymotic Research ER-3A insert earphones with full insertion depth as described by Killion *et al.* (1985).

The output of the earphones was calibrated using a Bruel and Kjaer 4134, $\frac{1}{2}$ " microphone in a Zwislocki coupler. The harmonic distortion of the sinusoids was determined by routing the output of the measuring amplifier to a spectrum analyzer. Third harmonic distortion was found to be at least 45 dB down from the primaries at a level of 90 dB SPL. All other harmonic distortion components were greater than 60 dB down at a primary level of 90 dB SPL.

3. Procedure

The data for this experiment were collected using a 2I-2AFC procedure with feedback. The interstimulus interval was 750 ms with an intertrial interval of 1 s. The left ear always received the low-frequency sinusoid (f_1) at a level of 80 dB SPL which was approximately 55 dB SL for the 200-Hz tone. The right ear always received the high-frequency sinusoid (f_2) at a level of 60 dB SPL.² This level of f_1 was chosen because it was found to be high enough to yield strong beats in pilot testing, yet it was low enough that it was felt unlikely that acoustic crossover would occur for these low frequencies of f_1 based on the data of Killion *et al.* (1985). A lower level, 60 dB SPL, was chosen for f_2 since interaural attenuation decreases in the high frequencies for these earphones. The range of interaural attenuation values approaches 60 dB by 2000 Hz (Killion *et al.*, 1985). The sinusoids formed a perfect ratio of small integers in one interval (either the octave or fifth). In the other interval, f_2 was mistuned by 0.75 Hz to form the beat stimulus. The probability of the first interval having the mistuned sinusoids was 0.5. The subject, who was seated in an Industrial Acoustics Company (IAC) double-walled sound attenuating room, was asked to indicate with a button push whether interval one or interval two contained a slowly beating stimulus.

According to Ohm's (1839) formula for BMCs, if two frequencies, $f_1:f_2(f_2>f_1)$, are mistuned from a ratio of small integers $m:n$, the resulting BMCs yield a beat rate of $|mf_2 - nf_1|$. Thus, for values of f_1 and f_2 of 200 and 400.75 Hz, respectively, the resulting beat rate would be 0.75 Hz. Previous research has shown that performance in beat detec-

tion may deteriorate if less than one beat is presented during a stimulus interval (Moore *et al.*, 1985). For this reason, the stimulus duration was set at 2 s to allow 1.5 beats for the octave given the 0.75-Hz mistuning. The beat rate for the mistuned fifth would be 1.5 Hz. The small mistuning was used to lessen the likelihood that listeners would use monaural frequency discrimination to distinguish the stimuli since the frequency difference limen in this frequency region for well-trained listeners is around 1 Hz (Wier *et al.*, 1977). Frequency discrimination for these stimuli was also tested directly in experiment 2 described below.

Subjects were initially trained in the detection of dichotic BMCs for the octave and fifth with a value of f_1 of 200 Hz. All four subjects performed well with a 2-Hz frequency change (Δf) of f_2 . The value of Δf was then reduced to 1 Hz and finally 0.75 Hz as training proceeded. All subjects reported that they heard a slower beat rate as the degree of mistuning was reduced. In later training sessions only the 0.75-Hz mistuning was used. Training and testing for the dichotic fifth were conducted with a single value of f_1 and f_2 : 200 and 300 Hz, respectively. For the octave, subjects started training with values of f_1 at 200, 300, and 400 Hz. If the subject's beat detection was consistently above chance at the highest value of f_1 , the next highest value of f_1 (in 100-Hz steps) was added and the lowest value of f_1 was dropped from the training so that in the actual experiment only three values of f_1 were used.

Extensive training in the detection of dichotic BMCs was conducted for each subject. The phenomenon is subtle and all subjects demonstrated some improvement in detection with training. Difficulty in detection of dichotic octave phase effects was also reported by Ayres and Clack (1984b) in which only four of nine subjects achieved better than chance performance.

Each subject received a minimum of 20 h of training in detection of dichotic BMCs before the test data were collected. A subject was presented with 15, 40-trial blocks in a 2-h training session. Before the final data were collected for each subject it was established that performance at the highest value of f_1 for the octave was near chance over several training sessions. The highest value of f_1 in training was selected as a test condition along with the next two lower values of f_1 . For example, if 500 Hz was the highest value of f_1 in training, the test values of f_1 for the dichotic octave would be 300, 400, and 500 Hz.

The formal data collection consisted of 320 trials for each of three dichotic octaves and the dichotic fifth. A Latin square was used to counterbalance presentation order in an attempt to control for order effects. Two blocks of 40 trials were presented per condition in each of the rows of the Latin square with at least a 1-min break between blocks. Twenty additional warm-up trials were used to familiarize the subject with each condition, but were not used in the final data analysis.

B. Results and discussion

All subjects reported hearing beats for the dichotic mistuned octave and fifth. The beats were reported to be either lateralized to the left ear (f_1) or to move back and forth

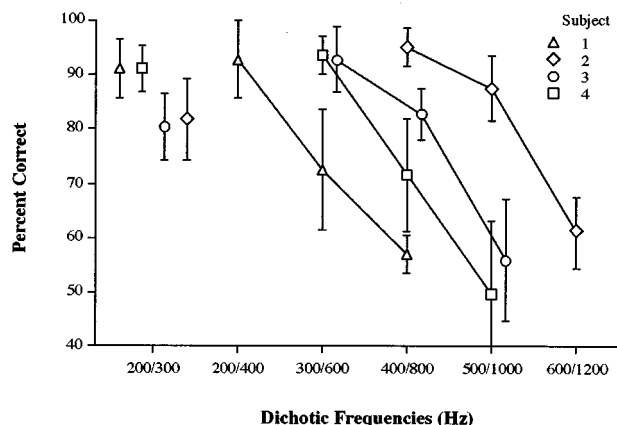


FIG. 1. The results of experiment 1 are shown for the detection of dichotic BMCs for four subjects: S1—triangle, S2—diamond, S3—circle, and S4—square. The abscissa represents the dichotic frequencies tested (fifth or octave) and the ordinate represents the percent-correct score. Each data point is the mean of eight blocks of 40 trials. The error bars represent ± 1 standard deviation of the mean. The results for the dichotic fifth and for subject 3 with the dichotic octave were offset for clarity.

between the ears. Figure 1 displays the data for the four subjects. Note that performance for the octave deteriorated for each subject as f_1 was raised, and no subject was above 70% correct for f_2 above 1000 Hz. There were obvious differences between subjects. For example, subject 2 scored about 95% correct performance for the dichotic octave for an f_1 of 400 Hz, compared to less than 60% for subject 1. Large differences between subjects have also been reported for the detection of simple binaural beats. In fact, Tobias (1965) reported that, in general, males perceived binaural beats at higher frequencies than females, with an average difference of 200 Hz higher for males. Tobias postulated a hormonal origin for the difference. However, this finding is not consistent with the present data since one of the female subjects in the study, subject 2, had the best performance for the higher frequency values of f_1 . Performance for the dichotic fifth approximated performance for the dichotic octave at the lowest frequency tested for each subject.

Figure 2 shows pilot data for subject 4 collected prior to experiment 1 on the detection of dichotic BMCs for the octave and the fifth using a 2I-2AFC procedure. Both sinusoids were presented at a level of 80 dB SPL through TDH-39 earphones in MX-41 AR cushions using the same signal generation equipment described above. A frequency change of 1 Hz was used to create the beating interval. Performance for this subject for the dichotic octave was similar to his performance in experiment 1 except for better detection of beats at the high frequencies in pilot testing. These data are not directly comparable to the data of experiment 1 due to the differences in Δf , level of f_2 , and transducer type. However, note that performance for the dichotic fifth rolled off more steeply in the high frequencies than performance for the octave.

The rolloff in performance in the high frequencies for the dichotic octave is consistent with an anecdotal account of dichotic BMCs by Thurlow and Bernstein (1957). They reported that dichotic beats were observed when the “fre-

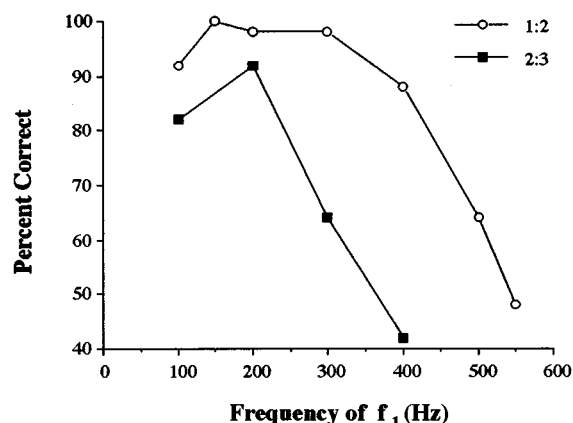


FIG. 2. Pilot data for subject 4 on the detection of beats for the dichotic octave (open circles) and fifth (filled squares). Each data point represents the percent-correct performance in the detection of dichotic BMCs for 50 trials in a 2I-2AFC experiment. Both sinusoids were at a level of 80 dB SPL and Δf was set at 1 Hz.

quency in one ear was a simple $n/1$ type multiple of the frequency in the other ear, provided that both frequencies were below 1000 Hz” (p. 519). The high frequency rolloff in performance has also been reported for *monaural* BMCs by Plomp (1967). For example, he reported that for an f_1 of 125 Hz at 90 dB SPL, no beats were heard for values of f_2 above 900 Hz, which corresponds to a frequency ratio ($f_1:f_2$) of 1:12. Plomp (1967) postulated that monaural BMCs for low-frequency sinusoids were caused by phase-induced changes in the combined waveform of the two sinusoids at the f_2 place. Thus, the low-pass detection function for monaural BMCs may be related to reduced phase locking in the high frequencies for the compound waveform of f_1 and f_2 . The high frequency rolloff would be expected for dichotic BMCs if the effect is due to a binaural process. For example, binaural beats of unisons, thought to be closely related to localization of low-frequency stimuli (Tobias, 1972), result from presenting a low-frequency sinusoid (f_L) to one ear and a second tone with a small frequency change from f_L in the other ear ($f_L + \Delta f$). Binaural beats are the most prominent for frequencies around 500 Hz. As f_L approaches 1000 Hz the detection of binaural beats diminishes. The upper limit for detection is around 1200–1500 Hz (Licklider *et al.*, 1950; Perrott and Nelson, 1969; Tobias, 1972).

The data of experiment 1 could be explained by a between-channel binaural phase effect between f_1 and f_2 . However, several other different mechanisms could also account for the data. The listener, for example, may have been able to distinguish between experimental intervals by using frequency discrimination of the 0.75-Hz increase in f_2 on signal trials. A second possibility is that the listener detected simple binaural beats between a stimulus component in one ear (f_2 mistuned by 0.75 Hz) and an aural harmonic ($2f_1$) in the other ear for the dichotic octave. For the dichotic fifth these binaural beats could possibly take place between the second harmonic of f_2 and the third harmonic of f_1 . Alternatively, monaural BMCs could have possibly been produced in the subject’s right ear by interaural crossover from

the high-level f_1 interacting with the f_2 stimulus component. Experiments 2–4 address these alternative explanations for the effect.

II. EXPERIMENT 2. FREQUENCY DISCRIMINATION

After the data from experiment 1 were collected, a frequency discrimination experiment was conducted with the same subjects to test each listener's ability to detect the 0.75-Hz mistuning of f_2 .

A. Method

The sinusoids were generated using the same equipment used in experiment 1. The data for this experiment were collected using a 2I-2AFC procedure with feedback. During one interval a sinusoid at a frequency of f_2 was presented to the subject's right ear at a level of 60 dB SPL. In the other interval the sinusoid was mistuned by 0.75 Hz. There was a probability of 0.5 that this was the first interval. The subject's task was to select the interval with the higher pitch. The interstimulus interval was again 750 ms with an inter-trial interval of 1 s. The frequency of f_2 , selected independently for each subject, was the same as the lowest value of f_2 (best performance) used in experiment 1. The values of f_2 in the present experiment were 400 Hz for subject 1, 600 Hz for subjects 3 and 4, and 800 Hz for subject 2.

Each subject was presented with five 40-trial blocks. No training was provided before this experiment since the goal was to determine if the subjects had already inadvertently trained themselves in frequency discrimination. Furthermore, since later experiments would again examine detection of dichotic beats, it was felt that a minimum number of trials should be used to limit subjects' training in frequency discrimination.

B. Results and discussion

Figure 3 displays the results for the four subjects for frequency discrimination (hatched bars). Also displayed are the results from experiment 1 on dichotic beat perception with the same value of f_2 (solid bars). The mean score for the four subjects for beat detection at the lowest octave was 93.5% (s.d.=0.90) compared to 60.8% (s.d.=7.2) for frequency discrimination [$t(3)=7.3$, $p<0.005$]. These data suggest that subjects were not using frequency discrimination as the cue in experiment 1.³ Furthermore, all subjects reported using beats as a basis for detection of the mistuned interval in experiment 1.

III. EXPERIMENT 3. DICHOTIC OCTAVE BMCs: EFFECT OF STIMULUS LEVEL AND MASKING NOISE

This experiment addressed three issues. The first issue was that the performance in experiment 1 could have been the result of a binaural within-channel effect between the mistuned f_2 and either a contralateral aural harmonic ($2f_1$) or the excitation pattern of f_1 . This was addressed first of all by reducing the level of the stimuli, and, thereby, the level of the proposed aural harmonic or excitation pattern of f_1 . Second, noise was presented to the left ear in the region of $2f_1$

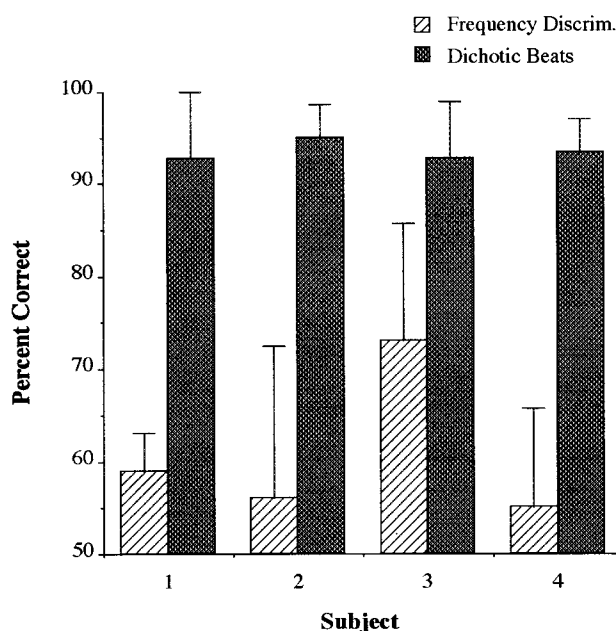


FIG. 3. The results of experiment 2 are shown for the percent-correct performance in frequency discrimination (hatched bars) for the four subjects. The solid bars represent the percent-correct performance for the detection of dichotic BMCs at the lowest octave tested for each subject in experiment 1. The error bars represent +1 standard deviation of the mean.

to mask either the aural harmonic or excitation pattern of f_1 and, thus, prevent binaural interaction with the mistuned f_2 .

The second issue addressed by this experiment was that there may have been acoustic crossover of f_1 to the ear with f_2 which could have led to monaural BMCs. This is not consistent with reports from the subjects that the beats were either lateralized to the left ear or appeared to move back and forth between the ears. Moreover, the likelihood of acoustic crossover was greatly diminished by the use of insert earphones. The minimum interaural attenuation for these earphones was reported to be 85 dB in this frequency region by Killion *et al.* (1985). Nevertheless, the reduction of the stimulus level in this experiment further reduced the likelihood of acoustic crossover as a source of dichotic BMCs. Dichotic beat detection was evaluated again in this experiment with the level of f_1 reduced to 70 dB SPL.

Finally, this experiment addressed the issue that the results of experiment 1 for the octave were based on binaural beats between upper aural harmonics of f_1 and f_2 (e.g., the fourth harmonic of f_1 and the second harmonic of f_2 : 800 and 801.5 Hz for a value of f_1 of 200 Hz). In order to reduce the possibility of this type of binaural interaction, the level of f_2 was reduced to 40 dB SPL, a level not expected to generate aural harmonics (Clack, 1977).

The purpose of this experiment was to see if the four subjects could still detect dichotic BMCs for the mistuned octave under conditions of reduced stimulus levels and with noise centered at $2f_1$ in the left ear. If performance under these conditions dropped to chance, it would suggest that beat detection was based on one of the effects just described.

A. Method

1. Apparatus

The sinusoids were generated using the same equipment as used for experiment 1. For the noise conditions one of the outputs from the D–A converter passed through an 8-kHz low-pass filter and digital attenuator (TDT-PA3) and was then mixed (TDT-ADD1) with noise before being amplified and routed to the earphone. A band-pass noise was generated by routing the output of a broad-band noise generator (TDT-GNS-40) through two low-pass programmable filters (90 dB/oct total rolloff). The output from these filters was then high passed (three Krohn-Hite 3323R filters in series: 72 dB/oct total rolloff) to create the band-pass noise. The noise was attenuated using an analog attenuator and then mixed (TDT-ADD1) with a sinusoid generated by one of the D–A converters.

Each subject's threshold for a sinusoid at f_2 in the left ear was tested in quiet and noise in a side experiment in order to establish masked threshold. Thresholds were estimated using a computer-controlled, Bekesy-tracking procedure. Sinusoids were generated by a Hewlett–Packard 3325A function generator. The sinusoids were routed to a programmable attenuator (TDT-PA3) and then a switch (TDT-SW1) that controlled the 20-ms rise–fall time with a \cos^2 time function. The signal was then routed to a mixer (TDT-ADD1) for testing in noise or directly to the headphone amplifier (Crown-D75) for thresholds in quiet.

2. Procedure

The data for this experiment were collected using a 2I-2AFC procedure with feedback. The level of the sinusoids was 70 dB SPL for f_1 and 40 dB SPL for f_2 . The frequencies of the lowest octave from experiment 1 were used for subjects 1, 2, and 4. For subject 3 the value of f_1 was 200 Hz using a 0.5-Hz value of Δf (see footnote 3). Each subject was tested in quiet at the lower stimulus levels for eight blocks of 40 trials and then in noise as described below for eight more blocks of 40 trials using the same stimulus levels.

The bandwidth of the noise presented with f_1 was approximately equal to the classical critical band: 100 Hz for values of f_2 of 600 Hz or below, and 15% of the center frequency for higher frequencies. The noise was set at an intensity that would just mask a 35 dB SPL tone at the frequency of $2f_1$. This level was chosen since it provided 10 dB greater masking than the average estimated level of the aural harmonic of a 70-dB SPL, 500-Hz tone based on the data of ten listeners using the tone-on-tone masking procedure from Clack (1977). Individual estimates of the level of the aural harmonic were not attempted. There has been some debate over using the tone-on-tone method for the estimation of the level of aural harmonics for low-frequency tones. Schubert (1969) argued that this technique is unusable for frequencies below 1000 Hz because phase effects will be caused by variations in the excitation pattern of f_1 at the $2f_1$ place. Nevertheless, Clack's average data provide a basis for establishing a masking level.

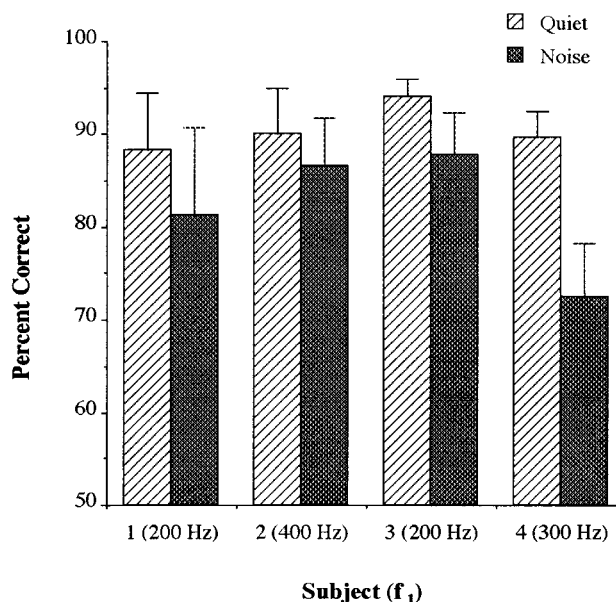


FIG. 4. Dichotic beat detection for the mistuned octave for levels of f_1 and f_2 of 70 and 40 dB SPL, respectively. The hatched bars represent performance in quiet and the solid bars represent performance in the presence of a band-pass masking noise presented to the left ear at the frequency of $2f_1$. The error bars represent ± 1 standard deviation of the mean.

B. Results and discussion

Figure 4 shows the results for the detection of dichotic beats at 70 dB SPL (f_1) and 40 dB SPL (f_2) in quiet (hatched bars) and with the narrow-band masker (solid bars). Each subject scored somewhat poorer in noise, but the mean difference between conditions only approached significance. The mean score in quiet was 90.5% (s.d.=2.1) compared to 82.0% in noise (s.d.=6.0) [$t(3)=2.84$, $p=0.066$]. It is clear from these results that performance at the reduced levels in quiet and with the addition of the masker was well above chance for each subject.

Results for the noise condition suggest that dichotic BMCs were not caused by beats between the mistuned f_2 and either the second aural harmonic of f_1 or the excitation pattern of f_1 . This is consistent with the data of Goldstein (1965), who found that monaural octave BMCs at low levels of f_1 and f_2 were not affected by raising the level of f_2 to a level sufficient to mask the second aural harmonic of f_1 . These results with a reduced level of f_1 are also consistent with the findings of Ayres and Clack (1984b) who simulated acoustic crossover by adding a 25-dB SPL, 400-Hz tone to the same ear as f_2 , a 10-dB SPL, 800-Hz sinusoid. Phase changes in these stimuli were not detected by subjects who had previously detected frozen dichotic phase differences between a 400-Hz sinusoid at 75 dB SPL in one ear and an 800-Hz sinusoid at 10 dB SPL in the other ear (supra-aural phones).

IV. EXPERIMENT 4. DICHOTIC OCTAVE BMCs: HIGH-LEVEL MASKER

An additional experiment was conducted in which band-pass noise at a higher level was presented to the left ear

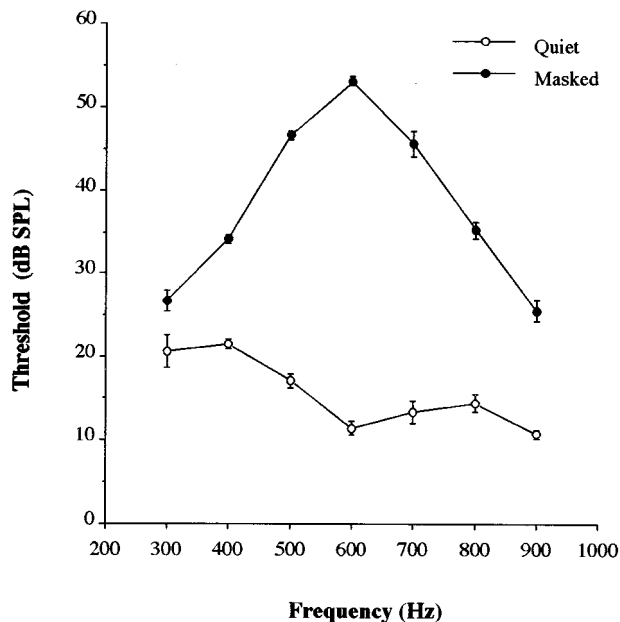


FIG. 5. Each data point represents the mean of five blocks of 40 trials for thresholds obtained in quiet (open symbol) and in the presence of the high-level bandpass masking noise (filled symbol) for subject 2. The error bars represent ± 1 standard deviation of the mean.

along with f_1 . As in experiment 3, the noise was centered at f_2 and served as a masker for either the aural harmonic of f_1 or its excitation pattern. The purpose of this experiment was to provide a more rigorous test of the aural harmonic and modified binaural correlator explanations of dichotic BMCs.

A. Method

Subject 2 participated in this experiment. The stimulus generation was identical to that of experiment 3. Additional masked thresholds were first obtained for subject 2. The masker was centered at 600 Hz with masker cutoff frequency and rolloff as described for experiment 3. In this case the masker was increased to a level resulting in maximal masking at 600 Hz without significant masking at 300 Hz. Thresholds for the frequencies 300–800 Hz were tested in 100-Hz steps in the presence of the masker in the left ear. Figure 5 displays the unmasked thresholds (open circles) and masked thresholds (filled circles) for subject 2 obtained using the Bekesy-threshold-tracking procedure as in experiment 3. Note that the masked threshold was 27 dB SPL at 300 Hz (the value of f_1) compared to 53 dB SPL at 600 Hz.

Subject 2 was then presented with five blocks of 40 trials in detection of dichotic BMCs in the noise condition described above. The dichotic octave for this experiment was chosen as 300 and 600 Hz at levels of 70 and 40 dB SPL. The value of Δf was 0.75 Hz. Note that the value of f_1 was 100 Hz lower than that used in experiment 3. The lower frequency was chosen to maximize this subject's performance in the high-level masker.

Following the masking experiment, subject 2 was also tested in frequency discrimination in quiet at 600 Hz in the right ear in the manner of experiment 2. The signal level was 40 dB SPL and the value of Δf was 0.75 Hz. Five blocks of

40 trials were used without feedback. The purpose of the frequency discrimination experiment was to see if subject 2 had learned to discriminate the dichotic stimuli on the basis of monaural frequency discrimination.

B. Results and discussion

The mean performance for subject 2 in the high-level masker was 90.5% for five blocks of 40 trials (s.d.=2.7). This compared to 55% (s.d.=6.7) for frequency discrimination using the same frequency and level of f_2 . It is clear from these results that frequency discrimination was not the basis for the detection of dichotic BMCs for subject 2 in the high-level noise.

The results of this experiment cast further doubt on the aural harmonic and modified binaural correlator explanations of dichotic BMCs.⁴ Moreover, the substantial amount of masking in the frequency range between f_1 and f_2 , as well as above f_2 , suggests that subject 2 was probably not able to rely on a cue at some place of spectral overlap of the neural excitation pattern of the two sinusoids in the central auditory nervous system. Rather, a mechanism would be needed that is independent of interactions within an auditory frequency channel.

V. EXPERIMENT 5: INTRACRANIAL IMAGE

Reports on dichotic BMCs dating back to Thompson (1881) have mentioned stimulus movement associated with the beats. Informal reports from the subjects in this study confirmed that stimulus movement was associated with dichotic BMCs. This experiment was designed to evaluate a listener's ability to detect differences in the location in intracranial space of BMCs under the conditions of masking noise as in experiment 3. A slight mistuning of f_2 is mathematically equivalent to a running phase change between f_1 and f_2 . In this experiment, the frequency of f_2 was held constant at $2f_1$ but it was phase shifted by 180° in one experimental interval. If listeners detected phase-induced changes in perceived stimulus location, it would provide evidence that dichotic BMCs were a true binaural phenomenon.

A. Method

1. Subjects

Subjects 2 and 4 participated in this study. At the time of this experiment, both subjects 1 and 3 had withdrawn from the study.

2. Apparatus

The equipment arrangement and stimulus generation parameters for this study were identical to those of experiment 3.

3. Procedure

The data for this experiment were collected using a two-cue, two-interval forced-choice procedure patterned after the method of Bernstein and Trahiotis (1982). The trial structure consisted of four stimulus intervals. The stimulus duration was 1 s with a 500-ms interstimulus interval and 1-s intertrial interval. As in experiment 3, the level of f_1 in the left ear

was 70 dB SPL and the level of f_2 in the right ear was 40 dB SPL. During intervals 1 and 4 the “standard” stimulus was presented. This consisted of dichotic sinusoids at an octave ratio with both sinusoids generated at 0° starting phase as measured at the input to the earphones. The predominant intracranial image of the standard was of a low-frequency sinusoid to the left of center. The standard was presented again in either interval 2 or 3 with a probability of 0.5, and the “signal” was presented in the other interval. The signal consisted of the same dichotic sinusoids, but the starting phase of f_2 was advanced 180° (“frozen” dichotic BMCs). The subject’s task was to select the interval (either 2 or 3) in which the low-frequency sinusoid on the left appeared to move in relation to the standard. The subject was encouraged to use any apparent movement of the low-frequency sinusoid as a clue.

The frequency of f_1 was 300 Hz for subject 2 and 200 Hz for subject 4. These values of f_1 were chosen to maximize temporal cues and were, therefore, 100 Hz lower than the test values in experiment 1. A 100-Hz narrow-band noise centered at $2f_1$ was presented continuously to the left ear throughout a block of trials as a masker for the second aural harmonic of f_1 . As in experiment 3, the level of the noise was sufficient to mask a 35-dB SPL sinusoid at the frequency of f_2 .

Each subject received a minimum of 50 trials of practice before the data reported below were collected. The test data consisted of five blocks of 40 trials for a total of 200 trials. Breaks were given as in experiment 1, and the data collection for each subject took place in a single experimental session.

B. Results and discussion

The detection of frozen dichotic BMCs was high for both subject 2 (mean=98.0%, s.d.=2.1%) and subject 4 (mean=84.0%, s.d.=3.4%). Given 200 trials, a score greater than 55.7% is significantly greater than chance at the 0.05 level. Subject 4 reported that on signal trials the low-frequency sinusoid on the left appeared to move in toward the midline as well as diagonally upward and backward. Subject 2 initially reported that on signal trials the location of the left sinusoid appeared to move upward. On later blocks of trials she reported that along with the upward movement there appeared to be movement further to the left on signal trials.

It would appear both from these experimental results, and from subject reports, that there is a perception of stimulus movement associated with dichotic BMCs. This is consistent with anecdotal reports in the literature (Lamore, 1975; Thompson, 1881; Thurlow and Bernstein, 1957; Thurlow and Elfner, 1959). Moreover, Ayres and Clack (1984b) reported that the subjects in their study used “a lateral shift in the perceived in-head location of the tonal image” to detect phase changes in an 800-Hz tone burst presented with a continuous 400-Hz sinusoid (p. 416). The results of the present experiment suggest that dichotic BMCs are a binaural phenomenon akin to binaural localization effects for low-frequency sinusoids.

VI. GENERAL DISCUSSION

Both the aural harmonic and the modified binaural correlator explanations of dichotic BMCs depend on input to the central auditory system originating at the f_2 place on the basilar membrane from the ear presented with f_1 : either an aural harmonic of f_1 or the excitation pattern of f_1 . Since masking in the frequency region of $2f_1$ had little effect on the detection of dichotic octave BMCs, neither of these explanations account for the data of this study. The binaural correlator model predicted poorer performance for the dichotic fifth than for the octave, which was indeed the case in the pilot data. However, the aural harmonic theory predicts that beats should not be detected for the dichotic fifth since the second aural harmonic of f_1 would occur at $2f_1$ rather than at $1.5f_1$.

Previous reports had cast doubt on the aural harmonic explanation of dichotic octave BMCs since beats were detected for stimuli at levels of 30 dB SPL (Thurlow and Bernstein, 1957) and 30 dB SL (Thurlow and Elfner, 1959). However, Demany and Semal (1988) suggested that harmonic distortion in the stimuli could have led to the perception of beats in these earlier studies. That explanation was not supported by the masking results of the present study. Ayres (1981) reported that with f_1 set at 400 Hz and a level of 70–75 dB SPL, the detection of dichotic octave phase effects was strongest for low levels of f_2 , 5–25 dB SL, fell to chance for f_2 at 35 dB SL and improved for f_2 at higher levels. These results could be interpreted to suggest a different mechanism for the detection of dichotic octave phase effects as a function of the level of f_2 . However, since Ayres (1981) did not employ a masker in the frequency region of f_2 in the ear with the f_1 sinusoid, it is difficult to interpret these findings. A systematic exploration of the effect of stimulus level on the perception of dichotic BMCs is warranted both in quiet and with the masking paradigm of the present study at several frequency and level ratios.

Recent models of the localization of low-frequency stimuli combine interaural cross correlations within each frequency channel to arrive at a judgment of the sound source. Stern *et al.* (1988) presented a weighted-image model that predicts the subjective lateral position of band-pass stimuli by examining the maxima of the cross-correlation functions across frequency. The trajectories of the cross-correlation maxima across frequency are given more weight if they share a given interaural delay (“straightness”), or if they fall near an interaural delay of zero (more central) since there are more binaural coincidence counting units with small versus large interaural delays. Shackleton *et al.* (1992) presented an across-frequency integration model of localization in which the cross-correlation functions are weighted for centrality and then summed across frequency. In this model straightness causes the summary cross-correlation function to have a large lobe corresponding to the common interaural delay across frequency. Stern and Trahiotis (1991) described a modification of the weighted-image model that corrects for an overemphasis on centrality weighting and predicts straightness weighting. A second-level coincidence mechanism receives input from a small number of first-level coincidence counters to arrive at a range of characteristic fre-

quencies with a common internal delay. Stern and Trahiotis (1991) cited physiological evidence for the second-level coincidence mechanism in the responses of interaural time sensitive units in the IC of the barn owl. Takahashi and Konishi (1986) recorded from IC units that demonstrated sensitivity to a characteristic interaural delay over a range of stimulus frequencies. The response of these units to binaural tones with a time difference yielding maximum firing was increased by the presentation of a second pair of binaural tones of different frequency with the same interaural delay.

The subjects in experiment 5 detected changes in the location of f_1 based on phase changes in a contralateral sinusoid at a frequency of $2f_1$. Similarly, Thurlow and Elfner (1959) reported localization effects for stimuli of the type $n:1$ for ratios up to 9:1. The current models of localization described above would not predict these localization effects since there is no interaural delay within any frequency channel from which to generate a cross-correlation function. Yin *et al.* (1987) attributed the finding of cyclic maxima in the histograms of IC units in cats presented with dichotic mistuned consonances to a cross-correlation process. However, they could not explain the large frequency ratios over which the effects were observed (up to 5:1). Clearly, a within-channel cross correlation would not be expected with these stimuli.

An alternative explanation for dichotic BMCs is based on the known firing patterns of medial superior olive (MSO) neurons combined with the Stern and Trahiotis (1991) second-level coincidence mechanism. Goldberg and Brown (1969) described the responses of MSO neurons in the dog that were excited by input from both ears (E-E neurons). They reported that the firing pattern of these binaural neurons to low frequency *monaural* sinusoids was phase locked, and with a firing rate that typically fell somewhere between the maximum and minimum firing rates established for these units by varying the interaural delay between binaurally presented sinusoids. Goldberg and Brown speculated that the monaural inputs to E-E neurons in the MSO had characteristic delays, inherent perhaps in the physical distance between ipsilateral and contralateral inputs to the MSO, that were independent of stimulus frequency over a limited frequency range.

Consider the case of dichotic octave sinusoids locked in phase. After peripheral processing, the half-wave rectified version of f_1 in the eighth nerve response would stimulate E-E neurons in the MSO within the critical band of f_1 to fire in a phase-locked fashion at a submaximal rate after some characteristic delay. A 180° phase shift in f_2 (experiment 5) would not only change the timing of the phase-locked response to f_2 but would change the temporal relationship between the two channels that were previously receiving information in phase. Takahashi and Konishi (1986) reported that the IC units that were sensitive to a characteristic interaural delay over a range of frequencies (the second-level coincidence mechanism) were not sensitive to monaural stimulation. However, given a strong temporal relationship between the frequencies of dichotic input such as the octave, it is proposed that an IC unit with broad tuning encompassing the octave would, first of all, be stimulated by that dichotic in-

put; and second, would have its firing pattern modulated by a change in interaural delay across channels simulated by a phase shift in one of the sinusoids. Recall, that the slight mistuning of f_2 (experiments 1, 3, and 4) is mathematically equivalent to a running phase shift between the two sinusoids. A cross correlation of the inputs to the IC unit from the two frequency channels stimulated by a mistuned octave would result in a period histogram with maxima occurring at the beat rate of mistuned consonances (Yin *et al.*, 1987).

Thus, it is speculated that the firing rate of units in the second-level coincidence mechanism (Stern and Trahiotis, 1991) may be modulated in response to dichotic stimulation if the inputs from each channel have a strong temporal relationship as in the case of dichotic mistuned consonances. The perception of dichotic BMCs based on this process would likely be subtle since the firing rate of MSO units to monaural stimulation is reduced compared to binaural stimulation. Recall that two subjects were dropped from the study because of their difficulty in hearing beats (see footnote 1). It would, furthermore, be expected that dichotic beat perception would increase with stimulus level, as was observed in pilot testing, since this would cause an increase in the monaural firing rate of separate MSO E-E units responding to dichotic stimulation. Moreover, an increased complexity of frequency ratio between the sinusoids would degrade their temporal relationship, accounting for the poorer performance for the dichotic fifth as shown in the pilot data. Finally, the effect would have a low-pass characteristic inherent in the localization of a sound source based on temporal information.

VII. CONCLUSIONS

The findings of this study fail to support either an aural harmonic explanation (Ayres and Clack, 1984b) or the binaural correlator model of Ayres (1981) for the phenomenon of dichotic BMCs. The subjects in this study reported stimulus movement associated with the beats, suggesting that dichotic BMCs are a binaural phenomenon. A new theory was proposed to account for dichotic BMCs as a between-channel phase effect. The proposed mechanism accounts for the findings of this study, predicts decreasing performance with increasing frequency ratio, and is consistent with recent models of localization for low-frequency stimuli that incorporate information across frequency channels.

ACKNOWLEDGMENTS

The author would like to thank Ed Burns for his assistance and guidance throughout this project. Robert Ling provided invaluable technical support. Lynne Werner, Doug Keefe, Rich Folsom, and Gary Thompson provided helpful comments on a previous version of this manuscript. Constantine Trahiotis suggested Experiment 5 after the preliminary data were presented at the 127th. Meeting of the Acoustical Society of America, May 1993, Ottawa, Canada. Raymond Dye and two anonymous reviewers provided extremely helpful comments on the manuscript and guidance in addressing the mechanism of the effect. This research was conducted in partial fulfillment of the requirements for the doctoral degree

at the University of Washington. Funding was provided by the Virginia Merrill Bloedel Hearing Research Center.

¹Two additional female subjects with normal hearing aged 19 and 21 years were dropped from the study because their performance in the detection of beats for the mistuned octave was less than 75% correct with sinusoids of 200 and 400 Hz at levels of 80 and 60 dB SPL, respectively.

²Near the end of training subject D found the 80-dB SPL level of f_1 to be annoyingly loud at the highest frequencies tested (500 and 600 Hz). For this reason the levels were reduced to 75 and 55 dB SPL for f_1 and f_2 , respectively. These levels were tolerated well and so all test trials in experiment 1 for this subject were run at these levels instead of 80 and 60 dB SPL.

³Although there was a mean difference in performance of 33% between the two tasks, it appears from an examination of Fig. 3 that subject 3 performed better in frequency discrimination than the other subjects. He scored only 52% on the first block of 40 trials in frequency discrimination, but was above 80% correct by the last block of trials. After the third block of trials this subject was asked if the cue he was using in the frequency discrimination task was similar to the one he heard in the beat detection experiment. He appeared surprised at the question and responded, "No, I can't hear beats now!" In order to discourage the use of frequency discrimination in subsequent beat-detection experiments, the value of Δf for subject 3 was reduced to 0.5 Hz. This change in Δf was found to reduce this subject's beat detection from 92.8% correct (320 trials) for stimuli at the lowest octave in experiment 1 to 84% correct (five blocks of 40 trials, s.d.=8.0). Subject 3's frequency discrimination was then retested with a 0.5-Hz value of Δf at 600 Hz and 60 dB SPL. He averaged 56.3% for five blocks of 40 trials (s.d.=12.7). This supports the results of the main frequency discrimination experiment, suggesting that, for these subjects, detection of dichotic BMCs was not based on frequency discrimination.

⁴An additional experiment was conducted with subject 1 using the dichotic fifth with f_1 (200 Hz) at 70 dB SPL and f_2 (300 Hz) at 60 dB SPL. Bandpass masking (500 to 1250 Hz) sufficient to provide a 20-dB threshold shift in the pass band was presented with f_2 to mask harmonics of f_2 at 600 and 1200 Hz that could have resulted in binaural beats with upper harmonics of f_2 . The level of the masker was chosen to provide 10 dB greater masking than the estimated level of the second aural harmonic of a 500-Hz sinusoid at 60 dB SPL based on the data of Clack (1977). Subject 1 achieved an average of 80% correct performance over eight blocks of 40 trials. Since detection was well above chance in the presence of the masker, the results suggest that beat detection for the dichotic mistuned fifth cannot be explained by interactions based on aural harmonics. This supports the results reported above for detection of beats for the dichotic octave in noise.

Ayres, T. J. (1981). "A dichotic probe investigation of octave phase effects," doctoral dissertation, University of Michigan, Ann Arbor, MI.

Ayres, T. J. (1982). "Aural harmonic distortion and the pulsation threshold procedure," *Acustica* **51**, 244–246.

Ayres, T. J., and Clack, T. D. (1984a). "Detection of interaural phase shift between a subaudible and an audible tone," *J. Acoust. Soc. Am.* **76**, 411–413.

Ayres, T. J., and Clack, T. D. (1984b). "Interaural octave phase-shift detection and aural harmonic distortion," *J. Acoust. Soc. Am.* **76**, 414–418.

Bernstein, L. R., and Trahiotis, C. (1982). "Detection of interaural delay in high-frequency noise," *J. Acoust. Soc. Am.* **71**, 147–152.

Clack, T. D. (1977). "Growth of the second and third aural harmonics of 500 Hz," *J. Acoust. Soc. Am.* **62**, 1060–1061.

Colburn, H. (1977). "Theory of binaural interaction based on auditory nerve data. II. Detection of tones in noise," *J. Acoust. Soc. Am.* **61**, 525–534.

Demany, L., and Semal, C. (1988). "Dichotic fusion of two tones one octave apart: Evidence for internal octave templates," *J. Acoust. Soc. Am.* **83**, 687–695.

Filip, M. (1970). "Sweep-tone effect in mistuned consonances," *Musica* **21**, 95–107.

Goldberg, J. M., and Brown, P. B. (1969). "Response of binaural neurons of dog superior olivary complex to dichotic tonal stimuli: some physiological mechanisms for sound localization," *J. Neurophysiol.* **32**, 613–636.

Goldstein, J. L. (1965). "An investigation of monaural phase perception," doctoral dissertation, University of Rochester, Rochester, NY.

Helmholtz, H. L. F. v. (1954). *On the Sensations of Tone as a Physiological Basis for the Theory of Music* (English translation of 4th German edition of 1877 edition, Dover, New York).

Jeffres, L. A. (1948). "A place theory of sound localization," *J. Comp. Physiol. Psychol.* **41**, 35–39.

Killion, M. C., Wilber, L. A., and Gudmundsen, G. I. (1985). "Insert ear-phones for more interaural attenuation," *Hear. Instrum.* **36**, 34–36.

Lamore, P. J. J. (1975). "Perception of two-tone octave complexes," *Acustica* **34**, 1–14.

Lamore, P. J. J. (1977a). "Investigation of two-tone interaction in octave complexes with the help of the pulsation-threshold method," *Acustica* **39**, 7–15.

Lamore, P. J. J. (1977b). "Pitch and masked threshold in octave complexes in relation to interaction phenomena in two-tone stimuli in general," *Acustica* **37**, 249–257.

Lamore, P. J. J. (1979). "Phase relations in an internal representation of two-tone octave complexes," *Acustica* **42**, 295–301.

Licklider, J. C. R., Webster, J. C., and Hedlund, J. M. (1950). "On the frequency limit of binaural beats," *J. Acoust. Soc. Am.* **22**, 468–473.

Moore, B. C. J., Peters, R. W., and Glasberg, B. R. (1985). "Thresholds for the detection of inharmonicity in complex tones," *J. Acoust. Soc. Am.* **77**, 1861–1867.

Ohm, G. S. (1839). "Bemerkungen uber combinationstone und stosse," *Ann. Phys. Chem.* **47**, 463–466.

Perrott, D. R., and Nelson, M. A. (1969). "Limits for the detection of binaural beats," *J. Acoust. Soc. Am.* **46**, 1477–1481.

Plomp, R. (1967). "Beats of mistuned consonances," *J. Acoust. Soc. Am.* **42**, 462–474.

Schubert, E. D. (1969). "On estimating aural harmonics," *J. Acoust. Soc. Am.* **45**, 790–791.

Shackleton, T. M., Meddis, R., and Hewitt, M. J. (1992). "Across frequency integration in a model of lateralization," *J. Acoust. Soc. Am.* **91**, 2276–2279.

Stern, R. M., and Trahiotis, C. (1992). "The role of consistency of interaural timing over frequency in binaural lateralization," in *Auditory Physiology and Perception*, edited by Y. Cazals, L. Demany, and K. Horner (Pergamon, Oxford), pp. 547–554.

Stern, R. M., Zeiberg, A. S., and Trahiotis, C. (1988). "Lateralization of complex binaural stimuli: A weighted-image model," *J. Acoust. Soc. Am.* **84**, 156–165.

Takahashi, T. A., and Konishi, M. (1986). "Selectivity for interaural time differences in the owl's midbrain," *J. Neurosci.* **6**, 3413–3422.

Thompson, S. P. (1881). "Phenomena of binaural audition. Part III," *Philos. Mag.* **12**, 351.

Thurlow, W. R., and Bernstein, S. (1957). "Simultaneous two-tone pitch discrimination," *J. Acoust. Soc. Am.* **29**, 515–519.

Thurlow, W. R., and Elfner, L. F. (1959). "Pure-tone cross-ear localization effects," *J. Acoust. Soc. Am.* **31**, 1606–1608.

Tobias, J. V. (1963). "Application of a 'relative' procedure to a problem in binaural-beat perception," *J. Acoust. Soc. Am.* **35**, 1442–1447.

Tobias, J. V. (1965). "Consistency of sex differences in binaural-beat perception," *Audiology* **4**, 179–182.

Tobias, J. V. (1972). "Curious binaural phenomena," in *Foundations of Modern Auditory Theory*, edited by J. V. Tobias (Academic, New York).

Wier, C. C., Jeasteadt, W., and Green, D. M. (1977). "Frequency discrimination as a function of frequency and sensation level," *J. Acoust. Soc. Am.* **61**, 178–184.

Yin, T. C. T., Chan, J. C. K., and Carney, L. H. (1987). "Effects of interaural time delays of noise stimuli on low frequency cells in the cat's inferior colliculus. III. Evidence for cross-correlation," *J. Neurophysiol.* **58**, 562–583.

Auditory localization, detection of spatial separateness, and speech hearing in noise by hearing impaired listeners

William Noble

Department of Psychology, University of New England, Armidale, NSW 2351, Australia

Denis Byrne

National Acoustic Laboratories, 126 Greville Street, Chatswood, NSW 2067, Australia

Kim Ter-Horst

Department of Psychology, University of New England, Armidale, NSW 2351, Australia

(Received 23 January 1996; revised 30 September 1996; accepted 5 April 1997)

In two groups, one with sensorineural and the other with conductive-mixed hearing loss, measures were made of single-source localization and speech intelligibility in both spatially separate and nonseparate noise. There was also a test for detecting when two sounds came from the same location or from separate ones. Localization test results confirmed earlier findings, namely, disruption of vertical plane ability generally, and a further, particular disturbance to horizontal plane localization in the conductive-mixed group. Compared with a normal control group, there were only slight signs of benefit from separation of speech and noise in the region lateral to the listener, and virtually none in the frontal region. The new test, spatial separateness, had elements in common with both of the other tests, and links were observed from localization to separateness detection, and from separateness to benefit from separation of speech and noise. Localization was also related to speech hearing in nonspatially separated noise. © 1997 Acoustical Society of America. [S0001-4966(97)04009-5]

PACS numbers: 43.66.Qp, 43.66.Sr, 43.72.Dv, 43.66.Dc [RHD]

INTRODUCTION

The aim of this investigation was to examine the relationship between decrement in speech hearing ability, in various conditions of competing noise, and decrement in aspects of localization ability, in two different sorts of hearing loss, namely, sensorineural and conductive-mixed. Studying this relationship can help understanding of the common factors among different auditory functions, and indicate the part that improved spatial hearing may hypothetically play in improved speech hearing.

Probably the most commonly reported problem in sensorineural hearing impairment is difficulty hearing speech in noise. This appears to be only moderately related to hearing threshold level (HTL) (Ter-Horst *et al.*, 1993) and has been shown to relate independently of HTL to such functions as pitch discrimination, temporal gap detection (Glasberg and Moore, 1989), and temporal resolution (Schorn and Zwicker, 1990). It has been assumed that there is also a relationship between free-field localization and speech hearing in competing noise. This stems from a study by Hirsh (1950) which suggested an advantage due to the spatial separateness of the signals. Hirsh identified differences in interaural phase as the mechanism explaining the effect; and altering phase differences under earphone listening certainly reduces the extent of masking by noise (Licklider, 1948). Such phase differences would arise in free-field listening. Recent studies which have simulated spatial separation using earphone delivery of signals recorded from ear canals have demonstrated both localizability and the advantage for speech intelligibility (Begault and Wenzel, 1993; McKinley *et al.*, 1994).

As Hirsh (1950) also observed, improvements in speech hearing in noise could arise from head shadow effects, which

will improve signal-to-noise ratios when signal and noise sources are separate, an effect that may be independent of spatial hearing. For example, if a speech signal is retained in the median vertical plane, and noise is displaced laterally, the acoustic shadow cast by the head for high-frequency components of the noise reduces its binaural loudness level relative to that of the speech. Although the head shadow generates an interaural level difference which assists in detection of the spatial displacement, this may be incidental to the separation effect. A study by Saberi *et al.* (1991) suggests that improvement may also occur from increases in signal-to-noise ratios in specific frequency bands, due to directionally different pinna filter effects. That effect can account for the observation of release from masking under monaural listening when noise and speech are separated in the median vertical plane, thus when there are no interaural differences.

It remains uncertain, therefore, what part, if any, spatial hearing ability plays in free-field speech hearing. Listeners may simply be exploiting different alterations in signal versus noise properties that result from their spatial separation, rather than finding speech easier to distinguish because it is heard as coming from a different place than the noise. Of relevance to this point, several studies (Bronkhorst and Plomp, 1989; Bronkhorst and Plomp, 1992; Ter-Horst *et al.*, 1993) have found that impaired hearing results in less advantage from spatial separation of speech and noise signals than occurs with normal hearing. Much of the effect turns out to be due to differential head shadow effects. These are greater at frequencies above about 2 to 3 kHz, hence they cannot be taken advantage of with hearing loss at higher frequencies. The difference in binaural loudness level between speech in the median plane, and noise displaced laterally, occurs at

higher frequencies, and hence is less audible to someone with high-frequency hearing loss. While such a consequence of impaired hearing will also affect localization ability, it remains unknown if there is a connection between localization and hearing speech in noise that cannot be accounted for by the common factor of hearing level.

There are only a few empirical studies relevant to this issue. One by Platte *et al.* (1978) reported observations in three people with apparently normal pure-tone thresholds but poorer than normal hearing for speech in noise, and also poorer than normal localization ability. Chocholle *et al.* (1975) reported a case of central disorder where the person showed slight loss in terms of HTL, but more severe disturbance in speech hearing, hearing brief stimuli, and free-field localization. Häusler *et al.* (1983) observed a relationship between minimum audible angle and speech discrimination ability (in quiet conditions), but it may not have been independent of hearing level, and the authors themselves are cautious about the reliability of the finding. There is a connection between self-assessed localization and speech hearing disabilities, in various conditions of noise and quiet (Noble *et al.*, 1995). A partial correlation of 0.56 remained between these factors when the cocorrelation with HTL was accounted for.

If a connection exists between localization and speech-in-noise disability, this could bear upon strategies for optimal signal delivery, such as in hearing aid fitting and design. Forms of design that have the effect of improving localization function could have the bonus effect of improving speech hearing in noise. This has always been one of the arguments for the advantage of bilateral fitting so as to make use of binaural hearing (Byrne *et al.*, 1992)

In the present study, a test of single-source localization in free field was used. This test was designed to assess ability in the vertical and horizontal planes, in two regions of two-dimensional auditory space, frontal and lateral. Different cues have different prominence in these regions (Middlebrooks and Green, 1991). In the frontal horizontal plane, interaural differences in time/phase and intensity dominate, especially low-frequency time cues (Wightman and Kistler, 1992). In the frontal vertical plane, pinna-derived spectral alterations are dominant, both monaural (Hebrank and Wright, 1974) and interaural (Searle *et al.*, 1975; Butler, 1994). Lateral horizontal and vertical plane discrimination appears to rest on a combination of classical interaural differences, pinna-derived cues—possibly at different frequency bands for horizontal and vertical discrimination (Weinrich, 1982; Butler *et al.*, 1990)—and spectral cues resulting from shoulder and torso reflections (Gardner, 1973; Kuhn, 1987). Thus performance in these four regions (frontal horizontal, frontal vertical, lateral horizontal, and lateral vertical) can be expected to differ, especially as a function of type and configuration of hearing impairment (Noble *et al.*, 1994). This merits the separate consideration of localization ability in the four regions.

The present study also included a test of speech hearing ability in free field under conditions where the speech and noise signal were presented from the same place, or the noise was presented from two locations symmetrically displaced

from that of the speech. Symmetrical displacement was used in an effort to overcome head shadow effects, such that the shadow cast on either side would be compensated by the opposite side noise source. Acoustic variations brought about by symmetrical separation of the noise from the speech signal are different in the horizontal and vertical planes, and in the frontal versus lateral regions (see Ter-Horst *et al.*, 1993). Thus separation effects were considered individually in each of the four spatial regions.

The localization task involves identifying the whereabouts of single acoustic events in otherwise “unoccupied” auditory space. The speech test, by contrast, involves the extent of spatial separation between signal and masker as a variable. We considered it appropriate to develop a further test, one that examines the factor of spatial separation as such. In this new test, the task is to distinguish when two different signals are coming from the same location or different ones; the whereabouts of either signal was not the issue, nor their intelligibility. Rather, listeners had to report if they judged two sounds to be together in space or apart. We reasoned that if “spatial hearing” is implicated in the ability to hear speech in spatially separated noise, a test of this kind is useful in addition to a test of single source localization.

In summary, this paper reports the effects of two types of hearing loss (sensorineural and conductive-mixed) on performance in three psychoacoustic tests: localization, speech hearing in noise, and detection of spatial separation. Additionally, we report on the inter-relationships in performance in these tests.

I. METHOD

A. Participants

Two groups of clients of Australian Hearing Services volunteered to participate: 88 with sensorineural hearing loss, 16 with conductive-mixed loss. They underwent the localization and speech tests, and a subset was tested on the spatial separateness task. Average age of the whole sample was 69.7 yr (s.d. 10.7), with no age difference between the two groups. Identification of conductive-mixed loss relied on criteria in Noble *et al.* (1994) except that the requirement for a 20-dB corrected air-bone gap at 0.5, 1, 2, and 4 kHz was relaxed in one or two cases where a difference at a single frequency was less than this, provided the average difference between air conduction and bone conduction was greater than 20 dB. Some participants had taken part in the earlier study. “Better ear” is defined as the ear with lower HTL at the frequency in question. We considered that, within the sensorineural group, the degree of hearing loss could be associated with qualitatively different outcomes, because of the likelier audibility of certain cues in those with less impairment. For this reason, in presentation of descriptive statistics, the sensorineural group has been split into equally sized lower and higher subgroups on the basis of better ear average air conduction HTL at 0.5 to 4 kHz, the point of division occurring at 41 dB. Figure 1 shows the average air conduction HTLs for the two types of hearing loss, the average

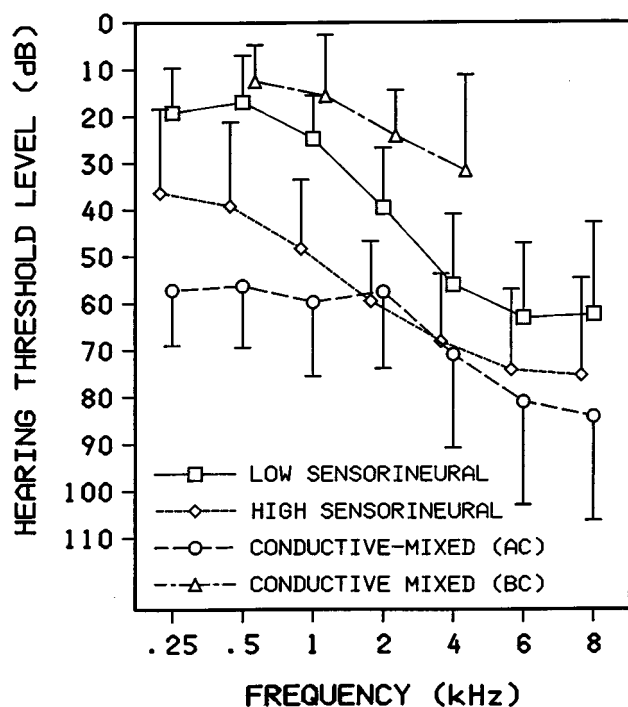


FIG. 1. Average air-conduction hearing threshold levels of sensorineural group (split into low and high subgroups), and bone- and air-conduction thresholds of conductive-mixed group (error bars show ± 1 or -1 s.d.).

HTLs for the two subgroups with sensorineural loss, and the average bone conduction HTLs for the conductive-mixed group.

B. Localization, speech in noise, and signal separateness testing

1. Localization

The localization test, described fully in Noble *et al.* (1994), used 20 numbered loudspeakers arrayed in two intersecting hemicircumferential arcs of 1.22-m radius, each source 18° apart from the next. Ten of the loudspeakers spanned the vertical plane, ten the horizontal plane (five on each side of the vertical array). One of the ten vertical loudspeakers was at the point of intersection common to both planes, there being five above that common one, and four below. The common source was assigned to the vertical plane for the purpose of calculation. The test used recorded pulsed pink noise (equal energy per third-octave band from 0.25 to 8 kHz), each pulse was of 150-ms duration, with 10-ms rise-fall times, and 50-ms interpulse intervals. Each signal comprised a minimum of four pulses and lasted 0.9 s overall. Successive signals were randomly varied by ± 3 dB about the nominal level.

All testing in this and the other two tasks was conducted, unaided, in a lighted anechoic room, with signal levels adjusted to the individual's unaided most comfortable level (MCL), and observation maintained by closed-circuit television. In the localization task there were 20 trials per test block, one trial per loudspeaker in random order, the task being to identify by number the loudspeaker judged to have been activated in a trial. Listeners were tested seated, their interaural axis level with the horizontal loudspeaker array,

and their head occupying the center of the implied sphere. They were free to move head and torso while the signal was active. Our previous observation has been that mobility offers little advantage in this experimental context, at least in the case of impaired hearing (Noble *et al.*, 1994). Testing occurred in two orientations: facing the center loudspeaker and facing the leftmost loudspeaker. No feedback was given.

2. Speech in spatially separated noise

The speech-in-noise test, described fully in Ter-Horst *et al.* (1993), used the above loudspeaker array and listening positions. A continuous narrative was presented from the center loudspeaker and speech spectrum noise (pink-noise filtered to match the long-term rms spectrum of the speech) was presented from that same loudspeaker or from the two on either side of it (18° horizontal separation), or from two at 54° on either side (three-loudspeaker separation), or from one above and one below (18° vertical separation), or 54° above and below. The noise was from a single channel, split to form correlated output whenever two sources were being used as the masker in a trial. We recognize that this approach to separation of speech from noise may not actually achieve true separation: the noise sources may perceptually "fuse." Results from a normal hearing control group (Ter-Horst *et al.*, 1993), reproduced in the present paper, suggest the arrangement used nonetheless can achieve separation benefit. The matter is addressed again in the Discussion.

Immobile listening was required in the speech test to ensure no variations in relative levels of speech and noise, which would have interfered with reliable threshold determination. Immobility was sustained voluntarily, monitored via the TV system, a procedure shown to be effective in previous experiments (e.g., Noble, 1981). The noise was adjusted to the listener's MCL, whose task was then to alter the speech level using a continuously variable attenuator until, as instructed, they could "follow half of what was being said." Listeners were free to use as many excursions as desired until that point was reached. In a given orientation, there were five practice trials, and, in random order, five determinations of threshold for each separation condition, as well as the nonseparate condition. For any condition, the median of the five observations was taken as the threshold. The speech test procedure has been shown to be reliable (Walker and Byrne, 1985), a feature confirmed in several subsequent experiments.

3. Detection of spatial separateness

This task involved presentation of continuous speech-spectrum noise simultaneously with eight-speaker speech babble, both signals preadjusted to be at the same acoustic level, as measured at a position corresponding to the center of the listener's head, and the dual signal presented at MCL. Over 80 trials (each 0.9 s) these sounds were randomly presented from the same (central) loudspeaker (40 trials), or with one from the center and the other from one removed to the left or right of center (five left, five right trials; 18° separation); or one from the center and the other removed 54° to the left or right; or one from the center and the other from

one above or below, or one centered and the other three above or below. Which sound was at which position was also randomly varied. Testing was in the two orientations used for the other tasks. The listener indicated on each trial whether the two sounds were from the same position or different ones, without regard to the direction or extent of difference, or which sound was where. An immobile posture was maintained during signal presentation, to ensure detection of separation was not on the basis of relative loudness variation. No feedback was given.

C. Data analysis and reduction

1. Localization

Scoring was based on the magnitude of erroneous responses (extent of deviation of responses from targets), and was computed as the arithmetic difference in number of loudspeakers between target and response. In cases where a response was to a location on the other plane than that of the target, counting proceeded from the target location to the central loudspeaker, and continued to the response location along the other plane.

2. Speech in noise

There are three components of measurement in this test: (1) signal-to-noise ratio required for 50% intelligibility when speech and noise are from the same loudspeaker [called the SIN (speech-in-noise) level]; (2) benefit from spatial separation in different planes and orientations (i.e., the difference between SIN level and the S/N ratio required under each of the separation conditions), and (3) the S/N ratio under different separation conditions.

3. Spatial separateness

This task has two components: percentage of correct calls when the sounds are from separate locations, and percentage correct when they are from the same place. In the initial description of results we show these components separately; for the purpose of comparative analysis, a signal detectability approach was adopted, to take account of both components together, as explained in Sec. II B.

II. RESULTS

A. Descriptive statistics

Initial analyses showed that there were certain interactions between type of hearing impairment, severity of sensorineural impairment, and task performance. For descriptive purposes, the sensorineural group data are presented for less and more severely impaired subgroups. About half the overall sample was tested on the spatial separateness test, and the conductive-mixed group was tested in the front-facing orientation only. In one or two individual cases not all tests were performed.

1. Localization

Results in Fig. 2 confirm previous observations (Noble *et al.*, 1994) that frontal vertical plane performance is severely affected by comparison with horizontal plane, even in the “low sensorineural” subgroup. The further effect of

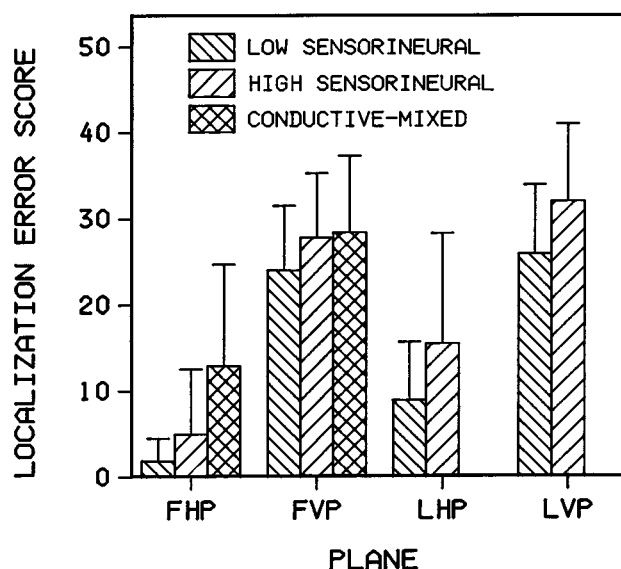


FIG. 2. Average localization total error magnitude scores of various hearing loss groups in four spatial regions: Frontal horizontal and vertical planes (FHP, FVP); lateral horizontal and vertical planes (LHP, LVP).

conductive-mixed disorder in the frontal horizontal plane is also confirmed. The difference between the “high sensorineural” and “conductive-mixed” groups is only partly due to differences in HTL. When samples were drawn, better matched on that variable ($N=14$ in each sample, 0.5 to 4 kHz HTL=58 dB in each), the difference in average total error magnitude scores between the two types of hearing loss, though reduced (from 7.9 to 6.9), remained significant.

Compared with the frontal orientation, there is a decrease in horizontal plane accuracy in the lateral orientation (sensorineural groups only). This is due to the increased incidence of front-rear reversals, which are reflected in larger error magnitudes. There was slightly greater absolute accuracy (number of correct responses) in performance in the lateral vertical plane (LVP) compared with the frontal vertical plane (FVP). The difference is not reflected in the magnitude of error scores across the two orientations, because of a greater incidence of cross-plane (“cone-of-confusion”) vertical errors laterally.

2. Speech in noise

Figure 3 shows the benefit from separation for the three hearing loss groups, for both planes and (sensorineural groups) both orientations. Also shown are the results for a group of 15 people with normal hearing, previously reported in Ter-Horst *et al.* (1993). The normal hearing and hearing impaired groups varied in the S/N ratio required for speech to be judged 50% intelligible when presented from the same loudspeaker as the noise (SIN). The SIN values for the four groups and two orientations were: normal hearing, frontal = -7.6 dB, lateral = -8.0 dB; low sensorineural, frontal = -6.9 dB, lateral = -7.0 dB; high sensorineural, frontal = -4.0 dB, lateral = -4.5 dB; conductive-mixed, frontal = -6.8 dB.

For the normal hearing group, separation benefit of 2–4 dB is observable at 18° separation in both planes and orientations. In the frontal horizontal plane, benefit is more or less

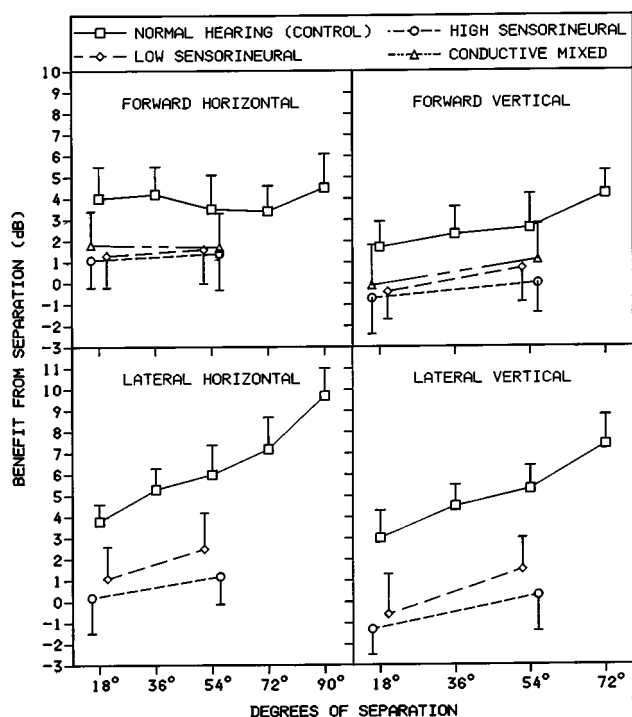


FIG. 3. Benefit from different degrees of separation of speech and noise in four spatial regions for normal hearing control group and the various hearing loss groups.

constant for all degrees of speech–noise separation, whereas benefit increases with increasing separation in the other three regions of auditory space.

The SIN and separation benefit measures both show poorer performance for all hearing loss groups compared with the normal control group. For nonseparated speech in noise (SIN), the low sensorineural and conductive-mixed groups required about 1 dB greater S/N ratio than the normal hearing listeners; the high sensorineural group needed a 3.5

dB greater S/N ratio. There is significant variation in performance among the three hearing loss groups in the SIN condition [$F(2,98)=4.5$, $p=0.01$]. *Post hoc* comparisons (Scheffé's test) showed that this is because the S/N ratios for the conductive-mixed and low sensorineural groups were better than for the high sensorineural group.

Compared with the normal hearing listeners, all hearing loss groups showed relatively little separation benefit, in fact, no benefit in some conditions. There was significant variation in the benefit from 54° of vertical separation [$F(2,98)=4$, $p=0.02$], the high sensorineural group receiving less benefit than the other two groups. The other separation conditions showed no significant variation across groups, though overall the average benefit was greatest for the conductive-mixed group. Compared with the frontal orientation, there was significantly more benefit from 54° of separation in the lateral horizontal ($p=0.004$) and vertical ($p=0.03$) planes for the low sensorineural subgroup, but no differences for the high subgroup.

3. Spatial separateness

This is a new test, and baseline data for nine normal hearing listeners are presented to compare with impaired hearing [Fig. 4(a) and (b)]. The normal group had HTLs less than 20 dB across the 0.25–8-kHz range. Results (percentages correct) are presented for each of the degrees and planes of separation, as well as for the nonseparate (same) condition. Separations were in one or the other direction relative to the central loudspeaker; for present purposes, data are combined over directions within a plane for each level of separateness. As the conductive-mixed group was tested in the frontal orientation only, a descriptive account of the data across groups is given for the two orientations separately.

The task is well within the capacity of normally hearing listeners when signals are at the same location or are sepa-

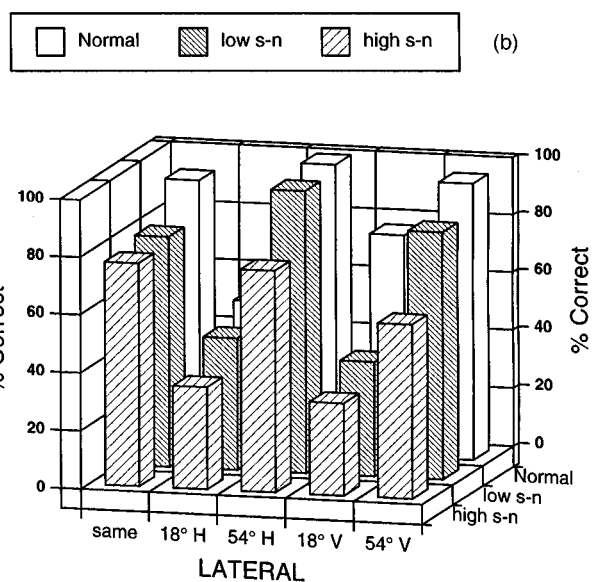
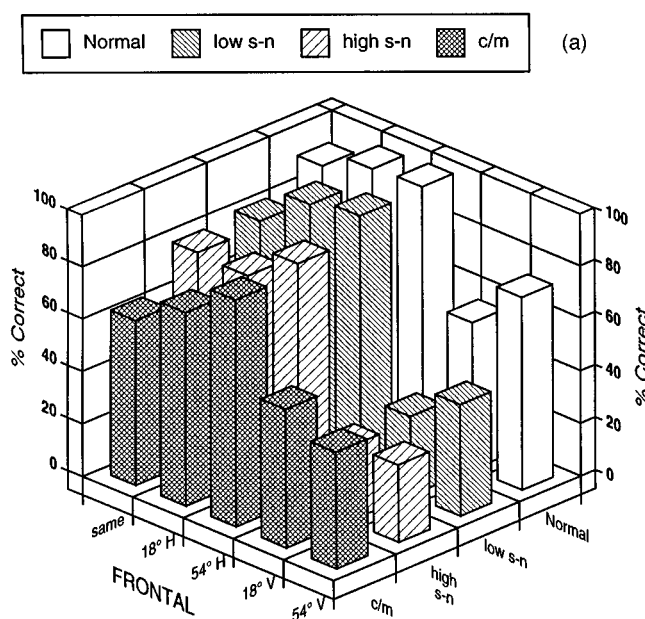


FIG. 4. (a) Percentages of correct responses in nonseparate ("same") and various separate conditions in the frontal orientation for normal hearing control group and various hearing loss groups. (b) Equivalent results in lateral orientation for normal and sensorineural loss groups.

TABLE I. Average values for d' on the spatial separateness test in normal, sensorineural, and conductive-mixed groups (s.d.'s in parentheses).

	FHP	FVP 18°	FVP 54°	Lateral 18°	Lateral 54°
Normal	4.5 (1.04)	2.02 (1.25)	2.72 (1.06)	2.31 (0.8)	4.36 (1.03)
Sensorineural	2.77 (1.59)	0.56 (0.8)	0.6 (0.79)	0.56 (0.6)	1.93 (1.11)
Conductive-mixed	1.62 (1.32)	0.45 (0.62)	0.23 (0.64)

rated in the horizontal plane; it becomes more challenging for separation in the frontal vertical plane. These observations hold for the low sensorineural group, although there is proportionately greater reduction in their vertical plane performance compared with the normal group. For the high sensorineural group, horizontal plane separation is poorer than in the low sensorineural group; as it is for the conductive-mixed group (the latter showing better vertical separation detection than the sensorineural subgroups, though there may be response bias affecting that result). In the lateral orientation the normal and low sensorineural groups do not differ markedly from each other, except in the 18° vertical separation condition, where both impaired groups have poorer performance than normal. In the 18° horizontal condition there are no differences among the groups, and in both of the 54° conditions the normal and low sensorineural groups are better than the high sensorineural group.

B. Comparative analyses

For the purpose of comparative statistical analysis, a signal detection approach was taken to results on the spatial separateness task, so as to control for effects of response bias. Proficiency was represented as d' , a quantity derived from the proportions of “hits” and “false alarms.” The higher the d' , the greater the degree of sensitivity in the task. “Hits” were counted as correct calls of “different” (sounds coming from spatially separate locations), “false alarms” as incorrect calls of “different,” “correct rejections” were counted as correct calls of “same” (sounds coming from the same location), “misses” were incorrect calls of “same.” The formula proposed by MacMillan and Creelman (1991, pp. 357–359) was used for calculating d' . If the number of hits or correct rejections was zero in any block of trials, that result was excluded from further consideration.

Values for d' in the frontal horizontal plane were highly correlated with each other, but uncorrelated with frontal vertical plane values; there was also a low correlation between 18° and 54° of frontal vertical plane separation. In the lateral orientation, d' values at 54° of separation in either plane tended to form one correlation cluster, and values at 18° of separation in either plane tended to form another. In view of these patterns, values for d' were derived from all FHP scores combined, from 18° and 54° FVP scores separately, and from LVP/LHP 18° and 54° scores separately. The d' scores thus derived are shown in Table I. A somewhat similar pattern of results was observed with the speech test, hence those results (S/N ratios) were considered in terms of horizontal and vertical planes in the frontal orientation, and in terms of 18° and 54° of separation (planes combined) in the lateral orientation.

We can expect performance differences across planes and orientations on theoretical grounds. Consistent with the “cone-of-confusion” principle, interaural time–phase and intensity differences for displacements from the interaural axis (i.e., in the lateral orientation) are virtually the same horizontally as vertically; these are probably the main cues available, in the case of hearing impairment, to permit detection of separateness or to derive benefit from speech–noise separation. Such cues are also in play in the frontal horizontal plane, but not in the frontal vertical plane, where pinna cues predominate. We also noted that, in the speech test, separation S/N ratios were highly correlated with respective SIN values. Because of this, separation S/N ratios are not included in the initial (correlation) analyses, as they add little to the picture derived from SIN scores. Finally, for the purposes of comparative analysis, the data from the low and high sensorineural groups have been combined.

1. Correlations between tests

The interest in the present study is to observe relations among the spatial and speech hearing tests when effects due to HTL are accounted for. As a first approach, partial correlations were calculated, to see whether connections remained among test results when common correlations with HTL were partialled out. This analysis suggested that, at least in the sensorineural group, there was little in the way of direct relationships between localization, separation benefit in the speech test, and sensitivity to spatial separateness. This was especially so in the frontal orientation, where partial correlations were either close to zero or in unexpected, hence uninterpretable, directions. In the lateral orientation, there were slight signs of direct relationships (Table II) between the spatial and speech tests, and, for the most part, in expected directions. Generally negative partial correlations remained between localization and both benefit and spatial separateness performance, indicating that as localization error score increased, benefit from separation and separateness sensitivity decreased. The positive partial correlation between LHP localization and SIN S/N ratio is expected: As the localization error score increases so does the S/N ratio required for 50% intelligibility.

In the conductive-mixed group the picture is clearer, as may be seen from the values in Table III. There are positive partial correlations between the magnitude of localization error and SIN S/N ratio, negative correlations between localization error and separateness detection, a negative relation between SIN and separateness detection in the horizontal plane, and positive correlations between separation benefit and separateness detection in the vertical plane. In

TABLE II. Partial correlations, controlling for HTL, among scores for localization, speech in nonspatially separate noise (SIN), separation benefit at 18° and 54°, and spatial separateness (SS) detection (d' scores) at 18° and 54°, in the lateral orientation, for the sensorineural group.

	SIN	Benefit 18°	Benefit 54°	SS 18°	SS 54°
LHP localization	0.28 ^a	0.16	−0.01	−0.06	−0.15
LVP localization	0.06	−0.03	−0.16	−0.1	−0.19
SIN		0.25 ^a	0.19	0.08	−0.14
Benefit 18°				0.02	0.04
Benefit 54°				0.17	0.02

^a $p < 0.05$.

some cases these partial correlation values are substantial, and in all cases they are in expected directions.

2. Multiple regression analyses

Our interest is also in the connections among the set of spatial hearing tests, and the ability to hear speech in noise, so it is appropriate to regress the former on the latter. For this purpose, the sensorineural group data provide a large enough data set, with results for between 32 and 41 people, depending on the variables included. Stepwise regression analysis, using a criterion of $F=2$ to enter, was undertaken on the three components of measurement on the speech test: SIN S/N ratio, separation S/N ratios, and separation benefit. For the SIN measure, the independent variables of interest were: localization, separateness detection, and HTL. For the frontal SIN condition both the FHP and FVP localization and separateness scores were included. For separation benefit and separation S/N ratios in the frontal horizontal plane, only horizontal plane spatial tests and HTL were included in regression on the speech test scores. Only vertical spatial tests and HTL were used for regression on VP speech test scores. In the lateral orientation, both HP and VP spatial test variables, plus HTL, were included in the regression analyses for 18° and 54° separation benefit and separation S/N ratios. The results of these analyses are shown in Table IV. Because of variations in the sample size and the number of independent variables, the critical value for R^2 varies, as indicated in the Table.

HTL enters the equation first in the regression on frontal plane SIN and separation S/N ratios, followed by localization. In the lateral orientation, localization and signal separateness tests dominate in the equivalent regressions. There is no relation among the other variables and frontal horizontal separation benefit scores, but a very slight involvement of FVP spatial separateness at 54° of separation (identified as

SS 54°V in the table) in frontal vertical separation benefit. Only HTL shows up in relation to lateral separation benefit. A further examination of separation benefit in each lateral plane revealed a weak involvement of 54° and then 18° spatial separateness detection for 18° LVP benefit (final $R^2 = 0.21$).

The conductive-mixed sample is too small for reliable regression analysis. Partial correlation between HP signal separateness and SIN, controlling for HP localization, was −0.44; localization controls the greater part of the variance in that relationship, yet the remaining correlation is in the expected direction. The partial correlation between HP separateness and separation S/N ratio, controlling for HP localization, is −0.43, again in the expected direction. Only the 18° vertical separateness score remains correlated in the expected direction with VP S/N ratio, after partialling out the effect of VP localization. The correlation between HP separateness and benefit from separation, controlling for HP localization, is 0.14; those between 18° and 54° VP separateness and VP benefit, controlling for VP localization, are 0.36, and 0.23, respectively, all in the expected direction.

III. DISCUSSION

Different outcomes were observed between the sensorineural and conductive-mixed groups. This can be expected given the nature of the two types of disorder. Both groups will show some common effects due to inaudibility of signal components, but the sensorineural group will also have various problems in time and frequency resolution which the conductive-mixed group will experience less or not at all (Zwicker and Schorn, 1978; Florentine *et al.*, 1980). By contrast, the conductive-mixed group will show reduced cochlear isolation compared with the sensorineural group due to an increased portion of energy transmitted to the cochleas via the skull (Zurek, 1986). We discuss the results obtained,

TABLE III. Partial correlations (controlling for HTL) among scores for localization, SIN, separation benefit, and spatial separateness (SS) detection at 18° and 54°, in the frontal orientation, for the conductive-mixed group.

	SIN	Benefit FHP	Benefit FVP	SS FHP	SS 18° FVP	SS 54° FVP
FHP localization	0.49	−0.09		−0.48		
FVP localization	0.71 ^a		0.08		0	−0.3
SIN		0.01	0.12	−0.57 ^a	0.04	−0.08
Benefit FHP				−0.06		
Benefit FVP					0.33	0.33

^a $p < 0.05$.

TABLE IV. Stepwise multiple regression analyses on three measures of speech hearing in noise: (1) Speech in nonseparated noise (SIN), (2) Separation S/N ratio, (3) Separation benefit. Dependent variables (DV, the speech measures) are in the frontal and lateral regions for SIN, in the frontal horizontal and vertical planes and 18° and 54° of lateral separation (across both planes) for separation S/N ratios and separation benefit scores. Independent variable/s (IV/s) that entered the equations on a criterion of $F=2$ are shown in their order of entry, and effect on R^2 . Critical values for $\alpha=0.05$ are shown in parentheses in respective cells.

Order	SIN			Separation S/N ratio			Separation benefit		
	DV	IV(s)	R^2	DV	IV(s)	R^2	DV	IV(s)	R^2
1	Frontal	HTL	0.29	FHP S/N	HTL	0.37	FHP benefit	none	-
2	(0.33)	FHP localization	0.34	(0.18)	FHP localization	0.42			
1	////////	//////	///	FVP S/N	HTL	0.31	FVP benefit	SS 54° V	0.1
	////////	//////	///	(0.27)			(0.27)		
1	Lateral	LHP localization	0.53	18° S/N	LHP localization	0.61	18° benefit	HTL	0.11
2	(0.26)	SS 54°	0.58	(0.26)			(0.26)		
1	////////	//////	///	54° S/N	LHP localization	0.66	54° benefit	HTL	0.18
2	////////	//////	///	(0.26)	SS 54°	0.68	(0.26)		
3	////////	//////	///		HTL	0.71			

looking at the two groups in order, but consider localization only briefly, as results confirmed earlier reported findings (Noble *et al.*, 1994).

A. Test outcomes

1. Localization

a. Sensorineural group. Whereas the audibility of dominant low-frequency time–phase cues can explain the relatively proficient FHP performance, the inaudibility (and distortion, if audible) of higher-frequency pinna-generated spectral transforms can explain the poor VP performance of the sensorineural group. A combination of lower-frequency interaural time differences with such slight pinna cues as remain audible may explain the small improvement in lateral over frontal VP performance, though, overall, VP sources were not well localized. The relative inaudibility and/or distortion of a cue around 4–6 kHz which seems to have significance for front–rear discrimination (Weinrich, 1982) may account for the reduction in lateral HP accuracy compared with frontal.

b. Conductive-mixed group. There is a marked effect on FHP localization of a conductive-mixed hearing loss. This has been argued to arise because cochlear isolation is not preserved, and normal interaural time–phase differences are disrupted (Noble *et al.*, 1994).

2. Speech in noise

a. Sensorineural group. This group shows considerable disability in hearing speech in noise, and very little sign of benefit from spatial separation, confirming earlier reports. This is seen especially in the VP, and even among those with lesser degrees of hearing loss (Fig. 3), suggesting that suprathreshold frequency distortion effects may make it difficult for these listeners to take advantage of spectral cues. We observed negative values in some separation conditions suggesting that spatial separation of signals from noise may worsen intelligibility. Caution is needed in generalizing such a conclusion. The measurement of speech and noise levels in different spatial positions is a complex procedure (Ter-Horst *et al.*, 1993), and we cannot be completely certain that mea-

sured levels of each type from each place will coincide with relative levels experienced by different listeners, as these will often be modified by head shadow effects that vary due to intra- and interaural disparities in hearing at different frequencies. It can certainly be concluded that the effect of separation in the case of even mild hearing loss contrasts markedly with its effect under normal hearing conditions.

There are different outcomes across planes and orientations between impaired and normal groups. With normal hearing, separation of speech and noise in the lateral orientation and in the frontal vertical plane has clearly beneficial effects that increase with increasing separation; by contrast the separation benefit in the frontal horizontal plane remains fairly constant with increasing (symmetrical) separation (Ter-Horst *et al.*, 1993). In the present study, the low sensorineural group followed this pattern, though at a much lower level of benefit than the normal group. The high sensorineural group showed even fewer signs of benefit, and a smaller amount of improvement with increasing separation. We interpret this result to indicate that, with lower levels of hearing loss, the possible benefit of a small amount of separation in lateral and frontal vertical regions of space is slight, while the possible benefit of a large amount of separation can be taken advantage of. With more severe levels of hearing loss, even a large amount of separation provides little increased benefit. The difference between frontal and lateral regions may be accounted for by the fact that, in the lateral region, interaural localization cues are less distinct than in front (Butler *et al.*, 1990), and with greater levels of hearing loss, particularly in the high frequencies, pinna-derived cues are less able to compensate.

The effect for hearing impaired listeners of spatially separating speech and noise was typically very minor, suggesting it may be difficult to observe the true correlates of separation benefit. The relative ineffectiveness is also seen in the very high correlations between SIN and separation S/N ratios. The hearing impaired listeners were not responding to the two forms of the task in obviously different ways, indicating they may not have been sensitive to the difference between the nonseparate versus separate conditions. As

stated earlier, the symmetrical arrangement of noise sources, and their being correlated, may not allow a genuine “separation” condition, as the noise could perceptually “fuse” and be heard as coming from the same place as the speech. The data for the normal control group in the FHP show a comparatively unchanging function with increasing extents of separation, a result consistent with a “fused” image account (there is nonetheless an immediate benefit from 18° of FHP separation, in both normal and impaired groups, which is hard to explain under a “fusion” account).

The normal hearing group showed clearly increasing benefit with increasing separation in the other three spatial regions. We see this as likely due to asymmetrical spectral changes introduced in those planes through directionally different head-related transfer functions for the two noise sources. For the low sensorineural subgroup, the slightly greater signs of separation benefit in the lateral orientation, especially at 54° of separation, is consistent with such an explanation as derived from the normal group’s performance. Some people in the low sensorineural subgroup would have been able to detect some of the distinctions introduced by displacements of the noise.

b. Conductive-mixed group. The lesser impact of noise on speech intelligibility in the conductive-mixed group, compared with the sensorineural group, and the slightly greater benefit from separation, may reflect the lower degree of distortion experienced by people with conductive loss relative to that experienced by people with sensorineural loss.

3. Spatial separateness

a. Sensorineural (and normal) groups. This is a new test, though it may be related to minimum audible angle. The question of detecting spatial separateness has been an issue in the study of intersensory interaction, as in the “ventriloquism” phenomenon (Warren *et al.*, 1981), but we are not aware of studies examining purely auditory detection of spatial separation. The task, which involved telling if two different signals were located in the same place or in different places, is distinctly more difficult in the frontal vertical than horizontal planes, which parallels the results for the localization test.

In the lateral orientation, both normal and hearing impaired listeners have difficulty with 18° of horizontal separation, which may best be explained by the fact that, because the rate of change of interaural differences is less marked in the region around the interaural axis, localization in that region is less acute also (Mills, 1972). Performance recovers at 54° of HP separation, but not fully for the high sensorineural subgroup [Fig. 4(b)]; the task may require access to spectral and loudness differences, as well as interaural time difference information, to enable proficient detection of the spatial gap, and those cues are likely to be inaudible or distorted for the poorer hearing group. This explanation is supported by the contrast, at 18° of lateral vertical separation, between normal and *both* of the sensorineural subgroups. Interaural time/level differences are about the same in the lateral vertical as in the lateral horizontal planes; the listeners with normal hearing presumably have greater access to fine differences in the spectra of the signals at high frequencies,

enabling them to detect the small vertical spatial gap more readily than those with high-frequency hearing loss. The differential recovery of the low versus high sensorineural subgroup at 54° of VP separation parallels the more marked difference in benefit from separation in the lateral region for the two groups, suggesting that the separateness task shares features with both the localization and speech tests.

b. Conductive-mixed group. The pattern of this group’s responses supports the argument for commonality of the separateness task with elements of both the localization and speech in noise measures. There is poorer VP than HP performance, which mirrors the localization test; there is proportionately less effect on VP performance compared with the sensorineural group, at 18° of separation (Table I), which is akin to the outcome for the speech test.

B. Relationships among tests

1. Sensorineural group

Scrutiny of the SIN result in relation to separation S/N ratios led to a recognition that, at least in frontal conditions, the two measures were almost identical. This suggests that separation is not very distinct from nonseparation as a condition, hence that the connections with localization are not specific to SIN or separation conditions, but reflect a more general feature common between elements of the two functions. (It needs to be accepted also that, at least in the frontal horizontal plane, perceptual “separation” of speech and noise may not have occurred.) The multiple regression analyses show a role for localization in prediction of either form of the speech test score. We observe in this context that a recent account of cortical representation of spatial whereabouts (Middlebrooks *et al.*, 1994) identifies a code based on temporal patterns. The common feature linking localization and SIN (or separation S/N ratio) may have to do with temporal properties of the auditory system. These are known to have a dominant place in the capacity to hear speech in noise (Schorn and Zwicker, 1990).

In the lateral orientation, localization and spatial separateness are the principal predictors of SIN and separation S/N ratios. With regard to separation benefit, a role for signal separateness is suggested when components of the speech separation benefit score are analyzed.

2. Conductive-mixed group

The results from the conductive-mixed sample show clear and meaningful links among localization, signal separateness, and SIN; and some signs of connection with separation benefit, at least in the vertical plane. The conductive-mixed group have lower levels of distortion of suprathreshold signals. Although HP localization is poorer than in the sensorineural group, this is more for reasons of mechanical transmission than due to distortions in the auditory system at and beyond the cochlea. The comparative absence of suprathreshold distortion may be why there is slightly better proficiency in VP signal separateness and separation benefit. The VP is a spatial region offering frequency-based (spectral) cues for detection of the spatial gap. The greater clarity in test inter-relationships in the

conductive-mixed group may also be a reflection of slightly better access to cues that are arguably common across elements of each test.

IV. CONCLUSION

Spatial hearing is a significant part of hearing function. The detection of the presence of critical signals, such as speech, in real conditions, is accomplished along with detection of their whereabouts. Such detection often goes on in contexts where there is competition between those signals requiring attention and those that represent interfering noise. Spatial separation of a speech sound from such interference seems to benefit perception of the speech signal.

The question pursued in this study was whether there is a role for spatial hearing ability in being able to benefit when hearing speech in conditions of spatially separated as opposed to nonseparated noise. Samples were tested in which hearing ability varied, and analysis was undertaken controlling for the factors of degree and type of hearing loss. Spatial hearing was tested in two ways: by means of single-source (identification) localization, and by a test for detection of the spatial separateness of two simultaneous sounds. Almost no consistent links could be observed between ability in the localization test and benefit from separation on the speech test. Somewhat more consistent signs were seen between separation benefit and results in the spatial separateness test. Furthermore, connections were evident between the two spatial hearing tasks. This pattern was clearer in a sample with conductive-mixed hearing loss than in one with sensorineural loss. We thus may conclude that spatial hearing does play a (limited) role in speech hearing in noise, with the connection between these functions being more readily observed in forms of impaired hearing that exhibit fewer signs of distortion in the auditory system itself.

ACKNOWLEDGMENTS

Thanks to Dean Davidson for computer programming at various levels of this project. Thanks also to Harvey Dillon, and to the journal's reviewers, for valuable comments on earlier versions of the paper. The study reported here was supported by a grant from the National Health and Medical Research Council of Australia.

- Begault, D. R., and Wenzel, E. M. (1993). "Headphone localization of speech," *Hum. Factors* **35**, 361–376.
- Bronkhorst, A. W., and Plomp, R. (1989). "Binaural speech intelligibility in noise for hearing-impaired listeners," *J. Acoust. Soc. Am.* **86**, 1374–1383.
- Bronkhorst, A. W., and Plomp, R. (1992). "Effect of multiple speechlike maskers on binaural speech recognition in normal and impaired hearing," *J. Acoust. Soc. Am.* **92**, 3132–3139.
- Butler, R. A. (1994). "Asymmetric performances in monaural localization of sound in space," *Neuropsychology* **32**, 221–229.
- Butler, R. A., Humanski, R. A., and Musicant, A. D. (1990). "Binaural and monaural localization of sound in two-dimensional space," *Perception* **19**, 241–256.
- Byrne, D., Noble, W., and Lepage, B. (1992). "Effects of long-term bilateral and unilateral fitting of different hearing aid types on the ability to locate sounds," *J. Am. Acad. Audiol.* **3**, 369–382.
- Chocholle, R., Chedru, F., Botte, M. C., Chain, F., and Lhermitte, F. (1975). "Etude psychoacoustique d'un cas de 'surdit  corticale'," *Neuropsychology* **13**, 163–172.
- Florentine, M., Buus, S., Scharf, B., and Zwicker, E. (1980). "Frequency selectivity in normally-hearing and hearing-impaired observers," *J. Speech Hear. Res.* **23**, 646–669.
- Gardner, M. B. (1973). "Some monaural and binaural facets of median plane localization," *J. Acoust. Soc. Am.* **54**, 1489–1495.
- Glasberg, B. R., and Moore, B. C. (1989). "Psychoacoustic abilities of subjects with unilateral and bilateral cochlear hearing impairments and their relationship to the ability to understand speech," *Scand. Audiol. Suppl.* **32**.
- H usler, R., Colburn, S., and Marr, E. (1983). "Spatial localization in subjects with impaired hearing," *Acta Oto-Laryngol. Suppl.* **400**, 1–61.
- Hebrank, J., and Wright, D. (1974). "Spectral cues used in the localization of sound sources on the median plane," *J. Acoust. Soc. Am.* **56**, 1829–1834.
- Hirsh, I. J. (1950). "The relation between localization and intelligibility," *J. Acoust. Soc. Am.* **22**, 196–200.
- Kuhn, G. F. (1987). "Physical acoustics and measurements pertaining to directional hearing," in *Directional Hearing*, edited by W. A. Yost and G. Gourevitch (Springer-Verlag, New York), pp. 3–25.
- Licklider, J. C. R. (1948). "The influence of interaural phase relations upon the masking of speech by white noise," *J. Acoust. Soc. Am.* **20**, 150–159.
- Macmillan, N. A., and Creelman, C. D. (1991). *Detection Theory: A User's Guide* (Cambridge U. P., Cambridge, England).
- McKinley, R. L., Erickson, M. A., and D'Angelo, W. R. (1994). "3-Dimensional auditory displays: Development, applications, and performance," *Aviat. Space Environ. Med.* **65**, A31–A38.
- Middlebrooks, J. C., and Green, D. M. (1991). "Sound localization by human listeners," *Annu. Rev. Psychol.* **42**, 135–159.
- Middlebrooks, J. C., Clock, A. E., Xu, L., and Green, D. M. (1994). "A panoramic code for sound location by cortical neurons," *Science* **264**, 842–844.
- Mills, A. W. (1972). "Auditory localization," in *Foundations of Modern Auditory Theory*, edited by J. V. Tobias (Academic, New York), Vol. II, pp. 303–348.
- Noble, W. (1981). "Earmuffs, exploratory head movements, and horizontal and vertical sound localization," *J. Aud. Res.* **21**, 1–12.
- Noble, W., Byrne, D., and LePage, B. (1994). "Effects on sound localization of configuration and type of hearing impairment," *J. Acoust. Soc. Am.* **95**, 992–1005.
- Noble, W., Ter-Horst, K., and Byrne, B. (1995). "Disabilities and handicaps associated with impaired auditory localization," *J. Am. Acad. Audiol.* **6**, 129–140.
- Platte, H.-J., D ring, W. H., and Schl ndorff, G. (1978). "Richtungsh ren und Sprachverstehen unter St rschalleinfl   bei Normalh renden," *Laryngol. Rhinol. Otol.* **57**, 672–680.
- Schorn, K., and Zwicker, E. (1990). "Frequency selectivity and temporal resolution in patients with various inner ear disorders," *Audiology* **29**, 8–20.
- Saberi, K., Dostal, L., Sadralobadi, T., Bull, V., and Perrott, D. R. (1991). "Free-field release from masking," *J. Acoust. Soc. Am.* **90**, 1355–1370.
- Searle, C. L., Braida, L. D., Cuddy, D. R., and Davis, M. F. (1975). "Binaural pinna disparity: Another auditory localization cue," *J. Acoust. Soc. Am.* **57**, 448–455.
- Ter-Horst, K., Byrne, D., and Noble, W. (1993). "Ability of hearing-impaired listeners to benefit from separation of speech and noise," *Aust. J. Audiol.* **15**, 71–84.
- Walker, G., and Byrne, D. (1985). "Reliability of speech intelligibility estimation for measuring speech reception threshold in quiet and in noise," *Aust. J. Audiol.* **7**, 23–31.
- Warren, D. H., Welch, R. B., and McCarthy, T. J. (1981). "The role of visual-auditory compellingness in the ventriloquism effect: Implications for transitivity among the spatial senses," *Percept. Psychophys.* **30**, 557–564.
- Weinrich, S. (1982). *The problem of front-back localization in binaural hearing*, Tenth Danavox Symposium, Klarskovg rd, Denmark (Scand. Audiol. Suppl. **15**, 135–146).
- Wightman, F. L., and Kistler, D. J. (1992). "The dominant role of low-frequency interaural time differences in sound localization," *J. Acoust. Soc. Am.* **91**, 1648–1661.
- Zurek, P. M. (1986). "Consequences of conductive auditory impairment for binaural hearing," *J. Acoust. Soc. Am.* **80**, 466–472.
- Zwicker, E., and Schorn, K. (1978). "Psychoacoustical tuning curves in audiology," *Audiology* **17**, 120–140.

The development of speech adaptation to an artificial palate

Shari R. Baum

School of Communication Sciences & Disorders, McGill University, 1266 Pine Avenue W., Montréal, Québec H3G 1A8, Canada

David H. McFarland^{a)}

École d'orthophonie et d'audiologie, Université de Montréal CP 6128, Succursale Centre-Ville, Montréal, Québec H3C 3J7, Canada

(Received 1 May 1997; accepted for publication 2 July 1997)

An investigation of adaptation to palatal modification in [s] production was conducted using acoustic and perceptual analyses. The experiment assessed whether adaptation would occur subsequent to a brief period of intensive, target-specific practice. Productions of [sa] were elicited at five time intervals, 15 min apart, with an artificial palate in place. Between measurement intervals, subjects read [s]-laden passages to promote adaptation. Results revealed improvement in both acoustic and perceptual measures at the final time interval relative to the initial measurement period. Interestingly, the data also suggested changes to normal (unperturbed) articulation patterns during the same interval. Results are discussed in relation to the development of speech adaptation to a structural modification of the oral cavity. © 1997 Acoustical Society of America. [S0001-4966(97)03910-6]

PACS numbers: 43.70.Aj [AL]

INTRODUCTION

A fundamental question, and one that has dominated much of the experimental inquiry into speech production, is to what extent, if any, sensory feedback interacts with central control signals in the control and coordination of speech movements (McFarland and Lund, 1995; Smith, 1992). Observing speech compensation to dynamic and static oral-articulatory perturbations has provided valuable insights into the potential role of sensory feedback in the control of speech gestures. Numerous investigations have demonstrated that speakers are able to relatively easily and rapidly adapt to many perturbations to the articulatory system (e.g., Abbs, 1986; Kelso and Tuller, 1983; Lindblom *et al.*, 1979; Warren *et al.*, 1980, 1984), suggesting predictive processes of speech motor programming. Nonetheless, more recent data suggest that compensation depends to some extent on the nature of the perturbation, the specific speech sounds targeted, and individual articulatory strategies adopted by speakers (Flege *et al.*, 1988; McFarland and Baum, 1995; Munhall *et al.*, 1994; Savariaux *et al.*, 1995).

Further, and in contrast to much of the data on perturbations that inhibit specific movements [e.g., fixation of the mandible by a bite block or application of a load to the lower lip (Gay *et al.*, 1981; Kelso and Tuller, 1983; Lindblom *et al.*, 1979; Lubker, 1979; but cf. Baum *et al.*, 1996; Flege *et al.*, 1988; Fowler and Turvey, 1980; McFarland and Baum, 1995)], a great deal of data have shown that compensation for a structural change to the oral environment (e.g., an artificial palate) may require a much more lengthy period of adaptation (Hamlet, 1973; Hamlet and Stone, 1974, 1978; Hamlet *et al.*, 1979). The presence of an artificial palate in the mouth has been found to result in increased duration of

the sibilant consonants and an increased number of articulatory errors, particularly as palatal thickness increases (Hamlet, 1973; Hamlet and Stone, 1974, 1978; Hamlet *et al.*, 1979). The sibilants tend to be most affected due to the apparent requirement of a precise positioning of the tongue relative to the palatal surface for their accurate production (Flege *et al.*, 1988).

In a previous experiment, McFarland *et al.* (1996) reported significant changes in fricative ([sʃ]) spectra with and without an artificial palate in place. The palates were found to be particularly perturbing to [s] articulation due to increased thickness at the alveolar ridge. Even after a 15-min period of conversation with the palate in place, spectral energy concentrations for [s] were significantly lower than under normal conditions. In addition, the differences were found to be perceptually salient to a group of naive listeners.

Studies have shown that speech gradually improves following the insertion of an artificial palate (Hamlet and Stone, 1976a, b; Hamlet *et al.*, 1978; Hamlet and Stone, 1978) but that normal speech may not be re-acquired for several days or weeks. The period of progressive improvement may reflect the development of new articulatory patterns to accommodate the structural change (McFarland *et al.*, 1996). It is of particular interest to determine the factors which contribute to the development of these new articulatory routines and the role that various types of sensory feedback may play in such adaptation. For example, many studies have suggested that sensory feedback (particularly auditory feedback) is very important in the development of speech motor control (Borden, 1979; Osberger and McGarr, 1982; Smith, 1992) but its role in mature speech production is less clear (e.g., Matthies *et al.*, 1994, 1996; Perkell *et al.*, 1992; Waldstein, 1990). By perturbing the articulatory system in certain specific ways, we can observe the response and requirements of a mature system in the development of novel articulatory movements.

^{a)}Electronic mail: mcfarlad@ere.umontreal.ca

TABLE I. Characteristics of the palate for each subject.

Subject	Shape of palate	Width of palate (at molars) (mm)	Length of palate (at molars) (mm)	Depth of palate (at molars) (mm)	Width of anterior palate (at cuspids) (mm)	Length of anterior palate (at cuspids) (mm)	Depth of anterior palate (at cuspids) (mm)
1	slightly V	43	36	17	32	13	7
2	V shaped	48	36	21	33	12.5	11.5
3	U shaped	46	38	19	32.5	14	11
4	U shaped	46	37	20	33	16	13.5
5	V shaped	45	40	20	32	14.5	14
6	U shaped	46.5	37	17	33.5	12	10
7	Slightly V	45	37	18	31.5	12	15

In so doing, we may identify the factors which are critical to successful adaptation, as well as those which impede compensation. We may also be able to determine whether adaptation can, by some means, be facilitated, perhaps by increasing the intensity of practice or adjusting the feedback provided.

In order to experimentally investigate the adaptation period in otherwise normal speakers, it is necessary to first determine whether the time required can be reduced to a period manageable in the laboratory. In previous studies that have examined compensation over time, observations of speech production were recorded longitudinally (e.g., over a period of several days or weeks (Hamlet, 1973; Hamlet and Stone, 1974, 1978; Hamlet *et al.*, 1979), but there were no controls on the speech activity during those intervals. Each individual subject may thus have had varying amounts of practice with the artificial palate in place, with varying degrees of target sound production even during similar time frames.

Our goal in the present investigation was to examine the adaptation process in order to facilitate the understanding of fundamental mechanisms involved and to ultimately explore the role of sensory feedback in speech adaptation. As a preliminary step, then, we sought to ascertain whether adaptation would occur subsequent to intensive, target-specific practice. If adaptation occurs within a relatively brief period (relative to the lengthy period reported in previous investigations; Hamlet, 1973; Hamlet and Stone, 1974, 1978; Hamlet *et al.*, 1979), various types of feedback can be systematically modified or eliminated in order to determine their role in articulatory compensation to a structural modification.

The objective of the present investigation was, therefore, to examine speakers' ability to compensate for the insertion of an artificial palate with a thicker than normal alveolar region in [s] production, over a relatively brief period of time, given intensive, focused practice. Both acoustic and perceptual analyses were utilized to determine whether a 1-h period of [s] practice would allow speakers to modify their established articulatory programs in order to compensate for the presence of an artificial palate to produce perceptually and acoustically adequate [s] tokens.

I. METHODS

A. Acoustic analyses

1. Subjects

The subjects included seven adult female native speakers of (Québec) French, with a mean age of 23 years. Six of the subjects (with the exception of S7) had participated in a previous study of compensation to palatal modification (McFarland *et al.*, 1996).¹ All subjects were free from current or prior history of speech, language, and hearing deficits. Measurements of palate width, depth, and length from specified landmarks were calculated from dental impressions made for each individual. These values are displayed in Table I.

2. Stimuli and procedures

An artificial palate was constructed for each subject from dental acrylic. The palate was fabricated such that a 6-mm ridge extruded near the alveolar ridge, at the midline of the cuspid-to-cuspid plane from the incisive papilla to 2 mm posterior to the cuspids, in order to perturb normal [s] production. The palate tapered to 1 mm posterior to that plane and was fitted with ball clasps to hold it in place. Figure 1 illustrates the palatal configuration in mid-sagittal (a) and inferior (b) views. (For six of the subjects, the palate had been made for a previous experiment.) The target stimulus, [sa], was elicited 30 times at each of five time intervals, 15 min apart, with the palate in place—that is, at 0, 15, 30, 45, and 60 min. In addition, at time 0 (prior to any practice) and time 60 (after 60 min of practice), 30 repetitions of [sa] were elicited under normal conditions (i.e., with no artificial palate). At these two test intervals, three blocks of ten tokens were produced alternately in the normal and perturbed conditions, beginning with the normal condition. That is, ten normal tokens were followed by ten tokens with the palate in place, and so on. At all other times during the 60-min interval the palate was in place; speakers were instructed to produce normal [s] but were given no specific instructions regarding maximizing the quality of their productions.

Stimuli were presented in orthographic form on a computer screen every 5 s and subjects were instructed to read each stimulus as it appeared. The palate was removed and inserted by the subject as necessary. Between time intervals, subjects were required to read aloud passages specially constructed to be heavily laden with [s] for 15 min in order to

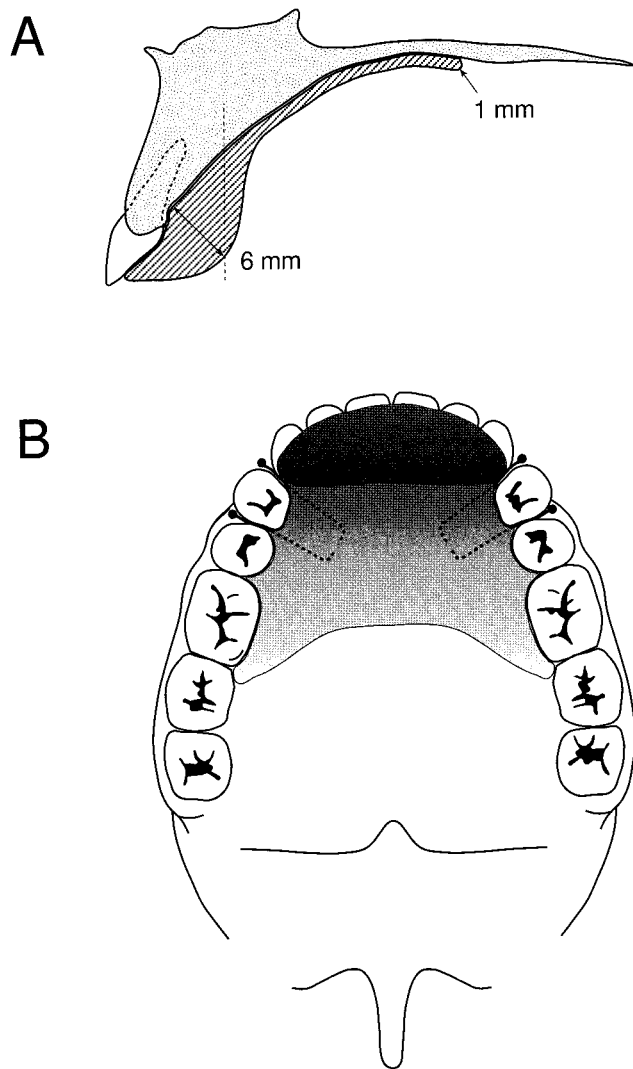


FIG. 1. Artificial palate configuration in mid-sagittal (a) and inferior (b) views. The vertical dotted line in (a) indicates the point at which (distal to the cuspids) the appliance begins to taper to 1-mm thickness.

promote adaptation to the perturbation. On average, during each 15 min interval, each subject produced 665 [s] tokens in a variety of phonetic environments, for an average total of 2660 productions. Recordings of the target utterances were made in a sound-treated room using a Sony DTC-57ES digital tape recorder and head-mounted directional microphone (AKG-HD421U) to ensure a constant distance from the microphone to the speaker's mouth.

3. Analyses

The 30 [sa] productions at each time interval with the palate in place, as well as the 30 repetitions produced under normal conditions at time 0 and time 60 were digitized at a rate of 20k samples/s with 12-bit quantization and a 9-kHz low-pass filter, using the BLISS speech analysis system (Mertus, 1989). A 20-ms full Hamming window was placed at the midpoint of each fricative and a centroid frequency was computed from Fourier analysis. The centroid is the first moment of the spectral distribution and represents a weighted average of the spectral peak frequencies. It has

been used previously to characterize the quality of fricative production and as an indicator of degree of adaptation to articulatory perturbation (Forrest *et al.*, 1988; McFarland and Baum, 1995; McFarland *et al.*, 1996). Although spectral moments may not reliably serve to singularly differentiate fricatives from one another (Shadle and Mair, 1997), under normal conditions with a constant frequency range and vowel environment, the centroid (or first spectral moment) remains relatively stable for a given fricative (Shadle and Mair, 1997) and may reflect, in part, the point of constriction within the vocal tract. We thus chose to concentrate our analyses on the centroid frequency (first spectral moment) as a reflection of the accuracy of [s] production.

B. Perceptual analyses

1. Subjects

The listeners in this experiment were ten native (Québec) French-speaking adults with training in speech-language pathology who were familiar with assessments of articulatory quality. None of the listeners had participated as a speaker in experiment 1.

2. Stimuli

From the recorded stimuli of experiment 1, those productions elicited at time 0 and time 60 in both the palate and normal conditions were utilized in the perception test. Five randomly selected tokens for each of seven speakers in each palate condition were included, for a total of 140 [sa] stimuli presented in random order. In addition, ten "high-quality" exemplars and ten "poor" exemplars were presented to listeners prior to the experimental stimuli as a training set. These stimuli had been selected by the experimenters based on their acoustic and perceptual attributes. The "poor" exemplars were those whose centroid frequencies were furthest from the normal (unperturbed) mean; the "high-quality" exemplars were all taken from the set of normal productions (at time 0), based on perceptual judgments by the experimenters.

3. Procedure

Auditory stimuli were presented to listeners individually over headphones (Sony MDR 7506) in a sound-treated room, along with a visual analogue scale of 10 cm in length, with the endpoints marked as "unintelligible" and "perfect." There was a 5-s interstimulus interval for the rating and subjects were given a short break at the midpoint of the experiment. Listeners were instructed to rate the quality of each production (concentrating solely on the fricative [s]), based on the training samples and their clinical experience, by making a mark at an appropriate point along the 10-cm scale.

II. RESULTS

A. Acoustic analyses

Mean centroid frequencies were calculated at each time interval for the normal and palate conditions separately. (The normal conditions only appeared at time 0 and time 60.) These data are displayed in Fig. 2, collapsed across subjects.

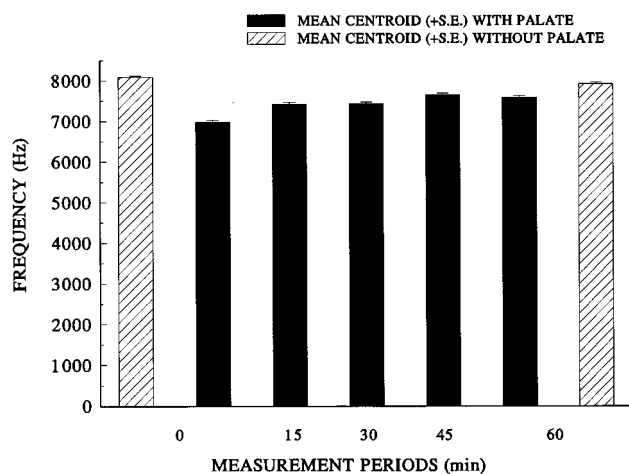


FIG. 2. Mean centroid frequencies (+s.e.) at each time interval for the normal and palate conditions. (The normal conditions only appeared at time 0 and time 60.)

A one-way analysis of variance (ANOVA) comparing centroids in the five palate conditions revealed a main effect for test interval [$F(4,24)=14.87$, $p<0.001$]. Multiple comparisons across intervals demonstrated significant differences between time 0 and all other intervals; in addition, time 15 and time 30 differed significantly from time 45. The improvement in compensation at the later time intervals (i.e., at time 60 relative to time 0) was shown by each individual subject, as may be seen in Table II which displays the centroid values for each subject at the five test intervals. Although one might have expected a reduction in variance across intervals, as shown in Table II, no consistent pattern emerged across subjects' standard error values.

ANOVAs were also conducted to assess the effect of the palatal perturbation at time 0 and time 60. A test interval \times palate condition ANOVA revealed significant main effects of test interval [$F(1,6)=6.12$, $p<0.05$] and palate condition [$F(1,6)=65.61$, $p<0.001$], and a significant test interval \times palate condition interaction [$F(1,6)=79.94$, $p<0.001$]. Simple effects analyses showed a significant effect of the palate at time 0 [$F(1,6)=141.97$, $p<0.001$], with centroids in the palate condition lower than those in the normal condition (an average difference of 1102 Hz). At time 60,

there was still a significant difference between centroids in the normal and palate conditions [$F(1,6)=11.63$, $p<0.02$], but the magnitude of the difference was much smaller (an average of 329 Hz). Three subjects (S2, S6, S7) displayed the smallest differences between conditions at time 60. An examination of the palatal characteristics of these three individuals revealed no apparent structural explanation for their better performance (see Table I). It is interesting to note that S7 was the one subject who had not had any previous experience with the palate in place and performed similarly to several other subjects.

Finally, a comparison of the normal conditions at time 0 and time 60 was undertaken. Somewhat surprisingly, a significant main effect of test interval was found [$F(1,6)=5.85$, $p<0.05$]. However, the difference in average centroid frequency at the two intervals was quite small, at 175 Hz. In contrast, the difference in average centroid frequency at those same two intervals in the palate conditions was 598 Hz. In addition, for all speakers, the standard errors were slightly higher in the normal condition at T60 relative to T0.

B. Perceptual analyses

The rating values were calculated in millimeters (mm) for each stimulus and means for each palate/time-interval condition were computed. The average ratings (with standard errors) for the four conditions are displayed in Fig. 3. As may be seen, at both time 0 and time 60, the ratings for the palate conditions were lower than those for the normal productions, but the values approximated one another more closely at the later test interval. A test interval \times palate condition ANOVA conducted on the ratings (with listener as a random factor) revealed a main effect for palate condition [$F(1,9)=98.118$, $p<0.001$] and a test interval \times palate condition interaction [$F(1,9)=33.552$, $p<0.001$].²

Post hoc analysis of the interaction using the Newman-Keuls procedure ($p<0.01$) demonstrated that all conditions were significantly different from one another. Of particular interest is the direction of change from time 0 to time 60 for the palate as compared to the normal conditions. In the palate conditions, quality ratings improved substantially from the initial test interval to the final interval; in stark contrast, quality ratings for the normal stimuli decreased over that same

TABLE II. Mean (+s.e.) of [s] centroid frequencies for each subject.

Subject	With palate						
	Without palate	Measurement periods					Without palate
	0	0	15	30	45	60	60
1	8233 (51)	7356 (70)	7646 (76)	7824 (81)	7992 (84)	8116 (59)	8381 (55)
2	7961 (40)	7299 (63)	7838 (65)	7972 (56)	7847 (65)	7721 (68)	7792 (68)
3	8232 (69)	6956 (80)	7485 (90)	7518 (134)	7681 (77)	7590 (119)	8124 (71)
4	8071 (58)	6854 (190)	7675 (157)	7515 (182)	7867 (72)	7509 (149)	8039 (58)
5	7829 (99)	6655 (88)	6958 (109)	6767 (76)	7069 (85)	6861 (75)	7440 (107)
6	8460 (89)	7069 (97)	6981 (130)	6934 (125)	7382 (93)	7722 (83)	8138 (117)
7	7827 (64)	6794 (66)	7377 (78)	7471 (66)	7732 (88)	7574 (63)	7517 (86)
Mean (s.e.)	8091 (30)	6989 (42)	7423 (45)	7429 (50)	7653 (37)	7587 (42)	7916 (38)

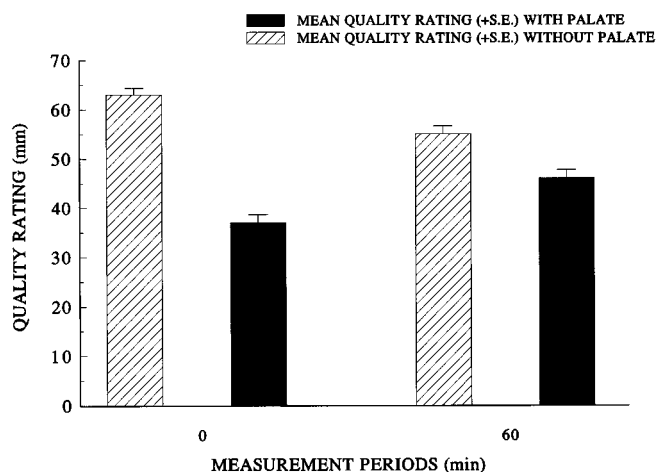


FIG. 3. Mean quality ratings (+ s.e.) for the normal and palate conditions at time 0 and time 60.

time period. These data suggest that modifications made to articulatory strategies for [s] to accommodate the artificial palate may have adversely affected the productions without the palate during that 1-h interval.³

III. DISCUSSION

The main finding of the present investigation was that adaptation to a structural modification of the oral cavity can occur relatively quickly with intensive, target specific practice. In agreement with our previous observations (McFarland *et al.*, 1996), lower centroid and quality ratings were found for [s] in palate as contrasted to normal (i.e., no palate) conditions, suggesting that this sound is highly susceptible to the perturbing effects of the artificial palate with a thicker than normal alveolar ridge. However, significant improvements in the acoustic and perceptual characteristics of [s] produced with the artificial palate in place were observed after a relatively brief one-hour practice period, although compensation was not complete. Previous reports have suggested that artificial palates placed in the mouths of otherwise normal speakers require a lengthy adaptation period. For example, in a previous study (McFarland *et al.*, 1996), we found no significant improvements in the acoustic characteristics of [s] after a 15-min adaptation interval with an artificial palate in place. Others have suggested that an adaptation period of days or weeks is required before normal speech is approached (Hamlet and Stone, 1976a, b; Hamlet *et al.*, 1978; Hamlet and Stone, 1978). In these earlier studies, however (as noted in the Introduction), there were no controls on the speech activity during the adaptation interval, and subjects may have had varying amounts of target sound production with the artificial palate in place. In the present study, subjects read specifically prepared texts heavily laden with [s], and this led to a relatively rapid improvement in articulatory accuracy.

It seems reasonable to assume that the lower centroid values in the palate as contrasted to normal conditions resulted from subjects moving the point of constriction for [s] production more posteriorly in the oral cavity due to the presence of the artificial palate. That is, subjects may have

been “searching” for an area of articulation more similar to the one used when normally producing [s] (i.e., with less alveolar thickness), or the presence of the buildup of acrylic in the alveolar area forced a more posterior tongue positioning. Alternatively, the altered centroids under conditions of perturbation may not have resulted from a more posteriorly placed constriction but rather may have been due to modification of the nature of the constriction (due to the increased thickness of the alveolar region) and changes in the direction of the airstream. We can only speculate as to the articulatory movements used in compensating for the presence of the artificial palate and the improvements in production accuracy during the period of adaptation. Perhaps subjects gradually moved the point of constriction more anteriorly and/or modified airflow turbulence in response to auditory and/or oral-sensory feedback.

The gradual improvement in articulation accuracy during the adaptation period suggests that articulatory processes for [s] production were continuously updated and refined (see Gentilucci *et al.*, 1995 for similar findings with reference to the control of precision grasp), perhaps by somatosensory and/or auditory feedback, in response to the change in oral form associated with the artificial palate. In fact, there appears to have been a “neural recalibration” (Anstis, 1995) of [s] articulation strategies under conditions of perturbation that persisted after the period of adaptation. While perturbed productions were steadily improving with practice, [s] productions without the artificial palate (normal conditions) were adversely affected, both in terms of quality ratings and acoustic measures, by the one-hour period of practice with the palate in place. “Normal” productions appeared to be approaching those of the adapted conditions with the palate in place, indicating that movement control parameters developed for the presence of the artificial palate were inappropriately applied to [s] productions without the palate in place. Similar negative “aftereffects” have been observed in other complex systems under conditions of adaptation. For example, in a recent study by Anstis (1995), subjects were asked to jog in place on solid ground after a 60-s period of adaptation to running on a treadmill. Once on solid ground, subjects tended to jog forwards, presumably because of persistent adaptive modifications of the gait control system for treadmill running (Anstis, 1995). Studies of second-language acquisition provide additional evidence for adaptive or common modes of speech articulatory programming (for a review, see Flege, 1988). Results reveal that learning a second language, particularly at a later age, may affect the production (and perception) of the native language, and the phonetic properties of the speech sounds (e.g., VOT) in the two languages may assimilate to common values (Flege, 1988). To extend and further evaluate the present findings, it would be important to observe normal and compensatory articulation during an even longer period of articulatory practice and at selected time intervals after the adaptation period.

The relatively short duration of the adaptation period in the current study sets the stage for the analysis of the potential influence of sensory feedback in the development of speech adaptation. As in a variety of complex motor behav-

iors (and as noted above), somatosensory and/or auditory feedback may have been utilized in updating the speech motor control system under conditions of perturbation (Gentilucci *et al.*, 1995). Auditory feedback may be particularly crucial for the development of speech motor control (Osberger and McGarr, 1982), and has been implicated in the on-line monitoring of at least some aspects of speech articulation (Perkell *et al.*, 1992; Waldstein, 1990). That there may be some auditory-based correction of speech articulatory gestures is also suggested by the clinical observation that adaptation to dentures is lengthened in patients with hearing loss (Martone, 1962). An obvious next step, and one that has been used rather frequently in speech motor control research (Smith, 1992), would be to modify or eliminate auditory feedback and to observe the effects, if any, on the duration or form of the adaptation process.

Somatosensory feedback which may participate in the adaptation process is also available from a variety of intraoral cutaneous afferents (Kent *et al.*, 1990; McFarland and Lund, 1995; Smith, 1992). Information from these sources might be used in assessing the status of the oral-motor system at the time of movement initiation and in modifying central command signals for speech articulation in the face of perturbation (Smith, 1992). Signals from intraoral afferents may be particularly important for certain sound classes, such as sibilants, which require a precise positioning of the tongue relative to the palatal surface. In fact, the presence of the artificial palate might be expected to modify or eliminate signals coming from palatal mucosal afferents. Subsequent work could focus on the further modification of these and other oral feedback channels, perhaps in combination with interruptions to auditory feedback (Kelso and Tuller, 1983).

The fact that intensive practice seems to modulate the time to adapt to a structural modification of the oral cavity [as indicated in comparison of the present study with our earlier findings (McFarland *et al.*, 1996) as well as those of others (e.g., Hamlet, 1973; Hamlet and Stone, 1974, 1978; Hamlet *et al.*, 1979)] may also have important clinical implications. Clinical observations suggest that the presence of dental prostheses and orthodontic appliances (Chaney *et al.*, 1978; Palmer, 1979; Tanaka, 1973) can result in significant speech articulation errors. Sibilants appear to be particularly impaired, and in fact, [s] production is often used to modify dental prostheses to improve their speech function (Pound, 1970, 1977). Although clinical reports suggest that most patients eventually compensate for the articulatory disturbances associated with dental appliances, there appear to be considerable differences between patients in their ability to adapt, and sibilants appear to be particularly resistant to adaptation (Tanaka, 1973). Perhaps intensive practice on target sound production would facilitate speech sound production in these clinical cases. Specific feedback on key articulatory configurations and/or movements may also facilitate the adaptation process. It would be important, in this regard, to record not only speech acoustics but also articulatory movements under conditions of perturbation, and although technically demanding, it seems particularly relevant to record movements of the tongue relative to the palatal surface. Previous investigations have shown that some speakers are able to alter tongue

groove shapes, apparently critical to accurate [s] production, in response to specific articulatory feedback (Fletcher and Newman, 1991).

IV. CONCLUSION

In conclusion, the results of the present investigation have revealed that speech compensation to the presence of an artificial palate can occur quickly during a relatively brief, target-specific period of practice. Future investigations may be directed toward exploring the potential contribution of sensory feedback in the adaptation process as well as the clinical utility of manipulating adaptation to dental prostheses and other clinically relevant modifications of the oral cavity. Further work is also needed in exploring the potential distributed effects of adapted articulatory strategies to non-perturbed speech articulation. Our preliminary data suggest that speech adaptation to oral-articulatory perturbations may result from a recalibration of the speech motor control system and a common or adaptive mode of articulatory programming distributed across perturbed (adapted) and normal [s] productions. Obvious parallels to similar effects in other complex systems provide added importance for further study of this preliminary finding.

ACKNOWLEDGMENTS

Our thanks to Mai Diab for assistance in data acquisition and analysis. This research was supported by funds from the Fonds de la Recherche en Santé du Québec (FRSQ). Thanks also to Ray Daniloff, Kevin Munhall, Gary Weismer, and one anonymous reviewer for their instructive comments on an earlier version of this paper.

¹Although these individuals had had some experience with [s] production with the palate in place, only 30 tokens had been produced in the previous experiment, which had been conducted more than 1 year earlier. As will be seen, there were no differences in production between the subject without prior experience and the others, suggesting that the previous limited experience with [s] production with the palate in place had little or no effect on performance in the current study.

²An ANOVA was also conducted using speaker as a random factor, and this analysis revealed the same pattern of results: a main effect for palate condition [$F(1,6) = 6.86, p < 0.05$] and a test interval \times palate condition interaction [$F(1,6) = 8.62, p < 0.05$].

³In a comparison of acoustic and perceptual data, although overall trends patterned similarly, there were some discrepancies for individual subjects. That is, for certain speakers, the perceptual ratings did not correspond well with the acoustic findings. This is most likely due to listeners' reliance on acoustic parameters other than those measured in the present investigation in making their perceptual judgments.

Abbs, J. H. (1986). "Invariance and variability in speech production: A distinction between linguistic intent and its neuromotor implementation," in *Invariance and Variability in Speech Processes*, edited by J. S. Perkell and D. H. Klatt (Erlbaum, Hillsdale, NJ), pp. 202–225.

Anstis, S. (1995). "Aftereffects from jogging," *Exp. Brain Res.* **103**, 476–478.

Baum, S. R., McFarland, D. H., and Diab, M. (1996). "Compensation to articulatory perturbation: Perceptual data," *J. Acoust. Soc. Am.* **99**, 3791–3794.

Borden, G. (1979). "An interpretation of feedback in established and developing speech," in *Speech and Language: Advances in Basic Research*, Vol. 3, edited by N. Lass (Academic, New York), pp. 223–242.

- Chaney, S. A., Moller, K. T., and Goodkind, R. J. (1978). "Effects of immediate dentures on certain structural and perceptual parameters of speech," *J. Prosthet. Dent.* **40**, 8–12.
- Flège, J. E. (1988). "The production and perception of foreign language speech sounds," in *Human Communication and Its Disorders, A Review—1988*, edited by H. Winitz (Ablex, Norwood, NJ), pp. 224–401.
- Flège, J. E., Fletcher, S. G., and Homiedan, A. (1988). "Compensating for a bite block in /s/ and /t/ production: Palatographic, acoustic, and perceptual data," *J. Acoust. Soc. Am.* **83**, 212–228.
- Fletcher, S. G., and Newman, D. G. (1991). "[s] and [ʃ] as a function of linguopalatal contact place and sibilant groove width," *J. Acoust. Soc. Am.* **89**, 850–858.
- Forrest, K., Weismer, G., Milenkovic, P., and Dougall, R. (1988). "Statistical analysis of word-initial voiceless obstruents: Preliminary data," *J. Acoust. Soc. Am.* **84**, 115–123.
- Fowler, C. A., and Turvey, M. T. (1980). "Immediate compensation in bite-block speech," *Phonetica* **37**, 306–326.
- Gay, T., Lindblom, B., and Lubker, J. (1981). "Production of bite-block vowels: Acoustic equivalence by selective compensation," *J. Acoust. Soc. Am.* **69**, 802–810.
- Gentilucci, M., Daprati, E., Toni, I., and Chieffi, S. (1995). "Unconscious updating of grasp motor program," *Exp. Brain Res.* **105**, 291–303.
- Hamlet, S. L. (1973). "Speech adaptation to dental appliances: Theoretical considerations," *J. Baltimore Coll. Dent. Surg.* **28**, 52–63.
- Hamlet, S., and Stone, M. (1974). "Reorganization of speech motor patterns following prosthodontic changes in oral morphology," *Speech Commun. Sem.* **2**, 79–86.
- Hamlet, S. L., and Stone, M. (1976a). "Observations on speech preparatory activity of the jaw in natural and compensatory speech," *J. Acoust. Soc. Am. Suppl.* **1** **59**, S85.
- Hamlet, S. L., and Stone, M. (1976b). "Compensatory vowel characteristics resulting from the presence of different types of experimental dental prostheses," *J. Phon.* **4**, 199–218.
- Hamlet, S. L., and Stone, M. (1978). "Compensatory alveolar consonant production induced by wearing a dental prosthesis," *J. Phon.* **6**, 227–248.
- Hamlet, S. L., Cullison, B. L., and Stone, M. L. (1979). "Physiological control of sibilant duration: Insights afforded by speech compensation to dental prostheses," *J. Acoust. Soc. Am.* **65**, 1276–1285.
- Hamlet, S., Stone, M., and McCarty, T. (1978). "Conditioning prostheses viewed from the standpoint of speech adaptation," *J. Prosthet. Dent.* **40**, 60–66.
- Kelso, J. A. S., and Tuller, B. (1983). "Compensatory articulation under conditions of reduced afferent information: A dynamic formulation," *J. Speech Hear. Res.* **26**, 217–224.
- Kent, R. D., Martin, R. E., and Suft, R. L. (1990). "Oral sensation: A review and clinical prospective," in *Human Communication and Its Disorders, A Review—1990*, edited by H. Winitz (Ablex, Norwood, NJ), pp. 135–191.
- Lindblom, B., Lubker, J., and Gay, T. (1979). "Formant frequencies of some fixed-mandible vowels and a model of speech motor programming by predictive simulation," *J. Phon.* **7**, 147–161.
- Lubker, J. (1979). "The reorganization times of bite-block vowels," *Phonetica* **36**, 273–293.
- Martone, A. L. (1962). "The phenomenon of function in complete denture prosthodontics. Clinical applications of concepts of functional anatomy and speech science to complete denture prosthodontics. Part VI. The diagnostic phase," *J. Prosthet. Dent.* **12**, 817–834.
- Matthies, M. L., Svirsky, M. A., Lane, H. L., and Perkell, J. S. (1994). "A preliminary study of the effects of cochlear implants on the production of sibilants," *J. Acoust. Soc. Am.* **96**, 1367–1373.
- Matthies, M. L., Svirsky, M., Perkell, J., and Lane, H. (1996). "Acoustic and articulatory measures of sibilant production with and without auditory feedback from a cochlear implant," *J. Speech Hear. Res.* **39**, 936–946.
- McFarland, D. H., and Baum, S. R. (1995). "Incomplete compensation to articulatory perturbation," *J. Acoust. Soc. Am.* **97**, 1865–1873.
- McFarland, D. H., and Lund, J. P. (1995). "The control of speech," in *Studies in Physiology, Vol. 3—Neural Control of Skilled Human Movement*, edited by F. W. J. Cody (Portland, London), pp. 61–74.
- McFarland, D. H., Baum, S. R., and Chabot, C. (1996). "Speech compensation to structural modifications of the oral cavity," *J. Acoust. Soc. Am.* **100**, 1093–1104.
- Mertus, J. (1989). *BLISS User's Manual* (Brown University, Providence, RI).
- Munhall, K. G., Lofqvist, A., and Kelso, J. A. S. (1994). "Lip-larynx coordination in speech: Effects of mechanical perturbations to the lower lip," *J. Acoust. Soc. Am.* **95**, 3605–3616.
- Osberger, M. J., and McGarr, N. S. (1982). "Speech production characteristics of the hearing impaired," in *Speech and Language: Advances in Basic Research and Practice*, edited by N. J. Lass (Academic, New York), pp. 221–283.
- Palmer, J. M. (1979). "Structural changes for speech improvement in complete upper denture fabrication," *J. Prosthet. Dent.* **41**, 507–510.
- Perkell, J. S., Lane, H., Svirsky, M. A., and Webster, J. (1992). "Speech of cochlear implant patients: A longitudinal study of vowel production," *J. Acoust. Soc. Am.* **91**, 2961–2978.
- Pound, E. (1970). "Utilizing speech to simplify a personalized denture service," *J. Prosthet. Dent.* **24**, 586–600.
- Pound, E. (1977). "Let /s/ be your guide," *J. Prosthet. Dent.* **38**, 482–489.
- Savariaux, C., Perrier, P., and Orliaguet, J. P. (1995). "Compensation strategies for the perturbation of the rounded vowel [u] using a lip tube: A study of the control space in speech production," *J. Acoust. Soc. Am.* **98**, 2428–2442.
- Shadle, C. H., and Mair, S. (1997). "Quantifying spectral characteristics of fricatives," *Proc. ICSLP* **96**, 1521–1524.
- Smith, A. (1992). "The control of orofacial movements in speech," *Crit. Rev. Oral Biol. Med.* **3**, 233–267.
- Tanaka, H. (1973). "Speech patterns of edentulous patients and morphology of the palate in relation to phonetics," *J. Prosthet. Dent.* **29**, 16–28.
- Waldstein, R. S. (1990). "Effects of postlingual deafness on speech production: Implications for the role of auditory feedback," *J. Acoust. Soc. Am.* **88**, 2099–2114.
- Warren, D. W., Allen, G., and King, H. A. (1984). "Physiologic and perceptual effects of induced anterior open bite," *Folia Phoniatr.* **36**, 164–173.
- Warren, D. W., Nelson, G. R., and Allen, G. (1980). "Effects of increased vertical dimension on size of constriction port and fricative sound intelligibility," *J. Acoust. Soc. Am.* **67**, 1828–1831.

Acoustic correlates of English and French nasalized vowels

Marilyn Y. Chen

Harvard-MIT Division of Health Sciences and Technology and Research Laboratory of Electronics,
Massachusetts Institute of Technology, Cambridge, Massachusetts 02139

(Received 5 February 1996; accepted for publication 26 June 1997)

Acoustic analysis of nasalized vowels in the frequency domain indicates the presence of extra peaks: one between the first two formants with amplitude $P1$ and one at lower frequencies, often below the first formant, with amplitude $P0$. The first-formant amplitude $A1$ is also reduced relative to its amplitude for an oral vowel. These acoustic characteristics can be explained by speech production theory. The objective of this study was to determine the values for the acoustic correlates $A1-P1$ and $A1-P0$ (dB) for quantifying nasalization. They were tested as measures of nasalization by comparing vowels between nasal consonants and those between stop consonants for English speakers. Also, portions of nasal vowels following a stop consonant were compared for speakers of French, which makes a linguistic distinction between oral and nasal vowels. In the analysis of English, the mean difference of $A1-P1$ measured in oral vowels and nasalized vowels had a range of 10 dB–15 dB; the difference of $A1-P0$ had a range of 6 dB–8 dB. In the study of French, the difference of $A1-P1$ measured between the least-nasalized portion and the most-nasalized portion of the vowel had a range of 9 dB–12 dB; for $A1-P0$, the difference ranged between 3 dB and 9 dB. In order to obtain an absolute acoustic measure of nasalization that was independent of vowel type, normalized parameters were calculated by adjusting for the influence of the vowel formant frequencies. © 1997 Acoustical Society of America. [S0001-4966(97)02010-9]

PACS numbers: 43.70.Aj, 43.70.Bk, 43.70.Hs, 43.70.Kv [AL]

INTRODUCTION

The degree of acoustic coupling between the vocal tract and the nasal tract is controlled by the velum (soft palate) as well as the posterior and lateral pharyngeal walls. The opening to the nasal tract (including the nasal passages and the sinuses) allows airflow through the nose as well as through the mouth and the acoustic coupling causes the vowel to be nasalized. In English, the velopharyngeal (v-p) port is opened during the production of the nasal consonants /m/, /n/, and /ŋ/, but it is raised for obstruent consonants to allow pressure buildup. During normal vowel production, the v-p port is bigger if the vowel is adjacent to a nasal consonant. In French, a few vowels are intentionally nasalized in order to be distinct from oral vowels.

For some populations, control of the v-p port is different from that of normal speakers, while for others variations in anatomy of the nasal tract lead to differences in the sound. Inadvertent nasalization, a speech disorder with the v-p port opened excessively during vowel production, is one of the most common problems of deaf speakers (Stevens *et al.*, 1976; Chen, 1995). It is also difficult for people with velopharyngeal insufficiency due to a cleft palate, paralyzed velum, or adenoidectomy to contrast nasal and nonnasal sounds (Kuehn and Dalston, 1989). Furthermore, patients who have had endonasal sinus surgery for treating severe sinusitis have often noticed a change in their speech post-operatively (Chen and Metson, in press).

The goal of this study is to quantify vowel nasalization objectively through measurements on the acoustic signal. It was motivated by the difficulty of obtaining consistent subjective judgments of nasality (especially when other speech disorders are present) and the inaccessibility of the velopharyngeal opening, the need of a better understanding of nasalization in order to synthesize more natural speech with nasals, and the desire to develop a more accurate speech production model of the nasal tract.

Analysis of the acoustic signal in the frequency domain is ideal in a clinical setting since measurements require only a microphone output. Furthermore, by examining the deviation of the nasalized vowel spectrum from that of the oral vowel, it is expected to reflect the overall condition of the nasal tract such as a larger total surface area and coupling to the paranasal sinuses.

The reduction in amplitude of the first formant spectral peak ($F1$) has been observed to be the primary cue of nasalization (Delattre, 1954; Fant, 1960; House and Stevens, 1956). Perceptual experiments of synthetic stimuli showed that $F1$ amplitude lowered by 6–8 dB is necessary to achieve a significant level of nasality perception (House and Stevens, 1956; Stevens *et al.*, 1988).

Nasal coupling during vowel production was also found to introduce a pole and a zero in the region of the first formant introducing a spectral peak around 1 kHz (House and Stevens, 1956; Maeda, 1982b; Huffman, 1990). The addition of such pole-zero pair synthetically to the spectrum also was found to be effective in enhancing nasality perception for different vowel types (Hawkins and Stevens, 1985; Maeda, 1982a).

Another nasal peak between 250 and 450 Hz has been observed in various studies of vowel nasalization (Hattori *et al.*, 1958; Fujimura and Lindqvist, 1971; Lindqvist-Gauffin and Sundberg, 1976; Maeda, 1982a; Båvegård *et al.*, 1993; Dang and Honda, 1995). Most of these researchers noted that the peak may be due to the pole-zero pair introduced by the paranasal sinuses. Introduction of this peak

synthetically with a pole-zero pair (Hattori *et al.*, 1958; Maeda, 1982a) or by raising the amplitude of the first harmonic (Klatt and Klatt, 1990) was found to be necessary for nasality perception, especially for nonhigh vowels.

Although some of the studies mentioned above suggested acoustic correlates for quantifying nasalized vowels, all except Maeda's study (1993) utilized only one spectral characteristic of nasalization (i.e., first-formant amplitude, nasal prominence in the vicinity of the first formant, or nasal prominence at low frequencies). Maeda's technique, however, only involved two of the three spectral characteristics and it was useful for just two vowel types. The author previously suggested an acoustic correlate $A1-P1$ (in decibels) that used the amplitude $A1$ of the first formant and the amplitude $P1$ of the nasal peak in the vicinity of the first formant (Chen, 1995). The measure was examined through acoustic analysis of normal-hearing and hearing-impaired children for mainly nonhigh vowels. In addition, Chen (1995) has applied an adjustment technique for vowel types to $A1-P1$ in synthetic vowels.

In this paper, an additional acoustic correlate $A1-P0$ involving the amplitude of the first formant and the amplitude $P0$ of a nasal peak at low frequencies is introduced. $A1-P1$ and $A1-P0$ were measured for normal-hearing adult speakers for six vowel types. The speech of adult English speakers was examined by comparing the relevant acoustic correlates in nasalized vowels due to coarticulation of adjacent nasal consonants with the respective values in oral vowels. Since English does not have linguistic vowel nasality, only phonetic nasality could be studied. To investigate phonemic nasality, French, with distinctive vowel nasality, was examined in a supplementary study by comparing the measures in the least-nasalized and more-nasalized portions of nasal vowels that are preceded by stop consonants. The influence of formant frequencies and nasal peak frequencies on the acoustic correlates was also addressed. In a separate study (Chen and Metson, in press), the effects of surgical alterations of the nasal anatomy on the acoustic characteristics of nasal vowels (as well as nasal consonants) were examined with the same techniques used in the present study and the acoustic data were related to the results of perceptual experiments.

I. THEORETICAL CONSIDERATIONS

Acoustic theory of nasalized vowel production can predict how coupling between the nasal tract and the rest of the vocal tract affect the acoustic spectra. Theoretical predictions are based on the physical dimensions of the vocal tract as well as the nasal tract. The nose is divided into two passages by the septum, beginning about 3 cm from the posterior end of the nasal tract. The turbinates, which augment the total surface area of the nasal passages, curve inferiorly and medially from the lateral wall to cover the corresponding meatus. From measurements of the effective cross-sectional area of the nose of an adult male cadaver, Bjuggren and Fant (1964) found that the total surface area of the nasal passages was about 3.5 times as large as that of a cylindrical tube with the same total cross-sectional area. Based on MRI of four subjects, Dang *et al.* (1994) found that the area function of

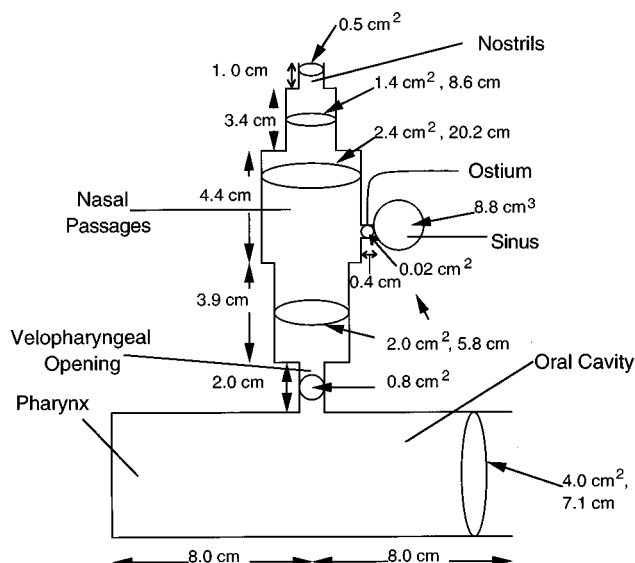


FIG. 1. The average physical dimensions of the vocal tract, nasal tract, and the maxillary sinus used in the theoretical modeling of nasalized neutral vowel are shown. They include length, cross-sectional area, circumference, and volume.

the nasal tract varied among subjects. There are also paranasal sinuses, including the maxillary, frontal, sphenoid, and ethmoid sinuses, connected to the lateral wall of the main nasal passages through narrow bony pathways called ostia. Asymmetry of the nasal passages along the septum may introduce pole-zero pairs in the transfer function of the nasal tract (Fujimura and Lindqvist, 1964; Lindqvist-Gauffin and Sundberg, 1976; Dang *et al.*, 1994). From their dual-tube model, Dang *et al.* concluded that the transfer function would be affected by an additional pole-zero pair in the 2 kHz–2.5 kHz range for nasal passages with an asymmetry coefficient of the area function as small as 0.3; this pole-zero pair would not affect the transfer function in the vicinity of the first formant.

If symmetry of the two channels is assumed, one can model the nasal tract as a side branch of the main vocal tract, consisting of an adjustable velopharyngeal opening followed by a fixed cavity and terminated by the nostrils. Figure 1 shows the average physical dimensions of the vocal tract, nasal tract, and the maxillary sinus used in the theoretical modeling of a nasalized neutral vowel. The dimensions are based on studies by Dang *et al.* (1994) and Stevens (in press), and include the length, cross-sectional area, circumference, and volume of the different portions of the tract.

As a result of the nasal side branch, extra poles and zeros are added to the all-pole system of the oral vowel (Fant, 1960). The locations of the pole-zero pairs can be determined by computing the sum of the driving-point susceptances B_n , B_m , and B_p , which are the (negative) reciprocal of the reactances at the junction looking toward the nose, the mouth, and the pharynx, respectively (Fujimura, 1960). The natural frequencies of the entire system are the frequencies for which $B_n + B_m + B_p = 0$. These frequencies can be determined by finding the intersections of curves of B_n and $-(B_m + B_p)$ versus frequency. The nasal reactance can be approximated as a series connection of an acoustic

mass, representing the velopharyngeal opening, and the reactance of the nasal tract. Based on the experimentally measured transfer function of the nasal tract from a sweep-tone source above the closed v-p port to the nostril output (Lindqvist and Sundberg, 1972), the susceptance B_n is estimated to have zeros at about 500 and 2000 Hz. This information can be used in constructing the B_n curves. The sum $B_m + B_p$ is determined by solving the one-dimensional wave equation for the particular vocal-tract shape with the mouth assumed to be open and the glottis assumed to be closed, as shown in Fig. 1.

The susceptance graphical analysis indicates the frequencies of the poles and zeros for the transfer function of the nasalized vowel. The first-formant frequency, $F1$, is shifted and there is an additional nasal pole. The zero for which the side branch acts as a short circuit when B_n goes to infinity and the zero for which the oral cavity acts as a short circuit when B_m goes to infinity are needed to calculate the lowest zero of the total system. An increase in coupling corresponds to an upward shift of nasal formant-antiformant frequencies and a larger magnitude of the extra peak. The abovementioned frequencies and the height of the extra peak (above that of the oral reference) introduced by adding the nasal pole and zero were calculated by Stevens (in press). A large velopharyngeal opening for the vowel /a/ can introduce a prominence as large as 12.1 dB with a pole at 910 Hz. Even with a small opening for the vowel /i/, a prominence of 13.5 dB can be introduced with a pole at 810 Hz.

A sinus can be modeled as a side cavity of the nasal tract system, as shown in Fig. 1. The narrow coupling allows one to model the sinus and its ostium as a Helmholtz resonator with a resonance frequency of

$$f_{zs} = \frac{c}{2\pi} \sqrt{\frac{S_o}{VL_o}}, \quad (1)$$

where S_o is the cross-sectional area of the ostium in cm^2 , L_o is its length in cm, and V is the volume of the paranasal cavity in cm^3 . The calculated antiresonance frequencies of the sinuses based on morphological data and modeling the sinuses as Helmholtz resonators corresponds well with the frequencies from measurement of the transmission characteristic (Dang and Honda, 1996). Larger sinuses, such as the maxillary and sphenoid sinuses, would introduce to the total system an extra zero and an extra pole below $F1$, at least for a nonhigh vowel. The zero frequency may be approximated by f_{zs} while the corresponding pole, which determines the location of the extra peak, is at a frequency lower than the zero due to the acoustic mass from the portion of the nasal tract anterior to the sinus ostium in parallel with the acoustic mass of the portions posterior to the ostium, including the nasal tract, the velopharyngeal opening, and the oral cavity.

Using dimensions derived from MRI, Dang *et al.* (1994) estimated f_{zs} of the sphenoid and maxillary sinuses for one subject to be between 534 and 989 Hz. They calculated the frequency of the pole to be lower than that of the zero by 33–127 Hz. In addition, Dang and Honda (1995) used the sound-pressure gradient in the nasal tract and at the nostril to

determine the volume-velocity transfer function, and showed that the nasal zero due to the sphenoid sinus as well as the maxillary sinus can be as low as 310 Hz. With the same technique, a four-zero model of sinus antiresonances with the lowest antiresonance frequency at 550 Hz attributed to the maxillary sinus was suggested (Dang and Honda, 1996). The discrepancy may be because of the wide variations of sinuses among subjects in the different studies and the inaccurate measurements of the ostium dimensions and the cavity volumes due to the limited MRI spatial resolution. By assuming that the zero is at 400 Hz (between the lowest values calculated from MRI and pressure gradient) and the pole is at 300 Hz (in the range of values calculated from MRI), the pole-zero pair would introduce a 3.1 dB increase at 270 Hz if the bandwidths of the pole and zero are 120 Hz. If the bandwidths are 80 Hz, the pole-zero pair would introduce a 5.5-dB increase at 290 Hz. From simulation of the transfer function for French nasal vowels, Feng and Castelli (1996) also found a low pole (250–300 Hz) for low nasal vowels.

In addition to introducing pole-zero pairs, coupling to the nasal tract also affects the first-formant bandwidth due to losses. The total surface area of the nasal tract is augmented due to the turbinates in the lateral walls of the nasal passages. Dang *et al.* (1994) used MRI to measure the three-dimensional geometry of the nasal tract and found a shape factor (Fant, 1960)

$$S_f = \frac{S}{\sqrt{4\pi A}} \quad (2)$$

equal to 1, 4, and 2 for the posterior, middle, and anterior portion of the nasal tract, respectively (see dimensions in Fig. 1). The shape factor is determined by the cross-sectional perimeter S and the cross-sectional area A . The losses due to wall vibration, viscous friction, and heat conduction that widen the bandwidth of the formants are all proportional to S/A (Flanagan, 1972). The approximate contributions of each region of the vocal tract and portions of the nasal tract to the formant bandwidth can be estimated from the dimensions and shape factors of the various components.

Based on the length and cross-sectional area dimensions of Fig. 1, wall losses in the pharyngeal and oral tract portions are estimated to contribute a total of 60 Hz to the first-formant bandwidth. For a large v-p opening, the posterior portion, the middle portion, and the anterior portion of the nasal tract are estimated to contribute on the average 15 Hz, 66 Hz, and 26 Hz, respectively, to the $F1$ bandwidth. For oral /æ/, the bandwidth, estimated from the decay of the bandpass-filtered first formant waveform, which included the glottal effect on bandwidth, was 131 Hz for males and 165 Hz for females (Chuang and Hanson, 1996). With nasalization, it would be increased to 238 Hz and 272 Hz, for males and females, respectively, giving a decrease of 5.2 dB and 4.3 dB in the amplitude of the $F1$ peak. There are other losses that were not taken into account, such as the sinuses augmenting the total surface area of the nose, and nasal resistance due to constrictions and nostril hairs.

II. PROPOSED ACOUSTIC CORRELATES OF NASALIZATION

A. $A1-P1$ (difference between $A1$ and $P1$ in dB)

One acoustic correlate used to quantify nasalized vowels was developed by considering the amplitudes of the first formant and the nasal prominence due to coupling to the nasal tract. As observed in Sec. I, the large shape factor S_f due to the septum and turbinates of the nasal passages contributes to broadening the first formant and to lowering the formant amplitude $A1$, which was estimated by the amplitude of the peak harmonic closest to the expected $F1$. Theoretically, it is expected that coupling to the nasal tract may lower $A1$ by about 5 dB. Also, a large velopharyngeal opening shifts the nasal zero to a higher frequency so that it moves farther away from the nasal pole, causing a more prominent extra peak above the first formant. The spectral effect of the extra peak is characterized by its amplitude, $P1$, which is estimated by using the amplitude of the highest peak harmonic around 950 Hz, based on a previous study consisting of four normal-hearing adults saying six vowel types between nasal consonants (Chen, 1995). This average frequency is close to the theoretical value of 910 Hz for the vowel /a/ with a large velopharyngeal opening (Stevens, in press). In the oral vowels, if no extra peak is observed, $P1$ is measured by using the highest harmonic close in frequency to the frequency of the peak in the nasalized vowel. From calculations, $P1$ of a nasalized vowel can be about 13 dB greater than for $P1$ of the oral vowel. The effect of the nasal zero can be assessed indirectly through its influence on $P1$ because it is often not obvious from the spectrum. Since both parameters $A1$ and $P1$ are changed by nasal coupling and they are inversely related to each other, they are lumped together by calculating the difference $A1-P1$. Also, a difference is used so that the measurements are independent of speech intensity. Theoretically, $A1-P1$ can decrease by about 18 dB when a vowel is nasalized with an average of 5-dB $A1$ lowering and 13-dB $P1$ raising. This theoretical value assumes a large opening for nonhigh vowels, which was observed by Moll (1962).

B. $A1-P0$ (difference between $A1$ and $P0$ in dB)

Another acoustic correlate used to quantify nasalized vowels is based on the nasal prominence due to coupling to the sinuses as well as the amplitude of the first formant. As observed in the theoretical analysis above, the paranasal sinuses, especially the maxillary and sphenoid sinuses, can introduce extra pole-zero pairs in the transfer function of the total system in a nasal vowel at very low frequencies. A larger velopharyngeal opening would cause greater coupling to the nasal sinuses and introduce a more prominent peak at the lower harmonics in the spectrum of a nasal vowel. The amplitude of this low-frequency peak in dB is designated as

$P0$. For both nasalized and oral vowels, the location of this extra peak is chosen based on which harmonic has the greatest amplitude at the low frequencies. Theoretical analysis in Sec. I, suggests that this amplitude can increase by 3 dB–6 dB due to coupling to the sinus. Furthermore, an increased open quotient of the glottal waveform can also cause $P0$ to be more prominent. As the open quotient (OQ) changes from 50% to 90%, for example, the first harmonic amplitude increases about 5 dB (Klatt and Klatt, 1990), assuming other aspects of the glottal waveform remain fixed. As noted above, coupling to the nasal tract would lower $A1$ by around 5 dB. Therefore, another acoustic correlate used for measuring the degree of nasal coupling is $A1-P0$: A nasal vowel would have a smaller $A1-P0$ by as much as 8 dB–11 dB due to the lowering of $A1$ and raising of $P0$. If the OQ is increased so that $P0$ is raised, $A1-P0$ may be decreased further. $A1-P0$ would be an especially useful measure of nasalization for vowels that have their first and/or second formant close to the frequency of $P1$, since peaks close in frequency influence each other and therefore obscure the $A1-P1$ measurement. On the other hand, $A1-P1$ would be more useful for vowels with $F1$ at a low frequency that affects $P0$. If the first formant occurs at the same frequency as the nasal peak $P0$, which sometimes happens in /i/, the influence of $P0$ may need to be subtracted from the measured $A1$. Doing so would show even a greater difference between $A1-P1$ of oral vowels and nasalized vowels.

C. Vowel-type adjustment

The parameters $A1-P1$ and $A1-P0$ can be adjusted for vowel types by correcting for the effects of the formants on the amplitude of the extra peaks. In addition, the adjustment technique would address the effect of formant transitions due to coarticulation of the adjacent consonants. Since $P1$ rides on the skirts of the first and second formants, it is dependent on the formant frequencies and, to a lesser extent, on the formant bandwidths. For a given degree of nasal coupling, if $F1$ and $F2$ move closer to each other and to the nasal peak, $P1$ is boosted up, resulting in a decrease of $A1-P1$. Also, $F1$ is expected to influence $P0$ due to the proximity in frequency of these spectral peaks: as $F1$ lowers, $P0$ is boosted, decreasing $A1-P0$.

The technique for adjusting $A1-P1$ for vowel type with approximations has been described by Chen (1995). In that study, the technique was applied to ten synthetic oral vowels. The unadjusted $A1-P1$ had a standard deviation (s.d.) of 12.0 dB; the adjusted $A1-P1$ had a much smaller s.d. of 2.1 dB. A similar technique can be used to determine the effect of the formants on $P0$. If the frequency of the extra peak is F_{P0} , the frequency of the first formant is $F1$, and the bandwidth of the first formant is $B1$, the effect of the first-formant component at F_{P0} is

$$T1(F_{P0}) = \frac{(0.5B1)^2 + F1^2}{[((0.5B1)^2 + (F1 - F_{P0})^2) \cdot ((0.5B1)^2 + (F1 + F_{P0})^2)]^{1/2}}. \quad (3)$$

The effect of the second-formant component at F_{P0} is

$$T2(F_{P0}) = \frac{(0.5B2)^2 + F2^2}{[(0.5B2)^2 + (F2 - F_{P0})^2] \cdot [(0.5B2)^2 + (F2 + F_{P0})^2]^{1/2}}, \quad (4)$$

where $F2$ is the frequency of the second formant and $B2$ its bandwidth. $T2$ is much smaller than $T1$ since the second formant is further away from the nasal peak in frequency than the first formant. The effects of higher formants at F_{P0} are small so they are not considered. By replacing $P0$ in dB by $(P0 - T1 - T2)$ in dB, the parameter $A1 - P0$ may be adjusted for vowel type. As for $A1 - P1$, approximations can be made if the bandwidths of the formants are much less than the formant frequencies (Chen, 1995). A similar technique can be used to determine the effect of $F2$ on $A1$ as well as the effect of $F1$ on $A1$, but the calculations show that there is small effect on the correlation between the nasality judgments and the acoustic correlates measured (Chen, 1995). Therefore, the adjustment only addresses the effects of $F1$ and $F2$ on $P1$ and $P0$ but not the effects of $F1$ and $F2$ on $A1$.

III. ACOUSTIC ANALYSIS

The recordings for the acoustic analysis were made with a ceiling-hung Electro-Voice model 054 omnidirectional dynamic microphone placed approximately six inches in front of the speaker's lips in a partially sound attenuated room. For this microphone position, the distances from the microphone to the mouth and to the nose were about equal, and the relative effect of reverberation was minimized. The microphone output was connected to a Shure microphone mixer followed by a Nakamichi LX-5 cassette recorder without Dolby and dbx so that the onsets were not distorted. All signals were low-pass filtered at 4.8 kHz using a TTE passive seven-pole elliptical low-pass filter, digitized at 10 kHz with 12-bit samples, and stored on a VAX-750 computer disk. The vowels were extracted from the digitized speech by editing the waveform files and were analyzed by using computer software. The frequency domain analysis of the vowels was done by using KLSPEC93, which is a revision of the software package developed by Klatt (1984). This research utilized the discrete Fourier transform (DFT) magnitude from the software package. Spectra throughout the vowel were generated by using a 30-ms Hamming window and computing a 512-pt. DFT.

A. English speakers: Minimal pairs of nasalized and oral vowels

To test the effectiveness of $A1 - P1$ and $A1 - P0$ as measures of nasalization, these correlates were measured and compared for the nasalized vowels and their corresponding oral vowels in English. Nasalized vowels were obtained by placing vowels in a nasal context that introduces nasal coarticulation, and oral vowels were generated by placing vowels between stop consonants that require pressure buildup.

1. Method

Eight native English speakers, four males (CM, MJ, NM, PG) and four females (JM, KT, LW, SM), participated

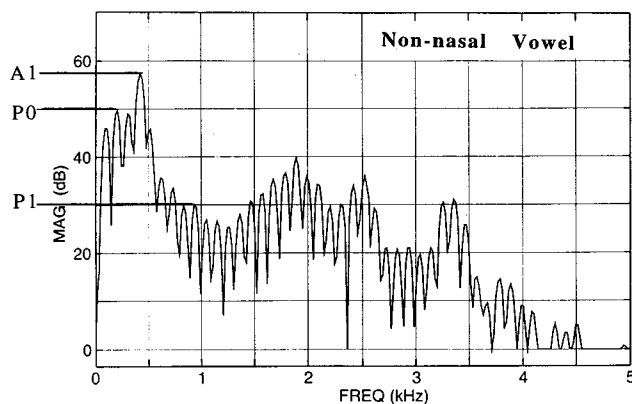
in this study. They said monosyllable words with the vowels /i/, /ε/, /æ/, /u/, /ɑ/, and /ʌ/ in the carrier phrase "think _____ clearly." The vowel was either between nasal consonants, e.g., *mean*, *men*, *man*, *moon*, *mom*, and *mum*, or between stops, e.g., *beeb*, *bed*, *bad*, *booed*, *bob*, and *bud*, so that a clear distinction between nasal and oral vowels was expected. Three repetitions of each token were recorded. The frequencies of the first and second formants, $F1$ and $F2$, respectively, the frequencies of $P1$ and $P0$, F_{P1} and F_{P0} , and the correlates $A1 - P1$ and $A1 - P0$ were measured at the beginning, the middle, and the end of the vowels. The measurements were made at different locations to observe any differences for vowel portions following a nasal consonant, preceding a nasal consonant, and further away from the nasal consonants, compared to the corresponding portions of the oral vowel. The beginning spectrum was obtained by aligning the left side of the window with the start of the first glottal pulse of the vowel; the end spectrum was calculated by aligning the right side of the window with the end of the glottal pulse just preceding the second consonant closure; the middle spectrum was obtained by centering the window at the midpoint between the beginning and end spectra.

Figure 2(a) shows the spectrum obtained from the middle of an oral vowel (i.e., in the word "bed") and Fig. 2(b) shows the spectrum from the middle of a nasalized vowel of the same type (i.e., in the word "men") spoken by a male speaker. The traces of the nasal prominences even in the oral vowel suggest that the velopharyngeal port may not be fully closed or there is coupling between the oral and nasal tracts through the muscles of the velum or the palate (Suzuki *et al.*, 1992). In the example, the values for the nasal vowel, $A1 - P1 = 15$ dB and $A1 - P0 = -1$ dB, are much less than those for the oral vowel, $A1 - P1 = 27$ dB and $A1 - P0 = 7$ dB.

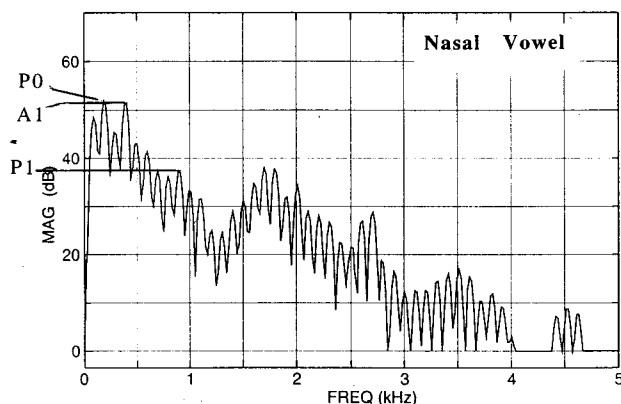
2. Results and discussion

Table I shows the measured frequencies of the spectral prominences for nasalized vowels averaged across locations and repetitions since no significant trend was seen among the locations for different speakers. For all of the vowels, except /i/, average F_{P0} ranged from 206 to 223 Hz with an average across vowels of 216 Hz. It was difficult to measure F_{P0} for /i/ because $F1$ is at a low frequency close to F_{P0} . For all of the vowels, average F_{P1} ranged from 924 to 1032 Hz with an average across vowels of 966 Hz. The formant frequencies differ from those values in the corresponding oral vowels measured by Hillenbrand *et al.* (1995), presumably due to the coupling to the nasal tract as well as the variations in the speaker dialect and measurement procedures.

The measurements of $A1 - P1$ and $A1 - P0$ made at the three points within the vowel are expected to show changes in the same direction with nasalization, i.e., lower values for the nasal vowel than for the oral vowel. Only 4.2% of the



(a)



(b)

FIG. 2. (a) The spectrum of an oral vowel is compared with (b) the spectrum of a nasalized vowel from the same speaker. The spectral peaks that determine A1, P1, and P0 are labeled. The amplitudes are measured by using the harmonic amplitudes closest to the expected peak according to theory. A1-P1 and A1-P0 are greater for the oral vowel than the nasal vowel.

A1-P0 values and 10.4% of A1-P1 values showed the contrary. On the other hand, there was no consistent trend of A1-P1 and A1-P0 values over time for either the nasal vowel or the oral vowel. (At most, only 59% of the timing contours showed the same pattern of variation of the parameters.) Therefore, only the averages across locations within the vowel and across repetitions were examined for eight speakers. Tables II and III show the average A1-P1 and A1-P0, respectively, measured in the oral and nasal vowels for each of the speakers. Since comparisons are made between the values of nasal and oral vowels of the same type, the adjustment technique was not used. The "O" columns show values for the oral vowel and the "N" columns show values for the nasal vowel. The boldfaced numbers indicate highly statistically significant ($p < 0.01$) differences and the italicized numbers indicate a lower significance ($p < 0.05$), according to one-sided dependent t -test between the oral and nasal values for the given vowel and speaker.

For /i/, all eight speakers and for /u/, six speakers showed highly statistically significant differences between A1-P1 measured in the oral vowels, $(A1-P1)_O$, and that of the nasal vowels, $(A1-P1)_N$. Only five speakers for /i/ and

TABLE I. Average frequencies of the nasal peaks and the first two formants measured in English nasalized vowels of eight speakers and three repetitions of each. The "avg." indicates averages across vowel types. F_{P0} and F_{P1} are the frequencies of the nasal peaks with amplitudes P0 and P1, respectively. F1 and F2 are the first- and second-formant frequencies, respectively.

Vowel	Nasalized			
	F_{P0} (Hz)	F1 (Hz)	F_{P1} (Hz)	F2 (Hz)
/i/	...	273	964	2529
/u/	206	397	1032	1213
/ε/	223	520	982	1895
/Λ/	223	627	938	1194
/æ/	212	562	924	1903
/ɑ/	217	655	953	1178
avg.	216	...	966	...

three speakers for /u/ showed highly statistically significant differences for $(A1-P0)_O$ and $(A1-P0)_N$. For /i/ and /u/ with low first-formant F1 which may influence the measurement of A1-P0, A1-P1 is a more robust measure of nasalization than A1-P0, even though the low F2 of /u/ may affect the measurement of A1-P1.

For /ε/ and /Λ/, there was a statistically significant difference between $(A1-P1)_O$ and $(A1-P1)_N$ for all of the speakers; six speakers for /ε/ and eight speakers for /Λ/ showed a highly statistically significant difference. In some cases, the second-formant F2 in /Λ/ was fairly close to the frequency of P1. As a result, the nasal peak and the second formant were less distinguishable, making the measurement of A1-P1 less reliable. Also, for /ε/ and /Λ/, there was a highly statistically significant difference between $(A1-P0)_O$ and $(A1-P0)_N$ and for all of the speakers, since F1 for these two vowels occurs at a high frequency, farther away from F_{P0} .

For /æ/ and /ɑ/, all of the speakers showed a highly statistically significant difference between $(A1-P0)_O$ and $(A1-P0)_N$ while five speakers for /æ/ and four speakers for /ɑ/ showed highly statistically significant difference for $(A1-P1)_O$ and $(A1-P1)_N$. As shown in Table I, for the low vowels F1 is at a much higher frequency than F_{P0} so that A1-P0 was measured reliably. However, F1 occurring at a high frequency would affect the measurement of A1-P1. In addition, F2 in /ɑ/ occurs at a low frequency close to F_{P1} , making the measurement of A1-P1 less reliable.

In summary, then, for the two high vowels /i/ and /u/, the difference between oral vowels and nasal vowels was significantly indicated by A1-P1 for six speakers, compared to four speakers when A1-P0 was used. On the other hand, A1-P0 showed significant difference between oral and nasal low vowels /æ/ and /ɑ/ for eight speakers, compared to the five speakers when A1-P1 was used. For /ε/ and /Λ/, both A1-P1 and A1-P0 showed significant differences between oral and nasal vowels for all of the speakers.

The difference $\Delta(A1-P1)$ between the average of $(A1-P1)_O$ and the average of $(A1-P1)_N$ among speakers was calculated for the nonlow vowels. The same was done

TABLE II. The correlate $A1-P1$ of English oral vowels (O) and nasal vowels (N) was measured at the beginning, the middle, and the end of the vowel for three repetitions and averaged. The boldfaced numbers indicate $p < 0.01$, and the italicized numbers indicate $p < 0.05$ between the oral and nasal values for the given speaker (Sp.).

Sp.	$A1-P1$ (dB)											
	$/i/$		$/u/$		$/ɛ/$		$/ʌ/$		$/æ/$		$/ɑ/$	
	O	N	O	N	O	N	O	N	O	N	O	N
CM	39.3	25.9	29.7	28.4	26.4	15.7	23.0	8.7	25.0	17.4	16.7	8.4
MJ	32.4	28.2	30.3	21.6	24.9	14.6	17.7	8.9	17.3	11.6	<i>9.4</i>	<i>5.6</i>
NM	41.9	27.3	24.3	20.7	25.2	16.3	18.6	1.4	20.1	15.2	7.1	-0.6
PG	38.6	26.4	29.2	19.3	31.6	20.4	20.6	13.0	26.3	17.2	16.3	10.7
JM	40.7	21.4	33.2	15.9	28.1	10.6	18.7	5.1	18.3	9.9	<i>11.1</i>	<i>4.6</i>
KT	40.6	27.4	33.0	25.3	31.6	18.9	20.0	8.2	12.2	11.4	8.7	4.7
LW	42.1	25.2	28.2	22.2	<i>22.7</i>	<i>17.0</i>	19.7	3.2	12.4	13.3	<i>7.2</i>	<i>2.6</i>
SM	43.4	21.1	34.9	24.9	<i>26.6</i>	<i>21.3</i>	15.1	6.3	<i>16.3</i>	<i>11.9</i>	<i>6.7</i>	<i>5.3</i>

for the difference $\Delta(A1-P0)$ between the average of $(A1-P0)_O$ and the average of $(A1-P0)_N$ for the nonhigh vowels. Table IV shows the average results from eight subjects. The mean for $\Delta(A1-P1)$ ranged from 10 dB to 15 dB with the minima ranging from 4 dB to 8 dB and the maxima from 17 dB to 23 dB. The vowel $/i/$ in general had higher $\Delta(A1-P1)$ than the other vowels. Although $A1$ is expected to decrease less for $/i/$ with its smaller velopharyngeal opening (Moll, 1962), $P1$ is expected to increase more than that of the other vowels (Stevens, in press). The mean for $\Delta(A1-P0)$ ranged from 6 to 8 dB with the minima ranging from 4 to 5 dB and the maxima from 8 to 16 dB. The mean values are consistent with the values predicted from theoretical calculations, 18 dB for $\Delta(A1-P1)$ and 8 dB–11 dB for $\Delta(A1-P0)$ (see Sec. II). The theoretical predictions of the differences are generally larger than the measured differences since the theory assumes a large velopharyngeal cou-

pling during the nasalized vowels. This may not occur when the vowel is nasalized due to coarticulation. Furthermore, the peak amplitude can only be approximated by using the amplitude of the closest harmonic, which varies with the fundamental frequency of the vowel. With better understanding of anatomy, physiology, and speech production from future research, the theory can be improved.

To show the effect of the adjustment technique for vowel types, the mean, standard deviation, and range of $A1-P1$ and $A1-P0$ with and without adjustment are listed in Table V. For $A1-P1$, with adjustment, the mean was lowered for both the oral and nasal vowels. The s.d. was reduced by 9.0 dB and 4.3 dB after adjustment for the oral vowels and the nasal vowels, respectively. The range for the oral vowels was larger than that of the nasal vowels before correction but it became smaller after correction. With adjustment, nasal vowels can still be distinguished from oral vowels.

TABLE III. The correlate $A1-P0$ of English oral vowels (O) and nasal vowels (N) was measured at the beginning, the middle, and the end of the vowel for three repetitions and averaged. The boldfaced numbers indicate $p < 0.01$, and the italicized numbers indicate $p < 0.05$ between the oral and nasal values for the given speaker (Sp.).

Sp.	$A1-P0$ (dB)											
	$/i/$		$/u/$		$/ɛ/$		$/ʌ/$		$/æ/$		$/ɑ/$	
	O	N	O	N	O	N	O	N	O	N	O	N
CM	10.8	9.9	3.0	4.0	8.6	1.1	8.9	2.0	8.6	3.1	9.1	1.1
MJ	10.9	7.7	<i>0.1</i>	<i>-4.6</i>	6.2	0.4	5.1	1.1	5.2	-0.9	5.6	1.6
NM	8.2	6.0	-2.3	-3.8	6.6	0.6	5.2	-7.7	3.9	-0.7	0.7	-6.7
PG	11.6	6.9	4.0	-0.9	9.0	-1.1	9.3	4.0	9.0	-6.7	10.7	4.9
JM	-0.2	-5.2	4.4	-5.8	4.4	-7.8	2.1	-8.2	2.0	-9.2	1.8	-6.0
KT	<i>-2.6</i>	<i>-5.6</i>	3.0	-3.8	6.9	-5.7	5.1	-6.3	-0.1	-8.9	-0.6	-7.1
LW	11.4	5.9	-7.0	-9.9	2.0	-3.3	3.4	-5.8	3.1	-1.7	2.7	-5.2
SM	3.6	6.3	6.4	6.2	10.1	5.6	7.8	3.2	8.4	4.8	7.7	3.4

TABLE IV. Mean, minimum (min.), and maximum (max.) differences between the average $A1-P1$ of nonlow vowels and $A1-P0$ of nonhigh vowels measured in oral and nasal English vowels for eight subjects.

Vowel	$\Delta(A1-P1)$ (dB)			$\Delta(A1-P0)$ (dB)		
	mean	min.	max.	mean	min.	max.
/i/	15	5	23
/u/	11	7	17
/e/	10	4	17	8	5	13
/ɛ/	12	8	17	8	4	13
/æ/	8	4	16
/ɑ/	6	4	8

els: for each vowel type, $A1-P1$ showed statistically significant difference between nasal and oral vowels with $p < 0.01$ by one-sided dependent t -test. The adjustment had a much smaller effect on $A1-P0$ than on $A1-P1$. For $A1-P0$, with adjustment, the mean was raised slightly for both oral and nasal vowels. The standard deviation remained about the same. The range was greater for the oral vowels than for the nasal vowels with or without adjustment.

B. French speakers: Most-nasalized and least-nasalized portions of nasal vowels

French has a nasal–nonnasal vowel distinction, but nasal vowels do not have corresponding oral vowel counterparts which have similar speech articulator positions except for the velum and the lateral pharyngeal walls. Although some languages have oral vowel counterparts to nasal vowels, we chose to study the French vowels since the main goal of this supplementary study was not to compare phonetic vowel nasality (e.g., in English) and phonemic vowel nasality (e.g., in French) but to observe the differences of acoustic correlates at preassigned locations in the nasal vowel that follows a stop consonant. The values at two locations with the greatest differences were examined in further detail.

1. Method

Eight native French speakers, three males (DH, DN, JS) and five females (AG, CL, CT, MT, VV), said words with a stop consonant followed by one of the four French nasal vowels / \tilde{e} /, / \tilde{a} /, / \tilde{o} /, and / $\tilde{ɔ}$ / (as in *bain*, *ban*, *bon*, and *quelqu'un*) in the carrier phrase “dites _____ pour moi.” Three repetitions were recorded for each type. The beginning of the vowel should be produced with the v-p port less open for pressure buildup in the stop than later in the vowel where

TABLE V. The effect of adjusting for vowel types of $A1-P1$ and $A1-P0$ is shown by examining the means, standard deviations (s.d.), and ranges for the oral and nasalized English vowels.

Acoustic correlate	Vowel nasalization	English					
		Unadjusted			Adjusted		
		mean	s.d.	range	mean	s.d.	range
$A1-P1$ (dB)	Oral	24.3	10.5	29.8	19.8	1.5	4.0
	Nasal	14.3	8.2	20.3	12.5	3.9	9.0
$A1-P0$ (dB)	Oral	7.4	1.6	9.0	8.4	2.0	6.0
	Nasal	1.0	1.6	6.0	2.9	1.5	4.0

TABLE VI. Average frequencies of the nasal peaks and the first two formants measured at the most-nasal portion (end) of French nasal vowels of eight speakers with three repetitions each. The “avg.” indicates averages across vowel types. F_{P0} and F_{P1} are the frequencies of the nasal peaks with amplitude $P0$ and $P1$, respectively. $F1$ and $F2$ are the first and second formants, respectively.

Vowel	Most-nasal (end)			
	F_{P0} (Hz)	$F1$ (Hz)	F_{P1} (Hz)	$F2$ (Hz)
/ \tilde{e} /	236	536	958	1302
/ \tilde{a} /	256	555	883	1019
/ \tilde{o} /	238	475	1029	828
/ $\tilde{ɔ}$ /	216	481	874	1277
avg	237	...	936	...

the port should be opened more to nasalize the vowel with minimal change in the positions of the other speech articulators.

For each vowel, the frequencies of the first and second formants, $F1$ and $F2$, and the frequencies of the extra peaks $P1$ and $P0$, F_{P1} and F_{P0} , as well as acoustic correlates $A1-P1$ and $A1-P0$ were measured at the beginning of the vowel, 20 ms into the vowel, the middle of the vowel, and the end of the vowel. The maximum deviations of $A1-P1$ and $A1-P0$ from the beginning of the vowel to the other three positions of the vowel were calculated for each speaker and repetition.

2. Results and discussion

The correlates $A1-P1$ and $A1-P0$ measured at the end of the vowel showed a greater deviation from the value at the vowel onset than did the other two locations in the vowel. The differences in the values over time may be explained by the closer contact of the velum and pharyngeal walls immediately following the stop consonant, followed by the increased lowering of the velum and the relaxing of the pharyngeal walls into the vowel. This difference was not as obvious in the study on English nasal vowels since those vowels were between nasal consonants. Table VI shows the average frequencies measured at the end of the nasal vowel, the most-nasalized portion. In cases where the formant frequency was close to the frequency of the extra peak, the more prominent peak throughout the vowel was labeled as the formant peak. According to the definition of $P0$, the second harmonic amplitude was used for measuring $P0$ for two male speakers while the first harmonic amplitude was used for measuring $P0$ for female speakers and one male speaker. (If the two subjects for whom F_{P0} was the second harmonic were omitted, the average F_{P0} would decrease by 6 to 15 Hz.) For all of the vowels, averaged F_{P0} ranged from 216 to 256 Hz with an average across vowels of 237 Hz, and average F_{P1} ranged from 874 to 1029 Hz with an average across vowels of 936 Hz. The frequency of the first formant indicates that the nasal vowels are nonlow and nonhigh vowels.

Tables VII and VIII show the average $A1-P1$ and $A1-P0$, respectively, measured in the nasal vowels, / \tilde{e} /, / \tilde{a} /, / \tilde{o} /, and / $\tilde{ɔ}$ / for each of the eight speakers. The adjustment

TABLE VII. The correlate $A1-P1$ was measured at the least-nasal portion of the French nasal vowels (L-n) and at the most-nasal portion of the nasal vowels (M-n) for three repetitions. The boldfaced numbers indicate $p < 0.01$, and the italicized numbers indicate $p < 0.05$ between the least-nasal and most-nasal values for the given speaker (Sp.).

Sp.	$A1-P1$ (dB)							
	$/\tilde{e}/$		$/\tilde{a}/$		$/\tilde{o}/$		$/\tilde{\text{œ}}/$	
	L-n	M-n	L-n	M-n	L-n	M-n	L-n	M-n
DH	26.3	18.7	21.7	27.3	30.3	27.0	36.0	18.3
DN	22.0	9.0	16.0	12.3	28.7	12.7	16.3	9.7
JS	31.0	27.0	16.7	9.7	14.0	9.3	28.0	23.7
AG	14.3	-1.0	12.0	-8.3	39.0	20.0	26.3	8.7
CL	22.3	12.7	15.7	4.0	31.7	19.0	8.0	13.7
CT	19.7	-1.3	13.0	-0.3	27.7	19.0	7.7	0.0
MT	21.7	7.7	16.7	4.7	19.3	9.7	18.7	4.3
VV	13.7	2.7	16.7	5.0	19.3	6.7	18.0	4.7

technique for vowel type was not needed since comparisons were made between the values for the same vowel. The “L-n” columns show values for the least-nasalized portion at the beginning of the vowel following the stop and the “M-n” columns show values for the most-nasalized portion at the end of the vowel. (The values from the other portions of the vowel are not presented since they differed less from the values at the beginning than the values from the end of the vowel.) The boldfaced numbers indicate $p < 0.01$ and the italicized numbers indicate $p < 0.05$ according to one-sided dependent t -test between the least-nasal and most-nasal values for the given vowel and speaker. Since the sample size is small, a technique suggested by Sachs (1984) incorporating the arithmetic means and the arithmetic mean of the ranges was used for the one-sided t -test.

For $/\tilde{e}/$, there was a statistically significant difference

TABLE VIII. The correlate $A1-P0$ was measured at the least-nasal portion of the French nasal vowels (L-n) and the most-nasal portion (M-n) for three repetitions. The boldfaced numbers indicate $p < 0.01$, and the italicized numbers indicate $p < 0.05$ between the least-nasal and most-nasal values for the given speaker (Sp.).

Sp.	$A1-P0$ (dB)							
	$/\tilde{e}/$		$/\tilde{a}/$		$/\tilde{o}/$		$/\tilde{\text{œ}}/$	
	L-n	M-n	L-n	M-n	L-n	M-n	L-n	M-n
DH	8.3	0.0	6.7	-1.0	5.7	-1.3	7.7	-3.0
DN	1.3	-5.3	4.3	-5.0	0.0	-8.7	-0.7	-5.0
JS	7.0	5.7	9.0	6.7	5.3	4.3	3.3	2.7
AG	3.7	-3.7	5.3	-1.3	4.0	-3.3	3.0	5.3
CL	1.7	-1.3	5.0	-1.7	4.3	-1.3	-6.3	-1.3
CT	5.3	-3.7	4.0	-7.0	0.7	-14.3	-6.0	-10.7
MT	6.7	1.3	4.0	-3.0	2.0	-7.0	-2.0	-10.7
VV	5.7	-11.0	6.7	-6.7	4.3	-11.3	-8.3	-9.7

between $A1-P1$ measured in the least-nasalized portion of the vowel $(A1-P1)_{L-n}$ and that of the most-nasalized portion $(A1-P1)_{M-n}$ for seven of the eight subjects. There was also a statistically significant difference between $(A1-P0)_{L-n}$ and $(A1-P0)_{M-n}$ for six of the eight subjects. For all speakers, the average measurements across vowels were larger at the beginning of the vowel with minimal nasalization than into the vowel where greater nasalization occurred, in agreement with $A1-P1$ and $A1-P0$ being inversely related to nasalization. For $/\tilde{a}/$, all of the speakers and for $/\tilde{o}/$, seven of the speakers showed statistically significant differences between $(A1-P0)_{L-n}$ and $(A1-P0)_{M-n}$, while for $A1-P1$, the differences were significant for only five speakers for $/\tilde{a}/$ and for six subjects for $/\tilde{o}/$. Table VI indicates that $F2$ is very close to F_{P1} for $/\tilde{a}/$, and $/\tilde{o}/$, making the measurement of $A1-P1$ less reliable. For $/\tilde{\text{œ}}/$, six of the speakers showed statistically significant differences between $(A1-P1)_{L-n}$ and $(A1-P1)_{M-n}$, while for $A1-P0$, the differences were significant for only three speakers. The smaller difference for $A1-P0$ may due to $/\tilde{\text{œ}}/$ being preceded by a voiceless stop. Although voiceless stops in French are only weakly aspirated, the spread glottal configuration in the stop would increase the first harmonic amplitude (used as $P0$ for six subjects) at the beginning of the vowel, giving it a more nasal characteristic.

The difference between $(A1-P1)_{L-n}$ and $(A1-P1)_{M-n}$, $\Delta(A1-P1)$, and the difference between $(A1-P0)_{L-n}$ and $(A1-P0)_{M-n}$, $\Delta(A1-P0)$, were calculated. Table IX shows the results from the averages of eight subjects. The mean for $\Delta(A1-P1)$ ranged from 9 dB to 12 dB with the minima ranging from -6 dB to 4 dB and the maxima from 18 dB to 21 dB, depending on the vowel type. The mean for $\Delta(A1-P0)$ ranged from 3 dB to 9 dB with the minima ranging from -5 dB to 2 dB and the maxima from 11 dB to 17 dB. The low minimum range was mainly due to speaker JS (50% of the time JS gave the lowest average difference among the speakers); also, for $/\tilde{\text{œ}}/$, $F2$ shifting to a lower frequency into the vowel may have decreased $\Delta(A1-P0)$.

TABLE IX. Mean, minimum (min.), and maximum (max.) differences between the averages A1-P1 and A1-P0 measured in least-nasal and most-nasal portions of French vowels for eight subjects are shown.

Vowel	$\Delta(A1-P1)$ (dB)			$\Delta(A1-P0)$ (dB)		
	mean	min.	max.	mean	min.	max.
/ɛ̃/	12	4	21	7	1	17
/ɑ̃/	9	-6	20	8	2	13
/ɔ̃/	11	3	19	9	1	16
/œ̃/	9	-6	18	3	-5	11

The theoretical values for the differences, 18 dB for $\Delta(A1-P1)$ and 8 dB–11 dB for $\Delta(A1-P0)$, are between the mean and maximum differences measured, as was also noted above for the contextually nasalized vowels in English. Any discrepancy between the theoretical difference and the measured difference for French may be due to some nasalization even at the beginning portion of the vowel and the varying degrees to which speakers nasalize the vowel. From high-speed cinefluorographic studies, Moll and Daniloff (1971) observed that in a stop consonant–vowel–nasal consonant sequence (CVN), velar movement began no later than the start of tongue movement toward the vowel.

To show the effect of the adjustment technique for vowel type, the means, standard deviations, and ranges of adjusted and unadjusted A1-P1 and A1-P0 are listed in Table X. For A1-P1, the mean was lowered slightly after adjustment for both portions of the vowels. The s.d. was reduced by 2.5 dB and 1.9 dB after adjustment for the least-nasalized portion and the most-nasalized portion, respectively. The amount of s.d., reduction was smaller than for English since the range of vowel height was much less for the French corpus. The range of the least-nasalized portion was larger than that of the most-nasalized portion before correction but it became about the same after correction. For A1-P0, with adjustment, the mean was raised for both portions. The standard deviation did not change much (on average) with adjustment and actually increased for the least-nasalized portion. The French vowels showed that, as in English, correction for vowel type has a smaller effect on A1-P0 than on A1-P1. The range of A1-P0 for the least-nasalized portions was greater than for the most-nasalized portions both before and after correction. The difference in range may be due to the nasal peak being more prominent in

TABLE X. The effect of adjusting for vowel types on A1-P1 and A1-P0 is shown by examining the means, standard deviations (s.d.), and ranges for the least-nasal and most-nasal portions of French vowels.

Acoustic correlate	Vowel nasalization	French Unadjusted			Adjusted		
		mean	s.d.	range	mean	s.d.	range
A1-P1 (dB)	Least-nasal	20.8	4.3	10.3	18.0	1.8	4.0
	Most-nasal	10.5	3.7	8.8	9.6	1.8	4.2
A1-P0 (dB)	Least-nasal	3.6	2.6	6.1	8.2	4.4	9.4
	Most-nasal	-2.3	1.5	3.5	-0.3	1.0	2.2

the most-nasalized portion. It is therefore measured more reliably, while for the least-nasalized portion the “nasal peak” is defined as the harmonic with the maximum amplitude in the vicinity of the peak in the most-nasalized portion. To evaluate this measure more closely, the minimum difference in A1-P0 between the least-nasal and the most-nasal for each speaker and each vowel was examined, and it was found that this difference was statistically significant for six speakers for three of the four vowels.

C. Differences between the English and French results

Some differences between the English and French results were observed. The mean of $\Delta(A1-P1)$ ranged from 10 to 15 dB for English and 9 to 12 dB for French; the mean of $\Delta(A1-P0)$ ranged between 6 and 8 dB for English and 3 to 9 dB for French. From Tables V and X, the unadjusted mean A1-P1 of the oral/least-nasalized vowels and nasal/most-nasalized vowels was 3.5 and 3.8 dB higher, respectively, for English than for French; the mean A1-P0 was similarly higher by 3.8 and 3.3 dB for the oral/least-nasalized vowels and nasal/most-nasalized vowels, respectively. The range of unadjusted A1-P1 was 19.5 dB and 11.5 dB greater for the English vowels than for French vowels in oral/least-nasalized vowels and nasal/most-nasalized vowels, respectively. The range of the unadjusted A1-P0 was 2.9 and 2.5 dB greater for English than for French in oral/least-nasalized vowels and nasal/most-nasalized vowels, respectively.

There were several causes for the differences between the English and French results. Only some vowels of each language were studied: the English vowels included high and low vowels while the French vowels were nonhigh and non-low vowels. In addition, for English, measurements for comparison were made in different tokens while for French, they were made in the same token at different times. These differences would cause the range of the English vowels to be greater than the French vowels, as reflected in the unadjusted values. On the other hand, there was no such trend in the ranges of the adjusted acoustic correlates between English and French vowels, particularly for A1-P1, suggesting that the adjustment technique compensates for vowel type and measurement differences. The fact that nasalization of the English vowels was due to context while the nasalization of the French vowels was due to contrast may introduce variations in the velopharyngeal opening size (Delattre, 1965; Mrayati, 1975), causing the means of A1-P1 and A1-P0 (both unadjusted and adjusted) for the most-nasalized portions in French to be smaller than for the nasal vowels in English. Furthermore, speaker differences or vowel environment affecting vowel breathiness may influence the values of A1-P0. A parameter characterizing breathiness, such as H1-H2 (the amplitude dB difference between the first and second harmonics) should be used to distinguish the effect of breathy voicing on A1-P0 from that of nasalization (Chen, 1996).

ACKNOWLEDGMENTS

The author would like to thank Kenneth N. Stevens for his guidance and editorial assistance. The editorial assistance of F. Bell-Berti, D. Kewley-Port, A. Löfqvist, and an anonymous reviewer is also gratefully acknowledged. This work was supported in part by an NSF fellowship, an NIH Grant (DC 00075), and a LeBel fellowship.

- Båvegård, M., Fant, G., Gauffin, J., and Liljencrants, J. (1993). "Vocal tract sweep-tone data and model simulations of vowels, laterals, and nasals," *STL-QPSR* **4**, 43–76.
- Bjuggren, G., and Fant, G. (1964). "The nasal cavity structures," *Speech Trans. Lab. Q. Prog. Stat. Rep.* **4**, Royal Institute of Technology, Stockholm, 5–7.
- Chen, M. Y. (1995). "Acoustic parameters of nasalized vowels in hearing-impaired and normal-hearing speakers," *J. Acoust. Soc. Am.* **98**, 2443–2453.
- Chen, M. Y. (1996). "Acoustic Correlates of Nasality in Speech," Ph. D. dissertation, Massachusetts Institute of Technology, Cambridge, MA.
- Chen, M. Y., and Metson, R. (1997). "Effects of sinus surgery on speech," *Arch. Oto-Laryngology—Head Neck Surg.* **123**, 845–852.
- Chuang, E. S., and Hanson, H. M. (1996). "Glottal characteristics of male speakers: Acoustic correlates and comparison with female data," *J. Acoust. Soc. Am.* **100**, 2657.
- Dang, J., and Honda, K. (1995). "An investigation of the acoustic characteristics of the paranasal cavities," *Proceeding of the XIIIth International Congress of Phonetic Sciences* **1**, 342–345.
- Dang, J., and Honda, K. (1996). "Acoustic properties of paranasal sinuses derived from transmission characteristic measurement and morphological observation," *J. Acoust. Soc. Am.* **100**, 3374–3383.
- Dang, J., Honda, K., and Suzuki, H. (1994). "Morphological and acoustical analysis of the nasal and the paranasal cavities," *J. Acoust. Soc. Am.* **96**, 2088–2100.
- Delattre, P. (1954). "Les attributs acoustiques de la nasalité vocalique et consonantique," *Stud. Linguist.* **8**, 103–109.
- Delattre, P. (1965). "La nasalité vocalique en français et en anglais," *The French Review* **39**, 92–109.
- Fant, G. (1960). *The Acoustic Theory of Speech Production* (Mouton, The Hague).
- Feng, G., and Castelli, E. (1996). "Some acoustic features of nasal and nasalized vowels: A target for vowel nasalization," *J. Acoust. Soc. Am.* **99**, 3694–3706.
- Flanagan, J. L. (1972). *Speech Analysis Synthesis and Perception* (Springer-Verlag, New York).
- Fujimura, O. (1960). "Spectra of nasalized vowels," *Q. Prog. Rep.* **58**, Massachusetts Institute of Technology, 214–218.
- Fujimura, O., and Lindqvist, J. (1964). "The sinewave response of the nasal tract," *Speech Trans. Lab. Q. Prog. Stat. Rep.* **1**, Royal Institute of Technology, Stockholm, 5–10.
- Fujimura, O., and Lindqvist, J. (1971). "Sweep-tone measurements of vocal-tract characteristics," *J. Acoust. Soc. Am.* **49**, 541–558.
- Hattori, S., Yamamoto, K., and Fujimura, O. (1958). "Nasalization of vowels in relation to nasals," *J. Acoust. Soc. Am.* **30**, 267–274.
- Hawkins, S., and Stevens, K. N. (1985). "Acoustic and perceptual correlates of the nonnasal–nasal distinction for vowels," *J. Acoust. Soc. Am.* **77**, 1560–1575.
- Hillenbrand, J., Getty, L. A., Clark, M. J., and Wheeler, K. (1995). "Acoustic characteristics of American English vowels," *J. Acoust. Soc. Am.* **97**, 3099–3111.
- House, A. S., and Stevens, K. N. (1956). "Analog studies of the nasalization of vowels," *J. Speech Hear. Dis.* **21**, 218–232.
- Huffman, M. (1990). "Implementation of nasal: Timing and articulatory landmarks," *UCLA Working Papers in Phonetics* **75**, 112–143.
- Klatt, D. H. (1984). "The new MIT speech VAX computer facility," *Speech Communication Group Working Papers IV*, Research Laboratory of Electronics, MIT, Cambridge, 73–82.
- Klatt, D. H., and Klatt, L. C. (1990). "Analysis, synthesis, and perception of voice quality variations among female and male talkers," *J. Acoust. Soc. Am.* **87**, 820–857.
- Kuehn, D. P., and Dalston, R. M. (1989). "Cleft palate and studies related to velopharyngeal function," in *Human Communication and Its Disorders*, edited by H. Winitz (Ablex, Norwood), pp. 1–106.
- Lindqvist, J., and Sundberg, J. (1972). "Acoustic properties of the nasal tract," *Speech Trans. Lab. Q. Prog. Stat. Rep.* **1**, Royal Institute of Technology, Stockholm, 13–17.
- Lindqvist-Gauffin, J., and Sunberg, J. (1976). "Acoustic properties of the nasal tract," *Phonetica* **33**, 161–168.
- Maeda, S. (1982a). "The role of the sinus cavities in the production of nasal vowels," *Proc. IEEE Int. Conf. ASSP* **2**, 911–914.
- Maeda, S. (1982b). "Acoustic cues of vowel nasalization: A simulation study," *J. Acoust. Soc. Am. Suppl.* **1** **72**, S102.
- Maeda, S. (1993). "Acoustics of vowel nasalization and articulatory shifts in French nasal vowels," in *Phonetics and Phonology Volume 5: Nasals, Nasalization and the Velum*, edited by M. K. Huffman and R. A. Krakow (Academic, New York), pp. 147–167.
- Moll, K. L. (1962). "Velopharyngeal closure on vowels," *J. Speech Hear. Res.* **5**, 30–37.
- Moll, K. L., and Daniloff, R. G. (1971). "Investigation of the timing of velar movements during speech," *J. Acoust. Soc. Am.* **50**, 678–684.
- Mrayati, M. (1975). "Etude des voyelles nasales françaises," *Bulletin de l'Institut de Phonétique de Grenoble* **IV**, 1–26.
- Sachs, L. (1984). *Applied Statistics*, 2nd ed. (Springer-Verlag, New York).
- Stevens, K. N. (in press). *Acoustic Phonetics* (MIT, Cambridge, MA).
- Stevens, K. N., Andrade, A., and Céu Viana, M. (1988). "Perception of vowel nasalization in VC contexts: A cross-language study," *J. Acoust. Soc. Am. Suppl.* **1** **82**, S119.
- Stevens, K. N., Nickerson, R. S., Boothroyd, A., and Rollins, A. M. (1976). "Assessment of nasalization in the speech of deaf children," *J. Speech Hear. Res.* **19**, 393–416.
- Suzuki, H., Nakai, T., Dang, J. and Lu, C. (1992). "Speech production model involving subglottal structure and oral-nasal coupling through closed velum," *Proceedings of the International Conference on Speech and Language Processing*, Banff, Alberta, Vol. 1, 441–444.

Correlation dimension of electroglottographic data from healthy and pathologic subjects

Alison Behrman^{a)}

Communication Sciences Program, Hunter College/CUNY, 425 East 25th Street, Room N1306, New York, New York 10010-2590

R. J. Baken

Department of Otorhinolaryngology, New York Eye and Ear Infirmary, 310 East 14th Street, New York, New York 10003

(Received 10 October 1996; accepted for publication 8 July 1997)

This paper considers the effects of nonstationarity, noise, and finite data sets on the estimation of the correlation dimension of time-series data characterizing the vibratory behavior of the vocal folds. The electroglottographic signal of sustained /a/ phonations from 10 healthy subjects and 20 subjects with vocal fold pathologies were used to reconstruct the state space in successively higher embeddings using the method of lags. The dimension values were calculated from the scaling region (the level area of the slope plots) which did not increase for higher embeddings. Reasonably defined scaling regions were found in all of the data from the healthy subjects and from five of the pathologic subjects, with values saturating between the first and second embeddings. The EGG data from those five pathologic subjects were nearly periodic. From the remaining 15 subjects, the scaling regions were highly constricted with nonconstant slopes, so that dimension values could not be confidently estimated. The results suggest that the correlation dimension is a highly subjective measure which is not usefully applied to abnormal EGG data. It is recommended that, if used, correlation dimension statistics need to be presented cautiously, and graphical presentation of the data should be included. © 1997 Acoustical Society of America. [S0001-4966(97)05010-8]

PACS numbers: 43.70.Bk, 43.70.Gr [AL]

INTRODUCTION

The power of nonlinear dynamics to characterize complex dynamical systems mathematically has resulted in its fruitful application to the analysis of diverse biological phenomena, including cardiovascular aging (Lipsitz, 1995), auditory perception (Ding *et al.*, 1995), and spinal cord neural structure (Smith and Neale, 1994). Exploration of the complex mechanisms of voice production, with its nonlinear biomechanical and aerodynamic forces, and with evidence of bifurcations and random-appearing output, would appear to similarly benefit from analyses within this theoretical framework. In that regard, dynamical analysis, the quantification of chaos from experimentally obtained time series, has played a dominant role in the characterization of the phonatory system as a chaotic oscillator (Kumar and Mullick, 1996; Narayanan and Alwan, 1995; Herzel *et al.*, 1994; Herzel, 1993; Titze *et al.*, 1993; Baken, 1990).

A prerequisite for chaotic systems is exquisite sensitivity to initial conditions (Eubank and Farmer, 1990) demonstrated by a positive Lyapunov exponent λ (Eckman and Ruelle, 1985; Sano and Sawada, 1985; Wolf *et al.*, 1985). Lyapunov exponent values for speech data are inconsistent. Kumar and Mullick (1996) found the maximum exponent λ_1 to be positive, characteristic of chaos, for normal vowel and consonant productions. In contrast, Narayanan and Alwan (1995) calculated a maximum exponent λ_1 of zero, indicating a limit cycle, for normal vowel phonation and a positive

value for voiced and voiceless fricative productions. Herzel (1993) found a maximum exponent λ_1 of zero for healthy vowel phonation, while a dysphonic vowel sample yielded a positive value. All authors cautioned, however, that calculation of the exponent is highly sensitive to short data sets and nonstationarity. In fact, critical sensitivity to noise (Schreiber and Kantz, 1995; Glass and Kaplan, 1993) makes calculation of a Lyapunov exponent highly suspect and inconclusive for voice data (Vaidya *et al.*, 1996).

Rigorous proof of chaotic dynamics may be unrealistic given current analytic limitations. Establishing the dynamics as dominantly low dimensional, however, may be more reasonable. Although low dimension is not a prerequisite for chaotic dynamics, a high-dimensional system is effectively a stochastic process. The distinction between chaos and noise is important. If the dynamics are periodic with additive Gaussian noise, then the periodic function and the standard deviation of the noise provide a complete description of the system. If the dynamics are low dimensional with the potential for chaos, then there is a complex determinism which holds the possibility of prediction, control, and manipulation. Therefore, demonstrating that the asymptotic behavior of the phonatory system is dominated by the interaction among relatively few degrees of freedom is a meaningful and practical goal. Low dimension may be demonstrated in a number of ways. The most popular, perhaps, is by calculation of the correlation dimension, an estimate of the complexity or irregularity of a system in space or time (Barnsley, 1988; Mandelbrot, 1983). The correlation dimension can be any real value which is less than or equal to the Euclidean di-

^{a)}Electronic mail: abehrman@hejira.hunter.cuny.edu

mension of the state space, and greater than or equal to the topological dimension. It is a scale-independent measure, which makes it appropriate for measuring fractal structures, which have no characteristic scale. One interpretation of the correlation dimension is that it defines the number of essential degrees of freedom of the attractor, and hence, of the dynamical system. A simplified voice production system can be approximately modeled with differential equations, and data from these models suggest that the phonatory system may be controlled by only a few operative degrees of freedom (Herzel *et al.*, 1994; Steinecke and Herzel, 1995; Baken, 1994; Berry *et al.*, 1994; Titze *et al.*, 1993; Awrejcewicz, 1990). Preliminary human data appear to support that assertion (Kumar and Mullick, 1996; Narayanan and Alwan, 1995; Kakita and Okamoto, 1994; Titze *et al.*, 1993; Hirose *et al.*, 1994).

The theories and tools of nonlinear dynamics have been developed within systems from which infinite and stationary data may be obtained. A signal is considered stationary if statistical characterizations of the time series are constant, and therefore no systematic changes, or trends, are evident (Chatfield, 1987). Rigorous application of nonlinear dynamical analyses, such as the correlation dimension, require stationary data. The difficulties of applying dynamical analysis to less than ideal data sets have been discussed in general (Grassberger *et al.*, 1993; Paulus *et al.*, 1993; Sauer and Yorke, 1993; Hammel, 1990; Kostelich and Yorke, 1988). Specifically, characteristics of physiologic data which complicate dynamical interpretation have been identified as short data sets, poor signal-to-noise ratios, nonstationarity, and high dimension (Schmid and Dünki, 1996; Schreiber and Kaplan, 1996; Kantz and Schreiber, 1995; Peng *et al.*, 1995; Wagner and Persson, 1995; Glass and Kaplan, 1993). The application of the theory of nonlinear dynamics to the phonatory system is based on the assumption that the system is deterministic, that initial transients die out relatively quickly after phonatory onset, that the signal is of adequate duration, and that the amount of noise in the system is low. In physiologic systems, transient events and noise (both additive, or measurement noise, as well as dynamic noise) are virtually always present. The larynx is situated in close physical proximity to major blood vessels, muscles, and nerves. A constantly changing environment, transient events, and the interaction between control systems results in both dynamic noise and nonstationarity. Distant events in the human body across all systems (neurologic, vascular, etc.) and hierarchical levels (peripheral, spinal, posterior fossa, etc.) are constantly affecting phonatory function, often in very small ways. Transient activity associated with phonatory onset, for example, is not very difficult to exclude from analytic data sets. But transients and dynamic noise associated with distant physiologic events may not be so obvious. In theory, the attractor describes the system's dynamics when stationarity has been achieved. One analytic solution for achieving a stationary data set is to sample relatively short segments of phonation, assuming that most transient effects are slower than the oscillatory behavior being observed. That is not necessarily always true, however. And the stationarity achieved by the short sampling duration may be outweighed by the negative

impact of missing information due to incomplete observation of the dynamics. Another solution is to constrain the subject during the experimental task in such a way as to produce the most constant signal possible. This is a limited solution, because constraining the system will not necessarily result in stationarity.

Notwithstanding these difficulties, the application of nonlinear dynamics to voice production holds great promise. Both the evidence that certain dysphonic characteristics may be related to nonlinear phenomena (Herzel, 1996), and the conceptualization of dysphonia as the disentrainment of a few principal vibratory modes (Steinecke and Herzel, 1995; Berry *et al.*, 1994) may ultimately result in greater understanding and control of abnormal voice production. Because of this great potential, further exploration of the application of dynamical analysis to voice data are needed. Specifically, the effect of longer data sets needs to be examined. While longer data sets may be considered more representative of phonatory dynamics than short data sets, the data may also be less stationary. In addition, more data from pathologic phonatory systems, which frequently contain significant intermittent phenomena, must be explored. The dimensionality of the "raw" physiologic signal, rather than derivative data, also bears examination. This paper explores the applicability of nonlinear dynamical systems theory to the analysis of normal and pathologic voice. The ultimate goal was a first approximation of the minimum number of independent variables (degrees of freedom) required to make meaningful assessment of healthy and dysphonic phonation. The specific purpose of this study was to explore the impact of nonstationarity, noise, and finite data sets on the calculation of the correlation dimension.

I. METHODS

A. Data collection

Ten healthy individuals and twenty dysphonic patients served as subjects. All dysphonic subjects were diagnosed with either bilateral nodules or a unilateral polyp of the vocal folds. Both pathologies are common benign lesions which have the potential to interfere with regular vibratory behavior in a variety of ways across a range of degrees of severity. Table I provides information on the sex and ages of all of the subjects, and the types of vocal pathologies of those who were dysphonic.

Data obtained on each subject consisted of the microphone and electroglottographic (EGG) signals of sustained /a/ at self-selected comfortable pitch and loudness. The EGG signal is currently one of the easiest and most noninvasive means of accessing information about vocal fold contact during vibration. Based on the principle of Ohm's law, it measures the change in electrical conductance across the neck in the region of the vocal folds, and the resulting output reflects the change in impedance due to changes in relative vocal fold contact area during phonation (Fig. 1) (Baken, 1992; Childers *et al.*, 1987; Fourcin, 1981). The source energy of the acoustic signal is substantially defined by the temporal and geometric characteristics of the changing vocal fold contact area throughout each vibratory cycle. Free of the reso-

TABLE I. Characteristics of healthy and pathologic subjects.

Patholog. Subject	Sex	Pathology	Age (yrs)	Healthy subject	Sex	Age (yrs)
1	F	Nodules	30	21	F	40
2	F	Nodules	78	22	M	34
3	F	Nodules	49	23	F	24
4	F	Nodules	42	24	F	25
5	F	Nodules	35	25	M	25
6	M	Nodules	30	26	M	24
7	M	Nodules	76	27	F	40
8	F	Nodules	21	28	M	27
9	F	Nodules	45	29	F	78
10	F	Nodules	18	30	M	71
11	M	Polyp	72			
12	M	Polyp	20			
13	F	Polyp	70			
14	M	Polyp	55			
15	M	Polyp	29			
16	M	Polyp	36			
17	M	Polyp	83			
18	M	Polyp	46			
19	M	Polyp	32			
20	F	Polyp	31			
Female						
mean			41.9			41.4
s.d.			20.7			21.9
range			18–78			24–78
Male						
mean			47.9			36.2
s.d.			22.4			19.8
range			20–83			24–71
All						
mean			44.9			38.8
s.d.			20.7			19.9
range			18–78			24–78

nant characteristics of the vocal tract, the EGG may be considered simpler than the acoustic signal. Salient characteristics of the EGG waveform of healthy, modal phonation produced at comfortable intensity include uniformity of successive periods and cycle amplitudes, a relatively sharper increase than decrease in vocal fold contact, and a relatively long maximal contact duration (Fourcin, 1981).

The EGG signal was transduced with a Kay Elemetrics Fourcin type electroglottograph, low-pass filtered -3 dB at 7 kHz. The microphone signal was obtained to confirm information derived from the EGG signal and to derive spectrographic and perturbation data, neither of which are addressed in this paper. All data were gathered by computer using the Kay Elemetrics A/D conversion hardware and software, with

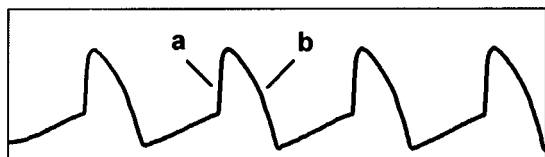


FIG. 1. Four cycles of a typical EGG waveform from a healthy subject, showing (a) increasing and (b) decreasing relative vocal fold contact.

16-bit resolution at a sampling rate of 25.0k samples/s/channel.

B. Data analysis

The first and last 0.4 s of the EGG signal were truncated to help remove some of the nonstationarity effects of phonation onset and offset. The data files were then trimmed to 2^{16} (65 536) data points in length (approximately 2.6 s) to facilitate calculation of the correlation dimension. All nonlinear analyses were performed on a Pentium-based PC using Tools For Dynamics Software.

1. State space embeddings

The EGG data were embedded in state space following the methods of Takens (1981), in which reconstruction of the attractor was accomplished using the method of lag variables. In such a representation, the value of a variable v at time (x) is lagged against itself, using a fixed time delay τ , to create a vector time series of the form

$$y(x) = \{v(x), v(x + \tau), v(x + 2\tau), \dots, v(x + (m-1)\tau)\}, \quad (1)$$

where each lagged time series is an m -dimensional embedding. The resulting values are used as coordinates in m -dimensional state space. Grassberger *et al.* (1991) note that choosing the lag values is somewhat arbitrary; the accurate reconstruction of the pseudo-state space should not be overly sensitive to the delay values. However, using too short a delay yields coordinates which are too correlated and results in a straight-line plot. Too long a delay distorts the geometry. One method of calculating the optimal delay is to use the minimum of the mutual information function (Fraser and Swinney, 1986) so that the lagged values share the least information with each other, or conversely, provide the most new information. Using this method, the means of the various optimal lag values used to embed the EGG data in m -dimensional state space was 1.1 ms for the female subjects and 1.4 ms for the male subjects.

2. Dimension analyses

The correlation dimension (d_A) (Grassberger and Procaccia, 1983), which is based on the comparison of pairwise distances between points and accounts for the density of points, provides information about the amount of state space filled by the attractor. One interpretation of the d_A is that it provides an estimate of the operational degrees of freedom of the dynamics. It is obtained by first calculating the correlation integral $C(r)$ for a number of embeddings. The $C(r)$ is the number of distances less than a given radius divided by the number of distances searched altogether. It is given by

$$C(r) = \lim_{n \rightarrow \infty} \frac{2}{n(n-1)} \sum_{j=1}^n \sum_{i=j+1}^n H(r - |v(i) - v(j)|), \quad (2)$$

where $v(i)$ and $v(j)$ are points on the attractor. H is the Heavyside function which tallies the number of distances which are found to be less than the given radius r . Equation (2) is modified, however, to exclude pairs of points which

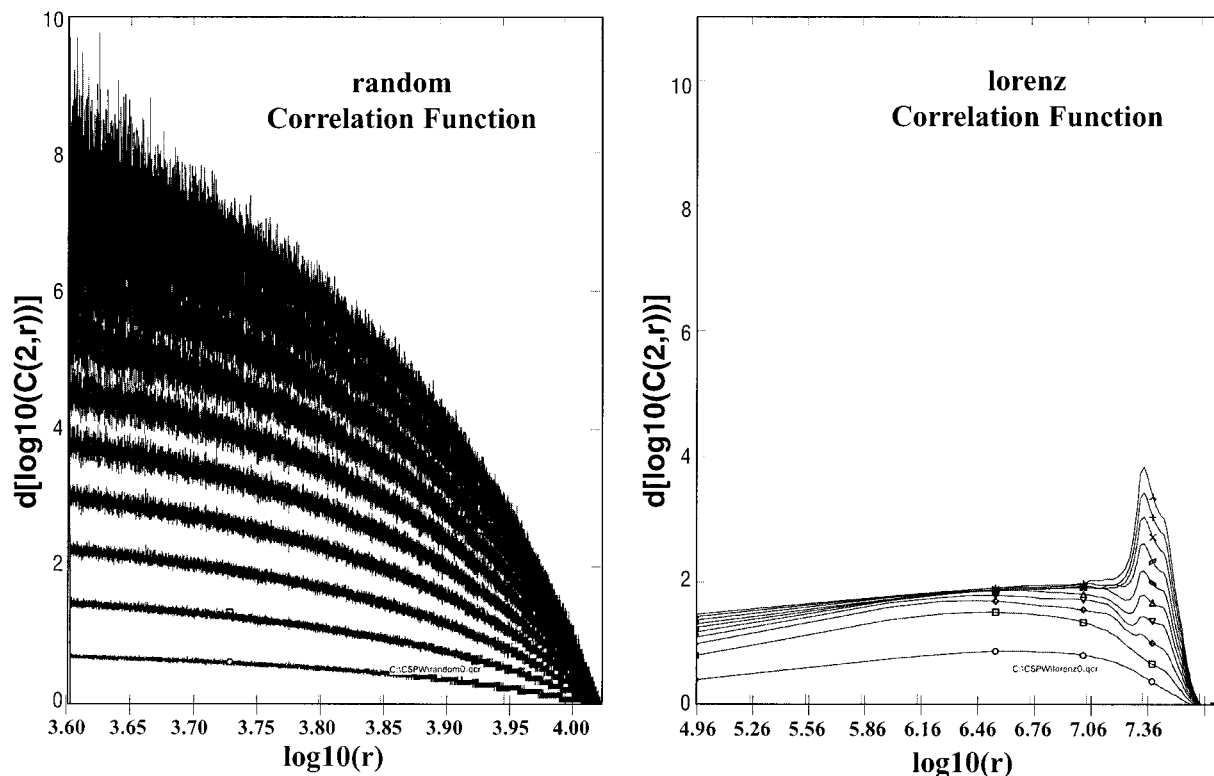


FIG. 2. Local slopes for correlation dimension calculations from (left) a software-generated random data set of 50k point; and (right) the Lorenz equations. Embedding dimensions 1–10 are shown from bottom to top.

are located near to one another in state space only because they are closely located in time. Theiler (1986) has shown that the inclusion of such strongly correlated points results in systematic artifact and makes dimension estimation difficult. The correlation dimension is then expressed as

$$d_A = \lim_{r \rightarrow 0} \lim_{N \rightarrow \infty} \frac{\log C(N, r)}{\log(r)}, \quad (3)$$

which is determined from the slope of the straight-line portion of a plot of the density of the data points as a function of the resolution for embedding dimension $m > d$, where m is the embedding dimension and d is the dimension of the attractor. That is, the estimated value of the correlation dimension is equal to the plateau region of the slope where the value is constant for increased embedding dimension. The constant values from successive embeddings are referred to here as saturation.

For a stochastic process with infinite operational degrees of freedom, each new embedding provides additional information, and saturation is never achieved. The left plot in Fig. 2 shows the local slope values from a data set which was produced using a computerized random number generator. The random data would be expected to completely fill each embedded dimension, and indeed, the number of pairs of points found as a function of resolution is a smoothly increasing function for each embedding with no evidence of a stable scaling region. In principle, for a deterministic system, whether it is chaotic or not, there are limited operational degrees of freedom, and therefore saturation will be reached when all essential degrees of freedom have been revealed.

The greater the number of degrees of freedom, the more rapid will be the variation in the average number of neighbors of any given data point as a function of distance from that point. The right plot in Fig. 2 shows the local slope values for the Lorenz equations (Lorenz, 1963), a set of three ordinary differential equations obtained as a model of convection fluid flow which have been used countless times to model chaotic flow. (The equations are not replicated here because they are so commonly found in the literature. The parameter values of $\sigma=16$, $b=4$, and $r=45.92$, while not meaningful in the domain of real-world physics, are the standard values used to model chaotic dynamics.) For this ideal (noiseless) chaotic system, the scaling region is long and unchanging for higher embeddings, and the slope is constant. From actual physiologic data, one expects less optimal plots. While the correlation dimension may be reasonably estimated if the plateau region (the scaling region) is constant and has a nonincreasing slope for higher embeddings, the required length of the scaling region is not rigorously defined. Kantz and Schreiber (1995) and Brandstater and Swinney (1987) show that even for well-behaved chaotic data, the scaling region is bounded by measurements of radius r which are smaller than the noise level at one end, and larger than the attractor size on the other end.

II. RESULTS AND DISCUSSION

A. EGG waveforms

Figure 3 shows EGG data from four of the subjects. Data from two healthy subjects (H28 and H29) are charac-

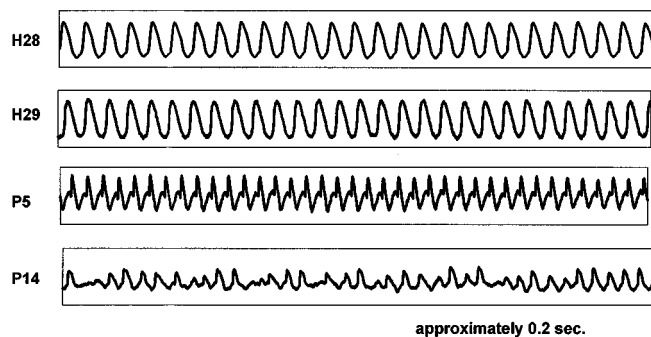


FIG. 3. EGG waveforms from healthy (H28, H29) and pathologic (P5, P14) subjects.

teristic of healthy, modal phonation; specifically, grossly regular (i.e., nearly periodic) in cycle-to-cycle periodicity and amplitude, with a faster increasing than decreasing contact phase. The EGG waveforms sampled from the pathologic subjects (P5 and P14) demonstrated considerable intersubject variability. Abnormal waveform shape (P5), apparent random amplitude and period irregularity (P14), as well as bifurcations and amplitude modulations (not shown) were observed. The waveforms from the pathologic subjects appeared more variable than the waveforms from the healthy subjects. No waveform may be considered representative of the pathologic group, for which there were no uniquely descriptive characteristics.

B. Correlation dimension

Figure 4 shows the plots of the local slopes of the correlation integral for ten embeddings from two healthy (H28, H29) and two pathologic subjects (P5, P14) corresponding to the waveforms shown in Fig. 3. The two noteworthy features of these plots are the estimated values of the correlation dimension, and the difficulty with which those estimates are made. In all instances, the determination of a stable scaling region was a subjective judgment.

All of the local slope plots from the healthy subjects' data were considered to have sufficiently stable scaling regions for estimation of the correlation dimension. Every data set from the healthy subjects clearly appeared to saturate well below the tenth embedding, between approximately 1.0 and 1.5, suggesting a noisy limit cycle. The data from subject H28 provide the best example of a stable scaling region from which the correlation dimension value could be estimated. Three of the data sets had similarly stable scaling regions. The other seven data sets from the healthy subjects looked similar to the plots from subject H29, in which the scaling area was reasonable, although not optimal. The decrease in stability of the scaling region with increasing dimension appeared to be the main factor causing the nonoptimal scaling region. The correlation dimension relies on the geometry of the data within small euclidean distances. It is primarily within these small spaces that noise most contaminates the dynamics. The result is that the higher dimensions are populated more dominantly by noise, causing the slope plots of the higher embeddings to more closely resemble the plots obtained from the random data of Fig. 2.

Five data sets from the pathologic subjects appeared similar to those from the healthy subjects, in that they contained scaling regions which were reasonably long, flat, and did not increase with higher embeddings. The correlation dimension from these five data sets was estimated to be between approximately 1.0 and 1.5. The corresponding EGG waveforms appeared grossly within normal limits and nearly periodic. The remaining 15 data sets from the pathologic subjects, however, all contained some intermittent phenomena as described above, and the power spectra revealed low-frequency energy and more broadly spread spectral peaks. These data sets provided limited scaling regions. The data from subjects P5 and P14 are representative of the constricted and nonstable scaling regions. In both of these examples, similar to the plot of H29, the slopes lose their stability with increasing embeddings. The plot from P14 also shows an upward creep of the scaling region with higher embeddings, likely due to the increasing dominance of noise with each embedding. The constricted scaling regions, unstable slopes and upward creep made it quite difficult to confidently estimate the correlation dimension.

The results show that the correlation dimension could be confidently estimated only from EGG data which was nearly periodic and representative of healthy, stable phonation (i.e., had an absence of bifurcations, modulations, or irregular segments). To determine whether shorter data sets would improve the quality of the scaling regions, the correlation dimension was estimated from the first 16 384 data points (approximately 0.66 s) and the first 32 768 data points (approximately 1.3 s) extracted from the full data sets of five healthy and five pathologic subjects. The plots of the local slopes from the extracted segments of H28 and P5 are shown in Fig. 5. Given the fact that all of the slope plots saturated below the fourth embedding, even the shorter extracted segments should theoretically contain sufficient data points to estimate the correlation dimension (Kantz and Schreiber, 1995; Nerenberg and Essex, 1990; Wolf *et al.*, 1985). Yet it is clear that the shorter data sets do not improve the confidence with which the correlation dimension can be estimated.

Another consideration relative to length of the data sets is the number of cycles sampled. Although the EGG was oversampled at 25k samples/s, the number of cycles is a function of the fundamental frequency and the sample duration. Because of limitations in computational file length, as well as limitations in the maximum phonation time for some of the pathologic subjects, the analyzed data files were trimmed to approximately 2.6 s. The mean fundamental frequency was 111 Hz (males) and 194 Hz (females), resulting in a mean number of cycles per data set of approximately 289 (males) and 504 (females). It is unknown if these vibratory cycles are sufficiently representative of the asymptotic behavior of the phonatory system. At least for the abnormal EGG data, however, it is unlikely.

III. CONCLUSIONS

This study sought to provide an estimate of the number of operative degrees of freedom of healthy and dysphonic phonation and to explore the impact of nonstationarity,

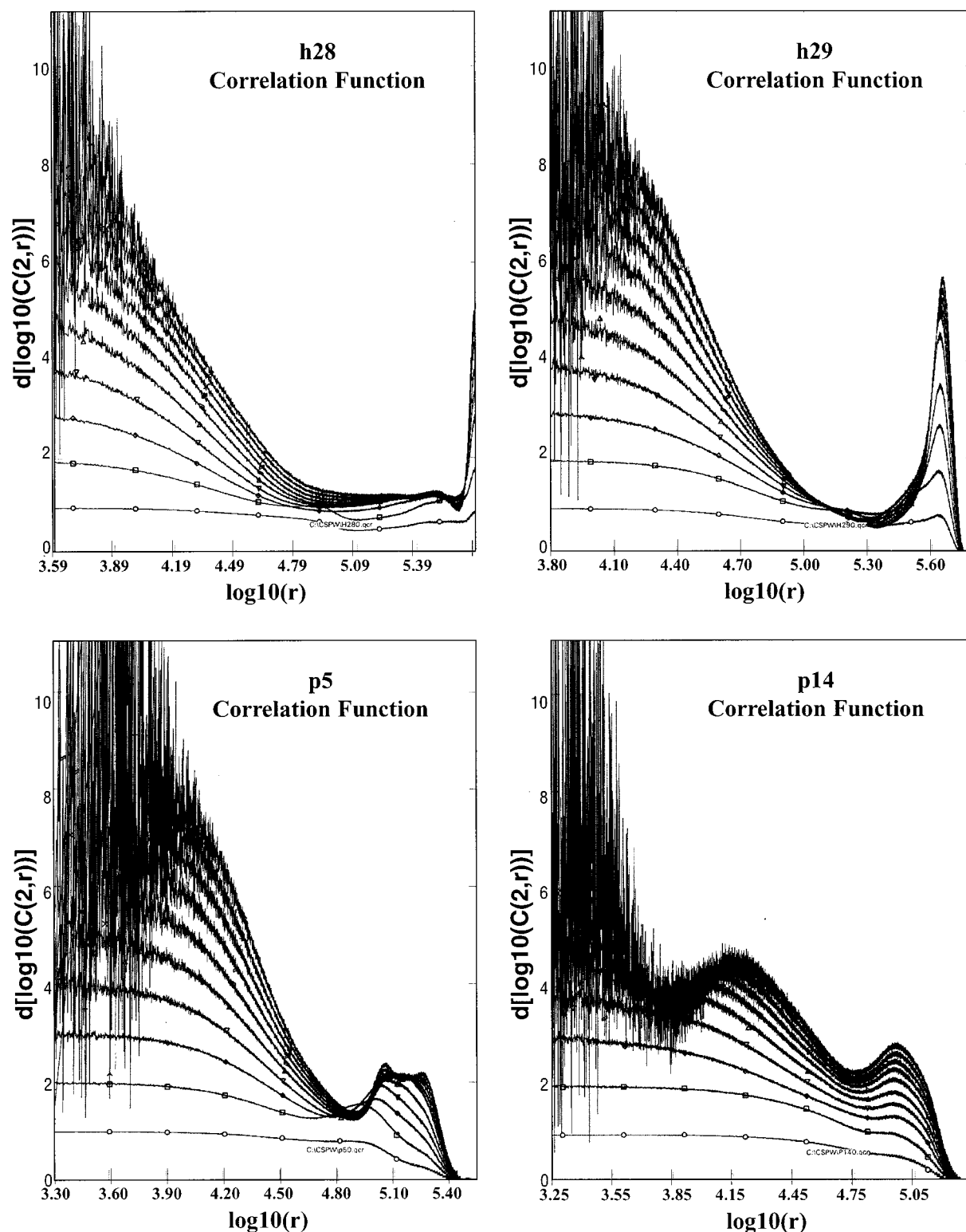


FIG. 4. Local slopes for correlation dimension calculations from healthy (H28, H29) (top) and pathologic (P5, P14) (bottom) subjects.

noise, and finite data sets on the calculation of the correlation dimension. The results provide preliminary evidence of low-dimensional determinism for only some of the EGG data sets and highlight some of the substantial problems in interpretation of the data.

The estimates of the correlation dimension are consistent with Titze *et al.* (1993), who found the correlation dimension

equaled 1 for one healthy subject and 2.6 for one dysphonic subject with polyposis. It is noteworthy that those data were derived from short (approximately 100 ms) and stationary segments, unlike the longer and generally nonstationary data segments analyzed herein. The results are also in agreement with Hirose *et al.* (1994), who used the time-series consecutive F_0 values extracted from the acoustic signal, and calcu-

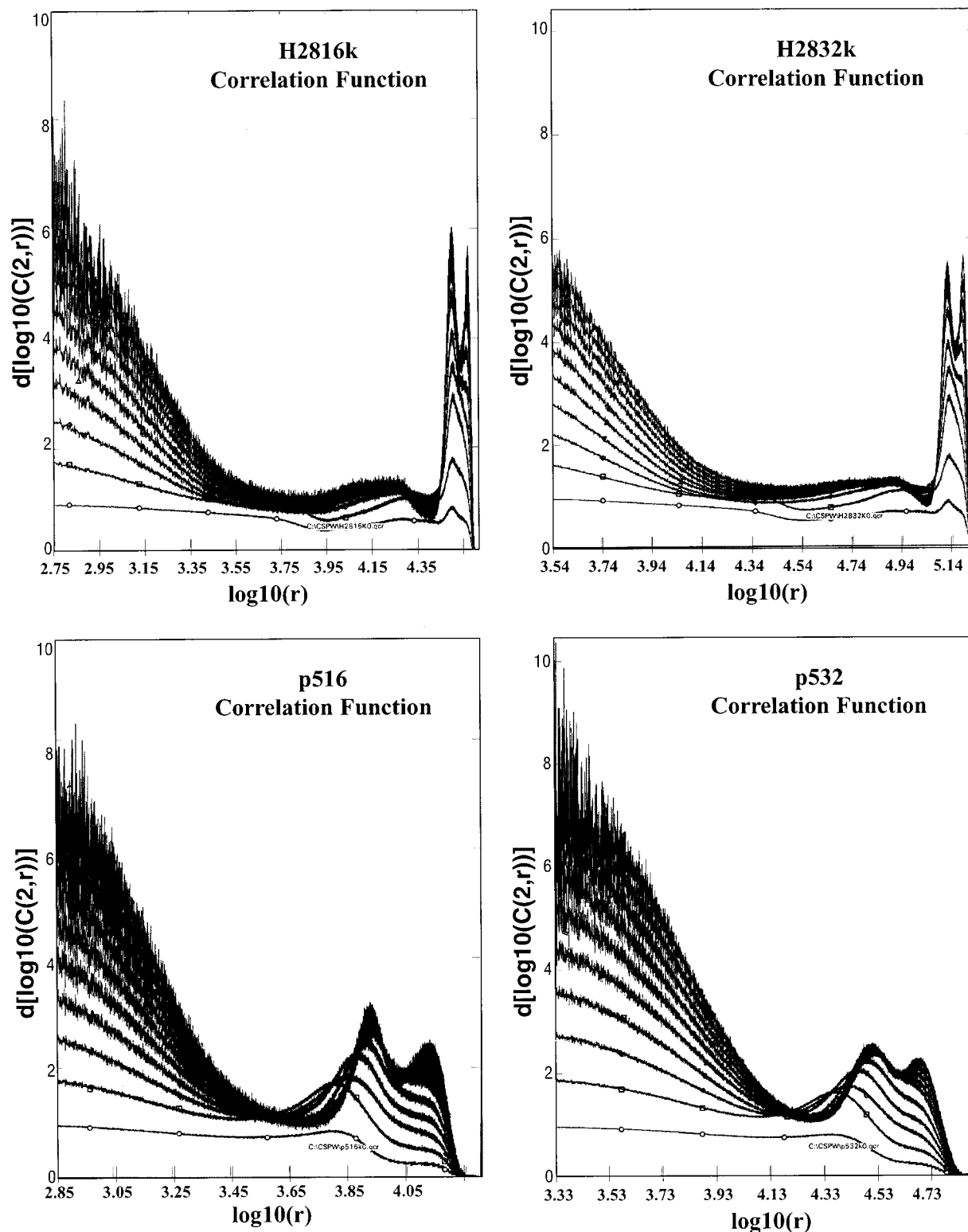


FIG. 5. Local slopes for correlation dimension calculations from the first 16 384 and 32 768 data points from H28 (top) and P5 (bottom).

lated similar values of capacity dimension ranging from approximately 1.3 to 1.7, which included both normal and dysphonic subjects. However, those authors failed to embed the time-series data in successively higher dimensions and measure the dimension from those higher embeddings, and therefore, a proper comparison cannot really be made.

The correlation dimension estimates from the healthy

subjects are lower than that obtained by Townshend (1992), who found a correlation dimension of approximately 3.3 for the microphone signal from one healthy subject. In comparing only the data from the healthy subjects, the estimates are also lower than the estimates found by Kumar and Mullick (1996), who calculated a mean correlation dimension of 2.89 for normal vowel phonation. That mean value, however, was

based on the correlation integral of the eighth embedding, for which all of the data did not saturate. In unpublished data, Kumar and Mullick found that saturation occurred at other slope values, typically less than 4, for embedding dimensions between 10 and 15 (personal communication). This suggests that their data may have been similarly affected by noise.

The findings for both healthy and pathologic subjects are also somewhat lower than those of Kakita and Okamoto (1994), who found a median correlation dimension value of approximately 3.5 for vowel phonation from 8 healthy subjects, and approximately 4.4 from 17 dysphonic subjects. Their calculations were based on embedded time-series data of sequential F_0 and amplitude values derived from the microphone signal. The authors did not report what percentage of their data sets saturated at the maximal embedding of 10, nor was information provided about the type and severity of their subjects' disorders, which could possibly have been quite different. Although no existing research absolutely demonstrates a correlation between dysphonic severity and degrees of freedom, there is accumulating evidence in other physiologic systems of specific pathophysiology resulting in a change in degrees of freedom as compared to healthy subjects (Newell *et al.*, 1995; Lipsitz and Goldberger, 1992). Therefore, it is conceivable that the severity of the dysphonia and/or the nature of the pathology may determine the dimensionality of the dynamics.

It is not immediately clear why the dimension estimates for the healthy data are lower than those estimates derived from sustained vowel phonation found by Townshend (1992), Kumar and Mullick (1996), and Kakita and Okamoto (1994). It could be attributable, in part, to differences in the underlying signal. EGG data may, in some ways, be considered less complex than microphone data, the latter of which reflects the coupling of the phonatory and resonatory subsystems. However, the data from Titze *et al.* (1993) are similarly based upon microphone data, and those values were consistent with the results presented here. It may well be that the differences may be due to the highly subjective nature of the statistical interpretation.

Kelso and Fuchs (1995), in a theoretical exploration of brain dynamics and metastable states, stated that for practical purposes, a system is stationary when the parameters and external inputs have not changed for an interval longer than the relaxation time of the system. The data sets from the pathologic subjects, with their frequent bifurcations to different vibratory regimes, demonstrated greater nonstationarity as a group, than did the data sets from the healthy subjects. This appeared to make a marked difference in the quality (i.e., "flatness" and duration) of the scaling regions of the slope plots for the two subject groups. The use of very short data sets in dimension analysis of voice data have likely been motivated, to a large extent, by the goal of obtaining stationary data segments (Kumar and Mullick, 1996; Narayanan and Alwan, 1995; Herzel *et al.*, 1994; Herzel, 1993; Titze *et al.*, 1993). Indeed, the results presented herein suggest that the effects of nonstationary time-series data make analysis of the scaling behavior more complicated. However, it was also shown that shorter data sets do not necessarily improve the scaling behavior, and it should be remembered that the non-

stationary characteristics of the data may themselves be the most interesting and revealing features of the system. Therefore, interpretations of overly short duration data sets should be made cautiously.

It is important to ask what new information is contributed by calculation of the correlation dimension. It is, after all, a computationally intensive measure. The dimension values clearly showed that the dynamics of healthy vocal fold vibratory behavior is defined by only a few significant degrees of freedom. Further, the correlation dimension values from a selected group of pathologic subjects showed that abnormal vibratory behavior was not stochastic, but rather was similarly dominated by a low (i.e., tractable) number of significant degrees of freedom. It would be hard to argue that this is new information, yet confirmation of what is already hypothesized and modeled is certainly helpful. However, the utility of a subjective measure which fails in the presence of data containing substantial irregularities, bifurcations, and modulations, must seriously be questioned. The lack of a substantial scaling region in the dimension analyses supports the statement that geometry-based fractal measures may not be the optimal tool with which to quantify the degrees of freedom (Kennel *et al.*, 1992), and highlights the need for careful (and cautious) interpretation of numerical data. It has been noted that determining the actual dimension value of biological data may not be as important as establishing that the dynamics of the system are low dimensional (Abarbanel, 1996; Kantz and Schreiber, 1995; Bassingthwaite *et al.*, 1994). Grassberger *et al.* (1991) have stated that examination of the qualitative features of the correlation integral might provide interesting information. Qualitative features may be of sufficient interest, especially in these early stages of dynamical analyses of voice and speech data, that a sampling of log-log plots, in addition to statistical data, should always be presented in any exploration of dimension analyses. It is suspected, however, that quite a large number of such plots would need to be examined before any meaningful conclusions could be drawn. Although the correlation integral plots from the 10 healthy subjects appeared generally consistent, the plots from the 20 pathologic subjects were highly variable and meaningful interpretation regarding underlying system dynamics was limited. Moreover, the fact remains that if the underlying data are nonstationary, the correlation integral is not the mathematically appropriate measure to use (Schreiber and Kantz, 1995; Theiler, 1986). Eckmann and Ruelle (1985) express the hope that the challenge of providing the required long and stationary time series for dynamical analyses can be met. It may well be that in the biological sciences, the challenge is to develop the appropriate tools for analysis of less than ideal data.

ACKNOWLEDGMENTS

We thank the three anonymous reviewers and Dr. Anders Löfqvist for their corrections, thoughtful comments, and suggestions. The first author also thanks Dr. James Yorke for his help and encouragement in the early stages of this project.

- Abarbanel, H. D. I. (1996). *Analysis of Observed Chaotic Data* (Springer-Verlag, New York), p. 74.
- Awrejcewicz, J. (1990). "Bifurcation portrait of the human vocal cord oscillations," *J. Sound Vib.* **136**, 151–156.
- Baken, R. J. (1990). "Irregularity of vocal period and amplitude: a first approach to the fractal analysis of voice," *J. Voice* **4**, 185–197.
- Baken, R. J. (1992). "Electroglottography," *J. Voice* **6**, 98–110.
- Baken, R. J. (1994). "The aged voice: A new hypothesis," *Voice: J. British Voice Assoc.* **3**, 57–73.
- Barnsley, M. F. (1988). *Fractals Everywhere* (Academic, Boston).
- Bassingthwaite, J. B., Liebovitch, L. S., and West, B. J. (1994). *Fractal Physiology* (Oxford U.P., New York).
- Berry, D. A., Herzel, H., Titze, I. R., and Krischer, K. (1994). "Interpretation of biomechanical simulations of normal and chaotic vocal fold oscillations with empirical eigenfunctions," *J. Acoust. Soc. Am.* **95**, 3595–3604.
- Brandstater, A., and Swinney, H. (1987). "Strange attractors in weakly turbulent Couette-Taylor flow," *Phys. Rev. Lett.* **66**, 2207.
- Chatfield, C. (1987). *The Analysis of Time Series* (Chapman & Hall, London).
- Childers, D. G., Alsaka, Y., Hicks, D., and Moore, G. P. (1987). "Vocal fold vibrations: an EGG model," in *Laryngeal Function in Phonation and Respiration*, edited by T. Baer, C. Sasaki, and K. Harris (College-Hill, Boston), pp. 181–202.
- Ding, M., Tuller, B., and Kelso, S. (1995). "Characterizing the dynamics of auditory perception," *CHAOS* **5**, 70–75.
- Eckmann, J. P., and Ruelle, D. (1985). "Ergodic theory of chaos and strange attractors," *Rev. Mod. Phys.* **57**, 617–656.
- Eubank, D., and Farmer, S. (1990). "An introduction to chaos and randomness," in *1989 Lectures in Complex Systems: SFI Studies in the Sciences of Complexity Vol. II*, edited by E. Jan (Addison-Wesley, Reading, MA), pp. 75–190.
- Fourcin, A. J. (1981). "Laryngographic assessment of phonatory function," in *Proceedings of the Conference on the Assessment of Vocal Pathology. ASHA Reports No. 11*, edited by C. Ludlow and M. Hart (American Speech-Language-Hearing Association, Rockville, MD), pp. 116–127.
- Fraser, A. M., and Swinney, H. L. (1986). "Independent coordinates for strange attractors from mutual information," *Phys. Rev. Lett. A* **33**, 1134–1146.
- Glass, L., and Kaplan, D. (1993). "Complex dynamics in physiology and medicine," in *Time Series Prediction: Forecasting the Future and Understanding the Past*, edited by A. S. Weigend and N. A. Gershenfeld (Addison-Wesley, Reading, MA), pp. 513–527.
- Grassberger, P., Hegger, R., Kantz, H., Schaffrath, C., and Schreiber, T. (1993). "On noise reduction methods for chaotic data," *CHAOS* **3**, 127–241.
- Grassberger, P., and Procaccia, I. (1983). "Measuring the strangeness of a strange attractor," *Physica D* **9**, 189–208.
- Grassberger, P., Schreiber, T., and Schaffrath, C. (1991). "Nonlinear time sequence analysis," *Int. J. Bifurcation Chaos* **1**, 521–547.
- Hammel, S. (1990). "A noise reduction method for chaotic systems," *Phys. Rev. Lett. A* **148**, 421–428.
- Herzel, H. (1996). "Possible mechanisms of vocal instabilities," in *Vocal Fold Physiology: Controlling Complexity and Chaos*, edited by P. J. Davis and N. H. Fletcher (Singular Publishing Group, San Diego), pp. 63–75.
- Herzel, H. (1993). "Bifurcations and chaos in voice signals," *Appl. Mech. Rev.* **46**, 399–413.
- Herzel, H., Berry, D., Titze, I. R., and Saleh, M. (1994). "Analysis of vocal disorders with methods from nonlinear dynamics," *J. Speech Hear. Res.* **37**, 1008–1019.
- Hirose, H., Imaizumi, S., and Yamori, M. (1994). "Voice quality in patients with neurological disorders," in *Vocal Fold Physiology: Voice Quality Control*, edited by O. Fujimura and M. Hirano (Singular Publishing Group, San Diego), pp. 235–248.
- Kakita, Y., and Okamoto, H. (1994). "Visualizing the characteristics of vocal fluctuation from the viewpoint of chaos: An attempt toward qualitative quantification," in *Vocal Fold Physiology: Voice Quality Control*, edited by O. Fujimura and M. Hirano (Singular Publishing Group, San Diego), pp. 79–95.
- Kantz, H., and Schreiber, T. (1995). "Dimension estimates and physiological data," *CHAOS* **5**, 143–154.
- Kelso, J. A. S., and Fuchs, A. (1995). "Self-organizing dynamics of the human brain: critical instabilities and Sil'nikov chaos," *CHAOS* **5**, 64–69.
- Kennel, M., Brown, R., and Abarbanel, H. (1992). "Determining embedding dimension for phase-space reconstruction using a geometrical construction," *Phys. Rev. Lett. A* **45**, 3403–3411.
- Kostelich, E. J., and Yorke, J. A. (1988). "Noise reduction in dynamical systems," *Phys. Rev. Lett. A* **38**, 1649–1652.
- Kumar, A., and Mullick, S. K. (1996). "Nonlinear dynamical analysis of speech," *J. Acoust. Soc. Am.* **100**, 615–629.
- Lipsitz, L. A. (1995). "Age-related changes in the 'complexity' of cardiovascular dynamics: A potential marker of vulnerability to disease," *CHAOS* **5**, 102–109.
- Lipsitz, L. A., and Goldberger, A. L. (1992). "Loss of 'complexity' and aging: Potential applications of fractals and chaos theory to senescence," *J. Am. Med. Assoc.* **267**, 1806–1809.
- Lorenz, E. N. (1963). "Deterministic nonperiodic flow," *J. Atmos. Sci.* **20**, 130–141.
- Mandelbrot, B. B. (1983). *The Fractal Geometry of Nature* (Freeman, San Francisco).
- Narayanan, S. S., and Alwan, A. (1995). "A nonlinear dynamical systems analysis of fricative consonants," *J. Acoust. Soc. Am.* **97**, 2511–2524.
- Nerenberg, M. A., and Essex, C. (1990). "Correlation dimension and systematic geometric effects," *Phys. Rev. Lett. A* **42**, 7065–7074.
- Newell, K. M., Gao, F., and Sprague, R. L. (1995). "The dynamical structure of tremor in tardive dyskinesia," *CHAOS* **5**, 43–47.
- Peng, C. K., Havlin, S., Stanley, H. E., and Goldberger, A. L. (1995). "Quantification of scaling exponents and crossover phenomena in nonstationary heartbeat time series," *CHAOS* **5**, 82–87.
- Paulus, M., Kadtke, J. B., and Menkello, F. V. (1993). "Statistical mechanics of biological and other complex experimental time series: assessing geometrical and dynamical properties," in *Complexity and Chaos: Proceedings of the Second Bryn Mawr Workshop on Measures of Complexity and Chaos*, edited by N. B. Abraham, A. M. Albano, A. Passamante, P. E. Rapp, and R. Gilmore (World Scientific, Singapore), pp. 233–244.
- Sano, M., and Sawada, Y. (1985). "Measurement of the Lyapunov spectrum from a chaotic time series," *Phys. Rev. Lett.* **55**, 1082–1085.
- Sauer, T., and Yorke, J. A. (1993). "How many delay coordinates do you need?" *Int. J. Bifurcation Chaos* **3**, 737–740.
- Schmid, G. B., and Dürki, R. M. (1996). "Indications of nonlinearity, intraindividual specificity and stability of human EEG: The unfolding dimension," *Physica D* **93**, 165–190.
- Schreiber, T., and Kantz, H. (1995). "Noise in chaotic data: Diagnosis and treatment," *CHAOS* **5**, 133–142.
- Schreiber, T., and Kaplan, D. T. (1996). "Nonlinear noise reduction for electrocardiograms," *CHAOS* **6**, 87–92.
- Smith, T. G., Jr., and Neale, E. A. (1994). "A fractal analysis of morphological differentiation of spinal cord neurons in cell culture," in *Fractals in Biology and Medicine*, edited by T. F. Nonnenmacher, G. A. Losa, and E. R. Weibel (Birkhäuser Verlag, Basel), pp. 10–220.
- Steinke, I., and Herzel, H. (1995). "Bifurcations in an asymmetrical vocal fold model," *J. Acoust. Soc. Am.* **97**, 1874–1884.
- Takens, F. (1981). "Detecting strange attractors in turbulence," in *Lecture Notes in Mathematics*, Vol. 898, edited by D. Rand and L. Young (Springer-Verlag, Berlin), p. 366.
- Theiler, J. (1986). "Spurious dimension from correlation algorithms applied to limited time-series data," *Phys. Rev. A* **34**, 2427–2432.
- Titze, I. R., Baken, R. J., and Herzel, H. (1993). "Evidence of chaos in vocal fold vibration," in *Vocal Fold Physiology: New Frontiers in Basic Science*, edited by I. R. Titze (Singular, San Diego), pp. 143–188.
- Tools For Dynamics (1997). [Computer software]. Applied Nonlinear Sciences, Inc., Del Mar, CA.
- Townsend, B. (1992). "Nonlinear prediction of speech signals," in *Nonlinear Modeling and Forecasting SFI Studies in the Sciences of Complexity Vol. XIII*, edited by M. Casdagli and S. Eubank (Addison-Wesley, Reading, MA), pp. 433–449.
- Vaidya, P. G., Behrman, A., Winkel, C., and Alford, S. (1996). "Comparison of caseygrams for healthy and pathological spec," *J. Acoust. Soc. Am.* **99**, 2594(A).
- Wagner, C. D., and Persson, P. B. (1995). "Nonlinear chaotic dynamics of arterial blood pressure and renal blood flow," *Am. J. Physiol.*, H621–627.
- Wolf, A. J., Swift, J. B., Swinney, H. L., and Vastano, J. A. (1985). "Determining Lyapunov exponents from a time series," *Physica D* **16**, 285–317.

Locus equations in the light of articulatory modeling

Samir Chennoukh^{a)} and René Carré

Département Signal, Unité Associée au CNRS, ENST, 46 rue Barrault, 75634 Paris Cedex 13, France

Björn Lindblom

Department of Linguistics, University of Stockholm, S-10691 Stockholm, Sweden

(Received 10 February 1997; accepted for publication 27 June 1997)

This paper examines the significance of the so-called ‘‘locus equation’’ by means of articulatory simulations of V_1CV_2 utterances with different intergestural timing, and, therefore, with varying degrees of consonant–vowel coarticulation. Movement toward the vowel V_2 started (i) at the beginning of the transition to the consonant, (ii) at the beginning of the complete consonant closure, or (iii) at the beginning of the release of the consonant. For each combination of vowels and each consonant, $F_{2\text{ onset}}$ of V_2 as a function of F_2 of V_2 was adequately described by straight lines corresponding to locus equations (referred to as *first-order* locus equations). The findings show that the derived locus equations depend on the consonant place on the one hand and on the degree of coarticulation on the other. The effect of varying intergestural timing was compared with published data on locus equation coefficients for individual speakers using the format of y-intercept plotted versus slope for each place of articulation (referred to as a *second-order* locus equation). These comparisons demonstrate that the model adequately captures the natural place-dependent variations in slope and intercept. Also it provides accurate numerical matches with their speaker-specific ranges suggesting the hypothesis that the variability derives, to a significant extent, from individual differences in intergestural timing. © 1997 Acoustical Society of America.

[S0001-4966(97)01910-3]

PACS numbers: 43.70.Bk [AL]

INTRODUCTION

Examining consonant–vowel sequences produced by a single speaker and with the same consonant in different vowel contexts, Lindblom (1963) observed a more or less linear relation between the values of the second formant measured at the onset of the consonant–vowel transition (F_{2o}) and at the midpoint of the vowel (F_{2v}) (Fig. 1). The equation for the line relating F_{2v} to F_{2o} has been called a ‘‘locus equation.’’ This first observation has since been confirmed by several different authors (Nearey and Shammass, 1987; Sussman *et al.*, 1991; Fowler, 1994).

Recently, a debate about the relation between locus equation coefficients and consonant place of articulation in vocalic contexts has developed in the speech community (Krull, 1987, 1988; Sussman *et al.*, 1991, 1993; Fowler, 1994; Sussman, 1994). The studies by Sussman and colleagues (1991, 1993) have shown a high correlation between the locus equation coefficients and consonant place of articulation. Sussman and colleagues (Sussman *et al.*, 1991) have proposed that listeners might use locus equations to determine place. But it has been pointed out that these locus equations exhibited variability both for individual speakers and for consonants sharing the same place of articulation whether with same or different manners of articulation (Fowler, 1994). Krull (1987, 1988) and Fowler (1994) propose that, for a specific place of consonant articulation, variations in locus equation slopes reflect differences in ‘‘degree of coar-

tication.’’ Fowler (1994, pp. 605) concludes that: ‘‘... locus equations provide poor information for place. First, in the data averaged over subjects, the patterning of significant differences in slope and y-intercept is not according to shared and different places of articulation; most seriously, /z/ and /d/, which share place of articulation, have distinct locus equations...’’

Moreover, Sussman’s perceptual claims for the locus equation seem additionally problematic because, being a statistical representation of data obtained from a set of utterances with the same consonant in varying vowel contexts (Sussman *et al.*, 1991; Fowler, 1994), the equation does not allow a listener to deduce place of articulation from a single token. In addition, the locus equations could change with the set of utterances and especially with different vowels. Finally, no method exists for automatic detection of the locus equation coefficients. Indeed, even detection of the second formant frequency at the onset of a CV syllabic transition is debatable and has often been questioned in different papers on the locus equation. We will therefore not consider possible perceptual function of the locus equation in this paper.

Our contribution to the debate consists in reporting some results on V_1CV_2 productions simulated under different conditions by means of the so-called distinctive region model (DRM). The questions are: (1) Is it possible to obtain linear relations between F_{2o} and F_{2v} with the model? (2) What do these linear relations represent?

I. THE DISTINCTIVE REGION MODEL

V_1CV_2 utterances were obtained using the so-called distinctive region model (DRM) which provides a representa-

^{a)}Current address: CAIP Center, Room 717, Core Building, Frelinghuysen RD, Piscataway, NJ 08854-1390.

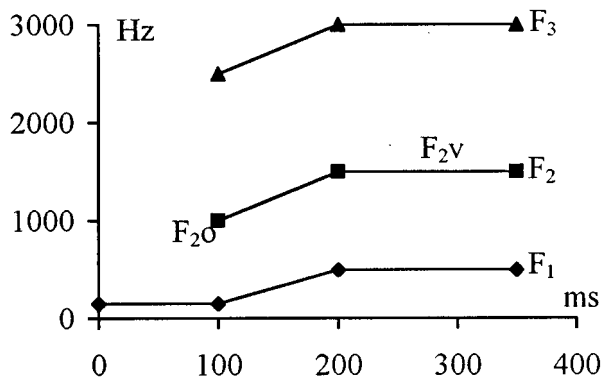


FIG. 1. The F_{2o} and F_{2v} measurements made on the CV second formant trajectory.

tion of the vocal tract area function (Mrayati *et al.*, 1988; Carré and Mrayati, 1992; Chennoukh, 1995; Chennoukh *et al.*, 1995) and whose parameters are motivated by acoustic theory. The model is an acoustic tube divided into “regions” (in the present application eight of them). The regions and the boundaries between them are derived from a criterion of “acoustic contrast” which maximizes each formant frequency’s range of variation. This criterion is defined as follows. When the area function of the uniform vocal tract is perturbed, formant frequencies undergo systematic changes which can be formally described in terms of “sensitivity functions” (Fant and Pauli, 1974). Region boundaries are deduced from the zero crossings of a given formant’s sensitivity function. These functions are formant specific and have the property of being asymmetric. For instance, the range for F_1 is maximized by dividing the tract into two equal halves and the asymmetrical behavior of the tract means that an increase in the area of the front part of the tract is acoustically equivalent to a decrease in the area of the back part. The corresponding behavior in F_2 and F_3 motivates other additional boundary points. The regions obtained from the criterion applied to F_1 , F_2 , and F_3 are shown in Fig. 2. Indeed the regions deduced from acoustic theory fit well with the anatomy of the human tract: Region 1 corresponds to the larynx, 3, 4, 5, and 6 to the oral cavity and 8 to the lip opening. Note also that the places of articulation that the DRM model makes available, are, in general, the regions which are preferred to produce the sounds of the world’s languages. For vowel production, regions 3 and 4 correspond to the back constriction, regions 5 and 6 to the front constriction, and regions 4 and 5 to the central constriction. The

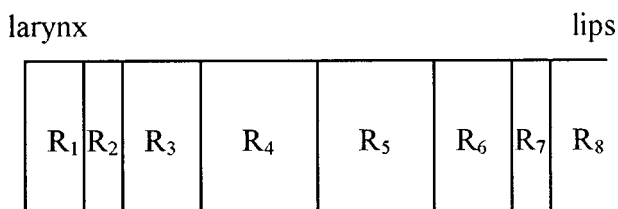
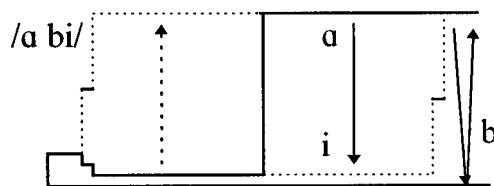
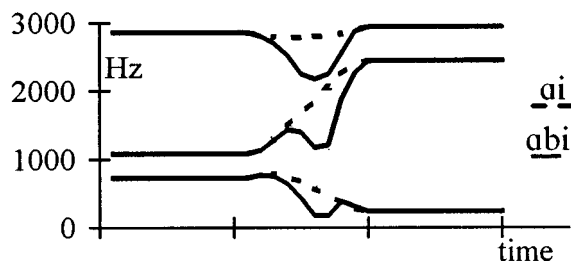


FIG. 2. The distinctive region model (DRM) and its eight regions. R_1 corresponds to the larynx cavity, R_3 , R_4 , R_5 , R_6 to the oral cavity, R_7 to the teeth, and R_8 to the lips. R_2 corresponds to the transition between the larynx and oral cavities.



(a)



(b)

FIG. 3. (a) /abi/ production with the DRM, the consonant gesture is superimposed on the vowel-to-vowel gesture; (b) the corresponding three formant variations for /ai/ and for /abi/.

vowel triangle can be predicted with the model (Carré *et al.*, 1994) and plausible V–V transitions are obtained (Carré and Mrayati, 1991). Moreover, vowel systems are predicted by the model (Carré, 1996). For consonant production, region 8 corresponds to /b/, region 6 to /d/, region 5 to /g/. The model has been used by Hill *et al.* (1995) for perceptually satisfactory synthesis-by-rule.

II. SIMULATIONS AND MEASUREMENTS

With the aid of the model, V_1CV_2 utterances were simulated as variations in DRM area functions over time and by superimposing consonant gestures on V_1V_2 transitions (Öhman, 1966) (see the example of superposition in Fig. 3, where the consonant gesture /b/ is superimposed in phase with the /ai/ gesture). For V_1CV_2 production, where C is /d/ or /g/, constant tongue volume constraint is taken into account (Chennoukh and Carré, 1995). The vowels V_1 and V_2 were chosen from the set /a, ø, o, u, y/. We note that the timing of a consonant gesture in relation to a given V_1V_2 movement specifies the extent of temporal overlap between C and V_2 production (i.e., the degree of coarticulation). In view of that observation three different phasing patterns [read: “degree of coarticulation” or, better, degree of coproduction (Fowler, 1993)] were chosen to control the relative timing of the consonant during the V_1V_2 transition. In Fig. 4 they are illustrated in terms of the anticipation of the second vowel V_2 . In phasing pattern 1 (Ph_1), the vowel V_2 was initiated at the beginning of the consonant gesture. This choice appears compatible with reports in the literature (Öhman, 1966). The transition V_1C depends on V_2 . The transition CV_2 depends on both vowels. In this case, the degree of CV_2 coarticulation can be considered maximal [Fig. 4(a)]. In phasing pattern 2 (Ph_2), the second vowel was started at the beginning of the complete consonant closure. This possibility has also been

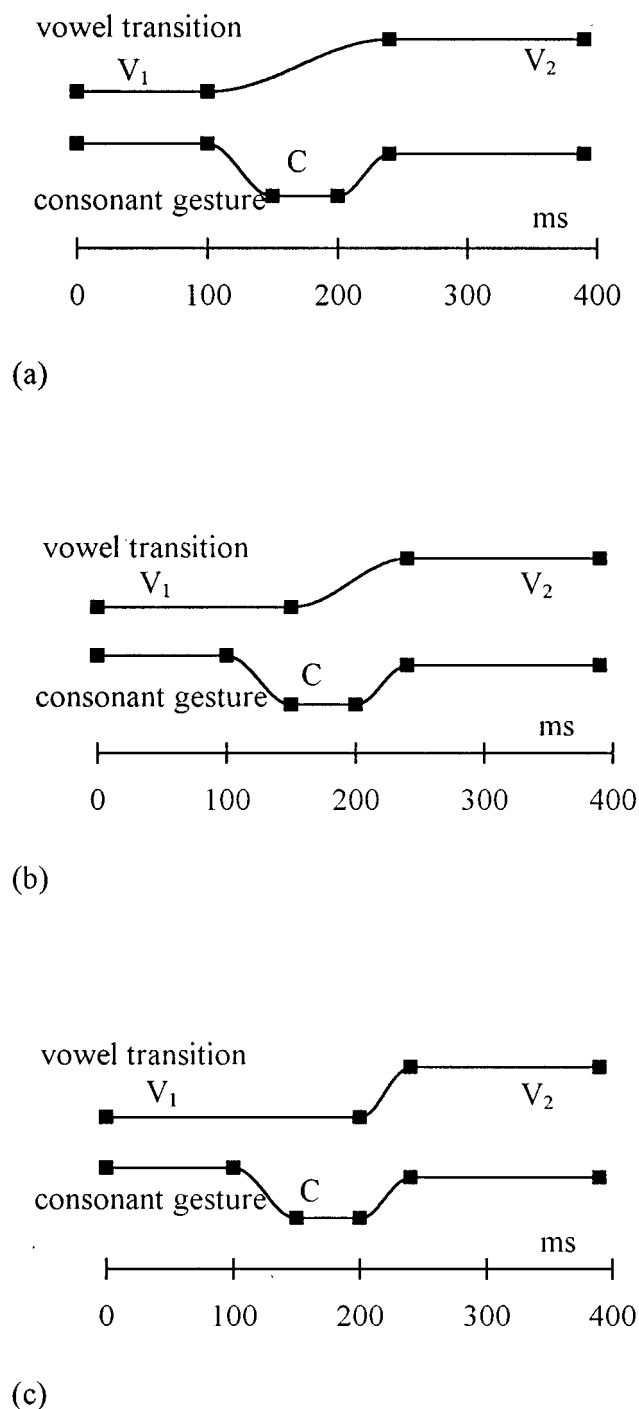


FIG. 4. Temporal organization of control parameters in the generation of V_1CV_2 utterances. The diagram shows three time points for initiating the gesture towards V_2 : (a) Phasing pattern Ph_1 ; (b) phasing pattern Ph_2 ; (c) phasing pattern Ph_3 . These phrasings represent three degrees of C- V_2 coarticulation.

discussed in experimental work (Gay, 1977). Here, the degree of coarticulation is less marked than in Ph_1 [Fig. 4(b)]. The transition V_1C does not depend on V_2 . But the transition CV_2 again depends on both vowels. In phasing pattern 3 (Ph_3), the transition towards the vowel V_2 was begun at the onset of the consonant release [Fig. 4(c)]. Here the degree of CV_2 coarticulation is accordingly very weak but the transition CV_2 depends even more strongly on V_1 .

Although obviously such a procedure provides only a crude first approximation to the degrees of freedom of the human speech production system, it was shown by Carré and Chennoukh (1995) that the model reproduces all the V_1CV_2 formant patterns observed by Öhman (1966) for /b/, /d/, and /g/. We take this finding to indicate that the output of DRM is of sufficient quality to investigate whether an articulatory model, incorporating discrete, invariant, and independent C and V gestures, constructed on principles totally independent of locus equations, can be extended to simulate such relations. Moreover, preliminary perceptual experiments (Chennoukh, 1995) show that subjects do perceive the present VCV stimuli that do not contain a stop burst, as speechlike and have no real problem categorizing them with respect to consonant place except for /b/ with low V_2 second formant (i.e., /u/ and /o/). In this case, it is known that the role of the burst is important to distinguish /b/ and /g/ (Dorman *et al.*, 1977).

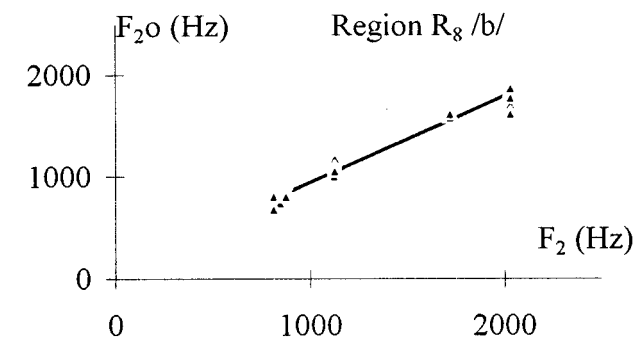
Below we will first examine the effect of intergestural timing on the locus equation coefficients, then the effect of the place of articulation on those coefficients.

For each degree of coarticulation and for regions 8, 6, and 5 of consonant articulation, 25 V_1CV_2 utterances (all pairings of the five possible V_1 's with the five possible V_2 's) were obtained, i.e., 75 V_1CV_2 utterances per region which corresponds to a total of 225 utterances. All these utterances were simulated using the same segment durations, namely, 100 ms for V_1 , 50 ms for the V_1C transition, 50 ms for the total consonant closure, 40 ms for the CV_2 transition, and 150 ms for the vowel V_2 . For each simulated utterance, the first three formant frequency trajectories were calculated every 5 ms from the transfer function of the model. A synthesized signal was then derived using the Klatt formant synthesizer (Klatt, 1980) with a sampling frequency of 16 kHz. Voicing was applied throughout the consonant closure. In order to obtain results temporally comparable with those obtained for natural data (Sussman *et al.*, 1991), the formant values were calculated from a spectrographic representation of the synthetic signal.

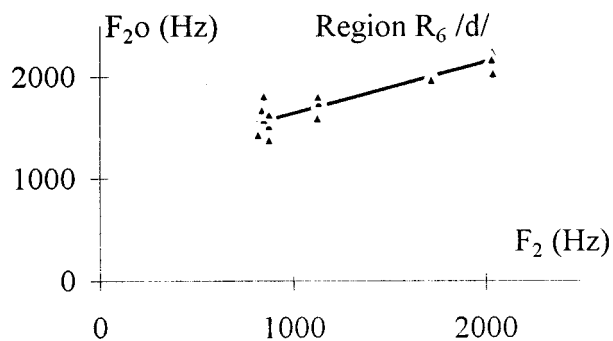
The synthetic signal was analyzed with software developed at the Département Signal, ENST (Chennoukh, 1995). After application of a 30-ms Hamming window to the signal and pre-emphasis filtering of +6 dB/octave, two analysis methods were used to provide spectral information for formant detection. These two methods were linear prediction coding (LPC) and cepstrum smoothing. F_2 onset (F_2o) was considered to be the value of F_2 10 ms after the release of the consonant, while the nucleus of the vowel (F_2v) was measured 110 ms after this release.

III. RESULTS

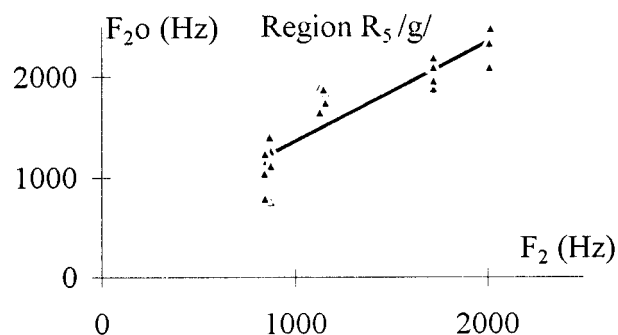
The results obtained for each degree of coarticulation and for the three regions of articulation are presented in Figs. 5–7. The five sets of different F_2v values correspond to the five different V_2 vowels; and within each set, there are five points corresponding to the five V_1 vowels. The reason why points on the graphs in these figures stack is because the model (in contrast to humans) always achieves the same F_2v for a given vowel. The linear orientation of the data points is



(a)



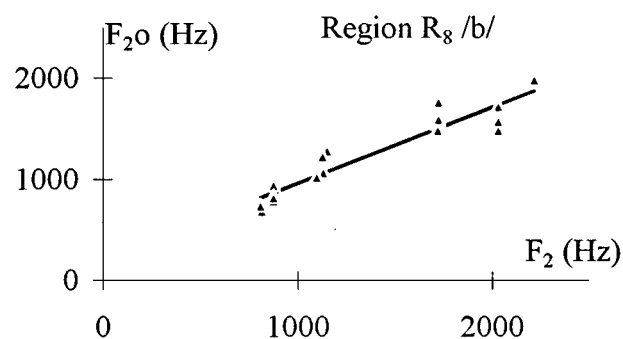
(b)



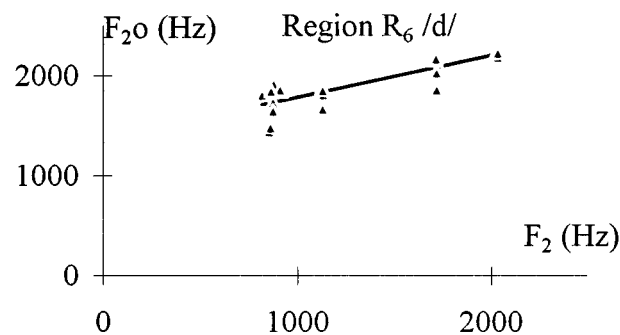
(c)

FIG. 5. Locus equations (F_2 onset- F_{2o} as a function of F_2 target- F_2v) for three regions of articulation R_5 (a), R_6 (b), R_8 (c) corresponding respectively to /b/, /d/, /g/, and for phasing pattern Ph_1 which corresponds to a large degree of C-V₂ coarticulation.

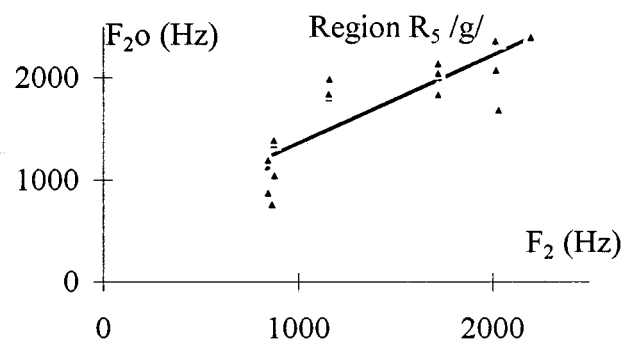
apparent and motivates the fitting of straight lines, so called locus equations. The locus equation coefficient values are summarized in Table I. They are close to those reported in the literature [for example, Sussman *et al.* (1991)]. The regression coefficients are all close to 1 except for those with Ph_3 .



(a)



(b)

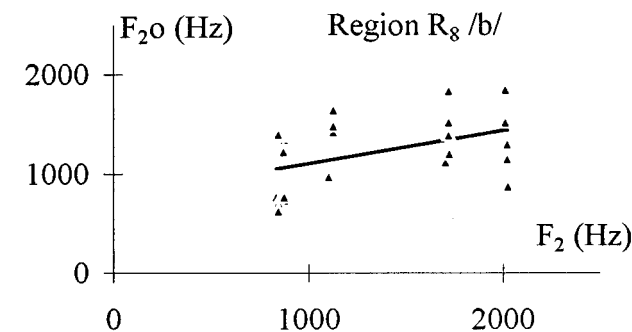


(c)

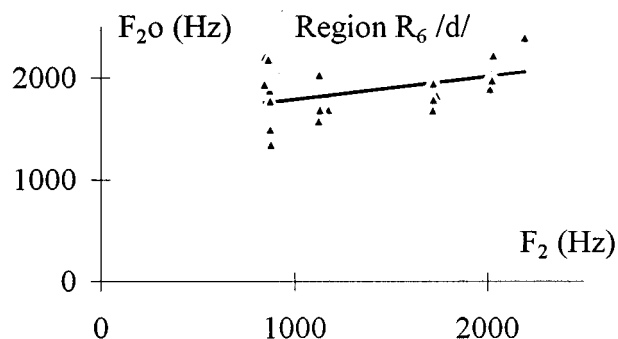
FIG. 6. Locus equations (F_2 onset- F_{2o} as a function of F_2 target- F_2v) for three regions of articulation R_5 (a), R_6 (b), R_8 (c) and for phasing pattern Ph_2 which corresponds to an intermediate degree of C-V₂ coarticulation.

The coefficients of the locus equation for the region R_6 (/d/) are clearly different from those of the other two regions. Indeed, the y intercept of the locus equation for this region has a range (1132–1566 Hz) beyond those of the other regions (i.e., R_5 : 378–1198 Hz and R_8 : 94–770 Hz). A similar result has been reported for natural speech (Sussman *et al.*, 1991).

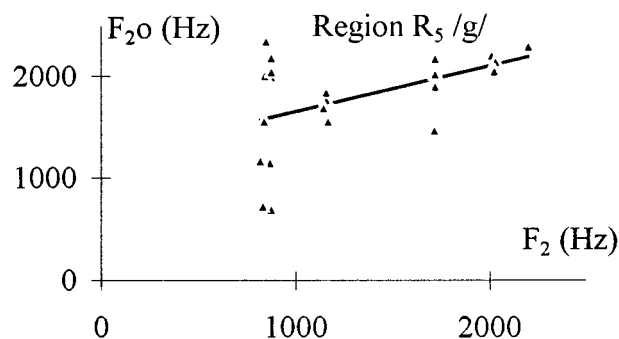
For each region of articulation, the locus equation coefficients vary as a function of the degree of coarticulation. In



(a)



(b)



(c)

FIG. 7. Locus equations (F_2 onset- F_2o as a function of F_2 target- F_2v) for three regions of articulation R_5 (a), R_6 (b), R_8 (c) and for phasing pattern Ph_3 which corresponds to a small degree of C- V_2 coarticulation.

all three cases, phasing pattern 1 (Ph_1) is consistently associated with the slope closest to 1 (which indicates near-maximum coarticulation), whereas phasing pattern 3 (Ph_3) shows the lowest slope value corresponding to minimum C- V_2 coarticulation. Ph_2 is intermediate.

To compare the three conditions of degree of coarticulation (phasing), we plotted the y-intercept of the locus equation versus the slope of the locus equation (Fig. 8). It gives rise to a linear relation (Sussman *et al.*, 1993; Chennoukh,

TABLE I. Locus equation coefficients for three regions of articulation (R_8 , R_6 , R_5) and for three degrees of coarticulation (Ph_1 , Ph_2 , Ph_3). The locus equation is $F_2o = m \cdot F_2v + b$; m is the slope, b is the y intercept, and " r " represents the regression coefficient.

	R_8 /b/			R_6 /d/			R_5 /g/		
	m	b	r	m	b	r	m	b	r
Ph_1	0.85	94	0.98	0.51	1132	0.92	0.98	378	0.91
Ph_2	0.75	212	0.95	0.42	1362	0.86	0.86	500	0.84
Ph_3	0.33	770	0.45	0.22	1566	0.42	0.45	1198	0.49

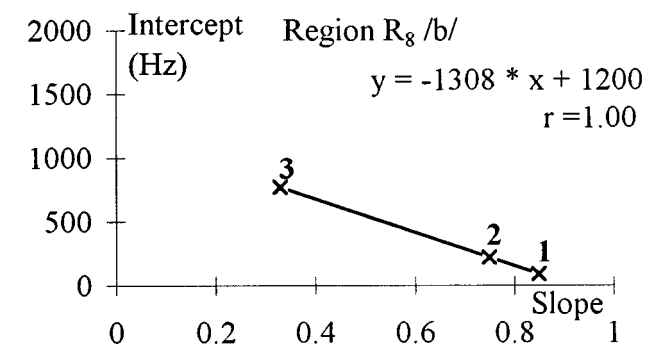
1995; Chennoukh *et al.*, 1995; Krull *et al.*, 1995). We refer to this linear relation as a second-order locus equation (SOLE) (Chennoukh, 1995), the first-order locus equation (FOLE) being the well-known locus equation.

To examine further the determinants of the locus equation, we computed the locus equations for all CV₂ combinations keeping V_1 constant. Five locus equations corresponding to V_1 being one of the following vowels /a, ø, o, u, y/ were obtained for each region of articulation. Their coefficients, listed in Table II, vary significantly with the first vowel. For example, the slopes for region 8 and for the Ph_1 phasing pattern are between 0.76 ($V_1 = /o/$) and 0.96 ($V_1 = /u/$) which should be compared with 0.85 (Table I). The dispersion is much more pronounced for region 5 and Ph_3 . Thus the first-order locus equation coefficients are apparently not invariant: They change with the preceding vowel and thus with the size and the content of the corpus. However, invariance does seem to be maintained for place at the level of second-order locus equation (Fig. 9). This diagram reproduces Fig. 8, but adds data points pertaining to intercept-slope coefficients obtained by fitting V_1 -specific lines rather than pooling V_1 -conditions (as in Figs. 5, 6, and 7 and Table I).

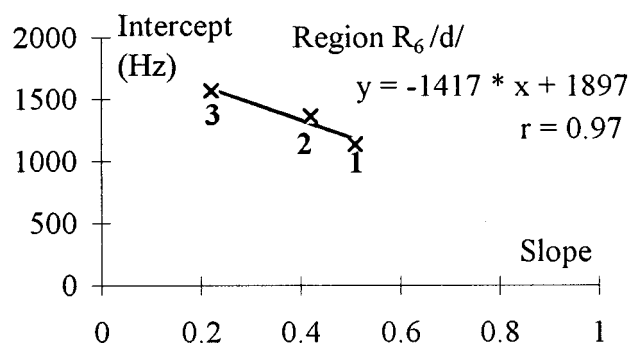
IV. COMPARING NATURAL AND SIMULATED DATA IN TERMS OF SECOND-ORDER LOCUS EQUATIONS

The present model simulations show that FOLE coefficients may vary although the region of articulation stays the same. They depend on the phasing of the vowel and consonant gestures and on the identity of the transconsonantal vowel (V_1). On the other hand, our results show that SOLE coefficients do provide constant correlates for specific regions of articulation (Fig. 9). For R_6 and R_5 , the coefficients are close in value although the ranges of variation are different (for R_6 the slope is between 0.2 and 0.5; for R_5 , the slope is between 0.5 and 1).

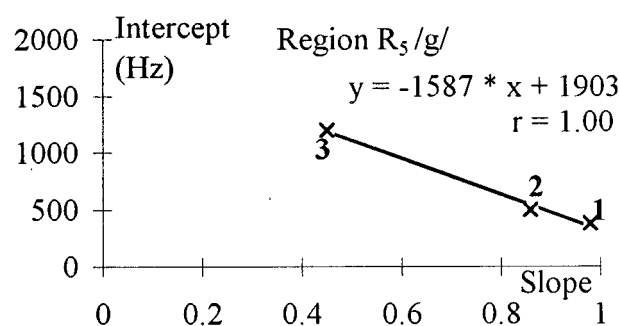
Why the representation, here called a second-order locus equation, also produces linearity is admittedly not well understood at present. We therefore limit ourselves to using this format descriptively. However, we can note that, at least in the present study, for a given place, manipulation of the identity of V_1 or changing intergestural timing, does not affect data points for high- F_2 as much as for low- F_2 contexts. The vowel-specific (or frequency-dependent) sensitivity of F_2 to these variations should be derivable from acoustic theory. Its effects on locus lines is to introduce a sort of



(a)



(b)



(c)

FIG. 8. Second-order locus equations fitted to the coefficients (slope and y-intercept of the first order locus equation) presented in Table I for the three phasing patterns Ph₁ (1), Ph₂ (2), Ph₃ (3) and three regions of articulation R₅ (a), R₆ (b), R₈ (c). The values in Table I were pooled across V₁ contexts.

“hinge point” near the high- F_2 points thereby generating the complementarity between slopes and intercepts that creates the second-order locus equation.

To further illustrate the second-order locus equation we next present observations based on modeling and compare them with locus equation data from natural speech. We shall here examine the data on stop consonants reported by Sussman *et al.* (1991), on homorganic consonants (Fowler, 1994;

TABLE II. Dependence of locus equations for /b/, /d/, and /g/ and the three phasings on first vowel of the V₁CV₂.

	V ₁	R ₈ /b/		R ₆ /d/		R ₅ /g/	
		m	b	m	b	m	b
Ph ₁	/y/	0.79	175.15	0.54	1071.43	0.94	410.68
	/ø/	0.85	144.58	0.48	1228.38	0.98	506.70
	/a/	0.88	23.43	0.42	1222.91	0.77	733.96
	/o/	0.76	173.01	0.58	1006.27	0.96	395.08
	/u/	0.96	-45.58	0.51	1135.21	1.28	-167.06
Ph ₂	/y/	0.89	110.44	0.43	1388.32	1.09	212.12
	/ø/	0.66	418.22	0.40	1305.30	0.94	545.81
	/a/	0.72	197.85	0.51	1248.97	0.37	1122.11
	/o/	0.68	216.17	0.33	1570.40	1.01	215.81
	/u/	0.74	191.41	0.43	1322.69	0.88	420.51
Ph ₃	/y/	0.43	1044.91	0.43	1339.71	0.04	2030.58
	/ø/	0.19	1178.84	0.25	1654.34	0.11	1915.37
	/a/	0.44	417.36	0.13	1687.70	0.23	1598.86
	/o/	0.37	494.35	0.21	1410.56	0.80	563.98
	/u/	0.23	733.88	0.03	1818.19	1.00	-12.25

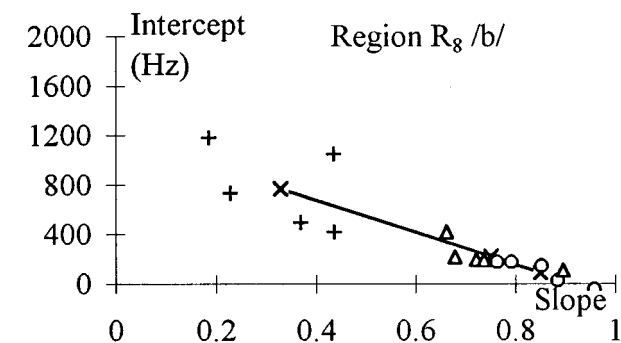
Sussman, 1994), and finally on consonants obtained from different languages (Sussman *et al.*, 1993).

A. Second-order locus equations and natural stop consonants

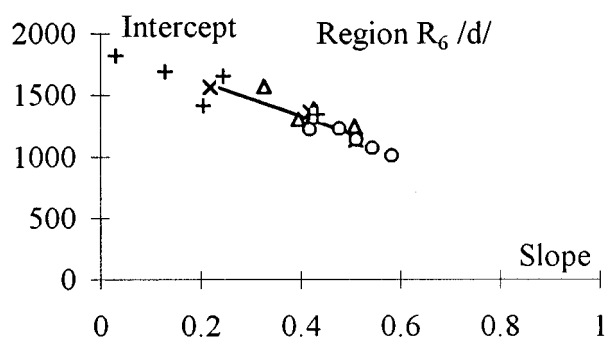
Figure 10 shows Sussman and colleagues’ results (1991) obtained from 20 subjects (10 males and 10 females) superimposed on the second-order locus equations simulated for three regions of articulation and for three degrees of coarticulation. Recall that the tokens in this study were CVC utterances while our observations come from V₁CV₂ utterances. Good agreement is observed between the two sets of results. Since the locus equation coefficients depend on the statistics of the corpus, the following conclusions can only be tentative.

First, although each speaker could have adopted a different strategy (different phasings) for coproducing the articulatory gestures of CV sequences, it happens to be the case that F_2 onsets are nevertheless more or less linearly related to vowel F_2 values. Presumably, that phenomenon could at least in part be associated with the fact that an individual speaker’s timing strategy remains the same for a specific consonant and is more or less independent of the adjacent vowels. In other words, for a specific speaker, the phasing of a given consonant in relation to vowel gestures stays more or less the same. This point must be balanced by the fact that the locus equation coefficients change with V₁ especially for Ph₃. We may therefore conclude that the apparently contradictory results of Öhman (1966) and Gay (1977) on the effect of V₂ on the V₁C transition can be explained by the fact that the speaker studied by Öhman used a strategy more or less corresponding to Ph₁, while the speaker studied by Gay used a strategy corresponding to Ph₂.

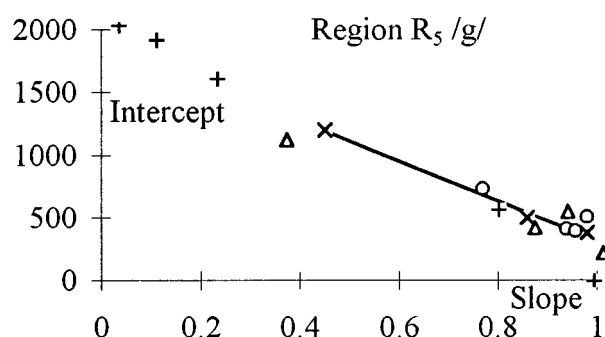
Second, in the case of /b/, the data points cluster near phasing pattern Ph₁ which indicates that most of the subjects anticipated the second vowel before executing the labial occlusion. That observation suggests a near-maximum degree



(a)



(b)

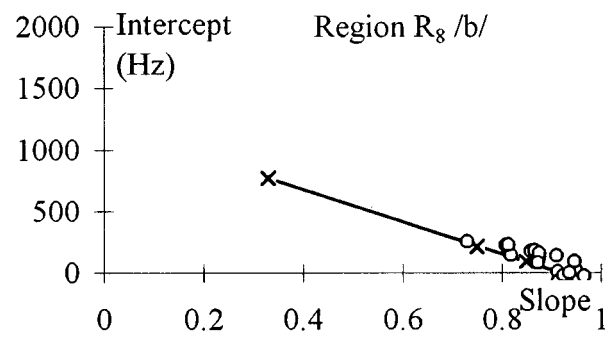


(c)

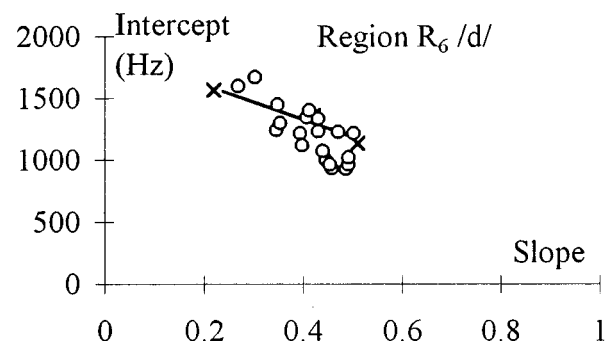
FIG. 9. Locus equation coefficients from Table II for three regions of articulation R_5 (a), R_6 (b), R_8 (c) superimposed on the second-order locus equation lines (represented by \times) of Fig. 8. The five \circ correspond to the five different V_1 with Ph_1 . The five Δ correspond to the five different V_1 with Ph_2 . The five $+$ correspond to the five different V_1 with Ph_3 .

of coarticulation. In the case of /d/, the data exhibit greater spread in relation to the phasing patterns. The anticipation of the second vowel shows a large range, from the maximum to the minimum degree of coarticulation. For /g/, the initiation of the second vowel typically occurs more frequently during the total closure.

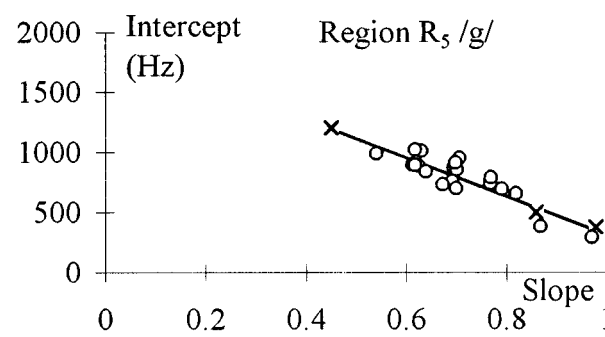
Third, the /d/ and the /g/ have more or less the same



(a)



(b)



(c)

FIG. 10. Comparisons of simulated second-order locus equations of Fig. 8 for three degrees of coarticulation (represented by \times) for three regions of articulation R_5 (a), R_6 (b), R_8 (c) with the Sussman *et al.* (1991) results (circles).

SOLE y -intercepts but different SOLE slopes. Moreover, the natural data and the simulated data have different ranges of distribution: The FOLE slope is between 0.2 and 0.5 for /d/ and between 0.5 and 1 for /g/.

Fourth, Ph_3 is less used by speakers than Ph_2 and Ph_1 . Evidently, the observed acoustic patterns tend to reflect co-production of consonant and vowel gestures rather than a sequence of these gestures. A preliminary perception test

TABLE III. Locus equations coefficients obtained by Fowler (1994) (F) and Sussman (1994) (S).

	Labial C (R_8 region)		Alveolar C (R_6 region)		Velar C (R_5 region)	
	Slope	y intercept	Slope	y intercept	Slope	y intercept
/b/ (F)	0.8	244
/p/ (S)	0.64	383				
/m/ (S)	0.83	116				
/m/ (S)	0.93	70				
/v/ (S)	0.62	420				
/v/ (F)	0.73	337
/ð/ (F)			0.5	903		
/ð/ (S)			0.24	1241		
/t/ (S)			0.35	1213		
/d/ (F)	0.47	1121
/z/ (S)			0.28	1217		
/z/ (F)	0.42	1078
/Z/ (S)			0.43	1276		
/ž/ (F)	0.34	1408
/n/ (S)			0.36	1310		
/k/ (S)					0.84	522
/k/ (S)					0.80	594
/k/ (S)					0.98	208
/k/ (S)					0.61	944
/g/ (F)	0.68	816

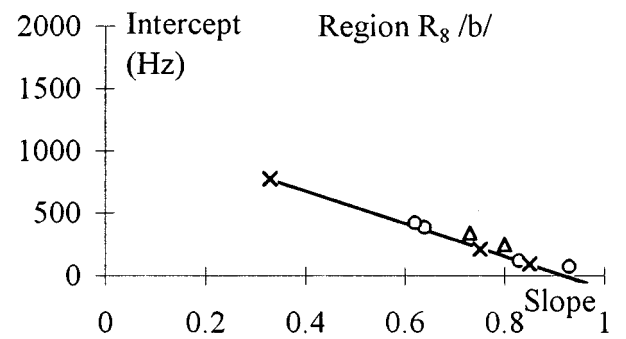
(Chennoukh, 1995) shows that the accuracy of identification of the place of articulation is less for Ph_3 than for Ph_2 and Ph_1 .

B. Second-order locus equations and the within-place variability of homorganic consonants

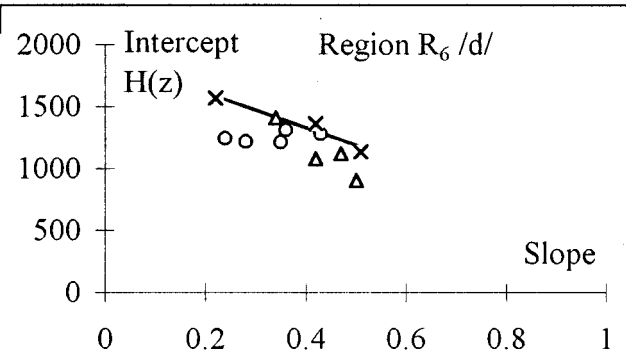
Fowler (1994) showed that the slope and y-intercept cannot give reliable information about place of articulation. Table III reproduces Fowler's data (1994) and those of Sussman (1994) for homorganic consonants (labial, alveolar, velar). Indeed, the locus equation coefficients are different, but when they are plotted together with the model-based second-order locus equations they are more or less on the SOLE lines (Fig. 11). For a given place of articulation, the slope changes because of the homorganic consonant. For example, we may conclude that, for the labial consonants, /b/ and /m/ are more coproduced than /v/ and /p/.

C. Second-order locus equations and some cross-linguistic data

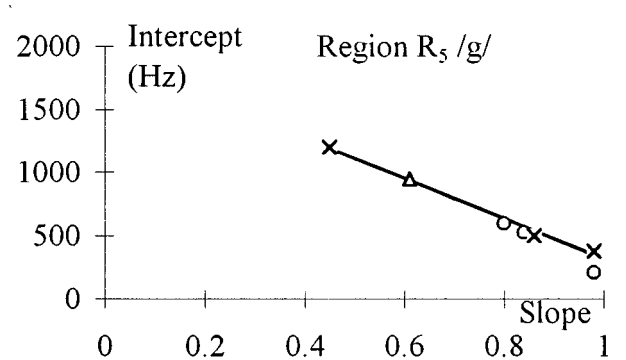
Sussman *et al.* (1993) reported locus equations for several languages. Once again, for a given articulatory place, locus equation coefficients show a certain language dependence, but when the coefficient values (Table IV) are plotted on the plane of y-intercept versus slope, a consistent and regular pattern emerges (Fig. 12). We first note that the slope-intercept data from Swedish, Thai, Arabic, Urdu, and English fall right on top of the model-based SOLE lines for all places of articulation. It is further seen that the five languages occupy different positions relative to the three patterns of gestural timing. This suggests that, for the labial, dental alveolar, and velar regions, the different languages use different patterns of C–V₂ coarticulation.



(a)



(b)



(c)

FIG. 11. Simulated second-order locus equations of Fig. 8 for three degrees of coarticulation (represented by \times) and three regions of articulation R_5 (a), R_6 (b), R_8 (c) are shown with Fowler's results (1994) (triangles) and Sussman's results (1994) (circles).

V. DISCUSSION AND CONCLUSION

In this investigation we have used the distinctive region model to simulate V_1CV_2 sequences in accordance with a coproduction strategy, that is by superimposing a consonant gesture on a vowel-to-vowel movement (Öhman, 1967). We have demonstrated that this modeling produces acoustic results that show significant parallels with several sets of published formant data (Sussman *et al.*, 1991, 1993; Fowler,

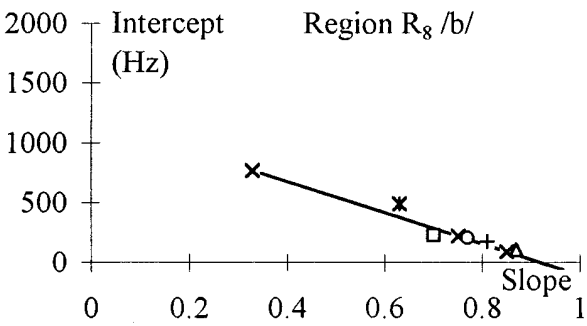
TABLE IV. Locus equations coefficients obtained from different languages (Sussman *et al.*, 1993).

Language	/b/- R_8		/d/- R_6		/g/- R_5	
	Slope	y intercept	Slope	y intercept	Slope	y intercept
Thai	0.7	228	0.3	1425
English	0.87	106	0.43	1073	0.66	807
Swedish	0.63	487	0.32	1096	0.95	360
Arabic	0.77	206	0.25	1307	0.92	229
Urdu	0.81	172	0.5	857	0.97	212

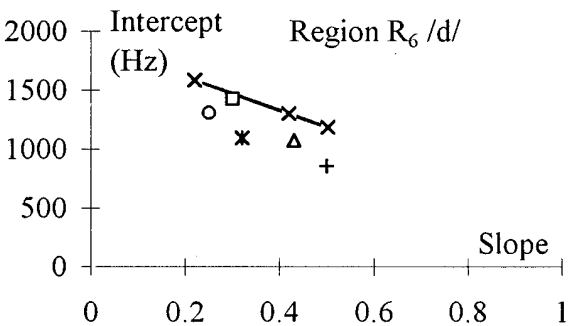
1994; Sussman, 1994). For instance, the model-based V_1CV_2 's exhibit the linear relationships, often documented for human speech, between F_2 at the CV_2 boundary and F_2 in the V_2 vowel. The numerical values of the slopes and intercepts for these locus equations were found to come close to those of published data.

Some insight into the issue of locus equation coefficients as invariant descriptors of place was gained by studying how they are affected by manipulating the relative timing of C and V_1V_2 movements. We found that, for a given place of articulation, variations in intergestural timing gave rise to changes in locus equation parameters. A certain systematicity in those variations was highlighted by examining the results in intercept-slope plots and by fitting straight lines (second-order locus equations, SOLEs) also to the data points of this format. When locus equation data published for individual speakers and for different languages were superimposed on the corresponding second-order locus equations, a close agreement between simulated and human data was evident. Furthermore, since the model-based SOLEs had been generated by varying gestural timing, i.e., the degree of C- V_2 coarticulation, a natural interpretation suggested itself of the speaker-specific and cross-linguistic variations in the locus equation place descriptors, namely the hypothesis that the observed within-place variability may be associated with differences in how the C and the V_2 gestures are temporally coordinated. Here, this coordination was studied by changing the phasing between the end of the stable part of V_1 and the beginning of the consonant closure. To complete our work, we intend now to study the phasing between the beginning of the stable part of V_2 and the end of the release of the consonant.

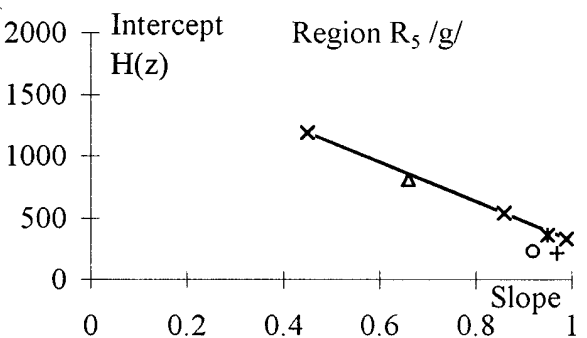
Claiming that FOLE coefficients exhibit place-specific invariance becomes problematic in the light of the present results. The question arises whether a similar claim could be made for SOLE coefficients. The data summarized in Figs. 10–12 seem to indicate that constancy was indeed maintained for place at the level of second-order locus equations. Our position is that, without a better understanding of the regularities underlying locus equations, speculations on their origins is of little use. Indeed, Lindblom (1996) has questioned the idea that speech signals should be expected to contain any invariants at all (absolute or relative), because such a claim is likely to overestimate signal information and underestimate the role played by accumulated, experience-



(a)



(b)



(c)

○ Arabic △ English × Swedish
 □ Thai + Urdu

FIG. 12. Language-dependence of slopes and intercepts illustrated with data from Sussman *et al.* (1993). The cross-linguistic observations are compared with simulated second-order locus equations of Fig. 8 for three degrees of coarticulation (represented by ×) and three regions of articulation R_5 (a), R_6 (b), R_8 (c).

based, signal-derived knowledge in normal perceptual processing. Therefore the role that articulatory constraints play in shaping “possible” and “actual” locus equations remains to be clarified by means of further work on articulatory mod-

eling. It would seem that only when such topics have been worked through comprehensively, will it be possible to address the issue of invariance in an insightful way.

ACKNOWLEDGMENTS

The authors wish to thank the anonymous reviewers and Michael Studdert-Kennedy for helpful comments.

- Carré, R. (1996). "Prediction of vowel systems using a deductive approach," *Proceedings of ICSLP-96* (Philadelphia), pp. 434–437.
- Carré, R., and Chennoukh, S. (1995). "Vowel–consonant–vowel modeling by superposition of consonant closure on vowel-to-vowel gesture," *J. Phonetics* **23**, 231–241.
- Carré, R., and Mrayati, M. (1991). "Vowel–vowel trajectories and region modeling," *J. Phonetics* **19**, 433–443.
- Carré, R., and Mrayati, M. (1992). "Distinctive regions in acoustic tubes. Speech production modeling," *J. Acoust.* **5**, 141–159.
- Carré, R., Lindblom, B., and MacNeilage, P. (1994). "Acoustic contrast and the origin of the human vowel space," *J. Acoust. Soc. Am. Suppl.* **1** **95**, S2924.
- Chennoukh, S. (1995). "Modélisation du conduit vocal en régions distinctives. Synthèse d'ensembles Voyelle–Voyelle et Voyelle–Consonne–Voyelle," Thèse en Signal et Images, ENST, Paris.
- Chennoukh, S., and Carré, R. (1995). "Vowel–vowel production on a Distinctive Region Model. A new command strategy," *Proceedings of the XIIIth ICPHS* (Stockholm), pp. 78–81.
- Chennoukh, S., Carré, R., and Lindblom, B. (1995). "On the 'locus equation' and its relation with the consonant place of articulation," *J. Acoust. Soc. Am.* **97**, 3242(A).
- Dorman, M. F., Studdert-Kennedy, M., and Raphael, L. J. (1977). "Stop-consonant recognition: Release bursts and formant transitions as functionally equivalent, context-dependent cues," *Percept. Psychophys.* **22**, 109–122.
- Fant, G., and Pauli, S. (1974). "Spatial characteristics of vocal tract resonance modes," in *Proceedings of the Speech Communication Seminar* (Almqvist & Wiksell, Stockholm), pp. 121–132.
- Fowler, C. A. (1993). "Phonological and articulatory characteristics of spoken language," in *Linguistic Disorders and Pathologies: An International Handbook*, edited by G. Blanken, J. Dittmann, H. Grimm, J. Marshall, and C.-W. Wallesch (Walther de Gruyter, Berlin), pp. 34–46.
- Fowler, C. A. (1994). "Invariants, specifiers, cues: an investigation of locus equations as information for place of articulation," *Percept. Psychophys.* **55**, 597–610.
- Gay, T. (1977). "Articulatory movements in VCV sequences," *J. Acoust. Soc. Am.* **62**, 183–193.
- Hill, D., Manzara, L., and Taube-Schock, C. R. (1995). "Real-time articulatory speech-synthesis-by-rules," *Proceedings of AVIOS'95* (San Jose).
- Klatt, D. H. (1980). "Software for a cascade/parallel formant synthesizer," *J. Acoust. Soc. Am.* **67**, 737–793.
- Krull, D. (1987). "Second formant locus patterns as a measure of consonant–vowel coarticulation," *Phonetic Experimental Research at the Institute of Linguistics, University of Stockholm (PERILUS)* **V**, 43–61.
- Krull, D. (1988). "Acoustic properties as predictors of perceptual responses: A study of Swedish voiced stops," *Phonetic Experimental Research at the Institute of Linguistics, University of Stockholm (PERILUS)* **VII**, 66–70.
- Krull, D., Lindblom, B., Shia, B. E., and Fruchter, D. (1995). "Cross-linguistic aspects of coarticulation: An acoustic and electropalatographic study of dental and retroflex consonants," *Proceedings of the 13th International Congress of Phonetic Sciences* (Stockholm), pp. 436–439.
- Lindblom, B. (1963). "On vowel reduction," Report No. 29. Stockholm: The Royal Institute of Technology, Speech Transmission Laboratory.
- Lindblom, B. (1996). "Role of articulation in speech perception: Clues from production," *J. Acoust. Soc. Am.* **99**, 1683–1692.
- Mrayati, M., Carré, R., and Guérin, B. (1988). "Distinctive region and modes: A new theory of speech production," *Speech Commun.* **7**, 257–286.
- Nearey, T. M., and Shammass, S. E. (1987). "Formant transitions as partly distinctive invariant properties in the identification of voiced stops," *Can. Acoust.* **15**, 17–24.
- Öhman, S. (1966). "Coarticulation in VCV utterances: spectrographic measurements," *J. Acoust. Soc. Am.* **39**, 151–168.
- Öhman, S. E. G. (1967). "Numerical model of coarticulation," *J. Acoust. Soc. Am.* **41**, 310–320.
- Sussman, H. (1994). "The phonological reality of locus equations across manner class distinctions: Preliminary observations," *Phonetica* **51**, 119–131.
- Sussman, H. M., Hoemeke, K., and Ahmed, F. (1993). "A cross-linguistic investigation of locus equations as a relationally invariant descriptor for place of articulation," *J. Acoust. Soc. Am.* **94**, 1256–1268.
- Sussman, H. M., McCaffrey, H. A., and Matthews, S. A. (1991). "An investigation of locus equations as a source of relational invariance for stop place categorization," *J. Acoust. Soc. Am.* **90**, 1309–1325.

Timing of pitch movements and accentuation of syllables in Dutch

Dik J. Hermes

Institute for Perception Research/IPO, P.O. Box 513, NL 5600 MB Eindhoven, The Netherlands

(Received 1 February 1996; revised 6 February 1997; accepted 26 May 1997)

In this study, the relation between the timing of a rising or falling pitch movement and the syllable it accentuates is investigated. The five-syllable utterance /mamamama/ was provided with a relatively fast rising or falling pitch movement. The timing of the movement was systematically varied and Dutch subjects were asked to indicate which syllable they perceived as accented. In order to find out where in the pitch movement the cue which induces the percept of accentuation is located, the duration of the pitch movement was varied. In order to find out which segments of the utterance this characteristic is linked to, the duration of the /m/ was varied. The results showed that the percept of accentuation is induced by a change in pitch at the start of the movement. The moment at which the course of pitch starts to change significantly determines which syllable is perceived as accented. If this moment lies some tens of milliseconds before the P-center, i.e., the perceptual moment of occurrence of the syllable, the preceding syllable is perceived as accented. For a rise, a high accent is perceived; for a fall, a low accent. If the pitch change occurs after this moment, the syllable with this P-center is perceived as accented. For the rise, a low accent is then perceived; for the fall, a high accent. This will be discussed in the light of earlier research on accentuation and of theoretical knowledge about pitch accents. © 1997 Acoustical Society of America. [S0001-4966(97)04309-9]

PACS numbers: 43.71.An, 43.71.Es, 43.70.Fq [WS]

INTRODUCTION

This paper is concerned with the relation between an accent-lending pitch movement and the syllable accented by this pitch movement. Two topics are addressed. The first topic has to do with the question of *which syllable is perceived as accented* as the temporal position of the pitch movement in an utterance is varied. To answer this, subjects were presented with a polysyllabic nonsense word with a pitch contour containing a rise or a fall, and they were asked to indicate the syllable they perceived as accented. The second topic deals with *what kind of accent is perceived by the listener*. To answer this, subjects were asked to indicate whether they perceived a high or a low accent, as the temporal position of a pitch movement was varied.

The first topic deals with the same question as addressed by Van Katwijk and Govaert (1967), who varied the position of a rising or a falling pitch movement within a synthetic four-syllable speech sound /χιχɔχɛχγ/. They asked subjects to rate the "level of accentuation" of the various syllables. They found that for the second, third, and fourth syllables higher levels of accentuation were attained when they were accented by a rise than when accented by a fall. The first syllable reached a higher level of accentuation when accented by a fall than when accented by a rise, but this could be attributed to a very strong declination. In the stimuli synthesized by Van Katwijk and Govaert (1967), pitch frequency decreased from 160 to 110 Hz in 1200 ms, the duration of the stimulus. This amounts to 42 Hz/s or 0.45 oct/s, about twice as much as is normal in neutral speech. Because of this strong declination the pitch in the utterance with the fall started at a very high level which probably caused the high ratings for the level of accentuation of the first syllable.

The second conclusion by Van Katwijk and Govaert was that the "pitch falls exert their prominence-lending force later than do pitch rises" (p. 115). This was based on the observation that falls in positions where they induced the highest level of accentuation of a syllable were positioned later in the syllable than rises in positions where they induced the highest level of accentuation. These experiments were carried out at a time when good speech synthesis was not yet possible. Furthermore, it is hard to decide from these experiments what attribute of the pitch contour induces the accentuation of a syllable and to what speech segment this attribute is linked.

Another related experiment is reported by Hasegawa and Hata (1992). They varied not only the position of a falling pitch movement in the nonsense utterance /mamama/, but also the steepness of the fall, which was completely situated within the vowel of the second syllable. They asked Japanese subjects to indicate whether they perceived an accent on the first or on the second syllable. They concluded, firstly, that the second syllable was only perceived as accented when the accenting fall started a certain distance into the vowel and, secondly, that, the steeper the fall, the more the subjects tended to indicate the first syllable as accented.

Much more is known about the temporal position of a pitch movement within a syllable and the kind of accent perceived. In various descriptions of intonation, pitch movements are divided into different categories on the basis of their position in the syllable. For example, in the description of Dutch intonation as given by 't Hart *et al.* (1990), two kinds of accent-lending rises are distinguished: an early rise starting before the vowel onset and a late rise starting after the vowel onset. Hill and Reid (1977) obtained a similar

result for English. They presented subjects with a pair of utterances which were identical except for the timing of a rising pitch movement. For a specific timing difference between the two pitch movements, subjects classified the utterances as more different when the two pitch movements started on different sides of the vowel onset than when they started both on the same side of the vowel onset. In the description by 't Hart *et al.* (1990), a realization of an early rise is indicated with "1," a late rise with "3." In autosegmental phonology, accents lent by these two types of pitch movements correspond with $L+H^*$ and L^*+H , respectively (Pierrehumbert, 1980).

For the accent-lending fall there is less agreement as to the division into different categories. 't Hart *et al.* (1990) give only one phonetic category of full-sized, accent-lending falls: the "A." Gussenhoven and Rietveld (1992/1993) distinguish two phonological categories, for Dutch, too, which they indicate with H^*L and $^H H^*L$. The second category is distinguished from the first by the presence of down-step (Pierrehumbert, 1980), a phenomenon for which there is no exact equivalence in the description by 't Hart *et al.* (1990). In the autosegmental phonology of English intonation (Pierrehumbert, 1980; Beckman and Pierrehumbert, 1986) two bi-tonal falls are distinguished, H^*+L and $H+L^*$. In Swedish, two lexical tones are distinguished. Bruce (1977) showed that timing differences between the falling pitch movements involved played a crucial role in distinguishing between the two.

Thus, various investigations have been carried out into the relation between the timing of a pitch movement and the kind of tonal event that is perceived. In the investigations reported in this paper, this problem also comes into play in the third experiment reported here, but in the first two experiments the main question is: which syllable is perceived as accented as the temporal position of a pitch movement is varied? Experiments are reported in which the timing of rising and falling pitch movements was systematically varied and Dutch subjects were asked to indicate which syllable they perceived as accented. The location in the utterance where the percept of accentuation shifts from one syllable to the next will be referred to as the *accentuation boundary*. In order to find out where the cue for accentuation of the pitch movement is located, at its onset or at its offset, pitch movements with three different durations were used. Furthermore, the duration of the speech segments was varied in order to investigate to which segment the attribute of the pitch contour which induces the accentuation of the syllable is coupled. The rationale of these two setups is given in the description of the experiments.

I. EXPERIMENT I

In this experiment, pitch movements of different durations were used: 80, 120, and 160 ms. The onset of these pitch movements was systematically varied over the utterance /mamamama/. Both rises and falls were used. When the timing of the pitch movement is gradually shifted to later in the utterance, the percept of accentuation will, at a certain

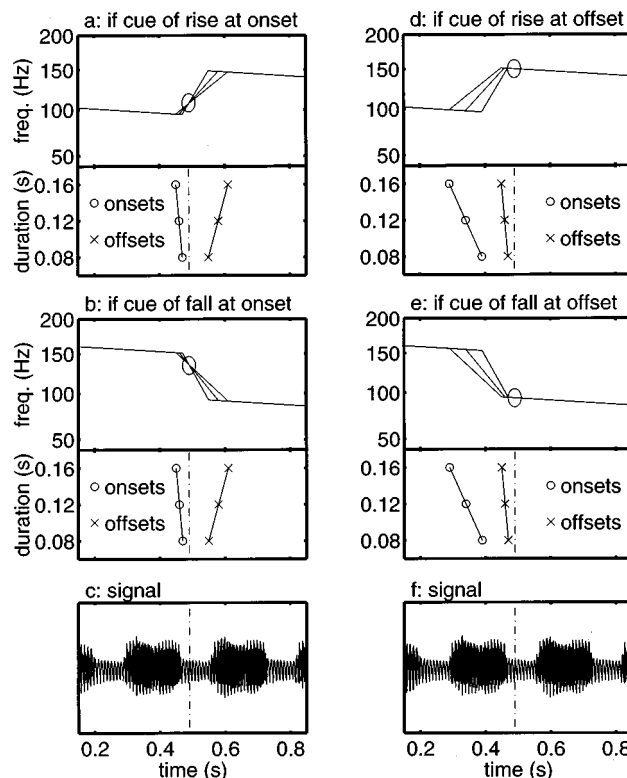


FIG. 1. Rationale of Experiment I. Pitch movements of three different durations at a hypothetical accentuation boundary. This hypothetical accentuation boundary is indicated by the vertical dashed-dotted line in the lower panels of (a), (b), (d), and (e), and in the oscillograms of the speech signal in (c) and (f). The three pitch movements are the three continuous lines consisting of straight-line segments shown in the upper panels of (a), (b), (d), and (e). The cue for accentuation is indicated by the circle. If this cue comes earlier than the accentuation boundary, the previous syllable is perceived as accented, while the next syllable is perceived as accented if it comes later. In (a) and (b), the situation is depicted if this cue for accentuation is at the onset of the pitch movement. In this case, the onset of the pitch movements at the accentuation boundary shift at most somewhat to the left as the duration of the movement gets longer, while the offsets shift to the right. This is shown in the lower panels of (a) and (b), where the onsets are indicated with small circles and the offsets with crosses. In (d) and (e), the situation is depicted if the cue for accentuation is at the offset of the pitch movement. Here, both the onset and the offset of the pitch movements at the accentuation boundaries shift to the left as the duration of the movement gets longer, the onset much more so than the offset.

location in the utterance, shift from one syllable to the next. The moment at which this occurs is the *accentuation boundary*.

A. Rationale

This experiment was carried out with pitch movements of three different durations in order to find out whether the cue for accentuation is at the onset or at the offset of the pitch movement. The rationale underlying this experimental setup is illustrated in Fig. 1. A hypothetical accentuation boundary between two syllables /ma/ is indicated by the dotted vertical lines in the lower panels of Fig. 1(a), (b), (d) and (e), and in the oscillograms in Fig. 1(c) and (f). The basic idea is that the location of the cue for accentuation at the accentuation boundary will be more or less independent of the duration of the pitch movement. So, if the pitch cue which induces the percept of accentuation is located at or

immediately after the *onset* of a pitch movement, the location of the *onset* of the pitch movement at the accentuation boundary will be more or less independent of the duration of the pitch movement. For the rise, this situation is depicted in Fig. 1(a), and in Fig. 1(b) for the fall. The location of the pitch cue is indicated by the ellipses. The position of this pitch cue is not exactly at the turning point of the pitch movement, since the perceptual process which determines where the cue is located will have an integration time, and this integration time may be somewhat longer for stimuli with weaker cues. It is supposed that the onset of the longer-duration pitch movements is less abrupt and, therefore, weaker than that of the shorter-duration pitch movements. The onset of the pitch movements at the accentuation boundary may, therefore, shift somewhat to the left. The offset of the pitch movement at the accentuation boundary will accordingly shift to the right as the duration of the pitch movement gets longer. This is shown in the lower panels of Fig. 1(a) and (b), where the position of the onsets of the pitch movements of three different durations at the accentuation boundary are indicated by circles and the position of the offsets of these pitch movements are indicated by crosses. If, on the other hand, the cue which accentuates the syllable is at or immediately after the *offset* of the pitch movement, the *offset* of the pitch movement at the accentuation boundary will be more or less independent of the duration of the pitch movement. This situation is illustrated in Fig. 1(d) for the rise, and in Fig. 1(e) for the fall. The hypothetical location of the pitch cue at the end of the pitch movement is again indicated by the ellipses. As argued before, the perceptual process which determines the moment at which the pitch movement has been completed will have an integration time. Therefore, the offset of the pitch movement at the accentuation boundary will at most shift a bit to the left as the duration of the pitch movement gets longer, but certainly not to the right. The onset of the pitch movement at the accentuation boundary will accordingly shift much more to the left. This is shown in the lower panels of Fig. 1(d) and (e), where the position of the onsets of pitch movements of three durations at the accentuation boundaries are indicated by circles and the position of the offsets of these pitch movements are indicated by crosses.

B. Method

1. Stimuli

The stimuli were derived from a natural three-syllable utterance /mamama/, spoken with an accent on the second syllable. Speech modifications were carried out with pitch-synchronous-overlap-add (PSOLA) techniques (Hammon *et al.*, 1989) with which pitch and time modifications can be applied to speech signals without affecting the speech quality too much. The first step was to triplicate the middle syllable, resulting in the utterance /mamamamama/ consisting of five syllables, of which the middle three were identical as to amplitude and spectral envelope. Next, the original pitch contour was replaced by a rising or a falling pitch movement superimposed on a declination line. The rises and falls had durations of 80, 120, or 160 ms. A stimulus con-

tinuum was created by shifting the pitch movement through the utterance in steps of 20 ms. The onset of the first element of the continuum was at the start of the stimulus. The offset of the last element was at the end of the stimulus. The declination rate was fixed at 0.7 E/s, where E is nr of ERB (Hermes and Van Gestel, 1991; Glasberg and Moore, 1990). In the male-voice range used in this study this amounts to about 24 Hz/s or 0.39 oct/s. The interval between successive onsets of the pitch movements in the continuum was 20 ms. The utterance lasted 1.32 s, so there were 62 stimuli with rises of 80 ms and 62 with falls of 80 ms, 60 stimuli with rises of 120 ms and 60 with falls of 120 ms, and 58 stimuli with rises of 160 ms and 58 with falls of 160 ms. Stimuli with rises and falls were mixed. There were 180 rises and 180 falls, so there were 360 different stimuli.

The order of presentation was random. The set of 360 stimuli was presented twice to each subject in the same random order. These stimuli were presented in six sessions of 120 stimuli. In each session, each set of 120 stimuli was preceded by 12 practice stimuli, during which the subjects were allowed to adjust the intensity of the stimuli to a comfortable loudness level. This set of practice stimuli approximately covered the range of the stimuli presented in the actual experiment.

2. Subjects and procedure

Eleven subjects took part in this experiment; all were students or research associates of the Institute of Perception Research. Some of them had experience in speech perception experiments, but there was no clear relation between the presence of this experience and the results. Their age ranged from about 20–40 years. All were native speakers of Dutch. Each subject did the test individually in an interactive computer session, seated in a quiet room. The subject started the presentation of a stimulus by pressing the return key on the keyboard or by clicking a button on the computer screen. He/she could listen to a stimulus as often as desired, by pressing or clicking repeatedly. The task was to indicate on which of the five syllables an accent was perceived. Thus, there were five response classes corresponding to whether an accent was perceived on the first, the second, the third, the fourth, or the fifth syllable. All responses, including the number of times a subject listened to each stimulus, were recorded.

C. Results and discussion

The results for the stimuli with the rises are presented in Fig. 2. The range of the onsets of the rises is shown in Fig. 2(a) for the stimuli with the 120-ms rise. For all five response classes, distributions were calculated of the onsets of the corresponding pitch movements. These distributions are presented in Fig. 2(b). They represent, for each response class, the number of these responses as a function of the onset time of the pitch movement. The upper part of the panel shows the results for the stimuli with the pitch movement of 80 ms, the middle part for the pitch movements of 120 ms, and in the lower part of the pitch movements of 180 ms. The onset distribution of the rises accenting the first

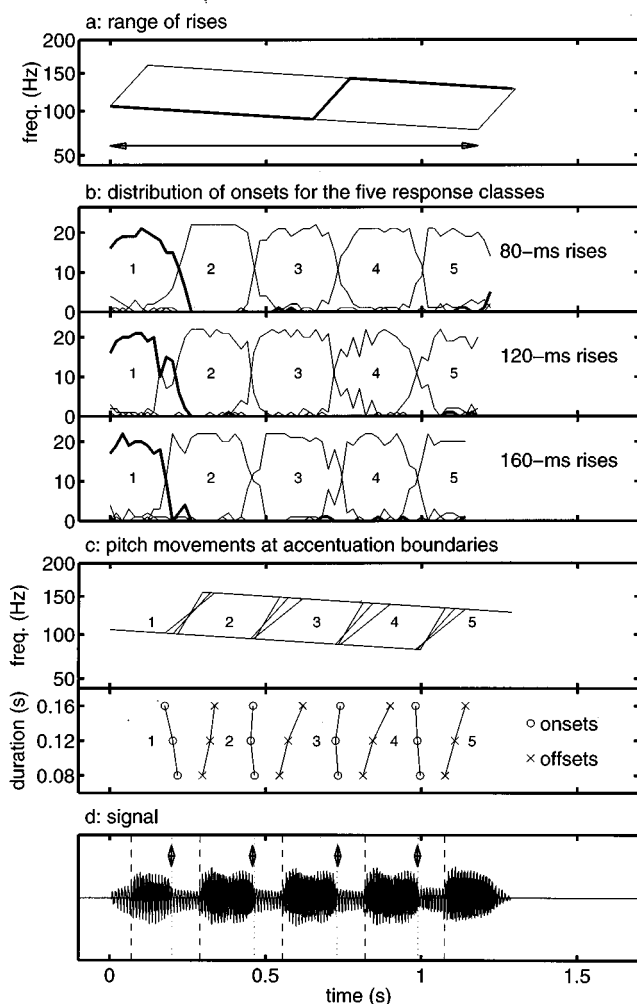


FIG. 2. Determination of the rises at the accentuation boundaries. In (a) the stimulus continuum is presented for the 120-ms rises. In (b), for each of the five response classes, the frequency distributions are presented of the onset times of the pitch movements accenting the responded syllable. The numbers in the plots indicate the syllable which, according to these distributions, is most often indicated as accented. The thick continuous line is the distribution of the onset times of the pitch movements accenting the first syllable. The lowest panel shows the oscillogram of the /mamamama/ stimulus monotonized at 100 Hz; the dotted lines are the transitions from the /a/'s to the /m/'s; the dashed lines are the transitions from the /m/'s to the /a/'s; the diamonds are the average of the onsets of the three rises at the accentuation boundary.

syllable is indicated with a thicker line than the other distributions. It can clearly be seen that, when the pitch movement starts early in the utterance, in almost all cases the first syllable is perceived as accented. However, after about 200 ms, more and more subjects start to indicate the second syllable as accented. Then, when the onset of the rise is later than about 250 ms, the listeners indicate in almost all cases the second syllable as accented. At about 450 ms there is a shift to the third syllable, etc. So, clear intervals can be seen where the corresponding syllable is almost always selected as the accented syllable. These regions are indicated by the numbers 1 to 5. What is most important at the moment are the locations in the speech signal where the percept of accentuation changes from one syllable to the next. These are the category boundaries on the continuum of onset and offset

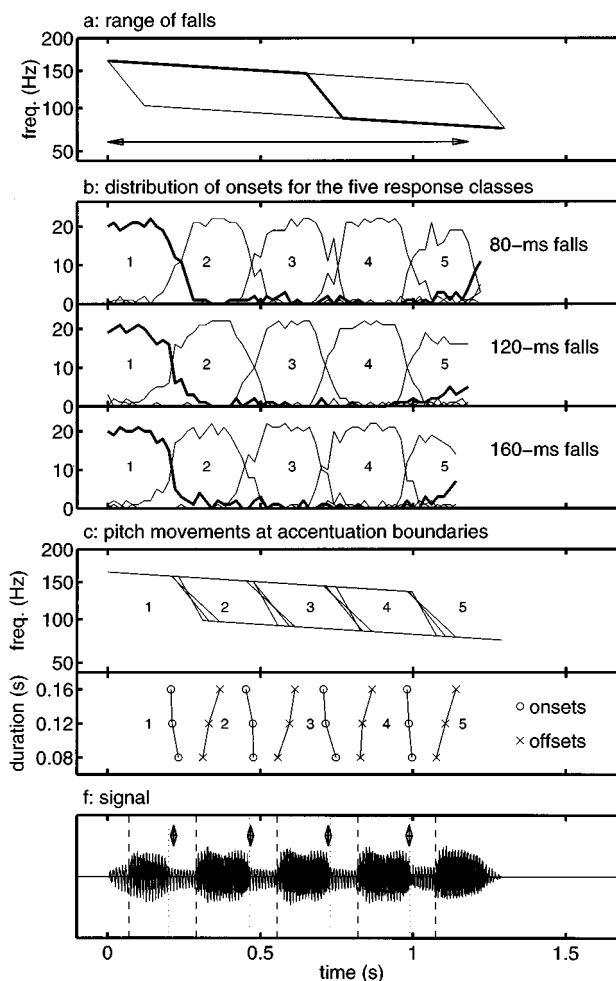


FIG. 3. Determination of the falls at the accentuation boundaries. Results are presented in the same way as in Fig. 4.

times before which a pitch movement accents one syllable and after which it accents the next. These are the moments in the speech signal where the distributions cross. They were calculated after smoothing the distributions, since without such smoothing the statistical fluctuations on the distributions could strongly influence the result. The results are presented in Fig. 2(c). The upper part shows the pitch movements at the accentuation boundaries as determined on the basis of the onset distributions. The lower part shows the position of the onsets and the offsets of these rises. Observe that the position of the onsets and offsets of the rises at the accentuation boundaries corresponds best with the situation presented in Fig. 1(a). The onset of the rises at the accentuation boundaries shift at most a bit to the left as the duration of the rise gets longer, while the offsets shift to the right. As argued in the rationale of this experiment, this shows that the cue for accentuation is *at the onset of the rise*. The relation with the segmental structure can be derived from the lowest panel representing the oscillogram of the stimulus monotonized at 100 Hz.

The results for the stimuli with the falls are presented in Fig. 3 in the same way as for the rises. In Fig. 3(a) the stimulus range of the falls is presented for the 120-ms fall. In Fig. 3(b) the onset distributions of the falls accenting each of

the five syllables are presented. As for the rises, clear intervals can be distinguished where in almost all cases either the first, the second, the third, the fourth, or the fifth syllable is perceived as accented. The locations where these distributions cross supply the accentuation boundaries of the syllable. The falls at these accentuation boundaries are presented in Fig. 3(c), in the lower part of which the onsets and offsets are presented. As for the rises, the onsets of the falls at the accentuation boundaries shift somewhat to the left, but the offsets shift to the right as the pitch movement gets longer. This is the situation presented in Fig. 1(b), which shows that, as for the rises, the cue for accentuation of the fall is located *at the onset of the fall*.

In Figs. 2(b) and 3(b), the onset distribution of the pitch movements accenting the first syllable is indicated by a thicker line than the onset distributions of the other syllables. Especially in the case of the fall, it can be seen that pitch movements starting very late in the utterance often induce the percept of an accent on the first syllable. This is probably due to the weakness of the accenting cue of such a late pitch movement. As has been shown elsewhere (Hermes, 1995), subjects tend to indicate the first syllable as accented in the absence of a clear accenting cue.

II. EXPERIMENT II

The previous experiment showed that the temporal location of the change in pitch at the onset of the pitch movement determined which syllable was perceived as accented. Inspection of Fig. 2(c) and (d) and Fig. 3(c) and (d) showed that this change in pitch was located close to the syllable onset (cf. Caspers and Van Heuven, 1993; Van Santen, 1995), about 90 ms before the vowel onset. To find out whether this segmental anchor point was indeed the vowel-consonant (VC) transition or some other point in the utterance, the duration of the /m/ was varied. In one set of stimuli the duration of the /m/ was halved, in the other it was doubled.

A. Rationale

The rationale of this experiment is presented in Fig. 4. The left three panels present the situation if the accentuation boundary is coupled with the syllable onset, i.e., the VC transition. This VC transition is indicated with the vertical dotted line, while the hypothetical accentuation boundary is represented by the continuous vertical line. In Fig. 4(a) three rises of different duration are depicted at the hypothetical accentuation boundary for the stimulus with the short /m/. In Fig. 4(b), these three rises are presented for the normal /m/, while in Fig. 4(c) these three rises at the hypothetical accentuation boundary are shown for the stimulus with the long /m/. Since in these three left panels the situation is depicted in which the cue for accentuation is coupled with the syllable onset, the distance between the syllable onset and the accentuation boundary, indicated by the double arrow in Fig. 4(a)–(c), remains constant, while the distance between the accentuation boundary and the vowel onset varies.

In the right three panels of Fig. 4, the situation is sketched in which the hypothetical accentuation boundary is coupled with the vowel onset, i.e., the consonant-vowel (CV) transition.

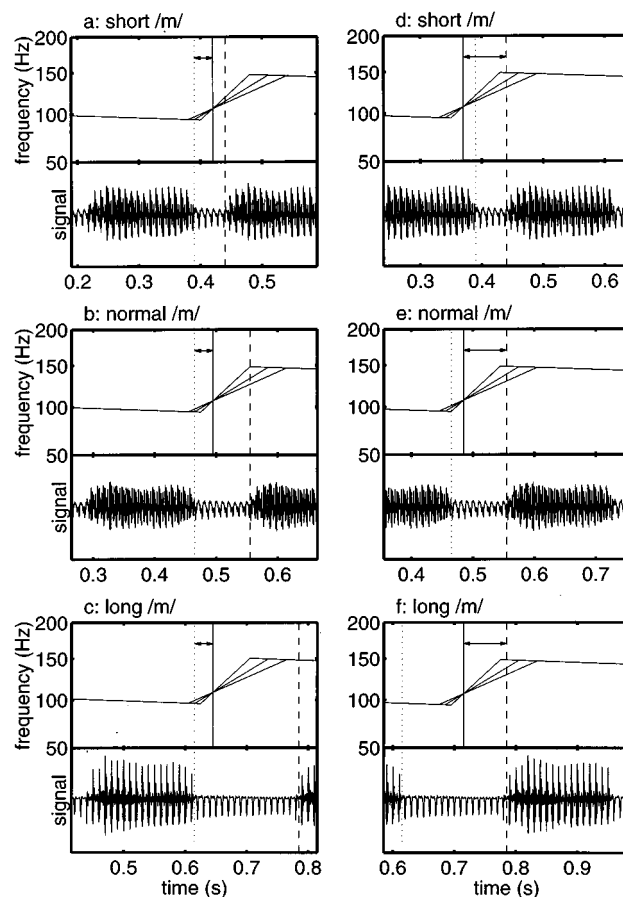


FIG. 4. Rationale of experiment II. In the left three panels, the three pitch movements of different durations are depicted at a hypothetical accentuation boundary under the hypothesis that the position of the accentuation boundary is linked up with the vowel-consonant (VC) transition. In (a) the stimulus with the short /m/ is presented, in (b) the stimulus with the normal /m/, and in (c) the stimulus with the long /m/. The dotted line represents the VC transition, the dashed line the CV transition, while the continuous vertical line represents the hypothetical accentuation boundary. Observe that the distance between the VC boundary and the hypothetical accentuation boundary, indicated by the double arrow, remains constant, while the distance between the accentuation boundary and the CV transition varies. In the right three panels, the pitch movements are depicted at a hypothetical accentuation boundary under the hypothesis that the position of the accentuation boundary is linked up with the consonant-vowel (CV) transition. Observe now that the distance between the accentuation boundary and the CV transition, indicated by the double arrow, remains constant, while the distance between the VC transition and the accentuation boundary varies.

(CV) transition. The hypothetical accentuation boundary is again indicated by the continuous vertical line, while the CV transition is indicated with the dashed vertical line. In Fig. 4(d)–(f), the three accent-lending rises at the accentuation boundary are presented for the stimuli with the short /m/, the normal /m/, and the long /m/, respectively. Since in these three right panels the situation is depicted in which the cue for accentuation is coupled with the vowel onset, the distance between the accentuation boundary and the vowel onset, indicated by the three double arrows in Fig. 4(d)–(f) remains constant, while the distance between the VC transition and the accentuation boundary varies.

So, the aim of this experiment was to find out whether the accentuation boundary is coupled with the syllable onset or the vowel onset. To this end, accentuation boundaries

were determined for /mamamama/ stimuli with /m/'s of three different durations. If the accentuation boundary is linked up with the syllable onset, the distance between syllable onset and accentuation boundary will remain constant. If, on the other hand, the accentuation boundary is linked up with the vowel onset, the distance between vowel onset and accentuation boundary will remain constant.

B. Method

1. Stimuli

In order to restrict the set of stimuli, only the accentuation boundary between the second and the third stimulus was investigated in this experiment. Hence, only stimuli were used in which the second or the third syllable was perceived as accented. For the stimuli with short /m/'s, the range of the onsets of the pitch movements is depicted in Fig. 5(a) for the rises and in Fig. 5(e) for the falls. For the stimuli with the short /m/, the onsets ranged from 260–460 ms after the onset of the utterance with intervals of 20 ms. The pitch movements again had a duration of 80, 120, and 160 ms, and there were rises and falls, resulting in a total of 66 stimuli with short /m/'s. In the stimuli with the long /m/'s the onsets of the pitch movements ranged from 460 to 780 ms after the onset of the utterance, again with intervals of 20 ms. The pitch movements had durations of 80, 120, or 160 ms, and there were rises and falls, resulting in a total of 102 stimuli with long /m/'s. The oscillograms of the stimuli are presented in Fig. 5(d) and (h) for the short-/m/ stimuli, and in Fig. 6(d) and (h) for the long-/m/ stimuli. The durations of the three /m/'s in the original /mamama/ were about 70, 80, and 70 ms. The duration of these /m/'s were doubled and halved by means of PSOLA techniques, as were the tripling of the second syllable and the pitch manipulations.

No subject complained about any unnaturalness of the stimuli, except that two subjects with a long experience of PSOLA-manipulated speech signals could identify the speech signals as manipulated with PSOLA. One of them heard a weak irregularity somewhere in the stimulus, probably due to some failure of PSOLA. It is assumed that this did not have a relevant influence on the results. Since excluding their data did not change the results, their data are included in the following description.

2. Subjects and procedure

The same 11 subjects were used as in the first experiment. Their task was to indicate whether they perceived an accent on the second or on the third syllable of the utterance. Stimuli with rises and falls were mixed as in Experiment I, but the stimulus set with the short /m/'s was presented in a separate session from the stimulus set with the long /m/'s. Both sets of stimuli were again presented twice in the same random order. Each time, each set was preceded by 12 practice stimuli covering the range of the stimuli presented in the actual experiment.

C. Results

The results are presented in Fig. 5 for the stimuli with the short /m/ and in Fig. 6 for the long /m/. Since the stimu-

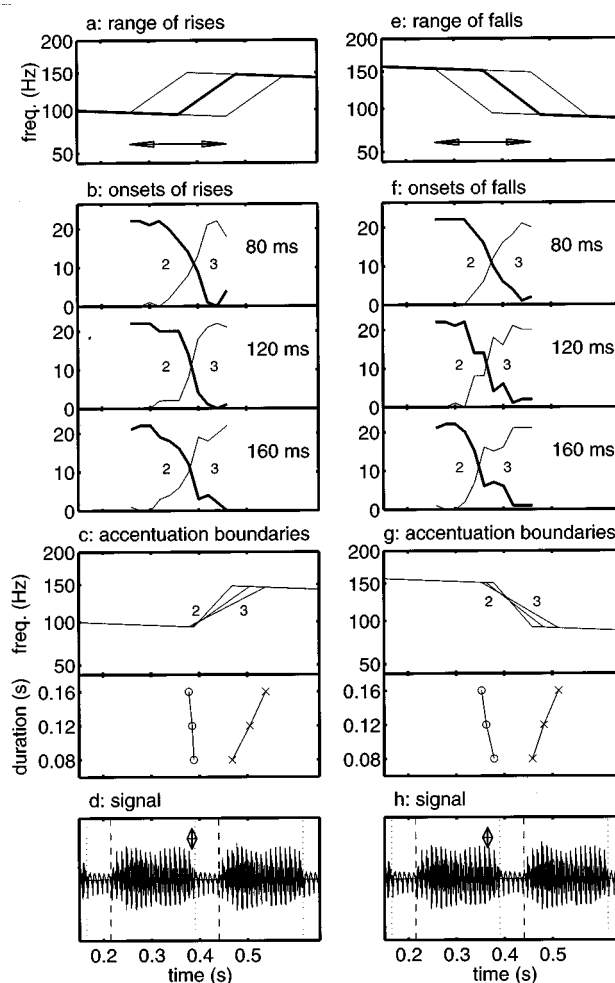


FIG. 5. Accentuation boundaries between the second and the third syllable for the /mamamama/ stimuli in which the duration of the /m/ was halved. In panels (a)–(d) the results for the rises are plotted, in panels (e)–(h) the results are for the falls. Panels (a) and (e) give the stimulus range of the rise and the fall of 120 ms. In (b) and (f) the onset distributions of the pitch movements of the three different durations are presented. The thicker line indicates the frequency distribution of the number of responses in which the subject indicated the second syllable as accented; the thinner line gives the number of times the third syllable was perceived as accented. The points where these two distributions cross yield the onsets of the pitch movement at the accentuation boundaries. The pitch movements at these accentuation boundaries as determined in this way are presented in panels (c) and (g), in which the lower part gives the onsets (small circles) and the offsets (crosses) of the pitch movements at the accentuation boundary. The two lowest panels present the oscillogram of the /mamamama/ stimulus monotonized at 100 Hz; the diamonds are the average of the onsets of the three pitch movements at the accentuation boundary.

lus range was limited to the stimuli accenting the second or the third syllable, only the accentuation boundaries between the second and the third syllable are presented. The results are similar to those obtained in Experiment I, except that the accentuation boundaries are positioned at different moments. For the stimuli with the short /m/'s, the accentuation boundary was located at about 65 ms before the vowel onset. For the stimuli with the long /m/'s, this was at 110 ms before the vowel onset. It is worth noting, as can be seen in Fig. 6, that this position is within the /m/.

The results for the three sets of stimuli are summarized in Fig. 7. The left three panels present the rises at the accentuation boundaries and the oscillogram of the stimuli, for the

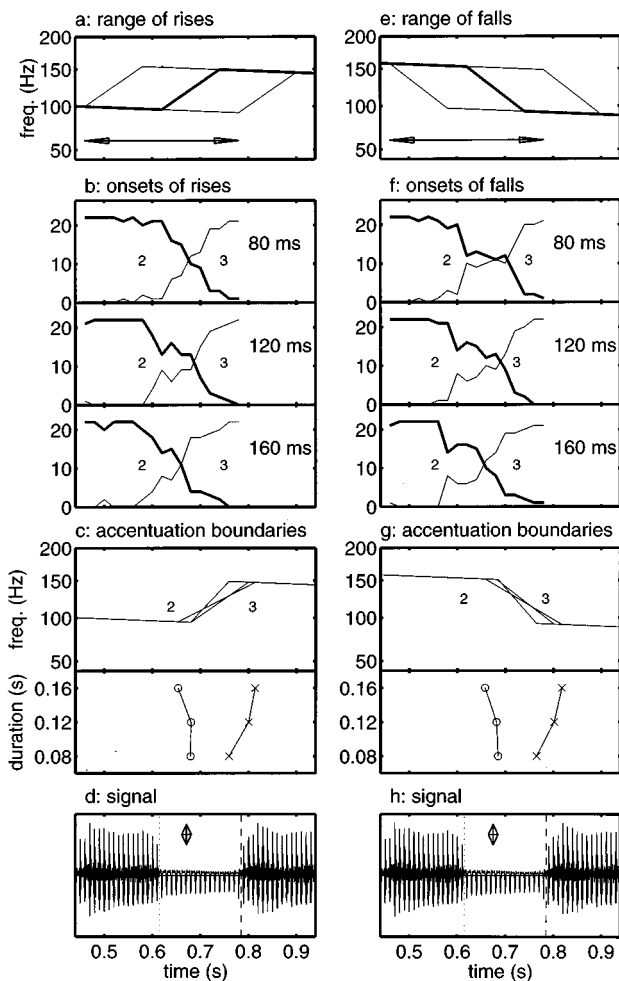


FIG. 6. Accentuation boundaries between the second and the third syllable for the stimuli in which the duration of the /m/ was doubled. Results are presented in the same way as in Fig. 4.

short /m/ at the upper panel, for the normal /m/ at the middle panel, and for the long /m/ at the lower panel. The falls at the accentuation boundaries are similarly presented in the right three panels. If these results are compared with the two situations sketched in Fig. 4, it can be concluded that the accentuation boundary is certainly not linked up with the syllable onset. For the short-/m/ and the normal-/m/ stimuli, the accentuation boundary is close to the syllable onset [Fig. 7(a), (b), (d), and (e)], but for the long-/m/ stimuli, the syllable boundary precedes the accentuation boundary by at least 60 ms. On the other hand, the distance between the accentuation boundary and the vowel onset, though less variable, is not really constant either. For the short /m/, this distance is about 65 ms, for the normal /m/ 90 ms, and for the long /m/ 110 ms. This will be discussed in more detail in the Discussion, where it will be argued that the accentuation boundary is neither strictly coupled with the syllable onset nor the vowel onset, but with the perceptual moment of occurrence of the syllable, the so-called P-center (Morton *et al.*, 1976).

III. EXPERIMENT IIIa

In this experiment, the main question was not which syllable was perceived as accented, but what kind of pitch

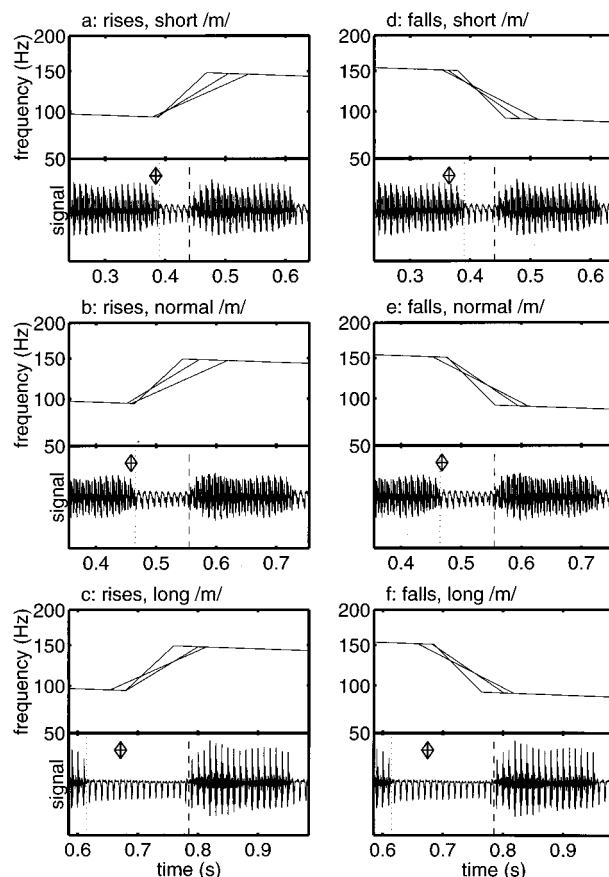


FIG. 7. Summary results of experiment II. Pitch movements of three different durations at the accentuation boundaries are presented together with the corresponding oscillograms of the stimuli monotonized at 100 Hz. In (a)–(c) the results for the rises are presented, while in (e)–(g) the results for the falls are shown. In the upper two panels (a) and (d) the results with the short /m/ are presented, in the middle two panels (b) and (e) are those with the normal /m/, and in the lower two panels (c) and (f) are those with the long /m/. The diamonds are the average of the onsets of the three pitch movements of different duration at the accentuation boundary.

accent was perceived. As described in the Introduction, in Dutch as well as in British English intonation, two kinds of rises are distinguished, an early rise starting before the vowel onset and a late rise starting after the vowel onset. For the fall, the situation is less clear.

Here, this issue was addressed by asking subjects to indicate, for a number of different timings and for three different durations of the pitch movement, whether they perceived a high or a low accent. Some informal tests showed that, in general, subjects could do this task easily, although perhaps not as easily as the task to indicate which syllable was perceived as accented. If a pitch movement occurs early in the interval where it accents a syllable, an accent lent by a rise is perceived as a high accent, while an accent lent by a fall is perceived as a low accent. If the pitch movement occurs late in the interval where it accents a syllable, a rise induces a low accent, while the fall induces a high accent. The location in the syllable where this transition occurs will be referred to as *high–low boundary*. This was examined both for the rise, where indeed the percept changes from high to low, and for the fall, where the percept actually changes from low to high.

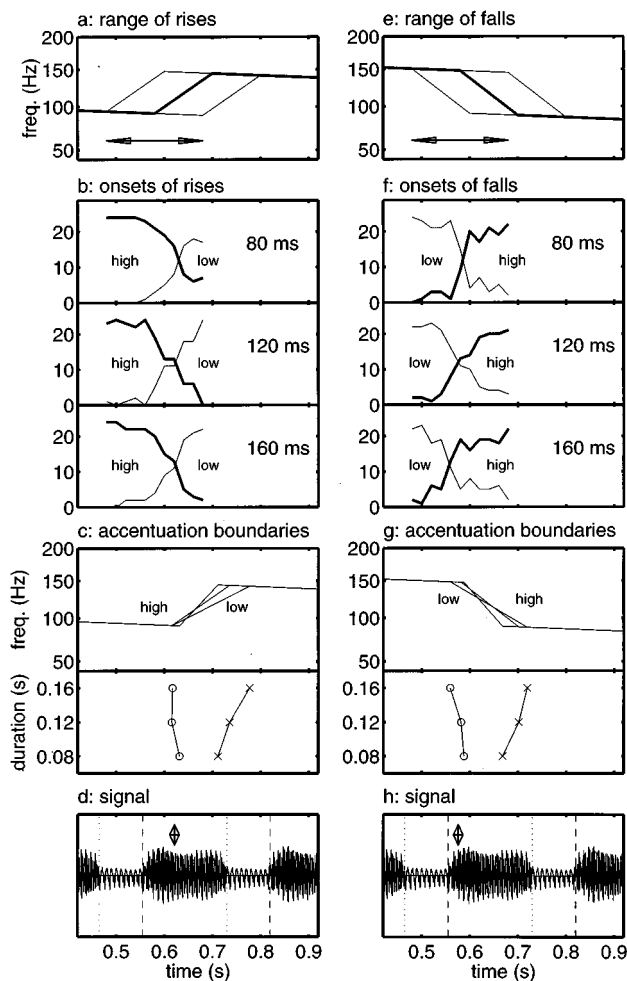


FIG. 8. Determination of the high–low boundary of the third syllable of the /mamamama/ stimulus. The stimulus range comprised those positions in which the third syllable is perceived as accented. For the 120-ms rise, this range is presented in panel (a), and for the 120-ms fall in panel (e). Distributions of the onset times of the pitch movements lending a high or a low accent to the third syllable are presented in panel (b) and (f). In (c) and (g), the pitch movements are presented at the high–low boundary as determined on the basis of the onset distributions. The two lowest panels present the oscillogram of the /mamamama/ stimulus monotonized at 100 Hz. The diamonds are the average of the onsets of the three pitch movements of different duration at the high–low boundary.

The aim of this experiment was to find out whether the timing of the onset or the offset of the pitch movement provided the cue for the perceptual distinction between the high and the low accent. The rationale was the same as that of Experiment I.

A. Method

1. Stimuli

The stimuli consisted of a restricted set of the stimuli used in Experiment I. The location of the onsets of the pitch movements ranged from 480–680 ms after the physical start of the utterance. This range, shown for the pitch movement of 120 ms in Fig. 8(a) and (e), was chosen in such a way that in almost all cases an accent was perceived on the third syllable. For some of the earliest pitch movements some subjects indicated having perceived an accent on the second syllable. Subjects were explicitly asked to concentrate on the

third syllable and indicate whether they perceived a high or a low third syllable. The interval between the elements of the continuum was 20 ms, so there were 11 rises, just as there were 11 falls. There were rises and falls of three durations: 80, 120, and 160 ms, resulting in 66 different stimuli.

2. Subjects and procedure

The same 11 subjects took part as in the previous two experiments. Their task now was not to indicate on which syllable they perceived an accent, but to indicate whether they heard a high or a low accent. The series of 66 stimuli was presented twice in the same random order. Each time, this series of 66 stimuli was preceded by 12 practice stimuli approximately covering the range of the stimuli used. During the presentation of these practice stimuli, subjects had the opportunity to adjust the volume of the stimuli to a comfortable loudness level.

B. Results and discussion

The results are shown in Fig. 8. As in the previous task, the boundary between the categories was quite well defined, showing that the subjects were capable of doing the task. The onset distributions of the accent-lending pitch movements are presented in Fig. 8(b) for the rises, and in Fig. 8(f) for the falls. The pitch movements at the high–low boundary as determined by the onset distributions are presented in Fig. 8(c) and (g). Just as for the accentuation boundary, it appears that the onset of the pitch movements at the high–low boundary shifted somewhat to the left, while the offset shifted to the right. This shows that here, too, the location of the onset of the movement determined whether a high or low accent was perceived.

In the previous experiments concerned with the accentuation boundary, these boundaries were at about the same position in the syllable for both the rises and the falls. The high–low boundaries for the rises, however, appeared to be later than those for the falls. The average of the onsets of the three rises is indicated with a diamond in Fig. 8(d); that of the onsets of the three falls in Fig. 8(h). The onsets of the falls at the high–low boundary were located some 20 ms after the vowel onset; those of the rises 45 ms later, some 65 ms after the vowel onset. Based on some comments by subjects, and by informal listening, the possibility was considered that this may be attributed to a systematic bias to identify an accent lent by rise with a high accent and an accent lent by fall with a low accent. Especially in the neighborhood of the high–low boundary the listener will hesitate between indicating a high or a low accent. As a consequence, the effect of this bias on the listener will be strong especially in this neighborhood. Hence, if, in this transition region, accents lent by rises are systematically indicated as high accents, the high–low boundary for the rise will show a bias to the right. If, similarly, in the neighborhood of the high–low boundary accents lent by falls are systematically indicated as low accents, the high–low boundary for the fall will also show a bias to the right. Hence, the difference between the high–low boundary of the rise and the fall cannot be explained by such a bias if this bias is equal for the rise and the

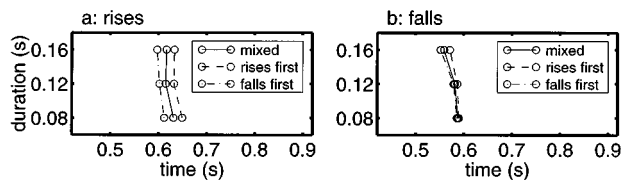


FIG. 9. Onsets of the pitch movements at the high-low boundary of the third syllable of the /mamamama/ stimulus under various experimental conditions. The stimulus range comprised those positions in which the third syllable is perceived as accented.

fall. Since the high-low boundary for the rise comes later than that of the fall, the bias should be larger for the rise than for the fall. It was felt that this bias may have been introduced by mixing the stimuli with the rises and the falls within one experimental session.

IV. EXPERIMENT IIIb

This experiment examined whether mixing stimuli with rises and falls within one experimental session might have introduced a systematic bias on the part of the subjects to classify an accent lent by a rise as a high accent and an accent lent by a fall as a low accent. Therefore, the same stimuli were presented, but this time rises and falls were presented in separate sessions.

A. Method

1. Stimuli

The stimuli presented in this experiment were exactly the same as in the previous experiment. There were 33 rises and these were presented twice in one experimental session. There were 33 falls, also presented twice, now presented in a separate session. So, the stimulus set of the rises and that of the falls both contained 66 stimuli. Within the set of rises the presentation of the stimuli was random, just as in the set of falls. The session with the rises was preceded by 12 practice stimuli approximately covering the range of the stimuli, all consisting of rises. The session with the falls was also preceded by 12 practice stimuli approximately covering the range of this set of stimuli, all consisting of falls.

2. Subjects and procedure

Twelve subjects participated, none of whom participated in the previous experiment. For six subjects, the stimulus set with the rises was presented first, while for the other six subjects the set with falls was presented first. Their task was again to indicate whether they heard a high or a low accent.

B. Results and discussion

The results are presented in Fig. 9, along with the results from the earlier experiment. The onset times of the rises at the high-low boundary are presented in Fig. 9(a), those for the falls in Fig. 9(b). It can be seen that, relative to the mixed experimental condition, the high-low boundary for the rises is about 35 ms later when the session with the rises is presented first, and that it is about 35 ms earlier when the falls are presented first. The size of the effect is about as large for the rises of 80, 120, and 160 ms. For the falls, the accentua-

tion boundary hardly changes with experimental condition. This shows that confusion of rises with high accents is a stronger effect than confusion of falls with low accents. It is, however, difficult to decide whether the effects are significant. If they are, and if indeed the difference in the high-low boundary between rises and falls is a consequence of an asymmetrical bias to classify accents lent by rises as high accents and accents lent by falls as low accents, it is difficult to explain why this effect is larger for the subjects who first carried out the session with the rises. Perhaps the session with the falls made the subjects aware of the relevant perceptual difference in this task, thereby avoiding the confusion of a high accent with an accent lent by a rise in the following experimental sessions. No other explanation could be found.

Observe furthermore that in all three conditions, the high-low boundary still comes later for the rises than for the falls. Whether this residual difference is still due to this confusion of high accents with accents lent by rises or is systematic is discussed later on.

What is not problematic is the conclusion that the location of the onset of the pitch movement determines whether a high or a low accent is perceived, just as it determines which syllable is perceived as accented. The timing of the offset is irrelevant.

V. GENERAL DISCUSSION

A. Large effects

The main conclusion of these experiments is that both the cue that determines which syllable is perceived as accented and the cue indicating whether a low or a high accent is perceived are located at the onset of the pitch movement. In all the results, the position of the onsets of the pitch movements at the category boundaries remain about constant or shift somewhat to the left as the pitch movement becomes longer. The offsets of the pitch movements at the category boundaries shift to the right. This situation was sketched in Fig. 1(a) and (b). This virtually excludes the possibility that the location of the offset of the pitch movement provides the cue for accentuation and the high-low distinction between accents. (In principle, it is still possible that a pattern recognition process in which the offset is taken into account plays a role. However, this would then require a complicated look-ahead strategy involving a delay of at least some 80 ms.)

The second important conclusion from these experiments, though less definite and in need of further experimentation, is concerned with the location of the category boundaries within the utterance. Based on the results described in this paper and on a review of the literature, it is argued that the temporal relation between the onset of the pitch movement and the perceptual moments of occurrence of the syllables, the so-called P-centers (Morton *et al.*, 1976), determines whether the pitch movement accents the syllable and what kind of accent is perceived.

The P-center is closely related to the vowel onset of a syllable, though three phenomena show that the P-center and the vowel onset cannot be identified with each other. The first two phenomena have to do with the relation of the

P-center with the segmental structure of the syllable (Marcus, 1981). First, as the consonant cluster preceding the vowel has a longer duration, the P-center comes earlier with respect to the vowel onset. Second, as the syllable rhyme, i.e., that part of the syllable which follows the vowel onset, has a longer duration, the P-center comes later with respect to the vowel onset. The third phenomenon is that the P-center depends on the kind of pitch movement realized on the syllable. Janker and Pompino-Marschall (1991) found a difference in P-center location of Thai words with a falling lexical tone and words with a rising lexical tone. The first of these phenomena will be linked with the shift to the left with respect to the vowel onset as the /m/'s become longer. The third will be linked with the difference in the high–low boundary of falls and rises as found in experiment III.

The accentuation boundaries as found for the syllables with /m/'s of different durations are located at 65 ms before the vowel onset for the stimuli with an /m/ halved in duration, at 90 ms for the stimuli with an /m/ of original duration, and at 110 ms for the stimuli with an /m/ doubled in duration. These shifts were unexpected, but they are exactly in the range of shifts in the perceptual center (P-center) found when varying the duration of the syllable onset (Marcus, 1981). Pompino-Marschall (1989) varied the duration of the /m/ in the syllable /ma/ and found about the same kind of shift as found in this study.

The category boundary of the high–low distinction for the fall is located 20 ms after the vowel onset. For the rise, this boundary is located 35–60 ms later, depending on the experimental context. If the experimental sessions with the falls preceded those with the rises, the difference between the high–low boundaries for the rises and the falls is smaller than when rises and falls are mixed within a session, and when the sessions with the rises are presented before those with the falls. So far there is no good explanation for this. Based on the results of experiment IIIb, it is suggested that listeners have a tendency to identify accents lent by rises with high accents. This may not, however, explain everything. Moreover, in this respect there is also a clear correspondence with results found for P-centers. This also relates to the finding by Janker and Pompino-Marschall (1991) of a difference in the P-center of Thai words with a falling lexical tone and words with a rising lexical tone. These rising and falling tones are both late in the syllable, so the correspondence between these results and those described here is remarkable. It is felt that these issues need further experimentation. As a last remark, it is tempting to identify the timing of the onset of the pitch movements found in this study with the timing of the “start of the accent command” in Fujisaki’s two-component theory of intonation (Fujisaki and Hirose, 1984; Fujisaki, 1993).

It is interesting to compare these conclusions with results obtained by House (1990). He found that sensitivity for pitch changes is reduced in speech segments of significant spectral change. Naturally, the vowel onset, or its presumed perceptual correlate, the P-center, lends itself preeminently to the timing of syllable events. If it is assumed that, some tens of milliseconds before the P-center, sensitivity to pitch change is reduced, we must conclude that for early rises and

falls, where the onset of the movement is located in this interval of reduced sensitivity, a jump to a pitch level different from what is expected on the basis of only declination will be perceived. So it will be this jump which induces the percept of accentuation. Still following House (1990), if the change in the course of pitch occurs after the vowel onset, so after the interval of reduced sensitivity to pitch change, we naturally perceive the change itself which then provides the listener with the cue for accentuation.

In summary, it now appears that two different mechanisms can induce the percept of an accent. If the change in pitch occurs at a location such as the P-center of the syllable where we are not very sensitive, the percept of a jump in pitch in the following vowel induces the accent. If the change in pitch takes place at a location where it is readily perceived, the pitch change itself induces the accent.

B. Small effects

The onsets of the pitch movements at the accentuation boundaries most often show a small shift to the left as the pitch movements become longer. This shift shows that the interval between the onset of the pitch movement and the moment after this onset at which the listener decides that an accent-lending change in the course of pitch has occurred, is longer for the longer pitch movements. This can be explained quite naturally, because, the excursion sizes of the different pitch movements being equal, the slope of the shorter pitch movements is differs more from the slope of declination than from the slope of the longer pitch movements. So, the change in the course of pitch is more abrupt for the shorter pitch movements. Therefore, the integration time of the perceptual process which decides whether an accent-lending change in the course of pitch has taken place is up to 40 ms longer for the longer pitch movements. What cannot be explained is that for the rises this shift is generally less than for the falls. Inspecting the data shows that for the rises this shift varies between –6 and 26 ms, and for the falls between 24 and 42 ms. Why this shift with longer pitch movement duration is in general a bit larger for the falls than for the rises still remains unclear. In general, the change in the slope of the pitch contour is more abrupt for the rise than for the fall, as a consequence of the falling declination. This should be coupled with a later category boundary for all falls, however, and cannot in itself explain why the shift with duration of the pitch movement is larger for the falls than for the rises.

C. Relation with previous studies

As mentioned in the Introduction, only a few previous studies have been carried out on the accentuation boundaries between two syllables. The oldest one is the study by Van Katwijk and Govaert (1967), who also varied the position of a rising or a falling pitch movement. Their first conclusion was that the rise was more effective in accenting a syllable than a fall. This conclusion is not clearly substantiated by the results obtained here, but this can be explained by the different experimental setup used by Van Katwijk and Govaert. First, the declination in their experiments was almost twice

as strong as the declination used in the experiments described here. The consequence of this is that the contrast in slope between declination and accent-lending fall becomes less. In addition, as the authors write, an utterance with such a strong declination starts so high that the subjects may perceive a “virtual rise” at the start. This virtual rise is a natural filling up of the so-called “hat pattern,” a sequence of a rise and a fall, which is very common in Dutch intonation. Furthermore, in a pilot experiment preceding the experiments described here (Hermes, 1995), it also appeared that for the /mamamamama/ stimuli used here, subjects most often indicated the first syllable as accented in the absence of any pitch movement besides declination.

The second conclusion by Van Katwijk and Govaert was that pitch falls exert their prominence lending force later than pitch rises. This cannot be explained by these differences in experimental setup. If, due to the strong falling declination, the fall becomes less conspicuous, the time to perceive the change in the course of pitch should be longer for the fall than for the rise. However, if this is the case, the accentuation boundary of the falls should be earlier than that of the rises. The easiest solution is then to attribute the difference to the bad synthesis quality of the stimuli used by Van Katwijk and Govaert. This may have interrupted the natural temporal relations of the vowel and the noise parts of the stimuli, but it is felt that here, too, more experimentation with syllables with fricative consonants as used by Van Katwijk and Govaert are needed.

Collier (1970) carried out an experiment in which he asked subjects to position an accent-lending rise in an utterance at the point where it lent optimum prominence to a specified syllable. He concluded that “subjects tend to relate its position to the vowel onset and not to the beginning of the syllable” (p. 83), and “The comparison of the location of pitch rises of different lengths is preferably made by considering the position of their tops” (p. 84). This last conclusion was also based on the observation in a pilot experiment that the distribution of the onsets of the pitch movements showed a much greater spread than the distribution of their peaks. This might seem contradictory to our results, but it follows from the different task of Collier’s subjects. He asked subjects to adjust the timing of the pitch movement in such a way that it lent optimal prominence to a specified syllable. This may amount to adjusting the timing of the pitch movement in such a way that the peak of the rise fell in the vowel. For the longer rises, this may have the consequence that their starts were located in the vowel of the previous syllable and, as Collier mentions, “the preceding syllable might become slightly stressed, thus weakening the optimal stress impression on the next, indicated one” (p. 84). Thus, Collier observed that in the adjusted position of the longer pitch movements the accent could shift to the previous syllable.

This, of course, raises the important issue of the relation between prominence, a gradual property of the syllable, and accentuation, a binary property of the syllable. Furthermore, the fact that a pitch movement may not lend an accent at all has been ignored. The experiment was deliberately carried out with /mamamamama/ stimuli in which the middle three syllables were identical in all respects except for the pitch

movement realized on them. In the original three-syllable utterance the middle syllable carried an accent, and, consequently, had the temporal and loudness properties of a stressed syllable (Sluijter, 1995). As has been argued (Hermes, 1995), in the absence of a clear accenting cue, the first syllable is mostly indicated as accented. Since this is not observed in the experiments reported here, all pitch movements used apparently lent an accent.

The results reported here may contradict results found by Hasegawa and Hata (1992). They used a three-syllable utterance /mamama/, which was provided with a pitch contour consisting of a gradual rise up to the vowel of the second syllable, an accent-lending fall starting within the vowel and a more gradual declination up to the end of the utterance. They concluded that the second syllable was only perceived as accented when the accenting fall started after the vowel onset. The main difference with our stimuli was that the first syllable had a gradually rising pitch contour, which in itself might have been a cue for an accent on the first syllable. Furthermore, if subjects have to choose between the first and the second syllable, they may have shown a bias for the first.

Some more literature is available on the high–low distinction between pitch accents. The results described in Experiment III corroborate a finding obtained by Bruce (1977) for Swedish word accents. In one of Bruce’s experiments, he varied the timing of a fall in such a way that somewhere between the two extremes of the continuum, the word accent and with it the meaning of the utterance changed. The duration of the fall varied between 40, 60, and 80 ms. He asked subjects to indicate what they heard. Bruce also found that the onset of the falls at the category boundary between the two Swedish word accents shifted to the left as the pitch movement became longer. The durations used by Bruce, 40, 60, and 80 ms, were smaller than the durations used here, 80, 120, and 160 ms, but they all agree in the sense that the perceptual decision was apparently taken between 20–50 ms after the onset of the pitch movement, and that this period was shorter for more rapid pitch movements. Bruce also found that the location of the category boundary was in the neighborhood of the vowel onset. For Swedish word accents, this boundary separates acute accent I, in the terms of this paper a fall lending a low accent, and the grave accent II, in the terms of this paper a fall lending a high accent. This conclusion by Bruce must perhaps be modified somewhat on the basis of results from Engstrand (1995). After analyzing a limited set of production data, Engstrand concludes that “one—and probably *the*—positive requirement on the word accent contrast is an F_0 fall on the primary stressed vowel in grave words. If the acute accent is at all associated with some such positive requirements, it remains to be specified” (p. 178). Translated into the results of this study, he explains that the grave accent II in Swedish is positively characterized as a late fall within the primary stressed vowel, while the acute accent I does not show this characteristic.

As to the difference between rises lending a high accent and rises lending a low accent, the results described in this paper are in agreement with the results found by Hill and Reid (1977) for British subjects. As described in the Introduction, they found that the boundary between the two cat-

egories was approximately at the vowel onset.

Van Dommelen (1995) found that, in Norwegian, the fall, in contrast to the rise, brought about a perceptual lengthening of the vowel of almost 20 ms. In fact, another interpretation would be that in the stimulus with the fall the P-center is about 20 ms earlier. If the perceived start of a vowel occurs at the P-center, the fall will last longer by the same amount as the P-center starts earlier. What is still unexplained is that Van Dommelen did not find the same lengthening of the vowel containing a fall in German syllables presented in sentence context.

More results on the category boundary between high and low accents, as lent by falls for Dutch, are provided by Gussenhoven and Rietveld (1992/1993). They showed that the boundary between these two categories is not exactly the vowel onset, but depends on the segmental structure of the onset and the rhyme of the syllable. They reported not to have found a direct relation with the P-center as determined by the algorithm by Pompino-Marschall (1989, 1991). These P-centers were not determined by a perception experiment, however, and inspection of their results shows that the locations of the category boundaries shifted in the same way with different syllable onsets as P-centers.

In most of the literature described, only separate rises or separate falls were taken into account. In many languages, an accent can also be lent by a combination of a rise and a fall, the rise–fall. At least in Dutch intonation, the location of these rise–falls is such that the rise starts about 50 ms before the vowel onset, while the fall starts about 80 ms after the vowel onset. The results of this study have been argued to indicate that an accent can be induced by two different mechanisms, a jump to a new pitch level in the syllable nucleus, and a change in pitch within the syllable nucleus. In terms of the results of this paper, this shows that rise–falls contain both cues for accentuation. The position of the rise effects that, in the following nucleus, a jump in pitch is perceived which induces a high accent in that syllable, while the onset of the fall within the syllable nucleus is also a cue for a high accent on this syllable. This may explain why the rise–fall is an effective cue for accentuation. In Hungarian the situation is more complicated. In this language, the timing of the accent-lending rise–fall on the last accented syllable determines whether a question or a statement is perceived (Gósy and Terken, 1994). The interpretation of these results in terms of the results described here is complicated by the presence of two movements. The same complication in this respect applies to results presented for German by Kohler (1991).

D. Conclusions

Combining all the evidence, it now appears that the moment at which the change in the course of pitch at the onset of a pitch movement is perceived determines which syllable is perceived as accented. If this moment occurs some tens of milliseconds before the P-center of the syllable, the syllable preceding the syllable with this P-center is perceived as accented. When it comes later, the syllable with this P-center itself is perceived as accented. If the change in the course of pitch at the onset of the pitch movement occurs before or at

the P-center, a high accent is perceived for the rise and a low accent for the fall. If the change in the course of pitch at the onset of the pitch movement occurs after the P-center, a low accent is perceived for the rise and a high accent for the fall.

Combined with the results obtained by House (1990), it is suggested that the perception of a pitch accent can arise from two different mechanisms. In the first, the perception of a *change in the course of pitch* at the onset of the pitch movement induces the perception of an accent. In the second, the perception of an accent is brought about by a *pitch level jump* between syllable nuclei. The perception of a pitch change gives rise to the perception of an accent on the syllable with the rhyme in which the pitch change is perceived. For a rise this induces a low accent, while for the fall it is high. If a pitch jump is perceived, the latter of the two syllables between which the jump takes place is perceived as accented. In this case the rise induces a high accent, while the fall induces a low accent.

ACKNOWLEDGMENTS

I would like to thank Jacques Terken, Frédéric Beau-gendre, and Marc Swerts for their critical reading of previous versions of this manuscript. I would also like to thank Jacques Terken for his suggestion for the third experiment to ask subjects to indicate whether they heard a high or a low accent, and David House for correcting my original view on Experiment IIIb.

- Beckman, M. E., and Pierrehumbert, J. B. (1986). "Intonational structure in Japanese and English," *Phonol. Yearbook* **3**, 255–309.
- Bruce, G. (1977). *Swedish word accents in sentence perspective* (Gleerup, Lund, Sweden).
- Caspers, J., and Van Heuven, V. J. (1993). "Perception of low-anchoring versus high-anchoring of Dutch accent-lending pitch rises," in *Proceedings of the European Speech Communication Association (ESCA) Workshop on Prosody*, 27–29 September 1993, Lund, Sweden, pp. 188–191.
- Collier, R. (1970). "The optimum position of prominence lending pitch rises," *IPO Annu. Progr. Rep.* **5**, 82–85.
- Engstrand, O. (1995). "Phonetic interpretation of the word accent contrast in Swedish," *Phonetica* **52**, 171–179.
- Fujisaki, H. (1993). "Dynamic characteristics of voice fundamental frequency in speech and singing," in *The production of speech*, edited by P. F. MacNeilage (Springer-Verlag, New York), pp. 39–55.
- Fujisaki, H., and Hirose, K. (1984). "Analysis of voice fundamental frequency contours for declarative sentences of Japanese," *J. Acoust. Soc. Jpn.* **5**, 233–242.
- Glasberg, B. R., and Moore, B. C. J. (1990). "Derivation of auditory filter shapes from notched-noise data," *Hearing Res.* **47**, 103–138.
- Gósy, M., and Terken, J. (1994). "Question marking in Hungarian: timing and height of pitch peaks," *J. Phonet.* **22**, 269–281.
- Gussenhoven, C., and Rietveld, T. (1992/1993). "The influence of syllable composition on the alignment of pitch targets," *Proc. Dept. Lang. Speech* **16/17**, 91–95.
- Hamon, C., Moulines, E., and Charpentier, F. (1989). "A diphone synthesis system based on time-domain prosodic modification of speech," in *Proceedings of the IEEE International Conference on Acoustics Speech and Signal Processing (ICASSP-89)*, pp. 238–241.
- Hasegawa, Y., and Hata, K. (1992). "Fundamental frequency as an acoustic cue to accent perception," *Lang. Speech* **35**, 87–98.
- Hermes, D. J. (1995). "Timing of pitch movements and accentuation of syllables," *IPO Ann. Progr. Rep.* **30**, 38–44.
- Hermes, D. J., and Van Gestel, J. C. (1991). "The frequency scale of speech intonation," *J. Acoust. Soc. Am.* **90**, 97–102.
- Hill, D. R., and Reid, N. A. (1977). "An experiment on the perception of intonation features," *Int. J. Man-Machine Studies* **9**, 337–347.
- House, D. (1990). *Tonal perception in speech* (Lund U.P., Lund, Sweden).

- Janker, P. M., and Pompino-Marschall, B. (1991). "Is the P-center position influenced by 'tone'?", in *Proceedings of the International Congress of Phonetic Sciences*, 1991, Aix-en-Provence, France, pp. 290–293.
- Kohler, K. J. (1991). "Prosody in speech synthesis: the interplay between basic research and TTS application," *J. Phonet.* **19**, 121–138.
- Marcus, S. M. (1981). "Acoustic determinants of perceptual center (P-center) location," *Percept. Psychophys.* **30**, 247–256.
- Morton, J., Marcus, S. M., and Frankish, C. R. (1976). "Perceptual centers (P-centers)," *Psychol. Rev.* **83**, 405–408.
- Pierrehumbert, J. (1980). "The phonology and phonetics of English intonation," Ph.D. dissertation, Massachusetts Institute of Technology, Cambridge, MA.
- Pompino-Marschall, B. (1989). "On the psychoacoustic nature of the P-center phenomenon," *J. Phonet.* **17**, 175–192.
- Pompino-Marschall, B. (1991). "The syllable as a prosodic unit and the so-called P-centre effect," *Forsch. Instit. Phonet. Sprachliche Kommun. Univ. München* **29**, 65–123.
- Sluijter, A. (1995). "Phonetic correlates of stress and accent," Ph.D. dissertation, Leiden University, Leiden, Holland.
- 't Hart, J., Collier, R., and Cohen, A. (1990). *A perceptual study of intonation: An experimental-phonetic approach to speech melody* (Cambridge U.P., Cambridge).
- Van Dommelen, W. A. (1995). "Interactions of fundamental frequency contour and perceived duration in Norwegian," *Phonetica* **52**, 180–187.
- Van Katwijk, A., and Govaert, G. A. (1967). "Prominence as a function of the location of pitch movement," *IPO Annu. Prog. Rep.* **2**, 115–117.
- Van Santen, J. P. H. (1995). "Template based speech timing," in *Proceedings of the ATR International Workshop on Computational modeling of prosody for spontaneous speech processing*, Kyoto, Japan, 12–14 April 1995, pp. 3–9–3–19.

Speech intelligibility as a function of the number of channels of stimulation for signal processors using sine-wave and noise-band outputs

Michael F. Dorman^{a)}

Department of Speech and Hearing Science, Arizona State University, Tempe, Arizona 85287-0102 and
University of Utah Health Sciences Center, Salt Lake City, Utah 84132

Philipos C. Loizou^{b)}

Department of Applied Science, University of Arkansas at Little Rock, Little Rock, Arkansas 72204-1099

Dawne Rainey

Arizona State University, Tempe, Arizona 85287-0102

(Received 12 August 1996; revised 17 June 1997; accepted 26 June 1997)

Vowels, consonants, and sentences were processed through software emulations of cochlear-implant signal processors with 2–9 output channels. The signals were then presented, as either the sum of sine waves at the center of the channels or as the sum of noise bands the width of the channels, to normal-hearing listeners for identification. The results indicate, as previous investigations have suggested, that high levels of speech understanding can be obtained using signal processors with a small number of channels. The number of channels needed for high levels of performance varied with the nature of the test material. For the most difficult material—vowels produced by men, women, and girls—no statistically significant differences in performance were observed when the number of channels was increased beyond 8. For the least difficult material—sentences—no statistically significant differences in performance were observed when the number of channels was increased beyond 5. The nature of the output signal, noise bands or sine waves, made only a small difference in performance. The mechanism mediating the high levels of speech recognition achieved with only few channels of stimulation may be the same one that mediates the recognition of signals produced by speakers with a high fundamental frequency, i.e., the levels of adjacent channels are used to determine the frequency of the input signal. The results of an experiment in which frequency information was altered but temporal information was not altered indicates that vowel recognition is based on information in the frequency domain even when the number of channels of stimulation is small. © 1997 Acoustical Society of America. [S0001-4966(97)04010-1]

PACS numbers: 43.71.Es, 43.71.Ky, 43.66.Ts [WS]

INTRODUCTION

Shannon *et al.* (1995) have reported nearly perfect scores on tests of speech recognition (vowels in /hVd/ context, consonants in /vCv/ context and sentences) when temporal information in the signals is preserved and spectral information is reduced to three or four bands of noise. This outcome is surprising from the point of view that vowel and consonant identity is specified by the location of formant frequencies and that small differences in formant frequencies can lead to changes in phonetic identity. For example, the formant frequencies of vowels can differ by as little as 100–200 Hz (Peterson and Barney, 1952) and 300–400 Hz differences in the onset frequency of the second-formant transition are sufficient to signal consonant place-of-articulation (/b d g/) in synthetic, two-formant syllables (Cooper *et al.*, 1952). These small, but critical, differences in formant frequencies would fall within a band of a 3- or 4-channel processor and, thus, would not be available to a listener for use in phonetic identification.

The Shannon *et al.* (1995) outcome is less surprising

from the view that for each segmental phone there are multiple cues to identity. In addition to cues in the time domain, which are known to provide some information about vowel identity (House, 1961) and considerable information about consonant voicing (e.g., Liberman *et al.*, 1958) and consonant manner (e.g., Liberman *et al.*, 1956), there are cues in the frequency domain which are relatively wide band, e.g., the burst spectra of stop consonants and the noise spectra of fricative consonants. These cues may be represented adequately with only a few channels of stimulation. Other factors may also enhance intelligibility when speech is presented via a few channels. A small number of items in the test set (e.g., 8 vowels and 16 consonants) would contribute to high levels of performance. In tests of sentence intelligibility, “top down” processing, or the use of multiple levels of linguistic knowledge, would aid subjects in word identification even if phonetic information was reduced, because of very poor frequency resolution, to only broad phonetic categories (see, for example, Zue, 1985).

Our interest in Shannon *et al.* (1995) stems from our experience with cochlear implant patients who use 4- and 6-channel signal processors. When individual channels are stimulated the patients report, most generally, that the signals

^{a)}Electronic mail: mdorman@imap2.asu.edu

^{b)}Electronic mail: loizou@ualr.edu

sound like “beep tones” and not like bands of noise. This observation led us to wonder about the intelligibility of speech, for normal-hearing listeners, when the speech is processed through a signal processor which outputs a sine wave at the center of each frequency band instead of a band of noise. Previous research with speech coding systems which resynthesized speech as the summation of the sine wave outputs of fixed channels suggest an asymptote in speech recognition with six to ten channels of stimulation (e.g., Hill *et al.*, 1968). This is approximately twice as many channels as Shannon *et al.* (1995) found to be necessary. The difference in the number of channels is striking and led us to investigate how the Shannon *et al.* (1995) processing scheme and a similar processing scheme using sine waves would compare when tested with the same materials. Thus, in experiment 1 we compared the intelligibility of vowels, consonants, and sentences when transmitted by a processor which output bands of noise, as in Shannon *et al.* (1995), and when transmitted by a processor which output sine waves at the center frequencies of the filters.

Shannon *et al.* (1995) interpreted their results as indicating that speech recognition, in the context of greatly reduced spectral information, can be achieved with primarily temporal cues. In experiment 2 we tested this hypothesis with the vowels used in experiment 1.

Consider the information available to a listener about vowel identity when signals are resynthesized as the summation of, for example, four bands of noise. The relative amplitudes of the noise bands indicates the approximate locations of the formants. Thus, the relative amplitudes across channels provide information, albeit very crude information, in the frequency domain. Temporal information is limited to a binary distinction along a continuum of vowel length, i.e., long versus short vowels. Now consider an experiment in which signal length is left unchanged, so short vowels are “short” and long vowels are “long”, but in which the amplitudes of the four noise bands are inverted. That is, the output of channel 1 is directed to channel 4, the output of channel 4 is directed to channel 1, the output of channel 3 is directed to channel 2, and the output of channel 2 is directed to channel 3. If temporal information is central to vowel recognition, then, in the situation just described, vowel recognition ought to be little changed since the temporal information was left unchanged. If, however, vowel recognition is based primarily on information in the frequency domain, then recognition ought to be very poor. In experiment 2 the outcome of such an experiment is reported.

I. EXPERIMENT 1

A. Method

1. Subjects

The subjects were eight young adults (all female, age range 22–31 years, mean=25 years) and one 63-year-old female.¹ All of the subjects passed a hearing screening at 25 dB HL for frequencies of 0.5, 1, 2, and 4 kHz.

TABLE I. Channel center frequencies for signal processors with 2–9 channels.

No. of channels	Channel								
	1	2	3	4	5	6	7	8	9
2	792	3392							
3	545	1438	3793						
4	460	953	1971	4078					
5	418	748	1339	2396	4287				
6	393	639	1037	1685	2736	4443			
7	377	572	866	1312	1988	3013	4565		
8	366	526	757	1089	1566	2252	3241	4662	
9	357	493	682	942	1301	1798	2484	3431	4740

2. Speech materials

Three tests of vowel recognition were used. One was the vowel test employed by Shannon *et al.* (1995)—the Iowa vowel test which used 8 vowels from a single male speaker (Tyler *et al.*, 1989). The second test was composed of 13 synthetic vowels in /bVt/ format (see Dorman *et al.*, 1989). These stimuli were used because the vowels were of equal duration and had identical pitch contour. Thus, temporal cues were not a factor in identification. The third test was composed of 11 vowels in the words “heed, hid, hayed, head, had, hod, hud, hood, hoed, who’d, heard,” each produced by three men, three women, and three girls. The stimuli were drawn from a set used by Hillenbrand *et al.* (1995).

The consonant test was the Iowa constant test—16 consonants in /aCa/ environment spoken by a single male speaker (Tyler *et al.*, 1986). This was the consonant test used by Shannon *et al.* (1995). The sentence material was from the H.I.N.T. test presented without competing noise (Nilsson *et al.*, 1994). Examples of sentences in this test are, “They met some friends at dinner,” “Yesterday he lost his hat,” “She spoke to her eldest son,” and “She is washing her new silk dress.”

All of the test materials were stored on computer disk and were output via custom software routines using MATLAB software and a 16-bit D/A converter.

3. Signal processing

The noise-band processor was implemented in the following manner. The signal was first processed through a pre-emphasis filter (low-pass below 1200 Hz, -6 dB per octave) and then bandpassed into N logarithmic frequency bands (where N varied from 2 to 9) using sixth-order Butterworth filters. The filter center frequencies and bandwidths, at 3 dB down from the passband level, are shown in Tables I and II. The envelope of the signal was extracted by half-wave rectification and low-pass filtering (second-order Butterworth) with a 160-Hz cutoff frequency. The envelope of each frequency band was used to modulate white noise, which was bandlimited with the same Butterworth bandpass filters. The noise-modulated envelopes of each band were finally combined, low-pass filtered (using sixth-order elliptic filters with 50-dB attenuation) at 5 kHz, and presented to the listeners at a comfortable level through headphones (Sennheiser HMD 410).

TABLE II. Channel bandwidths for signal processors with 2–9 channels.

No. of channels	Channel								
	1	2	3	4	5	6	7	8	9
2	984	4215							
3	491	1295	3414						
4	321	664	1373	2842					
5	237	423	758	1356	2426				
6	187	304	493	801	1301	2113			
7	154	234	355	538	814	1234	1870		
8	131	189	272	391	563	810	1165	1676	
9	114	158	218	302	417	576	796	1099	1519

Our implementation of a noise-band processor differed from that of Shannon *et al.* (1995) in several ways. In Shannon *et al.* (1995) the filters overlapped at -15 dB instead of at -3 dB as in the present experiment. In Shannon *et al.* (1995) filter 1 and filter 2 overlapped at 800 Hz, filters 2 and 3 overlapped at 1500 Hz, and filters 3 and 4 overlapped at 2500 Hz.

The sine-wave processor was implemented as follows. The signal was first processed through a preemphasis filter (low-pass below 1200 Hz, -6 dB per octave) and then band-passed into N logarithmic frequency bands (where N varied from 2 to 9) using sixth-order Butterworth filters (see Tables I and II). The envelope of the signal was extracted by full-wave rectification, and low-pass filtering (second-order Butterworth) with a 400-Hz cutoff frequency. [We used a 400-Hz cutoff frequency to conform to the cutoff frequency used in the Med El Corporation's cochlear-implant signal processor. Shannon *et al.* (1995) found no difference in performance for lowpass filters set at 160 Hz and above.] Sinusoids were generated with amplitudes equal to the root-mean-square (rms) energy of the envelopes (computed every 4 ms) and frequencies equal to the center frequencies of the bandpass filters. The sinusoids of each band were finally summed and presented to the listeners at a comfortable level.

4. Procedures

For the Iowa consonant, Iowa vowel, and synthetic vowel test sequences, five tokens of each stimulus were created. The stimuli were grouped into five blocks with each stimulus appearing once in a block. Stimulus order within each block was randomized. In the multitalker vowel test sequence, each stimulus appeared once. The stimuli were completely randomized. Ten sentences from the H.I.N.T. sentence lists were presented in each channel condition. Each ten-sentence list contained approximately 52 words. Different sentence lists were used for each condition. The sentence tests were conducted in open set format.

The tests were run in the order vowels (Iowa, synthetic, multitalker), consonants, and sentences. This test order was used because it was the order in which the stimulus materials became available for testing. After the experiment described here was conducted, we tested, in another experiment, other subjects with the consonant, multitalker vowel, and sentence material. In this experiment the order of tests was randomized. The mean scores were within 7 percentage points of the

mean scores in this report. For this reason we believe that the test order did not have a significant effect on performance.

For each type of material subjects were given practice before the test sequence began. Practice consisted of two repetitions of the test items with visual indication of item identity followed by a randomized sequence of stimuli with feedback of correct answers. Practice was given before each processor by channel-number condition. The test sessions were run in the order 9-channel processor to 2-channel processor, sequentially. For each type of material half of the patients were tested first with the noise-band processor and half were tested first with the sine-wave processor.

We chose a sequential test order starting with the largest number of channels, rather than a randomized test order, for two reasons. First, a completely randomized design would have required a heroic number of subjects. Second, we wanted to give the subjects time to adapt to the novel stimulation. There is, undoubtedly, a "warm up" effect for listening to altered speech signals of any kind. This effect was offset, to some degree, by our use of a sequential, rather than randomized, test order and by our familiarization procedure before each test condition. It is likely the case that *absolutely naive* subjects would not perform as well as the subjects in our experiments.

Responses were collected with custom software using a computer display of response alternatives (except for the sentence material) and a mouse as a response key. The subjects were allowed to use a "repeat" key during the consonant and vowel tests as many times as they wished. For the tests of word intelligibility in sentences the subjects were presented a sentence once, and were instructed to repeat as many of the words as they could. Each word in the sentence was scored.

B. Results

The results for vowel, consonant, and sentence identification are shown in Fig. 1, panels A–E. For the Iowa vowels a repeated measures analysis of variance indicated a main effect for channels ($F[7,56]=74.2$, $p<0.0001$) but no main effect for processors ($F[1,8]=0.004$, $p=0.85$). *Post hoc* tests according to Scheffe ($\alpha=0.05$) indicated no statistically significant differences in performance when the number of channels was increased beyond 6.² For the synthetic vowels a repeated measures analysis of variance indicated a main effect for channels ($F[7,56]=208.8$, $p<0.0001$) but no main effect for processors ($F[1,8]=3.05$, $p=0.12$). *Post hoc* tests according to Scheffe indicated no statistically significant differences in performance when the number of channels was increased beyond 8. For the multitalker vowels a repeated measures analysis of variance indicated a main effect for channels ($F[7,56]=330.3$, $p<0.0001$), a main effect for processors ($F[1,8]=8.98$, $p=0.02$), and a processor by channels interaction ($F[7,56]=4.88$, $p=0.0002$). The sine-wave processor produced slightly higher mean scores with 3–9 channels of stimulation. The largest difference between processors occurred with 7, 8, and 9 channels of stimulation. *Post hoc* tests according to Scheffe indicated no statistically significant differences in performance when the number of channels was increased beyond 8.

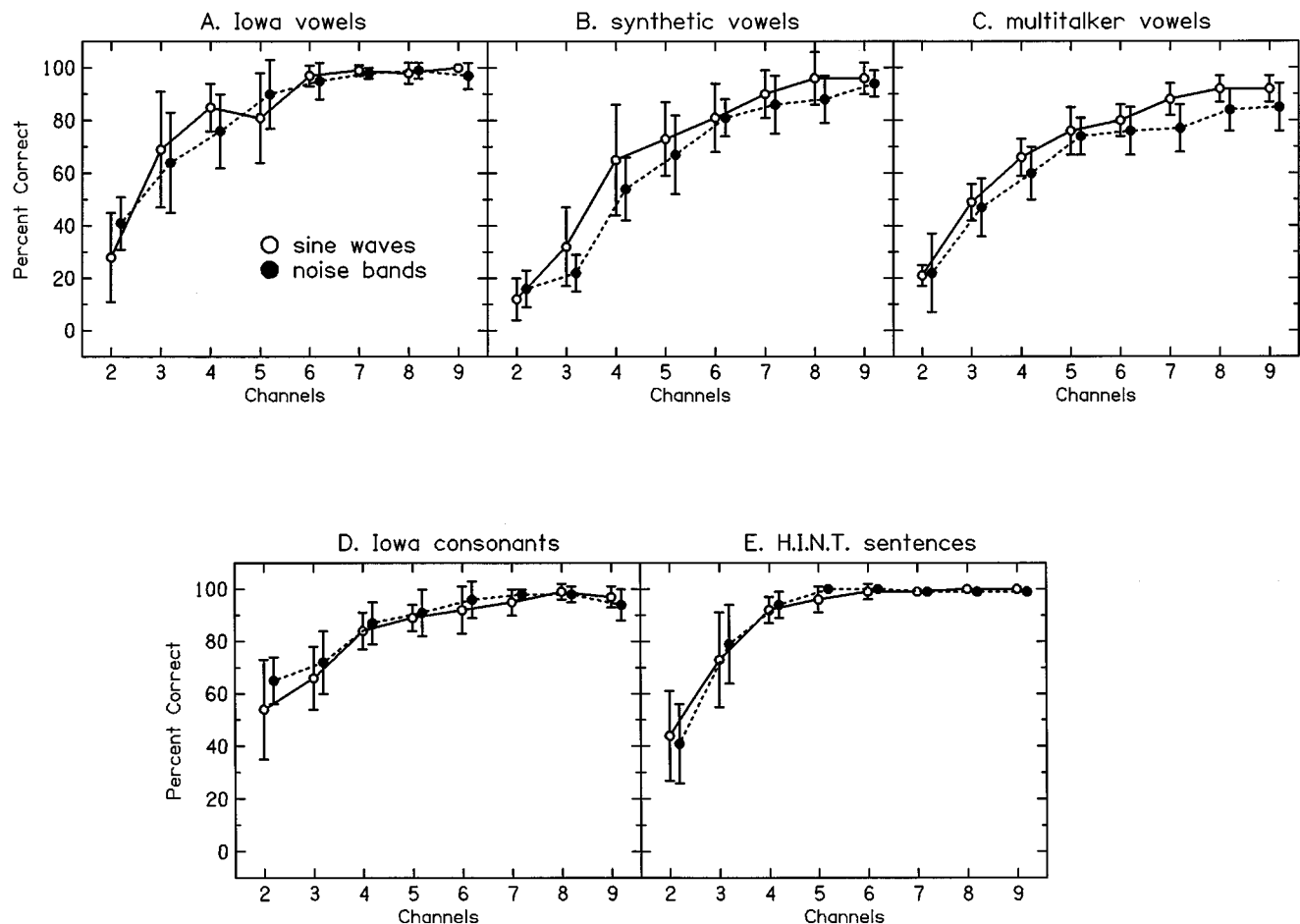


FIG. 1. Percent correct as a function of the number of channels of stimulation for vowels, consonants, and sentences. The parameter is processor type: sine-wave output (open circles) or noise-band output (filled circles). Error bars indicate ± 1 standard deviation.

For the Iowa consonants a repeated measures analysis of variance indicated a main effect for channels ($F[7,56] = 130.9$, $p < 0.0001$) but no main effect for processors ($F[1,8] = 3.26$, $p = 0.11$). *Post hoc* tests according to Scheffe indicated no statistically significant differences in performance when the number of channels was increased beyond 6.

The results of feature analyses for the consonants are shown in Fig. 2. For the feature “place of articulation” a repeated measures analysis of variance indicated a main effect for channels ($F[7,56] = 87.21$, $p < 0.0001$) and a main effect for processors (noise band = 76% correct and sine wave = 70% correct; $F[1,8] = 8.37$, $p = 0.02$). *Post hoc* tests according to Scheffe indicated no statistically significant differences in performance when the number of channels was increased beyond 6. The reduction in mean score with 9 channels relative to 8 channels for the noise-band processor was the result of a single subject’s low score in the 9-channel condition. This, most likely, reflects a warm-up effect as the 9-channel condition was always run first. For the feature “voicing” a repeated measures analysis of variance indicated a main effect for channels ($F[7,56] = 6.89$, $p < 0.0001$) but no main effect for processors ($F[1,8] = 0.01$, $p = 0.91$). *Post hoc* tests according to Scheffe indicated no statistically significant differences in performance

when the number of channels was increased beyond 3. Analysis of the data for the feature “manner” was complicated by a decrease in performance with 3 channels of stimulation for the noise-band processor. With the exception of this point, scores were 90% correct or better for 2–9 channels of stimulation for both processors. The dip in performance at three channels for the noise-band processor was due to errors on the nasal consonants which were identified as the semivowel /l/. This outcome appears to be an oddity of the cutoff frequencies for the three-channel condition because nasal manner was well identified with both fewer channels and a greater number of channels.

For the H.I.N.T. sentences a repeated measures analysis of variance indicated a main effect for channels ($F[7,56] = 80.1$, $p < 0.0001$) but no main effect for processors ($F[1,8] = 0.16$, $p = 0.91$). *Post hoc* tests according to Scheffe indicate no statistically significant differences in performance when the number of channels was increased beyond 5.

C. Discussion

The first issue to be considered is whether the Shannon *et al.* (1995) data are replicable. Our results indicate that they are. Our 4-channel, noise-band processor allowed intelligi-

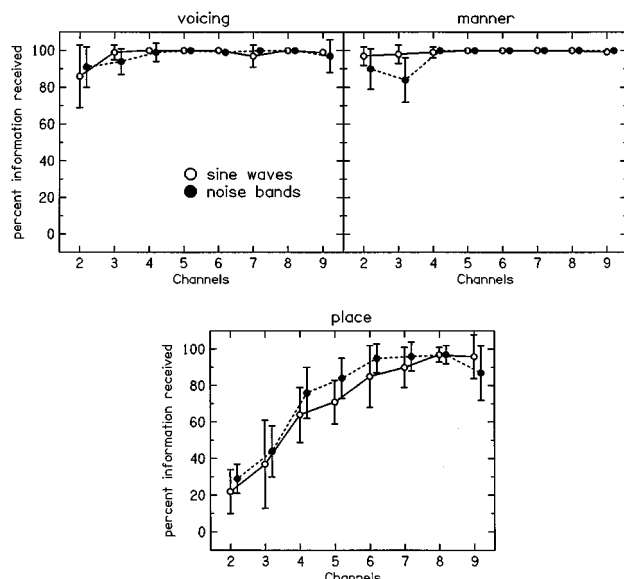


FIG. 2. Percent information received for the features “voicing,” “manner,” and “place” as a function of the number of channels of stimulation. The stimulus material was 16 consonants in “aCa” environment. Error bars indicate ± 1 standard deviation.

bility scores of 87% for consonants, with 76% correct for place, and 94% correct for sentences. Shannon *et al.* (1995) report approximately 90% for consonants, with 65% for place, and 95% correct for sentences. However, our 4-channel, noise-band processor allowed only 76% correct for the Iowa vowels while Shannon *et al.* (1995) report a mean of approximately 95%. Two factors may have contributed to the difference in outcome. One factor is practice. Shannon *et al.* (1995) allowed his subjects 8–10 hours of practice before testing began. Our subjects had less practice. A second factor is the configuration of the filters. The filters in the present experiment had different corner frequencies from those in Shannon *et al.* (1995) and were chosen so that similar logarithmic spacing could be employed with any number of channels. In addition, our filters were broadband, while Shannon’s filters were narrowband with small overlap between adjacent filters. Given the different results of the present experiment and Shannon *et al.* (1995) for the Iowa vowels, filter spacing deserves study in the design of signal processors with a small number of channels.

The second issue to be considered is whether the sine-wave processor and the noise-band processor produced different results. Different results were expected given the different stimulation along the cochlear partition produced by the two processors and given the results of Shannon *et al.* (1995), on the one hand, and Hill *et al.* (1968), on the other. However, differences in mean performance between the two processors were generally small and nonsignificant. Visual inspection of Fig. 1 indicates that the noise-band processor consistently allowed slightly lower vowel recognition scores than those allowed by the sine-wave processor. For one type of material—multitalker vowels—the scores were significantly lower. On the other hand, the noise-band processor allowed slightly, but significantly, higher scores for the feature place of articulation. The small disadvantage accruing to

the noise-band processor for vowels may have been due to the loss of frequency specific information within the noise-bands (see the discussion below). The same mechanism could mediate the *better* performance of the noise-band processor for consonant place of articulation. That is to say, energy distributed over the width of a band is more appropriate for many place cues than energy concentrated in a very narrow frequency region.

The third issue to be considered is how many channels are necessary to approach optimum performance with fixed-channel signal processors. The number of channels varies with test material. For material such as sentences, in which multiple levels of linguistic or “top-down” knowledge can be used, 5 channels allowed essentially 100% accuracy. For other material, such as multitalker vowels, or synthetic vowels, which needed fine-grained acoustic or “bottom-up” analyses, asymptotic performance was reached with 8 channels. It is possible, of course, that performance would reach asymptote at a larger number of channels if subjects were tested with more difficult materials, e.g., words with unreleased final stops.

If the present data with normal-hearing listeners can be extrapolated to cochlear implant patients, then it would be useful if signal processors for cochlear implants had 8 channels. More channels would not add greatly to intelligibility (at least in quiet) and fewer channels would detract from fine-grained acoustic analysis, although sentence understanding would not suffer with 5 channels, or even 4 channels, of stimulation.

The fourth issue to be considered is how information in the frequency domain is coded by processors which do not track formant frequencies. It is possible that the auditory system views the channels of fixed-channel processors in the same manner as harmonics of a high-pitched glottal source and derives an estimate of formant frequency from the amplitudes of adjacent channels in the same manner as formant frequencies are estimated from the amplitudes of adjacent harmonics of the glottal source. In the instance of normal speech signals with a high fundamental frequency, the location of formant peaks cannot be completely dependent on the location of the highest amplitude harmonics in the spectrum because the harmonics are too far apart. The relatively small difference limens for formant frequencies (e.g., 12 Hz at 550 Hz) indicates that the relative amplitudes of harmonics around a formant peak are used in the estimate of formant frequency (e.g., Sommers and Kewley-Port, 1996). Consider now the channel outputs in Fig. 3 for the 8-channel, sine-wave processor which allowed asymptotic performance for the multitalker vowel set. (For these plots the channel outputs were normalized into a 15-dB range. This allowed a common y axis for all of the plots in this figure and in Fig. 4). The formant frequencies of the vowels are indicated by the solid triangles. The formant frequencies are well represented by the relative amplitudes of the channels to the either side of the channels with the highest amplitude. For example, the low F_1 of /i/ is coded by a high-amplitude channel 1 and a low-amplitude channel 2. The higher frequency F_1 of /t/ is coded by a high-amplitude channel 1 and a similar amplitude for channel 2. For /ε/ F_1 is higher still and now channel 2 is

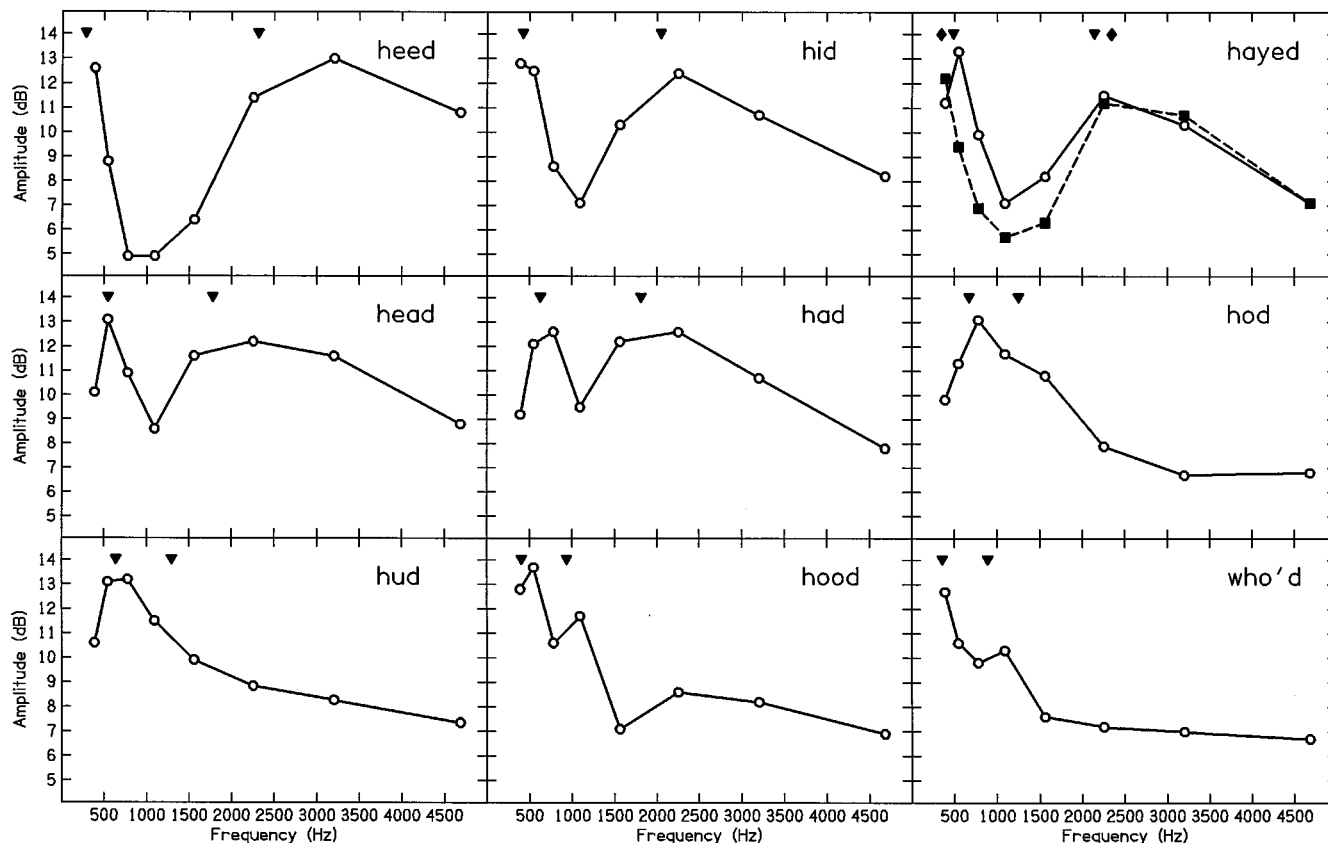


FIG. 3. Signal amplitude as a function of channel number for nine vowels produced by male speakers. The filled triangles and diamonds indicate the formant frequencies of the signal derived from 22nd-order LPC analyses. For “hayed” two sets of channel outputs are displayed. One was taken during the on-glide (open circles) and one (filled squares) was taken during the off-glide of the diphthong.

the highest amplitude channel. Finally, the high $F1$ of /æ/ is coded by high amplitudes in channels 2 and 3. Note also how the downward shift in frequency of $F1$ over the course of /e/ is coded by the change in the relative amplitudes of the first two channels. The location of $F2$ is coded in the same fashion as $F1$. For the high $F2$ in /i/ channel 7 has the highest amplitude. $F2$ is lower in /ɪ/ and channel 6 has the highest amplitude. $F2$ is lower still in /ε/ and channels 5 and 6 have similar amplitudes. The very low $F2$ of /u/ is coded by high amplitude in channel 4.

Not all vowels were coded by two peaks, corresponding to two formants, in the 8-channel outputs. Only one peak is present for “hod” and “hud.” It is not surprising that these vowels were well identified, in spite of the single peak, since experiments dating to Delattre *et al.* (1952) have shown that vowels with $F1$ and $F2$ close together in frequency space can be synthesized with a single formant.

As the number of channels is reduced, the definition of spectral peaks in the channel outputs is, of course, reduced. This is illustrated in Fig. 4 which shows the channel outputs for the vowels in “hid,” “head,” and “had” for processors with 8, 6, and 4 channels. As noted previously, 8 channels provide good resolution of the formant peaks, if we assume that the levels in adjacent channels are used in the estimation of formant frequency. For the 6-channel processor the relative amplitudes of the channels continue to provide a good estimate of formant frequencies and the mean score for mul-

titalker vowels remains high (80% correct). When the number of channels is reduced to 4, the output patterns look very different than those for 6 and 8 channels. However, adjacent channels, e.g., channels 1 and 2, continue to provide information about the relative frequencies of the input signal. Thus, the low $F1$ of /ɪ/ is coded by a large difference in signal level between channels 1 and 2. The higher $F1$ in /ε/ is coded by a smaller difference between channels 1 and 2. The still higher $F1$ of /æ/ is coded by a slightly higher signal level in channel 2 than channel 1. These differences, although not as visually salient as those for the 6- and 8-channel conditions, appear to be used by listeners since the mean score for the 4-channel condition was 66% correct. In this instance, e.g., for discriminating between /ɪ/ and /ε/, vowel length may be especially useful.

II. EXPERIMENT 2

The aim of experiment 2 was to test the hypothesis that vowel recognition, in the condition of a small number of channels of stimulation, is based primarily on temporal cues. As noted in the Introduction, the temporal cue to vowel identity is vowel length. In the experiment which follows the identification of three sets of vowels (Iowa vowels, synthetic vowels, and multitalker vowels) was assessed in a condition of “normal” 4-channel stimulation and in a condition in which vowel length was left unchanged but the signal level

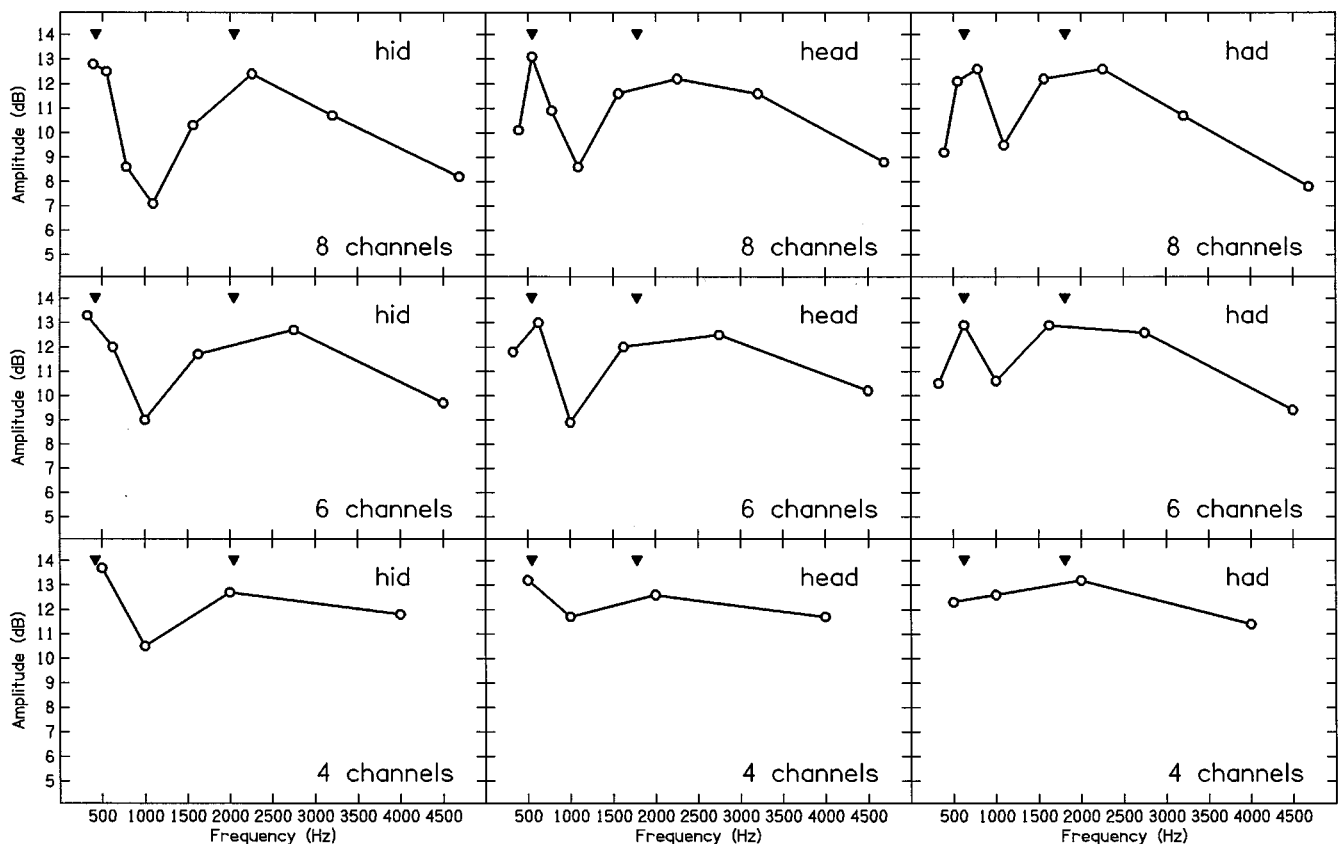


FIG. 4. Signal amplitude as a function of channel number for the vowels in “hid,” “head,” and “had.” In each column the output of processors with 8, 6, and 4 channels is shown. The stimuli were tokens of vowels produced by male speakers.

in each channel was altered. In the latter condition temporal information was normal but the information which specified frequency (the relative levels of the channels) was altered. If vowel recognition is determined primarily by temporal cues, then the altered stimuli should be well identified. If, however, vowel recognition is determined principally by information in the frequency domain, then the altered stimuli should not be well identified.

A. Method

1. Subjects

Eight subjects participated in the tests with the Iowa vowels and synthetic vowels. Six of the eight participated in the test with the multitalker vowels. The number of subjects varied solely as a function of availability for testing. All of the subjects had participated in experiment 1.

2. Speech materials

The three tests of vowel recognition used in experiment 1 were used in this experiment.

3. Signal processing

All stimuli were first processed through the 4-channel, noise-band processor described in experiment 1. To create stimuli with an altered representation of frequency the energy level of channel 1 was mapped onto channel 4, the energy level of channel 2 was mapped on channel 3, the

level of channel 3 was mapped onto channel 2, and the level of channel 4 was mapped onto channel 1. Vowel length was left unchanged.

4. Procedures

Following testing with the materials in experiment 1 the subjects were tested with the frequency altered stimuli. The patients were given the familiarization and practice with the altered 4-channel stimuli in the manner of the “normal” stimuli described in experiment 1. In the test sequence only the frequency-altered stimuli were presented. The order of testing for the Iowa vowels, the synthetic vowels and the multitalker vowels varied among the subjects in quasi-random fashion. Since all subjects had participated in experiment 1 the scores from that condition were used for the “normal” 4-channel scores.

Responses were collected in the same manner as in experiment 1.

B. Results and discussion

The averaged identification scores for the Iowa vowels, synthetic vowels, and multitalker vowels in the normal and frequency-altered stimulus conditions are shown in Fig. 5. For the Iowa vowels the mean score for the normal 4-channel stimuli was 76% correct. The mean score for the altered vowels was 35% correct. The two scores differed significantly [$t(7) = 6.8, p < 0.0002$]. For the synthetic vowels the mean score for the normal 4-channel stimuli was 54% cor-

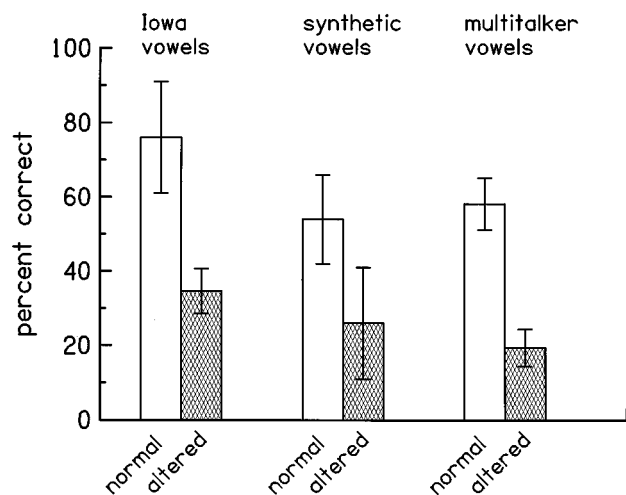


FIG. 5. Percent correct identification as a function of stimulus condition (normal or frequency altered) for three sets of 4-channel, noise-band vowels. The error bars indicate ± 1 standard deviation.

rect. The mean score for the altered vowels was 26% correct. The two scores differed significantly [$t(7) = 4.75$, $p < 0.001$]. For the multitalker vowels the mean score for the normal 4-channel stimuli was 58% correct. The mean score for the altered vowels was 19% correct. The two scores differed significantly [$t(5) = 9.71$, $p < 0.0006$]. Overall, our result, i.e., the significant and large drop in performance when frequency information was altered, suggests that information in the frequency domain is the principal factor determining the identification of vowels when vowels are processed and presented through a small number of channels. We suspect that this conclusion extends also to the identification of consonants. It is reasonable to suppose that the amplitude envelope in a channel specifies *when* energy is *where* in frequency space and it is the frequency domain information, *no matter how sparse*, on which the recognition routines for speech operate. There is no reason to believe that the nature of the recognition process changes in a fundamental fashion when the number of channels of stimulation becomes small. From this point of view, interest in the results of Shannon *et al.* (1995) and Hill *et al.* (1968) stems from a consideration of how sparse the representation of frequency can be and still support high levels of speech recognition.

In the forgoing discussion we have used the term “temporal cue” in the fashion commonly used to describe the acoustic cues for vowel and consonant identification, i.e., a portion of an acoustic signal which, when varied in duration, alters phonetic identification. However, the term “temporal cue” could also be used in another sense. As noted above, when speech signals are reduced to a small number of bands, the amplitude envelope in a channel specifies *when* energy is *where* in frequency space. The within- and across-channel changes in amplitudes over time specify changes in formant frequencies and, thus, are “temporal cues” for speech recognition.

III. CONCLUSIONS

The results of the present investigation indicate, as previous investigations have suggested, that high levels of

speech understanding can be obtained using signal processors with a small number of channels. The nature of the output signal, noise bands or sine waves, makes only a small difference in performance. The number of channels needed for high levels of performance varies with the nature of the test material. For the most difficult material—vowels produced by men, women and girls—8 channels were necessary to approach asymptotic performance. For the least difficult material—sentences—5 channels were sufficient. We suggest that the mechanism mediating the high levels of speech recognition achieved with only few channels of stimulation is the same one that mediates the recognition of signals produced by speakers with a high fundamental frequency, i.e., signal levels in adjacent channels are used to estimate the frequency of the input signal. Finally, our results suggest that vowel recognition is based principally on information in the frequency domain even when the number of channels of stimulation is small.

ACKNOWLEDGMENTS

This research was supported by NIDCD RO1 000654-6. We thank Jim Hillenbrand for permission to use the multitalker vowel materials and thank Michael Nilsson for permission to use the H.I.N.T. sentences. John Wygonski of the House Ear Institute graciously provided information about the implementation of the noise-band processor used in Shannon *et al.* (1995). A comment by Dr. Sid Bacon motivated experiment 2.

¹The 63-year-old subject performed as well as the younger subjects.

²A reviewer has pointed out that a conservative *post hoc* test would require that two mean scores be very different to find a difference between means. This would work against finding differences between mean scores when the number of channels is fairly large because performance is near asymptote. This, in turn, would lead to a conclusion of fewer, rather than more, channels being needed to achieve high levels of speech identification. The Scheffe test was chosen because it controls the experimentwise, or overall, error rate. Another option would be to use a *post hoc* test that uses an error rate that is comparisonwise. To see if this option would make a difference in outcome, we reran the *post hoc* tests with Fisher's LSD—a comparisonwise test. While there were some differences in outcome, there were no differences which affected the issue of asymptote.

- Cooper, F., Delattre, P., Liberman, A., Borst, J., and Gerstman, L. (1952). “Some experiments on the perception of synthetic speech,” *J. Acoust. Soc. Am.* **24**, 597–606.
- Delattre, P., Liberman, A., Cooper, F., and Gerstman, L. (1952). “An experimental study of the acoustic determinants of vowel color: Observations on one- and two-formant vowels synthesized from spectrographic patterns,” *Word* **8**, 195–210.
- Dorman, M., Dankowski, K., McCandless, G., and Smith, L. (1989). “Identification of synthetic vowels by patients using the Symbion multichannel cochlear implant,” *Ear Hear.* **10**, 40–43.
- Hill, J., McRae, P., and McClellan, R. (1968). “Speech recognition as a function of channel capacity in a discrete set of channels,” *J. Acoust. Soc. Am.* **44**, 13–18.
- Hillenbrand, J., Getty, L., Clark, M., and Wheeler, K. (1995). “Acoustic characteristics of American English vowels,” *J. Acoust. Soc. Am.* **97**, 3099–3111.
- House, A. (1961). “On vowel duration in English,” *J. Acoust. Soc. Am.* **33**, 1174–1178.

- Lieberman, A., Delattre, P., and Cooper, F. (1958). "Some rules for the distinction between voiced and voiceless stops in initial position," *Lang. Speech* **1**, 153–167.
- Lieberman, A., Delattre, P., Gerstman, L., and Cooper, F. (1956). "Tempo of frequency change as a cue for distinguishing classes of speech sounds," *J. Exp. Psychol.* **52**, 127–137.
- Nilsson, M., Soli, S., and Sullivan, J. (1994). "Development of the Hearing in Noise Test for the measurement of speech reception thresholds in quiet and noise," *J. Acoust. Soc. Am.* **95**, 1085–1099.
- Peterson, G., and Barney, H. (1954). "Control methods used in a study of vowels," *J. Acoust. Soc. Am.* **24**, 175–184.
- Shannon, R., Zeng, F.-G., Kamath, V., Wygonski, J., and Ekelid, M. (1995). "Speech recognition with primarily temporal cues," *Science* **270**, 303–304.
- Sommers, M., and Kewley-Port, D. (1996). "Modeling formant frequency discrimination of female vowels," *J. Acoust. Soc. Am.* **99**, 3770–3781.
- Tyler, R., Preece, J., and Tye-Murray, N. (1986). "The Iowa audiovisual speech perception laser videodisc," *Laser Videodisc and Laboratory Report*, Department of Otolaryngology, Head and Neck Surgery, University of Iowa Hospital and Clinics, Iowa City, IA.
- Zue, V. (1985). "The use of speech knowledge in automatic speech recognition," *Proc. IEEE* **73**, 1602–1615.

Development and evaluation of a German sentence test for objective and subjective speech intelligibility assessment

Birger Kollmeier^{a)} and Matthias Wesselkamp^{b)}

AG Medizinische Physik, Universität Oldenburg, D-26111 Oldenburg, Germany

(Received 26 July 1996; revised 7 April 1997; accepted 3 June 1997)

A German sentence test was developed which is comprised of 20 test lists of ten sentences each. The test corpus is a selection from sentences for speech quality evaluation recorded with a male unschooled speaker. Performance-intensity curves were measured for each individual sentence in a speech-simulating babble noise with a total of 40 normal-hearing listeners. Based on these data and the phonemic transcription of the 200 sentences selected from the underlying speech corpus, 20 test lists were composed using a numerical optimization process. These 20 test lists are highly equivalent with respect to their performance-intensity curves, the number of words within each test list, the number of phonemes within each test list, and approximately the frequency distribution of the phonemes which approximates the phoneme frequency distribution of the German language. The equivalence of the respective performance-intensity curves was demonstrated in an independent experiment with 20 normal-hearing listeners. In addition, a comparison was performed between the "objective" intelligibility measurements and two "subjective" speech intelligibility rating methods employing the same materials. As a result, both subjective assessment procedures correlate highly with each other and with the "objective" procedure across sentences. This underlines the applicability and validity of the test in combination with time-saving subjective assessment methods. Moreover, the variability in performance across different sentences correlates inversely with the RMS level of the respective sentence. This indicates that an adjustment of sentence material with respect to RMS level already yields reasonably homogeneous test material with respect to intelligibility. © 1997 Acoustical Society of America. [S0001-4966(97)00810-2]

PACS numbers: 43.71.Gv, 43.71.Es, 43.66.Sr [WS]

INTRODUCTION

The assessment of speech intelligibility plays an important role in a variety of areas such as, e.g., telecommunication, room acoustics, audiology, and evaluation of hearing aids. Although a variety of test materials and test methods has been developed and used so far (cf. Bosman, 1989; Kollmeier, 1990 for a review), the use of sentence materials for these purposes has many advantages over other materials. For instance, the understanding of a whole sentence appears to be more representative for a realistic communication situation than the intelligibility of a single word or phoneme. Moreover, the discrimination functions (i.e., the intelligibility as a function of speech level or signal-to-noise ratio, respectively, which is often referred to as performance-intensity curve) are steeper for sentence materials than for shorter speech segments and thus provide a very accurate measurement of a speech reception threshold, i.e., the speech level that corresponds to 50% intelligibility. Although some disadvantages occur (e.g., no possibility to test the same sentence twice with the same subject, higher weighting of low-frequency components versus high-frequency components in the speech spectrum as compared to monosyllables, no possibility to perform the test without an instructor), a variety of sentence intelligibility tests have been described in the literature so far. Plomp and Mimpfen (1979) developed a sentence

test for the Dutch language by first evaluating the intelligibility of all sentences at an intermediate speech level. For the composition of the actual test lists they only employed those sentences that yielded an intelligibility close to the average intelligibility of all sentences. Thus, a high homogeneity of the sentences both within each test list and across all test lists was achieved. A similar approach was employed for the hearing-in-noise test (HINT, Nilsson *et al.*, 1994).

The standardized procedure for the German language uses the "Marburger Satztest" (Niemeyer, 1967). It consists of ten test lists with ten sentences that are each phonemically balanced. However, the semantic construction is partially unusual and incomplete which has resulted in a relatively poor acceptance of this test in the German language. Moreover, the standardized recording of the sentence test by a schooled speaker is overarticulated and does not reflect an everyday communication situation. The test lists yield approximately the same intelligibility in quiet. However, the equivalence of the test lists and the homogeneity of the sentence intelligibility in noise was not considered when constructing the test. Recently, several speech intelligibility tests employing sentence materials were adopted into the German language. They are based on the minimum auditory capability test battery (Owens *et al.*, 1985; Dillier and Spillmann, 1992) or the speech-intelligibility-in-noise test (SPIN, Kalikow *et al.*, 1977; Tschopp and Ingold, 1992). These tests concentrate on certain aspects of speech intelligibility rather than total speech intelligibility. Moreover, all of the tests described so far employ scoring for correctly repeated phonemes, syl-

^{a)}Corresponding author.

^{b)}Present address: Siemens Audiologische Technik GmbH, Gebbertstr. 125, D-91058 Erlangen, Germany.

lables, words, or whole sentences. None of these tests employed subjective rating or subjective adjustment of intelligibility, although such methods provide considerable advantages over classical intelligibility scoring tests (Cox *et al.*, 1991; Peissig and Kollmeier, 1997). Thus, a new sentence test was developed for the German language which might be used both for sentence scoring methods and for subjective intelligibility ratings (Wesselkamp *et al.*, 1992). The development of this test is described in the next section, and the evaluation of the test material and its application to subjective speech intelligibility rating methods is described in the subsequent sections.

I. DEVELOPMENT OF THE SENTENCE TEST

A. Speech material

The underlying speech corpus consists of 400 sentences with three to seven words each that were recorded with a male unschooled speaker and were digitized by the German Telekom as part of the sentence materials used for quality evaluation of speech communication channels (Sotscheck, 1984). This inventory comprised the 100 sentences from the Marburger sentence test (Niemeyer, 1967), 100 sentences originally developed to supplement the Marburger sentences and 200 additional sentences that have not been published yet. From this basic inventory, syntactically incomplete sentences (“kein gutes Wetter, wenig Gäste”—“no good weather, few guests”) or sentences with an ambiguous articulation (“wird’s” instead of “wird es”) were removed as well as sentences with a content related to preceding or subsequent sentences within the test material. In addition, sentences were removed that showed a nonacceptable or obsolete content (e.g., “Jungen lieben Streit, Mädchen Eintracht”—“Boys love dispute, girls harmony”). The remaining 324 sentences were segmented and the resulting RMS-level of each single sentence as well as of the complete speech material was calculated. The average RMS level was -26.5 dB (respective digital maximal output) with a standard deviation of 2 dB. In addition, the actually recorded test sentences were phonemically transcribed.

B. Determination of the sentence-specific discrimination functions

For each of the 324 sentences, the discrimination function was measured, i.e., the number of correctly repeated words divided by the total number of words in the sentence as a function of the signal-to-noise ratio. For these purposes, the results from a total of 40 audiometrically normal listeners aged between 19 and 31 years were averaged for each signal-to-noise ratio and each sentence.

1. Apparatus

A computer-controlled speech audiometry workstation was employed which was developed within a German joint research project on speech audiometry (Kollmeier *et al.*, 1992). A PC 386 personal computer with a coprocessor board (Ariel DSP 32C) with 16-bit stereo AD-DA converters was used to control the complete experiment as well as stimulus presentation and recording of the subjects' re-

sponses. The stimulus levels were adjusted by a computer-controlled custom-designed audiometer comprising attenuators, anti-aliasing filters, and headphone amplifiers. Signals were presented monaurally to the subjects with a Beyer DT 48 headphones without free-field equalization. The subjects were situated in a sound-insulated booth. Their task was to orally repeat each sentence presented over headphone as closely as possible.¹ The instructor, also situated in the booth in front of the subject, marked each incorrectly repeated word. For this purpose, an Epson EHT 10S handheld computer was used with a LCD-touchscreen on which the target sentence was displayed. It was connected to the personal computer via serial interface. The exact test outcome (i.e., each correctly identified word for each subject) was stored by the computer for later statistical analysis.

2. Test material

The digitized sentences were stored on the hard disk of the computer. In addition, a speech-simulating continuous noise was stored digitally which is also available on Compact Disc and has been employed for a variety of speech tests (Kollmeier *et al.*, 1988). This noise was generated by statistically superimposing all words of a monosyllabic rhyme test produced by the same speaker. Thus, the long-term spectrum of the sentence material is very similar to the noise spectrum. Test sentence and noise were added digitally at a predefined signal-to-noise ratio and converted to analog (16 bits, 25-kHz sampling frequency, 10-kHz anti-aliasing low-pass filter). The noise was presented at a level of 65 dB SPL. The signal level varied according to the respective signal-to-noise ratio.

3. Measurement procedure

In a pilot experiment with four listeners, the signal-to-noise ratio (SNR) was determined which yields an average total intelligibility of the speech material of 50%. In the first experiment, sentence intelligibility was measured with twelve subjects with all 324 sentences at this signal-to-noise ratio. Based on these results, all sentences were grouped into six sets that only comprised sentences with approximately the same intelligibility at this SNR. Subsequently, a second experiment was performed with a different group of 12 subjects for all 324 sentences. The signal-to-noise ratio was selected for each set of sentences such that a two-point estimate of the discrimination function could be obtained from the results of the first two experiments. In a third experiment, another group of twelve subjects measured the intelligibility of all 324 sentences. In order to obtain a valid three-point estimate of the sentence-specific discrimination function, the SNR for the third experiment was determined such that for each set of sentences all three measurement points sample the region between 20% and 80% sentence intelligibility. During all experiments, each respective sentence was only presented once to each subject. A sentence-specific discrimination function with a logistic shape was fitted to the data as follows:

$$P(L)_{\text{sent.}} = \frac{100}{1 + \exp(-(L - L_{50, \text{sent.}})/s)} \quad (1)$$

The parameter $L_{50,\text{sent.}}$ denotes the level corresponding to 50% intelligibility for each respective sentence and s denotes the spread of the discrimination function which is inversely proportional to the slope m of the discrimination function ($s=25/m$). Due to the careful selection of the 3 SNR to be tested for each of the six sets of sentences, a reliable fit of the discrimination function could be obtained for all sentences.

4. Derivation of weighting factors

In order to reduce the inhomogeneities in the test material that might occur due to the varying intelligibility of different words within each sentence, weighting factors were derived for each word within each sentence. “Simple” words (i.e., words with an intelligibility higher than the average of the sentence) should have a lower weight than more “difficult” words. The word-specific weighting factor was derived at the sentence-specific $L_{50,\text{sent.}}$. This was achieved by fitting a word-specific discrimination function to each word of each sentence in the same way as the discrimination function that was fitted to the results of the complete sentence. If the discrimination function for the i th word in the respective sentence is denoted with $P(L)_{\text{word}(i)}$, then the corresponding correction factor k_i is computed as

$$k_i = \begin{cases} 5/7, & \text{for } P(L_{50,\text{sent.}})_{\text{word}(i)} > 70\%, \\ 0.5, & \text{for } 30\% \leq P(L_{50,\text{sent.}})_{\text{word}(i)} \leq 70\%, \\ 5/3, & \text{for } P(L_{50,\text{sent.}})_{\text{word}(i)} < 30\%. \end{cases} \quad (2)$$

By limiting the value of the correction factors, extreme values were avoided that might lead to the score of a single word dominating the score of a whole sentence. The factors k_i were normalized within each sentence to give a sum of 1, i.e.,

$$k'_i = \frac{k_i}{\sum_{j=1}^n k_j}, \quad (3)$$

where k'_i denotes the normalized factor and n denotes the number of words within the respective sentence. With the weighting factors thus obtained, the intelligibility score S of the sentence is calculated as

$$S = \frac{1}{n} \sum_{i=1}^n k'_i \tau_i, \quad (4)$$

where $\tau_i = 1$ if word i was correctly repeated and $\tau_i = 0$ otherwise.

The level-dependent intelligibility scores of the test sentences were recalculated using the word weighting factors k'_i and Eq. (4). For all sentences a strictly monotonic relationship was found between the score and the signal-to-noise ratio. After fitting discrimination functions to these weighted scores it was also found that the sentence-specific threshold level $L_{50,\text{sent.}}$ was always within the range of those signal-to-noise ratios originally employed in the measurements. Thus, the introduction of weighting factors is consistent with the data originally obtained without these factors.

5. Level correction

In order to increase the homogeneity of the test sentences, i.e., decrease the variation in sentence-specific threshold level $L_{50,\text{sent.}}$, the RMS levels of all test sentences were equalized.² After the level correction, 200 sentences were chosen that exhibited an intelligibility score between 30% and 70% at the global L_{50} . Figure 1 gives the frequency distribution of the sentence-specific $L_{50,\text{sent.}}$ of these sentences in comparison to the respective distribution of the 324 test sentences from the original speech material. The global L_{50} , i.e., the average value of these levels is -6.1 dB and the standard deviation is 1.83 dB before and 0.94 dB after the corrections. Thus, the level corrections and the selection criteria of the sentences produced a noticeable reduction of the variation in the sentence-specific $L_{50,\text{sent.}}$ and thus produced a marked increase in the homogeneity of the test material with respect to speech intelligibility.

C. Composition of optimized test lists

From the 200 sentences selected, 20 lists of ten sentences each were composed by a numerical optimization process using the following optimization criteria:

The parameters $L_{50,\text{list}}$ and spread s of the test-list-specific discrimination functions [cf. Eq. (1)] should be the same across all lists, the number of words as well as the number of phonemes should be the same within each test list, and the frequency distribution of the 39 different phonemes within the sentence material should also be equal across all lists. This resulted in a total set of 43 parameters that were optimized with a numerical optimization procedure similar to the “simulated annealing” algorithm (Otten and van Ginneken, 1989). As the initial distribution, the 200 sentences were grouped into 20 lists at random and the actual parameter values for the i th list were placed into a vector \mathbf{p}_i ($i=1-20$). The target vector \mathbf{v} was constructed from the “desired” parameter values, i.e., those values that should be achieved by each test list after optimization. Hence, the av-

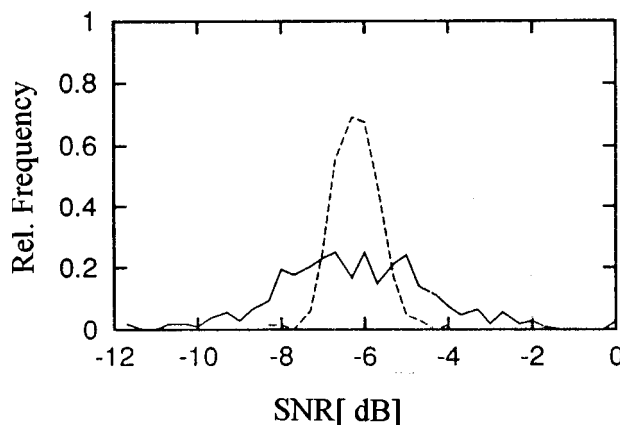


FIG. 1. Frequency distribution of sentence-specific speech reception thresholds $L_{50,\text{sent.}}$ for all 324 test sentences (solid line) in comparison to the distribution for the 200 sentences that were selected as the final test corpus after performing level corrections (dashed line).

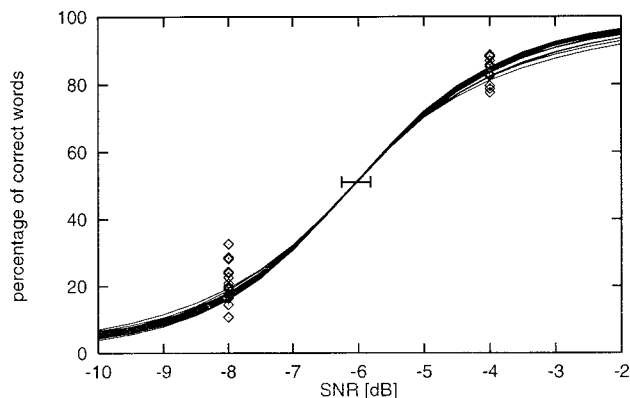


FIG. 2. Calculated discrimination functions (i.e., speech intelligibility as a function of signal-to-noise ratio SNR) for the 20 test lists that resulted from the numerical optimization procedure (solid lines). The symbols at -4 and -8 dB SNR denote the intelligibility scores for each of the 20 lists averaged across subjects that resulted from the independent experiment (Sec. II). The error bar at -6.1 dB denote the average value and standard deviation of the list-specific speech reception threshold $L_{50,\text{list}}$ estimated from this experiment (cf. Sec. II and Table I).

erage values of $L_{50,\text{sent}}$ and s across all 200 test sentences were placed as the “desired” value of L_{50} and s , respectively, into the vector \mathbf{v} . The number of words and number of phonemes were also selected as the total number of words and phonemes, respectively, divided by the number of test lists. The target frequency distribution of the phonemes was taken from the phoneme statistics of the German language according to Meier (1967). In addition, a vector \mathbf{g} of weighting factors was defined which determined the priority of the parameters to be optimized by the algorithm. By selecting appropriate elements of this vector, the algorithm tried to optimize the “more important” parameters L_{50} , s , number of phonemes, and number of words per list with a higher priority than the frequency distribution of the phonemes. The minimization algorithm thus had to minimize the function

$$d = \sum_{j=1}^{20} \|\mathbf{g} \cdot (\mathbf{p}_j - \mathbf{v})\|. \quad (5)$$

The global minimum of d was searched by a pairwise exchange of sentences between the test lists with the optimization algorithm. If a minimum of this function was obtained, a new random initial configuration was determined and the optimization process was repeated. The final result was taken as the minimum out of the results from all different optimization runs. This configuration was interpreted as the optimum configuration with respect to the criteria described above. The resulting test lists are listed in Wesselkamp (1994). The recording of these test lists together with the noise is available on compact disc.

1. Equivalence of the test lists

Figure 2 gives the discrimination functions calculated for each of the 20 resulting test lists. These functions were derived from the sentence-specific discrimination functions that had been fitted to the original data using the weighting factors for the single words and the level corrections for each sentence. The global L_{50} , i.e., the signal-to-noise ratio for

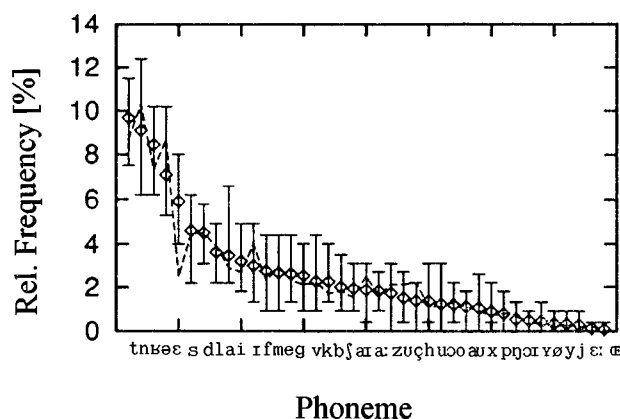


FIG. 3. Average phoneme frequency distribution (symbols) and minimum and maximum number of phonemes across test lists (error bars) for the 20 test lists that resulted from the numerical optimization procedure. The dashed line gives the corresponding expected value derived from the German speech statistics after Meier (1967). The phonemes are arranged according to their occurrence in the underlying test material.

50% sentence score, is -6.1 dB with a very small standard deviation across the test lists. Since the slopes of the list-specific discrimination functions coincide very well, approximately the same intelligibility score is expected for each test list over a wide range of signal-to-noise ratios. At the L_{50} , the slope of the discrimination function is approximately 20%/dB, which is considerably higher than for single-word test material. Thus, it is expected that these sentence lists yield a higher precision and efficiency in estimating speech reception thresholds in comparison to, e.g., tests employing single words.

If the derived test lists are employed without the weighting factors for the single words, the test list-specific discrimination functions no longer coincide as well as given in Fig. 2. However, the variation in the range of the list-specific $L_{50,\text{list}}$ remains below 1 dB across test lists.³ The number of phonemes is 226 for 15 test lists, 227 for three test lists, and 228 and 230 for one test list, respectively. Thus, the optimized test lists appear to be fairly homogeneous with respect to the number of phonemes. The frequency distribution of the phonemes within the test list is plotted in Fig. 3 as average values across test lists (diamonds) and minimum and maximum values of the respective phoneme frequency across all test lists. For comparison, the average phoneme frequency distribution of the German language after Meier (1967) is plotted as a dashed line. Obviously, the phoneme frequency distribution by the test list approximates the respective frequency distribution in the German language very well and no test list deviates substantially from this frequency distribution. One exception is the phoneme /ε/ which is over-represented in the underlying speech material.

II. EMPIRICAL VALIDATION OF THE TEST MATERIAL

In order to validate the test material optimized by the procedures described above, an independent set of experiments was performed. The aim of these experiments was to

estimate the discrimination function for each of the test lists and to test the hypothesis that all test lists are equivalent with respect to their discrimination function.

A. Subjects

Twenty subjects aged between 22 and 36 years (13 male, 7 female) participated in this study. They reported no previous hearing problems and were classified as normal listeners by clinical routine audiometry. They were paid on an hourly basis and had no prior experience with the sentence material.

B. Test procedure

The same stimuli, apparatus, and general test protocol were used as described above (Section I B). Each subject was tested with all 20 test lists at a signal-to-noise ratio of -4 or -8 dB, respectively, in such a way each test list was tested with ten subjects at each signal-to-noise ratio. The selection of signal-to-noise ratios for a given subject and test list was performed with a pseudo-random ordering. This was done in order to distribute the effect of subject and test list evenly across the two signal-to-noise ratios employed.

C. Results

The average intelligibility score across subjects for each of the both signal-to-noise ratios employed was evaluated for each test list separately. The average and spread across test lists of these values are plotted in Fig. 2 as open symbols at -4 and -8 dB signal-to-noise ratio, respectively. Apparently, a very good match is achieved between the values measured with the additional experiment and the “target” discrimination functions that resulted from the numerical optimization procedure.

In order to estimate the deviation of the discrimination functions that result from the independent measurements from the “target” functions plotted in Fig. 2, the following procedure was performed: For each test list, the resulting parameters $L_{50,\text{list}}$ and m were computed from the scores averaged at -4 and -8 dB across subjects, respectively. The parameters $L_{50,\text{list}}$ and m thus estimated for each test list are given in Table I together with their respective mean value and standard deviation averaged across test lists. Note that the standard deviation of $L_{50,\text{list}}$ is very low (0.27) indicating that only small differences occur across test lists in the empirical measurements. For comparison, the expected value of the sentence scores at -8 dB and -4 dB, L_{50} and m are also included in Table I. These values are derived from the average “target” function plotted in Fig. 2. They differ slightly from the empirical mean values obtained here.

In order to estimate if these deviations are significant, the “ideal” standard deviations for the respective parameters were calculated that would be expected on the basis of ten times ten complete, identical test lists presented to an ideal observer that performs according to the average target function from Fig. 2. The “ideal” standard deviation σ_{ideal} of the test score P is then given as:

$$\sigma_{\text{ideal}} = (P(1-P)/n_{\text{SUB}} \cdot n_{\text{SENT}}j)^{1/2}, \quad (6)$$

TABLE I. Intelligibility scores from the experiment described in Sec. II for each of the 20 lists averaged across ten subjects. In addition, the speech reception threshold and the slope m that are estimated from these results are listed. The last row gives the average value and standard deviation across test lists as well as the expected values that would result if all test lists were exactly equivalent and would be tested with an ideal observer.

Test list number	Score (%) at		Estimated	
	-8 dB	-4 dB	$L_{50,\text{list}}$ (dB)	Slope m (%/dB)
1	14.5	85.4	-6.00	22.1
2	17.6	82.7	-6.01	19.4
3	16.9	79.5	-5.84	18.4
4	28.2	88.7	-6.75	18.7
5	22.7	78.6	-6.06	15.8
6	16.6	82.5	-5.96	19.8
7	16.9	85.3	-6.10	20.9
8	10.8	85.8	-5.84	24.4
9	19.9	82.4	-6.10	18.3
10	20.0	82.9	-6.13	18.5
11	19.1	85.8	-6.22	20.3
12	24.4	88.4	-6.57	19.8
13	28.6	77.5	-6.30	13.5
14	16.4	85.1	-6.07	21.1
15	32.6	83.0	-6.74	14.4
16	23.9	85.3	-6.41	18.2
17	19.5	85.1	-6.21	19.8
18	20.9	86.9	-6.34	20.2
19	24.3	88.3	-6.56	19.7
20	19.5	88.1	-6.34	21.4
Mean	20.7	84.4	-6.23	19.2
Standard Deviation	5.22	3.22	0.27	2.51
Expected Mean	17.3	83.8	-6.07	19.8
“Ideal” Std.-Dev.	2.70	2.39	0.17	1.61

where $n_{\text{SUB}}=10$ represents the number of subjects, $n_{\text{SENT}}=10$ represents the number of sentences per test list and j represents the number of independent words in each sentence. This number j was evaluated from the current test results by a procedure proposed by Boothroyd and Nittrouer (1988). They use the following relation between the sentence score P_{sent} (i.e., the probability that all words in a sentence are repeated correctly) the word score P_{word} (i.e., the probability that a word is repeated correctly) and j :

$$P_{\text{sent}} = (P_{\text{word}})^j, \quad \text{i.e., } j = \log(P_{\text{sent}})/\log(P_{\text{word}}). \quad (7)$$

The values resulting from the current data are $j=1.95$ for -8 dB signal-to-noise ratio and $j=2.38$ for -4 dB, respectively. Note, however, that the test score P of the current test is a (weighted) average word score that does not coincide with the value P_{sent} computed to derive j from Eq. (7).

The resulting values of the standard deviations both for the sentence scores and the parameters $L_{50,\text{list}}$ and m , respectively, are given in the last row of Table I. They are lower than the empirical standard deviations which is due to inter-individual and interlist variations in the empirical data. However, the difference is comparably small and not statistically significant. In other words, the empirically observed standard deviation is not significantly different from the spread that would result if all test lists had exactly the same discrimination functions and were scored by the same observer. Also, the deviation between the empirical and expected mean

$L_{50,\text{list}}$ and slope m , respectively, is smaller than one “ideal” standard deviation. This indicates that the average performance of our subjects in this independent experiment is not statistically different from the performance of the group of subjects in the experiments from Sec. I. Thus, the equivalence of the test lists and the reproducibility of the test has been demonstrated with an independent experiment.

III. SUBJECTIVE RATING METHODS EMPLOYING THE SENTENCE MATERIALS

While the sentence intelligibility so far has been measured by the percentage of correctly repeated words of a sentence, a more time-saving estimate of speech intelligibility can be obtained by subjective rating methods. In order to test the possibility of using the sentence test developed here as material for subjective rating methods and to investigate the relation between the “objective” (i.e., scored) speech intelligibility with the subjective rating methods, two experiments were performed. In the first experiment, the subjects had to adjust the signal-to-noise ratio of each individual sentence until they approached the signal-to-noise ratio which corresponds to the subjective criterion of 50% intelligibility. In a second experiment, the subjects had to rate the amount of listening effort to understand the respective sentence at a given signal-to-noise ratio. Based on these judgements at various speech levels, a discrimination function was fitted to the data and the level corresponding to 50% subjective listening effort was evaluated. The difference in the subject’s task between experiments is that in the first experiment the sentence intelligibility was assessed directly and an adjustment in signal-to-noise ratio was performed until this assessment approached a (presumably constant) value. In the second experiment, however, speech intelligibility was assessed indirectly by asking the subjects to rate the listening effort to understand the sentence at a given (fixed) signal-to-noise ratio. By comparing the results from both experiments, the relation between the sentence-specific scored speech reception threshold L_{50} and the subjectively assessed thresholds can be evaluated. A detailed description of these experiments is given by Wesselkamp (1994).

A. Subjects

Twelve normal-hearing subjects (4 male, 8 female), aged 22–36 years, participated voluntarily in these measurements. They were experienced with other psychoacoustic and speech perception tests, but did not receive any special training prior to data collection. Four subjects participated both in experiment one and two.

B. Test procedure

1. Experiment 1

The same 324 original sentences, the same overall noise level of 65 dB SPL and the same general setup was used as described in Sec. I B. Each sentence was presented to each subject at an initial signal-to-noise ratio of 2 dB which corresponds to a high intelligibility. The subjects’ task was to indicate if the sentence level should be decreased or increased in order to achieve the subjective impression of 50%

intelligibility, i.e., the possibility to understand approximately half of the words in a given sentence. The subjects were instructed to build up their own respective criterion of 50% intelligibility during several practice runs and to adhere to this criterion throughout the subsequent experiments as closely as possible. Based on this criterion, they should judge if the target speech should be softer or louder in order to correspond to 50% intelligibility. For this purpose, a five-point scale was presented to the subject with the categories “much louder–louder–okay–softer–much softer.” The subjects were instructed to depress the appropriate categories until the intelligibility of the respective sentence was 50%. No further instructions were available to the subjects. According to the subject’s selection of one category, the speech level was increased or decreased by 1 dB or 0.5 dB, respectively, until the subject depressed the category “okay.” On the average, the subjects required approximately 10 presentations of each sentence at different levels which amounted to about 1 minute testing time per subject and sentence adjustment. Thus, three to four sessions of 60–90 minutes duration were performed for each subject.

2. Experiment 2

An absolute category rating procedure was performed with the same apparatus and the same sentence materials as in experiment 1 and Sec. I. Only the subset of 200 sentences was used that had been selected for the final version of the sentence test (see above). Since the subjective rating of listening effort correlates best with the intelligibility of speech material (cf. Sotscheck, 1992), the subjects were asked to rate their effort in understanding the respective sentence on a five-point scale according to CCITT (1980). In addition, four intermediate categories between these five main categories were allowed so that a total of nine categories were available to the subjects. They were associated with the letters from A to I as follows: A: complete relaxation possible, no effort necessary; C: attention required, no noticeable listening effort necessary; E: reasonable effort necessary; G: considerable effort required; I: meaning unclear despite all possible efforts. These response categories were listed on a sheet of paper and the subjects reported to the test conductor either the complete description of the category or the corresponding key letter.

Each sentence was presented at five predetermined signal-to-noise ratios to each of the eight subjects. They were selected in such a way that the sentence-specific $L_{50,\text{sent}}$ as well as 2 dB and 4 dB above and below this level were presented to the subjects. For some sentences, additional levels had to be tested in order to obtain a complete rated discrimination function. All sentences were grouped into 20 groups with ten sentences in random order and with a random selection of the respective predetermined value of the signal-to-noise ratio. Prior to the judgements, the complete group of sentences was played to the subjects to get them acquainted with the contents of the speech material. Thus, each sentence was judged by each of the eight subjects at least once at five different signal-to-noise ratios.

From the results, a discrimination function was fitted to the data in a similar way as described in Sec. I B. The aver-

TABLE II. Adjusted speech reception threshold $L_{50,adj}$ (average value and intraindividual standard deviation) and rated speech reception threshold $L_{50,rated}$ for each subject. These values were averaged across all sentences.

Subject	$L_{50,adj}$	Std. Dev.	$L_{50,rated}$ (dB)	Std. Dev.
1	-7.0	1.5		
2	-7.8	2.3	-5.8	1.8
3	-6.6	1.7		
4	-7.0	3.0		
5	-10.1	1.7	-7.6	1.8
6	-10.5	2.4	-5.2	1.8
7	-10.5	1.8	-3.2	1.8
8	-9.3	1.3		
9			-2.7	1.8
10			-6.3	1.6
11			-5.6	1.6
12			-6.2	1.7
Mean	-8.6	2.0	-5.3	1.7
Interindiv. Std.-Dev.	1.7		1.6	

age rated category was converted into a value between 0 and 100% and a discrimination function of the form given in Eq. (1) was fitted to the data. This procedure implicitly assumes a uniform distribution of categories across the numerical range between 0 and 100%, which might not be justified on the basis of the employed category ratings. However, the only outcome of the whole procedure were the sentence-specific subjective speech perception thresholds $L_{50,rated}$, i.e., the signal-to-noise ratios which correspond to category E (reasonable effort necessary). This result is expected to be fairly independent of any deviations between the scale employed and a scale with a uniformly distributed response pattern.

C. Results

Table II gives the average results from experiment 1 and experiment 2 for each subject averaged across all sentences. Obviously, substantial interindividual differences occur for the subjectively adjusted and rated thresholds. The maximum deviation is 3.9 dB for the adjusted thresholds and 3.9 dB for the rated thresholds. Although the mean results of the adjusted thresholds correspond to a lower signal-to-noise ratio than the rated thresholds, the rank order of individual thresholds across subjects is not the same for those subjects that participated in both experiments. This indicates that different subjective threshold criteria are assumed by the subjects in both types of measurement procedures. However, the intraindividual variations across sentences are remarkably small: The intraindividual standard deviations vary between 1.3 and 3.0 dB (average value: 1.96 dB) for the adjusted thresholds and 1.6 and 1.8 dB (average value: 1.74 dB) for the rated thresholds. This indicates that the intraindividual subjective criterion is very stable. Its variation is in the same range as the variations across subjects (i.e., the interindividual standard deviation which is represented in the last row of Table II), which is very similar both for the adjusted and rated thresholds. Taken together, both methods appear to have a good reproducibility because the variability in the repetitive

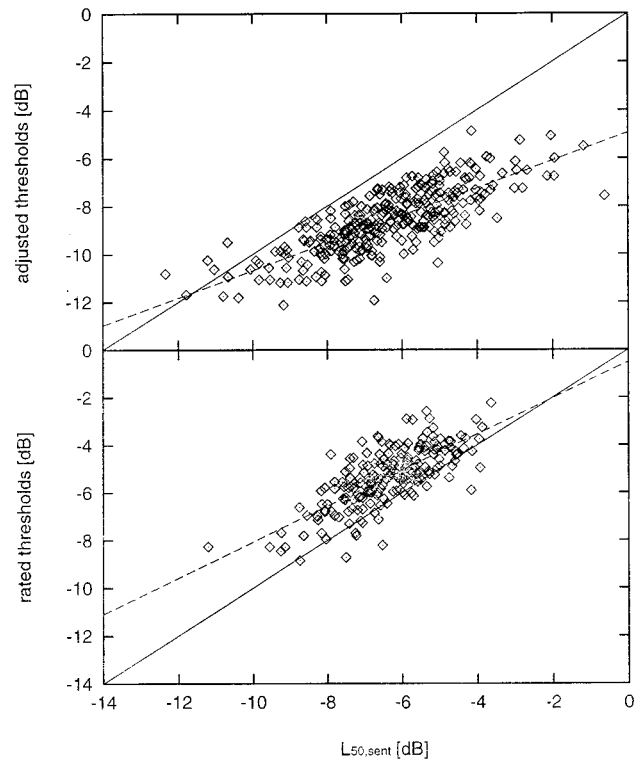


FIG. 4. Sentence-specific adjusted thresholds (upper panel) and subjectively rated thresholds (lower panel) as a function of the “objective” threshold $L_{50,sent}$ obtained from the scoring method. Each data point represents the average across all subjects that participated in the respective test. The solid lines represent an “ideal” relation between objective and subjectively rated threshold and the dashed line represent the respective regression line.

data of a particular subject is not larger than the variation in threshold across different normal-hearing subjects.

To assess the relation between the subjectively rated or adjusted thresholds with the thresholds obtained with the “objective” scoring method, Fig. 4 gives a scatter plot of the sentence-specific adjusted thresholds and rated thresholds versus the measured thresholds $L_{50,sent}$ obtained in Sec. I B. Note that all these results are obtained by averaging across subjects which is justified by the interindividual standard deviations being comparable to the intraindividual standard deviations in the adjustment and rating method employed here. Obviously, a very high correlation between both subjectively obtained thresholds and the scored threshold $L_{50,sent}$ is obtained. This correlation amounts to $r = +0.78$ for the adjusted thresholds and $r = 0.74$ for the rated thresholds. In the case of the adjusted thresholds, the regression line fitted to the data has a slope of 0.57 which indicates that the subjectively adjusted intelligibility thresholds are compressed within a much smaller range of signal-to-noise ratios than the measured ones. This might be due to the conservative adjustment procedure where extreme levels are not accepted by the subjects, whereas the discrimination function fitted to the “objective” speech scores might vary across a larger range. Similar arguments hold for the rated thresholds where the regression line has a slope of 0.76. Thus, this method provides less “compression” of the differences in intelligibility across test items and assumes a kind of compromise between

TABLE III. Factor loadings of the first, dominant component of the principal component analysis on the four parameters $L_{50,\text{sent}}$ (i.e., sentence-specific level corresponding to 50% scored speech intelligibility), $L_{50,\text{adj}}$ (i.e., sentence-specific level subjectively adjusted to 50% scored speech intelligibility), $L_{50,\text{rated}}$ (i.e., sentence-specific level corresponding to 50% intelligibility estimated by absolute category rating), and the RMS level of each sentence.

$L_{50,\text{sent}}$	$L_{50,\text{adj}}$	$L_{50,\text{rated}}$	RMS level
0.89	0.88	0.89	-0.87

the “objective” scoring method and the subjective method of adjustment.

In order to evaluate the number of underlying factors that describe the relation between measured speech intelligibility thresholds, adjusted and rated thresholds, a principal component analysis was performed which included for each specific sentence the scored speech reception thresholds $L_{50,\text{sent}}$, the adjusted thresholds $L_{50,\text{adj}}$, and the rated thresholds $L_{50,\text{rated}}$, as well as the sentence-specific RMS-level. These values were obtained from the 200 test sentences where all these results were accessible. As a result, one single factor was extracted as the most important component which explains 78% of the total variance and correlates very well with all values included. Table III gives the factor loadings of this principal factor on the four observed quantities for each sentence. All sentence-specific thresholds show a very high loading on this factor, whereas the RMS value shows a very high negative loading on this factor. This indicates that all three methods for assessing the speech reception thresholds for sentences correlate very highly with each other and also are highly influenced by the RMS level of each sentence. This principal factor can therefore be interpreted as the “effective” speech-to-noise ratio for each individual sentence that relates both to subjective measures (i.e., the speech reception threshold) and to objective measures (i.e., the deviation of the sentence-specific RMS value from the average RMS value).

IV. DISCUSSION

A. Value of the speech reception threshold

The average speech reception thresholds (SRT) reported here vary between -6.1 dB (scoring method), -8.6 dB (subjective adjustment of threshold), and -5.3 dB (subjective rating of intelligibility), respectively. Thus, they are somewhat lower than the values reported in the literature, e.g., Nilsen *et al.* (1994) who reported -2.9 dB, and Tschopp and Ingold (1992), who reported -3 and -8 dB, respectively. However, the absolute SRT value depends on several factors such as, e.g., the definition of the speech and noise level, the gender and articulation mode of the talker, the bandwidth of the recordings, and the spectral and temporal structure of the noise. In this study, the digitally computed RMS value was used to calculate the level, the male talker articulated the test material in a normal conversational mode, a reproduction bandwidth of 10 kHz was used, and the speech-simulating noise was generated by a statistical overlay of monosyllabic material recorded with the same talker.

Since these definitions and selections of experimental details partially differ from other studies reported in the literature, the deviation of several dB in speech reception threshold is not surprising.

It should be noted, however, that both the value of the average SRT and the close resemblance of the performance-intensity curves across test lists depend on the type of noise employed here. For a different type of noise, more variations across test lists may be expected because of the optimization procedure employed to assemble the lists. On the other hand, these variations will be limited because the optimization procedure also included nonacoustic features that are independent of the noise employed, such as the number of words and syllables in each list and the phoneme distribution.

B. Reliability and efficiency of the test procedures

For practical purposes, the accuracy in determining the SRT and the amount of time spent to achieve this accuracy is a major factor in assessing a particular test method. With the “objective” scoring method employed in Secs. I and II, respectively, the expected “ideal” standard deviation (s.d.) σ of the respective speech score P at a given signal-to-noise ratio depends only on P , the number of sentences in a list n_{SENT} , and the number j of independent words in a sentence:

$$\sigma = (P(1-P)/n_{\text{SENT}}j)^{1/2}. \quad (8)$$

Since j is approximately equal to 2 and $n_{\text{SENT}} = 10$, the maximum value of σ for $P=0.5$ is about 11% which corresponds to a s.d. in threshold level of approx. 0.5 dB (using the slope value of approx. 20%/dB). In practical applications, the variations across subjects and across test lists will increase the variability by up to a factor of two (cf. Sec. II C and the difference between empirical and “ideal” s.d. in Table I). Hence, the accuracy of determining the SRT with one test list (under the assumption that the signal level employed for testing is nearby the SRT value) amounts to somewhat below 2 dB.

Note that this value is very similar to the interindividual and intraindividual s.d. obtained with the subjective adjustment and rating methods evaluated in Sec. III (cf. Table II). Hence, the accuracy achieved with the different methods employed here appear to be approximately the same. On the other hand, the subjective adjustment procedure requires less time than the other methods to provide an SRT estimate (approx. 1 minute for adjusting one sentence level as compared to approx. 4 minutes for scoring a complete list). This indicates that the adjustment procedure is very efficient. One reason is that many different judgements can be performed by the subject within a short period of time. On the other hand, the efficiency of the “objective” scoring method can be enhanced if an adaptive procedure for adjusting the level is employed (cf. Brand *et al.*, 1996). Such a combination of speech test and adaptive procedure is only meaningful if the variability in intelligibility across test items is very small. This is the case for the sentence material employed here. However, the adaptive procedures can only adjust the presentation level towards its “optimal” value, but cannot further increase the accuracy of the test to values above the boundary estimated above. Hence, a further increase in ac-

curacy can only be achieved by increasing the number of test lists employed. Unfortunately, this requires more time. Therefore, the subjective adjustment methods are preferable in cases where the efficiency of the procedure is most important. If on the other hand the test items have to be more representative of the underlying language or if the results should be independent on a subjective criterion, the less efficient “objective” speech scoring methods should be employed.

C. Relations among the different measures of speech intelligibility

Although the three different methods for assessing speech intelligibility employed here aim at different aspects of speech intelligibility (e.g., scoring only correctly perceived words versus adjusting a subjective impression of intelligibility or rating the listening effort in understanding speech), the high correlation between the different measures is quite astonishing. Since all three measures also correlate highly with the sentence-specific RMS value (cf. Table III) it seems likely that the high correlation is caused by the variation of RMS level across sentences that influences all measures of sentence intelligibility in a similar way. This principal factor can therefore be interpreted as the “effective signal-to-noise ratio” for each individual sentence.

It should be noted, however, that this close relation between sentence-specific RMS level and SRT does not agree with findings of a high variability of the item-specific intelligibility especially for single words, which can neither be predicted with the RMS level of each item nor with more refined speech intelligibility prediction methods, such as the articulation index, speech transmission index, or perception models (Kollmeier, 1990; Wesselkamp, 1994). The reason for this comparatively high relation between speech intelligibility and RMS level might be the use of comparatively long speech items, i.e., sentences, where already some averaging is performed across different speech elements which is not the case for isolated words.

D. Applications

Due to its high precision and accuracy in measuring speech intelligibility in noise, the sentence test has already been employed in a variety of applications. In clinical audiology, it is used within a clinical joint research project to assess the “effective” impairment in noise for hearing-impaired patients and the possible use of a hearing aid (Kollmeier, 1996). Kießling *et al.* (1994) compared the performance-intensity functions of different computer-controlled speech tests for normal listeners and listeners with different configurations of hearing loss. Müller-Deile (1995) used the test for assessing the training progress of children wearing Cochlear Implants. Another application is the assessment of binaural interaction in normal and hearing-impaired subjects which can also be used for assessing the benefit of bilaterally worn hearing aids (Peissig and Kollmeier, 1997). Wesselkamp (1994) also used the test to validate a perception model to predict speech intelligibility under various conditions. Although this is not a complete list of

past and future applications of the test described here, it may provide some insights into the possible developments that are based on the concepts and results given above.

V. CONCLUSIONS

The German sentence test described here contains highly homogeneous test material and 20 highly equivalent sentence lists with ten short sentences each.

In separate sets of experiments, the discrimination functions obtained with each test list were shown to be very close to the “ideal” discrimination function achieved in the original design.

Two subjective speech intelligibility measurement methods (i.e., adjustment of thresholds and rating of listening effort for understanding speech) were shown to correlate highly with the speech reception thresholds obtained by scoring methods. The most dominant factor in predicting sentence-specific speech intelligibility appears to be the RMS value of each sentence.

The test appears to be useful for a variety of applications, such as, e.g., clinical audiology, hearing aid fitting, and the evaluation of communication systems both using conventional scoring methods and rapid subjective intelligibility assessment methods.

ACKNOWLEDGMENTS

Work supported by BMBF, PT-AUG. Thanks to A. Sievers for typing the manuscript, A. Gorges for technical support, and T. Brandt, I. Holube, K. Kliem and the other members of the AG Medizinische Physik for their encouragement and help. The valuable hints of two anonymous reviewers are gratefully acknowledged.

¹Although a permanent and objective record of the subject's responses can be obtained by tape recording the experimental session, such a procedure was not performed here. It would require an impractical experimental overhead for clinical purposes without significantly improving the reliability of the test scores, especially if a well-trained and experienced instructor performs the test with the subject.

²In order to keep the loudness impression approximately constant across all test sentences that have been recorded with a constant vocal effort of the speaker, the level correction was restricted to a range between -2.5 and $+2.5$ dB. Sentences with an intelligibility between 30% and 70% at the global L_{50} were not corrected in level. If the level correction was computed to be less than 0.5 dB, no correction was performed. In addition, the level for each sentence was only corrected, if the corresponding change in intelligibility for this sentence at the global L_{50} resulted in a more homogeneous test material (i.e., a reduction in standard deviation of the intelligibility averaged across sentences).

³If no weighting factors are employed, the calculated discrimination functions for the 20 test lists depicted in Fig. 2 would deviate by a maximum amount of approx. 4% or 0.25 dB in the range between 30% and 70% intelligibility. Since this variation across test lists is comparatively small, the test lists might as well be scored without weighting factors in certain practical applications. Thus, the test score is computed by directly obtaining a word score for each sentence. Moreover, since the number of words within each test list is 50 (for eleven lists), 51 (for eight test lists) and 52 (for one list), respectively, only a small error occurs, if simply the number of correctly repeated words within a complete test list is multiplied by a factor of 2 to yield the list score. Thus, the sentence test proposed here can also be used in a simple paper-and-pencil scoring method. However, the equivalence of the test lists is improved if the appropriate weighting factors are taken into account.

- Boothroyd, A., and Nittrouer, S. (1988). "Mathematical treatment of context effects in phoneme and word recognition," *J. Acoust. Soc. Am.* **84**, 101–114.
- Bosman, A. J. (1989). "Speech perception by the hearing impaired," Ph.D. thesis, University of Utrecht.
- Brand, T., Wesselkamp, M., and Kollmeier, B. (1996). "Adaptive estimation of psychometric functions in psychoacoustics and speech audiometry," in *Psychoacoustics, Speech and Hearing Aids*, edited by B. Kollmeier (World Scientific, Singapore), pp. 69–72.
- Comité consultatif International Télégraphique et Téléphonique (CCITT) Plenary Assembly Genève (1980) Yellow Book, Vol. V, Suppl. 2 to Recommendation P.74, Annex A.
- Cox, R. M., Alexander, G. C., and Rivera, I. M. (1991). "Comparison of objective and subjective measures of speech intelligibility in elderly hearing-impaired listeners," *J. Speech Hear. Res.* **34**, 904–915.
- Dillier, N., and Spillmann, T. (1992). "Deutsche Version der Minimal Auditory Capability (MAC)-Test-Batterie: Anwendungen bei Hörgeräte- und CI-Trägern mit und ohne Störlärm," in *Moderne Verfahren der Sprachaudiometrie*, edited by B. Kollmeier (Median Verlag, Heidelberg, Germany), pp. 238–263.
- Kalikow, D. N., Stevens, K. N., and Elliott, L. L. (1977). "Development of a test of speech intelligibility in noise using sentence materials with controlled word predictability," *J. Acoust. Soc. Am.* **61**, 1337–1351.
- Kießling, J., Schubert, M., and Wagner, I. (1994). "Sprachverständlichkeitsmessungen an Normalhörenden und Schallempfindungsschwerhörigen-fünf Sprachtests im Vergleich," *Audiol. Akustik* **33**(1), 6–19; **33**(2), 11–15.
- Kollmeier, B. (1990). "Messmethodik, Modellierung und Verbesserung der Verständlichkeit von Sprache," Habilitationsschrift, Universität Göttingen.
- Kollmeier, B. (1996). "Computer-controlled speech audiometric techniques for the assessment of hearing loss and the evaluation of hearing aids," in *Psychoacoustics, Speech, and Hearing Aids*, edited by B. Kollmeier (World Scientific, Singapore), pp. 57–68.
- Kollmeier, B., Sotscheck, J., and Kammermeier, A. (1988). "Digitalaufnahme eines Reimtests in deutscher Sprache," *Audiol. Akustik* **27**, 24–27.
- Kollmeier, B., Müller, C., Wesselkamp, M., and Kliem, K. (1992). "Weiterentwicklung des Reimtests nach Sotscheck," in *Moderne Verfahren der Sprachaudiometrie*, edited by B. Kollmeier (Median Verlag, Heidelberg, Germany), pp. 216–237.
- Meier, H. (1967). *Deutsche Sprachstatistik* (Georg Olms, Hildesheim, Germany).
- Müller-Deile, J. (1995). Personal communication.
- Niemeyer, W. (1967). "Sprachaudiometrie mit Sätzen I: Grundlagen und Testmaterial einer Diagnostik des Gesamtsprachverständnisses," *HNO* **15**, 335–343.
- Nilsson, M., Soli, S. D., and Sullivan, J. A. (1994). "Development of the Hearing in Noise Test for the measurement of speech reception thresholds in quiet and in noise," *J. Acoust. Soc. Am.* **95**, 1085–1099.
- Otten, R. H. J. M., and van Ginneken, L. P. P. (1989). *The Annealing Algorithm* (Kluwer, Boston).
- Owens, E., Kessler, D. K., Raggio, M., and Schubert, E. D. (1985). "Analysis and revision of the Minimal Auditory Capabilities (MAC) battery," *Ear Hear.* **6**, 280–290.
- Peissig, J., and Kollmeier, B. (1997). "Directivity of Binaural Noise Reduction in spatial multiple-noise-source arrangements for normal and impaired listeners," *J. Acoust. Soc. Am.* **101**, 1660–1670.
- Plomp, R., and Mimpen, A. M. (1979). "Improving the reliability of testing the speech reception threshold for sentences," *Audiology* **18**, 43–52.
- Sotscheck, J. (1984). "Sätze für Sprachgütemessungen und ihre phonologische Anpassung an die deutsche Sprache," in *Fortschritte der Akustik-DAGA'84* (DPG-Kongress-GmbH, Bad Honnef), pp. 873–876.
- Sotscheck, J. (1992). "Sprachqualitätstests in der Nachrichtentechnik," in *Moderne Verfahren der Sprachaudiometrie*, edited by B. Kollmeier (Median Verlag, Heidelberg, Germany), pp. 35–50.
- Tschopp, K., and Ingold, L. (1992). "Entwicklung einer deutschen Version des SPIN-Tests (Speech Perception in Noise)," in *Moderne Verfahren der Sprachaudiometrie*, edited by B. Kollmeier (Median Verlag, Heidelberg, Germany), pp. 311–329.
- Wesselkamp, M. (1994). "Messung und Modellierung der Verständlichkeit von Sprache," Ph.D. thesis, Universität Göttingen.
- Wesselkamp, M., Kliem, K., and Kollmeier, B. (1992). "Erstellung eines optimierten Satztests in deutscher Sprache," in *Moderne Verfahren der Sprachaudiometrie*, edited by B. Kollmeier (Median Verlag, Heidelberg, Germany), pp. 330–343.

Specifying spectra for musical scales

William A. Sethares^{a)}

Department of Electrical and Computer Engineering, University of Wisconsin, Madison,
Wisconsin 53706-1691

(Received 5 July 1996; accepted for publication 3 June 1997)

The sensory consonance and dissonance of musical intervals is dependent on the spectrum of the tones. The dissonance curve gives a measure of this perception over a range of intervals, and a musical scale is said to be *related* to a sound with a given spectrum if minima of the dissonance curve occur at the scale steps. While it is straightforward to calculate the dissonance curve for a given sound, it is not obvious how to find related spectra for a given scale. This paper introduces a “symbolic method” for constructing related spectra that is applicable to scales built from a small number of successive intervals. The method is applied to specify related spectra for several different tetrachordal scales, including the well-known Pythagorean scale. Mathematical properties of the symbolic system are investigated, and the strengths and weaknesses of the approach are discussed.

© 1997 Acoustical Society of America. [S0001-4966(97)05509-4]

PACS numbers: 43.75.Bc, 43.75.Cd [WJS]

INTRODUCTION

The motion from consonance to dissonance and back again is a standard feature of most Western music, and several attempts have been made to explain, define, and quantify the terms “consonance” and “dissonance.” For example, Tenney¹ provides a historical overview that identifies five separate uses of the terms, and a longstanding debate surrounds the “reductionist” explanations of Plomp and Levelt² and Terhardt,³ and the proponents of “cultural conditioning” such as Cazden.⁴ One of the most successful of the reductionist approaches is called tonal or *sensory* dissonance, in which the sensory dissonance between pairs of sine waves is determined from psychoacoustic experiments. The sensory dissonance of more complex sounds is then defined to be the sum of the dissonances between all simultaneously sounding sine wave partials. Because sensory dissonance depends on the partials, sounds with different spectra may function differently. For instance, an interval may be quite consonant when played with one sound, but quite dissonant when performed with another.

The dissonance curve $D_F(r)$ is a function that describes how the sensory dissonance of a sound with spectrum F varies when played at different intervals r . Figure 1, for instance, shows a plot of the dissonance curve for a sound with six harmonic partials over a range of intervals slightly larger than an octave. The minima of this curve occur at the simple integer ratios of the Just Intonation scale, reinforcing the familiar notion that the most consonant (least dissonant) intervals for sounds with harmonic spectra are those with small integer ratios. The top axis shows the steps of the 12-tone equal tempered scale, which can be viewed as approximating many of these just ratios. Techniques for drawing dissonance curves are described in detail in Ref. 5 and a computer program is given in Ref. 6. These are based on an explicit parametrization of the perceptual data gathered by Plomp and Levelt² (and replicated in Ref. 7). These are in

turn closely related to Helmholtz’⁸ “beat theory” of dissonance in which the beating between higher harmonics causes a roughness that is perceived as dissonance.

Nonharmonic sounds can have dissonance curves that differ dramatically from Fig. 1, indicating that intervals with the most sensory consonance depend strongly on the structure of the partials of the sound. A dramatic example of this is provided in the “Tones and tuning with stretched partials” selection of the Auditory Demonstrations recording by Houtsma *et al.*,⁹ in which stretched sounds appear more consonant when played in the corresponding stretched octaves than when played in “real” octaves. To talk about this kind of effect more generally, a spectrum and a scale are said to be *related* if the dissonance curve has minima at the scale steps. Thus Fig. 1 shows that the Just Intonation scale and harmonic sounds are related. It is easy to find the related scale for a given spectrum simply by drawing the dissonance curve. But the inverse problem of finding a spectrum that is related to a given scale is not as straightforward. This paper focuses on certain classes of scales (such as tetrachordal scales) which are defined by only a few different successive intervals, and presents an algorithm for constructing families of spectra related to these scales.

This is important because related spectra can provide the composer and/or performer with additional flexibility in terms of controlling the consonance and dissonance of a given piece. For example, the Pythagorean tuning is often criticized because its major third is sharp compared to the equal tempered third, which is itself sharper than the just third. This excessive sharpness is heard as a roughness or beating, and is especially noticeable in slow, sustained passages. Using a related spectrum that is specifically crafted for use in the Pythagorean tuning, however, can ameliorate much of this roughness. The composer or performer thus has the option of exploiting a smoother, more consonant third than is available when using unrelated spectra.

The next section reviews previous approaches to the spectrum selection problem, and recalls the principle of co-

^{a)}Electronic mail: sethares@ece.wisc.edu

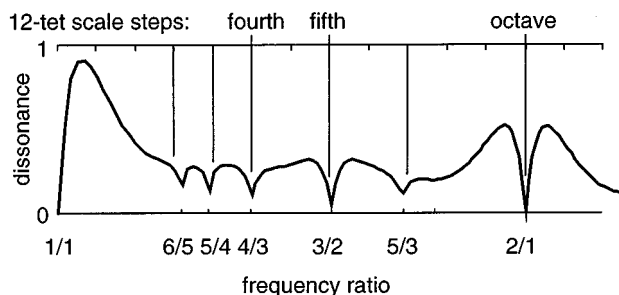


FIG. 1. Dissonance curve for a spectrum with fundamental at 500 Hz and six harmonic partials has minima at 1.0, 1.14, 1.2, 1.25, 1.33, 1.5, 1.67, 1.78, and 2.0, which are shown by the tick marks on the frequency axis. Observe that many of these coincide exactly with steps of the Just Intonation scale, and coincide approximately with 12-tet scale steps, which are shown above for comparison.

inciding partials, which can be used to transform the problem into simpler form. A symbolic system is then introduced along with a method of constructing related spectra. Several examples are given in detail, and related spectra are found for a Pythagorean scale and for a diatonic tetrachordal scale. A simple pair of examples then shows that it is not always possible to find such related spectra. The symbolic system is investigated in the Appendix, where several mathematical properties are revealed.

I. GENERAL TECHNIQUES

The problem of finding spectra for a specified scale was stated in Ref. 5 in terms of a constrained optimization problem that can sometimes be solved via iterative techniques such as the genetic algorithm¹⁰ or simulated annealing.¹¹ Though these approaches are very general, the problem is high dimensional (on the order of the number of partials in the desired spectrum), the algorithms run slowly (overnight, or worse), and they are not guaranteed to find optimal solutions (except “asymptotically”). Moreover, even when a good spectrum is found for a given scale, the technique gives no insight into the solution of other closely related spectrum selection problems. There must be a better way.

Several general properties of dissonance curves are given in Ref. 6. The fourth of these is the key to simplifying the spectrum selection problem:

Property of Coinciding Partial: Up to half of the $2n(n-1)$ minima of a dissonance curve occur at interval ratios r for which $r = f_i/f_j$, where f_i and f_j are partials of F .

In essence, whenever the j th partial of the lower tone coincides with the i th partial of the upper tone, there is a potential minimum of the dissonance curve. The minima corresponding to such intervals r typically “look like” the minima that occur at the simple integer ratios in Fig. 1. The other half of the potential minima are caused by more widely spaced partials that do not interact in a significant way. For instance, in Fig. 1, only the very shallow minimum at 1.78 is of this kind. Most musical tones are quite complex, with numerous partials, and the majority of minima are caused by

Pythagorean Diatonic Scale

ratio	cents	
1/1	0	
9/8	204	a=9/8
81/64	408	a
4/3	498	b=256/243
3/2	702	a
27/16	906	a
243/128	1110	a
2/1	1200	b

FIG. 2. Pythagorean major scale has intervals $a=9/8$ between all major seconds and $b=256/243$ between all minor seconds. It is laid out here in the “key” of C.

coinciding partials. This property of coinciding partials is the key to solving the spectrum selection problem in certain situations. The simplest case is for equal temperaments.

A. Spectra for equal temperaments

The ratio between successive scale steps in the 12-tone equal-tempered (abbreviated 12-tet) scale is the 12th root of 2, $\sqrt[12]{2}$, or about 1.0595. Similarly, m -tet has a ratio of $s = \sqrt[m]{2}$ between successive steps. Consider spectra for which successive partials are ratios of powers of s . Each partial of such a spectrum, when transposed into the same octave as the fundamental, lies on a note of the scale. Such a spectrum is said to be *induced* by the m -tet scale.

Induced spectra are good candidate solutions to the spectrum selection problem since the ratio between any pair of partials in an induced spectrum is s^k for some integer k . By the property of coinciding partials, the dissonance curve will tend to have minima precisely at steps of the scale. Thus such spectra will have low dissonance at scale steps, and many of the scale steps will be minima.

This insight can be exploited in two ways. First, it can be used to reduce the search space of the optimization routine. Instead of searching over all frequencies in a bounded region, the search need only be conducted over induced spectra. More straightforwardly, the spectrum selection problem for equal tempered scales can be solved by careful choice of induced spectra. In Ref. 5, this method was used to find spectra related to 10-tet, and other equal temperaments are equally straightforward. Unfortunately, it is not so clear how to proceed when confronted with nonequal tunings.

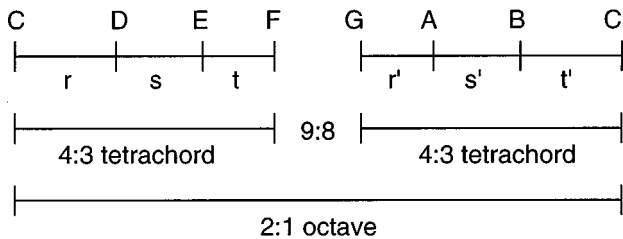


FIG. 3. Tetrachordal scales divide the octave into two 4:3 tetrachords separated by an interval of 9:8. The tetrachords are each divided into three intervals to form a seven note scale, which is labeled in the key of C.

B. Pythagorean scales and the tetrachord

To see why spectrum selection is more difficult for non-equal tunings, consider the Pythagorean diatonic scale, which is shown in Fig. 2 mapped to the “key” of C. This scale is created¹² from a series of pure 3/2 fifths (translated back into the original octave whenever necessary), and all seven of the fifths are pure. An interesting structural feature is that there are only two successive intervals, a “whole step” of $a=9/8$ and a “half step” of $b=256/243$. This whole step is 4 cents larger than the equal tempered version, while the half step is 10 cents smaller than in 12-tet.

In attempting to mimic the “induced spectrum” idea of the previous section, it is natural to attempt to place the partials at scale steps. Unfortunately, the intervals between scale steps are not necessarily scale steps themselves. For instance, if one partial occurred at the seventh ($f_i=243/128$) and the other at the fourth ($f_j=4/3$), then a minimum of the dissonance curve might occur at $r=f_i/f_j=a^3=729/512$, which is not a scale step. Similarly, the ratio between a partial at 4/3 and another at 81/64 is $256/243=b$, which again is not a scale step.

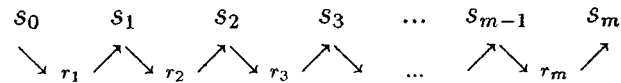
The Pythagorean scale is one example of a large class of scales based on “tetrachords”¹³ which were advocated by a number of ancient theorists such as Archytas, Aristoxenus, Didymus, Eratosthenes, and Ptolemy.¹⁴ A tetrachord is an interval of a pure fourth (a ratio of 4/3) that is divided into three subintervals. Combining two tetrachords around a central interval of 9/8 forms a seven tone scale spanning the octave. For instance, Fig. 3 shows two tetrachords divided into intervals r, s, t and r', s', t' . When $r=r', s=s',$ and $t=t'$, the scale is called an equal-tetrachordal scale. The Pythagorean scale is the special equal-tetrachordal scale where $r=r'=s=s'=9/8$. A modern treatment of tetrachords and tetrachordal scales is available in Ref. 15.

II. A SYMBOLIC SYSTEM

This section presents a symbolic system that uses the desired scale to define an operation that generates “strings” representing spectra, i.e., sets of partials. Admissible strings have all ratios between all partials equal to some interval in the scale, and thus are likely to be related spectra, via the property of coinciding partials.

A. Basic definitions

A desired scale S can be specified either in terms of a set of intervals $(s_0, s_1, s_2, \dots, s_m)$ with respect to some fundamental frequency f or by the successive ratios $r_i = s_i/s_{i-1}$.



For instance, for the Pythagorean diatonic scale of Fig. 2,

$$S = (1, 9/8, 81/64, 4/3, 3/2, 27/16, 243/128, 2/1),$$

and r_i is either $a=9/8$ or $b=256/243$ for all i . The intervals $s_i \in S$ are called the *scale intervals*.

A spectrum F is defined by a set of partials with frequencies at (f_1, f_2, \dots, f_n) . The property of coinciding partials suggests that related spectra can be constructed by ensuring that the ratios of the partials are equal to scale steps. The following definitions distinguish the situation where all ratios of all partials are equal to some scale step, from the situation where all scale steps occur as a ratio of some pair of partials.

Definition: If for each i and j there is a k such that $f_i/f_j = s_k$, then the spectrum is called *complementary* to the scale.

Definition: If for each k there is at least one pair of i and j such that $s_k = f_i/f_j$, then the spectrum is called *complete* with respect to the scale.

If a spectrum is both complete and complementary, then it is called *perfect* with respect to the given scale. Of course, scales and spectra need not be perfect in order to sound good or to be playable, and many scales have no perfect spectra at all. Nonetheless, when perfect spectra exist, they are ideal candidates.

B. An example

The simplest nonequal scales are those with only a small number of different successive ratios. For example, one scale generated by two intervals a and b has scale intervals

$$\begin{aligned} s_0 &= 1, \quad s_1 = a, \quad s_2 = ab, \quad s_3 = a^2b, \quad s_4 = a^2b^2, \\ s_5 &= a^3b^2, \quad \text{and} \quad s_6 = a^3b^3 = 2, \end{aligned} \quad (1)$$

where a and b are any two numbers such that $a^3b^3=2$. For this scale,

$$r_1 = a, \quad r_2 = b, \quad r_3 = a, \quad r_4 = b, \quad r_5 = a, \quad \text{and} \quad r_6 = b.$$

To see how it might be possible to build up a perfect spectrum for this scale, suppose that the first partial is selected arbitrarily at f_1 . Then f_2 must be

$$af_1, \quad abf_1, \quad a^2bf_1, \quad a^2b^2f_1, \quad a^3b^2f_1, \quad \text{or} \quad 2f_1 \quad (2)$$

since any other interval will cause f_2/f_1 to be outside the scale intervals. Suppose, for instance, that $f_2 = a^2bf_1$ is selected. Then f_3 must be chosen so that f_3/f_1 and f_3/f_2 are both scale intervals. The former condition implies that f_3 must be one of the intervals in (2) while the latter restricts f_3 even further. For instance, $f_3 = a^3b^2f_1$ is possible since $a^3b^2f_1/a^2bf_1 = ab$ is one of the scale intervals in (1). But $f_3 = a^3b^3f_1$ is not possible since $a^3b^3f_1/a^2bf_1 = ab^2$ is not one of the scale intervals. Clearly, building complementary

TABLE I. \oplus -table for the scale defined in (1).

\oplus	(0,0)	(1,0)	(1,1)	(2,1)	(2,2)	(3,2)
(0,0)	(0,0)	(1,0)	(1,1)	(2,1)	(2,2)	(3,2)
(1,0)	(1,0)	*	(2,1)	*	(3,2)	*
(1,1)	(1,1)	(2,1)	(2,2)	(3,2)	(0,0)	(1,0)
(2,1)	(2,1)	*	(3,2)	*	(1,0)	*
(2,2)	(2,2)	(3,2)	(0,0)	(1,0)	(1,1)	(2,1)
(3,2)	(3,2)	*	(1,0)	*	(2,1)	*

spectra for nonequal scales requires more care than in the equal tempered case where partials can always be chosen to be scale steps. For some scales, no complementary spectra may exist. For some, no complete spectra may exist.

C. Symbolic computation of related spectra

This process of building spectra rapidly becomes complex. A symbolic table called the \oplus -table (pronounced “Oh-plus-table”) simplifies and organizes the choices of possible partials at each step. The easiest way to introduce this is to continue with the example of the previous section.

Let the scalar intervals in (1) be written (1,0), (1,1), (2,1), (2,2), (3,2), and (3,3), where the first number is the exponent of a and the second is the exponent of b . Since the scale is generated by a repeating pattern, i.e., it is assumed to repeat at each octave, (3,3) is equated with (0,0). Basing the scale on the octave is not necessary, but it simplifies the discussion. The \oplus -Table I represents the relationships between all the scale intervals. The table shows, for instance, that the interval a^2b combined with the interval ab gives the scale interval a^3b^2 , which is notated $(2,1) \oplus (1,1) = (3,2)$.

The asterisk indicates that the given product is not permissible since it would result in intervals that are not scalar intervals. Thus $a^2b = (2,1)$ cannot be \oplus -added to $a = (1,0)$ since together they form the interval a^3b which is not an interval of the scale. Observe that the “octave” has been exploited whenever the product is greater than 2. For instance, $(1,1) \oplus (3,2) = (4,3)$. When reduced back into the octave, (4,3) becomes (1,0) as indicated in the table, expressing the fact that $a^4b^3/a^3b^3 = a^1b^0$. At first glance this may appear to be some kind of algebraic structure such as a group or a monad.¹⁶ However, algebraic structures require closure, i.e., that operations on members of the set give answers that remain within the set. The presence of the asterisks indicates that \oplus does not define a closed operator.

TABLE II. A perfect spectrum for the scale (1).

i	1	2	3	4	5	6	7	k
t_i	(3,3)	(5,5)	(6,6)	(9,8)	(10,9)	(11,10)	(13,12)	
s_i	(0,0)	(2,2)	(0,0)	(3,2)	(1,0)	(2,1)	(1,0)	
$r_{i,k}$		(2,2)	(1,1)	(3,2)	(1,1)	(1,1)	(2,2)	1
			(0,0)	(1,0)	(1,0)	(2,2)	(0,0)	2
				(3,2)	(2,1)	(2,1)	(1,1)	3
					(1,0)	(3,2)	(1,0)	4
						(2,1)	(2,1)	5
							(1,0)	6

TABLE III. \oplus -table for the Pythagorean scale defined in (4).

\oplus	(0,0)	(1,0)	(2,0)	(2,1)	(3,1)	(4,1)	(5,1)
(0,0)	(0,0)	(1,0)	(2,0)	(2,1)	(3,1)	(4,1)	(5,1)
(1,0)	(1,0)	(2,0)	*	(3,1)	(4,1)	(5,1)	*
(2,0)	(2,0)	*	*	(4,1)	(5,1)	*	*
(2,1)	(2,1)	(3,1)	(4,1)	*	(0,0)	(1,0)	(2,0)
(3,1)	(3,1)	(4,1)	(5,1)	(0,0)	(1,0)	(2,0)	*
(4,1)	(4,1)	(5,1)	*	(1,0)	(2,0)	*	*
(5,1)	(5,1)	*	*	(2,0)	*	*	*

D. Construction of spectra

The \oplus -Table I was constructed from the scale steps given in Eq. (1); other scales S define analogous tables. This section shows how to use such \oplus -tables to construct spectra related to a given scale.

Let S be a set of scale intervals with unit of repetition or “octave” s^* . Let $T = [S, s^* + S, 2s^* + S, 3s^* + S, \dots]$ be a concatenation of S and all its octaves. (The symbol “+” is used here in the sense of vector addition.) Each element of $s \in S$ represents an equivalence class $s + ns^*$ of elements in T .

Example: For the scale of the previous section,

$$S = [(0,0), (1,0), (1,1), (2,1), (2,2), (3,2)]$$

with octave $s^* = (3,3)$. Then

$$s^* + S = [(3,3), (4,3), (4,4), (5,4), (5,5), (6,5)],$$

$$2s^* + S = [(6,6), (7,6), (7,7), (8,7), (8,8), (9,8)],$$

etc., and T is a concatenation of these.

The procedure for constructing spectra can now be stated.

Symbolic Spectrum Construction:

(1) Choose $t_1 \in T$ and let $s_1 \in S$ be the corresponding representative of its equivalence class.

(2) For $i = 2, 3, \dots$, choose $t_i \in T$ with corresponding $s_i \in S$ so that there are $r_{i,i-j}$ with

$$s_i = s_j \oplus r_{i,i-j} \quad (3)$$

for $j = 1, 2, \dots, i-1$.

The result of this procedure is a string of t_i which defines a set of partials. By construction, the spectrum built from these partials is complementary to the given scale. If, in addition, all of the scale steps appear among either the s or the r , then the spectrum is complete, and hence perfect.

TABLE IV. A perfect spectrum for the Pythagorean scale (4).

i	1	2	3	4	5	6	7	k
t_i	(5,2)	(8,3)	(10,4)	(12,4)	(14,5)	(15,5)	(17,6)	
s_i	(0,0)	(3,1)	(0,0)	(2,0)	(4,1)	(5,1)	(2,0)	
$r_{i,k}$		(3,1)	(2,1)	(2,0)	(2,1)	(1,0)	(2,1)	1
			(0,0)	(4,1)	(4,1)	(3,1)	(3,1)	2
				(2,0)	(1,0)	(5,1)	(0,0)	3
					(4,1)	(2,0)	(2,0)	4
						(5,1)	(4,1)	5
							(2,0)	6

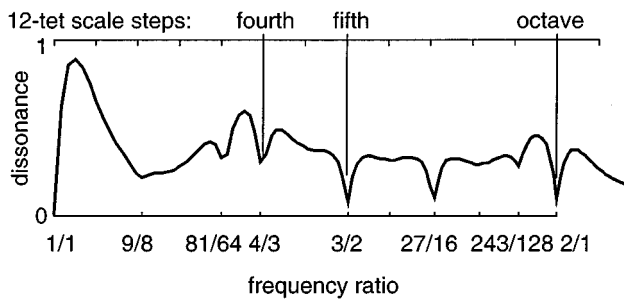


FIG. 4. Dissonance curve for the spectrum specially designed for play in the Pythagorean diatonic scale has minima at all the specified scale steps. Two extra "broad" minima are not caused by coinciding partials.

Equation (3) expresses the desire to have all of the intervals between all of the partials be scale intervals. A set of s_j are given (which are defined by previous choices of the t_j). Solving this requires finding a single s_i such that Eq. (3) is well defined for all j up to $i-1$. This can be done by searching all the columns s_j for an element s_i in common. If found, then the corresponding value of $r_{i,i-j}$ is given in the leftmost column. Whether this step is solvable for a particular i, j pair depends on the structure of the table and on the particular choices already made for previous s_i . Solution techniques for (3) are discussed at length in the Appendix.

It is probably easiest to understand the procedure by working through an example. One spectrum related to the scale (1) is given in Table II. This shows the choice of t_i , the corresponding scale steps s_i (which are the t_i reduced back into the octave), and the $r_{i,k}$ that complete Eq. (3). Since all the s_i and $r_{i,k}$ are scale steps, this spectrum is complementary. Since all scale steps can be found among the s_i or $r_{i,k}$, the spectrum is complete. Hence the spectrum of Table II is perfect for this scale. To translate the table into frequencies for the partials, recall that the elements t_i express the powers of a and b times an unspecified fundamental f . Thus the first partial is $f_1 = a^3 b^3 f$, the second is $f_2 = a^5 b^5 f$, etc.

III. PERFECT SPECTRA FOR PYTHAGOREAN SCALES

The Pythagorean diatonic scale of Fig. 2 is constructed from two intervals a and b in the order a, a, b, a, a, a, b . Thus the scale steps are given by

$$\begin{array}{cccccc} 1 & a & a^2 & a^2 b & a^3 b \\ (0,0) & (1,0) & (2,0) & (2,1) & (3,1) \\ & a^4 b & a^5 b & & a^5 b^2 = 2 \\ & (4,1) & (5,1) & \text{and} & (5,2) = (0,0). \end{array} \quad (4)$$

Typically, $a^2 b$ is a pure fourth. Along with the condition that $a^5 b^2 = 2$, this uniquely specifies $a = 9/8$ and $b = 256/243$, and so the scale contains two equal tetrachords separated by the standard interval $9/8$. The \oplus -table for this Pythagorean scale is shown in Table III. These exact values are not necessary for the construction of the perfect spectra that follow, and it is not necessary that (5,2) be an exact octave; any "pseudo-octave"¹⁷ or interval of repetition will do.

Spectra can be assembled by following the procedure for symbolic spectrum construction, and one such spectrum is given in Table IV. Observe that all of the s_i and $r_{i,k}$ are scale steps, and that all seven scale steps are present among the s_i and the $r_{i,k}$. Hence this spectrum is perfect for the Pythagorean scale (4). Assuming the standard values for a and b , this spectrum has its partials at

$$f, 2f, 3f, 4f, \frac{81}{16} = 5.0625f, \frac{27}{4} = 6.75f, \quad (5)$$

$$\frac{243}{32} \approx 7.594f, \quad \text{and} \quad \frac{81}{8} = 10.125f.$$

The first several partials are harmonic, and this is the "closest" perfect Pythagorean spectrum to harmonicity. For example, there are no suitable partials between $(12,4) \approx 5$ and $(14,5) = 6.75$, and thus no way to closely approximate the sixth harmonic partial $6f$. It is easy to check that $(13,4)$ and $(14,4)$ are not scale steps, and that $(13,5) = (3,1)$ forms the interval ab with $(12,4)$. Since ab is not a scale step, $(13,5)$ cannot occur in a complementary spectrum. [However, $(13,5) = 6$ can be used if $(12,4)$ is replaced by $(11,4) = 9/2$. This would then sacrifice the accuracy of the fifth harmonic in order to increase the accuracy of the sixth. Trade-offs such as this are common.]

The dissonance curve for the Pythagorean spectrum (5) is shown in Fig. 4, under the assumption that the amplitude of the i th partial is 0.9^i . As expected from the principle of coinciding partials, this curve has minima that align with the scale steps. Thus there are significant minima at the just fourth and fifths, and at the Pythagorean third $81/64$ and the Pythagorean sixth $27/16$, rather than at the just thirds and sixths as in the harmonic dissonance curve from Fig. 1. This spectrum will not exhibit rough beating when its thirds or sixths are played in long sustained passages in the Pythagorean tuning. There are also two extra minimum which are very shallow and broad, and are not due to coinciding partials. The exact location and depth of these minima changes significantly as the amplitude of the partials are changed. As is usual for such extra minima, they are only barely distinguishable from the surrounding regions of the curve. Thus perfect spectra, as constructed by the symbolic procedure, do give dissonance curves with minima that correspond closely with scale steps of the desired scale.

IV. SPECTRUM FOR A DIATONIC TETRACHORD

A more general diatonic tetrachordal scale is constructed from three intervals a , b , and c in the order a, a, b, c, a, a, b . The scale steps are given by

$$\begin{array}{cccccc} 1 & a & ab & a^2 b & a^2 bc \\ (0,0,0) & (1,0,0) & (1,1,0) & (2,1,0) & (2,1,1) \\ & a^3 bc & a^3 b^2 c & & a^4 b^2 c = 2 \\ & (3,1,1) & (3,2,1) & \text{and} & (4,2,1) = (0,0,0). \end{array} \quad (6)$$

As before, $a^2 b$ is a pure fourth that defines the tetrachord. The new interval c is typically given by the interval remain-

TABLE V. \oplus -table for the tetrachordal scale defined in (6).

\oplus	(0,0,0)	(1,0,0)	(1,1,0)	(2,1,0)	(2,1,1)	(3,1,1)	(3,2,1)
(0,0,0)	(0,0,0)	(1,0,0)	(1,1,0)	(2,1,0)	(2,1,1)	(3,1,1)	(3,2,1)
(1,0,0)	(1,0,0)	*	(2,1,0)	*	(3,1,1)	*	(0,0,0)
(1,1,0)	(1,1,0)	(2,1,0)	*	*	(3,2,1)	(0,0,0)	*
(2,1,0)	(2,1,0)	*	*	*	(0,0,0)	(1,0,0)	(1,1,0)
(2,1,1)	(2,1,1)	(3,1,1)	(3,2,1)	(0,0,0)	*	*	*
(3,1,1)	(3,1,1)	*	(0,0,0)	(1,0,0)	*	*	(2,1,1)
(3,2,1)	(3,2,1)	(0,0,0)	*	(1,1,0)	*	(2,1,1)	*

ing when two tetrachords are joined, and so $c=9/8$. There are no standard values for a and b . Rather, many different combinations have been explored over the years. The \oplus -table for this diatonic tetrachordal scale is given in Table V. As before, it is not necessary that (4,2,1) be an exact octave, though it must define the intervals at which the scale repeats.

Spectra can be constructed by following the symbolic spectrum construction procedure, and one such spectrum is given in Table VI. Observe that all of the s_i and $r_{i,k}$ are scale steps and that all seven scale steps are present among the s_i or $r_{i,k}$. Hence this spectrum is perfect for the specified tetrachordal scale (6).

In order to draw the dissonance curve, it is necessary to pick particular values for the parameters a , b , and c . As mentioned above, $c=9/8$ is the usual difference between two tetrachords and the octave. Somewhat arbitrarily, let $b=10/9$, which, combined with the condition that $a^2b=4/3$ (i.e., forms a tetrachord) implies that $a=\sqrt{6/5}$. With these values, the spectrum defined in Table VI is

$$f, 2f, 3f, 4f, 6.57f, 8f, 12f, \text{ and } 16f,$$

and the resulting dissonance curve is given in Fig. 5 when the amplitude of the i th partial is 0.9^i . Minima occur at all scale steps except the first, the interval a . While this may seem like a flaw, it is really quite normal for very small intervals (like the major second) to fail to be consonant; the Pythagorean spectrum of the previous section was quite atypical in this respect. Again, although a few broad minima occur, they are fairly undistinguished from the surrounding intervals. Thus the symbolic method of spectrum construction has again found a spectrum that is well suited to the desired scale.

TABLE VI. A perfect spectrum for the tetrachordal scale (6).

i	1	2	3	4	5	6	7	k
t_i	(4,2,1)	(6,3,2)	(8,4,2)	(11,5,3)	(12,6,3)	(14,7,4)	(16,8,4)	
s_i	(0,0,0)	(2,1,1)	(0,0,0)	(3,1,1)	(0,0,0)	(2,1,1)	(0,0,0)	
$r_{i,k}$		(2,1,1)	(2,1,0)	(3,1,1)	(1,1,0)	(2,1,1)	(2,1,0)	1
			(0,0,0)	(1,0,0)	(0,0,0)	(3,2,1)	(0,0,0)	2
				(3,1,1)	(2,1,0)	(2,1,1)	(1,1,0)	3
					(0,0,0)	(0,0,0)	(0,0,0)	4
						(2,1,1)	(2,1,0)	5
							(0,0,0)	6

V. WHEN PERFECTION IS IMPOSSIBLE

The above examples may lull the unsuspecting into a belief that perfect spectra are possible for any scale. Unfortunately, this is not so. Consider first a simple scale built from three arbitrary intervals a , b , and c in the order a, b, c, a . The scale steps are

$$\begin{array}{ccccccc} 1 & a & ab & abc & & a^2bc=2 & \\ (0,0,0) & (1,0,0) & (1,1,0) & (1,1,1) & \text{and} & (2,1,1)=(0,0,0) & \end{array} \quad (7)$$

As suggested by the notation, (2,1,1) serves as the basic unit of repetition which would likely be the octave. The \oplus -table for this scale is given in Table VII.

The difficulty with this scale is that the element (1,1,0) cannot be combined with any other. The symbolic construction procedure requires at each step that the s_i be expressible as a \oplus -sum of s_j and some $r_{i,k}$. But it is clear that the operation does not allow (1,1,0) as a product with any element [other than the identity (0,0,0)] due to the column of asterisks. In other words, if the interval (1,1,0) ever appears as a partial in the spectrum or as one of the $r_{i,k}$, then the construction process must halt since no more complementary partials can be added. In this particular example, it is possible to create a perfect spectrum by having the element (1,1,0) appear only as the very last partial. However, such a strategy will not work if there are two columns of asterisks.

An extreme example for which no perfect spectrum is possible is a scale defined by four different intervals a , b , c , and d taken in alphabetical order. The scale steps are

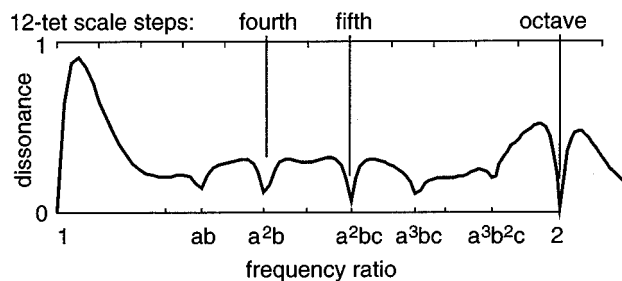


FIG. 5. The dissonance curve for the spectrum related to the diatonic tetrachord with $a^2=6/5$, $b=10/9$, and $c=9/8$, has minima at all scale steps except for the first. The broad minima at 1.16, 1.41, and 1.71 are not caused by coinciding partials.

$$\begin{array}{ccccccc} 1 & a & ab & abc & & abcd=2 & \\ (0,0,0,0) & (1,0,0,0) & (1,1,0,0) & (1,1,1,0) & \text{and} & (1,1,1,1) & = (0,0,0,0) \end{array} \quad (8)$$

As suggested by the notation, (1,1,1,1) serves as the basic unit of repetition which would likely be the octave. The \oplus -table for this scale is given in Table VIII.

Partials of a complementary spectrum for this scale can only have intervals that are multiples of the octave (1,1,1,1) due to the preponderance of disallowed asterisk entries in the \oplus -table. The only possible complementary spectrum is $(0,0,0,0)f$, $(1,1,1,1)f$, $(2,2,2,2)f$, etc., which is clearly not complete, and hence not perfect. Thus a given scale may or may not have perfect spectra, depending on the number and placement of the asterisk entries in the table.

VI. DISCUSSIONS AND CONCLUSIONS

A. Related versus perfect spectra

Do not confuse the idea of a spectrum related to a given scale with the notion of a perfect (complete and complementary) spectrum for the scale. The former is based directly on a psychoacoustic measure of the perceived sensory dissonance of the sound, while the latter is a construction based on the coincidence of partials within the spectrum. The latter is best viewed as an approximation and simplification of the former, in the sense that it leads to a tractable system for spectrum determination via the principle of coinciding partials.

Some scale intervals that appear in the spectrum (i.e., among the s_i or the $r_{i,k}$ of Tables II, IV, or VI) may not be minima of the dissonance curve. For instance, the tetrachordal spectrum of Sec. IV does not have a minimum at the first scale step even though the spectrum is complete. Alternatively, some minima may occur in the dissonance curve that are not explicitly ratios of partials. Three such minima occur in Fig. 5; they are the broad kind of minima that are due to wide spacing between certain pairs of partials.

The notion of a perfect spectrum shows starkly that the most important feature of related spectra and scales are the coincidence of partials of a tone, a result that would not have surprised Helmholtz. Perhaps the crucial difference is that related spectra take explicit account of the amplitudes of the partials, whereas perfect spectra do not. In fact, by manipulating the amplitudes of the partials, it is possible to make various minima appear or disappear. For instance, it is possible to “fix” the problem that the tetrachordal spectrum is missing its first scale step a by increasing the amplitudes of the partials that are separated by the ratio a . Alternatively, it is often possible to remove a minimum from the dissonance curve of a perfect spectrum by decreasing the amplitudes of the partials separated by that interval. Moreover, while a minimum due to coinciding partials may be extinguished by manipulating the amplitudes, its location (the interval it forms) remains essentially fixed. In contrast, the broad type minima that are not due to coinciding partials move continuously as the amplitudes vary; they are not a fixed feature of the dissonance curve of a perfect spectrum. In choosing the

amplitudes of the partials of a perfect spectrum, care must also be taken to avoid masking one partial by another.

B. Almost perfect spectra

As the number of different intervals in a desired scale increases, it becomes more difficult to find perfect spectra; the \oplus -tables become less full (i.e., have more disallowed asterisk entries) and fewer solutions to Eq. (3) exist. There are several simple modifications to the procedure that may result in spectra that are well matched to the given scale, even when perfection is impossible. One simple modification is to allow the spectrum to be incomplete. Since very small intervals are unlikely to be consonant with any reasonable amplitudes of the partials, they may be safely removed from consideration. A second simplifying strategy is to relax the requirement of complementarity, while it is certainly important that prominent scale steps occur at minima, it is not obviously harmful if some extra minima exist. Indeed, if an extra minimum occurs in the dissonance curve but never appears in the music, then its existence is transparent to the listener.

A third method of relaxing the procedure can be applied whenever the scale is specified only over an octave (or over some pseudo-octave), in which case the completeness and complementarity need only hold over each octave. For instance, a partial t_i might be chosen even though it forms a disallowed interval with a previous partial t_j , providing the two are more than an octave apart. Thus judicious relaxation of various elements of the procedure may allow specification of useful spectra even when perfect spectra are not possible.

C. The mathematician's view

From a mathematical point of view, the symbolic spectrum selection procedure raises a number of interesting issues. The \oplus operation defined here is not any kind of standard mathematical operator because of the disallowed asterisk entries. Though they do not form any recognizable algebraic structure, \oplus tables do have several features that would be familiar to an algebraist. For instance, the tables have an identity element, the operation \oplus is commutative, and it is associative when it is well defined. These are used in the Appendix to derive a set of properties that can be used to streamline the symbolic spectrum construction procedure.

\oplus -tables clearly have a significant amount of structure. For instance, any \oplus -table can be viewed as a subset of the commutative group of integer m vectors $(\sigma_1, \sigma_2, \dots, \sigma_m)$ where the i th entry is taken mod n_i , from which certain elements have been removed. Can this structure be exploited? Another obvious question concerns the possibility of decomposing \oplus -tables in the same kind of ways that arbitrary groups are decomposed into normal subgroups. Might such a decomposition allow the building up of spectra for larger scales in terms of spectra for simpler scales?

TABLE VII. \oplus -table for the scale defined in (7).

\oplus	(0,0,0)	(1,0,0)	(1,1,0)	(1,1,1)
(0,0,0)	(0,0,0)	(1,0,0)	(1,1,0)	(1,1,1)
(1,0,0)	(1,0,0)	*	*	(0,0,0)
(1,1,0)	(1,1,0)	*	*	*
(1,1,1)	(1,1,1)	(0,0,0)	*	*

D. The composer's view

From the musical point of view, perfect spectra raise a number of issues. For instance, a given nonequal scale sounds different in each key because the set of intervals is slightly different. How would the use of perfect spectra influence the ability to modulate through various keys? Certain chords will become more or less consonant when played with perfect spectra than when played with harmonic spectra. What patterns of (non)harmonic motion are best suited to perfect spectra and their chords? Will perfect spectra be useful for some part of the standard repertoire, or will they be only useful for new compositions that directly exploit their strengths (and avoid their weaknesses)?

E. Informal experiments

Preliminary experiments with perfect spectra are encouraging. A simple “organ” sound with eight harmonic partials was generated via additive synthesis. A second organlike sound which is perfect for the Pythagorean scale was generated with partials specified in (5). All parameters except for the frequencies of the partials were identical. Both sound pleasant, if somewhat bland and “electronic.” The Pythagorean spectrum, though nonharmonic, gives a definite sense of pitch, and is well fused. It also has a slightly “brighter” sound, probably because the highest partials occur at somewhat higher frequencies than in the harmonic version. The Bach chorale “Aus Meine Herzens Grunde” was recorded as a standard MIDI file and comparisons were made between the piece when played in (1) 12-tet with the harmonic spectrum, (2) Pythagorean tuning (in G) with the harmonic spectrum, (3) Pythagorean tuning (in G) with the Pythagorean spectrum, and (4) 12-tet with the Pythagorean spectrum. The differences between the four versions are subtle, but clear. For instance, there are several sustained major thirds between the alto and soprano lines, as in measures 4, 10, 13, and 16. In 12-tet, beats can be readily perceived between these two voices. The beats are even more pronounced in the Pythagorean tuning due to the stretching of the thirds. However, when the perfect spectrum is played in its related scale, the beats disappear, and the clarity of the chord increases. The fourth case is only marginally distinguishable from the first two, emphasizing that the Pythagorean spectrum itself is not overly bizarre.

It is certainly not true that all music will sound greatly improved (or even much different) when employing perfect spectra. For instance, the stylistically similar Bach chorale “Als der Gütige Gott” (as was used in Ref. 9 to demonstrate the effect of stretched spectra) does not show the same effect. With this piece, there is almost no noticeable difference (other than the brightness of the spectrum) between the per-

TABLE VIII. \oplus -table for the simple scale defined in (8).

\oplus	(0,0,0,0)	(1,0,0,0)	(1,1,0,0)	(1,1,1,0)
(0,0,0,0)	(0,0,0,0)	(1,0,0,0)	(1,1,0,0)	(1,1,1,0)
(1,0,0,0)	(1,0,0,0)	*	*	*
(1,1,0,0)	(1,1,0,0)	*	*	*
(1,1,1,0)	(1,1,1,0)	*	*	*

fect and harmonic versions. On investigation, it became clear that this is because there are no sustained major thirds in the chorale; the “held” chords are all inversions that avoid close position major thirds. Hence the piece avoids resolving to those chords that would sound most aggressive in the Pythagorean tuning.

F. Nonharmonic sounds

Exploiting nonharmonic sounds is a topic of considerable interest to the computer music community,^{18,19} and the notion of perfect spectra helps to specify classes of potentially useful nonharmonic sounds. Perfect spectra stipulate the frequencies of the partials, but leave the amplitudes free. Since spectrum is just one aspect of timbre, many different timbres may share a given spectrum. For instance, brassy timbres arise (at least in part) from a rise in the spectral energy in the higher partials, while flute timbres are dependent on a breathy puff in the attack. (For an overview of the physical correlates of timbre, see Ref. 20.) For spectra such as the Pythagorean, with partials that are detuned only a few percent from harmonic, it is likely that analogous increases in the energy of the higher partials will tend to be heard as trumpetlike, while breathy puffs of air in the attack will tend to cause the sound to appear flutelike. Thus each perfect spectrum defines a whole class of timbres which may sound as different from each other as a trumpet from a flute.

Finally, the method does not give any indication of how such sounds might be generated or created. One obvious way is via additive synthesis. Another is via the technique of “spectral mapping”,²¹ which directly manipulates the partials of a sampled sound. A much more difficult question is how acoustic instruments might be given the kinds of deviations from harmonicity that are specified by perfect spectra.

APPENDIX: PROPERTIES OF \oplus -TABLES

Given any set of scale intervals S , the \oplus -table derived from S has the following characteristics.

Identity: The “octave” or unit of repetition s^* acts as an identity element, i.e.,

$$s^* \oplus s = s \oplus s^* = s \quad \forall s \in S.$$

Commutativity: The \oplus -table is symmetric, i.e.,

$$s_1 \oplus s_2 = s_2 \oplus s_1 \quad \forall s_1, s_2 \in S. \quad (\text{A1})$$

If one side of (A1) is undefined (is “equal” to *), then so is the other. Commutativity of \oplus follows directly from the commutativity of products of powers of real numbers.

Associativity: The \oplus operator is associative whenever it is well defined. Thus

$$(s_1 \oplus s_2) \oplus s_3 = s_1 \oplus (s_2 \oplus s_3) \quad \forall s_1, s_2, s_3 \in S \quad (\text{A2})$$

provided that both sides of (A2) exist.

It is indeed possible for one side of (A2) to exist but not the other.

Example: The tetrachordal scale (6) has \oplus -Table V. Observe that $((2,1,1) \oplus (1,0,0)) \oplus (2,1,0)$ is well defined and equals $(1,0,0)$, but that $(2,1,1) \oplus ((1,0,0) \oplus (2,1,0))$ does not exist because $(1,0,0) \oplus (2,1,0)$ is disallowed. To further emphasize how unusual this construction is, observe that by commutativity, $(2,1,1) \oplus (1,0,0) = (1,0,0) \oplus (2,1,1)$. Substituting this in the above calculation gives $((1,0,0) \oplus (2,1,1)) \oplus (2,1,0)$ which is indeed equal to $(1,0,0) \oplus ((2,1,1) \oplus (2,1,0))$, since both sides are $(1,0,0)$.

The remaining properties of \oplus -tables concern “solutions” to the equation

$$s_i = s_j \oplus r_{i,i-j} \quad (\text{A3})$$

that arises in the symbolic spectrum construction procedure. Recall that in the procedure, a set of s_j are given (which are defined by previous choices of the t_j). The goal is to find a single s_i such that Eq. (A3) is well defined for all j up to $i-1$. The properties of \oplus -tables can help pinpoint viable solutions to (A3).

Theorem A.1: Suppose that $s_j \in S$ have been chosen for all $j < k$. Let \mathbf{S}_j be the set of all non-* entries in the s_j column of the \oplus -table. Then for all $i \geq k$, s_i must be an element of $\bigcap_{j < k} \mathbf{S}_j$.

Proof: First consider the case $i = k = 2$, with s_1 specified. Then (A3) requires choice of s_2 such that $s_2 = s_1 \oplus r_{1,1}$ for some $r_{1,1}$. Such $r_{1,1}$ will exist exactly when $s_2 \in \mathbf{S}_1$. For $i > 2$, $s_i = s_1 \oplus r_{i,i-1}$ must be solvable, which again requires that $s_i \in \mathbf{S}_1$. The general case $s_i = s_j \oplus r_{i,i-j}$ is similarly solvable exactly when $s_i \in \mathbf{S}_j$. Since this is true for every $j < k$, $s_i \in \bigcap_{j < k} \mathbf{S}_j$. \square

Thus when building spectra according to the procedure, the set $\mathcal{S}^k = \bigcap_{j < k} \mathbf{S}_j$ defines the allowable partials at the k th step. Clearly, \mathcal{S}^k can never grow larger since $\mathcal{S}^k \supset \mathcal{S}^{k+1} \forall k$, and it may well become smaller as k increases. This demonstrates that the order in which the partials are chosen is crucial in determining whether a perfect spectrum is realizable.

The easiest way to appreciate how the theorem A.1 simplifies (and limits) the selection problem is by example.

Example: In Table I, once $s_i = (3,2)$ for some i , then for all $k > i$, s_k must be $(3,2)$, $(1,0)$, or $(2,1)$.

Example: In Table III, once $s_i = (2,0)$ has been chosen, then for all $k > i$, s_k must be either $(2,0)$, $(4,1)$, or $(5,1)$. In particular, no s_k can be the identity $(0,0)$.

Corollary A.1: Suppose that an element $\hat{s} \in S$ appears in every column of the \oplus -table. Then for any choice of s_j , $j < i$, (A3) is always solvable with $s_i = \hat{s}$.

Proof: Since \hat{s} is in every column of the table, $\hat{s} \in \mathbf{S}_j \forall j$ and hence $\hat{s} \in \bigcap_{j < k} \mathbf{S}_j$ for any k . \square

In other words, for any $s \in S$, there is always a $r \in S$ such that $\hat{s} = s \oplus r$, and so \hat{s} is always permissible.

Example: In Table V, the identity $s^* = (0,0,0)$ appears in every column. Thus it is always possible to choose a partial t_i with the equivalence class s^* at any step.

Suppose, on the other hand, that an element $\bar{s} \in S$ appears nowhere in the \oplus -table other than in the column and row of the identity. Then \bar{s} cannot be used to define one of the s_i since $\bar{s} \notin \mathbf{S}_k$ for any k and so for any $s_i \neq s^*$, $s_i = \bar{s} + r$ has no solution. Although \bar{s} cannot occur among the s_i , it is still possible that it might appear among the $r_{i,k}$. Indeed, it will need to in order to find a complete spectrum.

Example: The element $\bar{s} = (2,1)$ appears nowhere in \oplus -table III defined by the Pythagorean scale. The spectrum was made complete by ensuring that \bar{s} appears among the $r_{i,k}$ of Table IV.

Another property of \oplus -tables is that elements are arranged in “stripes” from southwest to northeast. For instance, in Table III, a stripe of $(4,1)$ elements connects the $4,1$ entry with the $1,4$ entry. Similarly, a stripe of $(3,1)$ elements connect the $3,1$ with the $1,3$ entries, although the stripe is broken up by a *. The fact that such (possibly interrupted) stripes must exist is the content of the next theorem.

Given a m note scale S , the entries of the corresponding \oplus -table can be labeled as a matrix $\{a_{j,k}\}$ for $j = 1, 2, \dots, m$ and $k = 1, 2, \dots, m$. Let P_i denote the i th stripe of the \oplus -table, that is, $P_i = \{a_{j,k}\}$ for all j and k with $j+k = i+1$.

Example: For the Pythagorean \oplus -table,

$$P_1 = \{(0,0)\}, \quad P_2 = \{(1,0), (1,0)\},$$

$$P_3 = \{(2,0), (2,0), (2,0)\},$$

$$P_4 = \{(2,1), *, *, (2,1)\},$$

$$P_5 = \{(3,1), (3,1), *, (3,1), (3,1)\}, \text{ etc.}$$

Theorem A.2: For each i , all non-* elements of the stripe P_i are identical.

Proof: By construction, the elements s_i and $s_{i+1} \in S$ are integer vectors, and they may be ordered so that

$$s_{i+1} = s_i + e_{j,i} \forall i, \quad (\text{A4})$$

where $e_{j,i}$ is a unit vector with zeroes everywhere except for a single 1 in the j th entry. Let $\Sigma(s_i)$ represent the sum of the entries in $s_i = (\sigma_1, \sigma_2, \dots, \sigma_p)$, i.e., $\Sigma(s_i) = \sum_{j=1}^p \sigma_j$, and let Σ^* represent the sum of the entries in the element that forms the unit of repetition. Because the \oplus operation adds powers of the generating intervals,

$$\Sigma(s_j \oplus s_k) = \Sigma(s_j) + \Sigma(s_k) \pmod{\Sigma^*} \quad (\text{A5})$$

whenever $s_j \oplus s_k$ is well defined. Because of the ordering, the entries in the stripe P_i can be written

$$s_j \oplus s_k, \quad s_{j-1} \oplus s_{k+1}, \quad s_{j-2} \oplus s_{k+2} \dots$$

for all positive j and k with $j+k = i+1$. Hence

$$\Sigma(s_j \oplus s_k) = \Sigma(s_{j-1} \oplus s_{k+1}) = \dots \quad (\text{A6})$$

whenever these are defined. From (A4), $\Sigma(s_j) = \Sigma(s_k)$ implies that $s_j = s_k$. Hence (A6) shows that $s_j \oplus s_k = s_{j-1} \oplus s_{k+1} = \dots$ whenever the terms are defined, and hence all well-defined elements of the stripe are identical. \square

This is useful because stripes define whether a given choice for the t_i (and hence s_i) is likely to lead to complete

spectra. Suppose that \tilde{s} is a candidate for s_i at the i th step. Whether \tilde{s} will “work” for all previous s_j (i.e., whether $\tilde{s} = s_j \oplus r$ has solutions for all s_j) depends on whether \tilde{s} appears in all the corresponding \mathbf{S}_j . Theorem A.2 pinpoints exactly where \tilde{s} must appear, at the intersection of the column \mathbf{S}_j and the stripe containing \tilde{s} . Thus the procedure can be implemented without conducting a search for \tilde{s} among all possible columns.

A special case is when a column is “full,” i.e., when it contains no $*$ entries.

Theorem A.3: Let \mathbf{S}_f be a full column corresponding to $s_f \in S$. Then $s_i = s_f \oplus r_i$ is solvable for all $s_i \in S$.

Proof: Since there are m entries in the column \mathbf{S}_f and there are m different s_i , it is only necessary to show that no entries appear twice. Using the ordering (A4) of the previous proof, \mathbf{S}_f has elements

$$s_1 \oplus s_f, \quad s_2 \oplus s_f, \dots, s_m \oplus s_f, \quad (\text{A7})$$

which are well defined by assumption. Now proceed by contradiction, and suppose that the i th and j th elements of (A7) are the same, i.e., $s_i \oplus s_f = s_j \oplus s_f$. Then

$$\Sigma(s_i \oplus s_f) = \Sigma(s_j \oplus s_f) \pmod{\Sigma^*}$$

(where Σ and Σ^* were defined in the previous proof). This implies that

$$\Sigma(s_i) + \Sigma(s_f) = \Sigma(s_j) + \Sigma(s_f) \pmod{\Sigma^*}$$

which implies that $\Sigma(s_i) = \Sigma(s_j) \pmod{\Sigma^*}$. By the same argument as in the proof of theorem A.2, this implies that $s_i = s_j$. But each s_i appears exactly once in (A7), which gives the desired contradiction. \square

Thus when a column is full, it must contain every element. In this case, Eq. (A3) puts no restrictions on the choice of s_i . Let $\{s_j\}$ be all the elements of S that have full columns. Then a \oplus -subtable can be formed by these $\{s_j\}$ that has no illegal $*$ entries. For example, recall Table I which is generated by the scale (1). The elements (0,0), (1,1), and (2,2) have full columns and hence can be used to form a full \oplus -subtable. It is easy to generate perfect spectra for such full \oplus -subtables because Eq. (A3) puts no restrictions on the choice of partials for a complementary spectrum. Whether these extend to all elements of the scale, however, depends heavily on the structure of the nonfull part of the table. Finding spectra for full subtables is exactly the same as finding

spectra for equal temperaments, whose \oplus -tables have no disallowed $*$ entries. In fact, full \oplus -tables form a commutative group, which may explain why the equal tempered case is relatively easy to solve.

All of the above properties were stated in terms of the columns of the \oplus -table. By commutativity, the properties could have been stated in terms of the corresponding rows.

¹J. Tenney, *A History of ‘Consonance’ and ‘Dissonance’* (Excelsior, New York, 1988).

²R. Plomp and W. J. M. Levelt, “Tonal consonance and critical bandwidth,” *J. Acoust. Soc. Am.* **38**, 548–560 (1965).

³E. Terhardt, “Pitch, consonance, and harmony,” *J. Acoust. Soc. Am.* **55**, 1061–1069 (1974).

⁴N. Cazden, “The definition of consonance and dissonance,” *Int. Rev. Aesthetics Soc. Music* **11**, 123–168 (1980).

⁵W. A. Sethares, “Local consonance and the relationship between timbre and scale,” *J. Acoust. Soc. Am.* **94**, 1218–1228 (1993).

⁶W. A. Sethares, “Relating tuning and timbre,” *Exp. Musical Instrum.* **IX**, No. 2 (1993).

⁷A. Kameoka and M. Kuriyagawa, “Consonance theory part I: consonance of dyads,” *J. Acoust. Soc. Am.* **45**, 1452–1459 (1969); Also, “Consonance theory part II: consonance of complex tones and its calculation method,” *J. Acoust. Soc. Am.* **45**, 1460–1469 (1969).

⁸H. Helmholtz, *On the Sensations of Tone* (Dover, New York, 1954).

⁹A. J. M. Houtsma, T. D. Rossing, and W. M. Wagenaars, *Auditory Demonstrations* (Philips compact disc No. 1126-061 and text) (Acoustical Society of America, Woodbury, NY, 1987).

¹⁰S. Goldberg, *Genetic Algorithms in Search, Optimization, and Machine Learning* (Addison-Wesley, New York, 1989).

¹¹S. Kirkpatrick, C. D. Gelatt, and M. P. Vecchi, “Optimization by simulated annealing,” *Science* **220**, 4598 (1983).

¹²T. D. Rossing, *The Science of Sound* (Addison-Wesley, Reading, MA, 1990).

¹³D. B. Doty, *Just Intonation Primer* (Just Intonation Network, San Francisco, CA, 1993).

¹⁴J. M. Barbour, *Tuning and Temperament* (Michigan State College, East Lansing, 1951).

¹⁵J. Chalmers, Jr., *Divisions of the Tetrachord* (Frog Peak Music, Hanover, NH, 1993).

¹⁶S. Lang, *Algebra* (Addison-Wesley, Reading, MA, 1965).

¹⁷F. H. Slaymaker, “Chords from tones having stretched partials,” *J. Acoust. Soc. Am.* **47**, 1469–1571 (1968).

¹⁸W. Carlos, “Tuning: at the crossroads,” *Comput. Music J.* **Spring**, 29–43 (1987).

¹⁹M. V. Mathews and J. R. Pierce, “The Bohlen-Pierce scale,” in *Current Directions in Computer Music Research*, edited by M. V. Mathews and J. R. Pierce (MIT, Cambridge, MA, 1991).

²⁰D. M. Green, *An Introduction to the Psychology of Hearing* (Academic, New York, 1989), 3rd ed.

²¹W. A. Sethares, “Consonance-based spectral mappings,” *Comput. Music J.* (to appear in January 1998).

Optimal undercuts for the tuning of percussive beams

J. Petrolito and K. A. Legge

School of Science and Engineering, La Trobe University, Bendigo, Bendigo, VIC 3550, Australia

(Received 8 July 1996; revised 20 June 1997; accepted 25 June 1997)

The paper investigates the use of optimization techniques for the design of percussive beams. Profiles were generated to satisfy predetermined overtone tunings and specified optimization criteria. It is shown that there is no unique solution to the problem, and that the generated profiles need not be the same as traditionally used profiles. The vibration of the beams was modeled using a thick beam theory to take into account the possible effects of shear deformation on the natural frequencies. A number of beams were manufactured with the generated profiles, and their frequency characteristics were obtained experimentally. The experimental results confirm the validity of the numerically generated profiles. © 1997 Acoustical Society of America. [S0001-4966(97)01310-6]

PACS numbers: 43.75.Kk [WJS]

INTRODUCTION

The transverse modes generated when a uniform beam is struck between its two supports are not harmonic. In order to tune the beam so that at least the lowest of these modes is harmonically related, and therefore more pleasant to the ear, the makers of tuned idiophones, such as xylophones and marimbas, cut parabolic arches on the underside of the beams. Such an undercut results in a significant reduction to the frequency of the fundamental mode, with a lesser and variable effect on the higher modes. Hence, the length of the beam required for low notes is reduced, and the relationship between the various modes is controlled by the actual shape of the parabola. The extent to which xylophone and marimba bars are tuned and the actual ratio of the frequencies of the tuned overtones vary between instruments.¹ Typically, the lower notes have the first three modes tuned and the higher notes have only the first two modes tuned.

The actual dimensions of the undercut are an empirical design determined by tradition, and relate the subtleties of the sound produced with those favored by the human ear. In recent times, there has been an interest in investigating the effects of lateral cuts along the length of a beam, and in relating the empirical design to theory. The effect on the first four modes of the lateral cuts has been investigated by Bork,² and the optimal tuning of a xylophone bar preferred by the human ear has been experimentally determined by Bork and Meyer.^{3,4} Orduna-Bustamante⁵ applied numerical techniques to free, nonuniform beams, and was able to predict parabolic undercuts that closely resembled experimental results for requested tuning regimes. Summers *et al.*⁶ have simplified the undercut profile by replacing it with a rectangular cut. They have investigated the effect produced on the lowest two modes of the beam by variations in the height and length of a single rectangular undercut.

The current paper takes a more general approach to the problem, and follows previous work⁷ in which finite element analysis was used to determine the optimal undercut required to tune the xylophone bar. In this procedure, no assumption is made regarding the shape of the cut beyond ensuring that material is not added and that the structure remains a single beam. An optimization approach is then used to calculate the

profile of the beam to satisfy the prescribed frequencies. The calculated profile depends on the optimization criterion specified, and does not necessarily resemble the traditional cut. As is common, we have adopted a one-dimensional model to describe the behavior of the xylophone bar. However, the general procedure used can be extended to higher-order models if desired.

The precise definition of the xylophone supports is uncertain. Previous explanations for the response of xylophone bars generally assumed them to be free-free beams. In this study, we have designed the model so that it can account for a range of support conditions from completely free to simply supported. Hence, the model could also be used to study the effect of different support designs for xylophone bars.

I. GOVERNING EQUATIONS

The xylophone bar is modeled as a one-dimensional beam supported a small distance from each end, as shown in Fig. 1. The length of the overhangs is denoted L_1 and the length between the two supports is denoted L_2 . Since the dominant response of the struck beam is transverse, we will ignore any axial effects on the motion. There are various theories to describe the motion of beams under transverse loads, depending on the assumptions made regarding the effects of shear deformation on the motion. For beams with a large length to depth aspect ratio, classical beam theory is sufficient. While this theory will be applicable for the lower register of the xylophone, it has been shown to be an inappropriate model for the higher register when the length to thickness ratio is smaller.⁵

To account for both possibilities, the motion of the beam is therefore modeled using Timoshenko's beam theory,⁸ which is the simplest extension of the classical theory that can account for shear deformation. In this theory, the primary variables are the transverse displacement w and rotation θ , which are assumed to be independent. The moment M and shear force V in the beam are defined as

$$M = EI\theta', \quad V = kGA(w' - \theta), \quad (1)$$

where E is Young's modulus, $G = E/2(1 + \nu)$ is the shear modulus, ν is Poisson's ratio, I is the section modulus, A is

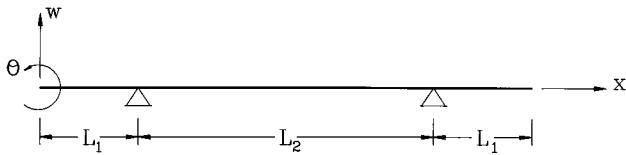


FIG. 1. Geometry and sign convention for the one-dimensional model of the xylophone bar.

the cross-sectional area, and k is the shear correction factor, which is usually taken as $5/6$ or $\pi^2/12$. A prime denotes differentiation with respect to x . As we are only interested in natural frequencies, we can formulate the problem in terms of the amplitudes of the displacement and rotation of the beam as it vibrates, which are denoted by $\bar{w}(x)$ and $\bar{\theta}(x)$. The theory results in a fourth-order system of coupled ordinary differential equations, namely

$$\begin{aligned} kGA(\bar{w}'' - \bar{\theta}') &= -\rho A \Omega^2 \bar{w}, \\ EI\bar{\theta}'' + kGA(\bar{w}' - \bar{\theta}) &= -\rho I \Omega^2 \bar{\theta}, \end{aligned} \quad (2)$$

where Ω is the natural frequency.

The beam is assumed to have a rectangular cross section with a constant width, b , and a varying height, $h(x)$. Hence, the sectional properties A and I are also functions of x with

$$A(x) = bh(x), \quad I(x) = bh(x)^3/12. \quad (3)$$

Finally, we consider the boundary conditions for a beam supported at $x=L_1$ and $x=L_1+L_2$. The supports are modeled by simple springs allowing motion in the vertical direction only. Each spring constant is selected as an option. Hence, each support can be selected as any condition within the range of simple support to completely free.

Analytical solutions of the governing equations can only be obtained for simple boundary conditions.⁸ In the present case with varying sectional properties, analytical solutions will not be possible, and hence a numerical solution is required. Moreover, the problem is not simply one of calculating the frequencies for a particular structure, but rather a case of finding a structure that will produce the required frequencies.

II. PROBLEM FORMULATION

The goal is to design a xylophone bar that responds with frequencies of specified ratios for the three lowest transverse modes without reference to the traditional parabolic undercut. Hence, we shall adopt a numerical approach as follows.⁷

In the current approach, the geometry of the beam is described by a number of parameters, which are the primary unknowns for the problem. An optimization procedure is used to determine the values of the parameters such that the beam has the desired frequency characteristics and satisfies other specified criteria. Clearly, a wide range of geometries could be adopted within this general framework. In this initial study, we have adopted a simple geometrical model for the beam, such that the vertical profile of the beam is divided into a number of sections of constant height. In addition, the beam is assumed to be symmetrical about its midlength point and its width is kept constant.

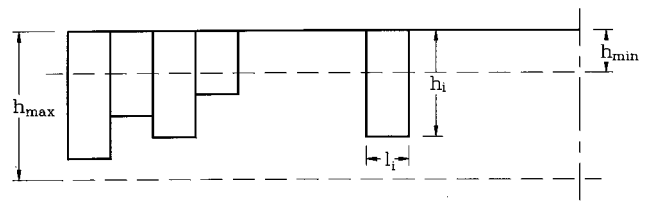


FIG. 2. The beam is discretised into N sections each with height h_i and length l_i . The uncut beam has height of h_{\max} .

Each half of the beam is discretised into N sections with height h_i , $i=1, \dots, N$ and length l_i , $i=1, \dots, N$ (see Fig. 2). In principle, both h_i and l_i can be treated as variables. However, there is no advantage in treating both as variables, and hence only the heights are taken as variables in this paper. The lengths l_i are fixed by the geometry of the beam and N . The response of the beam is thus a function of the h_i .

The problem is then treated as a constrained optimization problem where an optimization function $f(h_i)$, to be discussed below, is minimized subject to stated constraints $g_j(h_i)$, which in this case are the required natural frequencies together with some manufacturing constraints. Hence, we state the following optimization problem:

$$\text{Minimize } f(h_i) \quad \text{subject to } g_j(h_i) = 0, \quad j = 1, \dots, N_c, \quad (4)$$

where N_c is the number of constraints for the problem.

We associate the first N_f constraints with the required natural frequencies, and these constraints are nonlinear functions of the heights. The remaining $N_c - N_f$ constraints can be assumed to be associated with manufacturing constraints. As these constraints are difficult to specify without detailed knowledge of the manufacturing process, we will ignore them in this work and use $N_c = N_f$. However, we will impose restrictions on the permissible values of the heights.

We initially assume that the beam is uniform with all the h_i equal to h_{\max} , and, as previously stated, that the width of the beam is kept constant during manufacture. For ease of construction, it is desirable to restrict the variations in the h_i such that no material is added. Furthermore, to ensure that the beam remains structurally sound, a minimum height h_{\min} is specified. Hence, the variables h_i are bounded in the range

$$h_{\min} \leq h_i \leq h_{\max}, \quad i = 1, \dots, N. \quad (5)$$

Thus with the above formulation, the problem falls within the class of nonlinear optimization problems,⁹ and we have solved it using a sequential quadratic programming approach.¹⁰ Clearly, different solutions may be obtained by varying the function f . Moreover, we only attempt a local optimization, and hence the solution from this procedure may not be unique.

Two issues need to be resolved for the proposed procedure to be completed, namely (a) what optimization criterion is used, and (b) how the natural frequencies are calculated.

III. OPTIMIZATION CRITERIA

A number of optimizing criteria can be used and the use of different criteria will influence the results obtained. At this stage, there is no one criterion that can obviously be labeled

as the “best.” In practice, the ease of manufacture may well play a larger role than the mathematics can give credence to. For the present paper, we shall report on the investigation of two distinct classes of criteria.

In the first case, the amount of material removed from the beam is minimized, and the criterion is given as

$$f(h_i)=\sum_i^N (h_{\max}-h_i)l_i \tag{6}$$

since the width of the beam remains constant.

In the second case, an attempt is made to produce a profile that more closely mimics the standard profiles. To this aim, the criteria used depended on minimizing the difference between adjacent h_i to produce a smoother longitudinal profile of the beam. Three variations on this theme were reported previously.⁷ For brevity, we shall only explore one of these variations in this paper, namely the one that generally produced the smoothest profiles. For this case, two adjacent heights and a selectable weighting factor, α , are included in f , such that

$$f(h_i)=\sum_{i=1}^{N-1} (h_{i+1}-h_i)^2+\alpha\sum_{i=1}^{N-2} (h_{i+2}-h_i)^2. \tag{7}$$

The form of the above criterion has been chosen to ensure that f is always positive and differentiable. In addition, an

TABLE I. Frequency of the lowest three natural modes for a simply supported aluminium beam. All frequencies in Hz.

Mode No.	Theory	Measured
1	110	109
2	208	203
3	353	344

option was included that allowed the height changes to be restricted to the middle section of the beam, between the two supports.

IV. FREQUENCY CALCULATIONS

Due to the varying heights, a numerical approach is required for this phase of the solution. We have adopted a finite element approach with each section of the beam further discretized into a sufficient number of elements to ensure that the frequencies are calculated to a specified accuracy. A standard Timoshenko beam element with a consistent mass matrix was used,¹¹ and this element can also correctly model the classical beam theory if required. The formulation leads to a linear eigenvalue problem, which is solved using a Sturm sequence algorithm.¹²

Section	Height (a)	Height (b)
h_1	6.15	5.12
h_2	6.15	4.19
h_3	2.49	3.43
h_4	4.61	2.59
h_5	1.61	1.59

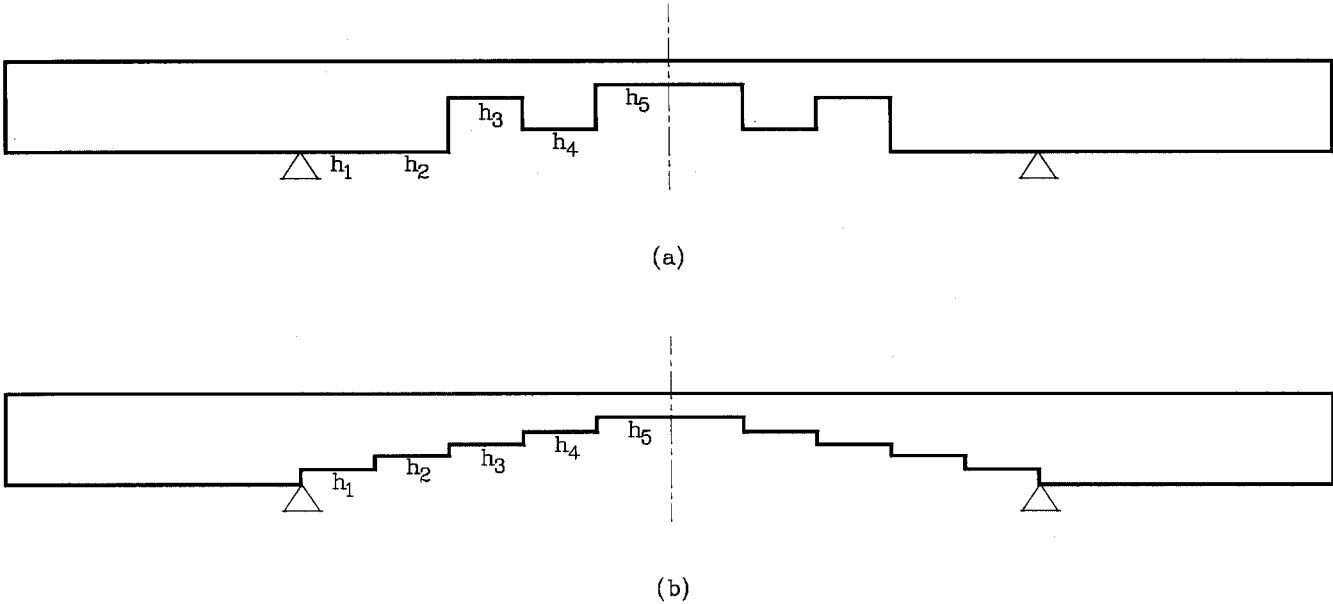


FIG. 3. Profiles of aluminum beams recorded in Table II. Optimization criterion: (a) minimum volume; (b) minimum height differences. Note that all dimensions are in millimeters and that the scale for length and height differ by a factor of 6.

TABLE II. A comparison of the measured frequencies of the first three modes for the aluminium beams depicted in Fig. 3 with the requested frequencies. All frequencies in Hz.

Mode No.	Requested	Measured profile Fig. 3(a)	Measured profile Fig. 3(b)
1	30	30	30
2	120	111	111
3	294	275	287

V. EXPERIMENT

A number of experimental investigations were performed with of the aim of supporting the theoretical formulation and the beam model. Generally, the bars of the xylophone and marimba are made from wood, although synthetic materials are sometimes used in modern instruments.¹ However, wood is a variable material, and it would be tempting to explain away inconsistencies by referring to its nonisotropic characteristics. With this in mind, we began with a simply supported aluminum beam to ascertain the accuracy of the theory, before attempting the investigations on a more problematic wooden beam.

Beams were constructed with profiles that had been generated by the aforementioned optimizing procedure. Normal mode frequencies were obtained for each of the beams by striking the beam with a xylophone beater and performing an FFT analysis on the resulting waveform. The waveform was detected by a Brüel & Kjaer subminiature accelerometer (type 4374) placed on the end of the beam under investigation. The output was fed via a Brüel & Kjaer charge amplifier (type 2651) to a 12-bit data acquisition board on a PC. It should be noted that the number of spectral lines in the FFT analysis limited the accuracy of the frequency measurements to 4 Hz. Such an accuracy would not be acceptable from a design point of view, particularly for low frequencies. However, since the goal of the present work is to verify the theoretical model, this accuracy was deemed acceptable.

The initial measurements were performed on a flat aluminum beam with $L_1=120$ mm and $L_2=300$ mm placed on two simple supports. The beam had a width of 20 mm and an uncut thickness of 6.15 mm. The physical properties of aluminum were taken as $E=71$ GPa, $\nu=0.3$, and $\rho=2700$ kg/m³. A shear correction factor of 5/6 was used in all calculations.

Table I compares the theoretical results with the results obtained experimentally. There is good agreement (within 3%) between theory and practice. The small discrepancies that do arise in the higher modes can be attributed to possible inaccuracies in the lengths L_1 and L_2 , the mass of the accelerometer (0.65 g) that was placed on the end of the beam, and inaccuracies in the material properties. The possible errors arising from such inaccuracies was investigated numerically. For example, a 1% change in L_1 and L_2 results in a shift of 1% in the frequencies of one or all of the modes. Similarly, a point mass of 0.65 g placed on the end of the beam alters the frequencies by up to 1%. The effect of reasonable variations in material properties amount to no more than one percent.

Next, a profile was generated for the same aluminum

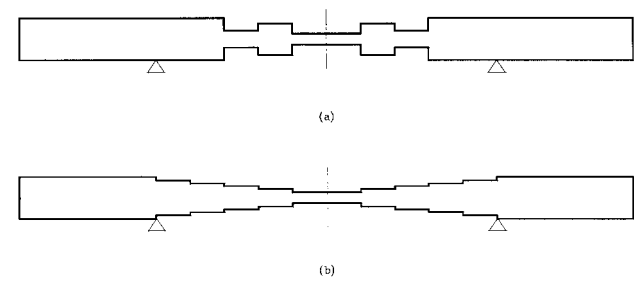


FIG. 4. Profiles of symmetric aluminum beams recorded in Table III. Optimization criterion: (a) minimum volume; (b) minimum height differences. Note scale for length and height differ by a factor of 6.

beam, such that the first three natural frequencies of the beam were 30, 120, and 294 Hz, respectively, thus following a possible marimba tuning regime⁴ of (1:4:9.8). Two different profiles were obtained using the optimizing criteria described earlier, and they are given in Fig. 3. For both cases, only the section of beam between the two supports was cut and five discretizations ($N=5$) were used. Profile (a) followed a request for minimum volume to be removed, whereas profile (b) followed a request for minimum height differences with $\alpha=0.5$. A comparison of the measured results for each beam against the requested frequencies are shown in Table II. The results again show good agreement, particularly in the prediction of the fundamental mode frequency. It is worth noting that the discrepancies between the predicted and measured values decrease for profile (b), which has less sharp steps between adjacent h_i . The one-dimensional model of the beam adopted cannot account for the complex stress state at the discontinuities of the beam profile. The significance of this effect increases with the sharpness of the step. For sharp steps, a two-dimensional model would improve the accuracy of the theory.

Both profiles were constructed with a flat top, consistent with a typical xylophone bar where ease of strike is important. However, there is a hidden assumption in the theory that the beam profile is symmetric about a horizontal axis along its center. In order to ascertain the effect such an assumption might have on the results, the two profiles were reconstructed with the implied symmetry (see Fig. 4) and the measurements were repeated. The results are depicted in Table III and show very little change from the previous results.

What the results do not show is the timbre of the sound generated by the aluminum beam. In order to produce a more musically satisfying note, the procedure was repeated on the wooden beam. As noted, both above and by Summers *et al.*,⁶

TABLE III. A comparison of the frequency of the lowest three modes for the aluminum beams depicted in Fig. 4 with the requested frequencies. All frequencies in Hz.

Mode No.	Requested	Measured profile Fig. 4(a)	Measured profile Fig. 4(b)
1	30	30	30
2	120	111	111
3	294	283	287

TABLE IV. Frequency of the lowest three natural modes for a wooden beam on spring supports. All frequencies in Hz.

Mode No.	Theory	Measured
1	377	378
2	1025	993
3	2002	1820

we are now dealing with a nonisotropic medium with variable mechanical properties.

The wooden beam used was a piece of kiln-dried Australian hardwood again with $L_1 = 120$ mm and $L_2 = 300$ mm. The beam had a width of 64 mm and an uncut thickness of 18.9 mm. The density was measured to be 648 kg m^{-3} . The elasticity of the sample was obtained by placing a sample of the wood in an extensometer, and obtaining a plot of the extension against the applied load. It was found to have a Young's modulus of 21 GPa to within an accuracy of 10%. Poisson's ratio was assumed to be 0.3. However, it should be noted that the effect of Poisson's ratio is limited since shear deformation is small for this example. Numerical tests confirmed that significant variations in Poisson's ratio had negligible effect on the frequencies. The beam was supported at L_1 and $L_1 + L_2$ on foam rubber strips that had a measured spring stiffness in the vertical direction of $2.9 \times 10^4 \text{ N m}^{-1}$.

Again, an uncut beam was initially investigated. Table IV compares the theoretical results with the results obtained experimentally. The results are reasonable given the nonisotropic nature of the material, with only the third frequency being outside the experimental error range. The accuracy of the results is consistent with the expectation that variations in material properties will have a greater influence on the higher modes.

Finally, two profiles were generated for the wooden beam using the minimum height difference criterion, and

TABLE V. Profiles of cut wooden beams. All heights in mm.

Section	Height
Profile (a)	
1	14.1
2	8.2
3	6.8
Profile (b)	
1	13.0
2	12.8
3	12.5
4	11.9
5	11.3
6	10.5
7	9.6
8	8.6
9	7.6
10	6.9
11	6.6
12	6.6
13	6.9
14	7.1
15	7.3

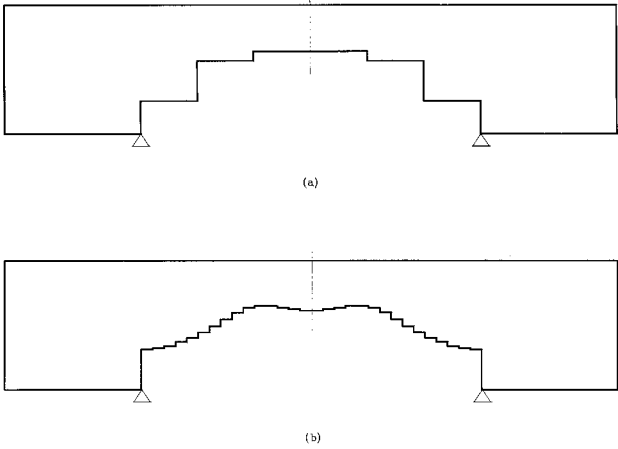


FIG. 5. Profiles of wooden beams with heights as specified in Table V. Note that the scale for length and height differ by a factor of 6.

with only the section between the two supports cut. The first profile (a) used 3 discretizations ($N = 3$) and the second profile (b) used 15 discretizations ($N = 15$) (see Table V and Fig. 5). In both cases, the beams were constructed with a flat top. The first three natural frequencies were requested to be 128, 512, and 1280 Hz, respectively. The results are given in Table VI.

The fundamental frequency compares well between prediction and measurement for profile (a). It should be noted that the measured results for the second profile (b) produced a fundamental discernibly flatter than predicted. Since the previous fundamental frequencies have been quite accurate, and given that the properties of wood can vary markedly between pieces, it has been assumed that this discrepancy is due to variations in the dominant physical properties, namely Young's modulus and density. That being so, we have adjusted the results so that the fundamental is as predicted, and the higher modes have the same ratio to the fundamental as those that were measured, and the adjusted results are also given in Table VI.

The measured frequencies of the higher modes are comparatively low, with the smoother profile again producing better agreement. Hence, the results suggest that the sophistication of the model used to describe the vibration of xylophone bars may be important for cases where high accuracy is required.

VI. CONCLUSIONS

This paper has presented a general, numerical technique for tuning xylophone bars, and compared the results with experimental data. As a specific example, the bar was modeled by a one-dimensional stepped beam. No other assump-

TABLE VI. Frequency of the lowest three natural modes for a wooden beam on spring supports. All frequencies in Hz.

Mode No.	Theory	Measured $N = 3$	Measured $N = 15$	Adjusted $N = 15$
1	128	125	117	128
2	512	475	461	504
3	1280	1148	1141	1248

tions were made regarding the profile of the bar, beyond ensuring that no material is added and that the structure remains a single beam. It was shown that different solutions that satisfy the constraints may be obtained depending on the optimizing criterion used, and that the resulting profiles are not necessarily the same as traditional profiles. The experimental data obtained validated the procedure, but indicated that the theoretical model does not completely account for the effects due to sharp steps in the beam profile. Hence, smoother profiles compared more favorably with the theoretical model used.

In summary, the present paper has established the use of optimization techniques in the general area of acoustic design. While the technique is general, the attainable accuracy depends on the appropriateness of the mathematical model used for the problem at hand. Hence, for the problem presented, the accuracy could be improved by using a higher-order theory or alternative specifications for the beam profile. Such studies are currently under investigation.

¹N. H. Fletcher and T. D. Rossing, *The Physics of Musical Instruments* (Springer-Verlag, New York, 1991).

- ²I. Bork, "Zur Abstimmung und Kopplung von Schwingenden Stäben und Hohlraumresonatoren," dissertation, Tech. Univ. Carolo-Wilhelmina, Braunschweig, 1983.
- ³I. Bork and J. Meyer, "On the tonal evaluation of xylophones," *Percussive Notes* **23**, 48–57 (1985).
- ⁴I. Bork, "Practical tuning of xylophone bars and resonators," *Appl. Acoust.* **46**, 103–127 (1995).
- ⁵F. Orduna-Bustamante, "Nonuniform beams with harmonically related overtones for use in percussion instruments," *J. Acoust. Soc. Am.* **90**, 2935–2941 (1991).
- ⁶I. R. Summers, S. Elsworth, and R. Knight, "Transverse vibrational modes of a simple undercut beam: An investigation of overtone tuning for keyed percussion instruments," *Acoust. Lett.* **17**, 66–70 (1993).
- ⁷J. Petrolito and K. A. Legge, "Optimizing the xylophone: A numerical approach," *Proceedings of the Computational Techniques and Applications Conference, CTAC95*, 625–630 (1996).
- ⁸C. L. Dym and I. H. Shames, *Solid Mechanics: A Variational Approach* (McGraw-Hill, New York, 1973).
- ⁹M. S. Bazaraa, H. D. Sherali, and C. M. Shetty, *Nonlinear Programming: Theory and Algorithms* (Wiley, New York, 1993), 2nd ed.
- ¹⁰D. Kraft, A Software Package for Sequential Quadratic Programming, DFVLRFB 88-28, Köln, Germany.
- ¹¹J. S. Przemieniecki, *Theory of Matrix Structural Analysis* (McGraw-Hill, New York, 1968).
- ¹²R. D. Cook, D. S. Malkus, and M. E. Plesha, *Concepts and Applications of Finite Element Analysis* (Wiley, New York, 1989), 3rd ed.

LETTERS TO THE EDITOR

This Letters section is for publishing (a) brief acoustical research or applied acoustical reports, (b) comments on articles or letters previously published in this Journal, and (c) a reply by the article author to criticism by the Letter author in (b). Extensive reports should be submitted as articles, not in a letter series. Letters are peer-reviewed on the same basis as articles, but usually require less review time before acceptance. Letters cannot exceed four printed pages (approximately 3000–4000 words) including figures, tables, references, and a required abstract of about 100 words.

Green's tensor function for Lamb's problem: The general anisotropic case

Martin Spies

Fraunhofer-Institut Zerstörungsfreie Prüfverfahren (IZFP), Universität des Saarlandes, Geb. 37, 66123 Saarbrücken, Germany

(Received 20 September 1996; revised 19 June 1997; accepted 2 July 1997)

The complete solution of Lamb's three-dimensional problem of determining the elastic disturbance resulting from a point force in a half-space is addressed. The derived expression for the half-space Green's function is valid for a general anisotropic medium and is given in a two-dimensional space–time spectral representation, which is well-suited for numerical evaluation. It is expressed with respect to the displacement and traction vectors involved as well as the full-space Green's dyadic (or displacement tensor) and triadic (or stress tensor) functions. © 1997 Acoustical Society of America. [S0001-4966(97)04410-X]

PACS numbers: 43.20.Bi, 43.20.Gp, 43.35.Cg, 43.35.Zc [JEG]

INTRODUCTION

Since Lamb's famous paper,¹ published in 1904, the problem of the elastic displacements resulting from a point force in a half-space has been the subject of numerous studies. The three-dimensional problem has been treated by several authors, representatively Cagniard,² Pekeris,^{3,4} and de Hoop⁵ are named here, all of them treating the case of an isotropic material. A solution in form of a Green's function, convenient for numerical evaluation, was given by Johnson,⁶ also for the isotropic case.

An extensive treatment of the half-space problem for a transversely isotropic (TI) medium has been performed by Kraut,⁷ the axis of material symmetry being perpendicular to the surface. Unlike the isotropic problem, the orientation of the axes relative to the half-space surface makes a considerable difference in the complexity of the analysis for the corresponding solid. Payton⁸ has complemented the studies on TI materials by giving explicit closed form solutions for specific two- and three-dimensional configurations. Burridge⁹ has analyzed Lamb's problem for a general anisotropic solid in which the surface has no particularly symmetrical orientation with respect to the (crystallographic) axes of the medium.

In this Letter, the case of a general anisotropic half-space is also considered. Its purpose is to provide a—relatively—simple expression directly reflecting the underlying physics. The solutions of Lamb's problem are thought of as the tensor Green's function for the elastic wave equation in a uniform half-space. Thus it represents the starting point for the consideration of sources, which are more

complicated than simple point sources. The dyadic function is derived in a two-dimensional space–time spectral representation in a way similar to Johnson.⁶ Accordingly, the relationships given there can be obtained by replacing the anisotropic material parameters by isotropic ones. The general relationships presented in this letter have previously been specialized to the transversely isotropic case, corresponding analytical and numerical evaluations can be found in Refs. 10–12.

I. PLANE WAVES IN FULL-SPACE MEDIA

The equation of motion for the displacement vector \mathbf{u} in a homogeneous anisotropic solid reads¹³

$$(\nabla \cdot \mathbf{C} \cdot \nabla) \cdot \mathbf{u}(\mathbf{R}, t) - \rho \frac{\partial^2}{\partial t^2} \mathbf{u}(\mathbf{R}, t) = -\mathbf{f}(\mathbf{R}, t), \quad (1)$$

and is explicitly dependent on space \mathbf{R} and time t . Here ∇ is the gradient vector and \mathbf{f} accounts for the volume force density. The material is characterized by the elastic stiffness tensor \mathbf{C} and the density ρ .

Applying Fourier transforms with respect to t and \mathbf{R} in terms of

$$\mathbf{u}(\mathbf{R}, \omega) = \int_{-\infty}^{\infty} \mathbf{u}(\mathbf{R}, t) e^{j\omega t} dt, \quad (2)$$

$$\mathbf{u}(\mathbf{K}, \omega) = \int_{-\infty}^{\infty} \int_{-\infty}^{\infty} \int_{-\infty}^{\infty} \mathbf{u}(\mathbf{R}, \omega) e^{-j\mathbf{K} \cdot \mathbf{R}} d^3\mathbf{R} \quad (3)$$

to the equation of motion (1) yields the dispersion equation

$$\tilde{\mathbf{W}}(\mathbf{K}, \omega) \cdot \tilde{\mathbf{u}}(\mathbf{K}, \omega) = \tilde{\mathbf{f}}(\mathbf{K}, \omega), \quad (4)$$

where the tilde denotes the transformed quantities. In this equation, the 3-D space-time Fourier representations of \mathbf{u} and \mathbf{f} appear as well as the wave matrix

$$\tilde{\mathbf{W}}(\mathbf{K}, \omega) = \mathbf{K} \cdot \mathbf{C} \cdot \mathbf{K} - \rho \omega^2 \mathbf{I}. \quad (5)$$

The plane wave solutions follow from the homogeneous dispersion equation

$$\tilde{\mathbf{W}}(\mathbf{K}, \omega) \cdot \tilde{\mathbf{u}}(\mathbf{K}, \omega) = \mathbf{0}, \quad (6)$$

the polarization vectors $\hat{\mathbf{u}}^\alpha$ and the wave numbers K_α can be obtained as the eigenvectors and the eigenvalues of the wave matrix $\tilde{\mathbf{W}}(\mathbf{K}, \omega)$. For transversely isotropic materials with arbitrary orientation of the rotational symmetry axis (TIA media), these solutions have been given previously.¹⁰

The differences between elastic wave propagation in isotropic and anisotropic media are already evident in the propagation of plane waves in a homogeneous region with a horizontal boundary. In an isotropic medium, one can distinguish between the compressional (P) and the horizontally or vertically polarized shear waves (SH and SV). The decomposition into these three eigenwaves is based on the orientation of the polarization vectors with respect to the horizontal plane. In a weakly anisotropic medium, the plane waves can still be labeled as quasi- P (qP), with approximately longitudinal polarization, and quasi- SH (qSH) and quasi- SV (qSV), with approximately transverse polarization. In a strongly anisotropic medium, there are three plane waves with mutually orthogonal polarizations in every direction of propagation. The identification of the waves according to specific dominant polarizations is now meaningless; therefore the three waves are designated according to their polarizations when propagated in certain symmetry directions. Thus the waves will in the following be labeled qP , $qS1$, and $qS2$.

II. FULL-SPACE GREEN'S FUNCTIONS

Green's dyadic function \mathbf{G} is defined by the differential equation¹³

$$(\nabla \cdot \mathbf{C} \cdot \nabla) \cdot \mathbf{G}(\mathbf{R}, t) - \rho \frac{\partial^2}{\partial t^2} \mathbf{G}(\mathbf{R}, t) = -\mathbf{I} \delta(\mathbf{R}) \delta(t), \quad (7)$$

where δ is Dirac's delta function. Application of spatial and temporal Fourier transforms (FT) with respect to \mathbf{R} and t results in

$$\tilde{\mathbf{W}}(\mathbf{K}, \omega) \cdot \tilde{\mathbf{G}}(\mathbf{K}, \omega) = \mathbf{I}. \quad (8)$$

Thus the 2-D space-time spectral representation—transformed with respect to x and y and indicated by a hat—is determined by one-dimensional inverse FT according to

$$\hat{\mathbf{G}}(K_x, K_y, z, \omega) = \frac{1}{2\pi} \int_{-\infty}^{\infty} \tilde{\mathbf{W}}^{-1}(\mathbf{K}, \omega) e^{jzK_z} dK_z, \quad (9)$$

where the inverse of $\tilde{\mathbf{W}}(\mathbf{K}, \omega)$ is given by

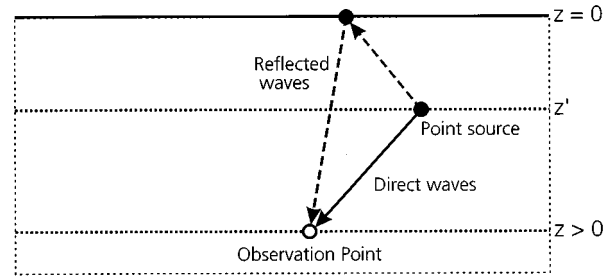


FIG. 1. Geometry for the determination of the disturbance due to a point source in an anisotropic half-space.

$$\tilde{\mathbf{W}}^{-1}(\mathbf{K}, \omega) = \frac{\text{adj } \tilde{\mathbf{W}}(\mathbf{K}, \omega)}{\det \tilde{\mathbf{W}}(\mathbf{K}, \omega)}. \quad (10)$$

Factorization of $\det \tilde{\mathbf{W}}(\mathbf{K}, \omega)$ with respect to K_z and definition of ($\alpha = qS1, qS2, qP$)

$$\mathbf{K}_\alpha^\pm = K_x \mathbf{e}_x + K_y \mathbf{e}_y + K_{z\alpha}^\pm \mathbf{e}_z, \quad (11)$$

where the sign accounts for up- and down-going wave components, provides

$$\begin{aligned} \hat{\mathbf{G}}(K_x, K_y, z, \omega) &= \hat{\mathbf{G}}_0^{qS1} e^{jzK_{zqS1}^\pm} + \hat{\mathbf{G}}_0^{qS2} e^{jzK_{zqS2}^\pm} \\ &+ \hat{\mathbf{G}}_0^{qP} e^{jzK_{zqP}^\pm}. \end{aligned} \quad (12)$$

Here, the positive sign applies for $z > 0$, the negative sign for $z < 0$.

In analogy to Hooke's law, Green's triadic function $\hat{\mathbf{\Sigma}}$ is defined as¹³

$$\hat{\mathbf{\Sigma}}(\mathbf{R}, \omega) = \mathbf{C} : \nabla \mathbf{G}(\mathbf{R}, \omega) = \hat{\mathbf{\Sigma}}^{213}(\mathbf{R}, \omega). \quad (13)$$

Thus $\hat{\mathbf{\Sigma}}(\mathbf{R}, \omega)$ is a third rank tensor, symmetrical in the first two indices. Using the \mathbf{K} vectors defined in Eq. (11), its 2-D spectral representation follows as

$$\begin{aligned} \hat{\mathbf{\Sigma}}(K_x, K_y, z, \omega) &= \hat{\mathbf{\Sigma}}_0^{qS1} e^{jzK_{zqS1}^\pm} + \hat{\mathbf{\Sigma}}_0^{qS2} e^{jzK_{zqS2}^\pm} \\ &+ \hat{\mathbf{\Sigma}}_0^{qP} e^{jzK_{zqP}^\pm}, \end{aligned} \quad (14)$$

where again the positive sign is valid for $z > 0$, the negative sign for $z < 0$. For TIA media, explicit expressions for $\hat{\mathbf{G}}_0^\alpha$ and $\hat{\mathbf{\Sigma}}_0^\alpha$ have been given in Ref. 11.

III. DERIVATION OF GREEN'S DYADIC FUNCTION FOR LAMB'S PROBLEM

In the following, an anisotropic half-space is considered, the free surface being identical with the x - y plane (Fig. 1). The problem is to determine the disturbance due to a point source in the half-space at position z' . As indicated in Fig. 1, the displacement at an observation point (position z) results from the three direct waves α with spectral components $\mathbf{K}_\alpha^{+/-}$ and nine reflected waves $\beta \rightarrow \alpha$, the respective spectral components being accordingly \mathbf{K}_β^- and \mathbf{K}_α^+ . While the direct contributions are described by full-space Green's function, the reflected contributions are to be determined. Mathematically, the basic problem is to solve Eq. (7) under the condition that the stresses vanish at the surface $z=0$.

The ansatz for the general solution of this problem is chosen as

$$\hat{\mathbf{G}}^{\text{half}} = \sum_{\alpha} \hat{\mathbf{G}}_0^{\alpha} e^{j(z-z')K_{z\alpha}^{\pm}} + \sum_{\alpha} \hat{\mathbf{u}}^{\alpha} \hat{\mathbf{b}}^{\alpha} e^{j(z+z')K_{z\alpha}^+}, \quad (15)$$

where $\hat{\mathbf{u}}^{\alpha}$ designates the plane wave polarization vectors. In Eq. (15), the first term represents the solution to the inhomogeneous problem (full-space Green's function), while the second term involving the arbitrary constant vectors $\hat{\mathbf{b}}^{\alpha}$ is the solution to the homogeneous problem that remains bounded as z goes to infinity.

In order to determine the unknown vectors $\hat{\mathbf{b}}^{\alpha}$, the next step is to apply the stress boundary conditions at the free surface according to

$$\mathbf{e}_z \cdot \mathbf{T}|_{z=0} = \mathbf{e}_z \cdot (\mathbf{C} : \nabla \mathbf{u})|_{z=0} = \mathbf{0}. \quad (16)$$

Transforming the stress tensor into the 3-D spectral representation yields

$$\tilde{\mathbf{T}} = j \mathbf{C} : \mathbf{K} \tilde{\mathbf{u}}. \quad (17)$$

Performing one-dimensional inverse Fourier transformation according to Eq. (9) and replacing $\hat{\mathbf{u}}$ by $\hat{\mathbf{G}}^{\text{half}} \cdot \hat{\mathbf{f}}$ allows—with respect to Eq. (13)—to formulate

$$\begin{aligned} \hat{\mathbf{t}}_z &\equiv \mathbf{e}_z \cdot \hat{\mathbf{T}} = \sum_{\alpha} j \mathbf{e}_z \cdot (\mathbf{C} : \mathbf{K}_{\alpha} \hat{\mathbf{G}}^{\text{half}, \alpha} \cdot \hat{\mathbf{f}}) = \mathbf{e}_z \cdot (\hat{\mathbf{S}}^{\text{half}} \cdot \hat{\mathbf{f}}) \\ &\equiv \hat{\mathbf{S}}^{\text{half}} \cdot \hat{\mathbf{f}}, \end{aligned} \quad (18)$$

where $\hat{\mathbf{S}}^{\text{half}} \equiv \mathbf{e}_z \cdot \hat{\mathbf{S}}^{\text{half}}$ has been introduced. It follows that

$$\begin{aligned} \hat{\mathbf{S}}^{\text{half}} &= \sum_{\alpha} \hat{\mathbf{S}}_0^{\alpha} e^{j(z-z')K_{z\alpha}^{\pm}} \\ &+ \sum_{\alpha} [j \mathbf{e}_z \cdot (\mathbf{C} : \mathbf{K}_{\alpha} \hat{\mathbf{u}}^{\alpha} \hat{\mathbf{b}}^{\alpha}) e^{j(z+z')K_{z\alpha}^+}], \end{aligned} \quad (19)$$

and

$$\hat{\mathbf{S}}^{\text{half}} = \sum_{\alpha} \hat{\mathbf{S}}_0^{\alpha} e^{j(z-z')K_{z\alpha}^{\pm}} + \sum_{\alpha} \hat{\mathbf{t}}_z^{\alpha} \hat{\mathbf{b}}^{\alpha} e^{j(z+z')K_{z\alpha}^+}. \quad (20)$$

Here $\hat{\mathbf{t}}_z^{\alpha}$ denotes the contribution to $\hat{\mathbf{t}}_z$ due to wave mode α . From Eq. (18) it follows that for arbitrary force density $\hat{\mathbf{f}}$ the stress boundary condition (16) is fulfilled if $\hat{\mathbf{S}}^{\text{half}}$ vanishes at $z=0$. Thus the arbitrary vectors $\hat{\mathbf{b}}^{\alpha}$ can be determined from

$$\sum_{\beta} \hat{\mathbf{S}}^{\beta} + \hat{\mathbf{t}}^{qS1} \hat{\mathbf{b}}^{qS1} + \hat{\mathbf{t}}^{qS2} \hat{\mathbf{b}}^{qS2} + \hat{\mathbf{t}}^{qP} \hat{\mathbf{b}}^{qP} = \mathbf{0}, \quad (21)$$

where

$$\hat{\mathbf{t}}^{\alpha} \equiv \hat{\mathbf{t}}_z^{\alpha} e^{jz'K_{z\alpha}^+}, \quad \hat{\mathbf{S}}^{\beta} \equiv \hat{\mathbf{S}}_0^{\beta} e^{-jz'K_{z\beta}^-}. \quad (22)$$

With $k=x, y, z$, it is

$$\sum_{\beta} \hat{\mathbf{S}}^{\beta} \cdot \mathbf{e}_k + \hat{\mathbf{t}}^{qS1} \hat{b}_k^{qS1} + \hat{\mathbf{t}}^{qS2} \hat{b}_k^{qS2} + \hat{\mathbf{t}}^{qP} \hat{b}_k^{qP} = 0, \quad (23)$$

which can be rewritten as

$$\sum_{\beta} \hat{\mathbf{S}}^{\beta} \cdot \mathbf{e}_k + (\hat{\mathbf{t}}^{qS1} \quad \hat{\mathbf{t}}^{qS2} \quad \hat{\mathbf{t}}^{qP}) \cdot \begin{pmatrix} \hat{b}_k^{qS1} \\ \hat{b}_k^{qS2} \\ \hat{b}_k^{qP} \end{pmatrix} = 0. \quad (24)$$

Defining the matrix

$$\hat{\mathbf{T}}_z \equiv (\hat{\mathbf{t}}^{qS1} \quad \hat{\mathbf{t}}^{qS2} \quad \hat{\mathbf{t}}^{qP}), \quad (25)$$

Eq. (24) yields the components \hat{b}_k^{α} according to

$$\begin{pmatrix} \hat{b}_k^{qS1} \\ \hat{b}_k^{qS2} \\ \hat{b}_k^{qP} \end{pmatrix} = -\hat{\mathbf{T}}_z^{-1} \cdot \sum_{\beta} \hat{\mathbf{S}}^{\beta} \cdot \mathbf{e}_k \quad (26)$$

or in vector notation:

$$\hat{\mathbf{b}}^{qS1} = -\mathbf{e}_x \cdot \hat{\mathbf{T}}_z^{-1} \cdot \sum_{\beta} \hat{\mathbf{S}}^{\beta}, \quad (27)$$

$$\hat{\mathbf{b}}^{qS2} = -\mathbf{e}_y \cdot \hat{\mathbf{T}}_z^{-1} \cdot \sum_{\beta} \hat{\mathbf{S}}^{\beta}, \quad (28)$$

$$\hat{\mathbf{b}}^{qP} = -\mathbf{e}_z \cdot \hat{\mathbf{T}}_z^{-1} \cdot \sum_{\beta} \hat{\mathbf{S}}^{\beta}. \quad (29)$$

Rewriting Eq. (25) according to

$$\hat{\mathbf{T}}_z = \hat{\mathbf{t}}^{qS1} \mathbf{e}_x + \hat{\mathbf{t}}^{qS2} \mathbf{e}_y + \hat{\mathbf{t}}^{qP} \mathbf{e}_z \quad (30)$$

and applying dyadic algebra allows to determine the inverse $\hat{\mathbf{T}}_z^{-1} = \text{adj } \hat{\mathbf{T}}_z / \det \hat{\mathbf{T}}_z$. The adjoint and the determinant are given by

$$\text{adj } \hat{\mathbf{T}}_z = \mathbf{e}_x \hat{\mathbf{t}}^{qS1} + \mathbf{e}_y \hat{\mathbf{t}}^{qS2} + \mathbf{e}_z \hat{\mathbf{t}}^{qP}, \quad (31)$$

$$\det \hat{\mathbf{T}}_z = \hat{\mathbf{t}}^{qS1} \cdot \hat{\mathbf{t}}^{qS1} (\hat{\mathbf{t}}^{qS2} \cdot \hat{\mathbf{t}}^{qS2} - \hat{\mathbf{t}}^{qP} \cdot \hat{\mathbf{t}}^{qP}), \quad (32)$$

where the vectors $\hat{\mathbf{T}}^{\alpha}$ are defined as

$$\hat{\mathbf{T}}^{qS1} = \hat{\mathbf{t}}^{qS2} \times \hat{\mathbf{t}}^{qP}, \quad \hat{\mathbf{T}}^{qS2} = \hat{\mathbf{t}}^{qP} \times \hat{\mathbf{t}}^{qS1}, \quad \hat{\mathbf{T}}^{qP} = \hat{\mathbf{t}}^{qS1} \times \hat{\mathbf{t}}^{qS2}. \quad (33)$$

Thus it is

$$\hat{\mathbf{b}}^{\alpha} = -\hat{\mathbf{T}}^{\alpha} \cdot \sum_{\beta} \hat{\mathbf{S}}^{\beta} / \det \hat{\mathbf{T}}_z \quad (34)$$

$$\equiv \sum_{\beta} \hat{\mathbf{b}}^{\beta\alpha} e^{-jz'(K_{z\alpha}^+ - K_{z\beta}^-)} / R(K_r). \quad (35)$$

Here the Rayleigh function $R(K_r) = \det \hat{\mathbf{T}}_z$ and the vectors $\hat{\mathbf{b}}^{\beta\alpha}$, directly indicating the reflection process $\beta \rightarrow \alpha$, have been introduced. Inserting Eq. (35) into (15) allows to finally formulate

$$\begin{aligned} \hat{\mathbf{G}}^{\text{half}} &= \sum_{\alpha} \hat{\mathbf{G}}_0^{\alpha} e^{j(z-z')K_{z\alpha}^{\pm}} \\ &+ \sum_{\alpha} \sum_{\beta} \hat{\mathbf{u}}^{\alpha} \hat{\mathbf{b}}^{\beta\alpha} e^{j(-z'K_{z\beta}^- + zK_{z\alpha}^+)} / R(K_r). \end{aligned} \quad (36)$$

This is the complete solution of Lamb's problem in the transform domain for any anisotropic half-space. An explicit representation of the Rayleigh function $R(K_r)$ and the vectors

$\hat{\mathbf{G}}^{\beta\alpha}$ for TI media has been given recently;¹² further details will follow.¹⁴

IV. DISCUSSION

For anisotropic half-spaces, a general solution to Lamb's problem has been derived in form of a dyadic Green's function. By application of a plane wave theory and the 2-D space-time spectral representation of Green's dyadic and triadic full-space functions explicit expressions for general anisotropic media have been obtained. Such a tensor Green's function plays a fundamental role, e.g., in the Knopoff-de Hoop representation theorem,¹⁵ which, e.g., provides an approach to the problem of earthquake modeling. In cases where the boundary conditions at buried sources are specified in terms of displacements, the spatial derivatives of the Green's function are required. These can be obtained from the dyadic (displacement tensor) function in form of the triadic (stress tensor) function according to Eq. (13). Crucial for the evaluation of the presented Green's dyad is evaluation of the Rayleigh function, since its zeroes produce singularities in the integral representation given above. Once these singularities have been determined, $\hat{\mathbf{G}}^{\text{half}}$ can in principle be evaluated as described in Ref. 16, where the generation of elastic waves by extended sources located on the half-space surface has been treated. In Ref. 12, the Rayleigh function singularities have been determined for several TI materials; details concerning the further numerical evaluation of the half-space Green's tensor using fast Fourier transformation will follow.¹⁴ Finally, it is worthwhile to mention that the introduction of isotropic material constants to the presented expressions leads to the results given by Johnson⁶ for isotropic half-spaces.

ACKNOWLEDGMENTS

The author would like to thank Professors M. Kröning and W. Arnold, IZFP, Saarbrücken, Germany, for their

steady support. This work was sponsored by the German Science Foundation DFG, which is gratefully acknowledged.

- ¹H. Lamb, "On the propagation of tremors over the surface of an elastic solid," *Philos. Trans. R. Soc. London, Ser. A* **203**, 1–42 (1904).
- ²L. Cagniard, *Réflexion et réfraction des ondes sismiques progressives* (Gauthier-Villars, Paris, 1939).
- ³C. L. Pekeris, "The seismic surface pulse," *Proc. Natl. Acad. Sci. USA* **41**, 469–480 (1955).
- ⁴C. L. Pekeris, "The seismic buried pulse," *Proc. Natl. Acad. Sci. USA* **41**, 629–639 (1955).
- ⁵A. T. de Hoop, "Theoretical determination of the surface motion of a uniform elastic half-space produced by a dilatational, impulsive point source," in *La Propagation des Ebranlements dans les Milieux Hétérogènes, Colloques Internationaux du Centre National de la Recherche Scientifique* (Marseille, 1961), pp. 21–32.
- ⁶L. R. Johnson, "Green's function for Lamb's problem," *Geophys. J. R. Astron. Soc.* **37**, 99–131 (1974).
- ⁷E. A. Kraut, "Advances in the theory of anisotropic elastic wave propagation," *Rev. Geophys.* **1**, 401–448 (1963).
- ⁸R. G. Payton, *Elastic Wave Propagation in Transversely Isotropic Media* (Martinus Nijhoff, The Hague, 1983).
- ⁹R. Burridge, "Lamb's problem for an anisotropic half-space," *Q. J. Mech. Appl. Math.* **24**, 81–98 (1971).
- ¹⁰M. Spies, "Elastic waves in homogeneous and layered transversely isotropic media: Plane waves and Gaussian wave packets. A general approach," *J. Acoust. Soc. Am.* **95**, 1748–1760 (1994).
- ¹¹M. Spies, "Elastic wave propagation in general transversely isotropic media. I: Green's functions and elastodynamic holography," *J. Acoust. Soc. Am.* **96**, 1144–1157 (1994).
- ¹²M. Spies and M. Kröning, "Green's function for Lamb's problem and Rayleigh wave propagation in general transversely isotropic materials," in *Review of Progress in QNDE*, Vol. 15, edited by D. O. Thompson and D. E. Chimenti (Plenum, New York, 1996), pp. 161–168.
- ¹³Y. H. Pao and V. Varatharajulu, "Huygens' principle, radiation conditions and integral formulas for the scattering of elastic waves," *J. Acoust. Soc. Am.* **59**, 1361–1371 (1976).
- ¹⁴M. Spies, "Green's function for Lamb's problem in anisotropic media. The general transversely isotropic case" (unpublished).
- ¹⁵R. Burridge and L. Knopoff, "Body force equivalents for seismic dislocations," *Bull. Seismol. Soc. Am.* **54**, 1875–1888 (1964).
- ¹⁶M. Spies, "Elastic wave in propagation in transversely isotropic media. II: The generalized Rayleigh function and an integral representation for the transducer field. Theory," *J. Acoust. Soc. Am.* **97**, 1–13 (1995).

Leaky-Rayleigh wave detection at air–solid interfaces by optical heterodyne interferometry

Michel de Billy, Laszlo Adler,^{a)} and Gerard Quentin

Groupe de Physique des Solides, Universités Paris 7 & Paris 6, C.N.R.S., URA 17, Tour 23,
2 place Jussieu, 75251 Paris Cedex 05, France

(Received 24 April 1997; accepted for publication 27 June 1997)

Recent developments have proven optical heterodyne interferometry to be a sensitive detector for ultrasonic amplitude and phase measurements in transparent materials. In this letter it is shown that this optical technique is sensitive enough to detect leaky-Rayleigh as well as leaky-Lamb waves in air reradiated from solids in the megaHertz region. Probing the leaky wave field at several positions parallel to the solid surface can yield the Rayleigh wave velocity of both transparent and opaque solids. This method can be used for low optical reflectivity solid surfaces: thus it can be extended for noncontact nondestructive evaluation applications. © 1997 Acoustical Society of America. [S0001-4966(97)03610-2]

PACS numbers: 43.20.Fn, 43.35.Zc [ANN]

INTRODUCTION

It is well known that when a Rayleigh wave propagates on a liquid-loaded solid surface, the energy of the wave “leaks” into the fluid if the sound velocity of the fluid is less than the velocity of the Rayleigh wave. These so-called leaky-Rayleigh waves have been studied extensively at liquid–solid interfaces in the last 30 years^{1–3} as have leaky-Lamb waves on plates immersed to liquids.⁴ Both leaky-Rayleigh and leaky-Lamb waves have found many applications in nondestructive evaluation, e.g., surface defect characterization, coated and composite materials characterization, etc.^{5,6} Because of the difficulties associated with ultrasonic wave generation and detection in air in the megaHertz region, air-coupled nondestructive evaluation has only recently been explored.^{7,8}

An optical method recently developed by Jia *et al.*⁹ used heterodyne interferometric probing of refractive index variation proportional to the pressure of acoustic waves in the medium. This allowed measurements of pulse propagation in air emitted by transducer in the megaHertz region. The same system was also applied to ultrasonic measurements of the dilatation associated with bulk waves as well as to measure guided waves, e.g., Rayleigh, Lamb, and interface waves in transparent solids.¹⁰

In this letter, measurements of leaky-Rayleigh and leaky-Lamb waves radiated into air are reported.

I. EXPERIMENTAL SETUP

The schematic diagram of the experimental system is shown in Fig. 1(a). The optical probe is a Mach–Zender heterodyne interferometer (BMI type SH130) used to measure the acoustical pressure of the leaky-Rayleigh wave in air. The probe beam shifted in frequency by an acousto-optic Bragg cell ($f_B = 70$ MHz) crosses a transparent medium where the index of refraction is modulated by the acoustic

wave and is then reflected by a mirror. The phase-modulated current measured by the photodiode is given as

$$i(t) \sim \cos[2\pi f_B t + v(t) + \phi_S - \phi_R], \quad (1)$$

where ϕ_R and ϕ_S are the phase constants corresponding to the reference and the probe beams of the interferometer, and $v(t)$ is the so-called Raman–Nath parameter,¹¹ the phase change due to the ultrasonic waves and is proportional the integrated acoustic pressure across the ultrasonic beam of width L ,

$$v(t) \approx \frac{2\pi\mu(2L)}{\lambda_L} P(t), \quad (2)$$

where μ is the piezo-optic coefficient, $P(t)$ is the pressure of the acoustic wave, and λ_L is the wavelength of the laser beam (633 nm). In order to detect the propagation of the ultrasonic pulses, a broadband electronic processing, similar to that used in the displacement measurements,^{12,13} has been used in this experiment.

The ultrasonic Rayleigh waves were generated on the surface of the sample by a so-called direct generation technique.¹⁴ A contact transducer is mounted directly over the edge of the specimen so that it can generate a bulk mode in the interior of the sample as well as surface modes along the surface. In this particular case, a 1-MHz shear transducer of vertical polarization, i.e., normal to the surface, is used. The samples are translated both in the vertical and horizontal positions with 10- μ m precision. Two types of experiments were carried out: in air and in transparent solids. The experimental setup for the measurements in air and in transparent solid is shown in Fig. 1(b) and (c), respectively. This method measures the ultrasonic pressure integrated on the path that the light travels in or above the sample.

II. EXPERIMENTAL RESULTS

In Fig. 2 the optically detected signals are shown at 0.1, 1, and 2 mm below the surface inside a Plexiglas sample. The laser beam intersects the sound field at 15 mm from the transducer surface. The first arrival signal is a longitudinal

^{a)}Department of Industrial, Welding and System Engineering, Ohio State University, Columbus, OH 43210.

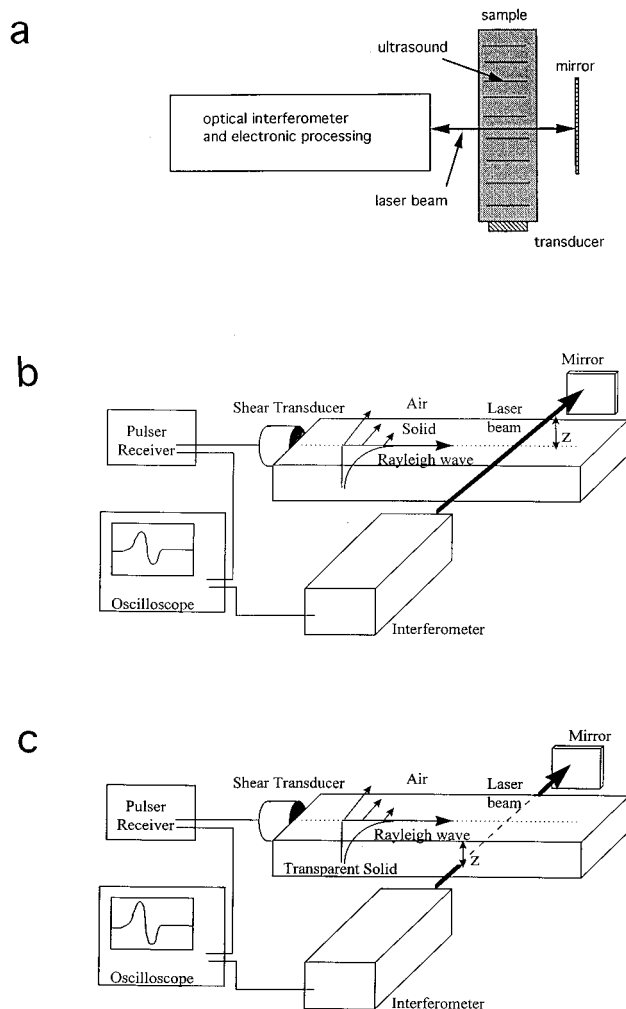


FIG. 1. (a) Experimental setup for leaky Rayleigh velocity measurements, (b) experimental setup for measurements in air, and (c) experimental setup for measurements in transparent solid.

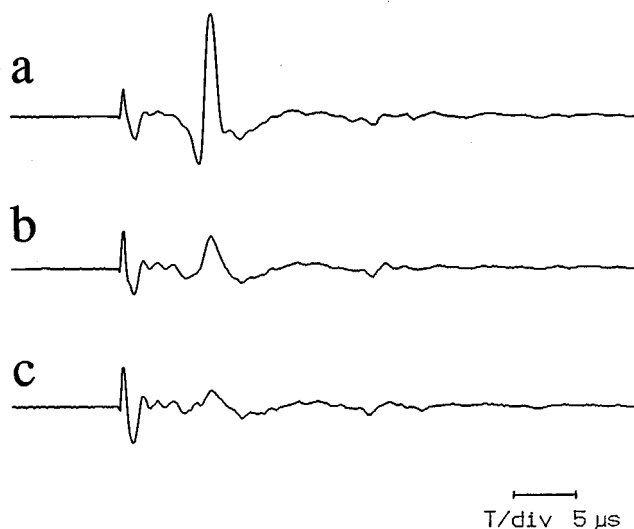


FIG. 2. Optically detected signals when the laser beam is inside a Plexiglas sample at a depth Z : $a-Z=0.1$ mm, $b-Z=1$ mm, and $c-Z=2$ mm.

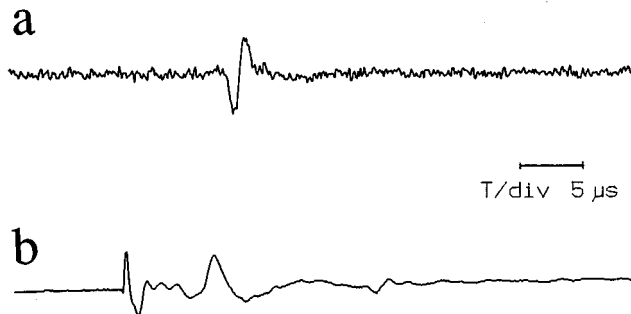


FIG. 3. Optically detected signals: (a) the probe is in air ($Z=1$ mm) and (b) the probe is in the Plexiglas sample ($Z=1$ mm).

wave generated by the shear transducer (This is concluded from velocity measurements, $Cl=2.75$ m/s in Plexiglas). The second arrival signal is a Rayleigh wave showing amplitude decay with depth (Z). The bulk transverse waves are not detected by the interferometer which detects dilatation only.¹⁰

When the probing laser is moved outside the sample to air, the signal amplitude drops significantly; nevertheless, after 500 times averaging a good measurable signal is obtained. In Fig. 3(a) is shown the pressure field of the leaky-Rayleigh wave measured in air above the interface 1 mm from the surface. The signal can be detected several centimeters away from the surface. For comparison, the ultrasonic field probed inside the Plexiglas at 1 mm below the surface is given in Fig. 3(b).

In order to measure the velocity of these waves, the field was probed parallel to the surface inside and outside the specimen. The detected signals recorded 20 mm apart in air and in the specimen are shown in Fig. 4(a) and (b), and 4(c) and (d), respectively. From these measurements, we obtained 1.28 km/s (V_R) and 1.26 km/s ($V_{L,R}$) for the Rayleigh and the leaky-Rayleigh wave velocities, respectively. The difference (less than 2%) is probably due to experimental error. In Fig. 5 the detected leaky-Rayleigh wave signals in air are shown again 20 mm apart for a duraluminum sample. The leaky-Rayleigh velocity ($V_{L,R}$) for this specimen was 2.96 km/s, which compares well with Rayleigh wave velocity (V_R) measurement of 2.88 km/s obtained by wedge technique measurements. Similar experiments were repeated for two other samples (glass and Polyvinyl). Table I summarizes the results for the four samples used. The leaky-Rayleigh wave velocity measured in air using the optical technique agrees well with the Rayleigh velocity measurements obtained either via the optical method (*) or via a conventional technique (+).

We have also demonstrated that the optical method is sensitive to detect leaky-Lamb waves in air from plates. In Fig. 6 the detected signals of a leaky-Lamb mode (mode S_0) are shown as measured at two points in air 20 mm apart for a 2-mm-thick Plexiglas plate.

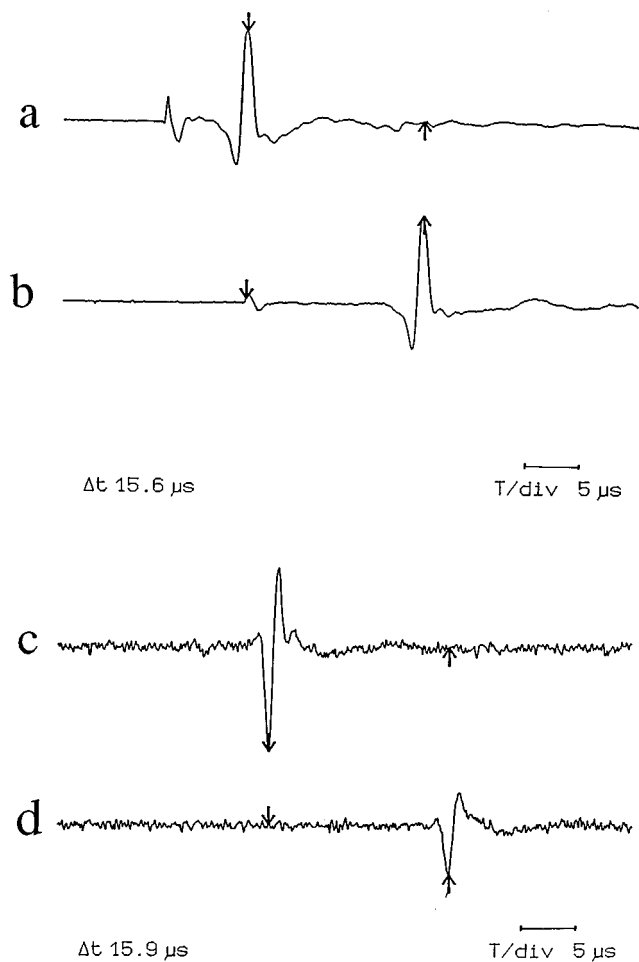


FIG. 4. Optically detected signals recorded at 20 mm apart along the interface for velocity measurements; the probe is moved in the Plexiglas specimen [(a) and (b)] and in air or above the Plexiglas sample [(c) and (d)].

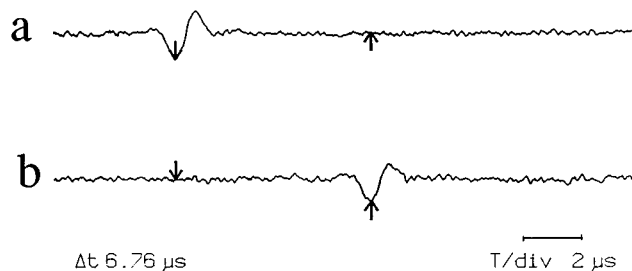


FIG. 5. Optically detected signals recorded at 20 mm apart along the interface (air-duraluminum) for velocity measurements of the leaky-Rayleigh wave.

TABLE I. Comparison between leaky-Rayleigh wave ($V_{L,R}$) and Rayleigh wave (V_R) for various materials.

Material	$V_{L,R}$ (km/s)	V_R (km/s)
Duraluminum	2.96	2.88+
Polyvinyl	1.02	0.99+
Glass	3.51	3.42*
Plexiglas	1.26	1.28*



FIG. 6. Optically detected signals recorded at 20 mm apart along the interface ($Z=2$ mm) for velocity measurements of a leaky-Lamb wave.

III. CONCLUSION

We have shown that the optical heterodyne interferometric method, which probes the refractive index variation in air, is sufficiently sensitive to detect leaky waves from semi-infinite solids and from plates. The method has potential applications for noncontact nondestructive evaluation problems.

- ¹H. L. Bertoni and T. Tamir, "Unified theory of Rayleigh angle phenomena for acoustic beams at liquid-solid interfaces," *Appl. Phys.* **2**, 157–172 (1973).
- ²W. Neubauer, "Ultrasonic reflection of bounded beam at Rayleigh and critical angles for a plane liquid-solid interface," *J. Appl. Phys.* **44**, 48–55 (1973).
- ³M. A. Breazeale, L. Adler, and L. Flax, "Reflection of a Gaussian ultrasonic beam from liquid-solid interface," *J. Acoust. Soc. Am.* **56**, 866–872 (1974).
- ⁴T. Y. Plona, L. E. Pitts, and W. G. Mayer, "Ultrasonic bonded beam reflection and transmission effects at a liquid/solid plate/liquid interface," *J. Acoust. Soc. Am.* **59**, 1324–1328 (1976).
- ⁵G. S. Scott and L. Adler, "The structure of ultrasonic leaky waves and their interaction with subsurface flows," *Mater. Eval.* **35**, 54–58 (1977).
- ⁶A. H. Nayfeh, D. E. Chimenti, L. Adler, and R. L. Crane, "Ultrasonic leaky waves in the presence of a thin layer," *J. Appl. Phys.* **52**(8), 4985–4994 (1981).
- ⁷B. T. Khuri Yakub, "Air coupled transducers," in *N. D. T. Handbook: Ultrasonic Testing*, edited by P. McIntire (ASNT, 1991), pp. 320–325.
- ⁸M. Castaings and P. Cawley, "The generation, propagation and detection of Lamb waves in plates using air coupled ultrasonic transducers," *J. Acoust. Soc. Am.* **100**, 3070–3077 (1996).
- ⁹X. Jia, G. Quentin, and M. Lassoued, "Optical heterodyne detection of pulsed ultrasonic pressures," *IEEE Trans. Ultrason. Ferroelectr. Freq. Control* **40**, 67–69 (1993).
- ¹⁰X. Jia, C. Mattei, and G. Quentin, "Analysis of optical interferometric measurements of guided acoustic waves in transparent solids," *J. Appl. Phys.* **77**, 5528–5537 (1995).
- ¹¹B. D. Cook, "Measurements of the optical nearfield of an ultrasonically produced phase grating," *J. Acoust. Soc. Am.* **60**, 95–199 (1976).
- ¹²D. Royer and E. Dieulesaint, "Optical detection of sub-Angström transient mechanical displacement," *IEEE Ultrason. Symp. Proc.*, 527–530 (1986).
- ¹³J. P. Monchalain, "Optical detection of ultrasound," *IEEE Trans. Ultrason. Ferroelectr. Freq. Control* **33**, 485–499 (1986).
- ¹⁴P. B. Nagy and L. Adler, "A novel technique for interface wave generation," in *Physical Acoustics*, edited by O. Leroy and M. A. Breazeale (Plenum, New York, 1991), pp. 529–535.

Comment on “Modal analysis of a structure in a compressible fluid using a finite element/boundary element approach” [J. Acoust. Soc. Am. 99, 1949–1957 (1996)]

Ardhendu G. Pathak and Purnima Jaliha

National Institute of Ocean Technology, IIT Campus, Madras 600 036, India

(Received 13 August 1996; accepted for publication 26 May 1997)

An approach to solve for the resonance frequency of fluid-loaded structures was recently suggested by McCollum and Siders [J. Acoust. Soc. Am. 99, 1949–1957 (1996)]. An iterative procedure was suggested to solve for eigenfrequencies by reducing the problem to the standard eigenvalue problem. Using an example of a single degree of freedom system with a piston radiating in fluid, it is shown that the proposed method can lead to incorrect results. © 1997 Acoustical Society of America. [S0001-4966(97)04509-8]

PACS numbers: 43.20.Tb, 43.30.Jx, 43.40.Rj [JEG]

INTRODUCTION

McCollum and Siders¹ have discussed in great detail an alternative procedure for calculating fluid-loaded response of structures using finite elements for structural response and boundary integral approach for acoustical response. The difficulties arise because the reaction of the fluid on a vibrating structure changes the structural response, which in turn leads to a change in fluid loading. In other words, there is a feedback loop due to fluid loading and the problem is to find the equilibrium point.

The loading due to the reaction of the fluid is characterized by the acoustical impedance Z_a . This quantity, in general, is complex. The real part, called radiation damping, signifies the energy loss due to acoustic radiation in the far field of the fluid. It is noted here that the harmonic force due to the radiation resistance term is not always proportional to the angular frequency and hence is not an exact analogue of the mechanical dashpot. The analogy is correct only in the high-frequency (“ ρc ”) limit where it reaches a constant value. The imaginary part of the radiation impedance characterizes the reactive power. At very low frequency ranges, the reactive part behaves as mass loading. Depending on the type of vibrator and the frequency range of operation, it can be shown to behave as a spring also.² When calculating the response of the fluid-loaded structures it is important to keep these physical interpretations in mind. The authors have suggested a way of incorporating the fluid loading (in particular, radiation damping) into the equations of motion in such a way as to reduce the problem to the standard eigenvalue problem. In the next section it is shown that the suggested procedure is not consistent with the underlying physics of the problem and can lead to errors in estimating fluid-loaded frequency of submerged vibrators.

I. THEORY

To fix the ideas, consider a single degree of freedom system as shown in Fig. 1. It consists of a baffled piston of mass m radiating in the fluid. The stiffness of the spring is k

and the external force acting on the system is $F(t)$. Equation (1), in the usual notation, describes the equation of motion for the system:

$$m \frac{d^2 x(t)}{dt^2} + kx(t) = F(t) - F_a(t), \quad (1)$$

where F_a denotes the force due to fluid loading. In the frequency domain this force can be represented as

$$F_a(\omega) = Z_a(\omega) * v(\omega) = [R_a(\omega) + jX_a(\omega)]v(\omega). \quad (2)$$

Here $Z_a(\omega)$ is the acoustic impedance and $v(\omega)$ is the velocity. Assuming harmonic loading and dropping the $\exp(j\omega t)$ factor, Eq. (1) above can be rearranged to solve for the free vibration frequency of the system as follows:

$$-m\omega^2 + j\omega R(\omega) - \omega X(\omega) + k = 0. \quad (3)$$

This is the frequency equation for the system, one of the roots of which gives the damped natural frequency of the system. To solve this analytically, consider the low-frequency ($ka < 1$) case. The acoustic resistance and reactance can be approximated by the first two terms in the series expansion as follows:³

$$R(ka) = Z[A_1(2ka)^2 - A_2(2ka)^4], \quad (4)$$

$$X(ka) = Z[B_1(2ka) - B_2(2ka)^3],$$

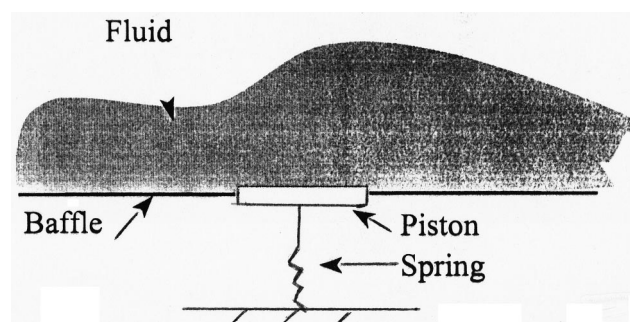


FIG. 1. A single degree of freedom system with a baffled piston radiating into fluid.

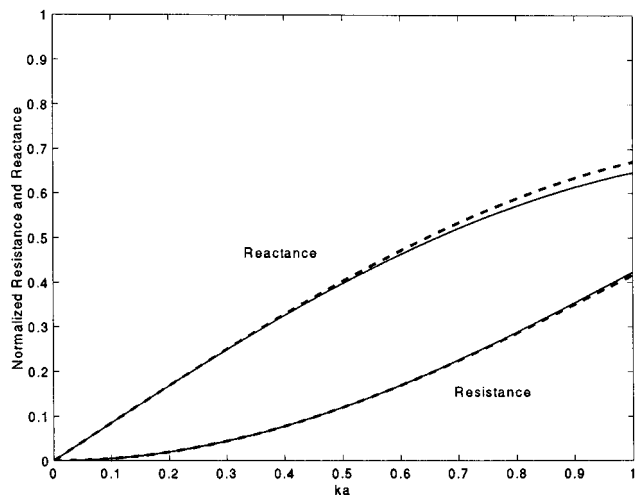


FIG. 2. Normalized resistance and reactance of a fluid-loaded piston. Continuous lines: exact solution; dashed lines: two term approximation.

where $Z = \rho c A_p$, ρ is density of the medium, c is the speed of sound, and A_p is area of the piston. Figure 2 shows the comparison of the values of the normalized radiation resistance and reactance for $ka < 1$. It can be seen that the two-term approximation given above matches with the exact solution in the range $ka < 1$. The expressions for $R(ka)$ and $X(ka)$ when substituted in Eq. (3) result in a fifth-order polynomial in frequency. The frequency equation for the case $ka < 1$ in nondimensional form can then be represented as

$$k_1 \Omega^5 + k_2 \Omega^4 + k_3 \Omega^3 + k_4 \Omega^2 - 1 = 0, \quad (5)$$

where

$$\begin{aligned} k_1 &= j A_2 \gamma \alpha^3, & k_2 &= -B_2 \gamma \alpha^2, \\ k_3 &= -j A_1 \gamma \alpha, & k_4 &= 1 + B_1 \gamma, \end{aligned} \quad (6)$$

$$\Omega = \omega / \omega_0, \quad \omega_0 = \sqrt{(k/m)},$$

$$\gamma = 2 \rho A_p a / (m c), \quad \alpha = 2 a \omega_0 / c.$$

This equation can be easily solved for the given values of system stiffness, mass, and piston diameter. In general

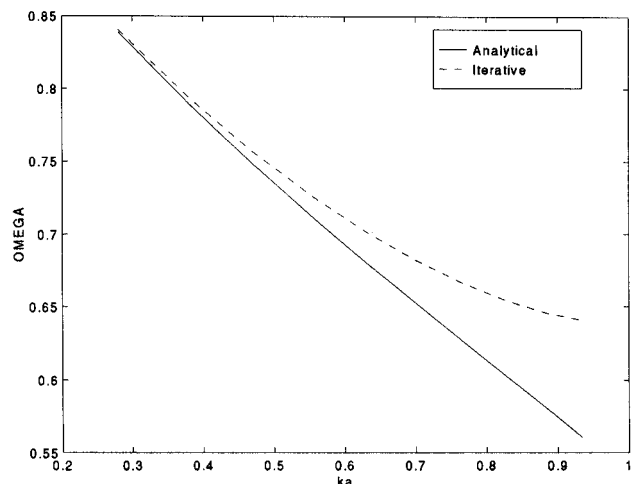


FIG. 3. Comparison of analytical and iterative solutions for $1 < \gamma < 5$ and $\gamma/\alpha = 1.5$.

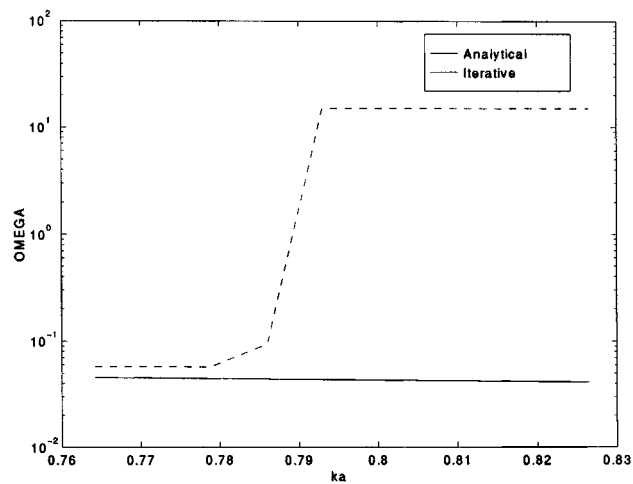


FIG. 4. Comparison of analytical and iterative solutions for $1000 < \gamma < 1200$ and $\gamma/\alpha = 30$.

there are five roots, only one of which has a real part corresponding to the damped natural frequency of the system.

Now consider the procedure outlined in the paper under discussion. It consists of writing Eq. (3) in the following form:

$$-(m + X(\omega)/\omega)\omega^2 + [k + j\omega R(\omega)] = 0. \quad (7)$$

The equation above can be recast in nondimensional form as

$$-(1 + \gamma X(2ka)/ka)\Omega^2 + (1 + j\Omega \gamma R(2ka)/\alpha) = 0. \quad (8)$$

The iterative solution suggested in the paper takes the following form:

$$\Omega_n^2 = \frac{1 + j\Omega_{n-1} \gamma R(2ka)/\alpha}{1 + \gamma X(2ka)/2ka}. \quad (9)$$

It is argued that the above iteration scheme correctly represents the in-fluid behavior of the system. However, this is not always the case. Figures 3 and 4 show two typical cases when the iterative solution does not match the analytical solution. In the case of Fig. 3 the absolute values do not match,

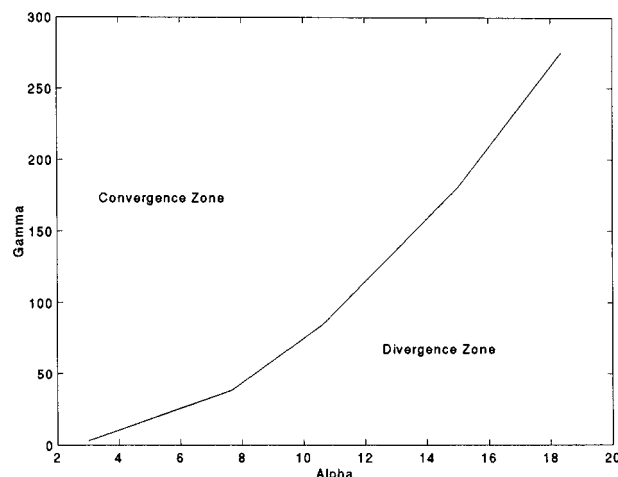


FIG. 5. Valid range of parameters for convergence of the iterative scheme obtained by trial and error.

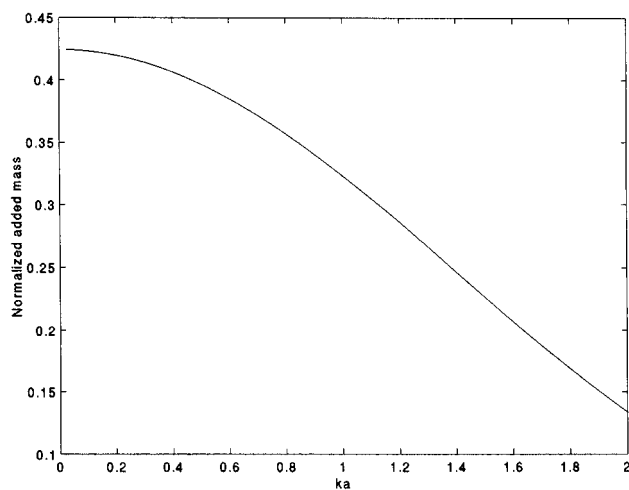


FIG. 6. Variation of normalized added mass of a fluid-loaded piston as a function of ka .

though the trend is same. However, in the case of Fig. 4, the iterative solution clearly converges to a wrong value since Ω cannot be greater than one. It is possible by trial and error to find the parameter ranges in which the iterative solution does not converge to the correct solution. Figure 5 shows the zone of convergence and divergence obtained using trial and error for the cases when $ka < 1$.

Further it is also stated with reference to Fig. 1 in the Ref. 1 that “as ka increases to value near one, the added mass changes very slowly.” That this is not the case is evident from the plot of nondimensional added mass versus ka shown in Fig. 6. The normalization factor used is $(2aZ/c)$. It is clear that the variation of nondimensional added mass is in fact rapid near $ka = 1$.

II. CONCLUSION

It has been shown that to solve for the in-fluid resonance frequency of a structure, grouping of the acoustic resistance term with stiffness is not consistent with the physics of the situation. Analytical solution for the in-fluid resonance frequency of a simple system consisting of a spring and piston radiating in the fluid was presented in a nondimensional form. The iterative scheme was compared with the analytical solution with numerical examples. It was shown that for a certain range of parameters the iterative scheme gives incorrect results.

¹M. D. McCollum and C. M. Siders, “Modal analysis of a structure in a compressible fluid using a finite element/boundary element approach,” *J. Acoust. Soc. Am.* **99**, 1949–1957 (1996).

²A. G. Pathak and P. R. Stepanishen, “Acoustic harmonic radiation from fluid-loaded elastic plates using elasticity theory,” *J. Acoust. Soc. Am.* **94**, 1700–1710 (1993).

³W. S. Burdic, *Underwater Acoustic System Analysis* (Prentice-Hall, Englewood Cliffs, NJ, 1984).

Response to “Comment on ‘Modal analysis of a structure in a compressible fluid using a finite element/boundary element approach’ ” [J. Acoust. Soc. Am. 102, 2445–2447 (1997)]

M. D. McCollum^{a)}

Harris Corporation-Electronic Systems Sector, Melbourne, Florida 32902-9100

Clementina M. Siders^{a)}

Naval Air Warfare Center, Orlando, Florida 32806

(Received 22 May 1997; accepted for publication 22 May 1997)

The authors thank Professors Pathak and Jaliha for their interest in our paper describing an iterative approach to estimating the in-water modal frequencies of a structure in a compressible fluid. Because of the requirement that the mode of interest remain uncoupled when the structure is submerged, the method is limited to nondimensional wave numbers, ka , of much less than one. In their Letter, Pathak and Jaliha showed that the method does not converge for some configurations of a piston in an infinite baffle, even though the in-water modal frequency is less than one. It is proposed that the lack of convergence is a result of the ideal nature of the piston problem. The particular configurations for which the method does not converge have one common characteristic. This is that the ka value corresponding to the *in vacuo* modal frequency is large, even though the final in-water ka is less than one. For these configurations, the radiation loading at the *in vacuo* frequency, which is the starting point for the iterative procedure, is dominated not by the radiation mass, but by the radiation damping. For realistic structures whose low-order modes remain uncoupled after submergence, the radiation mass is dominant at both the *in vacuo* and in-water modal frequencies. The proposed method is based on the assumption that this is the case, and was shown to be efficient and accurate for several modes of three multi-modal structures. Although it is believed that the piston variations presented by Pathak and Jaliha are outside of the realm of realistic structures, it will be shown that it is possible to achieve convergence to an accurate solution with a simple modification to the iterative procedure. © 1997 Acoustical Society of America. [S0001-4966(97)04609-2]

PACS numbers: 43.20.Tb, 43.30.Jx, 43.40.Rj [JEG]

INTRODUCTION

The iterative method proposed in the original paper¹ was presented as a solution to the problem of estimating a particular in-water resonance frequency of a finite element/boundary element model. This procedure was not limited by the usual assumption of an incompressible fluid, and was shown to be accurate for the low-order modes of a fluid-loaded spherical shell,² and for two- and three-dimensional models of a low-frequency acoustic projector. It was also shown that an accurate solution could be obtained using only the imaginary part of the radiation loading, that is, the radiation mass, since the radiation damping has little effect on the in-fluid resonance frequency of these modes. Although Pathak and Jaliha twice stated in their letter that the method focuses on the radiation damping, this is not the case. It is the radiation mass that is critical in determining the in-water modal frequency of low ka modes.

A key requirement for use of the method is that the modes remain uncoupled when the structure is submerged, which is generally the case at low ka in water.² In their letter, Pathak and Jaliha posed two very different variations of the classical piston-in-an-infinite-baffle problem, and presented the results of their analysis comparing the analytic

and iterative solutions, using the complex radiation load in both cases. Since the piston has only one mode, modal coupling is not an issue. In the second of the two problems, it was found that the solution failed to converge for final, that is, in-water, ka values greater than about 0.8. This behavior is a result of the large value of the *in vacuo* modal frequency of the piston. However, one can obtain an accurate solution in this situation simply by excluding the radiation damping from the iterative computation. For the problems we have encountered, this approach gives a solution that is very close to the harmonic resonance frequency. If one desires to include the radiation damping, one needs only to perform a second run of the iterative solution, starting at the frequency obtained from the first, purely real, solution. The second solution will converge very quickly since it begins at a point near the final solution. In practice, we generally exclude the radiation damping altogether because it has little effect on the in-water modal frequency, and because the resulting eigenvalue solution is purely real. For large numerical models, this can result in quite a large reduction in computational time.

I. THEORY

Before presenting our results for the two proposed problems, we would like to correct two typographical errors in Pathak's letter. Pathak cast the problem in nondimensional

^{a)}Formerly of the Naval Undersea Warfare Center, Underwater Sound Reference Division, Orlando, FL 32806.

form, combining three physical variables (mass, stiffness, and radius) into two nondimensional variables, α and γ . The variable γ , which combines the structural mass and the radius of the piston, should be written as follows:

$$\gamma = \frac{2\rho A_p a}{M}, \quad (1)$$

where ρ is the fluid density, A_p is the fluid-loaded area of the piston ($A_p = \pi a^2$), and M is the piston mass. (Pathak's expression included the speed of sound, c , in the denominator.) The second variable is defined by

$$\alpha = \frac{2a\omega_0}{c}, \quad (2)$$

where ω_0 is the *in vacuo* modal frequency ($\omega_0 = \sqrt{K/M}$) and K is the piston stiffness. It is interesting to note that one could rewrite Eq. (2) in terms of Pathak's nondimensional frequency, $\Omega = \omega/\omega_0$, and rearrange, to obtain the expression

$$\Omega = \frac{2ka}{\alpha}, \quad (3)$$

which would allow us to solve for Ω as a function of α and ka , without ever going through the formal solution process. This is a consequence of reducing the three-variable problem, in K , M , and a , to two variables in α and γ .

To obtain the iterative solution, Pathak and Jaliha wrote an expression for the normalized frequency in terms of the two nondimensional variables, following the derivation of the iterative procedure given in the original paper. The expression should be written as

$$\Omega_n^2 = \frac{1 + j\Omega_{n-1}\gamma R(2k_{n-1}a)/(Z \cdot \alpha)}{1 + \gamma X(2k_{n-1}a)/(Z \cdot 2k_{n-1}a)}, \quad (4)$$

where R and X are the normalized radiation damping and mass, respectively, and $Z = \rho c A_p$. (Pathak's expression omitted the normalizing factor Z in the numerator and denominator.) If one were to neglect the radiation damping contribution associated with the second term in the numerator, one would obtain a purely real expression for the iterative solution. Pathak included the radiation damping in the solution, in which case the eigenvalue is the real part of the complex square root of Eq. (4).

To use Eq. (4) with the complex radiation load, we would begin by describing the piston in terms of α and γ . Then, we would use the only known information, namely the nondimensional *in vacuo* modal frequency, Ω_0 , to compute the initial value of the radiation mass and damping. Note that in the nondimensional form, the *in vacuo* frequency is always $\Omega_0 = 1$. To obtain the radiation load, we first compute the initial value of ka , which is given by

$$(ka)_0 = \frac{\Omega_0 \alpha}{2}. \quad (5)$$

[This equation is a consequence of the definition of α given by Eq. (2).] With this value of ka , we can compute the nondimensional radiation mass and damping. Note that we have not specified the piston area, A_p , so we can compute

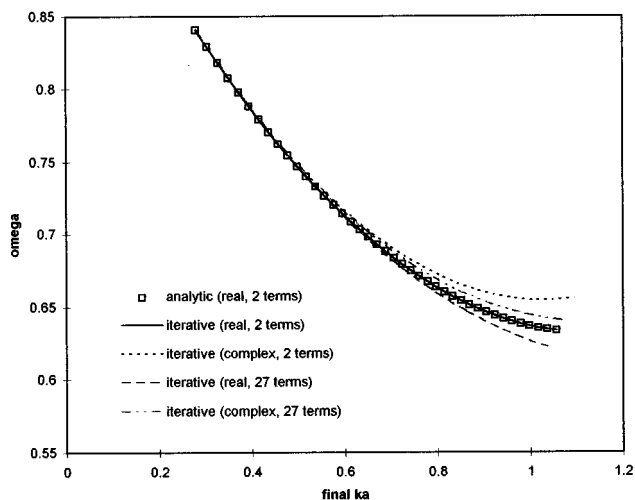


FIG. 1. Comparison of analytic (real) and iterative (real and complex) solutions for $1 \leq \gamma \leq 5$ and $\gamma/\alpha = 1.5$.

only the normalized values of the radiation loading. Now using Eq. (4) we compute a new value for Ω_n , and continue on until the value of Ω converges.

II. RESULTS

In the first problem posed by Pathak and Jaliha, the ratio γ/α was set to 1.5, and γ ranged from 1 to 5. For this problem, the *in vacuo* ka ranged from 0.33 to 1.67, over which values the radiation mass dominates. The results obtained by Pathak using the iterative solution matched the two-term analytic solution very well for ka values in the vicinity of 0.3, and as the value of ka increased, the difference between the two solutions became greater. It is implied that this difference is caused by the decreasing accuracy of the iterative solution with increasing ka . No statement was made about the number of terms used in computing the radiation loading for the iterative solution. Nor did the professors address the issue of the numerical precision of the results, which can be critical when several terms are included in the approximation.

Our results computed using the iterative solution with both the complex radiation load and the radiation mass alone (both represented by the first 2 and the first 27 terms), compared with the two-term analytic solution obtained with only the radiation mass, are shown in Fig. 1. These curves were computed using a FORTRAN program running in double precision on a Pentium processor. For each value of γ and α , the computed value of Ω was checked by substituting it back into the original equation. Note that for the range of ka values shown, the two-term real iterative solution exactly matches the two-term real analytic solution. This leads us to believe that the differences between Pathak's analytic and iterative results are caused by a difference in the number of terms in the radiation load approximation for the two solutions. The real (mass only) solution using 27 terms indicates that the two-term approximation becomes inadequate at $ka = 0.7$. The remaining two curves represent the complex iterative solutions for 2 and 27 terms, obtained using a modified procedure to be described in more detail later in the

paper. These results indicate that the radiation damping begins to have an effect at $ka=0.5$, but that the effect is fairly small for $ka<0.8$.

In Pathak’s second problem the ratio $\gamma/\alpha=30$, and γ varies from 1000 to 1200, and the *in vacuo* modal frequency ranges from 16.7 to 20, for which values the radiation damping completely dominates the radiation mass. In the results obtained by Pathak and Jaliha1, the n -term iterative solution (n unknown) was near the two-term analytic solution until ka reached about 0.78, at which point the iterative solution failed to converge. (Pathak’s curve implies convergence to an incorrect value, but our results showed an oscillation in the computed value.) The first point to be made is that in practice the proposed method is expected to work for $ka \ll 1$. For realistic multi-modal structures, the modes become coupled in water for higher values of ka . In this case, the method was found by Pathak to work for $ka \leq 0.78$, which is consistent with the claimed performance. However, this problem is special in that there exists only one mode, so we see no reason that this restriction should apply, so long as one uses enough terms in the representation of the radiation load for the highest ka of interest. Second, it is certain that Pathak’s iterative solution included more than two terms, because at the *in vacuo* ka values, the two-term approximation gives negative values of the radiation mass.

At large values of ka , the radiation mass is small, while the radiation damping is very large. At low ka , the mass dominates. Looking at Eq. (4), we see that with a large damping term and a small mass term, the expression approaches the following:

$$\Omega_n^2 = 1 + j \frac{\Omega_{n-1} \gamma R (2k_{n-1} a)}{(Z \cdot \alpha)} \tag{6}$$

Then we find that we are taking the square root of a number whose real part is one, and whose imaginary part is much greater than one. The result is a value of Ω which is greater than one, which is, of course, nonphysical. We can avoid this situation for problems with a large *in vacuo* ka in either of the following two ways: (i) perform the iterative procedure once through using only the radiation mass, then rerun using the complex radiation load and beginning with the values of ka and Ω obtained in the first run; or (ii) exclude the radiation damping term altogether. Our solution for this problem obtained using only the 27-term approximation (since the two-term mass is negative), compared with the purely real analytic solution for two terms, is shown in Fig. 2. We have presented the results for a wider range of γ values, $\gamma=100$ to 1200, in order to demonstrate the accuracy of the solution for $ka \ll 1$. This result shows that the 27-term approximation is valid for ka as high as 1 and the radiation damping begins to have an effect at $ka=0.5$. It is clear that the iterative procedure can be used to determine the in-fluid modal frequency using either the complex radiation load or the radiation mass alone, as long as one is careful to avoid the situation in which R is much greater than X .

For most, if not all, practical situations, one can obtain an acceptable estimate of the in-water modal frequency of uncoupled modes using only the radiation mass. Furthermore, for practical situations involving the lower order (low

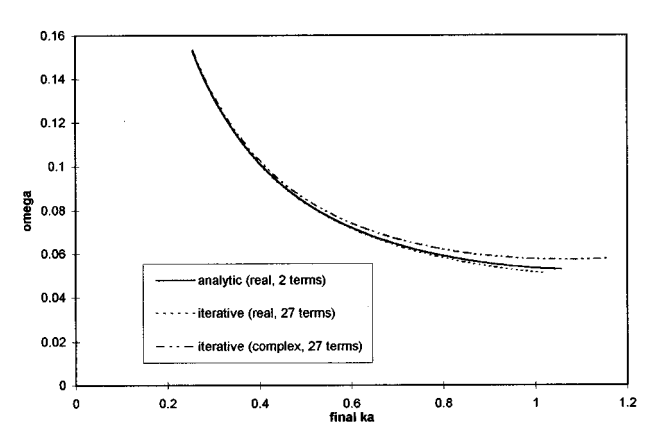


FIG. 2. Comparison of analytic (real) and iterative (real and complex) solutions for $100 \leq \gamma \leq 1200$ and $\gamma/\alpha=30$.

ka) modes of multi-mode structures, the *in vacuo* ka value will not be much greater than 1, and one can employ the complex formulation in one pass of the iterative procedure. Some *in vacuo* and in-water ka values from our original paper, compared with those of Pathak’s examples, are shown in Table I. The method was shown to work well for all of the modes described in the table, which includes *in vacuo* ka values up to 7.9, but for all of these problems, the radiation damping was excluded from the solution in the interest of computational efficiency in the finite element/boundary element solution. For the higher-order modes, it is likely that in order to use the complex radiation load it would have been necessary to use the two-part iterative solution. However, it was shown that the purely real modal solution was within 2% of the harmonic resonance frequency computed using the complex radiation load.

III. CONCLUSION

We have shown that the lack of convergence found by Pathak and Jaliha1 for a piston in an infinite baffle with a large ratio of γ to α is a result of the ideal nature of the

TABLE I. Comparison of *in vacuo* and in-water values of ka for various geometries.

Geometry	Mode	<i>in vacuo</i> ka	in-water ka
Spherical shell ^a	$n=2$ /lower branch	2.5	1.1
	$n=3$ /lower branch	2.9	1.4
	$n=4$ /lower branch	3.1	1.6
	$n=0$ /upper branch	5.7	4.3
Hydroacoustic transducer ^b (2-d)	1	0.4	0.2
	2	1.9	1.3
	4	3.6	2.8
	5	7.9	7
Hydroacoustic transducer ^b (3-d)	5	0.4	0.2
Piston/baffle ^c			
	($\gamma/\alpha=1.5$)		
	1	0.3 to 1.7	0.3 to 1.1
	($\gamma/\alpha=30$)		
	1	16.7 to 20	1.0 to 1.2

^aSee Ref. 2.
^bSee Ref. 1.
^cFrom Pathak and Jaliha1’s *Letter to the Editor*.

problem. Furthermore, we have shown that an accurate solution can be obtained for such a problem either by neglecting the radiation damping or by performing the iterative procedure in two passes. We assert that this situation is unlikely to occur in practice, and does not represent a limitation of the method for realistic structures. We thank Pathak and Jaliha for their interest in the proposed procedure, and for taking

the time to exercise it on a problem of wide academic interest.

¹M. D. McCollum and C. M. Siders, "Modal analysis of a structure in a compressible fluid using a finite element/boundary element approach," *J. Acoust. Soc. Am.* **99**, 1949–1957 (1996).

²M. C. Junger and D. Feit, *Sound, Structures, and Their Interaction* (MIT, Cambridge, MA, 1972).

Erratum: “Reflection and refraction of longitudinal wave at an interface between two micropolar elastic solids in welded contact” [J. Acoust. Soc. Am. 97, 822–830 (1995)]

S. K. Tomar

Department of Mathematics, Guru Nanak Khalsa College, Yamuna Nagar-135 001 (Haryana), India

M. L. Gogna

Department of Mathematics, Kurukshetra University, Kurukshetra-132 119 (Haryana), India

(Received 16 June 1997; accepted for publication 2 July 1997)

PACS numbers: 43.20.Gp, 43.20.Jr, 43.20.Mv, 43.10.Vx [JEG]

[S0001-4966(97)03510-8]

Expressions of E_2 and E_3 of Eq. (42) should be read as follows:

$$E_2 = z_2^2 \sqrt{1 - (V_3^2/V_1^2) \cos^2 \theta_1} [\mu + K + Kq_1]/(D_1 V_3^3/V_1^3),$$

$$E_3 = z_3^2 \sqrt{1 - (V_4^2/V_1^2) \cos^2 \theta_1} [\mu + K + Kq_2]/(D_1 V_4^3/V_1^3).$$

The last term of Eq. (16) should be read as $\cos \theta_p$ instead of $\cos \phi_p$.

Expression of m_{zx} in Eq. (19) should be read as

$$m_{zx} = \gamma(\Phi_{z,yz} - \Phi_{y,zz}).$$

Expression of P^* given just above Eq. (41) should read as

$$p^* = t_{lk} n_l \dot{u}_k + m_{lk} n_l \dot{\phi}_k.$$

TECHNICAL NOTES AND RESEARCH BRIEFS

Paul B. Ostergaard

10 Glenwood Way, West Caldwell, New Jersey 07006

Editor's Note: Original contributions to the Technical Notes and Research Briefs section are always welcome. Manuscripts should be double-spaced, and ordinarily not longer than about 1500 words. There are no publication charges, and consequently, no free reprints; however, reprints may be purchased at the usual prices.

Numerical estimation of the influence of ground impedance on sound propagation [43.28.En, 43.28.Fp]

L. Rahovich and M. Slonim

Department of Electrical and Computer Engineering, Ben-Gurion University of the Negev, Beer-Sheva, Israel

Ts. Zlotnick

EORD, Technion R&D, Haifa, Israel

The influence of ground impedance on sound propagation is estimated and analyzed using a specially developed fast field program. The Delany-Bazley-Chessell model of the ground impedance, which depends on only one parameter σ , is used in calculations. The σ values are varied from 10^2 to 10^5 . The calculations are carried out for six frequencies from 100 to 3200 Hz, three source-receiver positions, and with assumptions about the upward refracting linear profile. The conclusions drawn mention that excess sound attenuation always increases monotonously with increasing σ . It achieves a plateau afterwards, independent of change in σ . Explanations of the physical effects observed are given.

INTRODUCTION: PROBLEM DEFINITION

There are a number of computational tools available for predicting sound propagation through the atmosphere, including analytical solutions, ray tracing techniques, an approximate solution of the full wave equation, solution of the parabolic equation, and the fast field program (FFP).¹

The FFP is used for calculations of short- and long-range sound propagations.²⁻⁵ In these calculations it is assumed that a single frequency of sound propagates from source to receiver. The acoustic channel is represented by the layering scheme of a cascade connection of transmission lines. Each line has a discrete length with a constant characteristic impedance. The layer adjacent to the ground is loaded by the ground impedance. The parameters of the channel depend on the atmospheric conditions and ground impedance⁴⁻⁷ and they determine the decay of the acoustic signal, which is usually calculated as excess sound attenuation. This paper is devoted to the estimation of the influence of ground impedance on the excess sound attenuation. This determines the choice of model of ground impedance and assumptions accepted for calculations. The FFP is used in this article because it allows us to obtain accurate and reliable results.

I. MODEL USED FOR GROUND IMPEDANCE CALCULATIONS

The importance of ground impedance and its dependence on environmental conditions are understandable and widely discussed.^{1,7} This is the reason that various models for the ground impedance calculation have been proposed.⁵⁻⁹ In this paper the Delany-Bazley-Chessell model is applied because it is the one most frequently used for such calculations. The advantages of this model is that for the given atmospheric conditions the ground impedance depends on only one parameter, σ , which is the flow resistivity of the ground.

According to the Delany-Bazley-Chessell model the normalized resistance R and reactance X are, respectively,

$$\begin{aligned} R/\rho c &= 1 + 0.0571(f\rho/\sigma)^{-0.574}, \\ X/\rho c &= 0.08(f\rho/\sigma)^{-0.732}, \end{aligned} \quad (1)$$

where ρ is the air density, c is the sound velocity in air, f is the sound frequency and σ is a parameter of the ground. In our calculations we have used $\rho = 1.205 \text{ kg m}^{-3}$, $c = 340 \text{ m/s}$, and six frequencies 100, 200, 400, 800, 1600, and 3200 Hz. In order to cover as wide a range of ground impedance

values as possible, the σ values have been chosen as $10^2 \leq \sigma \leq 10^5$ Rayls/m. The value $\sigma = 100$ is smaller than 200 which is accepted for snow, grass, or forest,³ while the value $\sigma = 10^5$ is higher than that of asphalt, $\sigma = 4 \times 10^4$ (Ref. 3). The special fast field program (FFP) has been developed, which allows repeated calculations with discrete change of σ .

II. CONDITIONS AND PARAMETERS ACCEPTED FOR CALCULATIONS

The following conditions and parameters have been used for the calculations.

It is assumed that a sound source is located 1 m above the ground, i.e., $h_s = 1 \text{ m}$ and a receiver is on the ground, i.e., $h_r = 0$. The choice of locating the receiver on the ground is explained by the following. The receiver on the ground experiences the sum of the incident and reflected waves, where there are no propagation time delays between them. The existence of propagation time delays in the case where the receiver is located above the ground causes the appearance of oscillations in the calculated values of the excess sound attenuation.¹⁻³ These oscillations create additional difficulties in understanding and explaining the results obtained. Assuming $h_r = 0$ one may expect to obtain a smooth calculated curve clearly dependent on the ground impedance.

The ground impedance has a profound effect on the excess sound attenuation in the case of an upward refracting atmosphere. Under these atmospheric conditions a shadow zone arises where decay of the acoustic signal is especially large.^{10,11} Therefore the following assumptions have been used. A negative sound-speed gradient, characterized by upwind conditions, has been used. The real world conditions have been idealized to a linear profile with a constant gradient of sound speed $\partial c/\partial h = -0.1 \text{ s}^{-1}$. In the real situation the gradient of sound speed varies with height. However the main change occurs sufficiently close to the ground¹² and thereafter the gradient is kept constant. Therefore the assumption above is acceptable and widely used.¹

For the purpose of investigating the influence of a shadow zone, its beginning is estimated as²

$$R_s = \sqrt{\frac{2ch_s}{(\partial c/\partial h)}} = \sqrt{\frac{2 \cdot 340 \cdot 1}{0.1}} = 83 \text{ m}.$$

Three lengths between source and receiver, $l_1 = 80 \text{ m}$, $l_2 = 200 \text{ m}$, and $l_3 = 500 \text{ m}$ have been used in the calculations. Thus it has been possible to analyze the sound decay under the following conditions: without shadow zone ($l_1 = 80 \text{ m}$); with approximately equal zones, one without and another with shadow ($l_2 = 200 \text{ m}$, i.e., without shadow zone, 83 m and with it, 117 m) and, finally, the case where the shadow zone length is much bigger ($l_3 = 500 \text{ m}$, i.e., with shadow zone 417 m).

III. RESULTS OF CALCULATIONS, THEIR ANALYSIS AND DISCUSSION

The results of the calculations of excess sound attenuation are shown in Fig. 1 ($l_1 = 80 \text{ m}$), Fig. 2 ($l_2 = 200 \text{ m}$), and Fig. 3 ($l_3 = 500 \text{ m}$). It is necessary to mention that in Figs. 1-3 the results are presented as a function of σ and not as a function of f or a range as was done by most other authors. The reason is that the aim of this article is to investigate the influence of the ground impedance on sound propagation. Therefore σ is chosen as an independent variable.

Analyzing the results obtained one may draw some general conclusions.

(a) For each sound frequency with σ increasing, the excess sound attenuation increases monotonically until it achieves a plateau. This effect may be explained as follows. The equations of the sound channel solved by

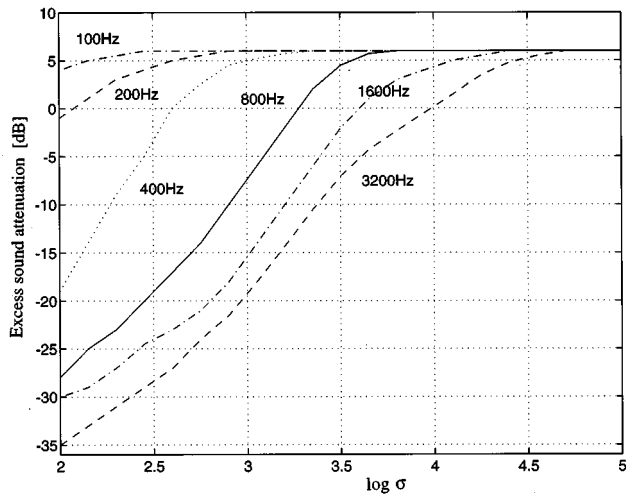


FIG. 1. Excess sound attenuation versus σ for various f and $l=80$ m. Shadow zone is laked of.

FFP are reminiscent of the “telegrapher’s equations” of a transmission line.⁴ According to the electroacoustic analogy the sound pressure and correspondingly the excess sound attenuation, proportional to the sound pressure, may be interpreted as a voltage across a receiver. In this article it is assumed that the receiver is located on the ground, i.e., the voltage across the receiver is the voltage across the ground impedance. A monotonically increasing σ leads to a monotonic increase of the ground impedance,¹ but the impedance of the sound channel is constant. Because the acoustic source is analogous to a current source, an increase of the ground impedance causes an increased voltage drop across it. But, as mentioned above, the voltage drop across the ground impedance is analogous to the sound pressure or to the excess sound attenuation, proportional to the sound pressure, therefore the excess increases with increasing σ . When the ground impedance starts to be much bigger than the impedance of the sound channel the sound pressure across the ground impedance is constant, i.e., the excess sound attenuation achieves a plateau.

(b) For each sound frequency the excess sound attenuation achieves its plateau value at the same σ_{\max} independent of length (Figs. 1–3). This effect is also explained using an electro-acoustic analogy. The acoustic channel is analogous to the transmission line, divided into two parts. One part consists of a cascade connection of discrete lengths of line; each discrete length is analogous to an atmospheric layer and starts from the sound source and ends at the topmost layer of atmosphere. The second part consists of a similar cascade which starts from the source but ends at the layer adjacent to the ground.⁴ Analyzing such an electrical connection one may assume that the

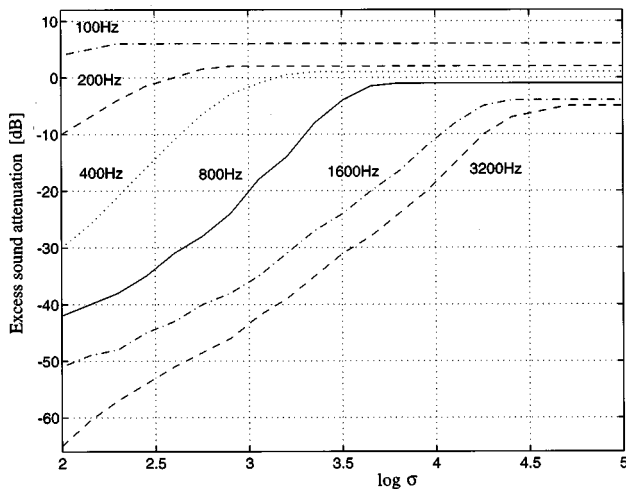


FIG. 2. Excess sound attenuation versus σ for various f and $l=200$ m. Nonshadow and shadow zones are approximately equal.

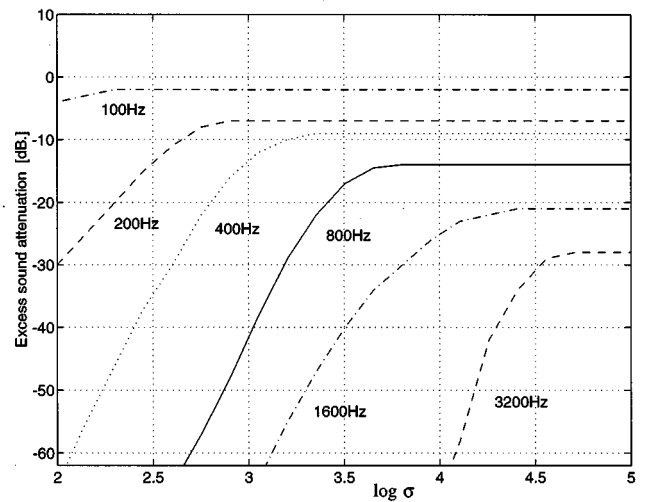
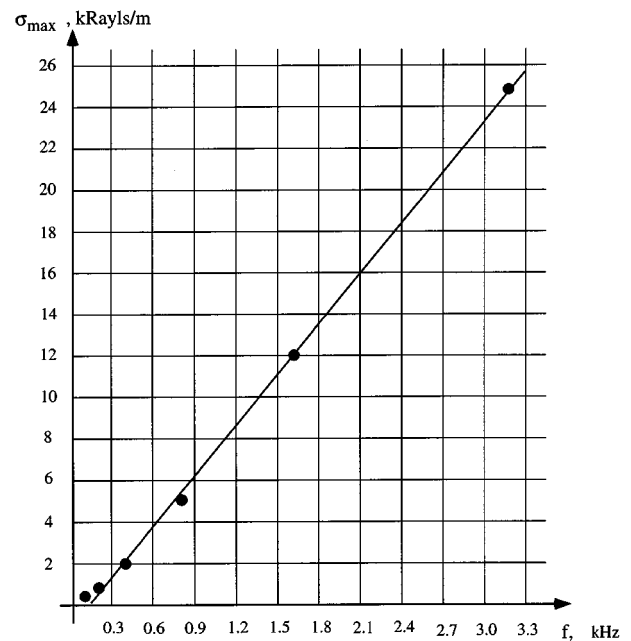


FIG. 3. Excess sound attenuation versus σ for various f and $l=500$ m. Shadow zone is much larger than nonshadow one.

voltage drop across the ground impedance will be kept constant with increasing impedance, if the ground impedance is large enough (the second part of the line will have close to open circuit conditions). This means that excess sound attenuation will achieve its plateau value and will stay constant with σ or ground impedance increasing. This analysis may accept an additional proof. In Fig. 4 the dependence of σ_{\max} on f is shown together with a table of σ_{\max} and f values. Analyzing the data in Fig. 4 one sees that there is a linear connection between σ_{\max} and f , for $400 \leq f \leq 3200$. This means that in this range the relation $f/\sigma \approx \text{const}$ and the ground impedance (1) has the same value for all σ_{\max} and f . In terms of the electrical analogy it is possible to say that the voltage drop across the ground impedance does not change if the ground impedance achieves its limit value, for $\sigma \geq \sigma_{\max}$. These limit values of the ground impedance are the same for all frequencies which are higher than 400 Hz. This conclusion verifies the above.



f , kHz	0.1	0.2	0.4	0.8	1.6	3.2
σ_{\max} kRayls/m	0.2	0.7	2	5	12	25

FIG. 4. Dependence of σ_{\max} on f .

(c) For the low frequencies where $f \leq 100$ Hz the ground impedance practically does not influence the excess sound attenuation even for very small σ ($\sigma \leq 200$). For the higher frequencies and particularly for the frequencies above 400 Hz the ground impedance has a very strong influence, especially for low σ . This result is explained by the above discussion. For low f the initial value of the ground impedance is high and the excess sound attenuation achieves its plateau value for small σ . For the high f the initial value of the ground impedance is low, therefore the excess sound attenuation achieves its plateau value for large σ .

(d) For each sound frequency the excess sound attenuation decreases with length increase for the same σ and f . This result is obvious. The impedance of the acoustic channel increases with the length increase; therefore the voltage drop across the ground impedance decreases, i.e., the excess sound attenuation decreases.

(e) In the case where the acoustic channel does not include the shadow zone (Fig. 1) the plateau value of the excess sound attenuation for all frequencies is the same and tends towards +6 dB. This result is well known for a hard surface (large σ). Here it is obtained for the more general case of wide changes of σ and f . The explanation of this is as follows. When the ground impedance achieves its limiting value ($\sigma \geq \sigma_{\max}$) the excess sound attenuation will be the same for all frequencies (see above discussion). Under these conditions, the receiver on the ground experiences the sum of the incident and the reflected waves without phase change. The values of both waves are the same, and therefore the excess attenuation is $20 \log(1+1) = 6$ dB.

(f) In the cases where the acoustic channels include the shadow zone (Figs. 2 and 3) the plateau values of the excess attenuations are different for different frequencies. These differences may be explained by the different decay of different sound frequencies through the shadow zone. A larger shadow zone causes more decay. Therefore the excess attenuations in Fig. 3 are lower than those in Fig. 2, for the same σ and f . However the σ_{\max} values virtually do not change with shadow zone.

It is necessary to mention that in Figs. 2 and 3 there are calculated values of the excess attenuations below -30 dB. This is because in the article the effects of turbulence have been ignored. Measured excess attenuations do not go below -30 dB because of scattering.

IV. CONCLUSIONS

The influence of ground impedance on sound propagation is analyzed. The Delaney-Bazley-Chessell model of the impedance, dependent on only one parameter σ , is used. The excess sound attenuation is calculated with σ varying over a wide range. Six sound frequencies and three distances between source and receiver, without and with the shadow zone, are used to calculate the excess sound attenuation.

It has been found that with a monotonically increasing σ the excess attenuation at first increases monotonically too. However when σ achieves σ_{\max} the excess attenuation reaches a plateau and does not change with increasing σ . Such a process is observed for all frequencies and it is explained using the analogy between a transmission line and an acoustic channel.

The σ_{\max} values are different for different frequencies. However it is shown that the ground impedances calculated for $\sigma = \sigma_{\max}$ are the same for all frequencies higher than 400 Hz. It is important to mention that the σ_{\max}

values are independent of, and the plateau values of the excess attenuations depend on, the presence or absence of a shadow zone. The plateau values are 6 dB for all frequencies when the shadow zone is absent. In the presence of shadow zones these values are lower and they fall with increasing frequency.

It is shown that for frequencies lower than 200 Hz the excess attenuation values achieve their plateau values for a small σ_{\max} , i.e., the ground impedance has only a small influence on the sound propagation. For frequencies higher than 400 Hz the plateau values of the excess attenuation are reached with high σ_{\max} values, i.e., the ground impedance strongly influences the sound propagation. All these effects are explained using the analogy between electrical and acoustic processes.

ACKNOWLEDGMENT

The authors are grateful to the reviewers for their constructive, serious, and detailed criticism which enabled them to improve the article.

- ¹K. Attenborough, S. Taherzadeh, H. E. Bass, X. Di, R. Raspet, G. R. Becker, A. Güdese, A. Chrestman, G. A. Daigle, A. L. L'Esperance, Y. Gabillet, Y. L. Li, M. J. White, P. Naz, J. M. Noble, and H. A. J. M. van Hoof, "Benchmark cases for outdoor sound propagation models," *J. Acoust. Soc. Am.* **97**, 173-191 (1995).
- ²R. Raspet, S. W. Lee, E. Kuester, D. C. Chang, W. F. Richards, R. Gilbert, and N. Bong, "A fast-field program for sound propagation in layered atmosphere above an impedance ground," *J. Acoust. Soc. Am.* **77**, 345-352 (1985).
- ³S. W. Lee, N. Bong, W. F. Richards, and R. Raspet, "Impedance formulation of the fast field program for acoustic propagation in the atmosphere," *J. Acoust. Soc. Am.* **79**, 628-634 (1986).
- ⁴S. J. Franke and G. W. Swenson, Jr., "A brief tutorial on the Fast Field Program (FFP) as applied to sound propagation in the air," *Appl. Acoust.* **27**, 203-215 (1989).
- ⁵M. West, R. A. Sack, and F. Walkden, "A brief tutorial on the Fast Field Program (FFP). A second tutorial: Application to sound propagation in the atmosphere," *Appl. Acoust.* **33**, 199-228 (1991).
- ⁶M. E. Delany and E. N. Bazley, "A note on the effect of ground absorption in the measurement of aircraft noise," *J. Sound Vib.* **16**, 315-322 (1971).
- ⁷C. I. Chessell, "Propagation of noise along a finite impedance boundary," *J. Acoust. Soc. Am.* **62**, 825-834 (1977).
- ⁸K. Attenborough, "Ground parameter information for propagation modeling," *J. Acoust. Soc. Am.* **92**, 418-427 (1992).
- ⁹S. Tooms, S. Taherzadeh, and K. Attenborough, "Sound propagation in a refracting fluid above a layered fluid-saturated porous elastic material," *J. Acoust. Soc. Am.* **93**, 173-181 (1993).
- ¹⁰S. J. Franke, R. Raspet, and C. H. Liu, "Numerical prediction of atmospheric sound pressure levels in shadow zones," *J. Acoust. Soc. Am.* **83**, 816-820 (1988).
- ¹¹W. E. McBride, H. E. Bass, R. Raspet, and K. E. Gilbert, "Scattering of sound by atmospheric turbulence: Predictions in a refractive shadow zone," *J. Acoust. Soc. Am.* **91**, 1336-1340 (1992).
- ¹²H. Klug, "Sound-speed profiles determined from outdoor sound propagation measurements," *J. Acoust. Soc. Am.* **90**, 475-481 (1991).

The influence of the oxygen mask on long-time spectra of continuous speech [43.72.Kb]

Milan Vojnović and Miomir Mijić

Faculty of Electrical Engineering, P.O. Box 816, 11001 Belgrade, Yugoslavia

This paper evaluates the general influence of the oxygen mask on the long-time speech spectrum. The influence of the oxygen mask was determined through a comparison of the long-time spectra of continual speech from the mask and the long-time spectra of normal speech. The most evident changes are in the frequency range above 800 Hz. The presence of the oxygen mask results in a change of the relative ratio of maximal values of particular formant areas.

INTRODUCTION

Voice and speaker recognition systems have to function under different circumstances, not always benign. In some situations speakers may be influenced by their physiological and psychological states which result in significant speech production changes. For example, there are circumstances when a kind of mask (diving, gas, oxygen) must be used for respiratory system protection. In speech communication systems which must function under such circumstances it seems feasible to introduce a mask as a part of the speech chain.

The mask influence in speech production were analyzed from different points. Bond *et al.* (1989) report an increase in duration of speech in an oxygen mask. Some investigators have reported a formant shift (Morrow, 1948; Rothenberg, 1973) as well as an increase in fundamental frequency (Bond *et al.*, 1989).

In considering how to generalize the influence of an oxygen mask in speech communication, four different effects can be involved:

- the effect of the mask cavity on the vocal tract transfer function,
- the effect of mask tightening on articulation,
- the effect of the mask respiratory valves noise, and
- the effect of the electroacoustical characteristics of the microphone built in the mask.

Speech produced while wearing an oxygen mask incorporates the first three factors mentioned above. The speech signal at the microphone output is also influenced by its electroacoustical characteristics, as well as the additive noise of inspiratory and expiratory valves.

This paper presents the results of the experiment conducted in order to analyze the composite influence of the oxygen mask on the long-time spectrum of continuous speech.

I. DESCRIPTION OF THE EXPERIMENT

For the purpose of this experiment the ULMER type 82PE oxygen mask was used (made in France). Interior mask volume is about 150 cm³. The mask required the talker to wear a standard flight helmet. During the experiment a standard aircraft oxygen supply installation was used as a part of the measuring system.

The main idea of the experiment was based on the comparison the long-time spectra of continuous speech from the oxygen mask and speech under normal conditions. The term "speech from the mask" implies the speech signal at the output of a microphone built in the mask, and the term "normal speech" assumes a signal at the output of an identical microphone when it is placed in front of the speaker's mouth at the position identical to this in the mask. The experiment was performed in order to obtain a comparison of the speech from the mask and normal speech. This should, as a result, determine the contribution of the oxygen mask.

The block diagram of measuring equipment is shown in Fig. 1. Two consecutive recordings of the same text read by the same talkers were performed. During the first recording the talkers read a selected text while wearing the oxygen mask (denoted by I in Fig. 1). As indicated in the figure, the subjects wore pilot helmets in order to enable the fixing of the mask with a constant pressure to the face. In the second case, the same text was read without the oxygen mask (denoted by II in Fig. 1). The microphone was fixed in the position frontal to the mouth by a flexible holder. The distance from the mouth, in this case, was equivalent to that in the oxygen mask. This distance was approximately 2 cm. Speech recording was performed by the tape recorder REVOX B77. Recorded continuous speech segments had a duration of a few minutes.

As indicated in Fig. 1, during the experiment talkers were located in separate rooms. The experiment was conducted from a control room, where interphone equipment, tape recorder, monitor loudspeaker, and microphone were placed. Within the interphone system a part of the signal from the talker's microphone was returned into his earphones to enable the subject's side tone during the speech process. Such conditions correspond to normal circumstances typical for oxygen mask application.

During the speech recording, 13 male talkers were involved. Their age ranged between 24 and 45. None of the subjects was trained for the experiment, nor did they have a previous experience in using such communication equipment and oxygen mask. Most of the talkers wore oxygen masks on their faces for the first time during this experiment.

After basic instructions on how to use the helmet and the oxygen mask, the talkers were allowed to choose the adequate mask size and set up the pressure of the mask to the face in order to feel comfortable during the experiment. The mask is available in three sizes, and two out of three available mask sizes were used during experiment ("medium"—8 talkers and "large"—5 talkers). Upon setting the talker in the recording position, there was a grace period of about 10 min, which was used for adaptation to the mask and this way of breathing. This time was also used to allow talkers to get acquainted with the text. The preparation was also used for adjusting the optimal level of recording. In both recordings (with and without mask) the subjects were reading the text in a sitting position.

The recorded text was composed in Serbian and prepared so as to represent a fair sample of normal speech. This feature was tested by performing a statistical analysis of phonemes occurrences. During an interval of about 30 s of reading by normal speed the text contains all 30 phonemes of this language. During a 60-s interval of reading the appearance of phonemes was nearly proportional to the probability of their occurrence in normal speech.

During the experiment an effort was made to minimize the influence of the microphone on the results. The microphone used was an EDM-MT-01 specially designed for application in oxygen masks. It is electrodynamical, noise canceling, with all other characteristics based on aeronautical standards. The same microphone was used for both recordings (with and without the mask). A measurement of microphone frequency characteristics was also performed. These results were used in an analysis of the speech signal to compensate the influence of the nonlinearities in microphone frequency characteristic on the calculated spectra.

II. RESULTS OF THE ANALYSIS

The analysis of the oxygen mask influence on the continuous speech spectrum was based on the comparison of the long-time 1/3 octave spectrum of the speech from the mask and the spectrum of normal speech. Both spectra were obtained by linear unweighted averaging into the time interval of 64 s. The frequency analyzer used for this purpose was Bruel & Kjaer type 2131. The analysis included the frequency range from 100 to 5000 Hz (eighteen 1/3 octave bands). Obtained spectra were normalized in such a way that the overall speech level of each speech sample was fixed to 0 dB.

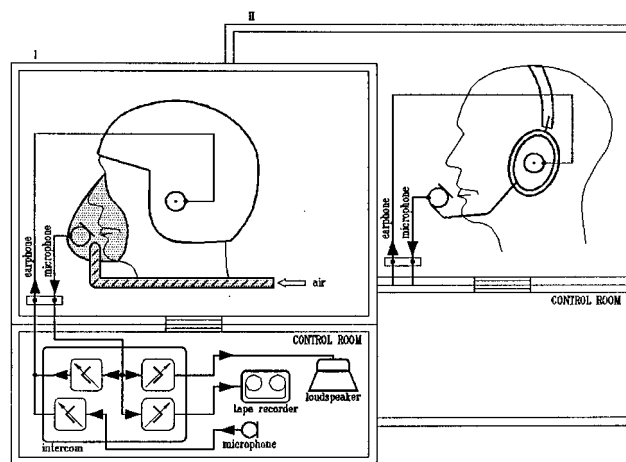


FIG. 1. The measuring equipment arrangement for recording a normal speech and the speech from the oxygen mask.

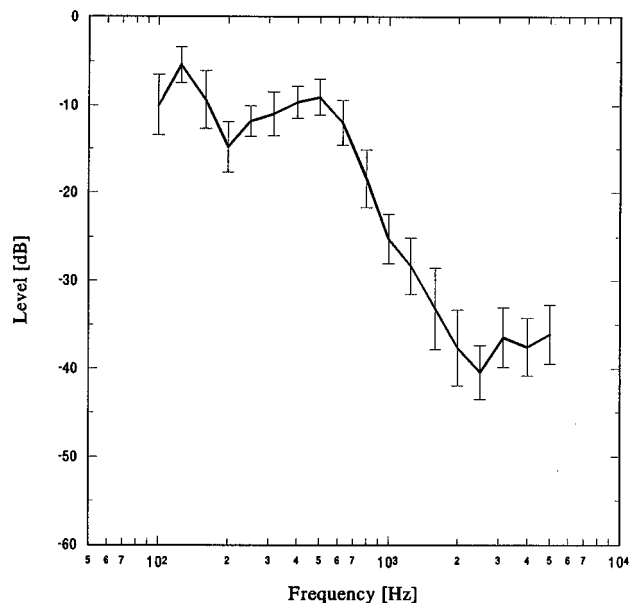


FIG. 2. Long-time average third octave spectrum of the speech from the oxygen mask.

As a result, a normalized long-time spectrum of continuous speech from the mask and a normalized long-time spectrum of normal speech were obtained for all 13 talkers. By their averaging the representative normalized mean spectrum of the speech from the mask (Fig. 2), and the representative normalized mean spectrum of the normal speech (Fig. 3) were determined. Standard deviations were also presented in these figures.

The influence of the oxygen mask on the speech spectrum, averaged for all 13 talkers, was derived as a difference between normalized long-time spectra of speech from the mask and normal speech. The result was presented in Fig. 4. The positive values on this diagram denote that the level of normalized speech from the mask was higher than the level of normal speech.

III. DISCUSSION

Considering the speech spectrum from the mask presented in Fig. 2, a few details can be observed: the spectrum has a local maximum in the 1/3

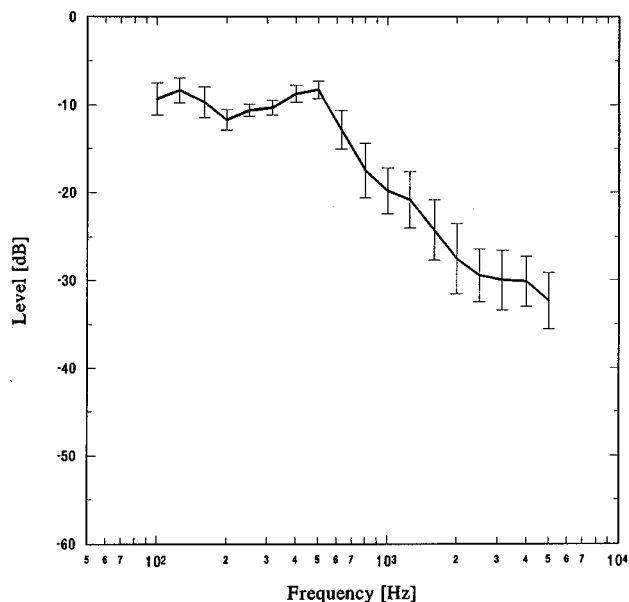


FIG. 3. Long-time average third octave spectrum of the normal speech.

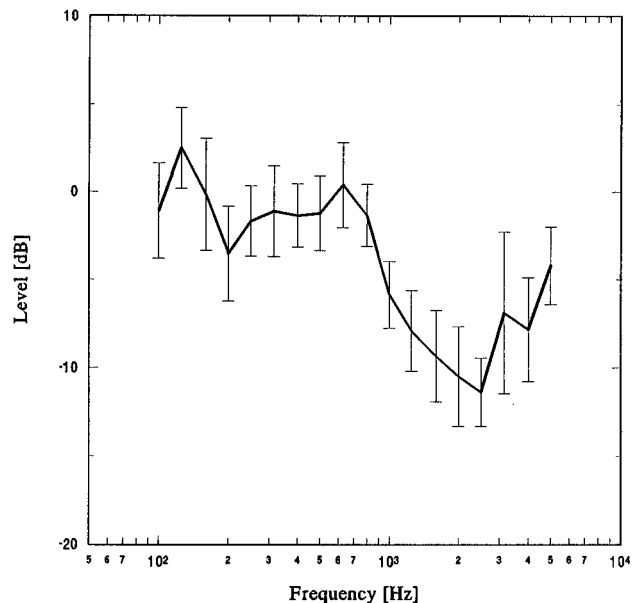


FIG. 4. The oxygen mask influence on the long-time average speech spectrum.

octave band with central frequency at 125 Hz, some enhancement in the area around 500 Hz, and a falling slope at about 12 dB per octave in the frequency range from 500 to 2500 Hz. An increase in spectrum level occurs in the frequency range over 2 kHz. The standard deviation of measured values considering the entire frequency range is within interval (3.2 ± 1.4) dB.

The spectrum of the normal speech (Fig. 3) is almost identical to those adopted from the literature (Byrne *et al.*, 1994). Its shape performs a maximum in the 1/3 octave band with the central frequency of 500 Hz, and a slope of about 6 dB/octave towards higher frequencies. The relative enhancement at low frequencies seems to be a consequence of microphone position in the near field. Frequency components in the 1/3 octave band at 125 Hz are approximately 3 dB lower, compared to the speech from the mask. Very good matches in shapes for both spectra can be observed in the frequency range from 250 to 800 Hz. The standard deviation in averaged normal speech spectrum of 13 talkers is 0.8 dB below the corresponding deviation obtained for the speech spectrum from the mask. Considering the entire frequency range standard deviation is located within the interval (2.3 ± 1.6) dB.

From the diagram presented in Fig. 4 it can be observed that the influence of the oxygen mask on the speech spectrum is minimal in the frequency range from 100 to 800 Hz. The exception is in 1/3 octave band with central frequency at 125 Hz, where the maximum relative enhancement with the mask is about 2.5 dB. Analysis has shown that the band at 125 Hz contains the fundamental speech frequencies of all talkers. The maximum relative attenuation by the presence of the mask was measured in the 1/3 octave band at 2500 Hz (11.5 dB). Within the frequency range between 630 and 2500 Hz a relative attenuation of the voice with the slope of about 6 dB/octave was achieved. For long-time spectra of continuous speech in the frequency range from 100 to 2500 Hz, as the rough approximation, it can be considered that the mask behaves as a first-order low-pass filter with cut-off frequency in the 1/3 octave band at 630 Hz. On the diagram in Fig. 4 the values of standard deviations are found within the interval of (3.2 ± 1.4) dB. The same applies in the case of speech with the mask.

The diagram in Fig. 4 shows that relative attenuation by the mask is smaller in frequencies over 2 kHz. In trying to explain that feature first assumption was based on the influence of inspiratory valve noise. The inspiratory valve noise appears in continuous speech while wearing the mask as a periodic sound phenomenon during inspirations. Such a position enables its cutting out from the recorded continuous speech signal. After such an editing process, a new spectrum analysis was performed. No difference between the long-time speech spectra with and without inspiratory valve noise was noted. Therefore, it appears that the inspiratory valve operation does not affect the long-time spectrum of speech from the mask.

The relative level increase at the highest frequencies (in Fig. 4) can be

a consequence of the expiratory valve function, which always follows the phonation. This valve adds some noise to the speech signal from the mask. Therefore, it cannot be removed from recorded speech by simple editing, as performed for inspiratory valve noise.

Finally, in this frequency range the first resonant frequencies of the oxygen mask interior occur due to the fact that interior dimensions of the mask have the same order of magnitude with the sound wavelength. Relative increases of sound level as shown in Fig. 4 may also be caused by the influence of standing waves at the microphone position in the mask.

IV. CONCLUSION

The results presented in this paper indicated that the oxygen mask has an obvious influence on the long-time spectrum of continual speech. The most evident changes caused by the presence of the mask on the speaker's face are in the frequency range over 800 Hz. In such a way the presence of the mask results in a change of the relative ratio of formant levels. These results for the oxygen mask are consistent with previously published results for the non-radiating type of mask (Badin *et al.*, 1990; Morrow *et al.*, 1971; Rothenberg, 1973).

The results presented in this paper should be considered in view of some initial limitations. The experiment involved 13 talkers without any

previous experience in using oxygen masks. Only one type of oxygen mask was used in the experiment (ULMER 82PE), though there are no significant differences in the size and shape of modern masks. Finally, the experiment was conducted using only one language. It would be interesting to perform the same experiment for other languages.

- Badin, P., Hertegard, S., and Karlsson, I. (1990). "Notes on the Rothenberg mask," *STL-QPSR* 1/1990, 1–7.
- Bond, Z. S., Moore, T. J., and Gable, B. (1989). "Acoustic-phonetic characteristics of speech produced in noise and while wearing an oxygen mask," *J. Acoust. Soc. Am.* **85**, 907–912.
- Byrne, D. *et al.* (1994). "An international comparison of long-term average speech spectra," *J. Acoust. Soc. Am.* **96**, 2108–2120.
- Morrow, C. T. (1948). "Reaction of Small Enclosures on the Human Voice. Part II. Analyses of Vowels," *J. Acoust. Soc. Am.* **20**, 487–497.
- Morrow, C. T., and Brouns, A. J. (1971). "Speech Communication in Diving Masks. I. Acoustics of Microphones and Mask Cavities," *J. Acoust. Soc. Am.* **50**, 1–9.
- Rothenberg, M. (1973). "A new inverse-filtering technique for deriving the glottal air flow waveform during voicing," *J. Acoust. Soc. Am.* **53**, 1632–1645.

Advanced-degree dissertations in acoustics

Editor's note: Abstracts of Donor and Master's theses will be welcomed at all times. Please note that they must be double spaced, limited to 200 words, must include the appropriate PACS classification numbers, and formatted as shown below (don't make the editor retype them, please!). The address for obtaining a copy of the thesis is helpful. Please submit two copies.

Adaptive piezoelectric sensoriaactuators for active structural acoustic control [43.50.Ki, 43.40.Vn, 43.40.Hb, 43.38.Fx]—Jeffrey Stuart Vipperman, *Department of Mechanical Engineering and Materials Science, Duke University, Durham NC 27708, also published through UMI, 800-521-3042, 1997 (Ph.D.)*. A new transducer technology with application to active control systems, modal analysis, and autonomous system health monitoring, is brought to fruition in this work. The transducer consists of a piezoceramic element which serves as both an actuator and a sensor and will be referred to in this work as a *sensoriaactuator*. Simple, adaptive signal processing in conjunction with a voltage controlled amplifier, reference capacitor, and a common-mode rejection circuit extract the mechanical response from the total response of the piezoelectric sensoriaactuator for sens-

ing. Adaptive compensation of the sensoriaactuator is necessary since the signal-to-noise ratio is typically greater than 40 dB, making it prohibitive to tune the circuit manually. In addition, the constitutive properties of piezoceramics vary with time and environment, necessitating that the circuit be periodically re-tuned. A multiple input multiple output (MIMO) implementation of the adaptive piezoelectric sensoriaactuator is developed using orthogonal white noise training signals for each sensoriaactuator. Lastly, \mathcal{H}_2 optimal feedback active structural acoustic control (ASAC) is demonstrated using the adaptive piezoelectric sensoriaactuators and the simply supported plate test bed. A cost function is formulated based upon control effort and predicted radiated acoustic power. Radiation filters are created to predict acoustic power based on the self- and mutual radiation efficiencies of the plate modes to be controlled. Both static output feedback and state-feedback compensation as well as dynamic (linear quadratic Gaussian) compensation are investigated and compared analytically. The importance of choosing an appropriate spatial aperture for the piezoceramic transducer for static compensation is discussed. Finally, multivariable LQG active vibration control (AVC) and ASAC are implemented experimentally on a simply supported plate test bed using an array of four adaptive piezoelectric sensoriaactuators as the control sensors and actuators.

Thesis advisor: Robert L. Clark.